Contribution to the numerical estimation of earthquake ground motions

Emmanuel Chaljub

Université Grenoble Alpes

Dossier de synthèse de l'activité scientifique présenté en vue d'obtenir le diplôme d'

Habilitation à Diriger les Recherches

par

Emmanuel Chaljub

Équipe Géophysique des Risques et de l'Environnement

Institut des Sciences de la Terre, Grenoble

Contribution to the numerical estimation of earthquake ground motions

Soutenu le 30 juin 2017, devant le jury composé de

- Hiroshi Kawase (Professeur, DPRI, Rapporteur)
- Donat Fäh (Professeur, ETH Zürich, Rapporteur)
- Jean-François Semblat (Directeur de Recherches, IFSTTAR, Rapporteur)
- Michel Bouchon (Directeur de Recherches, CNRS, Examinateur)
- Michel Campillo (Professeur, UGA, Examinateur)

ISTerre
Institut des Sciences de la Terre

UNIVERSITÉ Grenoble Alpes

Contents

Preamble

It is not useless to recall to a reader not aware of all the subtleties of the french system what the "Habilitation à Diriger les Recherches" (HDR) stands for.

The HDR – litterally, habilitation to lead research – is a french national diploma which gives its beneficiary the right (i) to officially supervise PhD students and (ii) to apply to professor-like positions. The HDR diploma can only be delivered by a french university to a candidate who has convinced an habilitation committee (HC) of his high-level scientific value, through an original research activity, an autonomous scientific strategy and the capacity to guide younger researchers.

The HDR manuscript is one of the media – the other being the oral defense – used by the candidate to convince the HC.

This HDR manuscript is made of 4 chapters:

— Chapter I presents my *Curriculum Vitæ*. It includes most of the elements of an administrative file which has already been successfully evaluated by a local committe of the Grenoble Alpes University. Because the chapter is only informative and doesn't have to be re-evaluated by the members of the HC, it is written in french.

— Chapter II presents a summary of my research activity. I made the choice to write this chapter as a digest of the articles I co-authored and of some unpublished work which either stimulated my mind in early years, or still require some more time to be analyzed but are worth being discussed.

— Chapter III presents some research perspectives for the next five years.

— Chapter IV is a collection of my scientific publications in the last decade. This makes a huge chapter (more than 250 pages!), which should only be consulted for details about a result presented in chapter II.

Chapitre I

Curriculum vitæ

Nom : **CHALJUB CHAR**
Prénom : **Emmanuel Orlando**
Date de Naissance : **09/02/1971**
Situation familiale : **marié, 2 enfants**
Grade : **physicien adjoint**
Etablissement d'affectation : **Observatoire des Sciences de l'Univers de Grenoble**
Unité de recherche d'appartenance : **Institut des Sciences de la Terre (UMR 5275)**

I.1 Formation

1994 : DEA d'Analyse Numérique, Paris VI.
2000 : Thèse de doctorat,≪ Modélisation numérique de la propagation des ondes sismiques en géométrie sphérique : application à la sismologie globale ≫, sous la direction d'A. Tarantola et J.-P. Vilotte, Institut de Physique du Globe de Paris.

I.2 Déroulement de carrière

2000-2002 : Hess fellow , Dep. of Geosciences, Université de Princeton, NJ, USA.
2002-2004 : Post-doctorant CNRS au Laboratoire de Géophysique Interne et Tectonophysique, équipe ≪ Ondes et Structure Interne du Globe ≫.
2005-présent : Physicien Adjoint à ISTerre, équipe ≪ Risques ≫, devenue ≪ Géophysique des Risques et de l'Environnement ≫.

I.3 Synthèse du parcours scientifique

Issu d'une formation de mathématiques appliquées, j'ai découvert la géophysique à l'Institut de Physique du Globe de Paris grâce à Albert Tarantola qui m'a proposé successivement deux stages de *master*, puis un sujet de thèse (associé à un financement du ministère). Mon travail de thèse a été consacré au développement de méthodes numériques de simulation de la propagation des ondes sismiques à l'échelle du globe. Après avoir développé un programme en différences finies pour simuler la propagation des ondes SH dans des modèles axisymétriques du manteau terrestre, j'ai contribué, sous la direction de Jean-Pierre Vilotte, au développement de la méthode des éléments spectraux pour la sismologie globale. J'ai poursuivi ce travail lors mon séjour post-doctoral à l'université de Princeton, grâce au financement de la Hess *fellowship*, pour inclure notamment les effets de la redistribution des masses pour les ondes élastiques à très longue période. Sur les conseils

de Bernard Valette, j'ai ensuite effectué un séjour post-doctoral (probablement le premier financé par le CNRS) au LGIT à Grenoble au sein de l'équipe « Ondes et Structures », pendant lequel je me suis peu à peu intéressé à l'estimation de l'aléa sismique et à la propagation des ondes en milieu fortement hétérogène.

Depuis 2005, j'occupe un poste de Physicien Adjoint à l'OSUG et mon activité de recherche à ISTerre, au sein de l'équipe « Risques » puis « Géophysique Risques Environnement », a principalement concerné l'estimation des mouvements sismiques, à la fois par une approche déterministe de simulation numérique, et empirique, en lien avec ma tâche de service de responsable du réseau accélérométrique nord-alpin (2005-2012). A l'occasion du IIIème symposium de l'ESG (*Effects of Surface Geology on earthquake motion*) organisé à Grenoble en 2006, j'ai démarré un travail de vérification des codes de calcul tridimensionnel du mouvement sismique dans le contexte de vallées alpines. J'ai poursuivi cet effort dans le cadre du projet international E2VP (*Euroseistest Verification and Validation Project*) dans le contexte du bassin sédimentaire mygdonien. Ces travaux, publiés entre 2010 et 2015, ont contribué à une meilleure compréhension de l'incertitude épistémique associée à la prédiction numérique des mouvements sismiques ; ils ont également permis de mettre au point des procédures robustes de construction de maillages et de modèles de vitesse associés pour les simulations numériques basées sur la méthode des éléments spectraux. Une fois identifié le domaine de validité de ces outils numériques, j'ai pu m'intéresser d'une part à la quantification de la variabilité des mouvements sismiques, par l'utilisation intensive de la simulation numérique, et à la validation des prédictions numériques, par la confrontation avec les enregistrements de mouvements faibles. J'ai également contribué, par le calcul simplifié de la réponse des ouvrages, à l'étude des interactions entre sol et structures (immeubles, barrages, digues).

Au cours de ces dix dernières années de recherche, j'ai eu la chance de pouvoir co-encadrer deux chercheurs post-doctorants et sept étudiants en thèse, dont trois sont en cours en 2016.

Par ailleurs, mes travaux utilisant intensivement les plateformes de calcul et de traitement hautes performances, j'ai été associé dès 2008 au pilotage du Service Commun de Calcul Intensif de l'OSUG. Et depuis 2009, on m'a confié la responsabilité du mésocentre de calcul de l'université de Grenoble, CIMENT. Cette activité est officiellement reconnue par la commission CNAP comme ma tâche de service depuis 2012.

I.4 Responsabilités scientifiques et collectives

2005-2012 : Responsable scientifique du réseau accélérométrique permanent des Alpes.
2008-présent : Responsable scientifique du Service Commun de Calcul Intensif de l'OSUG.
2009-présent : Responsable scientifique du mésocentre de calcul grenoblois CIMENT (Calcul Intensif, Modélisation, Expérimentation Numérique et Technologique, structure fédérative UJF-INP, 2 IR affectés).
2010-2012 : Membre du comité national de coordination des mésocentres de calcul.
2011-présent : Membre du comité de pilotage MaiMoSiNE (Maison de la Modélisation et de la Simulation, Nanosciences, Environnement).
2011-présent : Membre du comité de pilotage du projet Equipex Equip@Meso.
2013-2015 : Membre du comité de pilotage de l'informatique scientifique de l'Université Joseph Fourier, Grenoble.

I.5 Rayonnement

— Co-éditeur des comptes rendus du « Third International Symposium on the Effects of Surface Geology on Seismic Motion », LCPC éditions, Vol.1 (2006), Vol. 2 (2009).
— Expertise (2-4/an) pour les revues : Geophys. J. Int., Bull. Seismol. Soc. Am., PAGeoph,

Int. J. Num. Meth. Eng., CR-mécanique, Earthquake Spectra.
— Expertise projets : Swiss NSF (2009).
— Expert GENCI comité thématique « Astrophysique et Géophysique » (2010-présent).
— Chercheur invité (2009, 2010) à l'ITSAK (Thessalonique, Grèce) dans le cadre du TOK (Transfer of Knowledge, Marie Curie projet ITSAK-GR).
— Co-organisateur avec S. Day (UC San Diego) et P. Moczo (U. Bratislava) d'une session de sismologie numérique à la SSA (2010, 2012, 2015, 2016).
— 2 participations à des jurys de thèse en tant qu'examinateur.
— 2 participations à des comités de recrutement de maître de conférences.

I.5.1 Encadrement de la recherche

I.5.1.0.1 Stages de *master*

▷ Soline Hallier, « Etude numérique des résonances 2D des vallées Alpines », M1, 2005.
▷ Julie Verbecke (co-encadrement C. Cornou), « Analyse des effets de site dans la vallée de Grenoble », M1, 2006. J. V. a effectué une thèse à ETHZ, deux postdocs (Lamont, IPGP) et travaille à la CGG.
▷ Julien Converset (co-encadrement L. Margerin), « Mesures de l'amplification dans la coda des ondes sismiques », M1, 2006. J. C. a effectué une thèse à Géoazur et travaille maintenant chez Schlumberger.
▷ Laetitia Honoré, « Etude numérique des résonances 3D des vallées Alpines », M1, 2007. L. H. a effectué une thèse à Géoazur et est actuellement en post-doc au CEA Cadarache.
▷ Soline Hallier (co-encadrement M. Bouchon) : « L'effet de bord de bassin pendant le séisme de Kobe », M2, 2006.
▷ Christel Marchica (filière maths applis), « Simulation numérique de la propagation des ondes sismiques par une méthode d'éléments spectraux non-conformes », M1 (2011) et M2 (2012).
▷ Alexandre Hoffmann (filière maths applis), « Implémentation d'un solveur pour la simulation numérique de la redistribution des masses en sismologie globale longue-période », M2, 2014. A. H. est désormais en thèse en maths applis.
▷ Niels Hollard, « Développement de *GMPE* synthétiques et quantification des incertitudes », M2, 2015.

I.5.1.0.2 Thèses de doctorat

▷ Soline Hallier (co-encadrement M. Bouchon, ISTerre) : « Etude des mouvements forts en champ proche », 2006-2009, MESR. Abandon, 1 publication, reconversion professionnelle de S. H. actuellement embauchée par la société BULL S.A., dans le département 'benchmark pour le calcul haute performance'.
▷ Javed Iqbal (co-encadrement P.-Y. Bard, ISTerre) : « Contribution à l'analyse des effets macroscopiques de l'interaction sol-structure par modélisation simplifiée en éléments spectraux », 2008-2014, financement SFERE, **soutenue le 8 Décembre 2014**. J. I. est retourné travailler au Pakistan.
▷ Nizar Moussatat (co-encadrement L. Baillet, ISTerre) : « Simulation numérique de la dynamique de la rupture et mouvement du sol », 2009-2012, MESR. N. M. a abandonné pour raisons personnelles.
▷ Afifa Imtiaz (co-encadrement C. Cornou & P.-Y. Bard, ISTerre) : « Champ d'ondes, variabilité spatiale, et cohérence des mouvements sismiques : effets en champ proche et en vallée alluviale », 2011-2014, financement du projet NERA (EU-FP7). **Soutenue le 6 Janvier 2015**. Félicitations du jury. A. I. a été recrutée au BRGM en 2015.
▷ Christel Marchica (co-encadrement, B. Valette, ISTerre) : « Modélisation et simulation numérique en sismologie », 2012-2016, bourse handicap CNRS.

- ▷ Eleni Koufoudi (co-encadrement F. Dufour, 3SR) : « Analysis of spatial variability of seismic ground motion and application to the dynamic response of hydraulic dams », 2014-2017, financement EDF, chaire d'excellence industrielle Pereniti.
- ▷ Capucine Durand (co-encadrement P.-Y. Bard et F. Renalier [GéophyConsult]) : « Réponse sismique de digues et barrages en remblai : influence des caractéristiques du sol de fondation », 2015-2018, financement CIFRE (EDF, CNRS).

I.5.1.0.3 Chercheurs post-doctorants

- ▷ Seiji Tsuno, 2005-2007 : « Analyse expérimentale et numérique de la réponse sismique de la vallée de Grenoble ». S. T. est chercheur au *Railway Technical Institute*, Tokyo, Japon.
- ▷ Emeline Maufroy, 2011-2015 : « Vérification et validation des prédictions numériques de la réponse sismique du bassin mygdonien. Etude de la variabilité des effets source-site ».

I.6 Activités d'enseignement

Entre mon recrutement en 2005 et 2012, j'ai toujours effectué la totalité de mon service d'enseignement, qui se composait de l'encadrement du stage de géosciences marines de Villefranche/mer au niveau master 1 (et master 2 pendant 2 ans), de l'enseignement des méthodes numériques pour l'évaluation du mouvement sismique dans le cadre du master international MEEES (*Master in Earthquake Engineering and Engineering Seismology*), et de l'animation d'un module atelier en modélisation numérique au niveau master 2 qui implique l'encadrement pendant 3 mois de 1 à 5 étudiants par an. En 2012, j'ai transmis la responsabilité du stage de Villefranche/mer et fait jouer une décharge de 20 heures d'enseignement, qui m'avait été accordée depuis 2009 par la vice-présidence de l'UJF au titre de mon investissement dans le domaine du calcul intensif à l'échelle de l'Université.

Le volume de mes activités d'enseignement est le suivant :

- ▷ « Stage de géosciences marines de Villefranche/mer », 2005-2011, responsabilité au niveau Master 1, 36 heures ETD/an.
- ▷ « Stage de géosciences marines de Villefranche/mer », 2006-2008, encadrement au niveau Master 2P, 30 heures ETD/an.
- ▷ « Méthodes numériques pour l'estimation du mouvement sismique », 2005-2015, niveau Master 2 (MEEES et M2R), 20 à 25 heures ETD/an.
- ▷ « Atelier modélisation numérique », 2009-2015, encadrement et responsabilité pendant 2 ans, niveau Master 2, 6 à 22 heures ETD/an (2 heures cours + 4 heures par étudiant encadré).

I.7 Bibliographie

Code couleurs :

- ▷ **Chercheur post-doctorant en collaboration directe**
- ▷ **Etudiant en thèse co-encadré**
- ▷ **Etudiant en thèse en collaboration**
- ▷ **Etudiant en *master* co-encadré**

I.7.1 Articles

1. **Maufroy, E.**, **Chaljub, E.**, Theodoulidis, N. P., Roumelioti, Z., Hollender, F., Bard, P.-Y., de Martin, F., Guyonnet-Benaize, C., & Margerin, L., 2017. Source-related variability of site response in the Mygdonian basin (Greece) from accelerometric recordings and 3D numerical simulations, *Bull. Seismol. Soc. Am.*.
2. Kristek, J., Moczo, P., **Chaljub, E.**, & Kristekova, M., 2017. An orthorhombic representation of a heterogeneous medium for the finite-difference modelling of seismic wave propagation, *Geophys. J. Int.*, **208**, 1250–1264.
3. Cruz-Atienza, V. M., Tago, J., Sanabria-Gómez, J. D., **Chaljub, E.**, Etienne, V., Virieux, J., & Quintanar, L., 2016. Long duration of ground motion in the paradigmatic valley of Mexico, *Scientific Reports*, **6**, 38807.
4. **Maufroy, E.**, **Chaljub, E.**, Hollender, F., Bard, P.-Y., Kristek, J., Moczo, P., Martin, F. D., Theodoulidis, N., Manakou, M., Guyonnet-Benaize, C., Hollard, N., & Pitilakis, K., 2016. 3D numerical simulation and ground motion prediction : Verification, validation and beyond – Lessons from the E2VP project, *Soil. Dyn. Earthq. Eng.*, **91**, 53–71.
5. Blanc, E., Komatitsch, D., **Chaljub, E.**, Lombard, B., & Xie, Z., 2016. Highly-accurate stability-preserving optimization of the zener viscoelastic model, with application to wave propagation in the presence of strong attenuation, *Geophys. J. Int.*, **205**, 427–439.
6. **Chaljub, E.**, **Maufroy, E.**, Moczo, P., Kristek, J., Hollender, F., Bard, P.-Y., Priolo, E., Klin, P., de Martin, F., Zhang, Z., Zhang, W., & Chen, X., 2015. 3-D numerical simulations of earthquake ground motion in sedimentary basins : testing accuracy through stringent models, *Geophys. J. Int.*, **201**(1), 90–111.
7. **Imtiaz, A.**, Causse, M., **Chaljub, E.**, & Cotton, F., 2015. Is Ground-Motion Variability Distance Dependent ? Insight from Finite-Source Rupture Simulations, *Bull. Seismol. Soc. Am.*.
8. **Maufroy, E.**, **Chaljub, E.**, Hollender, F., Bard, P.-Y., Kristek, J., Moczo, P., Klin, P., Priolo, E., Iwaki, A., Iwata, T., **Etienne, V.**, De Martin, F., Manakou, M., Theodoulidis, N., & Pitilakis, K., 2015. Earthquale ground motion in the Mygdonian basin, Greece : the E2VP verification and validation of 3D numerical simulations up to 4 Hz, *Bull. Seismol. Soc. Am.*.
9. Moczo, P., Kristek, J., Galis, M., **Chaljub, E.**, & **Etienne, V.**, 2011. 3-D finite-difference, finite-element, discontinuous-Galerkin and spectral-element schemes analysed for their accuracy with respect to P-wave to S-wave speed ratio, *Geophys. J. Int.*, **187**, 1645–1667.
10. Souriau, A., **Chaljub, E.**, Cornou, C., Margerin, L., Calvet, M., Maury, J., Wathelet, M., Grimaud, F., Ponsolles, C., Pequegnat, C., Langlais, M., & Guéguen, P., 2011. Multimethod characterization of the french-pyrenean valley of Bagneres-de-Bigorre for seismic-hazard evaluation : Observations and models, *Bull. Seismol. Soc. Am.*, **101**(4), 1912–1937.
11. **Chaljub, E.**, Moczo, P., **Tsuno, S.**, Bard, P.-Y., Kristek, J., Kaser, M., Stupazzini, M., & Kristekova, M., 2010. Quantitative comparison of four numerical predictions of 3D ground motion in the Grenoble valley, France, *Bull. Seismol. Soc. Am.*, **100**(4), 1427–1455.

12. Etienne, V., **Chaljub, E.**, Virieux, J., & Glinsky, N., 2010. An hp-adaptive discontinuous Galerkin finite-element method for 3-D elastic wave modelling, *Geophys. J. Int.*, **183**(2), 941–962.
13. Causse, M., **Chaljub, E.**, Cotton, F., Cornou, C., & Bard, P.-Y., 2009. New approach for coupling k- 2 and empirical Green's functions : application to the blind prediction of broad-band ground motion in the Grenoble basin, *Geophys. J. Int.*, **179**(3), 1627–1644.
14. Hallier, S., **Chaljub, E.**, Bouchon, M., & Sekiguchi, H., 2008. Revisiting the basin-edge effect at Kobe during the 1995 Hyogo-Ken Nanbu earthquake, *Pure Appl. Geophys.*, **165**, 1751–1760.
15. **Chaljub, E.** & Valette, B., 2004. Spectral element modelling of three-dimensional wave propagation in a self-gravitating Earth with an arbitrarily stratified outer core, *Geophys. J. Int.*, **158**, 131–141.
16. **Chaljub, E.**, Capdeville, Y., & Vilotte, J.-P., 2003. Solving elastodynamics in a fluid-solid heterogeneous sphere : a parallel spectral element approximation on non-conforming grids, *J. Comput. Phys.*, **187**(2), 457–491.
17. Capdeville, Y., **Chaljub, E.**, Vilotte, J.-P., & Montagner, J.-P., 2003. Coupling the spectral element method with a modal solution for elastic wave propagation in global Earth models, *Geophys. J. Int.*, **152**, 34–67.
18. **Chaljub, E.** & Tarantola, A., 1997. Sensitivity of SS precursors to topography on the upper-mantle 660-km discontinuity, *Geophys. Res. Lett.*, **24**(21), 2613–2616.

I.7.2 Ouvrages et Chapitres d'Ouvrages

1. Moczo, P., Kristek, J., & Gális, M., 2014. *The Finite-difference Modelling of Earthquake Motions : Waves and Ruptures*, Cambridge University Press, With contributions by M. kristekova, **E. Chaljub**, M. Käser, P. Klin and C. Pelties.
2. Virieux, J., Etienne, V., Cruz-Atienza, V., Brossier, R., **Chaljub, E.**, Coutant, O., Garambois, S., Mercerat, D., Prieux, V., Operto, S., Ribodetti, A., & Tago, J., 2012. Modelling Seismic Wave Propagation for Geophysical Imaging, in *Seismic Waves - Research and Analysis*, pp. 253–304, Chap.13, Masaki Kanao.
3. **Chaljub, E.**, Komatitsch, D., Vilotte, J.-P., Capdeville, Y., Valette, B., & Festa, G., 2007. Spectral element analysis in seismology, in *Advances in Wave Propagation in Heterogeneous Media, Advances in Geophysics*, vol. 48, pp. 365–419, eds WU, R.-S. & Maupin, V., Elsevier Academic Press.
4. **Chaljub, E.**, 2000. *Modélisation numérique de la propagation d'ondes sismiques en géométrie sphérique : application à la sismologie globale (Numerical modeling of the propagation of seismic waves in spherical geometry : application to global seismology)*, Ph.D. thesis, Université Paris VII Denis Diderot, Paris, France, in French.

I.7.3 Actes de Congrès

1. Maufroy, E., **Chaljub, E.**, Hollender, F., Bard, P.-Y., Kristek, J., Moczo, P., de Martin, F., Theodoulidis, N., Manakou, M., Guyonnet-Benaize, C., Pitilakis, K., & Hollard, N., 2015. Validating the numerical simulation approach for ground motion prediction : General framework and latest lessons from the E2VP project, in *Proceedings of the 6th International Conference on Earthquake Geotechnical Engineering*, paper 452.
2. Iqbal, J., **Chaljub, E.**, Guéguen, P., & Bard, P.-Y., 2012. Soil-structure interaction simulations of 2D & 3-D block model with spectral element methods, in *Proceedings of the 15th world conference on Earthquake Engineering*, Lisboa, Portugal.

3. Maufroy, E., Bard, P.-Y., **Chaljub, E.**, Hollender, F., Kristek, J., Moczo, P., & E2VP-team, 2012. Validation of site-effect numerical predictions : New results from the Euroseistest Verification and Validation Project (E2VP), in *Proceedings of the 15th world conference on Earthquake Engineering*, Lisboa, Portugal.
4. Hollender, F., **Chaljub, E.**, Moczo, P., Bard, P.-Y., Manakou, M., Bielak, J., Theodoulidis, N., Cadet, H., Kristek, J., Tsuno, S., Pitilakis, K., Etienne, V., Gélis, C., & Bonilla, L. F., 2011. Evaluation du degré de validité des simulations numériques des mouvements sismiques : le projet de validation et de vérification Euroseistest (E2VP), in *8ème Colloque National AFPS*.
5. **Chaljub, E.**, 2009. Spectral element modeling of 3-D wave propagation in the alpine valley of Grenoble, in *Proceedings of the IIIrd International Symposium on the Effects of Surface Geology on Seismic Motion*, vol. 2, LCPC Editions, ISSN 1628-4704, 7 p.
6. **Chaljub, E.**, Cornou, C., & Bard, P.-Y., 2009. Numerical benchmark of 3-D ground motion simulation in the valley of Grenoble, french Alps, in *Proceedings of the IIIrd International Symposium on the Effects of Surface Geology on Seismic Motion*, vol. 2, LCPC Editions, ISSN 1628-4704, paper SB1, 11 p.
7. Cornou, C., **Chaljub, E.**, Verbeke, J., Converset, J., Voisin, C., Stehly, L., Margerin, L., Tsuno, S., Grasso, J., Guéguen, P., et al., 2009. Measurement and variability study of site effects in the 3-D glacial valley of grenoble, french alps, in *Third International Symposium on the Effects of Surface Geology on Seismic Motion*, vol. 2, pp. 1621–1627, LCPC Editions, ISSN 1628-4704.
8. Tsuno, S., **Chaljub, E.**, & Bard, P.-Y., 2009. Grenoble valley simulation benchmark : comparison of results and main learnings, in *Proceedings of the IIIrd International Symposium on the Effects of Surface Geology on Seismic Motion*, vol. 2, LCPC Editions, ISSN 1628-4704, paper SB2, 57 p.
9. Umeda, N., Tsuno, S., **Chaljub, E.**, Cornou, C., Bard, P.-Y., & Kawase, H., 2008. A study on the long duration of ground motion in the Grenoble basin, french Alps, in *Proceedings of the 14th world conference on Earthquake Engineering*, Beijing, China.
10. Douglas, J., Guéguen, P., **Chaljub, E.**, Cotton, F., Suhadolc, P., Costa, G., Faeh, D., Spühler, E., Gosar, A., Priolo, E., et al., 2006. Dissemination of alpine accelerometric data, in *Third International Symposium on the Effects of Surface Geology on Seismic Motion*, vol. 1, pp. 165–173, LCPC Editions, ISSN 1626-4704, paper 031.

I.7.4 Présentations récentes en conférences

1. Maufroy, E., **Chaljub, E.**, de Martin, F., Hollender, F., Bard, P.-Y., Hollard, N., Roumelioti, Z., & Theodoulidis, N., 2015. Understanding the variability of earthquake ground motion in sedimentary basins : insights from a numerical study in the Mygdonian basin, Greece., in *French-Japanese Symposium on Earthquake and Triggered Hazards*.
2. **Chaljub, E.**, Maufroy, E., deMartin, F., Hollender, F., Guyonnet-Benaize, C., Manakou, M., Savvaidis, A., Kiratzi, A., Roumelioti, Z., & Theodoulidis, N., 2014. How sensitive is earthquake ground motion to source parameters ? Insights from a numerical study in the Mygdonian basin, in *EGU General Assembly Conference Abstracts*, vol. 16, p. 11738.
3. **Chaljub, E.**, Maufroy, E., Moczo, P., Kristek, J., Priolo, E., Klin, P., De Martin, F., Zhang, Z., Hollender, F., & Bard, P.-Y., 2013. Identifying the origin of differences between 3D numerical simulations of ground motion in sedimentary basins : lessons from stringent canonical test models in the E2VP framework, in *EGU General Assembly Conference Abstracts*, vol. 15, p. 8736.

4. **Chaljub, E.**, Moczo, P., Kristek, J., Bard, P.-Y., & Hollender, F., 2011. Relevance of ground motion numerical simulations : what have we learned since the ESG2006 benchmark, in *Proceedings of the 4th IASPEI/IAEE International Symposium on Effects of Surface Geology on Seismic Motion*.

5. Moczo, P., Kristek, J., Galis, M., **Chaljub, E.**, & Etienne, V., 2010. FDM, FEM, SEM and DGM : Comparison, Accuracy and Efficiency, in Numerical Modeling of Seismic Motion, in *Eos Transactions AGU*, vol. 91(26), Invited.

6. **Chaljub, E.**, Bard, P.-Y., Hollender, F., Theodulidis, N., Moczo, P., **Tsuno, S.**, Kristek, J., Cadet, H., Franek, P., Bielak, J., et al., 2010. Euroseistest numerical simulation project : Comparison with local earthquake recordings for validation, *Seismological Research Letters*, **81**(2), 308–309.

7. **Chaljub, E.**, Bard, P.-Y., **Tsuno, S.**, Kristek, J., Moczo, P., Franek, P., Hollender, F., Manakou, M., Raptakis, D., & Pitilakis, K., 2009. Assessing the capability of numerical methods to predict earthquake ground motion : the Euroseistest verification and validation project, in *AGU Fall Meeting Abstracts*, vol. 1, p. 1968.

8. Bard, P.-Y. & **Chaljub, E.**, 2009. Effects of surface topography on seismic ground motion : recent results, remaining issues and needs, in *American Geophysical Union*, Invited.

Chapter II

Summary of research activity

II.1 Introduction

My research activity in the last 10 years has been dedicated to the estimation of Earthquake Ground Motions (EGM) with physics-based numerical methods. There are at least two obvious reasons for a seismologist to try to estimate EGM. The first one is to better understand and hopefully explain, the causes of the damages of past earthquakes. The second one is to help the society to better anticipate the motions that would affect the ground and the structures for future earthquakes that have been given a non-zero probability to occur. In the field of computational seismology, the first motivation has been central in the development of numerical methods in the last forty years, very often triggered by the occurrence of destructive earthquakes, whereas the second only appears now as a possibly affordable challenge to tackle, thank to the advent of mature numerical methods and codes, combined with continuously increasing computational resources.

However, as nicely stated in the research program of the Southern California Earthquake Center for the next five years (2017-2022), "Earthquakes are confoundingly simple in their gross statistical features but amazingly complex as individual events". EGM are indeed the consequences of a unique combination of complex individual processes: the source rupture, the propagation of seismic waves in the heterogeneous crust, and the response of sites with highly contrasted local geology. Understanding and modelling how each of those ingredients contribute to shape EGM, is thus a necessary step to build a prediction for future events.

In this chapter, I present my contributions to the numerical estimation of EGM in realistic frequency bands and when complex site effects occur. Some important topics, such as rupture dynamics or non-linear soil response, are not covered because I did not contribute to them. Other aspects which correspond to ongoing studies, such as the modeling of soil-structure interaction are not presented either. The chapter starts with a brief classification of the numerical methods which have been applied to the estimation of EGM in the last forty years. Then, the results of two long-term collaborative studies dedicated to verification, that is, the estimation of the epistemic uncertainty of 3D numerical simulations of EGM, are presented. Validation examples of 3D numerical simulations in realistic situations, corresponding to very different seismic contexts and levels of knowledge about the site conditions, follow. They illustrate the difficulty to apply fully deterministic physics-based models to predict EGM, given the level of uncertainty on their input parameters. Those results illustrate the reason why current predictions of EGM in seismic hazard analyses still rely on empirical methods, so-called Ground Motion Prediction Equations (GMPE) (see e.g. Douglas & Edwards (2016) for a recent review). The chapter closes with a summary of results obtained from a series of parametric studies, which quantify the dependence of EGM to variations of the source and site parameters and make the link with the estimation of the aleatory variability of GMPE.

II.2 Development and verification of numerical methods for deterministic prediction of EGM

II.2.1 Preamble

Many methods have been developed in the last forty years to evaluate EGM. They have been classified in Table II.1 following their ability to deal with realistic propagation media and seismic sources. The most general methods, i.e. which can in principle handle realistic seismic sources and arbitrary three-dimensional propagation media, fall into the category of grid-based (some would say brute-force) methods that compute approximate solutions to the wave equation at all discrete positions in space and time. Even though they were introduced in early years (one of the first review paper on the application of the FDM to the elastic wave equation was published by Boore (1972) and the applicability of the time domain FEM to seismological problems was studied in (Smith 1975)), grid-based methods were logically superseded during more than two decades, i.e. before the advent of the computational era [1], by the first set of methods described in Table II.1. Those rely on simplifying assumptions (e.g. plane wave excitation, periodic or piece-wise homogeneous propagation medium) but also on a deeper knowledge, or intuition, of the properties of the solutions to the wave equation (Weyl integral for plane wave decomposition, representation theorems, Rayleigh ansatz) which made them applicable to realistic situations and frequency bands. The DWM has been used extensively in source studies, and the Aki-Larner method and BIEM mainly to (lithological and topographical) site effect studies.

Note that the existence of easily accessible computer codes implementing each method (as illustrated in Table II.1) serves as an indicator of the vitality of their current use in the seismological community: codes implementing the DWM are quite widespread whereas implementations of the Aki-Larner method or even of BIEM have not survived the computational era, at least in seismology [2]. The present situation is quite clear for an average user who wants to compute EGM for its own research: either a 1D medium approximation is reasonable, and then any code implementing the DWM will make the job on his personal computer, or it is not and a code implementing a grid-based method in 2D or 3D will have to be used and ran on a dedicated high performance computing (HPC) platform, the size of which will depend on the frequency band adressed and the size of the physical domain [3].

The job of a developer has also pretty much changed over the years. The time when a single researcher would develop a computer program that would be used by an entire community is gone, as well as the time when a PhD student would spend years to develop a computer program from scratch [4]. Open-source codes are now being developped and maintained by large collaborative groups, formed by numerical seismologists, software engineers and HPC experts. The most advanced of those codes are often installed on the most powerful HPC platforms, and some of them even serve as benchmark to choose the platforms of the next generation.

But, as will be seen in the next section, this formidable improvement in computational performance does not necessarily ease the implementation of those 3D codes and it does not either prevent the solutions they compute to be sometimes wrong.

1. I arbitrarily chose the beginning of the computational era to be 2003, when two seismological codes were granted Gordon Bell awards at the Supercomputing conference (Komatitsch et al. 2003; Akcelik et al. 2003).

2. Boundary Element Methods and codes are more widespread in other disciplines as illustrated by the existence of community repositories.

3. The computational power follows the prediction of Moore's law and increases by a factor of two every 14 months. Nowadays' laptop computers offer about the same computational power than the biggest machine worlwide twenty years ago!

4. I personally experienced this life during my PhD and contributed to the development of the SEM at the global scale with my own code. But all my simulation results presented in this manuscript have been obtained with the open-source code SPECFEM implementing the SEM at the local scale.

Table II.1. Rough classification of numerical methods applied to EGM estimation in the last 40 years. The acronyms are as follows. DWM: Discrete Wavenumber Method, BIEM: Boundary Integral Equation Method, FDM: Finite-Difference Method, FEM: Finite Element Method, PSM: Pseudo-Spectral Method, SEM: Spectral Element Method, DGM: Discontinuous Galerkin Method. PW stands for plane wave, F for force and DC for double-couple. An asterisk means that the access to a code is subject to eligibility conditions. A question mark reflects a lack of information at the time the text was written. Note that a maximum of 3 references has been arbitrarily set to the list of available codes.

Method	Medium	Source	Reference	Available codes
DWM	1D	F+DC	Bouchon (2003)	AXITRA, HISADA, CPS
Aki-Larner	few interfaces	PW	Bard & Bouchon (1980a,b)	?
BIEM	piece-wise homog.	F+DC	Manolis et al. (2017)	?
FDM	3D	F+DC	Moczo et al. (2014)	FDSIM3D, SW4, OPENSWPC
FEM	3D	F+DC	Bao et al. (1998)	HERCULES*
PSM	3D	F+DC	Klin et al. (2010)	?
SEM	3D	F+DC	Chaljub et al. (2007)	SPECFEM3D, SPEED, EFISPEC
DGM	3D	F+DC	Dumbser & Kaeser (2006)	SEISSOL, NEXD

II.2.2 Verification

The development of a numerical method to estimate EGM and its implementation in a computer code comes naturally with the need for verification. Following Moczo et al. (2014) and Maufroy et al. (2015), I define the process of verification as "the demonstration of the consistency of the numerical method with the original mathematical–physical problem defined by the controlling equation, constitutive law, and initial and boundary conditions; and the quantitative analysis of its accuracy". In practice, each article referring to a new numerical development comes with an application to one or a few canonical situations where a reference solution exists. Analytical solutions served as early references: e.g. the Green function due to a force located at the surface of an elastic half-space (Lamb 1904), the solution of the buried line source problem in an elastic half-space (Garvin 1956) or the scattering of a plane SH wave by a semi-cylindrical canyon (Trifunac 1972), soon replaced by solutions produced with the DWM for layered visco-elastic propagation media (e.g. Day et al. (2001)). From there, one would have expected that a new method would become the reference for arbitrarily heterogeneous 2D or 3D media, and most of the developers would secretly hope that their method should be that reference.

The reality proved to be more complex, as illustrated by the results of a number of comparative exercises (Day et al. 2003, 2005) and of blind prediction tests organized in the seismological community: Turkey Flat in the Parkfield area, central California in 1989-1990 (e.g. Cramer (1995)), Ashigara Valley in the Kanagawa Prefecture, SW of Tokyo, Japan in 1992 (e.g. Bard (1994)), Osaka basin, Japan in 1998 (Kawase & Iwata (1998)). The main lesson that should be learned from those experiences is that each method has its advantages and disadvantages that often depend on a particular application. In other words, none of these methods can be chosen as the universally best (in terms of accuracy and computational efficiency) method for all important problems. One logical consequence and particular aspect of this situation is that, depending on a particular model of the medium, it might be not trivial to reach satisfactory agreement between solutions obtained by different methods.

My first motivation when I started to work on the topic of EGM estimation was to better understand the origin of the misfits between different numerical results. My interest was obvious: the problem was difficult and I wanted to be sure that the results I was obtaining with the spectral element method at the local scale were physically sound. I was lucky that the third edition of the

international symposium on the Effects of Surface Geology (ESG) on seismic motion was organized in Grenoble in 2006, just one year after I was recruited at the LGIT (Laboratoire de Géophysique Interne et Tectonophysique, now ISTerre). I was indeed soon enrolled in the design of a comparison exercise (Chaljub et al. 2009), without realizing that this would be the beginning of almost a decade of research work dedicated to verification studies, the results of which are summarized in the next sections.

II.2.2.1 Grenoble ESG2006

The ESG2006 symposium gave the opportunity to design a comparison exercise for numerical prediction of EGM in the context of alpine valleys, which was (and still is) quite a different target than large sedimentary basins considered in previous ESG exercises (Osaka basin in 1998 after the Kobe earthquake) or in the SCEC long-term comparison exercise (e.g. Los Angeles basin). The small spatial dimensions of the valley allowed to increase the frequency content up to 4 Hz, well beyond existing exercises, while the alpine context required to account for the effects of pronounced topographical variations. The project was ambitious: A series of imposed exercises featuring 2 weak motion events and 2 strong motion scenarios (see Fig. II.1) and a free-style exercise where the effect of a M6 event had to be predicted at one location in the valley together with an estimation of the uncertainty of the prediction. The set of exercises, which was improperly referred to as a "benchmark" [5], was tackled by 14 different teams providing 18 contributions, among which 9 3D predictions. The first results were quite disappointing, and because we had not anticipated that iterations would be needed to reach a decent agreement, they were presented "as is" at the ESG conference, triggering a few lazzi in the audience. As an example, Fig. II.2 shows the improvement of 3 solutions (that were among the closest in the initial round) after additional comparisons and investigation for implementation errors. It took a few more years of volunteer-based collaboration between 4 teams (Seiji Tsuno, Pierre-Yves Bard and myself in Grenoble, Peter Moczo and Jozef Kristek in Bratislava, Martin Käeser in Munich and Marco Stupazzini in Milano) to publish a quantitative analysis of the results obtained with 4 3D codes implementing 3 different methods (FDM, SEM and DGM) (Chaljub et al. 2010). The interested reader will find the article presenting the full results of this verification analysis in section IV.2 p. 170. In what follows, I briefly highlight some of those results as well as some lessons learned from the exercise.

As an example, Fig. II.3 shows the PGV maps that were obtained by the four groups for one of the strong motion case. The level of agreement was judged at that time to be satisfactory [6], given the complexity of the considered scenario (including finite fault effects and complex geometry of the sediment-bedrock interface). The remaining differences were attributed to the inherent complexity of the spatial distribution of peak values of ground velocity, which were shown to involve some interferences with late surface arrivals diffracted off the edges of the valley (in particular in the southeastern part of the valley where the largest values of PGV are reached).

Finally, the effect of surface topography on EGM could be investigated by 3 of the 4 teams. As shown in Fig. II.4, the overall effect was consistently predicted by all methods (and essentially located at rock sites for this source-valley configuration), even though more detailed numerical work would be needed to fully understand the differences in the predicted amplification/de-amplification values.

Those optimistic conclusions were balanced by the quite disappointing level of agreement reached for the supposedly simpler (at least in terms of source complexity) weak motion cases as shown in Fig. II.5. In spite of a more limited time devoted to the analysis of those cases, it was agreed that the main sources of differences between the numerical results were related to (i) the higher frequency

5. A benchmark has the much narrower meaning of comparing the performance of different codes to produce an already known solution with a given level of accuracy.

6. The article is often cited as an evidence of the maturity of 3D numerical simulation for EGM evaluation.

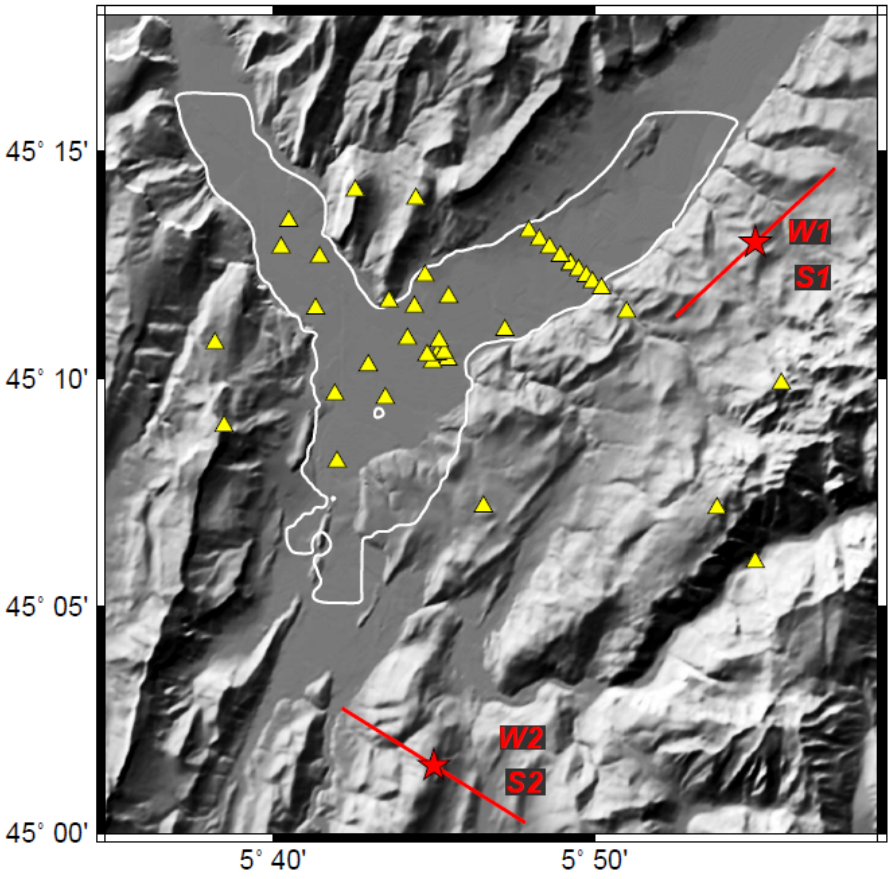

Figure II.1. Distribution of sources and receivers for numerical predictions of EGM in the valley of Grenoble as proposed during the ESG 2006 symposium. Four imposed exercises were proposed: two weak motion cases (W1 and W2) corresponding to past local events and two strong motion cases (S1 and S2) corresponding to extreme scenarios. After Chaljub et al. (2009).

content of the simulations and (ii) to differences in the approximation of intrinsic attenuation in one of the codes implementing the SEM.

Overall, the ESG2006 exercise was useful to illustrate the level-of-practice in numerical predictions of EGM and it helped to recall a few obvious statements, such that 3D simulation was far from being a press-button approach [7], or that the same numerical method (for example here SEM) implemented in different codes following different discretization strategies (for mesh design or realization of intrinsic attenuation) could lead to quite different results. It was also useful to test and improve some quantitative measures of the fit between time series: Anderson's engineering criteria (Anderson 2004) and the time-frequency misfits developed by the Bratislava team (Kristeková et al. 2006; Kristeková et al. 2009).

The main frustration stemmed from the lack of time to understand the origin of the quite large differences observed in the higher frequency band ([2-4] Hz), but it actually rooted the motivation to pursue a more methodological work on the verification of EGM simulations.

7. Ten years after, the statement is still essentially true.

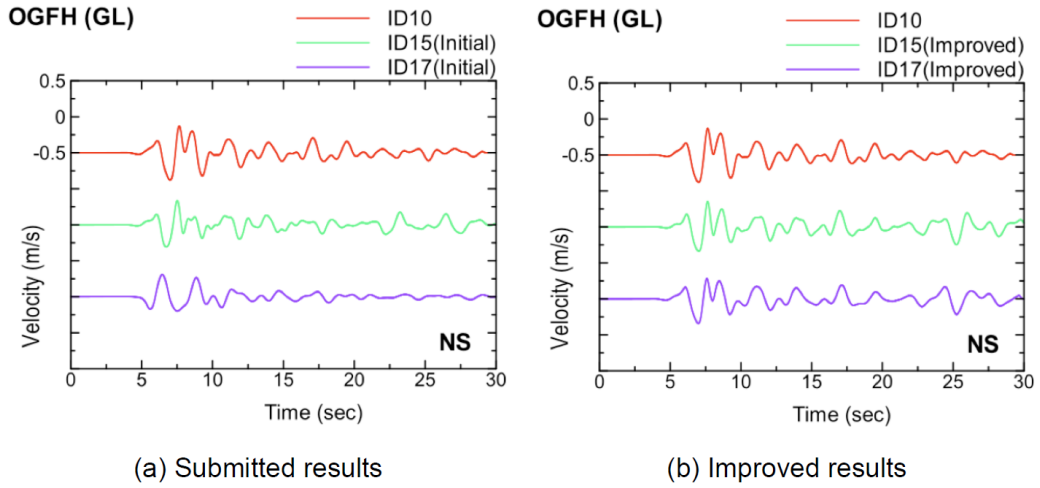

Figure II.2. Illustration of the reduction of misfit between numerical predictions due to the correction of implementation errors by participants between two stages of the ESG comparison exercise. After Tsuno et al. (2009).

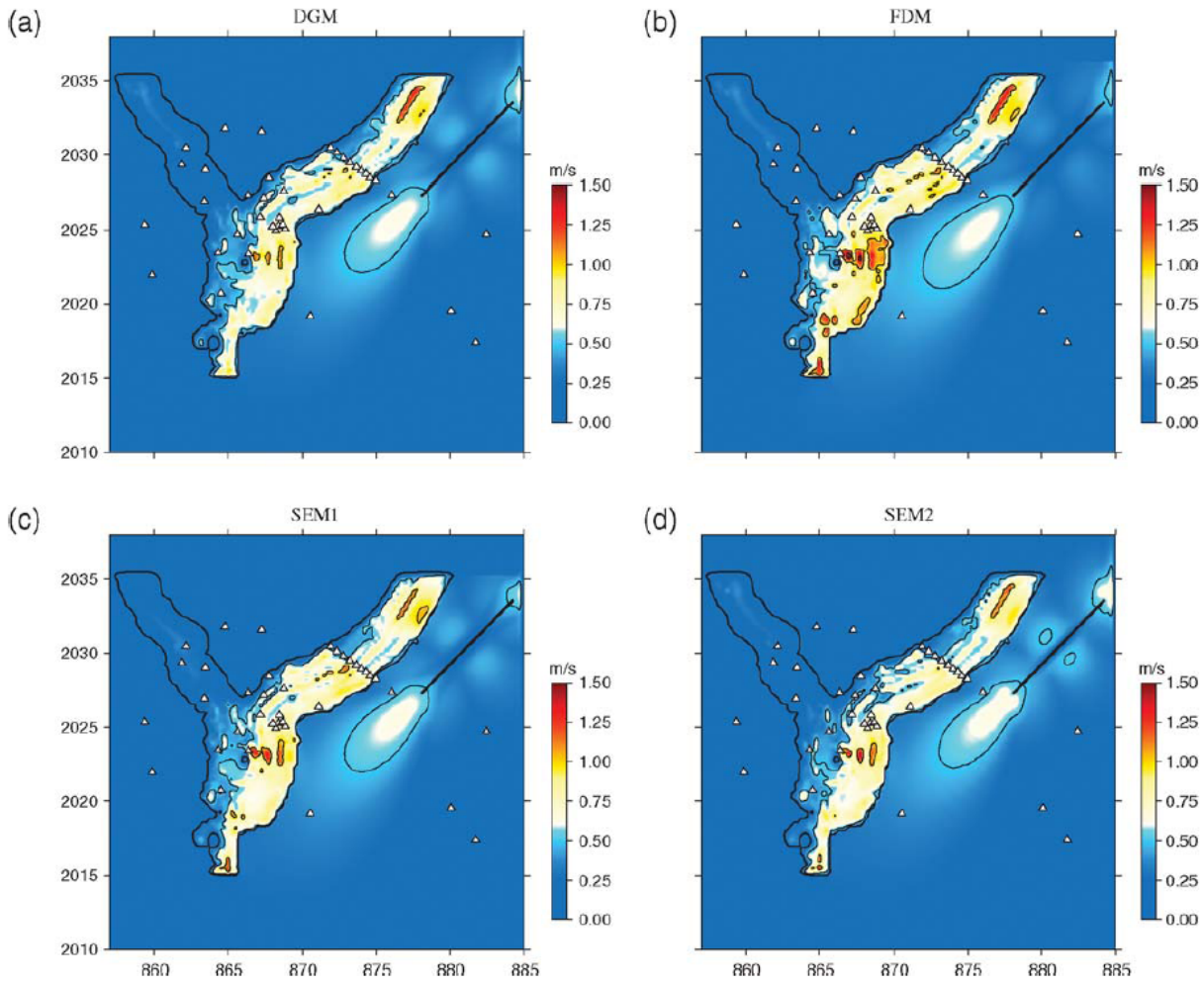

Figure II.3. Comparison of peak ground velocity maps in the Grenoble valley computed up to 2 Hz for a strong motion scenario by 4 different codes implementing 3 different numerical methods (FDM, SEM, DGM) and neglecting the surface topography. After Chaljub et al. (2010).

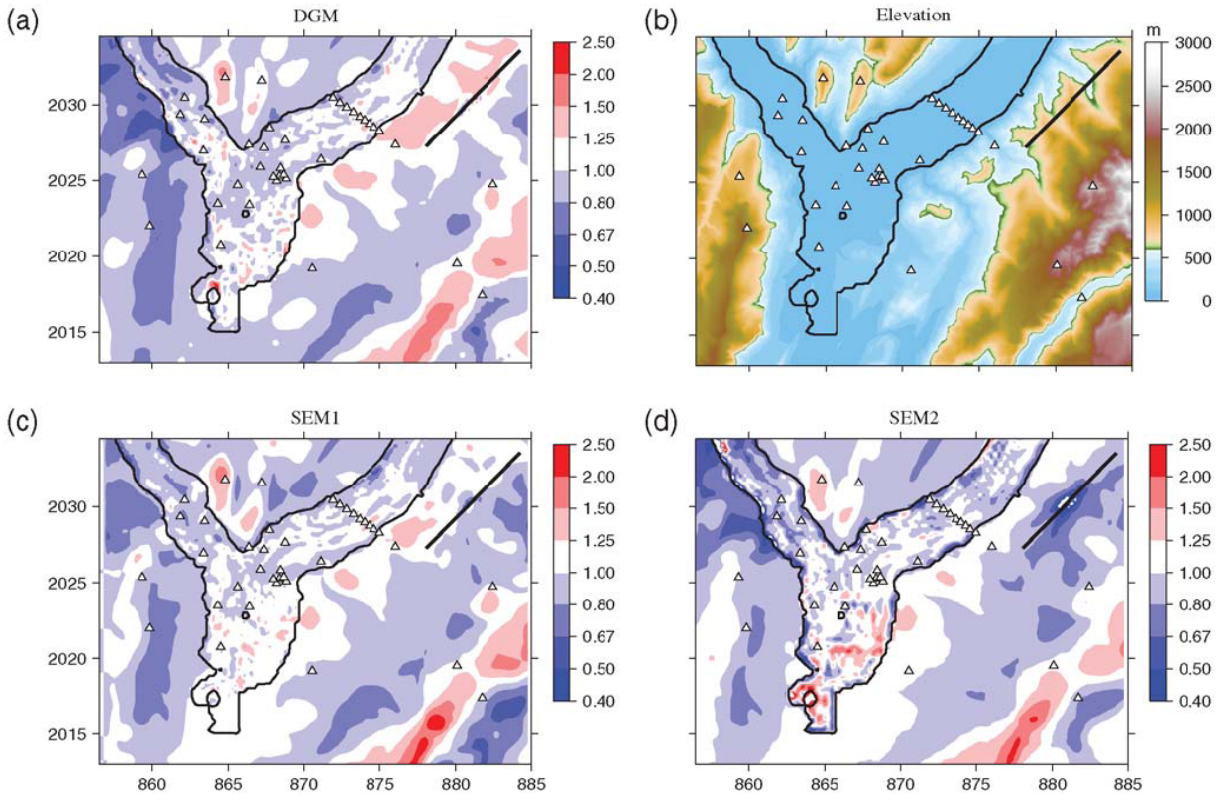

Figure II.4. Comparison of the effect of surface topography around the Grenoble valley computed up to 2 Hz for a strong motion scenario by 3 different codes implementing 2 different numerical methods (SEM, DGM). Red colors indicate amplification (PGV ratios with respect to a calculation with the same code in a flat model) and blue colors stand for de-amplification. After Chaljub et al. (2010).

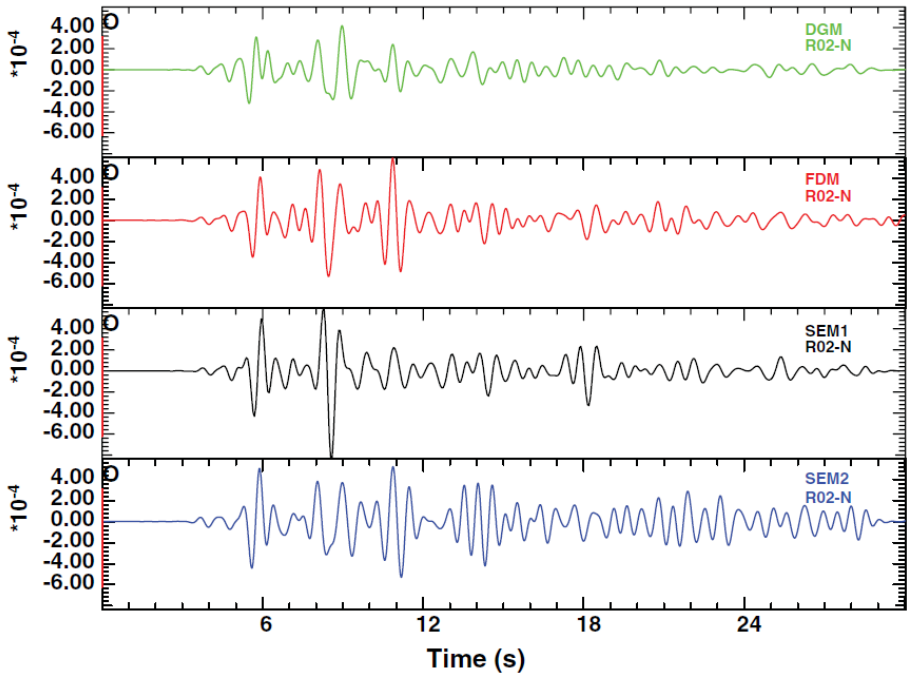

Figure II.5. Comparison of ground velocity computed up to 4 Hz for a weak motion event by 4 different codes implementing 3 different numerical methods (FDM, SEM, DGM) and neglecting the surface topography. After Chaljub et al. (2010).

II.2.2.2 Volvi E2VP

The opportunity to extend the verification effort came soon, in 2008, with the advent of the Euroseistest Verification and Validation Project (E2VP), funded by the Cashima project (supported by the French nuclear agency [CEA] in Cadarache and the Lau-Langevin Institute [ILL] in Grenoble) and organized jointly by ISTerre in Grenoble, CEA in Cadarache, ITSAK and the Aristotle University in Thessaloniki. The first objective of E2VP (the first of the two 'V') was indeed to evaluate the accuracy of the most-advanced numerical methods for EGM evaluation when applied to realistic 3D models. A large number of teams (from Europe, Japan and the USA) implementing a large panel of numerical methods (FDM, FEM, SEM, PSM, DGM) was recruited and, based upon the Grenoble experience, an efficient working group strategy was adopted relying on frequent meetings to evaluate and discuss current results and decide about performing more iterations or designing new test cases.

The target of E2VP was chosen in the central part of the Mygdonian basin, close to the Volvi lake in the epicentral area of the M6.5 event that struck Thessaloniki on June 20, 1978. The choice was motivated by the idea to capitalize on the results of previous European projects which constrained the geological structure of the basin and to exploit the recordings of the Euroseistest accelerometric network in the validation phase of the project (see section II.3). Fig. II.6 shows the geometry of the three-layer velocity model that was designed at the beginning of the project, based on the work of Manakou (2007) and Manakou et al. (2010). The geometrical complexity of the model stems from: the asymmetry between the slopes of the northern (gentle) and southern (sharp) basin edges, typical of graben-like basins, the saddle-point shape of the basin around the Euroseistest accelerometric array, and the large, uncorrelated variations of the thicknesses of the different sedimentary units filling the basin.

The numerical challenge was to compute the response of the basin for frequencies up to 4 Hz, i.e. more than 5 times the fundamental resonance frequency in the center of the basin (and ten times the one in the westernmost part), accounting for the large (up to 7.5) V_P/V_S ratios in the first sedimentary layers. Based upon the Grenoble experience, only point-like sources were considered.

After (months of) careful comparisons of the different predictions in visco-elastic and purely elastic media, a clear conclusion was drawn: the agreement between solutions was quantified to be very good to excellent for primary, mainly body-wave arrivals but would systematically degrade for late, surface wave arrivals diffracted at basin edges. Despite numerous iterations and improvements in the resolution of individual contributions, the large misfits related to late arrivals remained. A decisive observation was that the level of agreement for late phases would increase significantly in smoother velocity models (e.g. replacing the globally discontinuous piece-wise homogeneous original model by a globally continuous, piece-wise linear model), as shown in Fig. II.7.

Surprisingly, the (sometimes large) amplitude and phase differences seen for late arrivals between individual numerical solutions do not seem to affect the spatial distribution of peak ground motion even in the elastic regime where peak values may be attained at quite late times. This is illustrated in Fig. II.8, which shows some "stripes" of peak values corresponding to the paths taken by low velocity, large amplitude, Airy phases of surface waves diffracted off the northern basin edge. The locations and the level of amplitude of those stripes is shown to depend largely on the position of the source (here the source is located below the basin), and more importantly to decrease and almost vanish in the center of the basin when more realistic, visco-elastic simulations are considered (the peak values are then carried by earlier arrivals). They are nonetheless indicative of the spatial variability of EGM that can be expected in sedimentary basins close to complexly shaped edges, and the fact that even "not fully converged" numerical solutions can successfully predict their occurrence is certainly a message of hope for future studies.

It took another set of verification exercises (on canonical cases with existing reference solutions) to fully understand the impact of the roughness of the velocity model on the accuracy of numerical

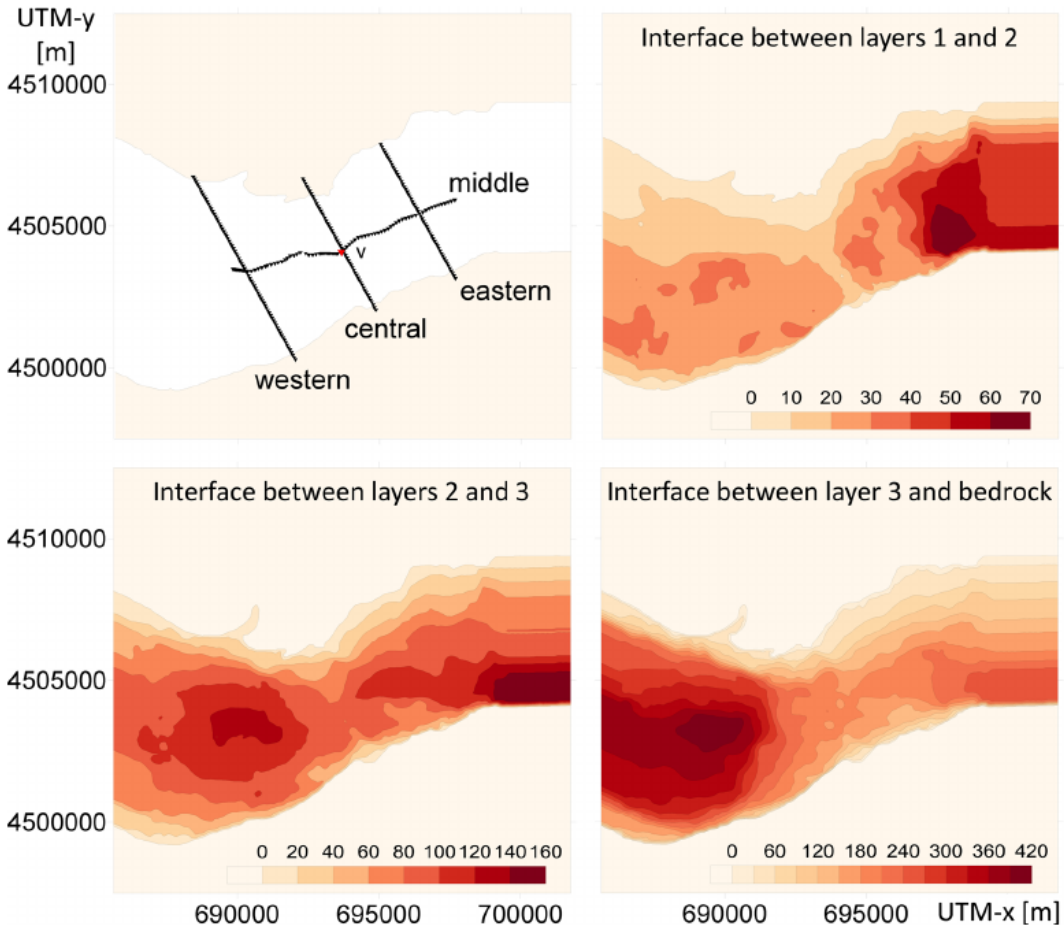

Figure II.6. Maps of sediment thickness of the three-layers velocity model of the Volvi basin used in the first phase of E2VP. The top left figure shows the location of receiver lines that were considered to compare numerical prediction of EGM. After Kristek et al. (2016).

prediction of EGM. The main results of these analyses are briefly recalled here. The reader is referred to Chaljub et al. (2015) and Kristek et al. (2016) for details.

In short, the main difficulty of the 3-layers velocity model shown in Fig. II.6 stems from its internal discontinuities, i.e. from variations of material properties which have an infinite spatial frequency spectrum. Since any grid-based numerical method has a limited spatial resolution to realize the discrete representation of a continuous model, the main question is to understand how the unresolved spatial scales are represented at the discrete level. Any error (for example aliasing) in the discrete representation of the high spatial frequencies will be the source of numerical inaccuracy. The resulting numerical error will also depend on the type of the simulated seismic waves: body waves that travel only a few times across the discontinuities will not be affected as much as surface waves which propagate along them and are continuously sensitive to the incorrect numerical representation of the interfaces.

This is illustrated in Fig. II.9 which corresponds to a careless implementation of the SEM, where one of the discontinuities of the model does not coincide with a boundary between spectral elements. In this particular case, the physical discontinuities are approximated within the spectral elements by high-order polynomials, giving rise to an undesired Gibbs effect. The effect of this crude approximation on the ground velocity computed after a few kilometers of horizontal propagation is shown on the right part of Fig. II.9. The deviation from the reference solution (in black) is spectacular. On the contrary, quasi vertically incident body waves computed with the same

approximation (left part of the figure) are not too severely affected (a small phase shift is clearly seen, which can be related to only a few percents of inaccuracy in the fundamental resonance frequency).

The discontinuities are in fact a particular case because a number of numerical methods (FEM, SEM, DGM) have the remarkable property to accurately account for them as long as they coincide with element's boundaries. This is not the case for the FDM, and their developers have been facing the issue of the discrete representation of the physical interfaces for a long time. For example Moczo et al. (2002) proposed to define an isotropic equivalent medium at the discrete level, by replacing elastic moduli in the vicinity of an interface by their volume harmonic average and mass densities by their volume arithmetic average. This corresponds to applying an approximate solution to the homogenization (or up-scaling) of an elastic medium. The general solution is a fully anisotropic medium (see e.g. Guillot et al. (2010); Capdeville et al. (2010)), which sometimes simplifies as noted by Backus (1962) who established that the long wavelength approximation of a stack of isotropic layers was a vertically transverse isotropic medium where the anisotropic parameters had to be defined by harmonic or arithmetic averages.

The set of canonical cases defined in Chaljub et al. (2015) helped to understand that the approximation of an isotropic equivalent medium proposed in (Moczo et al. 2002) was not sufficient to produce accurate results when surface waves propagating along the interfaces were involved. This motivated the development of a new, still approximate but anisotropic (orthorhombic), definition of the equivalent medium to be used at the discrete level (Moczo et al. 2014; Kristek et al. 2016). The comparison of the FDM results obtained with the old (isotropic) and new (anisotropic) equivalent media are represented in Fig. II.10 for a slightly modified version of the original three-layer velocity model of E2VP (the modification is such that the solution produced with the SEM can be considered as a reference). The results clearly show the gain of using the orthorhombic equivalent medium and suggest that this solution to the up-scaling problem, although approximate, can be considered as accurate enough for the numerical estimation of EGM in realistic situations.

These conclusions have important practical consequences for numerical estimation of EGM. They were stated in (Chaljub et al. 2015) and are reproduced here: " Whenever small-scale, or localized, strong variations of the material parameters have to be considered in the sediments, e.g. based on firm geological, geotechnical or geophysical evidence, an effective medium relevant for the chosen frequency range should be used. Depending on the degree of knowledge of the model heterogeneity and on the desired level of accuracy of the predictions, the effective media can be defined by procedures of increasing complexity. In the common situation where the level of uncertainty in the model (including the presence of interfaces) is large, a simple volume arithmetic average of the densities and slownesses, or a volume arithmetic average of the densities and harmonic average of the elastic moduli, should be used to provide an isotropic effective medium ready for numerical simulations. In all other situations, an up-scaling procedure should be adopted to design an anisotropic effective medium, either by solving a homogenization problem as suggested by Guillot et al. (2010) and Capdeville et al. (2010), or by following the explicit approach proposed by Moczo et al. (2014) and Kristek et al. (2016) based on the orthorhombic averaging. "

These recommendations were of course followed in the second phase of E2VP (2012-2014), during which a new model of the whole Mygdonian basin was built under the leadership of Fabrice Hollender (Maufroy et al. 2016) and served as a basis for sensitivity studies and quantification of the variability of EGM (see section II.3.3, p. 44).

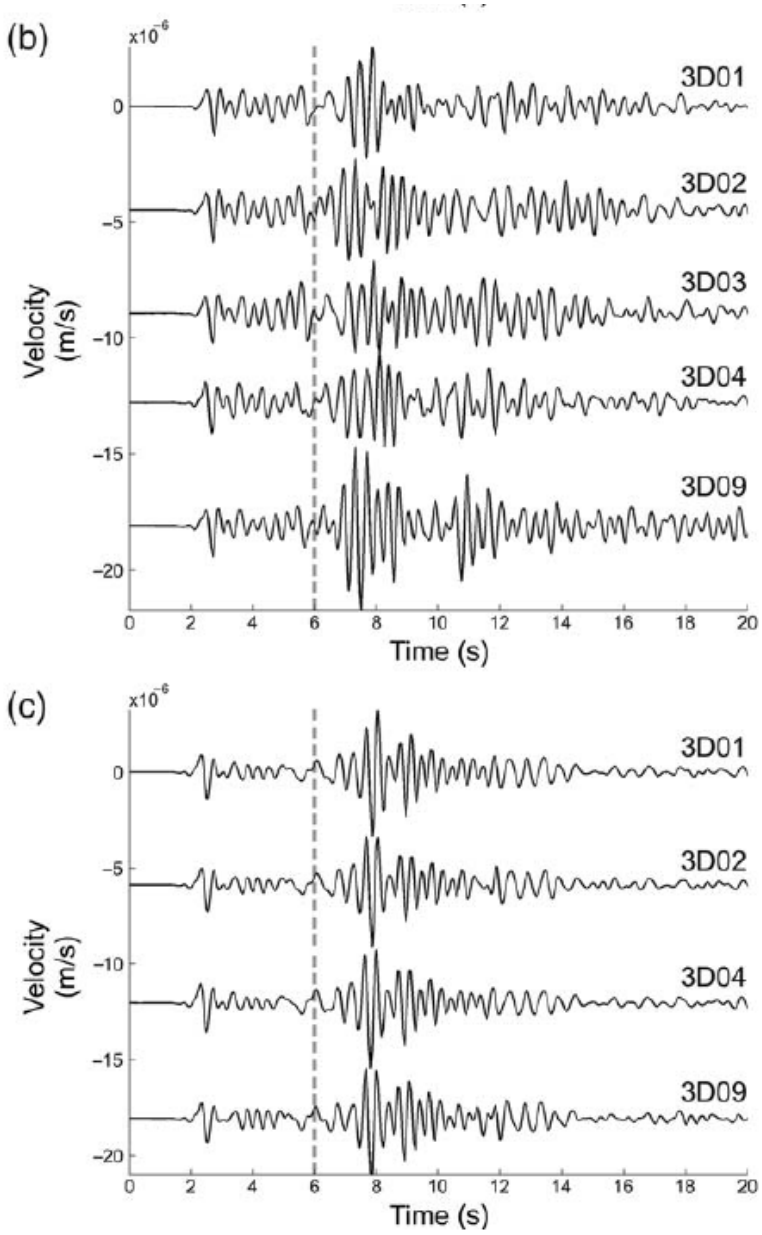

Figure II.7. Comparison of horizontal ground velocity computed in the center of the Volvi basin by various numerical methods. The top figure compares the elastic response of the discontinuous model shown in Fig. II.6, and the bottom figure shows the elastic predictions in a smoother, globally continuous velocity model. The vertical dashed line indicates a rough separation between body and surface waves arrivals. After Maufroy et al. (2015).

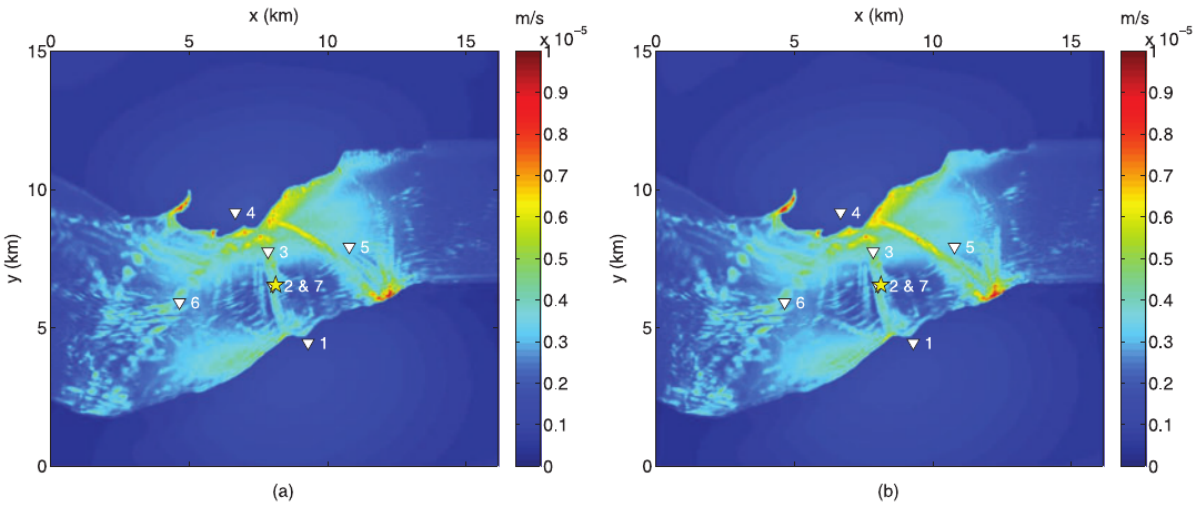

Figure II.8. Comparison of peak ground velocity maps obtained after computing the elastic response of the discontinuous velocity model shown in Fig. II.6 by two codes implementing the DGM (left) and the SEM (right) (respectively 3D09 and 3D02 in Fig. II.7). Despite significant differences in amplitude and arrival times of individual late phases, the distribution of peaks values are remarkably consistent. After Etienne et al. (2010).

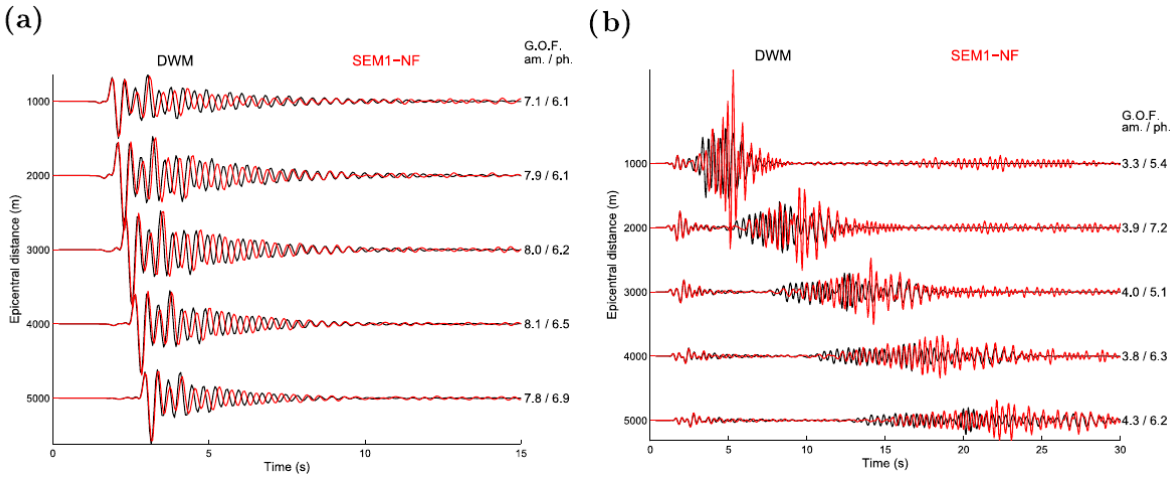

Figure II.9. After Chaljub et al. (2015).

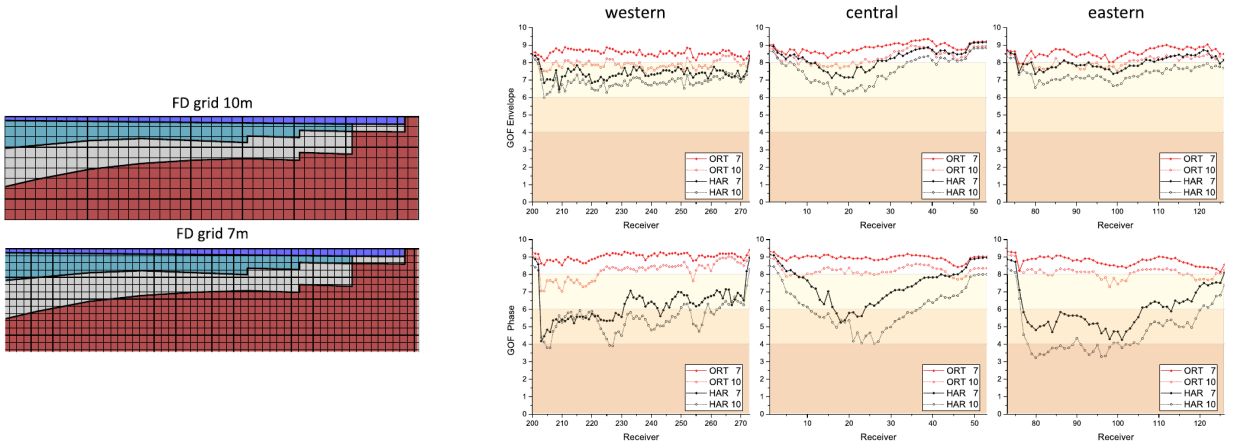

Figure II.10. Envelope and phase goodness-of-fit (right) between synthetic seismograms computed with the SEM and the FDM along three profiles of receivers shown in Fig. II.6. The properties of the discrete equivalent model in the FDM are computed in each FD cell (left) by taking volume average of the material parameters, either isotropic (HAR) or anisotropic (ORT). The SEM solution computed with homogeneous properties in each element has been taken as a reference. After Kristek et al. (2016).

II.2.3 Contributions to the development of numerical methods for EGM estimation

Although most of my research was dedicated to the application of numerical methods to the estimation of EGM, I contributed to a few studies dealing with the development or the numerical analysis of numerical methods.

In the course of the verification work done in the Mygdonian basin, we analyzed the performances of state-of-the-art numerical methods to account for large V_P/V_S ratios, as found in soft, water-saturated sediments (see Moczo et al. (2011) and section IV.1, p. 112). The originality of the article was to compute the total error (whereas most of analysis of numerical methods are limited to the estimation of the dispersion error) and to provide a common framework to analyze very different numerical schemes. The results revealed that the best method in terms of accuracy and insensitivity to the V_P/V_S ratio was a finite difference formulation and that the differences in performance of the spectral element method with this best method did not depend on the V_P/V_S ratio. Overall, the differences found among the analyzed methods were not large enough to explain the discrepancies observed between the different numerical predictions of the response of the Mygdonian basin (as confirmed a posteriori by the results shown in Figure II.10 which account for large V_P/V_S ratios).

The second contribution, which is described in Blanc et al. (2016) (see section IV.1, p. 125), deals with the implementation of attenuation in time-dependent numerical methods. The motivation of the study arose in the course of an comprehensive parametric study of 2D site effects (see section II.3.3.1, p. 44), where some configurations with very low Q values were found to be unstable numerically. The origin of the instability was related to the computation of the input parameters (frequencies and participation coefficients of the relaxation mechanisms) of the generalized Zener viscoelastic model. The article introduces a new method, based upon a nonlinear inversion of those parameters, which is shown to be always stable and more computationally efficient. It is now implemented in the open-source code SPECFEM3D implementing the spectral element method.

II.3 Validation and beyond: sensitivity analyses and variability of EGM prediction

II.3.1 Motivation

Once computationally efficient methods for EGM estimation have been developed and implemented into well verified numerical codes, they should be tested against observations in order to better understand how the individual ingredients of an earthquake (source, path and site) combine to produce a unique distribution of ground motions. Following Maufroy et al. (2015), I refer to this process as validation, that is, "as the demonstration of the capability of the theoretical model (i.e. the mathematical–physical model and its numerical approximation) to predict and reproduce observations". The validation process is a real challenge which has to be faced with limited or uncertain information (e.g. sparse earthquake recordings, insufficient knowledge of the propagation media, source location errors). In this context, the main talent for a seismologist is probably the ability to formulate well-posed questions that will not remain unanswered, and for a numerical seismologist to preserve the available computational power from useless calculations.

Keeping those preliminary remarks in mind, the validation approach should proceed as follows: First, the distance between observations and synthetic predictions has to be measured, which in particular requires to choose meaningful EGM parameters and to define an objective measure of the misfit. Second, the input parameters (geometrical, mechanical) controlling this distance have to be identified and their relative importance have to be evaluated, for example through sensitivity analyses. Third, the level of knowledge of the most important input parameters should be improved, for example through additional geophysical surveys and/or seismological or geological analyses. Eventually, the process should be iterated until a satisfactory level of agreement between observations and numerical predictions has been reached. Needless to say, this is a long lasting, site-dependent process the last steps of which are rarely, not to say never, achieved.

II.3.2 Validation studies

There are many reasons that can lead to choose a particular site to learn something about EGM: the level of hazard and risk of the site, the occurrence of past damaging earthquakes, the quality of existing seismological instrumentation, the quantity of available earthquake recordings, the level of knowledge (geological, geotechnical, geophysical) of the underground structure, the ease to access the site for additional measurements, the opportunity to get funding ...

In the following subsections, I briefly present my contributions to the validation of numerical estimation of EGM in frequency ranges of engineering interest and for a few sites corresponding to very different sets of the above conditions. Rather than a strict chronological order, I tried to gather those studies by increasing complexity of the scientific questions asked and, hopefully for the reader, by increasing interest of the answers provided.

II.3.2.1 Grenoble valley

In addition to be located "in the backyard" of any researcher working at ISTerre, there are many reasons that make the Grenoble valley a local site of great seismological interest. Indeed, although it is located in a moderate seismicity area (Thouvenot et al. 2003), it has been the target of many studies (e.g. Lebrun et al. (2002); Cornou et al. (2003)), most of them focusing on 3D site effects – and leaded by Grenoble seismologists. It has also been instrumented through the years with a few temporary velocimetric arrays and, since 1999, it has been hosting a part of the french permanent accelerometric network, in particular a vertical antenna located at the so-called Montbonnot borehole with 3 sensors distributed from the surface to the bedrock at 535 m depth.

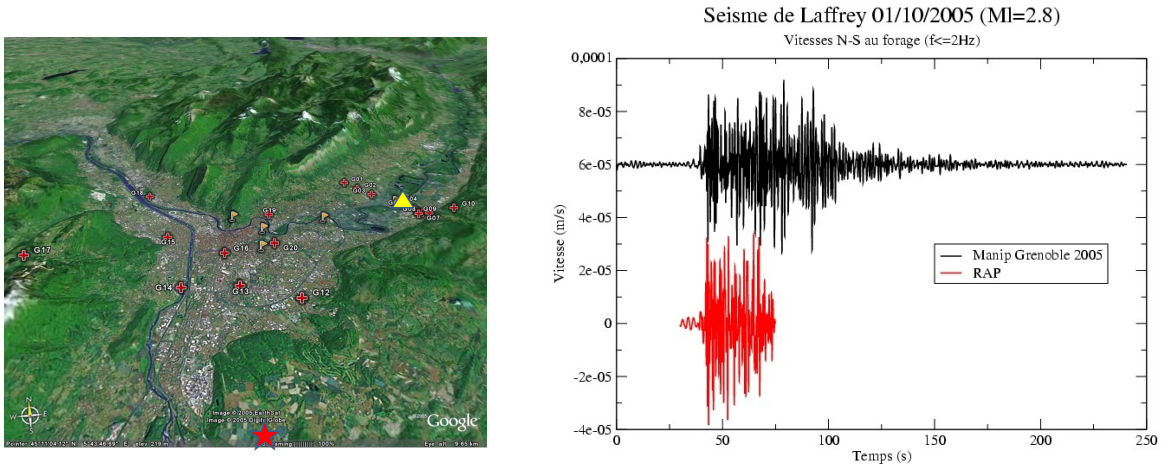

Figure II.11. Left: bird's-eye view of the 'Y'-shaped Grenoble valley showing the locations of the velocimetric sensors of the 2005 experiment (red crosses) and of the accelerometric stations of the french permanent network (yellow flags). The epicentre of the M2.8 (sismalp local magnitude) Laffrey event (2005/10/01) is shown by the red star and the location of the Montbonnot site by the yellow triangle. The epicentral distance is about 25 km. Right: low-pass ($\leq$ 2 Hz) filtered time series of ground velocity recorded by two collocated instruments at the Montbonnot site. The red trace corresponds to the time integration of the signal recorded by an accelerometer operating in triggered mode, and the black to the signal recorded by a broad-band velocimeter with continuous acquisition.

My interest in the validation work on the Grenoble valley started within the curse of the SISMOVALP European project and during the organization of the ESG 2006 symposium (see section II.2.2.1). The first motivation to compare observed and synthetic ground motions in the Grenoble valley is obviously related to complex site effects. The basic question was to know whether 3D simulations accounting for (i) the geometrical complexity of the surface and of the bedrock-sediment interface (obtained by inverting gravimetric measurements by Vallon (1999)) and (ii) a simple velocity model for the post-glacial sediments in the valley, were able to reproduce the level of amplification and the characteristics of recorded ground motions. In particular, one local event [8] recorded by a dense temporary velocimetric array deployed in 2005 (Cornou et al. 2009) shows unexpected duration of ground motion (see Figure II.11). The duration of low-frequency ($\leq$ 2 Hz) ground velocity is such that the decay of energy was not captured by the permanent accelerometers which were not operating in continuous mode at that time. Thank to the deployment of the temporary array of velocimeters, the low-frequency duration recorded at the Montbonnot site was shown to exceed 80 s, quite a large value for such weak (local magnitude M $\simeq$ 3), local (epicentral distance D $\simeq$ 25 km) event. The comparison with the ground velocity computed with the spectral element method (Chaljub 2009) using the ESG2006 propagation model shows a spectacular difference (see Figure II.12): while the amplitude of the computed ground velocity is comparable to the observed one, there is almost one order of magnitude between the respective durations! The severe underestimation of duration in the synthetics stems from the definition of the absorption used in the ESG2006 model. The shear quality factor was indeed assumed to be constant with depth and frequency. Its value, $Q_S = 20$, was taken to be half the Q_P value found by Cornou (2002) when analyzing the amplitude of explosive shots recorded at the Montbonnot site when the borehole was drilled (those crosshole measures, although done for P waves at much higher frequency [20 Hz] showed no dependence of Q_P with depth).

In order to reconcile the synthetic and observed durations, a few numerical experiments were

8. which was used as the weak event W2 in the ESG2006 "benchmark".

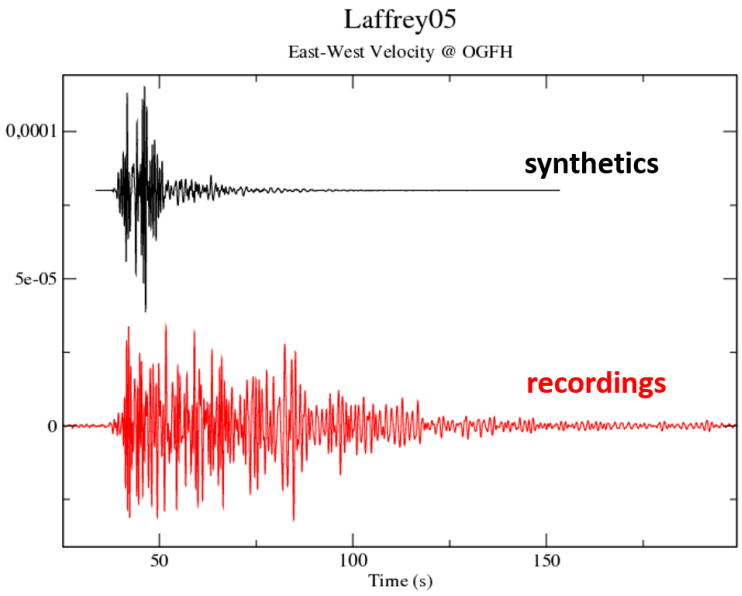

Figure II.12. Comparison of observed (red) and synthetic (black) EW component of ground velocity at the Montbonnot surface site. Both signals have been band-pass filtered between 0.5 Hz and 1.5 Hz.

performed, either consisting in increasing the shear quality factor with depth, or decreasing the shear wave velocity in the shallow part of the valley. Both effects are indeed expected to lengthen duration, either by decreasing the amplitude decay of late arrivals, in particular local surface waves, or by slowing them down. The effect of decreasing the absorption at depth is shown in Figure II.13. Setting the Q_S value to 80 for depth larger than 50 m is shown to increase the duration of the synthetics by a factor 3-4; the observed duration can be reproduced for deep (larger than 50 m) Q_S values reaching 200. Those values of the transition depth (H=50m) and of the deep Q_S values may seem quite unrealistic, but in fact there is a trade-off between those two quantities: considering for example a shallower transition depth (H=20m) and a lower deep Q_S value (100) also allows to match the observed duration. This suggests that the fundamental mode of local surface waves (of Love and Rayleigh type) diffracted off the valley edges may contribute significantly to the duration in the synthetics, but the composition of the wavefield was not investigated further at that time.

The last series of numerical experiments consisted in changing the shallower velocity values. One result is shown in Figure II.14. It corresponds to the case where a low-velocity layer is added to one of the previous models that already reproduced the observed duration. Instead of using the ESG2006 V_S model (which starts with a surface value of 300 m.s^{-1} and decays as the square root of depth), a constant V_S value of 200 m.s^{-1} is set in the first 50 m of the subsurface. Contrary to what could be expected, the overall duration is not strongly affected by this severe change of the velocity model. A strong amplification (corresponding to the fundamental resonance [at 1 Hz] of the additional low-velocity layer) is clearly seen in the first seconds of the signal, but it does not contribute significantly to the lengthening of ground motion duration. Those results suggests that local surface waves contribute the most to the lengthening of GM duration, and that there is a trade-off for those waves between the velocity and absorption values. In the case where a low-velocity layer is added to the model, the fundamental mode of surface waves is trapped into the layer and therefore damped more efficiently. The duration in this case is probably controlled by surface wave overtones, which are sensitive to the deeper, less attenuating parts of the valley. This effect, which can only be suggested here, is analyzed in more detail for the valley of Mexico in section II.3.2.2, p. 32.

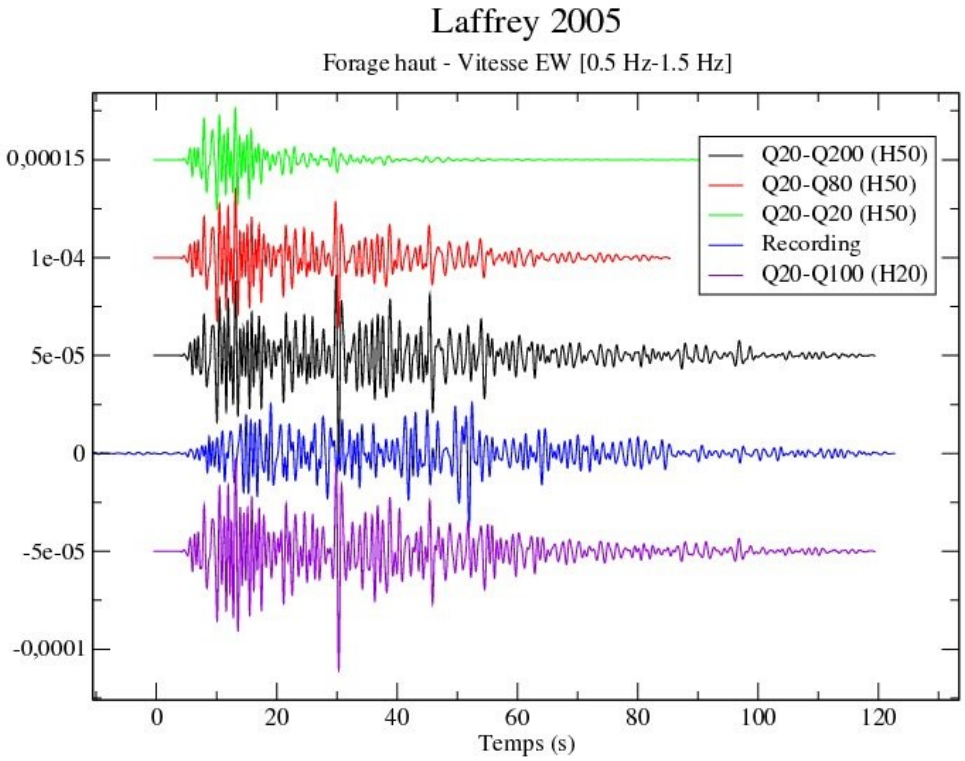

Figure II.13. EW component of ground velocity at the Montbonnot surface site for different models of attenuation in the valley. The recorded motion is the blue trace. The green trace corresponds to the black trace in Figure II.12. The red and black traces are obtained by increasing the Q_S value for depth larger than 50 m, to $Q_S = 80$ and $Q_S = 200$, respectively. The last, purple, trace corresponds to the results obtained for an increase of $Q_S = 100$ for depth larger than 20 m.

Those preliminary (and still unpublished) results illustrate the difficulty of the validation process when applied to realistic frequencies for which the parameters that control the EGM characteristics are either poorly constrained or known with a spatial resolution much lower than what would be needed. They were also characteristic of the more and more commonly faced situation where the limiting factor, that prevents to deepen our understanding of EGM through numerical experiments, is not related to available computational resources (the calculations presented here were not even challenging 10 years ago) but rather to the lack of knowledge of the input parameters needed to feed the numerical simulation codes. Much efforts have been devoted since that time to characterize the Grenoble valley model, in particular to map the shear velocity fluctuations in the shallower part (first tens of meters) of the valley, shaped by the complex river dynamics history. They should make possible in the next years to revisit the questions that were addressed in this section. In particular, explaining the duration of EGM in the Grenoble valley would require to analyze more systematically the largest possible set of earthquake recordings, to quantify the duration of EGM and the lengthening of duration with respect to outcrop and downhole references, to evaluate the influence of shallow heterogeneities inside the valley, as well as the importance of scattering outside of the valley, and to test possible correlations between shear wave velocities and quality factors (as a first step before to be able to map the absorption in the valley).

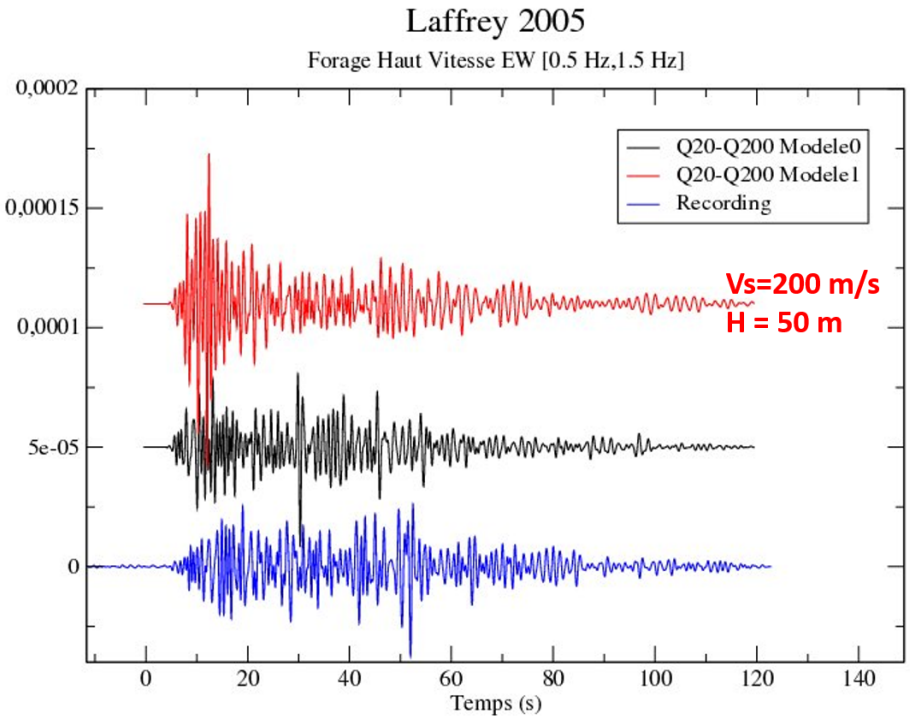

Figure II.14. EW component of ground velocity at the Montbonnot surface site for different velocity models in the valley. The recorded motion is the blue trace. The black trace is the same as the black trace in Figure II.13. The red trace is obtained after adding a 50 m thick low velocity layer to the model used to produce the black trace.

II.3.2.2 Mexico basin

The large damages which affected the city of Mexico during the 1985 Michoacán earthquake and the related human losses will remain in the seismological history as a dramatic evidence of the importance of local site effects. Many studies were conducted by the seismological and engineering communities to properly understand how the source, path and site effects shaped the particular EGM in the valley of Mexico, resulting in formidable amplifications in some frequency bands (reaching 500 around 0.3 Hz and 0.5 Hz) and huge durations (more than 3 minutes reported in the ancient lake-bed zone where the largest damages occurred). Despite those numerous contributions, the origin and physical causes of the duration of EGM in the valley of Mexico is still debated, and none of the many published studies succeeded to model the recorded durations. The main reason for the lack of consensus is certainly related to the challenge of modeling the source process in the subduction zone, the propagation effects along such a long path and such extreme site effects. Even the studies focusing only on site effects provided a very scattered set of estimations of the local contribution to the lengthening of duration of EGM.

As any seismologist working to understand site effects, my interest for the Mexico-Michóacan earthquake of 1985 had been triggered for a long time. But it is only through a collaboration with Víctor Cruz-Atienza and Josué Tago at UNAM and Jean Virieux in Grenoble, through the development of the viscoelastic part of their Discontinuous Galerkin code, that we decided to revisit the subject based upon 3D numerical experiments. The results of this validation work are briefly summarized hereafter, the full article reporting the study can be found in section IV.3 p. 240.

The main motivation of the study is to estimate the contribution of local site effects to the duration of EGM in the valley of Mexico through (i) the analysis of the recordings of a local earthquake by an array of broadband velocimeters recently deployed in the valley, and (ii) the design of a 3D model of the valley which allows numerical simulations of EGM for frequencies up to 1 Hz. The setting of the study is recalled in Figure II.15. The figure features the sediment thicknesses in the valley, as derived from extensive H/V measurements, the location of the epicenter of a local, shallow (4 km depth) M3.4 event that occurred in December of 2014, the locations of the array of broadband velocimeters and of instrumented boreholes which were used to measure the amplitude decay with depth of late, surface wave arrivals.

Despite the large size of the model and the extreme mechanical properties in the lake-bed zone of the valley (see the bottom Table in Figure II.15) the 3D simulation of EGM in the valley of Mexico for local events represents an affordable numerical effort for frequencies less than 1 Hz, once the access to typical university computational resources is granted [9].

A key result of the article is shown in Figure II.16, which compares observed ground velocities recorded for a local, shallow event to their synthetic counterparts. First, the recordings show large durations in the lake-bed zone, with harmonic beating in the long coda around 0.3 Hz that was thought to be typical of subduction events. Second, unlike previous 2D simulations which discarded the excitation of local surface waves to explain the duration in the valley, the 3D simulations succeed in predicting the observed EGM duration.

Furthermore, by comparing the average amplitude decay with depth of the late arrivals responsible for the large duration around 0.3 Hz and 0.5 Hz, it is clearly shown (see Figure II.17) that in the presence of attenuation, the long lasting seismic energy is systematically transported in the basin by higher modes of surface waves, as suggested by Shapiro et al. (2001). The fundamental mode of Rayleigh and Love surface waves, when it is excited, is systematically damped by the very high absorption in the first clay layers of the lake-bed zone. The global patterns of average amplification and lengthening of duration are shown in Figures II.17-b and II.17-d. The amplification pattern is quite complex and shows two ring-like zones of large amplification, located at the edges of the

9. Each viscoelastic simulation performed in the study required 24 hours of elapsed time on 512 modern CPU cores with at least 2Gb of RAM each.

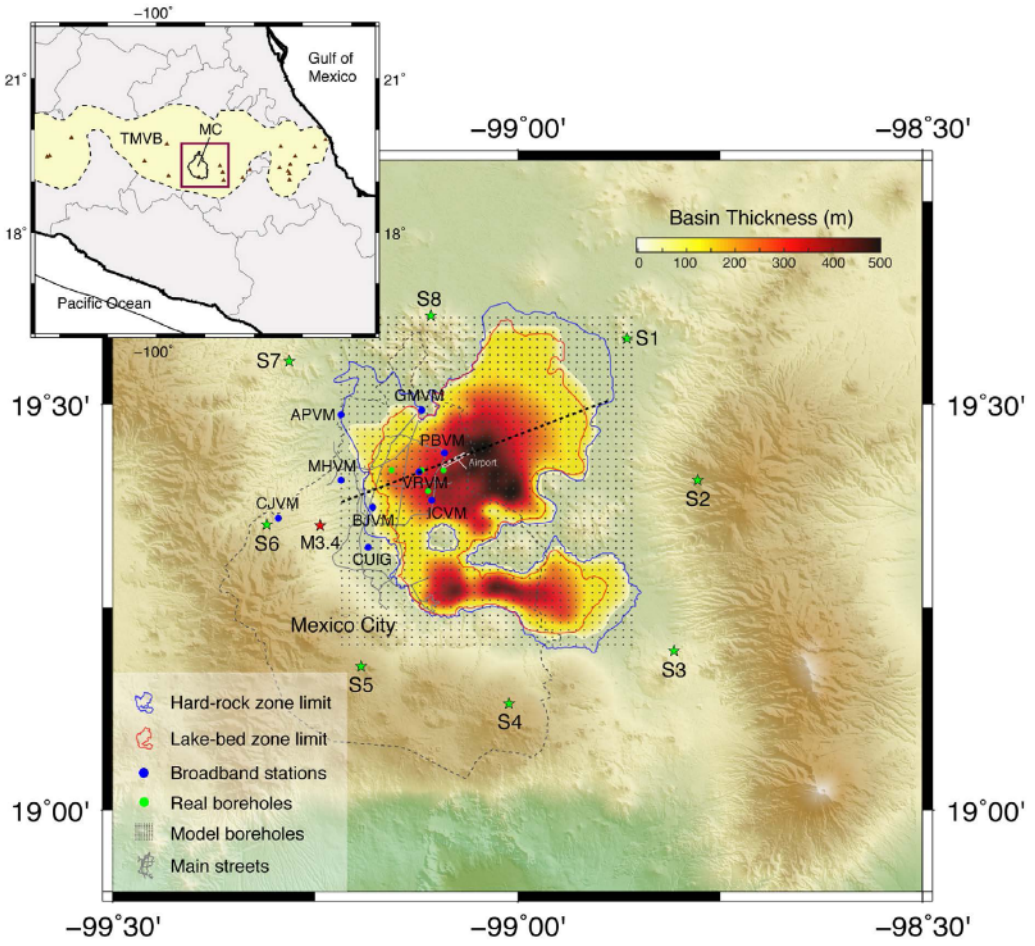

H (km)	Vp (km/s)	Vs (km/s)	Rho (gr/cm³)	Qp	Qs
0.03	0.8	0.05	2.0	30.0	15.0
0.02	1.2	0.1	2.0	60.0	30.0
0.25	2.0	0.4	2.05	80.0	40.0
0.25*	2.5	0.8	2.05	160.0	80.0
1.42*	2.70	1.56	2.20	312.0	156.0

Figure II.15. Topographic setting of Mexico City and the valley of Mexico. The red star is the local M3.4 event analyzed in the article and the green stars correspond to the locations of vertical forces applied at the free surface in the 3D simulations. The values of velocity, mass density and attenuation used in the model are given in the Table. After Cruz-Atienza et al. (2016).

external basin and at those of the deeper basin. Those ring-like, or belt-like, patterns probably correspond to zones where surface waves overtones interfere with incoming body waves, a kind of generalization of the physical process proposed by Kawase (1996) to explain the damage distribution caused by the 1995 Kobe earthquake. The interferences would also explain the general trend of anti-correlation observed between the amplification and lengthening of duration maps.

Finally, the reason why those 3D simulations succeed in reproducing the duration of EGM where previous 2D simulations failed is, I believe, due to the combined effect of (i) accounting for a more realistic basin geometry and (ii) considering shallow and surface sources which excite a richer incoming seismic wavefield than considered in older 2D studies. In particular, it is shown in the article that a non-negligible part of incoming fundamental mode of surface waves gets converted (transduced) into local surface waves overtones propagating in the basin. In the case of distant subduction earthquakes, which generate a lot of surface waves and crustal phases towards the valley of Mexico, this conversion effect is also expected to occur and to favor both amplification and lengthening of duration into the basin.

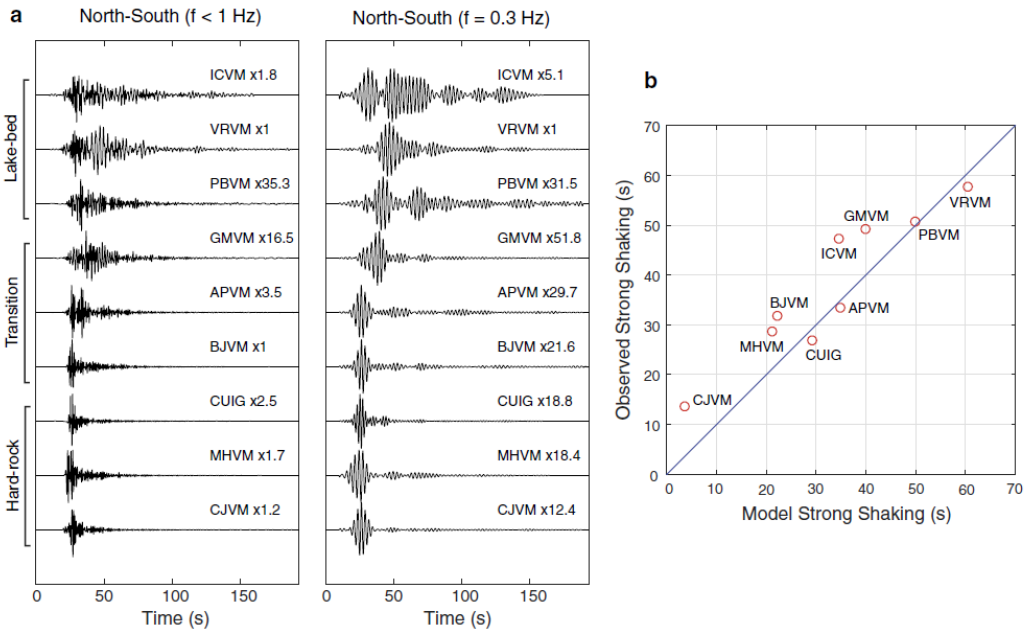

Figure II.16. Left: observed horizontal ground velocity filtered in different frequency bands for the M3.4 event which epicentre is shown in Figure II.15. Right: observed Vs simulated durations of the strong shaking phase for frequencies below 1 Hz. After Cruz-Atienza et al. (2016).

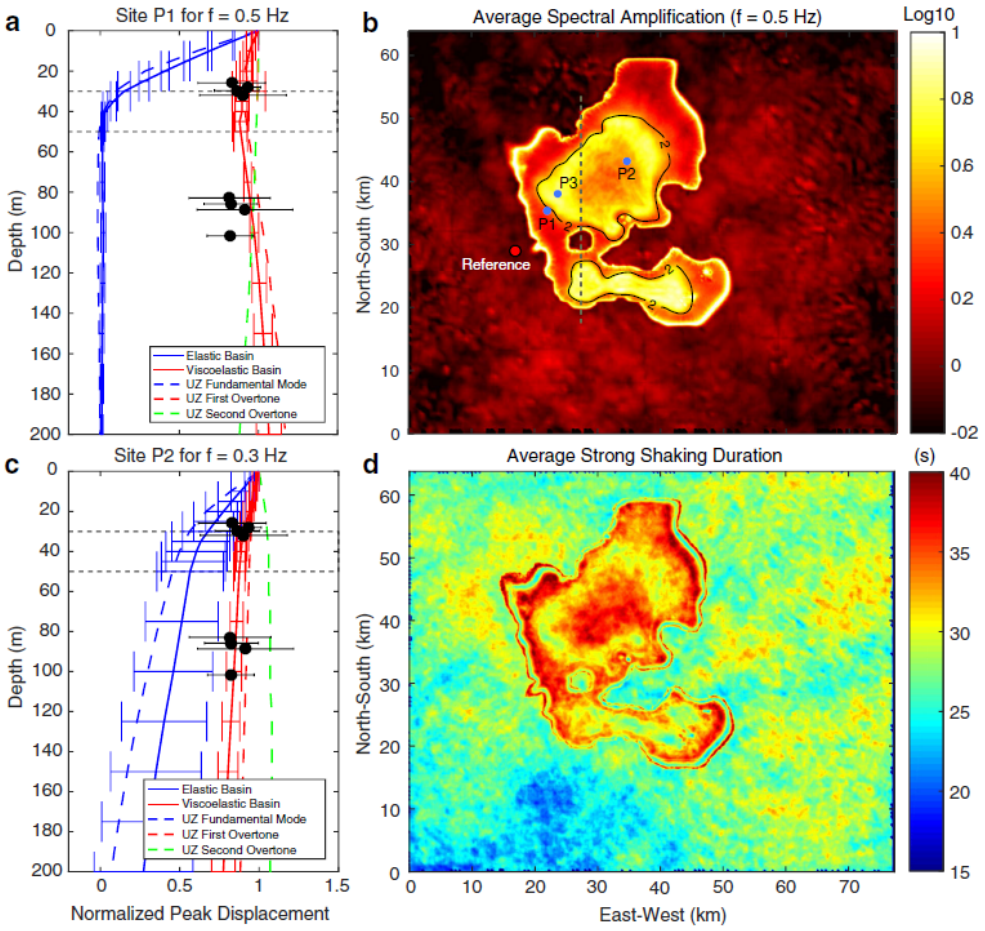

Figure II.17. **(a,c)** Comparison between observed (black dots) and average synthetic eigenfunctions (elastic in blue, viscoelastic in red) at two sites of interest in the basin and two different frequencies. **(b)** Average horizontal Fourier amplification at 0.5 Hz for the set of 8 surface forces. **(d)** Average strong shaking duration below 1 Hz for the set of 8 surface forces. After Cruz-Atienza et al. (2016).

II.3.2.3 Bagnères de Bigorre valley

The French Pyrenees are among the most seismically active regions of the, overall moderately active, french metropolitan area, with numerous destructive historical earthquakes in the central part of the range during the last centuries. The active zone being located "in the backyard" of our colleagues from the Toulouse Observatory, their enthusiastic leader, A. Souriau, easily convinced a group of young researchers working on seismic risk to join them and apply all available methods to estimate the seismic hazard in the small valley surrounding the city of Bagnères-de-Bigorre.

The idea was to deploy a seismological network for two years, to analyze the recordings of local earthquakes in order to track local site effects, then to apply and combine a series of characterization (H/V ratios and ellipticity of Rayleigh waves from microtremors or earthquake recordings, MASW active measurements) and prediction methods (among which 3D numerical simulation) to model the observations. The article presenting the obtained results can be found p. 192 in section IV.3. I hereafter summarize my contribution, related to 3D numerical simulation, to this study.

The challenge for numerical simulation, again, was not related to the size of the required computational resources, but to the level of knowledge on the substructure of the valley, which, using Bayesian inversion nomenclature, would probably correspond to the state of null a priori information. Nevertheless, a simple 3D model of the valley was elaborated: the basin structure was defined by a single layer with 150 m thickness, the contours of which were chosen based on local elevation and slope of the surface. A constant shear wave velocity, $V_S = 600$ m. s^{-1} was used in the layer, resulting in a fundamental resonance frequency of 1 Hz, consistent with the observed values. The seismic response of this model, computed up to 8 Hz and characterized by the peak ground acceleration (PGA), to a vertically incident, plane, shear wave with different polarization is shown in Figure II.18. The effects of surface topography are clearly identified: mountain ranges with east-west (resp. north-south) orientation get amplified when the polarization of the incoming plane wave is along the north-south (resp. east-west) direction. When the model of the valley is considered, the overall level of PGA is increased within the basin, the main amplifications being located close to the basin edges. This is a clear evidence of the so-called "basin-edge effect", as identified by Kawase (1996) and due to the interference between the incoming shear body wave and the surface waves diffracted off the basin edges. Given the particular orientation of the Bagnères-de-Bigorre valley (mainly north-south), and the nature of the interfering surface waves (Rayleigh or Love) following the polarization of the incoming plane wave, the effect occurs at different distances from the basin's edges. Another interesting pattern to note is the apparent de-amplification just outside of the valley, close to the edges of the basin, which is caused by a shadowing effect by the basin. This is clearly seen on the individual traces shown in Figure II.19. This pattern was also observed in the recorded and simulated response of the basin to a real event located 15 km southeast of the valley, as shown in Figure II.20 (in this case the shadow effect is expected to be even more pronounced close to the western side of the valley, given the southeastern azimuth of incoming seismic energy). Finally, the simulations were useful to estimate the effect of surface topography at the rock station BBAR. The simulated effect was indeed shown to be much lower than observed, suggesting a local complex velocity structure beneath that station, preventing it to be used as reference for the estimation of site effects in the valley.

Overall, and despite the interest of the study, the conclusions of the Bagnères-de-Bigorre experience as to the contribution of numerical simulation to better understand EGM were quite limited because of the sparsity of available earthquake recordings and the low level of knowledge of the geometrical and mechanical properties of the site.

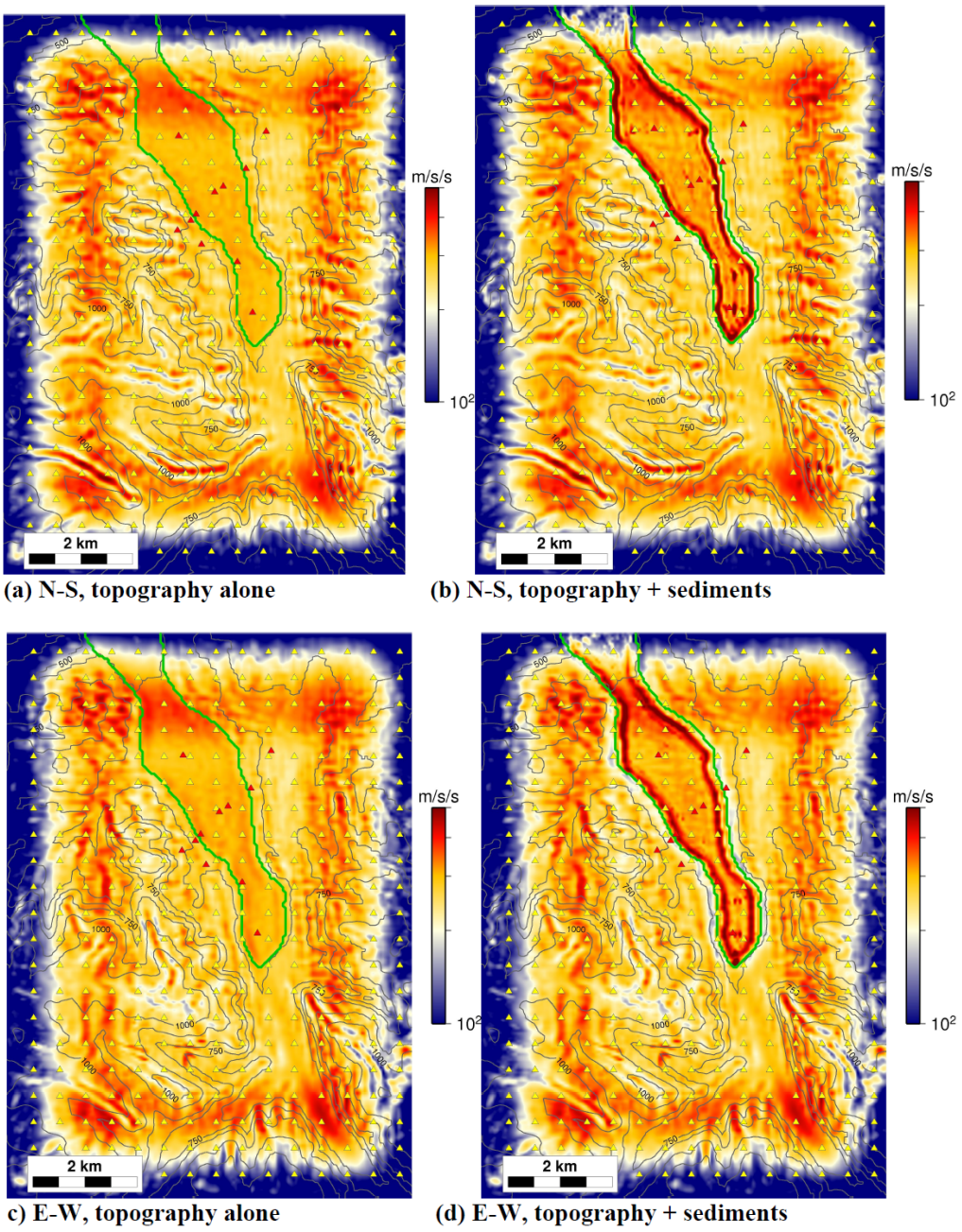

Figure II.18. Maps of peak ground acceleration computed for a plane, vertically incident shear wave beneath the Bagnères-de-Bigorre valley. The linear viscoelastic calculations include either the sole effect of surface topography (**a,c**), or the combined effect of surface topography and of a sediment filled basin (**b,d**). The incident plane wave is polarized either along the north-south (**a,b**) or east-west (**c,d**) direction. The color scale is arbitrary. After Souriau et al. (2011).

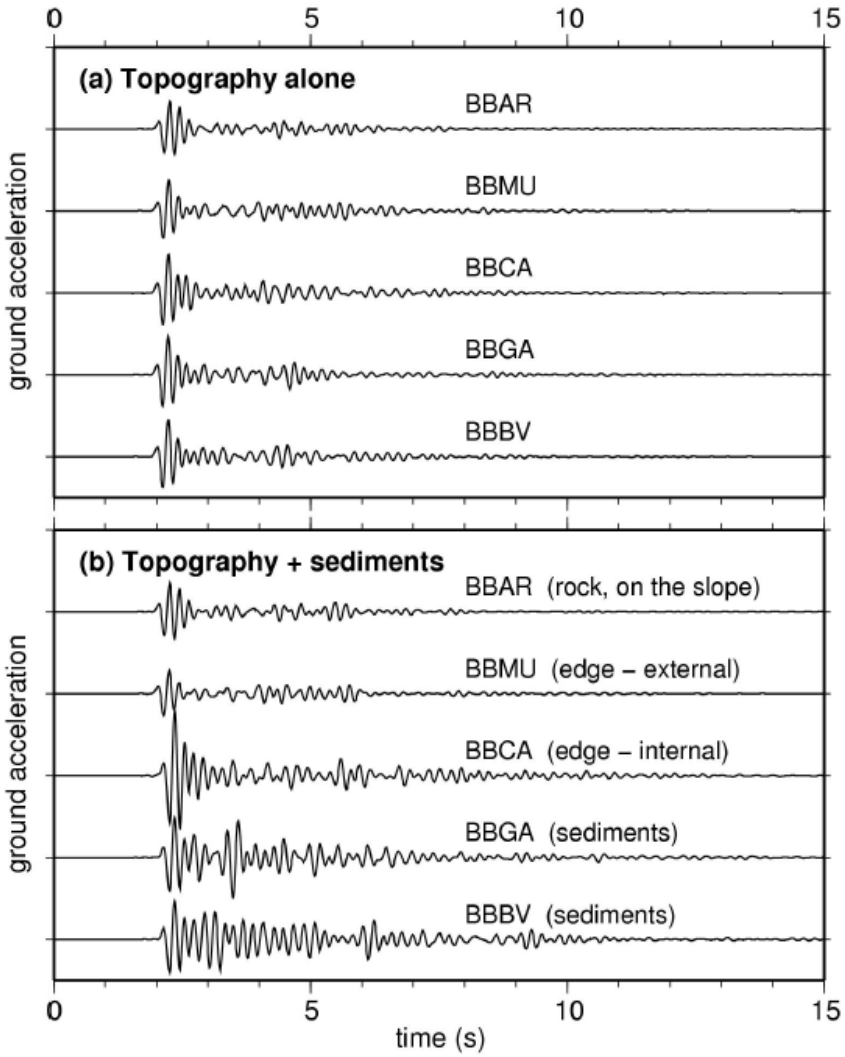

Figure II.19. Synthetic ground accelerations computed for a vertically incident plane wave with north-south polarization at a few stations which locations are indicated between parentheses. The calculations account for the sole effect of surface topography (**a**), or the combined effect of surface topography and of a sediment filled basin (**b**). After Souriau et al. (2011).

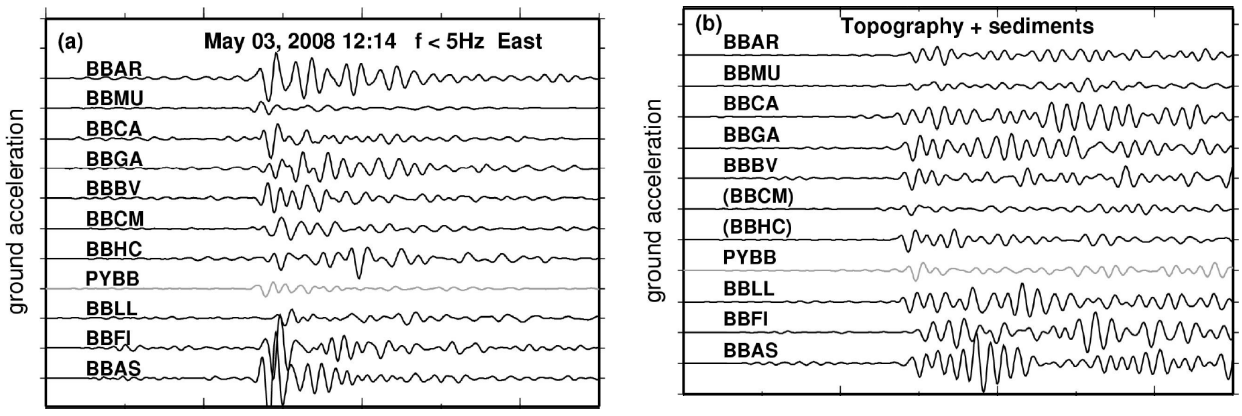

Figure II.20. Comparison of low-pass filtered ($f \leq 5$ Hz) observed (**a**) and synthetic (**b**) ground accelerations for a local M3.9 event located about 15 km from the centre of the valley. The total size of the time window is 7 s. After Souriau et al. (2011).

II.3.2.4 Mygdonian basin

Most of the previous studies only partially addressed the different steps of the validation process, as defined in section II.3.1. In particular, the evaluation of the differences between observed and simulated EGM was often restricted to visual inspection, and the origin of the misfits was, at best, only conjectured and never quantified. To go beyond those necessary but frustrating experiences, the choice of an optimal site – in terms of level of seismicity, quantity and quality of earthquake recordings and level of knowledge of the propagation medium between sources and stations – was mandatory. In the course of the Cashima project (see section II.2.2.2, p. 20), the Euroseistest site, in the central part of the Mygdonian basin, close to Thessaloniki, was elected as the best, among European sites for validation purpose.

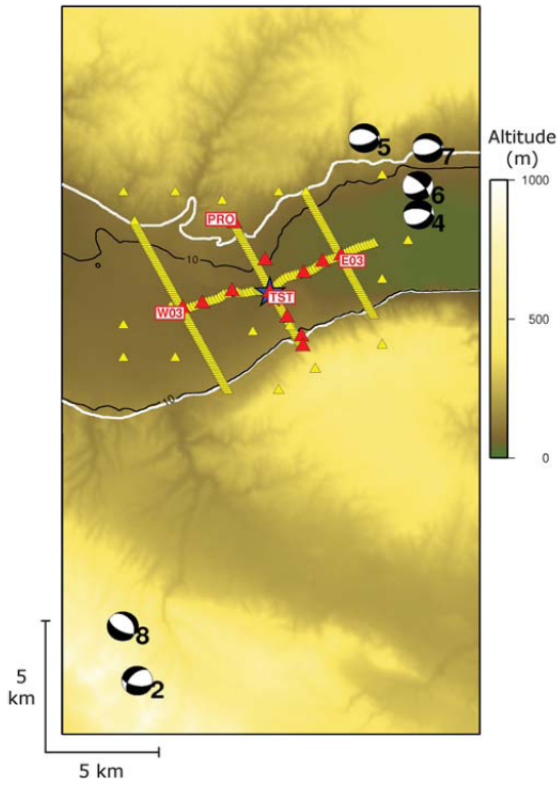

Figure II.21. Surface map of the central part of the Mygdonian basin, showing the accelerometric stations of the Euroseistest array (red triangles) and the epicentral locations of six local seismic events (beach-balls) which were used for the first stage of the validation process. After Maufroy et al. (2015).

It was therefore chosen as the target of a long-standing validation study, which followed a two-stages evolution: In the first phase, a set of 6 local events (see Figure II.21) was considered and the recordings of those events by the accelerometric stations of the Euroseistest array were compared to numerical predictions in the original 3-layers model of the basin presented in Figure II.6. Second, a new, larger, homogenized velocity model of the Mygdonian basin was built from a reanalysis of available geological, geotechnical and geophysical data and a larger set of 19 events was selected, based on the availability of high-quality accelerometric recordings and reliability of source parameters (focal mechanism and hypocentral location) as shown in Figure II.22. The model construction was leaded by Fabrice Hollender, and the work on sources and recordings was done in collaboration with Anastasia Kiratzi and Zafeiria Roumelioti (Aristotle University) and Nikos Theodoulidis (ITSAK). The results of the first phase were reported by Maufroy et al. (2015) (see section IV.3, p. 219), and those of the second phase by Maufroy et al. (2016) (see section IV.4, p. 312). Some of the most noticeable achievements of this validation study are briefly summarized

in what follows.

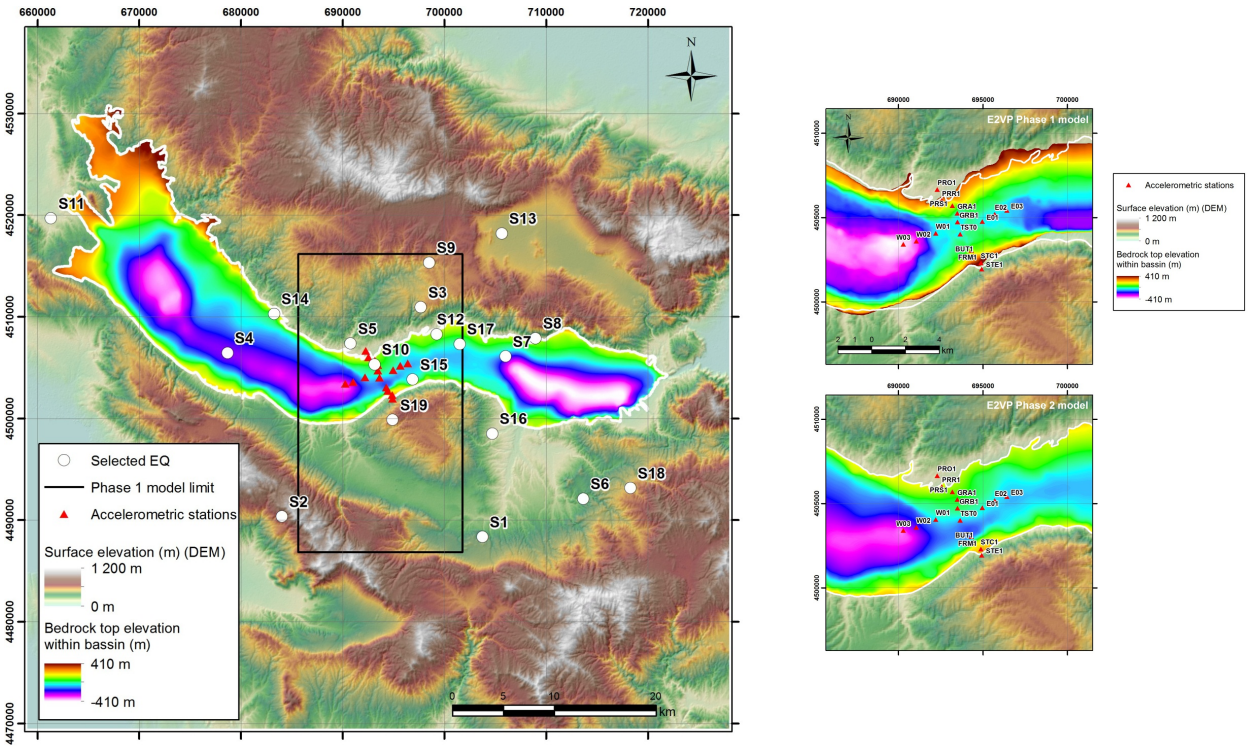

Figure II.22. Left: surface map of the whole model of the Mygdonian basin showing the epicentral locations of the 19 events considered in the second phase of the E2VP validation study. Right: geometrical differences between the velocity models used in the first and second phase of E2VP. After Maufroy et al. (2016).

The validation criteria were based on the selection of 5 ground motion parameters, which were proposed to (and accepted by) a panel of recognized experts in earthquake engineering and engineering seismology. For each of the 5 parameters (the PGA measured below 4 Hz, the spectral accelerations around 2 Hz and around 0.5 Hz, the cumulative absolute velocity, and the relative significant duration), a signed misfit value, measured in percents can be given, as shown in Figure II.23 for one of the 6 events of the first phase. Thank to those criteria, it was possible to quantify the distance between synthetics and observations using a meaningful metric, and to compare this distance to the epistemic uncertainty, i. e. with the distance between synthetics obtained by different numerical methods (see Figure II.24). The overall conclusion follows the expectation: the distance between synthetics is systematically, and significantly, smaller than the distance between any of the synthetics to the observations. This is certainly the gain of the in-depth verification work done on the synthetics. What is also apparent, and reassuring, is that the most similar numerical predictions also correspond to the smaller distances to the observations (Figure II.24-a).

Once the distance between observations and numerical predictions has been measured, the next challenge is to estimate the relative contributions of the source errors (location, magnitude, focal mechanism) and of the model errors to this distance. A first attempt to identify the source and model contributions is presented in Figures II.24-b and II.24-c, which respectively show the average misfits obtained at the central TST station (which corresponds to the location with the higher level of knowledge of the underground structure in the Mygdonian basin) and the average misfits computed for the most energetic (and hopefully best characterized) event among the 6 considered in the first phase. The misfits are seen to be slightly below the average in both situations, but it was demonstrated later in the second phase that those trends were not statistically robust (Maufroy et al. 2016). In particular, it was shown after relocation that the hypocentre of the most energetic event of the first catalog was in fact poorly known (the hypocentral location error for this local

event was of the same order as the distance to the centre of the Euroseistest array!).

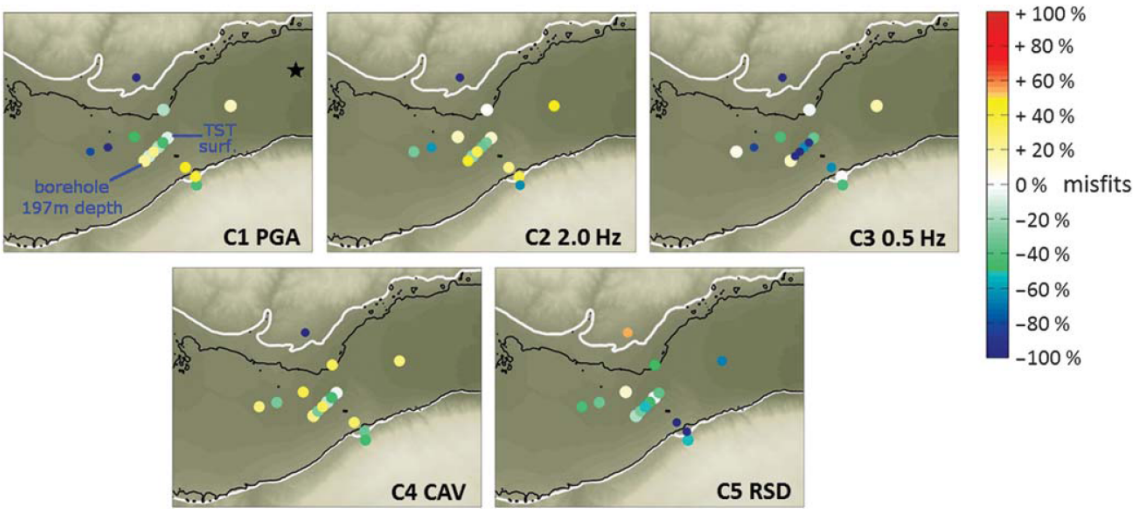

Figure II.23. Values of misfit between synthetics and recordings for one of the six local events (the epicentre of which is indicated by the black star in the top left figure) retained in the first validation phase of E2VP. The misfit values, in percents, are positive (resp. negative) whenever the synthetics overestimate (resp. underestimate) the real values. After Maufroy et al. (2015).

To go one step further and infer the contribution of the model error to the total misfit, one has to minimize the source error. This can be done by quantifying how errors on the source parameters "propagate" to the ground motion parameters (see for example section II.3.3.2), then restricting the validation approach to the recordings that correspond to those sources that minimize the propagation of the error. Another possibility is to compare relative, "source-independent" ground motion parameters. This approach was tested at the central TST station by forming the synthetic transfer function between the downhole and surface receivers and by convolving it with the real input signal at the downhole. The obtained time series, referred to as "hybrid", are shown to provide a better fit than the full synthetics to the observed ground motion parameters, whatever the set of events analyzed and the basin model considered (see Figure II.25-a, and Table 5 in Maufroy et al. (2016)). A closer look at the signed misfit values (Figure II.25-b) indicates that the hybrid synthetics tend to systematically underestimate the observed amplitudes (looking at the parameters C1-C4 which are sensitive to amplitude) and overestimate the observed durations (looking only at parameter C5). This suggests that the basin model considered in the first phase of E2VP tends to underestimate the observed amplification at TST (see also the direct comparison of downhole-to-surface transfer functions in Figure 13 of Maufroy et al. (2015)) and to overestimate the lengthening of duration. The new basin model considered in the second phase was shown to provide a globally better fit of the hybrid synthetics to the observations at TST (see the signed misfits given in Table 5 in Maufroy et al. (2016)), but this time to overestimate both the amplification and the lengthening of duration. Finally, the fact that in both models, the full synthetics are shown to overestimate the observed amplitudes and to underestimate the observed durations respectively suggests that the magnitudes of the local events could be systematically overestimated in the seismic catalogs, and that the level of heterogeneity in the model of the bedrock should be increased in order to produce more scattering along the path from the sources to the site. This last suggestion is also supported by the direct comparison of the duration sensitive parameter C5 at the rock sites of the accelerometric array (see Table 4 in Maufroy et al. (2016)). Those conclusions call for another iteration of the validation process at the Volvi site, but no volunteers have been found yet to perform this time-consuming task.

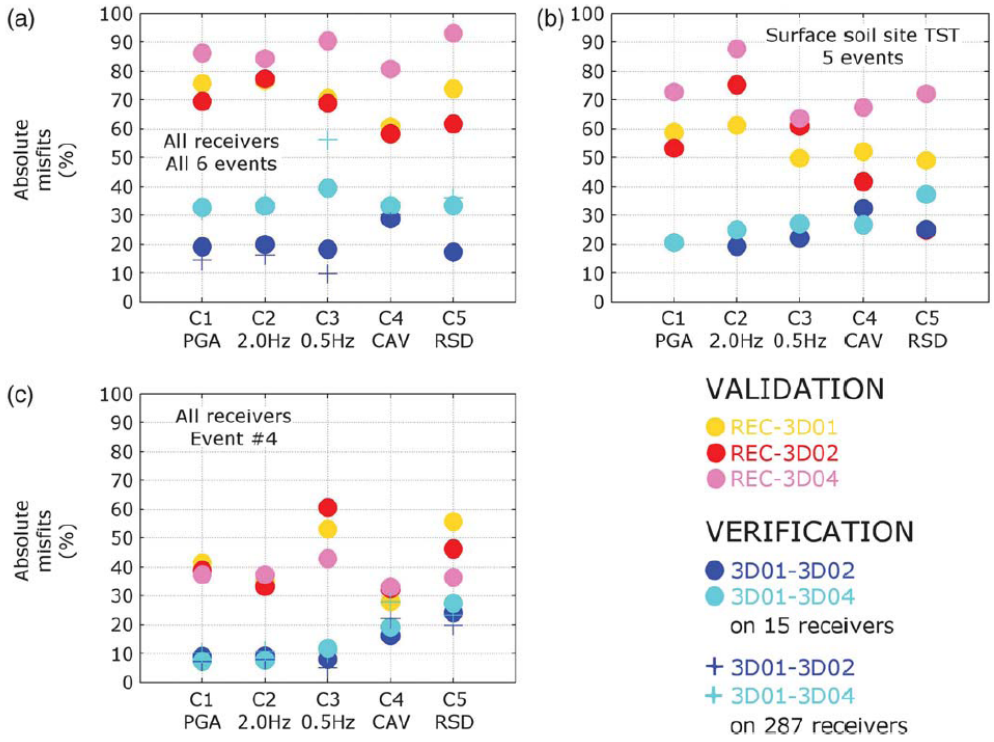

Figure II.24. Comparison of average absolute misfit values between different numerical predictions (blue circles) and between individual predictions and recordings (yellow, red and purple) for different sets of sources and real stations or receivers: **(a)** all events and stations/receivers ; **(b)** all events at the central surface station ; **(c)** one event at all stations/receivers. After Maufroy et al. (2015).

As a final remark, I would like to point out the tremendous amount of work that still needs to be done in order to be able to fit observed ground motions in realistic configurations and for frequencies of seismological and engineering interest. This is illustrated by the global, averaged over all events, values of misfits reported in Table 5 of Maufroy et al. (2016) and reproduced in Figure II.26, which are of the order of 100 %. But this somehow disappointing statement must be balanced by the quite good overall fit to the downhole-to-surface transfer function at the centre of the Mygdonian basin. It should also not prevent to use numerical simulation to better understand the origin of such differences to the observed EGM, as this will be illustrated in the next sections.

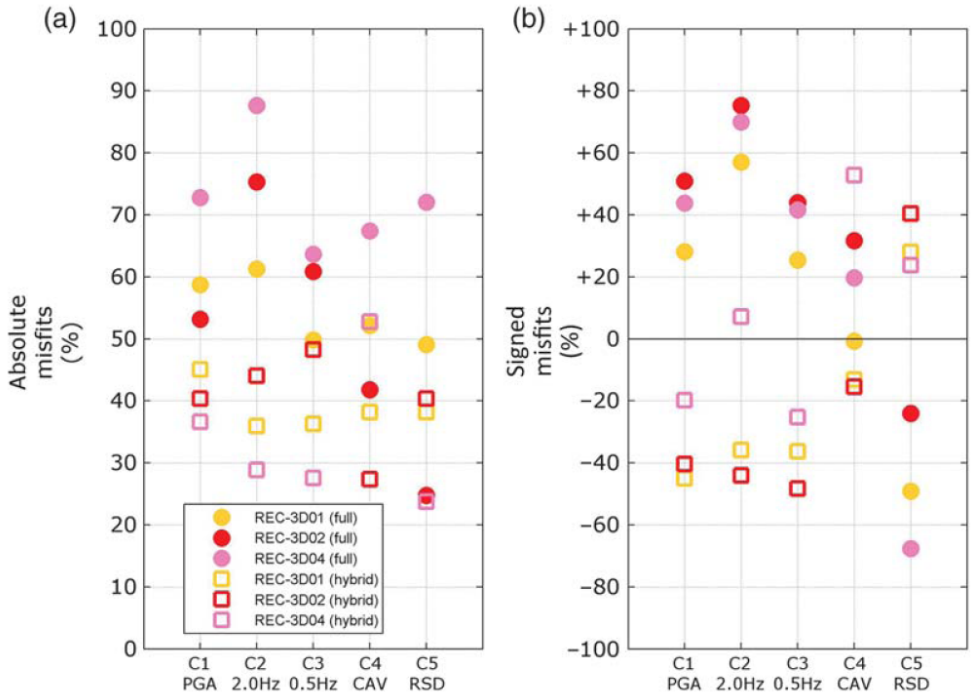

Figure II.25. Comparison of averaged absolute (left) and signed (right) misfit values for the full (circles) and hybrid (squares) synthetics. After Maufroy et al. (2015).

	FULL SYN. C1	HYBRIDS C1	FULL SYN. C2	HYBRIDS C2	FULL SYN. C3	HYBRIDS C3	FULL SYN. C4	HYBRIDS C4	FULL SYN. C5	HYBRIDS C5
AVERAGE	173	27	166	29	83	1	132	56	−79	32
AVERAGE without S10 S15	143	19	129	16	45	−22	107	50	−69	27

Figure II.26. Values of horizontal misfits for the five engineering parameters C1-C5 between the actual recordings at central soil site TST0 and their numerical (full or hybrid) predictions. The AVERAGE values correspond to an average over the 16 events that were recorded both at TST0 (surface) and TST5 (downhole). Adapted from Maufroy et al. (2015).

II.3.3 Understanding EGM variability

Even though physics-based numerical models have been shown in previous sections to be far from reproducing the observed EGM in realistic configurations and frequency bands, they do provide a powerful experimental framework to better understand and quantify the variability of EGM. Variability of EGM is usually understood in the context of Ground Motion Prediction Equations (GMPE) as the uncertainty related to the empirical prediction of a given ground motion intensity parameter obtained by averaging a statistically significant number of earthquake recordings corresponding to close-by values of magnitude and distance to the source. By variability, I understand here the variation of the output EGM that results from the variation of individual components of the physics-based model. This may also be referred to as sensitivity. To assess the uncertainty of the prediction of EGM by a physics-based model is therefore a two-step process: first, the variability (or sensitivity) to the individual components of the model have to be understood and quantified through a deterministic process; and second it has to be "convolved" with the uncertainty, resulting from lack of knowledge or from aleatory variability, of the values of the components of the model.

In what follows, I present a few contributions, either restricted to sensitivity analysis of EGM, or encompassing the estimation of the uncertainty of the prediction of EGM. Those studies are usually the most demanding in terms of computational resources since they require to explore the space of input parameters to the physics-based model, which may be large. However, the computational effort can be minimized when studying the sensitivity of EGM to source parameters. In this case indeed, a single propagation medium is considered and the heavy simulations can be restricted to the computation of its unit response (to a point source or a plane wave), the final results being obtained after a cost-less convolution phase. Whenever Green's functions are required for a small number of receivers and a large number of sources, the use of reciprocity can further reduce the number of computations needed by switching the role of sources and receivers. This is the main reason why source-related variability studies can be performed in three-dimensional realistic configurations, whereas site-related variability studies (which require to vary the propagation media) are usually restricted to 2D geometries.

II.3.3.1 Site-related variability

As stated in the introduction of (Maufroy et al. 2017), the physical mechanisms causing site effects have been known for a long time (see e.g. Bard & Bouchon (1980a,b) and Kawase (2003) for a review): impedance contrasts between soft sediments and stiffer underlying, and possibly outcropping, bedrock cause the amplification and trapping of seismic energy into the soft zones and the excitation of local surface waves at basins' or valleys' edges.

One of the most striking manifestation of site effect is the so-called basin edge effect, as labelled by Kawase (1996), that is, the interference between shear body waves impinging a basin and surface waves diffracted off the basin edges, which causes localized amplification of ground motion and increased ground deformation (Moczo & Bard 1993). This effect has been evoked already in this manuscript to explain the spatial patterns of EGM computed in the Bagnères-de-Bigorre valley and in the Mexico basin. We also studied it numerically during the PhD work of Soline Hallier. In particular, we looked at the influence of the geometry of the basin edge to the location and level of amplification of the interference belt in different frequency bands (see Hallier et al. (2008), p. 270 in section IV.4). We found that the basin edge effect occurred in a wider frequency band than previously reported and that it was enhanced in the case where the edge pends towards the basin, as expected if the edge coincides with a thrust fault (see Figure II.27).

The fact that the geometry of the basin edge plays a non-negligible role in the magnitude of the basin edge effect is not surprising and is related to the influence of the geometry on the efficiency of the conversion of incoming body waves to induced local surface waves. This is apparent in Figure II.28 which was obtained for a 2D canonical model of the central part of the Mygdonian basin,

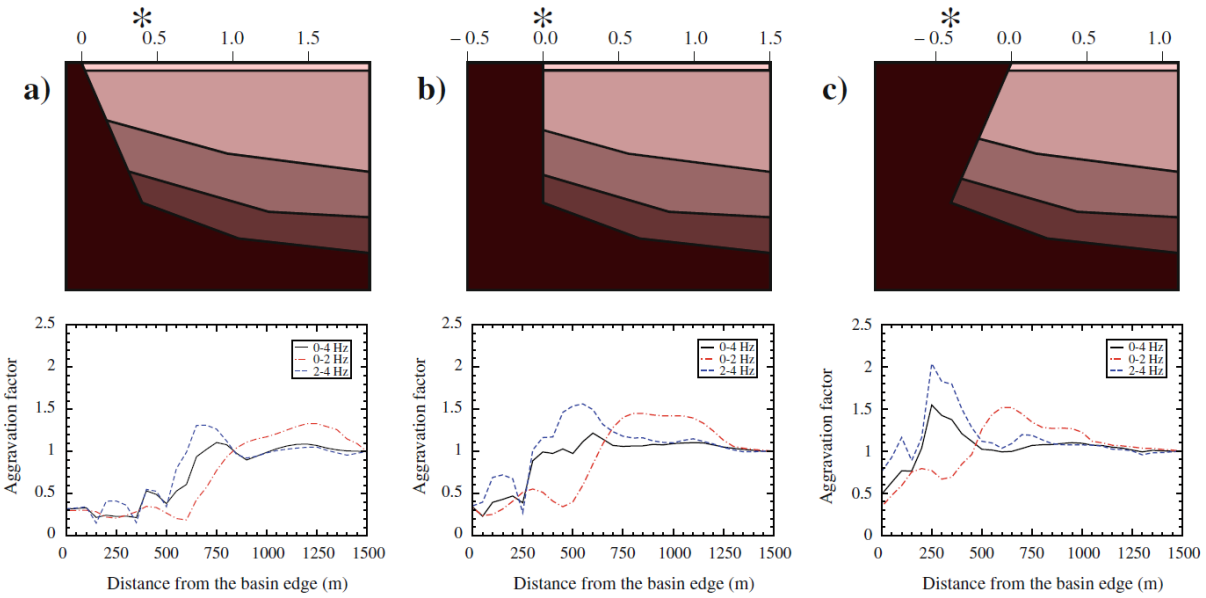

Figure II.27. Aggravation factors, defined as the ratio of peak ground velocity to a reference value corresponding to a station located in the centre of the basin, computed in a model of the Kobe basin for three geometries of the basin edge and different frequency bands. After Hallier et al. (2008).

where the influence of asymmetrical basin edges was studied. The presence of an edge with gentle slope seems to increase the chances for an incoming body wave to reach the grazing incidence that allow the generation of surface waves.

A more comprehensive study aiming at quantifying the sensitivity of EGM to geometrical and mechanical parameters was conducted in the course of the NERA project. The amount of simulations performed and of valley geometrical and mechanical properties is recalled in Figure II.29. Almost 2 thousand calculations of impulse response to a vertically incident plane wave with SH or SV polarization have been performed for frequencies up to 20 Hz and a time window of 60 s. An example of such $P-SV$ calculation for one of the largest valley is shown in Figure II.30. The ground motions (translations and deformations) have been recorded at a large number (between 100 to 400) of receivers per simulation, resulting in one of the largest databank of synthetic results which can be analyzed to better understand the contribution of site effects to EGM. A few results are presented hereafter, but most of the work is still ongoing and unpublished.

The impulse responses were further convolved with a set of real accelerograms extracted from the RESORCE collection (Akkar et al. 2014), and a few ground motion intensity parameters (GMIP) were computed on the obtained time series. The same procedure was applied to 1D synthetics, obtained from the same real accelerograms and from 1D impulse responses computed with the local models below each receiver. Then, the comparison between 1D and 2D synthetics was quantified through 2D/1D aggravation factors (AF) computed from each of the considered GMIP [10]. An example of such comparison is given in Figure II.31. It illustrates a general trend that the AF depend on the GMIP: parameters related to energy (e. g Arias intensity or Cumulative Absolute Velocity) result in larger aggravation values (up to 3-4) than high-frequency parameters (such as PGA, FA, or ARMS [see their definition in the caption of Figure II.31]).

The influence of the geometry of the valley on the AF is found to be significant, as illustrated in Figure II.32. For embanked valleys, the AF are found to be the largest in the centre of the valley

10. The reason to consider 2D/1D AF was motivated by the objective to propose a procedure to account for site effects in the European seismic design code.

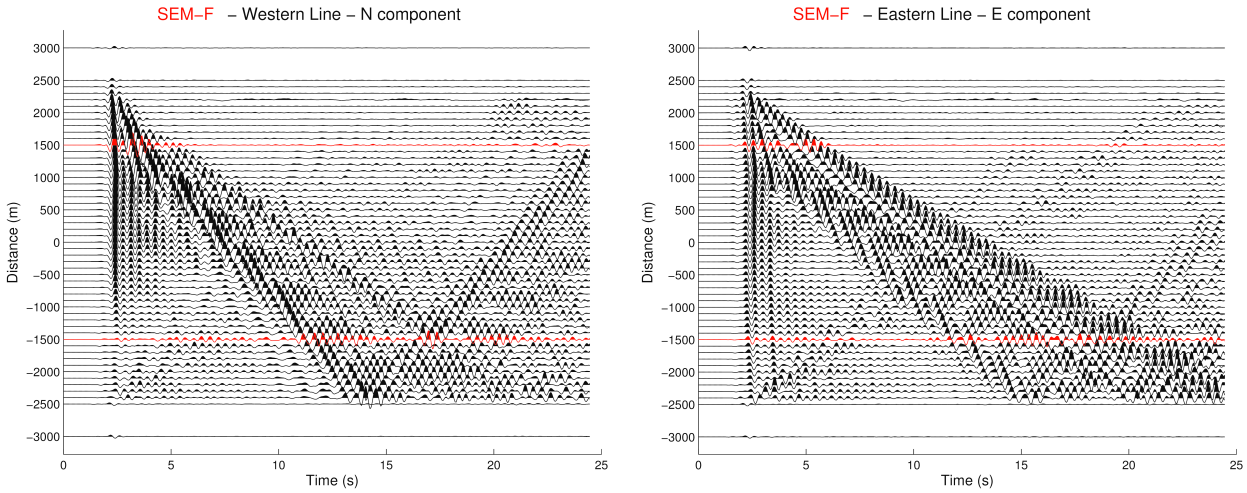

Figure II.28. Seismic sections of horizontal ground velocity computed in a canonical model of the Mygdonian basin with asymmetrical edges: a vertical southern edge and a northern edge with a gentle slope. The northern edge is much more efficient to excite local surface waves, either Rayleigh (left) or Love (right), towards the centre of the basin. After Chaljub et al. (2015).

because of constructive interferences between laterally propagating surface waves diffracted off the two edges. Steep edge slopes show large, but localized effects whereas gentle slopes have significant long-distance effects because of their higher efficiency to diffract local surface waves. It is worth to note that for steep edges, the AF are usually lower than 1 above the edge, because the main effect of the 2D edge is to deflect incoming energy towards the centre of the valley (which results in AF larger than 1 at the beginning of the flat part of the valley), contrary to the 1D case where the energy always propagates vertically.

Geometry of 2D valleys

- Trapezoidal or triangular shape
- Control parameters: H,W,α_1,α_2

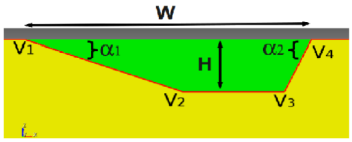

h(m) \ w (km)	0.5	1	2.5	5	10	20
30	0.06	0.03	0.012	-	-	-
60	0.12	0.06	0.024	0.012	-	-
120	0.24	0.12	0.048	0.024	0.012	-
250	0.5	0.25	0.1	0.05	0.025	0.0125
500	-	0.5	0.2	0.1	0.05	0.025
1000	-	-	0.4	0.2	0.1	0.05

27 (H,W) combinations * 6 (α_1,α_2) combinations = 162 geometries
31 with triangular shape, 131 with trapezoidal shape

Mechanical properties

- $VS(z) = VS_0 + (VS_1 - VS_0)\,[(z - z_0)/(z_1 - z_0)]^{0.5}$, z_0=0 m, z_1=1000 m

	1	2	3	4	5	6
VS_0 (m/s)	80	100	120	160	247	434
VS_1 (m/s)	480	700	835	950	1000	1000
VS_{30} (m/s)	125	167	200	250	333	500

162 geometries * 6 velocity models = 972 valleys

Computation of P-SV and SH response to vertically incident plane wave = 1944 simulations in 2D

Figure II.29. Summary of canonical 2D valleys considered in the NERA project. Each valley is characterized by its geometry (defined by the width (W) and height (H) of the valley and by the slopes of its two edges, Left) and by its mechanical parameters (defined by 6 different 1D velocity models, Right). A total of 1944 2D simulations for frequencies up to 20 Hz was performed for vertically incident *SH* and *SV* plane waves.

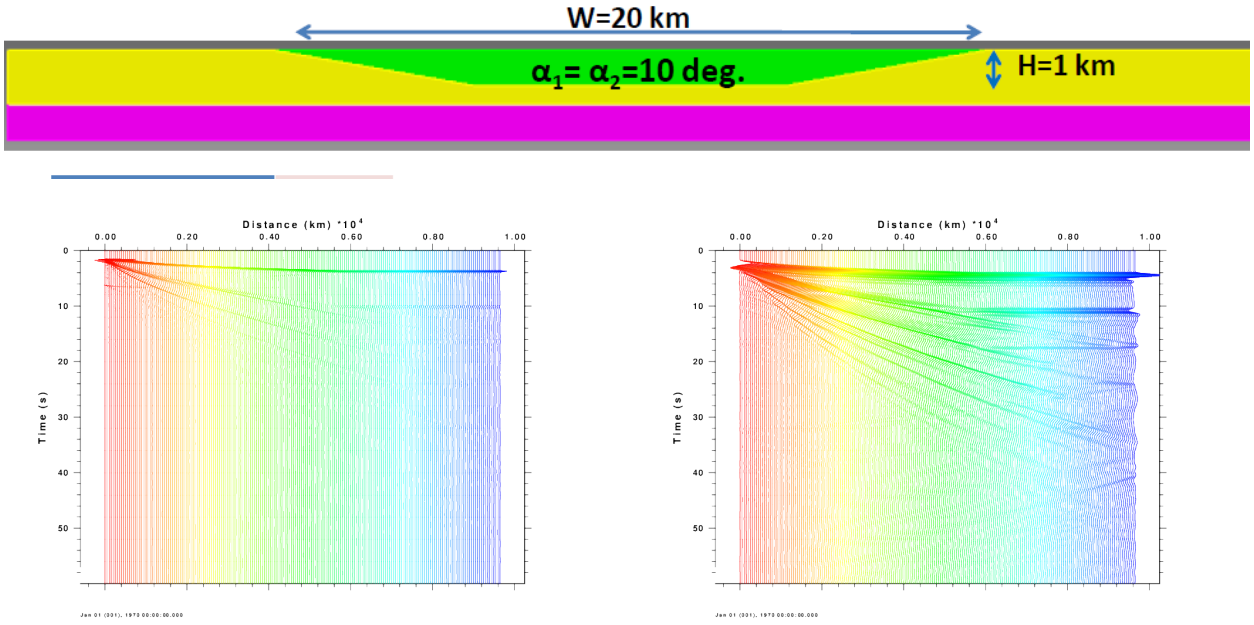

Figure II.30. Example of horizontal ground velocity computed for a large (W=20 km), deep (H=1 km), and soft ($V_{S_{30}}$=125 m/s) valley with gentle edge slope (10°). Left: unfiltered values, Right: filtered values below 1 Hz. The colors refer to the horizontal positions from valley edge (red) to valley centre (blue). The receiver interdistance is 50 m.

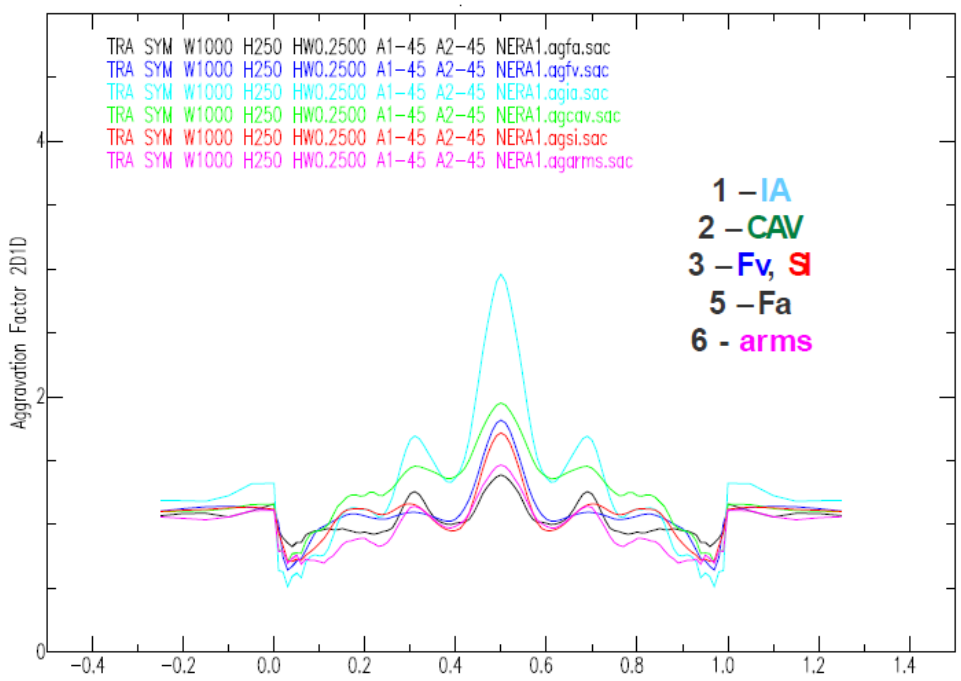

Figure II.31. Example of average aggravation factors computed for one valley model (W=2.5 km, H=250 m, slope=45°, $V_{S_{30}}$=125 m/s) and 6 different ground motion intensity parameters: IA=Arias Intensity, CAV=cumulative average velocity, Fv=intermediate period (1 s) averaged amplification factor, Fa=short period (0.1 s) averaged amplification factor, SI=spectral intensity averaged around 1s, arms=root mean squared acceleration. The horizontal distance is normalized to the valley width.

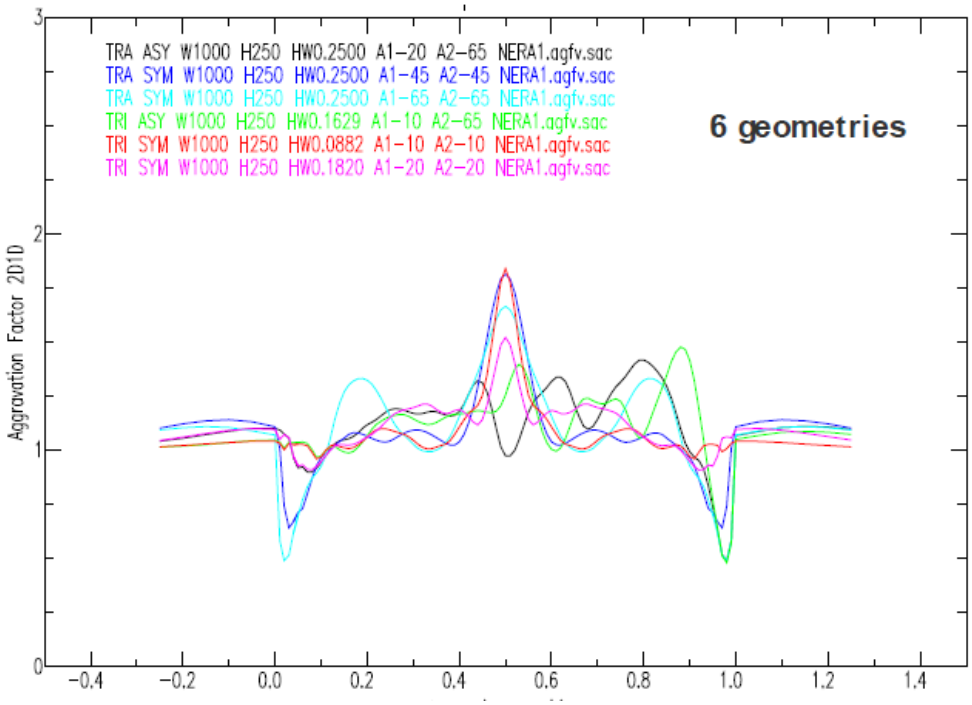

Figure II.32. Effect of the slopes of the edges on the aggravation factor of the average amplification at 1 s, Fv. The valley is defined as: W=1 km, H=250 m, $V_{S_{30}}$=125 m/s. The slopes of the edges take the following values: 10°, 20°, 45°, 65°. Note that some angle combinations correspond to asymmetrical valleys, whence the asymmetry in the results.

II.3.3.2 Source-related variability

Many published studies have been dedicated to the estimation of EGM in the vicinity of extended faults, and have tried to understand how the physical characteristics of the rupture can shape the ground motion. Given the challenge of assessing the parameters that drive the dynamics of the rupture, most of them have adopted a kinematic description of the rupture, decomposing the fault as a collection of sub-faults with constant properties (static slip, slip velocity, rise time). Then, depending on the frequency band considered and on the geometrical and geological complexities of the problem, the Green's functions are computed by methods of increasing computational cost, from discrete wavenumber methods to 3D grid-based methods.

I have contributed marginally to those topics, during the PhD theses of Mathieu Causse and of Afifa Imtiaz. Two articles presenting those contributions (Causse et al. 2009; Imtiaz et al. 2015) can be found in section IV.4, p. 281 and p. 299, respectively. In (Imtiaz et al. 2015), we have shown, from simple 1D Green's functions and available descriptions of past earthquake rupture kinematics, that the rupture type (unilateral or bilateral) could affect significantly the so-called within-event component of ground motion variability for distances up to a few tens of kilometers.

In (Causse et al. 2009), we have combined 3D numerical simulations of the response of the Grenoble valley to the recordings a small (M3) local event (the one presented in Figure II.11, in section II.3.2.1) to produce broad-band (0.1 Hz – 30 Hz) hybrid Green's functions (HGF). Those HGF have been summed according to a sophisticated model of the rupture process, consistent with a classical k^{-2} model of the static slip distribution. The parameters of the rupture model are: the K parameter, which controls the roughness of the static distribution of slip ; the location of the nucleation point Xnuc ; and the rupture velocity, v. The effect of varying those 3 parameters on the resulting ground velocity and acceleration is illustrated in Figure II.33. Finally, the three parameters were given realistic probability density functions which were further sampled in order to obtain the resulting distribution of ground motions for a M5.5 event at the locations where the original small event was recorded. The median (and median $\pm\sigma$) curves of the obtained horizontal acceleration spectra at 9 stations in the Grenoble valley are represented in Figure II.34, together with the corresponding EC8 design spectra. The figure shows that the design spectra are not adapted to the stiff alpine rock and that they can be exceeded in several frequency bands on the sediments.

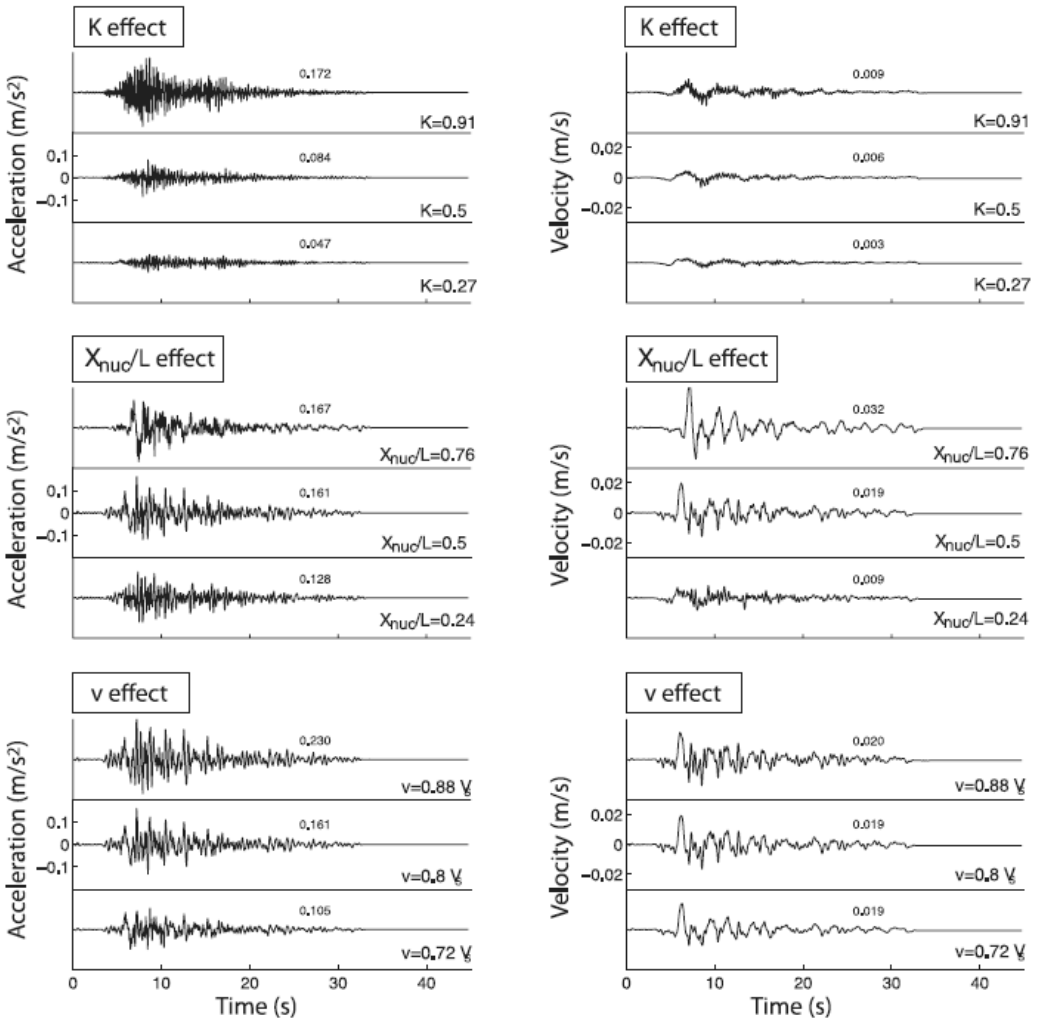

Figure II.33. Sensitivity of ground acceleration (left) and velocity (right) to variations (of $\pm\sigma$) of the three parameters controlling the rupture model: roughness (top), location of the nucleation point (middle) and rupture velocity (bottom). After Causse et al. (2009).

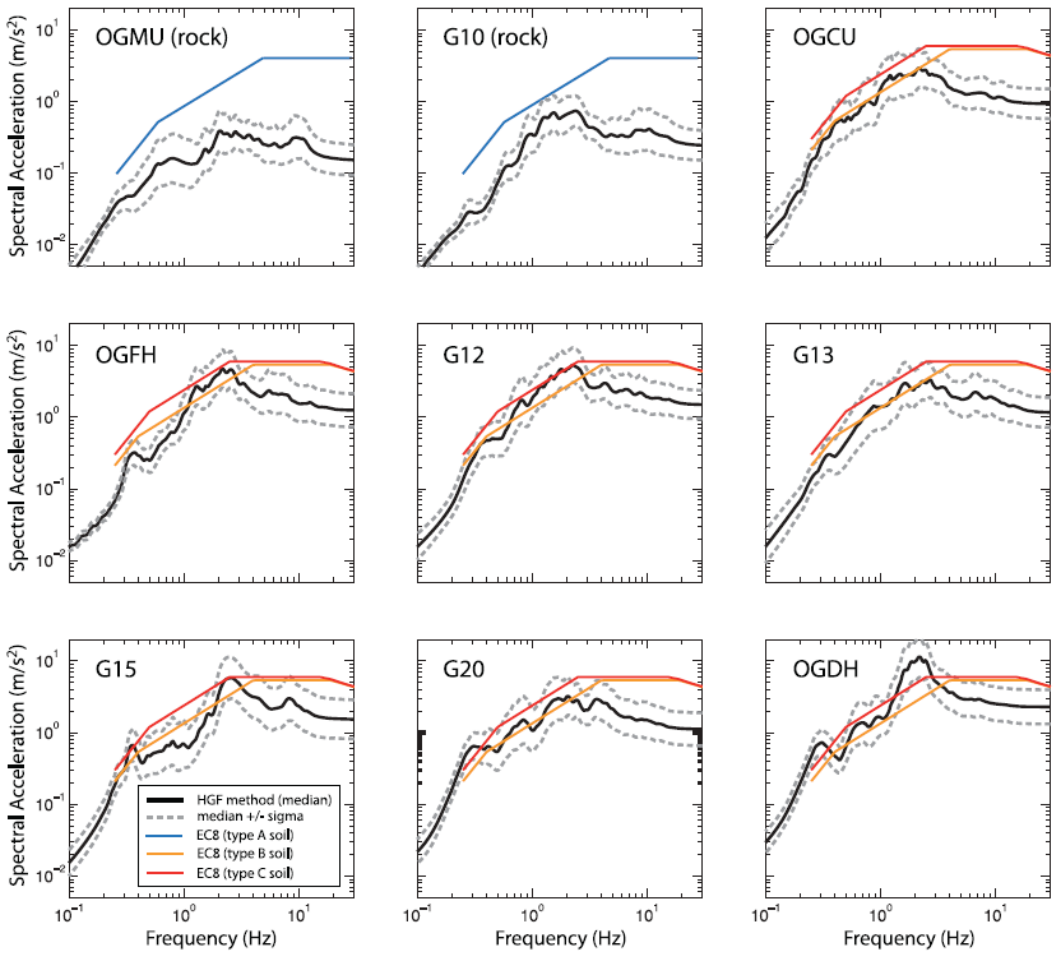

Figure II.34. Comparison of the distribution of EW spectral acceleration to EC8 spectra at 9 stations in the Grenoble valley. After Causse et al. (2009).

In (Maufroy et al. 2017, 2016), we investigated another aspect of source-related variability: the dependence of site response to the location of point-like seismic sources. The target of the study is the Mygdonian basin and the motivation was twofold: (i) investigate the sensitivity of different markers of site response (amplification and lengthening of duration) to available source catalogs, and (ii) better understand and quantify the sensitivity of ground motions to uncertain source parameters.

In order to address those questions, a large databank of Green's functions was constituted between 15 stations of the Euroseistest accelerometric array and three sets of point-like sources: A first set (S1) formed by 16 events (out of the 19 of the validation phase) for which both downhole and surface recordings were available at the central TST station, a second set (S2) where the hypocentral position of each event of set S1 was moved by up to ± two kilometers in (x, y, z) coordinates, resulting in 27 different possible locations within a 4 km edge cubic box, and a third set (S3) consisting of 1260 positions uniformly distributed around the central TST station (see Figure II.35).

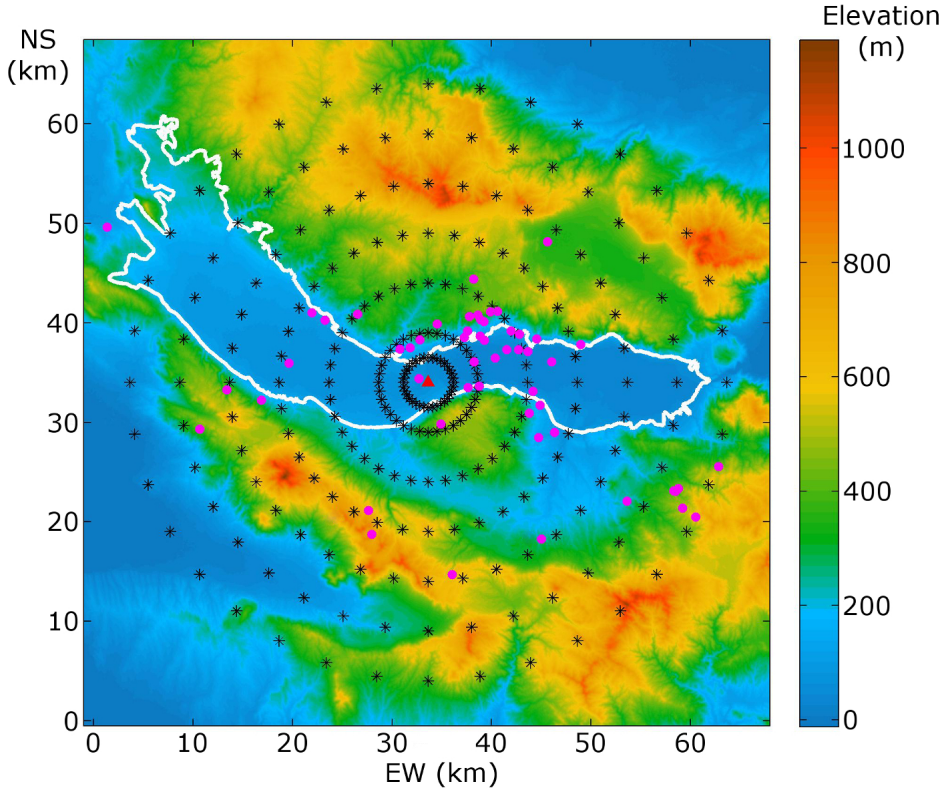

Figure II.35. Surface map of the Mygdonian basin showing the epicenters of the 1260 sources (black crosses) used to study the sensitivity of the site response to source locations. The pink dots correspond to the epicentral locations of 52 local events. After Maufroy et al. (2016).

Figure II.36 shows the comparison between observed and synthetics of 3 measures of site response: (i) amplification measured by standard spectral ratios (SSR) between the surface and downhole sensors at the TST station, (ii) lengthening of duration (LOD) measured by the group delay method for the same pair of sensors, and (iii) H/V ratios at the surface TST sensor. The figure shows that amplification (as measured by SSR) and LOD are two complementary, anti-correlated measures of the site response. The maximal ground motion durations are obtained at frequencies where the amplification is the most variable, and are shown to be caused by the excitation of local surface waves diffracted off the basin edges. A clear north-south asymmetry of both amplification and lengthening of duration is reported in the synthetics, which stems from the non-isotropic

excitation of local surface waves related to differences in the slopes of the basin edges. This effect could only be suggested in the observed ground motions, due to insufficient number of available recordings. The article by Maufroy et al. (2017) also investigated the influence of the choice of the reference station on the amplification measured by SSR, and the sensitivity of the amplification measured by SSR to the distribution of seismic sources. The largest variability of the measured site amplification is found for northern and southern clusters of shallow and far events (see Figure II.37).

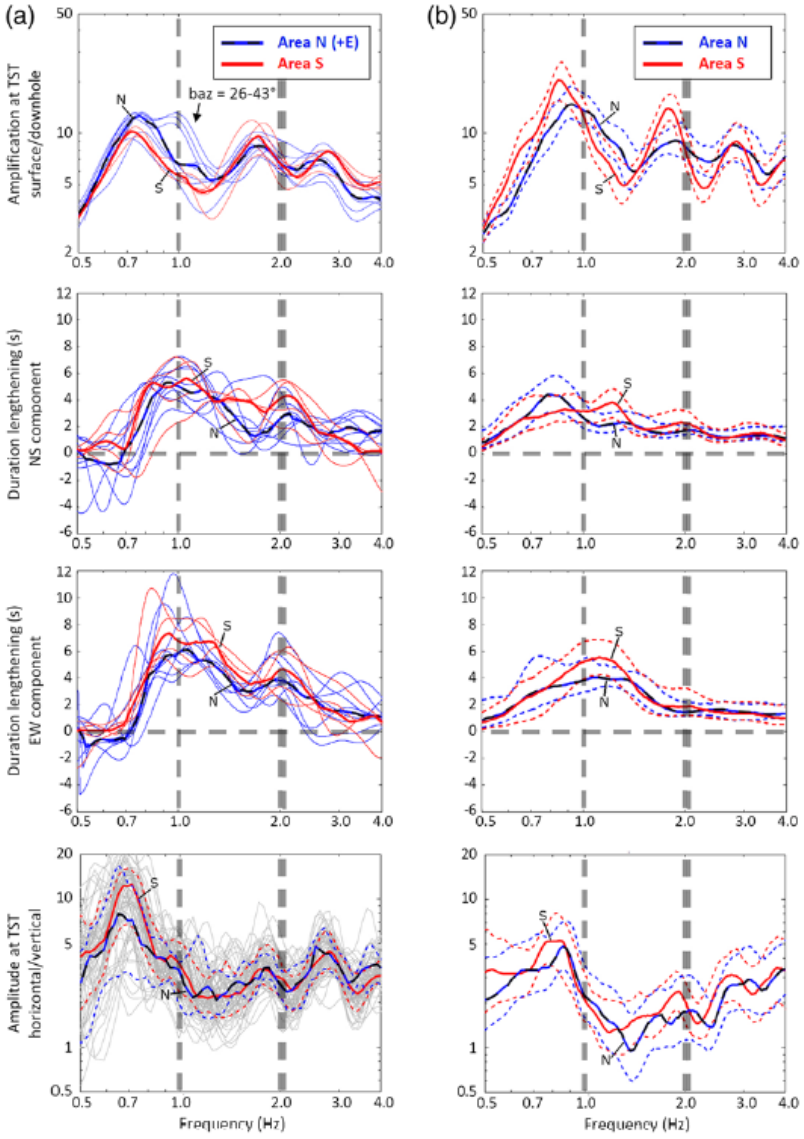

Figure II.36. Observed (left) and synthetic (right) measures of site response: amplification measured by surface-to-downhole spectral ratios at TST (top), lengthening of duration of horizontal motions (middle) and H/V rations at the surface TST station. The blue (resp. red) curves correspond to the measures restricted to northern (resp. southern) sources. Vertical dashed lines correspond to frequencies of maximal duration and most variable amplification. After Maufroy et al. (2017).

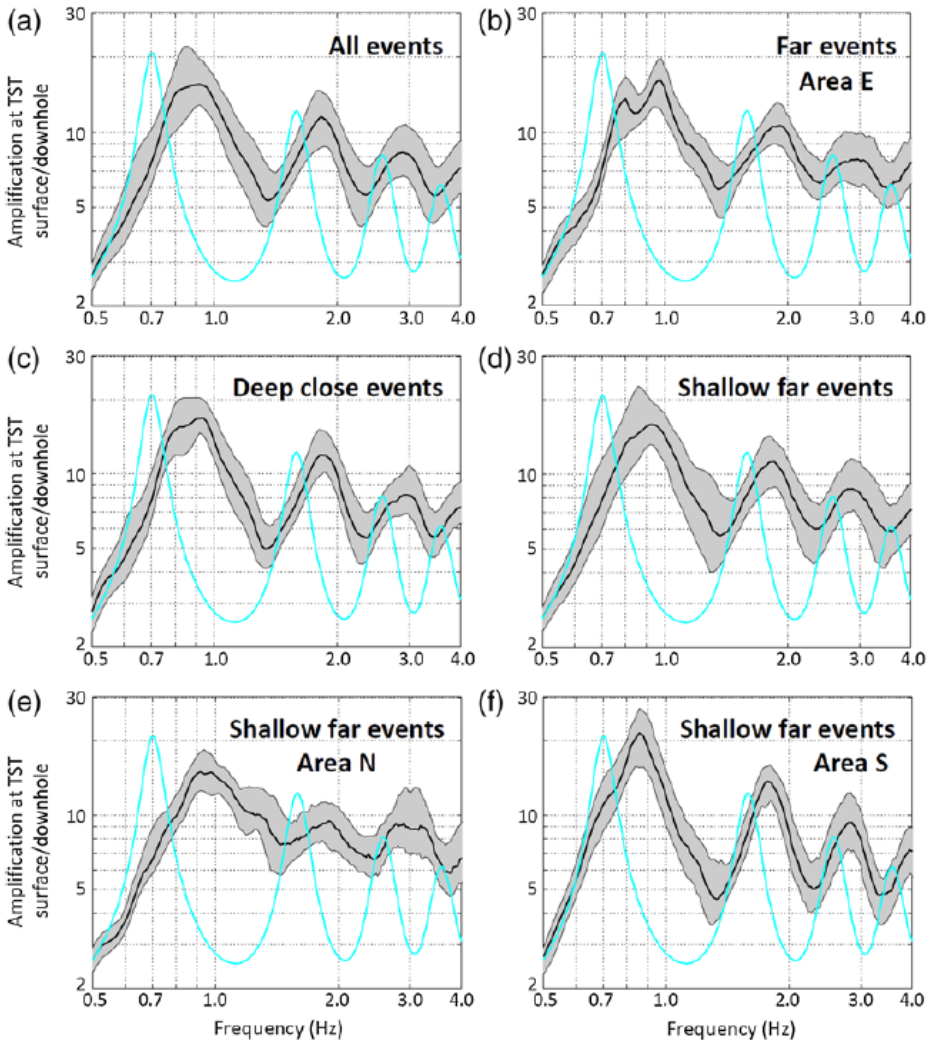

Figure II.37. Amplification at TST measured by surface-to-downhole SSR for different clusters of sources. The median of the distribution for each cluster is indicated by the bold black line and the grey shaded area corresponds to the values comprised between the 16th and 84th percentiles of the distribution. The cyan curve is the 1D prediction, that is, the SSR computed for a vertically incident shear wave in the local 1D model of the site. After Maufroy et al. (2017).

The sensitivity of EGM to hypocentral locations was further investigated in Maufroy et al. (2016). Figure II.38 shows how the spectral acceleration can be influenced by differences of a few km in hypocentre location. The influence on EGM is clearly source-dependent, with a larger sensitivity for shallow and close events compared to deep and far events, suggesting that the sensitivity is controlled by a combination of incidence angle and hypocentral distance to the site. Figure II.39 also shows that the sensitivity of EGM to uncertainties in the source position is site-independent and, most interestingly, that the measure of amplification by surface-to-downhole SSR is almost independent of the possible source location errors. This confirms the physical intuition that guided the design of hybrid time series in the validation phase (see section II.3.2.4): the surface-to-downhole transfer function is a robust measure of the site amplification, which may depend on the relative position of the source to the site (as seen previously) but not on smaller location errors.

Finally, the databank of Green's functions was exploited to produce a collection of synthetic seismograms for the set of real seismic events shown with pink circles in Figure II.35. The synthetics were then processed using an artificial neural network approach, following Derras et al. (2014), in order to produce GMPE for a set of classical GM intensity parameters (PGV, PGA, acceleration response spectra at different periods). Analyzing the uncertainty of the synthetic GMPE allows to understand and estimate its components and hopefully helps to provide some strategies to reduce it. For example, it is quite an easy game to artificially introduce some errors in the source catalog metadata (e. g. source location, or source magnitude) and estimate the resulting apparent prediction uncertainty. The results obtained for source location errors comprised between $\pm$ 1 km and $\pm$ 10 km, and source magnitude errors between $\pm$ 0.1 and $\pm$ 0.5 are shown in Figure II.40. They are expressed in terms of the between-event variability, τ, and the within-event variability, ϕ. As expected, only τ is affected by errors in the source parameters (because the error is the same for all stations that "recorded" the event). The sensitivity of τ is far from being negligible: 25% increase for a $\pm$ 3 km location error and a factor of 2 on τ for a magnitude error of $\pm$ 0.25. Those estimates, which seem quite realistic (see the discussion in Maufroy et al. (2016)), emphasize the usefulness of dense local networks to reduce source parameters errors for weak motion events.

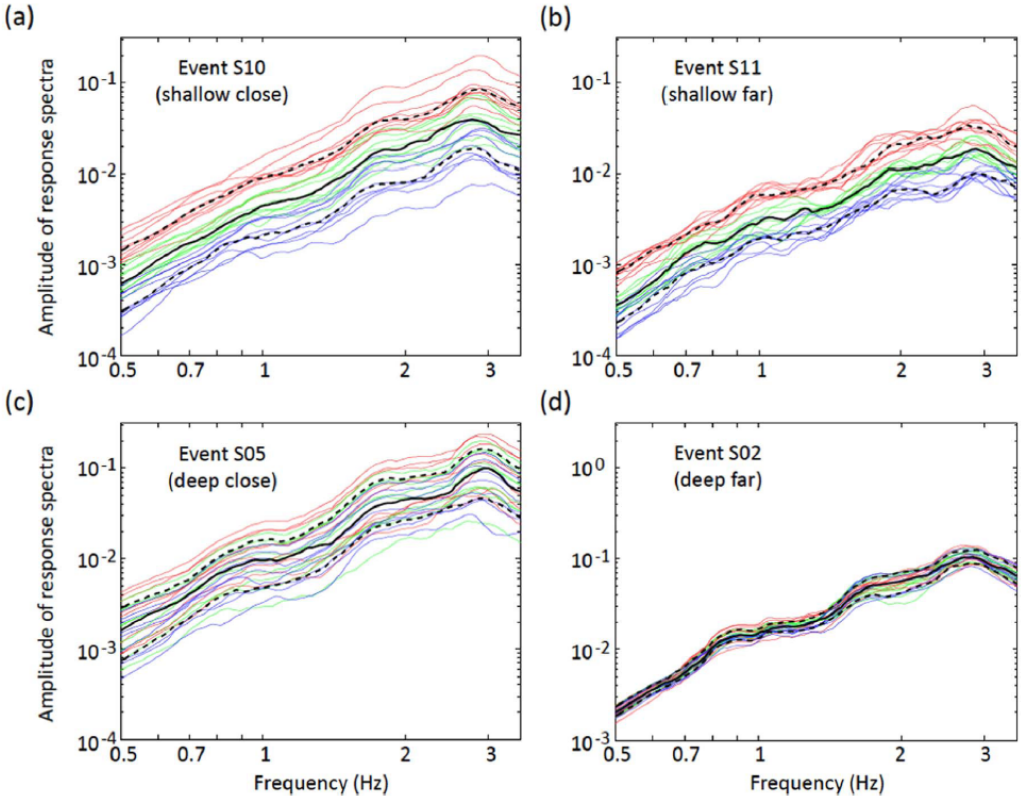

Figure II.38. Variability of the acceleration response spectrum at the surface TST station caused by moving the hypocentre location of a few sources by at most ± 2 km in each direction of space. The colors indicate the depth of the hypocentres, from deeper (blue) to shallower (red). After Maufroy et al. (2016).

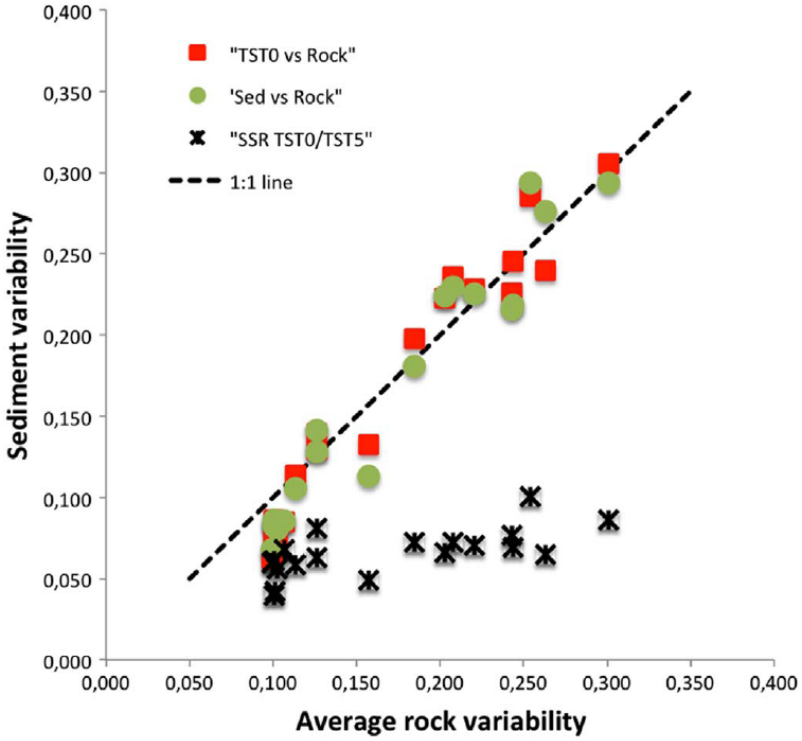

Figure II.39. Red squares: frequency-averaged variability of the acceleration response spectrum at TST plotted as a function of the corresponding variability averaged over the 4 rock stations. Green dots: same for the average of all stations at the sediments. Black crosses: frequency-averaged variability of the downhole-to-surface transfer function at TST. After Maufroy et al. (2016).

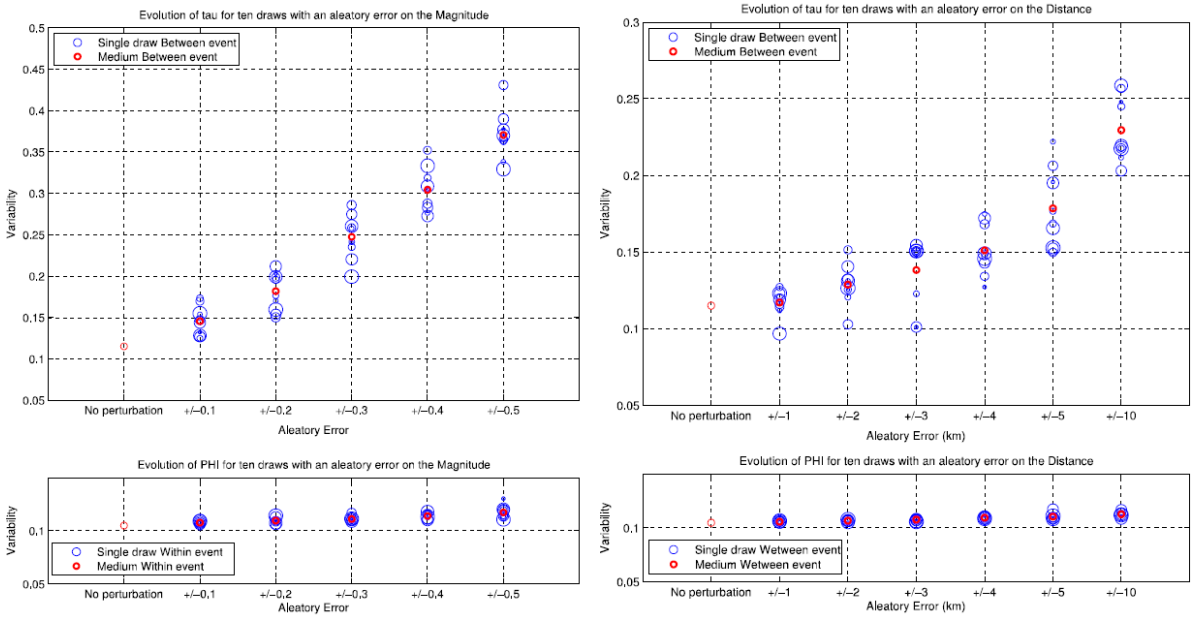

Figure II.40. Influence of uncertainties related to source magnitude (left) and to hypocentre location (right) on the between-event (top) and within-event (bottom) variability of synthetic GMPE. After Maufroy et al. (2016).

Chapter III

Perspectives

I hereafter present some research perspectives that should keep me busy in the next few years. They rely on intensive use of numerical simulation in order to (i) keep improving methods to predict EGM and understand its variability and (ii) develop methods to constrain the amplification and attenuation of EGM based upon the exploitation of diffuse seismic wavefields.

III.1 Better understanding EGM, its variability and its impact on man-made structures

My first perspective is naturally to pursue my effort to better understand and quantify how different physical ingredients contribute to the observed complexity and variability of EGM and its impact on structures. This will start with finalizing and/or extending the following studies:

1. The analysis of site-related variability of EGM based on the comprehensive databank of results produced during the NERA project (see section II.3.3.1). The same kind of parametric studies is about to be launched in the context of the PhD thesis of Capucine Durand (whom I am co-advising) in order to account for site-related variability on the seismic response of rivers dams (see e.g. Durand et al. (2017)).
2. The analysis of the synthetic GMPE obtained for the Mygdonian basin (see section II.3.3.2) in order (i) to quantify whether the within-event variability of EGM depends on the location of the stations in the basin; (ii) to test the performance of different proxies of the site condition (V_{S30}, f_0) and (iii) to quantify how uncertainties on those proxies propagate to apparent prediction uncertainty.
3. The analysis of site-city interaction, which was initiated during the PhD thesis of Javed Iqbal, based upon simplified spectral element modeling of the buildings response with macroscopically equivalent blocks (Iqbal 2014).
4. The characterization of the spatial variability of EGM and its impact on the response of arch dams, which has been initiated during the PhD work of Eleni Koufoudi (Koufoudi et al. 2017).

III.2 Exploiting the amplitude of H/V ratios in different wavefield regimes

The prediction of EGM at a given site requires in particular to constrain the amplification due to local geology as a function of frequency. This can be done in a full deterministic way by characterizing experimentally the necessary input parameters that will further allow a numerical

estimation of the amplification function (as was done for example during the E2VP project, see section II.3.2.4). But, as stated previously, this is a long-lasting, costly process, which can certainly not be deployed everywhere. Many studies (often motivated by operational needs) have adopted alternate, approximate approaches to estimate site response, for example based on non-invasive measures of seismic ambient noise. Among those, the H/V method has been successfully used for decades in order to constrain the frequency range in which site amplification is expected to occur (see Bard (1999) for a classical review article). Despite several attempts, the amplitude information carried by the H/V ratios measured on microtremors could not be related to the amplification level expected at a site. The main reason is that the H/V ratios depend strongly on the nature and composition of the seismic noise wavefield, which is not always known.

The subject has been revitalized in recent years, when some authors applied to seismic noise some concepts developed for diffuse seismic wavefields. In particular, assuming the equipartition of seismic energy (Hennino et al. 2001; Margerin et al. 2009; Nakahara & Margerin 2011), it is possible to predict the H/V ratios from the local velocity structure (Sánchez-Sesma et al. 2011), and therefrom to invert the ratios in order to retrieve the local structure (see Kawase et al. (2011) for an example of inversion of H/V ratios measured on earthquake coda, and Kawase et al. (2015) for a discussion of the inversion of microtremors H/V ratios). However, the state of equipartition is a particular consequence of the multiple scattering of seismic waves in heterogeneous media, and is thought to be only partially reached (not to say generally not reached). A nice example of equipartition is given in Figure III.1 for a local M4 Pyrenean earthquake recorded 40 km away from the source (see the complete analysis in Souriau et al. (2011), given in section IV.3, p. 192). The state of equipartition, which is precisely indicated by the stabilization of the H/V energy ratio, is only reached for about a minute in the earthquake coda for the tiny frequency band (around 15 Hz) considered in the analysis. Outside from the equipartition window, and in particular in the regime of seismic noise, the H/V energy ratio fluctuates by about one order of magnitude, which questions the possibility to perform a stable measure and to relate it to the equipartition value.

But the challenge is worth to tackle and there is certainly a different approach to adopt than the blind application of an elegant physical theory which validity conditions may not be met. I believe in particular that numerical simulations can be useful because they allow to explore the large variety of regimes of seismic energy partition that may be encountered in microtremors or seismic coda. As an example, I would recall a situation of interest which has been studied in Maufroy et al. (2017) and is illustrated in Figure III.2: the H/V ratios computed at the central TST station of the Mygdonian basin for a set of deviatoric double-couple and explosive sources are compared to the prediction of Kawase et al. (2011), which assumes that the incident wavefield consists of vertically propagating plane waves in a regime of equipartition (in this case the H/V ratio is simply obtained by forming the ratio of S to P transfer functions at the site). Although the proportion of shear and explosive sources was adjusted to match the equipartition hypothesis, the measured H/V ratios at the surface do not exactly follow the theoretical prediction. Additional simulations will thus be needed to identify the origin of this particular difference (for example 3D effects or differential attenuation between S and P wave modes, which are not accounted for in the reference theoretical solution). Then, the analysis should be extended to the regime of seismic noise, by comparing the prediction of full equipartition (which can be computed from 3D synthetics as done in Matsushima et al. (2014)) with the H/V ratios computed for realistic distributions of surface forces and of crustal and basin heterogeneities.

This part of my research perspectives can be seen as a revival, I would rather say an extension, of some of the work done during the former SESAME European project, and I will benefit from the expertise of many investigators of that project (and now close collaborators) to tackle the challenging questions raised above.

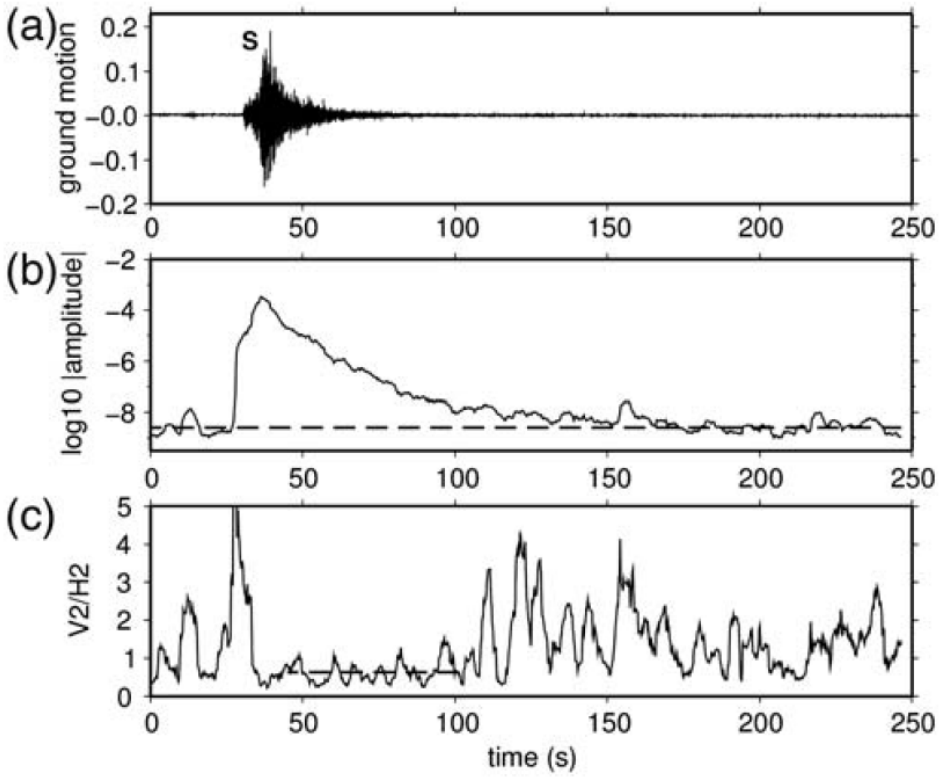

Figure III.1. Illustration of the equipartition of energy in the coda of a local M4 event recorded on a rock site outside of the Bagnères-de-Bigorre valley. The envelope of the seismogram is compared to that of the noise (dashed line). The ratio of vertical to horizontal kinetic energies is shown to stabilize during 40 s, 4 s after the S wave arrival. After Souriau et al. (2011).

III.3 Towards imaging absorption and scattering in different wavefield regimes

There are at least two physical ingredients which control EGM and are in general poorly constrained: the absorption of seismic energy along the path from source to site, and the level of scattering due to crustal heterogeneities. For example, the consequence of the lack of knowledge about local absorption has been illustrated in the Grenoble valley by the inability to explain observed ground motion duration (see section II.3.2.1), and the underestimation of synthetic EGM duration at rock sites around the Mygdonian basin has been suggested to result from the absence of crustal heterogeneities in the model of the bedrock used in the numerical simulations (see section II.3.2.4).

Because both absorption and scattering combine to influence the attenuation and the duration of EGM, their effects have to be separated, but the way to perform such separation has represented a long-term challenge in seismology. It is only recently that, thanks to advances in the numerical methods to solve the radiative transfer equation, Mayor et al. (2014); Margerin et al. (2016) have succeeded in quantifying the coda waves sensitivity to spatial variations of absorption and scattering, and have developed a regional absorption tomography model of the Alps based on coda Q_c measurements for regional earthquakes (Mayor et al. 2016).

The application of the sensitivity kernels to image absorption and scattering in sufficiently seismically active regions is an ongoing work by the group of L. Margerin in Toulouse, and we wish to collaborate to evaluate the possibility to extend this new kind of tomography to regions of low

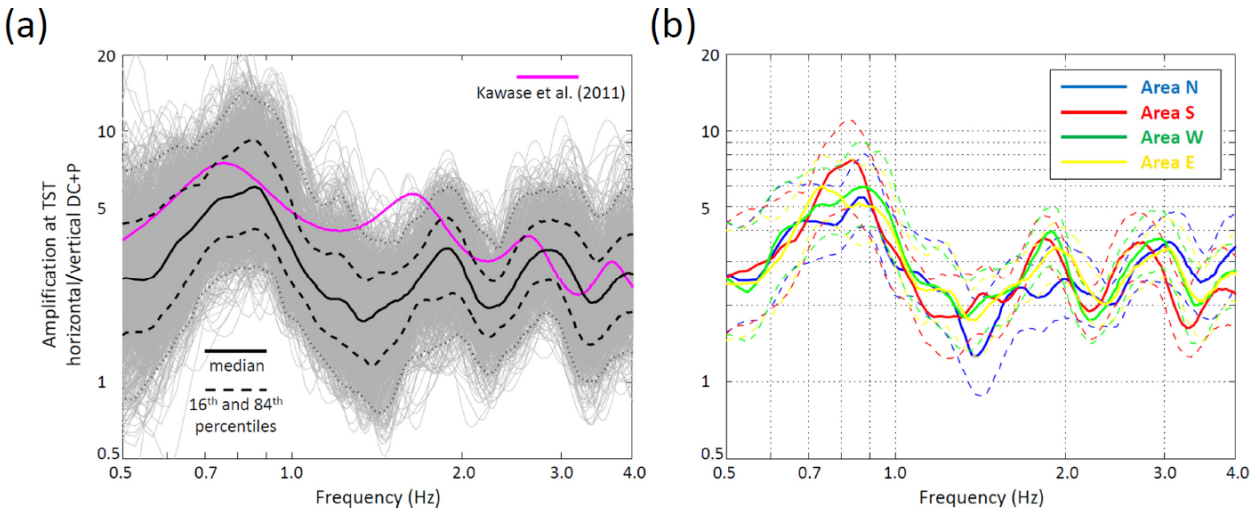

Figure III.2. Left: H/V ratios measured on 3D synthetics at the central station of the Euroseistest array for a distribution of sources consistent with a regime of equipartition of seismic energy between vertically propagating body waves. In this regime, the H/V ratio is given by the magenta line, which is obtained by the theoretical prediction of Kawase et al. (2011). Right: the H/V ratios are grouped into several clusters of source back-azimuths. The differences suggest that the condition of equipartition is not met in the surface synthetics. After Maufroy et al. (2017).

seismicity. In this case, the idea is to work with the coda of the Green's functions reconstructed from the correlations of seismic noise between neighbouring stations. This idea will be tested in 2D media thank to extensive numerical experiments. First, SH wave in unbounded heterogeneous (described by von Kármán auto-correlation functions) viscoelastic media will be simulated in order to understand the sensitivity of the Green's functions retrieved by cross-correlation to the distribution of the noise sources. Then, numerical sensitivity kernels will be constructed *ab initio* by computing the noise wavefield for local modifications of the absorption/scattering properties. The numerical experiments will then be extended to $P-SV$ wave propagation in a half-space to account for fluctuations in both S and P velocities, differential absorption between P and S waves, and conversion between body and surface wave modes close to the free surface.

A full proposal presenting this part of my research perspectives is presented in the Annex V.1. The proposal was rated as excellent by the French national research agency (ANR), who decided therefore not to fund it.

References

Akcelik, V., Bielak, J., Biros, G., Epanomeritakis, I., Fernandez, A., Ghattas, O., Kim, E. J., Lopez, J., O'Hallaron, D., Tu, T., et al., 2003. High resolution forward and inverse earthquake modeling on terascale computers, in *Proceedings of the 2003 ACM/IEEE conference on Supercomputing*, p. 52, ACM.

Akkar, S., Sandıkkaya, M., Şenyurt, M., Sisi, A. A., Ay, B., Traversa, P., Douglas, J., Cotton, F., Luzi, L., Hernandez, B., et al., 2014. Reference database for seismic ground-motion in Europe (RESORCE), *Bull. Earthq. Eng.*, **12**(1), 311–339.

Anderson, J. G., 2004. Quantitative measure of the goodness-of-fit of synthetic seismograms, in *13th World Conference on Earthquake Engineering Conference Proceedings, Vancouver, Canada, Paper*, vol. 243.

Backus, G. E., 1962. Long-wave elastic anisotropy produced by horizontal layering, *J. Geophys. Res.*, **67**(11), 4427–4440.

Bao, H., Bielak, J., Ghattas, O., Kallivokas, L. F., O'Hallaron, D. R., Shewchuk, J. R., & Xu, J., 1998. Large-scale simulation of elastic wave propagation in heterogeneous media on parallel computers, *Computer Methods in Applied Mechanics and Engineering*, **152**(1-2), 85–102.

Bard, P.-Y., 1994. Discussion session: Lessons, issues, needs and prospects. Special Theme session 5: Turkey Flat and Ashigara Valley experiments, in *Tenth World Conference of Earthquake Engineering, Proceedings*.

Bard, P.-Y., 1999. Microtremor measurements: a tool for site effect estimation, *The effects of surface geology on seismic motion*, **3**, 1251–1279.

Bard, P.-Y. & Bouchon, M., 1980a. The seismic response of sediment-filled valleys, Part 1: The case of incident SH waves, *Bull. Seismol. Soc. Am.*, **70**, 1263–1286.

Bard, P.-Y. & Bouchon, M., 1980b. The seismic response of sediment-filled valleys, Part 2: The case of incident P and SV waves, *Bull. Seismol. Soc. Am.*, **70**, 1921–1941.

Blanc, E., Komatitsch, D., Chaljub, E., Lombard, B., & Xie, Z., 2016. Highly accurate stability-preserving optimization of the Zener viscoelastic model, with application to wave propagation in the presence of strong attenuation, *Geophys. J. Int.*, **205**(1), 427–439.

Boore, D. M., 1972. Finite difference methods for seismic wave propagation in heterogeneous materials, *Methods in computational physics*, **11**, 1–37.

Bouchon, M., 2003. A review of the discrete wavenumber method, *Pure Appl. Geophys.*, **160**(3-4), 445–465.

Capdeville, Y., Guillot, L., & Marigo, J.-J., 2010. 2-D non-periodic homogenization to upscale elastic media for P–SV waves, *Geophys. J. Int.*, **182**(2), 903–922.

Causse, M., Chaljub, E., Cotton, F., Cornou, C., & Bard, P.-Y., 2009. New approach for coupling k^{-2} and empirical Green's functions: application to the blind prediction of broad-band ground motion in the Grenoble basin, *Geophys. J. Int.*, **179**(3), 1627–1644.

Chaljub, E., 2009. Spectral element modeling of 3D wave propagation in the alpine valley of Grenoble, in *Proceedings of the IIIrd International Symposium on the Effects of Surface Geology on Seismic Motion*, vol. 2, LCPC Editions, ISSN 1628-4704, 7 p.

Chaljub, E., Komatitsch, D., Vilotte, J.-P., Capdeville, Y., Valette, B., & Festa, G., 2007. Spectral element analysis in seismology, in *Advances in Wave Propagation in Heterogeneous Media, Advances in Geophysics*, vol. 48, pp. 365–419, eds WU, R.-S. & Maupin, V., Elsevier Academic Press.

Chaljub, E., Cornou, C., & Bard, P.-Y., 2009. Numerical benchmark of 3D ground motion simulation in the valley of Grenoble, french Alps, in *Proceedings of the IIIrd International Symposium on the Effects of Surface Geology on Seismic Motion*, vol. 2, LCPC Editions, ISSN 1628-4704, paper SB1, 11 p.

Chaljub, E., Moczo, P., Tsuno, S., Bard, P.-Y., Kristek, J., Kaser, M., Stupazzini, M., & Kristekova, M., 2010. Quantitative Comparison of Four Numerical Predictions of 3D Ground Motion in the Grenoble Valley, France, *Bull. Seismol. Soc. Am.*, **100**(4), 1427–1455.

Chaljub, E., Maufroy, E., Moczo, P., Kristek, J., Hollender, F., Bard, P.-Y., Priolo, E., Klin, P., de Martin, F., Zhang, Z., Zhang, W., & Chen, X., 2015. 3-D numerical simulations of earthquake ground motion in sedimentary basins: testing accuracy through stringent models, *Geophys. J. Int.*, **201**(1), 90–111.

Cornou, C., 2002. *Traitement d'antenne et imagerie sismique dans l'agglomération grenobloise (Alpes françaises) : implications pour les effets de site*, Theses, Université Joseph-Fourier - Grenoble I.

Cornou, C., Bard, P.-Y., & Dietrich, M., 2003. Contribution of dense array analysis to basin-edge-induced waves identification and quantification. application to grenoble basin, french alps (ii)., *Bull. Seismol. Soc. Am.*, **93**, 2624–2648.

Cornou, C., Chaljub, E., Verbeke*, J., Converset*, J., Voisin, C., Stehly, L., Margerin, L., Tsuno, S., Grasso, J., Guéguen, P., et al., 2009. Measurement and variability study of site effects in the 3d glacial valley of grenoble, french alps, in *Third International Symposium on the Effects of Surface Geology on Seismic*

Motion, vol. 2, pp. 1621–1627, LCPC Editions, ISSN 1628-4704.

Cramer, C. H., 1995. Weak-motion observations and modeling for the Turkey Flat, U.S., Site-Effects Test Area near Parkfield, California, *Bull. Seismol. Soc. Am.*, **85**(2), 440–451.

Cruz-Atienza, V. M., Tago, J., Sanabria-Gómez, J. D., Chaljub, E., Etienne, V., Virieux, J., & Quintanar, L., 2016. Long duration of ground motion in the paradigmatic valley of Mexico, *Scientific Reports*, **6**, 38807.

Day, S. M., Bielak, J., Dreger, D., Graves, R., Larsen, S., Olsen, K. B., & Pitarka, A., 2001. Tests of 3D elastodynamic codes: Final report for lifelines project 1a01, Tech. rep., Pacific Earthquake Engineering Research Center & Southern California Earthquake Center.

Day, S. M., Bielak, J., Dreger, D., Graves, R., Larsen, S., Olsen, K. B., & Pitarka, A., 2003. Tests of 3D elastodynamic codes: Final report for lifelines project 1a02, Tech. rep., Pacific Earthquake Engineering Research Center.

Day, S. M., Bielak, J., Dreger, D., Graves, R., Larsen, S., Olsen, K. B., & Pitarka, A., 2005. 3D ground motion simulation in basins: Final report for lifelines project 1a03, Tech. rep., Pacific Earthquake Engineering Research Center.

Derras, B., Bard, P. Y., & Cotton, F., 2014. Towards fully data driven ground-motion prediction models for Europe, *Bull. Earthq. Eng.*, **12**(1), 495–516.

Douglas, J. & Edwards, B., 2016. Recent and future developments in earthquake ground motion estimation, *Earth-Science Reviews*, **160**, 203 – 219.

Dumbser, M. & Kaeser, M., 2006. An arbitrary high-order discontinuous galerkin method for elastic waves on unstructured meshes - II. the three-dimensional isotropic case, *Geophys. J. Int.*, **167**(1), 319–336.

Durand, C., Chaljub, E., Bard, P.-Y., Baillet, L., Fry, J.-J., Granjon, R., & Renalier, F., 2017. Revisiting Sarma's method for seismic response of embankments: first results, in *Sixteenth World Conference on Earthquake Engineering*, Proceedings of the 16th World Conference on Earthquake Engineering, p. 4421, Santiago, Chile.

Etienne, V., Chaljub, E., Virieux, J., & Glinsky, N., 2010. An hp–adaptive discontinuous Galerkin finite-element method for 3-D elastic wave modelling, *Geophys. J. Int.*, **183**(2), 941–962.

Garvin, W. W., 1956. Exact transient solution of the buried line source problem, *Proceedings of the Royal Society A: Mathematical, Physical and Engineering Sciences*, **234**(1199), 528–541.

Guillot, L., Capdeville, Y., & Marigo, J.-J., 2010. 2-D non-periodic homogenization of the elastic wave equation: SH case, *Geophys. J. Int.*, **182**(3), 1438–1454.

Hallier, S., Chaljub, E., Bouchon, M., & Sekiguchi, H., 2008. Revisiting the basin-edge effect at Kobe during the 1995 Hyogo-Ken Nanbu earthquake, *Pure Appl. Geophys.*, **165**, 1751–1760.

Hennino, R., Trégourès, N., Shapiro, N., Margerin, L., Campillo, M., Van Tiggelen, B., & Weaver, R., 2001. Observation of equipartition of seismic waves, *Physical review letters*, **86**(15), 3447.

Imtiaz, A., Causse, M., Chaljub, E., & Cotton, F., 2015. Is ground-motion variability distance dependent? insight from finite-source rupture simulations, *Bull. Seismol. Soc. Am.*.

Iqbal, J., 2014. *Contribution to the analysis of macroscopic effects of structure-soil-structure interaction through simplified modeling by spectral elements method.*, Theses, Université Grenoble Alpes.

Kawase, H., 1996. The cause of the damage belt in Kobe: ???the basin-edge effect,??? constructive interference of the direct S-wave with the basin-induced diffracted/Rayleigh waves, *Seismol. Res. Lett.*, **67**(5), 25???34.

Kawase, H., 2003. Site effects on strong ground motions, *INTERNATIONAL GEOPHYSICS SERIES*, **81**(B), 1013–1030.

Kawase, H. & Iwata, T., 1998. A report on submitted results of the simultaneous simulation for Kobe, in *The Effects of Surface Geology on Seismic Motion, Recent Progress and new Horizon on ESG Study*, vol. 3, Balkema/CRC Press.

Kawase, H., Sánchez-Sesma, F. J., & Matsushima, S., 2011. The optimal use of horizontal-to-vertical spectral ratios of earthquake motions for velocity inversions based on diffuse-field theory for plane waves, *Bull. Seismol. Soc. Am.*, **101**(5), 2001–2014.

Kawase, H., Matsushima, S., Satoh, T., & Sánchez-Sesma, F. J., 2015. Applicability of theoretical horizontal-to-vertical ratio of microtremors based on the diffuse field concept to previously observed data, *Bull. Seismol. Soc. Am.*.

Klin, P., Priolo, E., & Seriani, G., 2010. Numerical simulation of seismic wave propagation in realistic 3-D geo-models with a Fourier pseudo-spectral method, *Geophys. J. Int.*, **183**(2), 905–922.

Komatitsch, D., Tsuboi, S., Ji, C., & Tromp, J., 2003. A 14.6 billion degrees of freedom, 5 teraflops, 2.5 terabyte earthquake simulation on the earth simulator, in *Supercomputing, 2003 ACM/IEEE Conference*,

pp. 4–4, IEEE.

Koufoudi, E., Chaljub, E., Dufour, F., Douste-Bacqué, I., Roussel, S., Bard, P.-Y., Humbert, N., Robbe, E., & Bourdarot, E., 2017. Experimental investigation of spatial variability of ground motions – monitoring of an arch dam, in *Sixteenth World Conference on Earthquake Engineering*, Proceedings of the 16th World Conference on Earthquake Engineering, p. 1737, Santiago, Chile.

Kristek, J., Moczo, P., Chaljub, E., & Kristekova, M., 2016. An orthorhombic representation of a heterogeneous medium for the finite-difference modelling of seismic wave propagation, *Geophys. J. Int.*.

Kristeková, M., Kristek, J., Moczo, P., & Day, S. M., 2006. Misfit criteria for quantitative comparison of seismograms, *Bull. Seismol. Soc. Am.*, **96**(5), 1836–1850.

Kristeková, M., Kristek, J., & Moczo, P., 2009. Time-frequency misfit and goodness-of-fit criteria for quantitative comparison of time signals, *Geophys. J. Int.*, **178**(2), 813–825.

Lamb, H., 1904. On the propagation of tremors over the surface of an elastic solid, *Philosophical Transactions of the Royal Society of London. Series A, Containing papers of a mathematical or physical character*, **203**, 1–42.

Lebrun, B., Hatzfeld, D., & Bard, P., 2002. Site effect study in urban area: experimental results in grenoble (france), in *Earthquake Microzoning*, pp. 2543–2557, Springer.

Manakou, M., 2007. *Contribution to the determination of a 3D soil model for site response analysis. The case of the Mygdonian basin*, Ph.D. thesis, Ph D Thesis (in Greek with English abstract), Department of Civil Engineering, Aristotle University of Thessaloniki.

Manakou, M., Raptakis, D., Ch??vez-Garc??a, F., Apostolidis, P., & Pitilakis, K., 2010. 3D soil structure of the Mygdonian basin for site response analysis, *Soil. Dyn. Earthq. Eng.*, **30**(11), 1198–1211.

Manolis, G. D., Dineva, P. S., Rangelov, T. V., & Wuttke, F., 2017. *Seismic Wave Propagation in Non-Homogeneous Elastic Media by Boundary Elements*, Springer International Publishing.

Margerin, L., Campillo, M., Van Tiggelen, B., & Hennino, R., 2009. Energy partition of seismic coda waves in layered media: Theory and application to Pinyon Flats Observatory, *Geophys. J. Int.*, **177**(2), 571–585.

Margerin, L., Planès, T., Mayor, J., & Calvet, M., 2016. Sensitivity kernels for coda-wave interferometry and scattering tomography: theory and numerical evaluation in two-dimensional anisotropically scattering media, *Geophys. J. Int.*, **204**(1), 650–666.

Matsushima, S., Hirokawa, T., De Martin, F., Kawase, H., & Sánchez-Sesma, F. J., 2014. The effect of lateral heterogeneity on horizontal-to-vertical spectral ratio of microtremors inferred from observation and synthetics, *Bull. Seismol. Soc. Am.*.

Maufroy, E., Chaljub, E., Hollender, F., Kristek, J., Moczo, P., Klin, P., Priolo, E., Iwaki, A., Iwata, T., Etienne, V., Martin, F. D., Theodoulidis, N. P., Manakou, M., Guyonnet-Benaize, C., Pitilakis, K., & Bard, P.-Y., 2015. Earthquake ground motion in the mygdonian basin, greece: The e2vp verification and validation of 3d numerical simulation up to 4 hz, *Bull. Seismol. Soc. Am.*, **105**(3), 1398–1418.

Maufroy, E., Chaljub, E., Hollender, F., Bard, P.-Y., Kristek, J., Moczo, P., Martin, F. D., Theodoulidis, N., Manakou, M., Guyonnet-Benaize, C., Hollard, N., & Pitilakis, K., 2016. 3D numerical simulation and ground motion prediction: Verification, validation and beyond – Lessons from the E2VP project, *Soil. Dyn. Earthq. Eng.*, **91**, 53–71.

Maufroy, E., Chaljub, E., Theodoulidis, N. P., Roumelioti, Z., Hollender, F., Bard, P.-Y., de Martin, F., Guyonnet-Benaize, C., & Margerin, L., 2017. Source-related variability of site response in the mygdonian basin (greece) from accelerometric recordings and 3d numerical simulations, *Bull. Seismol. Soc. Am.*.

Mayor, J., Margerin, L., & Calvet, M., 2014. Sensitivity of coda waves to spatial variations of absorption and scattering: radiative transfer theory and 2-d examples, *Geophys. J. Int.*, p. ggu046.

Mayor, J., Calvet, M., Margerin, L., Vanderhaeghe, O., & Traversa, P., 2016. Crustal structure of the Alps as seen by attenuation tomography, *Earth Planet Sci. Lett.*, **439**, 71–80.

Moczo, P. & Bard, P.-Y., 1993. Wave diffraction, amplification and differential motion near strong lateral discontinuities, *Bull. Seismol. Soc. Am.*, **83**(1), 85–106.

Moczo, P., Kristek, J., Vavryčuk, V., Archuleta, R. J., & Halada, L., 2002. 3D heterogeneous staggered-grid finite-difference modeling of seismic motion with volume harmonic and arithmetic averaging of elastic moduli and densities, *Bull. Seismol. Soc. Am.*, **92**(8), 3042–3066.

Moczo, P., Kristek, J., Galis, M., Chaljub, E., & Etienne, V., 2011. 3-D finite-difference, finite-element, discontinuous-Galerkin and spectral-element schemes analysed for their accuracy with respect to P-wave to S-wave speed ratio, *Geophys. J. Int.*, **187**, 1645–1667.

Moczo, P., Kristek, J., & Gális, M., 2014. *The Finite-difference Modelling of Earthquake Motions: Waves and Ruptures*, Cambridge University Press, With contributions by M. Kristekova, E. Chaljub, M. Käser, P. Klin and C. Pelties.

Nakahara, H. & Margerin, L., 2011. Testing equipartition for S-wave coda using borehole records of local earthquakes, *Bull. Seismol. Soc. Am.*, **101**(5), 2243–2251.

Sánchez-Sesma, F. J., Rodríguez, M., Iturrarán-Viveros, U., Luzón, F., Campillo, M., Margerin, L., García-Jerez, A., Suarez, M., Santoyo, M. A., & Rodríguez-Castellanos, A., 2011. A theory for microtremor H/V spectral ratio: Application for a layered medium, *Geophys. J. Int.*, **186**(1), 221–225.

Shapiro, N. M., Singh, S. K., Almora, D., & Ayala, M., 2001. Evidence of the dominance of higher-mode surface waves in the lake-bed zone of the Valley of Mexico, *Geophys. J. Int.*, **147**(3), 517–527.

Smith, W. D., 1975. The application of finite element analysis to body wave propagation problems, *Geophys. J. Int.*, **42**(2), 747–768.

Souriau, A., Chaljub, E., Cornou, C., Margerin, L., Calvet, M., Maury, J., Wathelet, M., Grimaud, F., Ponsolles, C., Pequegnat, C., Langlais, M., & Guéguen, P., 2011. Multimethod characterization of the french-pyrenean valley of Bagneres-de-Bigorre for seismic-hazard evaluation: Observations and models, *Bull. Seismol. Soc. Am.*, **101**(4), 1912–1937.

Thouvenot, F., Fréchet, J., Jenatton, L., & Gamond, J.-F., 2003. The belledonne border fault: identification of an active seismic strike-slip fault in the western alps, *Geophys. J. Int.*, **155**(1), 174–192.

Trifunac, M., 1972. Scattering of plane sh waves by a semi-cylindrical canyon, *Earthquake Engineering & Structural Dynamics*, **1**(3), 267–281.

Tsuno, S., Chaljub, E., & Bard, P., 2009. Grenoble valley simulation benchmark: Comparison of results and main learning, in *Proceedings of the IIIrd International Symposium on the Effects of Surface Geology on Seismic Motion*, vol. 2, LCPC Editions, ISSN 1628-4704, paper SB2, 57 p.

Vallon, M., 1999. Estimation de l???épaisseur d???alluvions et sédiments quaternaires dans la région grenobloise par inversion des anomalies gravimétriques, *Unpublished IPSN/CNRS report*, in french.

Chapter IV

Publications

IV.1 Development of numerical methods

1. Etienne, V., Chaljub, E., Virieux, J., & Glinsky, N., 2010. An hp-adaptive discontinuous Galerkin finite-element method for 3-D elastic wave modelling, *Geophys. J. Int.*, **183**(2), 941–962.
2. Moczo, P., Kristek, J., Galis, M., Chaljub, E., & Etienne, V., 2011. 3-D finite-difference, finite-element, discontinuous-Galerkin and spectral-element schemes analysed for their accuracy with respect to P-wave to S-wave speed ratio, *Geophys. J. Int.*, **187**, 1645–1667.
3. Blanc, E., Komatitsch, D., Chaljub, E., Lombard, B., & Xie, Z., 2016. Highly-accurate stability-preserving optimization of the zener viscoelastic model, with application to wave propagation in the presence of strong attenuation, *Geophys. J. Int.*, **205**, 427–439.
4. Kristek, J., Moczo, P., Chaljub, E., & Kristekova, M., 2017. An orthorhombic representation of a heterogeneous medium for the finite-difference modelling of seismic wave propagation, *Geophys. J. Int.*, **208**, 1250–1264.

Geophysical Journal International

Geophys. J. Int. (2010) **183,** 941–962 doi: 10.1111/j.1365-246X.2010.04764.x

An *hp*-adaptive discontinuous Galerkin finite-element method for 3-D elastic wave modelling

V. Etienne,[1] E. Chaljub,[2] J. Virieux[2] and N. Glinsky[3,4]

[1]*Géoazur - Université de Nice Sophia-Antipolis - CNRS, France. E-mail: etienne@geoazur.unice.fr*
[2]*Laboratoire de Géophysique Interne et Tectonophysique - Université Joseph Fourier - CNRS, France*
[3]*LCPC/CETE de Nice, France*
[4]*INRIA Sophia Antipolis Méditerannée, France*

Accepted 2010 August 4. Received 2010 July 21; in original form 2010 February 12

SUMMARY

We present a discontinuous Galerkin finite-element method (DG-FEM) formulation with Convolutional Perfectly Matched Layer (CPML) absorbing boundary condition for 3-D elastic seismic wave modelling. This method makes use of unstructured tetrahedral meshes locally refined according to the medium properties (*h*-adaptivity), and of approximation orders that can change from one element to another according to an adequate criterion (*p*-adaptivity). These two features allow us to significantly reduce the computational cost of the simulations. Moreover, we have designed an efficient CPML absorbing boundary condition, both in terms of absorption and computational cost, by combining approximation orders in the numerical domain. A quadratic interpolation is typically used in the medium to obtain the required accuracy, while lower approximation orders are used in the CPMLs to reduce the total computational cost and to obtain a well-balanced workload over the processors. While the efficiency of DG-FEMs have been largely demonstrated for high approximation orders, we favour the use of low approximation orders as they are more appropriate to the applications we are interested in. In particular, we address the issues of seismic modelling and seismic imaging in cases of complex geological structures that require a fine discretization of the medium. We illustrate the efficiency of our approach within the framework of the EUROSEISTEST verification and validation project, which is designed to compare high-frequency (up to 4 Hz) numerical predictions of ground motion in the Volvi basin (Greece). Through the tetrahedral meshing, we have achieved fine discretization of the basin, which appears to be a *sine qua non* condition for accurate computation of surface waves diffracted at the basin edges. We compare our results with predictions computed with the spectral element method (SEM), and demonstrate that our method yields the same level of accuracy with computation times of the same order of magnitude.

Key words: Surface waves and free oscillations; Site effects; Computational seismology; Wave propagation.

1 INTRODUCTION

Over the last decades, simulations of wave propagation in complex media have been efficiently tackled with finite-difference methods (FDMs) and applied with success to numerous physical problems (Graves 1996; Moczo *et al.* 2007). Nevertheless, FDMs suffer from some critical issues that are inherent to the underlying Cartesian grid, such as parasite diffractions in cases where the boundaries have a complex topography. To reduce these artefacts, the discretization should be fine enough to reduce the 'stair-case' effect at the free surface. For instance, a second-order rotated FDM requires up to 60 gridpoints per wavelength to compute an accurate seismic wavefield in elastic media with a complex topography (Bohlen & Saenger 2006). Such constraints on the discretization drastically restrict the possible field of realistic applications. Some interesting combinations of FDMs and finite-element methods (FEMs) might overcome these limitations (Galis *et al.* 2008). The idea is to use an unstructured FEM scheme to represent both the topography and the shallow part of the medium, and to adopt for the rest of the model a classical FDM regular grid. For the same reasons as the issues related to the topography, uniform grids are not suitable for highly heterogeneous media, since the grid size is determined by the shortest wavelength. Except in some circumstances, like mixing grids (Aoi & Fujiwara 1999) or using non uniform Cartesian grids (Pitarka 1999) in the case of a low velocity layer, it is almost impossible to locally adapt the grid size to the medium properties in the

general case. From this point of view, FEMs are appealing, since they can use unstructured grids or meshes. Due to ever-increasing computational power, these kinds of methods have been the focus of a lot of interest and have been used intensively in seismology (Aagaard *et al.* 2001; Akcelik *et al.* 2003; Ichimura *et al.* 2007). Usually, the approximation order remains low, due to the prohibitive computational cost related to a non-diagonal mass matrix. However, this high computational cost can be avoided by mass lumping, a standard technique that replaces the large linear system by a diagonal matrix (Marfurt 1984; Chin-Joe-Kong *et al.* 1999). Another class of FEMs that relies on the Gauss–Lobatto–Legendre quadrature points has removed these limitations, and allows for spectral convergence with high approximation orders. This high-order FEM, called the spectral element method (SEM, Seriani & Priolo 1994; Komatitsch & Vilotte 1998), has been applied to large-scale geological models, up to the global scale (Chaljub *et al.* 2007; Komatitsch *et al.* 2008). The major limitation of SEM is the exclusive use of hexahedral meshes, which makes the design of an optimal mesh cumbersome in contrast to the flexibility offered by tetrahedral meshes. With tetrahedral meshes (Frey & George 2008), it is possible to fit almost perfectly complex topographies or geological discontinuities and the mesh width can be adapted locally to the medium properties (*h*-adaptivity). The extension of the SEM to tetrahedral elements represents ongoing work, while some studies have been done in two dimensions on triangular meshes (Mercerat *et al.* 2006; Pasquetti & Rapetti 2006). On the other hand, another kind of FEM has been proven to give accurate results on tetrahedral meshes: the discontinuous Galerkin finite-element method (DG-FEM) in combination with the arbitrary high-order derivatives (ADER) time integration (Dumbser & Käser 2006). Originally, DG-FEM was developed for the neutron transport equation (Reed & Hill 1973). It has been applied to a wide range of applications such as electromagnetics (Cockburn *et al.* 2004), aeroacoustics (Toulopoulos & Ekaterinaris 2006) and plasma physics (Jacobs & Hesthaven 2006), just to cite a few examples. This method relies on the exchange of numerical fluxes between adjacent elements. Contrary to classical FEMs, no continuity of the basis functions is imposed between elements, and therefore the method supports discontinuities in the seismic wavefield, as in the case of a fluid–solid interface. In such cases, the DG-FEM allows the same equation to be used for both the elastic and the acoustic media, and it does not require any explicit conditions on the interface (Käser & Dumbser 2008), which is, on the contrary, mandatory for continuous formulations, like the SEM (Chaljub *et al.* 2003). Moreover, the DG-FEM is completely local, which means that elements do not share their nodal values, contrary to conventional continuous FEM. Local operators make the method suitable for parallelization and allow for the mixing of different approximation orders (*p*-adaptivity).

However, in most studies, the DG-FEM is generally used with high approximation orders. Here, we present a low-order DG-FEM formulation with the convolutional perfectly matched layer (CPML) absorbing boundary condition (Roden & Gedney 2000; Komatitsch & Martin 2007) that is suitable for large-scale 3-D seismic wave simulations. In this context, the DG-FEM provides major benefits. Our approach relies intensively on the *p*-adaptivity. This last feature is crucial for efficient simulations, in order to mitigate the effects of the very small elements that are generally encountered in refined tetrahedral meshes. Indeed, the *p*-adaptivity allows an optimized time stepping to be achieved, by adapting the approximation order according to the size of the elements and the properties of the medium. The benefit of such a numerical scheme is particularly important with strongly heterogeneous media. Due to the mathematical formulation we consider, the medium properties are assumed to be constant per element. Therefore, meshes have to be designed in such a way that this assumption is compatible with the expected accuracy. In particular, we address the issues of seismic modelling and seismic imaging in complex media. In the first application, the discretization must be able to represent the geological structures fairly, without oversampling, while in the second, the spatial resolution of the imaging process puts constraints on the coarsest parametrization of the medium. If we consider full waveform inversion (FWI) applications, the expected imaging resolution reaches half a wavelength, as shown by Sirgue & Pratt (2004). Therefore, following the Shannon theorem, a minimum number of four points per wavelength is required to obtain such accuracy. These reasons have motivated our development of DG-FEM with low orders. In this study, we focus on the quadratic interpolation, which yields a good compromise between accuracy, discretization and computational cost.

This paper is structured as follows. In Section 2, we review in detail the DG-FEM formulation, and introduce the concept of *p*-adaptivity. The implementation of the method on distributed memory machines is discussed in Section 3. The source excitation and two kinds of boundary conditions are explained in Section 4: the free surface, and the absorbing boundary conditions. Special attention is paid to the latter with the detailed CPML formulation. The efficiency of the CPML is demonstrated with validation tests that in some cases reveal instabilities inside the absorbing layers. The strategy for saving CPU time and memory with low-order CPML is then presented. In Section 5, we study the convergence of the method, and the ability to compute accurate surface waves when a free surface is considered. The advantages of the *hp*-adaptivity in the context of tetrahedral meshes are discussed in Section 6. Finally, in Section 7, we illustrate the efficiency of our method, with a challenging seismological model, where the computation of surface waves is critical for the prediction of site effects.

2 THE DG-FEM FORMULATION

2.1 Elastodynamic system

The equations governing particle velocity and stress in an isotropic elastic medium, namely the elastodynamic system (Virieux 1986), is a first-order hyperbolic system. Following the approach of BenJemaa *et al.* (2009), the elastodynamic system can be written in the following pseudo-conservative form

$$\begin{aligned} \rho \partial_t \vec{v} &= \sum_{\theta \in \{x,y,z\}} \partial_\theta (\mathcal{M}_\theta \vec{\sigma}) + \vec{f} \\ \Lambda \partial_t \vec{\sigma} &= \sum_{\theta \in \{x,y,z\}} \partial_\theta (\mathcal{N}_\theta \vec{v}) + \Lambda \partial_t \vec{\sigma}_0, \end{aligned} \tag{1}$$

with the definitions of the velocity and stress vectors as

$$\begin{aligned} \vec{v} &= (v_x \; v_y \; v_z)^T \\ \vec{\sigma} &= (\tau \; \tau' \; \tau'' \; \sigma_{xy} \; \sigma_{xz} \; \sigma_{yz})^T, \end{aligned} \tag{2}$$

and

$$\begin{aligned} \tau &= \frac{1}{3}(\sigma_{xx} + \sigma_{yy} + \sigma_{zz}) \\ \tau' &= \frac{1}{3}(2\sigma_{xx} - \sigma_{yy} - \sigma_{zz}) \\ \tau'' &= \frac{1}{3}(-\sigma_{xx} + 2\sigma_{yy} - \sigma_{zz}). \end{aligned} \tag{3}$$

Due to the change of variables defined in eq. (3), the right-hand side of (1) does not include any terms that relate to the physical

properties. $\mathcal{M}_\theta$ and $\mathcal{N}_\theta$ are constant real matrices (Appendix B). Λ is a diagonal matrix given by

$$\Lambda = \mathrm{diag}\left(\frac{3}{3\lambda+2\mu}, \frac{3}{2\mu}, \frac{3}{2\mu}, \frac{1}{\mu}, \frac{1}{\mu}, \frac{1}{\mu}\right),$$

where λ and μ are the Lamé parameters. Moreover, the diagonality of Λ is an essential point of our formulation since the inverse of this matrix is required for the computation of the stress components (eq. 1). The extension of the pseudo-conservative form for the anisotropic or viscoelastic cases should be further analysed since the change of variable may depend on the physical parameters while the isotropic purely elastic case requires the simple global change of variables as shown in this study. Finally, in eq. (1), ρ is the medium density, while $\vec{f}$ and $\vec{\sigma}_0$ are the external forces and the initial stresses, respectively.

2.2 Spatial discretization

As is usual with FEMs (Zienkiewicz *et al.* 2005), we want to approximate the solution of eq. (1) by means of polynomial basis functions defined in volume elements. The spatial discretization is carried out with non-overlapping and conforming tetrahedra. We adopt the nodal form of the DG-FEM formulation (Hesthaven & Warburton 2008), assuming that the stress and velocity vectors are approximated in the tetrahedral elements as follows

$$\begin{aligned}\widehat{\vec{v}}_i(\vec{x},t) &= \sum_{j=1}^{d_i} \vec{v}_{ij}(\vec{x}_j,t)\,\varphi_{ij}(\vec{x})\\ \widehat{\vec{\sigma}}_i(\vec{x},t) &= \sum_{j=1}^{d_i} \vec{\sigma}_{ij}(\vec{x}_j,t)\,\varphi_{ij}(\vec{x}),\end{aligned} \tag{4}$$

where i is the index of the element, $\vec{x}$ is the spatial coordinates inside the element, and t is the time. d_i is the number of nodes or degrees of freedom (DOF) associated with the interpolating Lagrangian polynomial basis function φ_{ij} relative to the jth node located at position $\vec{x}_j$. The expressions of the Lagrangian basis functions are given in Appendix A. $\vec{v}_{ij}$ and $\vec{\sigma}_{ij}$ are the velocity and stress vectors, respectively, evaluated at the jth node of the element. Although it is not an intrinsic limitation, we have adopted here the same set of basis functions for the interpolation of the velocity and the stress components. In the following, the notation P_k refers to a spatial discretization based on polynomial basis functions of degree k, and a P_k element is a tetrahedron in which a P_k scheme is applied. The number of DOF in a tetrahedral element is given by $d_i = (k+1)(k+2)(k+3)/6$. For instance, in a P_0 element (Fig. 1a), there is only one DOF (the stress and velocity are constant per element), while in a P_1 element (Fig. 1b), there are four DOF located at the four vertices of the tetrahedron (the stress and velocity are linearly interpolated). It is worth noting that the P_0 scheme corresponds to the case of the finite-volume method (BenJemaa *et al.* 2007, 2009; Brossier *et al.* 2008). For the quadratic approximation order P_2, one node is added at the middle of each edge of the tetrahedron, leading to a total of 10 DOF per element (Fig. 1c).

The first step in the finite-element formulation is to obtain the weak form of the elastodynamic system. To do so, we multiply eq. (1) by a test function φ_{ir} and integrate the system over the volume of the element i. For the test function, we adopt the same kind of function as used for the approximation of the solution. This case corresponds to the standard Galerkin method and can be written as

$$\begin{aligned}\int_{V_i} \varphi_{ir}\,\rho\,\partial_t\vec{v}\,\mathrm{d}V &= \int_{V_i} \varphi_{ir} \sum_{\theta\in\{x,y,z\}} \partial_\theta(\mathcal{M}_\theta\vec{\sigma})\,\mathrm{d}V\\ \int_{V_i} \varphi_{ir}\,\Lambda\,\partial_t\vec{\sigma}\,\mathrm{d}V &= \int_{V_i} \varphi_{ir} \sum_{\theta\in\{x,y,z\}} \partial_\theta(\mathcal{N}_\theta\vec{v})\,\mathrm{d}V \quad \forall r\in[1,\ d_i],\end{aligned} \tag{5}$$

where V_i is the volume of the tetrahedral element i. For the purpose of clarity, we have omitted the external forces and stresses in (5). Integration by parts of the right-hand side of (5) leads to

$$\begin{aligned}\int_{V_i} \varphi_{ir}\,\rho\,\partial_t\vec{v}\,\mathrm{d}V &= -\int_{V_i} \sum_{\theta\in\{x,y,z\}} \partial_\theta\varphi_{ir}\,(\mathcal{M}_\theta\vec{\sigma})\,\mathrm{d}V\\ &\quad + \int_{S_i} \varphi_{ir}\Big(\sum_{\theta\in\{x,y,z\}} \mathcal{M}_\theta\,n_\theta\Big)\vec{\sigma}\,\mathrm{d}S\\ \int_{V_i} \varphi_{ir}\,\Lambda\,\partial_t\vec{\sigma}\,\mathrm{d}V &= -\int_{V_i} \sum_{\theta\in\{x,y,z\}} \partial_\theta\varphi_{ir}\,(\mathcal{N}_\theta\vec{v})\,\mathrm{d}V\\ &\quad + \int_{S_i} \varphi_{ir}\Big(\sum_{\theta\in\{x,y,z\}} \mathcal{N}_\theta\,n_\theta\Big)\vec{v}\,\mathrm{d}S,\end{aligned} \tag{6}$$

with S_i as the surface of the element i, and $\vec{n} = (n_x, n_y, n_z)^T$ as the outward pointing unit normal vector with respect to the surface S_i. In the second term of the right-hand side of eq. (6), the fluxes of the stress and velocity wavefields across the faces of the element i appear. For evaluation of these fluxes, we adopt the centred flux scheme for its non-dissipative property (Remaki 2000; BenJemaa *et al.* 2009; Delcourte *et al.* 2009). Using eq. (4) and assuming constant physical properties per element, eq. (6) can be approximated

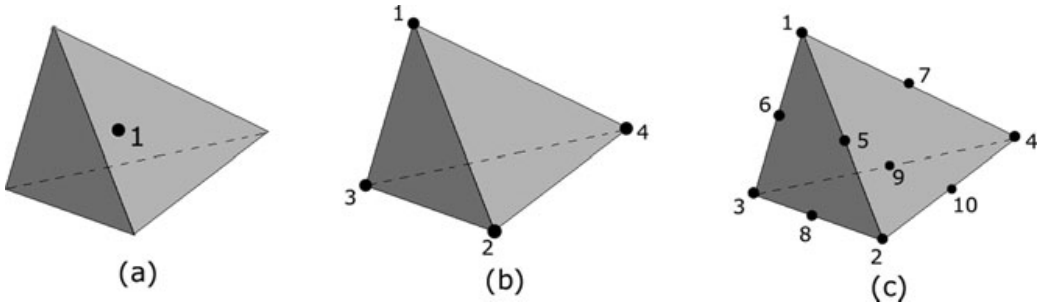

Figure 1. (a) P_0 element with one unique DOF. (b) P_1 element with four DOF. (c) P_2 element with 10 DOF.

with

$$\rho_i \int_{V_i} \varphi_{ir}\, \partial_t \widehat{\vec{v}}_i \,\mathrm{d}V = -\int_{V_i} \sum_{\theta\in\{x,y,z\}} \partial_\theta \varphi_{ir}\, (\mathcal{M}_\theta \widehat{\vec{\sigma}}_i)\,\mathrm{d}V + \frac{1}{2}\sum_{k\in N_i}\int_{S_{ik}} \varphi_{ir}\, \mathcal{P}_{ik}(\widehat{\vec{\sigma}}_i + \widehat{\vec{\sigma}}_k)\,\mathrm{d}S$$

$$\Lambda_i \int_{V_i} \varphi_{ir}\, \partial_t \widehat{\vec{\sigma}}_i \,\mathrm{d}V = -\int_{V_i} \sum_{\theta\in\{x,y,z\}} \partial_\theta \varphi_{ir}\, (\mathcal{N}_\theta \widehat{\vec{v}}_i)\,\mathrm{d}V + \frac{1}{2}\sum_{k\in N_i}\int_{S_{ik}} \varphi_{ir}\, \mathcal{Q}_{ik}(\widehat{\vec{v}}_i + \widehat{\vec{v}}_k)\,\mathrm{d}S, \qquad (7)$$

with $k \in N_i$ representing the elements k adjacent to the element i, and S_{ik} the face between elements i and k. $\mathcal{P}$ and $\mathcal{Q}$ are defined as follows

$$\mathcal{P}_{ik} = \sum_{\theta\in\{x,y,z\}} n_{ik\theta}\, \mathcal{M}_\theta$$

$$\mathcal{Q}_{ik} = \sum_{\theta\in\{x,y,z\}} n_{ik\theta}\, \mathcal{N}_\theta,$$

where $n_{ik\theta}$ is the component along the θ axis of the unit vector $\vec{n}_{ik}$ of the face S_{ik} that points from element i to element k. Eq. (7) indicates that the computations of the stress and velocity wavefields in one element require information from the directly neighbouring elements. This illustrates clearly the local nature of DG-FEM. Using the tensor product $\otimes$, we obtain the expression

$$\rho_i(\mathcal{I}_3 \otimes \mathcal{K}_i)\partial_t \vec{v}_i = -\sum_{\theta\in\{x,y,z\}} (\mathcal{M}_\theta \otimes \mathcal{E}_{i\theta})\vec{\sigma}_i + \frac{1}{2}\sum_{k\in N_i}\Big[(\mathcal{P}_{ik}\otimes\mathcal{F}_{ik})\vec{\sigma}_i + (\mathcal{P}_{ik}\otimes\mathcal{G}_{ik})\vec{\sigma}_k\Big]$$

$$(\Lambda_i \otimes \mathcal{K}_i)\partial_t \vec{\sigma}_i = -\sum_{\theta\in\{x,y,z\}} (\mathcal{N}_\theta \otimes \mathcal{E}_{i\theta})\vec{v}_i + \frac{1}{2}\sum_{k\in N_i}\Big[(\mathcal{Q}_{ik}\otimes\mathcal{F}_{ik})\vec{v}_i + (\mathcal{Q}_{ik}\otimes\mathcal{G}_{ik})\vec{v}_k\Big], \qquad (8)$$

where $\mathcal{I}_3$ represents the identity matrix. In eq. (8), the vectors $\vec{v}_i$ and $\vec{\sigma}_i$ should be read as the collection of all nodal values of the velocity and stress components in the element i. We now introduce the mass matrix

$$(\mathcal{K}_i)_{rj} = \int_{V_i} \varphi_{ir}\,\varphi_{ij}\,\mathrm{d}V \qquad j,r \in [1,\ d_i], \qquad (9)$$

the stiffness matrix

$$(\mathcal{E}_{i\theta})_{rj} = \int_{V_i} (\partial_\theta \varphi_{ir})\,\varphi_{ij}\,\mathrm{d}V \qquad j,r \in [1,\ d_i], \qquad (10)$$

with $\theta \in \{x, y, z\}$, and the flux matrices

$$(\mathcal{F}_{ik})_{rj} = \int_{S_{ik}} \varphi_{ir}\,\varphi_{ij}\,\mathrm{d}S \qquad j,r \in [1,\ d_i] \qquad (11)$$

$$(\mathcal{G}_{ik})_{rj} = \int_{S_{ik}} \varphi_{ir}\,\varphi_{kj}\,\mathrm{d}S \qquad r \in [1,\ d_i] \qquad j \in [1,\ d_k]. \qquad (12)$$

It is worth noting that in eq. (12), the DOF of elements i and k appear (d_i and d_k, respectively) indicating that the approximation orders are totally decoupled from one element to another. Therefore, the DG-FEM allows for varying approximation orders in the numerical scheme. This feature is referred to as p-adaptivity. Moreover, given an approximation order, these matrices are unique for all elements (with a normalization according to the volume or surface of the elements) and they can be computed before hand with appropriate integration quadrature rules. The memory requirement is therefore low, since only a collection of small matrices is needed according to the possible combinations of approximation orders. The maximum size of these matrices is $(d_{\max} \times d_{\max})$ where $d_{\max}$ is the maximum number of DOF per element and the number of matrices to store is given by the square of the number of approximation orders mixed in the numerical domain. Details regarding the computation of the matrices are given in Appendix B. It should be mentioned that to retrieve both the velocity and the stress components, eq. (8) requires the computation of $\mathcal{K}_i^{-1}$, which can also be performed before hand.

Note that if we want to consider variations in the physical properties inside the elements, the pseudo-conservative form makes the computation of flux much easier and computationally more efficient than in the classical elastodynamic system. These properties come from the fact that in the pseudo-conservative form, the physical properties are located in the left-hand side of eq. (1). Therefore, no modification of the stiffness and flux matrices nor additional terms are needed in eq. (8) to take into account the variation of properties. Only the mass matrix needs to be evaluated for each element and for each physical property according to the expression

$$(\mathcal{K}_i)_{rj} = \int_{V_i} \chi_i(\vec{x})\,\varphi_{ir}(\vec{x})\,\varphi_{ij}(\vec{x})\,\mathrm{d}V \qquad j,r \in [1,\ d_i], \qquad (13)$$

where $\chi_i(\vec{x})$ represents the physical property (ρ_i or one of the Λ_i components) varying inside the element.

2.3 Time discretization

For the time integration of eq. (8), we adopt a second-order explicit leap-frog scheme that allows to compute alternatively the velocity and the stress components between a half time step. Eq. (8) can be written as

$$\rho_i(\mathcal{I}_3 \otimes \mathcal{K}_i)\frac{\vec{v}_i^{\,n+\frac{1}{2}} - \vec{v}_i^{\,n-\frac{1}{2}}}{\Delta t} = -\sum_{\theta\in\{x,y,z\}} (\mathcal{M}_\theta \otimes \mathcal{E}_{i\theta})\vec{\sigma}_i^{\,n} + \frac{1}{2}\sum_{k\in N_i}\Big[(\mathcal{P}_{ik}\otimes\mathcal{F}_{ik})\vec{\sigma}_i^{\,n} + (\mathcal{P}_{ik}\otimes\mathcal{G}_{ik})\vec{\sigma}_k^{\,n}\Big]$$

$$(\Lambda_i \otimes \mathcal{K}_i)\frac{\vec{\sigma}_i^{\,n+1} - \vec{\sigma}_i^{\,n}}{\Delta t} = -\sum_{\theta\in\{x,y,z\}} (\mathcal{N}_\theta \otimes \mathcal{E}_{i\theta})\vec{v}_i^{\,n+\frac{1}{2}} + \frac{1}{2}\sum_{k\in N_i}\Big[(\mathcal{Q}_{ik}\otimes\mathcal{F}_{ik})\vec{v}_i^{\,n+\frac{1}{2}} + (\mathcal{Q}_{ik}\otimes\mathcal{G}_{ik})\vec{v}_k^{\,n+\frac{1}{2}}\Big], \qquad (14)$$

where the superscript n indicates the time step. We chose to apply the definition of the time step as given by Käser *et al.* (2008), which links the mesh width and time step as follows

$$\Delta t < \min_i \left(\frac{1}{2k_i + 1}\cdot\frac{2r_i}{V_{Pi}}\right), \qquad (15)$$

where r_i is the radius of the sphere inscribed in the element indexed by i, V_{Pi} is the P-wave velocity in the element, and k_i is the polynomial degree used in the element. Eq. (15) is a heuristic stability criterion that usually works well. However, there is no mathematical proof for unstructured meshes that guarantees numerical stability.

3 COMPUTATIONAL ASPECTS

As mentioned in Section 2, the DG-FEM is a local method, and therefore it is naturally suitable for parallel computing. In our implementation, the parallelism relies on a domain-partitioning strategy, assigning one subdomain to one CPU. This corresponds to the

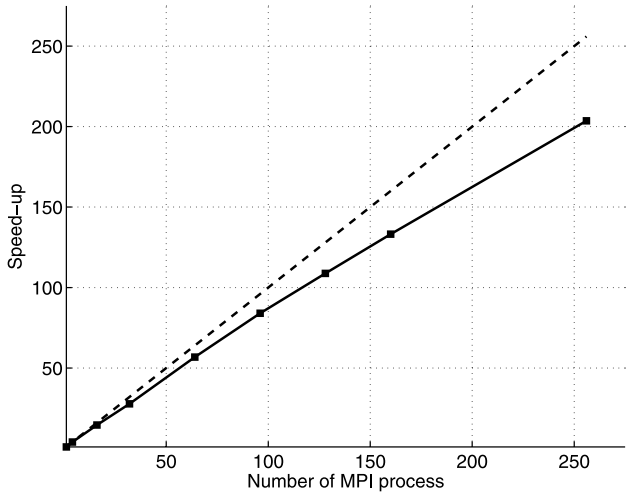

Figure 2. Speed-up observed when the number of MPI processes is increased from 1 to 256 for modelling with a mesh of 1.8 million P_2 elements. The ideal speed-up is plotted with a dashed line, the observed speed-up with a continuous line. These values were observed on a computing platform with bi-processor quad core Opteron 2.3 GHz CPUs interconnected with Infiniband at 20 Gb s^{-1}.

single program mutiple data (SPMD) architecture, which means that there is only one program and each CPU uses the same executable to work on different parts of the 3-D mesh. Communication between the subdomains is performed with the message passing interface (MPI) parallel environment (Aoyama & Nakano 1999), which allows for applications to run on distributed memory machines. For efficient load balancing among the CPUs, the mesh is divided with the partitioner METIS (Karypis & Kumar 1998), to balance the number of elements in the subdomains, and to minimize the number of adjacent elements between the subdomains. These two criteria are crucial for the efficiency of the parallelism on large-scale numerical simulations. Fig. 2 shows the observed speed-up (i.e. the ratio between the computation time with one CPU, and the computation time with N CPUs) when the number of MPI processes is increased from 1 to 256, for strong scaling calculations on a fixed mesh of 1.8 million P_2 elements. This figure shows good efficiency of the parallelism, of around 80 per cent.

In our formulation, another key point is the time step, which is common for all of the subdomains. The time step should satisfy the stability condition given in eq. (15) for every element. Consequently, the element with the smallest time step imposes its time step on all of the subdomains. We should mention here a more elaborate approach with local time stepping (Dumbser *et al.* 2007) that allows for elements to have their own time step independent of the others. Nevertheless, the p-adaptivity offered by DG-FEM allows mitigation of the computational burden resulting from the common time step. This point is detailed in section 6. From a technical point of view, we implemented the method in the FORTRAN 90 language without the use of specific mathematical libraries like Basic Linear Algebra Subroutines (BLAS). Indeed, the matrix products in the DG-FEM formulation involve relatively small matrices (typically 10×10 in P_2). Therefore, we did not experience substantial gains when calling mathematical libraries, as already observed by Komatitsch *et al.* (2008) for SEM.

4 SOURCE EXCITATION AND BOUNDARY CONDITIONS

We consider here the implementation of a point source in the DG-FEM, and we detail two types of boundary conditions that are generally encountered in seismic modelling: the free surface, and the absorbing boundary conditions. Special attention is given to the latter, based on the CPML (Drossaert & Giannopoulos 2007; Komatitsch & Martin 2007). To our knowedge, this point has not been studied intensely in a DG-FEM framework.

4.1 Source excitation

The excitation of a point source is projected onto the nodes of the element that contains the source as follows

$$\vec{s}_i^n = \frac{\vec{\varphi}_i(\vec{x}_s)}{\sum_{j=1}^{d_i} \varphi_{ij}(\vec{x}_s) \int_{V_i} \varphi_{ij}(\vec{x}) \mathrm{d}V} s(t), \tag{16}$$

with $\vec{s}_i^n$ the nodal values vector associated to the excited component, $t = n\Delta t$, $\vec{x}_s$ the position of the point source and $s(t)$ the source function. Eq. (16) gives the source term that should be added to the right-hand side of eq. (14) for the required components. It should be noticed that this term is only applied to the element containing the source. Depending on the approximation order, the spatial support of the source varies. Fig. 3(a) shows that the support of a P_0 element is actually the whole volume of the element (represented on the cross-section with a homogeneous white area). In this case, no precise localization of the source inside the element is possible due to the constant piecewise interpolation approximation. On the other hand, in a P_1 element (Fig. 3b), the spatial support of the source is linear and allows for a rough localization of the source. In a P_2

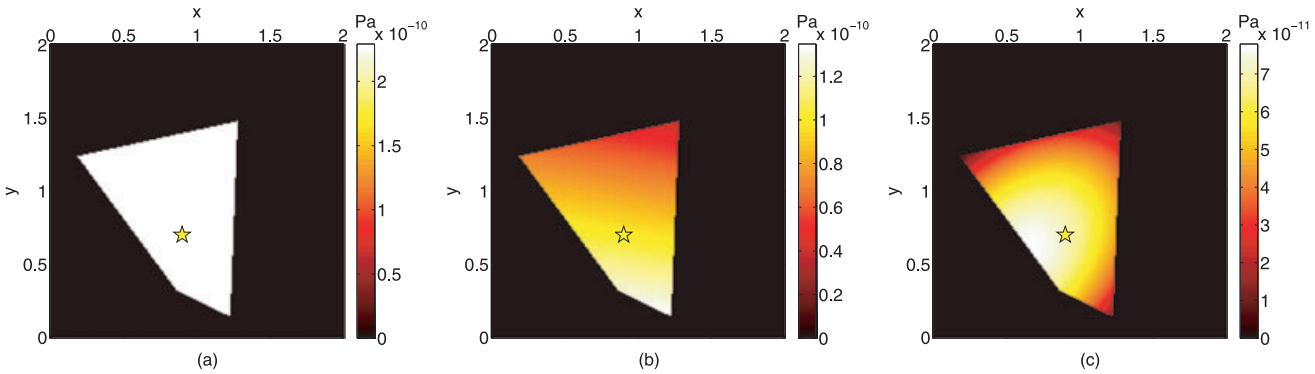

Figure 3. (a) Cross-section of the mesh near the source position, indicated with a yellow star in the xy plane. This view represents the spatial support of the stress component in a P_0 element containing the point source. (b) Same as (a) with a P_1 element. (c) Same as (a) with a P_2 element.

element (Fig. 3c), the quadratic spatial support tends to resemble the expected Dirac in space close to the source position. It should be noted that the limitations concerning source localization also apply to the solution extraction at the receivers, according to the approximation order of the elements containing the receivers.

4.2 Free surface condition

For the element faces located on the free surface, we use an explicit condition by changing the flux expression locally. This is carried out with the concept of virtual elements, which are exactly symmetric to the elements located on the free surface. Inside the virtual elements, we impose a velocity wavefield that is identical to the wavefield of the corresponding inner elements, and we impose an opposite stress wavefield. As a result, the velocity is seen as continuous across the free surface, while the stress is equal to zero on the faces related to the free surface.

4.3 Absorbing boundary condition

For simulations in an infinite medium, an absorbing boundary condition needs to be applied at the edges of the numerical model. An efficient way to mimic such an infinite medium can be achieved with PMLs, which was initially developed by Berenger (1994) for electromagnetics, and adapted for elastodynamics by Chew & Liu (1996). PMLs are anisotropic absorbing layers that are added at the periphery of the numerical model. The classical PML formulation is based on splitting of the elastodynamic equations. In the following, we use a new kind of PML, known as CPML, which does not require split terms. The CPML originated from Roden & Gedney (2000) for electromagnetics and was applied by Komatitsch & Martin (2007) and Drossaert & Giannopoulos (2007) to the elastodynamic system. CPML is based on an idea of Kuzuoglu & Mittra (1996), who obtained a strictly causal form of PML by adding some parameters in the standard damping function of Berenger (1994), which enhanced the absorption of waves arriving at the boundaries of the model with grazing incidence angles.

4.3.1 CPML formulation

Inside the CPML, a damping function is applied only onto the spatial derivative perpendicular to the boundary. In the CPML formulation, the damping function is defined in the frequency domain as follows

$$s_\theta = \kappa_\theta + \frac{d_\theta}{\alpha_\theta + \mathrm{i}\omega} \qquad \forall \theta \in \{x, y, z\}, \tag{17}$$

with angular frequency ω and coefficients $\kappa_\theta \geq 1$ and $\alpha_\theta \geq 0$. The damping profile d_θ varies from 0 at the entrance of the layer, up to a maximum real value $d_{\theta\max}$ at the end (Collino & Tsogka 2001) such that

$$d_\theta = d_{\theta\max}\left(\frac{\delta_\theta}{L_{\mathrm{cpml}}}\right)^2, \tag{18}$$

and

$$d_{\theta\max} = -3V_P\frac{\log(R_{\mathrm{coeff}})}{2L_{\mathrm{cpml}}} \qquad \forall \theta \in \{x, y, z\}, \tag{19}$$

with δ_θ as the depth of the element barycentre inside the CPML, L_{cpml} the thickness of the absorbing layer, and R_{coeff} the theoretical reflection coefficient. For all of the tests presented in the following, we chose $R_{\mathrm{coeff}} = 0.1$ per cent. α_θ is a coefficient that varies from a maximum value ($\alpha_{\theta_{\max}} = \pi f_0$) at the entrance of the CPML, to zero at its end. If $\kappa_\theta = 1$ and $\alpha_\theta = 0$, the classical PML formulation is obtained. In the CPML, the spatial derivatives are replaced by

$$\partial_{\tilde{\theta}} \rightarrow \frac{1}{\kappa_\theta}\partial_\theta + \zeta_\theta * \partial_\theta \qquad \forall \theta \in \{x, y, z\}, \tag{20}$$

with

$$\zeta_\theta(t) = -\frac{d_\theta}{\kappa_\theta^2}H(t)e^{-(d_\theta\kappa_\theta+\alpha_\theta)t} \qquad \forall \theta \in \{x, y, z\}, \tag{21}$$

where *H(t)* denotes the Heaviside distribution. Roden & Gedney (2000) have demonstrated that the time convolution in eq. (20) can be performed in a recursive way using memory variables defined by

$$\psi_\theta = \zeta_\theta * \partial_\theta \qquad \forall \theta \in \{x, y, z\}. \tag{22}$$

ψ_θ represents a memory variable in the sense that it is updated at each time step. Komatitsch & Martin (2007) showed that the term κ_θ has a negligible effect on the absorbing abilities, and it can be set to 1. If we take $\kappa_\theta = 1$ and derive eq. (22) using eq. (21), we get

$$\partial_t\psi_\theta = -d_\theta\partial_\theta - (d_\theta + \alpha_\theta)\psi_\theta \qquad \forall \theta \in \{x, y, z\}. \tag{23}$$

We can introduce the memory variables into the initial elastodynamic system of eq. (1) with the definition of vectors

$$\begin{aligned}\vec{\psi}_\theta(\vec{v}) &= [\psi_\theta(v_x)\ \psi_\theta(v_y)\ \psi_\theta(v_z)]^T\\ \vec{\psi}_\theta(\vec{\sigma}) &= [\psi_\theta(\tau)\ \psi_\theta(\tau')\ \psi_\theta(\tau'')\ \psi_\theta(\sigma_{xy})\ \psi_\theta(\sigma_{xz})\ \psi_\theta(\sigma_{yz})]^T\\ &\qquad \forall \theta \in \{x, y, z\}.\end{aligned} \tag{24}$$

If we apply the change of variables in eq. (20), eq. (1) becomes

$$\begin{aligned}\rho\partial_t\vec{v} &= \sum_{\theta\in\{x,y,z\}}\partial_\theta(\mathcal{M}_\theta\vec{\sigma}) + \sum_{\theta\in\{x,y,z\}}\mathcal{M}_\theta\vec{\psi}_\theta(\vec{\sigma})\\ \Lambda\partial_t\vec{\sigma} &= \sum_{\theta\in\{x,y,z\}}\partial_\theta(\mathcal{N}_\theta\vec{v}) + \sum_{\theta\in\{x,y,z\}}\mathcal{N}_\theta\vec{\psi}_\theta(\vec{v}).\end{aligned} \tag{25}$$

Eq. (25) is the initial elastodynamic system augmented by the memory variables on the right-hand side. In combination, another extra system dealing with the memory variables is

$$\begin{aligned}\partial_t\vec{\psi}_\theta(\vec{\sigma}) &= -d_\theta\partial_\theta(\vec{\sigma}) - (d_\theta + \alpha_\theta)\vec{\psi}_\theta(\vec{\sigma})\\ \partial_t\vec{\psi}_\theta(\vec{v}) &= -d_\theta\partial_\theta(\vec{v}) - (d_\theta + \alpha_\theta)\vec{\psi}_\theta(\vec{v}) \quad \forall \theta \in \{x, y, z\}.\end{aligned} \tag{26}$$

The collection of memory variables associated with each element located in the CPMLs is made of 22 memory variables per DOF. These variables correspond to the 22 spatial derivatives involved in eq. (1). If we apply the DG-FEM formulation as presented in the previous section to eqs (25) and (26), we get

$$\begin{aligned}\rho_i(\mathcal{I}_3 \otimes \mathcal{K}_i)\frac{\vec{v}_i^{\,n+\frac{1}{2}} - \vec{v}_i^{\,n-\frac{1}{2}}}{\Delta t} &= -\sum_{\theta\in\{x,y,z\}}(\mathcal{M}_\theta \otimes \mathcal{E}_{i\theta})\vec{\sigma}_i^{\,n}\\ &+ \frac{1}{2}\sum_{k\in N_i}\left[(\mathcal{P}_{ik} \otimes \mathcal{F}_{ik})\vec{\sigma}_i^{\,n} + (\mathcal{P}_{ik} \otimes \mathcal{G}_{ik})\vec{\sigma}_k^{\,n}\right]\\ &+ (\mathcal{I}_3 \otimes \mathcal{K}_i)\sum_{\theta\in\{x,y,z\}}\mathcal{M}_\theta\vec{\psi}_\theta\left(\vec{\sigma}_i^{\,n}\right)\\ (\Lambda_i \otimes \mathcal{K}_i)\frac{\vec{\sigma}_i^{\,n+1} - \vec{\sigma}_i^{\,n}}{\Delta t} &= -\sum_{\theta\in\{x,y,z\}}(\mathcal{N}_\theta \otimes \mathcal{E}_{i\theta})\vec{v}_i^{\,n+\frac{1}{2}}\\ &+ \frac{1}{2}\sum_{k\in N_i}\left[(\mathcal{Q}_{ik} \otimes \mathcal{F}_{ik})\vec{v}_i^{\,n+\frac{1}{2}} + (\mathcal{Q}_{ik} \otimes \mathcal{G}_{ik})\vec{v}_k^{\,n+\frac{1}{2}}\right]\\ &+ (\mathcal{I}_3 \otimes \mathcal{K}_i)\sum_{\theta\in\{x,y,z\}}\mathcal{N}_\theta\vec{\psi}_\theta\left(\vec{v}_i^{\,n+\frac{1}{2}}\right),\end{aligned} \tag{27}$$

incombination with the memory variable system

$$
\begin{aligned}
&(\mathcal{I}_3 \otimes \mathcal{K}_i)\frac{\vec{\psi}_\theta\left(\vec{\sigma}_i^{\,n}\right) - \vec{\psi}_\theta\left(\vec{\sigma}_i^{\,n-1}\right)}{\Delta t} = d_{i\theta}(\mathcal{I}_6 \otimes \mathcal{E}_{i\theta})\vec{\sigma}_i^{\,n-1} \\
&- d_{i\theta}\frac{1}{2}\sum_{k\in N_i} n_{ik\theta}\left[(\mathcal{I}_6 \otimes \mathcal{F}_{ik})\vec{\sigma}_i^{\,n-1} + (\mathcal{I}_6 \otimes \mathcal{G}_{ik})\vec{\sigma}_k^{\,n-1}\right] \\
&- (\mathcal{I}_3 \otimes \mathcal{K}_i)(d_{i\theta} + \alpha_{i\theta})\vec{\psi}_\theta\left(\vec{\sigma}_i^{\,n-1}\right) \\
&(\mathcal{I}_3 \otimes \mathcal{K}_i)\frac{\vec{\psi}_\theta\left(\vec{v}_i^{\,n+\frac{1}{2}}\right) - \vec{\psi}_\theta\left(\vec{v}_i^{\,n-\frac{1}{2}}\right)}{\Delta t} = \sum_{\theta\in\{x,y,z\}} d_{i\theta}(\mathcal{I}_3 \otimes \mathcal{E}_{i\theta})\vec{v}_i^{\,n-\frac{1}{2}} \\
&- d_{i\theta}\frac{1}{2}\sum_{k\in N_i} n_{ik\theta}\left[(\mathcal{I}_3 \otimes \mathcal{F}_{ik})\vec{v}_i^{\,n-\frac{1}{2}} + (\mathcal{I}_3 \otimes \mathcal{G}_{ik})\vec{v}_k^{\,n-\frac{1}{2}}\right] \\
&- (\mathcal{I}_3 \otimes \mathcal{K}_i)(d_{i\theta} + \alpha_{i\theta})\vec{\psi}_\theta\left(\vec{v}_i^{\,n-\frac{1}{2}}\right) \qquad \forall\theta \in \{x, y, z\}.
\end{aligned}
\tag{28}
$$

Eqs (27) and (28) indicate that *p*-adaptivity is also supported in the CPMLs. At the end of the CPMLs, we apply a simple free surface condition as explained in the previous section.

4.3.2 Validation tests

To validate the efficiency of the CPML, we present some simulations of wave propagation in a homogeneous, isotropic and purely elastic medium. The model size is 8 km × 8 km × 8 km, and the medium properties are: $V_P = 4000\ \mathrm{m\,s^{-1}}$, $V_S = 2310\ \mathrm{m\,s^{-1}}$ and $\rho = 2000\ \mathrm{kg\,m^{-3}}$. An explosive source is placed at coordinates ($x_s = 2000$ m, $y_s = 2000$ m, $z_s = 4000$ m) and a line of receivers is located at coordinates (3000 m $\leq x_r \leq$ 6000 m, $y_r = 2000$ m, $z_r = 4000$ m) with 500 m between receivers. The conditions of the tests are particularly severe, since the source and the receivers are located close to the CPMLs (at a distance of 250 m), thus favouring grazing waves. The source signature is a Ricker wavelet with a dominant frequency of 3 Hz and a maximum frequency of about 7.5 Hz. Due to the explosive source, only *P*-wave is generated and the minimum wavelength is about 533 m. The mesh contains 945 477 tedrahedra with an average edge of 175 m, making a discretization of about 3 elements per $\lambda_{\min}$. Figs 4(c) and (d) show the results obtained with the P_2 interpolation and CPMLs of 10-elements width ($L_{\mathrm{cpml}} = 1750$ m) at all edges of the model. With the standard scale, no reflection can be seen from the CPMLs. When the amplitude is magnified by a factor of 100, some spurious reflections are visible. This observation is in agreement with the theoretical reflection coefficient ($R_{\mathrm{coeff}} = 0.1$ per cent) in eq. (19). Fig. 5(a) allows to compare the seismograms computed with CPMLs of 10-elements width and the seismograms computed in a larger model without reflection in the time window.

As shown by Collino & Tsogka (2001), the thickness of the absorbing layer plays an important role in the absorption efficiency. In Figs 4(a) and (b), the same test was performed with CPMLs of five-elements width ($L_{\mathrm{cpml}} = 875$ m) at all edges of the model.

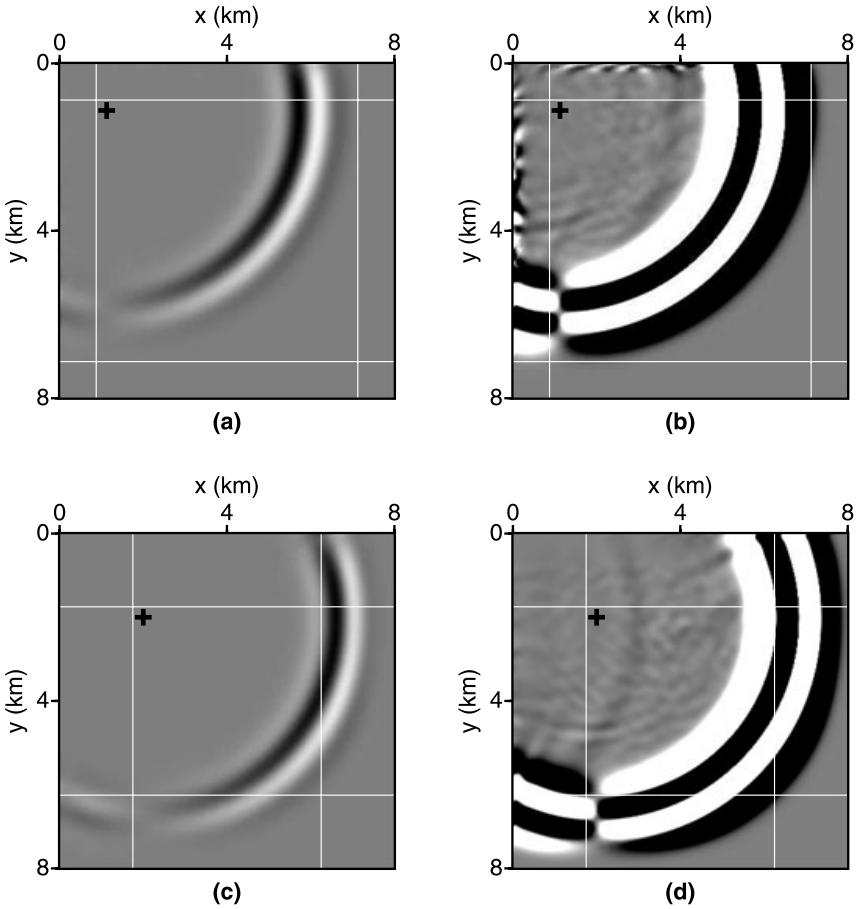

Figure 4. Snapshots at 1.6 s of the velocity component v_x in the plane *xy* that contains the source location. CPMLs of five-elements width are applied at all edges of the model. The modelling was carried out with P_2 interpolation. White lines, the limits of the CPMLs; black cross, the position of the source. (a) Real amplitude. (b) Amplitude magnified by a factor of 100. (c) and (d) Same as (a) and (b) with CPMLs of 10-elements width.

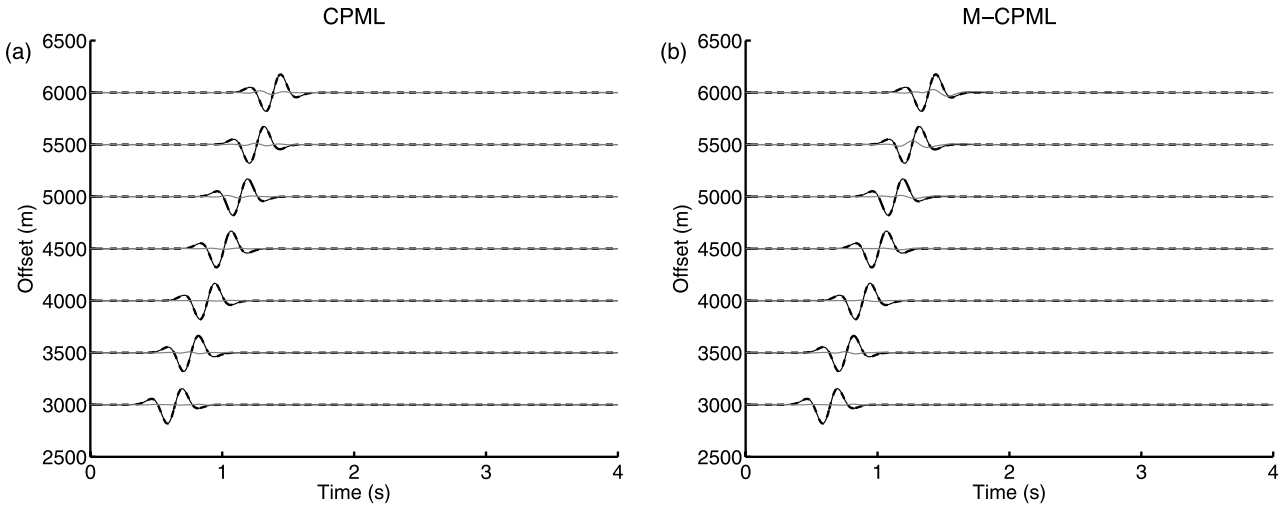

Figure 5. (a) Seismograms of the velocity component v_x. The amplitude of each seismogram is normalized. Black continuous line, numerical solution in large model without reflection in the time window; dashed line, numerical solution with 10-elements width CPMLs; grey line, residuals magnified by a factor of 10. (b) Same as (a) with 10-elements width M-CPMLs.

Compared to Figs 4(c) and (d), the amplitude of the reflections have the same order of magnitude. Nevertheless, in the upper and left parts of the model, some areas with a strong amplitude appear close to the edges. These numerical instabilities arise at the outer edges of the CPMLs, and they expand over the complete model during the simulations. Instabilities of PML in long time simulations have been studied in electromagnetics (Abarbanel *et al.* 2002; Bécache *et al.* 2004). In the following, we present a numerical stability study of CPML combined with DG-FEM for the elastodynamics. The results are shown in Fig. 6, with snapshots at long times for CPMLs of 5- and 10-elements widths. In these snapshots, the instabilities arise at the four corners of the model (at 20 s for the 10-elements width CPML). Tests with larger CPMLs (not shown) demonstrate that when the CPML width is 20 elements, these instabilities do not appear. Such instabilities were experienced by Meza-Fajardo & Papageorgiou (2008) with standard PML, for an isotropic medium. These authors proposed the application of an additional damping in the PML, onto the directions parallel to the layer, leading to a multiaxial PML (M-PML). Fig. 7 is equivalent to Fig. 6, instead that 10 per cent of the damping profile defined in eq. (18) has been added onto the directions parallel to the CPMLs (in the latter named M-CPMLs). As a result, instabilities do not appear when the CPML width is at least 10 elements while the efficiency of the absorption is preserved as shown by Fig. 5(b) with similar residuals compared to Fig. 5(a).

4.3.3 Saving computation time and memory

Table 1 gives the computation times for updating the velocity and stress wavefields in one element for one time step, for different approximation orders, without or with the update of the CPML memory variables (i.e. elements located outside or inside the CPMLs). These computation times illustrate the significant increase with respect to the approximation order, and they allow an evaluation of the additional costs of the CPML memory variables computation from 40 per cent to 60 per cent. The effects of this additionnal cost have to be analysed in the context of a domain-partitioning strategy. As introduced in Section 3, the mesh is divided into subdomains, using a partitioner. Fig. 8(a) shows the layout of the subdomains that were obtained with the partitioner METIS (Karypis & Kumar 1998) along the *xy* plane used in the previous validation tests. The mesh was divided into 32 partitions, although only a few of these are visible on the cross-section in Fig. 8(a). We used an unweighted partitioning, meaning that each partition contains approximately the same number of elements. The subdomains, partially located in the CPMLs, contain different numbers of CPML elements. In large simulations, some subdomains are totally located inside the CPMLs, and some others outside the CPMLs. In such a case, the extra computation costs of the subdomains located in the absorbing layers penalize the whole simulation. Indeed, most of the subdomains spend 40–60 per cent of the time just waiting for the subdomains located in the CPMLs to complete the computations at each time step. For a better load balancing, we propose to benefit from the *p*-adaptivity of DG-FEM, using lower approximation orders in the CPMLs. Indeed, inside the absorbing layers, we do not need a specific accuracy, and consequently the approximation order can be decreased. Table 1 indicates that such a mixed numerical scheme is advantageous, since the computation time required for a P_0 or P_1 element located in the CPML is shorter than the computation time of a standard P_2 element. Fig. 8(b) shows the approximation order per element when P_1 is used in the CPMLs and P_2 in the rest of the medium. We should note here that the interface between these two areas is not strictly aligned to a cartesian axis, and has some irregularities due to the shape of the tetrahedra. Although it is possible to constrain the alignment of the element faces parallel to the CPML limits, we did not observe significant differences in the absorption efficiency whether the faces are aligned or not.

Fig. 9(a) shows the seismograms computed when the modelling was carried out with P_2 inside the medium and P_1 in the CPMLs. Absorbing layers of 10-elements width are applied at all edges of the model. For comparison, Fig. 9(b) shows the results obtained with P_0 in the CPMLs and P_2 for the rest of the medium. In this case, the spurious reflections have significant amplitudes. The snaphots (not presented here) reveal a large number of artefacts both in the CPMLs and in the medium. These artefacts make it impossible to use these seismograms for practical applications. On the other hand, the seismograms computed with the mixed scheme P_2/P_1 show weak artefacts, and are reasonably comparable with the

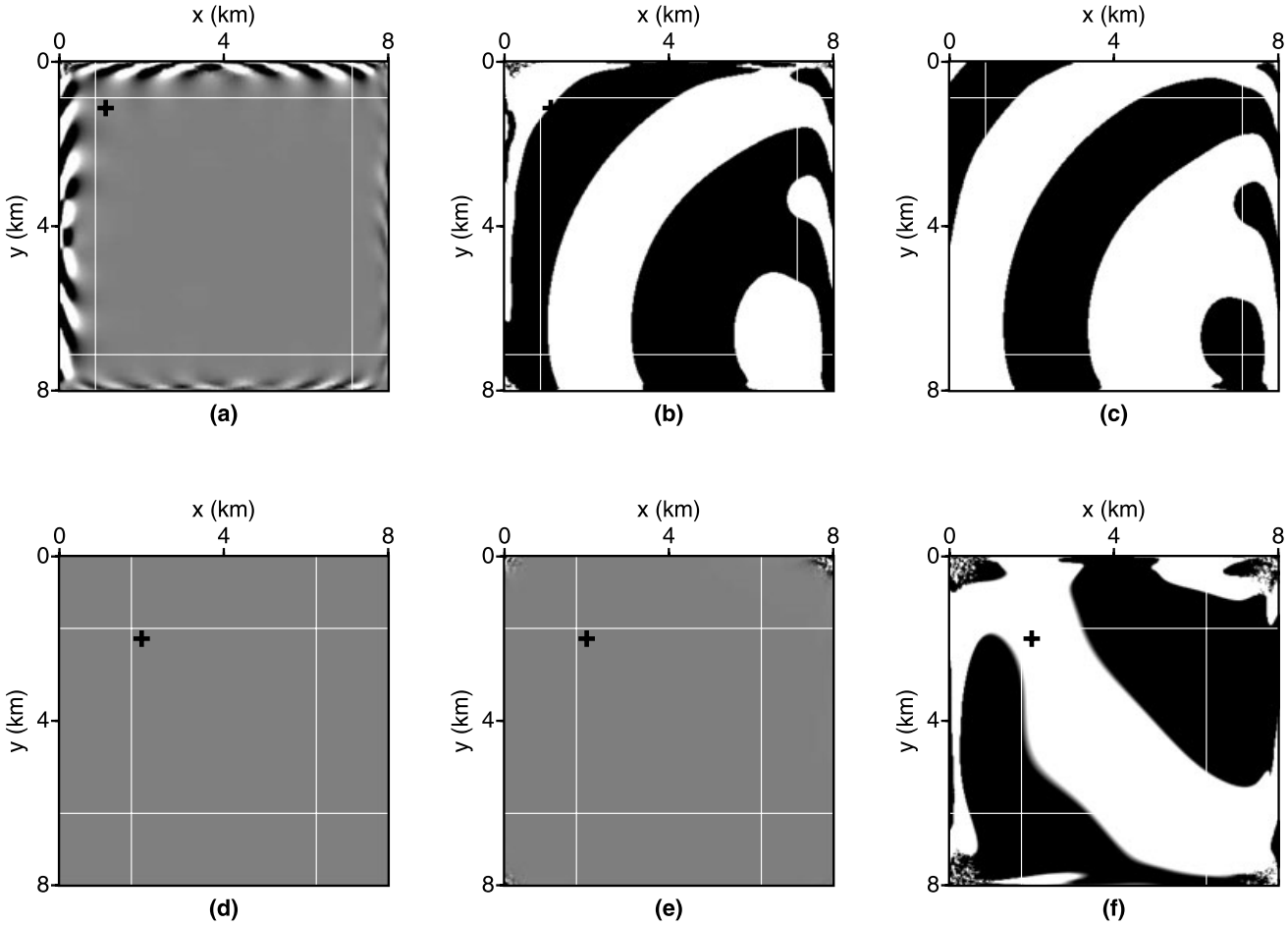

Figure 6. (a), (b) and (c) Snapshots of the velocity component v_x in the plane xy that contains the source location at 10, 20 and 30 s, respectively. The amplitude is plotted without any magnification factor. The modelling was carried out with P_2 interpolation. CPMLs with five-elements width are applied at all edges of the model. White lines, the limits of the CPMLs; black cross, the position of the source. (d), (e) and (f) Same as (a), (b) and (c), respectively, except with CPMLs of 10-elements width.

seismograms obtained with complete P_2 modelling (compare Figs 9a and 5a). Therefore, taking into account that the computation time and the memory consumption of the P_2/P_1 simulation are nearly half of those required with the full P_2 modelling, we can conclude that this mixed numerical scheme is of interest. It should be noticed that it is possible to adopt a weighted partitioning approach to overcome partly load balancing issues. Nevertheless, it does not prevent from using our mixed scheme approach which allows a significant reduction of the number of CPML memory variables. Actually, our strategy is totally compatible with a weighted partitioning and the combination of both would be more efficient than using only one of them. We should also stress that the saving in CPU time and memory provided with this kind of low-cost absorbing boundary condition is crucial for large 3-D simulations, and this becomes a must in the context of 3-D seismic imaging applications that require a lot of forward problems, such as FWI.

5 ACCURACY OF DG-FEM WITH TETRAHEDRAL MESHES

There are a variety of studies in the literature concerning the dispersive and dissipative properties of DG-FEM with reference to wave-propagation problems. To cite but a few examples: Ainsworth *et al.* (2006) provided a theoretical study for the 1-D case; Basabe *et al.* (2008) analysed the effects of basis functions on 2-D periodic and regular quadrilateral meshes; and Käser *et al.* (2008) discussed the convergence of the DG-FEM combined with ADER time integration and 3-D tetrahedral meshes. More related to our particular concern here, Delcourte *et al.* (2009) provided a convergence analysis of the DG-FEM with a centred flux scheme and tetrahedral meshes for elastodynamics. They demonstrated the sensitivity of the DG-FEM to the mesh quality, and they proved that the convergence is limited by the second-order time integration we have used in this study, despite the order of the basis function.

5.1 Convergence study

We present a convergence analysis of the DG-FEM P_2, P_1 and P_0 schemes following the approach of Delcourte *et al.* (2009). The analysis is based on the propagation of an eigenmode in a unit cube with a free surface condition applied at all faces. The properties of the cube are $V_P = 1\ \mathrm{m\,s^{-1}}$, $V_S = 0.5\ \mathrm{m\,s^{-1}}$ and $\rho = 1\ \mathrm{kg\,m^{-3}}$. According to these parameters, the solution of the eigenmode (1,1,1)

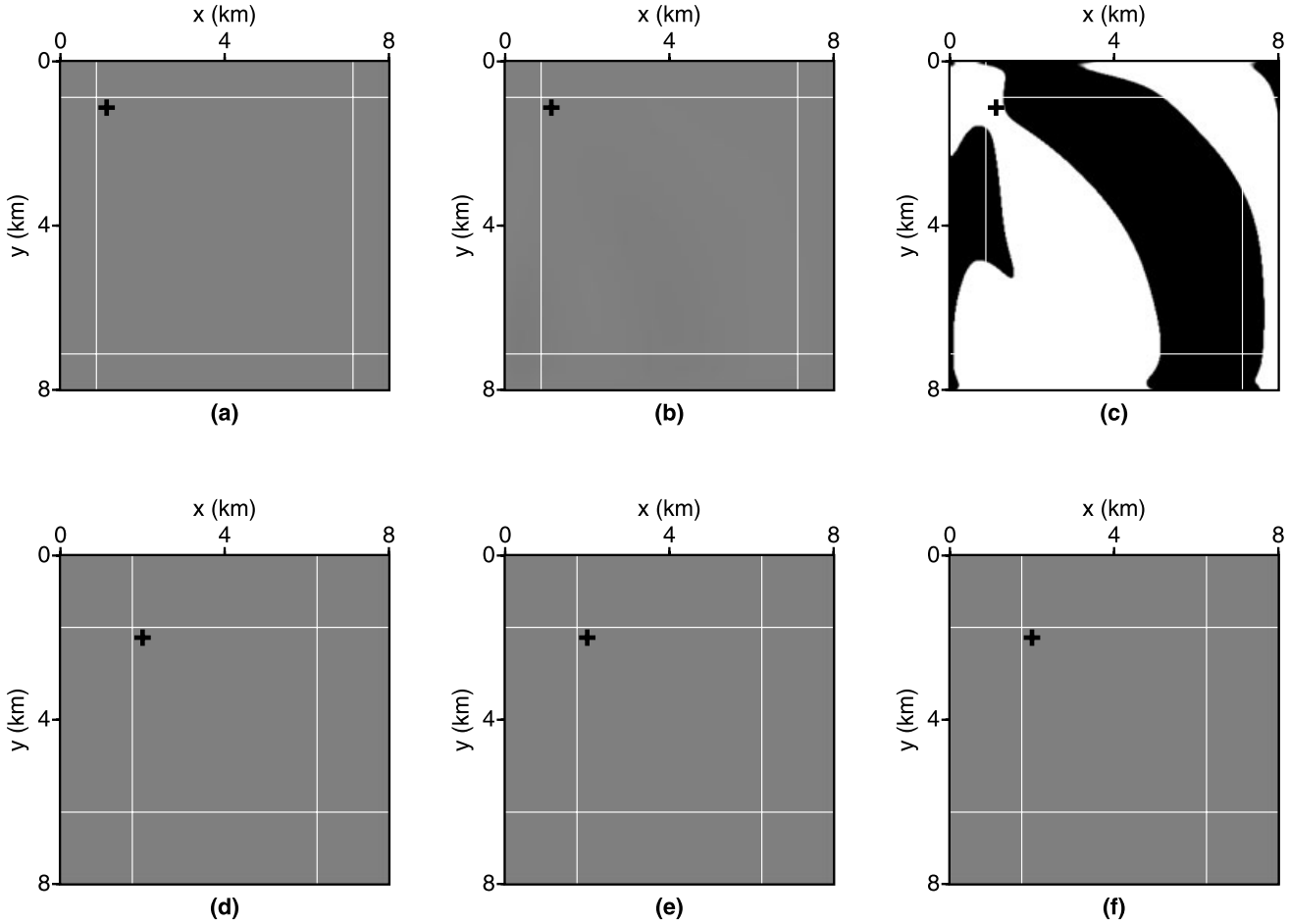

Figure 7. (a), (b) and (c) Snapshots of the velocity component v_x in the plane xy that contains the source location at 10, 20 and 30 s, respectively. The amplitude is plotted without any magnification factor. The modelling was carried out with P_2 interpolation. M-CPMLs with five-elements width and 10 per cent of the damping profile added onto the directions parallel to the layer were applied at all edges of the model. White lines, the limits of the M-CPMLs; black cross, the position of the source. (d), (e) and (f) Same as (a), (b) and (c), respectively, except with M-CPMLs of 10-elements width.

Table 1. Computation times for updating the velocity and stress wavefields in one element for one time step. These values correspond to average computation times for a computing platform with bi-processor quad core Opteron 2.3 GHz CPUs interconnected with Infiniband 20 at Gb s^{-1}.

Approximation order	Element outside CPML (μs)	Element inside CPML (μs)
P_0	2.6	3.6
P_1	5.0	8.3
P_2	21.1	29.9

is given by

$$\begin{aligned}
v_x &= \cos(\pi x)\,[sin(\pi y) - \sin(\pi z)]\cos(\Omega t)\\
v_y &= \cos(\pi y)\,[sin(\pi z) - \sin(\pi x)]\cos(\Omega t)\\
v_z &= \cos(\pi z)\,[sin(\pi x) - \sin(\pi y)]\cos(\Omega t)\\
\sigma_{xx} &= -A\sin(\pi x)\,[sin(\pi y) - \sin(\pi z)]\sin(\Omega t)\\
\sigma_{yy} &= -A\sin(\pi y)\,[sin(\pi z) - \sin(\pi x)]\sin(\Omega t)\\
\sigma_{zz} &= -A\sin(\pi z)\,[sin(\pi x) - \sin(\pi y)]\sin(\Omega t)\\
\sigma_{xy} &= \sigma_{xz} = \sigma_{yz} = 0,
\end{aligned} \tag{29}$$

where $A = 1/\sqrt{2}$ and $\Omega = \pi/\sqrt{2}$. In order to assess the convergence rate of the method, we made several tests with different unstructured tetrahedral meshes with the characteristics summarized in Table 2. The initial conditions are imposed at each node of the elements by setting the velocities at $t = 0$ and the stresses at $t = \Delta t/2$ following eq. (29). We place a bunch of receivers according to a cartesian grid that matches the size of the cube. The spacing between receivers is 0.1 m, making a total number of 1331 receivers ($11 \times 11 \times 11$). At each receiver, a sinusoidal signal with a period of $T = 2\sqrt{2}$s should be observed. This monochromatic signal corresponds to the propagation of P-waves across the cube that are continuously reflected at the cube faces. Consequently, we can establish a relationship between the simulation time and the propagated distance. In the Fig. 10(a), we present the normalized rms error between the analytical and numerical solutions at $t = 5T$ and at $t = 50T$, corresponding to a propagation of 5 and 50 wavelengths, respectively. We can observe that no convergence is achieved with P_0 while a second-order convergence is observed for both P_1 and P_2 at $t = 5T$. As expected, an increase of the error is seen at longer times, resulting from the accumulation of errors with time iterations. At $t = 50T$, a second-order convergence is still observed for P_1 while the convergence of P_2 becomes more

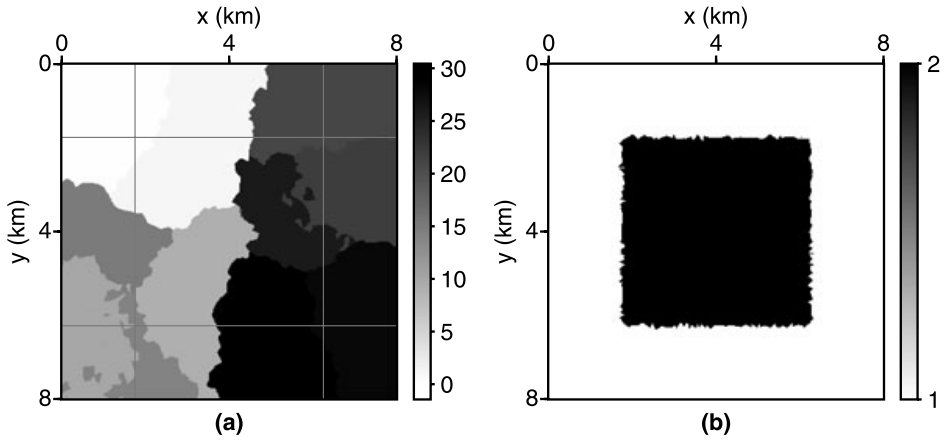

Figure 8. (a) Layout of the subdomains obtained with the partitioner METIS (Karypis & Kumar 1998) along the *xy* plane that contains the source location. Grey lines, the limits of the CPMLs. The mesh was divided into 32 partitions, although only a few of these are visible on this cross-section. (b) View of the approximation order per element along the same plane. Black, the P_2 elements; white, the P_1 elements.

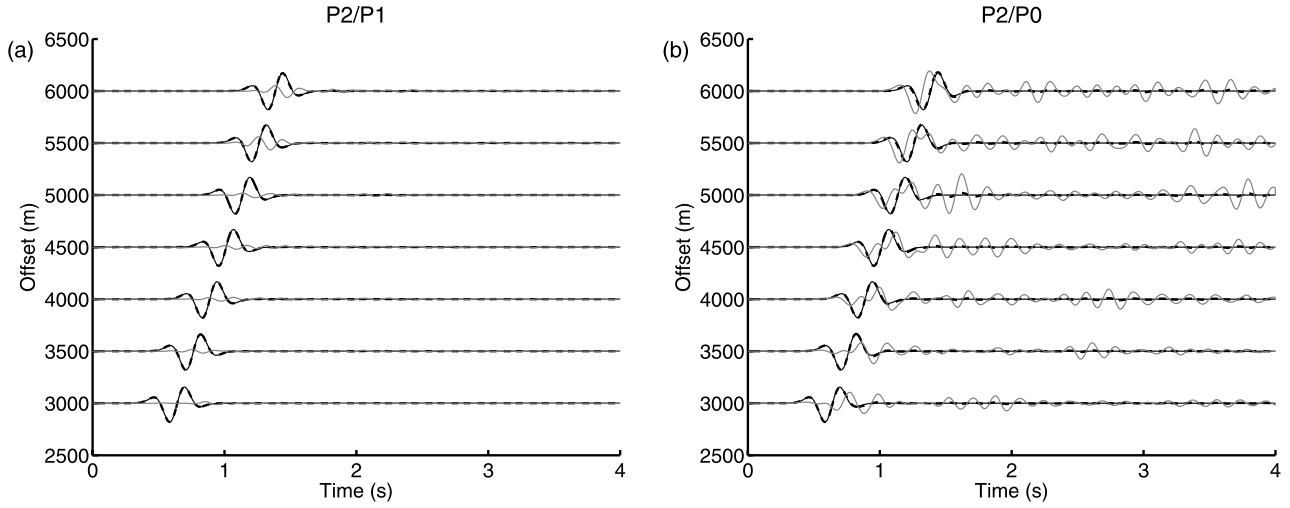

Figure 9. (a) Seismograms of the velocity component v_x. The amplitude of each seismogram is normalized. The modelling is done with P_1 in the CPMLs and P_2 inside the medium. Black continuous line, numerical solution in large model without reflection in the time window; dashed line, numerical solution with 10-elements width CPMLs; grey line, residuals magnified by a factor of 10. (b) Same as (a) except the modelling is done with P_0 in the CPMLs and P_2 inside the medium.

Table 2. Average edge length, minimum and maximum insphere radius and number of elements of the unstructured tetrahedral meshes used for the convergence study.

Mesh	1	2	3	4	5	6
Average edge (m)	0.19	0.12	0.08	0.05	0.04	0.03
Min. insphere radius (m)	0.0203	0.0132	0.0078	0.0048	0.0030	0.0019
Max. insphere radius (m)	0.0486	0.0304	0.0211	0.0155	0.0117	0.0087
Number of elements	1561	5357	17 932	49 822	154 297	388 589

erratic. The seismograms of Figs 11(a) and (a) represent the v_x component observed at short and long times, respectively. These seismograms have been recorded at the position ($x = 0$ m, $y = 0$ m, $z =$ 0.5 m) with the mesh # 4. At short times, we can see a good match between the numerical and analytical solutions for both P_1 and P_2 schemes. Concerning the P_0 scheme, we can notice a strong distortion of the sinusoidal signal with a apparent period that is shorter than the analytical one. We can conclude that the P_0 scheme does not provide accurate results with unstructured tetrahedral meshes. At long times, the agreement is still good for P_2 (thus explaining the slow convergence observed when using finer meshes) but we can observe a strong delay for the P_1 scheme. The delay is reduced when using finer meshes as indicated by the convergence curve in Fig. 10(a). In terms of precision and efficiency, the gain from the P_2 scheme compared with the P_1 scheme can be evaluated from Fig. 10(b). For the same level of precision, the computation time of the P_2 modelling is nearly two orders of magnitude lower than the computation time of the P_1 modelling.

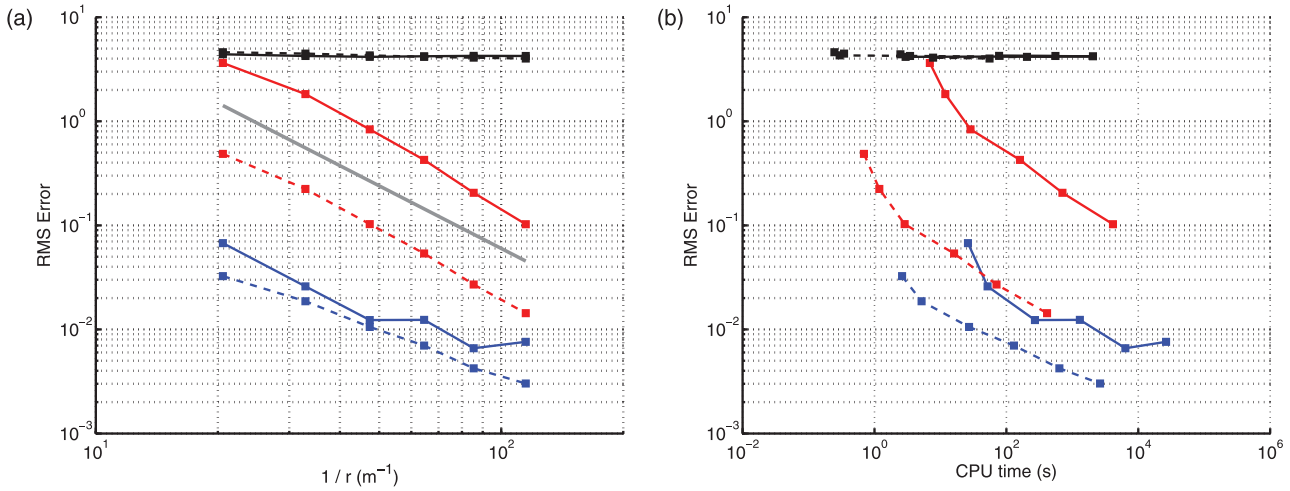

Figure 10. (a) Root mean square error between the analytical and numerical solutions versus the inverse of the maximum insphere radius r. Black dashed line, the error against the P_0 solution at $t = 5T$; black continuous line, the error against P_0 at $t = 50T$; red dashed line, the error against the P_1 solution at $t = 5T$; red continuous line, the error against P_1 at $t = 50T$; blue dashed line, the error against the P_2 solution at $t = 5T$; blue continuous line, the error against P_2 at $t = 50T$; grey curve, second-order slope. (b) Same as (a) except the root mean square error is plotted versus the elapsed computation time. The tests have been performed with 32 CPUs on a computing platform with bi-processor quad core Opteron 2.3 GHz CPUs interconnected with Infiniband at 20 Gb s^{-1}.

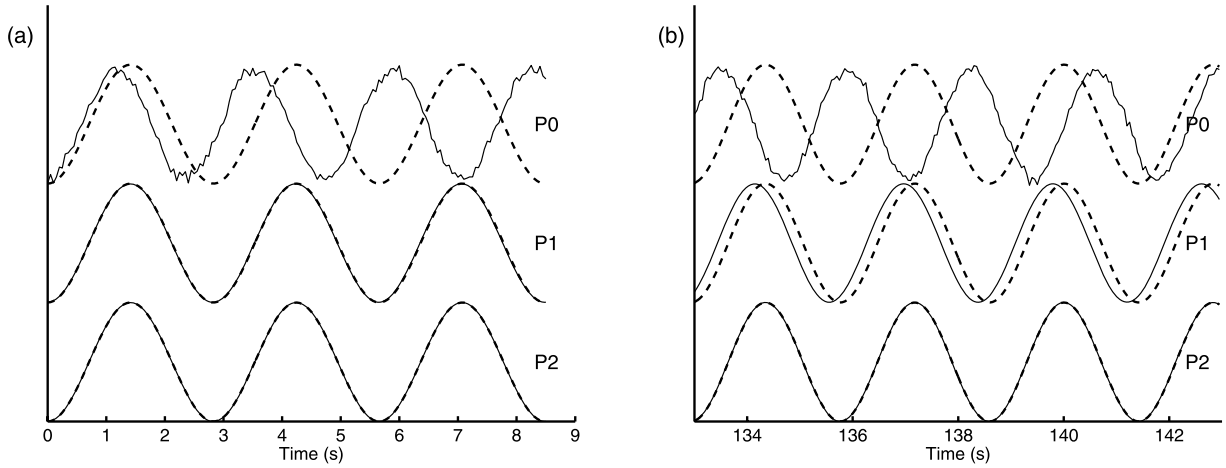

Figure 11. (a). Seismograms of velocity component v_x computed with the P_2, P_1 and P_0 schemes for $t \in [0, 3\,T]$. Continuous line, the DG-FEM solution; dashed line, the analytical solution. (b) Same as (a) for $t \in [47T, 50T]$.

5.2 Accurate modelling of surface waves

Accurate modelling of surfaces wave is crucial for seismological studies, such as for the prediction of site effects or FWI of land seismic data, where the receivers are usually located on the free surface. For simple geometries, some analytical solutions exist. The propagation of waves along the surface of an elastic half space was discussed by Lamb (1904) for a force located on the surface, and an analytical solution was defined by Garvin (1956) for the buried line-source problem. Nevertheless, in the case of complex topographies, a numerical method needs to be used. For this, a method suitable for unstructured meshes has major advantages. In the following, for validation purposes, we consider a homogeneous, isotropic and purely elastic medium with a planar free surface, and we adopt the experimental set-up defined in the WP1_HHS1 test case of the SPICE test code validation project (Moczo *et al.* 2005). The model dimensions are 20 km × 20 km × 10 km in the directions x, y and z, respectively. The physical properties are given by $V_P = 6000$ m s^{-1}, $V_S = 3464$ m s^{-1} and $\rho = 2700$ kg m^{-3}. The source is a point dislocation with the only non-zero moment tensor component M_{xy}. The moment-rate time history is given by

$$M_{xy}(t) = M_0 \frac{t}{T^2} \exp\left(-\frac{t}{T}\right),$$

with $M_0 = 10^{18}$ Nm and $T = 0.1$ s. Considering a maximum frequency of 5 Hz, the minimum wavelength is 693 m. The source and receiver locations are given in Table 3. The distance between the source and the receivers varies from 1 to 16 $\lambda_{\min}$. We performed the computation with the mixed scheme, with P_2 elements in the medium and P_1 elements in the CPMLs. Absorbing layers were applied at all edges of the model, except at the top, where a free surface condition was used. Figs 12(a) and (b) allow a comparison of the seismograms of the components v_x and v_z, respectively, obtained with DG-FEM and with the reflectivity method (Bouchon 1981; Coutant 1989). All of these seismograms were filtered between 0.13 and 5 Hz. With an average mesh spacing of 3 elements per wavelength, a good match is seen between the analytical and numerical solutions for all of the traces. Exceptions are found for

Table 3. Source and receiver locations for the planar free-surface modelling.

Type	X (m)	Y (m)	Z (m)
Source	0	0	–693
Receiver #1	0	693	0
Receiver #2	0	5543	0
Receiver #3	0	10 932	0
Receiver #4	490	490	0
Receiver #5	3919	3919	0
Receiver #6	7348	7348	0
Receiver #7	577	384	0
Receiver #8	4612	3075	0
Receiver #9	8647	5764	0

the component v_z in traces #1, 2 and 3, where the DG-FEM fails to reproduce strictly null signals, but exhibits weak residuals. These residuals might be due to the spatial support of the source, which does not coincide with a pure Dirac in space, as depicted in Fig. 3(c).

6 *HP*-ADAPTIVITY

6.1 Two-step refinement approach

One of the most interesting aspects of the DG-FEM is the possibility to mix approximation orders without any special efforts. This feature relies on the local support of the basis functions, which are discontinuous between the elements, as was introduced in Section 2, and is referred to as *p*-adaptivity. When combined with mesh refinement, this method becomes *hp*-adaptive. As in the initial study of Babuska & Suri (1990), *hp*-adaptive FEMs associated with *a posteriori* error estimates have gained a lot of interest due to the exponential rates of convergence seen with the correct combination of *h*- and *p*- refinements. In the present study, we propose to define a simple *a priori* error estimate to predict the required approximation order for each element. Our approach is based on two major steps. The first refers to the mesh construction, with the intention to build a tetrahedral mesh that is locally adapted to the media properties. Initially, a mesh is generated that roughly satisfies the discretization required by the target approximation order. At the very beginning of the procedure, the mesh can even be regular. Afterwards, the elements are checked against the physical properties of the medium, and the list of elements that need to be refined is used for the next iteration. The process is repeated until the list of elements to refine is empty. We used to build and refine our meshes with the tool TETGEN (Si & Gärtner 2005) which allows to specify for each element the maximum authorized volume. To compute the optimal volume for each element, we usually define a maximum ratio between the insphere radius and the wavelength and then we evaluate the corresponding volume of an equilateral tetrahedron. Given the complexity of the medium to be discretized, tetrahedral mesh generators can produce ill-shaped tetrahedra even if quality criteria are used. A common practice is to limit the aspect ratio, which is defined by the ratio between the maximum side length and the minimum height of the elements. Nevertheless, despite robust algorithms, like the Delaunay refinement algorithm of Shewchuk (1998), some almost flat elements can be present at the end of the refinement process, which are known as slivers. Besides these slivers, another critical phenomenon can occur where there are abrupt contrasts in the physical properties. In these situations, the refinement algorithm might not be able to perform the optimal discretization. This occurs when the size of the elements cannot vary as fast as the medium properties for geometrical reasons. In that case, some elements are necessarily undersized. Consequently, the construction of an ideal mesh is a difficult task, and a large range of element sizes is often seen in constrained meshes. To mitigate the negative effects of the badly sized elements, we propose to downgrade these elements with lower approximation orders. This is done in the second step of our refinement approach, which is devoted to the *p*-adaptivity.

6.2 Numerical results

Our intention here, is to illustrate the benefits of the *p*-adaptivity. For that purpose, we consider the case of the eigenmode propagation in the unit cube presented in Section 5.1 and introduce a refined area in meshes #1, 2 and 3 in order to create artificially a large range of element sizes. We obtain the new meshes #1′, 2′ and 3′ by defining a cubic zone of size 0.1 m × 0.1 m × 0.1 m in the middle of the model where the average edge length is ten times smaller than *h*, the average edge length in the surrounding mesh. The characteristics of the meshes can be found in Table 4. The ratio between the maximum and minimum insphere radius have been significantly increased compared to the uniform meshes used

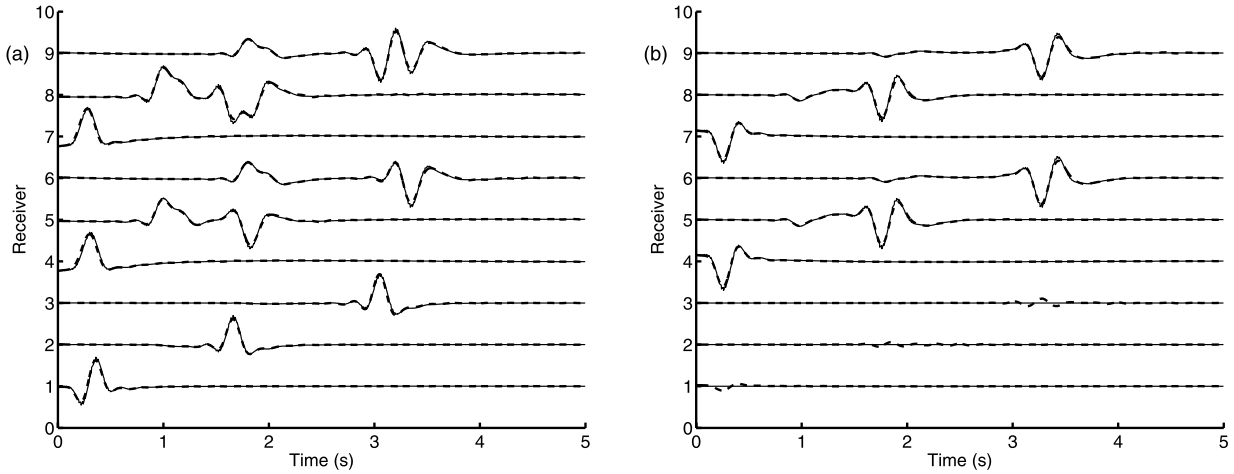

Figure 12. (a) Seismograms of the velocity component v_x computed for the planar free-surface modelling of the SPICE test code validation project. Continuous line, the analytical solution provided by the reflectivity method; dashed line, the DG-FEM solution. (b) Same as (a) with the component v_z.

Table 4. Minimum and maximum insphere radius and number of elements of the unstructured tetrahedral meshes with a refined area.

Mesh	1′	2′	3′
Min. insphere radius (m)	0.0017	0.0010	0.0007
Max. insphere radius (m)	0.0425	0.0292	0.0198
Number of elements	6952	26 374	82 668

previously (compare with Table 2). The cross section of the mesh #3′ in Fig. 13(a). allows to see the refined area in the center of the model. For the *p*-adaptivity, we adopted the following criteria: if the insphere radius is comprised between $h/30$ and $h/10$, the approximation order is downgraded to P_1, and if the radius is smaller than $h/30$, the approximation order is downgraded to P_0. This strategy is depicted in Fig. 14, where for each approximation order, the time step evaluated with eq. (15) *versus* the insphere radius of one single equilateral tetrahedron is shown. When applying these criteria, the time step does not decrease uniformly according to the size of the element. Instead, two jumps (Fig. 14, dashed line) allow the time step to increase despite the reduction in the element size. These jumps are due to the decrease in the approximation order from P_2 to P_1, and from P_1 to P_0. According to the adopted criteria, we obtain the distribution of approximation orders indicated in Table 5. The number of downgraded elements is quite important and represent for all meshes approximatively 60 per cent. Nevertheless, the downgraded elements are mostly located in the vicinity of the refined area as shown in Fig. 13(b) and represent in average only 3 per cent of the volume of the model. Moreover, despite the fact that the P_0 scheme does not provide accurate results, the introduction of such elements allows a drastic increase of the time step by a factor of five. The impact of the downgraded elements can be analysed with Fig. 15(a) showing the normalized rms error between the analytical, the P_2 and the *p*-adaptive numerical solutions at $t = 50T$. Actually, the *p*-adaptive scheme exhibits an error which is comparable to the complete P_2 modelling except for the mesh #3′, where we observe a particular behavior of the P_2 scheme with an increase of the error despite the mesh spacing has been reduced. This indicates that a large distribution of element sizes has an effect on the convergence on the P_2 scheme. On the contrary, the *p*-adaptive scheme seems

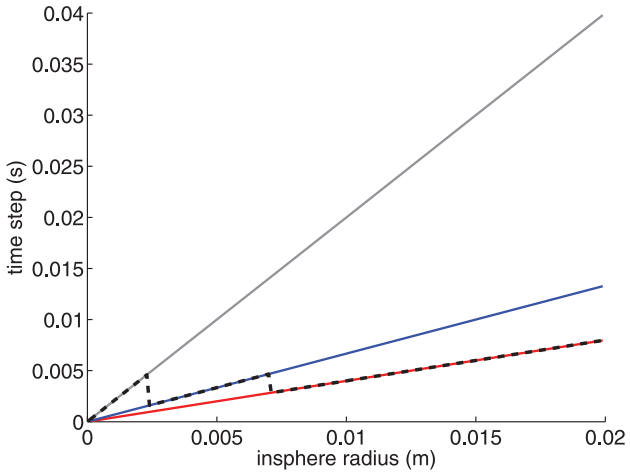

Figure 14. Time step *versus* the insphere radius of one single equilateral tetrahedron computed with eq. (15), for different approximation orders. Grey curve, P_0; blue curve, P_1; red curve, P_2; dashed line, the *p*-adaptive approach used for mesh #3′.

less sensitive and preserves the second-order convergence. From a computational point of view, the benefit of the approach appears in Fig. 15(b) where the error is represented versus the computation time. For the same computation time, the *p*-adaptive approach shows a better misfit than the full P_2 modelling, as indicated by the position of the *p*-adaptive curve at the left of the P_2 curve. The *hp*-refinement provided by DG-FEM is particularly interesting in the case of complex refined meshes where small elements are generally produced by tetrahedral mesh generators. The efficiency of our approach in such cases is illustrated in the next section.

7 APPLICATION TO COMPLEX MEDIUM

We here demonstrate the potential of DG-FEM with *hp*-adaptivity in a challenging seismological model, where the computation of the surface waves is critical for the prediction of site effects. These phenomena arise when the ground motion caused by an earthquake

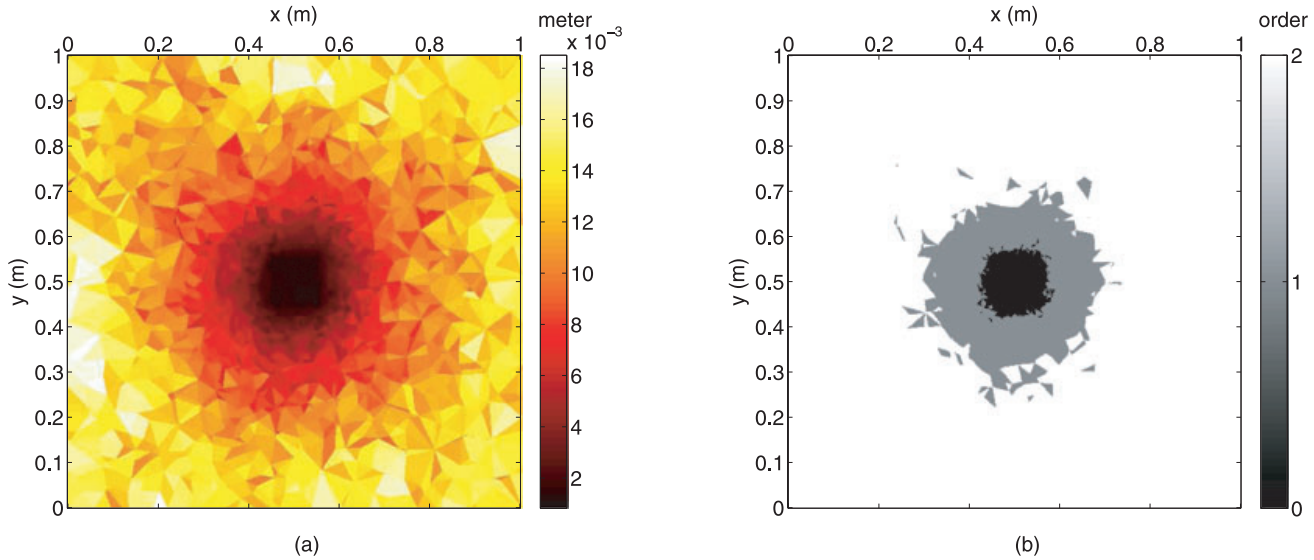

Figure 13. (a) View of the mesh in the *xy* plane at $z = 0.5$ m, showing the size of the elements (insphere radius) in the mesh #3′. (b) Same as (a) with the approximation order associated with each element. White, P_2 elements; grey, P_1 elements; black, P_0 elements.

Table 5. Number of elements per approximation orders and time steps for the complete P_2 and the *p*-adaptive modelling.

	Nb P_0 elements	Nb P_1 elements	Nb P_2 elements	Time step
Full P_2 scheme with mesh 1′	0	0	6952	0.0006745
p-adaptive scheme with mesh 1′	2520	1606	2826	0.0033372
Full P_2 scheme with mesh 2′	0	0	26 374	0.0004187
p-adaptive scheme with mesh 2′	10 883	5849	9642	0.0020934
Full P_2 scheme with mesh 3′	0	0	82 668	0.0002737
p-adaptive scheme with mesh 3′	34 176	17 483	31 009	0.0013687

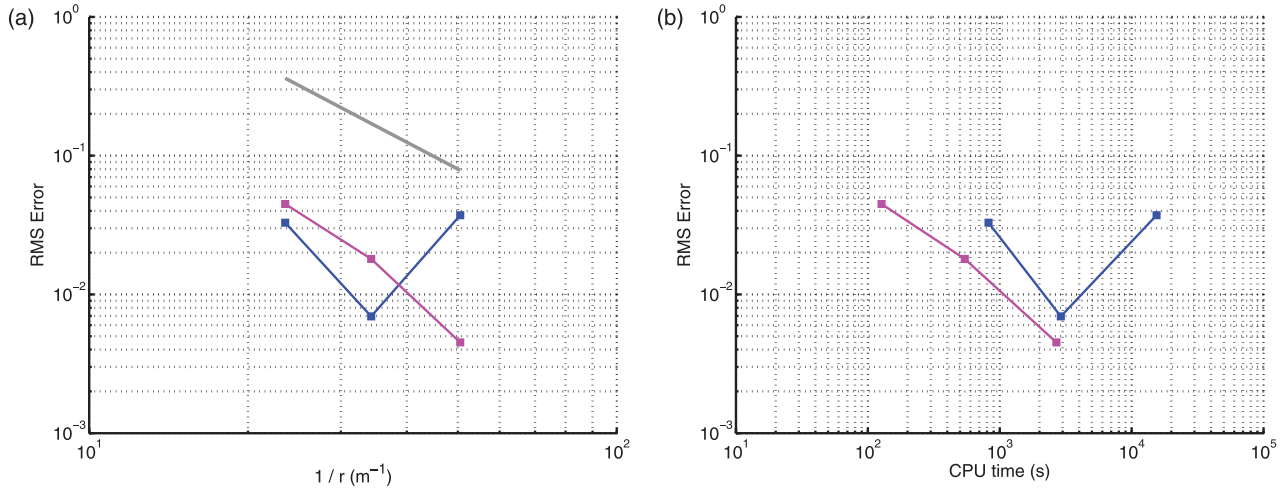

Figure 15. (a) Root mean square error between the analytical and numerical solutions versus the inverse of the maximum insphere radius r at $t = 50T$. Blue line, the error against the P_2 solution; pink line, the error against the *p*-adaptive solution; grey curve, second-order slope. (b) Same as (a) except the root mean square error is plotted versus the elapsed computation time. The tests have been performed with 32 CPUs on a computing platform with bi-processor quad core Opteron 2.3 GHz CPUs interconnected with Infiniband at 20 Gb s^{-1}.

is amplified by geological structures. Site effects can be related to a sedimentary basin, like for the great earthquake in Mexico in 1985 (Campillo *et al.* 1989; Kawase 2003). The importance of site effects and their study were the main motivation for setting-up worldwide test sites. Here, we consider the EUROSEISTEST verification and validation project (Chaljub *et al.* 2009), and address the issue of modelling the ground motion in a basin structure. We compare the results obtained with our method against results computed with SEM.

7.1 Description of EUROSEISTEST verification and validation project

The EUROSEISTEST verification and validation project refers to the geological structure of the Mygdonian sedimentary basin about 30 km E–NE of the city of Thessaloniki (northern Greece). It mainly consists of a sedimentary basin with extreme low velocities and a high Poisson ratio, embedded in high velocity bedrock. The velocity structure of the area is well known along the central section *AB* (Fig. 16b), following a large number of geophysical and geotechnical measurements (Jongmans *et al.* 1998), surface and borehole seismic prospecting, and electrical soundings and microtremor recordings. The 3-D structure in the whole graben was then extrapolated from this central profile, taking into account information from many single-point microtremor measurements, some array microtremor recordings, one EW refraction profile, and old deep boreholes drilled for water-exploration purposes (Raptakis *et al.* 2005; Manakou *et al.* 2007). The sediment thickness indeed increases both to the West and the East of the central profile, which corresponds to a buried pass between two thicker subbasins. For the verification part of the EUROSEISTEST project, a smooth vertical gradient without any lateral variation was considered. Inside the basin, the velocities vary with the depth as follows

$$V_P = 1000 + 100\sqrt{d}$$
$$V_S = 200 + 32\sqrt{d},$$

where V_P and V_S are expressed in m s^{-1}, and d is the depth in m. Table 6 summarizes the properties of the EUROSEISTEST model. The ratio between the maximum and minimum *S*-wave velocities is 17.2. This high factor favours the use of unstructured meshes, as a large range of different element sizes is expected. Indeed, small elements are required in the basin area while larger ones can be used in the bedrock. The size of the model is 16 km × 15 km × 8 km in the directions x, y and z, respectively. M-CPMLs of 2 km width are applied at all edges of the model, except at the top, where a free surface condition is used. The model topography is flat. Figs 16(a) and (b) show the *P*- and *S*-wave velocities, respectively, on the free surface in the xy plane. In these figures, the complex shape of the basin and the abrupt contrast of velocity at the basin border can be seen. The source is located 5 km below the basin, and it acts as a double-couple mechanism that represents a small earthquake with a corner frequency of 4 Hz (Fig. 17). The epicentre is indicated with a yellow star in Fig. 16(a). The minimum propagated wavelength is 50 m, and the largest dimension of the model is 320 λ. We considered seven receivers, as marked with numbered green triangles in Fig. 16(a), at strategic positions of the true EUROSEISTEST array. All of these receivers lie on the free surface, except receiver #7,

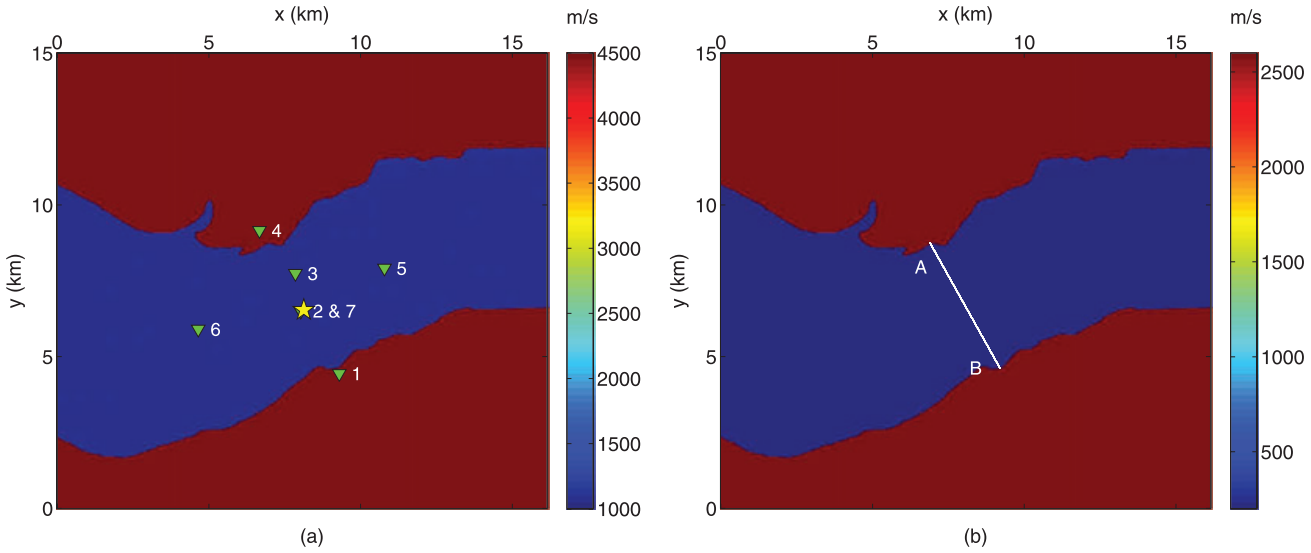

Figure 16. (a) View of the mesh in the xy plane at $z = 0$ m, showing the P-wave velocity associated with each element in the EUROSEISTEST model. Numbered green triangles, the receivers; yellow star, source epicentre. (b) Same with the S-wave velocity associated with each element. The position of the cross-section AB is indicated by the white line.

Table 6. The properties of the geological structures of the EUROSEISTEST model.

	P-wave velocity ($m\,s^{-1}$)	S-wave velocity ($m\,s^{-1}$)	Density	Ratio V_P / V_S	Max. depth
Basin	1000–3027	200–848	2100 $kg\,m^{-3}$	5.00–3.57	411 m
Bedrock	4500–6144	2600–3444	2600–2755 $kg\,m^{-3}$	1.73–1.78	8 km

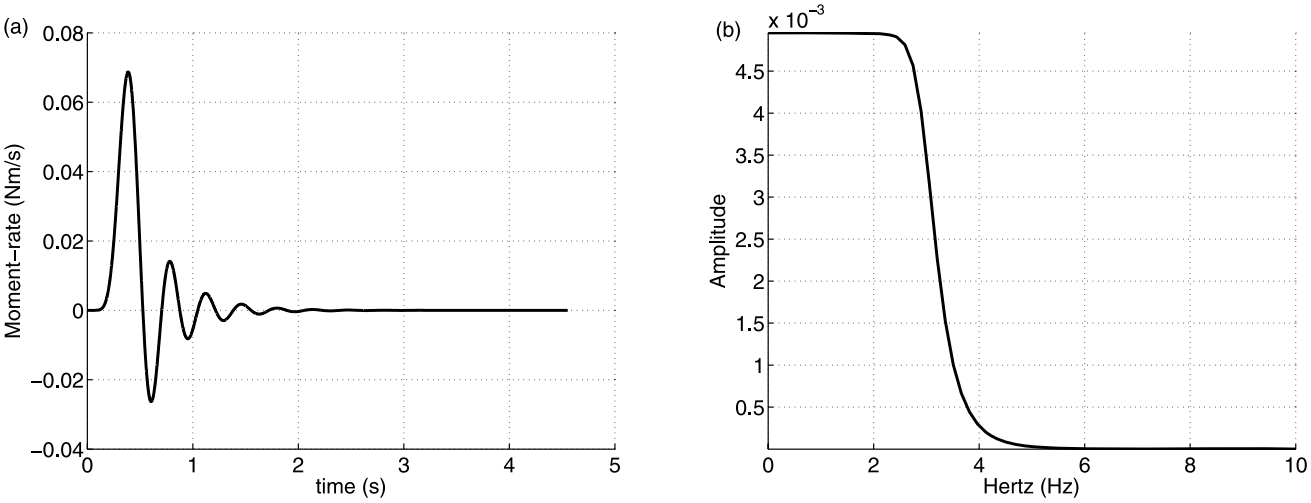

Figure 17. (a) Moment-rate function of the source used for the EUROSEISTEST modelling. (b) Amplitude spectrum of the source.

which is buried at 197 m depth just above the source. Receivers #1 and #4 are located on the bedrock, and the others are located within the basin area.

7.2 Numerical results

For the SEM calculations, the size of the computational domain was 16.14 km × 29.31 km × 7.86 km, and local absorbing boundary conditions were imposed at the lateral and bottom boundaries, following Komatitsch & Vilotte (1998). The mesh is based on a conforming layer-cake topology (Komatitsch *et al.* 2004) where the elements are deformed to follow the sediment-bedrock interface, except for depths shallower than a threshold value, which was set to 80 m for the basin. For the elements close to the valley edges, the sediment-bedrock discontinuity is approximated by assigning different material values to the collocation points inside the elements. Note that because of the large P-wave velocity in the shallow bedrock, the choice of the threshold depth directly controls the time step authorized by the CFL stability condition, and therefore the total CPU time of the simulation. For the DG-FEM calculations, the size of the numerical model was 20.14 km × 19 km × 8 km in the directions x, y and z, respectively, including M-CPMLs of 2 km width at all edges of the model, except at the top, where a free-surface condition was used. We adopted the two-step refinement

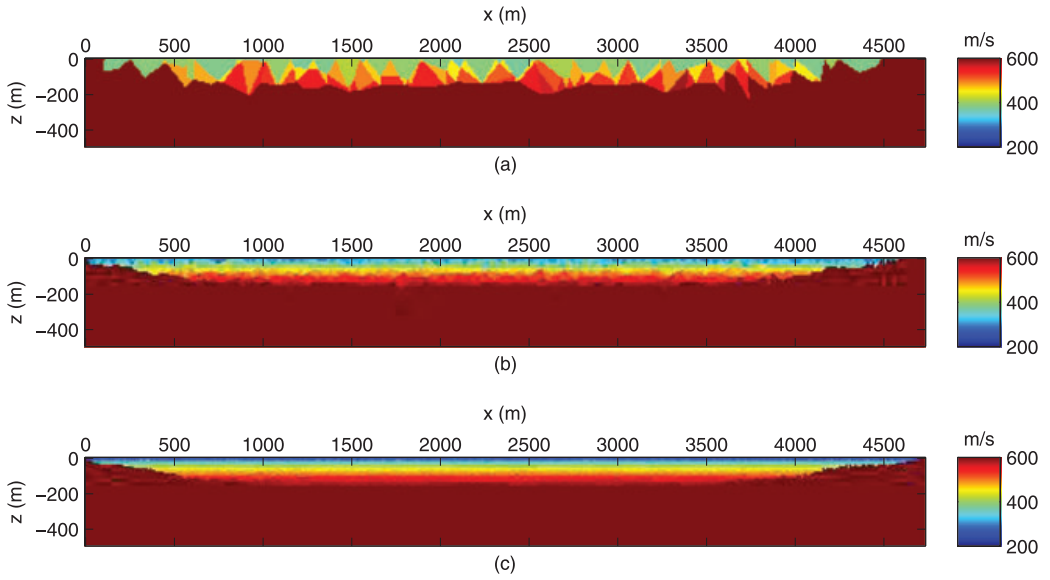

Figure 18. (a) Cross-section *AB* of the mesh at the first iteration of the *h*-refinement showing the *S*-wave velocity associated with each element in the EUROSEISTEST model. (b) Same as (a) at the second iteration of the *h*-refinement. (c) Same as (a) at the sixth and last iteration of the *h*-refinement.

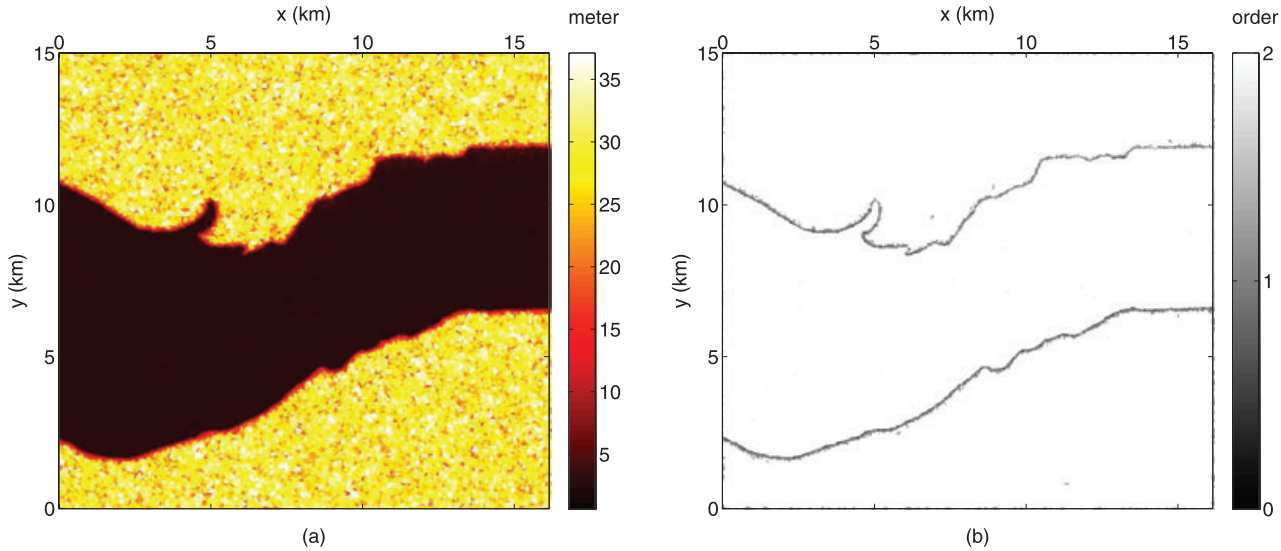

Figure 19. (a) View of the mesh in the *xy* plane at $z = 0$ m, showing the size of the elements (insphere radius) in the EUROSEISTEST model. (b) Same as (a) with the approximation order associated with each element. White, P_2 elements; grey, P_1 elements; black, P_0 elements.

approach explained in the previous section. In the first step, we built an *ad hoc* tetrahedral mesh with TETGEN. A total of six mesh refinement iterations were required to reach an adaptive discretization of three elements per λ_S. Figs 18(a), (b) and (c) show the distribution of the *S*-wave velocity in the cross-section *AB* for the first, second and last iterations of the *h*-refinement process, respectively. Due to the extremely low velocities in the basin, the automatic refinement process produced very small elements, which resulted in a fine and regular discretization of the basin shape. Fig. 19(a) shows the size of the elements (insphere radius) on the free surface. As expected, smaller elements are found in the basin area rather than in the bedrock. In this example, we have taken advantage of the tetrahedral mesh refinement. Indeed, the volume of the basin represents 0.8 per cent of the complete volume of the model and it contains 72 per cent of the total number of mesh elements. In the second step, we made use of *p*-adaptivity to reduce the number of time steps. We adopted the following criteria: if the insphere radius is between $\lambda_S/120$ and $\lambda_S/40$, the approximation order is downgraded to P_1, and if the insphere radius is smaller than $\lambda_S/120$, the approximation is downgraded to P_0. While most of the tetrahedral elements are adequate for P_2, the badly sized elements are computed with lower approximation orders. We end up with a mesh that contains in total 16.3 million elements and 131.0 million DOF. The approximation orders are distributed as follows: 67.04 per cent P_2 elements, 32.67 per cent P_1 elements (with 28.66 per cent elements in the M-CPMLs), and 0.29 per cent P_0 elements. This strategy is shown in Fig. 19(b), where the approximation order is shown for each element located on the free surface. Almost all of the elements are P_2 elements, except for those with inappropriate sizes, which are downgraded to P_1 or to P_0 in the worst cases. Indeed, the contact

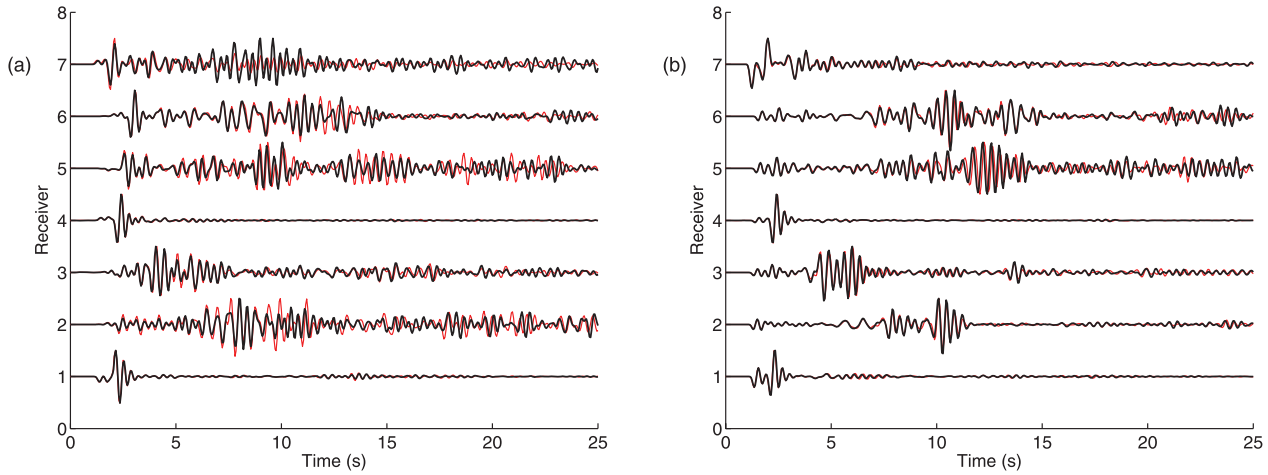

Figure 20. (a) Seismograms of the component v_x computed in the EUROSEISTEST model. Black line, with DG-FEM; red line, with SEM. (b) Same as (a) with the component v_z.

Table 7. Mesh statistics, computation time and memory allocation relative to the EUROSEISTEST modelling. the DG-FEM and SEM computations were both performed with 18 bi-xeon Quadcore CPU IBM E5420 at 2.5 GHz (making a total of 144 cores).

Method	Order	Min. edge (m)	Max. edge (m)	Nb elem.	Nb DOF	Nb steps	Nb CPUs	Elapse time (hr)	Memory (GB)
DG-FEM	$P_2/P_1/P_0$	2.5	399.8	16.3×10^6	131.0×10^6	122 565	144	52	~26
SEM	P_4	20.0	906.0	1.4×10^6	91.7×10^6	75 000	144	7	~25

between the basin and the bedrock produces a high velocity contrast that is not ideally accommodated by the tetrahedra. Therefore, some elements located in the bedrock have smaller sizes than expected, and thus can be treated with lower approximation orders. These latter are particularly visible in Fig. 19(b). Some P_1 elements also appear at the border in Fig. 19(b) where the M-CPMLs start.

The seismograms of the components v_x and v_z computed with DG-FEM and with SEM are shown in Figs 20(a) and (b), respectively. The fit between the DG-FEM and SEM solutions is almost perfect for the vertical component v_z, whatever the position of the receivers, and even at long times. On the other hand, for the horizontal component v_x, good agreement is seen for short times, of up to 6–7 s. At later times, some amplitude misfits are seen. Nevertheless, for all of the traces, the overall fit of the waveforms between the two solutions is remarkable, which indicates that the same and complex wave propagation phenomena are represented. Contrary to the SEM, for the DG-FEM, constant physical properties per element were assumed, given by the average of the properties at the four vertices of the elements. Therefore, the amplitude misfits seen in the DG-FEM seismograms might be the consequence of the approximations used in the model discretization, rather than the accuracy of the numerical method itself. The statistics related to the DG-FEM and SEM modelling are given in Table 7. Compared to DG-FEM, the number of DOF used in the SEM modelling is 30 per cent lower, and the number of time steps is nearly two-fold lower. Both of the simulations were performed on the same computing platform with 18 bi-xeon Quadcore CPU IBM E5420 at 2.5 GHz (giving a total of 144 cores). The methods required similar amounts of memory, and to obtain 30 s of wave propagation, the computation time was 7 hr with SEM and 52 hr with DG-FEM. The computation time per DOF and per step is on average 1.67 µs for DG-FEM, and 0.52 µs for SEM. Taking into account that the number of unknowns per DOF is nine with DG-FEM (with first-order velocity–stress formulation) and three with SEM (with second-order velocity formulation), these two methods yield comparable computation times per unknown. Therefore, the relative cost of the methods depends mainly on the mesh characteristics. However, a detailed analysis is required and goes beyond the scope of this study. We can expect, that in more complicated cases (like a set of thin geological layers), the DG-FEM would be more efficient, due to the flexibility of tetrahedral meshes. In the following, we present another comparison tool that allows for a study of the misfits on the complete free surface of the model. An objective in earthquake engineering is to predict the ground motion for a realistic scenario. The map of peak ground velocity (PGV) provides a convenient representation that shows the maximum value of the norm of the velocity vector for each position on the free surface. PGV maps computed with 30 s of seismic signals are shown in Fig. 21. The fit between the PGV map computed with DG-FEM and the PGV map computed with SEM is almost perfect. On these maps, the paths followed by energetic bundles of surface waves can be seen. When they reach the basin borders, these bundles are reflected and diffracted. This behaviour can be be seen in the PGV map in the southeast part of the basin.

8 PERSPECTIVES AND CONCLUSIONS

We have proposed a DG-FEM with CPML absorbing boundary condition that benefits most from *hp*-adaptivity combined with tetrahedral meshes. The gain obtained with this method in the context of 3-D seismic elastic modelling is important when complex geological structures are considered, especially if the medium has highly contrasting physical properties. In our approach, we favour the use of low approximation orders which allows fine discretization of the medium with piecewise constant properties per element. From this point of view, an optimal compromise between precision, computational cost and adequate discretization is achieved with the P_2 interpolation. For efficient reduction of the computation time, CPMLs were designed with lower approximation orders and they allowed a saving of between 40 and 60 per cent of CPU time on large

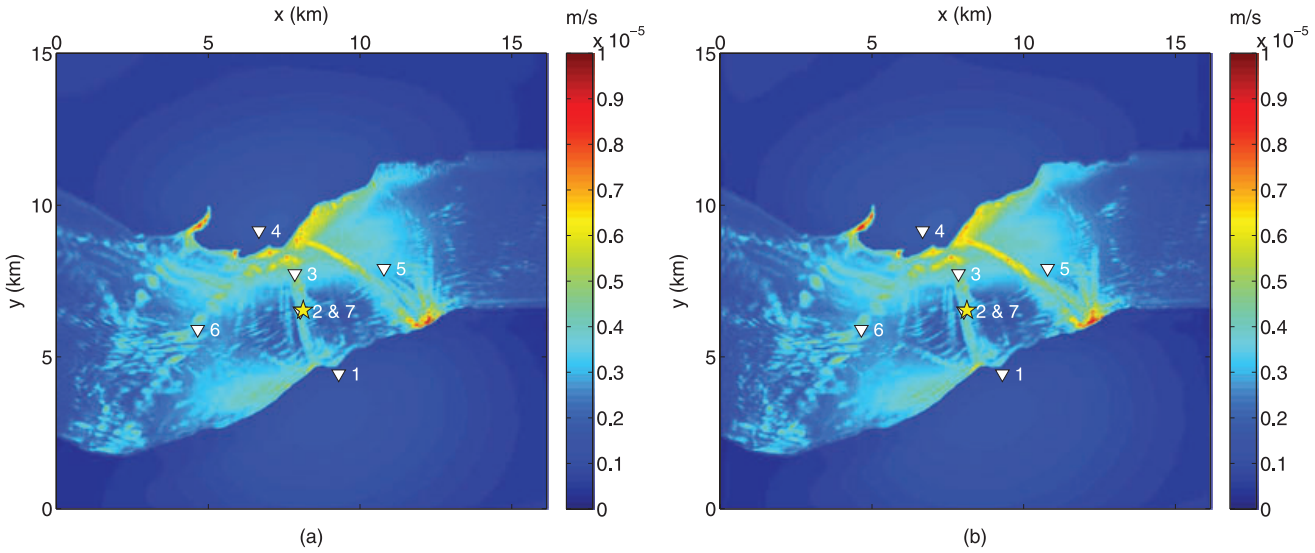

Figure 21. (a) Peak ground velocity map computed for the EUROSEISTEST modelling with DG-FEM. Numbered white triangles, the receivers; yellow star, the source epicentre. (b) Same as (a) computed with SEM.

clusters. Moreover, we mitigated the effects of ill-sized tetrahedral elements by automatically choosing the appropriate approximation order for each element, and hence we have kept the number of time steps as low as possible. In our case, the so-called *p*-adaptivity technique can reduce the number of time steps by a factor of five. Consequently, when combined with the low-cost CPMLs, computation times are generally reduced by nearly one order of magnitude, compared with the times observed with standard DG-FEM modelling using a unique approximation order. The potential and the perspectives concerning this method are numerous. For the limitations of our formulation, we note the possibility of attributing varying physical properties inside the elements. This would release the discretization constraint and would allow the use of higher approximation orders, thus reducing the number of elements and the computational cost of the simulations. For completeness, we note another possible means of releasing the discretization constraint, with non-conforming meshing, although the expected gain does not appear as crucial in the case of tetrahedral meshes as it is with hexahedral meshes. Apart from these possible evolutions, we intend to include viscoelastic rheologies (Käser *et al.* 2007) and to apply the method to realistic problems requiring appropriate discretizations of geological structures and/or large material contrasts. Due to the discontinuous nature of the method, rupture mechanisms, like earthquake dynamic rupture, might be modelled (BenJemaa *et al.* 2007, 2009; de la Puente *et al.* 2009). This method can also be applied to seismic modelling in cases of complex topographies, or be used as a forward modelling tool for FWI techniques (Tarantola 1987; Pratt *et al.* 1998).

ACKNOWLEDGMENTS

This study was funded by the SEISCOPE consortium, which is sponsored by BP, CGG-VERITAS, EXXON MOBIL, SHELL and TOTAL. It has also benefited from the support of the CEA/CASHIMA project. All of the numerical simulations were performed on the high performance computing facilities of IDRIS/CNRS (Project #92280) and the Observatoire de la Côte d'Azur (OCA), except the EUROSEISTEST ground predictions which were performed at the *Service Commun de Calcul Intensif de l'Observatoire de Grenoble* (SCCI-CIMENT). We would like to thank Romain Brossier and Stéphane Operto for the fruitful discussions. The remarks and suggestions of Martin Käser and an anonymous reviewer are greatly acknowledged as well.

REFERENCES

Aagaard, B.T., Hall, J.F. & Heaton, T.H., 2001. Characterization of near-source ground motion with earthquake simulations, *Earthq. Spectra.,* **17,** 177–207.

Abarbanel, S., Gottlieb, D. & Hesthaven, J.S., 2002. Long-time behavior of the perfectly matched layer equations in computational electromagnetics, *J. Scient. Comput.,* **17,** 405–422.

Ainsworth, M., Monk, P. & Muniz, W., 2006. Dispersive and dissipative properties of discontinuous Galerkin finite element methods for the second-order wave equation, *J. Scient. Comput.,* **27**(1–3), 5–40.

Akcelik, V. *et al.*, 2003. High resolution forward and inverse earthquake modeling on terascale computers, in *SC'03: Proceedings of the 2003 ACM/IEEE Conference on Supercomputing,* IEEE Computer Society, Washington, DC, USA, p. 52.

Aoi, S. & Fujiwara, H., 1999. 3D finite-difference method using discontinuous grids, *Bull. seism. Soc. Am.,* **89,** 918–930.

Aoyama, Y. & Nakano, J., 1999, *RS/6000 SP: Practical MPI Programming,* IBM Corporation, Red Book edition, Texas.

Babuska, I. & Suri, M., 1990. The p and the hp versions of the finite element method: an overview, *Comp. Meth. Appl. Mech. Engng.,* **80**(1–3), 5–26.

Basabe, J.D., Sen, M. & Wheeler, M., 2008. The interior penalty discontinuous galerkin method for elastic wave propagation: grid dispersion, *Geophys. J. Int.,* **175,** 83–93.

Bécache, E., Petropoulos, P.G. & Gedney, S.G., 2004. On the long-time behavior of unsplit perfectly matched layers, *IEEE Trans. Anten. Propagat.,* **52,** 1335–1342.

BenJemaa, M., Glinsky-Olivier, N., Cruz-Atienza, V.M. & Virieux, J., 2009. 3D Dynamic rupture simulations by a finite volume method, *Geophys. J. Int.,* **178,** 541–560.

BenJemaa, M., Glinsky-Olivier, N., Cruz-Atienza, V.M., Virieux, J. & Piperno, S., 2007. Dynamic non-planar crack rupture by a finite volume method, *Geophys. J. Int.,* **171,** 271–285.

Berenger, J.-P., 1994. A perfectly matched layer for absorption of electromagnetic waves, *J. Computat. Phys.,* **114,** 185–200.

Bohlen, T. & Saenger, E.H., 2006. Accuracy of heterogeneous staggered-grid finite-difference modeling of Rayleigh waves, *Geophysics,* **71,** 109–115.

Bouchon, M., 1981. A simple method to calculate green's functions for elastic layered media, *Bull. seism. Soc. Am.,* **71**(4), 959–971.

Brossier, R., Virieux, J. & Operto, S., 2008. Parsimonious finite-volume frequency-domain method for 2-D P-SV-wave modelling, *Geophys. J. Int.,* **175**(2), 541–559.

Campillo, M., Gariel, J., Aki, K. & Sanchez-Sesma, F., 1989. Destructive strong ground motion in Mexico city: source, path, and site effects during great 1985 Michoacan earthquake, *BSSA,* **79**(6):1718–1735.

Chaljub, E. *et al.*, 2009. Assessing the capability of numerical methods to predict earthquake ground motion: the Euroseistest verification and validation project, *EOS, Trans. Am. geophys. Un.,* Abstract S43A-1968.

Chaljub, E., Capdeville, Y. & Vilotte, J.-P., 2003. Solving elastodynamics in a fluid-solid heterogeneous sphere: a parallel spectral element approximation on non-conforming grids, *J. Computat. Phys.,* **187,** 457–491.

Chaljub, E., Komatitsch, D., Vilotte, J.-P., Capdeville, Y., Valette, B. & Festa, G., 2007. *Adv. Geophysics,* **48,** 365–419.

Chew, W.C. & Liu, Q.H., 1996. Perfectly matched layers for elastodynamics: a new absorbing boundary condition, *J. Comput. Acous.,* **4,** 341–359.

Chin-Joe-Kong, M.J.S., Mulder, W.A. & Van Veldhuizen, M., 1999. Higher-order triangular and tetrahedral finite elements with mass lumping for solving the wave equation, *J. Eng. Math.,* **35,** 405–426.

Cockburn, B., Li, F. & Shu, C.W., 2004. Locally divergence-free discontinuous Galerkin methods for the Maxwell equations, *J. Computat. Phys.,* **194,** 588–610.

Collino, F. & Tsogka, C., 2001. Application of the perfectly matched absorbing layer model to the linear elastodynamic problem in anisotropic heterogeneous media, *Geophysics,* **66,** 294–307.

Coutant, O., 1989. Program of Numerical Simulation AXITRA, Research report, LGIT, Grenoble.

de la Puente, J., Ampuero, J.-P. & Käser, M., 2009. Dynamic rupture modeling on unstructured meshes using a discontinuous Galerkin method, *J. geophys. Res.,* **114,** B10302, doi:10.1029/2008JB006271.

Delcourte, S., Fezoui, L. & Glinsky-Olivier, N., 2009. A high-order discontinuous Galerkin method for the seismic wave propagation, *ESAIM: Proc.,* **27,** 70–89.

Drossaert, F.H. & Giannopoulos, A., 2007. A nonsplit complex frequency-shifted PML based on recursive integration for FDTD modeling of elastic waves, *Geophysics,* **72**(2), T9–T17.

Dumbser, M. & Käser, M., 2006. An arbitrary high order discontinuous Galerkin method for elastic waves on unstructured meshes II: the three-dimensional isotropic case, *Geophys. J. Int.,* **167**(1), 319–336.

Dumbser, M., Käser, M. & Toro, E., 2007. An arbitrary high order discontinuous Galerkin method for elastic waves on unstructured meshes V: local time stepping and p-adaptivity, *Geophys. J. Int.,* **171**(2), 695–717.

Dunavant, D.A., 1985. High degree efficient symmetrical gaussian quadrature rules for the triangle, *Int. J. Numer. Methods Eng.,* **21,** 1129–1148.

Frey, P. & George, P., 2008, *Mesh Generation*. ISTE Ltd, London & John Wiley Sons Inc, Hoboken, NJ.

Galis, M., Moczo, P. & Kristek, J., 2008. A 3-D hybrid finite-difference - finite-element viscoelastic modelling of seismic wave motion, *Geophys. J. Int.,* **175,** 153–184.

Garvin, W.W., 1956. Exact transient solution of the buried line source problem, *Proc. Roy. Soc. Lond.,* **234,** 528–541.

Graves, R., 1996. Simulating seismic wave propagation in 3D elastic media using staggered-grid finite differences, *Bull. seism. Soc. Am.,* **86,** 1091–1106.

Hesthaven, J.S. & Warburton, T., 2008, *Nodal Discontinuous Galerkin Method. Algorithms, Analysis, and Application,* Springer, New York.

Ichimura, T., Hori, M. & Kuwamoto, H., 2007. Earthquake motion simulation with multi-scale finite element analysis on hybrid grid, *Bull. seism. Soc. Am.,* **97**(4), 1133–1143.

Jacobs, G. & Hesthaven, J.S., 2006. High-order nodal discontinuous Galerkin particle-in-cell methods on unstructured grids, *J. Comput. Phys.,* **214,** 96–121.

Jongmans, D., Pitilakis, K., Demanet, D., Raptakis, D., Riepl, J., Horrent, C., Lontzetidis, K. & Bard, P.Y., 1998. Determination of the geological structure of the Volvi basin and validation of the basin response, *Bull. seism. Soc. Am.,* **88**(2), 473–487.

Karypis, G. & Kumar, V., 1998, METIS—a software package for partitioning unstructured graphs, partitioning meshes and computing fill-reducing orderings of sparse matrices, Version 4.0, University of Minnesota.

Käser, M. & Dumbser, M., 2008. A highly accurate discontinuous Galerkin method for complex interfaces between solids and moving fluids, *Geophysics,* **73**(3), 23–35.

Käser, M., Dumbser, M., de la Puente, J. & Igel, H., 2007. An arbitrary high order discontinuous Galerkin method for elastic waves on unstructured meshes III: viscoelastic attenuation, *Geophys. J. Int.,* **168**(1), 224–242.

Käser, M., Hermann, V. & de la Puente, J., 2008. Quantitative accuracy analysis of the discontinuous Galerkin method for seismic wave propagation, *Geophys. J. Int.,* **173**(2), 990–999.

Kawase, H., 2003, Site effects on strong ground motions, in *International Handbook of Earthquake and Engineering Seismology, Part B,* eds Lee, W.H.K. and Kanamori, H., Academic Press, London.

Keast, P., 1986. Moderate-degree tetrahedral quadrature formulae, *Comput. Methods Appl. Mech. Eng.,* **55,** 339–348.

Komatitsch, D. & Martin, R., 2007. An unsplit convolutional perfectly matched layer improved at grazing incidence for the seismic wave equation, *Geophysics,* **72**(5), SM155–SM167.

Komatitsch, D. & Vilotte, J.P., 1998. The spectral element method: an efficient tool to simulate the seismic response of 2D and 3D geological structures, *Bull. seism. Soc. Am.,* **88,** 368–392.

Komatitsch, D., Liu, Q., Tromp, J., Suss, P., Stidham, C. & Shaw, J.H., 2004. Simulations of ground motion in the Los Angeles basin based upon the spectral-element method, *Bull. seism. Soc. Am.,* **94,** 187–206.

Komatitsch, D., Labarta, J. & Michéa, D., 2008. A simulation of seismic wave propagation at high resolution in the inner core of the Earth on 2166 processors of MareNostrum, *Lecture Notes Comput. Sci.,* **5336,** 364–377.

Kuzuoglu, M. & Mittra, R., 1996. Frequency dependence of the constitutive parameters of causal perfectly matched anisotropic absorbers, *IEEE Microwave Guided Wave Lett.,* **6,** 447–449.

Lamb, H., 1904. On the propagation of tremors over the surface of an elastic solid, *Phil. Trans. R. Soc. Lond. Ser.,* **A 203,** 1–42.

Manakou, M., Raptakis, D., Apostolidis, P., Chavez-Garcia, F.J. & Pitilakis, K., 2007. The 3D geological structure of the Mygdonian basin (Greece), in *proceedings of the 4th International Conference on Earthquake Geotechnical Engineering,* Ref. 1686, ICEGE, Thessaloniki.

Marfurt, K., 1984. Accuracy of finite-difference and finite-elements modeling of the scalar and elastic wave equation, *Geophysics,* **49,** 533–549.

Mercerat, E.D., Vilotte, J.P. & Sanchez-Sesma, F.J., 2006. Triangular spectral element simulation of two-dimensional elastic wave propagation using unstructured triangular grids, *Geophys. J. Int.,* **166,** 679–698.

Meza-Fajardo, K. & Papageorgiou, A., 2008. A nonconvolutional, split-field, perfectly matched layer for wave propagation in isotropic and anisotropic elastic media: stability analysis, *Bull. seism. Soc. Am.,* **98**(4), 1811–1836.

Moczo, P., Ampuero, J.P., Kristek, J., Galis, M., Day, S.M. & Igel, H., 2005. The European Network SPICE Code Validation, *EOS, Trans. Am. geophys. Un.*, Abstract S13A-0180.

Moczo, P., Kristek, J., Galis, M., Pazak, P. & Balazovjech, M., 2007. The finite-difference and finite-element modeling of seismic wave propagation and earthquake motion, *Acta Physica Slovaca,* **52**(2), 177–406.

Pasquetti, R. & Rapetti, F., 2006. Spectral element methods on unstructured meshes: comparisons and recent advances, *J. Scient. Comput.,* **27,** 377–387.

Pitarka, A., 1999. 3D elastic finite-difference modeling of seismic motion using staggered grids with nonuniform spacing, *Bull. Seism. Soc. Am.,* **89**(1), 54–68.

Pratt, R.G., Shin, C. & Hicks, G.J., 1998. Gauss-Newton and full Newton methods in frequency-space seismic waveform inversion, *Geophys. J. Int.,* **133,** 341–362.

Raptakis, D.G., Manakou, M.V., Chavez-Garcia, F.J., Makra, K.A. & Pitilaks, K.D., 2005. 3D configuration of Mygdonian basin and preliminary estimate of its site response, *Soil Dyn. Earthq. Eng.,* **25,** 871–887.

Reed, W. & Hill, T., 1973. Triangular mesh methods for the neuron transport equation. Technical Report LA-UR-73-479, Los Alamos Scientific Laboratory.

Remaki, M., 2000. A new finite volume scheme for solving Maxwell's system, *COMPEL,* **19**(3), 913–931.

Roden, J.A. & Gedney, S.D., 2000. Convolution PML (CPML): an efficient FDTD implementation of the CFS-PML for arbitrary media, *Microwave Opt. Technol. Lett.,* **27**(5), 334–339.

Seriani, G. & Priolo, E., 1994. Spectral element method for acoustic wave simulation in heterogeneous media, *Finite Elements Anal. Des.,* **16,** 337–348.

Shewchuk, J.R., 1998. Tetrahedral mesh generation by delaunay refinement, in *Proceedings of the 14th Annual Symposium on Computational Geometry,* pp. 86–95, SCG, Minneapolis, MN.

Si, H. & Gärtner, K., 2005. Meshing piecewise linear complexes by constrained delaunay tetrahedralizations, in *Proceedings of the 14th International Meshing Roundtable,* pp. 147–163, IMR, San Diego, CA.

Sirgue, L. & Pratt, R.G., 2004. Efficient waveform inversion and imaging: a strategy for selecting temporal frequencies, *Geophysics,* **69**(1), 231–248.

Tarantola, A., 1987, *Inverse Problem Theory: Methods for Data Fitting and Model Parameter Estimation,* Elsevier, New York.

Toulopoulos, I. & Ekaterinaris, J.A., 2006. High-order discontinuous Galerkin discretizations for computational aeroacoustics in complex domains, *AIAA J.,* **44,** 502–511.

Virieux, J., 1986. P-SV wave propagation in heterogeneous media, velocity-stress finite difference method, *Geophysics,* **51,** 889–901.

Zienkiewicz, O.C., Taylor, R.L. & Zhu, J.Z., 2005, *The Finite Element Method its Basis and Fundamentals,* 6th edn, Elsevier, London.

APPENDIX A: LAGRANGIAN BASIS FUNCTIONS

For the definition of the Lagrangian basis functions, the barycentric or tetrahedral coordinates $(\zeta_1, \zeta_2, \zeta_3, \zeta_4)$ that are linked to the cartesian coordinates (x, y, z) are defined inside an element as follows:

$$\begin{pmatrix} 1 \\ x \\ y \\ z \end{pmatrix} = \begin{pmatrix} 1 & 1 & 1 & 1 \\ x_1 & x_2 & x_3 & x_4 \\ y_1 & y_2 & y_3 & y_4 \\ z_1 & z_2 & z_3 & z_4 \end{pmatrix} \begin{pmatrix} \zeta_1 \\ \zeta_2 \\ \zeta_3 \\ \zeta_4 \end{pmatrix},$$

where (x_j, y_j, z_j) are the coordinates of the jth node of the element. Then, the Lagrangian basis functions can be defined with a linear combination of the tetrahedral coordinates depending on the approximation order. Following the node numbering convention given in Fig. 1, these functions are given by for the P_0 interpolation

$$\varphi_1 = 1,$$

for the P_1 interpolation

$$\varphi_1 = \zeta_1 \qquad \varphi_2 = \zeta_2 \qquad \varphi_3 = \zeta_3 \qquad \varphi_4 = \zeta_4,$$

and for the P_2 interpolation

$$\varphi_1 = (2\zeta_1 - 1)\zeta_1 \qquad \varphi_2 = (2\zeta_2 - 1)\zeta_2 \qquad \varphi_3 = (2\zeta_3 - 1)\zeta_3 \qquad \varphi_4 = (2\zeta_4 - 1)\zeta_4$$

$$\varphi_5 = 4\zeta_1\zeta_2 \qquad \varphi_6 = 4\zeta_1\zeta_3 \qquad \varphi_7 = 4\zeta_1\zeta_4 \qquad \varphi_8 = 4\zeta_3\zeta_2 \qquad \varphi_9 = 4\zeta_3\zeta_4 \qquad \varphi_{10} = 4\zeta_2\zeta_4.$$

APPENDIX B: MATRICES USED IN THE DG-FEM FORMULATION

$\mathcal{M}_\theta$ and $\mathcal{N}_\theta$ are constant real matrices defined by

$$\mathcal{M}_x = \begin{pmatrix} 1 & 1 & 0 & 0 & 0 & 0 \\ 0 & 0 & 0 & 1 & 0 & 0 \\ 0 & 0 & 0 & 0 & 1 & 0 \end{pmatrix} \qquad \mathcal{N}_x = \begin{pmatrix} 1 & 2 & -1 & 0 & 0 & 0 \\ 0 & 0 & 0 & 1 & 0 & 0 \\ 0 & 0 & 0 & 0 & 1 & 0 \end{pmatrix}^T$$

$$\mathcal{M}_y = \begin{pmatrix} 0 & 0 & 0 & 1 & 0 & 0 \\ 1 & 0 & 1 & 0 & 0 & 0 \\ 0 & 0 & 0 & 0 & 0 & 1 \end{pmatrix} \qquad \mathcal{N}_y = \begin{pmatrix} 0 & 0 & 0 & 1 & 0 & 0 \\ 1 & -1 & 2 & 0 & 0 & 0 \\ 0 & 0 & 0 & 0 & 0 & 1 \end{pmatrix}^T$$

$$\mathcal{M}_z = \begin{pmatrix} 0 & 0 & 0 & 0 & 1 & 0 \\ 0 & 0 & 0 & 0 & 0 & 1 \\ 1 & -1 & -1 & 0 & 0 & 0 \end{pmatrix} \qquad \mathcal{N}_z = \begin{pmatrix} 0 & 0 & 0 & 0 & 1 & 0 \\ 0 & 0 & 0 & 0 & 0 & 1 \\ 1 & -1 & -1 & 0 & 0 & 0 \end{pmatrix}^T.$$

For P_k, with $k \leq 2$, the volume integral in eqs (9) and (10) can be computed with the 11 Gauss points integration rule for tetrahedra (Keast 1986) and the surface integral in eqs (11) and (12) can be computed with the six Gauss points integration rule for triangles (Dunavant 1985).

Below, we give the expression of the matrices relevant for P_1 elements following the node numbering convention given in Fig. 1(b).

$$\mathcal{K}_i = \frac{vol_i}{20}\begin{pmatrix} 2 & 1 & 1 & 1 \\ 1 & 2 & 1 & 1 \\ 1 & 1 & 2 & 1 \\ 1 & 1 & 1 & 2 \end{pmatrix}, \tag{B1}$$

with vol_i as the volume of element i.

$$\mathcal{E}_{i\theta} = \frac{1}{12}\begin{pmatrix} S_{i1}n_{i1_\theta} & S_{i1}n_{i1_\theta} & S_{i1}n_{i1_\theta} & S_{i1}n_{i1_\theta} \\ S_{i2}n_{i2_\theta} & S_{i2}n_{i2_\theta} & S_{i2}n_{i2_\theta} & S_{i2}n_{i2_\theta} \\ S_{i3}n_{i3_\theta} & S_{i3}n_{i3_\theta} & S_{i3}n_{i3_\theta} & S_{i3}n_{i3_\theta} \\ S_{i4}n_{i4_\theta} & S_{i4}n_{i4_\theta} & S_{i4}n_{i4_\theta} & S_{i4}n_{i4_\theta} \end{pmatrix} \qquad \forall\theta \in \{x, y, z\}, \tag{B2}$$

with S_{ik} the surface of the face opposite to the kth node of element i and $\vec{n}_{ik} = (n_{ik_x}, n_{ik_y}, n_{ik_z})^T$ as the outward pointing unit normal vector with respect to the surface S_{ik}. For the computation of the flux matrices, we adopt a specific node numbering scheme. First, the neighbour element k is given by the node number of element i which is not shared between elements i and k. For instance, in Fig. 1(b), the neighbour element $k = 1$ is the element sharing the face (234) of element i. Second, the neighbour element nodes share the same node numbers of element i on the common face. Therefore, the opposite nodes of element i and k have also the same number. With this node numbering scheme, $\mathcal{F}_{ik}$ and $\mathcal{G}_{ik}$ are identical when both elements are P_1. We use this property to perform an efficient computation of the flux. In that case, we get

$$\mathcal{F}_{i1} = \frac{S_{i1}}{12}\begin{pmatrix} 0 & 0 & 0 & 0 \\ 0 & 2 & 1 & 1 \\ 0 & 1 & 2 & 1 \\ 0 & 1 & 1 & 2 \end{pmatrix} \qquad \mathcal{F}_{i2} = \frac{S_{i2}}{12}\begin{pmatrix} 2 & 0 & 1 & 1 \\ 0 & 0 & 0 & 0 \\ 1 & 0 & 2 & 1 \\ 1 & 0 & 1 & 2 \end{pmatrix}$$

$$\mathcal{F}_{i3} = \frac{S_{i3}}{12}\begin{pmatrix} 2 & 1 & 0 & 1 \\ 1 & 2 & 0 & 1 \\ 0 & 0 & 0 & 0 \\ 1 & 1 & 0 & 2 \end{pmatrix} \qquad \mathcal{F}_{i4} = \frac{S_{i4}}{12}\begin{pmatrix} 2 & 1 & 1 & 0 \\ 1 & 2 & 1 & 0 \\ 1 & 1 & 2 & 0 \\ 0 & 0 & 0 & 0 \end{pmatrix}. \tag{B3}$$

Geophysical Journal International

Geophys. J. Int. (2011) **187,** 1645–1667 doi: 10.1111/j.1365-246X.2011.05221.x

3-D finite-difference, finite-element, discontinuous-Galerkin and spectral-element schemes analysed for their accuracy with respect to *P*-wave to *S*-wave speed ratio

Peter Moczo,[1,2] Jozef Kristek,[1,2] Martin Galis,[1,2] Emmanuel Chaljub[3] and Vincent Etienne[4]

[1]*Faculty of Mathematics, Physics and Informatics, Comenius University Bratislava, Mlynska dolina F1, 84248 Bratislava, Slovak Republic. E-mail: moczo@fmph.uniba.sk*
[2]*Geophysical Institute, Slovak Academy of Sciences, Dubravska cesta* 9, 84528 *Bratislava, Slovak Republic*
[3]*ISTerre, Université Joseph Fourier, BP* 53, 38041 *Grenoble, France*
[4]*Géoazur,* 250 *rue Albert Einstein, Sophia Antipolis,* 06560 *Valbonne, France*

Accepted 2011 September 5. Received 2011 August 15; in original form 2011 April 19

SUMMARY

We analyse 13 3-D numerical time-domain explicit schemes for modelling seismic wave propagation and earthquake motion for their behaviour with a varying *P*-wave to *S*-wave speed ratio (V_P/V_S). The second-order schemes include three finite-difference, three finite-element and one discontinuous-Galerkin schemes. The fourth-order schemes include three finite-difference and two spectral-element schemes. All schemes are second-order in time. We assume a uniform cubic grid/mesh and present all schemes in a unified form. We assume plane *S*-wave propagation in an unbounded homogeneous isotropic elastic medium. We define relative local errors of the schemes in amplitude and the vector difference in one time step and normalize them for a unit time. We also define the equivalent spatial sampling ratio as a ratio at which the maximum relative error is equal to the reference maximum error. We present results of the extensive numerical analysis.

We theoretically (i) show how a numerical scheme sees the *P* and *S* waves if the V_P/V_S ratio increases, (ii) show the structure of the errors in amplitude and the vector difference and (iii) compare the schemes in terms of the truncation errors of the discrete approximations to the second mixed and non-mixed spatial derivatives.

We find that four of the tested schemes have errors in amplitude almost independent on the V_P/V_S ratio.

The homogeneity of the approximations to the second mixed and non-mixed spatial derivatives in terms of the coefficients of the leading terms of their truncation errors as well as the absolute values of the coefficients are key factors for the behaviour of the schemes with increasing V_P/V_S ratio.

The dependence of the errors in the vector difference on the V_P/V_S ratio should be accounted for by a proper (sufficiently dense) spatial sampling.

Key words Numerical approximations and analysis; Computational seismology; Theoretical seismology.

1 INTRODUCTION

When numerically modelling seismic wave propagation and earthquake ground motion in a local or regional scale, we often consider a finite volume of the Earth. Typically, the volume has a shape of a cuboid (a rectangular parallelepiped) with the top face representing a flat free surface and other faces representing transparent boundaries or planes of symmetry. In a more realistic case, the free Earth's surface has a non-planar topography. The medium inside is often considered a heterogeneous isotropic viscoelastic continuum. If we cover the computational domain by a space–time grid of points or elements, then the overall accuracy of the numerical modelling for the given space–time discretization and source–receiver configuration may depend on some or all of the following factors:

(1) accuracy in
  (i) a homogeneous medium (V_P/V_S—*P*-wave to *S*-wave speed ratio)
  (ii) a smoothly spatially varying medium (spatial variability of material parameters)
(2) accuracy at
  (i) a material interface (geometry, continuity of displacement and traction)
  (ii) a free surface (geometry, zero traction)
(3) accuracy of
  (i) a grid boundary (transparency or symmetry)
  (ii) simulation of source (location, mechanism, time function)
  (iii) incorporation of attenuation (frequency dependence, spatial variability)

Articles presenting numerical methods or schemes usually include and some of them focus first of all on the stability and grid dispersion in an unbounded homogeneous medium. This is fundamental and necessary. Not all articles sufficiently address the other factors determining the overall accuracy of the numerical modelling. Surprisingly enough, the least attention has been paid to the accuracy with respect to the V_P/V_S ratio.

At the same time, in surface sediments, and mainly in sedimentary basins and valleys, the ratio V_P/V_S is often as large as five or more (e.g. larger than 10 in the unconsolidated lake sediments in Ciudad de México). Recent numerical-modelling exercises focused on the deep Alpine sediment valley beneath Grenoble, France and the sedimentary Mygdonian Basin near Thessaloniki, Greece (e.g. Chaljub *et al*. 2010a,b; Moczo *et al*. 2010a), also confirm the necessity to account for large V_P/V_S ratios with sufficient accuracy.

Moczo *et al*. (2010b) investigated accuracy of four finite-difference (FD) and three finite-element (FE) schemes with respect to the V_P/V_S ratio. Their investigation was restricted to the basic second-order 2-D schemes. They aimed to identify and select the very basic inherent aspects of the schemes responsible for their behaviour with respect to the varying V_P/V_S ratio, and to compare different schemes at the most fundamental level. They indicated that consistency in approximating first spatial derivatives and, consequently, the second mixed and non-mixed spatial derivatives appears to be the key factor for the behaviour of a scheme with respect to the V_P/V_S ratio.

Moczo *et al*. (2010b) introduced the problem of the accuracy with respect to the V_P/V_S ratio in sufficient extent and detail. Therefore, we do not repeat here the extensive introduction and rather refer readers to the latter paper.

In this paper, we focus on investigating the accuracy of 3-D time-domain explicit numerical schemes of second-order in time and second- and fourth-order in space with respect to the V_P/V_S ratio in an unbounded homogeneous medium. We include schemes based on the FD, FE, spectral-element (SE) and discontinuous-Galerkin (DG) methods.

We present all the investigated schemes in a unified form and define (full) local errors in one time integration step. Because different schemes use different time steps (according to appropriate stability conditions), we normalize the errors with respect to time. Consequently, we can directly compare numerically evaluated errors of different schemes. We perform extensive numerical analysis for wide ranges of values of the V_P/V_S ratio and spatial sampling ratio, and for the entire range of directions of propagation with respect to the spatial grid. We analyse and interpret the numerical results in terms of the inherent structures of the numerical schemes. We eventually develop general conclusions on the accuracy of the numerical schemes with respect to the V_P/V_S ratio and on the numerical efficiency of the schemes in practical applications.

2 EQUATIONS OF MOTION FOR A HOMOGENEOUS MEDIUM

Consider a Cartesian coordinate system (x, y, z) and an unbounded homogeneous perfectly elastic isotropic medium. Let ρ denote density, λ and μ Lamé elastic moduli, $\alpha = [(\lambda + 2\mu)/\rho]^{1/2}$ and $\beta = (\mu/\rho)^{1/2}$ *P*-wave and *S*-wave speeds (i.e. V_P and V_S). Let displacement components $u_i \; ; \; i \in \{x, y, z\}$ and stress-tensor components $\sigma_{ij} \; ; \; i, j \in \{x, y, z\}$ be functions of the spatial coordinates and time t. Denote

$$\varphi_{,\zeta} = \frac{\partial \varphi}{\partial \zeta}; \quad \varphi \in \{u_i, \; \sigma_{ij}\}, \quad i, j \in \{x, y, z\}, \quad \zeta \in \{t, x, y, z\}. \tag{1}$$

We will consider two strong forms of the equation of motion without the body force term. The displacement-stress (DS) formulation of the equation of motion is

$$\begin{aligned}
\rho u_{x,tt} &= \sigma_{xx,x} + \sigma_{xy,y} + \sigma_{xz,z} \\
\rho u_{y,tt} &= \sigma_{yy,y} + \sigma_{yz,z} + \sigma_{yx,x} \\
\rho u_{z,tt} &= \sigma_{zz,z} + \sigma_{zx,x} + \sigma_{zy,y}
\end{aligned} \tag{2}$$

$$\begin{aligned}
\sigma_{xx} &= (\lambda + 2\mu) u_{x,x} + \lambda u_{y,y} + \lambda u_{z,z} \\
\sigma_{yy} &= (\lambda + 2\mu) u_{y,y} + \lambda u_{z,z} + \lambda u_{x,x} \\
\sigma_{zz} &= (\lambda + 2\mu) u_{z,z} + \lambda u_{x,x} + \lambda u_{y,y} \\
\sigma_{xy} &= \mu \, (u_{x,y} + u_{y,x}) \\
\sigma_{yz} &= \mu \, (u_{y,z} + u_{z,y}) \\
\sigma_{zx} &= \mu \, (u_{z,x} + u_{x,z}).
\end{aligned} \tag{3}$$

The displacement (D) formulation is

$$\rho u_{x,tt} = (\lambda + 2\mu)u_{x,xx} + \lambda\,(u_{y,yx} + u_{z,zx}) + \mu\,(u_{x,yy} + u_{y,xy} + u_{z,xz} + u_{x,zz})$$
$$\rho u_{y,tt} = (\lambda + 2\mu)u_{y,yy} + \lambda\,(u_{z,zy} + u_{x,xy}) + \mu\,(u_{y,zz} + u_{z,yz} + u_{x,yx} + u_{y,xx})$$
$$\rho u_{z,tt} = (\lambda + 2\mu)u_{z,zz} + \lambda\,(u_{x,xz} + u_{y,yz}) + \mu\,(u_{z,xx} + u_{x,zx} + u_{y,zy} + u_{z,yy}). \quad (4)$$

Eqs (4) can be written as

$$u_{x,tt} = \alpha^2(u_{x,xx} + u_{y,yx} + u_{z,zx}) + \beta^2\,(u_{x,yy} - u_{y,yx} + u_{x,zz} - u_{z,zx})$$
$$u_{y,tt} = \alpha^2(u_{y,yy} + u_{z,zy} + u_{x,xy}) + \beta^2\,(u_{y,zz} - u_{z,zy} + u_{y,xx} - u_{x,xy})$$
$$u_{z,tt} = \alpha^2(u_{z,zz} + u_{x,xz} + u_{y,yz}) + \beta^2\,(u_{z,xx} - u_{x,xz} + u_{z,yy} - u_{y,yz}). \quad (5)$$

The weak form of the equation of motion (e.g. Zienkiewicz & Taylor 1989; Hughes 2000; Moczo *et al*. 2007a) is

$$\int_\Omega w\,(\rho\,u_{i}{}_{,tt})\,\mathrm{d}\Omega + \int_\Omega w_{,k}\;\sigma_{ik}\,\mathrm{d}\Omega - \int_{\Gamma_N} w\,h_i\,\mathrm{d}\Gamma = 0, \quad (6)$$

where Ω is a volume of a medium with boundary Γ, h_i is a prescribed traction on part Γ_N of boundary Γ and the equations have to be satisfied for all possible choices of weight functions w.

3 NUMERICAL SCHEMES

Several numerical methods can be used to solve the strong-form and weak-form equations of motion. The analysis by Moczo *et al*. (2010b) was restricted to the basic 2-D second-order FD and FE schemes. Here, we investigate 13 3-D time-domain numerical schemes of second- and fourth-order in space based on four important numerical methods—FD, FE, DG and SE methods. We use three uniform spatial grids in the FD schemes—conventional, partly-staggered and staggered (Fig. 1a). The other schemes are constructed on the mesh of uniform cubic elements. The elements considered for the FE and SE schemes are illustrated in Figs 1(b) and (c), respectively. All schemes are explicit and second-order accurate in time. The choice of the explicit schemes well reflects the fact that the explicit schemes are strongly dominant in recent numerical modelling of seismic wave propagation and earthquake ground motion. The same is true about the second-order accuracy in time. The powerful and sophisticated ADER-DG method (Arbitrary high-order DERivative Discontinuous Galerkin, for details see Section 3.3) makes a significant exception. We do not include possible ADER-DG of higher order because so far they have been developed for tetrahedral grids, and the higher order in time would have no comparison among the other schemes.

Given the variety of methods, grids, approximation orders and integrations in elements, we have to introduce easy-to-follow acronyms to be used throughout the paper.

An acronym of each investigated scheme starts with two letters indicating a method. FD stands for the finite-difference method. Similarly, FE, DG or SE indicate the finite-element, discontinuous-Galerkin or spectral-element method, respectively.

The FD schemes differ from each other by the equation formulation, grid and order of approximation. D indicates the displacement formulation, DS the displacement-stress formulation. CG indicates conventional grid, PSG partly-staggered grid, and SG staggered grid. 2 or 4 indicates the second- or fourth-order approximation in space. The lower-case 'a' or 'b' indicates one of two variants of the fourth-order approximation. The acronyms of the six considered schemes are FD D CG 2, FD DS PSG 2, FD DS SG 2, FD D CG 4a, FD D CG 4b and FD DS SG 4.

All three of the FE schemes considered solve the weak-form of the equation of motion on the mesh of uniform cubic elements and are second-order accurate in space. The schemes differ in the integration applied within an element. Consequently, the method indicator is followed by the indicator of the integration. L8, G1 or G8 indicates Lobatto 8-point, Gauss 1-point or Gauss 8-point integration, respectively. The acronyms of the three considered schemes are FE L8, FE G1 and FE G8.

In the case of the DG schemes, we explicitly indicate the polynomial degree of the basis functions, P0 or P1, and the centred flux, CF, to clearly distinguish the schemes from a large variety of possible DG schemes. The acronyms are DG P0 CF and DG P1 CF.

The order of approximation is explicitly indicated for two SE schemes. Indicators cn and vn then distinguish the central node and vertex node. The acronyms are SE 4 cn and SE 4 vn.

The acronyms and essential characteristics of all 13 considered numerical schemes are given in Fig. 2.

3.1 The finite-difference schemes

Reviews of the FD schemes on the conventional, partly-staggered and staggered grids, including original references, can be found, for example, in extensive texts by Moczo *et al*. (2007a,b).

3.1.1 FD D CG 2, FD D CG 4a, FD D CG 4b

FD D CG 2, the second-order FD scheme solving the strong-form equation of motion for displacement on the conventional grid, is obtained if derivatives in eqs (5) are replaced using standard second-order centred FD formulae approximating second non-mixed and mixed derivatives.

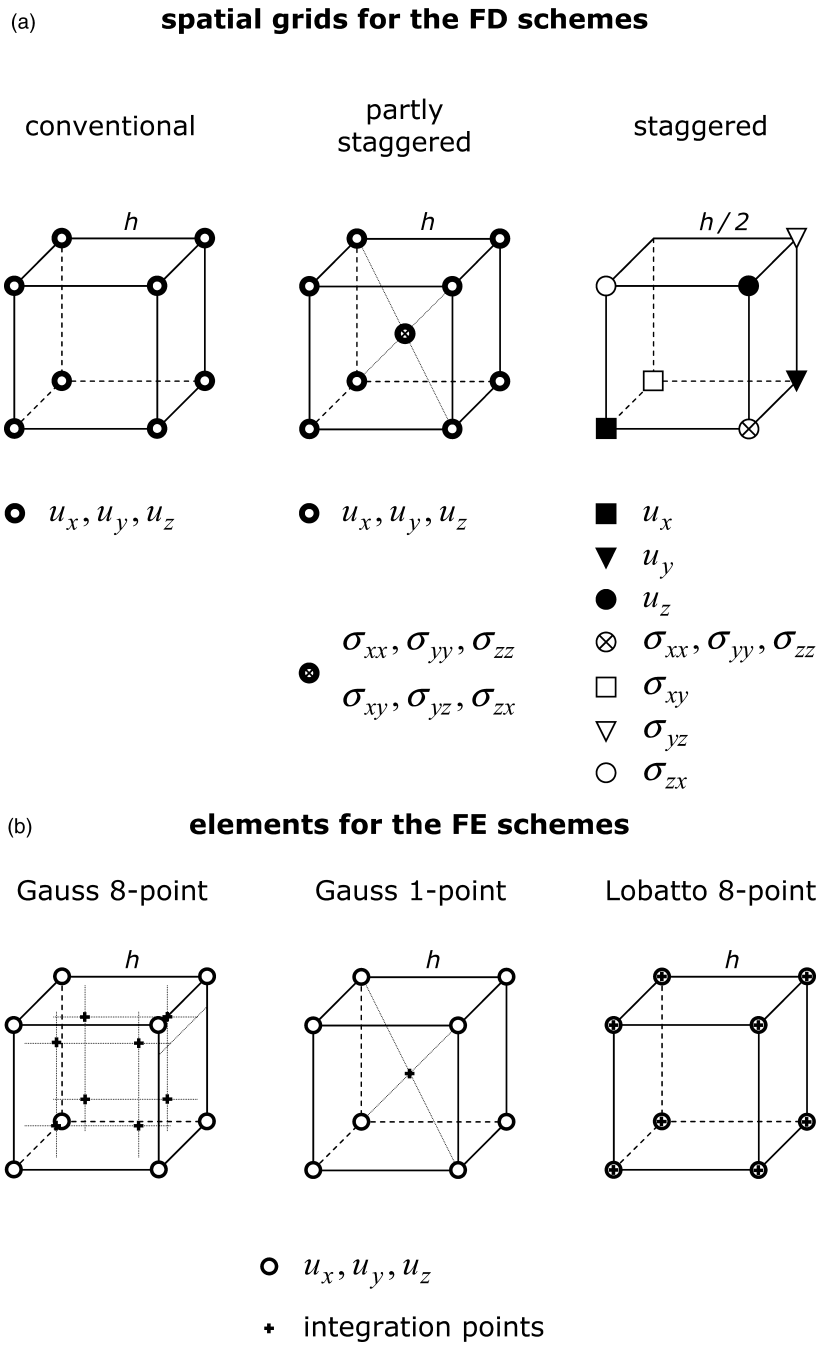

Figure 1. (a) Spatial grids for the FD schemes considered in this study. Left-hand panel: conventional grid-–all displacement components are located at each grid point (position). Centre panel: partly-staggered grid—all displacement components share the same grid points whereas all stress-tensor components share other grid points. Right-hand panel: staggered grid—each of the quantities has its own grid position except the normal stress-tensor components sharing one grid position. (b) The cubic element used for the FE schemes. The nodal points are represented by empty circles. The integration points used in the Gauss 8-point, Gauss 1-point and Lobatto 8-point integrations are represented by crosses. The integration points in the Gauss 8-point integration define vertices of a centred cube with the edge equal to $2h/\sqrt{3}$. The positions of the other integration points are obvious. (c) The cubic element used for the SE schemes. The nodal points are also the integration points. The vertex and central nodes are explicitly indicated by empty circles. For the positions of the nodal points we refer to Chaljub *et al*. (2007).

On the conventional grid, we can find several fourth-order approximations to the second non-mixed and mixed spatial derivatives. Therefore, we include two different approximations to the second non-mixed and mixed spatial derivatives and, thus, two different schemes. Based on the indication found by Moczo *et al*. (2010b), we constructed one scheme with the minimum possible equal coefficients of the leading terms of the truncation errors for the mixed and non-mixed derivatives—FD D CG 4a. The other scheme, FD D CG 4b, has the minimum possible spatial stencil and a relatively large difference between values of coefficients of the leading terms of the truncation errors.

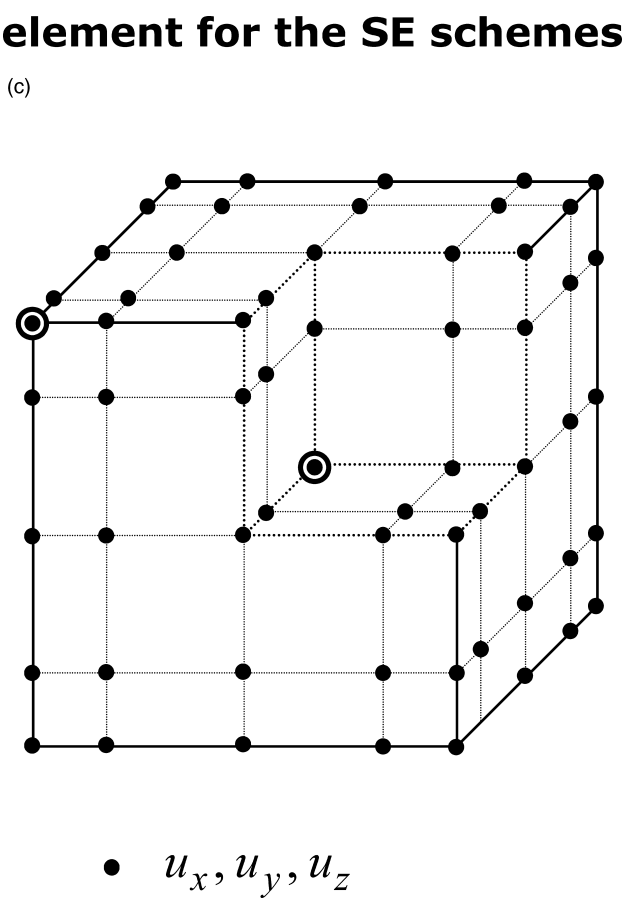

Figure 1. (*Continued.*)

3.1.2 FD DS SG 2, FD DS SG 4

FD DS SG 2 is obtained in the following way: The second time derivatives in eqs (2) are replaced using the standard second-order centred FD formula approximating the second derivative. The first spatial derivatives of the stress-tensor components in eqs (2) are replaced using the standard second-order centred FD formula approximating the first derivative. Then, all discrete stress-tensor components on the right-hand side (r.h.s.) of the obtained schemes are replaced by their FD approximations. The approximations are obtained from eqs (3), in which the first derivatives are replaced using the standard second-order centred FD formula approximating the first derivative. In the resulting final scheme only displacement components appear. This is important to note, given the fact that the scheme solves the DS formulation of the equation of motion on the staggered grid. Note that this type of scheme is also called the parsimonious scheme.

FD DS SG 4 is obtained in the same way except that fourth-order FD approximations are used to replace the first spatial derivatives of the stress-tensor and displacement components.

3.1.3 FD DS PSG 2

For comparison with FD D CG 2 and FD DS SG 2, we also include the second-order scheme solving the DS formulation of the equation of motion on the partly-staggered grid. The scheme is obtained in the same way as FD S SG 2 except that the FD approximations are more complicated. The complication is due to the fact that the stress-tensor components are displaced from the displacement components by a half-grid spacing in all three Cartesian directions (see Fig. 1). For example, in approximating the x-derivative of the stress-tensor component at a grid position of the displacement component, the required values of the stress-tensor components are obtained as arithmetic averages of the values at four stress-tensor component grid positions in the corresponding yz-grid planes.

We do not include the velocity–stress (VS) staggered grid schemes. They differ from the FD DS SG schemes only in approximating time derivatives. They approximate second spatial derivatives of the particle-velocity components (in the resulting final schemes) in the same way as the FD DS SG schemes approximate the second spatial derivatives of the displacement components. Moczo *et al*. (2010b) showed that the difference between the behaviours of the corresponding 2-D schemes with respect to the V_P/V_S ratio due to different time derivatives is negligible. Conclusions for the FD VS SG schemes related to the approximations to the spatial derivatives are the same as those for the FD DS SG schemes.

3D numerical schemes					
method		equation formulation	grid	add. specif.	order
FD D CG 2	finite-difference	displacement	conventional		2
FD DS PSG 2		displacement-stress	partly-staggered		
FD DS SG 2		displacement-stress	staggered		
FE L8	finite-element	displacement	conventional	Lobatto 8-point integr.	
FE G1				Gauss 1-point integr.	
FE G8				Gauss 8-point integr.	
DG P0 CF	discontinuous-Galerkin	displacement	conventional	polynomial order zero, centred flux	
DG P1 CF				polynomial order one, centred flux	
FD D CG 4a	finite-difference	displacement	conventional		4
FD D CG 4b					
FD DS SG 4		displacement-stress	staggered		
SE 4 cn, vn	spectral-element	displacement	conventional	GLL integr.	

Figure 2. Acronyms and essential characteristics of the investigated numerical schemes. Although the FE, DG and SE schemes are constructed on the uniform mesh of cubic elements, we use the term conventional grid also for these schemes because, effectively, all displacement components are located at each node, and stress-tensor components are not explicitly treated. 'order' in the rightmost column means the order of approximation in space.

3.2 The finite-element schemes

Detailed expositions of the FE method can be found, for example, in books by Zienkiewicz & Taylor (1989), Ottosen & Petersson (1992), Hughes (2000), Belytschko *et al*. (2000) and Reddy (2006). For the FE modelling of seismic wave propagation see, for example, Bielak *et al*. (2003), Ma & Liu (2006), Moczo *et al*. (2007a) and Galis *et al*. (2008).

We consider a uniform mesh of cubic elements with eight nodes in vertices and with tri-linear basis functions. Given this, we can get different final FE schemes by considering different volume integrations within an element. The standard full Gauss 8-point integration leads to scheme FE G8. Because the mesh is uniform and medium is homogeneous, the integration is exact. The reduced 8-point Lobatto integration leads to scheme FE L8. Eventually, the application of the simplest possible reduced 1-point Gauss integration leads to scheme FE G1. All the three situations are illustrated in Fig. 1(b).

In the case of the homogeneous medium, uniform FD grids with cubic cells, and mesh of cubic elements, the FE L8 scheme is exactly the same as FD D CG 2, and FE G1 is exactly the same as FD DS PSG 2. Because these are important equalities, we highlight them (for reader's convenience) in the explicit symbolic equations

$$\begin{aligned} &\text{FE L8} = \text{FD D} \quad \text{CG 2} \\ &\text{FE G1} = \text{FD DS PSG 2}. \end{aligned} \tag{7}$$

3.3 The discontinuous-Galerkin scheme

The DG method (e.g. Hesthaven & Warburton 2008) is a discontinuous FE method. Contrary to the classical FE method, no continuity of the basis functions is imposed between elements. Instead, the concept of a numerical flux, taken from the framework of the finite-volume (FV) method (LeVeque 2002) is used for exchanging quantities (e.g. displacements) between elements. Therefore, the DG method supports discontinuities in the seismic wavefield, and provides interesting features for dynamic rupture modelling or wave propagation modelling when high contrasts of the medium properties have to be considered. The DG method has been applied to seismology rather recently (Dumbser &

Käser 2006; Käser & Dumbser 2006; Dumbser *et al*. 2007; Käser *et al*. 2007, 2008; de la Puente *et al*. 2007, 2008; De Basabe *et al*. 2008; de la Puente 2008; Delcourte *et al*. 2009). A wide range of the DG schemes can be obtained depending on the choice of the basis functions (modal or nodal basis functions), the type of flux (upwind or centred flux) or the numerical scheme used for the time integration. Here, we consider a nodal DG scheme with the centred flux (Etienne *et al*. 2010) and we restrict to two of the simplest formulations. The first scheme, DG P0 CF (P0 indicating the zero polynomial of the basis functions, CF centred flux), assumes a uniform representation of wavefields inside the elements (only one constant basis function is used). The second scheme, DG P1 CF, assumes a linear representation of the wavefields inside the elements (via tri-linear basis functions and 8-point Gauss integration). For the homogeneous medium, uniform mesh of cubic elements and the second-order time integration we have the following identities:

$$\begin{aligned}&\text{DG P0 CF} = \text{FV P0 CF} = \text{FE L8} = \text{FD D CG 2}\\ &\text{DG P1 CF} = \text{FE G8}.\end{aligned} \tag{8}$$

Note that in the case of the homogeneous medium, the numerical flux mimics the continuities of quantities and thus leads to direct relation to the classical FE schemes. We may also explicitly emphasize the equivalence of DG P0 CF and FV P0 CF.

3.4 The spectral-element schemes

The power of the SE method to numerically model seismic wave propagation is now well evident from many applications and publications. For details on the method, we refer to the original papers by Komatitsch & Vilotte (1998) and Komatitsch & Tromp (1999) as well as to the comprehensive reviews by Komatitsch *et al*. (2005) and Chaljub *et al*. (2007).

The SE method is a special kind of the FE method that relies on the use of a high-order polynomial basis function. Although in the other investigated schemes, one and the same formula is applied to update a displacement-vector component at all grid positions, in the SE scheme it is necessary to distinguish different schemes for different nodes even in the cubic element. In this paper, we restrict to two representative nodes—the vertex node and the central node. Consequently, we distinguish two schemes—SE 4 cn for the central node and SE 4 vn for the vertex node. The element with the central and vertex nodes is illustrated in Fig. 1(c).

We may also mention the choice of the fourth order. The spectral element calculations in elastodynamics use polynomial orders between 3 and 8. This range of values allows benefiting from the low level of numerical dispersion of the spectral methods (De Basabe & Sen 2007; Seriani & Oliveira 2008) while preventing the use of too severe CFL constraints (due to the quadratic stretching of the grid points near the element edges). The fourth order is, therefore, among the best choices in terms of accuracy and computational costs.

3.5 Unified representation of the numerical schemes

All 13 numerical schemes can be represented in a unified form. Define the V_P/V_S ratio r:

$$r = \alpha/\beta. \tag{9}$$

Throughout the text, r and V_P/V_S, α and V_P, and β and V_S will be used interchangeably. Let h be a grid spacing in each of the three Cartesian directions and Δt be a time step. Let $U_\xi^m = U_\xi^m(I,K,L)$ be a discrete approximation to $u_\xi(Ih, Kh, Lh, m\Delta t) = u_\xi(x_I, y_K, z_L, t_m)$; $\xi \in \{x, y, z\}$. Each numerical scheme can be then written as (compare with eqs (5))

$$\begin{aligned}
U_x^{m+1} &= 2\,U_x^m - U_x^{m-1}\\
&\quad + (\Delta t)^2\,\beta^2\,\{\, r^2\left(D_{xx}\left[U_x^m\right] + D_{yx}\left[U_y^m\right] + D_{zx}\left[U_z^m\right]\right)\\
&\qquad + D_{yy}\left[U_x^m\right] - D_{yx}\left[U_y^m\right] + D_{zz}\left[U_x^m\right] - D_{zx}\left[U_z^m\right]\}\\
U_y^{m+1} &= 2\,U_y^m - U_y^{m-1}\\
&\quad + (\Delta t)^2\,\beta^2\,\{\, r^2\left(D_{yy}\left[U_y^m\right] + D_{zy}\left[U_z^m\right] + D_{xy}\left[U_x^m\right]\right)\\
&\qquad + D_{zz}\left[U_y^m\right] - D_{zy}\left[U_z^m\right] + D_{xx}\left[U_y^m\right] - D_{xy}\left[U_x^m\right]\}\\
U_z^{m+1} &= 2\,U_z^m - U_z^{m-1}\\
&\quad + (\Delta t)^2\,\beta^2\,\{\, r^2\left(D_{zz}\left[U_z^m\right] + D_{xz}\left[U_x^m\right] + D_{yz}\left[U_y^m\right]\right)\\
&\qquad + D_{xx}\left[U_z^m\right] - D_{xz}\left[U_x^m\right] + D_{yy}\left[U_z^m\right] - D_{yz}\left[U_y^m\right]\}\,.
\end{aligned} \tag{10}$$

The numerical schemes differ from each other by the difference operators $D_{\xi\xi}$ and $D_{\xi\eta}$; $\xi, \eta \in \{x, y, z\}$ for approximating second non-mixed and mixed spatial derivatives. Here, we explicitly present D_{xx} and D_{zx} operators. The other operators can be easily obtained by the even permutation of the Cartesian indices.

In the set of the considered 13 numerical schemes, we can recognize two types of non-mixed operators. The first type can be expressed as

$$D_{xx}\,[\Psi(I,K,L)] = \frac{1}{h^2}\sum_{j=0}^{J} w_j^{xx}\,\left[\Psi\left(I-\Delta_j, K, L\right) + \Psi\left(I+\Delta_j, K, L\right)\right]. \tag{11}$$

Table 1. Grid positions for the D_{xx} operators defined by eq. (11).

D_{xx}^{scheme}	Δ_j				
	$j=0$	$j=1$	$j=2$	$j=3$	$j=4$
$D_{xx}^{\text{FD D CG 2}}$					
$D_{xx}^{\text{FE L8}}$	0	1			
$D_{xx}^{\text{DG P0 CF}}$					
$D_{xx}^{\text{FD DS SG 2}}$	0	1			
$D_{xx}^{\text{FD D CG 4}a}$	0	1	2	3	
$D_{xx}^{\text{FD D CG 4b}}$	0	1	2		
$D_{xx}^{\text{FD DS SG 4}}$	0	1	2	3	
$D_{xx}^{\text{SE 4 cn}}$	0	$\sqrt{12/7}$	2		
$D_{xx}^{\text{SE 4 vn}}$	0	$2-\sqrt{12/7}$	2	$2+\sqrt{12/7}$	4

Table 2. Weight coefficients for the D_{xx} operators defined by eq. (11).

D_{xx}^{scheme}	$576\, w_j^{xx}$				
	$j=0$	$j=1$	$j=2$	$j=3$	$j=4$
$D_{xx}^{\text{FD D CG 2}}$					
$D_{xx}^{\text{FE L8}}$	−576	576			
$D_{xx}^{\text{DG P0 CF}}$					
$D_{xx}^{\text{FD DS SG 2}}$	−576	576			
$D_{xx}^{\text{FD D CG 4}a}$	−400	288	144	−32	
$D_{xx}^{\text{FD D CG 4b}}$	−720	768	−48		
$D_{xx}^{\text{FD DS SG 4}}$	−730	783	−54	1	
$D_{xx}^{\text{SE 4 cn}}$	−480	588	−108		
$D_{xx}^{\text{SE 4 vn}}$	−2520	$294(5+\sqrt{21})$	−384	$294(5-\sqrt{21})$	–36

Here Ψ represents a displacement component. According to eq. (11), operators of different schemes may differ from each other by the number of the grid positions at which displacement components are used for the approximation and the weight coefficients of the considered displacement component at those grid positions. The grid positions and weight coefficients are given in Tables 1 and 2, respectively.

The second type can be expressed as

$$D_{xx}\,[\Psi(I,K,L)] = \frac{1}{h^2}\sum_{l=L-1}^{L+1}\sum_{k=K-1}^{K+1} \alpha^{xx}_{l-L+2,\,k-K+2}\; D_{xx}^{\text{FD D CG 2}}\;\Psi(I,k,l). \tag{12}$$

The weight coefficients are given in Table 3.

Note that the grid spacing h represents the average spacing between the nodes in the SE schemes. We may emphasize that we consider the exact SEM schemes with no assumption of the regular grid spacing. The average grid spacing h is introduced just to make it possible to directly compare the SE schemes with the other schemes in terms of the spatial sampling ratio. The average grid spacing thus only means how many grid points of the SEM element are used to sample the S wavelength.

Similarly, we can recognize two types of the mixed operators. The first type can be expressed as

$$\begin{aligned} D_{zx}\,[\Psi(I,K,L)] = \frac{1}{h^2}\sum_{n=1}^{N}\sum_{j=1}^{N} w^{zx}_{nj}\,[\;&\Psi(I+\Delta_j,K,L+\Delta_n)-\Psi(I+\Delta_j,K,L-\Delta_n)\\ &-\Psi(I-\Delta_j,K,L+\Delta_n)+\Psi(I-\Delta_j,K,L-\Delta_n)\;]. \end{aligned} \tag{13}$$

The grid positions and weight coefficients are given in Tables 4 and 5, respectively.

The second type can be expressed as

$$D_{zx}\,[\Psi(I,K,L)] = \frac{1}{h^2}\sum_{k=K-1}^{K+1} \alpha^{zx}_{k-K+2}\; D_{zx}^{\text{FD D CG 2}}\;\Psi(I,k,L). \tag{14}$$

The weight coefficients are given in Table 6.

3.6 Truncation errors of the discrete spatial operators

The truncation error, the difference between the discrete approximation to a derivative and the exact derivative, is an important characteristic of accuracy of the discrete approximation. The lowest power of the argument increment (here, the grid spacing h) determines the order of

Table 3. Weight coefficients for the D_{xx} operators defined by eq. (12).

D_{xx}^{scheme}	α^{xx}
$D_{xx}^{\text{FD DS PSG 2}}$ $D_{xx}^{\text{FE G1}}$	$\frac{1}{16}\begin{bmatrix}1&2&1\\2&4&2\\1&2&1\end{bmatrix}$
$D_{xx}^{\text{FE G8}}$ $D_{xx}^{\text{DG P1 CF}}$	$\frac{1}{36}\begin{bmatrix}1&4&1\\4&16&4\\1&4&1\end{bmatrix}$

Table 4. Grid positions for the D_{zx} operators defined by eq. (13).

D_{zx}^{scheme}	$\Delta_j,\ \Delta_n$			
	$j,n=1$	$j,n=2$	$j,n=3$	$j,n=4$
$D_{zx}^{\text{FD D CG 2}}$				
$D_{zx}^{\text{FE L8}}$	1			
$D_{zx}^{\text{DG P0 CF}}$				
$D_{zx}^{\text{FD DS SG 2}}$	1/2			
$D_{zx}^{\text{FD D CG 4}a}$	1	2		
$D_{zx}^{\text{FD D CG 4b}}$	1	2		
$D_{zx}^{\text{FD DS SG 4}}$	1/2	3/2		
$D_{zx}^{\text{SE 4 cn}}$	$\sqrt{12/7}$	2		
$D_{zx}^{\text{SE 4 vn}}$	$2-\sqrt{12/7}$	2	$2+\sqrt{12/7}$	4

accuracy of the discrete approximation. The coefficients of terms in the truncation error are also important. Table (A1) of the Appendix gives the leading and first higher terms of the truncation errors of all operators defined by eqs (11)–(14). We will discuss the truncation errors in the analysis and interpretation of the numerical results.

4 LOCAL ERROR OF THE NUMERICAL SCHEMES

4.1 Concept of the local error

To evaluate accuracy of the numerical schemes, we define a local error of a numerical scheme. First, we can symbolically express all schemes in a unified form

$$U_{\xi}^{m+1}(I,K,L) = \textit{numerical\_scheme}\ \{U^{m-1},\ U^{m}\}, \tag{15}$$

or, equivalently,

$$U_{\xi}(I,K,L,\ t+\Delta t) = \textit{numerical\_scheme}\ \{U(t-\Delta t),\ U(t)\}. \tag{16}$$

Here, $\xi \in \{x,y,z\}$ and $U(t-\Delta t)$ and $U(t)$ represent displacement components at relevant grid positions around (I,K,L) at times $t-\Delta t$ and t, respectively. Define a numerical solution in one time step as

$$U_{\xi}^{\mathrm{N}}(I,K,L,\ t+\Delta t) = \textit{numerical\_scheme}\ \{U^{\mathrm{E}}(t-\Delta t),\ U^{\mathrm{E}}(t)\}, \tag{17}$$

where the upper index N indicates the numerical solution and the upper index E indicates an exact value. Thus, if we know the exact value of displacement at any time, we can define and calculate a relative local error in amplitude as

$$\varepsilon_{\text{ampl}}^{\text{Rel}} = \left(\frac{\Delta t_{\text{ref}}}{\Delta t}\right)^2 \left|\frac{A^{\mathrm{N}}-A^{\mathrm{E}}}{A^{\mathrm{E}}}\right|. \tag{18}$$

Here, A^{N} is the amplitude of the numerical solution (modulus of the displacement vector) in one time step and A^{E} is the exact amplitude—both evaluated at time $t+\Delta t$. Because different numerical schemes use different time steps Δt, we have to normalize the error for a unit time. Because the time derivative is approximated by the second-order FD formula, we have to normalize with the square of Δt. The division of the relative error by $(\Delta t)^2$, however, artificially increases the value of the error. This can be compensated, for example, by multiplication by some time step value taken as a reference. We specify this later.

In their analysis of the 2-D second-order FD and FE schemes, Moczo *et al*. (2010b) also defined the relative error in the direction of the displacement vector (or error in polarization or angle). The 3-D problem involves three displacement-vector components and two angles. This considerably complicates the quantification of the polarization error and direct comparison of their values with the values of the error

Table 5. Weight coefficients for the D_{zx} operators defined by eq. (13).

D_{zx}^{scheme}	w^{zx}
$D_{zx}^{\text{FD D CG 2}}$	
$D_{zx}^{\text{FE L8}}$	$\frac{1}{4}$
$D_{zx}^{\text{DG P0 CF}}$	
$D_{zx}^{\text{FD DS SG 2}}$	1
$D_{zx}^{\text{FD D CG 4}a}$	$\frac{1}{576}\begin{bmatrix} 256 & -32 \\ -32 & 4 \end{bmatrix}$
$D_{zx}^{\text{FD D CG 4b}}$	$\frac{1}{576}\begin{bmatrix} 240 & -24 \\ -24 & 0 \end{bmatrix}$
$D_{zx}^{\text{FD DS SG 4}}$	$\frac{1}{576}\begin{bmatrix} 729 & -27 \\ -27 & 1 \end{bmatrix}$
$D_{zx}^{\text{SE 4 cn}}$	$\frac{1}{768}\begin{bmatrix} 343 & -21\sqrt{21} \\ -21\sqrt{21} & 27 \end{bmatrix}$
$D_{zx}^{\text{SE 4 vn}}$	$\frac{1}{1152}\begin{bmatrix} 343(5+\sqrt{21}) & -112(7+\sqrt{21}) & 686 & -21(7+\sqrt{21}) \\ -112(7+\sqrt{21}) & 512 & -112(7-\sqrt{21}) & 96 \\ 686 & -112(7-\sqrt{21}) & 343(5-\sqrt{21}) & -21(7-\sqrt{21}) \\ -21(7+\sqrt{21}) & 96 & -21(7-\sqrt{21}) & 18 \end{bmatrix}$

Table 6. Weight coefficients for the D_{zx} operators defined by eq. (14).

D_{zx}^{scheme}	α^{zx}
$D_{zx}^{\text{FD DS PSG 2}}$ $D_{zx}^{\text{FE G1}}$	$\frac{1}{4}[\,1 \quad 2 \quad 1\,]$
$D_{zx}^{\text{FE G8}}$ $D_{zx}^{\text{DG P1 CF}}$	$\frac{1}{6}[\,1 \quad 4 \quad 1\,]$

in amplitude. Therefore, instead of defining errors analogous to the error used by Moczo *et al*. (2010b), we define the error in the vector difference as

$$\varepsilon_{\text{vdiff}}^{\text{Rel}} = \left(\frac{\Delta t_{ref}}{\Delta t}\right)^2 \frac{1}{A^{\text{E}}}\left[\left(U_x^{\text{N}} - U_x^{\text{E}}\right)^2 + \left(U_y^{\text{N}} - U_y^{\text{E}}\right)^2 + \left(U_z^{\text{N}} - U_z^{\text{E}}\right)^2\right]^{1/2}. \tag{19}$$

This absolute value of the vector difference between the numerically calculated displacement vector and the exact displacement vector comprises both errors in amplitude and polarization in one reasonable value. This value can be directly compared with the error in amplitude.

4.2 Note on the local error and grid dispersion

It is clear that the local error in amplitude, as defined by eq. (18), quantifies, how the exact amplitude changes in one time step due to inaccuracy of a numerical scheme.

In an analysis of stability the problem is different: one investigates condition for propagation of a harmonic plane wave by a numerical scheme in a discrete grid in a stable manner. For example, Moczo *et al*. (2000) investigated condition for propagation of a plane harmonic wave with a constant amplitude by the fourth-order DS staggered grid FD scheme. They obtained the standard stability condition and the grid-dispersion relation. The price for propagating the harmonic plane wave with the constant amplitude in a discrete grid is a grid velocity that differs from the true velocity, and the difference depends on the size of the grid spacing.

4.3 The exact solution–-a harmonic plane *S* wave in an unbounded homogeneous medium

It is reasonable to consider a harmonic plane S wave propagating in an unbounded homogeneous elastic isotropic medium as the exact solution in definitions of the local errors. We will consider a harmonic plane S wave polarized in a vertical plane determined by the z-axis and wavenumber vector $\vec{k}$. The displacement components are

$$u_\xi\,(x, y, z, t\,;\omega\,;\varphi, \delta) = A_\xi E^t E^x E^y E^z\,; \quad \xi \in \{x, y, z\}\,, \tag{20}$$

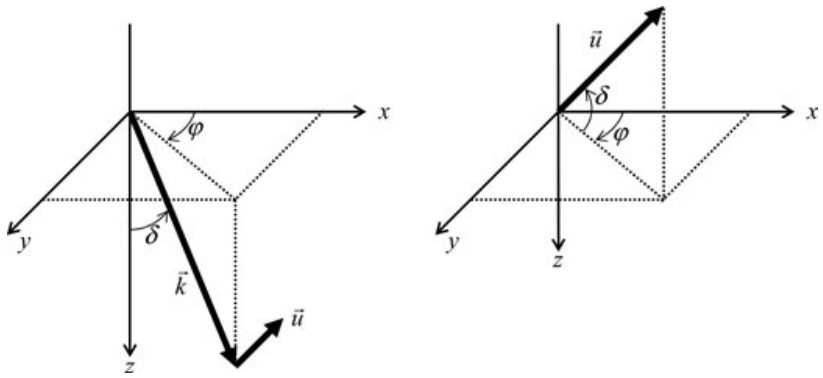

Figure 3. Cartesian coordinate system, angles φ and δ for defining a direction of propagation, displacement vector and displacement components of the plane *S* wave.

where

$$E^t = \exp[-i\omega t]$$

$$E^x = \exp[ik_x x] \qquad E^y = \exp[ik_y y] \qquad E^z = \exp[ik_z z]$$

$$k_x = k\cos\varphi\sin\delta \qquad k_y = k\sin\varphi\sin\delta \qquad k_z = k\cos\delta$$

$$A_x = A\cos\varphi\cos\delta \qquad A_y = A\sin\varphi\cos\delta \qquad A_z = -A\sin\delta$$

$$k = \omega/\beta\,, \quad 0 \le \delta \le \pi\,, \quad 0 \le \varphi \le 2\pi, \tag{21}$$

ω is the angular frequency, $k = |\vec{k}|$ is the wavenumber, δ is the angle between the positive z-axis and the wavenumber vector $\vec{k}$ (the direction of propagation), φ is the angle between the positive x-axis and the vertical plane determined by the z-axis and wavenumber vector $\vec{k}$ (Fig. 3). Note that i in the arguments of the exponential function denotes the imaginary unit throughout the entire text. Otherwise, i will be used to indicate a Cartesian component of the displacement vector or spatial coordinate.

It is known from the numerical experience that modelling of the *P* wave poses a minor problem compared to the modelling of the *S* wave if the modelling comprises both waves. Later, we explain why it is so.

4.4 Evaluation of the exact and numerical values of displacement in a grid

Let h and λ be the grid spacing and wavelength, respectively. The spatial sampling ratio s is defined as

$$s = h/\lambda. \tag{22}$$

Then

$$k = \omega/\beta = 2\pi s/h, \tag{23}$$

$$k_x h = 2\pi s\cos\varphi\sin\delta\,, \quad k_y h = 2\pi s\sin\varphi\sin\delta\,, \quad k_z h = 2\pi s\cos\delta, \tag{24}$$

$$\omega = 2\pi s\beta/h. \tag{25}$$

Considering the stability condition for any of the numerical schemes in the form

$$\Delta t \le \Phi(h, \alpha, \beta) \tag{26}$$

and the stability ratio p

$$p = \Delta t/\Phi\,, \quad p \le 1, \tag{27}$$

the time step can be expressed as

$$\Delta t = p\,\Phi(h, \alpha, \beta)\,. \tag{28}$$

(Note that the stability parameter sometimes is defined as $p = \Delta t\,\alpha/h$.)

Without loss of generality, consider for simplicity

$$x_I = 0\,, \quad y_K = 0\,, \quad z_L = 0\,, \quad t_m = 0. \tag{29}$$

Then the errors are evaluated at

$$x_I = 0\,, \quad y_K = 0\,, \quad z_L = 0\,, \quad t_{m+1} = \Delta t. \tag{30}$$

The real exact displacement at this space–time grid position is [see eqs (20) and (21)]

$$\mathrm{Re}\left\{u_\xi(0, 0, 0, \Delta t)\right\} = A_\xi\cos\omega\Delta t \tag{31}$$

Table 7. Quantities entering the numerical schemes and formulas for the errors.

	$\omega\,\Delta t$	$\Delta t\,\beta/h$	Δt
FD D CG 2 FE L8 DG P0 CF	$2\pi p\,s\,\dfrac{1}{(1+r^2)^{1/2}}$	$\dfrac{p}{(1+r^2)^{1/2}}$	$p\dfrac{s}{(1+r^2)^{1/2}}\dfrac{\lambda}{\beta}$
FD DS PSG 2 FE G1 FE G8 DG P1 CF	$2\pi p\,s\,\dfrac{1}{r}$	$\dfrac{p}{r}$	$p\dfrac{s}{r}\dfrac{\lambda}{\beta}$
FD DS SG 2	$2\pi\dfrac{1}{\sqrt{3}}p\,s\,\dfrac{1}{r}$	$\dfrac{1}{\sqrt{3}}p\dfrac{1}{r}$	$\dfrac{1}{\sqrt{3}}p\dfrac{s}{r}\dfrac{\lambda}{\beta}$
FD D CG 4a FD D CG 4b	$2\pi 0.7p\,s\,\dfrac{1}{(1+r^2)^{1/2}}$	$0.7\dfrac{p}{(1+r^2)^{1/2}}$	$0.7p\dfrac{s}{(1+r^2)^{1/2}}\dfrac{\lambda}{\beta}$
FD DS SG 4	$2\pi\dfrac{6}{7\sqrt{3}}p\,s\,\dfrac{1}{r}$	$\dfrac{6}{7\sqrt{3}}p\dfrac{1}{r}$	$\dfrac{6}{7\sqrt{3}}p\dfrac{s}{r}\dfrac{\lambda}{\beta}$
SE 4 cn, vn	$2\pi 0.55\left(\dfrac{1}{2}-\sqrt{\dfrac{3}{28}}\right)p\,s\,\dfrac{1}{r}$	$0.55\left(\dfrac{1}{2}-\sqrt{\dfrac{3}{28}}\right)\dfrac{p}{r}$	$0.55\left(\dfrac{1}{2}-\sqrt{\dfrac{3}{28}}\right)p\dfrac{s}{r}\dfrac{\lambda}{\beta}$

and

$$A^{\mathrm{E}}=\left[(A_x\cos\omega\,\Delta t)^2+\left(A_y\cos\omega\,\Delta t\right)^2+(A_z\cos\omega\,\Delta t)^2\right]^{1/2}=A\,|\cos\omega\,\Delta t|\,. \tag{32}$$

The exact values of (complex) displacements entering the r.h.s. of schemes (10) are evaluated as

$$\begin{aligned}
&U_\xi^{m-1}(I,K,L)\\
&\quad=u_\xi\,(0,0,0,\ t=-\Delta t\,;\omega\,;\varphi,\delta)\\
&\quad=A_\xi\exp[+i\omega\,\Delta t]\\
&U_\xi^{m}(I,K,L)\\
&\quad=u_\xi\,(0,0,0,\ t=0\,;\omega\,;\varphi,\delta)\\
&\quad=A_\xi\\
&U_\xi^{m}(I+\Delta_I,K+\Delta_K,L+\Delta_L)\\
&\quad=u_\xi\ (h\,\Delta_I,\ h\,\Delta_K,\ h\,\Delta_L,\ t=0\,;\omega\,;\varphi,\delta)\\
&\quad=A_\xi\ \exp[+ik_xh\,\Delta_I]\ \exp[+ik_yh\,\Delta_K]\ \exp[+ik_zh\,\Delta_L]\,.
\end{aligned} \tag{33}$$

The grid-index increments Δ_I, Δ_K and Δ_L depend on a numerical scheme. Quantities k_xh, k_yh and k_zh are given by eq. (24).

It is clear from schemes (10) and definitions of the difference operators (11)–(14) that each scheme effectively includes the second power of quantity $\Delta t\,\beta/h$. Quantities $\omega\,\Delta t$, $\Delta t\,\beta/h$ and Δt entering the numerical schemes and formulae for the errors are summarized in Table 7.

U_x^{m+1}, U_y^{m+1} and U_z^{m+1}, evaluated at (I,K,L), are obtained using schemes (10). Then

$$A^{\mathrm{N}}=\left(\left[\mathrm{Re}\left\{U_x^{m+1}\right\}\right]^2+\left[\mathrm{Re}\left\{U_y^{m+1}\right\}\right]^2+\left[\mathrm{Re}\left\{U_z^{m+1}\right\}\right]^2\right)^{1/2}. \tag{34}$$

In principle, we can take any of the time steps as the reference time step Δt_{ref} appearing in formulae (18) and (19) for the errors. As a reasonable choice we consider

$$\Delta t_{\mathrm{ref}}=\Delta t\quad\text{for FD DS SG 4}\,;\quad p=0.9,\ \ s=1/6,\ \ r=1.42. \tag{35}$$

The argument for the choice is: as it will be clear from the numerical calculations, scheme FD DS SG 4 is least sensitive to increasing V_P/V_S ratio r, $s=\frac{1}{6}$ is the most common choice for the spatial sampling ratio in the numerical modelling of earthquake motion in surface sedimentary basins using the fourth-order staggered-grid FD scheme, $r=1.42$ is taken in this article instead of the exact minimum value $r=\sqrt{2}$.

Note that the time steps in Table 7 include factor $\frac{s\lambda}{\beta}$. It could be replaced by $\frac{h}{\beta}$ but in both cases the time steps include explicitly the S-wave speed β in addition to the V_P/V_S ratio r. Because, however, the errors (18) and (19) include ratio $(\frac{\Delta t_{\mathrm{ref}}}{\Delta t})^2$ the explicit presence of λ and β is removed from the errors. Consequently, apart from the absolute quantities φ and δ (angles determining the direction of propagation), errors $\varepsilon^{\mathrm{Rel}}_{\mathrm{ampl}}$ and $\varepsilon^{\mathrm{Rel}}_{\mathrm{vdiff}}$ depend only on relative dimensionless quantities—the spatial sampling ratio s, stability ratio p and the V_P/V_S ratio r.

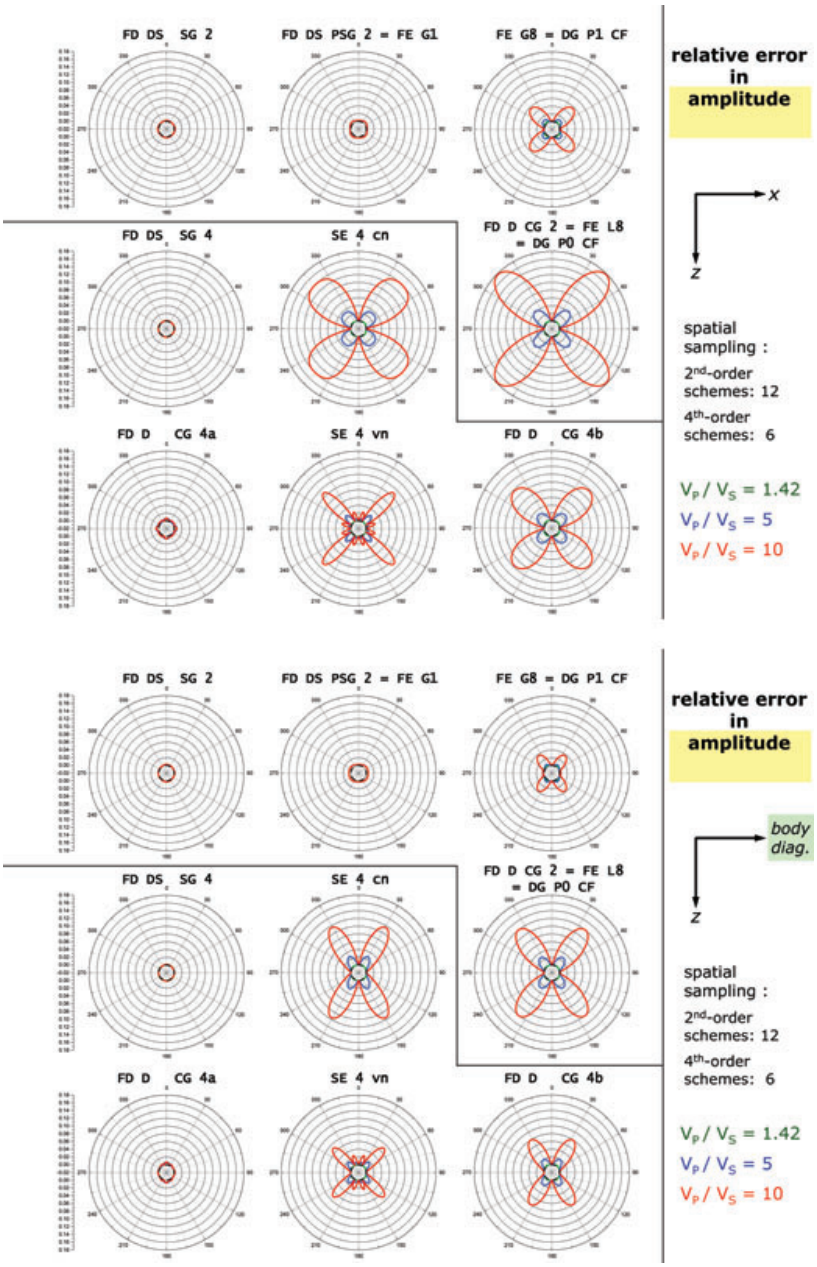

Figure 4. Relative local errors in amplitude for the plane *S* waves propagating in all directions of the *xz*-plane (angle $\varphi = 0^\circ$, top panel) and in the vertical plane of the body diagonal (angle $\varphi = 45^\circ$, bottom panel). The errors are calculated for the stability ratio $p = 0.9$, the spatial sampling ratio s corresponding to 12 and 6 grid spacings per wavelength in the second- and fourth-order schemes, respectively, and three values of the V_P/V_S ratio r: 1.42, 5 and 10. In each graph, the innermost circle (black thick solid) of the scale grid corresponds to the zero error.

5 NUMERICAL RESULTS

5.1 Relative local errors in amplitude for plane *S* waves propagating in any direction in the *xz*-plane and vertical plane of the body diagonal

Because the medium is isotropic, it is enough to look at the errors of the schemes for waves propagating in all directions in two planes—for example, the *xz*-plane and the vertical plane determined by the *z*-axis and body diagonal.

Fig. 4 shows the relative local errors in amplitude, see definition eq. (18), of all numerical schemes for the plane *S* waves as functions of direction of propagation in the *xz*-plane (angle $\varphi = 0^\circ$; top panel) and in the vertical plane of the body diagonal (angle $\varphi = 45^\circ$; bottom panel), that is for all angles δ in both planes. The errors are calculated for the stability ratio $p = 0.9$. The values of the spatial sampling ratio s correspond to 12 and 6 grid spacings per wavelength in the second- and fourth-order schemes, respectively. These spatial samplings are common in the numerical modelling of the earthquake ground motion in sedimentary basins (later, we investigate the error as a function

of s). Recall that in the SE schemes, the grid spacing h represents the average spacing between the nodes to directly compare the SE schemes with the other schemes in terms of the spatial sampling ratio.

The errors were calculated for three values of the V_P/V_S ratio r: 1.42, 5 and 10. The speed ratio $r = 1.42$ represents the minimum possible value of the V_P/V_S ratio r (the exact value being $\sqrt{2}$), $r = 5$ is a common value in surface sediments, mainly under the water level, and $r = 10$, though relatively large, certainly is not the maximum possible value in the unconsolidated surface water-saturated sediments. Practically taken, $r \geq 5$ often have to be accounted for in the numerical modelling of seismic motion in sedimentary basins and valleys.

The thin broken line separates the second- and fourth-order schemes. Within these two parts of the figure, the spatial arrangement of the schemes roughly reflects sensitivity and thus inaccuracy of the schemes with respect to the varying V_P/V_S ratio r. The least sensitive schemes are placed on the left-hand side (l.h.s.).

The figure indicates that the staggered-grid schemes FD DS SG 2 and FD DS SG 4 are both least sensitive and most accurate in the range of the considered V_P/V_S ratio values. Close to them is the partly-staggered-grid scheme FD DS PSG 2 = FE G1. The fourth-order conventional-grid scheme FD D CG 4a comes out as a surprise given the well-known poor behaviour of the most classical conventional-grid scheme FD D CG 2. An immediate notion from comparing FD D CG 4a with FD D CG 4b is that the sensitivity and accuracy with respect to the V_P/V_S ratio r is not dominantly linked to the order of the schemes. An important conclusion also comes from comparison of the three FE schemes. They differ from each other only by the integration within the element but their behaviours with respect to the varying V_P/V_S ratio r differ considerably. The two SE schemes also appear sensitive to the increasing V_P/V_S ratio r and surprisingly inaccurate for V_P/V_S equal to 5 and 10.

5.2 Relative local errors in the vector difference for plane *S* waves propagating in any direction in the *xz*-plane and vertical plane of the body diagonal

The arrangement of Fig. 5 is the same as that of Fig. 4 but Fig. 5 shows the relative errors in the vector difference, see definition eq. (19). The striking difference between Figs 4 and 5 is that for each scheme the error in the vector difference clearly depends on the V_P/V_S ratio r. This difference is the most apparent with the four schemes, FD DS SG 4, FD DS SG 2, FD DS PSG 2 = FE G1 and FD D CG 4a, which were most accurate and least sensitive to the increasing r in terms of the relative error in amplitude. Still, however, the maximum errors of FD DS SG 4 and FD DS SG 2 are smaller than the errors of the other schemes—as in the case of the relative errors in amplitude.

Recall that the relative local error in the vector difference comprises the errors in individual components and, thus, also the error in polarization (difference between the true and numerical directions of the displacement vector). This means that the difference between errors in Fig. 5 and errors in Fig. 4 is due to the polarization errors. Clearly, the polarization errors of each scheme depend on the V_P/V_S ratio r.

5.3 Equivalent spatial sampling for the errors in amplitude and the vector difference

Because the errors shown in Figs 4 and 5 were calculated for the commonly used values of the spatial sampling ratio s, they have only indicative meaning. To quantitatively compare the accuracy of the schemes with respect to varying V_P/V_S ratio r, we proceed as follows. We choose a reference maximum error as the maximum relative error in amplitude of FD DS SG 4 for $r = 10$ and $s = 1/6$. This error is equal to 0.00112. For each individual numerical scheme, we then calculate an equivalent spatial sampling ratio s_{equiv} as a function of r. The equivalent spatial sampling ratio s_{equiv} is defined as a ratio at which the maximum relative error of the scheme is equal to the reference maximum error. The maximum relative error is determined as maximum of errors calculated for angles $\varphi \in [0, 90]^\circ$ and $\delta \in [0, 90]^\circ$ with angle increment of 0.5°. We find the equivalent spatial-sampling ratio based on the relative error in amplitude and the equivalent spatial-sampling ratio based on the relative error in the vector difference.

Fig. 6(a) shows the $1/s_{\text{equiv}}(r)$ curves based on the relative error in amplitude for all the investigated schemes (recall that $1/s_{\text{equiv}}$ is equal to the number of the grid spacings per wavelength). The left-hand panel shows the curves for the stability ratio $p = 0.3$, the right-hand panel for $p = 0.9$. The solid lines are used for the fourth-order schemes, the dashed lines for the second-order schemes.

The curves for the two values of the stability ratio differ from each other only negligibly. Small differences can be seen only for the lowest values of r.

At first sight, we realize that the curves are consistent with the indicative Fig. 4. FD DS SG 4, FD D CG 4a, FD DS SG 2 and FD DS PSG 2 = FE G1 make one distinct group of schemes. The equivalent sampling ratios of these schemes only little depend on the V_P/V_S ratio r.

FD D CG 4b, SE 4 cn, SE 4 vn, FE G8 = DG P1 CF and FD D CG 2 = FE L8 = DG P0 CF make the other distinct group of schemes whose equivalent spatial sampling ratios considerably change with increasing V_P/V_S ratio r. Among the schemes of the second group, we can distinguish the subgroup of the FD D CG 4b, SE 4 cn and SE 4 vn schemes, distinct FE G8 = DG P1 CF, and, finally, the worst FD D CG 2 = FE L8 = DG P0 CF.

Fig. 6(b) shows the $1/s_{\text{equiv}}(r)$ curves based on the relative error in the vector difference. As indicated by Fig. 5 the $1/s_{\text{equiv}}$ increase with increasing r for each scheme.

Fig. 6 clearly shows that, in terms of the equivalent spatial sampling, FD DS SG 4 is more accurate and more efficient than the other schemes for media with $r > 2$.

Table 8 lists the $1/s_{\text{equiv}}$ values for $p = 0.9$ and three values of the V_P/V_S ratio r—1.42, 5 and 10.

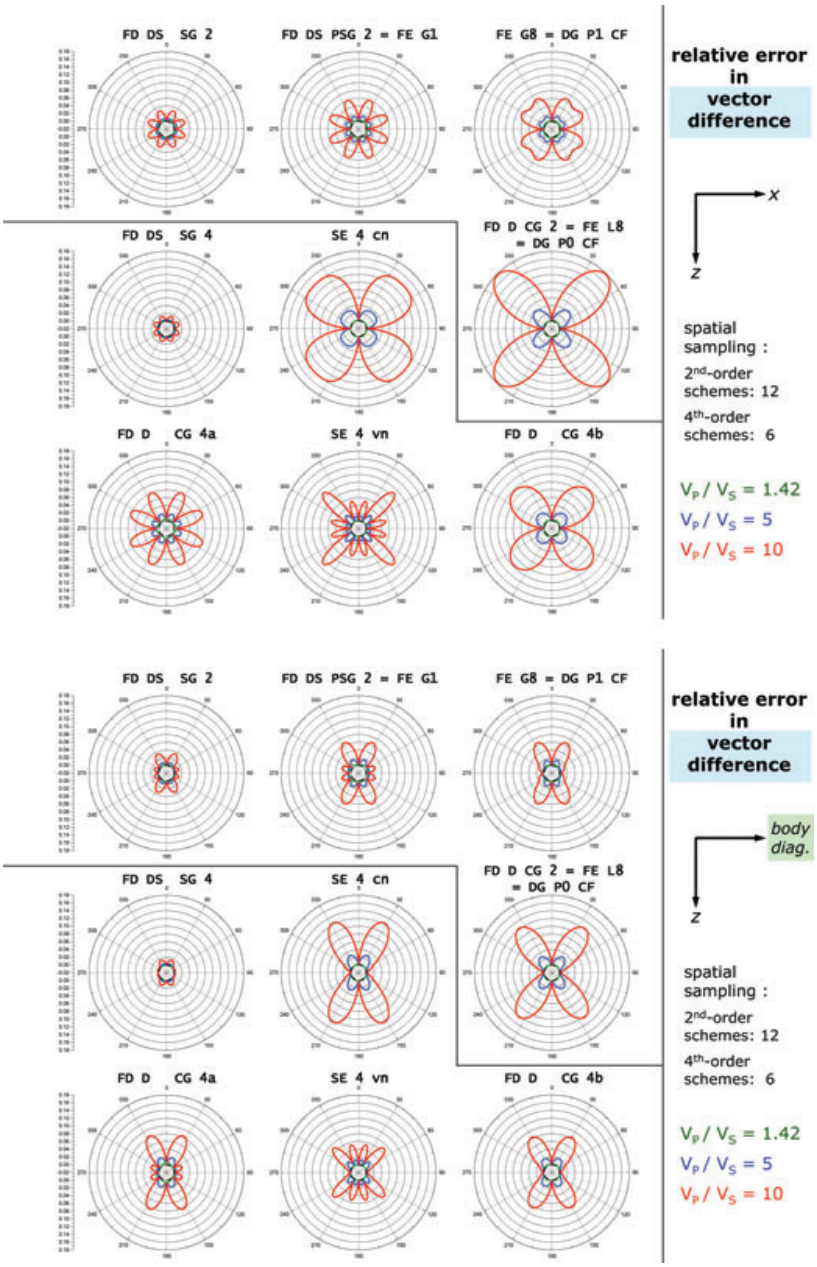

Figure 5. The same as Fig. 4 but for the errors in the vector difference.

5.4 Essential summary of the numerical results

The relative local error in amplitude of schemes FD DS SG 4, FD D CG 4a, FD DS SG 2 and FD DS PSG 2 = FE G1 is almost independent on the V_P/V_S ratio r. However, the error in the vector difference increases with increasing V_P/V_S ratio. This can be explained only by the dependence of the polarization errors of all schemes on the V_P/V_S ratio. The dependence of the error in the vector difference on the V_P/V_S ratio has to be accounted for by a proper spatial sampling.

FD D CG 2 = FE L8 = DG P0 CF is the most sensitive to increasing V_P/V_S ratio and for $V_P/V_S > 2$ requires considerably denser spatial sampling than any other scheme.

The maximum errors in the vector difference of schemes FD DS SG 2, FE G8 = DG P1 CF and FD DS PSG 2 = FE G1 increase with the increasing V_P/V_S ratio in the same way. Schemes FD DS PSG 2 = FE G1 and FE G8 = DG P1 CF require denser spatial sampling than FD DS SG 2 to achieve the same accuracy.

The maximum errors in the vector difference of all fourth-order schemes increase for $V_P/V_S > 3$ in the same way. Schemes FD D CG 4a, FD D CG 4b, SE 4 cn and SE 4 vn require denser spatial sampling than FD DS SG 4 to achieve the same accuracy.

The fourth-order schemes are for $V_P/V_S > 3$ less sensitive to increasing V_P/V_S ratio than the second-order schemes.

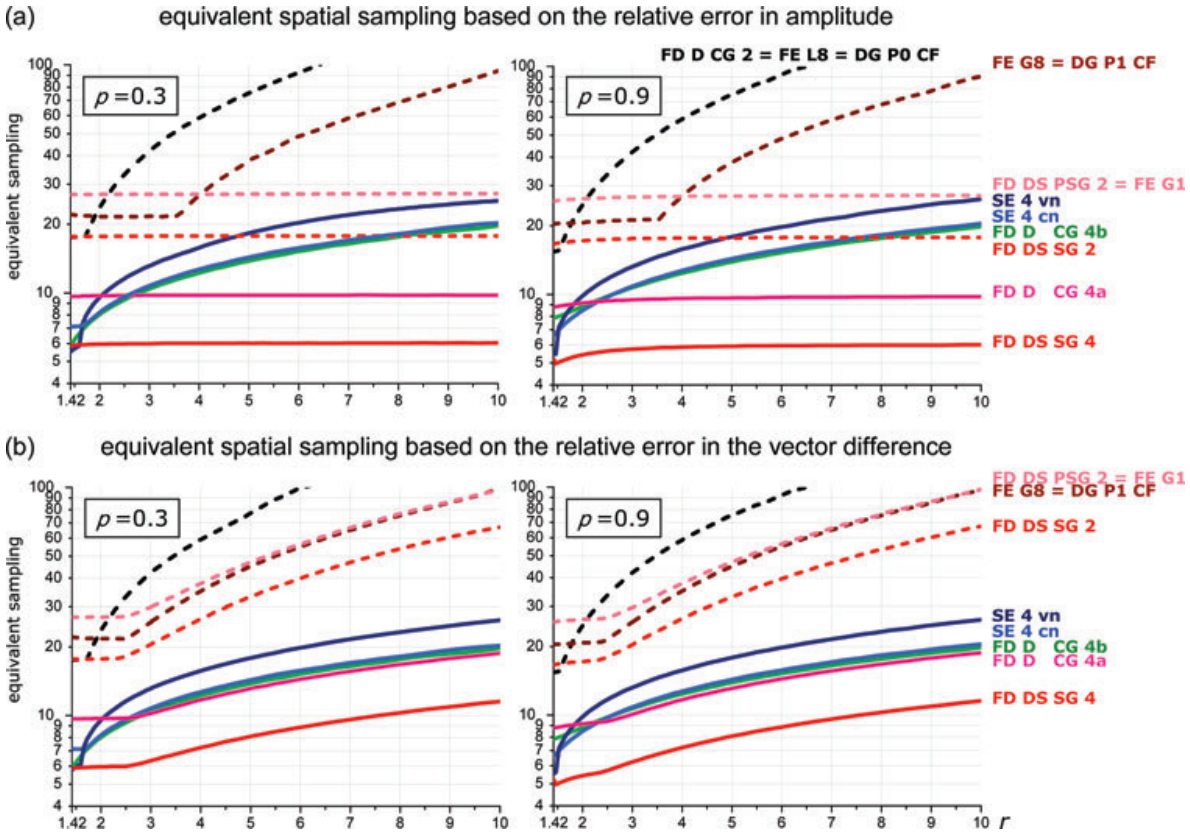

Figure 6. The $1/s_{\text{equiv}}(r)$ curves. The equivalent spatial sampling ratio s_{equiv} is defined as a ratio at which the maximum absolute value of the relative error of the scheme is equal to the reference maximum error. The chosen reference maximum error, 0.00112, is equal to the maximum relative error in amplitude of FD DS SG 4 for the V_P/V_S ratio $r = 10$ and spatial sampling ratio $s = 1/6$. The left-hand panel shows the curves for the stability ratio $p = 0.3$, the right-hand panel for $p = 0.9$.

Table 8. The $1/s_{\text{equiv}}$ values for the stability ratio $p = 0.9$ and reference maximum error equal to 0.00112. Boldface indicates schemes for which the $1/s_{\text{equiv}}$ based on the relative error in amplitude varies with the V_P/V_S ratio r only negligibly.

V_P/V_S ratio r	**FD DS SG 4**	**FD D CG 4a**	**FD DS SG 2**	FD D CG 4b	SE 4 cn	**FD DS PSG 2 = FE G1**	SE 4 vn	FE G8 = DG P1 CF	FD D CG 2 = FE L8 = DG P0 CF
				$1/s_{\text{equiv}}$ based on the relative error in amplitude					
1.42	**5.3**	**8.8**	**16.6**	7.8	6.6	**25.6**	5.5	17.7	15.4
5	**5.9**	**9.7**	**17.7**	14.0	14.4	**26.9**	18.0	38.7	75.4
10	**6.0**	**9.7**	**17.8**	19.7	20.4	**27.1**	26.2	85.3	153.5
				$1/s_{\text{equiv}}$ based on the relative error in the vector difference					
1.42	**5.3**	**8.8**	**16.6**	7.8	6.6	**25.6**	5.5	20.4	15.4
5	**8.1**	**13.1**	**33.3**	14.0	14.4	**47.5**	18.0	45.6	76.3
10	**11.5**	**18.7**	**67.3**	19.8	20.5	**97.5**	26.2	97.0	162.1

6 ANALYSIS AND INTERPRETATION OF THE NUMERICAL RESULTS

6.1 How does the equation of motion see the *S* and *P* waves?

Recall the equation of motion (5) in the concise form

$$u_{i,tt} = \alpha^2 u_{j,ji} + \beta^2 (u_{i,jj} - u_{j,ji}). \tag{36}$$

The *S* wave is solenoidal, that is, div $\vec{u} = u_{j,j} = 0$. Consequently, in the case of the *S* wave, we have

$$u_{j,ji} = 0, \quad u_{i,jj} - u_{j,ji} = \frac{1}{\beta^2} u_{i,tt}. \tag{37}$$

The P wave is irrotational, that is, $\mathrm{rot}\,\vec{u} = 0$ or $\varepsilon_{kji}\,u_{i,j} = 0$, where ε_{kji} is the Levi-Civita symbol. Consequently, in the case of the P wave it is

$$u_{j,ji} = \frac{1}{\alpha^2} u_{i,tt} \quad , \quad u_{i,jj} - u_{j,ji} = 0. \tag{38}$$

6.2 How does a numerical scheme see the S and P waves?

A numerical scheme solving equation of motion (36) can be written in the form

$$DA\{u_{i,tt}\} \approx \alpha^2 DA\{u_{j,ji}\} + \beta^2 DA\{\, u_{i,jj} - u_{j,ji}\,\}, \tag{39}$$

where DA means a discrete approximation. Eq. (39) is, in fact, a concise symbolic form of eqs (10). A discrete approximation to any operator in general can be expressed as a sum of the exact differential operator and a truncation error (for which we will use symbol TrE). Eq. (39) can be written as

$$u_{i,tt} + TrE\{u_{i,tt}\} \approx \alpha^2(\, u_{j,ji} + TrE\{u_{j,ji}\}\,) + \beta^2(\, u_{i,jj} - u_{j,ji} + TrE\{\, u_{i,jj} - u_{j,ji}\,\}\,). \tag{40}$$

6.2.1 The case of the harmonic plane S wave

Considering the first of eqs (37), equality $u^S_{i,tt} = -\omega^2 u^S_i$, and the fact that each second spatial derivative of a displacement-vector component is proportional to $-\omega^2 u^S_i/\beta^2$, eq. (40) can be rewritten as

$$\left(1 + error_i^{t\,S}\right)\left(-\omega^2 u_i^S\right) \approx \alpha^2\left(0 + error_i^{\alpha S}\right)\frac{-\omega^2 u_i^S}{\beta^2} + \beta^2\left(1 + error_i^{\beta S}\right)\frac{-\omega^2 u_i^S}{\beta^2} \tag{41}$$

and

$$u_i^S \approx \left(r^2\, error_i^{\alpha S} + 1 + error_i^{\beta S} - error_i^{t\,S}\right)\; u_i^S. \tag{42}$$

Note that the double-index summation rule does not apply to index i from eqs (41)–(57).

The error terms

$$error_i^{\alpha S} = \frac{\beta^2\; TrE\left\{u^S_{j,ji}\right\}}{-\omega^2\, u_i^S} \quad , \quad error_i^{\beta S} = \frac{\beta^2\; TrE\left\{u^S_{i,jj} - u^S_{j,ji}\right\}}{-\omega^2\, u_i^S} \tag{43}$$

do not depend on r. The error term $error_i^{t\,S}$ does depend on r

$$error_i^{t\,S} = \frac{TrE\left\{u^S_{i,tt}\right\}}{-\omega^2\, u_i^S} = c_1\frac{1}{r^2} + c_2\frac{1}{r^4} + \cdots \tag{44}$$

Coefficients c_l ; $l = 1, 2, \ldots$ do not depend on r. Note that the series in powers of $\frac{1}{r^2}$ is due to the second-order approximation to the second time derivative. The squares of the time step, $(\Delta t)^2$, are expressed using $\frac{1}{r^2}$.

6.2.2 The case of the harmonic plane P wave

Considering the second of eqs (38), equality $u^P_{i,tt} = -\omega^2 u^P_i$, and the fact that each second spatial derivative of a displacement-vector component is proportional to $-\omega^2 u^P_i/\alpha^2$, eq. (40) can be rewritten as

$$\left(1 + error_i^{t\,P}\right)\left(-\omega^2 u_i^P\right) \approx \alpha^2\left(1 + error_i^{\alpha P}\right)\frac{-\omega^2 u_i^P}{\alpha^2} + \beta^2\left(0 + error_i^{\beta P}\right)\frac{-\omega^2 u_i^P}{\alpha^2} \tag{45}$$

and

$$u_i^P \approx \left(1 + error_i^{\alpha P} + \frac{1}{r^2}\, error_i^{\beta P} - error_i^{t\,P}\right)\; u_i^P. \tag{46}$$

Analogously to the error terms in eqs (43), $error_i^{\alpha P}$ and $error_i^{\beta P}$ do not depend on r. The dependence of $error_i^{t\,P}$ on r is analogous to that of $error_i^{t\,S}$ in eq. (44).

6.2.3 Comparison

We see the important difference between eq. (42) for the S wave and eq. (46) for the P wave: In the case of the S wave, term $r^2 error_i^{\alpha S}$ increases with increasing V_P/V_S ratio r, whereas in the case of the P wave, term $\frac{1}{r^2} error_i^{\beta P}$ decreases with increasing V_P/V_S ratio r. This is why a large value of the V_P/V_S ratio r does not pose a problem for the P wave.

Because we restrict our investigation to the S wave, in the following section, we will omit the explicit indication of the S wave in the displacement-vector components and error terms.

6.3 Structure of the relative errors in amplitude and vector difference

Recall eq. (39)

$$DA\{u_{i,tt}\} \approx \alpha^2 DA\{u_{j,ji}\} + \beta^2 DA\{u_{i,jj} - u_{j,ji}\}. \tag{47}$$

The investigated numerical schemes differ from each other by the approximations on the r.h.s. They share the same approximation to the second time derivative

$$DA\{u_{i,tt}\} \approx \left(u_i^{m+1} - 2u_i^m + u_i^{m-1}\right) \frac{1}{(\Delta t)^2}. \tag{48}$$

After substituting $DA\{u_{i,tt}\}$ in eq. (47) by approximation (48), we can get the scheme for the numerical displacement component at the time level $m+1$ in the form

$${}^{\mathrm{N}}u_i^{m+1} = 2u_i^m - u_i^{m-1} + (\Delta t)^2 \left(\alpha^2 DA\{u_{j,ji}\} + \beta^2 DA\{u_{i,jj} - u_{j,ji}\}\right). \tag{49}$$

Recalling the concept of the local error, eqs (15)–(19), we distinguish the numerical value, labelled N, on the l.h.s., from the exact values of the displacement components on the r.h.s. (not labelled). Subtracting u_i^{m+1} from both sides of eq. (49), dividing the equation by $(\Delta t)^2$ and using eq. (48), we get

$$\left({}^{\mathrm{N}}u_i^{m+1} - u_i^{m+1}\right) \frac{1}{(\Delta t)^2} = -DA\{u_{i,tt}\} + \alpha^2 DA\{u_{j,ji}\} + \beta^2 DA\{u_{i,jj} - u_{j,ji}\}. \tag{50}$$

Each of the discrete approximations on the r.h.s. can be replaced by the sum of the exact operator and truncation error. Then

$$\begin{aligned}\left({}^{\mathrm{N}}u_i^{m+1} - u_i^{m+1}\right) \frac{1}{(\Delta t)^2} &= -u_{i,tt} + \alpha^2 u_{j,ji} + \beta^2 (u_{i,jj} - u_{j,ji}) \\ &\quad - TrE\{u_{i,tt}\} + \alpha^2 TrE\{u_{j,ji}\} + \beta^2 TrE\{u_{i,jj} - u_{j,ji}\}.\end{aligned} \tag{51}$$

The sum of the first three terms on the r.h.s. is equal to zero, see eq. (36), and thus

$$\left({}^{\mathrm{N}}u_i^{m+1} - u_i^{m+1}\right) \frac{1}{(\Delta t)^2} = -TrE\{u_{i,tt}\} + \alpha^2 TrE\{u_{j,ji}\} + \beta^2 TrE\{u_{i,jj} - u_{j,ji}\}. \tag{52}$$

Considering eqs (43) and (44), the case of the harmonic plane S wave,

$$\left({}^{\mathrm{N}}u_i^{m+1} - u_i^{m+1}\right) \frac{1}{(\Delta t)^2} = \left(error_i^{tS} - r^2 error_i^{\alpha S} - error_i^{\beta S}\right) \omega^2 u_i. \tag{53}$$

Referring to definition (19) of the error in the vector difference and eq. (32), we can consider an auxiliary error-component term

$$\begin{aligned}\tilde{\varepsilon}_{i,\,\mathrm{vdiff}} &= \frac{\left({}^{\mathrm{N}}u_i^{m+1} - u_i^{m+1}\right)}{A^{\mathrm{E}}} \frac{1}{(\Delta t)^2} \\ &= \left(error_i^{tS} - r^2 error_i^{\alpha S} - error_i^{\beta S}\right) \frac{\omega^2 u_i}{|A \cos \omega\, \Delta t|}.\end{aligned} \tag{54}$$

Referring now to definition (18) of the error in amplitude and eq. (32), we can rearrange eq. (54) and consider an auxiliary error-component term

$$\begin{aligned}\tilde{\varepsilon}_{i,\,\mathrm{ampl}} &= \frac{{}^{\mathrm{N}}u_i^{m+1}}{A^{\mathrm{E}}} \frac{1}{(\Delta t)^2} \\ &= \left(error_i^{tS} - r^2 error_i^{\alpha S} - error_i^{\beta S}\right) \frac{\omega^2 u_i}{|A \cos \omega\, \Delta t|} + \frac{u_i^{m+1}}{|A \cos \omega\, \Delta t|} \frac{1}{(\Delta t)^2}.\end{aligned} \tag{55}$$

Accounting for eqs (20) and (21), we have

$$u_i^{m+1} = u_i(t + \Delta t) = \exp[-i\,\omega\,\Delta t]\; u_i(t). \tag{56}$$

Consequently,

$$\begin{aligned}\tilde{\varepsilon}_{i\,,\,\mathrm{ampl}} &= \frac{{}^{\mathrm{N}}u_i^{m+1}}{A^{\mathrm{E}}} \frac{1}{(\Delta t)^2} \\ &= \left(error_i^{tS} - r^2 error_i^{\alpha S} - error_i^{\beta S} + \frac{\exp[-i\,\omega\,\Delta t]}{(\omega\,\Delta t)^2}\right) \frac{\omega^2 u_i}{|A \cos \omega\, \Delta t|}.\end{aligned} \tag{57}$$

The errors in the vector difference (19) and amplitude (18) can be then written as

$$\varepsilon^{\mathrm{Rel}}_{\mathrm{vdiff}} = (\Delta t_{\mathrm{ref}})^2 \left[\tilde{\varepsilon}^2_{x,\,\mathrm{vdiff}} + \tilde{\varepsilon}^2_{y,\,\mathrm{vdiff}} + \tilde{\varepsilon}^2_{z,\,\mathrm{vdiff}}\right]^{1/2} \tag{58}$$

and

$$\varepsilon^{\mathrm{Rel}}_{\mathrm{ampl}} = (\Delta t_{\mathrm{ref}})^2 \left| \left[\tilde{\varepsilon}^2_{x,\,\mathrm{ampl}} + \tilde{\varepsilon}^2_{y,\,\mathrm{ampl}} + \tilde{\varepsilon}^2_{z,\,\mathrm{ampl}}\right]^{1/2} - 1 \right|. \tag{59}$$

Although the auxiliary error-component terms eqs (54) and (57) do not quantitatively represent the entire values of the relative errors in amplitude and the vector difference, they indicate where the difference between the error in amplitude and error in the vector difference comes from. The r.h.s of eqs (54) and (57) differ by the fourth term in the parenthesis in eq. (57). The absolute value of this term is proportional to r^2, see Table 7. The fact that the errors in amplitude of schemes FD DS SG 4, FD D CG 4a, FD DS SG 2 and FD DS PSG 2 = FE G1 are almost independent on r is likely related to the interaction of the second and fourth terms, as they are both proportional to r^2.

6.4 Truncation errors of the discrete approximations to the second non-mixed and mixed spatial derivatives

It is also reasonable to look at the truncation errors of the discrete approximations to the second non-mixed and mixed spatial derivatives. The leading and first higher terms of the truncation errors of the second- and fourth-order operators are listed in Table A1 in Appendix. Here, we compare coefficients of these terms.

Denote the truncation errors of the operators for the mixed and non-mixed derivatives as $TrE\{D_{zx}\}$ and $TrE\{D_{xx}\}$, respectively. Define ratios for each scheme

$$C_{LT} = \frac{\text{coeff. of the leading term of } TrE\{Dzx\}}{\text{coeff. of the leading term of } TrE\{Dxx\}}$$
$$C_{kHT} = \frac{\text{coeff. of the k-th higher term of } TrE\{Dzx\}}{\text{coeff. of the k-th higher term of } TrE\{Dxx\}}; \quad k = 1, 2, 3, \ldots \tag{60}$$

C_{LT} and C_{1HT} are shown in Fig. 7. Fig. 7(a) includes the four schemes for which the errors in amplitude are almost independent on the V_P/V_S ratio r, Fig. 7(b) includes all other schemes. All the four schemes in Fig. 7(a) have $C_{LT} = 1$. It is easy to find that schemes FD DS SG 4, FD DS SG 2 and FD DS PSG 2 = FE G1 have also $C_{kHT} = 1$. On the other hand, none of schemes in Fig. 7(b) has C_{LT} or C_{1HT} equal to 1.

Let c_2^2 and c_4^2 be coefficients of the leading term and first higher term of $TrE\{D_{xx}\}$ or $TrE\{D_{zx}\}$ of the second-order FD DS SG 2 operators. The upper index indicates the second-order, the lower index the power of the grid spacing h. Similarly, let c_4^4 and c_6^4 be coefficients of the leading term and first higher term of $TrE\{D_{xx}\}$ or $TrE\{D_{zx}\}$ of the fourth-order FD DS SG 4 operators. Fig. 7 shows the corresponding coefficients of other second-order operators as multiples of c_2^2 and c_4^2. Similarly, the figure also shows coefficients of other fourth-order operators as multiples of c_4^4 and c_6^4.

In general, for the schemes of the same order (that is either second or fourth) for given C_{LT} or C_{1HT} the errors in amplitude and the vector difference increase with increasing absolute values of coefficients of terms in the truncation errors. This can be well seen in the case of schemes FD DS SG 2 and FD DS PSG 2 = FE G1 and schemes SE 4 cn and SE 4 vn. In both comparisons, the C_{LT} or C_{1HT} ratios are the same for the compared schemes but the coefficients of terms in the truncation errors are different.

It is interesting to compare FD DS SG 4 and FD D CG 4a. Although they have different C_{1HT}, the ratio of the coefficients of the leading terms (7.1, see Fig. 7a) well quantifies the difference in their errors (see Fig. 6).

7 CONCLUSIONS

We considered an unbounded homogeneous isotropic elastic medium and uniform cubic grid, and analysed 13 3-D time-domain explicit numerical schemes of the second-order in time for modelling seismic wave propagation and earthquake motion for their behaviour with a varying *P*-wave to *S*-wave speed ratio (V_P/V_S or r).

The schemes of the second-order in space are:

FD D CG 2—finite-difference displacement conventional grid
FD DS PSG 2—finite-difference displacement-stress partly-staggered grid
FD DS SG 2—finite-difference displacement-stress staggered grid
FE L8—finite-element Lobatto 8-integration points
FE G1—finite-element Gauss 1-integration point
FE G8—finite-element Gauss 8-integration points
DG P0 CF—discontinuous-Galerkin polynomial order zero centred-flux
DG P1 CF—discontinuous-Galerkin polynomial order one centred -flux

The schemes of the fourth-order in space are:

FD D CG 4a—finite-difference displacement conventional grid variant a
FD D CG 4b—finite-difference displacement conventional grid variant b
FD DS SG 4—finite-difference displacement-stress staggered grid
SE 4 cn—spectral-element central node
SE 4 vn—spectral-element vertex node.

We wrote all schemes in the unified form. Some of the schemes are equivalent

FD D CG 2 = FE L8 = DG P0 CF
FD DS PSG 2 = FE G1
FE G8 = DG P1 CF.

We defined the numerical solution as the displacement vector at time level $m + 1$ obtained from the numerical scheme entered by the exact values of displacement of the plane *S* wave at time levels $m - 1$ and m. We defined the relative local error in amplitude and the relative local error in the vector difference based on the difference between the numerical solution and the exact solution. Because different schemes use different time steps, we normalized the errors for a unit time.

(a)

2nd-order schemes			4th-order schemes		
operator	C_{LT} C_{1HT}		operator	C_{LT} C_{1HT}	
$D_{xx}^{\text{FD DS SG 2}}$	1 1	c_2^2 c_4^2	$D_{xx}^{\text{FD DS SG 4}}$	1 1	c_4^4 c_6^4
$D_{zx}^{\text{FD DS SG 2}}$		c_2^2 c_4^2	$D_{zx}^{\text{FD DS SG 4}}$		c_4^4 c_6^4
$D_{xx}^{\text{FD DS PSG 2}}$ $D_{xx}^{\text{FE G1}}$	1 1	$7.0\,c_2^2$ $53.5\,c_4^2$	$D_{xx}^{\text{FD D CG 4}a}$	1 0.53	$7.1\,c_4^4$ $26.7\,c_6^4$
$D_{zx}^{\text{FD DS PSG 2}}$ $D_{zx}^{\text{FE G1}}$		$7.0\,c_2^2$ $53.5\,c_4^2$	$D_{zx}^{\text{FD D CG 4}a}$		$7.1\,c_4^4$ $14.2\,c_6^4$

(b)

2nd-order schemes			4th-order schemes		
operator	C_{LT} C_{1HT}		operator	C_{LT} C_{1HT}	
$D_{xx}^{\text{FE G8}}$ $D_{xx}^{\text{DG P1 CF}}$	1.2 1.73	$5.0\,c_2^2$ $31.0\,c_4^2$	$D_{xx}^{\text{FD D CG 4b}}$	8.5 22	$1.2\,c_4^4$ $1.8\,c_6^4$
$D_{zx}^{\text{FE G8}}$ $D_{zx}^{\text{DG P1 CF}}$		$6.0\,c_2^2$ $53.5\,c_4^2$	$D_{zx}^{\text{FD D CG 4b}}$		$10.1\,c_4^4$ $39.1\,c_6^4$
$D_{xx}^{\text{FD D CG 2}}$ $D_{xx}^{\text{FE L8}}$ $D_{xx}^{\text{DG P0 CF}}$	4 16	c_2^2 c_4^2	$D_{xx}^{\text{SE 4 cn}}$	6 8	$2.03\,c_4^4$ $3.5\,c_6^4$
$D_{zx}^{\text{FD D CG 2}}$ $D_{zx}^{\text{FE L8}}$ $D_{zx}^{\text{DG P0 CF}}$		$4.0\,c_2^2$ $16.0\,c_4^2$	$D_{zx}^{\text{SE 4 cn}}$		$12.2\,c_4^4$ $27.9\,c_6^4$
			$D_{xx}^{\text{SE 4 vn}}$	6 8	$5.4\,c_4^4$ $106.8\,c_6^4$
			$D_{zx}^{\text{SE 4 vn}}$		$32.5\,c_4^4$ $854.5\,c_6^4$

Figure 7. Comparison of coefficients of the leading and the first higher terms of the truncation errors $TrE\{D_{xx}\}$ and $TrE\{D_{zx}\}$. (a) schemes with the error in amplitude almost independent on the V_P/V_S ratio r. (b) schemes with the error in amplitude dependent on the V_P/V_S ratio r.

We also defined the equivalent spatial sampling ratio as a ratio at which the maximum relative error of the scheme is equal to the reference maximum error.

The numerical evaluations of the errors and equivalent spatial sampling ratios led to the following conclusions:

The relative local error in amplitude of schemes FD DS SG 4, FD D CG 4a, FD DS SG 2 and FD DS PSG 2 = FE G1 is almost independent on the V_P/V_S ratio. The error in the vector difference increases with increasing V_P/V_S ratio. This can be explained only by the dependence of the polarization errors of all schemes on the V_P/V_S ratio.

FD D CG 2 = FE L8 = DG P0 CF is the most sensitive to the increasing V_P/V_S ratio and for $V_P/V_S > 2$ requires considerably denser spatial sampling than any other scheme.

The maximum errors in the vector difference of the second-order schemes FD DS SG 2, FE G8 = DG P1 CF and FD DS PSG 2 = FE G1 increase with the increasing V_P/V_S ratio in the same way. Schemes FD DS PSG 2 = FE G1 and FE G8 = DG P1 CF require denser spatial sampling than FD DS SG 2 to achieve the same accuracy.

The maximum errors in the vector difference of all the fourth-order schemes increase with the increasing V_P/V_S ratio for $V_P/V_S > 3$ in the same way. Schemes FD D CG 4a, FD D CG 4b, SE 4 cn and SE 4 vn require denser spatial sampling than FD DS SG 4 to achieve the same accuracy.

The fourth-order schemes are for $V_P/V_S > 3$ less sensitive to the increasing V_P/V_S ratio than the second-order schemes.

We theoretically showed how a numerical scheme sees the *P* wave and *S* wave if the V_P/V_S ratio increases. In this study, we show that the increasing V_P/V_S ratio does not pose a problem for a scheme to model the *P* wave.

We also showed the structure of the errors in amplitude and the vector difference.

We compared the schemes in terms of the truncation errors of the discrete approximations to the second mixed and non-mixed spatial derivatives. The most important finding is this: Schemes FD DS SG 4, FD D CG 4a, FD DS SG 2 and FD DS PSG 2 = FE G1 with the errors in amplitude almost independent on the V_P/V_S ratio have the same coefficients of the leading terms of the truncation errors of approximations to the second mixed and non-mixed spatial derivatives. None of the other schemes have those coefficients equal.

Scheme FD DS SG 2 with the smallest errors among the second-order schemes and scheme FD DS SG 4 with the smallest errors among the fourth-order schemes have the same coefficients also at each higher term of the truncation errors of approximations to the second mixed and non-mixed spatial derivatives. The absolute values of the coefficients are smaller than the absolute values of coefficients of the truncation errors of the other schemes.

The general theoretical conclusion based on the investigation of the 13 numerical schemes is that the homogeneity of the approximations to the second mixed and non-mixed spatial derivatives in terms of the coefficients of the leading terms of their truncation errors as well as the absolute values of the coefficients are key factors for the behaviour of the numerical schemes with increasing V_P/V_S ratio.

The practical conclusion for the existing numerical schemes is that the dependence of the errors in the vector difference on the V_P/V_S ratio should be accounted for by a proper (sufficiently dense) spatial sampling. We quantified the proper sampling with respect to the local errors in amplitude and in the vector difference.

ACKNOWLEDGMENTS

This work was supported in part by the Slovak Research and Development Agency under the contract number APVV-0435-07 (project OPTIMODE) and bilateral APVV Slovak–French project SK-FR-0028-09. We gratefully acknowledge the funding by the European Union through the Initial Training Network QUEST (Grant agreement number 238007), a Marie Curie Action under the People Programme. We thank Jean Virieux and Jacobo Bielak for discussions. We very much appreciate careful and useful reviews by Diego Mercerat and Josep de la Puente that helped us to improve the article.

REFERENCES

Belytschko, T., Liu, W.K. & Moran, B., 2000. *Nonlinear Finite Elements for Continua and Structures,* John Wiley & Sons, New York, NY.

Bielak J., Loukakis, K., Hisada, Y. & Yoshimura, Ch., 2003. Domain reduction method for three-dimensional earthquake modeling in localized regions. Part I: theory, *Bull. seism. Soc. Am.,* **93,** 8170–824.

Chaljub, E., Komatitsch, D., Vilotte, J.-P., Capdeville, Y., Valette, B. & Festa, G., 2007. Spectral element analysis in seismology, in *Advances in Wave Propagation in Heterogeneous Earth,* Advances in Geophysics Series Vol. 48, pp. 365–419, eds Wu, R.-S. & Maupin, V., Elsevier–Academic Press, London.

Chaljub, E. *et al*. 2010a. Euroseistest Numerical Simulation Project: comparison with local earthquake recordings for validation, *Seismol. Res. Lett.,* **81,** 1427–1455.

Chaljub, E., Moczo, P., Tsuno, S., Bard, P.-Y., Kristek, J., Käser, M., Stupazzini, M., Kristekova, M., 2010b. Quantitative comparison of four numerical predictions of 3D ground: motion in the Grenoble Valley, France, *Bull. seism. Soc. Am.,* **100,** 1427–1455.

De Basabe, J.D. & Sen, M.K., 2007. Grid dispersion and stability criteria of some common finite-element methods for acoustic and elastic wave equations, *Geophysics,* **72,** T81–T95.

De Basabe, J.D., Sen, M.K. & Wheeler, M., 2008. The interior penalty discontinuous Galerkin method for elastic wave propagation: grid dispersion. *Geophys. J. Int.,* **175,** 83–93.

de la Puente, J., 2008. *Seismic Wave Propagation for Complex Rheologies,* VDM Verlag, Saarbrücken.

de la Puente, J., Dumbser, M., Käser, M. & Igel, H., 2008. Discontinuous Galerkin methods for wave propagation in poroelastic media, *Geophysics,* **73,** 77–97.

de la Puente, J., Käser, M., Dumbser, M. & Igel, H., 2007. An arbitrary high order discontinuous Galerkin method for elastic waves on unstructured meshes – IV. Anisotropy, *Geophys. J. Int.,* **169,** 1210–1228.

Delcourte, S., Fezoui, L. & Glinsky-Olivier, N., 2009. A high-order discontinuous Galerkin method for the seismic wave propagation, *ESAIM: Proc.,* **27,** 70–89.

Dumbser, M. & Käser, M., 2006. An arbitrary high order discontinuous Galerkin method for elastic waves on unstructured meshes – II. The three-dimensional case, *Geophys. J. Int.,* **167,** 319–336.

Dumbser, M., Käser, M. & Toro, E., 2007. An arbitrary high order discontinuous Galerkin method for elastic waves on unstructured meshes – V. Local time stepping and p-adaptivity, *Geophys. J. Int.,* **171,** 695–717.

Etienne, V., Chaljub, E., Virieux, J. & Glinsky, N., 2010. An hp-adaptive discontinuous Galerkin finite-element method for 3D elastic wave modelling, *Geophys. J. Int.,* **183,** 941–962.

Galis, M., Moczo, P. & Kristek, J., 2008. A 3-D hybrid finite-difference—finite-element viscoelastic modelling of seismic wave motion, *Geophys. J. Int.,* **175,** 153–184.

Hesthaven, J.S. & Warburton, T., 2008. Nodal discontinuous Galerkin Method, in *Algorithms, Analysis, and Application,* Springer, New York, NY.

Hughes, T.J.R., 2000. *The Finite Element Method: Linear Static and Dynamic Finite Element Method Analysis,* Prentice Hall, New York, NY.

Käser, M. & Dumbser, M., 2006. An arbitrary high order discontinuous Galerkin method for elastic waves on unstructured meshes – I. The two-dimensional isotropic case with external source terms, *Geophys. J. Int.,* **166,** 855–877.

Käser, M., Dumbser, M., de la Puente, J. & Igel, H., 2007. An arbitrary high order discontinuous Galerkin method for elastic waves on unstructured meshes – III. Viscoelastic attenuation, *Geophys. J. Int.,* **168,** 224–242.

Käser, M., Hermann, V. & de la Puente, J., 2008. Quantitative accuracy analysis of the discontinuous Galerkin method for seismic wave propagation, *Geophys. J. Int.,* **173,** 990–999.

Komatitsch, D. & Tromp, J., 1999. Introduction to the spectral element method for three-dimensional seismic wave propagation, *Geophys. J. Int.,* **139,** 806–822.

Komatitsch, D., Tsuboi, S. & Tromp, J., 2005. The spectral-element method in seismology, *Geophys. Monogr. Ser.*, **157**, 205–227.

Komatitsch, D. & Vilotte, J.-P., 1998. The spectral-element method: an efficient tool to simulate the seismic response of 2D and 3D geological structures, *Bull. seism. Soc. Am.,* **88,** 368–392.

LeVeque, R.J., 2002. *Finite Volume Methods For Hyperbolic Problems*.*Cambridge Texts in Applied Mathematics,* Cambridge University Press, Cambridge.

Ma, S. & Liu, P., 2006. Modeling of the perfectly matched layer absorbing boundaries and intrinsic attenuation in explicit finite-element methods, *Bull. seism. Soc. Am.,* **96,** 1779–1794.

Moczo, P. *et al*., 2010a. Numerical modeling of earthquake ground motion in the Mygdonian Basin, Greece: verification of the 3D numerical methods, *Seism. Res. Lett.,* **81,** 310.

Moczo, P., Kristek, J., Galis, M., Pazak, P., 2010b. On accuracy of the finite-difference and finite-element schemes with respect to P-wave to S-wave speed ratio, *Geophys. J. Int.,* **182,** 493–510.

Moczo, P., Kristek, J., Galis, M., Pazak, P. & Balazovjech, M., 2007a. The finite-difference and finite-element modeling of seismic wave propagation and earthquake motion, *Acta Phys. Slovaca,* **57,** 177–406.

Moczo, P., Kristek, J. & Halada, L., 2000. 3D 4th-order staggered-grid finite-difference schemes: stability and grid dispersion. *Bull. seism. Soc. Am.,* **90,** 587–603.

Moczo, P., Robertsson, J.O.A. & Eisner, L., 2007b. The finite-difference time-domain method for modeling of seismic wave propagation, in *Advances in Wave Propagation in Heterogeneous Earth,* Advances in Geophysics Series Vol. 48, pp. 421–516, eds Wu, R.-S., Maupin, V. & Dmowska, R., Elsevier/Academic Press, San Diego, CA.

Ottosen, N.S. & Petersson, H., 1992. *Introduction to the Finite Element Method,* Prentice Hall, New York, NY.

Reddy, J.N., 2006. *An Introduction to the Finite Element Method,* McGraw-Hill, New York, NY.

Seriani, G. & Oliveira, S.P., 2008. Dispersion analysis of spectral element methods for elastic wave propagation, *Wave Motion* **45,** 729–744.

Zienkiewicz, O.C. & Taylor, R.L., 1989. *The Finite Element Method,* 4th edn, Vol. 1, McGraw-Hill, New York, NY.

APPENDIX

Table A1. The leading and first higher terms of the truncation errors of the non-mixed and mixed spatial operators defined by eqs (11)–(14). Part a: second-order operators, part b: fourth-order operators.

Operator	Truncation error × 20160
Part (a)	
$D_{xx}^{\text{FD D CG 2}}$ $D_{xx}^{\text{FE L8}}$ $D_{xx}^{\text{DG P0 CF}}$	$1680\,\Psi^{(4,0,0)}\,h^2$ $+\,56\,\Psi^{(6,0,0)}\,h^4$
$D_{zx}^{\text{FD D CG 2}}$ $D_{zx}^{\text{FE L8}}$ $D_{zx}^{\text{DG P0 CF}}$	$6720\left(\frac{1}{2}\Psi^{(1,0,3)}+\frac{1}{2}\Psi^{(3,0,1)}\right)h^2$ $+\,896\left(\frac{3}{16}\Psi^{(1,0,5)}+\frac{10}{16}\Psi^{(3,0,3)}+\frac{3}{16}\Psi^{(5,0,1)}\right)h^4$
$D_{xx}^{\text{FD DS PSG 2}}$ $D_{xx}^{\text{FE G1}}$	$11760\left(\frac{3}{7}\Psi^{(2,0,2)}+\frac{1}{7}\Psi^{(4,0,0)}+\frac{3}{7}\Psi^{(2,2,0)}\right)h^2$ $+\,2996\left(\frac{1}{107}\left(2\Psi^{(6,0,0)}+15\Psi^{(4,2,0)}+15\Psi^{(4,0,2)}+15\Psi^{(2,4,0)}+45\Psi^{(2,2,2)}+15\Psi^{(2,0,4)}\right)\right)h^4$
$D_{zx}^{\text{FD DS PSG 2}}$ $D_{zx}^{\text{FE G1}}$	$11760\left(\frac{2}{7}\Psi^{(1,0,3)}+\frac{3}{7}\Psi^{(1,2,1)}+\frac{2}{7}\Psi^{(3,0,1)}\right)h^2$ $+\,2996\left(\frac{1}{107}\left(6\Psi^{(1,0,5)}+30\Psi^{(1,2,3)}+15\Psi^{(1,4,1)}+20\Psi^{(3,0,3)}+30\Psi^{(3,2,1)}+6\Psi^{(5,0,1)}\right)\right)h^4$

Table A1. (*Continued.*)

Operator	Truncation error × 20160
$D_{xx}^{\text{FD DS SG 2}}$	$1680\ \Psi^{(4,0,0)}\ h^2$
	$+ 56\ \Psi^{(6,0,0)}\ h^4$
$D_{zx}^{\text{FD DS SG 2}}$	$1680\ \left(\frac{1}{2}\Psi^{(1,0,3)} + \frac{1}{2}\Psi^{(3,0,1)}\right)\ h^2$
	$+ 56\ \left(\frac{3}{16}\Psi^{(1,0,5)} + \frac{10}{16}\Psi^{(3,0,3)} + \frac{3}{16}\Psi^{(5,0,1)}\right)\ h^4$
$D_{xx}^{\text{FE G8}}$ $D_{xx}^{\text{DG P1 CF}}$	$8400\ \left(\frac{2}{5}\Psi^{(2,0,2)} + \frac{1}{5}\Psi^{(4,0,0)} + \frac{2}{5}\Psi^{(2,2,0)}\right)\ h^2$
	$+ 1736\ \left(\frac{1}{31}\left(\Psi^{(6,0,0)} + 5\Psi^{(4,2,0)} + 5\Psi^{(4,0,2)} + 5\Psi^{(2,4,0)} + 10\Psi^{(2,2,2)} + 5\Psi^{(2,0,4)}\right)\right)\ h^4$
$D_{zx}^{\text{FE G8}}$ $D_{zx}^{\text{DG P1 CF}}$	$10080\ \left(\frac{1}{3}\Psi^{(1,0,3)} + \frac{1}{3}\Psi^{(1,2,1)} + \frac{1}{3}\Psi^{(3,0,1)}\right)\ h^2$
	$+ 2996\ \left(\frac{1}{41}\left(3\Psi^{(1,0,5)} + 10\Psi^{(1,2,3)} + 5\Psi^{(1,4,1)} + 10\Psi^{(3,0,3)} + 10\Psi^{(3,2,1)} + 3\Psi^{(5,0,1)}\right)\right)\ h^4$
Part (b)	
$D_{xx}^{\text{FD D CG 4}a}$	$-1344\ \Psi^{(6,0,0)}\ h^4$
	$-300\ \Psi^{(8,0,0)}\ h^6$
$D_{zx}^{\text{FD D CG 4}a}$	$-1344\ \left(\frac{1}{2}\Psi^{(1,0,5)} + \frac{1}{2}\Psi^{(5,0,1)}\right)\ h^4$
	$-160\ \left(\frac{1}{2}\Psi^{(1,0,7)} + \frac{1}{2}\Psi^{(7,0,1)}\right)\ h^6$
$D_{xx}^{\text{FD D CG 4b}}$	$-224\ \Psi^{(6,0,0)}\ h^4$
	$-20\ \Psi^{(8,0,0)}\ h^6$
$D_{zx}^{\text{FD D CG 4b}}$	$-1904\ \left(\frac{6}{17}\Psi^{(1,0,5)} + \frac{5}{17}\Psi^{(3,0,3)} + \frac{6}{17}\Psi^{(5,0,1)}\right)\ h^4$
	$-440\ \left(\frac{4}{22}\Psi^{(1,0,7)} + \frac{7}{22}\Psi^{(3,0,5)} + \frac{7}{22}\Psi^{(5,0,3)} + \frac{4}{22}\Psi^{(7,0,1)}\right)\ h^6$
$D_{xx}^{\text{FD DS SG 4}}$	$-189\ \Psi^{(6,0,0)}\ h^4$
	$-\frac{45}{4}\ \Psi^{(8,0,0)}\ h^6$
$D_{zx}^{\text{FD DS SG 4}}$	$-189\ \left(\frac{1}{2}\Psi^{(1,0,5)} + \frac{1}{2}\Psi^{(5,0,1)}\right)\ h^4$
	$-\frac{45}{4}\ \left(\frac{1}{2}\Psi^{(1,0,7)} + \frac{1}{2}\Psi^{(7,0,1)}\right)\ h^6$
$D_{xx}^{\text{SE 4 cn}}$	$-384\ \Psi^{(6,0,0)}\ h^4$
	$-\frac{1920}{49}\ \Psi^{(8,0,0)}\ h^6$
$D_{zx}^{\text{SE 4 cn}}$	$-2304\ \left(\frac{1}{2}\Psi^{(1,0,5)} + \frac{1}{2}\Psi^{(5,0,1)}\right)\ h^4$
	$-\frac{15\,360}{49}\ \left(\frac{1}{2}\Psi^{(1,0,7)} + \frac{1}{2}\Psi^{(7,0,1)}\right)\ h^6$
$D_{xx}^{\text{SE 4 vn}}$	$-1\,024\ \Psi^{(6,0,0)}\ h^4$
	$-\frac{58\,880}{49}\ \Psi^{(8,0,0)}\ h^6$
$D_{zx}^{\text{SE 4 vn}}$	$-6144\ \left(\frac{1}{2}\Psi^{(1,0,5)} + \frac{1}{2}\Psi^{(5,0,1)}\right)\ h^4$
	$-\frac{471\,040}{49}\ \left(\frac{1}{2}\Psi^{(1,0,7)} + \frac{1}{2}\Psi^{(7,0,1)}\right)\ h^6$

Geophysical Journal International

Geophys. J. Int. (2016) **205,** 427–439
GJI Seismology

doi: 10.1093/gji/ggw024

Highly accurate stability-preserving optimization of the Zener viscoelastic model, with application to wave propagation in the presence of strong attenuation

Émilie Blanc,[1,2] Dimitri Komatitsch,[1] Emmanuel Chaljub,[3] Bruno Lombard[1] and Zhinan Xie[1,4]

[1] *LMA, CNRS UPR* 7051, *Aix-Marseille University, Centrale Marseille, F*-13453 *Marseille cedex* 13, *France. E-mail: komatitsch@lma.cnrs-mrs.fr*
[2] *Division of Scientific Computing, Department of Information Technology, Uppsala University, Box* 337, *SE*-751 05 *Uppsala, Sweden*
[3] *Université Grenoble Alpes and CNRS, ISTerre, BP* 53, *F*-38041 *Grenoble, France*
[4] *Institute of Engineering Mechanics, China Earthquake Administration, Harbin* 150080, *China*

Accepted 2016 January 15. Received 2015 December 20; in original form 2015 November 14

SUMMARY

This paper concerns the numerical modelling of time-domain mechanical waves in viscoelastic media based on a generalized Zener model. To do so, classically in the literature relaxation mechanisms are introduced, resulting in a set of the so-called memory variables and thus in large computational arrays that need to be stored. A challenge is thus to accurately mimic a given attenuation law using a minimal set of relaxation mechanisms. For this purpose, we replace the classical linear approach of Emmerich & Korn with a nonlinear optimization approach with constraints of positivity. We show that this technique is more accurate than the linear approach. Moreover, it ensures that physically meaningful relaxation times that always honour the constraint of decay of total energy with time are obtained. As a result, these relaxation times can always be used in a stable way in a modelling algorithm, even in the case of very strong attenuation for which the classical linear approach may provide some negative and thus unusable coefficients.

Key words: Numerical solutions; Numerical approximations and analysis; Body waves; Seismic attenuation; Computational seismology; Wave propagation.

1 INTRODUCTION

Taking dissipation mechanisms, that is, viscoacoustic or viscoelastic behaviour into account is often important in fields that involve acoustic or elastic wave propagation. This has led to significant research effort for instance in seismology, seismic wave propagation and imaging in the oil and gas industry, non-destructive industrial evaluation based on ultrasonic waves, or medical imaging. A large number of articles can be found in the literature about modelling of viscoelastic media characterized by their quality factor Q, with recent reviews available for instance in Petersson & Sjögreen (2012) and Carcione (2014). Of particular interest is the case of a Q factor that is constant over a wide range of frequencies because that is observed in many cases of practical interest (see e.g. Liu *et al.* 1976; Dahlen & Tromp 1998; Komatitsch & Tromp 1999).

In pioneering work, Liu *et al.* (1976) demonstrated that a finite and constant quality factor can be modelled by superimposing N standard linear solid (SLS) damping mechanisms. Day & Minster (1984) developed a Padé approximant of the viscoelastic modulus for time-domain wave propagation simulations. Emmerich & Korn (1987) then showed that the rheological model of a generalized Maxwell body can be used to represent the rational approximation of the viscoelastic modulus and developed a linear least-squares technique to compute the coefficients of the rational approximation involved (i.e. the points and weights that are needed in the case of time-domain simulations) in an optimized fashion. This latter work has resulted in an improved approximation of a viscoelastic solid having a given quality factor Q and has become the classical way of representing such a material. It has been used in numerous subsequent articles, for example, Carcione *et al.* (1988a,b), Kristek & Moczo (2003), Komatitsch *et al.* (2004), Moczo & Kristek (2005), Käser *et al.* (2007), Martin & Komatitsch (2009), Savage *et al.* (2010), Lombard & Piraux (2011), Dhemaied *et al.* (2011) and Petersson & Sjögreen (2012). It is also worth mentioning that Moczo & Kristek (2005) proved the equivalence between the different rheological models mentioned previously, as also analysed by Cao & Yin (2014). Because of this equivalence, in what follows for simplicity we will call it the Zener model and will mostly refer to the formulation of Carcione (2014) for that model.

In the context of time-domain simulations, these methods are often expensive in terms of memory storage when implemented numerically because they require the use of the so-called

memory variables that need to be stored and marched in time (see e.g. Moczo & Kristek 2005; Carcione 2014). To alleviate this, Day (1998), Day & Bradley (2001), Graves & Day (2003) and van Driel & Nissen-Meyer (2014) have suggested spreading the relaxation mechanisms and thus the related memory variables over adjacent grid points, using a single mechanism per grid point and trying to get a good approximation of the damping behaviour in average over a local volume, in particular when attenuation is weak (van Driel & Nissen-Meyer 2014). However, there are open questions regarding the overall accuracy of such an approach, in particular when propagating waves over a large number of wavelengths, which is very often the case in practice. Kristek & Moczo (2003) have also pointed out the fact that the presence of discontinuities, that is, of interfaces in the material model under study, can lead to inaccuracies in this spreading technique.

In practice, the Zener model requires fitting $Q(\omega)$ over a range of angular frequencies $[\omega_{\min}, \omega_{\max}]$, which implies determining a set of N points and N weights. As mentioned above, this is classically done based on the linear approach of Emmerich & Korn (1987), in which one sets the N points and then optimizes and solves for the N weights. Casula & Carcione (1992) have proposed an approximation to simplify the way of computing the weights, in particular in the case of low-loss solids. However, two important drawbacks can appear with this technique. First, the accuracy of the approach can be relatively poor, that is, the error compared with the real constant Q can be large when the frequency range under study is large and/or when the number of relaxation mechanisms N used is small. This amounts to introducing a physical modelling error, independent of the numerical error induced in addition by the chosen numerical scheme. Second, some weights can be negative because the linear approach of Emmerich & Korn (1987) does not enforce their positivity. This is particularly true when attenuation is strong (say $Q < 20$ or so), which is a case that can occur for instance in site effect and earthquake hazard assessment studies (poorly consolidated sediments), in soil-structure interaction studies where values of the critical damping ratio $\xi = \frac{1}{2Q}$ larger than 5 per cent are often considered in the structures, as well as in non-destructive industrial testing or medical imaging. In such a case the physical and also mathematical constraint of decay of total energy with time can be broken, as we will see in Section 2, and using such negative weights can make wave propagation modelling algorithms become unstable. Peyrusse *et al.* (2014) pointed out the problem of negative weights in the approach of Emmerich & Korn (1987) and proposed to impose their positivity in the inversion, as also addressed by Withers *et al.* (2015). However, they did not invert jointly for the points and weights and found that their approach was at best as accurate as that of Emmerich & Korn (1987).

Alternative approaches exist to represent viscoelastic damping mechanisms and to compute their coefficients. For instance, Xu & McMechan (1998) used simulated annealing to find the weights of the Zener body, the relaxation times being evenly distributed in logarithmic scale over N points in the band of angular frequencies. Russo & Zollo (2003) developed an analytical approach for optimization of the relaxation times; however, they used a less general relaxation function by assigning the same ratio of relaxed and unrelaxed moduli to all Zener bodies, and they did not introduce the positivity of the weights as a constraint. Liu & Archuleta (2006) used a simulated annealing approach to compute the relaxation points and weights for only two extreme values of the quality factor, $Q = 5$ and $Q = 5000$, and proposed a regression methodology to derive the coefficients for intermediate values of Q. However, they also did not impose the positivity of the weights as a constraint and their approximation of the Q values is limited to a 5 per cent accuracy. Furthermore, their expression of the viscoelastic modulus is different from the classical one of, for example, Moczo & Kristek (2005), Lombard & Piraux (2011), Petersson & Sjögreen (2012) and Carcione (2014). Bielak *et al.* (2011) introduced an internal friction model with optimized memory efficiency based on a Kelvin–Voigt body put in parallel with two Maxwell bodies and managed to mimic an almost constant Q quality factor over two decades in frequency. Other attempts at improving the coefficient optimization process can be found in the literature: Robertsson *et al.* (1994) and Robertsson (1996) developed a quasi-analytical approach, but an important limitation is that it is valid only when Q is large; Asvadurov *et al.* (2004) minimized the error in L_∞ norm in an elegant way, but their approach is quite involved and, more importantly, valid for a constant Q only.

In this paper, our goal is thus to develop a nonlinear optimization technique that (i) will be significantly more accurate than the classical approach of Emmerich & Korn (1987) and (ii) will always lead to physically meaningful relaxation times that honour the constraint of decay of total energy with time, by enforcing the positivity of all the coefficients obtained, including in the case of strong attenuation, thus ensuring stable simulations. Compared to Emmerich & Korn (1987) we will not set the points but rather solve and optimize for them jointly with the weights, imposing strict positivity as a constraint in the process. Instead of solving for N unknowns, we will thus solve for $2N$ unknowns. Having more degrees of freedom to solve for, we will be able to significantly improve the accuracy of the approximation. This strategy has successfully been used in other fields such as viscoelastic models in solid mechanics (Rekik & Brenner 2011) and high-frequency poroelasticity (Blanc *et al.* 2013). To some extent, this idea has some similarities with switching from Newton–Cotes (trapezoidal, Simpson...) quadrature to Gauss quadrature in numerical integration in order to get a more accurate integration rule by determining optimized points and weights instead of weights only. The methodology that we will introduce is independent of the numerical scheme used to solve the wave equation in time, that is, it is general and can be used in numerical techniques as diverse as finite differences, finite elements, spectral elements, discontinuous Galerkin, etc. The coefficients are computed once and for all in a preprocessing step.

The paper is organized as follows: in Section 2.1, we briefly recall some elementary notions about viscoelasticity and discuss the decay of total energy with time. In Section 2.2, we recall the approach of Emmerich & Korn (1987) and reformulate it within our framework. In Section 2.3, we introduce the nonlinear optimization approach that will allow us to define the new methodology. In Section 3, we perform numerical experiments to show the dispersion and quality factor curves obtained, which illustrates the improved accuracy of the results. Finally, in Section 4, we perform a numerical experiment for 3-D wave propagation in a tabular medium, which confirms the robustness and the improved accuracy of the nonlinear optimization approach.

2 PHYSICAL MODELLING

As mentioned above, viscoelastic models are widely used in the case of the propagation of acoustic or seismic waves in dissipative media, among other applications. The 2-D or 3-D linear viscoelastic wave equation then writes:

$$\rho \frac{\partial^2 \mathbf{u}}{\partial t^2} = \nabla \cdot \boldsymbol{\sigma} + \mathbf{f}, \tag{1}$$

where $\boldsymbol{\rho}$ is the distribution of density and $\mathbf{u}$ denotes the displacement field produced by the source $\mathbf{f}$. The symmetric stress tensor $\boldsymbol{\sigma}$ is linearly related to the strain tensor $\boldsymbol{\varepsilon} = \frac{1}{2}(\boldsymbol{\nabla}\mathbf{u} + (\boldsymbol{\nabla}\mathbf{u})^T)$ by Hooke's law, which in an elastic, anisotropic linear solid may be written in the form

$$\boldsymbol{\sigma} = \mathbf{c} : \boldsymbol{\varepsilon}\,, \tag{2}$$

where the colon denotes a double tensor contraction operation. The elastic properties of the medium are determined by the fourth-order elastic tensor $\mathbf{c}$, which in an isotropic medium is $c_{ijk\ell} = \lambda\delta_{ij}\delta_{k\ell} + \mu(\delta_{ik}\delta_{j\ell} + \delta_{i\ell}\tilde{}\delta_{jk})$, where δ is the Kronecker delta symbol and λ and μ are the two Lamé parameters, related to the pressure and shear wave celerities and to density by $\mu = \rho\, c_s^2$ and $\lambda = \rho\, c_p^2 - 2\mu$. In an attenuating medium, Hooke's law (2) needs to be modified such that the stress is determined by the entire strain history:

$$\boldsymbol{\sigma}(t) = \int_{-\infty}^{t} \frac{\partial}{\partial t}\mathbf{c}(t-t') : \boldsymbol{\varepsilon}(t')\ \mathrm{d}t'\,. \tag{3}$$

In the 1-D case without attenuation this reduces to

$$\begin{aligned} \rho\,\frac{\partial^2 u}{\partial t^2} &= \frac{\partial \sigma}{\partial x} + f \\ \varepsilon &= \frac{\partial u}{\partial x} \\ \sigma &= (\lambda + 2\,\mu)\varepsilon \end{aligned} \tag{4}$$

with scalar unknowns, and in an attenuating medium Hooke's law becomes

$$\sigma(t) = \int_{-\infty}^{t} \frac{\partial}{\partial t}(\lambda(t-t') + 2\,\mu(t-t'))\,\varepsilon(t')\ \mathrm{d}t'\,. \tag{5}$$

2.1 Constitutive law

Let us briefly recall elementary notions about viscoelasticity in 1-D. In higher spatial dimensions, the discussion below is then straightforwardly applied to the compressional and shear relaxation functions, respectively. The reader is referred, for example, to Carcione (2014) for a detailed presentation. The integro-differential expression of 1-D linear viscoelasticity writes

$$\sigma = \psi * \frac{\partial \varepsilon}{\partial t}, \tag{6}$$

where $*$ denotes time convolution. The relaxation function of the Zener model writes

$$\psi(t) = E_r\left(1 - \frac{1}{N}\sum_{\ell=1}^{N}\left(1 - \frac{\tau_{\varepsilon\ell}}{\tau_{\sigma\ell}}\right)\mathrm{e}^{-\dfrac{t}{\tau_{\sigma\ell}}}\right) H(t), \tag{7}$$

where E_r is the relaxed modulus, N is the number of relaxation mechanisms, $\tau_{\varepsilon\ell}$ and $\tau_{\sigma\ell}$ are relaxation times and H is the Heaviside step function. It is worth mentioning that the $1/N$ factor in eq. (7) is not present in earlier publications (Liu *et al.* 1976; Carcione *et al.* 1988a,b). This has been changed in Carcione (2001) and Moczo & Kristek (2005) as well as in many subsequent publications. The model with the $1/N$ factor is physically more meaningful because the model without it cannot be represented by mechanical elements, since it requires a spring with negative constant (Casula & Carcione 1992); but calculations not shown here demonstrate that these two ways of expressing the Zener model are equivalent. Another issue that is sometimes found in the literature is that waves speed up instead of slowing down when attenuation is turned on because the reference used is the relaxed state instead of the more traditional unrelaxed state (e.g. in Carcione 1993).

At $t = 0$, the relaxation function (7) is equal to the unrelaxed modulus E_u

$$E_u = \frac{1}{N}\sum_{\ell=1}^{N}\frac{\tau_{\varepsilon\ell}}{\tau_{\sigma\ell}}\,E_r. \tag{8}$$

As time increases, ψ decreases monotonically from E_u to E_r, and as frequency increases, the phase velocity increases monotonically from c_0 to c_∞ defined by

$$c_0 = \sqrt{\frac{E_r}{\rho}}, \qquad c_\infty = \sqrt{\frac{E_u}{\rho}}. \tag{9}$$

Instead of writing the constitutive law as a convolution product (6), one can equivalently use the differential form

$$\begin{cases} \sigma = \displaystyle\sum_{\ell=1}^{N}\sigma_\ell, \\ \sigma_\ell + \tau_{\sigma\ell}\,\dfrac{\partial \sigma\ell}{\partial t} = E_{r\ell}\left(\varepsilon + \tau_{\varepsilon\ell}\dfrac{\partial \varepsilon}{\partial t}\right), \qquad \ell = 1, \ldots, N, \\ E_{r\ell} = \dfrac{E_r}{N}\,. \end{cases} \tag{10}$$

This form is useful to prove the decay of energy (Bécache *et al.* 2004).

Property 1. Let us define

$$\mathcal{E} = \mathcal{E}_1 + \mathcal{E}_2 + \mathcal{E}_3, \tag{11}$$

with

$$\begin{aligned} \mathcal{E}_1 &= \frac{1}{2}\int_{\mathbb{R}} \rho\, v^2\,\mathrm{d}x, \\ \mathcal{E}_2 &= \frac{1}{2}\int_{\mathbb{R}} E_r\left(\frac{\partial u}{\partial x}\right)^2\mathrm{d}x, \\ \mathcal{E}_3 &= \frac{1}{2}\sum_{\ell=1}^{N}\int_{\mathbb{R}}\frac{\tau_{\sigma\ell}}{E_{r\ell}\,(\tau_{\varepsilon\ell} - \tau_{\sigma\ell})}\left(\sigma_\ell - E_{r\ell}\frac{\partial u}{\partial x}\right)^2\mathrm{d}x, \end{aligned} \tag{12}$$

where $v = \frac{\partial u}{\partial t}$ is velocity and ρ is density. $\mathcal{E}_1$ corresponds to the kinetic energy, $\mathcal{E}_2$ to the elastic potential energy in the relaxed state and $\mathcal{E}_3$ to the sum of the inelastic potential energies. The total energy $\mathcal{E}$ then obeys

$$\frac{\mathrm{d}\mathcal{E}}{\mathrm{d}t} = -\sum_{\ell=1}^{N}\int_{\mathbb{R}}\frac{1}{E_{r\ell}\,(\tau_{\varepsilon\ell} - \tau_{\sigma\ell})}\left(\sigma_\ell - E_{r\ell}\frac{\partial u}{\partial x}\right)^2\mathrm{d}x. \tag{13}$$

To prove (13), the conservation of momentum in eq. (4) combined with system (10) can be written as

$$\begin{cases} \rho\,\dfrac{\partial v}{\partial t} = \dfrac{\partial \sigma}{\partial x}, & \text{(14a)} \\ \sigma = \displaystyle\sum_{\ell=1}^{N}\sigma_\ell, & \text{(14b)} \\ \sigma_\ell + \tau_{\sigma\ell}\,\dfrac{\partial \sigma\ell}{\partial t} = E_{r\ell}\left(\dfrac{\partial u}{\partial x} + \tau_{\varepsilon\ell}\dfrac{\partial v}{\partial x}\right), \qquad \ell = 1, \ldots, N. & \text{(14c)} \end{cases}$$

Let us multiply eq. (14a) by v and integrate by parts:

$$\int_{\mathbb{R}} \rho\, v\, \frac{\partial v}{\partial t}\, \mathrm{d}x + \int_{\mathbb{R}} \frac{\partial v}{\partial x}\, \sigma\, \mathrm{d}x = 0. \tag{15}$$

We can then transform the stress σ into σ_ℓ thanks to eq. (14b)

$$\int_{\mathbb{R}} \rho\, v\, \frac{\partial v}{\partial t}\, \mathrm{d}x + \sum_{\ell=1}^{N} \int_{\mathbb{R}} \frac{\partial v}{\partial x}\, \sigma_\ell\, \mathrm{d}x = 0, \tag{16}$$

and split the resulting equation into two terms:

$$\underbrace{\int_{\mathbb{R}} \left(\rho\, v\, \frac{\partial v}{\partial t} + E_r\, \frac{\partial u}{\partial x}\, \frac{\partial}{\partial t} \left(\frac{\partial u}{\partial x} \right) \right) \mathrm{d}x}_{\Delta_1}$$

$$+ \sum_{\ell=1}^{N} \underbrace{\int_{\mathbb{R}} \left(\sigma_\ell - E_{r\ell}\, \frac{\partial u}{\partial x} \right) \frac{\partial v}{\partial x}\, \mathrm{d}x}_{\Delta_2} = 0. \tag{17}$$

Eq. (14c) then yields

$$\sigma_\ell - E_{r\ell}\, \frac{\partial u}{\partial x} + \tau_{\sigma\ell}\, \frac{\partial}{\partial t} \left(\sigma_\ell - E_{r\ell}\, \frac{\partial u}{\partial x} \right) = E_{r\ell}\, (\tau_{\varepsilon\ell} - \tau_{\sigma\ell})\, \frac{\partial v}{\partial x}, \tag{18}$$

and thus

$$\frac{\partial v}{\partial x} = \frac{1}{E_{r\ell}\, (\tau_{\varepsilon\ell} - \tau_{\sigma\ell})} \left(\sigma_\ell - E_{r\ell}\, \frac{\partial u}{\partial x} + \tau_{\sigma\ell}\, \frac{\partial}{\partial t} \left(\sigma_\ell - E_{r\ell}\, \frac{\partial u}{\partial x} \right) \right). \tag{19}$$

Injecting eq. (19) into Δ_2 in eq. (17) and using straightforward algebra recovers eq. (13).

An important remark follows from Property 1: if $\tau_{\varepsilon\ell} > \tau_{\sigma\ell} > 0$ $\forall \ell$ then $\mathcal{E}$ in eq. (11) is a definite-positive quadratic form, and

$$\frac{\mathrm{d}\mathcal{E}}{\mathrm{d}t} < 0\,. \tag{20}$$

The condition $\tau_{\varepsilon\ell} > \tau_{\sigma\ell} > 0$ $\forall \ell$ is therefore a sufficient condition to obtain a decreasing total energy. It is worth mentioning that we have not shown that it is necessary in the mathematical sense because we cannot exclude that there can be cases in which the sum in eq. (13) remains positive even if some of the coefficients are negative. In higher spatial dimensions a similar energy analysis can be performed; computations are slightly more involved but the conclusion is unchanged (Bécache *et al.* 2004). Let us also mention that a standard linear solid in which $\tau_\sigma > \tau_\varepsilon$ instead of $\tau_\varepsilon > \tau_\sigma$ is sometimes called an anti-Zener body (Mainardi 2010). Such a body is non-causal, that is, its energy in the unrelaxed state is smaller than its energy in the relaxed state; This means that one of its two springs has a negative modulus.

2.2 Linear optimization

The relaxation function of the generalized Zener model involves $2N + 1$ parameters. The relaxed modulus E_r can be deduced from the phase velocity at zero frequency (eq. 9). Determination of the relaxation times $\tau_{\varepsilon\ell}$ and $\tau_{\sigma\ell}$ is more involved. The most classical approach originates in the work of Emmerich & Korn (1987), which we are going to briefly recall. For the sake of simplicity, we perform the calculations with new unknowns:

$$\kappa_\ell = \frac{1}{N} \left(\frac{\tau_{\varepsilon\ell}}{\tau_{\sigma\ell}} - 1 \right), \qquad \theta_\ell = \frac{1}{\tau_{\sigma\ell}}, \tag{21}$$

from which the original coefficients can be recovered using

$$\tau_{\varepsilon\ell} = \frac{1 + N\, \kappa_\ell}{\theta_\ell}, \qquad \tau_{\sigma\ell} = \frac{1}{\theta_\ell}. \tag{22}$$

These coefficients will also be useful in future sections because imposing $\tau_{\varepsilon\ell} > \tau_{\sigma\ell} > 0$ $\forall \ell$ simply means imposing $\kappa_\ell > 0$ and $\theta_\ell > 0$. The viscoelasticity modulus $M = \mathcal{F}(\frac{\partial \Psi}{\partial t})$, where $\mathcal{F}$ is the Fourier transform in time, is deduced from (7):

$$M(\omega) = E_r \left(1 + i\, \omega \sum_{\ell=1}^{N} \frac{\kappa_\ell}{\theta_\ell + i\, \omega} \right). \tag{23}$$

We determine the relaxed modulus E_r so that the phase velocity of the Zener model equals c_r at a given reference frequency f_r: $c(\omega_r) \equiv c_r$, with $\omega_r = 2\,\pi\, f_r$. The wavenumber is

$$k = \left(\frac{\rho\, \omega^2}{M(\omega)} \right)^{1/2} = \sqrt{\frac{\rho}{E_r}}\, \omega \left(1 + \sum_{\ell=1}^{N} \frac{\kappa_\ell}{\theta_\ell + i\omega} \right)^{-1/2}. \tag{24}$$

Denoting $\Re(k)$ the real part of k, the phase velocity is

$$c(\omega) = \frac{\omega}{\Re(k)} = \sqrt{\frac{E_r}{\rho}}\, \mathcal{F}(\omega), \tag{25}$$

with

$$\mathcal{F}(\omega) = 1/\Re \left\{ \left(1 + \sum_{\ell=1}^{N} \frac{\kappa_\ell}{\theta_\ell + i\omega} \right)^{-1/2} \right\}. \tag{26}$$

The requirement $c(\omega_r) \equiv c_r$ is then reached by taking

$$E_r = \frac{\rho\, c_r^2}{\mathcal{F}(\omega_r)}. \tag{27}$$

The quality factor Q is defined as the ratio of the imaginary part to the real part of M. Its reciprocal writes

$$Q^{-1}(\omega) = \frac{\displaystyle\sum_{\ell=1}^{N} \frac{\omega\, \theta_\ell\, \kappa_\ell}{\theta_\ell^2 + \omega^2}}{\displaystyle 1 + \sum_{\ell=1}^{N} \frac{\omega^2\, \kappa_\ell}{\theta_\ell^2 + \omega^2}}. \tag{28}$$

The main idea in Emmerich & Korn (1987) is then to minimize the distance between $Q^{-1}(\omega)$ and a given $Q_{\mathrm{ref}}^{-1}(\omega)$ in a band of angular frequencies $[\omega_{\min}, \omega_{\max}]$, which of course depends on the spectrum of the source under study, that is, on the frequency content of the data or experiment that one wants to model. For this purpose in Emmerich & Korn (1987) the relaxation frequencies θ_ℓ are evenly distributed over N points in logarithmic scale

$$\theta_\ell = \omega_{\min} \left(\frac{\omega_{\max}}{\omega_{\min}} \right)^{\frac{\ell-1}{N-1}}, \qquad \ell = 1, \ldots, N, \tag{29}$$

in the band of angular frequencies $[\omega_{\min}, \omega_{\max}]$. The coefficients κ_ℓ are then obtained by identifying the reciprocal of the quality factor (28) with a given $Q_{\mathrm{ref}}^{-1}(\omega)$. From eq. (28), one obtains the set of equations

$$\sum_{\ell=1}^{N} \frac{\omega_k \left(\theta_\ell - \omega_k\, Q_{\mathrm{ref}}^{-1}(\omega_k) \right)}{\theta_\ell^2 + \omega_k^2}\, \kappa_\ell = Q_{\mathrm{ref}}^{-1}(\omega_k), \quad k = 1, \ldots, K, \tag{30}$$

where the angular frequencies are distributed linearly on a logarithmic scale of K points

$$\omega_k = \omega_{\min} \left(\frac{\omega_{\max}}{\omega_{\min}} \right)^{\frac{k-1}{K-1}}, \quad k = 1, \ldots, K. \tag{31}$$

If $K = N$, one obtains a square linear system. The choice $K = 2N - 1$ is often made (Groby & Tsogka 2006), leading to an overdetermined system. Nothing in this method prevents from obtaining negative values $\kappa_\ell < 0$ when solving eq. (30), yielding $\tau_{\varepsilon\ell} < \tau_{\sigma\ell}$ via eq. (22), which is unsuitable both physically and mathematically as mentioned in Property 1. In practice, this can (and does) happen in particular when N is large, typically $N \geq 5$ or so, as we will see in Section 3.

Emmerich & Korn (1987) suggest that ω_k/ω_{k-1} should be chosen equal to about 10 in practice, however, such a choice is not always convenient or even possible in all situations because it means that when the number of mechanisms N is large then the total bandwidth should be extremely large (10^{N-1}), while in some situations in order to improve accuracy one wants to have standard linear solids that are located much closer to one another and be able to increase N to improve the accuracy of the approximation without having to use a large distance $\omega_k/\omega_{k-1} \simeq 10$ between two mechanisms. Also, from a mathematical point of view imposing that ω_k/ω_{k-1} be around 10 does not automatically ensure the positivity of the coefficients obtained; if positivity is not imposed explicitly as a constraint, there is no particular mathematical reason for it to be ensured in practice.

2.3 Optimization with constraints

Let us introduce the objective function

$$\mathcal{J}\left(\{\kappa_\ell, \theta_\ell\};\, N,\, K\right) = \sum_{k=1}^{K} \left(\sum_{\ell=1}^{N} \frac{\omega_k\, Q_{\text{ref}}(\omega_k)\left(\theta_\ell - \omega_k\, Q_{\text{ref}}^{-1}(\omega_k)\right)}{\theta_\ell^2 + \omega_k^2}\, \kappa_\ell - 1 \right)^2 . \tag{32}$$

Minimizing eq. (32) with respect to the κ_ℓ only recovers the Emmerich & Korn (1987) expressions (30). Here we propose to minimize eq. (32) in terms of both variables, imposing decay of total energy with time as in eq. (20), that is, imposing $\tau_{\varepsilon\ell} > \tau_{\sigma\ell} > 0\ \forall \ell$, which in turn means imposing the positivity constraints $\kappa_\ell > 0$ and $\theta_\ell > 0$. We introduce the additional constraint $\theta_\ell < \theta_{\max}$ in order to avoid too large values of θ_ℓ, which could result in stiff equations and thus in numerical instabilities in the time-marching of memory variables (Blanc *et al.* 2013).

These $3N$ constraints are relaxed by setting $\kappa_\ell = \kappa_\ell'^2$ and $\theta_\ell = \theta_\ell'^2$ and solving the following problem with only N constraints:

$$\min_{\{\kappa_\ell', \theta_\ell'\}} \mathcal{J}\left(\{\kappa_\ell'^2, \theta_\ell'^2\};\, N,\, K\right), \quad \text{with } \theta_\ell'^2 \leq \theta_{\max} \text{ for } \ell = 1, \ldots, N. \tag{33}$$

As problem (33) is nonlinear and non-quadratic with respect to abscissas θ_ℓ', to solve it we resort to the *SolvOpt* algorithm (Kappel & Kuntsevich 2000; Rekik & Brenner 2011), which is based on the iterative Shor's method (Shor 1985). As starting values for that iterative optimization technique we use the values $\kappa_\ell'^{(0)}$ and $\theta_\ell'^{(0)}$ obtained based on the Emmerich & Korn (1987) procedure (29)–(30) (even if some of them are negative, since our nonlinear optimization procedure will then ensure positivity).

To determine the $2N$ coefficients κ_ℓ' and θ_ℓ', the minimal number of relaxation frequencies is $K = 2N$. In practice, we have observed better accuracy when taking the larger value $K = 4N$. The angular frequencies ω_k are chosen evenly spaced in logarithmic scale over the optimization band $[\omega_{\min}, \omega_{\max}]$, as in the linear approach, and thus eq. (31) remains valid.

3 NUMERICAL VALIDATION OF THE APPROACH

3.1 Approximation and coefficients obtained

Let us illustrate the improved accuracy of the approximation obtained as well as the fact that the coefficients κ_ℓ and θ_ℓ obtained are always positive. To do so, let us perform several numerical experiments with different numbers of relaxation mechanisms N. Optimization is performed over $K = 4N$ angular frequencies ω_k (31), as explained in Section 2.3. We set the lower and upper bounds of the angular frequency range to

$$\omega_{\min} = \omega_c/10, \qquad \omega_{\max} = 10\,\omega_c, \tag{34}$$

where $\omega_c = 2\pi f_c$ is the dominant angular frequency of the source.

We first take a constant quality factor $Q_{\text{ref}} = 5$ and a dominant frequency of the source $f_c = 1.5$ Hz. Fig. 1 shows the exact value of Q_{ref}^{-1} and the numerical approximation (28) obtained using optimization based on $N = 2$ to $N = 7$ relaxation mechanisms in the angular frequency band $[\omega_{\min}, \omega_{\max}]$. In the interval of optimization, the linear approach of Emmerich & Korn (1987) yields oscillations whereas the nonlinear optimization with constraints gives a curve that is almost constant and fits the exact value very well.

The numerical values of the coefficients κ_ℓ and θ_ℓ obtained with $N = 6$ are given in Table 1. The κ_5 weight is negative in the linear Emmerich & Korn (1987) procedure, which could lead to unstable results if used in a numerical simulation, as illustrated in Section 4, because the set of coefficients does not necessarily honour the constraint of decay of energy with time of eq. (20).

To evaluate the effect of the optimization more quantitatively, it is useful to introduce the following quantities:

(1) u_{ex}^{Q} the unknown exact solution of the model with a truly constant Q_{ref} factor, which obeys a fractional-order partial differential equation (Carcione *et al.* 2002);

(2) u_{ex}^{Z} the unknown exact solution of the Zener model approximation of that constant Q_{ref}, which obeys a standard partial differential equation with memory variables;

(3) u_{num}^{Z} the known numerical solution of the partial differential equation with memory variables, obtained using the numerical scheme selected to solve the wave eq. (1).

The triangular inequality then yields the total error

$$\varepsilon_t = ||u_{\text{ex}}^{Q} - u_{\text{num}}^{Z}|| \leq \underbrace{||u_{\text{ex}}^{Q} - u_{\text{ex}}^{Z}||}_{\varepsilon_m} + \underbrace{||u_{\text{ex}}^{Z} - u_{\text{num}}^{Z}||}_{\varepsilon_n}, \tag{35}$$

in which ε_n is the numerical error due to discretization. That error depends on the numerical scheme chosen to discretize the wave

Table 1. Coefficients of eq. (21) obtained when resorting to (a) the method of Emmerich & Korn (1987) and (b) nonlinear optimization with constraints, for a quality factor $Q = 5$ modelled with $N = 6$ relaxation mechanisms. One can note that one gets a negative weight for $\ell = 5$ in the case of the linear approach of Emmerich & Korn (1987).

(a)	κ_ℓ	θ_ℓ	(b)	κ_ℓ	θ_ℓ
$\ell = 1$	$+2.81\,10^{-1}$	$1.50\,10^{-1}$	$\ell = 1$	$+2.93\,10^{-1}$	$9.18\,10^{-2}$
$\ell = 2$	$+1.29\,10^{-1}$	$3.77\,10^{-1}$	$\ell = 2$	$+1.92\,10^{-1}$	$3.57\,10^{-1}$
$\ell = 3$	$+1.07\,10^{-1}$	$9.46\,10^{-1}$	$\ell = 3$	$+2.00\,10^{-1}$	$1.01\,10^{0}$
$\ell = 4$	$+3.54\,10^{-1}$	$2.38\,10^{0}$	$\ell = 4$	$+2.26\,10^{-1}$	$2.75\,10^{0}$
$\ell = 5$	$-1.00\,10^{-1}$	$5.97\,10^{0}$	$\ell = 5$	$+2.84\,10^{-1}$	$7.75\,10^{0}$
$\ell = 6$	$+7.85\,10^{-1}$	$1.50\,10^{1}$	$\ell = 6$	$+7.39\,10^{-1}$	$3.38\,10^{1}$

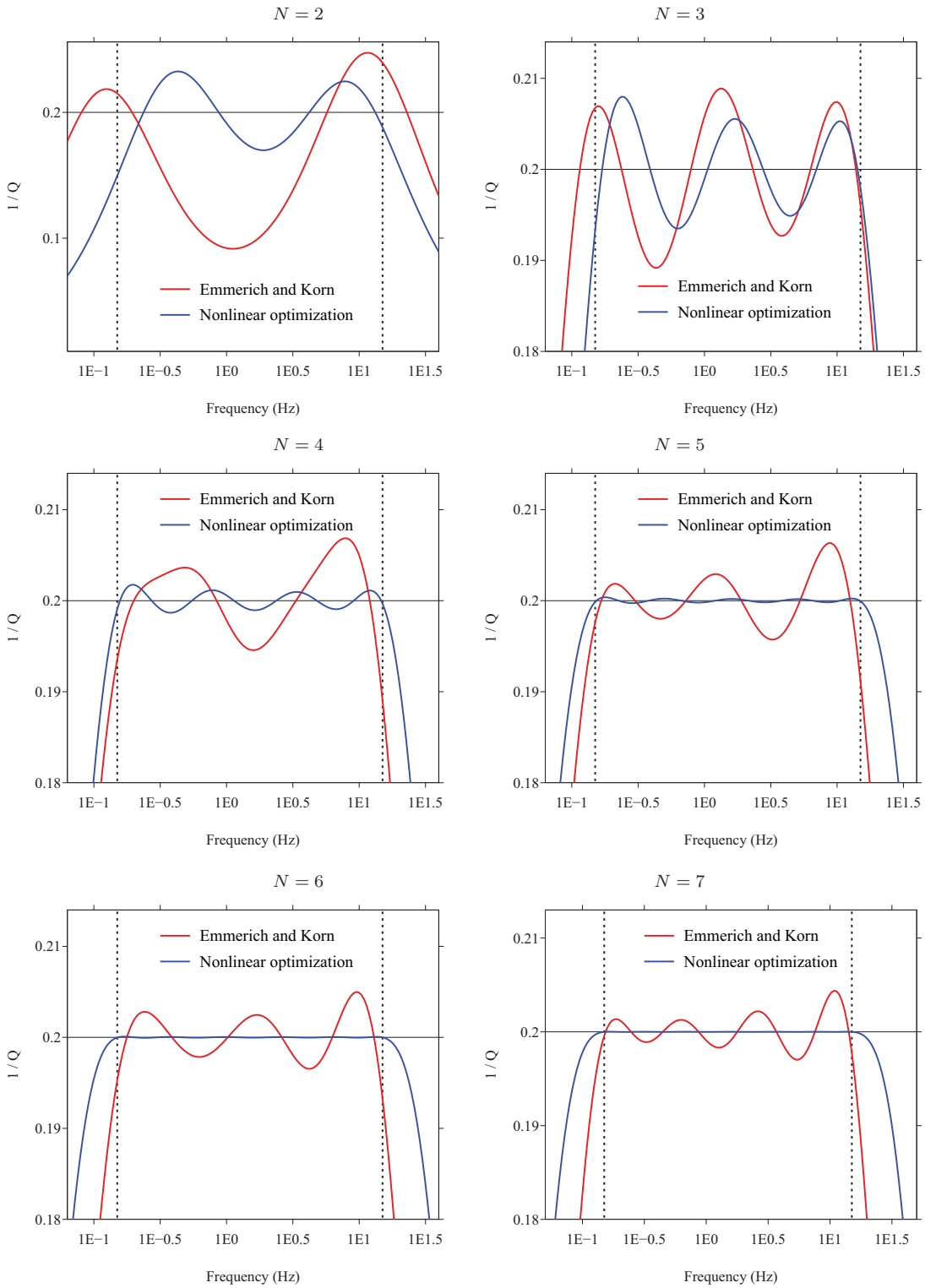

Figure 1. Reciprocal of the quality factor when using a Zener approximation with $N = 2$ (upper left) to $N = 7$ (bottom right) relaxation mechanisms based on the linear approach of Emmerich & Korn (1987) (red line) and nonlinear optimization (blue line). The vertical dotted lines denote the interval of optimization $[f_{\min}, f_{\max}]$. The horizontal axis is in logarithmic scale.

equation and can be analysed using standard numerical analysis tools (which is classical in the literature and out of the scope of this paper). Here we focus on the physical modelling error ε_m, which is related to the quality of the optimization process:

$$\varepsilon_m \sim ||Q_{\text{ref}}^{-1}(\omega) - Q^{-1}(\omega)||_2 \tag{36}$$

in the interval of optimization. Values of ε_m for $Q_{\text{ref}} = 5$ and various values of the number of relaxation mechanisms N are given in Table 2. With $N = 6$ we get $\varepsilon_m = 1.21$ per cent in the case of Emmerich & Korn (1987) and $\varepsilon_m = 0.0156$ per cent in the case of nonlinear optimization with constraints. When making the number of relaxation mechanisms N vary from 2 to 6 we get the relative

Table 2. Relative physical modelling error (36) in the case of the linear approach of Emmerich & Korn (1987) and in the case of nonlinear optimization, when making the number of relaxation mechanisms vary from $N = 2$ to $N = 7$. Nonlinear optimization always leads to more accurate results.

N	Linear optimization	Nonlinear optimization
2	$\varepsilon_m = 34.2$ per cent	$\varepsilon_m = 10.7$ per cent
3	$\varepsilon_m = 3.08$ per cent	$\varepsilon_m = 2.17$ per cent
4	$\varepsilon_m = 1.99$ per cent	$\varepsilon_m = 0.42$ per cent
5	$\varepsilon_m = 1.49$ per cent	$\varepsilon_m = 0.08$ per cent
6	$\varepsilon_m = 1.21$ per cent	$\varepsilon_m = 0.0156$ per cent
7	$\varepsilon_m = 0.86$ per cent	$\varepsilon_m = 0.0030$ per cent

errors of Table 2. For $N = 2$ we get improvement, for $N = 3$ the difference is less pronounced but then for $N \geq 4$ the difference becomes significant again. These errors are displayed in Fig. 2. When nonlinear optimization is used the error keeps decaying in a very significant fashion, while in the case of the linear approach of Emmerich & Korn (1987) it does not.

Let us illustrate the effect of the physical modelling error ε_m on time-domain results of 1-D wave propagation. The only linear and causal model of viscoelasticity having a constant quality factor Q was introduced by Kjartansson (1979). We compare the exact solution for the velocity obtained with that truly constant Q model (u_{ex}^{Q}), which is the reference solution, with the exact solution obtained with the Zener model approximation of that constant Q (u_{ex}^{Z}). These exact solutions are computed semi-analytically based on Fourier synthesis. Details about how to compute the solution in the case of the Zener model can be found in appendix D of Favrie *et al.* (2015). We consider a homogeneous 1-D domain extending from $x_{\min} = -5000$ m to $x_{\max} = +5000$ m. The constant density is $\rho = 2000$ kg m^{-3}, the reference frequency is $f_r = 1.5$ Hz and the celerity at that frequency is $c_r = 2000$ m s^{-1}. The source is a Ricker wavelet force with dominant frequency $f_c = f_r$ located at $x = 0$. Fig. 3 shows the time history of velocity recorded at two receivers r_1 and r_2 located in $x_{r1} = 1000$ m and $x_{r2} = 3000$ m, respectively. Since dispersion is a cumulative effect, as expected the errors are more pronounced after a larger distance of propagation. In the case of linear optimization a visible error remains even when using $N = 4$ relaxation mechanisms; on the contrary an almost perfect agreement is obtained if nonlinear optimization is used with $N = 4$ relaxation mechanisms.

3.2 Dispersion curves

The dispersion of the Kjartansson (1979) model is

$$c(\omega) = c_r \left(\frac{\omega}{\omega_r} \right)^{\frac{1}{\pi} \arctan \frac{1}{Q}} . \tag{37}$$

An important remark from eq. (37) is that one can see that the phase velocity of this model is not bounded at infinite frequency, contrary to that of the Zener model. A consequence is that in such a model the reference velocity needs to be given at a finite frequency, it cannot be an unrelaxed value at infinite frequency as in the Zener model.

Fig. 4 compares the phase velocities of the Zener model (obtained with the two methods of optimization) with the reference phase velocity of the Kjartansson (1979) model. The parameters used are $c_r = 2000$ m s^{-1}, $f_r = 1.5$ Hz and $Q = 5$. The optimization is performed in the frequency range $[f_c/10, 10f_c]$, where $f_c = f_r$. The choice $f_r = f_c$ is natural, it amounts to choosing the dominant frequency of the source as the reference frequency. For $N = 2$ relaxation mechanisms, the linear optimization largely overestimates the phase velocity of the Zener model (a), whereas nonlinear optimization underestimates the phase velocity of the Zener model at $f > f_c$ (b). For $N = 4$, a good agreement is observed between the Zener model and the Kjartansson (1979) model if nonlinear optimization is used (b).

3.3 Case of a non-constant Q factor

We now select a varying quality factor (e.g. Dahlen & Tromp 1998)

$$Q(\omega) = Q_0 \left(\frac{\omega}{\omega_0} \right)^{-\alpha} , \tag{38}$$

with $Q_0 = 20$, $f_0 = 1.5$ Hz, $\omega_0 = 2\pi f_0$ and $\alpha = 0.1$. Since the exponent is negative, this leads to $1/Q$ increasing with frequency, that is, to higher attenuation at higher frequency. As in Fig. 1 for the case of a constant Q, in Fig. 5 we show the exact value of $Q^{-1}(\omega)$ and the numerical approximation (28) obtained using optimization

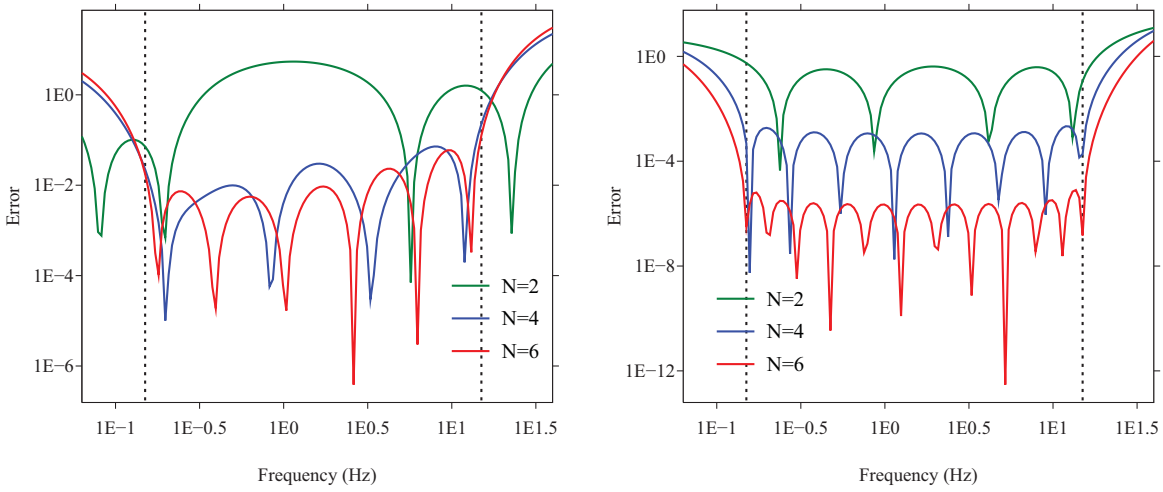

Figure 2. Value of the objective function of eq. (32) as a function of frequency, using a Zener approximation with $N = 2$ (green curve), $N = 4$ (blue curve) and $N = 6$ (red curve) relaxation mechanisms, with the linear approach of Emmerich & Korn (1987) (left) and with nonlinear optimization (right). The vertical dotted lines denote the interval of optimization $[f_{\min}, f_{\max}]$. Both axes are in logarithmic scale. Note that the vertical logarithmic scale has about twice more decades on the right figure than on the left figure, that is, the error levels are very significantly different.

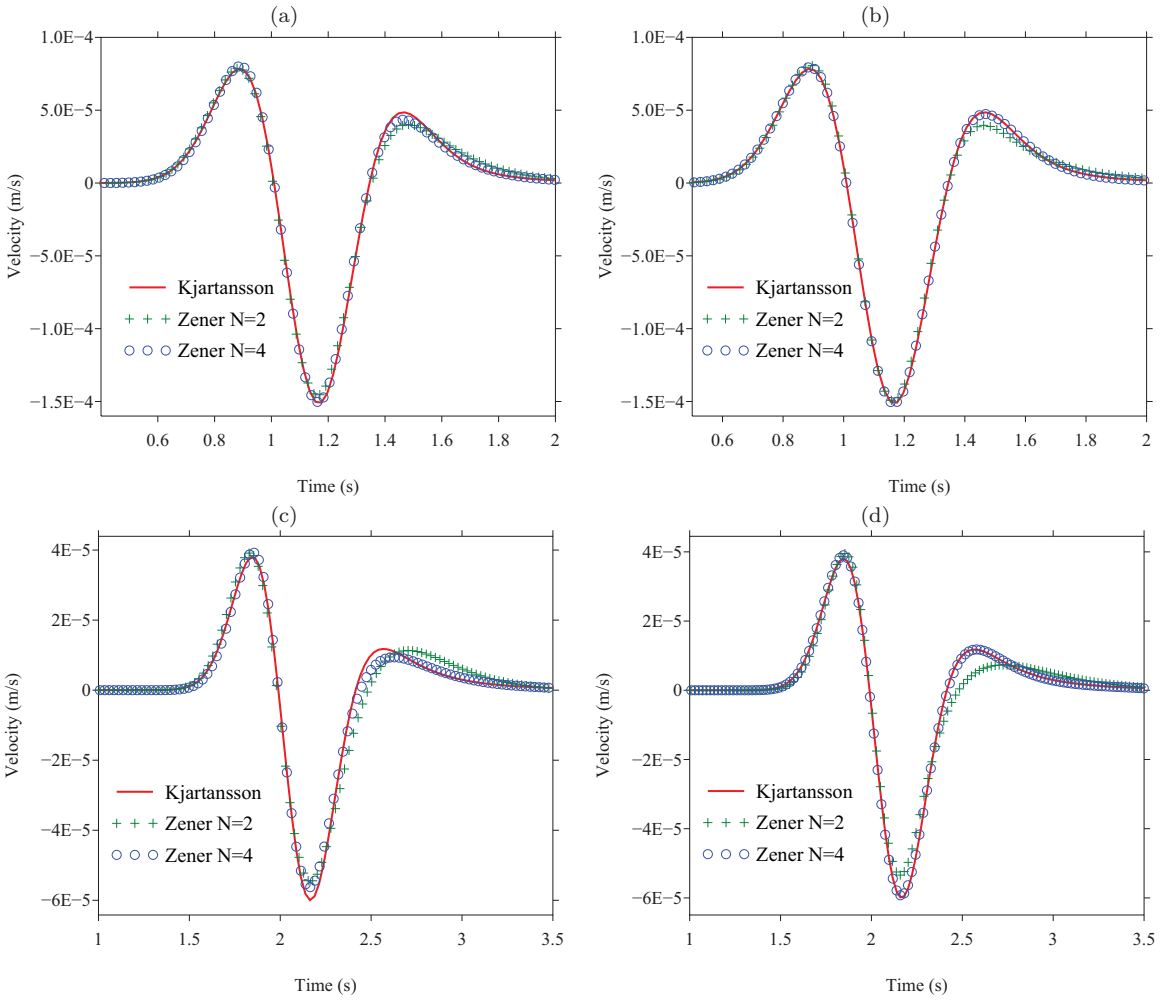

Figure 3. Time history of velocity recorded at receivers r_1 (top) and r_2 (bottom), comparing the exact solution of the Kjartansson (1979) model (red curve) to the exact solution of the Zener model obtained with linear optimization (left row) and with nonlinear optimization (right row), for $N = 2$ (green curve) and $N = 4$ (blue curve) relaxation mechanisms.

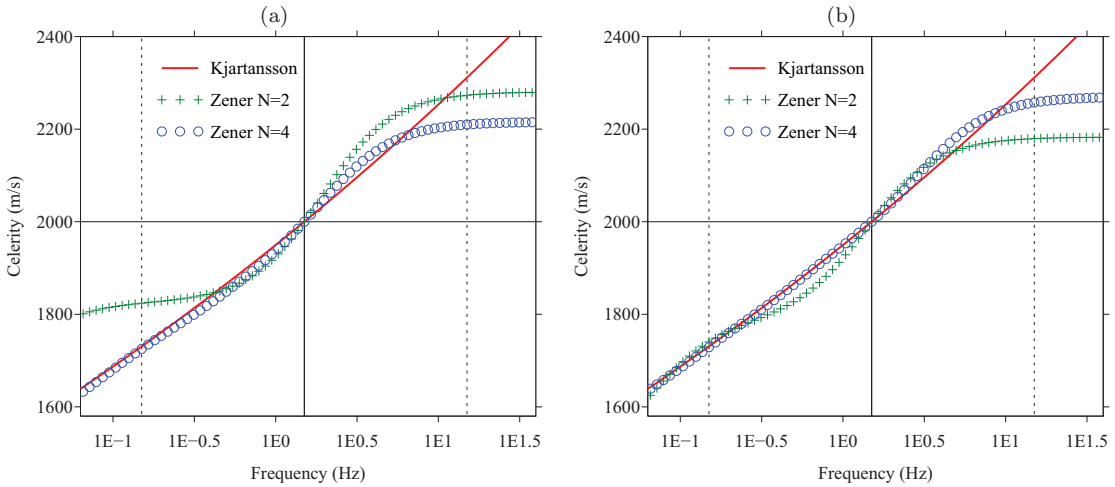

Figure 4. Dispersion curves obtained with linear optimization (a) and with nonlinear optimization (b) in the case of the Kjartansson (1979) model (red curve), the Zener model with $N = 2$ relaxation mechanisms (green curve) and the Zener model with $N = 4$ relaxation mechanisms (blue curve). The solid vertical line indicates the reference frequency $f_r = 1.5$ Hz. The vertical dotted lines denote the frequency range $[f_c/10, 10f_c]$ in which optimization is performed. The horizontal line denotes the celerity $c(f_r) = 2000$ m s^{-1} on which all the models are locked, that is, where they are by definition identical.

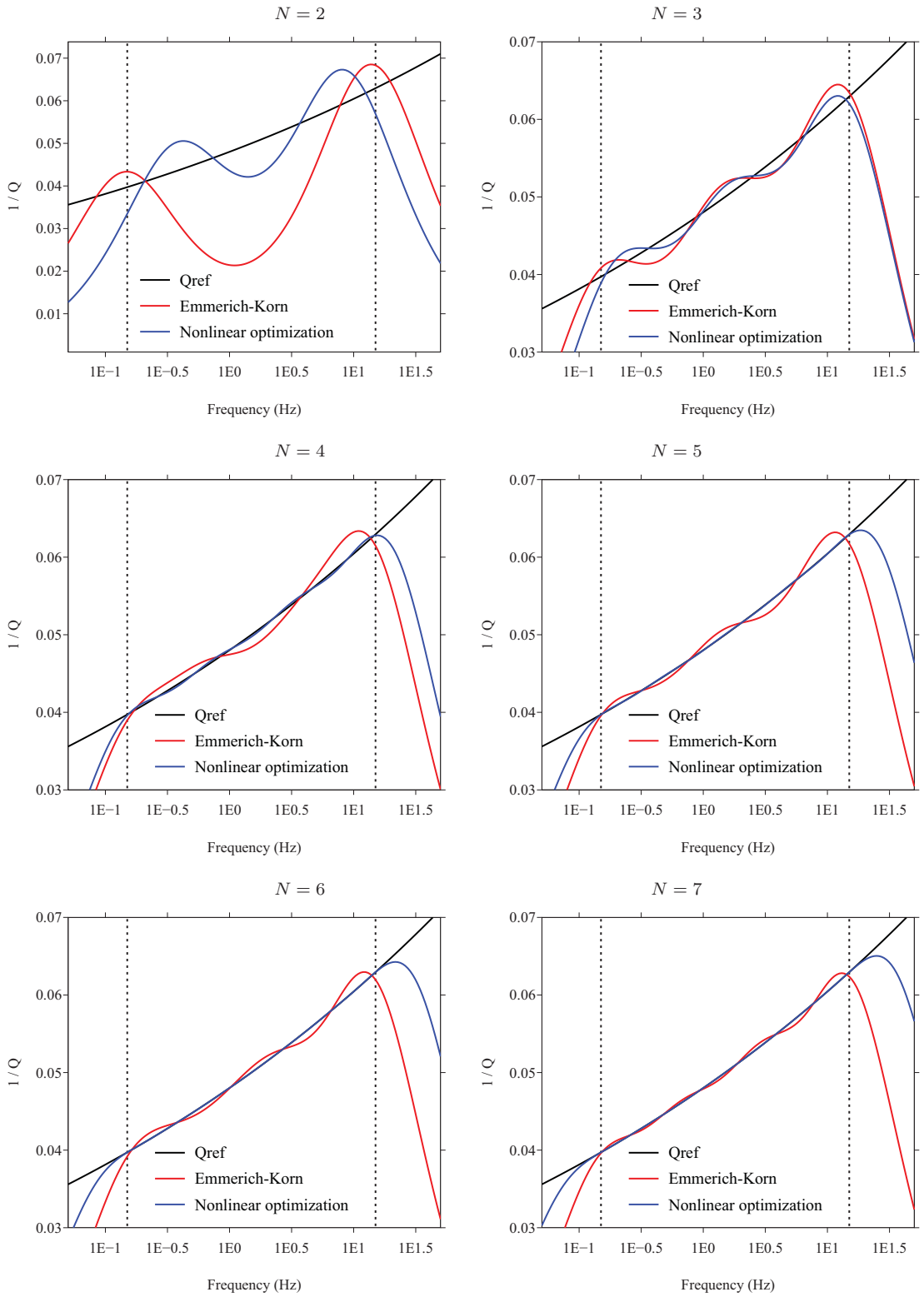

Figure 5. Same as Fig. 1 but for a non-constant quality factor $Q(\omega) = Q_0(\frac{\omega}{\omega_0})^{-\alpha}$, with $Q_0 = 20, f_0 = 1.5$ Hz, $\omega_0 = 2\pi f_0$ and $\alpha = 0.1$.

based on $N = 2$ to $N = 7$ relaxation mechanisms in the angular frequency band $[\omega_{\min}, \omega_{\max}]$. In the interval of optimization, the linear approach of Emmerich & Korn (1987) yields more oscillations than the result obtained with the nonlinear optimization approach with constraints.

4 VALIDATION FOR 3-D WAVE PROPAGATION IN A LAYER-CAKE MEDIUM

In Section 3, we have illustrated how the choice of the relaxation times in the Zener model affects the accuracy of time domain

Table 3. Layered viscoelastic model used in the validation examples of Section 4. The L_i, $i = 1...3$ refer to the sedimentary layers and B to the surrounding bedrock. h stands for layer thickness, V_S, V_P, Q_S, Q_P stand for S and P seismic velocities and quality factors and ρ stands for mass density.

	h (m)	V_P (m s^{-1})	V_S (m s^{-1})	ρ (kg m^{-3})	Q_P	Q_S
L_1	17.3	1500	200	2100	40	20
L_2	72.5	1800	350	2100	70	35
L_3	115.6	2500	650	2200	130	65
B	–	4500	2600	2600	∞	∞

solutions of the viscoelastic wave equation in a homogeneous medium. Let us now turn to a more realistic example of 3-D propagation in a tabular medium with strong contrasts in viscoelastic properties. For this purpose, we consider the viscoelastic medium described in Table 3. The elastic version of this model was used by Chaljub *et al.* (2015) to study the accuracy of numerical predictions of earthquake ground motion in the Mygdonian basin in northern Greece. The model consists in a stiff elastic half-space overlaid by three sedimentary layers with lower seismic impedances, which cause large amplification of earthquake ground motion (the so-called site effects). The shear quality factors in the sediments are approximated by a simple, frequency-independent scaling from the shear velocities, $Q_S = V_S/10$, as done in site effect studies in the (general) situation in which no other constraints on intrinsic attenuation can be used; the P quality factors are defined by $Q_P = 2\,Q_S$.

The viscoelastic medium is excited by a double-couple point source with a vertical strike-slip focal mechanism. The source is set at 80 m depth in order to excite high-frequency surface waves propagating within the sedimentary layers. In realistic cases, those surface waves would be generated locally by conversion of incoming body waves at strong lateral heterogeneities located close to the surface (for example at basin edges) and would contribute to the amplification and duration lengthening of ground motion. The source time function is a step with a rising time $\tau = 0.1$ s. It radiates a far-field displacement with a flat spectrum up to 1 Hz and gradual decay between 1 Hz and 10 Hz.

The computations are performed with the AXITRA software package (Coutant 1989), which implements a discrete wavenumber method (Bouchon 1981). As in Section 3, we compute the solutions for the truly constant Q model of Kjartansson (1979), and for Zener models with different numbers of mechanisms, whose relaxation times are obtained based either on linear or nonlinear optimization. We use a reference frequency $f_r = 1$ Hz and solve for the relaxation times of the Zener models in the two-decade frequency range $[f_r/10, 10f_r]$.

Fig. 6(a) shows 25 s of horizontal ground acceleration computed at 4-km epicentral distance for the truly constant Q model (black line) and for the Zener models with $N = 3$ mechanisms and relaxation times inverted using linear (red line) or nonlinear (blue line) optimization. Note that the overall agreement between traces is quite good even for late surface waves, mainly because anchoring the dispersion of the different models at the reference frequency has the effect of minimizing phase misfit. The differences in amplitude can be analysed by comparing Fourier amplitude spectra (Fig. 6b). The solutions of the Zener models either underpredict (around $f_r = 1$ Hz) or overpredict (around 2.5 Hz) the amplitude of the constant Q solution, as expected from Fig. 1. The maximum differences reach about 10 per cent around the dominant, reference frequency. A more precise measure is to quantify time–frequency misfits, or goodness-of-fit scores as proposed by Kristeková *et al.* (2009). When applied to very similar signals, the envelope (resp. phase) misfits or goodness-of-fit scores mainly reflect the differences or similarities in amplitude (resp. phase) between the traces. In Fig. 6c, we plot the envelope goodness-of-fit scores as a function of time. Each goodness-of-fit value $g(t)$ corresponds to a frequency average over the range [0.2–5 Hz] of the envelope time–frequency misfit, $m(t)$,

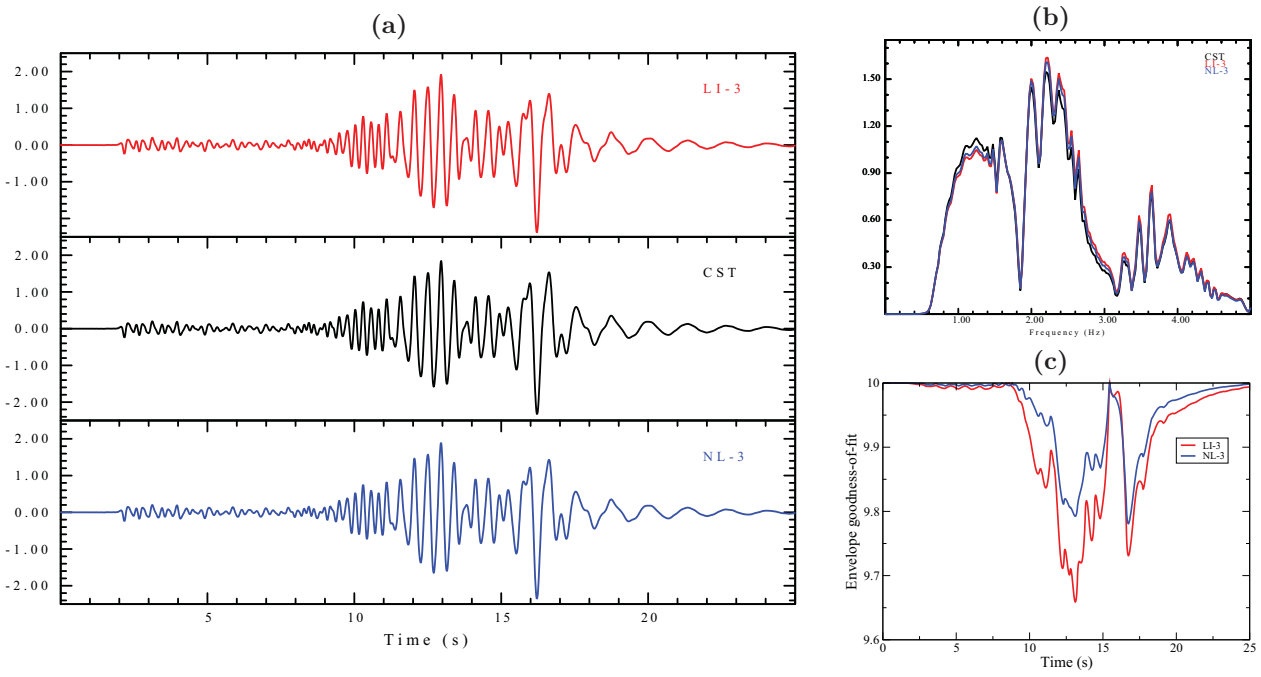

Figure 6. (a) Time evolution of horizontal ground acceleration in cm s^{-2} at 4-km epicentral distance for a constant Q model (black line) and for the Zener model with $N = 3$ relaxation mechanisms obtained based on linear (red) or nonlinear (blue) optimization. (b) Corresponding Fourier amplitude spectra. (c) Time evolution of the envelope goodness-of-fit with respect to the reference solution of the constant Q model.

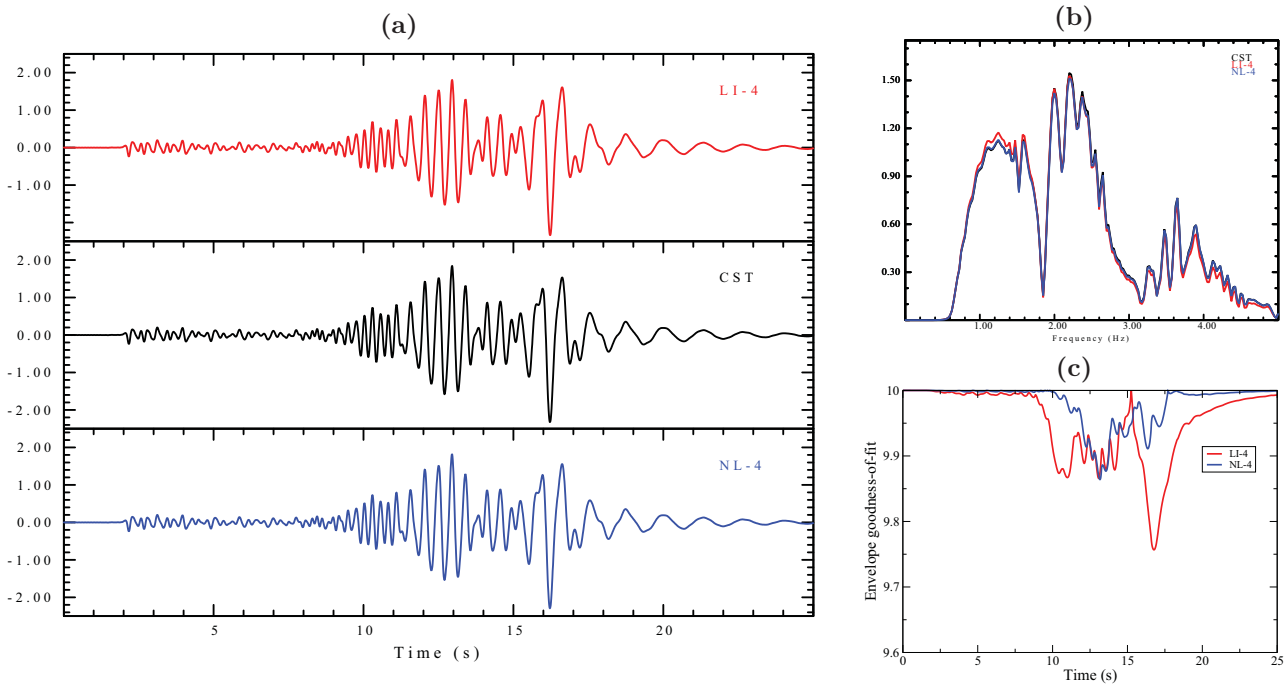

Figure 7. Same as Fig. 6 but using $N = 4$ relaxation mechanisms.

Table 4. Average envelope (E) and phase (P) goodness-of-fits of horizontal ground acceleration for the Zener viscoelastic models with relaxation times obtained based on linear and nonlinear optimization.

N	Linear optimization	Nonlinear optimization
3	$E = 9.36$ $P = 9.76$	$E = 9.57$ $P = 9.82$
4	$E = 9.64$ $P = 9.88$	$E = 9.84$ $P = 9.93$
6	$E = 9.83$ $P = 9.90$	$E = 9.90$ $P = 9.95$
10	$E = 9.89$ $P = 9.94$	$E = 9.90$ $P = 9.96$

which is further scaled to a score between 0 (no fit) and 10 (perfect fit) based on the nonlinear mapping $g(t) = 10 \exp[-m(t)]$. The figure shows that nonlinear optimization of the relaxation times in the Zener model always yields a more accurate approximation of the constant Q model, even for $N = 3$.

From the analysis of Fig. 1, we expect that this trend should be even more pronounced if we increase the number of relaxation mechanisms. This is indeed the case for the results obtained with $N = 4$ relaxation mechanisms, which are shown in Fig. 7: the improvement of the prediction of the Zener model with nonlinear optimized relaxation times is clearly seen, both in the Fourier amplitude spectra and in the time evolution of the goodness-of-fit scores.

The global (i.e. time- and frequency-averaged) phase and envelope goodness-of-fit scores are given in Table 4 for $N = 3$, 4, 6, 10. They confirm (i) that the phase misfits are negligible after the adjustment of the physical dispersion at the reference frequency and (ii) that for $N \geq 4$ mechanisms, the solution of the Zener model with nonlinear optimization of the relaxation times matches the solution of the constant Q model almost perfectly, whereas $N \geq 6$ mechanisms are needed to obtain the same accuracy when the relaxation times are computed based on classical linear optimization.

5 CONCLUSIONS AND FUTURE WORK

We have developed a nonlinear methodology based on the *SolvOpt* algorithm of Kappel & Kuntsevich (2000) to optimize the coefficients of the Zener viscoelastic model that is significantly more accurate, for a given number of relaxation mechanisms, than the classical linear approach of Emmerich & Korn (1987), or equivalently that can reach similar accuracy for a smaller number of relaxation mechanisms. The approach also ensures the positivity of the coefficients obtained, thus always honouring the constraint of decay of total energy with time and resulting in a stable algorithm when used in viscoelasticity applications, even in the case of very strong attenuation. We have illustrated the improved accuracy obtained based on several numerical experiments, first for a simple wave pulse propagating in a homogeneous 1-D medium with strong attenuation and then for a more realistic 3-D wavefield propagating in a stratified medium with large contrasts in seismic velocities and attenuation.

In future work, we plan to extend our applications of this technique to fitting a non-constant $Q(\omega)$ profile; such an extension could be useful, for example, for non-destructive testing or in ocean acoustics. Since the approach used is not specific to the Zener model, we also plan to apply it to other, more complex or less classical models, which may even involve fractional derivatives (e.g. Zhu & Carcione 2014); in viscoelasticity, one can think of the Andrade model (e.g. Ben Jazia *et al.* 2014), the fractional Kelvin–Voigt model (Caputo 1967) or the fractional Zener model (Nasholm & Holm 2013), and in poroelasticity of the widely used model based on the Biot–Johnson–Koplik–Dashen theory (e.g. Blanc *et al.* 2013).

Our SEISMIC_CPML finite-difference and SPECFEM spectral-element software packages are available open source at geodynamics.org; they both include our implementation of the *SolvOpt* technique presented in this paper.

ACKNOWLEDGEMENTS

The *SolvOpt* algorithm was developed by Franz Kappel and Alexei V. Kuntsevich in Kappel & Kuntsevich (2000). We thank Pierre Suquet for introducing us to the article of Rekik & Brenner (2011),

and Chang-Hua Zhang, Eric Rosenkrantz and Cédric Bellis for fruitful discussion. We thank the two reviewers Jozef Kristek and José M. Carcione for useful comments that improved the manuscript. Calculations were performed using the computing resources of the CIMENT infrastructure. Part of this work was funded by the Simone and Cino del Duca / Institut de France / French Academy of Sciences Foundation under grant #095164, by the European 'Mont-Blanc: European scalable and power efficient HPC platform based on low-power embedded technology' #288777 project of call FP7-ICT-2011-7 and by the European 'WAVES: Waves and Wave-Based Imaging in Virtual and experimental Environments' #641943 project of call H2020-MSCA-ITN-2014. ZX thanks the continuous support of Prof Liao Zhenpeng, the China Scholarship Council for financial support during his stay at LMA CNRS, and the NSF of the Heilongjiang Province of China under grant #LC201403.

REFERENCES

Asvadurov, S., Knizhnerman, L. & Pabon, J., 2004. Finite-difference modeling of viscoelastic materials with quality factors of arbitrary magnitude, *Geophysics,* **69**(3), 817–824.

Bécache, E., Ezziani, A. & Joly, P., 2004. A mixed finite element approach for viscoelastic wave propagation, *Comput. Geosci.,* **8,** 255–299.

Ben Jazia, A., Lombard, B. & Bellis, C., 2014. Wave propagation in a fractional viscoelastic Andrade medium: diffusive approximation and numerical modeling, *Wave Motion,* **51**(6), 994–1010.

Bielak, J., Karaoglu, H. & Taborda, R., 2011. Memory-efficient displacement-based internal friction for wave propagation simulation, *Geophysics,* **76**(6), T131–T145.

Blanc, E., Chiavassa, G. & Lombard, B., 2013. Biot-JKD model: simulation of 1D transient poroelastic waves with fractional derivatives, *J. Comput. Phys.,* **237,** 1–20.

Bouchon, M., 1981. A simple method to calculate Green's functions for elastic layered media, *Bull. seism. Soc. Am.,* **71,** 959–971.

Cao, D. & Yin, X., 2014. Equivalence relations of generalized rheological models for viscoelastic seismic-wave modeling, *Bull. seism. Soc. Am.,* **104**(1), 260–268.

Caputo, M., 1967. Linear models of dissipation whose *Q* is almost frequency independent: Part II, *Geophys. J. R. astr. Soc.,* **13,** 529–539.

Carcione, J.M., 1993. Seismic modeling in viscoelastic media, *Geophysics,* **58**(1), 110–120.

Carcione, J.M., 2001. *Wave Fields in Real Media: Wave Propagation in Anisotropic, Anelastic and Porous Media,* 1st edn, Elsevier Science.

Carcione, J.M., 2014. *Wave Fields in Real Media: Wave Propagation in Anisotropic, Anelastic, Porous and Electromagnetic media,* 3rd edn, Elsevier Science.

Carcione, J.M., Kosloff, D. & Kosloff, R., 1988a. Wave propagation simulation in a linear viscoelastic medium, *Geophys. J. Int.,* **95,** 597–611.

Carcione, J.M., Kosloff, D. & Kosloff, R., 1988b. Viscoacoustic wave propagation simulation in the Earth, *Geophysics,* **53**(6), 769–777.

Carcione, J.M., Cavallini, F., Mainardi, F. & Hanyga, A., 2002. Time-domain modeling of constant-*Q* seismic waves using fractional derivatives, *Pure appl. Geophys.,* **159,** 1719–1736.

Casula, G. & Carcione, J.M., 1992. Generalized mechanical model analogies of linear viscoelastic behaviour, *Bollettino di Geofisica Teorica ed Applicata,* **34**(136), 235–256.

Chaljub, E. *et al.*, 2015. 3-D numerical simulations of earthquake ground motion in sedimentary basins: testing accuracy through stringent models, *Geophys. J. Int.,* **201**(1), 90–111.

Coutant, O., 1989. Program of numerical simulation AXITRA, Tech. rep., LGIT, Université Joseph Fourier, Grenoble, France, (in French).

Dahlen, F.A. & Tromp, J., 1998. *Theoretical Global Seismology,* Princeton Univ. Press.

Day, S.M., 1998. Efficient simulation of constant *Q* using coarse-grained memory variables, *Bull. seism. Soc. Am.,* **88,** 1051–1062.

Day, S.M. & Bradley, C., 2001. Memory-efficient simulation of anelastic wave propagation, *Bull. seism. Soc. Am.,* **91,** 520–531.

Day, S.M. & Minster, J.B., 1984. Numerical simulation of attenuated wavefields using a Padé approximant method, *Geophys. J. R. astr. Soc.,* **78**(1), 105–118.

Dhemaied, A., Rejiba, F., Camerlynck, C., Bodet, L. & Guérin, R., 2011. Seismic-wave propagation modeling in viscoelastic media using the auxiliary differential equation method, *Bull. seism. Soc. Am.,* **101**(1), 413–420.

Emmerich, H. & Korn, M., 1987. Incorporation of attenuation into time-domain computations of seismic wave fields, *Geophysics,* **52,** 1252–1264.

Favrie, N., Lombard, B. & Payan, C., 2015. Fast and slow dynamics in a nonlinear elastic bar excited by longitudinal vibrations, *Wave Motion,* **56,** 221–238.

Graves, R.W. & Day, S.M., 2003. Stability and accuracy of coarse-grain viscoelastic simulations, *Bull. seism. Soc. Am.,* **93,** 283–300.

Groby, J.P. & Tsogka, C., 2006. A time domain method for modeling viscoacoustic wave propagation, *J. Comput. Acoust.,* **14**(2), 201–236.

Kappel, F. & Kuntsevich, A., 2000. An implementation of Shor's *r*-algorithm, *Comput. Optim. Appl.,* **15**(2), 193–205.

Käser, M., Dumbser, M., De La Puente, J. & Igel, H., 2007. An arbitrary high-order discontinuous Galerkin method for elastic waves on unstructured meshes—III. Viscoelastic attenuation, *Geophys. J. Int.,* **168**(1), 224–242.

Kjartansson, E., 1979. Attenuation of seismic waves in rocks and applications in energy exploration, *PhD thesis,* Stanford University, California, USA.

Komatitsch, D. & Tromp, J., 1999. Introduction to the spectral-element method for 3-D seismic wave propagation, *Geophys. J. Int.,* **139**(3), 806–822.

Komatitsch, D., Liu, Q., Tromp, J., Süss, P., Stidham, C. & Shaw, J.H., 2004. Simulations of ground motion in the Los Angeles basin based upon the spectral-element method, *Bull. seism. Soc. Am.,* **94**(1), 187–206.

Kristek, J. & Moczo, P., 2003. Seismic-wave propagation in viscoelastic media with material discontinuities: a 3D fourth-order staggered-grid finite-difference modeling, *Bull. seism. Soc. Am.,* **93**(5), 2273–2280.

Kristeková, M., Kristek, J. & Moczo, P., 2009. Time-frequency misfit and goodness-of-fit criteria for quantitative comparison of time signals, *Geophys. J. Int.,* **178**(2), 813–825.

Liu, P. & Archuleta, R.J., 2006. Efficient modeling of *Q* for 3D numerical simulation of wave propagation, *Bull. seism. Soc. Am.,* **96**(4A), 1352–1358.

Liu, H.P., Anderson, D.L. & Kanamori, H., 1976. Velocity dispersion due to anelasticity: implications for seismology and mantle composition, *Geophys. J. R. astr. Soc.,* **47,** 41–58.

Lombard, B. & Piraux, J., 2011. Numerical modeling of transient two-dimensional viscoelastic waves, *J. Comput. Phys.,* **230**(15), 6099–6114.

Mainardi, F., 2010. *Fractional Calculus and Waves in Linear Viscoelasticity: An Introduction to Mathematical Models,* Imperial College Press.

Martin, R. & Komatitsch, D., 2009. An unsplit convolutional perfectly matched layer technique improved at grazing incidence for the viscoelastic wave equation, *Geophys. J. Int.,* **179**(1), 333–344.

Moczo, P. & Kristek, J., 2005. On the rheological models used for time-domain methods of seismic wave propagation, *Geophys. Res. Lett.,* **32,** L01306, doi:10.1029/2004GL021598.

Nasholm, S.P. & Holm, S., 2013. On a fractional Zener elastic wave equation, *Fract. Calc. Appl. Anal.,* **16,** 26–50.

Petersson, N.A. & Sjögreen, B., 2012. Stable and efficient modeling of anelastic attenuation in seismic wave propagation, *Commun. Computat. Phys.,* **12,** 193–225.

Peyrusse, F., Glinsky, N., Gélis, C. & Lanteri, S., 2014. A nodal discontinuous Galerkin method for site effects assessment in viscoelastic media: verification and validation in the Nice basin, *Geophys. J. Int.,* **199,** 315–334.

Rekik, A. & Brenner, R., 2011. Optimization of the collocation inversion method for the linear viscoelastic homogenization, *Mech. Res. Commun.,* **38**(4), 305–308.

Robertsson, J.O.A., 1996. A numerical free-surface condition for elastic/viscoelastic finite-difference modeling in the presence of topography, *Geophysics,* **61**(6), 1921–1934.

Robertsson, J.O.A., Blanch, J.O. & Symes, W.W., 1994. Viscoelastic finite-difference modeling, *Geophysics,* **59**(9), 1444–1456.

Russo, G. & Zollo, A., 2003. A constant-Q technique for the numerical simulation of attenuation of seismic body waves, *Geophysics,* **68**(5), 1744–1748.

Savage, B., Komatitsch, D. & Tromp, J., 2010. Effects of 3D attenuation on seismic wave amplitude and phase measurements, *Bull. seism. Soc. Am.,* **100**(3), 1241–1251.

Shor, N., 1985. *Minimization Methods for Non-Differentiable Functions,* Springer-Verlag.

van Driel, M. & Nissen-Meyer, T., 2014. Optimized viscoelastic wave propagation for weakly dissipative media, *Geophys. J. Int.,* **199**(2), 1078–1093.

Withers, K.B., Olsen, K.B. & Day, S.M., 2015. Memory-efficient simulation of frequency-dependent Q, *Bull. seism. Soc. Am.,* **105**(6), 3129–3142.

Xu, T. & McMechan, G.A., 1998. Efficient 3-D viscoelastic modeling with application to near-surface land seismic data, *Geophysics,* **63**(2), 601–612.

Zhu, T. & Carcione, J.M., 2014. Theory and modelling of constant-Q P- and S-waves using fractional spatial derivatives, *Geophys. J. Int.,* **196**(3), 1787–1795.

Geophysical Journal International

Geophys. J. Int. (2017) **208,** 1250–1264
Advance Access publication 2016 December 5
GJI Seismology

doi: 10.1093/gji/ggw456

An orthorhombic representation of a heterogeneous medium for the finite-difference modelling of seismic wave propagation

Jozef Kristek,[1,2] Peter Moczo,[1,2] Emmanuel Chaljub[3,4] and Miriam Kristekova[1,2]

[1] *Faculty of Mathematics, Physics and Informatics, Comenius University Bratislava, Mlynska dolina F1,* 842 48 *Bratislava, Slovak Republic. E-mail: kristek@fmph.uniba.sk*
[2] *Earth Science Institute, Slovak Academy of Sciences, Dubravska cesta* 9, 845 28 *Bratislava, Slovak Republic*
[3] *Univ. Grenoble Alpes, ISTerre, F-*38041 *Grenoble, France*
[4] *CNRS, ISTerre, F-*38041 *Grenoble, France*

Accepted 2016 December 1. Received 2016 November 30; in original form 2016 April 1

SUMMARY

The possibility of applying one explicit finite-difference (FD) scheme to all interior grid points (points not lying on a grid border) no matter what their positions are with respect to the material interface is one of the key factors of the computational efficiency of the FD modelling. Smooth or discontinuous heterogeneity of the medium is accounted for only by values of the effective grid moduli and densities. Accuracy of modelling thus very much depends on how these effective grid parameters are evaluated. We present an orthorhombic representation of a heterogeneous medium for the FD modelling. We numerically demonstrate its superior accuracy. Compared to the harmonic-averaging representation the orthorhombic representation is more accurate mainly in the case of strong surface waves that are especially important in local surface sedimentary basins. The orthorhombic representation is applicable to modelling seismic wave propagation and earthquake motion in isotropic models with material interfaces and smooth heterogeneities using velocity–stress, displacement–stress and displacement FD schemes on staggered, partly staggered, Lebedev and collocated grids.

Key words: Numerical approximations and analysis; Earthquake ground motions; Computational seismology; Theoretical seismology; Wave propagation.

1 INTRODUCTION

Sufficiently realistic models are necessary for numerical modelling of seismic wave propagation as well as for prediction of earthquake ground motion especially in local surface sedimentary structures capable to produce anomalous earthquake motion. The realistic physical model has to be sufficiently accurately and efficiently represented by discrete grid models in the (spatial) domain numerical methods such as the finite-difference (FD) methods.

Models of the Earth's interior and surface geological structures have to include layers/blocks of different materials. Inside a layer/block, material parameters (*P* and *S* wave speeds, density, *P* and *S* wave quality factors) may change continuously. The material parameters may change discontinuously at a contact of two layers/blocks. In local surface sedimentary structures the ratio of the *S* wave speeds in the bedrock and sediments commonly reaches values considerably larger than 2, and even 10 is not exceptional. Large velocity contrasts at material interfaces can dominantly contribute to forming seismic wave propagation. It is therefore obvious that accuracy of representation of the interfaces in the discrete grid model considerably affects the overall accuracy of the numerical modelling.

Recent FD schemes represent a large variety of approaches with considerable differences in accuracy and computational efficiency in realistic models with large velocity contrasts and complex geometry of material interfaces. This is mainly due to a level of (in)consistency of the various discrete representations of the interfaces with the boundary conditions at the interfaces. Let us note that the FD schemes also differ in accuracy in models with large *P*-wave to *S*-wave speed ratio; see Moczo *et al*. (2010, 2011).

At the welded material interface the displacement or particle-velocity and traction vectors are continuous. Consequently, a discrete representation of a welded material interface in a grid should sufficiently well approximate the boundary conditions.

One possible approach is to apply different FD schemes to different grid points: a FD scheme for the smoothly heterogeneous medium to the grid points away of the interface, and specific FD schemes to the grid points at and near (this depends on the stencil) the interface. The latter schemes have to be obtained by a proper incorporation of the boundary conditions at the interface. Such approach has been called homogeneous. Clearly, the schemes are specific for a particular geometry of the interface. Whereas feasible for simple interface geometry, the application of the homogeneous approach to non-planar interfaces is difficult and therefore has been considered impractical. In any case, the approach requires stable and sufficiently accurate FD approximation of the boundary conditions which is not a trivial problem.

In the alternative heterogeneous approach only one FD scheme is used for all interior grid points (points not lying on boundaries of a grid) no matter what their positions are with respect to the material interface. The presence of the interface is accounted for only by values of effective material parameters assigned to grid positions. Therefore, the heterogeneous approach has been commonly applied to incorporate both continuous and discontinuous heterogeneities of medium.

If a FD scheme should be applicable to any interior grid point, it should approximate equation of motion and stress–strain relation (SSR) valid for both the smoothly heterogeneous medium and interface. In other words, for finding a FD scheme applicable to the grid points at, near and away of the material interface we need SSR for a point at the interface that would (i) have the same form as SSR for a point in a smooth medium and (ii) be consistent with the interface boundary conditions.

SSR (Hooke's law) for a smooth isotropic elastic medium may be written in the matrix form

$$\vec{\sigma} = \mathbf{E}\vec{\varepsilon}, \tag{1}$$

where the stress vector, strain vector and elasticity matrix are, respectively,

$$\vec{\sigma} \equiv \left[\sigma_{xx}, \sigma_{yy}, \sigma_{zz}, \sigma_{xy}, \sigma_{yz}, \sigma_{zx}\right]^T,$$
$$\vec{\varepsilon} \equiv \left[\varepsilon_{xx}, \varepsilon_{yy}, \varepsilon_{zz}, \varepsilon_{xy}, \varepsilon_{yz}, \varepsilon_{zx}\right]^T \tag{2}$$

$$\mathbf{E} \equiv \begin{bmatrix} \lambda+2\mu & \lambda & \lambda & 0 & 0 & 0 \\ \lambda & \lambda+2\mu & \lambda & 0 & 0 & 0 \\ \lambda & \lambda & \lambda+2\mu & 0 & 0 & 0 \\ 0 & 0 & 0 & 2\mu & 0 & 0 \\ 0 & 0 & 0 & 0 & 2\mu & 0 \\ 0 & 0 & 0 & 0 & 0 & 2\mu \end{bmatrix}. \tag{3}$$

(The defined quantities do not correspond to Voigt notation. This aspect is not important in the article.) Thus we need SSR for a point at an interface which has the same form as Hooke's law (1) for the considered stress and strain vectors. Although Backus (1962) and Schoenberg & Muir (1989) addressed the problem of the equivalent medium consistent with the interface boundary condition, and Muir *et al*. (1992) explicitly pointed out its relation to the FD schemes, apparently this fundamental task had not attracted sufficient attention of developers of FD schemes for several decades until the article by Moczo *et al*. (2002). They suggested a simplified approach for the (2,4) staggered-grid schemes: an effective grid elastic modulus at the grid position of the stress-tensor component evaluated as a volume integral harmonic average of the modulus within a volume of the grid cell centred at the grid position. Numerical tests confirmed that the scheme was more accurate than the staggered-grid schemes presented earlier. The historical overview can be found in the book by Moczo *et al*. (2014).

The SCEC (Southern California Earthquake Center) code comparative exercise (Day *et al*. 2003 and also Bielak *et al*. 2010) as well as the ESG2006 (ESG – Effects of Surface Geology 2006) international comparative exercise for a typical deep Alpine Grenoble valley, France (Chaljub *et al*. 2006; Tsuno *et al*. 2006; Chaljub *et al*. 2010) clearly demonstrated that it had been far from trivial to reach satisfactory level of agreement among numerical predictions by different methods and, specifically among predictions by different FD schemes. In the ESG2006 only four predictions reached a reasonable level of agreement, the FD predictions based on approach by Moczo *et al*. (2002) among them. See the article by Chaljub *et al*. (2010) for details.

The direct impulse for developing a new discrete representation of material interface came from the quantitative iterative analysis of numerical predictions in the unprecedented international comparative E2VP exercise (E2VP – Euroseistest Verification and Validation Project 2008–2012; Chaljub *et al*. 2015; Maufroy *et al*. 2015) for the shallow sedimentary Mygdonian basin, Greece. The iterative analysis eventually included a set of complex realistic models and a set of related canonical models. The stringent canonical models made it possible to identify insufficient accuracy in the FD modelling of strong surface waves along horizontal interface with large velocity contrast. This is understandable—the harmonic averaging is strictly accurate only in 1-D problem. In the previous reported modelling studies the approximate discrete representation by Moczo *et al*. (2002) based on volume harmonic averaging proved sufficiently accurate. The reason was that the simulated wavefields were not so strongly dominated by surface waves propagating along horizontal material interfaces.

Let us eventually mention the general alternative homogenization approach for effective representation of medium heterogeneity developed by Capdeville and his colleagues (e.g. Capdeville & Marigo 2007; Capdeville *et al*. 2013).

For treating material heterogeneity in the spectral-element, discontinuous Galerkin, and pseudospectral methods we refer to the articles by Chaljub *et al*. (2010, 2015) and relevant chapters in the book by Moczo *et al*. (2014). These references are also relevant for the FD method.

First we explain SSR for a point at the planar material interface parallel to a Cartesian coordinate plane. We present an alternative (as compared to Moczo *et al*. 2002) derivation that makes it possible to identify the resulting effective discrete representation in relation to continuous and discontinuous field quantities. The derivation provides the necessary basis for the new representation. Then we consider shear and normal stress-tensor components in a heterogeneous cell. We present and discuss effective representation of a heterogeneous grid cell based on orthorhombic averaging. We demonstrate the accuracy of the representation by numerical tests.

2 THE SSR FOR A PLANAR MATERIAL INTERFACE

Consider a planar welded interface parallel to a Cartesian coordinate plane. Continuity of displacement implies continuity of three strain-tensor components, and continuity of traction implies continuity of three stress-tensor components across the interface. Fig. 1 summarizes continuous and discontinuous stress- and strain-tensor components for the three Cartesian orientations. In the following sections we analyse the shear and normal stresses in terms of discontinuous and continuous components.

2.1 Shear stress-tensor components at an interface perpendicular to the *x*-axis

Discontinuous shear stress-tensor component. For the two half-spaces (indicated by the $-$ and $+$ superscripts) in a welded contact we can write in general

$$\sigma_{yz}^{-} = 2\mu^{-}\varepsilon_{yz}$$
$$\sigma_{yz}^{+} = 2\mu^{+}\varepsilon_{yz}. \tag{4}$$

interface perpendicular to the					
x axis		y axis		z axis	
continuous	discontinuous	continuous	discontinuous	continuous	discontinuous
σ_{xx}	ε_{xx}	σ_{yy}	ε_{yy}	σ_{zz}	ε_{zz}
σ_{xy}	ε_{xy}	σ_{yz}	ε_{yz}	σ_{zx}	ε_{zx}
σ_{zx}	ε_{zx}	σ_{xy}	ε_{xy}	σ_{yz}	ε_{yz}
ε_{yy}	σ_{yy}	ε_{zz}	σ_{zz}	ε_{xx}	σ_{xx}
ε_{zz}	σ_{zz}	ε_{xx}	σ_{xx}	ε_{yy}	σ_{yy}
ε_{yz}	σ_{yz}	ε_{zx}	σ_{zx}	ε_{xy}	σ_{xy}

Figure 1. Continuous and discontinuous stress- and strain-tensor components for the three Cartesian orientations of a material interface.

Considering continuity of ε_{yz} and an arithmetic average $\langle\sigma_{yz}\rangle^x$ of the stress-tensor components at the interface,

$$\langle\sigma_{yz}\rangle^x \equiv \tfrac{1}{2}\left(\sigma_{yz}^- + \sigma_{yz}^+\right), \tag{5}$$

the summation of eq. (4) leads to SSR

$$\langle\sigma_{yz}\rangle^x = 2\langle\mu\rangle^x \varepsilon_{yz}, \tag{6}$$

with the arithmetic average of the shear moduli

$$\langle\mu\rangle^x \equiv \tfrac{1}{2}\left(\mu^- + \mu^+\right). \tag{7}$$

Continuous stress-tensor components. For example, for σ_{xy} we may write

$$\begin{aligned}\sigma_{xy} &= 2\mu^- \varepsilon_{xy}^-\\ \sigma_{xy} &= 2\mu^+ \varepsilon_{xy}^+\end{aligned} \tag{8}$$

or

$$\begin{aligned}\frac{1}{\mu^-}\sigma_{xy} &= 2\varepsilon_{xy}^-\\ \frac{1}{\mu^+}\sigma_{xy} &= 2\varepsilon_{xy}^+.\end{aligned} \tag{9}$$

Considering continuity of σ_{xy} and an arithmetic average $\langle\varepsilon_{xy}\rangle^x$ at the interface,

$$\langle\varepsilon_{xy}\rangle^x \equiv \tfrac{1}{2}\left(\varepsilon_{xy}^- + \varepsilon_{xy}^+\right) \tag{10}$$

the summation of eq. (9) leads to SSR

$$\sigma_{xy} = 2\,\langle\mu\rangle^{Hx}\,\langle\varepsilon_{xy}\rangle^x \tag{11}$$

with the harmonic average of the shear moduli

$$\langle\mu\rangle^{Hx} \equiv \frac{2}{\frac{1}{\mu^-} + \frac{1}{\mu^+}}. \tag{12}$$

Analogously we obtain a relation for σ_{zx}. The relations for the shear stress-tensor components at the interface perpendicular to the x-axis are then

$$\begin{aligned}\sigma_{xy} &= 2\langle\mu\rangle^{Hx}\langle\varepsilon_{xy}\rangle^x\\ \langle\sigma_{yz}\rangle^x &= 2\langle\mu\rangle^x \varepsilon_{yz}\\ \sigma_{zx} &= 2\langle\mu\rangle^{Hx}\langle\varepsilon_{zx}\rangle^x.\end{aligned} \tag{13}$$

Partial summary. SSRs for the shear stress-tensor components at the interface perpendicular to the x-axis:

(1) Continuity of ε_{yz} and the arithmetic averaging of the discontinuous σ_{yz} imply the arithmetic averaging of the shear moduli, $\langle\mu\rangle^x$.

(2) Continuity of σ_{xy} (or σ_{zx}) and the arithmetic averaging of the discontinuous ε_{xy} (or ε_{zx}) imply the harmonic averaging of the shear moduli, $\langle\mu\rangle^{Hx}$.

(3) SSRs (13) have the same forms as SSRs for a point in a smooth medium and are consistent with the interface boundary conditions.

2.2 Normal stress-tensor components at an interface perpendicular to the *x*-axis

SSRs in a smooth medium are:

$$\begin{aligned}\sigma_{xx} &= M\varepsilon_{xx} + \lambda\varepsilon_{yy} + \lambda\varepsilon_{zz}\\ \sigma_{yy} &= \lambda\varepsilon_{xx} + M\varepsilon_{yy} + \lambda\varepsilon_{zz}\\ \sigma_{zz} &= \lambda\varepsilon_{xx} + \lambda\varepsilon_{yy} + M\varepsilon_{zz}.\end{aligned} \tag{14}$$

Here

$$M \equiv \lambda + 2\mu \tag{15}$$

For two half-spaces in contact we may write

$$\begin{aligned}\sigma_{xx} &= M^-\,\varepsilon_{xx}^- + \lambda^-\varepsilon_{yy} + \lambda^-\varepsilon_{zz}\\ \sigma_{xx} &= M^+\,\varepsilon_{xx}^+ + \lambda^+\varepsilon_{yy} + \lambda^+\varepsilon_{zz}\end{aligned} \tag{16}$$

$$\begin{aligned}\sigma_{yy}^- &= \lambda^-\varepsilon_{xx}^- + M^-\varepsilon_{yy} + \lambda^-\varepsilon_{zz}\\ \sigma_{yy}^+ &= \lambda^+\varepsilon_{xx}^+ + M^+\varepsilon_{yy} + \lambda^+\varepsilon_{zz}\end{aligned} \tag{17}$$

$$\begin{aligned}\sigma_{zz}^- &= \lambda^-\varepsilon_{xx}^- + \lambda^-\varepsilon_{yy} + M^-\,\varepsilon_{zz}\\ \sigma_{zz}^+ &= \lambda^+\varepsilon_{xx}^+ + \lambda^+\varepsilon_{yy} + M^+\,\varepsilon_{zz}.\end{aligned} \tag{18}$$

Continuous stress-tensor component. Because the interface is perpendicular to the x-axis, relations for σ_{xx} are simpler for averaging compared to σ_{yy} and σ_{zz}: they include only one discontinuous quantity – ε_{xx}. Relations (16) may be written as

$$\begin{aligned}\varepsilon_{xx}^- &= \frac{1}{M^-}\sigma_{xx} - \frac{\lambda^-}{M^-}\varepsilon_{yy} - \frac{\lambda^-}{M^-}\varepsilon_{zz}\\ \varepsilon_{xx}^+ &= \frac{1}{M^+}\sigma_{xx} - \frac{\lambda^+}{M^+}\varepsilon_{yy} - \frac{\lambda^+}{M^+}\,\varepsilon_{zz}.\end{aligned} \tag{19}$$

Continuity of σ_{xx}, ε_{yy} and ε_{zz}, and the arithmetic averaging of ε_{xx}^- and ε_{xx}^+ lead to

$$\langle\varepsilon_{xx}\rangle^x = \left[\langle M\rangle^{Hx}\right]^{-1}\sigma_{xx} - \left\langle\frac{\lambda}{M}\right\rangle^x \varepsilon_{yy} - \left\langle\frac{\lambda}{M}\right\rangle^x \varepsilon_{zz} \tag{20}$$

and

$$\sigma_{xx} = \langle M\rangle^{Hx}\langle\varepsilon_{xx}\rangle^x + \left\langle\frac{\lambda}{M}\right\rangle^x \langle M\rangle^{Hx}\varepsilon_{yy} + \left\langle\frac{\lambda}{M}\right\rangle^x \langle M\rangle^{Hx}\varepsilon_{zz}. \tag{21}$$

Discontinuous stress-tensor component. Consider, for example, σ_{yy}. It is clear from eq. (17) that before we average σ_{yy}^- and σ_{yy}^+, we have to express ε_{xx}^- and ε_{xx}^+ using continuous field quantities. Using (19) in (17) we obtain

$$\begin{aligned}\sigma_{yy}^- &= \frac{\lambda^-}{M^-}\sigma_{xx} + \left(M^- - \lambda^-\frac{\lambda^-}{M^-}\right)\varepsilon_{yy} + \left(\lambda^- - \lambda^-\frac{\lambda^-}{M^-}\right)\varepsilon_{zz}\\ \sigma_{yy}^+ &= \frac{\lambda^+}{M^+}\sigma_{xx} + \left(M^+ - \lambda^+\frac{\lambda^+}{M^+}\right)\varepsilon_{yy} + \left(\lambda^+ - \lambda^+\frac{\lambda^+}{M^+}\right)\varepsilon_{zz}.\end{aligned} \tag{22}$$

Continuity of σ_{xx}, ε_{yy} and ε_{zz}, and the arithmetic averaging of σ_{yy}^- and σ_{yy}^+ give

$$\begin{aligned}\langle\sigma_{yy}\rangle^x &= \left\langle\frac{\lambda}{M}\right\rangle^x \sigma_{xx} + \left[\langle M\rangle^x - \left\langle\frac{\lambda^2}{M}\right\rangle^x\right]\varepsilon_{yy}\\ &\quad + \left[\langle\lambda\rangle^x - \left\langle\frac{\lambda^2}{M}\right\rangle^x\right]\varepsilon_{zz}.\end{aligned} \tag{23}$$

Substituting the r.h.s. of eq. (21) for σ_{xx} gives the sought SSR

$$\begin{aligned}\langle\sigma_{yy}\rangle^x &= \left\langle\frac{\lambda}{M}\right\rangle^x \langle M\rangle^{Hx}\langle\varepsilon_{xx}\rangle\\ &\quad + \left\{\langle M\rangle^x - \left\langle\frac{\lambda^2}{M}\right\rangle^x + \left[\left\langle\frac{\lambda}{M}\right\rangle^x\right]^2\langle M\rangle^{Hx}\right\}\varepsilon_{yy}\\ &\quad + \left\{\langle\lambda\rangle^x - \left\langle\frac{\lambda^2}{M}\right\rangle^x + \left[\left\langle\frac{\lambda}{M}\right\rangle^x\right]^2\langle M\rangle^{Hx}\right\}\varepsilon_{zz}.\end{aligned} \tag{24}$$

Analogously we easily obtain

$$\begin{aligned}\langle\sigma_{zz}\rangle^x &= \left\langle\frac{\lambda}{M}\right\rangle^x \langle M\rangle^{Hx}\langle\varepsilon_{xx}\rangle\\ &\quad + \left\{\langle\lambda\rangle^x - \left\langle\frac{\lambda^2}{M}\right\rangle^x + \left[\left\langle\frac{\lambda}{M}\right\rangle^x\right]^2\langle M\rangle^{Hx}\right\}\varepsilon_{yy}\\ &\quad + \left\{\langle M\rangle^x - \left\langle\frac{\lambda^2}{M}\right\rangle^x + \left[\left\langle\frac{\lambda}{M}\right\rangle^x\right]^2\langle M\rangle^{Hx}\right\}\varepsilon_{zz}.\end{aligned} \tag{25}$$

Partial summary. SSRs for the normal stress-tensor components at the interface perpendicular to the x-axis:

(1) Continuity of σ_{xx}, ε_{yy} and ε_{zz}, and the arithmetic averaging of the discontinuous ε_{xx} imply two averaged elastic coefficients, $\langle M\rangle^{Hx}$ and $\langle\frac{\lambda}{M}\rangle^x\langle M\rangle^{Hx}$.

(2) Continuity of ε_{yy} and ε_{zz}, and the averaging of discontinuous σ_{yy} and ε_{xx} (or σ_{zz} and ε_{xx}) imply $\langle\frac{\lambda}{M}\rangle^x\langle M\rangle^{Hx}$ and two more averaged elastic coefficients: $\langle\lambda\rangle^x - \langle\frac{\lambda^2}{M}\rangle^x + [\langle\frac{\lambda}{M}\rangle^x]^2\langle M\rangle^{Hx}$ and $\langle M\rangle^x - \langle\frac{\lambda^2}{M}\rangle^x + [\langle\frac{\lambda}{M}\rangle^x]^2\langle M\rangle^{Hx}$.

(3) Considering the averaged elastic coefficients, stress- and strain-tensor components, SSRs (21), (24) and (25) have the same forms as SSRs for a point in a smooth medium and are consistent with the interface boundary conditions.

2.3 Elasticity matrices for interfaces perpendicular to the coordinate axes

Define

$$\begin{aligned}A^\xi &= \langle M\rangle^{H\xi}\\ B^\xi &= \left\langle\frac{\lambda}{M}\right\rangle^\xi \langle M\rangle^{H\xi}\\ C^\xi &= \langle M\rangle^\xi - \left\langle\frac{\lambda^2}{M}\right\rangle^\xi + \left[\left\langle\frac{\lambda}{M}\right\rangle^\xi\right]^2\langle M\rangle^{H\xi}\\ D^\xi &= \langle\lambda\rangle^\xi - \left\langle\frac{\lambda^2}{M}\right\rangle^\xi + \left[\left\langle\frac{\lambda}{M}\right\rangle^\xi\right]^2\langle M\rangle^{H\xi},\end{aligned} \tag{26}$$

where $\xi \in \{x, y, z\}$. Then SSRs (13), (21), (24) and (25) for a point at the interface perpendicular to the x-axis may be concisely written as

$$\begin{bmatrix}\sigma_{xx}\\ \langle\sigma_{yy}\rangle^x\\ \langle\sigma_{zz}\rangle^x\\ \sigma_{xy}\\ \langle\sigma_{yz}\rangle^x\\ \sigma_{zx}\end{bmatrix} = \begin{bmatrix}A^x & B^x & B^x & 0 & 0 & 0\\ B^x & C^x & D^x & 0 & 0 & 0\\ B^x & D^x & C^x & 0 & 0 & 0\\ 0 & 0 & 0 & 2\langle\mu\rangle^{Hx} & 0 & 0\\ 0 & 0 & 0 & 0 & 2\langle\mu\rangle^x & 0\\ 0 & 0 & 0 & 0 & 0 & 2\langle\mu\rangle^{Hx}\end{bmatrix}\begin{bmatrix}\langle\varepsilon_{xx}\rangle^x\\ \varepsilon_{yy}\\ \varepsilon_{zz}\\ \langle\varepsilon_{xy}\rangle^x\\ \varepsilon_{yz}\\ \langle\varepsilon_{zx}\rangle^x\end{bmatrix}. \tag{27}$$

For the interface perpendicular to the y-axis it is

$$\begin{bmatrix}\langle\sigma_{xx}\rangle^y\\ \sigma_{yy}\\ \langle\sigma_{zz}\rangle^y\\ \sigma_{xy}\\ \sigma_{yz}\\ \langle\sigma_{zx}\rangle^y\end{bmatrix} = \begin{bmatrix}C^y & B^y & D^y & 0 & 0 & 0\\ B^y & A^y & B^y & 0 & 0 & 0\\ D^y & B^y & C^y & 0 & 0 & 0\\ 0 & 0 & 0 & 2\langle\mu\rangle^{Hy} & 0 & 0\\ 0 & 0 & 0 & 0 & 2\langle\mu\rangle^{Hy} & 0\\ 0 & 0 & 0 & 0 & 0 & 2\langle\mu\rangle^y\end{bmatrix}\begin{bmatrix}\varepsilon_{xx}\\ \langle\varepsilon_{yy}\rangle^y\\ \varepsilon_{zz}\\ \langle\varepsilon_{xy}\rangle^y\\ \langle\varepsilon_{yz}\rangle^y\\ \varepsilon_{zx}\end{bmatrix} \tag{28}$$

and for the interface perpendicular to the z-axis

$$\begin{bmatrix}\langle\sigma_{xx}\rangle^z\\ \langle\sigma_{yy}\rangle^z\\ \sigma_{zz}\\ \langle\sigma_{xy}\rangle^z\\ \sigma_{yz}\\ \sigma_{zx}\end{bmatrix} = \begin{bmatrix}C^z & D^z & B^z & 0 & 0 & 0\\ D^z & C^z & B^z & 0 & 0 & 0\\ B^z & B^z & A^z & 0 & 0 & 0\\ 0 & 0 & 0 & 2\langle\mu\rangle^z & 0 & 0\\ 0 & 0 & 0 & 0 & 2\langle\mu\rangle^{Hz} & 0\\ 0 & 0 & 0 & 0 & 0 & 2\langle\mu\rangle^{Hz}\end{bmatrix}\begin{bmatrix}\varepsilon_{xx}\\ \varepsilon_{yy}\\ \langle\varepsilon_{zz}\rangle^z\\ \varepsilon_{xy}\\ \langle\varepsilon_{yz}\rangle^z\\ \langle\varepsilon_{zx}\rangle^z\end{bmatrix}. \tag{29}$$

2.4 Elasticity matrix for an interface—interpretation

Transversely isotropic medium. Any of the matrix relations (27), (28) and (29) has the same form as the matrix relation for a point in a smooth medium, see eq. (1), with nine non-zero elements (considering the symmetry of the matrix). Matrix in any of relations (27), (28) and (29) may be considered the elasticity matrix of an averaged medium representing contact of two materials and consistent with the boundary conditions at the welded material interface.

Matrix in eq. (1) has only 2 independent non-zero elements (e.g. 2μ and $\lambda + 2\mu$) because it represents an isotropic medium. Matrix

for an averaged medium has 5 independent non-zero elements, for example, A^{ξ}, B^{ξ}, C^{ξ}, $2\langle\mu\rangle^{H\xi}$ and $2\langle\mu\rangle^{\xi}$ considering that $D^{\xi} = C^{\xi} - 2\langle\mu\rangle^{\xi}$. This means that the averaged medium is transversely isotropic with the axis of symmetry perpendicular to the interface.

Why is the averaged medium representing contact of two isotropic media at a planar interface transversely isotropic? SSRs for the continuous shear stress-tensor components need the harmonic average $\langle\mu\rangle^{H\xi}$ whereas the relation for the discontinuous shear stress-tensor component needs the arithmetic average $\langle\mu\rangle^{\xi}$. It is then clear that relations for the normal stress-tensor components at the interface need other independent coefficients—increasing thus the total number of coefficients: the continuous normal stress-tensor component needs 2 more independent coefficients, and the discontinuous normal stress-tensor components need, in addition to the latter 2 coefficients, also the 5th independent coefficient. The transversely isotropic medium is understandable: if it cannot be isotropic then there is no reason why it should not have the axial symmetry about the axis perpendicular to the interface.

Meaning of the harmonic averages. Consider, for example, a planar interface perpendicular to the z-axis and a 1-D problem with a wave propagating in the direction of the z-axis. Propagation of the plane P wave in any of two half-spaces is described by

$$\rho\frac{\partial^2 u_z}{\partial t^2} = \frac{\partial \sigma_{zz}}{\partial z}, \quad \sigma_{zz} = (\lambda + 2\mu)\ \frac{\partial u_z}{\partial z} = (\lambda + 2\mu)\ \varepsilon_{zz}. \tag{30}$$

Propagation of the plane S wave in any of two half-spaces is described by

$$\rho\frac{\partial^2 u_x}{\partial t^2} = \frac{\partial \sigma_{zx}}{\partial z}, \quad \sigma_{zx} = \mu\frac{\partial u_x}{\partial z} = 2\mu\,\varepsilon_{zx} \tag{31}$$

if the wave is polarized in the x direction, and by

$$\rho\frac{\partial^2 u_y}{\partial t^2} = \frac{\partial \sigma_{zy}}{\partial z}, \quad \sigma_{zy} = \mu\frac{\partial u_y}{\partial z} = 2\mu\,\varepsilon_{zy} \tag{32}$$

if the wave is polarized in the y direction. SSRs at the interface are then for the three cases:

$$\sigma_{zz} = \langle\lambda + 2\mu\rangle^{Hz}\langle\varepsilon_{zz}\rangle^{z}, \tag{33}$$

$$\sigma_{zx} = 2\langle\mu\rangle^{Hz}\langle\varepsilon_{zx}\rangle^{z}, \tag{34}$$

$$\sigma_{zy} = 2\langle\mu\rangle^{Hz}\langle\varepsilon_{zy}\rangle^{z}. \tag{35}$$

These SSRs for the welded interface and the matrix for the averaged transversely isotropic medium representing contact of two materials and consistent with the boundary conditions at the welded material interface were presented by Moczo *et al.* (2002) using a matrix formalism. In this section we (i) presented an alternative derivation which explicitly shows all relations between the continuous and discontinuous field quantities on one hand and the effective averaged elastic coefficients on the other hand, (ii) showed matrices (27)–(29) necessary for explanation of the orthorhombic averaging and (iii) explained structure of the elasticity matrix for the averaged transversely isotropic medium.

2.5 Planar interface in a general orientation

Assume such an interface in the Cartesian coordinate system xyz. The interface is parallel to one of the coordinate planes in some rotated system $x'y'z'$. The elasticity matrix in the rotated system has nine non-zero elements from which 5 are independent. If we transform SSR from $x'y'z'$ into xyz, the transformed elasticity matrix has 5 independent elements (the transformation does not change the physics of the interface) but has all 21 (considering the matrix symmetry) elements non-zero. This means that all strain-tensor components are necessary for calculating each stress-tensor component at a point of the interface.

2.6 Non-planar interface

A non-planar smooth surface may be locally approximated by a planar interface tangential to the surface at a given point. There are two options: (1) Calculate 21 non-zero elastic coefficients for each grid point and store them in memory during the entire FD time-integration. (2) Store only $2 + 2$ elastic coefficients (2 per medium in contact) and 2 angles (specifying orientation of an approximating tangential planar interface) for each grid point and calculate the elasticity matrix at each time step at each grid point. It is clear that we face either considerably increased memory requirement or considerably increased computing time.

2.7 A simple computational compromise—harmonic averaging

Given the situation described, Moczo *et al.* (2002) suggested the computational compromise: an effective grid elastic modulus at a given grid position is evaluated as the volume integral harmonic average over a grid cell centred at that grid position. Consequently, an interface between two isotropic media is represented by a harmonically averaged isotropic medium. The advantageous aspect of the approach is that the effective grid moduli are directly applicable, for example, to the standard velocity-stress FD scheme—they do not change the structure and number of arithmetic operations in the FD scheme.

2.8 Structure of the equation of motion in relation to a planar interface

Consider a planar interface between two homogeneous elastic half-spaces perpendicular to the z-axis. Fig. 2 shows the structure of the equation of motion with respect to the stress-tensor components continuous and discontinuous across the interface. The continuous stress-tensor components are in blue, the discontinuous ones are in red. The colour frames on the right-hand sides of the equations indicate parts relevant for different wavefield configurations.

In any of the three simplest 1-D problems with waves propagating in the $\pm z$ direction, that is, 1-D P-wave, 1-D S-wave polarized in the y direction and 1-D S-wave polarized in the x direction (indicated by the violet frames), only one continuous stress-tensor component is involved. As shown in Section 2.4, the harmonic averaging of elastic moduli is exact in any of the three simplest 1-D problems.

The 2-D SH problem (green frames) involves one continuous and one discontinuous shear stress-tensor components. The harmonic averaging is exact for the continuous component whereas it is only approximate for the discontinuous one.

The 2-D P-SV problem (brown frames) involves one continuous shear stress-tensor component, one continuous normal stress-tensor component and one discontinuous normal stress-tensor component. The harmonic averaging is exact for the continuous shear stress-tensor component whereas it is only approximate for the two others.

In the 3-D problem the harmonic averaging is exact for two continuous shear stress-tensor components whereas it is only approximate for the four others.

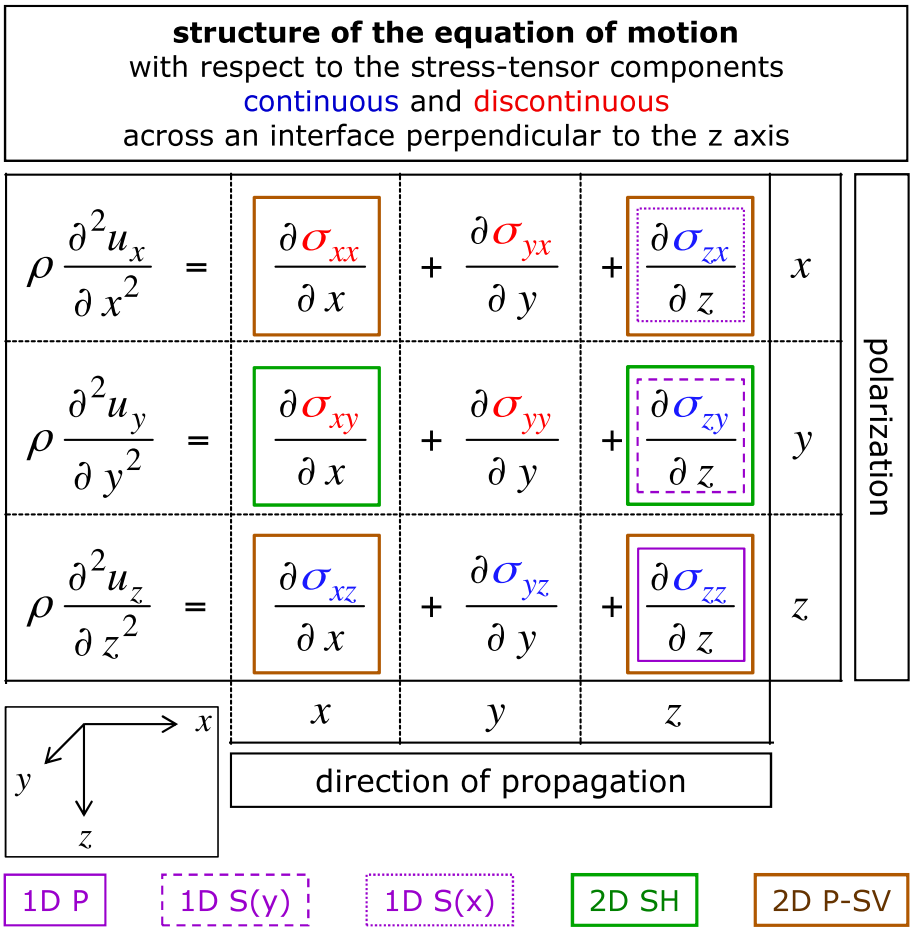

Figure 2. Structure of the equation of motion illustrating relation of the continuous and discontinuous stress-tensor components to effective medium averaging.

Stringent numerical tests (Moczo *et al*. 2002; Chaljub *et al*. 2015) show that the harmonic averaging of moduli for all stress-tensor components is surprisingly accurate except the case when the wavefield is dominated by surface wave propagating along the contrast interface. The analysis of the stringent tests that involve dominant surface waves propagating in the horizontal direction along the strong-contrast interface (within the verification phase of the E2VP project, Chaljub *et al*. 2015) led us to improve the way of representing the material interface by an averaged medium. We present the new method in the following sections.

3 SSR FOR A JOINT POINT OF EIGHT CUBES – SEQUENTIAL AVERAGING

Consider a joint grid point of eight grid cells. In a simple representation of a heterogeneous medium material of each cell is homogeneous while different from materials of the other cells. It is important to find an effective material grid parameter representing heterogeneity of the medium around that grid point. There is, however, a more important reason for considering the canonical situation of a joint point of eight cubes. Consider non-planar interfaces inside a grid cell. Then we can think of dividing the cell into homogeneous subcells and approximating the non-planar interfaces by a staircase interfaces separating homogeneous subcells.

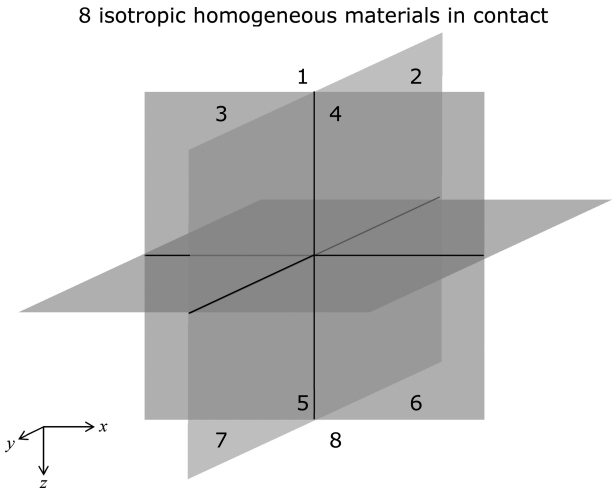

Figure 3. Illustration of interfaces separating eight infinitely large cubes in contact. Each cube is assumed elastic and homogeneous. In general, the cubes differ from each other by values of elastic moduli and density.

3.1 Shear stress-tensor components

Consider a configuration in Fig. 3: eight homogeneous elastic infinitely large cubes in contact. The cubes may differ from each other by values of moduli. With reference to eq. (11) let us write SSRs for

σ_{xy} at each of eight planar interfaces perpendicular to the horizontal Cartesian directions:

$$\sigma_{xy}^{12} = 2\langle\mu\rangle^{Hx,12}\,\langle\varepsilon_{xy}\rangle^{x,12}, \quad \sigma_{xy}^{34} = 2\langle\mu\rangle^{Hx,34}\,\langle\varepsilon_{xy}\rangle^{x,34}$$
$$\sigma_{xy}^{13} = 2\langle\mu\rangle^{Hy,13}\,\langle\varepsilon_{xy}\rangle^{y,13}, \quad \sigma_{xy}^{24} = 2\langle\mu\rangle^{Hy,24}\,\langle\varepsilon_{xy}\rangle^{y,24} \tag{36}$$

and

$$\sigma_{xy}^{56} = 2\langle\mu\rangle^{Hx,56}\,\langle\varepsilon_{xy}\rangle^{x,56}, \quad \sigma_{xy}^{78} = 2\langle\mu\rangle^{Hx,78}\,\langle\varepsilon_{xy}\rangle^{x,78}$$
$$\sigma_{xy}^{57} = 2\langle\mu\rangle^{Hy,57}\,\langle\varepsilon_{xy}\rangle^{y,57}, \quad \sigma_{xy}^{68} = 2\langle\mu\rangle^{Hy,68}\,\langle\varepsilon_{xy}\rangle^{y,68}. \tag{37}$$

Here the superscripts indicate the interface—for example, 12 indicates the interface between cubes 1 and 2. Considering averaging along joint contact lines of the four upper and lower cubes (the four horizontal contact lines in Fig. 3), respectively, and continuity of σ_{xy} in any horizontal direction (Fig. 1), we define σ_{xy}^{-} and σ_{xy}^{+}:

$$\sigma_{xy}^{-} \equiv \sigma_{xy}^{12} = \sigma_{xy}^{34} = \sigma_{xy}^{13} = \sigma_{xy}^{24}$$
$$\sigma_{xy}^{+} \equiv \sigma_{xy}^{56} = \sigma_{xy}^{78} = \sigma_{xy}^{57} = \sigma_{xy}^{68}. \tag{38}$$

Then averaging of moduli and strains in relations (36) and (37), respectively, leads to

$$\sigma_{xy}^{-} = 2\,\langle\mu\rangle^{Hxy,-}\,\langle\varepsilon_{xy}\rangle^{xy,-}$$
$$\sigma_{xy}^{+} = 2\,\langle\mu\rangle^{Hxy,+}\,\langle\varepsilon_{xy}\rangle^{xy,+}, \tag{39}$$

where

$$\langle\mu\rangle^{Hxy,-} = 4\left[\frac{1}{\langle\mu\rangle^{Hx,12}} + \frac{1}{\langle\mu\rangle^{Hx,34}} + \frac{1}{\langle\mu\rangle^{Hy,13}} + \frac{1}{\langle\mu\rangle^{Hy,24}}\right]^{-1}$$
$$\langle\mu\rangle^{Hxy,+} = 4\left[\frac{1}{\langle\mu\rangle^{Hx,56}} + \frac{1}{\langle\mu\rangle^{Hx,78}} + \frac{1}{\langle\mu\rangle^{Hy,57}} + \frac{1}{\langle\mu\rangle^{Hy,68}}\right]^{-1} \tag{40}$$

and

$$\langle\varepsilon_{xy}\rangle^{xy,-} = \frac{1}{4}\left(\langle\varepsilon_{xy}\rangle^{x,12} + \langle\varepsilon_{xy}\rangle^{x,34} + \langle\varepsilon_{xy}\rangle^{y,13} + \langle\varepsilon_{xy}\rangle^{y,24}\right)$$
$$\langle\varepsilon_{xy}\rangle^{xy,+} = \frac{1}{4}\left(\langle\varepsilon_{xy}\rangle^{x,56} + \langle\varepsilon_{xy}\rangle^{x,78} + \langle\varepsilon_{xy}\rangle^{y,57} + \langle\varepsilon_{xy}\rangle^{y,68}\right). \tag{41}$$

Considering averaging at a joint point of eight cubes and continuity of ε_{xy} in the z direction, we define

$$\langle\varepsilon_{xy}\rangle^{xy} \equiv \langle\varepsilon_{xy}\rangle^{xy,-} = \langle\varepsilon_{xy}\rangle^{xy,+}. \tag{42}$$

Defining also

$$\langle\sigma_{xy}\rangle^{z} \equiv \frac{1}{2}\left(\sigma_{xy}^{-} + \sigma_{xy}^{+}\right) \tag{43}$$

and

$$\left\langle\langle\mu\rangle^{Hxy}\right\rangle^{z} = \frac{1}{2}\left(\langle\mu\rangle^{Hxy,-} + \langle\mu\rangle^{Hxy,+}\right) \tag{44}$$

we finally obtain from (39) SSR for the joint point of eight cubes:

$$\langle\sigma_{xy}\rangle^{z} = 2\left\langle\langle\mu\rangle^{Hxy}\right\rangle^{z}\langle\varepsilon_{xy}\rangle^{xy}. \tag{45}$$

We have obtained this relation by averaging first in the horizontal directions x and y, and then averaging in the z direction. We may try also the opposite way: averaging first in the z direction and then in the horizontal directions.

With reference to eq. (6), consider therefore, instead of eqs (36) and (37), the following relations for the four interfaces perpendicular to the z-axis:

$$\langle\sigma_{xy}\rangle^{z,15} = 2\langle\mu\rangle^{z,15}\,\varepsilon_{xy}^{15}, \quad \langle\sigma_{xy}\rangle^{z,26} = 2\,\langle\mu\rangle^{z,26}\,\varepsilon_{xy}^{26}$$
$$\langle\sigma_{xy}\rangle^{z,37} = 2\langle\mu\rangle^{z,37}\,\varepsilon_{xy}^{37}, \quad \langle\sigma_{xy}\rangle^{z,48} = 2\,\langle\mu\rangle^{z,48}\,\varepsilon_{xy}^{48}. \tag{46}$$

Consider now interfaces perpendicular to the x- and y-axes. Because σ_{xy} is continuous in both x and y directions, we may define

$$\langle\sigma_{xy}\rangle^{z} \equiv \langle\sigma_{xy}\rangle^{z,15} = \langle\sigma_{xy}\rangle^{z,26} = \langle\sigma_{xy}\rangle^{z,37} = \langle\sigma_{xy}\rangle^{z,48}. \tag{47}$$

Then averaging of moduli and strains in relations (46) in the x and y directions, respectively, leads to

$$\langle\sigma_{xy}\rangle^{z} = 4\left[\frac{1}{\langle\mu\rangle^{z,15}} + \frac{1}{\langle\mu\rangle^{z,26}}\right]^{-1}\frac{1}{2}\left(\varepsilon_{xy}^{15} + \varepsilon_{xy}^{26}\right)$$
$$\langle\sigma_{xy}\rangle^{z} = 4\left[\frac{1}{\langle\mu\rangle^{z,37}} + \frac{1}{\langle\mu\rangle^{z,48}}\right]^{-1}\frac{1}{2}\left(\varepsilon_{xy}^{37} + \varepsilon_{xy}^{48}\right) \tag{48}$$

and

$$\langle\sigma_{xy}\rangle^{z} = 4\left[\frac{1}{\langle\mu\rangle^{z,15}} + \frac{1}{\langle\mu\rangle^{z,37}}\right]^{-1}\frac{1}{2}\left(\varepsilon_{xy}^{15} + \varepsilon_{xy}^{37}\right)$$
$$\langle\sigma_{xy}\rangle^{z} = 4\left[\frac{1}{\langle\mu\rangle^{z,26}} + \frac{1}{\langle\mu\rangle^{z,48}}\right]^{-1}\frac{1}{2}\left(\varepsilon_{xy}^{26} + \varepsilon_{xy}^{48}\right) \tag{49}$$

Summation of the four relations (48) and (49) eventually leads to

$$\langle\sigma_{xy}\rangle^{z} = 2\,\langle\langle\mu\rangle^{z}\rangle^{Hxy}\langle\varepsilon_{xy}\rangle^{xy}, \tag{50}$$

where $\langle\langle\mu\rangle^{z}\rangle^{Hxy}$ denotes the harmonic average of the four harmonic averages in relations (48) and (49), and $\langle\varepsilon_{xy}\rangle^{xy}$ denotes the arithmetic average of the four arithmetic averages of strain in relations (48) and (49).

It is obvious from comparison of relations (45) and (50) that the order of averaging leads to relations with differently averaged moduli. At the same time, we immediately see two common features of both averages, $\langle\mu^{Hxy}\rangle^{z}$ and $\langle\langle\mu\rangle^{z}\rangle^{Hxy}$: (1) continuity of σ_{xy} in the x and y directions implies the harmonic averaging in both directions, (2) discontinuity of σ_{xy} in the z direction implies the arithmetic averaging in that direction. Both obtained SSRs are just different approximations and it is difficult to say which one is better. We may use, however, an additional criterion to choose one of them. Consider, for example, one of cubes representing a liquid or vacuum. Then the corresponding harmonic average $\langle\mu\rangle^{Hxy}$ would give a zero average value for the four cubes. This would be not the case with the arithmetic averaging applied first. Consequently we choose relation (50). In summary, all SSRs are

$$\langle\sigma_{xy}\rangle^{z} = 2\,\langle\langle\mu\rangle^{z}\rangle^{Hxy}\langle\varepsilon_{xy}\rangle^{xy}$$
$$\langle\sigma_{yz}\rangle^{x} = 2\,\langle\langle\mu\rangle^{x}\rangle^{Hyz}\langle\varepsilon_{yz}\rangle^{yz}$$
$$\langle\sigma_{zx}\rangle^{y} = 2\,\langle\langle\mu\rangle^{y}\rangle^{Hzx}\langle\varepsilon_{zx}\rangle^{zx}. \tag{51}$$

Important property of the averaged moduli. Consider a 3-D grid cell and evaluation of the average moduli over the volume of the cell. Assume, for example, that the grid cell contains only one interface perpendicular to the x-axis. Then relations (51) reduce to

$$\sigma_{xy} = 2\,\langle\mu\rangle^{Hx}\langle\varepsilon_{xy}\rangle^{x}$$
$$\langle\sigma_{yz}\rangle^{x} = 2\,\langle\mu\rangle^{x}\varepsilon_{yz}$$
$$\sigma_{zx} = 2\,\langle\mu\rangle^{Hx}\langle\varepsilon_{zx}\rangle^{x} \tag{52}$$

that is to SSRs for the transversely isotropic medium—see eq. (27). Analogously, relations (51) reduce to relations for the transversely isotropic medium with the axis of symmetry parallel with the y- or z-axis for an interface perpendicular to the y- or z-axis, respectively.

3.2 Normal stress-tensor components

Formal averaging of the normal stress-tensor components at the joint point of eight homogeneous cubes (Fig. 3) is considerably more complicated and rather lengthy. Therefore we just outline essential aspects.

We may start, for example, with SSRs (27) at the interfaces perpendicular to the x-axis and average them first at the interfaces perpendicular to the y-axis. It is the simplest to start with SSR for σ_{yy}, that is, $\langle\sigma_{yy}\rangle^x(\langle\varepsilon_{xx}\rangle^x,\ \varepsilon_{yy},\ \varepsilon_{zz})$. Because only ε_{yy} from the four field quantities in the relation is discontinuous across the interface perpendicular to the y-axis, the averaging can be achieved by averaging the relation $\varepsilon_{yy}(\langle\varepsilon_{xx}\rangle^x,\ \varepsilon_{zz},\ \langle\sigma_{yy}\rangle^x)$. The result of the averaging is $\langle\varepsilon_{yy}\rangle^y(\langle\varepsilon_{xx}\rangle^x,\ \varepsilon_{zz},\ \langle\sigma_{yy}\rangle^x)$ from which we obtain the sought SSR for $\langle\sigma_{yy}\rangle^x$ at the interface perpendicular to the y-axis: $\langle\sigma_{yy}\rangle^x(\langle\varepsilon_{xx}\rangle^x,\ \langle\varepsilon_{yy}\rangle^y,\ \varepsilon_{zz})$.

We may continue with σ_{xx}. In SSR for σ_{xx} at the interface perpendicular to the x-axis, $\sigma_{xx}(\langle\varepsilon_{xx}\rangle^x,\ \varepsilon_{yy},\ \varepsilon_{zz})$, two quantities are discontinuous across the interface perpendicular to the y-axis: σ_{xx} and ε_{yy}. Therefore, before we average σ_{xx} at the interface, we must express ε_{yy} from SSR $\langle\sigma_{yy}\rangle^x(\langle\varepsilon_{xx}\rangle^x,\ \varepsilon_{yy},\ \varepsilon_{zz})$ at the interface perpendicular to the x-axis. We obtain $\sigma_{xx}(\langle\varepsilon_{xx}\rangle^x,\ \varepsilon_{zz},\ \langle\sigma_{yy}\rangle^x)$. Because $\langle\varepsilon_{xx}\rangle^x,\ \varepsilon_{zz},\ \langle\sigma_{yy}\rangle^x$ are continuous across the interface perpendicular to the y-axis, we may average σ_{xx}. The result of averaging is $\langle\sigma_{xx}\rangle^y(\langle\varepsilon_{xx}\rangle^x,\ \varepsilon_{zz},\ \langle\sigma_{yy}\rangle^x)$. In this relation we express $\langle\sigma_{yy}\rangle^x$ from relation for σ_{yy} at the interface perpendicular to the y-axis, $\langle\sigma_{yy}\rangle^x(\langle\varepsilon_{xx}\rangle^x,\ \langle\varepsilon_{yy}\rangle^y,\ \varepsilon_{zz})$, and eventually obtain SSR at the interface perpendicular to the y-axis: $\langle\sigma_{xx}\rangle^y(\langle\varepsilon_{xx}\rangle^x,\ \langle\varepsilon_{yy}\rangle^y,\ \varepsilon_{zz})$.

Analogously we could continue with σ_{zz}. Having SSRs for the normal stress-tensor components averaged across the interfaces perpendicular to the x- and y-axes, we could then continue with averaging across the interface perpendicular to the z-axis.

It is obvious, however, that we could start the averaging procedure from SSRs (28) for the interfaces perpendicular to the y-axis, continue with averaging across the interfaces perpendicular to the z-axis and finish with averaging across the interfaces perpendicular to the x-axis. Eventually and alternatively, the order of averaging might be $z \to x \to y$.

The problem, indicated already by averaging the shear stress-tensor components, is that the three different sequences of averaging (that is, $x \to y \to z$, $y \to z \to x$ and $z \to x \to y$) give three different averaged moduli in SSRs for the joint point of eight cubes. This is not acceptable because the averaged medium should not depend on the order of averaging. The three different results are consequence of the fact that such averaging is not rigorous and justified. It is just approximate.

4 DECISION ON AVERAGING IN THE CELL VOLUME: THE ORTHORHOMBIC MEDIUM

It is obvious that we are facing two problems: (1) We do not want to have 21 non-zero coefficients in the elasticity matrix (see Sections 2.5 and 2.6). That would considerably decrease computational efficiency. (2) The sequential averaging (Sections 3.1 and 3.2) is not applicable. In this situation we have to decide how to average medium in order to obtain sufficiently accurate and computationally efficient representation of a material interface.

It is reasonable to impose two requirements in this decision-making:

(1) Keeping the number of non-zero coefficients in the elasticity matrix the same as for the isotropic or transversely isotropic media, that is, nine (considering the matrix symmetry). This means that the averaged medium would neither change the structure of calculating stress-tensor components nor increase the number of arithmetic operations.

(2) If a grid cell contains a planar interface (between two homogeneous materials) perpendicular to the ξ-axis, then the averaged medium in the cell is the transversely isotropic medium with axis of symmetry parallel to the ξ-axis.

Consequently, the elasticity matrix should have the following general form:

$$\begin{bmatrix} \Pi_x & \lambda_{xy} & \lambda_{zx} & 0 & 0 & 0 \\ \lambda_{xy} & \Pi_y & \lambda_{yz} & 0 & 0 & 0 \\ \lambda_{zx} & \lambda_{yz} & \Pi_z & 0 & 0 & 0 \\ 0 & 0 & 0 & 2\mu_{xy} & 0 & 0 \\ 0 & 0 & 0 & 0 & 2\mu_{yz} & 0 \\ 0 & 0 & 0 & 0 & 0 & 2\mu_{zx} \end{bmatrix}. \tag{53}$$

As we explained in Section 3.1 we can take eq. (51) for the shear stress-tensor components:

$$\begin{aligned} \mu_{xy} &= \langle\langle\mu\rangle^z\rangle^{Hxy} \\ \mu_{yz} &= \langle\langle\mu\rangle^x\rangle^{Hyz} \\ \mu_{zx} &= \langle\langle\mu\rangle^y\rangle^{Hzx}. \end{aligned} \tag{54}$$

With the normal stress-tensor components it is more complicated. For finding a solution, it is instructive and helpful to see the coefficients for transversely isotropic media representing the planar interfaces perpendicular to the coordinate axes at once. We show them in Fig. 4. According to the 2nd requirement, for example, Π_x has to give $\langle M\rangle^{Hx}$ or $\langle M - \frac{\lambda^2}{M}\rangle^y + [\langle\frac{\lambda}{M}\rangle^y]^2\langle M\rangle^{Hy}$ or $\langle M - \frac{\lambda^2}{M}\rangle^z + [\langle\frac{\lambda}{M}\rangle^z]^2\langle M\rangle^{Hz}$ if the grid cell contains interface perpendicular to the x- or y- or z-axis, respectively. Analogous requirements apply to the other Π_ξ and $\lambda_{\xi\eta}$ coefficients. All these requirements are met by the following averages:

$$\begin{aligned} \Pi_x &= \left\langle \left\langle M - \frac{\lambda^2}{M}\right\rangle^{yz} + \left[\left\langle\frac{\lambda}{M}\right\rangle^{yz}\right]^2 \langle M\rangle^{Hyz} \right\rangle^{Hx} \\ \Pi_y &= \left\langle \left\langle M - \frac{\lambda^2}{M}\right\rangle^{zx} + \left[\left\langle\frac{\lambda}{M}\right\rangle^{zx}\right]^2 \langle M\rangle^{Hzx} \right\rangle^{Hy} \\ \Pi_z &= \left\langle \left\langle M - \frac{\lambda^2}{M}\right\rangle^{xy} + \left[\left\langle\frac{\lambda}{M}\right\rangle^{xy}\right]^2 \langle M\rangle^{Hxy} \right\rangle^{Hz} \end{aligned} \tag{55}$$

and

$$\begin{aligned} \lambda_{xy} &= \left\langle \left\langle M - \frac{\lambda^2}{M}\right\rangle^{z} + \left[\left\langle\frac{\lambda}{M}\right\rangle^{z}\right]^2 \langle M\rangle^{Hz} \right\rangle^{Hxy} \\ &\quad \times \left\langle \frac{\langle\lambda - \frac{\lambda^2}{M}\rangle^z + [\langle\frac{\lambda}{M}\rangle^z]^2\langle M\rangle^{Hz}}{\langle M - \frac{\lambda^2}{M}\rangle^z + [\langle\frac{\lambda}{M}\rangle^z]^2\langle M\rangle^{Hz}} \right\rangle^{xy} \end{aligned} \tag{56}$$

$$\begin{aligned} \lambda_{yz} &= \left\langle \left\langle M - \frac{\lambda^2}{M}\right\rangle^{x} + \left[\left\langle\frac{\lambda}{M}\right\rangle^{x}\right]^2 \langle M\rangle^{Hx} \right\rangle^{Hyz} \\ &\quad \times \left\langle \frac{\langle\lambda - \frac{\lambda^2}{M}\rangle^x + [\langle\frac{\lambda}{M}\rangle^x]^2\langle M\rangle^{Hx}}{\langle M - \frac{\lambda^2}{M}\rangle^x + [\langle\frac{\lambda}{M}\rangle^x]^2\langle M\rangle^{Hx}} \right\rangle^{yz} \end{aligned} \tag{57}$$

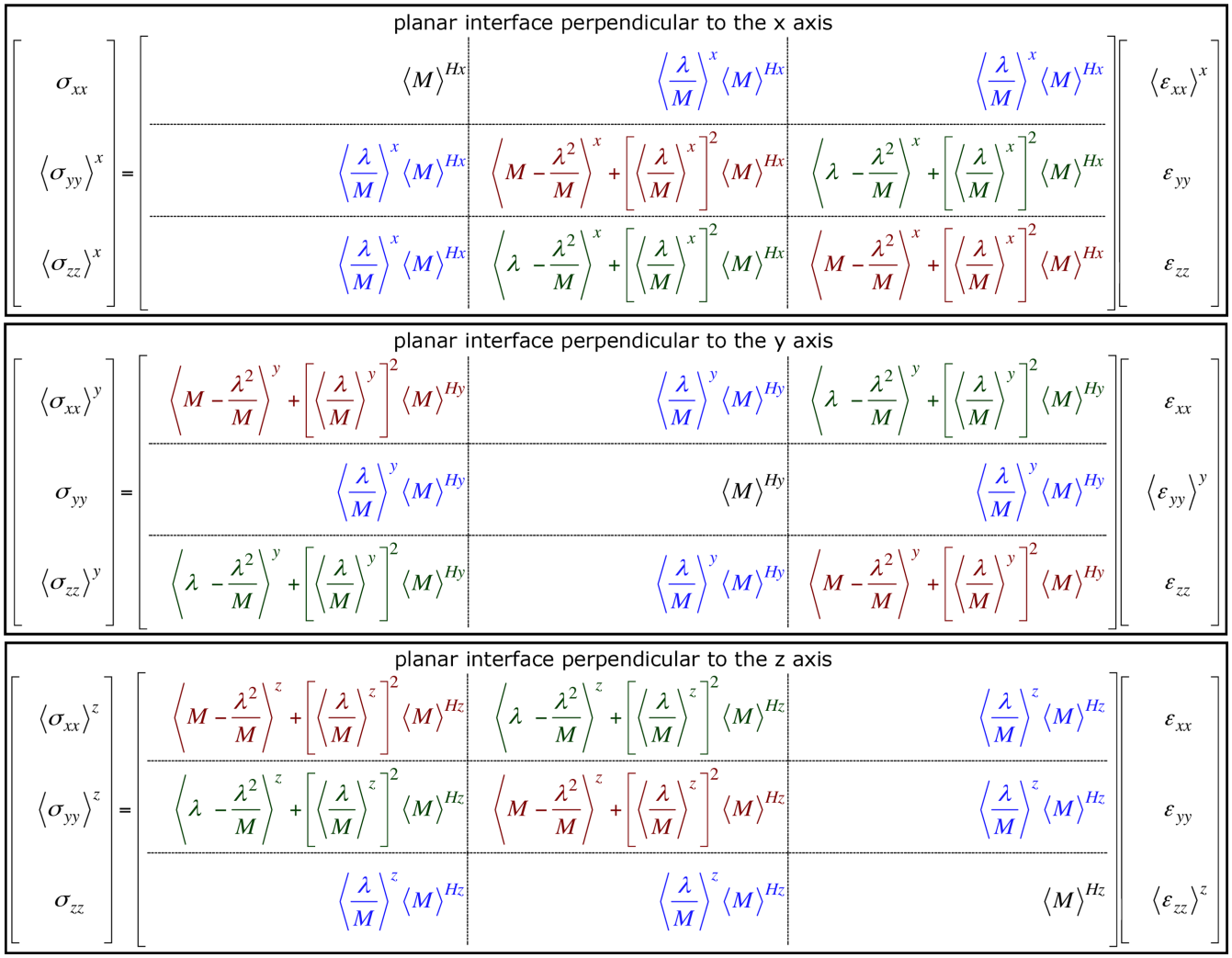

Figure 4. Coefficients for the normal stress-tensor components in the transversely isotropic media representing the planar interfaces perpendicular to the coordinate axes. Colours help to distinguish different averaged moduli.

$$\lambda_{zx} = \left\langle \left\langle M - \frac{\lambda^2}{M} \right\rangle^y + \left[\left\langle \frac{\lambda}{M} \right\rangle^y \right]^2 \langle M \rangle^{Hy} \right\rangle^{Hzx} \times \left\langle \frac{\langle \lambda - \frac{\lambda^2}{M} \rangle^y + [\langle \frac{\lambda}{M} \rangle^y]^2 \langle M \rangle^{Hy}}{\langle M - \frac{\lambda^2}{M} \rangle^y + [\langle \frac{\lambda}{M} \rangle^y]^2 \langle M \rangle^{Hy}} \right\rangle^{zx} \tag{58}$$

Each average applies to a volume of the grid cell $h \times h \times h$ centred at a position of the stress-tensor component. We see that the nine coefficients are independent. This means that the averaged medium has an orthorhombic anisotropy with three axes of symmetry that are identical with coordinate axes.

5 NUMERICAL VERIFICATION

Because the developed discrete representation is approximate it is necessary to test it numerically by comparing the FD seismograms with seismograms obtained using independent verified methods. Whereas for a 1-D model it is possible to use the very accurate semianalytical discrete-wavenumber method (DWM), for 2-D and 3-D models we can only use an approximate but sufficiently accurate numerical method. We have chosen the spectral-element method (SEM). Tests for 1-D and 2-D models were performed and published—we will just briefly mention the substantial aspects. In this article we present 3-D tests.

5.1 1-D models

Moczo *et al.* (2014) and Chaljub *et al.* (2015) presented numerical tests for a set of canonical 1-D models. One model, denoted as Can2, consists of three horizontal homogeneous elastic isotropic layers over half-space. The model represents the vertical profile beneath the TST seismic station in the Mygdonian basin near Thessaloniki in Greece. A 3-D wavefield is generated by a single vertical force at the free surface and a point double-couple (DC) source in the half-space—in order to include both intensive surface and body waves. The simulations are performed for frequencies up to 4 Hz. The other model, Can3, is a modification of Can2: there are vertical constant gradients of material parameters in the layers. The reference solutions are obtained using two DWN codes - Axitra (Bouchon 1981; Coutant 1989) for the DC source and the code developed by Hisada (1994, 1995) for the surface force. The FD seismograms are obtained for four alternative representations: LOC

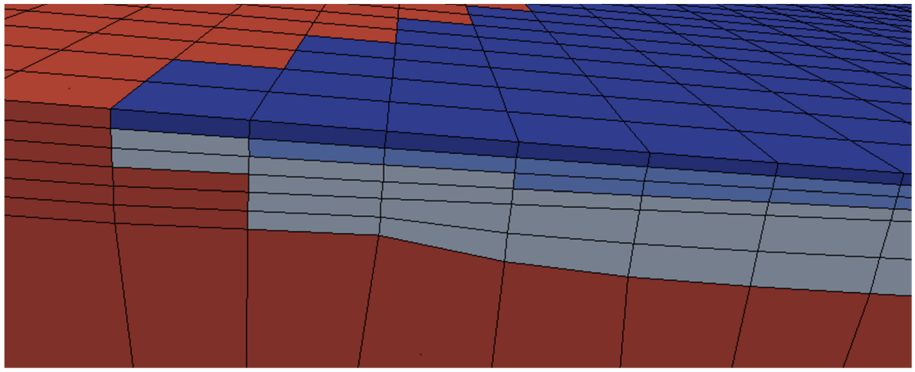

Figure 5. Illustrative detail of the reference SEM model. Different colours represent different homogeneous materials. Element faces exactly follow interfaces. This specific feature makes it possible for SEM to produce sufficiently accurate seismograms. Exactly the same model is considered in the FD simulation.

– local (point) values of the elastic moduli and density, ARI – volume arithmetic averages of moduli and volume arithmetic averages of density evaluated using numerical integration over a grid cell centred at the grid position of the modulus or density, HAR – volume harmonic averages of moduli and volume arithmetic averages of density, and ORT – volume effective coefficients corresponding to the orthorhombic averaged medium. The level of agreement between the FD and DWN seismograms in phase and amplitude is quantified using the time-frequency phase and envelope goodness-of-fit (GOF) criteria (Kristekova *et al*. 2009). The orthorhombic representation yields the best results.

5.2 2-D model

Testing the orthorhombic representation in a 2-D model is much more complicated. Moczo *et al*. (2014) and Chaljub *et al*. (2015) used a 2-D model representing a simplified NS profile of the Mygdonian basin going through the TST seismic station and 3-D wavefield due the point DC source in the half-space. They compared the HAR and ORT FD seismograms with seismograms simulated by the Florent De Martin's SEM code efispec (De Martin 2011). Accuracy of the SEM solution is strongly determined by discretization of the wedge-type Northern margin of the basin. Florent De Martin developed an extremely fine SEM mesh following all material interfaces (though obviously relative, the minimum size of the element is only 0.5 m in simulation up to 4 Hz and minimum *S*-wave speed of 200 m s^{-1}). Consequently, the SEM simulation was computationally extremely demanding. It provided, however, the best feasible reference solution for testing the orthorhombic discretization. The ORT representation yields FD seismograms that are in excellent agreement with the SEM reference seismograms. The HAR representation yields FD seismograms that are in excellent agreement with the SEM seismograms except at receivers where the motion is dominated by surface waves propagating along the horizontal interfaces.

5.3 3-D model

The approach applied in testing the orthorhombic representation in 2-D was not feasible in 3-D due to extreme computational time and memory requirements. In order to obtain a sufficiently accurate reference SEM seismograms, we developed a special model. In the available realistic 3-D model of the Mygdonian basin we modified geometry of material interfaces so that the element faces can exactly follow interfaces. This means that the SEM simulation exactly accounts for the geometry of material interfaces and consequently the SEM seismograms are adequately accurate. Fig. 5 illustrates the SEM mesh. Contact of elements with different colours is a material interface. There are 5 interfaces in the figure showing a detail of the basin edge.

The original model of the Mygdonian basin is shown in Fig. 6. The upper left-hand panel shows margins of the sedimentary basin at the flat free surface, four horizontal profiles of receivers at the free surface and position of the vertical profile of receivers in the central part of the basin. The FD and SEM seismograms are compared along the receiver profiles.

Material parameters of the model are shown in Fig. 7.

The wavefield is generated by a DC point source located at a depth of 5 km. The source time function is shown in Fig. 8. The slip-rate time function is defined as a low-pass filtered Gaussian pulse. The slip is obtained by integration of the slip rate.

The reference SEM seismograms were computed using the SPECFEM3D code developed by Komatitsch and Tromp (e.g. Komatitsch & Tromp 1999; Tromp *et al*. 2008; Peter *et al*. 2011). The FDM seismograms were computed using the FDSim3D code (Kristek & Moczo 2014; Moczo *et al*. 2014). Figs 9 and 10 summarize the SEM and FDM computational parameters.

We calculated the ORT FD seismograms using two spatially discontinuous grids. The size of the fine-grid spacing is 10 m in the first grid and 7 m in the second grid. As in the 1-D and 2-D models, it is reasonable to compare the ORT FD seismograms not only with the reference SEM seismograms but also with HAR FD seismograms. The HAR seismograms were also calculated using the two discontinuous grids. Fig. 11 shows the envelope and phase GOFs (goodness-of-fit) between the reference SEM seismograms and FDM seismograms along the western, central and eastern receiver profiles. Each curve represents GOF between the SEM and respective FD seismograms. GOFs are calculated for the entire 30-s window in the frequency range [0.1, 5] Hz from the arithmetic average of the single-valued misfits evaluated separately for each component (Kristekova *et al*. 2009). Fig. 12 shows the envelope and phase GOFs for the middle and vertical receiver profiles. Recall that GOF = 10 means the perfect agreement.

Overall for a given discrete representation (ORT or HAR) the GOF values for the 7-m grid spacing are larger than the GOF values for the 10-m grid spacing. This means that, for a given discrete representation, the FD seismograms for the smaller size of the grid

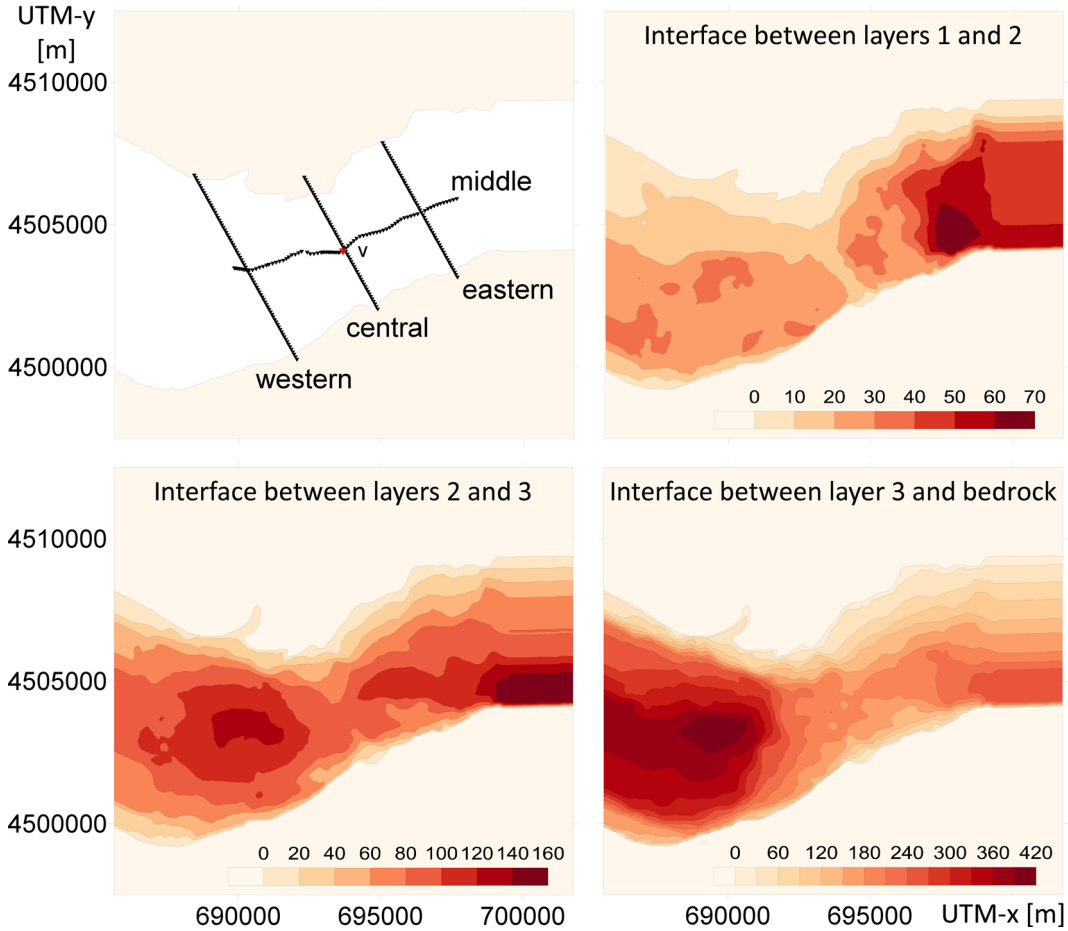

Figure 6. Geometry of the original 3-D model of the Mygdonian basin. Upper left-hand panel: margins of the sedimentary basin at the flat free surface, four horizontal profiles of receivers at the free surface and position of the vertical profile of receivers (v) in the central part of the basin. Upper right-hand panel: interface between the uppermost and middle sedimentary layers. Lower left-hand panel: interface between the middle and bottom sedimentary layers. Lower right-hand panel: interface between the bottom sedimentary layer and bedrock.

Layer	V_S	V_P	ρ
	(m/s)	(m/s)	(kg/m^3)
1	200	1500	2100
2	350	1800	2200
3	650	2500	2200
Bedrock	2600	4500	2600

Figure 7. Material parameters of the 3-D model of the Mygdonian basin.

spacing are closer to the SEM seismograms compared to the FD seismograms for the larger size of the grid spacing. This is what one expects.

The more important is comparison of the two discrete representations. Overall for a given spatial grid the phase GOF values for the ORT discrete representation are significantly larger than the phase GOF values for the HAR representation. In other words, the ORT FD seismograms are significantly closer in phase to the SEM seismograms than the HAR FD seismograms are. The improvement in terms of the envelope GOFs due to the ORT representation compared to the HAR representation is considerable although not as significant as in the phase GOFs.

It is also interesting and important to compare the HAR 7-m FD seismograms with the ORT 10-m FD seismograms. Despite the larger grid spacing the ORT 10-m FD seismograms are significantly more accurate in phase than the HAR 7-m FD seismograms. They are comparably-to-slightly-more accurate in envelope.

Fig. 13 shows seismograms for receiver 166 at the middle profile. The phase GOF values between the four FD seismograms and the reference SEM seismogram at this receiver range approximately from 3.5 to 9. Although we look at just one receiver, the relatively large range of the GOF values makes it possible to reasonably illustrate differences in seismograms corresponding to different GOF values.

6 ACCURACY AND EFFICIENCY OF THE ORTHORHOMBIC REPRESENTATION AND FD MODELLING

Recall Fig. 5 illustrating an important aspect of the SEM modelling. It is natural to cover the spatial computational domain with elements of different shapes and sizes. Consequently, it is possible for SEM to follow geometry of a material interface piece-wise by element faces. This is significant for accuracy of the SEM modelling but, at the same time, can considerably increase the number of elements e.g. in the case of a wedge of a sedimentary layer. In fact, this aspect led to the computationally very much demanding 2-D model developed by Florent De Martin (Section 5.2) as well as to the necessity to adjust geometry of material interfaces in the reference 3-D model

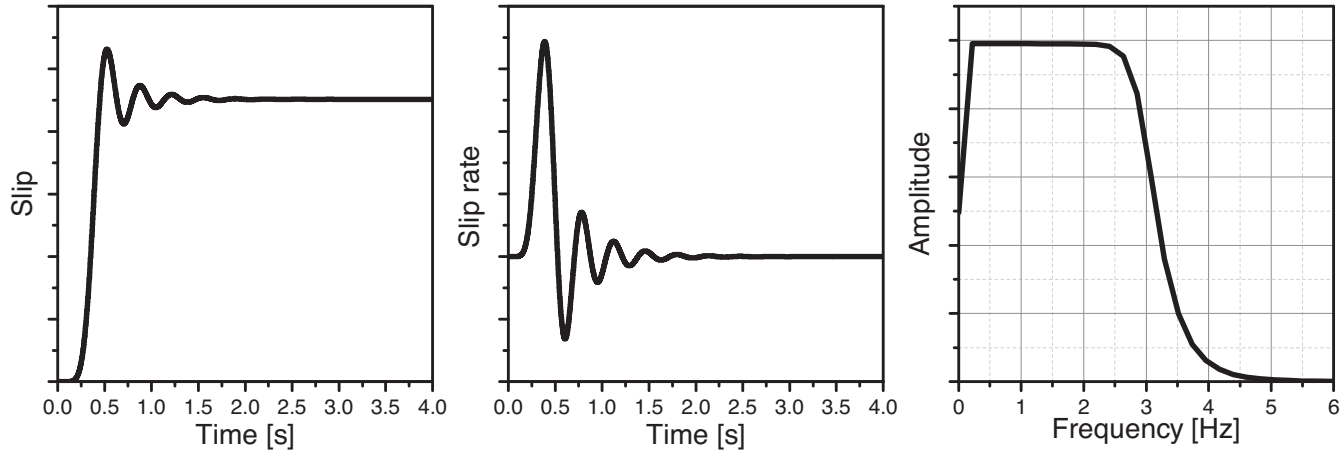

Figure 8. The source time function. Left-hand panel: slip, centre: slip rate, right-hand panel: Fourier amplitude spectrum of the slip rate.

computational domain	16.14 km x 29.31 km x 7.86 km		
number of elements	1 751 040		
polynomial degree	N=4 (5 GLL points per direction)		
number of points (each counted once)	115 605 072		
		vertical	horizontal
(upper) fine mesh	element size	2.5-7.5 m	50 m
	average grid spacing	0.62-1.87 m	12.5 m
	minimum grid spacing	0.43-1.30 m	8.63 m
(lower) coarse mesh	element size	860 m	200 m
	average grid spacing	215 m	50 m
	minimum grid spacing	148.50 m	34.53 m
time step	0.0001 s		
time window	30 s		
note: minimum grid spacing = 0.691 % of average gridsize for N=4			

Figure 9. Computational parameters of the SEM simulation. GLL means Gauss–Lobatto–Legendre.

		FDM 10 m	FDM 7 m
fine grid	size	1585 x 1475 x 59	2113 x 2113 x 84
	grid spacing	10 m	7 m
	PML zone	55 grid planes	55 grid planes
coarse grid	size	145 x 135 x 140	193 x 193 x 200
	grid spacing	110 m	77 m
	PML zone	5 grid planes	5 grid planes
time step		0.001 s	0.0007 s
time window		30 s	30 s

Figure 10. Computational parameters of the FDM simulations with the 10-m and 7-m grid spacings.

of the Mygdonian basin for verification in this study. Obviously, the smaller size of an element, the smaller size of the time step and, consequently, the larger number of time levels to be computed.

The FD modelling is computationally most efficient on the uniform grid and in the heterogeneous formulation. The latter means that one FD scheme is applied to all grid points except those forming a border of the grid. The use of one scheme everywhere means that both smooth and discontinuous heterogeneity has to be accounted for by effective values of moduli and density at respective grid points. An effective grid modulus is evaluated numerically as a volume orthorhombic average in a grid cell centred at the grid position of the corresponding stress-tensor component. An effective density is evaluated numerically as a volume arithmetic average in a grid cell centred at the grid position of the corresponding particle-velocity component. The geometry as well as material properties on both sides of the interface are accounted for by the effective grid moduli and densities. In other words, in a chosen spatial grid, geometry of an interface may be arbitrary. For a given frequency range, change of interface geometry neither requires a new grid, nor changed computational demands. This is the significant advantage of the FD modelling. We illustrate this advantage in Fig. 14.

Note that the size of the FD grid cell should not be directly compared with the size of the SEM element. A SEM element for a given polynomial degree includes certain number of the GLL integration points per direction. For example, in the reference SEM calculation the polynomial degree is 4 and thus the number of GLL points per direction is 5. Therefore, for computational efficiency it is reasonable to compare the total number of the FD grid points with the total number of the GLL points. Usually, in the case of local surface

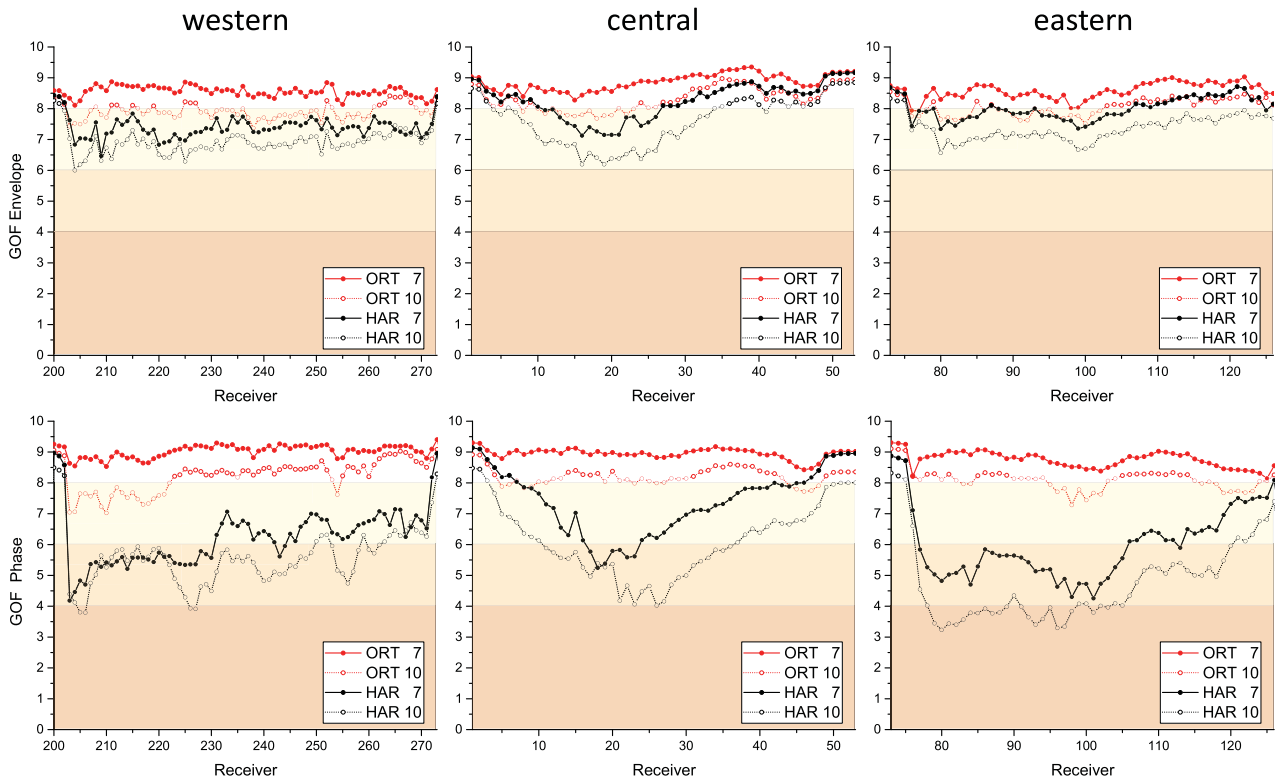

Figure 11. The envelope and phase GOFs (goodness-of-fit) between the reference SEM seismograms and FDM seismograms along the western, central and eastern receiver profiles. The FDM seismograms were obtained using the orthorhombic (ORT) and harmonic (HAR) averaging for the 10-m and 7-m grid spacings.

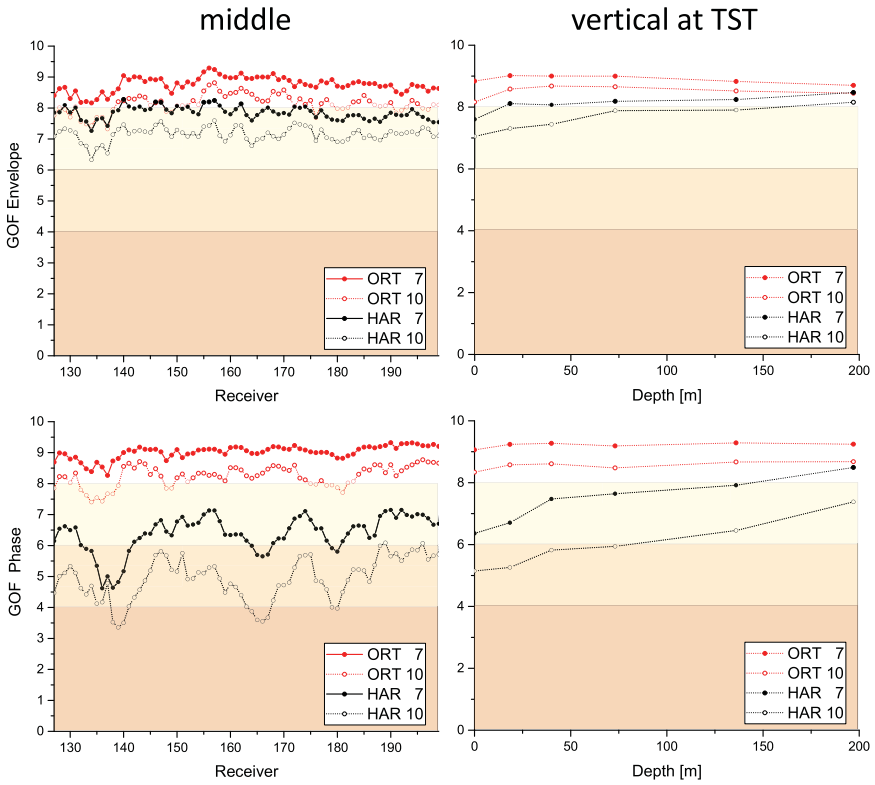

Figure 12. The envelope and phase GOFs (goodness-of-fit) between the reference SEM seismograms and FDM seismograms along the middle profile and vertical profile. The FDM seismograms were obtained using the orthorhombic (ORT) and harmonic (HAR) averaging for the 10-m and 7-m grid spacings.

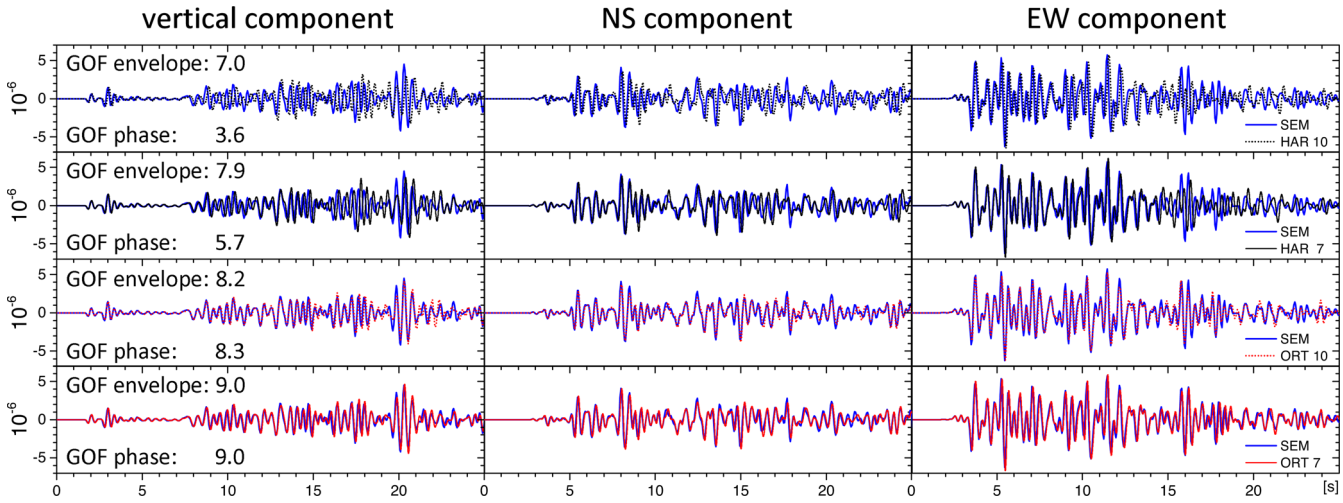

Figure 13. Comparison of the four FD seismograms with the reference SEM seismogram for receiver 166 at the middle profile.

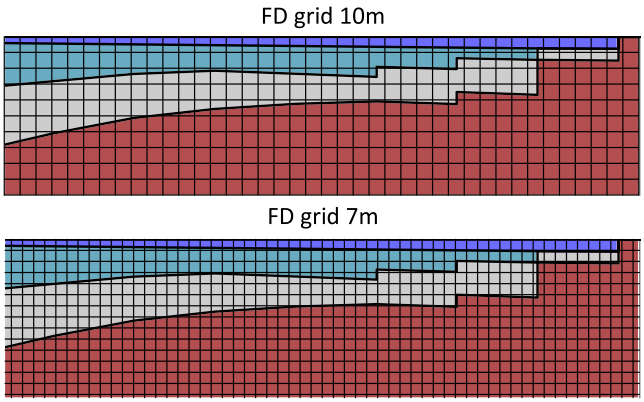

Figure 14. Illustration of the FD grid and material interfaces—a detail of one vertical grid plane crossing the sediment layers in the Mygdonian basin model. Assuming a proper evaluation of the effective grid moduli and densities at grid points there is no need for the grid to be conformable with interfaces.

sedimentary structures with flat free surface, the application of a FD discontinuous spatial grid and effective grid moduli is computationally more efficient than the application of SEM for a given frequency range and level of accuracy. The SEM computational requirements should be decreased if the orthorhombic representation is applied and interfaces are not followed by element faces.

7 CONCLUSIONS

We presented derivation of the stress–strain relation for a point at a planar interface between two homogeneous half-spaces. The derivation is an alternative to the matrix derivation by Moczo *et al.* (2002). Contrary to that the presented derivation makes it possible to interpret the obtained average elastic moduli with respect to continuous and discontinuous stress- and strain-tensor components.

We showed that the approach applicable to the planar interface is not applicable to the joint point of eight homogeneous infinitely large cubes. The average moduli depend on the sequence of averaging (that is, $x \to y \to z$, $y \to z \to x$ and $z \to x \to y$). This is not acceptable because the averaged medium should not depend on the order of averaging.

We have developed a new orthorhombic representation of material heterogeneity. Heterogeneity of the medium in a FD cell is represented by an averaged medium with an orthorhombic anisotropy with three axes of symmetry that are identical with the coordinate axes. An effective grid modulus is evaluated numerically as a volume orthorhombic average in a grid cell centred at the grid position of the corresponding stress-tensor component.

We numerically tested the orthorhombic representation for a complex 3-D model of the Mygdonian sedimentary basin. We compared the FD seismograms with seismograms calculated using the spectral element method (SEM). For achieving sufficient accuracy of the reference SEM solution, we modified geometry of material interfaces so that the element faces exactly follow interfaces. For quantitative comparison of the FD and SEM seismograms we evaluated goodness-of-fit in envelope and phase.

The performed numerical tests show that the orthorhombic representation is more accurate than that developed by Moczo *et al.* (2002). As demonstrated by tests for 1-D and 2-D models, the orthorhombic representation is more accurate mainly for strong surface waves propagating along horizontal material interfaces.

The orthorhombic representation is applicable to modelling seismic wave propagation and earthquake motion in isotropic models with material interfaces and smooth heterogeneities using velocity-stress, displacement-stress and displacement FD schemes on staggered, partly staggered, Lebedev and collocated grids.

ACKNOWLEDGEMENTS

This work was supported in part by the Slovak Research and Development Agency under the contract number APVV-0271-11 (project MYGDONEMOTION), by the Slovak Foundation Grant VEGA-2/0188/15, project Cashima and SIGMA (EDF, AREVA, CEA and ENEL). Part of the calculations were performed in the Computing Centre of the Slovak Academy of Sciences using the supercomputing infrastructure acquired in project ITMS 26230120002 and 26210120002 (Slovak infrastructure for high-performance computing) supported by the Research & Development Operational Programme funded by the ERDF. The SEM calculations were performed using HPC resources from GENCI-TGCC under grants (2013-046060, 2014-046060) and using the Froggy platform from the CIMENT HPC center of Grenoble Alpes University (https://ciment.ujf-grenoble.fr, last accessed March 2016) which is supported by the Rhône-Alpes region (GRANT CPER07_13

CIRA), the OSUG@2020 labex (reference ANR10 LABX56) and the Equip@Meso project (reference ANR-10-EQPX-29-01) of the Programme Investissements d'Avenir supervised by the Agence Nationale pour la Recherche. We appreciate critical and constructive comments by Wei Zhang and an anonymous reviewer.

REFERENCES

Backus, G.E., 1962. Long-wave elastic anisotropy produced by horizontal layering, *J. geophys. Res.,* **67,** 4427–4440.

Bielak, J. *et al.*, 2010. The ShakeOut earthquake scenario: verification of three simulation sets, *Geophys. J. Int.,* **180,** 375–404.

Bouchon, M., 1981. A simple method to calculate Green's functions for elastic layered media, *Bull. seism. Soc. Am.,* **71,** 959–971.

Capdeville, Y. & Marigo, J.-J., 2007. Second order homogenization of the elastic wave equation for non-periodic layered media, *Geophys. J. Int.,* **170,** 823–838.

Capdeville, Y., Stutzmann, E., Wang, N. & Montagner, J.P., 2013. Residual homogenization for seismic forward and inverse problems in layered media, *Geophys. J. Int.,* **194,** 470–487.

Chaljub, E., Cornou, C. & Bard, P.-Y., 2006. Numerical benchmark of 3D ground motion simulation in the valley of Grenoble, French Alps, in *Third International Symposium on the Effects of Surface Geology on Seismic Motion,* Grenoble, France, 2006, August 30th–September 1st, paper number SB1, Vol. 2.

Chaljub, E., Moczo, P., Tsuno, S., Bard, P.-Y., Kristek, J., Käser, M., Stupazzini, M. & Kristekova, M., 2010. Quantitative comparison of four numerical predictions of 3D ground motion in the Grenoble Valley, France, *Bull. seism. Soc. Am.,* **100,** 1427–1455.

Chaljub, E. *et al.*, 2015. 3D numerical simulations of earthquake ground motion in sedimentary basins: testing accuracy through stringent models, *Geophys. J. Int.,* **201,** 90–111.

Coutant, O., 1989. *Program of Numerical Simulation Axitra. Res. Rep. LGIT (in French),* Université Joseph Fourier, Grenoble.

Day, S.M., Bielak, J., Dreger, D.S., Graves, R.W., Larsen, S., Olsen, K.B. & Pitarka, A., 2003. Tests of 3D elastodynamic codes: final report for Lifelines Project 1A02. Pacific Earthquake Engineering Research Center.

De Martin, F., 2011. Verification of a spectral-element method code for the Southern California Earthquake Center LOH.3 viscoelastic case, *Bull. seism. Soc. Am.,* **101,** 2855–2865.

Hisada, Y., 1994. An efficient method for computing Green's functions for a layered half-space with sources and receivers at close depths, *Bull. seism. Soc. Am.,* **84,** 1456–1472.

Hisada, Y., 1995. An efficient method for computing Green's functions for a layered half-space with sources and receivers at close depths (Part 2), *Bull. seism. Soc. Am.,* **85,** 1080–1093.

Komatitsch, D. & Tromp, J., 1999. Introduction to the spectral-element method for 3-D seismic wave propagation, *Geophys. J. Int.,* **139,** 806–822.

Kristek, J. & Moczo, P., 2014. 'FDSim3D – The Fortran95 code for numerical simulation of seismic wave propagation in 3D heterogeneous viscoelastic media'. Available at: www.cambridge.org/moczo, last accessed 30 June 2016.

Kristekova, M., Kristek, J. & Moczo, P., 2009. Time-frequency misfit and goodness-of-fit criteria for quantitative comparison of time signals, *Geophys. J. Int.,* **178,** 813–825.

Maufroy, E. *et al.*, 2015. Earthquake ground motion in the Mygdonian basin, Greece: the E2VP verification and validation of 3D numerical simulation up to 4 Hz, *Bull. seism. Soc. Am.,* **105,** 1398–1418.

Moczo, P., Kristek, J., Vavryčuk, V., Archuleta, R.J. & Halada, L., 2002. 3D heterogeneous staggered-grid finite-difference modeling of seismic motion with volume harmonic and arithmetic averaging of elastic moduli and densities, *Bull. seism. Soc. Am.,* **92,** 3042–3066.

Moczo, P., Kristek, J., Galis, M. & Pazak, P., 2010. On accuracy of the finite-difference and finite-element schemes with respect to P-wave to S-wave speed ratio, *Geophys. J. Int.,* **182,** 493–510.

Moczo, P., Kristek, J., Galis, M., Chaljub, E. & Etienne, V., 2011. 3-D finite-difference, finite-element, discontinuous-Galerkin and spectral element schemes analysed for their accuracy with respect to P-wave to S-wave speed ratio, *Geophys. J. Int.,* **187,** 1645–1667.

Moczo, P., Kristek, J. & Galis, M., 2014. *The Finite-Difference Modelling of Earthquake Motions: Waves and Ruptures,* Cambridge Univ. Press.

Muir, F., Dellinger, J., Etgen, J.T. & Nichols, D., 1992. Modeling elastic fields across irregular boundaries, *Geophysics,* **57,** 1189–1193.

Peter, D. *et al.*, 2011. Forward and adjoint simulations of seismic wave propagation on fully unstructured hexahedral meshes, *Geophys. J. Int.,* **186,** 721–739.

Schoenberg, M. & Muir, F., 1989. A calculus for finely layered anisotropic media, *Geophysics,* **54,** 581–589.

Tromp, J., Komatitsch, D. & Liu, Q., 2008. Spectral-element and adjoint methods in seismology, *Commun. Comput. Phys.,* **3,** 1–32.

Tsuno, S., Chaljub, E. & Bard, P.-Y., 2006. Results from numerical benchmark of 3D ground motion simulation in the alpine valley of Grenoble, in *Proceedings of the 3rd International Symposium on the Effects of Surface Geology on Seismic Motion,* Grenoble, 29 August–1 September, 2006, eds Bard, P.-Y., Chaljub, E., Cornou, C., Cotton, F. & Guéguen, P., LCPC Editions.

IV.2 Verification of numerical simulations

1. Chaljub, E., Moczo, P., Tsuno, S., Bard, P.-Y., Kristek, J., Kaser, M., Stupazzini, M., & Kristekova, M., 2010. Quantitative comparison of four numerical predictions of 3D ground motion in the Grenoble valley, France, *Bull. Seismol. Soc. Am.*, **100**(4), 1427–1455.
2. Chaljub, E., Maufroy, E., Moczo, P., Kristek, J., Hollender, F., Bard, P.-Y., Priolo, E., Klin, P., de Martin, F., Zhang, Z., Zhang, W., & Chen, X., 2015. 3-D numerical simulations of earthquake ground motion in sedimentary basins: testing accuracy through stringent models, *Geophys. J. Int.*, **201**(1), 90–111.

Bulletin of the Seismological Society of America, Vol. 100, No. 4, pp. 1427–1455, August 2010, doi: 10.1785/0120090052

Quantitative Comparison of Four Numerical Predictions of 3D Ground Motion in the Grenoble Valley, France

by Emmanuel Chaljub, Peter Moczo, Seiji Tsuno, Pierre-Yves Bard,* Jozef Kristek, Martin Käser, Marco Stupazzini, and Miriam Kristekova

Abstract This article documents a comparative exercise for numerical simulation of ground motion, addressing the seismic response of the Grenoble site, a typical Alpine valley with complex 3D geometry and large velocity contrasts. Predictions up to 2 Hz were asked for four different structure wave-field configurations (point source and extended source, with and without surface topography). This effort is part of a larger exercise organized for the third international symposium on the effects of surface geology (ESG 2006), the complete results of which are reported elsewhere (Tsuno *et al.*, 2009).

While initial, blind computations significantly differed from one another, a remarkable fit was obtained after correcting for some nonmethodological errors for four 3D methods: the arbitrary high-order derivative discontinuous Galerkin method (ADER-DGM), the velocity-stress finite-difference scheme on an arbitrary discontinuous staggered grid (FDM), and two implementations of the spectral-element method (SEM1 and SEM2). Their basic formulation is briefly recalled, and their implementation for the Grenoble Valley and the corresponding requirements in terms of computer resources are detailed.

Besides a visual inspection of PGV maps, more refined, quantitative comparisons based on time-frequency analysis greatly help in understanding the origin of differences, with a special emphasis on phase misfit. The match is found excellent below 1 Hz, and gradually deteriorates for increasing frequency, reflecting differences in meshing strategy, numerical dispersion, and implementation of damping properties.

While the numerical prediction of ground motion cannot yet be considered a mature, push-button approach, the good agreement reached by four participants indicates that, when used properly, numerical simulation is actually able to handle correctly wave radiation from extended sources in complex 3D media. The main recommendation to obtain reliable numerical predictions of earthquake ground motion is to use at least two different but comparably accurate methods, for instance the present formulations and implementations of the FDM, SEM, and ADER-DGM.

Introduction

The very fact that a large part of the world's populations lives in earthquake-prone areas implies that seismologists must predict earthquake ground motion during potential future earthquakes, no matter whether they can or cannot timely predict earthquake occurrence. Prediction of the earthquake motion at a site of interest is extremely important for designing new buildings and reinforcing existing ones, as well as for undertaking actions that could help mitigate losses during future earthquakes.

Theory and numerical simulation are irreplaceable tools in the earthquake ground-motion research, mainly for two reasons. Considering the present-day limitations of direct controlled physical experiments in seismology, it is extremely difficult to scale laboratory experiments to real structures. Moreover, in most cases, there is a drastic lack of earthquake recordings at the sites of interest.

Given the present state of our knowledge of the processes and structures that form earthquake ground motion, and, at the same time, capabilities of modern seismic arrays, realistic 3D computational models have to include nonplanar interfaces between layers, gradients in velocity, density, and quality

*Also at Laboratoire Central des Ponts-et-Chaussées, 58 Bd Lefebvre, 75732, Paris Cedex 15, France.

factors inside layers, and often free-surface topography. In particular, the rheology of the medium has to allow for realistic broadband attenuation. Realistic strong ground-motion simulations should also account for nonlinear behavior in soft soils, which will, however, be neglected here for the sake of simplicity.

Only approximate computational methods are able to account for the structural complexity of the realistic models. The most important aspects of each method are accuracy and computational efficiency (in terms of computer memory and time). These two aspects are in most cases contradictory. A reasonable balance between the accuracy and computational efficiency in case of complex realistic structures made the numerical modeling methods dominant among all approximate methods.

A number of different numerical modeling methods have been developed within the last few decades. Each method has its advantages and disadvantages that often depend on the particular application. Therefore, it is very unlikely that one of the existing or recently developed numerical modeling methods can be systematically and simultaneously the most accurate and the most efficient for all important medium wave-field configurations.

In general, a sufficiently high level of agreement or sufficiently small level of misfit between data and theoretical prediction can be considered a confirmation of a theoretical model of an investigated process. In particular, the agreement between recorded and numerically predicted earthquake motion can be considered an ultimate criterion for capability of seismologists to simulate earthquake ground motion. A procedure of evaluating the capability of the theoretical model to describe the reality can be called validation. Clearly, in the validation it is necessary to understand what is a reasonable level of agreement. Given the complexity and inevitable uncertainty of realistic models (earthquake source and material structure), this is not a simple problem. Certainly, first we have to be sure that the numerical simulation method and its implementation in the computer code are correct. A procedure of evaluating the capability of the method to solve the elastodynamic equations with initial and boundary conditions can be called verification. Without the method verification, it is impossible to properly evaluate the level of agreement between recorded and simulated motions. Consequently, verification of the recent numerical modeling methods for complex realistic models is an important task.

The importance of the objective comparison, verification, and validation of the numerical modeling methods is evidenced by different initiatives. On one hand, the Southern California Earthquake Center (SCEC) has recently organized 3D numerical simulation code validation projects for wave propagation (Day *et al.*, 2003) and dynamic rupture simulations (Harris *et al.*, 2009). The goal was to validate and compare 3D earthquake simulation methods, and foster their application by the engineering community. On the other hand the EU FP6 SPICE project (Seismic Wave Propagation and Imaging in Complex Media: A European Network, www.spice-rtn.org, 2004–2007) aimed at development of computational tools for seismic wave propagation, earthquake motion, and seismic imaging. SPICE has established an open Internet-based digital library (Gallovic *et al.*, 2007; www.spice-rtn.org/library), which comprises computer codes, training materials, simulation exercises, and an interactive web interface for code validation (Moczo *et al.*, 2006; www.nuquake.eu/SPICECVal/). The main goal of the SPICE Code Validation is to provide an open long-term basis for possible tests and comparisons of the numerical methods and codes for the seismic wave propagation and earthquake motion simulations. The objective evaluation of accuracy and comparison is facilitated using the time-frequency misfit criteria (Kristekova *et al.*, 2006) interactively applicable to a solution one wants to compare with any of the previously uploaded solutions.

In parallel, real sites and realistic models were prime targets of the blind prediction tests in framework of three international symposia on the effects of surface geology (ESG) in Odawara, Japan (1992), Yokohama, Japan (1998), and Grenoble, France (2006). The ESG 2006 symposium provided an excellent opportunity to focus on numerical modeling of earthquake motion in the Grenoble Valley for local weak and moderate earthquakes. The Grenoble Valley is a very interesting and typical deep Alpine sediment-filled structure. The Grenoble urban area, mostly built over the sedimentary area, gathers a significant population (around 500,000), a number of high-tech and/or sensitive industrial facilities, and educational and research institutions. Therefore, despite an only moderate regional seismic hazard (with known historical events hardly reaching magnitude 6) and considerable broadband site effects, Lebrun *et al.* (2001) raised the concern about the seismic risk in such Alpine valley configurations, which are also met in different other areas within the European Alps, and in other mountainous areas with embanked valleys filled with young, postglacial lacustrine sediments.

Our article presents results of a multi-institution project and an unprecedented comparison of very different and important methods applied to a structurally complex model of a real site. The scope of our article is not to benchmark computer codes that solve a well-referenced problem with a known analytical solution. Rather, our article considers a realistic 3D problem for which we do not have a reference solution. There is no objective way of defining an absolute level of accuracy for the different predictions of the seismic response of the Grenoble Valley.

The applied methods have been developed by various teams in different institutions using different computer facilities. It was not technically feasible to perform presented simulations on the same computer. It is important to realize that the use of the same computer is of marginal importance compared with the main aspect of the article.

The scope and goal of our article match those of the SCEC code validation project that targeted the Los Angeles basin to demonstrate the reachable level of agreement among

the leading U.S. modeling teams. Our article has a similar goal; in addition, it considers a wider set of numerical methods and a significantly higher maximum frequency.

Compared with the Los Angeles basin, the modeling of the Grenoble Valley is complicated by the relatively large velocity contrast and the complex interface geometry. The level of the reached agreement was not possible to anticipate and thus is not trivial.

Structurally complex models of real sedimentary valleys pose great challenges. Even though there have been a number of attempts at validation, the agreement between synthetics and data remains far from satisfactory, except for very low frequencies, say < 0.1 Hz. This is because one cannot isolate the validity of the simulation from that of other factors, such as the material model, including possible nonlinearities, and the source description. One common way to reduce the influence of these factors is to use small earthquakes, whose rupture can be modeled as a point source.

Given the model complexity and methodological differences among the applied methods, we found a surprisingly good level of agreement for four of the submitted predictions obtained by different teams: Käser *et al.* (2006) used the arbitrary high-order derivative discontinuous Galerkin method (ADER-DGM), Chaljub (2009) used the spectral-element method (SEM), Kristek *et al.* (2009) used the finite-difference method (FDM), and Stupazzini (2009) and Stupazzini *et al.* (2009) used another implementation of the SEM. The ADER-DGM, FDM, and SEM differ both in the basic formulations of the equations of motion and boundary conditions, and the way they construct discrete models and the resulting systems of algebraic equations. They also differ in the required computer memory and time. At the same time these three methods, together with the finite-element method (FEM), are at present the most powerful numerical modeling methods for earthquake ground motion. Whereas the FDM and FEM have a relatively long tradition, the SEM has been used since the early 1990s; ADER-DGM has been elaborated and applied to seismology rather recently. Despite this relatively long tradition of the FDM and FEM, they are still being developed in terms of accuracy and efficiency, and it is reasonable to expect considerable improvements.

In this article we first present the structural model of the Grenoble Valley and definition of the numerical simulations. In the next section we briefly introduce the ADER-DGM, FDM, and SEM. Computational aspects of the simulations for the Grenoble Valley are then discussed. The main part of the article presents comparison of the numerical results obtained with the ADER-DGM, FDM, and two implementations of the SEM. We conclude with main lessons learned and recommendations for future blind predictions and benchmark tests.

Structural Model of the Grenoble Valley

Grenoble is settled on Quaternary fluvial and postglacial deposits at the junction of three large valleys of the French external Alps (Fig. 1), surrounded by three mountain ranges. This junction mimics the letter Y (the so-called Grenoble Y), with three legs:

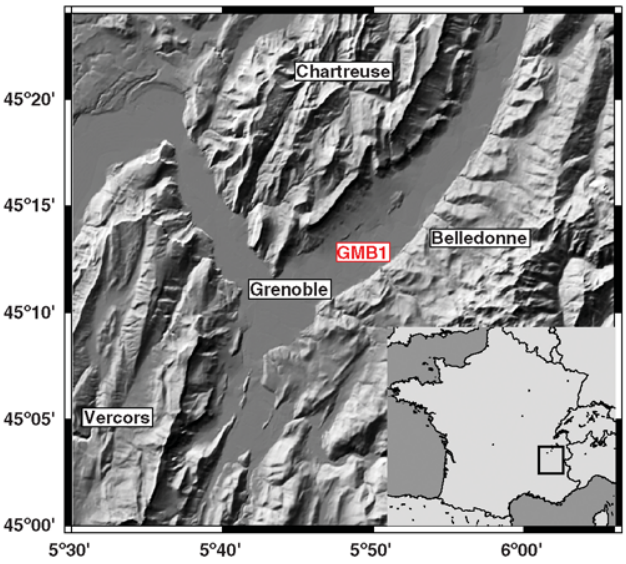

Figure 1. Situation map of the Grenoble area in the French Alps, showing the Y-shaped Grenoble Valley surrounded by the Vercors and Chartreuse limestone massifs with maximal elevation of 2000 m, and the crystalline Belledonne chain where elevation reaches 3000 m. GMB1 indicates the location of the Montbonnot borehole (see text).

1. The northeastern branch of the Y is the N30°–40° trending Grésivaudan Valley, extending about 60 km upstream along the Isère River.
2. The northwestern branch is the N150° trending, Cluse-de-l'Isère Valley, extending from Grenoble to Moirans (about 20 km), where the Isère River flows to the northwest.
3. The southern branch follows the Drac River, flowing from the south and arriving in a small plain about 15 km upstream of Grenoble.

The three massifs delineated by these valleys are the Belledonne crystalline massif to the east and two subalpine foothills consisting of sedimentary rocks (limestone) to the north (Chartreuse) and the southwest (Vercors). These foothills were formed when the Alpine shortening displaced the sedimentary cover to the northwest, forming folds and related thrusts (7 to 5 m.y. B.P.) and uplifted the crystalline basement (5 m.y. B.P.) to the east of the study area (Belledonne massif).

The IsèreValley (from upper Grésivaudan to downstream Cluse-de-l'Isère) therefore extends for about 110 km from Albertville in the northwest to Rovon west of the Vercors massif; it is 3 to 5 km wide and quasi-flat, with slowly decreasing altitudes (330 m in Albertville, 211 m in Grenoble, 180 m in Rovon). The surrounding mountains exhibit, however, a pronounced topography with maximum elevations slightly above 2000 m in Vercors and Chartreuse and above 3000 m in the Belledonne massif. As explained by Gamond *et al.*

(2009), this course runs along several hundred meters deep paleovalley carved in the Mesozoic sedimentary cover of the Alpine foothills. The northeast-southwest Grésivaudan Valley was dug by erosion around 5 m.y. B.P. through the tributaries of the paleo-Isère River, while the northwest-southeast Cluse-de-l'Isère was carved by epigenesis between 5 and 2 m.y. B.P. when the foothills were uplifted.

Its present morphology presents asymmetrical inclined sides and longitudinal moraines typical of glacial valleys. During the last glacial-interglacial cycles, as all valleys in the western Alps, it was successively eroded and overdeepened by thick Alpine glaciers (Isère glacier, local glaciers of the Belledonne massif, Drac-Romanche glacier) feeding large ice lobes at the piedmont and then filled essentially by lake sediments as glaciers were melting and retreating higher up in the catchments during warm phases. In the IsèreValley, both proglacial and deltaic lacustrine sediments completely filled an up to 900 m deep and 100 km long fjordlike basin during the last deglaciation, while only a thin, fluvial sequence formed during our interglacial period (Chapron *et al.*, 2009).

Despite the relatively good mechanical characteristics of these quaternary deposits, the large impedance contrast with the embedding rocks, together with the large embankment ratio, cause huge amplifications as observed by Lebrun *et al.* (2001), Cornou *et al.* (2003a, 2003b), and Cornou *et al.* (2009). A series of geotechnical and geophysical investigations has thus been carried out in the Grenoble area to improve the knowledge of the underground structure. A summary of these investigations can be found in the series of dedicated articles included in Volume 2 of the ESG 2006 proceedings (Chapron *et al.*, 2009; Cornou *et al.*, 2009; Dietrich *et al.*, 2009; Gamond *et al.*, 2009; Guéguen *et al.*, 2009; Jerram *et al.*, 2009; Ménard, Blein, Fournier *et al.*, 2009; Ménard, Dietrich, Vallon *et al.* 2009) and in Guéguen *et al.* (2007). Their primary focus was to constrain the deep structure responsible for the low-frequency effects; once this objective was met, a secondary objective was assigned to better understand the shallow structure controlling the higher-frequency amplification and its short-wavelength lateral variations. Because the ESG 2006 numerical simulations were limited to a 2 Hz maximum frequency, only the deep underground structure and large-scale geometry and topography are presented here.

The first deep investigations consisted in several hundreds of gravimetric measurements that allowed constraining the geometry of the sediment/bedrock interface and indicating a large thickness close to 1 km in the deepest part (Vallon, 1999). This information was checked and calibrated through the drilling of one deep borehole in the Grésivaudan Valley (the Montbonnot GMB1 site in Fig. 1, now instrumented with three accelerometers at the surface, GL-42 m, and GL-550 m), which reached the bedrock at a depth of 535 m, very close to the expectations from the gravimetric survey. Above a thin (4 m thick) glacial till, the post-Würm filling sequence consists in 520 meters of monotonous lacustrine sandy-silty formations corresponding to the postglacial lake, and ends with 15 meters of sandy-pebbly alluvium deposited when the presently working Isère fluviatile regime started again (Nicoud *et al.*, 2002).

As described by Chapron *et al.* (2009), Dietrich *et al.* (2009) and Ménard, Dietrich, Vallon *et al.* (2009), the nature of this postglacial sedimentary infill has also been documented by a set of seismic reflection profiles acquired both on land in the Isère Valley and in large valley lakes, such as the Le Bourget Lake 50 km to the north of Grenoble. All highlight very thick, rather homogeneous quaternary deposits with nonnegligible *P*- and *S*-wave velocity gradients. All these measurements have been complemented by several hundreds of microtremor measurements processed with the H/V technique (Guéguen *et al.*, 2007, 2009), which consistently exhibit a low-frequency peak (usually between 0.3 and 0.5 Hz) associated with the thick lacustrine filling, and in some parts, a second higher frequency peak (ranging from 2 to 5–6 Hz).

In summary, the main conclusions of all these deep investigations are:

- 20 km of seismic reflection profiles at different cross sections along the Isère Valley, together with the information collected in the borehole drilled near Grenoble and reaching the sediment-bedrock, allowed us to calibrate or confirm the information provided by gravimetric surveys and background noise H/V measurements on distribution of the sediment thickness in the valley.
- The bottom of the valley is marked by an irregular topography. The bottom of the Isère Valley shows a great variety of shapes: flat bottom, wide open V-shape, V-shape interlocked in a larger U-shaped valley. At some places, there exist underground substratum highs, such as a hillock (probably of tithonic age) that could be identified just south of the Grenoble downtown (see Fig. 2).
- The depth of the substratum increases downstream the Isère River from about 200 m in the upper Grésivaudan, 500 m in the lower Grésivaudan, and more than 800 m in the Cluse of Grenoble.
- The seismic velocities are roughly laterally homogeneous at depths larger than 20–40 m, in line with the filling of the valley by the postglacial lacustrine deposits.
- The *P*- and *S*-wave velocity distributions within the sediments are characterized by moderate to strong vertical gradients, with the V_P/V_S ratio varying between 6 near the surface and 2.7 at several hundred meters depth.

Given the limitation of our numerical simulation exercise to an upper frequency of 2 Hz, we thus considered a simple depth-varying sediment velocity model derived from the deep borehole measurements. The valley model is thus described by two main components:

- A 3D geometry consisting of a free-surface topography and a sediment-basement interface.
- Sediment and bedrock velocity models exhibiting only a 1D depth dependence.

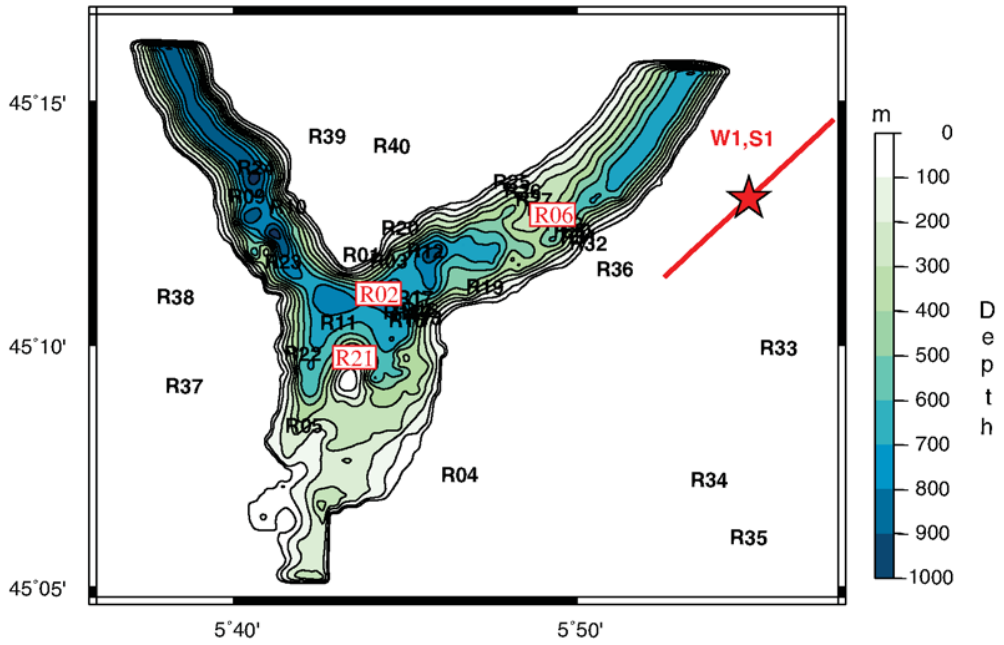

Figure 2. Map of sediment thickness in the Grenoble Valley showing 40 receivers (R01 to R40) used in the simulations. Contour lines every 100 m are shown; the bold black line indicates the points where the sediment thickness equals 50 m. The positions of the point source W1 and extended source S1 are shown in red. Red boxes indicate particular receivers for which a detailed comparison is shown further in the article. Receiver R06 corresponds to the GMB1 location in Figure 1.

The geometry of the surface topography is shown in Figure 1, and the underground topography is depicted in Figure 2. The velocity model is detailed in Table 1. This model is still distant from the reality, especially for the shallow part. It constitutes, however, a good starting model that is able to reproduce the main features of the low-frequency response, and it is complex enough to enable a meaningful comparison between different numerical methods.

The quality factor values were chosen infinite in the underlying bedrock. The bedrock is very stiff and the computations are performed only for local, shallow sources, so that crustal damping effects may be thought negligible in a first step. The quality factor was taken slightly larger than that actually measured in the Montbonnot borehole ($Q_P = 35$, see Cornou, 2002), but these measurements were obtained at higher frequencies (several tens of Hertz); higher Q values are needed to reproduce the observed low-frequency duration within the valley (Chaljub, 2009).

Selected Earthquakes

Various active tectonic features such as basement thrusts and strike-slip faults have been described in this part of the Alps (Thouvenot *et al.*, 2003, 2009). However, the known history reports only moderate earthquakes with intensities reaching VIII on the Medvedev, Sponheuer, and Karnik (MSK) scale, and estimated magnitudes between M 5 and M 6. The last significant earthquake in the Grenoble immediate surroundings was an M 5.3 earthquake that occurred in Corrençon (Vercors, about 30 km to the southwest of Grenoble) in 1962, which caused some chimney falls in the city.

The densification of the seismic monitoring networks undertaken in the late 1980s revealed some clear, previously unsuspected seismic alignments. In particular, the Belledonne Border Fault (BBF) has been identified as the most active of these new features: it consists of a 50 to 70 km long, northeast-southwest trending segment, characterized by

Table 1
Mechanical Parameters for the Grenoble Valley Model

Unit	Thickness	Unit Mass (kg/m^3)	S-Wave Velocity β (m/sec)	P-Wave Velocity α (m/sec)	Quality Factor Q_S	Quality Factor Q_P
Sediments	Up to 1000 m	$2140 + 0.125z$*	$300 + 19\sqrt{z}$	$1450 + 1.2z$	50	$37.5\ \alpha^2/\beta^2$
Bedrock	0–3 km	2720	3200	5600	∞	∞
	3–27 km	2720	3430	5920	∞	∞
	27–35 km	2920	3810	6600	∞	∞
	>35 m	3320	4450	8000	∞	∞

*z refers to depth expressed in meters.

many small earthquakes exhibiting a right-lateral strike-slip motion consistent with an east–west compressive tectonic environment. Such a segment could therefore easily accommodate an M 6 event, with recurrence rates, however, well beyond the 500- to 1000-year historic period. This fault runs indeed east of and parallel to the northeast branch of the Y, with a distance of approximately 5–7 km from the eastern edge of the Isère–Grésivaudan Valley.

Because several recordings could be obtained at different sites from a small magnitude event on this fault near the village of Lancey in 2003, it was decided to simulate the ground motion for two earthquakes (Chaljub *et al.*, 2009):

- A real, weak one, called W1, corresponding to this 2003 event. This event had a moment magnitude M 2.9, and was assumed to be a point source with a 45° strike angle and a 90° dip angle, located at a 3 km depth. (There is, however, a significant uncertainty on the depth estimate, which could be up to 8 km).
- A hypothetical, stronger event (S1), corresponding to an M 6 event rupturing the Belledonne Border Fault along a segment centered at the W1 hypocenter. The fault length and width were assumed to be 9 and 4.5 km, respectively. A very simple (and, indeed, somewhat pessimistic and unrealistic) kinematics was assumed. The rupture nucleates at the fault center, propagates circularly with a rupture velocity equal to 2.8 km/sec, and stops abruptly when it reaches the boundary of the rectangular fault area. In addition, the slip distribution is flat (i.e., constant slip over the whole ruptured area). Such a fault mechanism generates very strong stopping phases, especially as the rupture is very shallow: the resulting ground-motion values are thus unrealistically high, and should be taken with much caution if applied to hazard estimates. Such a scenario nevertheless constitutes a good case for a comparison between different numerical methods, because it includes very strong pulses with high directivity.

For both cases, the source function was defined as

$$s(t) = 0.5(1 + \mathrm{erf}[4(t - 2\tau)/\tau]), \qquad (1)$$

where τ is the rise time chosen to provide an average slip velocity on the fault plane equal to 1 m/sec. It was thus taken equal to 0.03 sec for the weak event (W1) case, and to 1.16 sec for the strong event case (S1).

The ground motion from each of these events was computed at a series of 40 receivers displayed in Figure 2 (some of them corresponding to the location of a few seismological or accelerometric stations that recorded the M 2.9, 2003 Lancey earthquake). Most of these receivers are located at the surface, but two are located at depth and correspond to the Montbonnot downhole sensors (receiver R06 corresponds to the GMB1 location in Fig. 1). Receivers R01, R04, and R33 to R40 are located on rock outcrops, whereas all the others are located within the valley.

The simulation exercise proposed for the ESG 2006 symposium also included another set of twin events (W2, S2), located 20 km to the south of Grenoble, corresponding to a conjugate strike-slip fault with a west-northwest–east-southeast strike. A more complete description of the simulation exercise can be found in Chaljub *et al.* (2009) and Tsuno *et al.* (2009). In the present article, however, only the (W1, S1) set of events is considered.

Fourteen different groups from eight countries contributed to the ESG 2006 comparison, providing a total of 18 prediction sets; three groups used the empirical Green's function technique for the few receivers collocated with strong motion stations, two used a 1D (horizontal layering) approach for the borehole site, three modeled the response of a 2D cross section, and seven addressed the 3D problem, out of which three could account for the effects of both underground and surface topography. The numerical schemes used for 3D contributions belong to the finite-difference, spectral-element and discontinuous-Galerkin finite-element methods. Four participants whose 3D predictions were surprisingly close updated their results after the ESG meeting, after correcting some nonmethodological errors (evidenced by comparing to other predictions) in preparation of the numerical simulations. Only the results from the corrected predictions are considered here. Further details on all other methods and results can be found in Tsuno *et al.* (2009).

Computational Methods

3D Fourth-Order Velocity-Stress Finite-Difference Scheme on an Arbitrary Discontinuous Staggered Grid

Although the FDM has been used in seismology since the late 1960s, its elaboration for the structurally complex media is certainly far from being completed. Recent elaboration of the staggered-grid schemes for viscoelastic media with material interfaces as well as the development of the optimally accurate schemes are two examples soundly indicating that the best times of the finite-difference modeling are still ahead of us. Because we do not have space here for more details, we refer to the recent comprehensive review (Moczo, Robertsson, Eisner, 2007) and monograph (Moczo *et al.*, 2007).

For the numerical simulations we used a 3D fourth-order velocity-stress finite-difference scheme on an arbitrary discontinuous staggered grid. A complete theory can be found in articles by Moczo *et al.* (2002, 2004), Kristek *et al.* (2002), Kristek and Moczo (2003), and Moczo and Kristek (2005). Here we restrict our focus to the essential aspects of the simulation method.

The scheme solves the equation of motion and Hooke's law for viscoelastic medium with rheology of the generalized Maxwell body,

$$\rho \dot{v}_i = \sigma_{ij,j} + f_i, \qquad (2)$$

and

$$\dot{\sigma}_{i,j} = \kappa\dot{\varepsilon}_{kk}\delta_{ij} + 2\mu\left(\dot{\varepsilon}_{ij} - \frac{1}{3}\dot{\varepsilon}_{kk}\delta_{ij}\right) - \sum_{l}^{4}\left[\kappa Y_l^{\kappa}\xi_l^{kk}\delta_{ij} + 2\mu Y_l^{\mu}\left(\xi_l^{ij} - \frac{1}{3}\xi_l^{kk}\delta_{ij}\right)\right], \quad (3)$$

$$\dot{\xi}_l^{ij} + \omega_l\xi_l^{ij} = \omega_l\dot{\varepsilon}_{ij}; \qquad l = 1, \ldots, 4. \quad (4)$$

Here, in a Cartesian coordinate system (x_1, x_2, x_3), $\rho(x_i)$; $i\in\{1, 2, 3\}$, is density; $\kappa(x_i)$ and $\mu(x_i)$ unrelaxed (elastic) bulk and shear moduli; Y_l^{κ} and Y_l^{μ} anelastic coefficients; $\vec{u}(x_i, t)$ displacement vector; t time; $\vec{f}(x_i, t)$ body force per unit volume; $\sigma_{ij}(x_k, t)$, $\varepsilon_{ij}(x_k, t)$, i, j, and $k\in\{1, 2, 3\}$ stress and strain tensors; ξ_l^{ij} material-independent anelastic functions; and ω_l relaxation angular frequencies. Summation convention does not apply to index l. The anelastic coefficients are obtained from

$$Y_l^{\kappa} = \left(\alpha^2 Y_l^{\alpha} - \frac{4}{3}\beta^2 Y_l^{\beta}\right)\Big/\left(\alpha^2 - \frac{4}{3}\beta^2\right),$$
$$Y_l^{\mu} = Y_l^{\beta}; \qquad l = 1, \ldots, 4, \quad (5)$$

where α and β are elastic (corresponding to the unrelaxed moduli) P- and S-wave velocities, and anelastic coefficients Y_l^{α} and Y_l^{β} are obtained from the desired/measured quality factor values

$$Q_{\nu}^{-1}(\tilde{\omega}_k) = \sum_{l=1}^{n}\frac{\omega_l\tilde{\omega}_k + \omega_l^2 Q_{\nu}^{-1}(\tilde{\omega}_k)}{\omega_l^2 + \tilde{\omega}_k^2}Y_l^{\nu};$$
$$k = 1, \ldots, 7, \qquad \nu\in\{\alpha, \beta\}. \quad (6)$$

The schemes for solving the equation of motion and time derivative of Hooke's law have the same structure as standard fourth-order velocity staggered-grid schemes. The accuracy of our scheme is determined by how we treat smooth material heterogeneity and material discontinuity. The effective grid density for a corresponding particle velocity component is evaluated as an integral volume arithmetic average of density inside a grid cell centered at the grid position of the corresponding particle velocity component; for example

$$\rho^{A}_{I,J+1/2,K+1/2} = \frac{1}{h^3}\int_{x_{I-1/2}}^{x_{I+1/2}}\int_{y_J}^{y_{J+1}}\int_{z_K}^{z_{K+1}}\rho\,\mathrm{d}x\mathrm{d}y\mathrm{d}z. \quad (7)$$

The effective grid, unrelaxed bulk, and shear moduli are evaluated as integral volume harmonic averages of moduli in respective grid cells centered at grid positions of the stress-tensor components; for example

$$\kappa^{H}_{I+1/2,J+1/2,K+1/2} = \left[\frac{1}{h^3}\int_{x_I}^{x_{I+1}}\int_{y_J}^{y_{J+1}}\int_{z_K}^{z_{K+1}}\frac{1}{\kappa}\mathrm{d}x\mathrm{d}y\mathrm{d}z\right]^{-1}. \quad (8)$$

The integrals are evaluated numerically, and the grid cell can contain a material discontinuity. The anelastic coefficients Y_l^{κ} and Y_l^{μ} are determined as follows: An average viscoelastic modulus in the frequency domain is numerically determined for a cell as an integral harmonic average. A corresponding quality factor is then determined from the averaged viscoelastic modulus at specified frequencies. Equation (6) for the bulk and shear moduli is then used to determine average anelastic functions. A coarse spatial distribution of the anelastic functions is applied in order to reduce the memory requirements.

The free surface is simulated using the AFDA technique (Kristek *et al.*, 2002; Moczo *et al.*, 2004).

If the near-surface sedimentary body with lower seismic wave velocities is covered by a fine spatial grid and underlying stiffer bedrock with larger velocities is covered by a coarser spatial grid, the number of grid points and, consequently, the computer memory and time requirements are significantly reduced compared with the uniform grid. In order to make such a combined (or discontinuous) spatial grid efficient, the ratio of the size of the spatial grid spacing in the coarser grid and that in the finer grid should correspond to the ratio of the shear-wave velocities in the stiffer bedrock and softer sediments. Therefore, Kristek *et al.* (2009) and Moczo *et al.* (2007) developed an algorithm that enables us to adjust a discontinuous spatial grid accordingly except that, due to the structure of the staggered grid, the ratio of the spatial grid spacings in the coarser and finer grids has to be an odd number. In other words, depending on the model of medium, we can choose a 1:1 (uniform) grid, or 1:3, 1:5, … discontinuous grid. The grid is illustrated in Figure 3. A Fortran 95 computer code 3DFD_VS has been developed for performing the finite-difference scheme. PML absorbing boundary conditions are implemented. The code is MPI parallelized (see the Data and Resources section for details).

3D Spectral-Element Method

The spectral-element method (SEM) has been introduced quite recently for seismological applications (Seriani and Priolo, 1991, 1994; Faccioli *et al.*, 1997; Komatitsch and Vilotte, 1998). The SEM is a special kind of the finite-element method (FEM) that relies on the use of a high-order spectral polynomial basis. Like the FEM, the SEM can naturally handle media with complex geometries, including surface topography and nonplanar interfaces, and it allows local mesh refinement to account for variations in seismic wavelengths. Moreover, compared with the traditional low-order FEM, the high-order spectral basis yields very accurate results by minimizing numerical dispersion and numerical anisotropy (Seriani and Oliveira, 2007; de Basabe and Sen, 2007). In practice, polynomial orders $N = 4$ to $N = 8$ are used and provide sufficiently accurate results for both body and surface waves, as soon as 5 to 6 points are used to sample the seismic wavelengths.

In the classical SEM, as in the two implementations presented hereafter, the choice of the element shapes, polynomial basis, and numerical integration rule relies on tensorization, that is, on separation of variables. The advantage is the possibility to increase significantly the computational

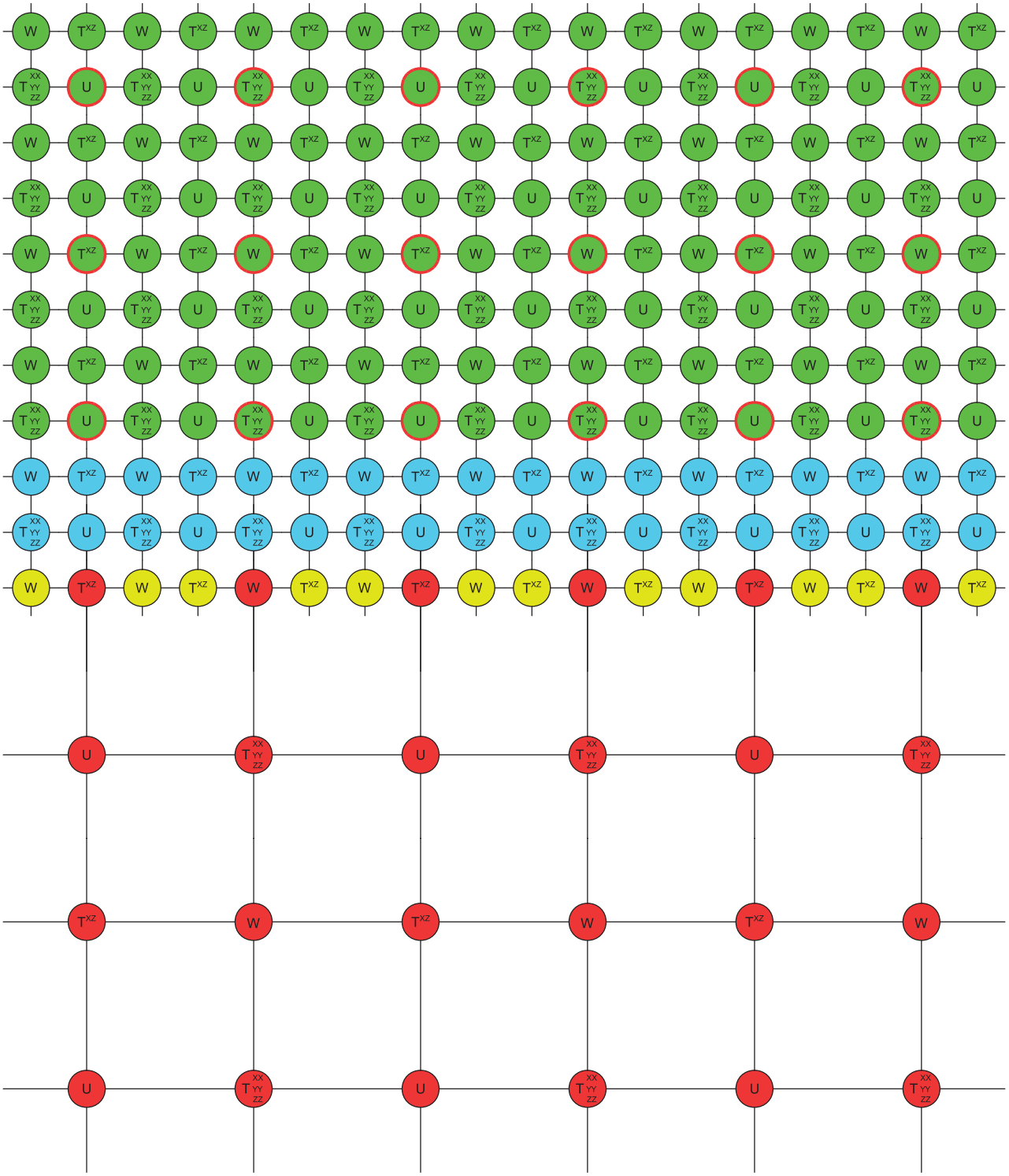

Figure 3. A vertical grid plane in the arbitrary discontinuous spatial staggered grid in the case of the coarser-to-finer spatial grid spacing equal to 3. The interior grid positions of the finer grid: green, 4th-order FD scheme; blue, 2nd-order FD scheme; yellow, bicubic interpolation. The interior grid positions of the coarser grid: red, 4th-order FD scheme. The red-circumscribed green positions define the boundary of the coarser grid.

efficiency by (1) leading to a diagonal mass matrix, allowing fully explicit schemes to be used for time evolution; and (2) decreasing the computational cost of the internal forces. The drawback is the restriction of the geometry of spectral elements to quadrangles in 2D and to hexahedra in 3D. Recall indeed that in order to account properly for discontinuities in elastic parameters, the spectral elements must not intersect the physical interfaces. This condition is not always easy to account for in a hexahedra-based SEM, for example, near valley or basin edges. Extensions of the SEM to 2D meshes of triangular elements have been proposed recently at the price of either losing the diagonal character of the mass matrix (Mercerat *et al.*, 2005) or decreasing the spectral accuracy (Komatitsch *et al.*, 2001).

Review papers presenting the numerous developments of the SEM for global or regional seismology applications can be found in Komatitsch *et al.* (2005) and Chaljub *et al.* (2007). Here, we briefly recall the key features of the SEM discretization.

Through the principle of virtual work, the dynamic equilibrium problem for the medium Ω can be stated in the following weak or variational form: find $\boldsymbol{u} = \boldsymbol{u}(\boldsymbol{x}, t)$, displacement vector, such that $\forall t \in (0, T)$

$$\frac{\partial^2}{\partial t^2}\int_\Omega \rho \boldsymbol{u}\cdot\boldsymbol{v}d\Omega + \int_\Omega \sigma_{ij}(\boldsymbol{u})\varepsilon_{ij}(\boldsymbol{v})d\Omega = \int_{\Gamma_N} \boldsymbol{t}\cdot\boldsymbol{v}d\Gamma + \int_\Omega \boldsymbol{f}\cdot\boldsymbol{v}d\Omega, \quad i,j = 1\ldots d \quad \text{for all } \boldsymbol{v}, \tag{9}$$

where t is time, $\rho = \rho(\boldsymbol{x})$ the material density, σ_{ij} the stress-tensor, ε_{ij} the infinitesimal strain tensor, $\boldsymbol{f} = \boldsymbol{f}(\boldsymbol{x}, t)$ the known body force distribution, $\boldsymbol{t} = \boldsymbol{t}(\boldsymbol{x}, t)$ the vector of external traction prescribed on Γ_N, and $\boldsymbol{v} = \boldsymbol{v}(x)$ is the generic function (candidate to represent admissible displacements). Note that the free-surface condition is obtained implicitly, or naturally, in the weak formulation. The stress and strain tensors in (9) are related to the displacement by Hooke's law (3).

An appropriate numerical solution of (9) can be achieved through discretization in the space and time domain. Herein, the latter is done via finite differences; the best trade-off in terms of accuracy, stability, and computational complexity is obtained using the explicit second-order leapfrog scheme (LF2-LF2) (Maggio and Quarteroni, 1994) that must satisfy the well-known Courant-Friedrichs-Lewy (CFL) stability condition.

The spatial discretization is based upon the Galerkin approximation to equation (9). It starts with a decomposition of the computational domain Ω into a family of nonoverlapping, unstructured quadrilaterals Ω_k (or hexahedra in 3D). Each element Ω_k is obtained by a regular mapping of a reference element Ω_{ref} (the unit square $[-1, +1]^2$ in 2D and the unit cube $[-1, +1]^3$ in 3D). Then, admissible displacements are approximated by polynomials of degree N on each element. This writes formally

$$\sum_{k=1}^{K}\frac{\partial^2}{\partial t^2}\int_{\Omega_k}\rho u_N^{(i)}\cdot v^{(i)}d\Omega + \sum_{k=1}^{K}\int_{\Omega_k}\sigma_{lm}(\boldsymbol{u}_N^{(i)})\varepsilon_{lm}(\boldsymbol{v}_N^{(i)})d\Omega = \sum_{k=1}^{K}\int_{\Gamma_N^{(k)}} t^{(i)}v^{(i)}d\Gamma_N + \sum_{k=1}^{K}\int_{\Omega_k} f^{(i)}v^{(i)}d\Omega, \tag{10}$$

where $\boldsymbol{u}_N$ and $\boldsymbol{v}_N$ denote the approximations of $\boldsymbol{u}$ and $\boldsymbol{v}$, and $u_N^{(i)}$, $v_N^{(i)}$, $t_N^{(i)}$, $f^{(i)}$ the scalar components of the vectors $\boldsymbol{u}_N$, $\boldsymbol{v}_N$, $\boldsymbol{t}$ and $\boldsymbol{f}$. Note that equation (10) implicitly assumes that the displacements are globally continuous, but the material properties can be discontinuous across elements.

The integrals in (10) are evaluated numerically by a high-order quadrature formula based on the Gauss-Lobatto-Legendre (GLL) points (Davis and Rabinowitz, 1984; Canuto *et al.*, 1988). The polynomials used to approximate the displacements are then defined as the shape functions of the GLL points. Thanks to this particular choice, the SEM inherits the exponential accuracy of spectral methods in space: for problems with sufficiently smooth exact solution $\boldsymbol{u}$, the numerical solution $\boldsymbol{u}_N$ obtained in the SEM converges more rapidly than those based upon the classical FEM. This property is known as spectral accuracy in the literature, and the convergence of the spectral methods is referred to as exponential or geometrical, as opposed to the algebraic convergence of the classical FEM. Note that this does not hold for the numerical realization of the free-surface condition: the convergence of numerical traction toward the prescribed traction is only algebraical (Deville *et al.*, 2002). For the wave propagation applications, the numerical accuracy is more properly assessed by the analysis of numerical dispersion, which has been shown recently to be optimal for the SEM (Seriani and Oliveira, 2007; de Basabe and Sen, 2007).

Assembling the elementary contributions to account for the continuity of displacements, equation (10) can be written as a global system of ordinary differential equations in time,

$$[M]\ddot{\boldsymbol{U}}(t) + [K]\boldsymbol{U}(t) = \boldsymbol{F}(t) + \boldsymbol{T}(t), \tag{11}$$

where vectors $\boldsymbol{F}$ and $\boldsymbol{T}$ stem from the contributions of the external forces and applied tractions, $\boldsymbol{U}$ stores the displacement values $\boldsymbol{u}_N(x, t)$ at the GLL nodes, and $[M]$ and $[K]$ denote the mass and the stiffness matrices, respectively. An important consequence of the choice of the polynomial basis is that the mass matrix is diagonal, which, as stated previously, allows for the use of fully explicit finite-difference schemes for the time evolution.

In the following we will present two different implementations of the SEM. In the first SEM-based code, hereafter referred to as SEM1, viscoelasticity is accounted for using a superposition of the standard linear solids (SLS; Liu *et al.*, 1976), which are implemented via memory variables (see Chaljub *et al.*, 2007, and references therein). Note that a parallel superposition of the SLS is also called the generalized Zener body. Also note that the rheology of the generalized Zener body is equivalent to that of the generalized Maxwell body as shown by Moczo and Kristek (2005). Thus,

the rheology in the SEM1 is equivalent to that implemented in the FD and ADER-DGM methods described in the article. The Lysmer and Kuhlemeyer (1969) absorbing boundary conditions are applied. (See the Data and Resources section for details on the SEM1 software package.)

In the second implementation, hereafter referred to as SEM2, the viscoelastic behavior is implemented with a frequency linear dependent quality factor, implying that all frequency components are equally attenuated (Faccioli *et al.*, 1997). Kosloff and Kosloff (1986) showed that this can be easily obtained by replacing the inertia term into the wave equation with an *ad hoc* expression. The absorbing boundaries are implemented following Stacey's (1988) first-order P3 paraxial conditions. A more detailed description of the software package adopted for the SEM2 simulation can be found in Stupazzini *et al.* (2009) (also see the Data and Resources section for details on the SEM2 software).

3D Velocity-Stress Discontinuous Galerkin Scheme with ADER-Time Integration of Unstructured Tetrahedral Meshes

The proposed numerical method combines a discontinuous Galerkin (DG) finite-element scheme with a time-integration technique using Arbitrarily high-order DERivatives (ADER) in order to solve the governing PDE with arbitrarily high approximation order in time and space. The system of the 3D seismic wave equations formulated in velocity-stress leads to a hyperbolic system of the form

$$\frac{\partial Q_p}{\partial t} + A_{pq}\frac{\partial Q_q}{\partial \xi} + B_{pq}\frac{\partial Q_q}{\partial \eta} + C_{pq}\frac{\partial Q_q}{\partial \zeta} = E_{pq}Qq + S_p, \tag{12}$$

where the vector Q of unknowns contains the six stress and the three velocity components. The Jacobian matrices A, B, and C include the material values and can include anisotropic, viscoelastic, or poroelastic material properties as explained in detail in Dumbser and Käser (2006), Käser *et al.* (2007), de la Puente *et al.* (2007) and (2008). The viscoelastic medium and the attenuation is defined by rheology of the GMB-EK, the same as described in the section on the finite-difference method. Furthermore, the reactive source term E is necessary, if viscoelastic attenuation is considered, and S is an external source term accommodating force of moment tensor sources. In the discontinuous Galerkin approach, the solution is approximated inside each tetrahedral element by a linear combination of space-dependent polynomial basis functions and time-dependent degrees of freedom as expressed through

$$(Q_h)_p(\xi,\eta,\zeta,t) = \hat{Q}_{pl}(t)\Phi_l(\xi,\eta,\zeta), \tag{13}$$

where the basis functions Φ_l form an orthogonal modal basis and are defined on the canonical reference tetrahedron. Note that there are no integration points necessary, because the basis is a modal basis and not a nodal basis as typically used in the SEM.

As the fully detailed derivation of the numerical scheme would go beyond the scope of this article, we refer to the previous work of Käser and Dumbser (2006) and Dumbser and Käser (2006) for a detailed mathematical formulation of the discontinuous Galerkin method. The unique property of the ADER-DGM scheme is, that the time accuracy of the scheme is automatically coupled to the space accuracy determined by the degree of approximation polynomials used in equation (13). This is due to the ADER time-integration approach (Titarev and Toro, 2002), where the fundamental idea is to expand the solution of equation (12) via a Taylor series in time

$$Q_p(\xi,\eta,\zeta,t) = \sum_{k=0}^{N}\frac{t^k}{k!}\frac{\partial^k}{\partial t^k}Q_p(\xi,\eta,\zeta,0), \tag{14}$$

where we then replace all time derivatives in equation (14) by space derivatives using the governing PDE in equation (12). It can be shown that the k-th time derivative can be expressed recursively as

$$\frac{\partial^k}{\partial t^k}Q_p = (-1)^k\left(A_{pq}\frac{\partial}{\partial \xi} + B_{pq}\frac{\partial}{\partial \eta} + C_{pq}\frac{\partial}{\partial \zeta}\right)^k Q_q + E_{pq}\frac{\partial^{k-1}}{\partial t^{k-1}}Q_p + \frac{\partial^{k-1}}{\partial t^{k-1}}S_p. \tag{15}$$

Using equations (13) and (15) in (14), the Taylor series expansion only depends on space derivatives of the basis functions Φ_l and lower order time derivatives of the source terms. The resulting expression for the degrees of freedom can be integrated in time analytically as shown in detail by Dumbser and Käser (2006) or Käser *et al.* (2007). Therefore, this new approach, termed ADER-DG method, provides arbitrarily high-order approximation in space and time depends on the degree of the used basis polynomials Φ_l in equation (13) and the corresponding order of the time Taylor series chosen in equation (14).

Once the high-order time-integrated degrees of freedom are computed, the evolution of the numerical solution in time is calculated via local stiffness and flux terms (Dumbser and Käser, 2006). Especially, the flux computations contribute as the major part with more than 80% to the overall computational cost. A numerical flux out of the element and a numerical flux into the element have to be calculated for each element boundary, that is, triangular surface, for each tetrahedral element. Each flux computation requires a multiplication of two matrices F and Q of the sizes:

size of F: (number of degrees of freedom) × (number of degrees of freedom) and
size of Q: (number of degrees of freedom) × (number of variables in the system).

The stiffness terms, however, are relatively cheap as only one matrix-matrix-multiplication of the same computational complexity has to be carried out. Nevertheless, all

operations use only local data, that is, data from the element itself and its direct neighbor sharing a common element boundary. Due to this local character of the numerical scheme, a number of different optimization approaches have been developed (Dumbser *et al.*, 2007) to enhance computational efficiency, in particular for parallel computing.

p_τ-Adaptation. In most applications, the computational domain is larger than a particular zone of interest. Therefore, a large number of elements is needed to discretize the entire geometry of the model. However, high-order accuracy might only be required in a relatively small portion of the computational domain, which makes it desirable to choose the accuracy adaptively in space. With the ADER-DG approach, it is possible to vary the degree p of the approximation polynomials Φ_l in equation (13) from one element to the other. Due to the direct coupling of the time and space accuracy via the ADER approach, the scheme automatically becomes adaptive in time accuracy, which is referred to as p_τ-adaptation.

Local Timestepping. Geometrically complex computational domains or spatial resolution requirements often lead to meshes with small or possibly degenerate elements. The timestep for explicit numerical schemes is determined by the ratio of the mesh size h of the smallest element and the corresponding maximum wave speed in this element. For global timestepping schemes, all elements are updated with this extremely restrictive timestep length, leading to a large amount of iterations. With the ADER approach, time accurate local timestepping can be used, so that each element is updated by its own, optimal timestep. An element can be updated to the next time level if its actual time level and its local timestep Δt fulfill the condition with respect to all neighboring tetrahedrons n,

$$t + \Delta t \leq \min(t_n + \Delta t_n). \tag{16}$$

Information exchange between elements across interfaces appears when numerical fluxes are calculated. These fluxes depend on the length of the local time interval over which a flux is integrated and the corresponding element is evolved in time. Therefore, when the update criterion (16) is fulfilled for an element, the flux between the element itself and its neighbor n has to be computed over the local time interval:

$$\tau_n = [\max(t, t_n), \min(t + \Delta t, t_n + \Delta t_n)]. \tag{17}$$

This can reduce the overall amount of flux calculations dramatically because only the small elements have to be updated frequently according to their small timestep lengths. A full description of the p_τ-adaptation and local timestepping of the ADER-DG scheme is given by Dumbser *et al.* (2007).

Grouped Mesh Partitioning. For large-scale applications it is essential to design a parallel code for supercomputing facilities, where load balancing is an important issue. However, if p_τ-adaptivity and especially local timestepping are applied, the partitioning is sophisticated because a subdomain can have different polynomial orders and timestep lengths. We split the computational domain into zones that usually contain geometrical or geological entities that are meshed individually. Then, each of these zones is partitioned separately into subdomains of equal numbers of elements, which now include tetrahedral elements with roughly the same sizes and orders of accuracy. Finally, each processor receives a subdomain from each zone and therefore gets a similar computational load. In Figure 4a we show a partition of the full tetrahedral mesh used for the Grenoble model, where each subdomain is color-coded. In Figure 4b we show the grouped partitioning used to improve load balance.

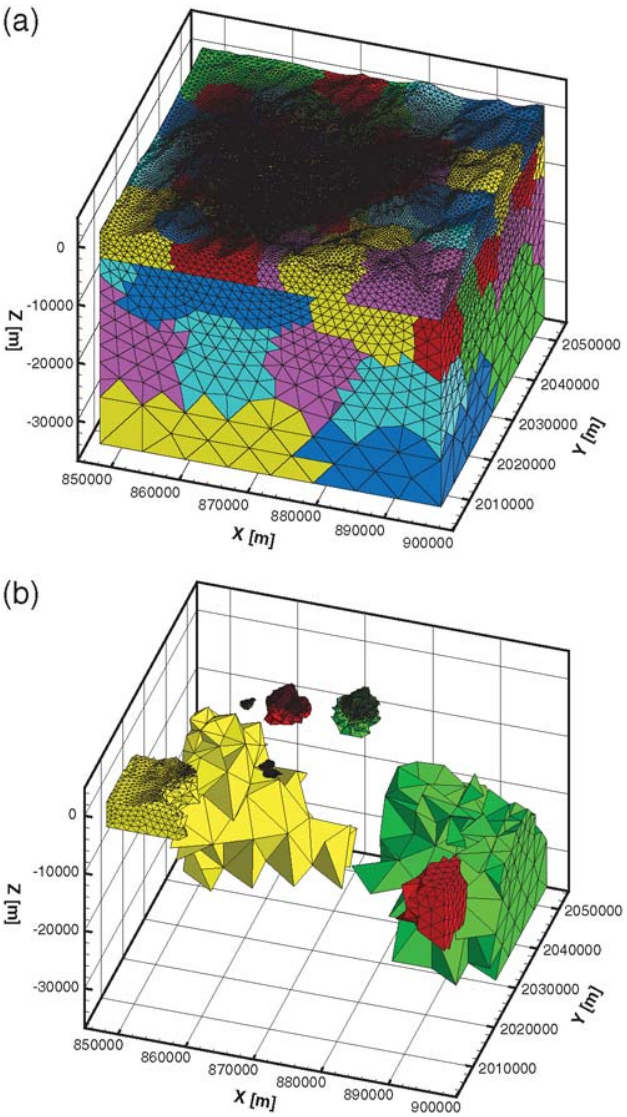

Figure 4. (a) Partitioning of an unstructured tetrahedral discretization of the Grenoble model. (b) Separate subdomains that contain a balanced number of small and large tetrahedrons from different zones are given to each processor, as indicated by the same color, to optimize the load balance.

Comparison of Computational Aspects in Modeling Earthquake Motion in Grenoble Basin

3D Fourth-Order Velocity-Stress Finite-Difference Scheme on an Arbitrary Discontinuous Staggered Grid

Space-Time Grid. The computational domain is a rectangular parallelepiped covered by a discontinuous staggered grid. The upper part of the model with a sedimentary body, 1125 m thick, is covered by a finer grid with a grid spacing of 25 m. The finer grid is made of $1321 \times 1431 \times 45$ grid cells. The lower part of the model, covering a major part of the bedrock, 8125 m thick, is covered by a coarser grid with a grid spacing of 125 m. The coarser grid is made of $265 \times 287 \times 65$ grid cells. The coarser grid is overlapping 187.5 m of the finer grid. The 1:5 discontinuous spatial grid means 87% reduction in the total number of grid cells compared to the uniform grid with a grid spacing of 25 m (approximately 90 mil. of grid cells in the discontinuous grid instead of 700 mil. of grid cells in the uniform grid). Fifty and ten grid spacings are grid thicknesses of the PML boundary regions in the finer and coarser grids, respectively. The timestep is 0.0022 sec. The used spatial grid means that the simulation should be sufficiently accurate up to 2.5 Hz.

Material Heterogeneity and Attenuation. The true model geometry of the material interfaces as well as the smooth material heterogeneity inside the sedimentary body are accounted for in the evaluation of the effective material elastic and anelastic grid parameters grid using relations (5)–(8) and the approach described therein. We can note that the scheme using the integral volume harmonic averages of the moduli and integral volume arithmetic average of density, evaluated for each cell centered at a relevant grid position, is capable to sense the true position of the material interfaces within the cell.

The constant $Q(\omega)$ law is simulated using the rheology of the generalized Maxwell body. The so-called coarse grid graining is applied in the spatial discretization of the anelastic coefficients and functions. The Q values are specified at four frequencies: 0.07 Hz, 0.225 Hz, 0.71 Hz, and 2.25 Hz. This should accurately cover the frequency range of 0.04 to 4 Hz. The P- and S-wave velocities are specified at a frequency of 1 Hz.

Treatment of the Kinematic Source. The finite kinematic model of the rupturing surface is simulated using 1836 regularly distributed point double-couple sources over a fault area 9 km × 4.5 km for the S1 event. Each point source is simulated using a discrete system of body forces acting at the grid positions centered at the grid position of the normal stress-tensor component. All point sources have the same focal parameters and source-time functions. The action of the individual point sources in time is prescribed and corresponds to the specified rupture velocity.

Accuracy versus Efficiency. All simulations were performed on a small cluster of the Opteron 2.2 machines (6 CPUs, 10 GB RAM in total). The computational parameters are given in Table 2.

3D Spectral-Element Method: The SEM1 Implementation

Model Geometry and Mesh Generation. In the first implementation of the SEM, SEM1, a simple meshing strategy, as proposed by Komatitsch *et al.* (2004), is adopted. The topology of the mesh is that of a layer-cake model in which the interfaces are deformed to follow, as much as possible, the physical interfaces. This strategy has the advantage of being easy to implement, but it also has some drawbacks. First, the size of the elements does not vary horizontally, which prevents the use of very large models as the ones that would be needed to propagate the seismic wave field from a distant earthquake to the Grenoble Valley. For the Grenoble simulation, which considers only local sources, this point is not critical; it has the nice consequence of providing a more accurate discretization of the free-surface topography, which is rather stiff in the Grenoble area (see Fig. 5). Second, the sediment-bedrock interface is not accounted for at depths shallower than about 350 m (see Fig. 6). The velocity

Table 2
Comparison of the Computational Parameters

Test Case	Number of Grid Cells or Elements	Order in Space/Time	Timestep	Number of Central Processing Units	Central Processing Unit Time	Memory
DSG Velocity-Stress FD						
W1 Flat	90,009,370	4/2	0.0022 sec	6	~33 hr	~10 GB
S1 Flat	90,009,370	4/2	0.0022 sec	6	~33 hr	~10 GB
SEM1						
W1 Flat	332,160	4/2	0.0005 sec	32	~9 hr	~10 GB
S1 Topography	332,160	4/2	0.0005 sec	32	~9 hr	~10 GB
SEM2						
S1 Topography	216,972	3/2	0.0003 sec	63	~10 hr	~18 GB
ADER-DG						
W1, S1 Flat	870,613	5/5	0.0001 sec	510	~32 hr	~50 GB
S1 Topography	1,259,721	5/5	0.0001 sec	510	~48 hr	~70 GB

contrasts near the valley edges are thus approximated by continuous variations using the polynomial basis within each spectral element. Although not quantified, the error due to this approximation is not expected to be too large because the size of the near-surface elements close to the valley edges is that of the smallest wavelength in the simulation (that is, about 150 m for a 2 Hz calculation). The mesh is coarsened with depth using the conforming strategy proposed by Komatitsch *et al.* (2004) as shown in Figure 6. We use a polynomial order $N = 4$ within each element. For calculations accurate for frequencies up to 2 Hz, the mesh contains 332,160 elements and 22,062,624 grid points.

Material Heterogeneity and Attenuation. For the attenuation model provided in the ESG exercise, the generalized Zener body with three relaxation mechanisms was used in order to mimic a constant shear quality factor in the sediments within the frequency band (0.2 Hz–10 Hz). The reference frequency, which was not imposed, is chosen to be the fundamental frequency of the Grenoble Valley, $f0 = 0.3$ Hz. Time extrapolation was handled by a second-order explicit Newmark finite-difference scheme, with an additional Runge-Kutta scheme being used to march in time the memory variables needed to model viscoelasticity (see details in Komatitsch and Tromp, 1999).

Treatment of the Kinematic Source. To model the strong motion case S1, we considered a set of 1250 point sources regularly distributed on the prescribed fault plane. Each point source was assigned a moment magnitude M 2.9 and an onset time consistent with the imposed rupture kinematics.

Accuracy versus Efficiency. All simulations were performed on a cluster of 42 SUN-V40Z nodes equipped with four AMD-Opteron 2.6 GHz processors, each having 8 GB RAM. The computational parameters are summarized in Table 2.

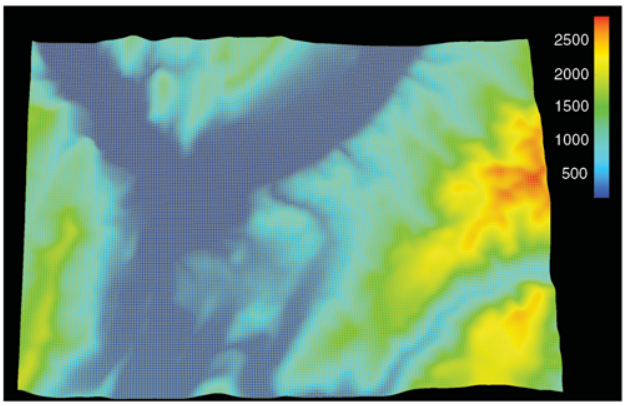

Figure 5. Surface view of the mesh of 192 × 160 elements used in the SEM1 calculations. The colors indicate surface elevation. The mesh contains 192 × 160 elements for 2 Hz calculations. The length of the elements does not vary horizontally and is kept smaller than 150 m. Each surface element contains 125 gridpoints (not shown here).

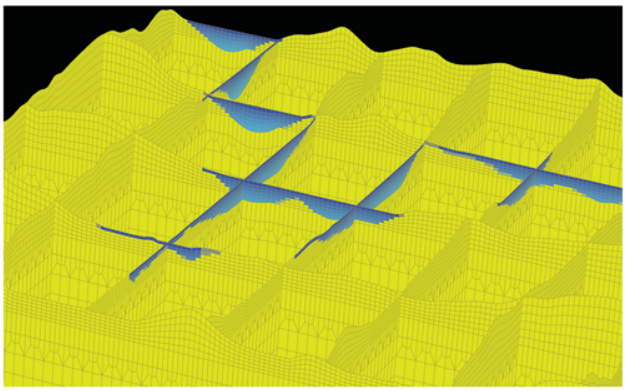

Figure 6. View of the 3D mesh of elements used in the SEM1 calculations. Golden colors indicate elements that are entirely within the bedrock, whereas blue colors stand for elements that intersect the sediments. The bedrock-sediment interface is not accounted for at depths shallower than 350 m, in particular for elements close to valley edges. The mesh is coarsened with depth following a simple conforming strategy proposed in (Komatitsch *et al.*, 2004).

3D Spectral-Element Method: The SEM2 Implementation

Model Geometry and Mesh Generation. In the second implementation of the SEM, SEM2, the meshing strategy adopted aims at accounting for true positions of material interfaces. This task was successfully solved thanks to the software CUBIT, which incorporates a set of powerful and advanced meshing schemes specifically developed to handle the hexahedral unstructured meshing problem (see the Data and Resources section for details). A thorough description of the meshing strategy adopted to strictly account for the geometry of the Grenoble Valley can be found in Stupazzini (2009). The final mesh is depicted in Figure 7 and consists of 216,972 elements, the size of which ranges from a minimum of about 20 m (inside the alluvial valley) up to 900 m. The mesh is designed to propagate frequencies up to 2 Hz with $N = 3$ (5,659,551 nodes) and up to around 3 Hz with $N = 4$ (13,300,892). A detailed zoom of a portion of the computational domain is presented in Figure 8, showing the strategy adopted to account for the discontinuity between the soft soil and bedrock. The computational domain is subdivided into small chunks; each of them is sequentially meshed starting from the alluvial basin down to the bedrock.

Material Heterogeneity and Attenuation. Inside the alluvial deposit the smooth vertical variation is taken into account assigning at each GLL point the mechanical properties evaluated according to the prescribed depth variation. The layer stratification is considered in the bedrock. The discontinuity between the soft soil and bedrock is strictly accounted for as previously mentioned. With respect to the constant quality factor model, frequencies smaller than 0.5 Hz will be overdamped, whereas higher frequencies will be enhanced in the alluvial deposits.

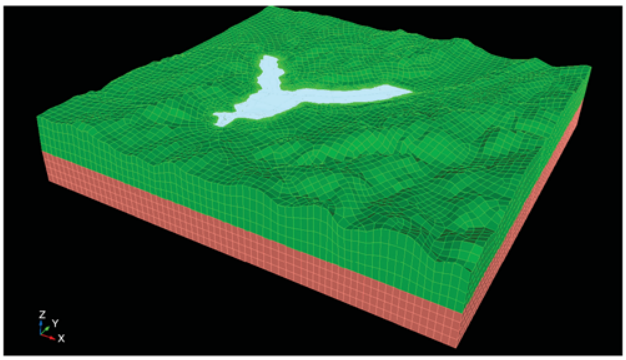

Figure 7. Three-dimensional view of the mesh used in the SEM2 calculations. The mesh contains 216,972 elements, ranging from 20 m (inside the alluvial basin) up to 900 m; for 2 Hz calculations $N = 3$ is sufficient. Different colors refer to different mechanical properties.

Treatment of the Kinematic Source. The seismic source is introduced through an appropriate distribution of the seismic moment tensor density (Aki and Richards, 2002). To model the strong motion case S1, we considered a set of 750 point sources regularly distributed on the prescribed fault plane.

Accuracy versus Efficiency. The simulations were performed on AMD Opteron 250 (64 bit single core 2.4 GHz) with 2 GB RAM and 1000T Ethernet (Oeser *et al.*, 2006). The computational parameters are summarized in Table 2.

3D Velocity-Stress Discontinuous Galerkin Scheme with ADER Time Integration of Unstructured Tetrahedral Meshes

Model Geometry and Mesh Generation. The ADER-DG method uses a tetrahedral mesh that accounts for the given geometry of the internal and external boundaries. Both the digital elevation model of the topography and the interface between the basin structure and the bedrock are provided on a regular grid with x-, y-, and z-coordinates, which is imported into a CAD tool to construct parameterized surfaces.

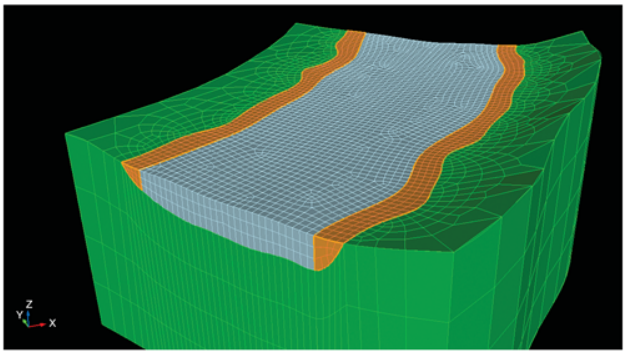

Figure 8. In order to account for the discontinuity between soft soil and bedrock the computational domain is subdivided into small chunks, each of them is sequentially meshed starting from the alluvial basin down to the bedrock.

These surfaces are then triangulated with an appropriate mesh size, and finally the volumes between the surfaces are filled with tetrahedral elements. Hereby the tetrahedral elements are conformingly connected to the surface triangulations. Furthermore, variable element sizes are chosen in order to account for the variable seismic velocity structure. Therefore, the edge lengths of the tetrahedral elements vary between 200 m inside the basin up to 5000 m at the bottom of the model, smoothly growing with increasing distance from the basin. Within the whole basin structure the mesh size increases vertically up to 500 m at the bottom of the basin.

In order to capture the topography sufficiently accurately the lateral growths factor along the free surface is chosen to result in a maximum edge length of 1000 m at the top lateral boundaries.

Material Heterogeneity and Attenuation. The smooth vertical heterogeneities inside the basin and in the surrounding bedrock are approximated in the ADER-DG approach by piecewise constant material; that is, the material parameters are evaluated at the barycenter of a tetrahedral element and are then assumed to be constant within the volume covered by the element. Similarly, the Q-factor for the viscoelastic material properties inside the basin is evaluated at the barycenter. The given wave velocities at that position are then assumed to be given for a central frequency of 1 Hz within the absorption band from 0.1 to 10 Hz. The frequency-independent constant Q-law is approximated with three relaxation mechanisms defined by a generalized Maxwell body.

Treatment of the Kinematic Source. The ADER-DG method treats the source term in both cases (W1 and S1) as a kinematic seismic source. Whereas the W1 case uses a single, double-couple point source with given location and source parameters, the S1 source is represented by 5000 aligned slip patches of a dimension of 90 m × 90 m to cover the specified 9 km × 4.5 km fault surface. Each slip patch is treated as a point source with the same parameters (strike, dip, rake) and the same shape of the source time function and possess different onset times as derived from the given rupture velocity. Therefore, the resulting seismic wave field is generated as a superposition of all individual slip patches.

Accuracy versus Efficiency. The simulations were performed on Intel Itanium2 Madison processors 1.6 GHz, 4 GB RAM per node. The computational parameters are summarized in Table 2.

Comparison of Numerical Predictions

Outline of the Comparison Method

Comparing numerical predictions of ground motion in a realistic 3D application is not straightforward because no reference solution is available, and each prediction may come with its own errors, either intrinsic (due to the limita-

tions of the numerical method used) or case-dependent (due to implementation and human errors). While it can be assumed that intrinsic errors can be identified by a proper knowledge of the numerical method being used, implementation errors need more user experience and often a complex iterative process to be tracked and hopefully minimized.

Here we present the results of such comparison process for the Grenoble Valley between four implementations of the numerical techniques presented before: DGM based on the discontinuous Galerkin method, FDM based on the finite-difference method, and SEM1 and SEM2, two implementations of the spectral-element method. We carefully checked that the presented numerical predictions are not affected by technical mistakes in individual implementations and simulations.

We compare the ground-motion predictions for the weak and strong motion cases W1-FLAT and S1-FLAT, respectively. The comparison includes a visual inspection of ground acceleration at selected receivers and global maps of peak ground velocity, as well as a quantitative analysis based on two different measures introduced recently: the goodness-of-fit score proposed by Anderson (2004), which consists of an average of ground-motion indicators of common use in engineering seismology, and the misfit measure proposed by Kristekova *et al.* (2006), which is based on the time-frequency representation of the seismograms.

Finally, we present the results obtained for the strong motion case S1-TOPO and compare the different predictions of the effects of surface topography.

Peak Velocities

Figure 9 shows the global maps of PGV (i.e., the peak values of the norm of the ground velocity vector) computed for the strong case motion case S1-FLAT by the four codes: DGM, FDM, SEM1, and SEM2.

Note the high level of ground motion for this M 6 event, especially in the eastern part of the valley. Lower values would be obtained by choosing a more physical source kinematics (instead of the Haskell model considered here, which produces a very strong directivity effect on the S wave) and depth (the top of the fault for the S1 event is located only 750 m below sea level, or about 1.5 km below surface). All maps show little correlation with the sediment thickness, except near the receiver R21, where the low values of ground velocity are consistent with the presence of steep bedrock uplift (see Fig. 2). The strongest amplitudes occur in the southeast part of the valley, with peak velocities exceeding 1.5 m/sec. These localized high values are caused by late interferences of surface waves diffracted off the eastern edge of the valley with surface waves backscattered off the bedrock uplift.

The PGV maps computed by the four codes look remarkably similar. Subtle differences can be seen, for example, in the source region where the patterns differ slightly. This could indicate small differences in the implementations of the extended source. Also, the level of the peak values displayed by the FDM code seems systematically larger than that of the other predictions. However, given the intrinsic difficulty of comparing peak values, the level of agreement shown in Figure 9 is found to be satisfactory.

Quantitative Comparison

Similarity Score and Misfit Measure. The issue of assessing the reliability of numerical predictions of ground motion has received renewed interest in recent years with the introduction of new tools to quantify the fit, either between synthetics and observations or between numerical predictions.

Anderson (2004) proposed a measure of the goodness-of-fit between two seismograms that is based on the comparison of 10 criteria that are commonly used in engineering applications: Arias duration (criterion1, or C1), energy duration (C2), Arias integral (C3), energy integral (C4), peak acceleration (C5), peak velocity (C6), peak displacement (C7), response spectrum (C8), Fourier spectrum (C9), and cross correlation (C10). These criteria are evaluated in narrow frequency bands and scaled between 0 and 10. A global average (between individual criteria and different frequency bands) is then applied to end up with one number, the so-called similarity score. Based on the systematic comparison of the horizontal components of recorded motions, Anderson (2004) introduced the following verbal scale for goodness-of-fit: a score below 4 is a poor fit, between 4 and 6 is a fair fit, between 6 and 8 is a good fit, and beyond 8 is an excellent fit.

Figure 10 shows an example of calculation of the similarity between the predictions of the north–south ground acceleration at the borehole receiver R06 for the S1-FLAT case. Solution SEM1-FLAT is used as a reference for all measurements, and only one frequency band, 0.1,2 Hz, is considered. Figure 10 confirms the impression of good fit from visual inspection of seismograms. It also shows that the differences between predictions obtained by different codes are smaller than the difference between predictions obtained by the same code with and without including the effect of surface topography (SEM1-FLAT and SEM1-TOPO).

Kristekova *et al.* (2006) proposed a measure of the misfit between two seismograms, which relies on the time-frequency representations of the signals. Their time-frequency misfit measure (hereafter referred to as TF misfit measure or simply TF misfit) allows separating amplitude (envelope) and phase differences both in the time and frequency domains.

Figure 11 shows an example of application of the TF misfit to the predictions of north–south ground acceleration at R06 for the S1-FLAT case by the FDM and SEM1 codes. The figure shows the time-frequency envelope (amplitude) and phase misfits, respectively, denoted by TFEM and TFPM. An average of the absolute values of TFEM and TFPM over time and frequency results in single-valued estimations of the envelope (EM) and of the phase (PM) misfits. A single,

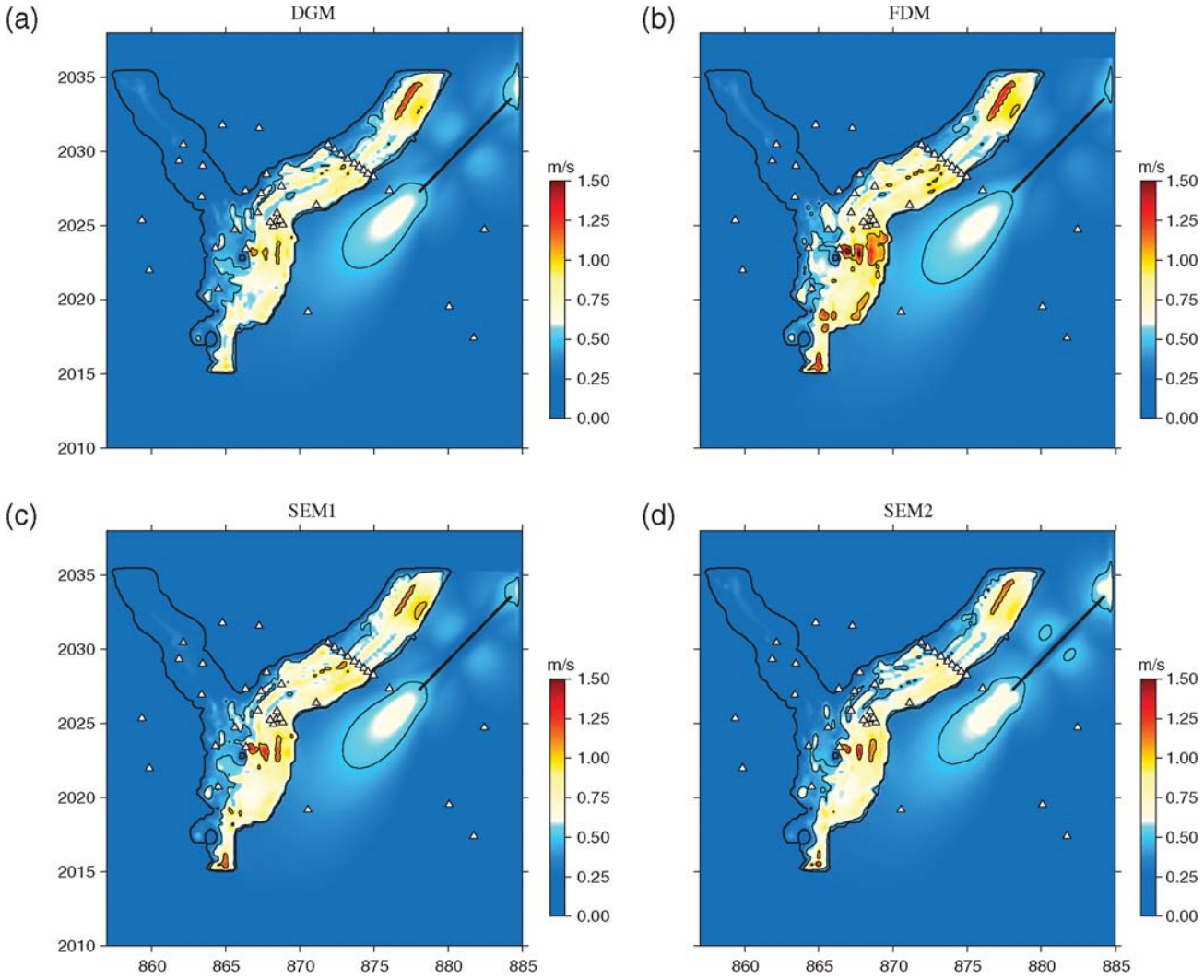

Figure 9. PGV maps obtained by the four codes (a) DGM, (b) FDM, (c) SEM1, (d) SEM2 for the strong motion case S1 without surface topography (S1-FLAT). Receiver locations are indicated by the triangles. The X and Y labels denote distances (in km) in the local Lambert coordinate system. The bold curve indicates the 50 m contour line in the sediment thickness map and the bold straight line shows the surface projection of the fault for the S1 event.

global score (denoted by EPM) is finally obtained by averaging EM and PM.

Application to the S1-FLAT and W1-FLAT Cases. We computed both the similarity score and the TF misfit for all 40 receivers and all predictions, taking the SEM1 result as a reference. We chose to use a single reference to alleviate the task of computing the misfits for each pair of predictions. Our analysis was performed for a time window 0,20.48 sec (2048 samples with timestep $\Delta t = 0.01$ sec) for each component of ground acceleration.

The correspondence between the similarity score and the TF misfit is summarized in Figure 12. Each dot represents a pair of measures evaluated at a single receiver, on a single component of ground acceleration for one of the cases S1-FLAT, S1-TOPO, or W1-FLAT. The figure shows a linear trend between the results of the two measures, which is particularly accurate for well-matching predictions. The level of the excellent fit, defined by Anderson (2004) as the similarity score above 8, corresponds to a TF misfit level below 0.4. The equation of the linear regression writes $(10\text{-}S) = 5M$, where S and M stand for the similarity score and TF misfit, respectively. Based on this equivalence, we will hereafter represent the results of the comparison of numerical predictions using the sole TF misfit measure.

We found no significant dependence of the TF misfit on the ground-motion component considered: the mean difference (averaged over the 40 receivers) between different single-component TF misfits does not exceed 0.04 (or 0.2 in terms of the similarity scores). We will therefore use a unique misfit value at each receiver, referred to as the total misfit, and defined as the arithmetic mean of the three individual TF misfits computed for the X, Y, and Z components.

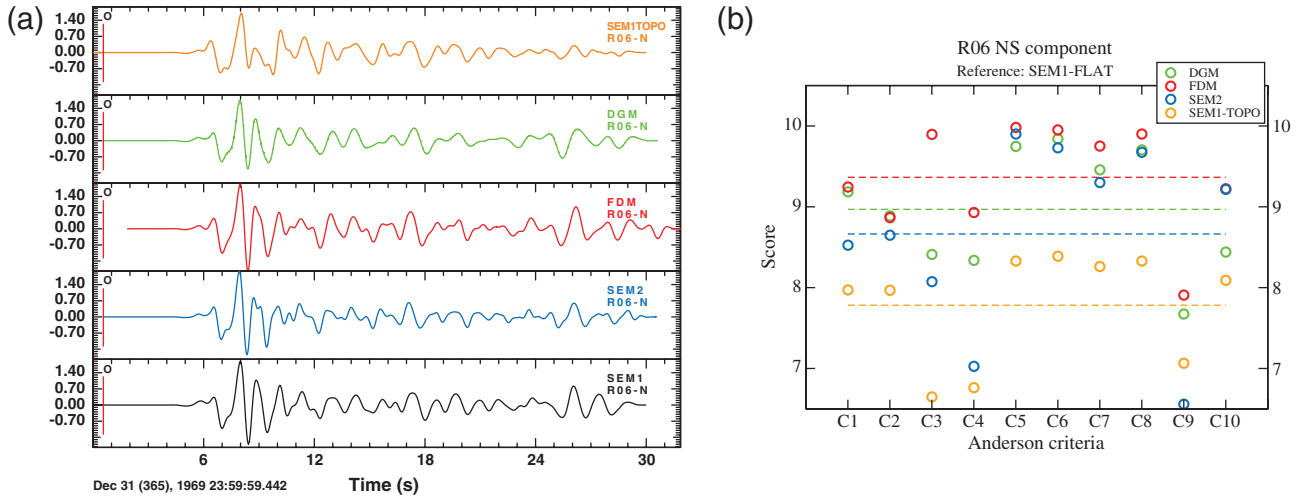

Figure 10. (a) Time series of the NS ground acceleration computed at receiver R06 by 4 different codes for the strong motion case S1-FLAT: DGM (green), FDM (red), SEM1 (black), and SEM2 (blue). The topmost trace (orange curve) was computed by the code SEM1 including surface topography (S1-TOPO). (b) Goodness-of-fit as measured by the 10 criteria proposed by Anderson (2004). The SEM1-FLAT prediction is used as reference in each case. The dashed lines indicate the levels of the global similarity scores for each prediction. Note that the fit between different predictions of the same simulation case (S1-FLAT) is better than the fit between predictions of different simulation cases (S1-TOPO and S1-FLAT) by the same code (SEM1).

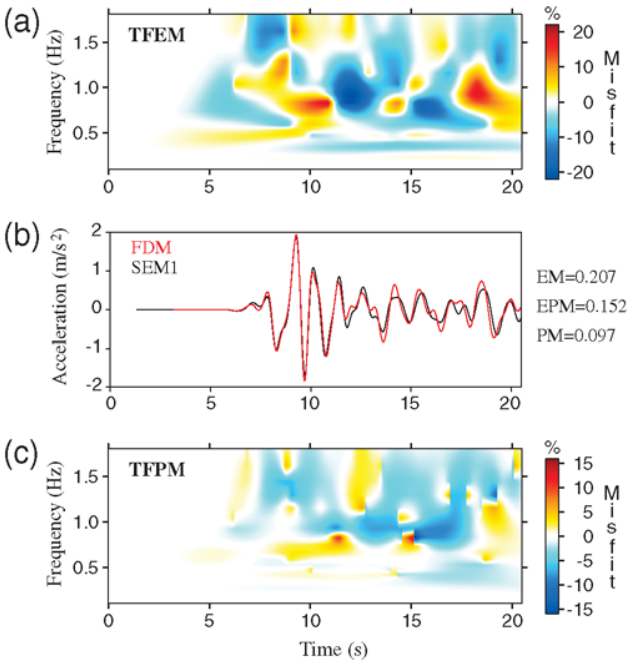

Figure 11. Example of application of the TF misfit analysis to the predictions of the NS ground acceleration at receiver R06 for the S1-FLAT case. (a),(c) Panels show the time-frequency envelope (TFEM) and phase (TFPM) misfits, respectively, taking the SEM1 prediction as a reference. (b) Time series of acceleration predicted by codes FDM (red) and SEM1 (black) are shown. Single-valued envelope (EM) and phase (PM) misfits are obtained by averaging the absolute values of TFEM and TFPM over time and frequency. The total TF misfit is obtained by averaging the envelope and phase misfits EM and PM.

Figure 13 shows the TF misfits between the different predictions of the S1-FLAT and W1-FLAT cases computed at the 40 receivers in the frequency band 0.1–2 Hz. Each dot corresponds to the total TF misfit averaged over the three components of ground acceleration.

For the S1-FLAT case, the misfit between the different predictions is almost everywhere lower than 0.4, which corresponds to the level of the excellent fit defined by Anderson (2004). Note the high similarity between the predictions of the FDM and SEM1 codes, despite the systematic amplitude shift observed in Figure 9. This illustrates the importance of

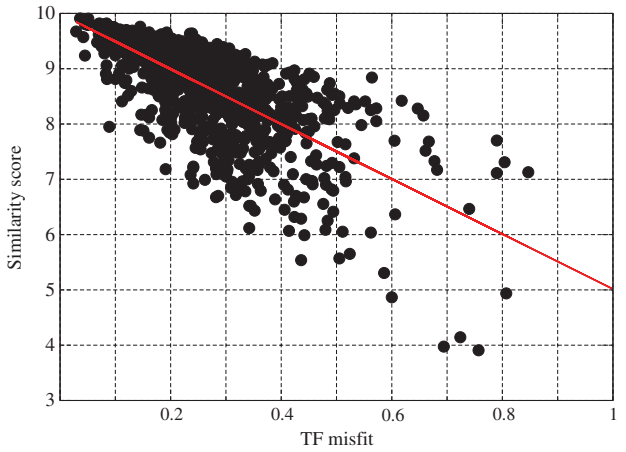

Figure 12. Comparison of results obtained with the TF misfit (M) plotted against those using the similarity score (S). Both measures have been applied to the 3 components of the 40 receivers for the benchmark cases S1-FLAT, S1-TOPO, and W1-FLAT. A global linear trend (red line) with equation (10-$S = 5M$) is found.

using a quantitative misfit measure instead of a single ground-motion parameter. Although the implementation of the point source is expected to be much simpler, the level of misfit is higher for the weak-motion case W1-FLAT than for the strong-motion case S1-FLAT. This is related to the larger high-frequency content of the W1 source, compared with the S1 source, which challenges the numerical methods at hand. Individual time series and amplitude spectra of the three components of ground acceleration at receiver R02, located in the center of the Grenoble Valley, are shown in Figure 14 and Figure 15 for the S1-FLAT case and W1-FLAT case, respectively.

Visual inspection of the traces and spectra confirms the high similarity between the different predictions of the S1-FLAT case, including at late arrival times, whereas larger differences in amplitude and phase arise for the predictions of the W1-FLAT case. Note in particular in Figure 15 the differences in timing and amplitude between the predictions of the diffracted Rayleigh wave arriving around 8 sec. Because of the wider frequency content of the source, the weak motion case also tends to highlight the differences in the implementation of intrinsic attenuation as described in the previous section (see, for example, the larger high-frequency content of the SEM2 prediction compared with the others).

Figure 16 and Figure 17 show the results obtained for the S1-FLAT case at two other locations: R06 (Montbonnot borehole ground-level station) in the middle of the 2D profile across the Grésivaudan Valley and R21 close to the steep bedrock uplift (see Fig. 2). Note the high similarity between all predictions at receiver R06 and the differences in amplitude and phase that lead to the large misfit between SEM1 and DGM at R21. This last example (R21) is one of the only cases where the level of misfit is surprisingly high in one component only (Z).

The global TF misfit distributions displayed in Figure 13 do not show any particular dependence on either the soil condition or the receiver location within the valley. The main trend is a systematic increase of the misfit with increasing distance to the source. This is expected because intrinsic errors (e.g., numerical dispersion) or differences in physical modeling (e.g., intrinsic attenuation) tend to accumulate with time and with the distance propagated. In the remainder of this section, we will therefore represent the misfit as a function of the source-receiver distance. The detail of the TF misfits in terms of amplitude and phase is shown for the S1-FLAT case in Figure 18. Both measures show the same pattern, with the highest similarity being found between the FDM and SEM1 predictions. However, the phase misfit seems to be more helpful in tracking differences between predictions. For example, the amplitude misfit between DGM and SEM1 is roughly identical to the one between SEM1 and SEM2, but larger phase misfits are seen between SEM1 and SEM2. Note also that the increase of the total TF misfit between FDM and SEM1 predictions with distance only appears in the amplitude (envelope) misfit, the difference in phase being roughly constant for all 40 receivers.

To better understand the differences between numerical predictions for the S1-FLAT case, we plot in Figure 19 the amplitude and phase misfits computed in three frequency bands: low-frequency (LF) 0.2,0.5 Hz; intermediate frequency (IF) 0.5,1.0 Hz; and high-frequency (HF) 1.0,2.0 Hz. Note that the LF band is roughly centered at the fundamental frequency of the Grenoble Valley (around 0.3 Hz); the energy radiated by the source in the S1-FLAT case decreases significantly in the HF band, suggesting that the weight of the HF misfit in the total TF misfit is weak. There is a global trend for the TF misfits (amplitude and phase) to increase with frequency. Therefore, it becomes more difficult at higher frequencies to assume a linear dependence on the source-receiver distance. This can be mainly explained by the fact that intrinsic errors of each numerical method (in particular numerical dispersion) increase with frequency.

We finally remark that there is a strong dependence of the amplitude misfit between DGM and SEM1 with frequency, which results in large differences in the HF band. The TF misfits computed for the W1-FLAT case (see Fig. 13) suggest that these discrepancies become dominant when the high-frequency content of the source is larger.

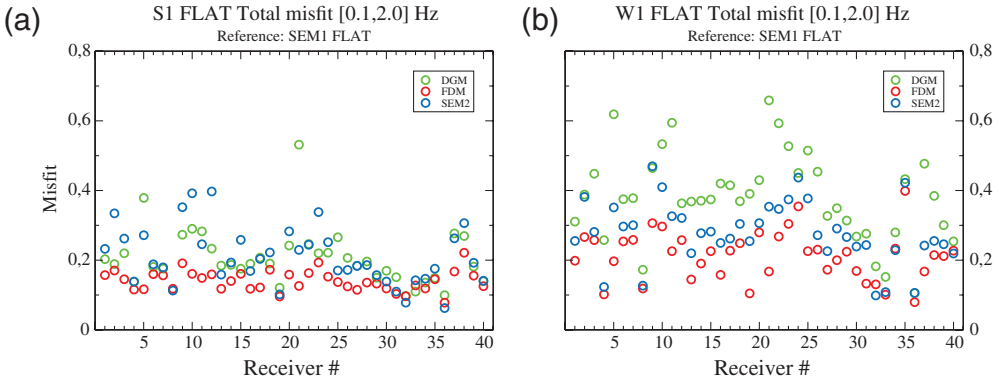

Figure 13. (a) TF misfits computed for the S1-FLAT case and (b) for the W1-FLAT case, taking the SEM1 prediction as reference. Each dot corresponds to the average of the 3 components of total misfit (average of envelope and phase) measured on the predictions of ground acceleration at each receiver in the frequency band 0.1,2.0 Hz. Receivers R01, R04, R08, and R33–R40 are located on rock sites.

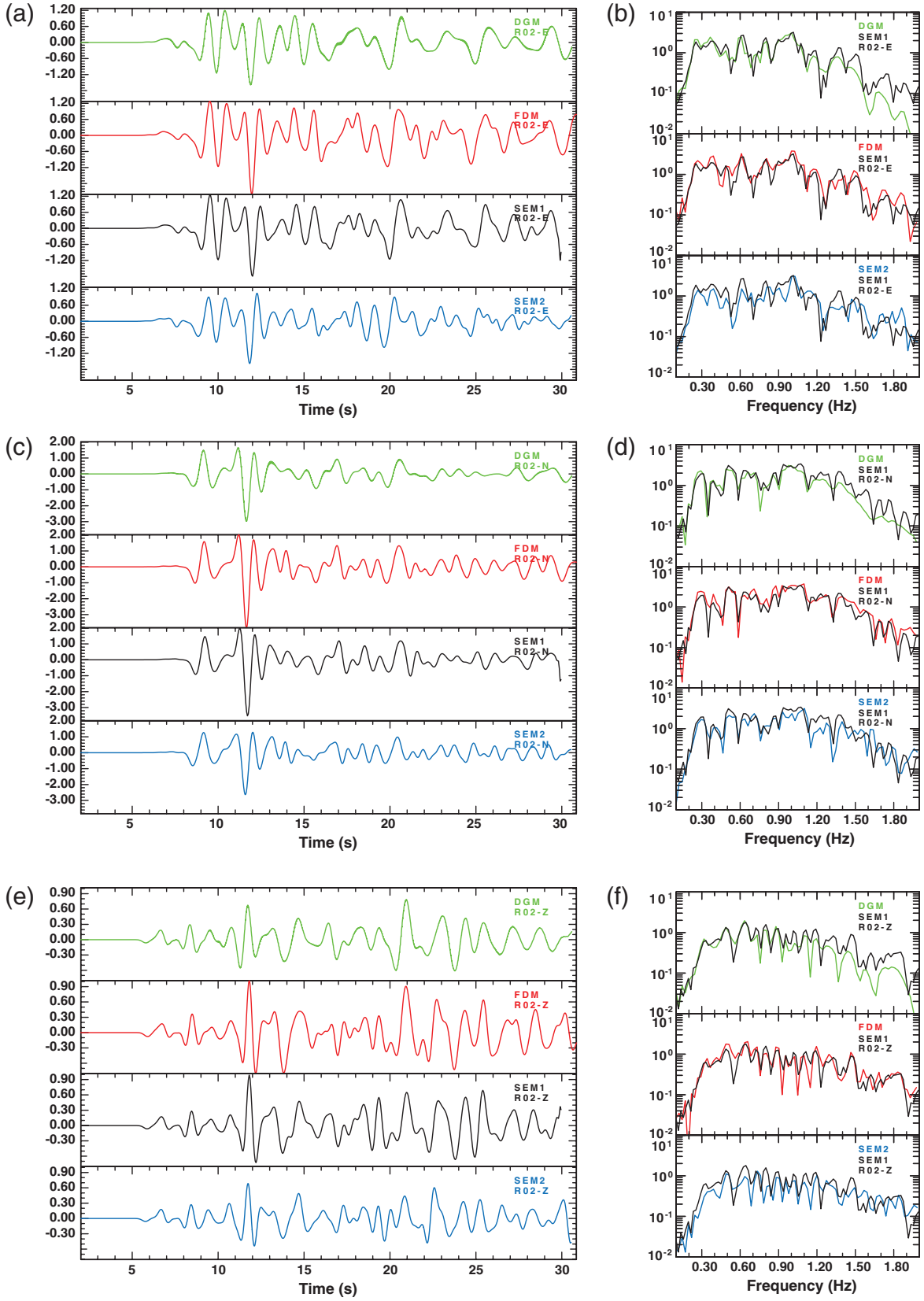

Figure 14. (a),(c),(e) Time series and (b),(d),(f) amplitude spectra of ground acceleration (EW, NS, UD) computed at receiver R02 by the four different codes for the strong motion case S1-FLAT.

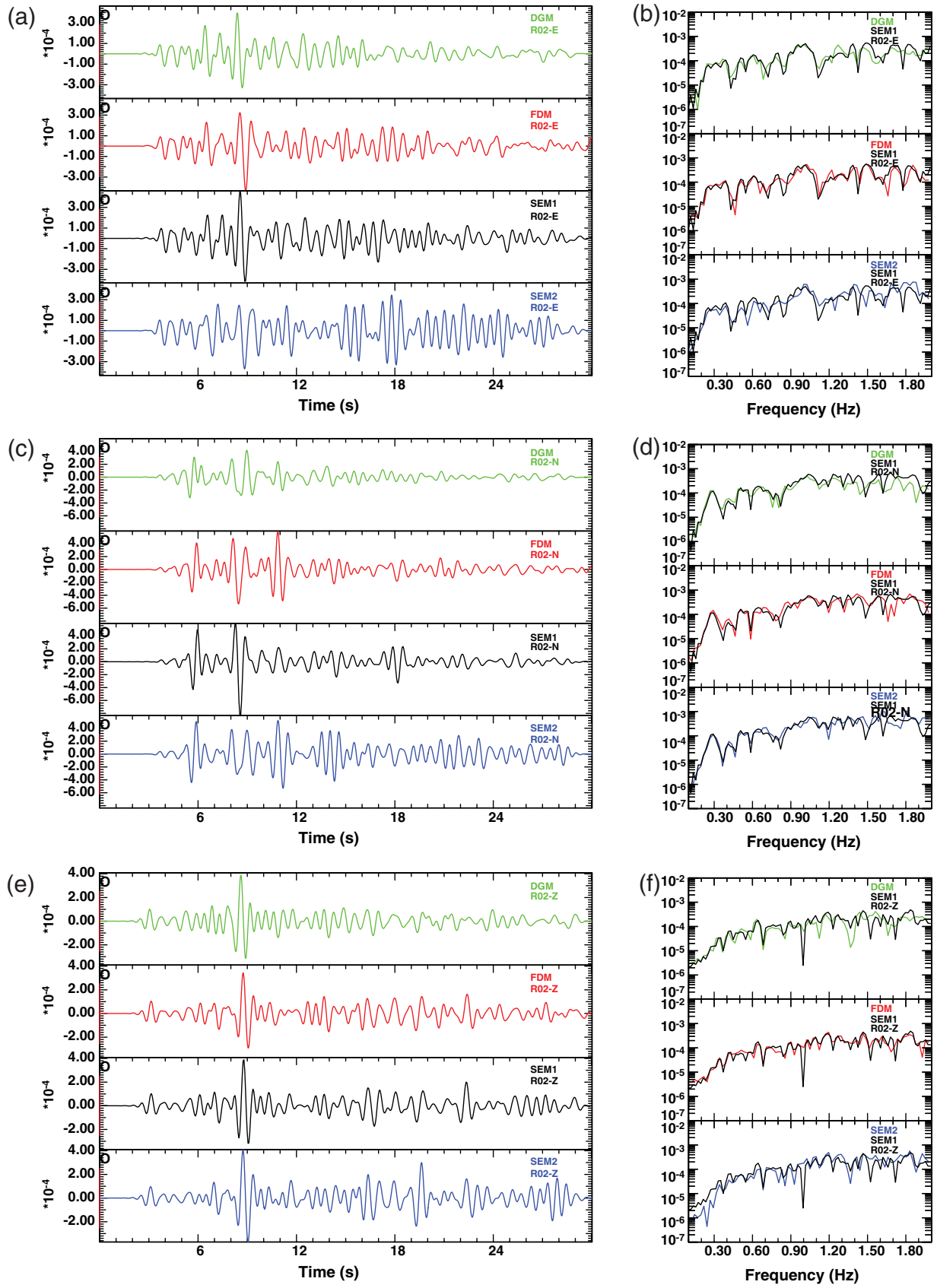

Figure 15. Same as Figure 14 for the weak motion case W1-FLAT.

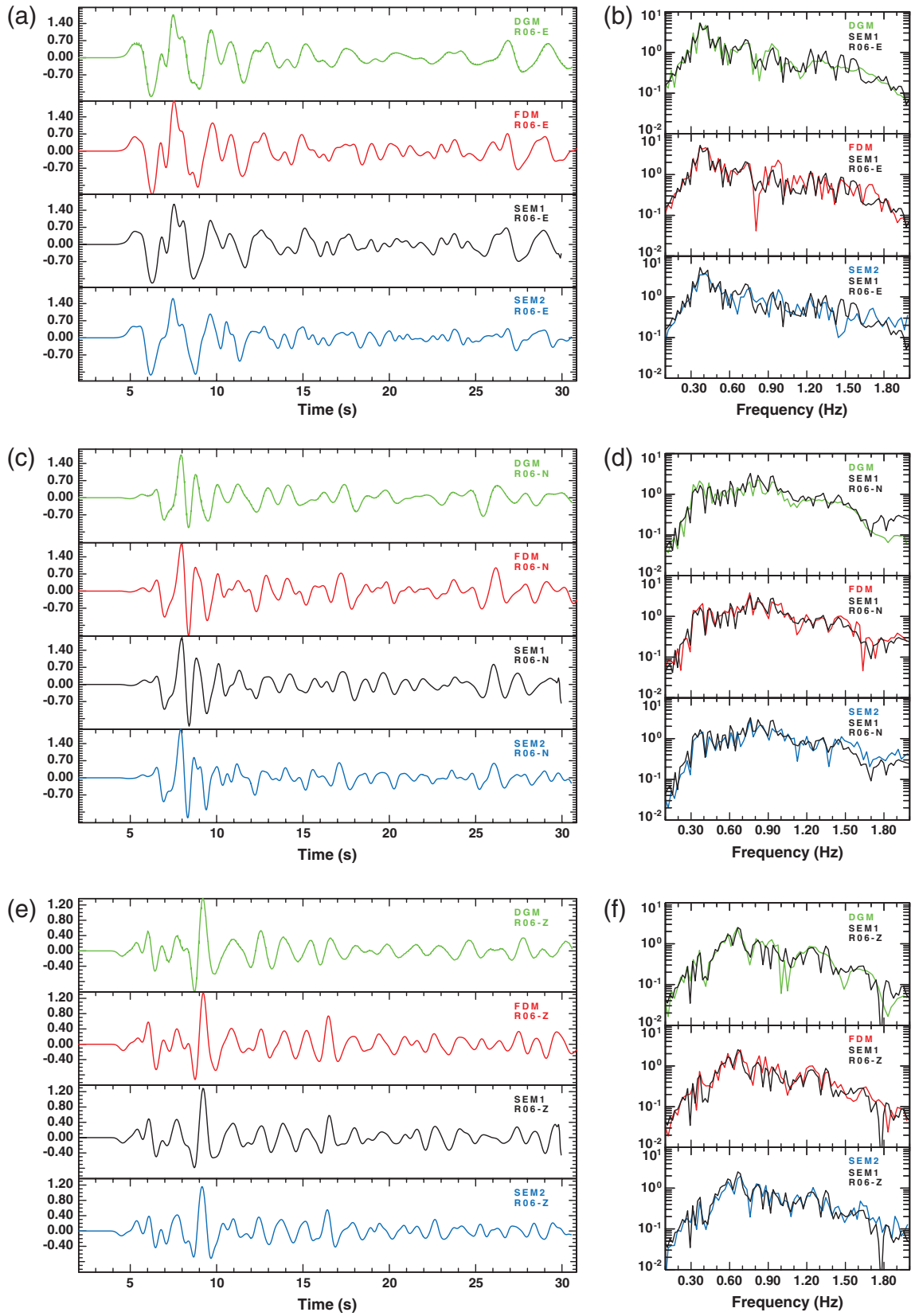

Figure 16. (a),(c),(e) Time series and (b),(d),(f) amplitude spectra of ground acceleration (EW, NS, UD) computed at receiver R06 by the four different codes (DGM, FDM, SEM1, and SEM2) for the strong motion case S1-FLAT.

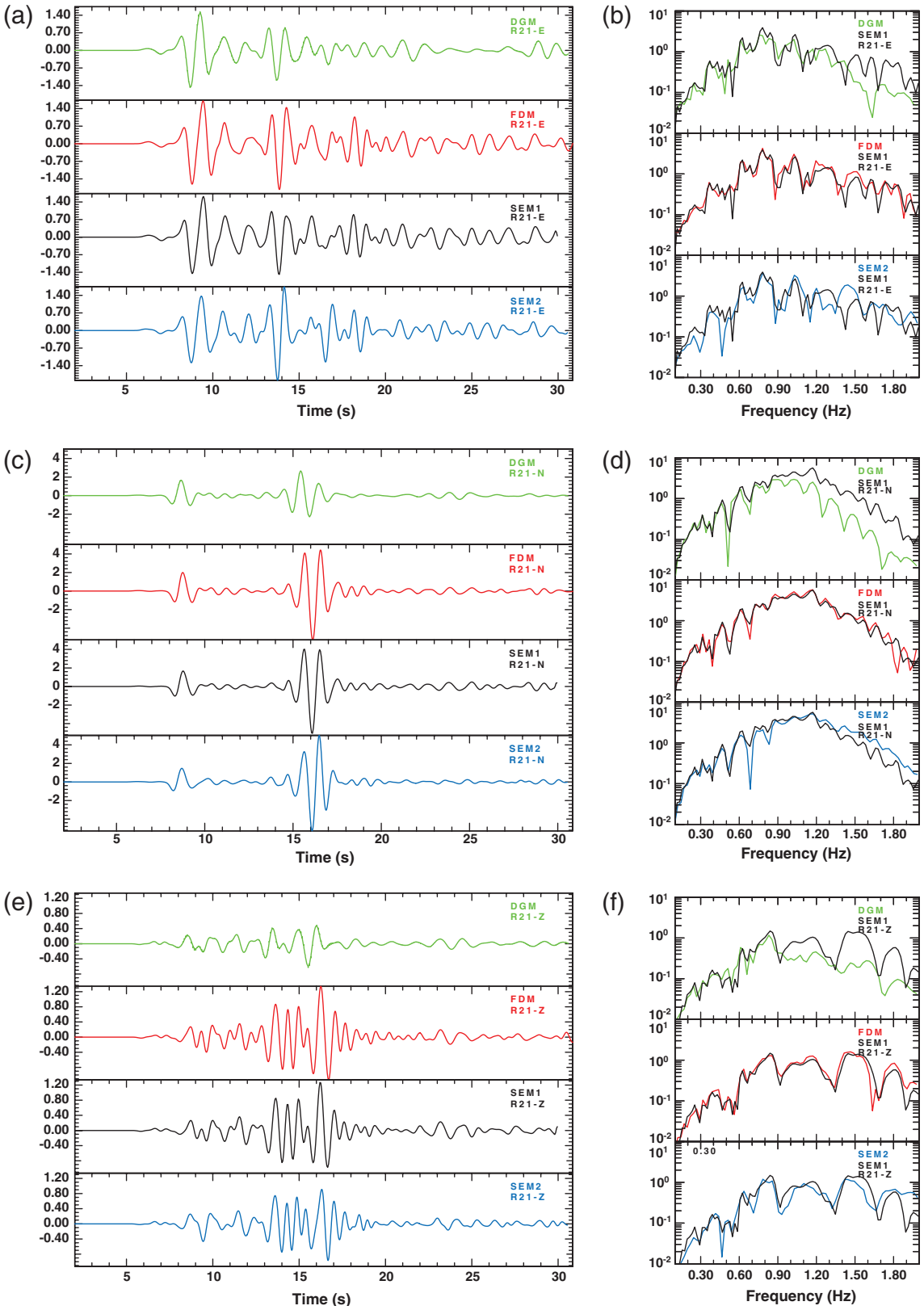

Figure 17. (a),(c),(e) Time series and (b),(d),(f) amplitude spectra of ground acceleration (EW, NS, UD) computed at receiver R21 by the four different codes for the strong motion case S1-FLAT. Note the low similarity between the DGM and SEM1 predictions on the vertical component.

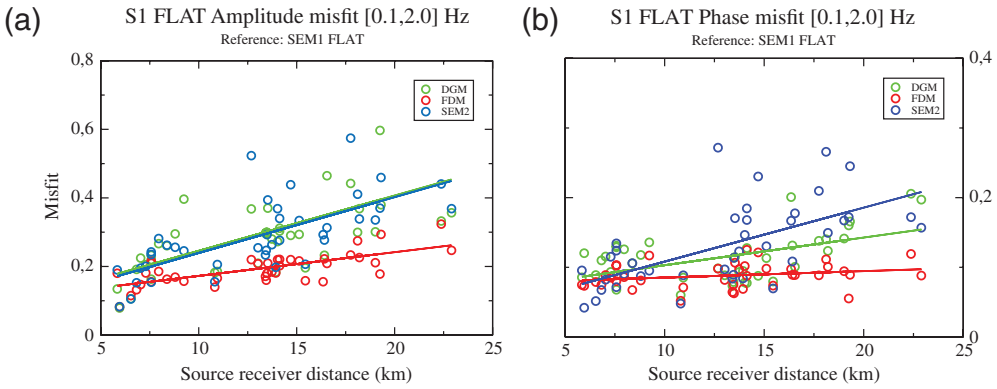

Figure 18. (a) Envelope and (b) phase misfits computed for the S1-FLAT case and plotted against source-receiver distance. Solid lines indicate linear regressions through the sets of points.

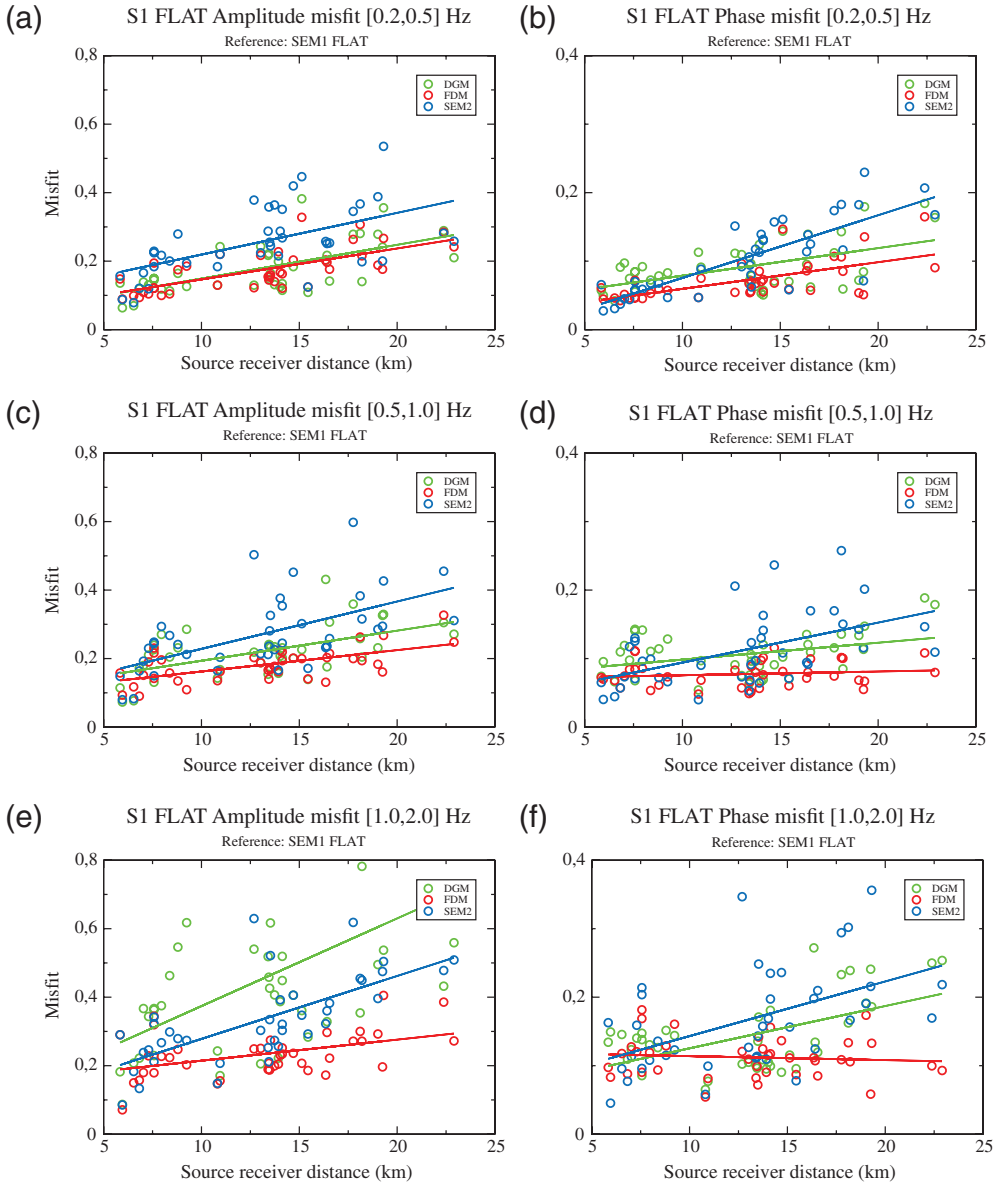

Figure 19. Same as Figure 18 for different frequency bands: (a),(b) 0.2,0.5 Hz; (c),(d) 0.5,1.0 Hz; and (e),(f) 1.0,2.0 Hz.

Effect of Surface Topography

Three codes (DGM, SEM1, and SEM2) computed the strong motion case S1-TOPO, which includes the effect of surface topography. The PGV maps obtained for the S1-TOPO case are shown in Figure 20. Note the deformation of the predicted patterns (compare with Fig. 9) close to the source due to the presence of surface topography on top of the fault plane. The overall distributions of peak values look quite similar inside the valley, suggesting that the main differences with respect to the S1-FLAT case occur on the rock sites. This is only partly confirmed by Figure 21, which shows the maps obtained by dividing the PGV by those obtained in the S1-FLAT case. Noticeable differences are indeed observed in the southwestern part of the valley, a region where strong variations of the sediment thickness occur. The patterns observed on the three maps of PGV ratios are quite consistent outside of the valley: systematic amplification is found on the mountain peaks (see, for example, receivers R33 and R34 in the eastern Belledonne chain and receivers R39 and R40 in the northern Chartreuse massif), whereas deamplification is found in valleys (see receiver R35). Seismic motion on slopes is more complex because amplification or deamplification can occur depending on the slope orientation with respect to the seismic event (see the two flanks bordering the Romanche Valley around receiver R35 at coordinates $X = 880$ km, $Y = 2015$ km). Extreme and mean values of amplification and deamplification are given in Table 3.

The average effect of surface topography inside the valley, as measured by the ratio of the PGV, is found to be negligible, but large differences in extreme values occur: the maximal predicted amplifications vary significantly on

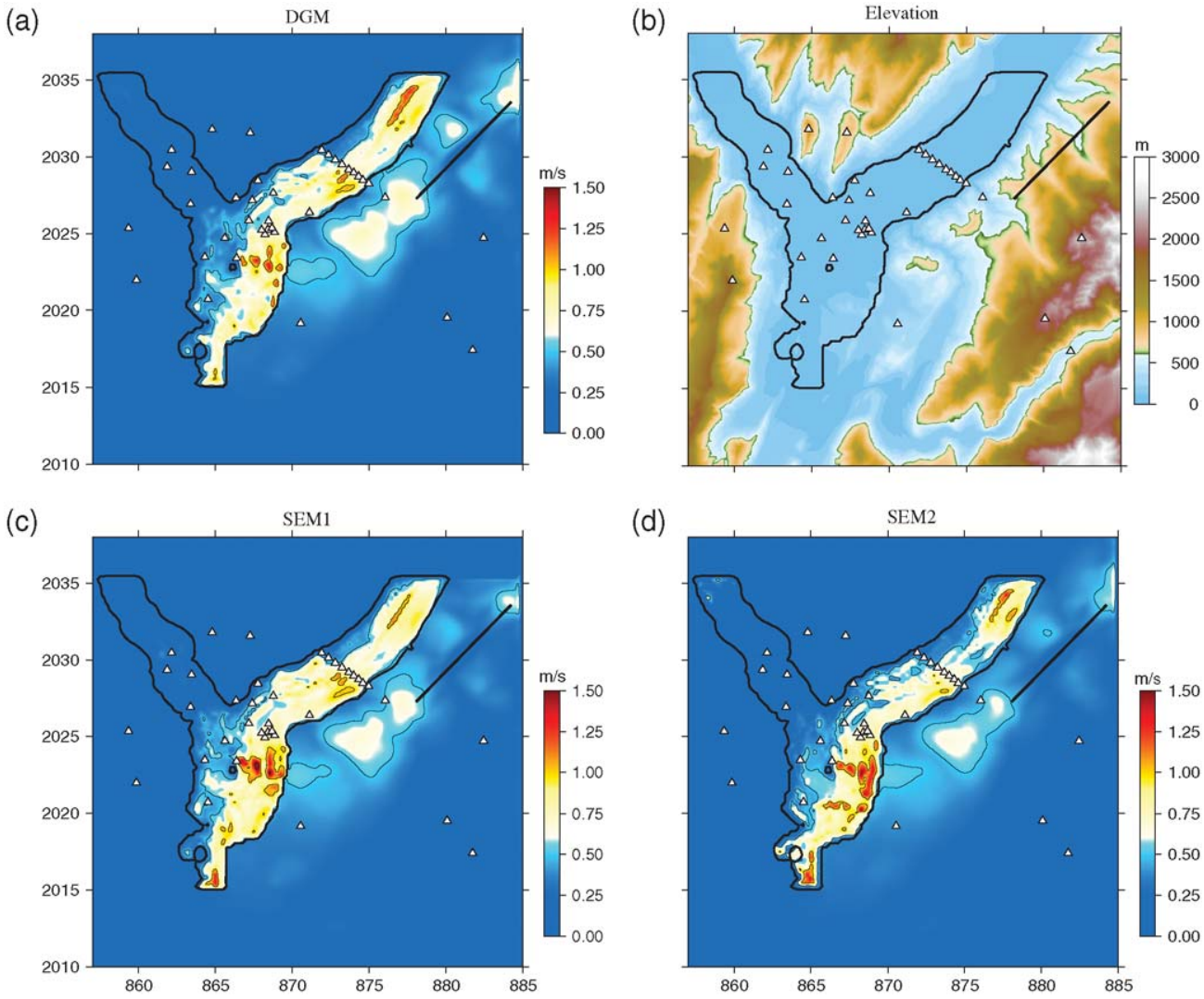

Figure 20. PGV maps obtained by three codes: (a) DGM, (c) SEM1, (d) SEM2 for the strong motion case S1-TOPO. (b) The map of surface elevation is shown. Receiver locations are indicated by the triangles; the X and Y labels denote distances (in km) in the local Lambert coordinate system. The bold curve indicates the 50 m contour line in the sediment thickness map; the bold straight line shows the surface projection of the fault for the S1 event.

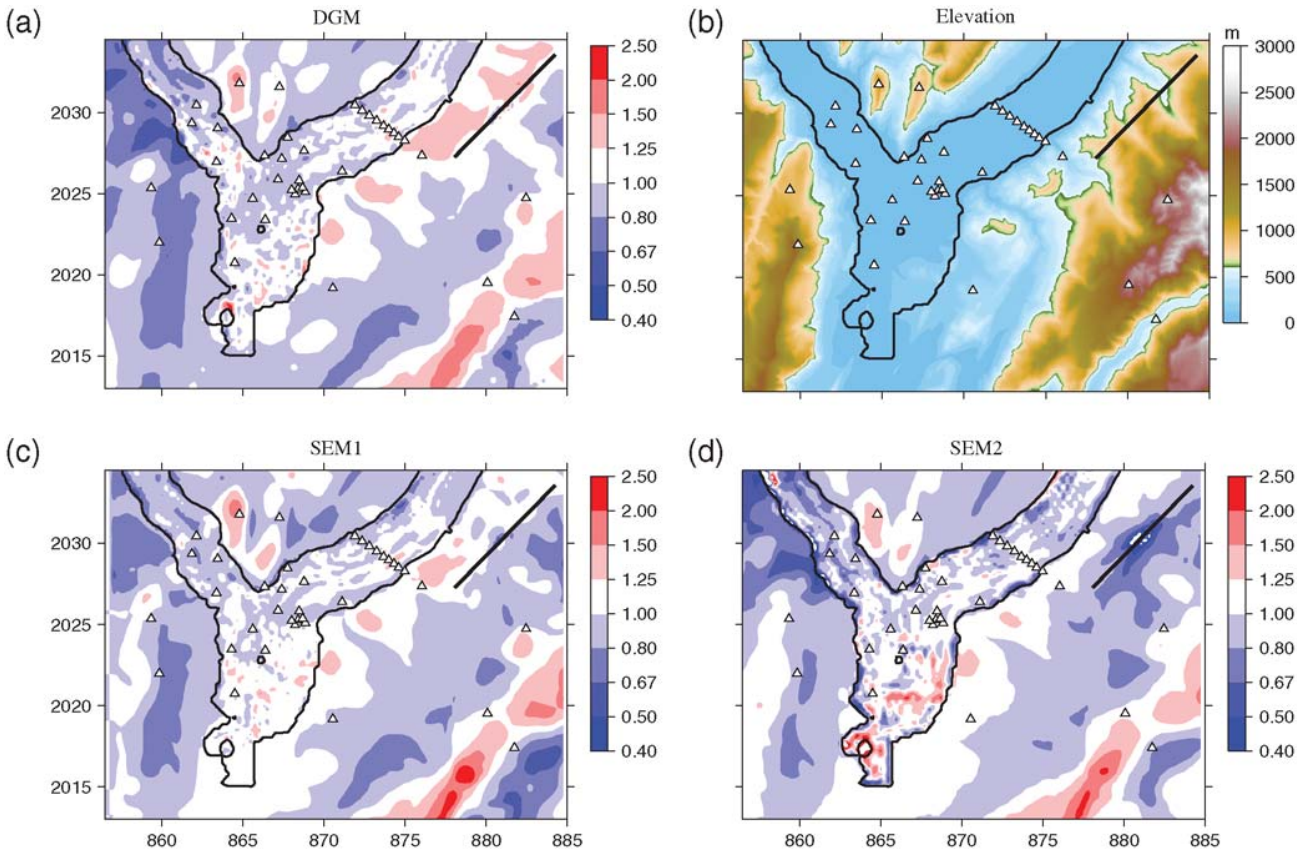

Figure 21. Maps of ratios between the PGV obtained with the surface topography and PGV obtained for the flat free surface by the three codes: (a) DGM, (c) SEM1, and (d) SEM2. (b) The map of surface elevation is shown. Receiver locations are indicated by the triangles and the *X* and *Y* labels denote distances (in km) in the local Lambert coordinate system. The bold curve indicates the 50 m contour line in the sediment thickness map and the bold straight line shows the surface projection of the fault for the S1 event.

rock sites and, more surprisingly, within the valley. This could result from differences in the implementation of surface topography, in the representation of velocity contrasts near the valley edges, and in the design of the meshes for the S1-FLAT and S1-TOPO cases.

Conclusions

The third international symposium on the effects of surface geology in Grenoble, France (ESG 2006), provided an excellent opportunity to focus the traditional blind prediction experiment on numerical modeling of earthquake motion in a typical deep Alpine sediment-filled structure, the Grenoble Valley.

The Grenoble urban area gathers a significant population of around 500,000, a number of high-tech and sensitive industrial facilities, and educational and research institutions. This and observed broadband site effects imply that the moderate regional seismic activity poses a concern about the seismic risk in the area. Moreover, similar conditions are also met in other areas within the European Alps and in other mountainous areas with embanked valleys filled with young, postglacial lacustrine sediments. This specific area also presents a further interest in relation to its relatively small extent, which allows performing deterministic numerical simulation up to higher frequencies than is usually considered in much wider areas such as the Los Angeles basin.

The present article reports partial results from this simulation exercise for four structure wave-field configurations that were specified for voluntary participants: W1-FLAT, S1-FLAT, W1-TOPO, S1-TOPO, with *W* and *S* meaning weak and strong, FLAT and TOPO meaning geometry of the free surface, respectively. The weak configurations comprised

Table 3
Extreme and Average Values of the Ratio of Peak Ground Velocity Computed by the Codes DGM, SEM1, and SEM2*

	DGM	SEM1	SEM2
Minimum ratio (valley)	0.447	0.549	0.133
Maximum ratio (valley)	2.255	1.641	3.599
Mean ratio (valley)	0.996	0.998	0.991
Minimum ratio (rock)	0.543	0.533	0.277
Maximum ratio (rock)	3.222	2.464	2.095

*With and without accounting for the effects of surface topography.

double-couple point sources, the strong ones finite kinematic source models.

Fourteen groups from eight countries contributed to the ESG 2006 comparison with at least one numerical method and possibly different cases, providing a total of 18 prediction sets; seven groups addressed the 3D problem, out of which three could account for the effects of both underground and surface topography. The numerical schemes used for the 3D contributions belong to the finite-difference, spectral-element, and discontinuous-Galerkin finite-element methods. Four participants whose 3D predictions were surprisingly close updated their results after the ESG meeting, after correcting some nonmethodological errors (evidenced by comparing to other predictions) in preparation of the numerical simulations. Only the results from the corrected predictions were considered here.

One of the main lessons of this comparative exercise concerns the present capabilities of numerical simulation and is indeed a lesson of modesty: all the submitted predictions exhibit a very large variability. This variability confirms that the numerical prediction of ground motion in general certainly cannot be considered a mature, push-button approach, and the variability in direct uncorrected numerical predictions can be significantly larger than the variability associated with empirical predictions. This is also because not all applied numerical codes implement the best methodologically possible algorithms; some of the codes are not yet bug free. Much care should be also given to an unambiguous definition of the input solicitation (input signal and/or source kinematics). Not sufficiently elaborated numerical predictions may yield wrong results and therefore will lead to large mistrust from end users.

However, there is also another lesson, which is a lesson of hope: the striking similarity between predictions by completely different numerical methods is a very encouraging result. Despite the structural complexity, that is geometry and relatively large velocity contrast at the sediment-basement interface as well as smooth heterogeneity, and the methodological differences among the simulation methods, we found a surprisingly good level of agreement among four of the submitted predictions obtained by the finite-difference method (FDM), two implementations of the spectral-element method (SEM1 and SEM2), and arbitrary high-order derivative, the discontinuous Galerkin method (ADER-DGM). It clearly shows that, when used with caution, numerical simulation is actually able to handle wave radiation correctly from an extended source and their subsequent propagation in complex 3D media.

The expression good agreement is not simply a matter of subjective feeling. It indeed results from a detailed, quantitative comparison between the four numerical predictions using the misfit criteria proposed by Kristekova *et al.* (2006). These misfit criteria are based on the time-frequency representations of the signals and allow proper quantification and characterization of disagreement between signals. This misfit measurement is found to be consistent with the engineering-oriented similarity score proposed by Anderson (2004). Another instructive comparison was achieved by looking at predicted PGV maps.

The main conclusions from the detailed comparison are explained in the following list:

- The objective quantification of the mismatch between the different predictions proves to be effective and useful. The two different comparison tools used for quantification, although very different, do provide very consistent results. While Anderson's engineering-based criteria are probably enough for validating numerical predictions for end users, more refined comparisons based on time-frequency analysis greatly help in understanding the origin of differences. In particular, the analysis of the phase misfit with the technique of Kristekova *et al.* (2006) proves very instructive in identifying differences in propagation properties from one numerical method to another, and thus in orienting further investigations to refine computational tools.
- The match is found to be good at low frequencies (below 1 Hz) and to gradually deteriorate with increasing frequency, as expected. The reasons for that could not be unambiguously individualized, but may be related both to differences in the numerical methods (numerical dispersion, implementation of damping) and differences in the model implementation.
- An important component to explain the differences is certainly related to the meshing. While the applied finite-difference scheme authorizes a good automatic accounting for the details of the sediment-basement interface, different strategies were used by the three other groups: some used a rather coarse meshing that did not follow details of the valley boundaries, especially at shallow depth, while some others spent much time in refining the mesh. The 2 Hz maximum frequency considered here is still too low to actually clearly identify the effects of the valley boundaries, considering also the rather smooth velocity variation in the sediments and the absence of shallow weathered layers in the bedrock. This issue is presently investigated within the framework of another numerical comparative exercise on the Volvi–Euroseistest site in Greece, where both sediments and bedrock exhibit complex shallow structures with inner interfaces between different units.
- The effects of free-surface topography were found significant in elevated areas in the three surrounding mountain ranges, but less important within the valley. However, while they are negligible in the S1 case, they slightly increase in the W1 case corresponding to higher predominant frequencies. This result cannot therefore be extrapolated to frequencies higher than 2 Hz, and the question is still open.

The comparison of the numerical predictions obtained with the FDM, two implementations of the SEM, and ADER-DGM indicates that each of these methods can be applied to simulation of the earthquake motion in structurally complex sediment-filled valleys with the flat free surface. In addition to being methodologically relatively simpler than the SEM

and ADER-DGM, the presented implementation of the FDM can be computationally more efficient because the volume harmonic averaging of moduli and volume arithmetic averaging of density allows to account for irregular interfaces in regular grids well-suited to parallel implementation, while abrupt changes in the grid size are also allowed at the transition between sediments and much stiffer bedrock. In the case of the presented predictions, the FDM needed approximately 65% of the computational time used by SEM, but obviously the difference may depend on the used computer and on the particular case under study. On the other hand, for the SEM and ADER-DGM the incorporation of the nonplanar free surface poses no methodological problem; thus, the methods can be equally easily applied to both the flat and nonplanar free surface. In general, it is far from easy and natural to implement free-surface condition in the FDM. The applied DSG Velocity-Stress FDM cannot account for the free-surface topography. If the incorporation of the topography is inevitable, for example, at particular sites and at higher frequencies, a hybrid combination with the finite-element method (Galis *et al.*, 2008) might be an alternative to the applied DSG VS FDM.

We would like to stress two main conclusions based on the ESG 2006 simulation exercise and the detailed comparison of the four closest numerical predictions:

1. No single numerical modeling method can be considered as the best for all important medium wave-field configurations in both computational efficiency and accuracy.

2. Reliable predictions of the earthquake ground motion in complex structures should be made using at least two different but comparably accurate methods to enhance reliability of the prediction. Our study indicates that the proper formulations and implementations of the FDM, SEM, and ADER-DGM can be applied.

Data and Resources

All data used in this article came from published sources listed in the references. The Fortran 95 computer code for performing the finite-difference scheme is available at www.nuquake.eu/Computer_Codes/ (last accessed June, 2010). A detailed description of the SEM1 software package can be found at www.geodynamics.org/cig/software/packages/seismo/specfem3d (last accessed June, 2010). A detailed description of the software package adopted for the SEM2 simulation can be found at http://geoelse.stru.polimi.it (last accessed June, 2010). The software CUBIT is available at http://cubit.sandia.gov/ (last accessed June, 2010).

Acknowledgments

This work was supported in part by the Slovak Research and Development Agency under the contract number APVV-0435-07 (project OPTIMODE) and VEGA Project 1/4032/07. All the computations using the SEM1 code were performed at the Service Commun de Calcul Intensif (SCCI) of the Grenoble Observatory. The authors providing the ADER-DG solutions thank the Deutsche Forschungsgemeinschaft (DFG), who supported the work through the Emmy Noether program (KA 2281/2-1). The cooperation of P. Bunge and J. Oeser for allowing the extensive use of the Tethys cluster is also gratefully acknowledged, as well as the support by the Leibniz Rechenzentrum in München. This comparison work was made possible through various financial helps and grants from ILL (Institut Laue-Langevin) and CEA (French Atomic Energy Commission) through the Cashima project, from the INTERREG IIIB Alpine Space Program of the European Commission through the Sismovalp project, and from the French National Research Agency (ANR) through the QSHA project.

References

Aki, K., and P. Richard (2002). *Quantitative Seismology*, Second Ed., University Science Books, Sausalito, California, 700 pp.

Anderson, J. G. (2004). Quantitative measure of the goodness-of-fit of synthetic seismograms, *13th World Conf. on Earthquake Engineering Conference Proc.*, Paper 243.

Canuto, C., M. Y. Hussaini, A. Quarteroni, and T. A. Zang (1988). *Spectral Methods in Fluid Dynamics*, Springer-Verlag, New York.

Chaljub, E. (2009). Spectral element modeling of 3D wave propagation in the Alpine valley of Grenoble, France, in *ESG 2006, Third Intl. Symposium on the Effects of Surface Geology on Seismic Motion*, P.-Y. Bard, E. Chaljub, C. Cornou, F. Cotton, and P. Guéguen (Editors), LCPC Editions, ISSN 1628-4704, Vol. 2**,** 1467–1473.

Chaljub, E., C. Cornou, and P.-Y. Bard (2009). Numerical benchmark of 3D ground motion simulation in the valley of Grenoble, French Alps, in *ESG 2006, Third Intl. Symposium on the Effects of Surface Geology on Seismic Motion*, P.-Y. Bard, E. Chaljub, C. Cornou, F. Cotton, and P. Guéguen (Editors), LCPC Editions, ISSN 1628-4704, Vol. **2,** 1365–1375.

Chaljub, E., D. Komatitsch, J.-P. Vilotte, Y. Capdeville, B. Valette, and G. Festa (2007). Spectral element analysis in seismology, in *Advances in Wave Propagation in Heterogeneous Media*, R.-S. Wu and V. Maupin (Editors), Vol. **365–419,** Elsevier Academic Press, New York.

Chapron, E., M. Dietrich, C. Beck, P. Van Rensbergen, P. Finckh, G. Menard, G. Nicoud, F. Lemeille, F. Anselmetti, and M. De Batist (2009). High-amplitude reflections in proglacial lacustrine basin fills of the NW Alps: Origin and implications, in *ESG 2006, Third Intl. Symposium on the Effects of Surface Geology on Seismic Motion*, P.-Y. Bard, E. Chaljub, C. Cornou, F. Cotton, and P. Guéguen (Editors), LCPC Editions, ISSN 1628-4704, Vol. 2**,** 1587–1596.

Cornou, C. (2002). Traitement d'antenne et imagerie sismique dans l'agglomération grenobloise (Alpes Françaises): Implications pour les effets de site, *Ph.D. Thesis*, (260 pages, www-lgit.obs.ujf-grenoble.fr/~cornouc/PUBLIS_CECILE/These_Version_Finale_Cecile.pdf), Joseph Fourier University, Grenoble (in French).

Cornou, C., P.-Y. Bard, and M. Dietrich (2003a). Contribution of dense array analysis to the identification and quantification of basin-edge-induced waves, part I: Methodology, *Bull. Seismol. Soc. Am.* **93,** 2604–2623.

Cornou, C., P.-Y. Bard, and M. Dietrich (2003b). Contribution of dense array analysis to the identification and quantification of basin-edge-induced waves, part II: Application to Grenoble basin (French Alps), *Bull. Seismol. Soc. Am.* **93,** 2624–2648.

Cornou, C., E. Chaljub, J. Verbeke, J. Converset, C. Voisin, L. Stehly, L. Margerin, S. Tsuno, J.-R. Grasso, P. Guéguen, S. Roussel, P. Roux, S. Hatton, and M. Campillo (2009). Measurement and variability study of site effects in the 3D glacial valley of Grenoble, French Alps, in *ESG 2006, Third Intl. Symposium on the Effects of Surface Geology on Seismic Motion*, P.-Y. Bard, E. Chaljub, C. Cornou, F. Cotton, and P. Guéguen (Editors), LCPC Editions, ISSN 1628-4704, Vol. **2,** 1621–1627.

Davis, P. and P. Rabinowitz (Editors) (1984). *Methods of Numerical Integration*, Academic Press, New York.

Day, S. M., J. Bielak, D. Dreger, R. Graves, S. Larsen, K. Olsen, and A. Pitarka (2003). *Tests of 3D Elastodynamic Codes: Final Report*

for Lifelines Project 1A02, Pacific Earthquake Engineering Research Center, Berkeley, California.

de Basabe, J. D., and M. K. Sen (2007). Grid dispersion and stability criteria of some common finite-element methods for acoustic and elastic wave equations, *Geophysics* **72,** T81–T95.

de la Puente, J., M. Dumbser, M. Käser, and H. Igel (2008). Discontinuous Galerkin methods for wave propagation in poroelastic media, *Geophysics* **73,** T77–T97.

de la Puente, J., M. Käser, M. Dumbser, and H. Igel (2007). An arbitrary high order discontinuous Galerkin method for elastic waves on unstructured meshes IV: Anisotropy, *Geophys. J. Int.* **169,** 1210–1228.

Deville, M. O., P. F. Fischer, and E. H. Mund (2002). *High-Order Methods for Incompressible Fluid Flow*, Cambridge University Press, New York.

Dietrich, M., C. Cornou, G. Ménard, F. Lemeille, F. Guyoton, and R. Guiguet (2009). Seismic profiling and borehole measurements in the Isère Valley near Grenoble, France: 1—Data acquisition and processing, in *ESG 2006, Third Intl. Symposium on the Effects of Surface Geology on Seismic Motion*, P.-Y. Bard, E. Chaljub, C. Cornou, F. Cotton, and P. Guéguen (Editors), LCPC Editions, ISSN 1628-4704, Vol. **2,** p. 1597–1608.

Dumbser, M., and M. Käser (2006). An arbitrary high order discontinuous Galerkin method for elastic waves on unstructured meshes II: The three-dimensional case, *Geophys. J. Int.* **167,** 319–336.

Dumbser, M., M. Käser, and E. Toro (2007). An arbitrary high order discontinuous Galerkin method for elastic waves on unstructured meshes V: Local time stepping and *p*-adaptivity, *Geophys. J. Int.* **171,** 695–717.

Faccioli, E., F. Maggio, R. Paolucci, and A. Quarteroni (1997). 2D and 3D elastic wave propagation by a pseudo-spectral domain decomposition method, *J. Seismol.* **1,** 237–251.

Galis, M., P. Moczo, and J. Kristek (2008). A 3-D hybrid finite-difference–finite-element viscoelastic modelling of seismic wave motion, *Geophys. J. Int.* **175,** 153–184.

Gallovic, F., R. Barsch, J. de la Puente Alvarez, and H. Igel (2007). Digital library for computational seismology, *Eos* **88,** 559.

Gamond, J.-F., J.-P. Gratier, and F. Thouvenot (2009). Seismotectonic frame of the Grenoble Valley, in *ESG 2006, Third Intl. Symposium on the Effects of Surface Geology on Seismic Motion*, P.-Y. Bard, E. Chaljub, C. Cornou, F. Cotton, and P. Guéguen (Editors), LCPC Editions, ISSN 1628-4704, Vol. 2**,** p. 1569–1575.

Guéguen, P., C. Cornou, S. Garambois, and J. Banton (2007). On the limitation of the H/V spectral ratio using seismic noise as an exploration tool: Application to the Grenoble Valley (France), a small apex ratio basin, *Pure Appl. Geophys.* **164,** 115–134.

Guéguen, P., S. Garambois, S. Tadenuma, B. Lebrun, and F. Cotton (2009). Geotechnical, geophysical and seismological data used for the estimate of the highest amplified frequency in the basin of Grenoble, in *ESG 2006, Third Intl. Symposium on the Effects of Surface Geology on Seismic Motion*, P.-Y. Bard, E. Chaljub, C. Cornou, F. Cotton, and P. Guéguen (Editors), LCPC Editions, ISSN 1628-4704, Vol. 2**,** 1629–1637.

Harris, R. A., M. Barall, R. Archuleta, E. Dunham, B. Aagaard, J. P. Ampuero, H. Bhat, V. Cruz-Atienza, L. Dalguer, P. Dawson, S. Day, B. Duan, G. Ely, Y. Kaneko, Y. Kase, N. Lapusta, Y. Liu, S. Ma, D. Oglesby, K. Olsen, A. Pitarka, S. Song, and E. Templeton (2009). The SCEC/USGS dynamic earthquake rupture code verification exercise, *Seism. Res. Lett.* **80,** 119–126.

Jerram, J., P. Foray, S. Labanieh, and E. Flavigny (2009). Characterizing the nonlinearities of the lacustrine clays in the Grenoble basin, in *ESG 2006, Third Intl. Symposium on the Effects of Surface Geology on Seismic Motion*, P.-Y. Bard, E. Chaljub, C. Cornou, F. Cotton, and P. Guéguen (Editors), LCPC Editions, ISSN 1628-4704, Vol. 2**,** 1639–1648.

Käser, M., and M. Dumbser (2006). An arbitrary high order discontinuous Galerkin method for elastic waves on unstructured meshes I: The two-dimensional isotropic case with external source terms, *Geophys. J. Int.* **166,** 855–877.

Käser, M., M. Dumbser, and J. de la Puente Alvarez (2006). An efficient ADER-DG method for 3-dimensional seismic wave propagation in media with complex geometry, in *ESG 2006, Third Intl. Symposium on the Effects of Surface Geology on Seismic Motion*, P.-Y. Bard, E. Chaljub, C. Cornou, F. Cotton, and P. Guéguen (Editors), LCPC EditionsVol. 1**,** pp. 455–464, Grenoble.

Käser, M., M. Dumbser, J. de la Puente, and H. Igel (2007). An arbitrary high order discontinuous Galerkin method for elastic waves on unstructured meshes III: Viscoelastic attenuation, *Geophys. J. Int.* **168,** 224–242.

Komatitsch, D., and J. Tromp (1999). Introduction to the spectral element method for three-dimensional seismic wave propagation, *Geophys. J. Int.* **139,** 806–822.

Komatitsch, D., and J. P. Vilotte (1998). The spectral-element method: an efficient tool to simulate the seismic response of 2D and 3D geological structures, *Bull. Seismol. Soc. Am.* **88,** 368–392.

Komatitsch, D., Q. Y. Liu, J. Tromp, P. Suss, C. Stidham, and J. H. Shaw (2004). Simulations of ground motion in the Los Angeles basin based upon the spectral-element method, *Bull. Seismol. Soc. Am.* **94,** 187–206.

Komatitsch, D., R. Martin, J. Tromp, M. A. Taylor, and B. A. Wingate (2001). Wave propagation in 2-D elastic media using a spectral element method with triangles and quadrangles, *J. Comp. Acoustics* **9,** 703–718.

Komatitsch, D., S. Tsuboi, and J. Tromp (2005). The spectral-element method in seismology, in *Seismic Earth: Array Analysis of Broadband Seismograms*, A. Levander, and G. Nolet (Editors), American Geophysical Union Monograph 157, 205–228.

Kosloff, R., and D. Kosloff (1986). Absorbing boundaries for wave propagation problems, *J. Comp. Physics* **63,** 363–373.

Kristek, J., and P. Moczo (2003). Seismic-wave propagation in viscoelastic media with material discontinuities: A 3D fourth-order staggered-grid finite-difference modeling, *Bull. Seismol. Soc. Am.* **93,** 2273–2280.

Kristek, J., P. Moczo, and R. J. Archuleta (2002). Efficient methods to simulate planar free surface in the 3D 4(th)-order staggered-grid finite-difference schemes, *Stud. Geophys. Geod.* **46,** 355–381.

Kristek, J., P. Moczo, and P. Pazak (2009). Numerical modeling of earthquake motion in Grenoble basin, France, using a 4th-order velocity-stress arbitrary discontinuous staggered-grid FD scheme, in *ESG 2006, Third Intl. Symposium on the Effects of Surface Geology on Seismic Motion*, P.-Y. Bard, E. Chaljub, C. Cornou, F. Cotton, and P. Guéguen (Editors), LCPC Editions, ISSN 1628-4704, Vol. 2**,** p. 1517–1526.

Kristekova, M., J. Kristek, P. Moczo, and S. M. Day (2006). Misfit criteria for quantitative comparison of seismograms, *Bull. Seismol. Soc. Am.* **96,** 1836–1850.

Lebrun, B., D. Hatzfeld, and P. Y. Bard (2001). Site effect study in urban area: Experimental results in Grenoble (France), *Pure Appl. Geophys.* **158,** 2543–2557.

Liu, H. P., D. L. Anderson, and H. Kanamori (1976). Velocity dispersion due to anelasticity: Implications of seismology and mantle composition, *Geophys. J. Roy. Astron. Soc.* **47,** 41–58.

Lysmer, J., and R. L. Kuhlemeyer (1969). Finite dynamic model for infinite media, *J. Eng. Mech. Div. Proc. Amer. Soc. Civil Eng.* **95,** 859–877.

Maggio, F., and A. Quarteroni (1994). Acoustic wave simulation by spectral methods, *East–West J. Num. Math* **2,** 129–150.

Ménard, G., O. Blein, C. Fournier, A. Guyomard, C. Julian, J.-F. Gamond, and A. Paillet (2009). Relations between present vertical movements and sedimentary fill in the Grenoble area, in *ESG 2006, Third Intl. Symposium on the Effects of Surface Geology on Seismic Motion*, P.-Y. Bard, E. Chaljub, C. Cornou, F. Cotton, and P. Guéguen (Editors), LCPC Editions, ISSN 1628-4704, Vol. 2**,** 1577–1585.

Ménard, G., M. Dietrich, M. Vallon, S. Tadenuma, C. Bordes, O. Méric, F. Lemeille, and A. Paillet (2009). Seismic profiling and borehole mea-

surements in the Isère Valley near Grenoble, France: 2—Interpretation, in *ESG 2006, Third Intl. Symposium on the Effects of Surface Geology on Seismic Motion*, P.-Y. Bard, E. Chaljub, C. Cornou, F. Cotton, and P. Guéguen (Editors), LCPC Editions, ISSN 1628-4704, Vol. 2**,** 1609–1620.

Mercerat, E. D., J. P. Vilotte, and F. J. Sanchez-Sesma (2005). Triangular spectral-element simulation of 2D elastic wave propagation using unstructured triangular grids, *Geophys. J. Int.* **166,** 679–698.

Moczo, P., and J. Kristek (2005). On the rheological models used for time-domain methods of seismic wave propagation, *Geophys. Res. Lett.* **32,** L01306.

Moczo, P., J.-P. Ampuero, J. Kristek, S. M. Day, M. Kristekova, P. Pazak, M. Galis, and H. Igel (2006). Comparison of numerical methods for seismic wave propagation and source dynamics—the SPICE Code Validation, in *ESG 2006, Third Intl. Symposium on the Effects of Surface Geology on Seismic Motion*, P.-Y. Bard, E. Chaljub, C. Cornou, F. Cotton, and P. Guéguen (Editors), LCPC Editions, Vol. 1**,** 495–504, Grenoble.

Moczo, P., J. Kristek, and M. Galis (2004). Simulation of the planar free surface with near-surface lateral discontinuities in the finite-difference modeling of seismic motion, *Bull. Seismol. Soc. Am.* **94,** 760–768.

Moczo, P., J. Kristek, M. Galis, P. Pazak, and M. Balazovjech (2007). The finite-difference and finite-element modeling of seismic wave propagation and earthquake motion, *Acta Phys. Slovaca* **57,** 177–406.

Moczo, P., J. Kristek, V. Vavrycuk, R. J. Archuleta, and L. Halada (2002). 3D heterogeneous staggered-grid finite-difference modeling of seismic motion with volume harmonic and arithmetic averaging of elastic moduli and densities, *Bull. Seismol. Soc. Am.* **92,** 3042–3066.

Moczo, P., J. O. A. Robertsson, and L. Eisner (2007). The finite-difference time-domain method for modeling of seismic wave propagation, in *Advances in Wave Propagation in Heterogeneous Media*, R.-S. Wu and V. Maupin (Editors), Vol. **421–516**, Elsevier Academic Press, New York.

Nicoud, G., G. Royer, J. C. Corbin, F. Lemeille, and A. Paillet (2002). Creusement et remplissage de la vallée de l'Isère au Quaternaire récent. Apports nouveaux du forage GMB1 (1999) dans la région de Grenoble (France), *Géologie de la France* **4,** 39–49 (in French).

Oeser, J., H. P. Bunge, and M. Mohr (2006). Cluster design in the Earth Sciences tethys, in *High Performance Computing and Communications—Second Intl. Conf.*, *HPCC 2006*, Munich, Germany, Lecture Notes in Computer Science, vol. 4208**,** M. Gerndt and D. Kranzlmuller Vol. 31–40**,** Springer-Verlag Berlin.

Seriani, G., and S. P. Oliveira (2007). Dispersion analysis of spectral element methods for elastic wave propagation, *Wave Motion* **45,** 729–744.

Seriani, G., and E. Priolo (1991). High-order spectral element method for acoustic wave modeling, *Expanded Abstracts of the Soc. Expl. Geophys.* 1561–1564.

Seriani, G., and E. Priolo (1994). A spectral element method for acoustic wave simulation in heterogeneous media, *Finite Elem. Anal. Des.* **16,** 337–348.

Stacey, R. (1988). Improved transparent boundary formulations for the elastic wave equation, *Bull. Seismol. Soc. Am.* **78,** 2089–2097.

Stupazzini, M. (2009). 3D Ground Motion Simulation of the Grenoble Valley by GeoELSE, in *ESG 2006, Third Intl. Symposium on the Effects of Surface Geology on Seismic Motion*, P.-Y. Bard, E. Chaljub, C. Cornou, F. Cotton, and P. Guéguen (Editors), LCPC Editions, ISSN 1628-4704, Vol. **2,** 1551–1560.

Stupazzini, M., R. Paolucci, and H. Igel (2009). Near-fault earthquake ground motion simulation in the Grenoble Valley by a high-performance spectral element code, *Bull. Seismol. Soc. Am.* **99,** 286–301.

Thouvenot, F., J. Frechet, L. Jenatton, and J. F. Gamond (2003). The Belledonne Border Fault: Identification of an active seismic strike-slip fault in the western Alps, *Geophys. J Int.* **155,** 174–192.

Thouvenot, F., L. Jenatton, and R. Guiguet (2009). Seismicity of the Grenoble area, in *ESG 2006, Third Intl. Symposium on the Effects of Surface Geology on Seismic Motion*, P.-Y. Bard, E. Chaljub, C. Cornou, F. Cotton, and P. Guéguen (Editors), LCPC Editions, ISSN 1628-4704, Vol. 2**,** 1563–1567.

Titarev, V. A., and E. F. Toro (2002). ADER: Arbitrary high order Godunov approach, *J. Sci. Comput.* **17,** 609–618.

Tsuno, S., E. Chaljub, and P. Y. Bard (2009). Grenoble Valley simulation benchmark—comparison of results and main learnings, in *ESG 2006, Third Intl. Symposium on the Effects of Surface Geology on Seismic Motion*, P.-Y. Bard, E. Chaljub, C. Cornou, F. Cotton, and P. Guéguen (Editors), LCPC Editions, ISSN 1628-4704, Vol. 2**,** 1377–1433.

Vallon, M. (1999). Estimation de l'épaisseur d'alluvions et sédiments quaternaires dans la région grenobloise par inversion des anomalies gravimétriques, Unpublished IPSN/CNRS report, 33 pp. (in French).

Laboratoire de Géophysique Interne et Tectonophysique
CNRS
Observatoire de Grenoble, Université J. Fourier, France
Maison des Géosciences
BP 53, 38041 Grenoble
Cedex 9, France
Emmanuel.Chaljub@obs.ujf-grenoble.fr
Seiji.Tsuno@obs.ujf-grenoble.fr
bard@obs.ujf-grenoble.fr
(E.C., S.T., P.-Y.B.)

Faculty of Mathematics
Physics and Informatics
Comenius University Bratislava
Mlynska dolina F1
842 48 Bratislava, Slovakia
Peter.Moczo@fmph.uniba.sk
Jozef.Kristek@fmph.uniba.sk
(P.M., J.K.)

Department für Geo-und Umweltwissenschaften
Ludwig-Maximilians-Universität München
Theresienstrasse 41 80333 München, Germany
martin.kaeser@geophysik.uni-muenchen.de
(M.K.)

Department of Structural Engineering
Politecnico di Milano
Piazza Leonardo da Vinci, 32
20133 Milano, Italy
stupa@stru.polimi.it
(M.S.)

Geophysical Institute
Slovak Academy of Sciences
Dubravska cesta 9
845 28 Bratislava, Slovakia
kristekova@savba.sk
(M.K.)

Manuscript received 23 February 2009

Geophysical Journal International

Geophys. J. Int. (2015) **201,** 90–111 doi: 10.1093/gji/ggu472
GJI Seismology

3-D numerical simulations of earthquake ground motion in sedimentary basins: testing accuracy through stringent models

Emmanuel Chaljub,[1] Emeline Maufroy,[1] Peter Moczo,[2,3] Jozef Kristek,[2,3] Fabrice Hollender,[1,4] Pierre-Yves Bard,[1] Enrico Priolo,[5] Peter Klin,[5] Florent de Martin,[6] Zhenguo Zhang,[7] Wei Zhang[7] and Xiaofei Chen[7]

[1] *Univ. Grenoble Alpes/CNRS/IRD/IFSTTAR, ISTerre, F-*38000 *Grenoble, France. E-mail: Emmanuel.Chaljub@obs.ujf-grenoble.fr*
[2] *Faculty of Mathematics, Physics and Informatics, Comenius University Bratislava, Mlynska dolina F*1, 84248 *Bratislava, Slovak Republic*
[3] *Geophysical Institute, Slovak Academy of Sciences, Dubravska cesta* 9, 84528 *Bratislava, Slovak Republic*
[4] *French Alternative Energies and Atomic Energy Commission (CEA), Saint-Paul-lez-Durance, France*
[5] *Istituto Nazionale di Oceanografia e Geofisica Sperimentale, Trieste, Italy*
[6] *Bureau de Recherches Géologiques et Minières, Risks and Prevision Division,* 3 *avenue C. Guillemin, BP* 36009, *F-*45060 *Orléans Cedex* 2, *France*
[7] *School of Earth and Space Sciences, University of Science and Technology of China, Hefei, Anhui* 230026, *China*

Accepted 2014 December 4. Received 2014 December 1; in original form 2014 July 10

SUMMARY

Differences between 3-D numerical predictions of earthquake ground motion in the Mygdonian basin near Thessaloniki, Greece, led us to define four canonical stringent models derived from the complex realistic 3-D model of the Mygdonian basin. Sediments atop an elastic bedrock are modelled in the 1D-sharp and 1D-smooth models using three homogeneous layers and smooth velocity distribution, respectively. The 2D-sharp and 2D-smooth models are extensions of the 1-D models to an asymmetric sedimentary valley. In all cases, 3-D wavefields include strongly dispersive surface waves in the sediments. We compared simulations by the Fourier pseudo-spectral method (FPSM), the Legendre spectral-element method (SEM) and two formulations of the finite-difference method (FDM-S and FDM-C) up to 4 Hz.

The accuracy of individual solutions and level of agreement between solutions vary with type of seismic waves and depend on the smoothness of the velocity model. The level of accuracy is high for the body waves in all solutions. However, it strongly depends on the discrete representation of the material interfaces (at which material parameters change discontinuously) for the surface waves in the sharp models.

An improper discrete representation of the interfaces can cause inaccurate numerical modelling of surface waves. For all the numerical methods considered, except SEM with mesh of elements following the interfaces, a proper implementation of interfaces requires definition of an effective medium consistent with the interface boundary conditions. An orthorhombic effective medium is shown to significantly improve accuracy and preserve the computational efficiency of modelling.

The conclusions drawn from the analysis of the results of the canonical cases greatly help to explain differences between numerical predictions of ground motion in realistic models of the Mygdonian basin.

We recommend that any numerical method and code that is intended for numerical prediction of earthquake ground motion should be verified through stringent models that would make it possible to test the most important aspects of accuracy.

Key words: Numerical solutions; Numerical approximations and analysis; Earthquake ground motions; Site effects; Computational seismology; Wave propagation.

1 INTRODUCTION

Seismologists must predict earthquake ground motion during potential future earthquakes in densely populated areas and sites of special importance. This is very important for land-use planning, designing new buildings and reinforcing existing ones. It is also very important for undertaking actions that could help mitigate losses during future earthquakes.

Prediction of the earthquake ground motion for a site of interest can be based on empirical approach if sufficient earthquake records

at that site or at a sufficiently similar site are available. In most cases, however, this is not so and seismologists face a drastic lack of data. In such situations it is the theory and numerical simulations that have to be applied for predicting the earthquake motion.

Structural and rheological complexity of the realistic models imply that only approximate computational methods can be applied. Among the approximate methods, the domain (in the spatial sense) numerical-modelling methods are dominant due to relatively reasonable balance between the accuracy and computational efficiency. Some of the more widely used numerical-modelling methods are the time-domain finite-difference, finite-element, Fourier pseudo-spectral, spectral-element and discontinuous Galerkin methods.

Each method has its advantages and disadvantages that often depend on a particular application. In other words, none of these methods can be chosen as the universally best (in terms of accuracy and computational efficiency) method for all important problems. One logical consequence and particular aspect of this situation is that, depending on a particular model of the medium, it might be not trivial to reach satisfactory agreement between solutions obtained by different methods. And indeed, this is the important lesson learned from the dedicated international blind predictions tests and comparative exercises for the Turkey Flat in the Parkfield area, central California in 1989–1990 (e.g. Cramer 1995), Ashigara Valley in the Kanagawa Prefecture, SW of Tokyo, Japan in 1992 (e.g. Bard 1994), Osaka basin, Japan in 1998 (Kawase & Iwata 1998), Grenoble valley in French Alps in 2006 (Chaljub *et al.* 2006, 2010) as well as from the Southern California Earthquake Center (SCEC) code comparison (Day *et al.* 2001, 2003, 2005; Bielak *et al.* 2010).

The SCEC comparison included relatively simple models of a homogeneous half-space and layer over half-space (Day *et al.* 2001), and a realistic model of the San Fernando Valley and Los Angeles Basin (Day *et al.* 2003, 2005). In the simple models the *P*- to *S*-wave velocity ratio was as low as 1.73 and the *S*-wave velocity contrast less than 1.5. Due to the material parameters and source position, strong surface waves were not generated in the models. Bielak *et al.* (2010) analysed results of verification for the ShakeOut scenario earthquake for the realistic SCEC community velocity model and frequency range [0.1, 0.5] Hz. They concluded that the independent simulations were, given the complexity and size of the problem, satisfactorily close. They attributed the observed differences mainly to differences in discrete representations of the model heterogeneity and models of attenuation.

The ESG2006 (Effects of Surface Geology 2006) exercise was focused on the Grenoble valley in the French Alps (Chaljub *et al.* 2006, 2010). Compared with the Los Angeles basin, the modelling of the Grenoble Valley is complicated by the larger *P*- to *S*-wave velocity ratio, larger velocity contrast and the complex interface geometry. The simulations were performed for the frequency range [0.1, 2] Hz. Four teams reached a very good level of agreement up to 1 Hz. The differences above 1 Hz were attributed to differences in discrete representations of the model heterogeneity, numerical dispersion and models of attenuation, that is, similar to reasons found by Bielak *et al.* (2010).

The individual named reasons for differences in both comparisons for realistic models are probably correct but they were not really separated and quantified. In other words, none of the three comparisons (SCEC simple models, SCEC ShakeOut and ESG2006) provides sufficient methodological basis for estimating accuracy of individual numerical solutions and possible differences among independent numerical solutions for relatively simple but stringent models or for other complex realistic models. This, however, is an important aspect in relation to application of the numerical-modelling methods in practical predictions.

Given the state-of-the-art in the numerical modelling of earthquake motion it was logical to develop a project focused on systematic and quantitative comparison of the most advanced numerical methods. The Aristotle University of Thessaloniki, Greece, the Cashima research project (supported by CEA—the French Alternative Energies and Atomic Energy Commission, and the Laue-Langevin Institute, ILL, Grenoble) and ISTerre at Joseph Fourier University, Grenoble, France, jointly organized the Euroseistest Verification and Validation Project (E2VP) which aims at: (i) evaluating accuracy of the current most advanced numerical methods when applied to realistic 3-D models and (ii) quantitative comparison of the recorded and numerically simulated earthquake ground motion. E2VP thus includes both verification and validation (e.g. Bielak *et al.* 2010; Moczo *et al.* 2014). The E2VP target site is the Mygdonian basin near Thessaloniki, Greece, the international research and test site of many international seismological and earthquake-engineering projects (for more on the site see Maufroy *et al.* 2014).

In this paper, we address the verification part of E2VP. From the originally 18 teams from around the world intended to participate, eight teams contributed to the 3-D modelling over the whole duration of the first verification phase and four teams were able to reach a satisfactory level of agreement for the complex 3-D models of the Mygdonian basin [one team applied its finite-difference scheme, one team Fourier pseudo-spectral scheme and two teams independent implementations of the spectral-element method (SEM)].

Importantly and consistently with the previous comparative efforts mentioned above, there were differences among individual solutions by the four teams mainly in the configurations with strong surface waves and at high frequencies—despite the effort to make the individual discrete models as close as possible. The differences led us to develop 4 canonical models derived from the realistic 3-D model of the Mygdonian basin. Two models are 1-D, two models are 2-D. Wavefields are in the all models 3-D. The solutions for the canonical models were computed by the four original teams and by a fifth team which applied the velocity–stress collocated-grid finite-difference scheme.

The quantitative analysis of the results explains how the accuracy of individual solutions and level of agreement between solutions vary with the type of seismic waves and depend on the discretization of the spatial variations of material parameters.

2 EUROSEISTEST VERIFICATION AND VALIDATION PROJECT

The target site of E2VP is the Mygdonian basin located in the northeastern part of Greece, 30 km ENE from Thessaloniki, in the epicentral area of the *M*6.4 seismic event which occurred on 1978 June 20 (e.g. Soufleris *et al.* 1982; Theodulidis *et al.* 2006). E2VP focuses on the part of the basin between the Lagada and Volvi lakes, a site which has been extensively investigated in several European projects (e.g. Euroseistest, Euroseismod, Euroseisrisk, ISMOD, ITSAK-GR; see `http://euroseisdb.civil.auth.gr`, last accessed 16 January 2015) and monitored with a dense accelerometric array since the mid-nineties. The project makes use of a detailed 3-D model of the intralake basin zone (about 5 km wide and 15 km long) based upon work by Manakou (2007) and Manakou *et al.* (2010). The model consists of three sedimentary layers with significant lateral variations in thickness as shown in

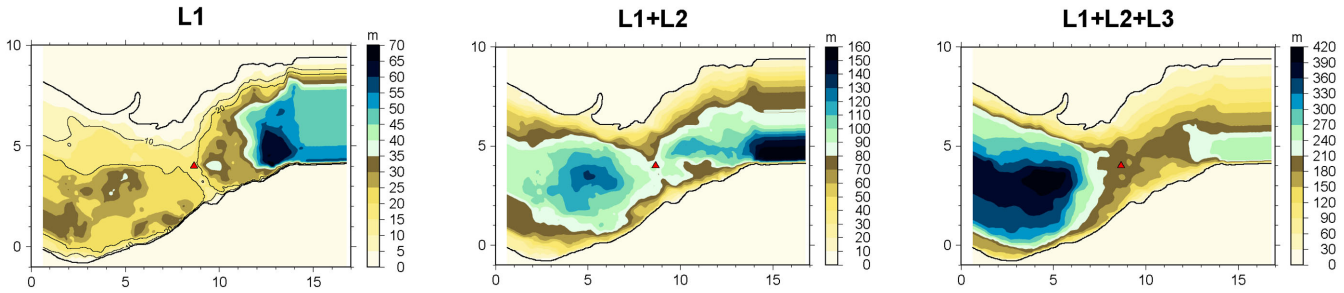

Figure 1. Thicknesses of the sedimentary layers of the Mygdonian basin's velocity model used within the E2VP project. The red triangle denotes the position of TST, the central station of the Euroseistest accelerometric array.

Table 1. Thicknesses (h) and material parameters (S and P seismic velocities V_S and V_P, respectively, and mass density ρ) in the model with three homogeneous layers used in E2VP. L_i, $i = 1 \ldots 3$ denote the sedimentary layers and H the surrounding bedrock.

	h (m)	V_P (m s^{-1})	V_S (m s^{-1})	ρ (kg m^{-3})
L_1	17.3	1500	200	2100
L_2	72.5	1800	350	2100
L_3	115.6	2500	650	2200
H	1000	4500	2600	2600

Table 2. Same as Table 1 for the smooth, piecewise linear, three-layer model used in E2VP.

	h (m)	V_P (m s^{-1})	V_S (m s^{-1})	ρ (kg m^{-3})
L_1	17.3	[1500–1600]	[200–250]	2100
L_2	72.5	[1600–2200]	[250–500]	[2100–2130]
L_3	115.6	[2200–2800]	[500–900]	[2130–2250]
H	1000	4500	2600	2600

Fig. 1. Note that the TST station at the centre of the Euroseistest site is located at a saddle point, with the sedimentary thickness increasing both eastward and westward, and decreasing towards the edges of the basin. The central NS profile passing through TST appears as a buried pass between two thicker sub-basins, the maximum thickness (about 400 m) being reached in the westernmost one. Based upon this three-layer structure of the basin, two different velocity models have been considered in E2VP: a piecewise homogeneous model with physical interfaces within the sediments, and a smooth, piecewise linear model without internal discontinuities. The depth distribution of seismic velocities and mass densities in each sedimentary layer and in the surrounding bedrock is given for both models in Tables 1 and 2, respectively. The intrinsic attenuation is modelled through a linear scaling of the quality factor with shear wave velocity as $Q_S = V_S/10$, neglecting the bulk attenuation, $Q_\kappa = \infty$.

Many different numerical methods were compared during the verification phase of E2VP, to evaluate the epistemic uncertainty in numerical prediction of earthquake ground motion in sedimentary basins. Here we consider a subset of those methods which provided the most similar results: the velocity–stress finite-difference method on the staggered grid (FDM-S), the Fourier pseudo-spectral method (FPSM) and the Legendre SEM. They are are briefly described in Section 4. The reader is referred to Maufroy *et al.* (2014) for a presentation of the results obtained by a wider set of methods and codes, which allows to better appreciate the difficulty to obtain acceptable levels of agreement in realistic 3-D verification exercises.

In Fig. 2, we compare synthetics simulated at the TST station by the three methods for frequencies up to 4 Hz for the viscoelastic model with three homogeneous layers. The basin is excited by a double-couple point source located at 3 km depth. The level of similarity is excellent for the first arrivals (i.e. for $t \leq 5$ s), which consist mainly of body waves, and it decreases for late arrivals consisting mostly of surface waves diffracted at the basin edges. In Fig. 3, we compare synthetics for the elastic model with homogeneous layers. The neglect of attenuation reveals significant differences in amplitude and phase in the time window dominated by the local surface waves, that is for $t \geq 6$ s. Note that those differences remain even after increasing the grid resolution used in each of the numerical

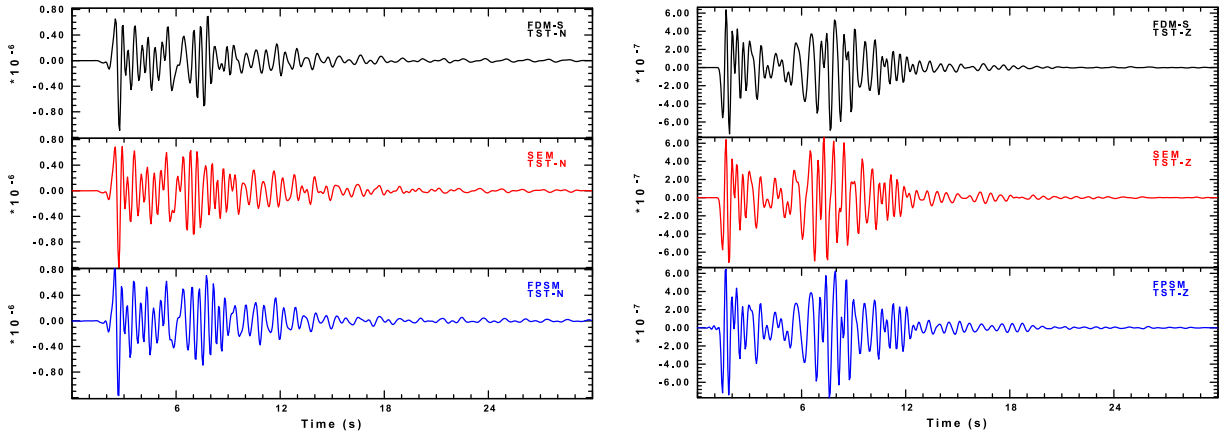

Figure 2. Comparison of predictions of the NS (left-hand panel) and vertical (right-hand panel) components of ground velocity at the central TST station obtained by three different numerical methods: FDM-S (black), SEM (red) and FPSM (blue). The sedimentary basin is modelled with three homogeneous viscoelastic layers of varying thicknesses described in Fig. 1 and Table 1.

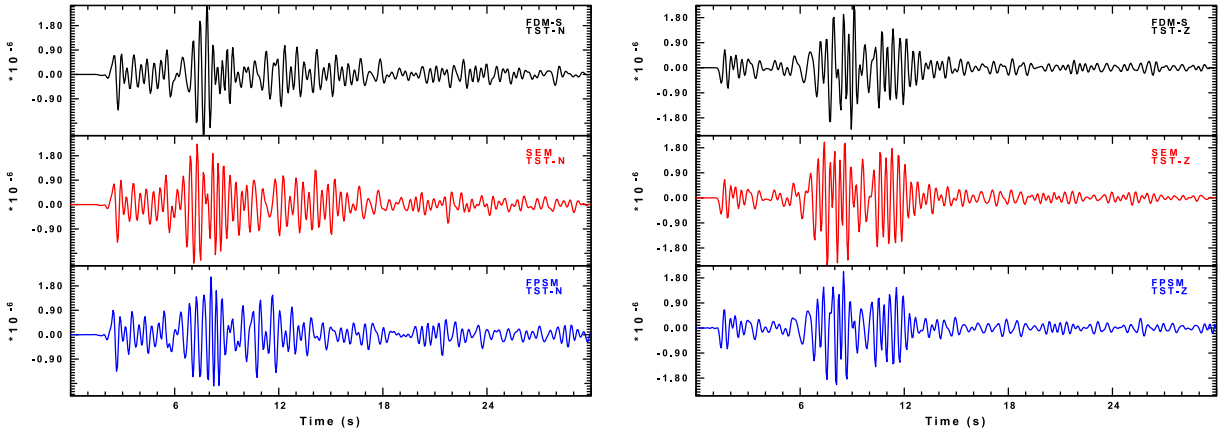

Figure 3. Same as Fig. 2 for the elastic model (neglecting intrinsic attenuation) with homogeneous layers. Note the good agreement on the first arrivals and the differences in phase and amplitude for later arrivals (between $t = 6$ and 12 s).

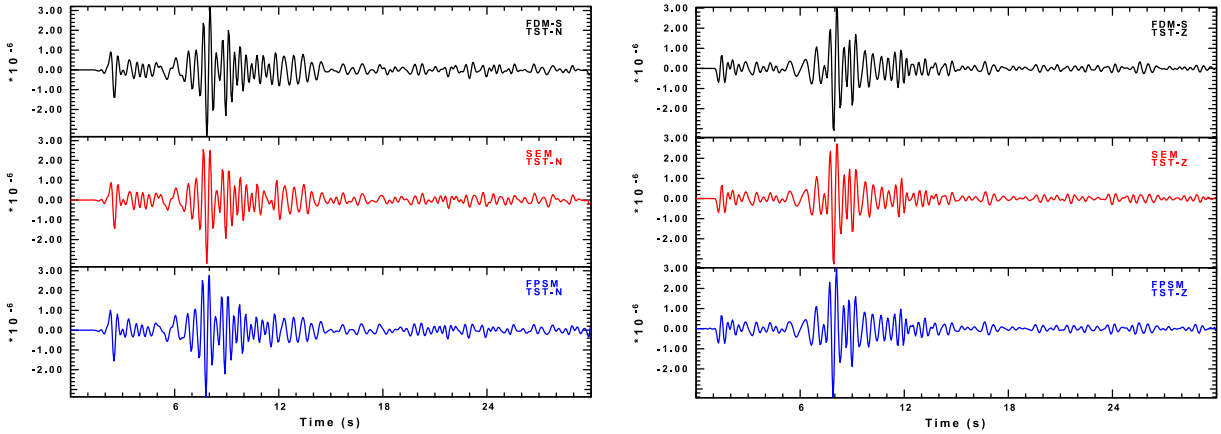

Figure 4. Same as Fig. 3 for the smooth basin model of Table 2: no internal material discontinuities in sediments. Note the overall good agreement obtained, even on late arrivals.

solutions. These results suggest that the epistemic uncertainty of numerical prediction of earthquake ground motion may be large for local surface waves. Several factors may contribute to this. They are investigated and discussed later in the paper.

Another important observation is that the level of epistemic uncertainty on the late arrivals was found smaller whenever a smooth basin model was considered. This is illustrated in Fig. 4 where we compare the predictions of the elastic response of the smooth piecewise linear model of Table 2. Despite the neglect of attenuation, the level of fit is excellent on the whole wavefield.

3 CANONICAL TEST CASES

In order to better understand the origin of the differences between numerical predictions of ground motion observed in the course of E2VP, we designed a set of test cases with relevant characteristics.

We focus on the perfectly elastic models because we checked that the differences between individual solutions were much larger when attenuation was neglected. The verification of solutions in the viscoelastic models is left for a further, second level analysis. We may note that reaching a satisfactory level of agreement in the elastic models represents a real numerical challenge.

In this paper, we present four test cases: two for which the velocity model is varying only in the vertical direction (1-D geometry), and two for which the velocity model is a simplified, 2-D cross-section of the Mygdonian basin model (2-D geometry). For each geometry (1-D or 2-D), two kinds of structural models were considered: one model, referred to as sharp, with internal discontinuities of the material parameters in the sedimentary part; and one model, referred to as smooth, where the vertical variation of the material parameters is continuous, piecewise linear within the sediments. The four test cases are denoted as 1D-sharp, 1D-smooth, 2D-sharp and 2D-smooth. The 3-D seismic wavefields include surface waves trapped in the sediments: for models with 1-D geometry, the surface waves are excited by a surface force, whereas they are spontaneously generated from the conversion of body waves at the basin edges for models with 2-D geometry.

3.1 Models with 1-D geometry

The problem configuration for the test cases with 1-D geometry (1D-sharp and 1D-smooth) is depicted in Fig. 5. The model consists of three sedimentary layers overlying an elastic, homogeneous half-space. The layer thicknesses, densities and seismic velocities for the 1D-sharp and 1D-smooth models are given in Tables 1 and 2, respectively. The total sediment thickness is 205.4 m and the fundamental resonance frequencies are $f_0 \simeq 0.67$ and $\simeq 0.74$ Hz for the 1D-sharp and 1D-smooth models, respectively. Note that although the 1D-smooth model was not designed to be a smooth approximation of the 1D-sharp model, whence the difference in the fundamental frequency, both models are consistent with the geological and geophysical information gathered at the TST site.

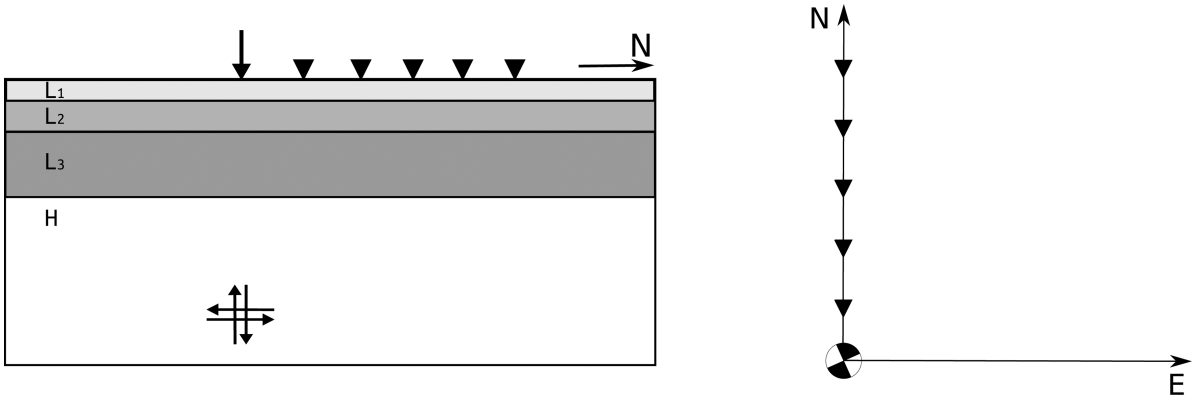

Figure 5. Schematic representation (left: vertical cross-section, right: surface view) of the 3 layers (L_1, L_2, L_3) over half-space (H) models used in the test cases 1D-sharp and 1D-smooth. The values of thicknesses, densities and seismic velocities are given in Tables 1 and 2. The positions of the sources and surface receivers are indicated with bold arrows and triangles, respectively. The beach ball at the epicentre indicates the focal mechanism of the double-couple point source plotted. The distance between the receivers along the northern surface profile is 1 km.

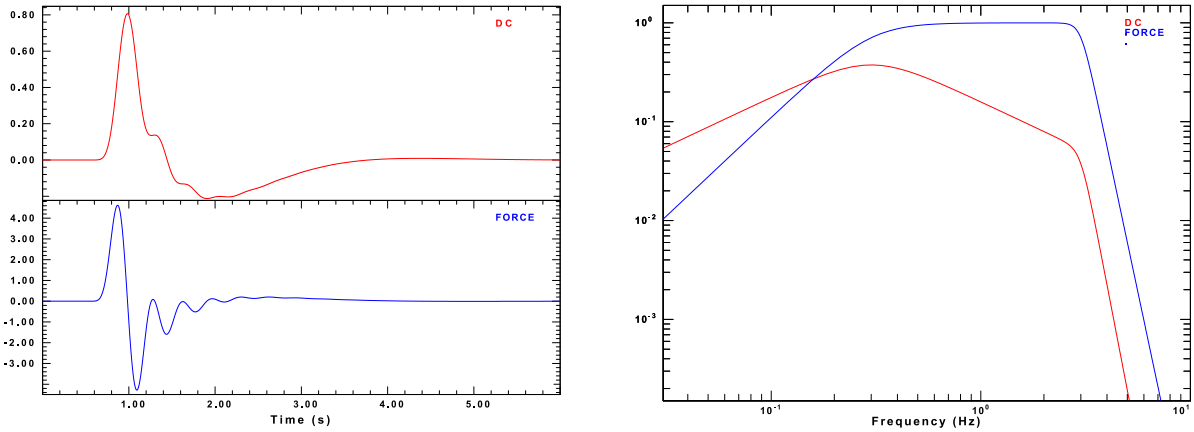

Figure 6. Source time functions used in the test cases 1D-sharp and 1D-smooth. Left-hand panel: dimensionless time histories for the deep double-couple source (red) and the surface force (blue). Right-hand panel: corresponding amplitude Fourier spectra.

The impact of the strategy used for constructing a geophysical model on the level of epistemic uncertainty in the numerical prediction of earthquake ground motion is discussed at the end of the paper.

A double-couple point source with strike ϕ_S, dip δ_S and rake λ_S is set at 3 km depth. The focal mechanism is that of a vertical strike-slip fault ($\delta_S = 90^\circ$, $\lambda_S = 0^\circ$), rotated such that the horizontal coordinate axes do not lie in any nodal plane of the radiation patterns for the P or S waves: $\phi_S = 22.5^\circ$. An additional vertical force is considered at the free surface in order to excite Rayleigh surface waves trapped in the sedimentary layers. Both sources act synchronously with the time functions shown in Fig. 6. The source time function for the surface force is a bandpass filtered Dirac pulse with almost no spectral content beyond $f_{max} = 4$ Hz and a flat part in the band [0.3–3 Hz]; its integral is used to define the time history of the double-couple source. The seismic moment of the double-couple source is set to $M_0 = 10^{18}$ N.m and the amplitude of the surface force is multiplied by a factor $A = 5 \times 10^{11}$ in order to obtain synthetic seismograms with realistic ratios of body- to surface wave amplitudes.

3.1.1 Reference solutions

The reference solutions for the 1D-sharp and 1D-smooth cases were computed with the discrete wavenumber method (DWM; Bouchon 1981, 2003): we used the `axitra` program (Coutant 1989) to compute the wavefield generated by the deep double-couple source and a code implementing Hisada's asymptotic approximation at high wavenumbers (Hisada 1995) to compute the wavefield generated by the surface force.

Fig. 7 shows the synthetic seismograms computed at a few receivers located at the surface along the northern profile for the 1D-sharp case. The east–west component of ground velocity consists only of *SH* body waves and shows a typical 1-D resonance pattern at about 2.7 Hz, whereas the vertical component is dominated by the propagation of strongly dispersed Rayleigh surface waves. The time-frequency representation of the vertical ground velocity at 4 km epicentral distance is shown in Fig. 8. It helps to identify the contributions of the different Rayleigh modes to the 15 s long wave train recorded after 10 s: seismic phases arriving between 12 and 16 s consist mainly of the high-frequency ($\geq$2 Hz) first higher mode, whereas phases arriving after 18 s are made of the moderate- to low-frequency fundamental mode ($\leq$3 Hz). Note the large amplitude related to the arrival of the Airy phase of the fundamental Rayleigh mode around 17 s, which is well predicted by the analysis of the group velocity.

The surface seismograms for the 1D-smooth case are shown in Fig. 9. Note that, compared to the 1D-sharp case, the high-frequency resonance effect is less pronounced in the body wave part and that a simpler surface wave dispersion pattern is observed on the vertical component. Looking at the time-frequency representation of the vertical ground velocity at 4 km epicentral distance (Fig. 10), one

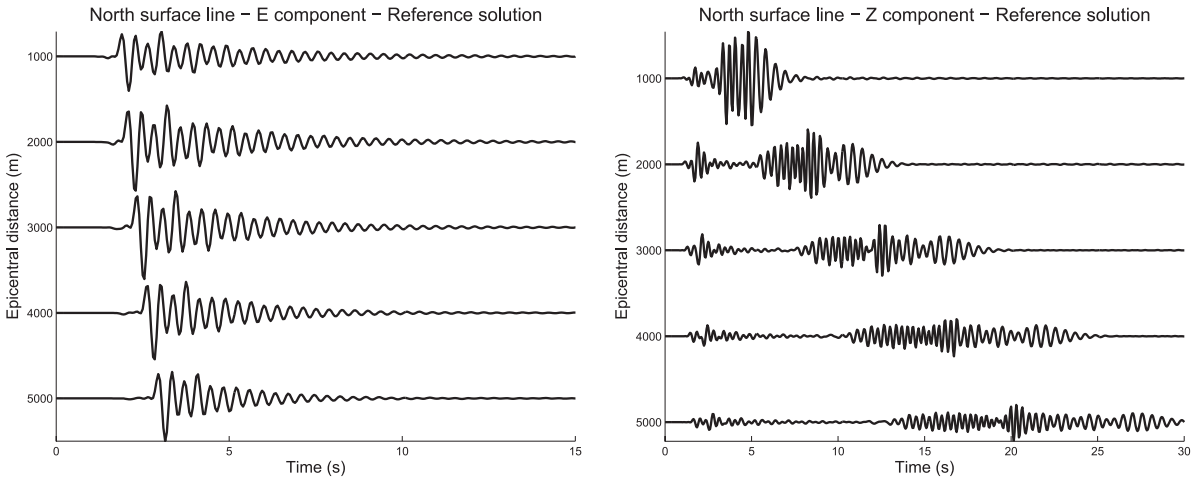

Figure 7. East–west (left-hand panel) and vertical (right-hand panel) components of ground velocity along the northern surface profile computed with the discrete wavenumber method for the 1D-sharp model.

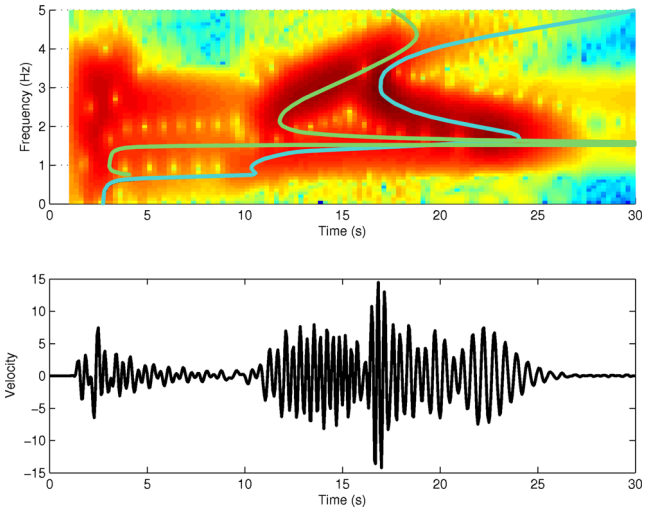

Figure 8. Time (bottom panel) and time-frequency (top panel) representations of the vertical ground velocity at 4 km epicentral distance for the 1D-sharp case. The background colours on the top image indicate the amplitude of the seismic arrivals, from blue (small) to red (medium) and bordeaux (large). The solid lines superimposed on the image indicate the theoretical group arrival times of the fundamental (blue) and first higher (green) modes of Rayleigh waves.

sees indeed that the fundamental and first higher modes of Rayleigh waves are well separated in time, the fundamental mode being much less dispersed than in the 1D-sharp case.

3.2 Models with 2-D geometry

The problem configuration for the test cases with 2-D geometry (2D-sharp and 2D-smooth) is shown in Fig. 11. The model corresponds to a 5-km-long valley bounded at one side by a vertical wall and at the other side by a gentle slope, in order to mimic the geometry of the north–south cross-section of the Mygdonian basin passing through the central TST station (Fig. 1). The layering for the 2D-sharp (resp. 2D-smooth) model is the same as that for the 1D-sharp (resp. 1D-smooth) model, except close to the northern edge where the thickness of each layer linearly decreases from its value given in Table 1 (resp. Table 2) to zero over a distance of 1.5 km. The resulting angle of the bedrock-sediment interface at the northern boundary is about 8°.

Both 2-D models are excited by the same deep double-couple source used for the 1D-sharp and 1D-smooth cases. In these models, contrary to the 1-D models, the surface waves (of Rayleigh and Love type) are generated at the edges of the valley and trapped in the sediments.

4 NUMERICAL METHODS

The numerical solutions presented in this paper were obtained by three kinds of numerical approximation in space: two velocity–stress formulations of the finite-difference method – on the staggered grid and on the collocated grid, the FPSM and the Legendre SEM. Time evolution in all cases is solved by an explicit, conditionally stable, finite-difference scheme. In what follows, we briefly present each method and explain how it should be implemented to provide an accurate solution to the canonical cases.

4.1 Legendre SEM

The SEM is a high-order finite-element approximation in which the consistent choice of an orthogonal polynomial basis and of a Gauss numerical quadrature allows to achieve the convergence properties of spectral methods. In its early applications to seismology (Priolo *et al.* 1994; Seriani & Priolo 1994), a set of Chebyshev polynomials and Gauss–Chebyshev quadrature were used. Using instead Legendre polynomials and Gauss–Legendre–Lobatto quadrature yields SEM, which still holds the convergence rate of spectral methods while providing a diagonal mass matrix resulting in costless implementation of explicit finite-difference schemes in time. The Legendre formulation of the SEM was introduced in seismology by Faccioli *et al.* (1997) and Komatitsch & Vilotte (1998), and is the most widely used nowadays. It relies on the tensorization of the 1-D SEM, and therefore on the use of quadrangles in 2-D and hexahedras in 3-D. The reader is referred to Komatitsch *et al.* (2005) and Chaljub *et al.* (2007) for review articles presenting the numerous developments of SEM, and to Moczo *et al.* (2014, chapter 5, p. 76) for a historical presentation and recent applications to seismic wave propagation in sedimentary basins or alluvial valleys.

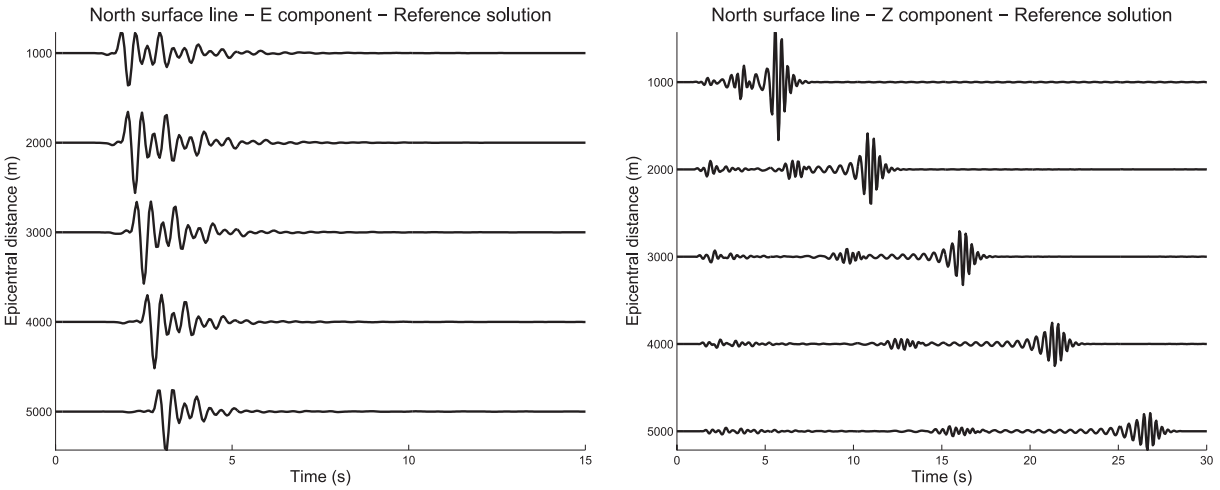

Figure 9. East–west (left-hand panel) and vertical (right-hand panel) components of ground velocity along the northern surface profile computed with the discrete wavenumber method for the 1D-smooth model.

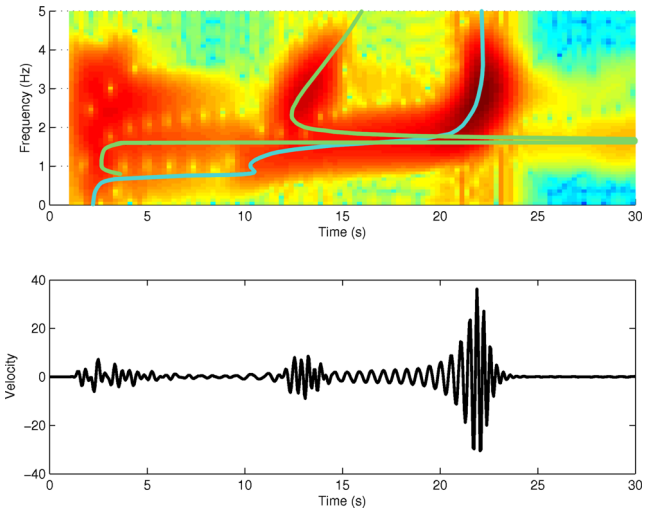

Figure 10. Same as Fig. 8 for the 1D-smooth case.

In the finite-element method (FEM), and therefore in SEM, the free-surface condition (and more generally the continuity of traction) is said to be a natural boundary condition because it is accounted for in the weak form of the equations to be solved and does not have to be explicitly enforced at the discrete level. This allows surface topography to be accounted for in SEM, as long as the variations of the free surface can be accurately represented at the discrete level. No particular effort, or care, was therefore needed when implementing the free-surface condition in SEM for the canonical cases considered here, since they all deal with a flat free surface.

Two kinds of material heterogeneities can be accounted for in SEM: intra-element, continuous variations approximated by their projection on the high degree (typically $N \in [4 - 6]$) local polynomial bases, and inter-element discontinuities, thank to the FEM functional framework. Note that the representation of small-scale variations by the local spectral element polynomial bases is intrinsically limited. Trying to represent localized variations, for example material discontinuities, can lead to aliasing effects and/or Gibbs oscillations just like in the traditional spectral methods (e.g. Boyd 2001). However, practical situations occur where discontinuities exist but can hardly be represented at the discrete level due to geometrical complexity in the design of hexahedral meshes (e.g. when large variations of interface elevation occur on small spatial scales) or due to prohibitive computational cost to respect the Courant–Friedrichs–Lewy (CFL) stability condition (e.g. close to the valley or basin edges). Some approximate mesh design strategies are sometimes adopted in those cases. In these strategies, the element boundaries do not follow the shape of the material interfaces (they do not coincide with the interfaces). We may use acronym 'NF' (not following) for these strategies. In the remainder of the paper, the performance of some NF strategies is evaluated and compared to

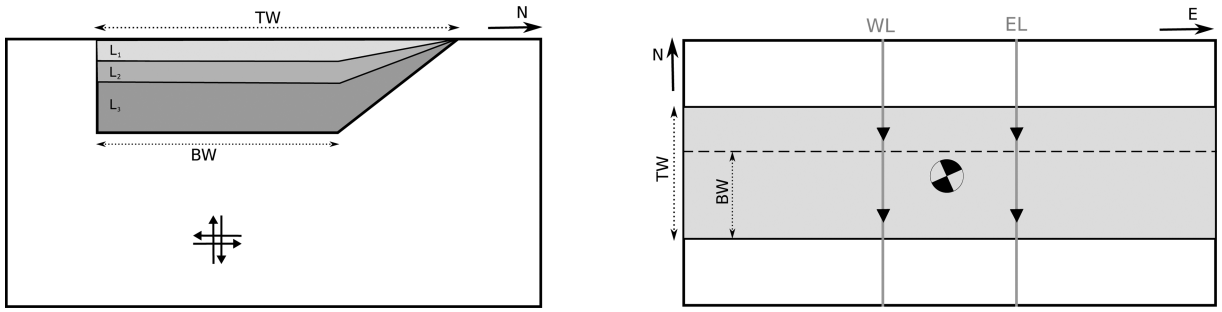

Figure 11. Schematic representation (left: vertical cross-section, right: surface view) of the valley model used in the test cases 2D-sharp and 2D-smooth. The bottom and total widths are BW = 3.5 km and TW = 5 km, respectively, and the maximum sediment thickness is about 205 m. The location of the source is indicated by the double-couple in the left figure and by the beach ball in the right one. The triangles along the western line (WL) and eastern line (EL) indicate the receiver positions where numerical predictions are further compared.

the optimal strategy, referred to as 'F' strategy, in which the element boundaries follow the interfaces (i.e. material interfaces never intersect the elements). Note that the spectral element meshes considered here are always geometrically conforming, that is such that neighbouring elements share either a corner or an entire edge or face.

Two open-source codes implementing SEM have been used in this study: `specfem3D` (Peter *et al.* 2011) and `efispec` (De Martin 2011). Both codes implement the P1 paraxial formulation of Stacey (1988) at the absorbing boundaries. We always used a polynomial order $N = 5$ and, away from the interfaces, we imposed the size of the spectral elements to be smaller than or equal to the local minimum S wavelength. The results obtained with the two codes are strictly similar when using the same mesh of elements. In the remainder of the paper, the results obtained with `specfem3D` (resp. `efispec`) will be referred to as SEM1 (resp. SEM2).

4.2 FPSM

The FPSM combines the optimal accuracy of the global spectral differential operators with the simplicity of the spatial discretization using a structured rectangular grid. The peculiarity of FPSM consists in the evaluation of the spatial derivatives by means of a multiplication in the wavenumber domain. Time evolution is usually solved using non spectral approaches, as, for example the 2nd-order explicit finite-difference scheme used in this paper. The transition from the spatial domain to the wavenumber domain, and back, is performed by means of the fast Fourier transform. Thanks to the Nyquist sampling theorem, FPSM works with a relatively coarse spatial sampling (Fornberg 1987), which represents a valuable advantage when solving 3-D problems.

On the other hand, the nature of the global differential operators implies that possible numerical artifacts are spread across the whole space domain. There are two common sources of numerical errors. One is the discontinuity of the fields that are being differentiated, which produces singularity in the calculated wavefield (Gibbs phenomenon). The other is the representation of material discontinuities (interfaces): since FPSM solves the heterogeneous formulation of the equation of motion, artefacts may be due to the staircase approximation interfaces with sharp impedance contrast. The free-surface condition—a typical feature of models used for earthquake ground motion simulations—can be seen as an extreme case of a sharp material interface and therefore is particularly challenging for FPSM.

The FPSM implementation used in this paper (Klin *et al.* 2010) tackles the aforementioned problems in the following way. The occurrence of Gibbs phenomenon is significantly reduced using the Fourier differential operators on staggered grids (Özdenvar & McMechan 1996). The staircase approximation of the material interfaces is avoided using the volume harmonic averaging of the elastic moduli and volume arithmetic averaging of density proposed by Moczo *et al.* (2002). The free-surface boundary condition—discontinuity of displacement and vanishing traction at the free surface—is solved by the following approach: (1) before applying the differential operator a linear function is subtracted from the displacement field in order to remove its discontinuity at the free surface, and it is added back after differentiation is performed; (2) a stress imaging technique accomplishes the vanishing of the stress field. In order to sample adequately the surface wave wavefield, which features higher vertical-component wavenumbers close to the free surface, the vertical spatial sampling step is gradually squeezed towards surface. Finally, the wavefield absorption at lateral and bottom boundaries of the computational domain is performed with the convolutional perfectly matching layer (CPML; Komatitsch & Martin 2007).

A more comprehensive review of FPSM and related discussions can be found in Klin *et al.* (2010) and Moczo *et al.* (2014).

4.3 3-D (2-4) Velocity–stress finite-difference scheme on an arbitrary discontinuous staggered grid (FDM-S)

Here we very briefly describe the finite-difference methodology that has been developed based on several partial approaches starting from the introduction of the staggered-grid schemes into seismology (Madariaga 1976; Virieux 1984, 1986) up to developing the orthorhombic effective grid modules (Moczo *et al.* 2014). Because the description of the methodology below is very concise, we refer for a complete theory to the book by Moczo *et al.* (2014).

The scheme solves the strong differential form of the equation of motion and time derivative of Hooke's law for the viscoelastic medium with rheology of the generalized Maxwell body. The schemes have the same structure as standard velocity–stress staggered-grid schemes which are 2nd-order accurate in time and 4th-order accurate in space. The accuracy of the scheme in the heterogeneous medium is mainly determined by the way how a smooth material heterogeneity and material interface are represented by the effective material grid parameters. Two approaches are applied in this study. The first one has been presented by Moczo *et al.* (2002). The effective grid density is evaluated as an integral volume arithmetic average of density inside a grid cell centred at the grid position of the corresponding particle velocity component. The effective grid unrelaxed bulk and shear moduli are evaluated as integral volume harmonic averages of moduli in respective grid cells centred at grid positions of the stress-tensor components. The integrals are evaluated numerically and the grid cell can contain a material interface. In the second approach, the effective averaged medium has, in general, an orthorhombic anisotropy. If a material interface is parallel to a Cartesian coordinate plane, the averaged medium is transversely isotropic. The transverse anisotropy is the correct representation of a planar material interface consistent with the boundary conditions in the long wavelength approximation (as shown originally by Backus (1962) and discussed also by Moczo *et al.* (2002)). For a detailed exposition see chapter 9 of the book by Moczo *et al.* (2014). The free surface is simulated using the AFDA technique (Kristek *et al.* 2002; Moczo *et al.* 2004). The non-reflecting boundaries of the spatial grid are simulated by using PML. For efficient modelling of earthquake motion in surface sedimentary structures a spatially discontinuous staggered grid is used. The stable algorithm of the discontinuous grid (Kristek *et al.* 2010) enables one to use the ratio between the bottom coarser grid and upper finer grid as large as 25. For the computer codes we refer to `http://www.nuquake.eu/FDSim` (last accessed 16 January 2015).

4.4 3-D Velocity–stress collocated-grid finite-difference method (FDM-C)

The FDM-C (Zhang & Chen 2006; Zhang *et al.* 2012) solves the first-order hyperbolic velocity–stress elastodynamic equations using finite-difference approximations with all the wavefield components and model parameters defined at the same grid point. Having quantities collocated, the method is well suited to utilize curvilinear grids for solving elastodynamic equations in curvilinear

coordinates. This makes it suitable for implementing irregular free surface. The collocated grid is also a natural choice to simulate seismic waves in a general anisotropic medium. A simple application of the central differences on the collocated grid to approximate the first-order derivative would lead to odd-even decoupling problem as a grid-to-grid oscillation in the simulation results. Either a spatial filtering or artificial damping would be necessary to suppress the non-physical grid-to-grid oscillations. The FDM-C in this paper uses the DRP/opt MacCormack scheme (Hixon 1998) with a 7-point stencil for one derivative. Usually the accuracy of a 7-point stencil can reach 6th order. However, in the DRP MacCormack scheme, two points are sacrificed to achieve optimal dispersion accuracy by the dispersion-relation preserving (DRP) methodology (Tam & Webb 1993), which results in an optimized 4th-order accuracy in terms of dispersion error. To get minimal dissipation error, DRP/opt MacCormack of (Hixon 1998) optimizes the coefficients of the DRP MacCormack at 8 points per wavelength and higher. In the DRP/opt MacCormack scheme, the central spatial difference operator is split into forward and backward one-sided difference operators, which are alternately used in the 4th-order Runge-Kutta time marching schemes. The one-sided operators introduce inherent dissipation, which can damp the spurious short-wavelength numerical (non-physical) waves to avoid the odd-even decoupling. The central difference is recovered when the forward and backward differences are added together. As we can use different operators in three dimensions, there are in total eight biased different operators, and they are used sequentially in an 8-steps cycle to get minimal error. More details can be found in Zhang & Chen (2006) and Zhang *et al.* (2012). The free-surface boundary condition on curvilinear grids is implemented by the traction-imaging method (Zhang & Chen 2006; Zhang *et al.* 2012) which antisymmetrically images the traction components to the ghost points and is an extension of the stress-imaging technique for the flat free surface. For a discrete representation of material heterogeneity, the effective media approach by Moczo *et al.* (2002) is adopted. The density at a point is evaluated as the volume arithmetic average whereas λ and μ at a point are calculated as the volume harmonic averages. PML is used as the absorbing technique surrounding the lateral and bottom boundaries. If the grid is rectangular in the absorbing layers, the auxiliary differential equations implementation of the complex frequency-shifted PML (ADE CFS-PML; Zhang & Shen 2010) is used. If the grid is curvilinear in the absorbing zones, a multi-axial extension (ADE CFS-MPML) towards stable simulations on curvilinear grids (Zhang *et al.* 2014) is applied.

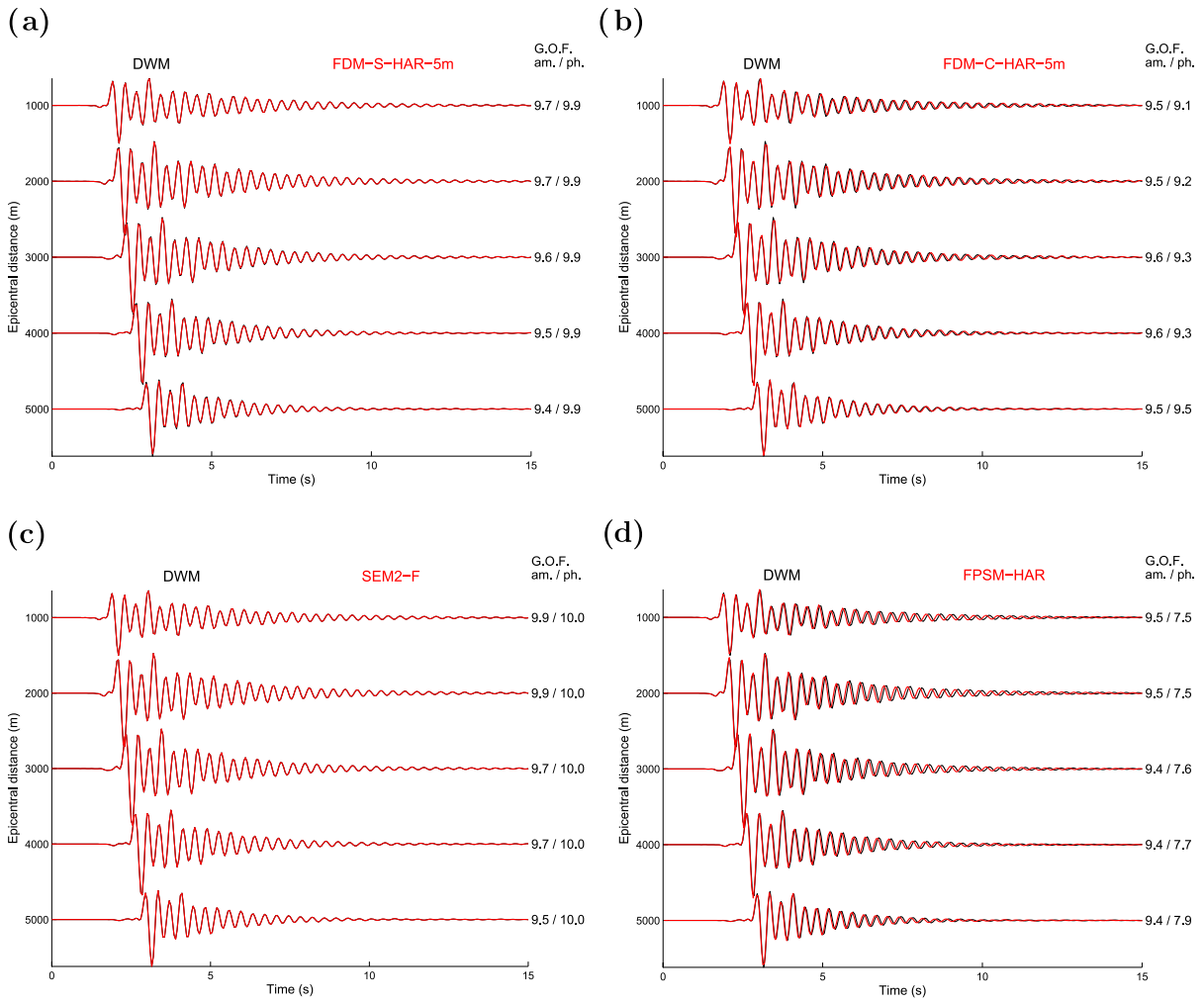

Figure 12. East–west component of ground velocity along the northern surface profile computed for the 1D-sharp case by 4 different methods: (a) FDM-S; (b) FDM-C; (c) SEM2-F; (d) FPSM. HAR indicates the harmonic averaging of the elastic moduli. Each of the seismograms (plotted in red) is superimposed on the reference solution computed with DWM (in black). The numbers to the right of each trace correspond to the goodness-of-fit scores in envelope (labelled to as 'am') and phase (labelled to as 'ph') with respect to the reference solution. A perfect match corresponds to a score of 10.

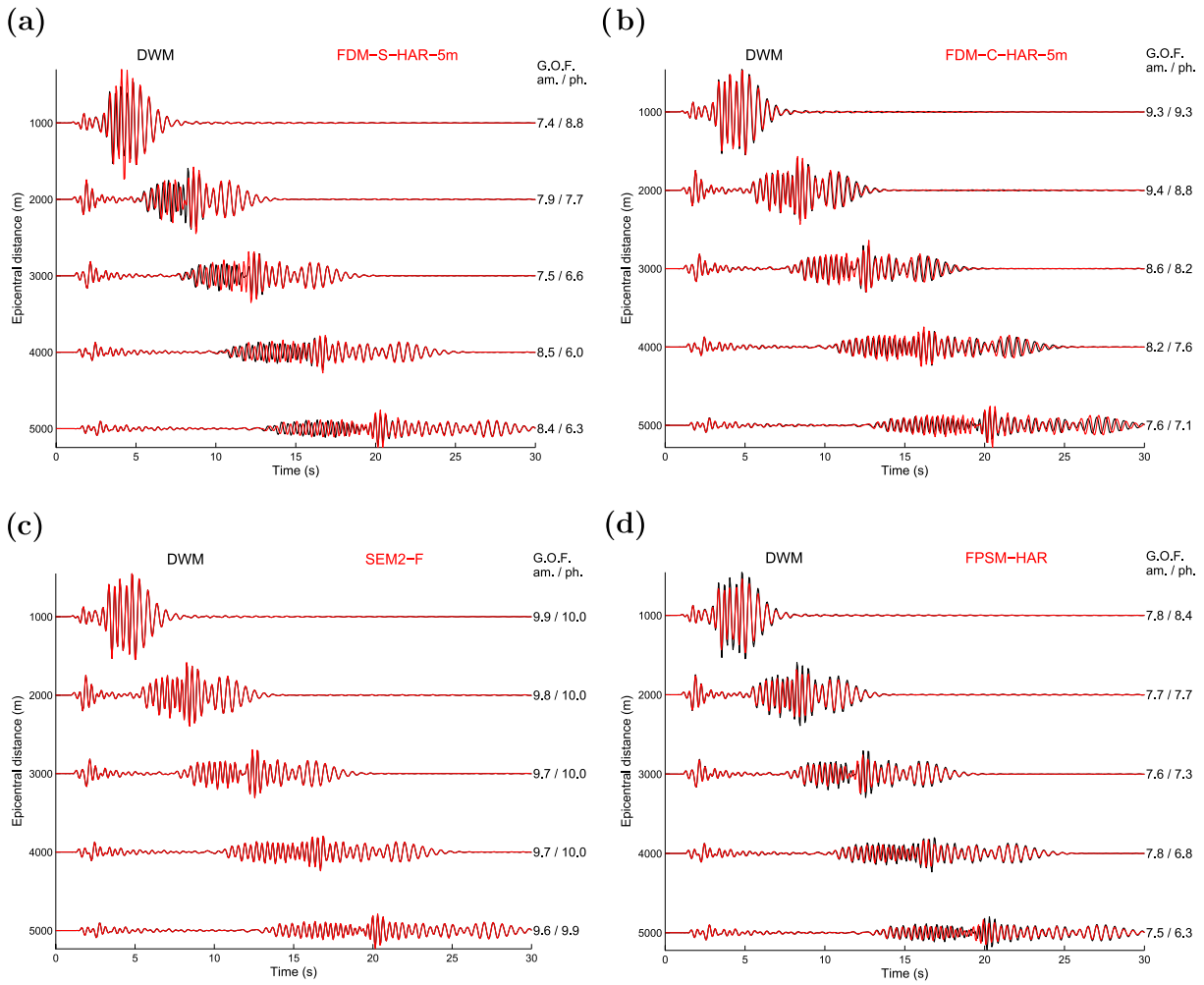

Figure 13. Same as Fig. 12 for the vertical component of ground velocity.

5 RESULTS FOR 1-D GEOMETRY

5.1 1-D layered model with sharp interfaces

Fig. 12 shows the EW component of ground velocity along the northern surface profile (Fig. 5) computed for the 1D-sharp case by the four methods: FDM-S, FDM-C, FPSM and SEM2-F. Note that in FDM-S, FDM-C and FPSM calculations, the volume harmonic averaging of the elastic moduli and volume arithmetic averaging of mass density proposed by Moczo *et al.* (2002) is used to approximate the physical interfaces of the 1D-sharp model, and that the SEM2-F calculations are performed following the F strategy, that is imposing that the interfaces of the model coincide with the spectral elements' boundaries. In FDM-S and FDM-C, the grid spacing is 5 m, which corresponds to a minimum of 10 gridpoints per S wavelength at the surface. The horizontal grid spacing is 20 m for FPSM and 10 m in average for SEM2-F at the surface (i.e. the horizontal size of the surface spectral elements is 50 m and the polynomial order is $N = 5$). The vertical grid spacing increases in FPSM from 3 m at the surface to 100 m in the bedrock. In SEM2-F it is set in average to 3.46 m in the first layer and to 14.5 m in the second layer. The spectral element mesh is further coarsened twice with depth using a three-to-one elementary brick (e.g. Peter *et al.* 2011), yielding an average horizontal and vertical resolution of 90 m in the bedrock. Each numerical solution is superimposed on the reference one–computed with DWM as detailed in Section 3.1.1.

The goodness-of-fit (GOF) in amplitude and phase between the two solutions are also shown. The GOF values were obtained as

$$G = 10 \exp(-|M|),$$

where M represents the time-frequency misfit in amplitude or phase evaluated for the time-frequency window $[0 - 30]\,\mathrm{s} \times [0 - 4]\,\mathrm{Hz}$. G attains values from 0 (no fit) to 10 (perfect fit); see Kristeková *et al.* (2009) for details. As expected from the spatial resolution used and given the fact that the analysed traces contain only body waves, the level of agreement obtained in Fig. 12 is excellent with amplitude GOF values well above 9 for all solutions, and with only FPSM exhibiting non-optimal phase GOF values, slightly below 8.

The same comparison for the vertical component of ground velocity is shown in Fig. 13. Except for the SEM2-F calculations, clear differences in phase and amplitude are now seen in all the predicted surface wave trains. Whereas for the solutions computed with FDM-S and FPSM the phase error seems to increase with frequency, it looks more uniformly distributed for the FDM-C solution. The overall GOF scores are, however, similar for the three solutions. They are even slightly higher for the FDM-C solution which, surprisingly, shows a minimal phase error on the high-frequency Airy phase of the fundamental Rayleigh mode. Note that the GOF values decrease with epicentral distance as expected from the accumulation of error during propagation.

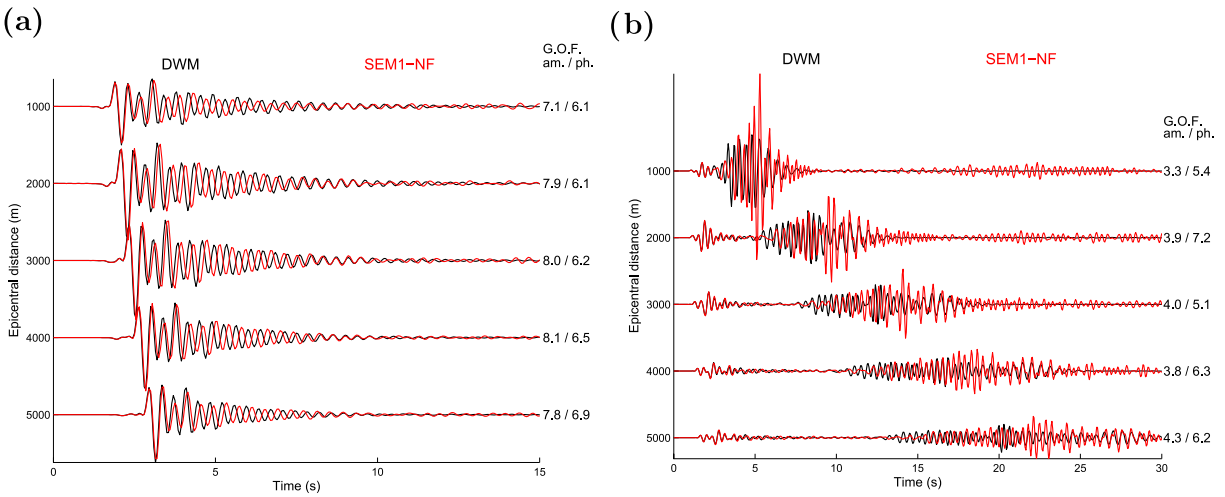

Figure 14. East–west (left-hand panel) and vertical (right-hand panel) components of ground velocity computed for the 1D-sharp case using SEM1-NF.

The excellent fit obtained for SEM2-F is intrinsically related to the correct discrete representation of the interfaces in the 1D-sharp model by the F strategy. In Fig. 14, we present the results obtained with SEM1 using a NF strategy, where instead of squeezing one element in the first layer, L_1, two spectral elements of the same vertical size ($= 44.9$ m) are used to describe the first two layers, L_1 and L_2. Note that only the first physical interface is approximated in this modified mesh, the other two still coincide with elements'

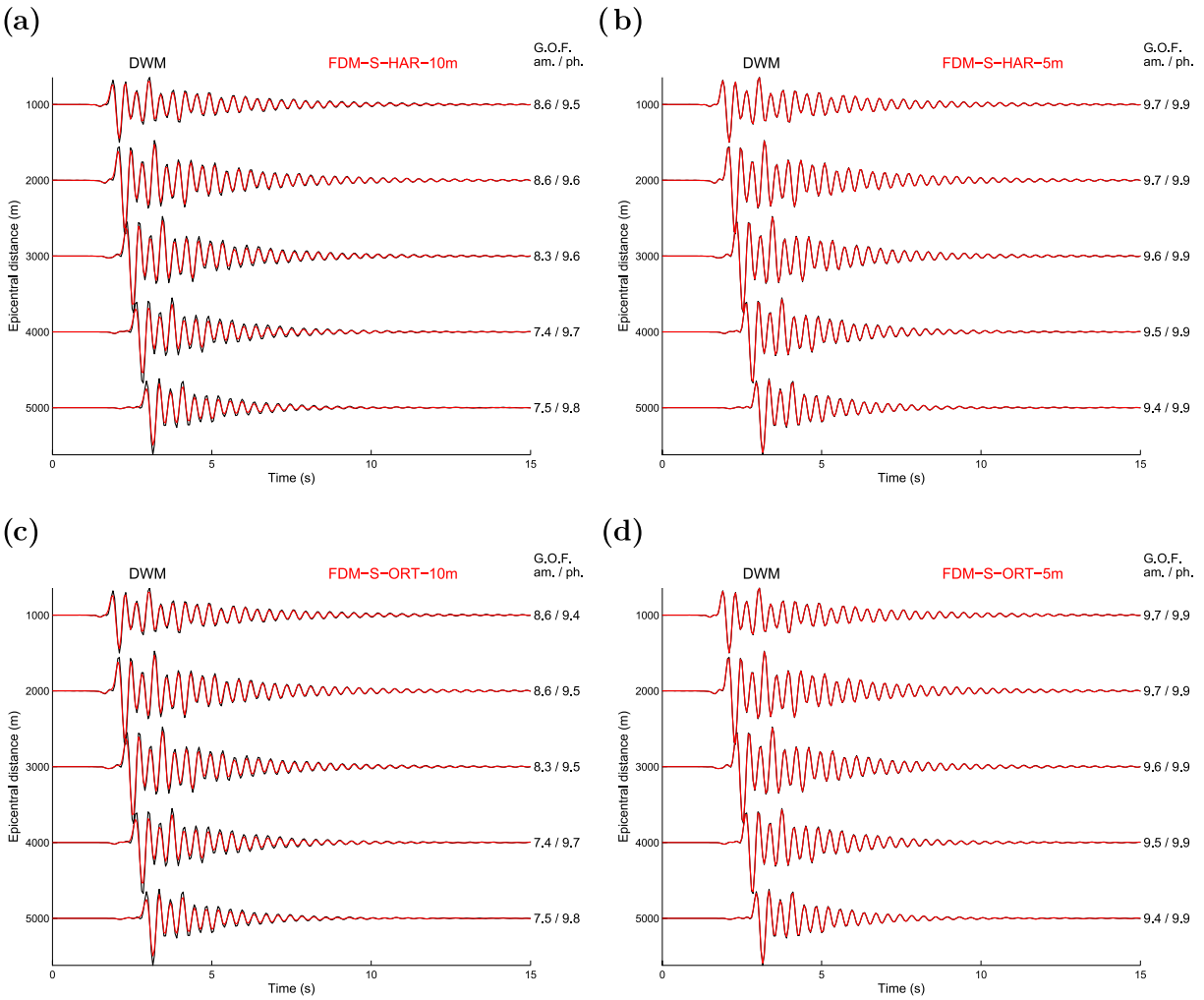

Figure 15. East–west component of ground velocity along the northern surface profile for the 1D-sharp case computed with FDM-S using different grid spacings and definitions of the effective media: (a) harmonic averaging, 10 m; (b) harmonic averaging, 5 m; (c) orthorhombic averaging, 10 m; (d) orthorhombic averaging, 5 m.

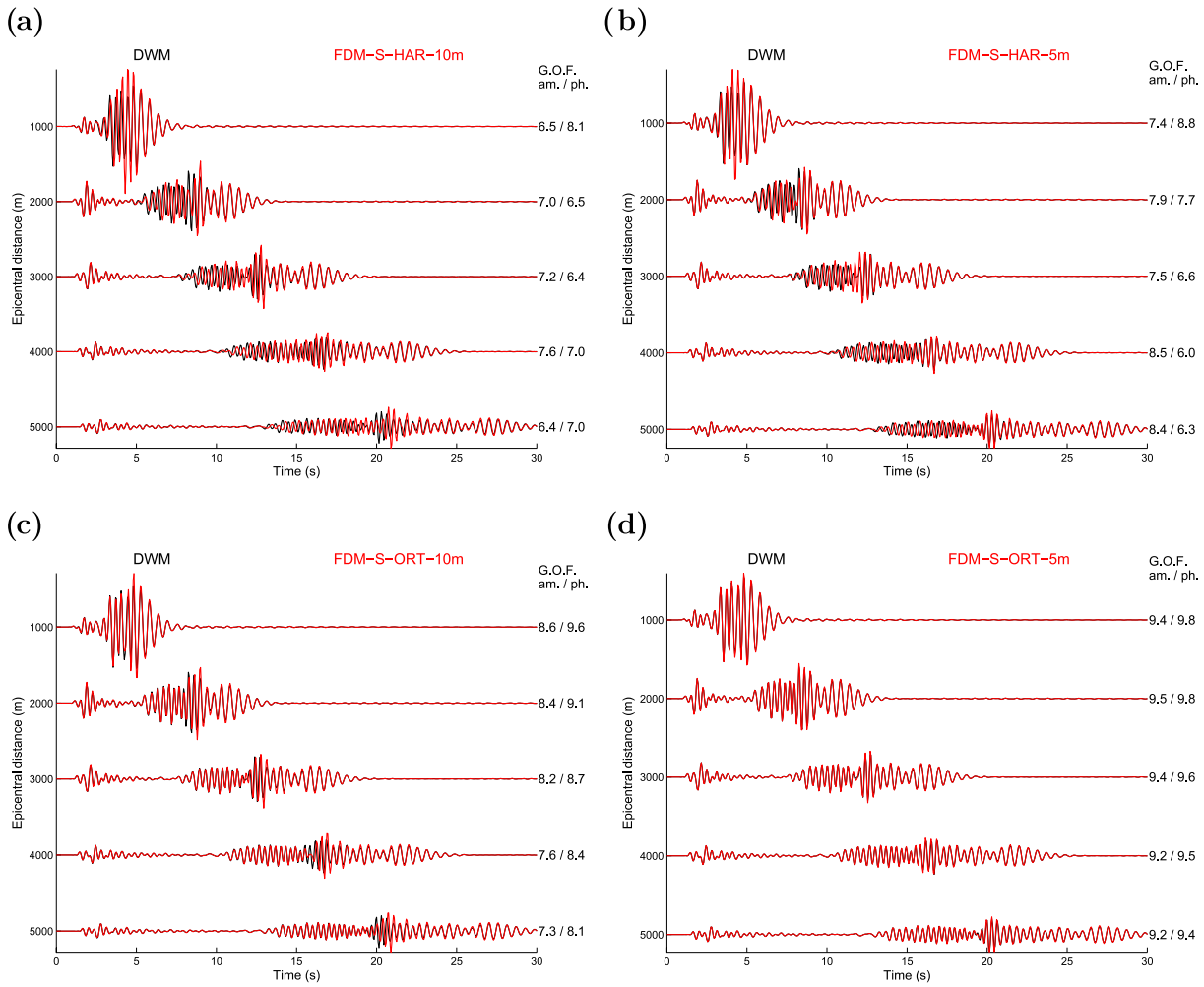

Figure 16. Same as Fig. 15 for the vertical component of ground velocity.

boundaries (i.e. the vertical size of the elements is further adapted to the thickness of the L_3 layer). The effect on the accuracy of the resulting numerical solution is tremendous. Apart from the direct *S* wave, all the other arrivals are affected by large phase and amplitude errors: the high-frequency 1-D resonance occurs at a slightly lower frequency (around 2.5 Hz instead of 2.7 Hz) and the surface wave dispersion pattern is completely different. This is not a straightforward matter of the vertical spatial resolution in terms of the number of nodes per wavelength, but rather a problem of how the discontinuity in the material parameters is represented at the discrete level by the local spectral polynomial bases: everything happens as if we had computed an accurate solution in a wrong discrete model. Note that some of the inaccurate late arrivals in the SEM1-NF solution (e.g. around 20 s at 1 km epicentral distance) are due to weak reflections off the western (not perfectly absorbing) boundary of the computational domain, which was not as distant as in the mesh used in computation of the reference SEM2-F solution. Those spurious arrivals, however, contribute only marginally to the misfit with the reference solution.

The sensitivity of the surface wave dispersion properties on the discrete implementation of the model in SEM was reported by Capdeville & Marigo (2008) in the context of global seismology. It can be recast under the general issue, faced by any grid-based numerical method, of how to represent spatial variations of the elastic parameters which are smaller than the size of the numerical grid cell (the extreme case being that of a material discontinuity). The main challenge is to 'up-scale' the medium, that is to design an effective medium which realizes a physically consistent, low-pass filtering of the original model. Several up-scaling procedures have been derived in the last years: Moczo *et al.* (2002) proposed to use the volume harmonic average of the elastic moduli and arithmetic average of the mass density in the vicinity of a material discontinuity; Fichtner & Igel (2008) presented a non-linear minimization approach to design smooth models which preserve the phase velocities of a few target Love and Rayleigh modes; more recently Capdeville *et al.* (2010a,b) and Guillot *et al.* (2010) introduced a general numerical procedure to derive a fully anisotropic effective model using the framework of the homogenization theory; Moczo *et al.* (2014) extended their 2002 formulation to a more general effective medium with the orthorhombic anisotropy.

In Figs 15 and 16, we illustrate the performance of this new orthorhombic effective medium for numerical solutions for the 1D-sharp case computed with FDM-S. Note that because the interfaces are horizontal, the anisotropy simplifies to the vertical transverse isotropy, that is, the effective medium reduces to the one predicted by Backus (1962). For the seismograms consisting of body waves crossing the discontinuities (Fig. 15), the two approaches are comparable, the accuracy being controlled by the resolution of the grid rather than by the choice of the effective medium. The advantage of using the orthorhombic approach is much clearly seen in Fig. 16, which involves Rayleigh waves propagating parallel to the

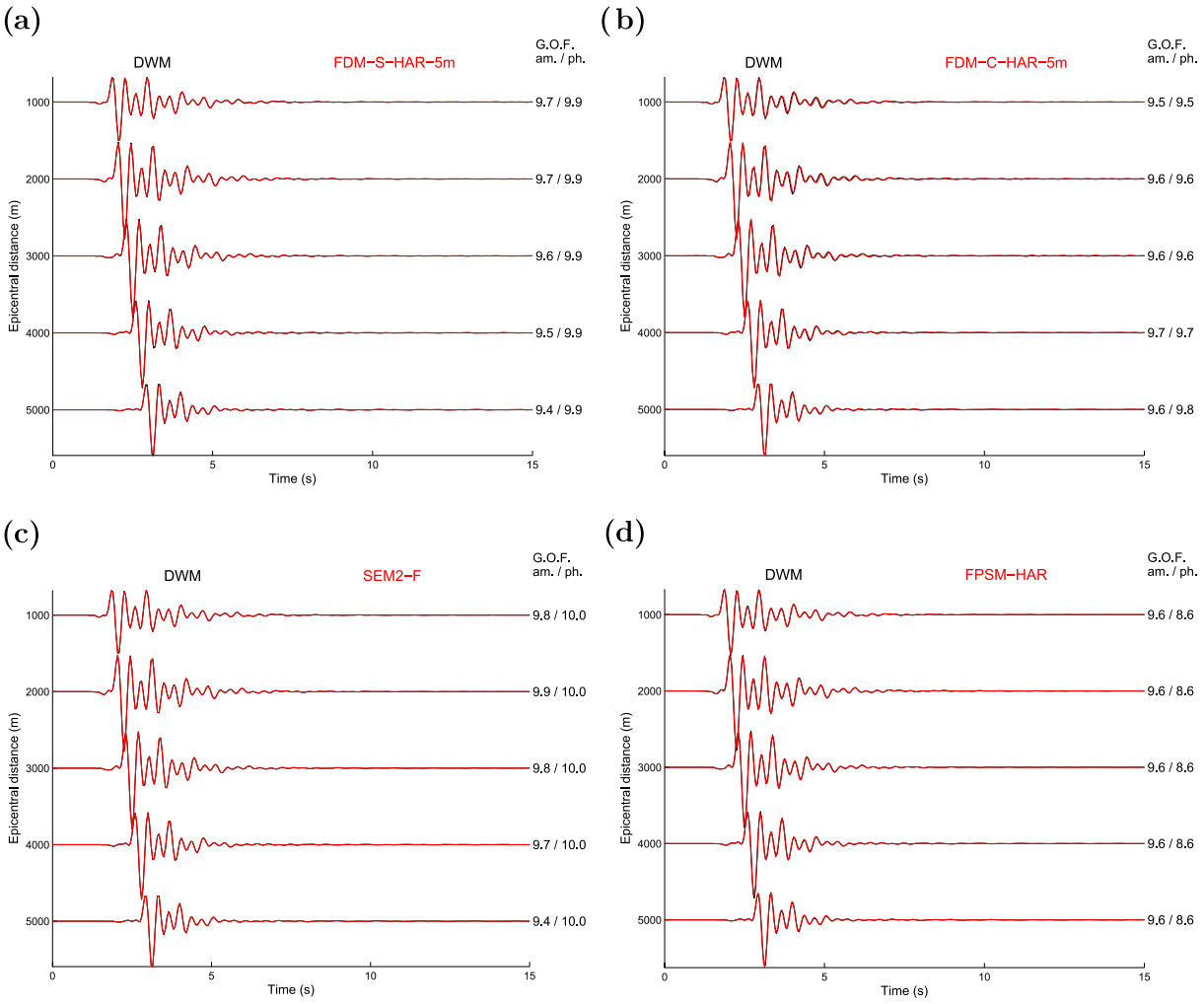

Figure 17. East–west component of ground velocity along the northern surface profile computed for the 1D-smooth case by four different methods: (a) FDM-S; (b) FDM-C; (c) SEM2-F; (d) FPSM.

discontinuities: the anisotropic solution computed with a grid spacing of 10 m (Fig. 16c) outperforms the isotropic solution obtained with a grid spacing twice smaller (Fig. 16b), having inaccuracy only in the high-frequency Airy phase of the fundamental Rayleigh mode. Further reducing the grid spacing to 5 m in the anisotropic solution (Fig. 16d) allows to reach the same level of accuracy as with SEM2-F.

Note that the applied number of grid points per wavelength in the 1D-sharp model may not be sufficient in other (velocity) models for obtaining the same level of accuracy.

5.2 1-D gradient layer model

The numerical solutions for the 1D-smooth case computed with the four methods (FDM-S, FDM-C, FPSM and SEM2-F) are shown in Fig. 17 (EW component) and Fig. 18 (vertical component). Compared to the 1D-sharp case, the level of goodness-of-fit with respect to the reference solution is systematically increased for both body and surface waves.

Most interestingly, the solution obtained with SEM1-NF, in which the mesh design follows the NF strategy, is also sufficiently accurate, as shown in Fig. 19. This is related to the ability of the polynomial bases used in the shallow spectral elements to represent the 1D-smooth velocity model, which consists of a gentle kink—the S velocity gradients in layers L_1 and L_2 are 2.89 and 3.45 s^{-1}, respectively. The comparison of the FDM-S solutions obtained with different effective medium implementations and grid spacings is shown in Fig. 20. The same conclusion drawn for the body waves in the 1D-sharp model, that numerical accuracy was mostly controlled by the resolution of the grid rather than by the choice of the effective medium, now applies to the entire simulated wavefield.

The comparison suggests that the material interface of the first order (discontinuity of the first derivative only) does not produce significant effective anisotropy.

6 RESULTS FOR 2-D GEOMETRY

We now consider more realistic canonical cases with a 2-D geometry. The aim of this section is to highlight how the discrete representation of the model, in particular at valley edges, where surface waves are generated, influences the accuracy of the numerical prediction of earthquake ground motion.

6.1 2-D valley with sharp interfaces

We first consider the 2D-sharp model with geometry shown in Fig. 11. The flat part corresponds to the three-layer-over-half-space model 1D-sharp.

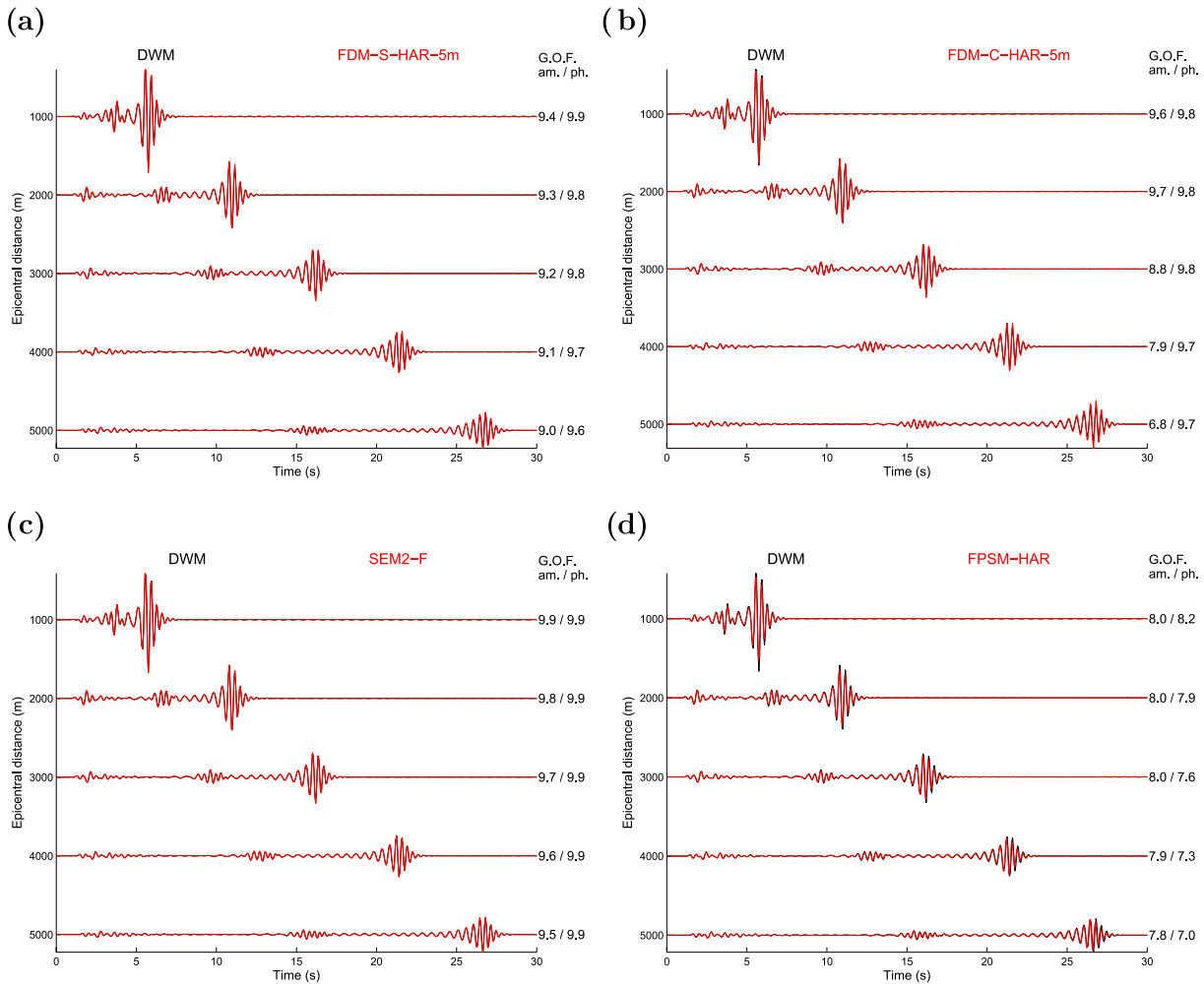

Figure 18. Same as Fig. 17 for the vertical component of ground velocity.

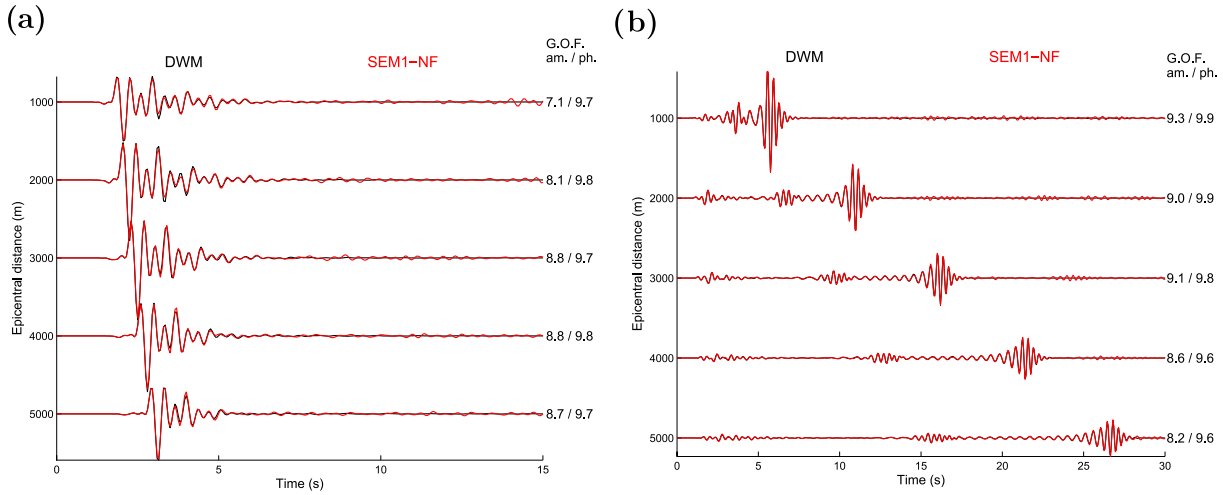

Figure 19. East–west (left-hand panel) and vertical (right-hand panel) components of ground velocity for the 1D-smooth case computed with SEM1-NF.

Relying on the results for the 1D-sharp case, we consider as a reference the solution computed with SEM2-F with the mesh (shown in Fig. 21) designed following the F strategy. Because of the deformation of the hexahedra close to the northern edge of the valley, the distance between the grid points tends towards a very tiny value, yielding an extremely severe CFL stability condition on the time step. In such realistic situations, the F strategy can drastically decrease the computational efficiency of SEM. In the remainder of the paper, some alternative strategies are presented and their efficiency is discussed.

The seismograms of the SEM2-F solution are shown in Fig. 22 for two horizontal components along two different surface profiles.

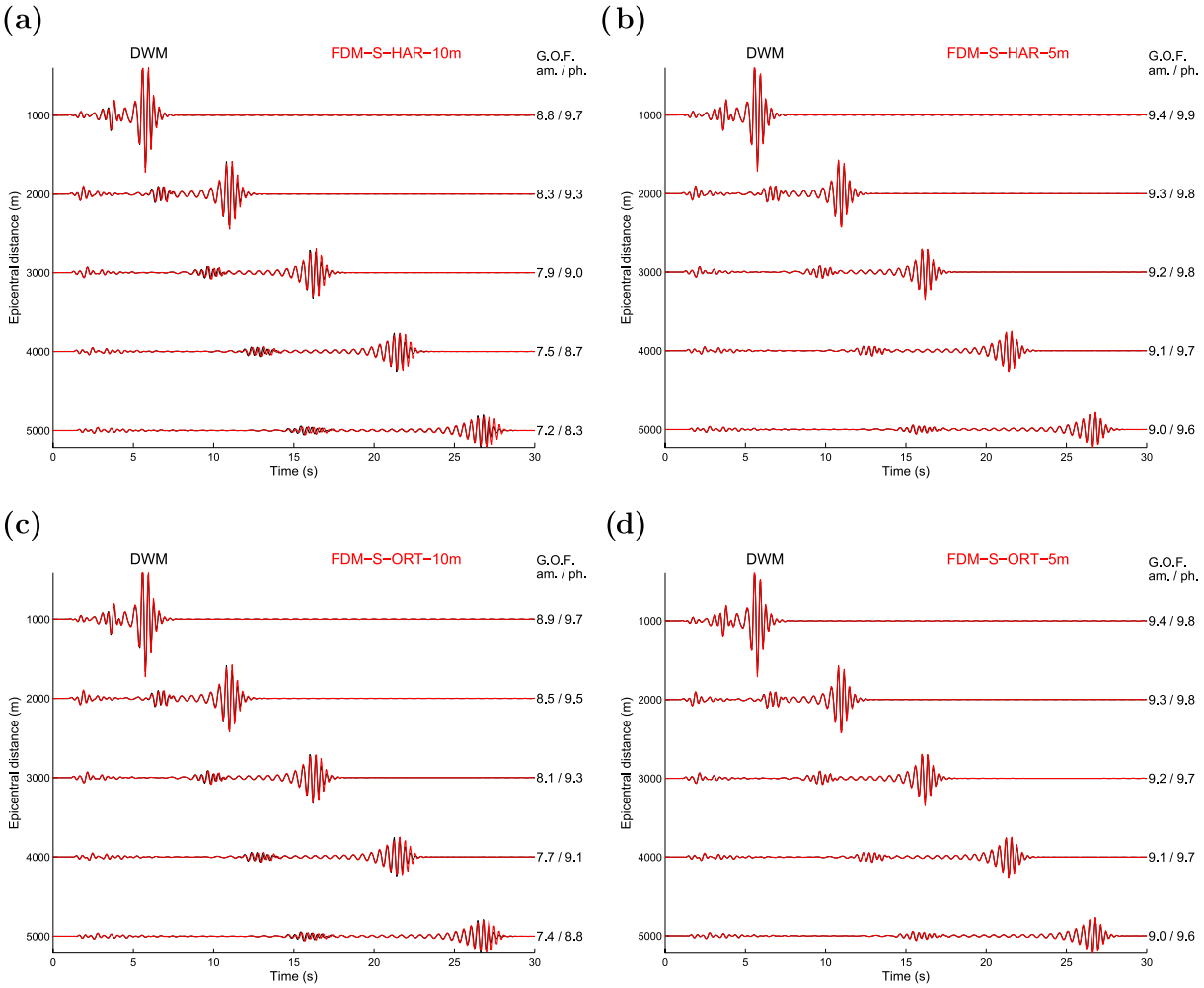

Figure 20. Vertical component of ground velocity along the northern surface profile for the 1D-smooth case computed with FDM-S using different grid spacings and definitions of the effective media: (a) harmonic averaging, 10 m; (b) harmonic averaging, 5 m; (c) orthorhombic averaging, 10 m; (d) orthorhombic averaging, 5 m.

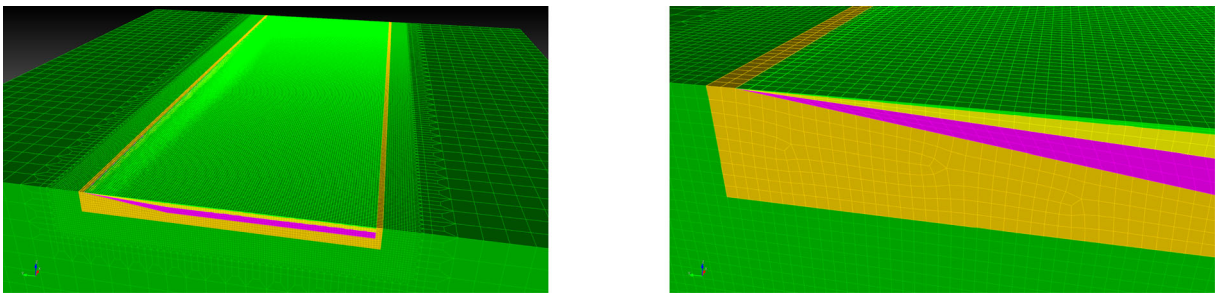

Figure 21. Spectral element mesh, designed following the F-strategy, used to compute a reference solution of the 2D-sharp case. The mesh consists of a 2-D section of unstructured quadrilaterals which is further 'sweeped' along the direction transverse to the valley in order to define hexahedra. The mesh is further coarsened in the horizontal and vertical directions, from the orange 'shoe-box' intermediate region to the outside green region.

Because the model has a 2-D geometry, the left seismic section is dominated by the in-plane component of motion corresponding to a pseudo-2-D *P–SV* case (the wavefield would be fully 2-D if it was excited by a line of sources parallel to the axis of the valley) and the right section by the out-of-plane component of motion corresponding to a pseudo-2-D *SH* case. A clear asymmetry in the excitation of surface waves is observed between the edges of the valley. At the (northern) edge with the gentle slope, very energetic and strongly dispersed Rayleigh and Love surface waves are generated, whereas the surface wave trains generated at the vertical (southern) edge are hardly seen. The red lines indicate the seismic traces that are used as reference for comparing with the other numerical predictions. They correspond to receivers located 1 km away from the edges of the valley.

Fig. 23 shows the horizontal in-plane component of the ground motion computed at the northern receiver by FDM-S, FDM-C, FPSM and SEM1-BE. The numerical solutions were computed using the same spatial resolution as for the 1D-sharp case, except for

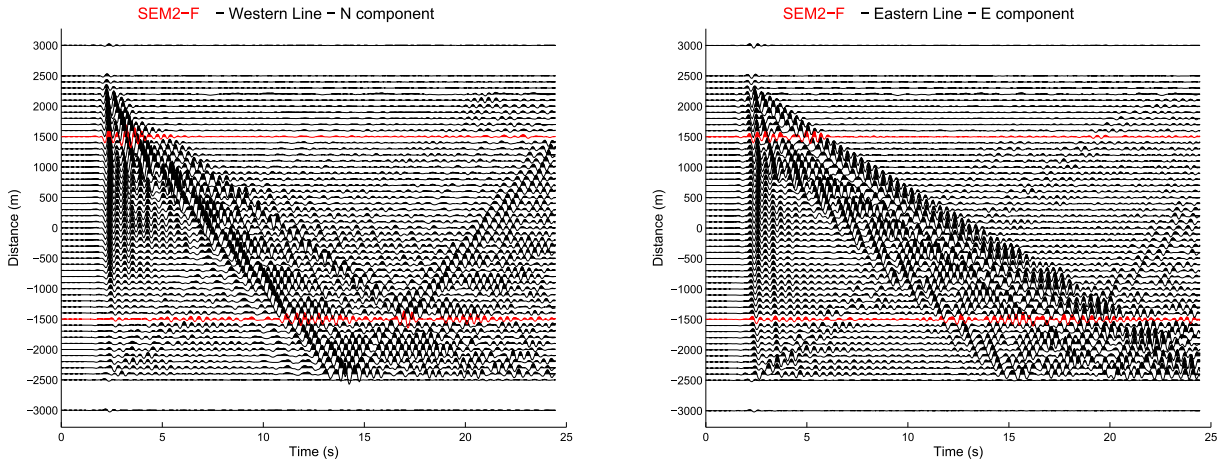

Figure 22. Seismic sections of the north–south (left-hand panel) and east–west (right-hand panel) components of ground velocity along the western (left-hand panel) and eastern (right-hand panel) profiles (Fig. 11) computed for the 2D-sharp case with SEM2-F. The distance is measured from the centre of the valley and increases towards north. The left (resp. right) panel shows a strongly dispersed Rayleigh (resp. Love) wave train excited at the northern edge. Red traces correspond to locations where the different numerical predictions are further compared (see text).

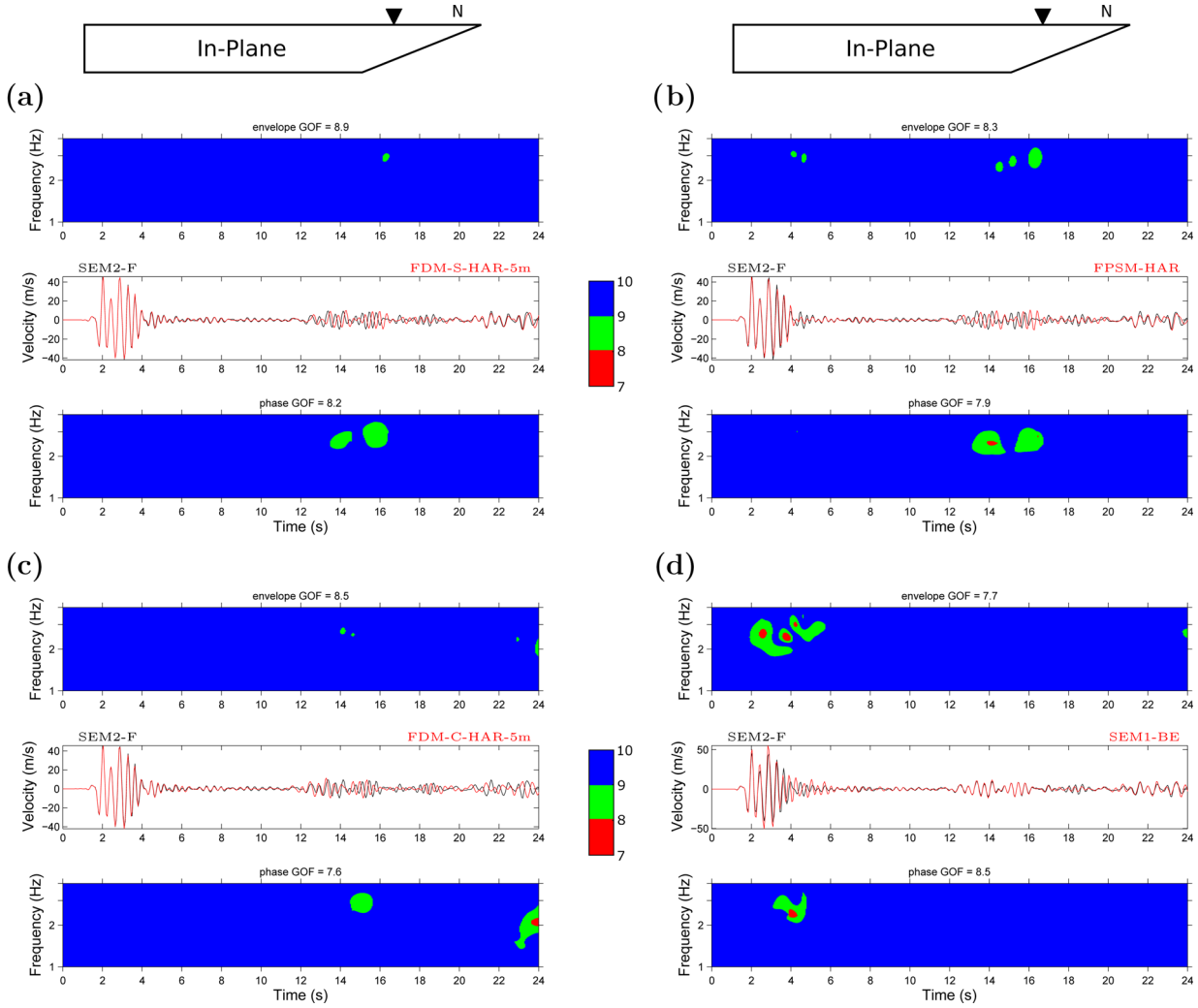

Figure 23. North–south component of ground velocity at a receiver along the western surface profile of Fig. 11, 1 km away from the northern edge, computed for the 2D-sharp case by four teams using (a) FDM-S, (b) FPSM, (c) FDM-Cand (d) SEM1-BE. The SEM2-F solution is taken as a reference and is plotted in black. The level of agreement between each solution and the reference is quantified by the time-frequency goodness-of-fit (GOF) in amplitude (top panel) and phase (bottom panel). The colour scale indicates the level of GOF, from 7 to 10 (perfect fit). The average GOF is indicated on top of the time-frequency subplots.

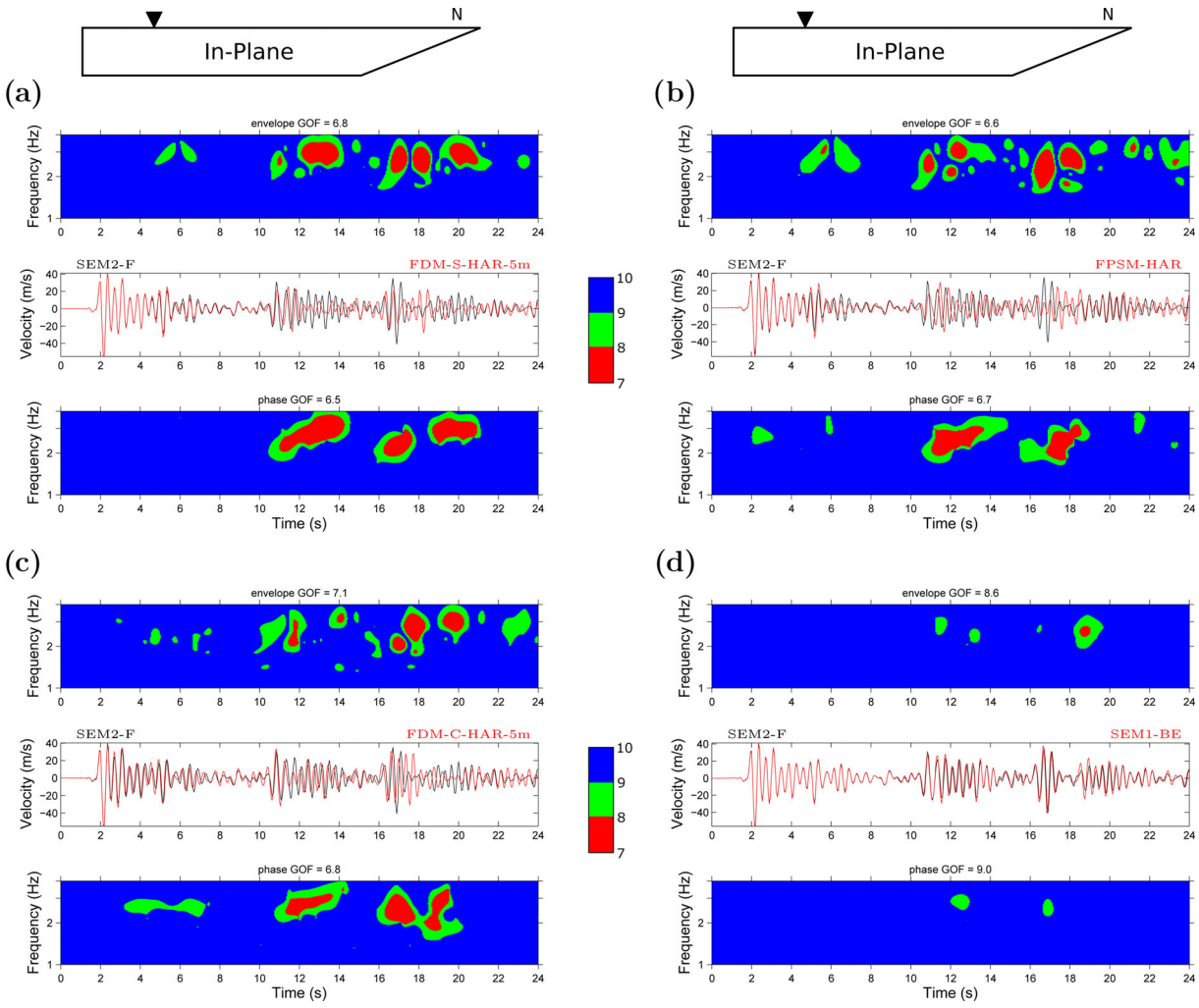

Figure 24. Same as Fig. 23 at a receiver which is 1 km away from the southern edge of the valley.

FPSM where the vertical grid spacing varies from 7 m (instead of 3 m) at the surface to 84 m (instead of 100 m) in the bedrock. In the SEM1-BE solution, the mesh is designed in the 'best-effort' (BE) mode, which is a compromise between the F and NF strategies: the boundaries of the elements follow the material interfaces only when these are horizontal or vertical. This results in a 'shoebox' high-resolution mesh coinciding at the southern edge with the mesh designed following the F strategy, but with elements intersected by the material interfaces at the northern edge. Note that the BE strategy makes it possible to increase the time step compared to the F strategy, and consequently decrease the total CPU time of the calculation, by a factor $p \simeq 13$.

Each prediction in Fig. 23 is superimposed on the SEM2-F reference, and the time-frequency GOF (in amplitude and in phase) with respect to the reference are shown as colour images. The agreement with the reference is very good, even excellent in the first arrival, around 2 s. Some discrepancies appear around 3 s, in the Rayleigh waves generated at the nearby northern edge, for the FPSM solution and more noticeably for the SEM1-BE solution which, among all solutions, is the one that makes the crudest approximation of the northern edge geometry. The level of GOF generally decreases with time, except for the SEM1-BE solution because the BE strategy used to design the mesh is optimal to accurately model the generation of Rayleigh waves at the southern edge and their propagation along the flat part of the valley.

In Fig. 24, we compare the same horizontal in-plane component of ground motion but at the southern receiver. The agreement is very good for the first 10 s of the seismogram which consists of body and Rayleigh waves generated at the vertical southern edge. The level of agreement considerably decreases for later arrivals consisting of Rayleigh waves excited at the northern edge of the valley. The best fit is obtained with the SEM1-BE solution, suggesting that the error in the numerical modelling of the surface wave generation at the northern edge is not increased by the propagation of the surface waves towards the centre of the valley. For all the other solutions, the numerical error accumulates during propagation of the surface waves along the horizontal interfaces—as in the 1D-sharp case. Note that the phase of the FDM-C solution seems again optimally accurate for the most energetic Rayleigh surface wave arrivals around 11 and 17 s, which probably correspond to Airy phases.

In Fig. 25 we compare the horizontal in-plane component at the southern receiver computed with FDM-S for different resolutions and definitions of the effective medium. As in the 1D-sharp case, the advantage of using the orthorhombic effective medium is clearly seen on the late Rayleigh waves generated at the northern edge: the GOF levels for the anisotropic solution computed with 10 m grid spacing (Fig. 25c) are much higher than for the 5 m isotropic solution (Fig. 25b). Halving the size of the grid in the anisotropic solution (Fig. 25d) yields perfect match with the SEM2-F solution,

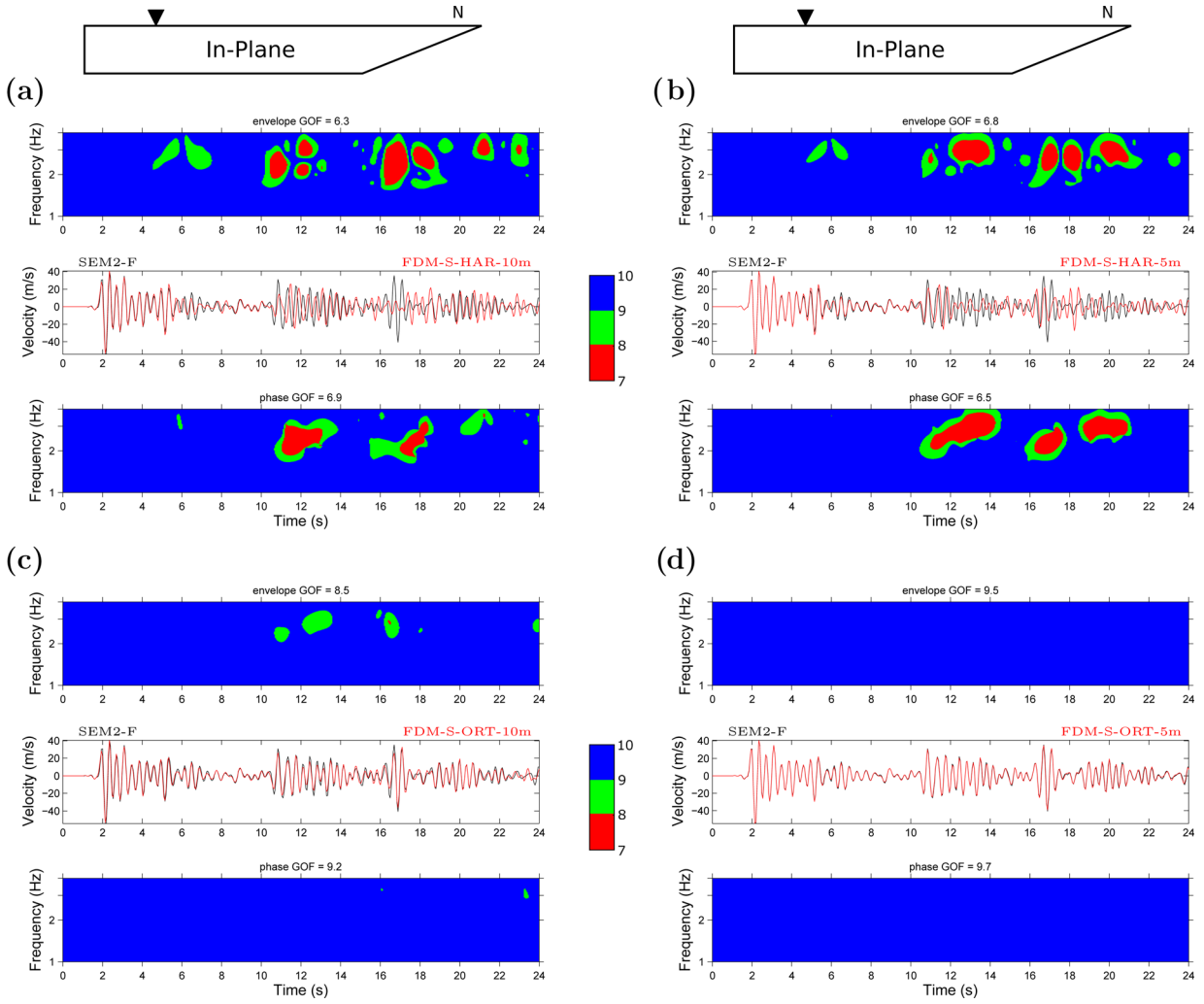

Figure 25. Same as Fig. 24 for solutions computed with FDM-S using different grid spacings and definitions of the effective medium: (a) harmonic averaging, 10 m; (b) harmonic averaging, 5 m; (c) orthorhombic averaging, 10 m; (d) orthorhombic averaging, 5 m.

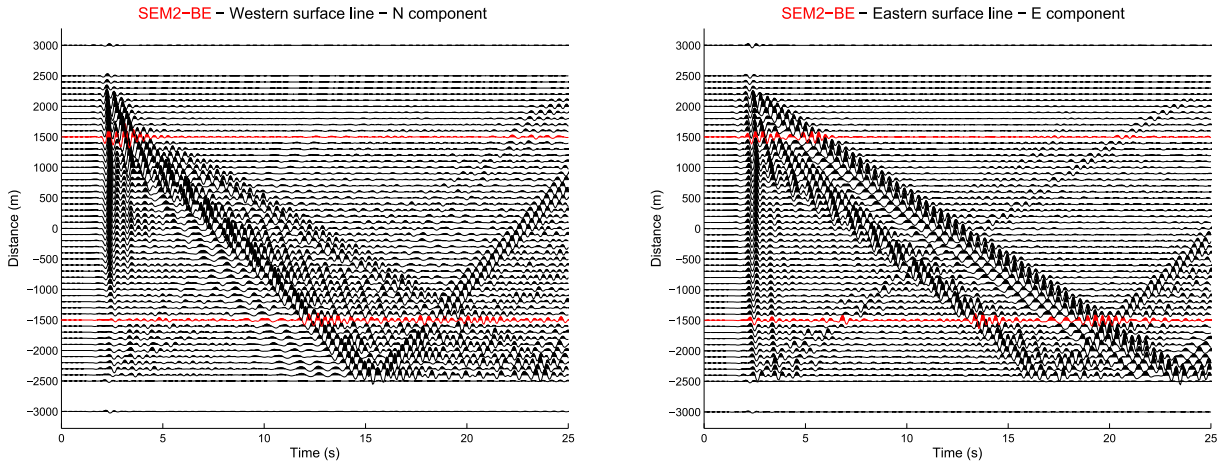

Figure 26. Seismic sections of the north–south (left-hand panel) and east–west (right-hand panel) components of ground velocity along the western (left-hand panel) and eastern (right-hand panel) profiles (Fig. 11) computed with SEM2-BE for the 2D-smooth case. The distance is measured from the centre of the valley and increases towards north. The left (resp. right) panel shows strong Rayleigh (resp. Love) wave trains excited at the northern edge. Red traces correspond to locations where the different numerical predictions are further compared.

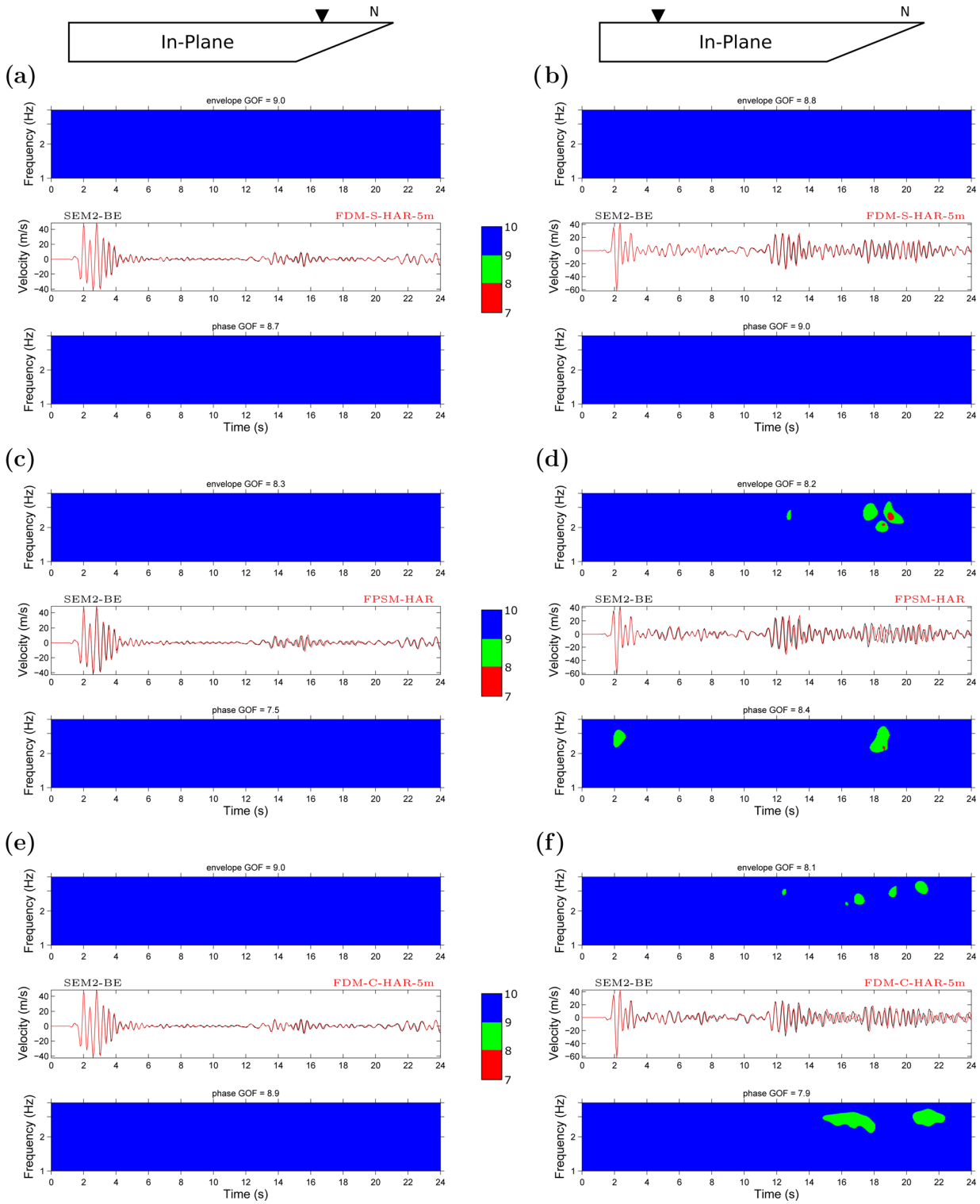

Figure 27. North–south component of ground velocity at receivers along the western surface profile of Fig. 11, 1 km away from the northern (left-hand panel) or southern (right-hand panel) edge, computed for the 2D-smooth case by three teams using (a–b) FDM-S, (c–d) FPSM, (e–f) FDM-C. The SEM2-BE solution is taken as a reference and is plotted in black. The level of agreement between each solution and the reference is quantified by the time-frequency goodness-of-fit (GOF) in amplitude (top panel) and phase (bottom panel). The colour scale indicates the level of GOF, from 7 to 10 (perfect fit). The average GOF is indicated on top of the time-frequency subplots.

which provides an a posteriori justification for considering the latter a reference.

The out-of-plane component (which mainly consists of *SH* and Love waves) computed by FDM-S, FDM-C, FPSM and SEM1-BE at the northern and southern receivers are shown in Figs S1 and S2, respectively, and the FDM-S solutions computed with different grid spacings and implementations of the effective medium are shown in Fig. S3. The same conclusions as for

the in-plane component can be drawn and are thus not repeated here.

6.2 2-D valley with gradient in sediments

Given the considerable cost to compute the solution of the 2D-sharp case with SEM2-F, we consider instead the SEM2-BE solution computed with the BE strategy as a reference. The seismograms of the horizontal ground velocity, computed with SEM2-BE along the two surface profiles of Fig. 11, are shown in Fig. 26. As for the 2D-sharp case, we observe a strong asymmetry in the spontaneous generation of surfaces waves following the slope of the valley edge. Note also that the surface waves, in particular Love waves, are less dispersed than in the 2D-sharp case (compare with Fig. 22), as expected from the analysis of the 1D-sharp and 1D-smooth solutions (Figs 8 and 10).

Fig. 27 shows the horizontal component of the in-plane component of the ground velocity computed at the northern and southern receivers by FDM-S, FDM-C and FPSM, and their comparison with the reference SEM2-BE solution. Note the excellent level of agreement in the early part of the signals, including the Rayleigh waves recorded at the northern receiver, and the overall good fit obtained for the late Rayleigh waves (generated at the northern valley edge) at the southern receiver.

The effect of varying the grid resolution and the definition of the effective medium in the FDM-S solution is shown in Fig. S4. Consistently with the analysis of the 1D-smooth results, we observe only a slight increase of GOF with respect to the SEM2-BE solution when switching from the isotropic to the orthorhombic effective medium, the accuracy being mainly controlled by the spatial resolution of the grid. Note also that the SEM2-BE solution, although not optimal, can be reasonably considered a reference. The tiny remaining difference between the 5 m orthorhombic FDM-S solution and the SEM2-BE solution can be partly attributed to the fact that the latter is not exact.

For the sake of completeness, we show in Fig. S5 the comparison of the horizontal out-of-plane component at the northern and southern receivers. Similar conclusions can be drawn as for the in-plane component: the overall level of agreement between solutions is very good, even for some of the late Love wave arrivals. Finally, in Fig. S6 we compare the predictions by FDM-S at the southern receiver for different grid spacings and definitions of the effective medium. We conclude again that due to the smoothness of the velocity model, the solution for the orthorhombic effective medium only slightly differs from that obtained using the harmonic averaging of moduli.

7 CONCLUSION

In order to better understand the origin of differences between 3-D numerical predictions of earthquake ground motion in realistic models of the Mygdonian basin, we have designed four canonical models and have compared several numerical solutions of the four cases for frequencies up to 4 Hz. The solutions were computed with the FPSM, the Legendre SEM and two formulations of the finite-difference method (FDM-S and FDM-C).

The comparisons show that both the accuracy of individual solutions and level of agreement between solutions vary with the type of seismic waves and depend on the smoothness of the velocity model. The level of accuracy is high for the body waves in the numerical solutions for all the models considered, whereas it systematically decreases in the sharp models for the surface waves. This is also observed for the realistic models of the Mygdonian basin (Maufroy *et al.* 2014).

The accuracy of the numerical solutions for the sharp models is shown to depend strongly on the discrete representation of the material interfaces (at which material parameters change discontinuously) inside the sediments. We have illustrated the dual nature of the implementation of interfaces in SEM: solutions computed with a mesh of elements whose boundaries follow the interfaces (F strategy) are optimally accurate, whereas solutions computed by approximating the discontinuities with the polynomial basis local to the elements can be extremely inaccurate for surface waves propagating along the interfaces. For all the numerical methods considered, except SEM if the F strategy can be applied, a proper implementation of interfaces requires the definition of an effective medium consistent with the interface boundary conditions. We have tested the efficiency of two explicit effective media: the isotropic volume harmonic and arithmetic averaging of elastic moduli and densities, respectively (Moczo *et al.* 2002), and its generalization to an orthorhombic effective medium (Moczo *et al.* 2014). Our results show that using the isotropic effective medium yields numerical solutions of limited accuracy for surface waves. They also indicate that reaching an acceptable accuracy by solely decreasing the size of the numerical grid may be extremely computationally expensive. Using instead the orthorhombic effective medium is shown to significantly improve the accuracy of the solutions and to preserve the computational efficiency of the methods.

The conclusions drawn from the analysis of the results of the canonical cases greatly help to explain the origin of the differences between numerical predictions of ground motion in realistic models of the Mygdonian basin (Maufroy *et al.* 2014). The persistent misfit between even the most similar solutions can be fairly attributed to the differences in the discrete representation of the material interfaces in sediments: The SEM solution was computed following the best-effort strategy in which the element boundaries do not follow the interfaces for depths smaller than a threshold value (the choice of which is the result of a compromise between accuracy and computational efficiency); the FDM-S and FPSM solutions used an isotropic effective medium with insufficiently small grid spacing (10 m for FDM-S and 7 m for FPSM, respectively).

These results have important implications regarding the accuracy of numerical prediction of earthquake ground motion in sedimentary basins, in particular with respect to local surface waves which play a critical role in the lengthening of ground motion duration and local amplifications at the basins' edges (e.g. Kawase 1996; Hallier *et al.* 2008). An improper discrete representation of the interfaces can cause considerably inaccurate numerical modelling of surface waves. Therefore, preparation of the computational model needs special care in this respect. Homogeneous layers within sediments should not be artificially introduced.

Whenever small-scale, or localized, strong variations of the material parameters have to be considered in the sediments, for example based on firm geological, geotechnical or geophysical evidence, an effective medium relevant for the chosen frequency range should be used. Depending on the degree of knowledge of the model heterogeneity and on the desired level of accuracy of the predictions, the effective media can be defined by procedures of increasing complexity. In the common situation where the level of uncertainty in the model (including the presence of interfaces) is large, a simple volume arithmetic average of the densities and slownesses, or a volume arithmetic average of the densities and harmonic average of the elastic moduli, should be used to provide an isotropic effective

medium ready for numerical simulations. In all other situations, an upscaling procedure should be adopted to design an anisotropic effective medium, either by solving a homogenization problem as suggested by Guillot *et al.* (2010) and Capdeville *et al.* (2010b), or by following the explicit approach proposed by Moczo *et al.* (2014) based on the orthorhombic averaging.

Finally, our results confirm that there is no single numerical-modelling method that can be considered the best—in terms of accuracy and computational efficiency—for all structure-wavefield configurations. We recommend that any numerical method and code that is intended to be applied for numerical prediction of earthquake ground motion should be verified through stringent models that would make it possible to test the most important aspects of accuracy. We believe that the canonical cases presented in this paper, and made freely available to the seismological community (http://www.sismowine.org, last accessed 16 January 2015), can serve this purpose.

ACKNOWLEDGEMENTS

The authors are grateful to all the participants of E2VP and to Y. Capdeville for fruitful discussions about homogenization. F. de Martin thanks P. Thierry (Intel) for allowing access to the latest Sandy Bridge processors. The careful reading of the manuscript by one reviewer was very much appreciated.

The research presented in this paper was supported by the following projects or funding agencies: Cashima, Sigma, Stefanik, BRGM, MYGDONEMOTION APVV-0271-11 funded by the Slovak grant agency APVV, National Natural Science Foundation of China (Nos. 41090293, 41274053).

The SEM calculations were performed using the resources of the BRGM, of the CIMENT infrastructure (https://ciment.ujf-grenoble.fr, last accessed 16 January 2015) and of the CEA TGCC center acquired in the GENCI projects t2011046060, t2012046060 and t2013046060. The SEM meshes were designed using the commercial software Cubit (https://cubit.sandia.gov/, last accessed 16 January 2015). The FPSM calculations used the computational resources of CINECA—Consorzio Interuniversitario per il Calcolo Automatico (Bologna, Italy). Part of the FDM-S calculations were performed in the Computing Centre of the Slovak Academy of Sciences using the supercomputing infrastructure acquired in project ITMS 26230120002 and 26210120002 (Slovak infrastructure for high-performance computing) supported by the Research & Development Operational Programme funded by the ERDF.

REFERENCES

Backus, G.E., 1962. Long-wave elastic anisotropy produced by horizontal layering, *J. geophys. Res.,* **67**(11), 4427–4440.

Bard, P.-Y., 1994. Discussion session: lessons, issues, needs and prospects. Special Theme session 5: Turkey Flat and Ashigara Valley experiments, in *Proceedings of the Tenth World Conference of Earthquake Engineering,* Madrid, 19–24 July 1992, Vol. 11, pp. 6985–6988.

Bielak, J. *et al.*, 2010. The ShakeOut earthquake scenario: verification of three simulation sets, *Geophys. J. Int.,* **180**(1), 375–404.

Bouchon, M., 1981. A simple method to calculate Green's functions for elastic layered media, *Bull. seism. Soc. Am.,* **71**(4), 959–971.

Bouchon, M., 2003. A review of the discrete wavenumber method, *Pure appl. Geophys.,* **160**(3–4), 445–465.

Boyd, J.P., 2001. *Chebyshev and Fourier Spectral Methods,* Courier Dover Publications.

Capdeville, Y. & Marigo, J.-J., 2008. Shallow layer correction for spectral element like methods, *Geophys. J. Int.,* **172**(3), 1135–1150.

Capdeville, Y., Guillot, L. & Marigo, J.-J., 2010a. 1-D non-periodic homogenization for the seismic wave equation, *Geophys. J. Int.,* **181**(2), 897–910.

Capdeville, Y., Guillot, L. & Marigo, J.-J., 2010b. 2-D non-periodic homogenization to upscale elastic media for P–SV waves, *Geophys. J. Int.,* **182**(2), 903–922.

Chaljub, E., Cornou, C. & Bard, P.-Y., 2006. Numerical benchmark of 3D ground motion simulation in the valley of Grenoble, French Alps, in *Proceedings of the Third International Symposium on the Effects of Surface Geology on Seismic Motion,* LCPC edn, Vol. 2, pp. 1365–1375.

Chaljub, E., Komatitsch, D., Vilotte, J.-P., Capdeville, Y., Valette, B. & Festa, G., 2007. Spectral element analysis in seismology, in *Advances in Wave Propagation in Heterogeneous Media,* Vol. 48, Advances in Geophysics Series, pp. 365–419, eds WU, R.-S. & Maupin, V., Elsevier.

Chaljub, E., Moczo, P., Tsuno, S., Bard, P.-Y., Kristek, J., Kaser, M., Stupazzini, M. & Kristekova, M., 2010. Quantitative comparison of four numerical predictions of 3D ground motion in the Grenoble valley, France, *Bull. seism. Soc. Am.,* **100**(4), 1427–1455.

Coutant, O., 1989. *Program of numerical simulation AXITRA, Tech. rep.,* LGIT, Université Joseph Fourier, Grenoble, in French.

Cramer, C.H., 1995. Weak-motion observations and modeling for the Turkey Flat, U.S., Site-Effects Test Area near Parkfield, California, *Bull. seism. Soc. Am.,* **85**(2), 440–451.

Day, S.M., Bielak, J., Dreger, D., Graves, R., Larsen, S., Olsen, K.B. & Pitarka, A., 2001. *Tests of 3D elastodynamic codes: final report for lifelines project 1a01, Tech. rep.,* Pacific Earthquake Engineering Research Center & Southern California Earthquake Center.

Day, S.M., Bielak, J., Dreger, D., Graves, R., Larsen, S., Olsen, K.B. & Pitarka, A., 2003. *Tests of 3D elastodynamic codes: final report for lifelines project 1a02, Tech. rep.,* Pacific Earthquake Engineering Research Center.

Day, S.M., Bielak, J., Dreger, D., Graves, R., Larsen, S., Olsen, K.B. & Pitarka, A., 2005. *3D ground motion simulation in basins: final report for lifelines project 1a03, Tech. rep.,* Pacific Earthquake Engineering Research Center.

De Martin, F., 2011. Verification of a spectral-element method code for the Southern California Earthquake Center LOH.3 viscoelastic case, *Bull. seism. Soc. Am.,* **101**(6), 2855–2865.

Faccioli, E., Maggio, F., Paolucci, R. & Quarteroni, A., 1997. 2D and 3D elastic wave propagation by a pseudo-spectral domain decomposition method, *J. Seismol.,* **1**(3), 237–251.

Fichtner, A. & Igel, H., 2008. Efficient numerical surface wave propagation through the optimization of discrete crustal modelsa technique based on non-linear dispersion curve matching (DCM), *Geophys. J. Int.,* **173**(2), 519–533.

Fornberg, B., 1987. The pseudo-spectral method: comparisons with finite differences for the elastic wave equation, *Geophysics,* **52**(4), 483–501.

Guillot, L., Capdeville, Y. & Marigo, J.-J., 2010. 2-D non-periodic homogenization of the elastic wave equation: SH case, *Geophys. J. Int.,* **182**(3), 1438–1454.

Hallier, S., Chaljub, E., Bouchon, M. & Sekiguchi, H., 2008. Revisiting the basin-edge effect at Kobe during the 1995 Hyogo-Ken Nanbu earthquake, *Pure. appl. Geophys.,* **165**, 1751–1760.

Hisada, Y., 1995. An efficient method for computing Green's functions for a layered half-space with sources and receivers at close depths (part 2), *Bull. seism. Soc. Am.,* **85**(4), 1080–1093.

Hixon, R., 1998. Evaluation of a high-accuracy MacCormack-type scheme using benchmark problems, *J. Comput. Acoust.,* **6**(03), 291–305.

Kawase, H., 1996. The cause of the damage belt in Kobe: "the basin-edge effect," constructive interference of the direct *S*-wave with the basin-induced diffracted/Rayleigh waves, *Seism. Res. Lett.,* **67**(5), 25–34.

Kawase, H. & Iwata, T., 1998. A report on submitted results of the simultaneous simulation for Kobe, in *The Effects of Surface Geology on Seismic Motion, Recent Progress and new Horizon on ESG Study,* Vol. 3, eds Irikura, K., Kudo, K., Okada, H. & Sasatani, T., Balkema/CRC Press.

Klin, P., Priolo, E. & Seriani, G., 2010. Numerical simulation of seismic wave propagation in realistic 3-D geo-models with a Fourier pseudo-spectral method, *Geophys. J. Int.,* **183**(2), 905–922.
Komatitsch, D. & Martin, R., 2007. An unsplit convolutional perfectly matched layer improved at grazing incidence for the seismic wave equation, *Geophysics,* **72**(5), SM155–SM167.
Komatitsch, D. & Vilotte, J.P., 1998. The spectral-element method: an efficient tool to simulate the seismic response of 2D and 3D geological structures, *Bull. seism. Soc. Am.,* **88**(2), 368–392.
Komatitsch, D., Tsuboi, S. & Tromp, J., 2005. The spectral-element method in seismology, in *Seismic Earth: Array Analysis of Broadband Seismograms, Vol. 157 of Geophysical Monograph,* pp. 205–228, eds Levander, A. & Nolet, G., American Geophysical Union.
Kristek, J., Moczo, P. & Archuleta, R.J., 2002. Efficient methods to simulate planar free surface in the 3D 4th-order staggered-grid finite-difference schemes, *Stud. Geophys. Geod.,* **46**(2), 355–381.
Kristek, J., Moczo, P. & Galis, M., 2010. Stable discontinuous staggered grid in the finite-difference modelling of seismic motion, *Geophys. J. Int.,* **183**(3), 1401–1407.
Kristeková, M., Kristek, J. & Moczo, P., 2009. Time-frequency misfit and goodness-of-fit criteria for quantitative comparison of time signals, *Geophys. J. Int.,* **178**(2), 813–825.
Madariaga, R., 1976. Dynamics of an expanding circular fault, *Bull. seism. Soc. Am.,* **66**(3), 639–666.
Manakou, M., 2007. Contribution to the determination of a 3D soil model for site response analysis. The case of the Mygdonian basin, *PhD thesis*, (in Greek with English abstract), Department of Civil Engineering, Aristotle University of Thessaloniki.
Manakou, M.V., Raptakis, D.G., Chvez-Garca, F.J., Apostolidis, P.I. & Pitilakis, K.D., 2010. 3D soil structure of the Mygdonian basin for site response analysis, *Soil. Dyn. Earthq. Eng.,* **30**(11), 1198–1211.
Maufroy, E. *et al.*, 2014. Earthquake ground motion in the Mygdonian basin, Greece: the E2VP verification and validation of 3D numerical simulations up to 4 Hz, *Bull. seism. Soc. Am.,* in press.
Moczo, P., Kristek, J., Vavryčuk, V., Archuleta, R.J. & Halada, L., 2002. 3D heterogeneous staggered-grid finite-difference modeling of seismic motion with volume harmonic and arithmetic averaging of elastic moduli and densities, *Bull. seism. Soc. Am.,* **92**(8), 3042–3066.
Moczo, P., Kristek, J. & Gális, M., 2004. Simulation of the planar free surface with near-surface lateral discontinuities in the finite-difference modeling of seismic motion, *Bull. seism. Soc. Am.,* **94**(2), 760–768.
Moczo, P., Kristek, J. & Gális, M., 2014. *The Finite-Difference Modelling of Earthquake Motions Waves and Ruptures,* Cambridge Univ. Press.
Özdenvar, T. & McMechan, G.A., 1996. Causes and reduction of numerical artifacts in pseudo-spectral wavefield extrapolation, *Geophys. J. Int.,* **126,** 819–828.
Peter, D. *et al.*, 2011. Forward and adjoint simulations of seismic wave propagation on fully unstructured hexahedral meshes, *Geophys. J. Int.,* **186**(2), 721–739.
Priolo, E., Carcione, J.M. & Seriani, G., 1994. Numerical simulation of interface waves by high-order spectral modeling techniques, *J. acoust. Soc. Am.,* **95**(2), 681–693.
Seriani, G. & Priolo, E., 1994. A spectral element method for acoustic wave simulation in heterogeneous media, *Finite Elem. Anal. Des.,* **16,** 337–348.
Soufleris, C., Jackson, J.A., King, G. C.P., Spencer, C.A. & Scholz, C.H., 1982. The 1978 earthquake sequence near Thessaloniki (northern Greece), *Geophys. J. Int.,* **68**(2), 429–458.
Stacey, R., 1988. Improved transparent boundary formulations for the elastic-wave equation, *Bull. seism. Soc. Am.,* **78**(6), 2089–2097.
Tam, C.K.W. & Webb, J.C., 1993. Dispersion-relation-preserving finite difference schemes for computational acoustics, *J. Comput. Phys.,* **107**(2), 262–281.
Theodulidis, N., Roumelioti, Z., Panou, A., Savvaidis, A., Kiratzi, A., Grigoriadis, V., Dimitriu, P. & Chatzigogos, T., 2006. Retrospective prediction of macroseismic intensities using strong ground motion simulation: the case of the 1978 Thessaloniki (Greece) earthquake (M6.5), *Bull. Earthq. Eng.,* **4**(2), 101–130.
Virieux, J., 1984. SH-wave propagation in heterogeneous media: Velocity-stress finite-difference method, *Geophysics,* **49**(11), 1933–1942.
Virieux, J., 1986. P-SV wave propagation in heterogeneous media: velocity-stress finite-difference method, *Geophysics,* **51**(4), 889–901.
Zhang, W. & Chen, X., 2006. Traction image method for irregular free surface boundaries in finite difference seismic wave simulation, *Geophys. J. Int.,* **167**(1), 337–353.
Zhang, W. & Shen, Y., 2010. Unsplit complex frequency-shifted pml implementation using auxiliary differential equations for seismic wave modeling, *Geophysics,* **75**(4), T141–T154.
Zhang, W., Zhang, Z. & Chen, X., 2012. Three-dimensional elastic wave numerical modelling in the presence of surface topography by a collocated-grid finite-difference method on curvilinear grids, *Geophys. J. Int.,* **190**(1), 358–378.
Zhang, Z., Zhang, W. & Chen, X., 2014. Complex frequency-shifted multi-axial perfectly matched layer for elastic wave modelling on curvilinear grids, *Geophys. J. Int.,* **198**(1), 140–153.

SUPPORTING INFORMATION

Additional Supporting Information may be found in the online version of this article:

Figure S1. East–west component of ground velocity at a receiver along the eastern surface profile of Fig. 11, 1 km away from the northern edge, computed for the 2D-sharp case by (a) FDM-S, (b) FPSM, (c) FDM-C, (d) SEM1-BE. The SEM2-F solution is taken as a reference and is plotted in black. The level of agreement between each solution and the reference is quantified by the time-frequency goodness-of-fit (GOF) in amplitude (top panel) and phase (bottom panel). The colour scale indicates the level of GOF, from 7 to 10 (perfect fit). The average GOF is indicated on top of the time-frequency subplots.
Figure S2. Same as Fig. S1 at a receiver 1 km away from the southern edge of the basin.
Figure S3. Same as Fig. S2 for solutions computed with FDM-S using different grid spacings and definitions of the effective medium: (a) harmonic averaging, 10 m; (b) harmonic averaging, 5 m; (c) orthorhombic averaging, 10 m; (d) orthorhombic averaging, 5 m.
Figure S4. North–south component of ground velocity at the southern receiver for solutions computed with FDM-S using different grid spacings and definitions of the effective medium: (a) harmonic averaging, 10 m; (b) harmonic averaging, 5 m; (c) orthorhombic averaging, 10 m; (d) orthorhombic averaging, 5 m. The level of agreement between each solution and the reference is quantified by the time-frequency goodness-of-fit (GOF) in amplitude (top panel) and phase (bottom panel). The colour scale indicates the level of GOF, from 7 to 10 (perfect fit). The average GOF is indicated on top of the time-frequency subplots.
Figure S5. Same as Fig. 27 for the east–west component of ground velocity at receivers along the eastern surface profile of Fig. 11, 1 km away from the northern (left-hand panel) or southern (right-hand panel) edge.
Figure S6. Same as Fig. S4 for the east–west component of ground velocity at the southern receiver. (http://gji.oxfordjournals.org/lookup/suppl/doi:10.1093/gji/ggu472/-/DC1).

Please note: Oxford University Press is not responsible for the content or functionality of any supporting materials supplied by the authors. Any queries (other than missing material) should be directed to the corresponding author for the article.

IV.3 Validation of numerical simulations

1. Souriau, A., Chaljub, E., Cornou, C., Margerin, L., Calvet, M., Maury, J., Wathelet, M., Grimaud, F., Ponsolles, C., Pequegnat, C., Langlais, M., & Guéguen, P., 2011. Multimethod characterization of the french-pyrenean valley of Bagneres-de-Bigorre for seismic-hazard evaluation: Observations and models, *Bull. Seismol. Soc. Am.*, **101**(4), 1912–1937.
2. Maufroy, E., Chaljub, E., Hollender, F., Bard, P.-Y., Kristek, J., Moczo, P., Klin, P., Priolo, E., Iwaki, A., Iwata, T., Etienne, V., De Martin, F., Manakou, M., Theodoulidis, N., & Pitilakis, K., 2015. Earthquale ground motion in the Mygdonian basin, Greece: the E2VP verification and validation of 3D numerical simulations up to 4 Hz, *Bull. Seismol. Soc. Am.*.
3. Cruz-Atienza, V. M., Tago, J., Sanabria-Gómez, J. D., Chaljub, E., Etienne, V., Virieux, J., & Quintanar, L., 2016. Long duration of ground motion in the paradigmatic valley of Mexico, *Scientific Reports*, **6**, 38807.

Bulletin of the Seismological Society of America, Vol. 101, No. 4, pp. 1912–1937, August 2011, doi: 10.1785/0120100293

Multimethod Characterization of the French-Pyrenean Valley of Bagnères-de-Bigorre for Seismic-Hazard Evaluation: Observations and Models

by Annie Souriau, Emmanuel Chaljub, Cécile Cornou, Ludovic Margerin, Marie Calvet, Julie Maury, Marc Wathelet, Franck Grimaud, Christian Ponsolles, Catherine Pequegnat, Mickaël Langlais, and Philippe Guéguen

Abstract A narrow rectilinear valley in the French Pyrenees, affected in the past by damaging earthquakes, has been chosen as a test site for soil response characterization. The main purpose of this initiative was to compare experimental and numerical approaches. A temporary network of 10 stations has been deployed along and across the valley during two years; parallel various experiments have been conducted, in particular ambient noise recording, and seismic profiles with active sources for structure determination at the 10 sites. Classical observables have been measured for site amplification evaluation, such as spectral ratios of horizontal or vertical motions between site and reference stations using direct *S* waves and *S* coda, and spectral ratios between horizontal and vertical (H/V) motions at single stations using noise and *S*-coda records. Vertical shear-velocity profiles at the stations have first been obtained from a joint inversion of Rayleigh wave dispersion curves and ellipticity. They have subsequently been used to model the H/V spectral ratios of noise data from synthetic seismograms, the H/V ratio of *S*-coda waves based on equipartition theory, and the 3D seismic response of the basin using the spectral element method. General good agreement is found between simulations and observations. The 3D simulation reveals that topography has a much lower contribution to site effects than sedimentary filling, except at the narrow ridge crests. We find clear evidence of a basin edge effect, with an increase of the amplitude of ground motion at some distance from the edge inside the basin and a decrease immediately at the slope foot.

Online Material: Comparison of H/H_{ref} ratios, and maps of simulated PGVs and PGDs.

Introduction

France is considered to be a country of moderate seismicity, if we exclude the French Antilles, where several $M > 6$ events occurred during the last decade. At the historical timescale, however, the metropolitan territory has experienced strong destructive events causing fatalities, in particular in the Alps, in the Rhine graben, on the French Riviera near Nice, and in the Pyrenees. If similar events were to occur today, they would induce dramatic situations from both human and economical points of view. For this reason, the French government has devoted special effort to evaluate and mitigate seismic risk in both metropolitan territory and the Antilles, and to develop educational programs concerning seismic risk. A six-year Earthquake Plan has been decided by the Ministry of Ecology for the period 2005–2010. In parallel, three urban centers have been selected as pilot sites by the French Accelerometric Network for developing instrumentation and methods for seismic-hazard evaluation: the city of Nice, built on complex geological structures bordering the Mediterranean (Courboulex *et al.*, 2007; Bertrand *et al.*, 2007); the city of Grenoble, located at the convergence of two deep alpine valleys (LeBrun *et al.*, 2001; Cornou *et al.*, 2003; Guéguen *et al.*, 2007); and the two cities of Lourdes and Bagnères-de-Bigorre in the central Pyrenees (Dubos *et al.*, 2003; Souriau *et al.*, 2007). These cities have either a dense permanent population or important sites for tourism.

We present the results obtained at Bagnères-de-Bigorre in the central Pyrenees. The choice of this site was first motivated

by its proximity to the seismic sources, with a significant seismicity located less than 20 km away from the city. On the other hand, the Bagnères Valley is nearly rectilinear, with a much simpler geometry than that of the nearby city of Lourdes, where several experiments had been previously conducted (Dubos *et al.*, 2003; Souriau *et al.*, 2007). These conditions are favorable to test different approaches of seismic-hazard evaluation, based both on field experiments and on numerical simulations, and to evaluate the performances and limitations of the different methods.

For this purpose, a variety of experiments have been conducted. In addition to the permanent accelerometric observatory PYBB, a temporary network of 10 accelerometric stations has been deployed along and across the valley. The network operated during two years, thereby providing a database of about 100 events with magnitudes ranging from 2.5 to 5.0. The data have been processed using classical methods such as H/H_{ref} and V/V_{ref} (spectral ratio between the horizontal or vertical signals recorded at one site and those recorded at a reference station on rock), and H/V (ratio of horizontal-to-vertical signals), which give an estimate of the soil response to seismic excitation. In order to model the observations, the structure beneath the stations has been characterized from active surface wave methods. Based on the obtained 1D-velocity profiles, numerical simulations of the 3D response of the valley to various kinds of seismic excitation have been performed and compared with the observations.

After a short description of the geological context, we present a description of the experimental set-up and the data processing. The various experimental approaches to the evaluation of the site response are examined and discussed. The results of 3D numerical simulations are used to elucidate the role of topography and surface heterogeneity in observed amplifications. Finally, we discuss the lessons that may be drawn from these various results, not only for the seismic risk in the Bagnères Valley, but also, from a general point of view, for the performances and limitations of the different experimental and numerical methods used.

Geological and Tectonic Context

The Pyrenees are an elongated range of mountains extending about 400 km from the Atlantic to the Mediterranean, resulting from the convergence of the Iberian and Eurasian plates during the last 65 m.y., after a rifting episode that opened a shallow sea between the two plates (Choukroune, 1992). The limit between the two plates, the North Pyrenean fault, is located at the northern foot of the range on the French side. It coincides with a sharp Moho jump, the Iberian crust being up to 20 km thicker than the Eurasian one in the central Pyrenees (Hirn *et al.*, 1980; ECORS Pyrenees Team, 1988). The paleo-rift remains as a narrow sedimentary zone north of the North Pyrenean fault (the North Pyrenean zone). South of the North Pyrenean fault, the Paleozoic axial zone contains the highest summits, which reach a 3400 m height in the central part of the range.

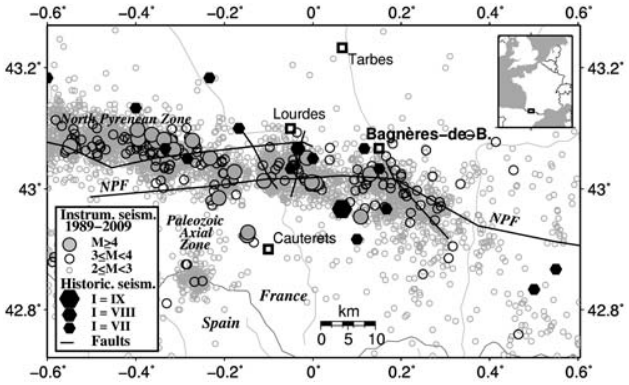

Figure 1. Map of central Pyrenees, with instrumental and historical seismicity, and the location of the pilot site at Bagnères-de-Bigorre. NPF denotes the North Pyrenean fault, the boundary of the Iberian and Eurasian plates.

The seismic activity is moderate, with about 600 events located each year. It exhibits a general east–west trend, with a greater occurrence of events in the western and central Pyrenees and the presence of several clusters, one of them being located south of Bagnères (Fig. 1). On average only one or two events with $M \geq 5$ occur every 10 years (Souriau and Pauchet, 1998; Dubos *et al.*, 2004; Rigo *et al.*, 2005; Sylvander *et al.*, 2008).

The historical seismicity, well-documented back to the fourteenth century (Lambert *et al.*, 1996), reveals a maximum activity in the central part of the range on the French side (Fig. 1), with about 25 events of intensity larger than VII since the beginning of the seventeenth century (in the intensity scale of Medvedev, Sponheuer, and Karnik). Parts of the cities of Lourdes and Bagnères-de-Bigorre were destroyed in 1660 by an event of intensity IX that killed 30 people 17 km southeast of Lourdes and 13 km southwest of Bagnères. Its magnitude is estimated at 6.0–6.1 (Levret *et al.*, 1994). Two other events caused severe damage to these cities in 1750 (intensity VIII) and 1854 (intensity VII).

In a narrow flat valley in the North Pyrenean zone, Bagnères stretches along the south-southeast–north-northwest direction at an altitude of about 500 meters (Fig. 2a). The city is located along the Adour River, which runs to the north-northwest. The Bagnères Valley is filled with fluvial deposits, but imprints of the Quaternary glaciations are visible on the border of the valley. During the Riss episode, the limit of the glaciers was about 3 km north of Bagnères, whereas the Würm glaciation stopped more uphill, 5 km south of the city (Alimen, 1964). Therefore, glacial deposits may be present beneath the fluvial deposits. Drillings performed by the Bureau de Recherches Géologiques et Minières in the valley detected blocks of glacial origin in the southern part of the valley only, and sand and pebble at many places; unfortunately, these drillings do not sample depths larger than 26 m and never reach the bedrock. Bagnères is built at a location where the valley broadens and intercepts a wide crest stretching to the northeast with a road accessing the valley.

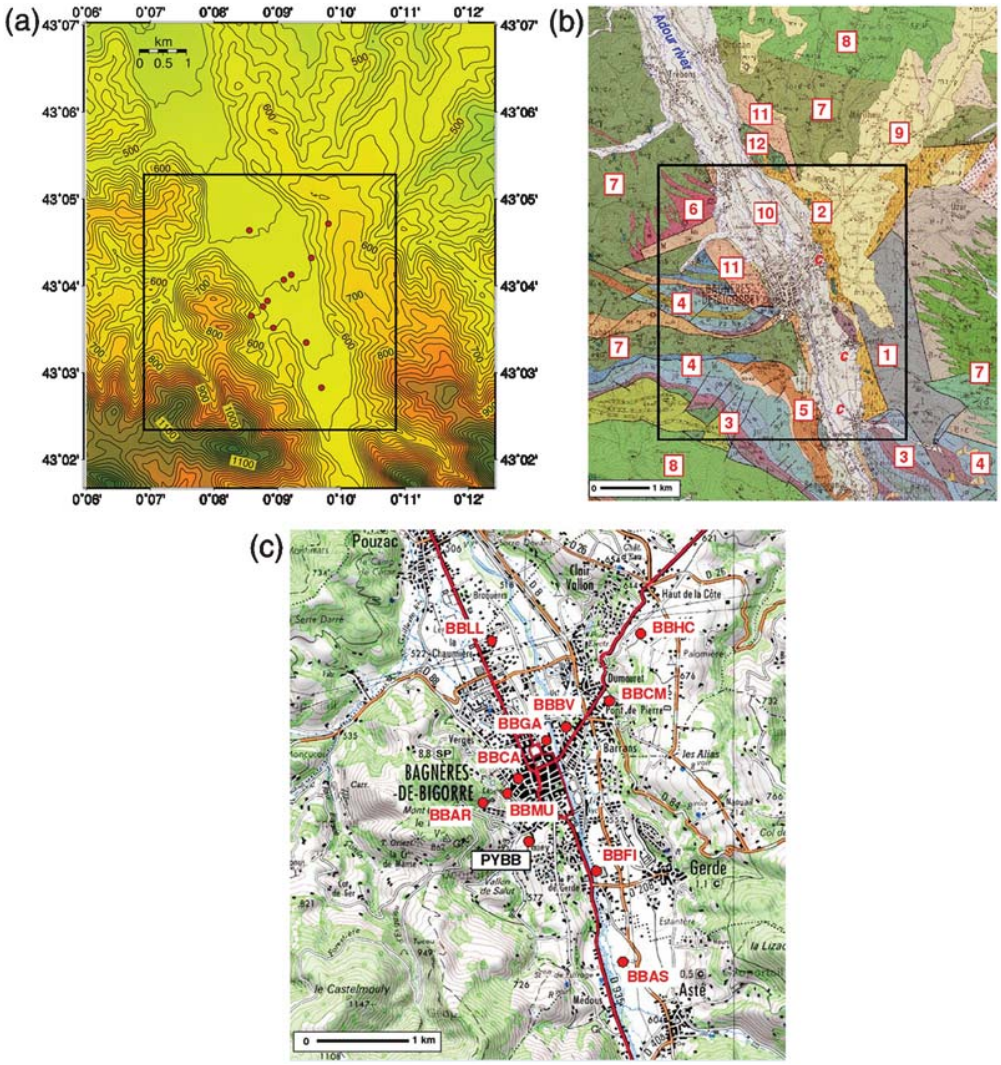

Figure 2. (a) Topographic map of the Adour Valley (from Institut Géographique National), with the location of the accelerometric stations (red dots); (b) geological map of the Adour Valley with the city of Bagnères-de-Bigorre (Azambre *et al.*, 1989). In (a) and (b), the box delineates Fig. 2c; (c) topographic map of the valley, the location of the 10 temporary accelerometric stations, and the permanent accelerometric observatory PYBB. Geological map caption in (b): (1) Paleozoic Ordovician (schist and sandstone), (2) Upper Trias (marls and limestone), (3) Lias (breccias), (4) Dogger and Malm (dolomite, breccias, limestone), (5) Lower Albian (limestone, calcarenites), (6) Mesozoic breccias with granite and gneiss elements, (7) Albian and Cenomanian black flysch, (8) Upper Cretaceous schistous marls, (9) Miocene and Pliocene clay with pebbles, (10) Quaternary fluviatile sediments, (11) Migmatites, (12) Ophites, *c*- main erosion fans.

This crest is covered with Miocene–Pliocene clay and rises 150 m above the valley (Fig. 2b). It is interpreted as a paleotopography preserved between two basins that were affected by a vigorous quaternary erosion (Babault *et al.*, 2005). West of the Adour Valley the mountain rises steeply to a height of 800–1000 m (Fig. 2a). The complex geological nature of the rocks of these mountains, with numerous east–west oriented faults, reflects the tormented history of the structures along the North Pyrenean fault (Fig. 2b).

Bagnères is a small city of 8000 permanent inhabitants, but it is an important tourist center with thermalism, mountain activities, and hotel business induced by the proximity of the pilgrimage city of Lourdes and the Pic-du-Midi astronomical observatory. It also has some industrial activities (electronics, high precision mechanics, cable factory, railway industry, aeronautics). This economical context and the high historical seismicity were additional reasons to choose this city as a pilot site for seismic risk evaluation, an initiative supported by the French Accelerometric Network.

The Temporary Network

Description of the Network and Data

A network of 10 accelerometers has been deployed in Bagnères from November 2006 to November 2008 (Table 1), in addition to the permanent station PYBB of the Réseau Accélérométrique Permanent (RAP; Pequegnat *et al.*, 2008). Each station includes a three-component accelerometer

Table 1
Stations Used

Code	Station Location	Latitude (°N)*	Longitude (°E)*	Altitude (m)
BBAR	Hospital (Arbizon)	43.0609	0.1431	630
BBMU	Salies Museum	43.0627	0.1462	550
BBCA	School (Carnot)	43.0638	0.1474	550
BBGA	Social center (Gambetta)	43.0678	0.1516	545
BBBV	Vacation center (Bonvouloir)	43.0688	0.1536	550
BBCM	Senior center (Castelmouly)	43.0720	0.1588	555
BBHC	Private house (Haut-de-la-Côte)	43.0786	0.1633	625
BBLL	Private house (Lotissement de Laître)	43.0773	0.1426	545
BBFI	Centre Laurent Fignon hotel	43.0558	0.1575	565
BBAS	Private house (Asté)	43.0471	0.1615	600
PYBB	Bagnères Observatory	43.0586	0.1489	560

*Coordinates in the WGS84 system.

Episensor ES-T from Kinemetrics and a Agecodagis Titan3 data logger with a sampling rate of 125 Hz. The recording is continuous for the temporary stations and triggered for the permanent station PYBB, based on a STA/LTA algorithm. Seven of the temporary stations are aligned across the valley (Fig. 2c), with two stations, BBMU and BBCM, at the edge of the valley. The mean distance between these stations is about 500 m. The three remaining stations are set up along the valley axis. Three stations are installed on rock: BBAR, BBMU, PYBB; the other ones are installed on soils.

Most of the stations are located on the floor inside small size buildings of one to three stories or inside individual houses; the resonance frequency of these buildings may be typically of the order of 10 Hz or more (Goel and Chopra, 1998). Only BBAR and BBCM are located in more complex buildings. The frequencies of interest for soil response range from 0.1 to 20 Hz. Hence, the high-frequency spectrum may possibly be perturbed by the resonance of the buildings. This will be clarified later with the aid of horizontal-to-vertical (H/V) ratio measurements. On the other hand, no high building can be found in the vicinity of our stations, the vibrations of which could generate a signal perturbing our measurements (Guéguen *et al.*, 2000; Castellaro and Mulargia, 2010). The permanent accelerometer observatory PYBB is installed inside a historical seismological observatory on a pillar that is anchored to the rock and decoupled from the nearby ground, as was usual practice in the early twentieth century. The instrument and sampling rate are the same as for the temporary network.

The earthquakes recorded by the temporary network are extracted on the basis of the catalog provided by the Seismic Survey Service of the Pyrenees. The catalog includes events with magnitudes as low as 1.0. The accelerometric records are validated and distributed by the Réseau Accélérométrique Permanent (RAP) in Grenoble. All data are high quality, except the north component at the southernmost station BBAS until May 2008, where technical problems have been *a posteriori* detected. Figure 3 (black traces) shows an example of accelerometric records for an M 4.3 event located 13 km to the west-southwest of Bagnères. These records reveal important variations in the amplitudes and frequency content of the signals, depending on the location of the station. The stations in the valley (BBCA, BBFI, BBAS) recorded a large amplitude, high-frequency signal,

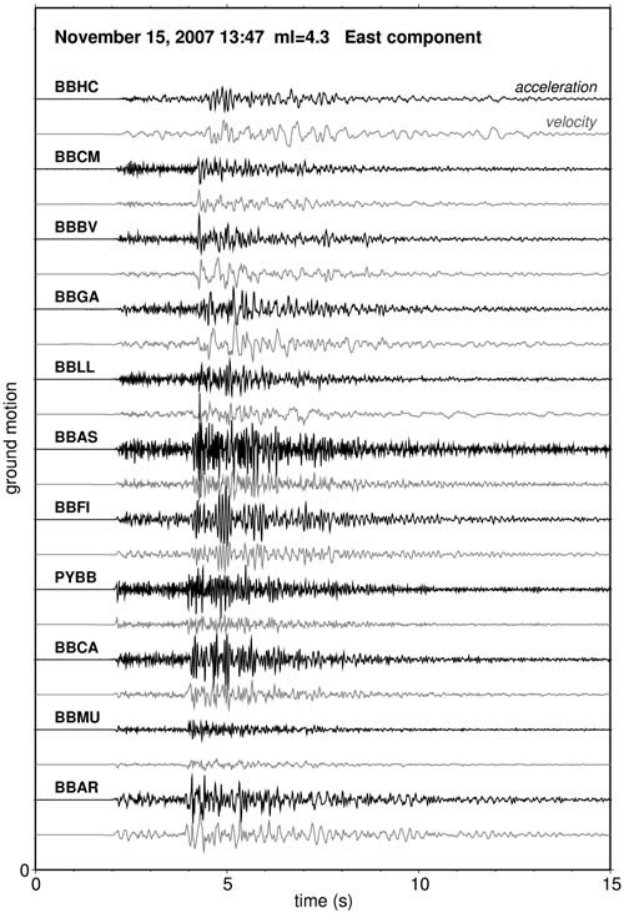

Figure 3. Example of accelerometric records (in black) for the 15 November 2007 event of magnitude 4.3 located 13 km to the west-southwest of Bagnères (east component). Station codes refer to Figure 2c. Ground velocity is plotted in gray to make the low frequencies more apparent. Note the strong variations in amplitude, frequency content, and coda length.

whereas the amplitude is low at the foot of the mountain (BBMU). The signals at the stations on the flank of the valley (BBAR, BBHC) have an important low frequency content with a long coda, which appears still more prominent when velocity signals are considered (Fig. 3, gray traces). Site effects are thus very clear from these records, although it is not possible at this stage to know what are the respective contributions of topography and sedimentary filling.

Characterization of Soil Structure

A good knowledge of the structure beneath the stations is essential for the interpretation of experimental results and the design of numerical models. Active seismic measurements, such as multichannel analyses of surface waves (MASW; Park *et al.*, 1999) were performed a few tens of meters away from the temporary sites. The experiment consisted in deploying linear profiles from 34.5 to 92 meters in length (Table 2) equipped with 24 Mark Products 4.5 Hz vertical geophones. The waves were generated with a hammer blow on a metallic plate at various offsets from the last geophones in both directions; this offset ranged from one to several times the geophone interspacing. Rayleigh waves dispersion curves for the fundamental and higher modes obtained for each shot points were then processed to get average phase velocities with their confidence level (one standard deviation). Table 2 summarizes the minimum and maximum measured frequencies and wavelengths at each site. Because very inconsistent phase velocities were obtained for different shot points at BBCM, this site has been discarded.

The retrieval of the vertical profiles of shear-wave velocity is performed in two steps. First, fundamental and higher mode Rayleigh waves are inverted using the conditional neighborhood algorithm (Wathelet, 2008), as implemented in the Geopsy package (see Data and Resources). Model parameterization consisted of two or three uniform layers overlaying a half-space, the bottom depth of each layer being defined by a geometrical progression based on the wavelength range, namely from half the minimum measured wavelength to half the maximum measured wavelength. For each site, 20,000 velocity models have been generated. From this model ensemble, we randomly extracted 1000 models having a misfit of 1. The misfit m is defined according to the concept of acceptable solution (Lomax and Snieder, 1994); it has the value $m = 1$ when the calculated dispersion curve is completely inside the uncertainty bounds, and a greater value outside. This allowed us to obtain an ensemble of statistically acceptable models explaining the data within their uncertainty bounds. Superficial shear-wave velocities are varying from site to site (Fig. 4a). At most sites, however, a velocity contrast is detected within the first 10 to 20 m below the surface. This result is consistent with the electrical and gravimeteric prospecting (Perrouty, 2008), which revealed a thickness of quaternary sediments of about 15–20 m close to BBAS, 25–30 m close to BBFI, and about 42 m close to BBLL.

Deriving the velocity structure at larger depth, especially down to bedrock depth, would require larger aperture acquisition based on active techniques (MASW) or passive techniques such as the frequency-wavenumber (f-k) method (Capon, 1969) or the spatial autocorrelation (SPAC) method (Aki, 1957). Such deployments were not planed in the framework of the present project. However, joint inversion of dispersion and H/V curves has shown its ability to better constrain shear-wave velocity especially at large depths (Fäh *et al.*, 2001; Scherbaum *et al.*, 2003; Parolai *et al.*, 2005; Arai and Tokimatsu, 2005), with *a priori* assumptions on the energy partition of Rayleigh and Love waves in the noise wave field, or on the ratio between horizontal and vertical loading forces. In order to avoid such prior assumptions, the ellipticity of Rayleigh waves has been measured directly by applying a time-frequency analysis with continuous wavelet transform to the noise wave field (Fäh *et al.*, 2009; Hobiger, 2011). This technique allows us to identify *P-SV* wavelets in the signal, and ellipticity is estimated by computing the spectral ratio from these wavelets only. In general, reliable measurements of the ellipticity are obtained for the right flank of the ellipticity peak, which carries the most important information on the velocity structure in the intermediate to large depth range (Fäh *et al.*, 2009). Ellipticites were obtained at frequencies lower than those of dispersion curves (Table 2), allowing us to extend the shear-wave velocity

Table 2
MASW Profile Characteristics

	Profile Length (m)	Minimum Wavelength (m)	Maximum Wavelength (m)	Minimim Frequency (Hz)	Maximum Frequency (Hz)	Ellipticity Frequency Range (Hz)
BBFI	69	9.6	60	8.9	29.5	1.4–1.8
PYBB	57.5	3.6	55.3	15.1	44.9	10.7–14.2
BBAR	69	3.4	33.7	13.1	59	6.3–10.3
BBLL	92	5.7	45.3	12.9	49.2	1.4–1.7
BBGA	69	6.6	48.6	9.6	39.9	1.7–6.13
BBBV	57.5	11	61.3	11.7	28.1	1.5–2.4
BBCM	57.5	–	–	–	–	–
BBAS	92	7.3	73.8	13.1	40	–
BBCA	34.5	3.7	20	23	48.3	1.6–7
BBMU	34.5	3.8	34.7	16.1	48.2	–
BBHC	57.5	7.9	45.9	6.2	26.2	2.8–4.4

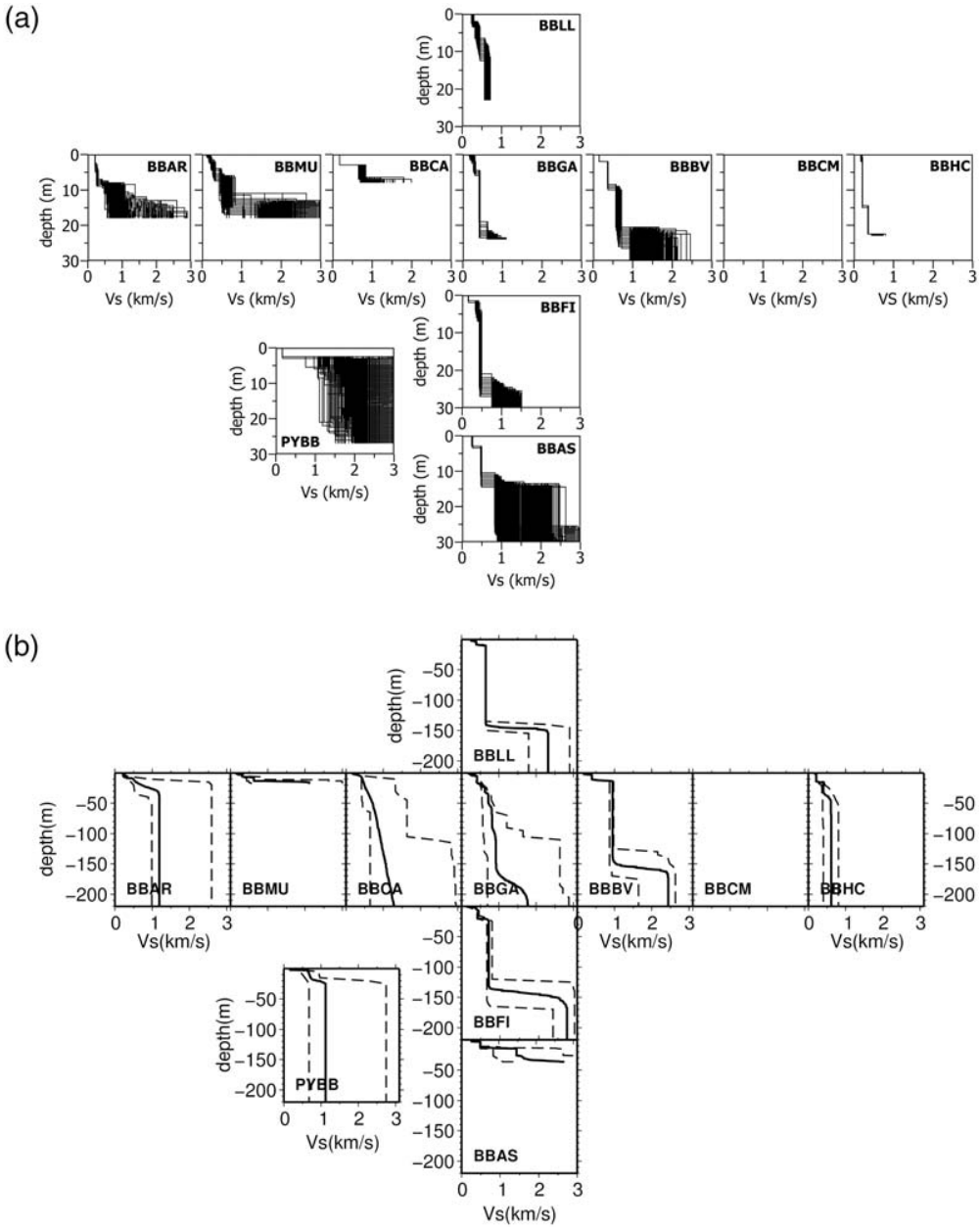

Figure 4. Shear-wave velocity profiles obtained near the sites of the temporary stations from MASW experiments. (a) Inversion of Rayleigh wave dispersion curves, the 1000 best models; (b) simultaneous inversion of dispersion curves and ellipticity (except at BBMU and BBAS, obtained from dispersion curves alone, and BBCM, where no reliable model could be obtained). The thick lines show the mean models; dashed lines delineate the limits of all acceptable models. The velocity profiles can be obtained at greater depth when ellipticity is considered.

profiles at larger depths. For the joint inversion of dispersion and ellipticity, the global misfit was computed by summing single misfit functions obtained from each dataset (ellipticity and dispersion), datasets having similar weight. Weights are indeed useless when considering misfits based on the acceptable solution concept, for which each curve fits the data within its uncertainty bounds with a misfit of one.

Model parameterization is the same as before, except for a layer with linear velocity increase down to 400 m, which has been added above the half-space. The inversion scheme is also the same as before. Figure 5 illustrates the improvement in *S*-velocity profile when ellipticity and dispersion curves are jointly inverted. Approximate models of shear-wave velocity may be derived from the surface down to about 200 m at most sites. Note, however, that when large frequency gaps exist in the ellipticity and dispersion curves measurements, the retrieved *S*-velocity profiles may be biased at intermediate depths (Hobiger *et al.*, 2010; Hobiger 2011). This is possibly the case at BBFI, BBLL, BBBV, and BBCA sites.

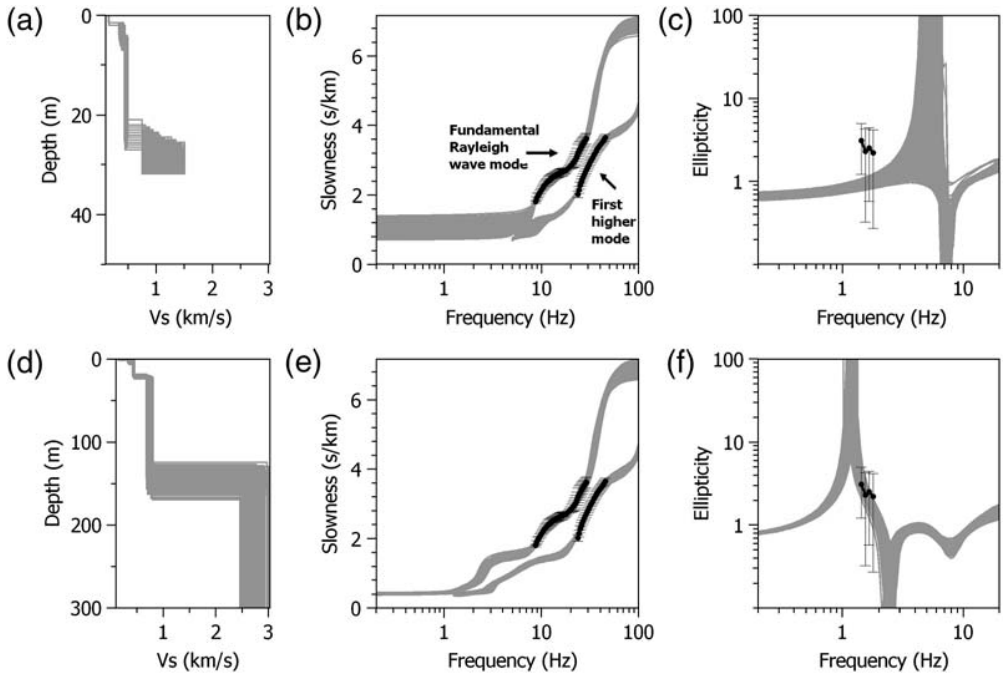

Figure 5. Example of determination of the 1D *S*-velocity profile from MASW experiment, at site near BBFI. (a) Set of possible structures determined from the phase velocity dispersion curves alone; the fit of the observations (in black) with the model predictions (in gray) is shown in (b) for the dispersion curves (fundamental and first higher mode), and in (c) for the ellipticity of the fundamental mode; (d) structure obtained from simultaneous inversion of phase velocities and ellipticity; comparison with observations is shown in (e) and (f). The introduction of the ellipticity as an additional constraint allows us to retrieve the structure at greater depth.

Figure 4b displays the *S*-velocity profiles obtained in the vicinity of the different temporary stations. At most sites, it has been possible to invert simultaneously phase velocities (fundamental mode and higher modes at a few sites) and ellipticities. At BBMU and BBAS, no stable measurement of ellipticity could be obtained, and the velocity profile is derived from the fundamental Rayleigh wave dispersion curve. The different velocity profiles reveal that, inside the valley, the bedrock is reached at depths of about 100–150 m. The sedimentary layer is thus very thin compared with that observed in Alpine valleys, for example, up to about 1000 m in the Grenoble basin (LeBrun *et al.*, 2001). Moreover, no large variation of the thickness of sediments is observed along the valley. The most significant differences concern the rather strong impedance contrast in the uppermost 20 m, as already mentioned. For numerical modeling based on spectral element method, the following generic *S*-velocity 1D-profile inside the valley has been derived:

$$\begin{aligned} V_S(\text{m/s}) &= 200 + 100 \times (z)^{1/2} \quad \text{for } z = 0\text{–}25 \text{ m} \\ V_S(\text{m/s}) &= 655 + 1.7 \times z \quad \text{for } z = 25\text{–}150 \text{ m} \\ V_S(\text{m/s}) &= 2200 \text{ m/s} \quad \text{for } z > 150 \text{ m (bedrock)}, \end{aligned} \tag{1}$$

where z is depth in meters.

The three rock sites BBAR, BBMU, and PYBB display rather different characteristics. BBMU appears as the stiffer site, but the V_S profile could not be retrieved below the depth of 17 m. At BBAR and PYBB, the bedrock velocity is retrieved with a very large uncertainty, with possible V_S values ranging from 1000 to 2500 m/s, thus compatible with those ($V_S \sim 2200$ m/s) found in the middle of the valley, even though the mean value ($V_S \sim 1200$ m/s) may suggest a weathered or fractured bedrock. On the other hand, MASW profiles at BBAR, BBMU, and near PYBB reveal the presence of a soft, thin layer at the surface that may amplify the seismic motion at high frequency. However, this surficial layer does not affect the signal at station PYBB, as the instrument is set up on a pillar anchored in the bedrock. The profile at BBHC reveals a thick, soft layer as expected from the local geology, the station being installed on a crest of Miocene and Pliocene sediments.

Experimental Site Effect Determination

Brief Description of the Methods

Three methods are commonly used to determine site effects at one site. The first one is based on the computation of the spectral ratios H/H_{ref} of the horizontal components for local or regional events, at site i, and at a nearby reference site located on bedrock without topography (Borcherdt, 1970). It assumes that the ground motion induced by the earthquake is the same at the sediment-bedrock interface at site i and beneath the surface at the reference site (after correcting the free-surface effect). The H/H_{ref} ratio is thus the transfer function of the sedimentary layers at site i. This

is valid only if source radiation and propagation effects can be neglected, thus the distance between source and stations must be large compared with the distance between sites. The method is generally applied to *S* waves, which are very sensitive to site conditions (in particular to the presence of soft layers) and which are at the origin of most of the damages. It may also be applied to the coda of earthquakes, which results from the scattering of seismic waves in a large volume around the ballistic path from source to station (Phillips and Aki, 1986). In this case, the use of a reference station eliminates statistically most of the contributions of the structures inside this volume. The main difficulty is generally to find a good reference station. The method may also be applied to the vertical component (V/V_{ref}), even though vertical acceleration is less important than horizontal acceleration for seismic hazard.

The second method relies on the ratio between horizontal and vertical components of ambient noise at station *i* (H/V method, Nakamura, 1989). Horizontal-to-vertical measurement of noise is particularly popular because it does not require earthquake recording; only a few tens of minutes of noise record are necessary, and no reference station is necessary. It is thus very easy to implement. However, it leads to results that are sometimes difficult to interpret, because they depend on the way the different components of noise are amplified by the soil structure (Bard, 1999). Difficulties stem from the complexity of ambient noise (which includes Rayleigh waves, Love waves, and body waves) and from its great variability in space and time (Bonnefoy-Claudet, Cotton, and Bard, 2006). However, if high impedance contrasts are present in soil structure, resonances in the uppermost layers generate peaks in the H/V spectral ratios. For a single homogeneous flat layer of thickness h and *S*-velocity V_S overlying a flat bedrock, a resonance peak is observed at frequency $f = V_S/4h$. The spectral ratio is more complex if impedance contrasts are weak (Malischewsky and Scherbaum, 2004) or if several layers are present. Generally, the frequency of the main peak gives the fundamental resonance frequency, but its amplitude is controlled by the proportion of Love waves and generally underpredicts site amplification (Picozzi *et al.*, 2005; Bonnefoy-Claudet *et al.*, 2008; Haghshenas *et al.*, 2008; Endrun, 2010). At rock site conditions and in the absence of topography, H/V is close to unity in a large frequency domain (Lachet and Bard, 1994; Bard, 1999).

The third method relies on the measurement of energy partitioning of coda waves on horizontal and vertical components (H/V-coda). This method was first proposed by Lermo and Chávez-García (1993), who showed that the site resonance frequency can be estimated by analyzing the H/V ratio of shear waves and their early coda at a single station. They found good agreement between H/V measurements on *S* waves and the classical spectral ratio results. In a recent study, Margerin *et al.* (2009) performed an analysis of H/V for coda waves measured at the Pynion Flats observatory in California. They showed that shallow low-velocity layers have a clear impact on the frequency dependence of the H/V ratio in the coda. Just as in the case of noise wave fields, the H/V peak may be related to the resonance frequency of the structure.

The three methods described previously have been applied to data collected at the temporary and permanent stations. Moreover, systematic H/V measurements on noise have been performed to evaluate soil response variability through the whole city using CityShark™, an instrument with a software package Geopsy especially adapted to record urban noise (see Data and Resources; Chatelain *et al.*, 2000; Wathelet *et al.*, 2008). CityShark is connected to a 3D-Lenhartz velocimeter of period 5 s whose passband and sensitivity are more adapted to record noise than accelerometers. We first present the results for the methods that do not require a reference station (H/V on noise and H/V on *S*-wave coda), then those where a reference station is necessary (H/H_{ref} on *S* wave and H/H_{ref} on *S* coda).

H/V on Noise: Results

This method is first considered because it may help to define the reference station, in addition to the MASW results. The processing of the data at the temporary stations follows the procedure described in Souriau *et al.* (2007). The mean H/V spectral ratio and its confidence level are computed from 30 noise records of 40 s each. The spectra are smoothed using a moving average window whose width is 20% of the central frequency, and the north (N) and east (E) spectra are combined into a single horizontal spectrum according to $H = (|N|^2 + |E|^2)^{1/2}$, assuming the absence of phase coherence between the two components. We have checked that, despite the geometry of the valley, the north to vertical (N/V) and the east to vertical (E/V) spectral ratios are nearly identical. An experiment using the CityShark seismic station has been conducted at the exact location of the temporary stations. For these data, the software package Geopsy provides a quasi-automatic computation of H/V.

The Influence of the Instrument. Figure 6a shows the comparison between the results obtained from the accelerometers and from the CityShark velocimeter at BBCA and BBCM. For the accelerometric data, we selected one day (1 February 2008) where the microseismic noise is rather strong. The CityShark experiment has been conducted during a day with rather low microseismic noise. The results obtained at these two stations are well representative of what is obtained at the different stations: there is generally a good coherency of the results at high frequency, but significant discrepancies may be observed at low frequency. This may be explained by the self-noise of the accelerometer compared with the noise level (Strollo *et al.*, 2008), a problem that is not encountered with the CityShark velocimeter. It is illustrated in Figure 6b, which shows the power spectral density of the ambient noise with a clear peak due to the microseismic noise, superimposed on the accelerometer self-noise. The ambient noise is lower than the instrument self-noise at frequencies lower

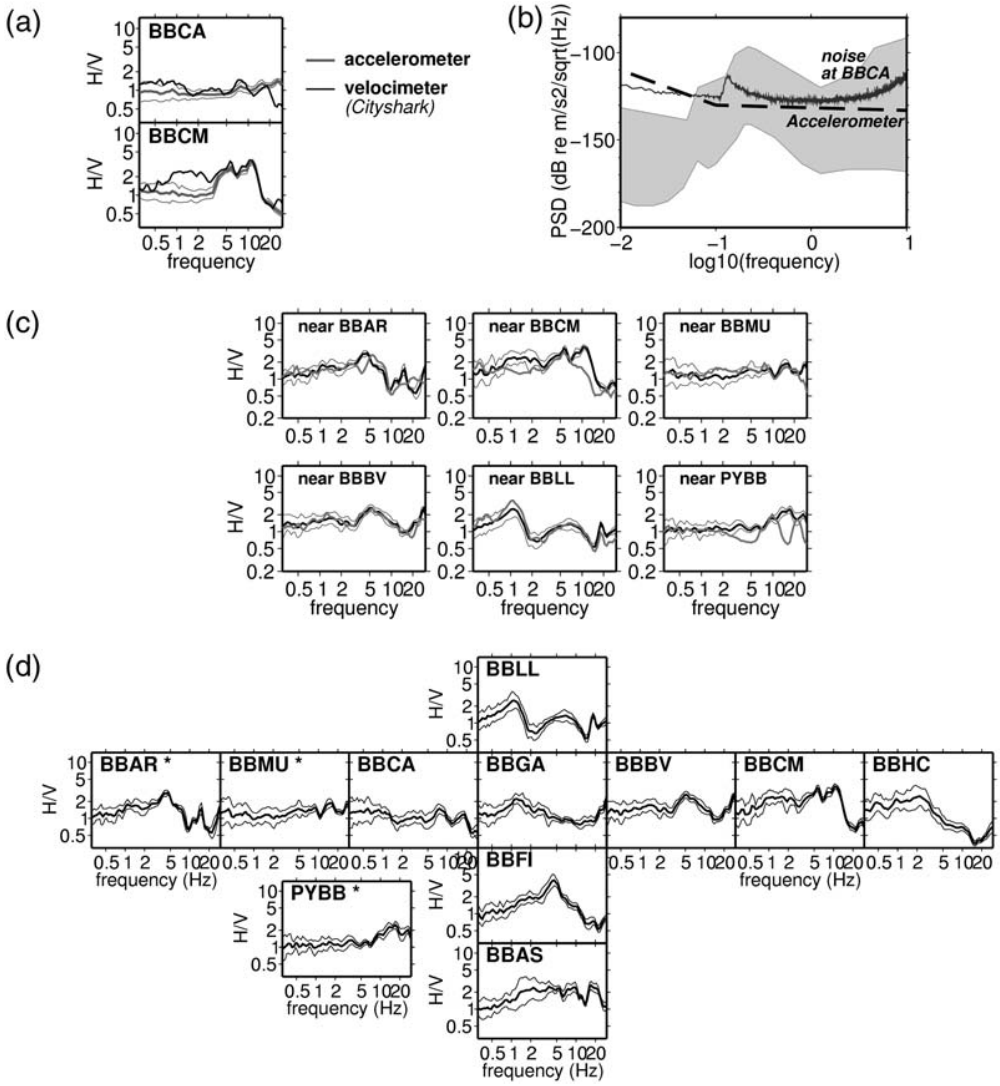

Figure 6. The horizontal-to-vertical spectral ratios on ambient noise. (a) Examples of results obtained at BBCA and BBCM with the accelerometer of the temporary stations (gray), and with the velocimeter of the CityShark instrument (black). For clarity, the confidence level (one standard deviation) is reported for the accelerometer only, it is similar for the velocimeter. (b) Comparison between the power spectral density of the noise at BBCA and the self-noise of the accelerometer. The gray domain is bounded by the low-noise/high-noise curves of Peterson (1993). (c) Influence of the buildings at a few sites. The horizontal-to-vertical ratio is shown in black (with 1σ-confidence level) inside the building and in gray outside the building. (d) Horizontal-to-vertical ratio values with 1σ-confidence level obtained from CityShark at the different stations. Stations denoted by an asterisk (*) are located on rock.

than about 0.1 Hz. Even around 1 Hz the level of ambient noise is sometimes only slightly above the instrumental noise. Thus, our accelerometers are inappropriate to H/V measurements. In what follows, we will thus consider only the CityShark results.

Effect of the Buildings. As most stations are set up inside buildings, it is useful to estimate the perturbations they may induce on the records. Figure 6c shows H/V measurements inside the building and immediately outside for a few typical sites, obtained with the CityShark instrument. BBAR and BBCM are located at one end of the basement of recent concrete elongated buildings of 5–6 levels. A small peak at 15 Hz is observed inside the building at BBAR, and at 11 Hz at BBCM. The instrument of BBMU is on the floor in an old, massive stone building of three levels, which does not generate any perturbation. The same conclusion holds at BBBV, BBLL, which are inside individual houses. The spectral ratio perturbation due to the buildings is thus limited to the high-frequency domain of the spectrum, and it appears significantly lower than the spectral ratio variations due to site effects, except perhaps at BBCM. At PYBB, the location of the instrument on a seismological pillar (which is supposed to be anchored to the bedrock) clearly simplifies the site response, as it removes the resonance of the uppermost layers. This shows the efficiency of this observatory installation.

Note that using a pillar at the reference station is equivalent to replace soft soil by a stiff structure. It is thus very different from using a reference station in a borehole, where downgoing waves perturb the reference signal, which must be corrected for this effect (Steidl *et al.*, 1996; Assimaki *et al.*, 2008).

Results at the Different Stations and Choice of the Reference Station. Figure 6d shows the H/V spectral ratios obtained from CityShark. For the choice of a reference station, we are primarily concerned by the three stations located on rock, BBAR, BBMU, PYBB. We observe a consistent peak at 4.5 Hz at BBAR, possibly due to a topographic effect, and/or to a thin soft layer surface as observed from MASW experiment. At BBMU and PYBB, the spectral ratios are nearly flat and close to unity in the frequency range 0.3–10 Hz. However, as noted in Figure 3, the amplitudes at BBMU immediately at the slope foot are small compared with those at other stations, suggesting a local topographic or geological effect, as will be discussed later. We will thus choose PYBB as a reference station, keeping in mind that a small peak is present at 17 Hz. This permanent station has in addition the advantage of being maintained at the standard of an observatory, thereby ensuring high-quality data. Note that some stations in the middle of the valley, located on soft soils, have nearly flat H/V spectral ratios, probably because of the absence of strong impedance contrast between stiff sediments and bedrock, as will be discussed later. This illustrates the difficulty of choosing the reference station on the sole basis of the H/V ratio if geological conditions are ignored (Steidl *et al.*, 1996; Cadet *et al.*, 2010).

H/V Dense Measurements on Noise: Variability of Site Effects in the Valley. Measurements of H/V spectral ratios on noise are the simplest and least expensive way to have an appraisal of the structure variability throughout the basin, even though only the fundamental resonance frequency could be obtained with this method. They are also of practical interest for risk mitigation, which was one of the motivations of the pilot site experiment. Figure 7a shows the CityShark sample points inside the Bagnères basin. They consist of three transverse profiles and one profile along the valley axis. The middle transverse profile and the profile along the valley include the temporary stations.

The H/V spectral ratios are given in Figure 7b. There is no straightforward feature coming out from these results; in particular, it is not possible to draw a map of fundamental resonance frequency, as is sometimes done (e.g., Parolai *et al.*, 2001; Souriau *et al.*, 2007). Even if a change in the noise composition from one measurement to another may be responsible for some variability (due, for example, to the traffic increase at some hours during the experiment), the observed spectral variations mostly reflect the complexity of the structures. In the northern profile where the valley is broad, we observe low frequency peaks close to the valley axis (sites 04, 05, 06), where the sedimentary filling is the thickest. The profile along the valley reveals an important variability of the resonance peaks, with frequency of about 1 Hz at sites 38–39 and about 7 Hz at sites 43–44. As for the H/H_{ref} spectra, it may be due to the increase of sediment thickness downward in the valley. The H/V signal shows some complexity on the flanks of the valley, with sometimes a spectral drop above 10 Hz (sites 02, 08, 09, 19, 24, 29). This is not systematic (e.g., sites 14 and 32 at the foot of the hill, which have a flat spectrum). Sites on the Miocene–Pliocene crest east of the valley (sites 35, 36, 21, 22) exhibit a broad, low frequency peak. We also note a great variability for nearby stations (e.g., 24 and 25). This complexity shows that the detailed geology and geometry of the valley may play an important role at the frequencies we consider; local topography and structures must be taken into account as accurately as possible in the modeling.

H/V on Coda: Results

The *S* coda corresponds to the signal after the direct *S*-wave arrival, due to wave scattering by crustal heterogeneities. At the distances we consider, the coda regime (defined from energy equipartitioning) is reached only a few seconds after the *S* arrival, as illustrated in Figure 8. Figure 8a shows a local earthquake record (M 2.9) at station BBAR. Figure 8b shows the typical slow decay of coda energy with time. Coda duration largely exceeds the ballistic propagation time between source and station, as a result of multiple scattering from small-scale heterogeneities in the crust. Figure 8c illustrates the rapid stabilization of the H/V ratio in the coda, typically only a few seconds after the direct shear-wave arrival. This fact is characteristic of coda waves and has previously been reported by Hennino *et al.* (2001) and Margerin *et al.* (2009). The return to the noise level is also very clear from the energy analysis: H/V on noise shows very large fluctuations compared with the coda (Fig. 8c).

H/V-coda has been measured on a selection of events at distances larger than 10 km from Bagnères, and with magnitudes larger than 2.5, to get enough energy in the coda (Fig. 9a). The distribution of events around the city exhibits a gap in azimuth to the north and the east (Fig. 1). Moreover, the strong attenuation in the Pyrenees (Drouet *et al.*, 2005) limits the number of remote events that could be recorded. We obtain a total of 83 events with epicentral distances, depths, and magnitudes ranging from 12 to 212 km, 3 to 18 km, and 2.5 to 5.0, respectively (Fig. 9a).

For data processing, we selected an *S*-wave coda window starting 10 s after the *S* arrival, with a total duration of 30 s. As for noise records, H/V is defined as the square root of the ratio between the sum of the kinetic energies on the two horizontal components and the kinetic energy on the vertical component. The H/V ratio appears very reproducible and shows little (if any) dependence on source location. This stabilization of the energy ratio in the coda is interpreted as the effect of mode mixing due to multiple scattering. It results in a phenomenon known as equipartition where all the propagation modes, both surface and body

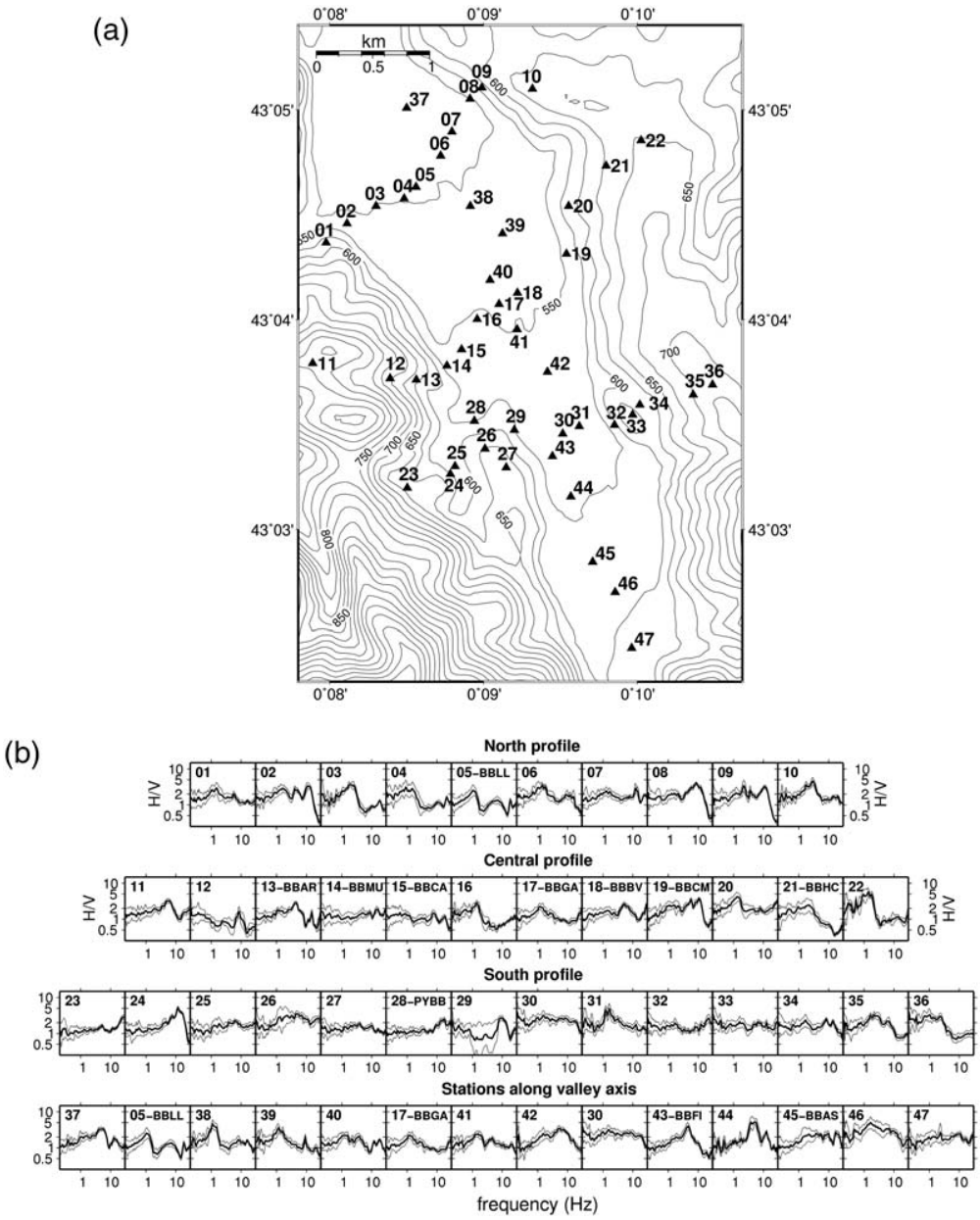

Figure 7. (a) Map of selected sites for H/V measurements on noise with CityShark in the Bagnères Valley; (b) H/V spectral ratios (numbers refer to the sampled locations).

waves, get excited by equal energy (Margerin *et al.*, 2009). Results are given in Figure 9b, with 1σ confidence intervals estimated from the variability of the spectra for the different events.

There is overall agreement with H/V on noise, with peaks at the same frequencies and amplitudes ranging roughly from 0.5 to 7. A steady decrease of the H/V ratio at high frequencies ($f > 17$ Hz) is observed at some stations, whereas it is not observed for noise measurements (e.g., BBBV, BBGA, BBLL). This illustrates that at high frequencies, the wave contents of noise and coda are significantly different. However, the stability and reproducibility of H/V-coda is advantageous over H/V on noise records, which may exhibit large fluctuations.

H/H_{ref} and V/V_{ref} on *S* Wave and on *S* Coda: Results

S *Waves.* This method has been applied to the same selection of events (Fig. 9a), with magnitudes larger than 2.5 that ensure a good *Sn* ratio at low frequency and distances to the network larger than 10 km for the reference station method to be valid. *S*-wave arrivals have been handpicked. A window of length l starting 0.5 s before *S* has been selected, l increasing with epicentral distance D from $l = 5$ s (for $D < 35$ km) to $l = 15$ s (for $D > 100$ km). The spectral ratios have been

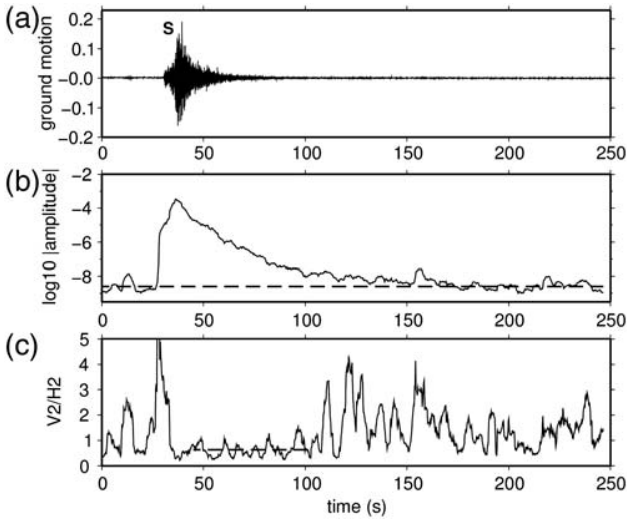

Figure 8. Illustration of equipartition energy in the coda (diffusion regime). (a) Record of the 3 October 2007, M_L 2.9 event, located 38 km to the west of Bagnères (east component at BBAR); (b) plot of the seismogram envelope and the mean noise level measured on the first 20 s of the record (dotted line); (c) ratio between the kinetic energy of the vertical and horizontal components, V^2/H^2, for the record filtered at 15 Hz. Note the stabilization of the ratio between 40 s (i.e., only 4 s after the *S*-wave arrival) and 100 s. After 100 s, the large fluctuations correspond to the decay of the signal below the noise level.

computed with the same procedure as for H/V (where V is replaced by H at the reference station PYBB). We have first processed independently the north and east components; it shows that there is no variation of horizontal polarization related to the basin north-northwest–south-southeast elongation (Ⓔ see Fig. S1, available in the electronic supplement to this paper).

Figure 10a shows the H/H_{ref} spectral ratios obtained after combining the two horizontal components, as well as the V/V_{ref} ratios. In most cases, H/H_{ref} and V/V_{ref} have peaks at the same frequencies and with similar amplitudes, however, V/V_{ref} is generally larger than H/H_{ref} at high frequency. At a few stations (BBLL, BBAR, BBHC), the V/V_{ref} peak is slightly shifted toward high frequency compared with the H/H_{ref} peak, as often observed (e.g., Dubos, 2003). From the H/H_{ref} ratios, two interesting results emerge: (1) High ratios (up to 10) are obtained at BBAR and BBHC on the flanks of the valley, even though one of the stations (BBAR) is set up on rock. Note, however, that the resonance frequencies are not the same, about 5 Hz at BBAR and 2.5 Hz at BBHC (on thick soft sediments). By contrast, the stations at the slope foot have smooth spectral ratios. This suggests a possible topographic effect, with amplification at the crest and flank, and amplitude decrease at the slope foot. (2) The spectra of the stations along the valley are highly variable, with a resonance frequency decreasing from south (BBAS and BBFI) to north (BBLL). This corresponds to the downhill increase of the sediment layer thickness, possibly related to the front of the glaciers.

Coda Waves. For H/H_{ref} analysis in the coda, we retained the same events and time windows as those used for H/V coda (Fig. 9a). The coda window thus does not generally overlap the window used for *S*-wave analysis, except for a few remote events. Just as for the *S* wave ratio, the N/N_{ref} and E/E_{ref} ratios are nearly identical (Ⓔ see Fig. S1c, available in the electronic supplement to this paper), denoting the absence of variation in horizontal polarization inside the network. Figure 10b gives the H/H_{ref} spectra, which combines the two horizontal components. They are remarkably consistent with those obtained on *S* waves. The same conclusion holds for V/V_{ref} (in gray in Fig. 10b). The H/H_{ref} ratios appear, however, slightly smoother and with smaller error bars for coda waves than for *S* waves, as the result of stabilization of energy partitioning in the coda.

Comparison of the Different Methods

Figure 10c shows the intercomparison of the spectral ratios obtained with the different methods. The most prominent feature is the significant difference between the H/V ratios (on noise or coda waves) on one side and the H/H_{ref} ratios (on *S* waves or coda waves) on the other side. H/H_{ref} exhibits clear peaks at some stations (e.g., BBGA, BBAR) whose amplitude is lower on H/V, sometimes with a nearly constant H/V ratio over a large frequency range (BBMU, BBGA, BBBV). By contrast, the low frequency ratios (for $f < 1$–2 Hz) are similar.

These differences may hardly be ascribed to the reference station, which is set up on a pillar anchored to the rock and whose H/V ratio is flat up to about 7 Hz. The H/V amplitudes are controlled by the Rayleigh wave ellipticity and by the presence of Love waves that affect the horizontal components. Low H/V may have different origins. (1) Low impedance contrasts between sediments and bedrock combined with low-noise excitation level (Haghshenas *et al.*, 2008). This is probably the case in Bagnères, where rather stiff sediments are overlaying a soft bedrock, leading to moderate shear-wave velocity contrast. (2) Strong lateral variations of the underground structure, especially at sites close to valley edge. In this case, additional lateral interferences of edge-diffracted waves may be generated, which were not present for simple 1D structures where only vertical interferences occur (Uebayashi, 2003; Hagshenas *et al.*, 2008). Differences observed between H/H_{ref} and H/V ratios at some valley sites (BBLL, BBGA) may possibly be attributed to locally diffracted surface waves as previously observed at other sites (e.g., Cornou and Bard, 2003; Bindi *et al.*, 2009).

We have shown the interest of H/V on ambient noise for testing various properties of the sites, for choosing a reference station, and for determining rapidly site effect spatial variability. The comparison of H/V and H/H_{ref} confirms that H/V is at best able to give the fundamental resonance frequency (e.g., at BBLL, BBHC), but that it may strongly underestimate the amplification (Haghshenas *et al.*, 2008), and in some cases (BBGA) H/V may fail in estimating the

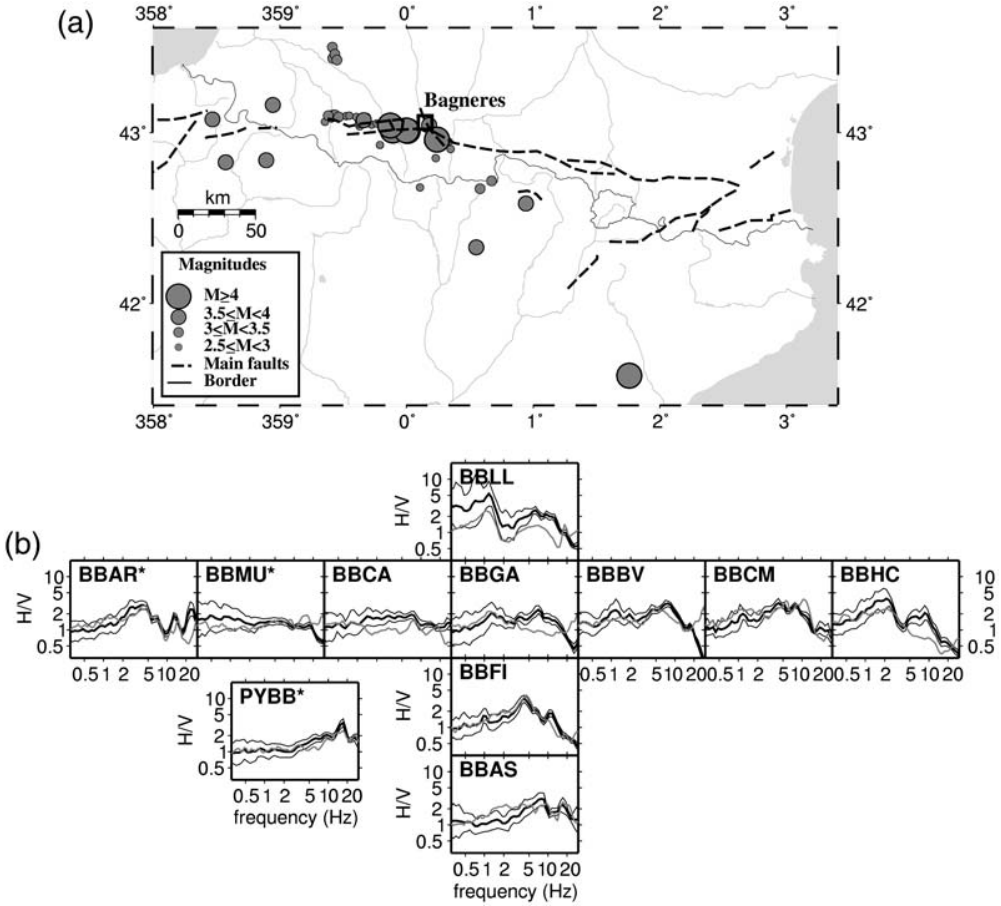

Figure 9. (a) Map of events used for the determination of the H/V ratios on *S*-coda-waves and the H/H_{ref} ratios on *S* wave and *S* coda; (b) H/V ratio on *S* coda (in black), with 1σ-confidence level. The H/V ratios on noise are reported in gray for comparison. Station codes with an asterisk (*) correspond to locations on rock.

overall shape of site response (e.g., Cornou and Bard, 2003; Bindi *et al.*, 2009). If earthquakes may be easily recorded, and if a reference station is available, H/H_{ref} on *S* coda gives the most reliable and most stable results.

Numerical Models

The confrontation of experimental results with numerical simulations may help to understand the origin of amplification or amplitude decrease at some sites and to specify the role of the various parameters (topography, soils, wave field composition) in site response. Modeling will concern the local response to seismic excitation at the temporary stations, as well as the global response of the basin.

H/V Modeling with Synthetic Seismograms: A Test of the 1D S-Velocity Profiles

As the *S*-velocity models in the vicinity of the temporary stations are known from joint inversion of dispersion curves and ellipticities, it is interesting to check the coherency between these models and the observed H/V measurements on noise records. Because the thickness of the soft layer is small compared with the width of the basin, global resonance of the whole basin is not expected to occur (Bard and Bouchon, 1985); a 1D-modeling relying on the *S*-velocity profile beneath the station will be appropriate.

In traditional approaches, one considers the response of a stack of plane layers to shear waves arriving at vertical incidence beneath the structures (e.g., Stephenson *et al.*, 2009). A more realistic modeling may, however, be obtained using the complete seismograms. Following Bonnefoy-Claudet, Cornou, *et al.* (2006), synthetic noise of 13 minutes duration is generated using the discrete wavenumber code developed by Hisada (1994, 1995), which computes Green's functions due to point sources for viscoelastic horizontally stratified media, using the reflectivity method. Green's functions are then convolved with different source time functions, and synthetic seismograms obtained for each source are summed. In this study, source time functions are approximated by surface and subsurface forces, distributed randomly in space, direction (vertical or horizontal), amplitude, and time. The time function is a delta-like signal with a flat spectrum between 0.2 and 20 Hz. Sources are located at 0.5 m depth and

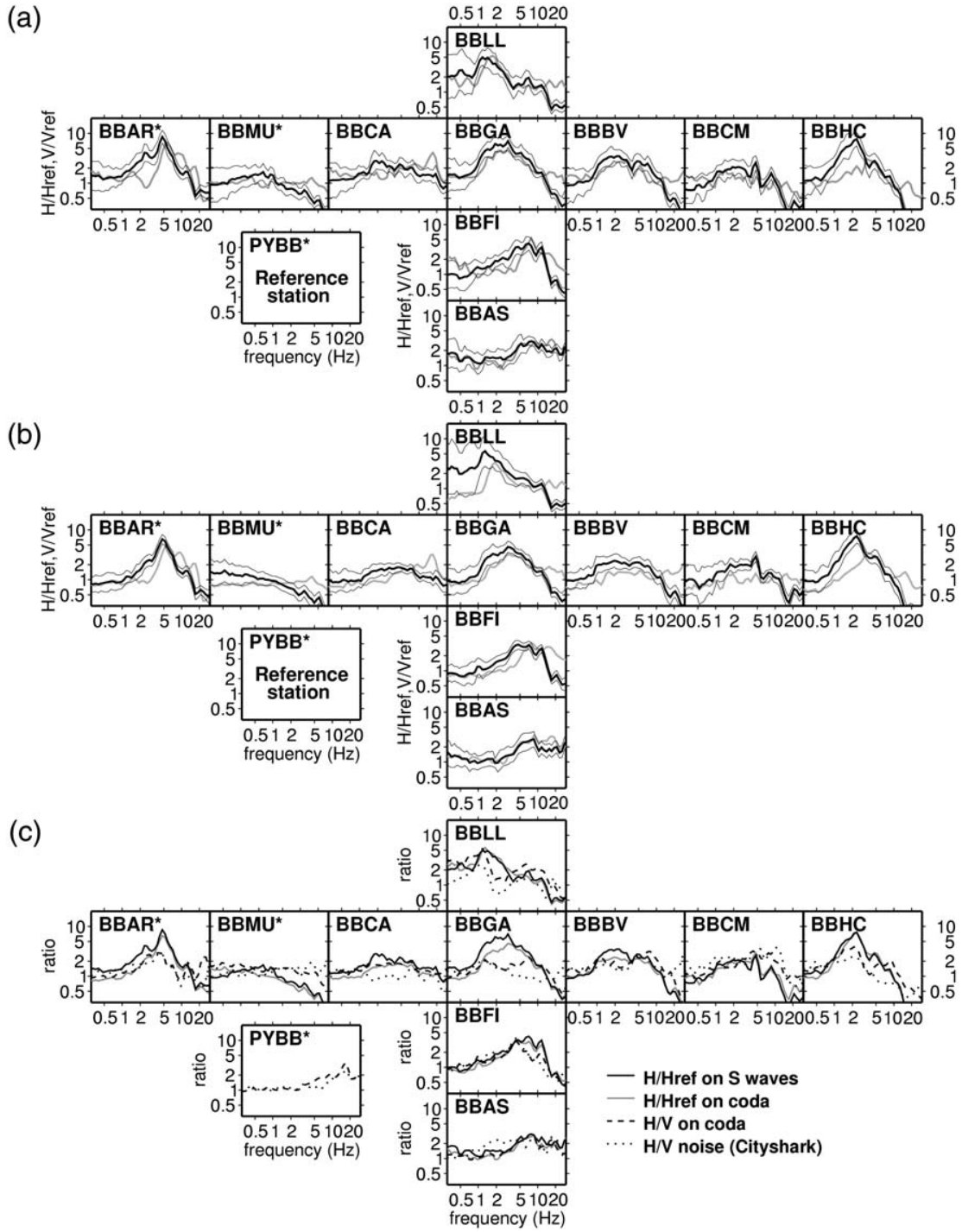

Figure 10. Spectral ratio of horizontal motion (black) and vertical motion (gray) with respect to a reference station (PYBB) (a) for *S* waves, (b) for the coda of *S* wave. Events used are shown in Figure 9a. 1σ-confidence level is given for H/H_{ref} only, it is similar for V/V_{ref}. In (c) a comparison of the different methods is shown. Station codes with an asterisk (*) correspond to locations on rock.

distributed at distances ranging from 5 to 500 m away from the site in order to ensure the excitation of the entire sedimentary column. The modeling has been restricted to the stations for which the structure is well constrained (Fig. 4b). The *S*-velocity model used is the mean velocity structure previously derived at each site down to the bedrock (at about 100–150 m depth), *P* velocity is twice *S* velocity, and Q_S (respectively, Q_P) is varying from 15 (respectively, 20) for surficial layers to 100 (respectively, 150) for the deepest structure.

Figure 11 compares the results of the modeling with the H/V spectra of the CityShark experiment obtained near the temporary stations outside the buildings. The agreement between observations and models is satisfying over a large frequency range from 0.2 to 15 Hz. In particular, H/V peak positions at low and high frequencies are rather well retrieved, the high-frequency peak being controlled by the surficial velocity structure. Moreover, the synthetic data do not predict sharp H/V peaks, in agreement with the observations. They generally slightly overpredict the peak amplitudes, suggesting either that the velocity contrasts in the models are slightly stronger than in the real structures or that the proportion between horizontal and vertical forces excitation is not properly modeled.

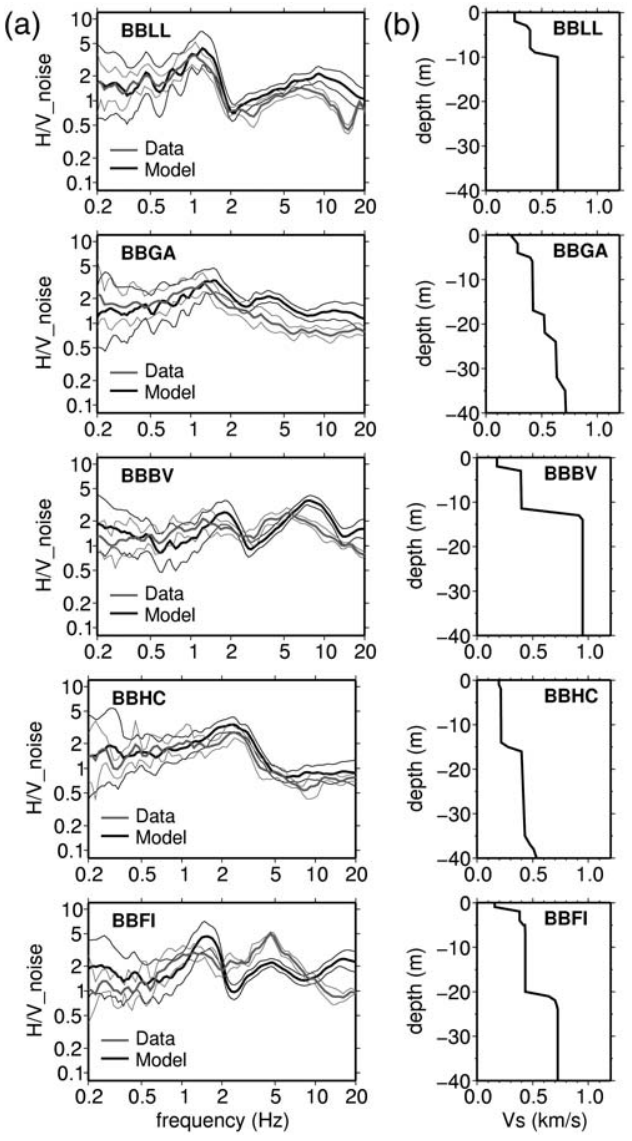

Figure 11. (a) Modeling of the H/V spectral ratio at the temporary stations from noise generated by summing synthetic seismograms. Predicted ratios are in black; experimental spectra of H/V on noise measured outside the buildings are in gray. Values are given with one standard deviation confidence level (thin lines). (b) The uppermost 40 m of the *S*-velocity models used (defined down to 150 m); only stations with well-defined structure are considered.

Simulation of H/V for Coda Waves

Similar to the analysis performed with noise records, we use the velocity models to calculate the theoretical H/V ratio in the coda, neglecting the possible role of confinement due to basin edges. In the framework of equipartition theory, we write a modal decomposition of the coda wave field in terms of eigenfunctions of the layered medium under the station. The modal amplitudes are uncorrelated (complex) random variables with zero mean and equal variance. Clearly, the true medium under the station is only approximately layered and also displays small-scale fluctutations superimposed on the background structure. In loose terms, equipartition theory says that, as far as average energetic quantities are concerned, the true medium can be replaced by a laterally averaged medium, and the coda wave field can be represented as a sum of surface and body waves coming from all possible azimuths. With these assumptions, we perform a summation over all modes and compute the kinetic energy on each component of the seismogram. Further details on the computational procedure can be found in Margerin (2009). Note that there is no adjustable parameter in the theory. This is an important difference with noise simulations, where the amount of vertical and horizontal sources may be adjusted to fit the data.

The outcome of the calculations is displayed in Figure 12. In the 0.2–2 Hz frequency band, the agreement between observations and data is satisfactory at most stations. The only notable exception is the station BBLL, which shows a broad peak around 1 Hz. At frequencies higher than 2 Hz, the theoretical calculations may sometimes differ significantly from the measurements. As an example, at BBCA, the theory predicts a peak around 10 Hz, which is absent in the data. At BBAS, the predicted peak is observed in the data but with a smaller amplitude. This comparison validates the gross features of the velocity structure as sensed by low frequency waves. However, the finest details of the observed H/V ratio in the coda are not reproduced by our calculations. Some moderate site effects revealed by coda waves at some stations (BBAR, BBLL, BBHC) are not easily modeled with the available velocity profiles. It would be interesting to adjust the local velocity structure to improve the fit between data and theory. However, solving such an inverse problem goes far beyond the goal of our study.

Modeling the 3D Response of the Valley with the Spectral Element Method

In order to quantify the respective contributions of surface topography and basin structure to the observed amplifications, we performed 3D simulations of the response of the Bagnères basin to various seismic excitations using the

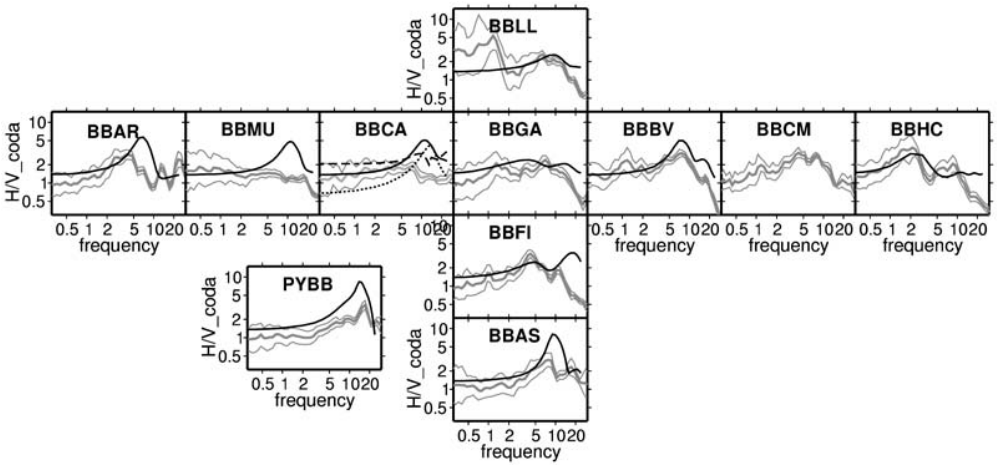

Figure 12. Analysis of energy partitioning in the coda (from the H/V ratio) at the temporary stations. Observed ratios, with 1σ confidence level are in gray. Results of simulations based on equipartition theory with both surface waves and body waves are in black. Structure not available for modeling at BBCM.

spectral element method (SEM) (e.g., Komatitsch and Vilotte, 1998; Komatitsch and Tromp, 1999; Komatitsch *et al.*, 2005; Chaljub *et al.*, 2007). If the 3D structure is known with sufficient resolution, the SEM provides an efficient tool to model the variability of the ground motion in space and time by accurately accounting for the complexity of seismic wave propagation in the presence of free-surface topography and 3D heterogeneities, in particular mode conversion from body to surface waves in sedimentary basins (e.g., Chaljub *et al.*, 2010), or from surface to body waves at a nonplanar free-surface (Komatitsch and Vilotte, 1998). The associated local effects on strong ground motion are of particular interest for seismic risk evaluation.

The response of the structure is investigated in two steps: (1) considering the topography alone and (2) considering both the topography and the filling of the valley by sediments. Two types of sources are investigated: (1) a vertically incident plane shear wave with polarization either in the north–south or east–west direction and (2) a realistic double-couple point source with characteristics close to an M 3.9 event, which occurred on 3 May 2008 to the south-southeast of Bagnères.

Structure Parametrization and Numerical Implementation. Figure 13a shows a 3D view of the computational domain used for plane waves, the size of which is about 5 km in the vertical direction and 8 km × 11 km in the east–west and north–south directions, respectively. With the mean crustal structure beneath the Bagnères basin being unknown, we adapted a model previously obtained at the nearby city of Lourdes (Dubos *et al.*, 2003; Table 3). The model is made of homogeneous layers, except the topmost layer, where we imposed a velocity and density gradient from the surface down to 179 m above sea level (Table 3). The base of the computational domain is the planar surface with elevation $z = -4451$ m, and the free surface is given by a digital elevation map (DEM) with spatial resolution 50 m. Surface elevation inside the domain of computation varies from about $z = 430$ m to the northwest to $z = 1560$ m to the southwest. From the DEM, we define the surface imprint of the quaternary sediments as the set of points for which the elevation is less than 600 m, and the local slope does not exceed 10% (see the red line showing the obtained basin edge on Fig. 13b). This *ad hoc* criterion was adjusted in order to have the basin edge separating the BBMU (rock) and BBCA (soil) stations, but it was not possible to find a simple proxy to also include the eastern station BBCM in the sediments.

The basin structure is defined as a single layer with uniform thickness $h = 150$ m, and homogeneous P and S velocities, consistent with the results of the seismic profiles (Table 3). The fundamental resonance frequency of this layer is 1 Hz, in agreement with the observations. The structure of the Miocene sedimentary crest to the east beneath BBHC is not known well enough to be safely introduced in the model. Thus, the comparison between simulations and observations will disregard the eastern slope of the profile (BBCM and BBHC). Throughout the model, the S wave quality factor is chosen to be independent of frequency and to scale with the shear-wave velocity as $Q_S = V_S/10$ (V_S in m/s). Neglecting the bulk attenuation yields the definition of the P-wave quality factor: $Q_P = (3/4) \times (V_P/V_S)^2 \times Q_S$.

The 3D computational domain for plane waves (Fig. 13a) is discretized with a mesh of 284,256 spectral elements with polynomial order $N = 4$, which results in 19,356,750 grid points. The mesh is designed to sample the wavelengths with a minimum of 5 grid points (i.e., we use at least one spectral element per minimum wavelength), and it is coarsened with depth following a simple conforming strategy as explained in previous studies (Komatitsch *et al.*, 2004; Chaljub *et al.*, 2007). The minimum element size in the basin is 75 m, which results in accurate simulations for frequencies up to

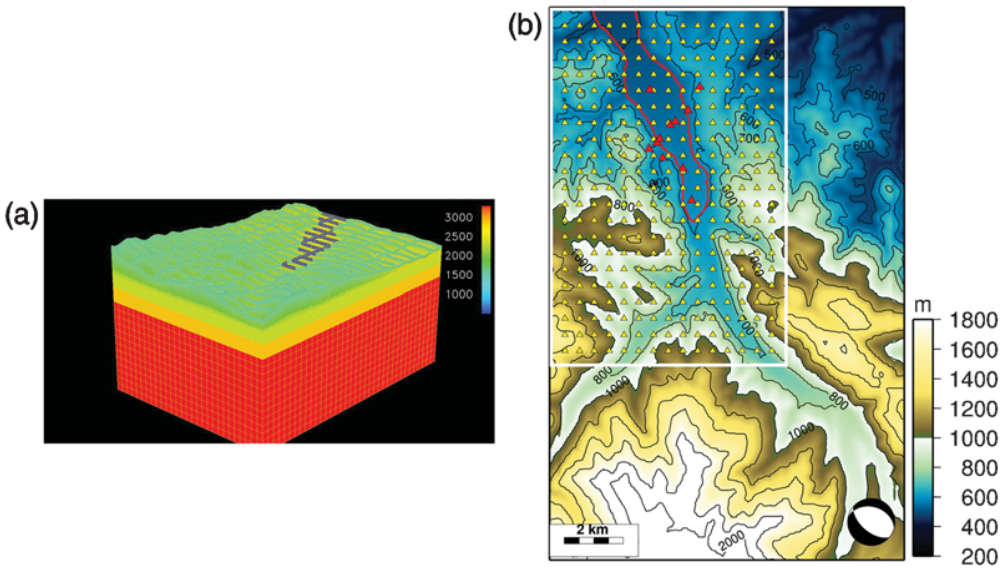

Figure 13. Grid for the spectral element method computations. (a) 3D grid used for the vertically incident plane waves with the location of the basin (in blue); (b) domain of investigation, the white box corresponds to (a); points at the surface indicate where the signal is computed, on a regular grid with spacing 500 m (yellow triangles), and at the sites of the accelerometric stations (red triangles). The domain of investigation is superimposed on the topography in (b). The sedimentary filling is located inside the red contour. The whole map corresponds to the domain considered for modeling the realistic source, whose focal mechanism is plotted at its epicentral location.

8 Hz. For each seismic excitation, we compute 30 s of ground displacement, velocity, and acceleration at the 11 temporary and permanent stations (red triangles in Fig. 13b), as well as at 315 virtual stations distributed on a regular grid of size 500 m (yellow triangles in Fig. 13b). When a realistic source is considered, the computational domain is extended laterally and in depth in order to include the focus. The computational domain is 12 km × 12 km × 17 km in the vertical, east–west, and north–south directions, respectively (Fig. 13b). It is discretized with the same grid spacing as the computational domain used for plane waves, which results in 47,331,770 grid points.

The source time function is given by a low-pass filtered Dirac pulse for plane wave excitation and by a low-pass filtered Heaviside pulse for the realistic double-couple source. In each case, the source does not radiate energy for frequencies above 8 Hz, allowing us to compute maps of peak ground displacement, velocity, and acceleration without having to store the full time series at all the surface grid points.

Intrinsic attenuation is modeled using the rheology of the generalized Zener body, which is equivalent to the superposition of standard linear solids (Moczo *et al.*, 2007) and implemented through the introduction of memory variables (see Chaljub *et al.*, 2007, and references therein). We use three relaxation mechanisms to model a constant Q in the frequency range 0.5–8 Hz.

Absorbing boundary conditions are implemented using a simple radiation equation (Lysmer and Kuhlemeyer, 1969; Komatitsch and Vilotte, 1998). This is certainly not the best performing technique, but it is known to be insensitive to Poisson's ratio, a useful property when the absorbing boundaries intersect the sedimentary layers (as is the case here for the northern boundary of the computational domain).

Results for a Plane Wave. The seismic source consists in a vertically incident plane S wave with particle displacement polarized either in the north–south direction (thus, nearly parallel to the valley axis) or in the east–west direction. This

Table 3
Model for Spectral Element Method Simulations

z (m) Above Sea Level	V_S (m/s)	V_P (m/s)	Density (kg/m^3)
Surface*	1000	1900	2000
179 to −251	2400	4500	2500
−251 to −851	3000	5400	3000
Below −851	3400	6000	3200
Sediments (h = 150 m)†	600	1500	2000

*There is a velocity gradient in the top layer from the surface down to z = 179 m.

†This last line corresponds to the homogeneous sediment filling of the basin.

exercise is mostly academic, however, it may give an idea of the response of the valley to a large remote event (for example, from the south of Spain or from Catalonia), for which *S* waves arrive with steep incidence beneath the Bagnères basin. Figure 14 shows the maps of peak ground accelerations (PGA) obtained for the two polarizations, when we consider the topography alone (Fig. 14a,c) and when the basin structure is added (Fig. 14b,d). [Ⓔ The equivalent maps for peak ground velocities (PGV) and peak ground displacement (PGD) are available in the electronic supplement to this paper; see Figs. S2, S3.] In all maps, there is a contamination of the values along the computational domain boundaries caused by the poor performance of absorbing conditions for vertically incident plane waves travelling at grazing incidence along the lateral boundaries of the domain. Therefore, we avoid interpreting peak values for locations closer than about 2 km from the edges of the computational domain.

The simulations with topography alone clearly show amplifications related to short wavelength crests. The amplifications occur inside the east–west oriented structures for incoming plane wave with north–south polarization and in the north–south oriented structures for east–west polarization.

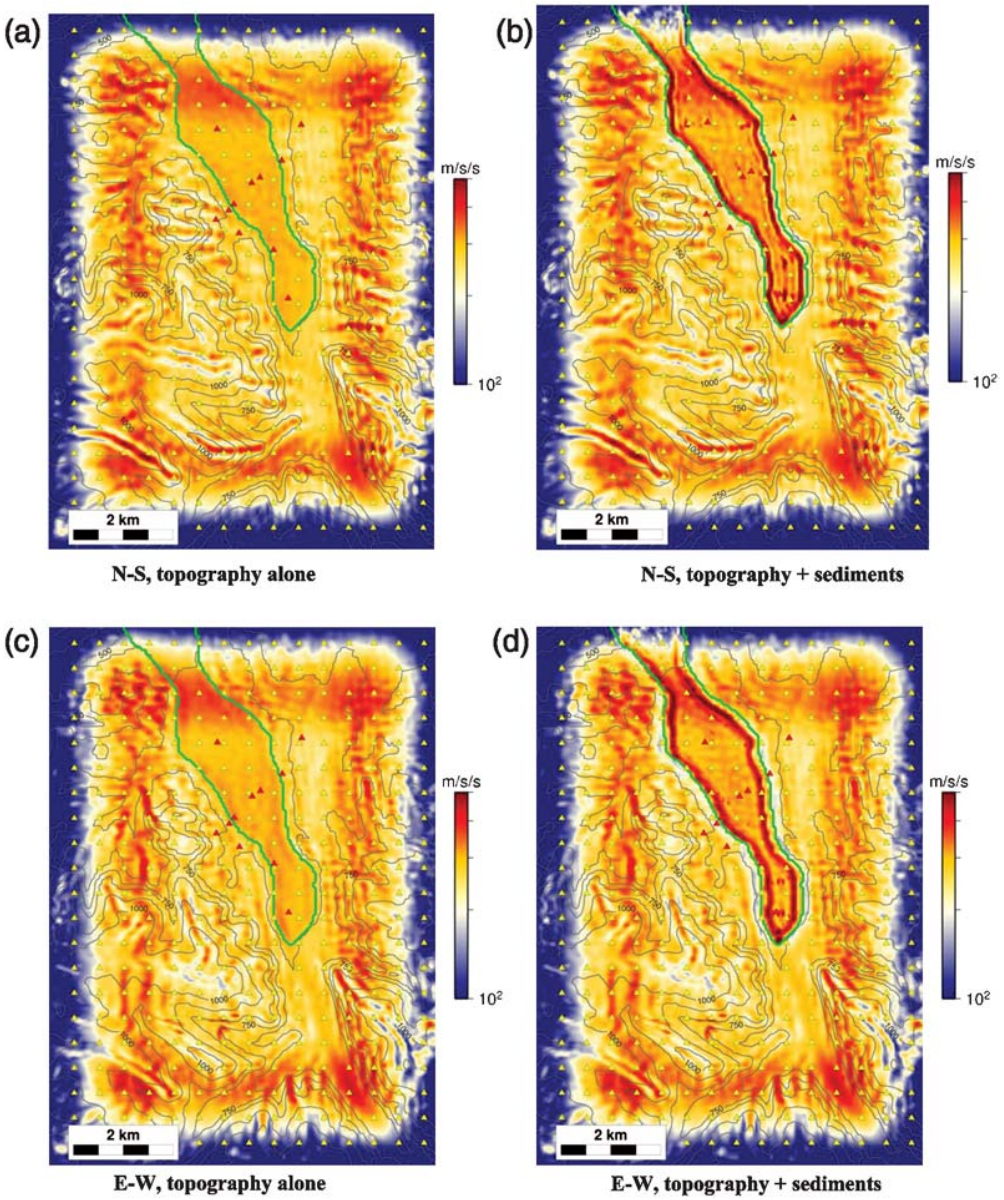

Figure 14. Peak ground acceleration for a plane *S*-wave incident beneath the structure, with topography alone (a,c) and with the basin filled with sediments (b,d). The location of the basin is shown by a green line. The plane wave has either (a,b) a north–south polarization or (c, d) an east–west polarization. Edge effects are observed along the border of the valley, with an amplitude increase (in red) and an amplitude decrease (in blue) immediately outside. Scale is arbitrary. Numerical artefacts are observed at the border of the plots, over a width of about 2 km.

The resonant structures have typically 200–300 m lateral extension, and wave focusing occurs at the top of the crests, whereas defocusing occurs on the slopes. This focusing–defocusing effect is well observed for PGA and PGV; it appears smoother on PGD, as displacement representation favors long wavelength signal (Ⓔ see Fig. S3a,c, available in the electronic supplement to this paper). Figure 14a brings to light the numerous east–west oriented structures related to the Pyrenean tectonics (Ⓔ see Fig. S2a, available in the electronic supplement to this paper). The PGA, PGV, and PGD inside the Adour basin have medium values and do not exhibit significant variations. We just note a small edge effect with an amplitude increase at the border of the basin, followed by a small amplitude decrease immediately at the mountain foot. It is best observed on the synthetic signal (Fig. 15a, note the small amplitude decrease at BBMU). This effect is more visible for the east–west polarization (Fig. 14c), thanks to the north–south orientation of the valley.

The introduction of the sedimentary layer completely modifies the ground motion pattern, as it is seen on PGA maps (Fig. 14b,d) and on time-series of ground accelerations (Fig. 15b). Whatever the polarization of the incoming wave, both the PGA and the duration of ground motion are seen to increase within the basin (see stations BBCA, BBGA, BBBV in Fig. 15b), as well as PGV and PGD. The most striking feature in the basin is a clear increase, by a factor of 2–3, of the PGA values close to the edges (but slightly offset from the basin edge toward the basin axis), as shown for station BBCA in Figure 15b. This is a manifestation of the so-called basin edge effect, caused by the interference between the incoming shear wave and surface waves diffracted off the basin edge, and first invoked by Kawase (1996) to explain the occurrence of the damage belt during the 1995 Kobe event. The characteristics of the amplification zone and its distance to the basin edge strongly depend on the basin structure (in particular on the geometry of the edge, the thicknesses and velocities of the sedimentary layers) and on the characteristics (in particular, the spectral content) of the incoming signal (Kawase, 1996; Pitarka *et al.*, 1998; Hallier *et al.*, 2008). Note, for example, that the maximum is not at the same distance of the edge for north–south (Fig. 14b) and east–west (Fig. 14d) polarization, an effect easier to observe in the narrow uppermost basin to the south. In addition to the amplification close to the basin edge, we note a systematic PGA decrease immediately outside the basin, at the mountain foot, as shown for station BBMU in Figure 15b (Ⓔ see also Fig. S2b,d, available in the electronic supplement to this paper). Such an amplitude decrease outside the narrow amplified zone has been observed in other similar contexts, for example, at Kobe (Pitarka *et al.*, 1998; Hallier *et al.*, 2008) or in the Gubbio basin (Bindi *et al.*, 2009). For the north–south polarization, we also observe in the uppermost basin north–south-oriented stripes distant one to another by about 250 m (Fig. 14b), some amplitude variations resulting likely from stationary resonant modes in the east–west direction. By contrast, the PGD inside the basin appears nearly uniform, due to the prevalence of low frequencies in displacement signal (Ⓔ see Fig. S3b,d, available in the electronic supplement to this paper). The SEM thus allows us to obtain a picture of the valley response with a great accuracy and to understand the origin of most of the observed features.

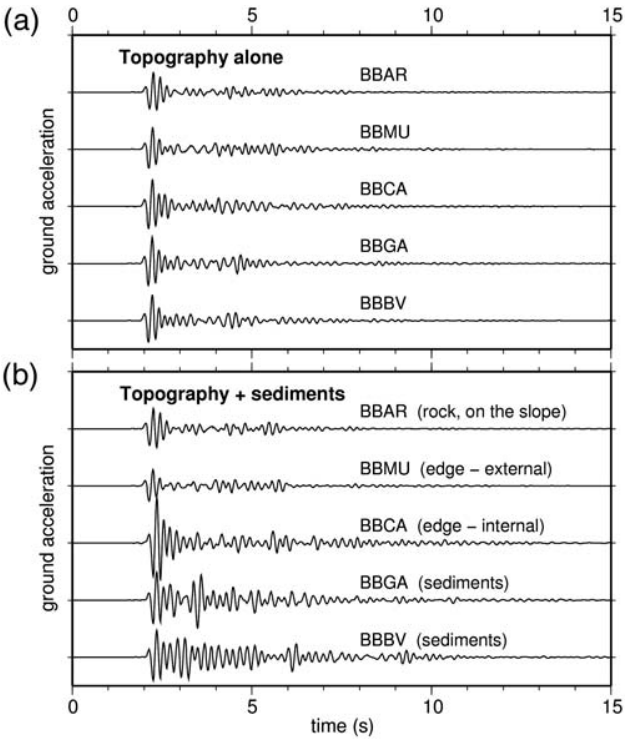

Figure 15. Synthetic ground acceleration for a plane *S*-wave incident beneath the stations, with north–south polarization. North component at stations of the transverse profile, illustrating the influence of the sediments. (a) Numerical results for topography alone; (b) topography and basin filled with sediments. Note the large amplitudes and long duration inside the basin (BBGA, BBBV), the edge effect appearing as an amplitude decrease immediately outside the basin (BBMU), and as an amplitude increase at the border of the basin (BBCA).

Results for a Realistic Source. Next we simulate the response of the Bagnères basin to a local event close to an *M* 3.9 event that occurred on 3 May 2008 and was well recorded by all the stations of the temporary array. The distance of the epicenter to PYBB is about 13 km, and the focal depth is 11 km. We used a double-couple point source with the same focal mechanism as the real event (Fig. 13b), and the source time function was defined as a low-pass filtered step function. The displacement field radiated by the simulated source has therefore a flat amplitude spectrum up to the maximum frequency of 8 Hz.

Figure 16a,b shows the maps of PGA obtained from the simulations with topography alone and with topography and basin structure, respectively. Similar maps are obtained for PGV and PGD (Ⓔ see Figs. S4a,b and S5a,b, respectively, available in the electronic supplement to this paper).

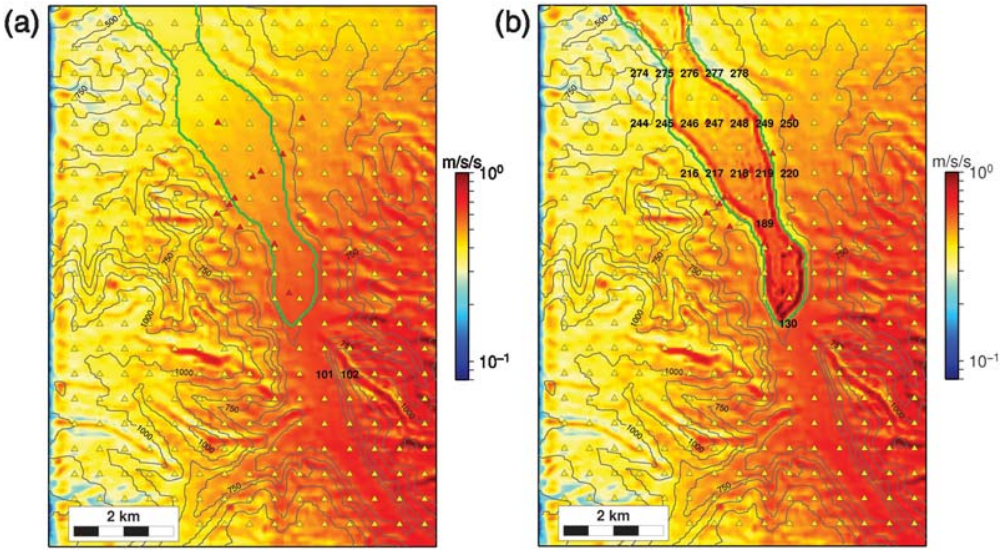

Figure 16. Peak ground acceleration computed for a double-couple point source close to that of the 3 May 2008 event (see location and focal mechanism on Fig. 13b), in a structure with (a) topography alone and (b) topography and sedimentary filling in the basin. Because of the high corner frequency, the absolute PGA values are unrealistic; only the PGA pattern can be analyzed (see text). Note in (a) the predominant influence of radiation pattern on the distribution of PGA, in (b) the general increase of PGA inside the basin and the edge effect with an increase of amplitude inside the basin and a decrease immediately outside. The virtual stations numbered in black correspond to sites considered in Figures 17 and 18.

Maximal PGA values are around 0.4 g on rock sites close to the source. These high values are mainly due to the use of a source time function with corner frequency $f_c = 8$ Hz, instead of $f_c = 2$ to 5 Hz for Pyrenean events of such magnitude (Drouet *et al.*, 2005). The PGA values should therefore not be directly compared with the observations. In the absence of sediments (Fig. 16a), the dominant pattern is due to the combined effects of epicentral distance and radiation pattern. Topographic effects with PGA increase at the top of the crests and PGA decrease immediately below are observed systematically along the narrow crests, in particular to the east of the investigated area. No amplitude variation is observed at the foot of the slopes bordering the basin. The introduction of sediments (Fig. 16b) yields a general PGA increase inside the basin, which is reinforced by the basin edge effect, as well as a clear PGA decrease immediately at the foot of the slopes. The same observations hold for PGV and PGD. On the PGD map, we observe an asymmetry of the basin edge effect, which appears stronger to the east than to the west. It could be a consequence of the relative *S*-wave incidence with respect to the dip angle of the structures sampled by the waves: the amplitude decreases if the ray arrives parallel to the slope (Bouchon, 1973; Kawase and Aki, 1990; Pedersen *et al.*, 1994).

In order to better quantify the role of the sediments, the spectral ratios obtained for the north–south and east–west components from the simulations with and without sediments are given along three profiles across the valley and at a few additional stations in the higher part of the basin (Fig. 17, with location of the stations used in Fig. 16b). The influence of the sediments almost disappears outside the basin (e.g., at site 130 to the south). By contrast, a strong amplification up to 8 is observed around 1 Hz in the valley. We note the amplification due to the basin edge effect (site 219, for example) and a slight amplitude decrease at high frequency at the foot of the slopes (e.g., at site 245), consistent with the PGA maps. In the frequency range of the simulations, the two horizontal components show similar results outside the basin, with a ratio close to 1. Inside the basin, the amplification is generally slightly larger on the east–west component than on the north–south component, indicating a small effect of the valley orientation.

Figure 18 compares the simulations with the observations at the temporary stations. It shows the recorded east–west ground accelerations (Fig. 18a) and the synthetics obtained with (Fig. 18b) and without (Fig. 18c) sediments. The records have been low-pass filtered below 5 Hz, where the displacement spectrum radiated by the source is supposed to be flat (this filtering explains the disappearance of the *P* wave). As absolute amplitudes are not valid, the synthetic records have been scaled to the observations by normalizing the simulated signals to the observed one at the reference station PYBB. It has also to be kept in mind that the structures beneath the eastern flank (BBCM and BBHC) could not be modeled. The comparison of simulated signals with records is, however, of great interest to validate the model and to understand the origin of the PGA values.

In the absence of sediments, the dominant feature in the synthetic seismograms is the topographic effect. This is illustrated by the two lower traces in Figure 18c, BB102 being at the top of the crest and BB101 in the valley (see their locations in Fig. 16a). The amplification concerns not only

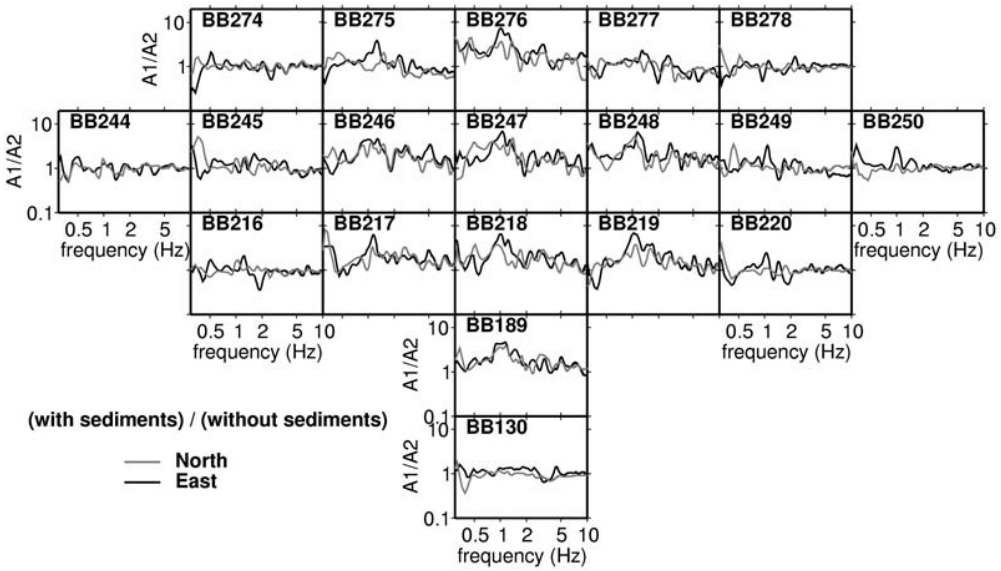

Figure 17. Influence of the sediments on the spectral ratios. Ratios between acceleration spectra obtained from numerical simulations, with topography and sediments, and with topography alone, at selected points (see Fig. 16b), for the double-couple source.

the *S* wave, but also its coda, which is responsible for the PGA value (unfortunately, there are no observations at these sites). When sediments are added (Fig. 18b), the signal inside the valley becomes more complex than in the absence of sediments. The coda becomes very energetic and can be responsible for the PGA value. By contrast, the direct *S* wave is generally not significantly amplified. A clear amplitude decrease related to basin edge effect is predicted and observed at the base of the slope at BBMU (Fig. 18a,b). The signal at BBAR remains difficult to explain, as the large amplitude and complex *S* wave observed at this station are poorly compatible with its location on rock. This suggests either that the rock is strongly weathered (MASW profiles show rather slow shallowest layers that are not modeled here), or that strong wave scattering is induced by the very complex geological nature of the slope, with many lithological contrasts (Fig. 2b) and caves due to karst erosion. The characteristics of the record at the reference station PYBB are, by contrast, in good agreement with rock site conditions.

Discussion and Conclusions

The Bagnères experiment has been conducted for two reasons: (1) to test experimental and numerical methods in a context that is relatively simple from the geometrical and structural point of view (which thus permits a relatively light instrumentation), (2) to infer some guidelines to mitigate the seismic hazard in the Bagnères Valley, which experienced strong historical damaging events. The main interest of a pilot site for seismic-hazard evaluation is to have control of all the steps from observation to simulation. This implies the deployment of appropriate experiments, specific analyses of the shallow structure, a good understanding of the nature and origin of the observed signals, and finally the confrontation of the observations with numerical simulations. As shown by previous studies, this approach may be very fruitful as soon as a dense seismic array may be set up, for example, the Euro-seistest site at Volvi in Greece (Chávez-García *et al.*, 2000; Manakou *et al.*, 2010), or the San Jose site in California (Hartzell *et al.*, 2003; Hartzell *et al.*, 2010), or the Gubbio basin in central Italy (Bindi *et al.*, 2009).

Classical semiempirical methods of site characterization (H/H_{ref} and V/V_{ref} on *S* waves and *S* coda, H/V on noise and on *S* coda) have been implemented along and across the valley. Both H/H_{ref} and H/V give a very local picture of the soil response, as noted in previous studies (e.g., Stephenson *et al.*, 2009). Contrary to some other studies (e.g., Satoh *et al.*, 2001), we have not considered *P*-wave spectra, whose interest for seismic risk is minor, nor H/V on *S* waves, which may be strongly dependent on focal mechanisms. The systematic analysis of the energy partitioning following the *S* wave reveals that the equipartition regime is reached a few seconds after the *S* arrival only (Fig. 8). As noted by Chávez-García *et al.* (2002) and Cornou *et al.* (2003) in similar contexts (narrow valleys in New Zealand and in the French Alps), the small size of the basin implies that locally generated surface waves appear quickly in the records, so that the direct *S*-wave window is very short. Figure 10c, which summarizes the experimental results, shows that H/H_{ref} ratios are very similar for *S* wave and *S* coda. They give access to a broad response spectrum at the sites, provided that a good reference station could be found. This justifies the interest of these spectra for seismic-hazard assessment. By contrast, the H/V spectra on noise give at best the fundamental resonance frequency without a reliable access to the amplification. The horizontal-to-vertical ratio for *S* coda is somewhat similar to H/V on noise (Fig. 9b), but it is more stable, due to energy

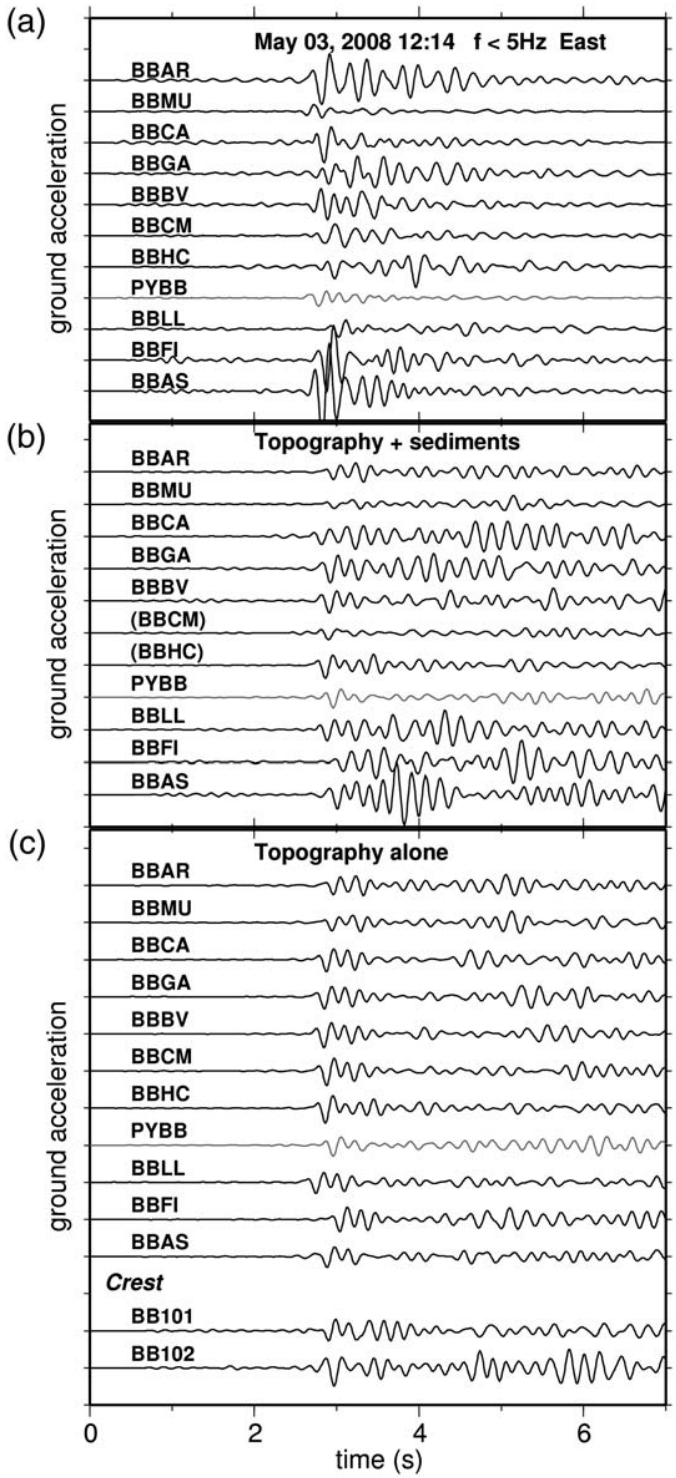

Figure 18. Comparison of the accelerometric records (a) with the synthetics obtained from the 3D-modeling of the valley with the spectral element method. Numerical results for topography alone (c) and for a basin filled with a homogeneous layer of sediments (b). For this last case, results at BBHC and BBCM are not valid (structure unknown). In each panel, the upper, lower, and gray traces correspond to the transverse profile, the longitudinal profile, and the reference station PYBB, respectively. (c) Two synthetic records show the amplification at the top of a crest compared with the hill foot (see station locations and corresponding PGAs on Fig. 16a). The scale is the same for all the traces in (b) and (c) and is normalized to the recorded *S*-wave amplitude at PYBB.

equipartitioning in *S* coda, whereas noise content may vary with time.

In the Bagnères Valley, the H/H_{ref} spectra reveal the presence of resonance peaks with large amplifications (up to 8) along the valley axis, with a frequency decrease downhill, which is well explained by the valley structure (Fig. 10a). By contrast, H/V on noise appears very difficult to interpret, because some stations with large H/H_{ref} amplifications give a nearly flat H/V spectrum (e.g., BBGA on Fig. 10c). The horizontal-to-vertical ratio on noise may, however, be useful to detect rapid lateral variations in the soil response (Fig. 7), which may sometimes vary drastically at the scale of a few tens of meters only. In the Bagnères experiment, H/V has also been used to detect a possible influence of the buildings where the temporary stations were set up (Fig. 6c); in particular, it illustrates the advantage of the seismological pillar at the PYBB observatory. The choice of this reference station rather than BBMU is also *a posteriori* justified by the 3D-modeling that reveals an amplitude decrease at the basin edge where BBMU is set up.

The determination of the structure is key to model the basin response to seismic excitation. Thus, it was important to retrieve the structure as deep and as accurately as possible. The use of ellipticity together with wave dispersion, and when possible the higher modes of surface waves, allowed us to reach depths up to about 200 m with profiles of maximum length 90 m, thereby providing a convenient experimental method in mountainous regions or in urban contexts. The *S*-velocity structure has been checked by modeling H/V spectral ratios for noise and for *S* coda with two different, though certainly related, modeling approaches (Figs. 11, 12). The agreement between simulations and observed ratios is generally satisfying for noise in the whole frequency band, which validates the MASW results. The results of the modeling for coda waves are more contrasted and suggest that some finer details of the local structure remain to be understood.

The 3D-simulations of the basin response using the spectral element method are very informative, even though the adopted structure is a somewhat simplified version of the real one. A modeling at higher frequency would be necessary to account for the finest details of the structure and of the source spectrum but would require extensive geophysical measurements (array noise techniques, noise correlation, active refraction, and reflection seismics). Despite these limitations, the success of the model is certainly due to the simplicity of the geometry and structure of the basin, compared with other sites (e.g., the Los Angeles basin, Komatitsch *et al.*, 2004). This justifies *a posteriori* the choice of this valley as a pilot site. In particular, the simulations allowed us to study the relative contributions of topography and sediments to site effects which, from an experimental viewpoint, would only be achievable by setting up very dense surface and borehole instrumentation. In the Bagnères basin, the sedimentary filling is clearly at the origin of the dominant contribution (Figs. 14, 16). Significant topographic amplifications may, however, be observed in some cases along the narrow crests in the mountains; they depend on the wave polarity with respect to crest direction (Fig. 14), a geometrical effect previously observed at other sites (e.g., Lovati *et al.*, 2010; Pischiutta *et al.*, 2010). By contrast, no significant influence of the valley orientation could be observed on peak ground acceleration inside the basin (except some resonances in the uppermost narrow valley, see Fig. 14b and Ⓔ Fig. S2b, available in the electronic supplement to this paper). This is because the wavelengths considered are small with respect to the size of the basin, whereas they are comparable to the width of the topographic crests. The numerical simulations also suggest that the high amplifications on the flanks of the valley (close to 8 at BBHC and BBAR, Fig. 10) are probably not of topographic origin, but an effect of local geological characteristics.

The most prominent feature of the amplification maps, as revealed by the 3D-modeling, is the basin edge effect, which predicts an overamplification of the PGA by a factor of about 2 in the basin at some distance of the mountain foot. This distance is about 100–200 m for the moderate events we considered, but could become larger for large magnitude events that excite lower frequencies. A PGA decrease by a factor of about 2 is also observed immediately at the edge of the basin. These predictions are in general good agreement with the observations. Note that without this modeling, it would have been difficult to guess the origin of the very low amplitudes at BBMU (Figs. 3, 18a). It is also interesting to note that, at some stations, the PGA is not due to the direct *S* wave, but to some energetic coda waves arriving a few seconds later.

Important lessons had been drawn from previous studies devoted to large earthquakes (such as Northridge in 1994 and Kobe in 1995). In regions of moderate seismicity, a light experiment similar to that conducted in Bagnères is an efficient and nonexpensive way to analyze in a systematic way the influence of different parameters describing the valley response to seismic excitation. Our results are mostly based on observations of local small to moderate events and on simulations in a limited frequency range. It is likely that large, regional earthquakes would reveal different soil responses, in particular at low frequency, some effects that would require a much longer and heavier experiment to be investigated. Our study shows, however, that numerical modeling may offer now a good way to tackle such issues at somewhat low cost.

Data and Resources

Accelerometric data are available at the Réseau Accélérométrique Permanent in Grenoble, France, on request, or at http://www-rap.obs.ujf-grenoble.fr (last accessed March 2011). The topographic map is from the French Institut Géographique National (Saint-Mandé, France); the geological map is from the Bureau de Recherches Géologiques et Minières (Orléans, France). The spectral element simulations were performed on the high-performance computing

facilities of the Service Commun de Calcul Intensif de l'Observatoire de Grenoble for the plane wave cases. Simulations for the realistic source were performed at the Commissariat à l'Energie Atomique CCRT (GENCI project 2011046060). They required 290 cores for calculation during 5.5 hours. CityShark™, an instrument with a software package Geopsy (http://www.geopsy.org, last accessed March 2011), was used to measure the impact of urban noise on soil response variability through the whole city of Bagnères (Chatelain *et al.*, 2000; Wathelet *et al.*, 2008). Most of the figures in this study have been drawn with the Generic Mapping Tool software (Wessel and Smith, 1991).

Acknowledgments

We thank the different organizations that support the French Accelerometric Network and the French Ministry of Ecology, which supported this project. Part of the funding was also provided by the European Regional Development Fund (ERDF/FEDER), POCTEFA program, in the frame of the SISPyr (Système d'Information Sismique des Pyrénées) project. We also thank the persons and institutions who hosted stations, the mayor of Bagnères-de-Bigorre, M. Sylvander for extraction of the Digital Elevation Model and focal solution computations, and the Commissariat à l'Energie Atomique (CEA) for the access to its high-performance computing facilities. We also thank two anonymous reviewers and the associate editor, S. Parolai, for helpful comments.

References

Aki, K. (1957). Space and time spectra of stationary stochastic waves, with special reference to microtremors, *Bull. Earthq. Res. Inst. Tokyo* **35,** 415–457.

Alimen, H. (1964). Le Quaternaire des Pyrénées de la Bigorre, *Mém. Carte Géol. France*, Paris, Imp. Nat., 394 pp. (in French).

Arai, H., and K. Tokimatsu (2005). *S*-wave velocity profling by joint inversion of microtremor dispersion curve and horizontal-to-vertical (H/V) spectrum, *Bull. Seismol. Soc. Am.* **95,** 1766–1778.

Assimaki, D., W. Li, J. H. Steidl, and K. Tsuda (2008). Site amplification and attenuation via downhole array seismogram inversion: A comparative study of the 2003 Miyagi-Oki aftershock sequence, *Bull. Seismol. Soc. Am.* **98,** 301–330.

Azambre, B., F. Crouzel, E.-J. Debroas, J.-C. Soulé, and Y. Ternet (1989). *Carte géologique, Notice explicative de la feuille Bagnères-de-Bigorre à 1/50000*, Ed. B. R. G. M., Orléans, France (in French).

Babault, J., J. Van den Driessche, S. Bonnet, S. Castelltort, and A. Crave (2005). Origin of the highly elevated Pyrenean peneplain, *Tectonics* **24,** 2010–2019.

Bard, P.-Y. (1999). Microtremor measurements: A tool for site effect estimation? in *The Effects of Surface Geology on Seismic Motion*, Kudo Irikura, Okada, and Sasatani (Editors), Balkema, Rotterdam, 1251–1279.

Bard, P. Y., and M. Bouchon (1985). The two-dimensional resonance of sediment-filled valleys, *Bull. Seismol. Soc. Am.* **75,** 519–541.

Bertrand, E., A. Duval, M. Castan, and S. Vidal(2007). 3D Geotechnical Soil Model of Nice, France, Inferred from Seismic Noise Measurements, for Seismic Hazard Assessment, *American Geophysical Union, Fall Meeting 2007*, abstract #NS11D-0798.

Bindi, D., S. Parolai, F. Cara, G. Di Giulio, G. Ferretti, L. Luzi, G. Monachesi, F. Pacor, and A. Rovelli (2009). Site amplifications observed in the Gubbio Basin, Central Italy: Hints for lateral propagation effect, *Bull. Seismol. Soc. Am.* **99,** 741–760.

Bonnefoy-Claudet, S., F. Cotton, and P. Y. Bard (2006). The nature of noise wavefield and its applications for site effects studies: A literature review, *Earth Sci. Rev.* **79,** 205–227.

Bonnefoy-Claudet, S., C. Cornou, P. Y. Bard, F. Cotton, P. Moczo, J. Kristek, and D. Fäh (2006). H/V ratio: A tool for site effects evaluation. Results from 1D noise simulations, *Geophys. J. Int.* **167,** 827–837.

Bonnefoy-Claudet, S., A. Köhler, C. Cornou, M. Wathelet, and P. Y. Bard (2008). Effects of Love waves on microtremor H/V ratio, *Bull. Seismol. Soc. Am.* **98,** 288–300.

Borcherdt, R. D. (1970). Effects of local geology on ground motion near San Francisco Bay, *Bull. Seismol. Soc. Am.* **60,** 29–81.

Bouchon, M. (1973). Effect of topography on surface motion, *Bull. Seismol. Soc. Am.* **63,** 615–632.

Cadet, H., P.-Y. Bard, and A. Rodriguez-Marek (2010). Defining standard rock site: Proposition based on the KiK-net database, *Bull. Seismol. Soc. Am.* **100,** 172–195.

Capon, J. (1969). High-resolution frequency-wavenumber spectrum analysis, *Proc. of the IEEE* **57,** 1408–1419.

Castellaro, F., and F. Mulargia (2010). How far from a building does the ground-motion free-field start? The case of the three famous towers and a modern building, *Bull. Seismol. Soc. Am.* **100,** 2080–2094.

Chaljub, E., D. Komatitsch, J.-P. Vilotte, Y. Capdeville, B. Valette, and G. Festa (2007). Spectral-element analysis in seismology, in *Advances in Wave Propagation in Heterogeneous Media, Advances in Geophysics*, R. Wu and V. Maupin (Editors), Elsevier Academic Press, Amsterdam, 365–419.

Chaljub, E., P. Moczo, S. Tsuno, P.-Y. Bard, M. Käser, M. Stupazzini, and M. Kristekova (2010). Quantitative comparison of four numerical predictions of 3D ground motion in the Grenoble Valley, France, *Bull. Seismol. Soc. Am.* **100,** 1427–1455.

Chatelain, J. L., P. Guéguen, B. Guillier, J. Fréchet, F. Bondoux, J. Sarrault, P. Sulpice, and J. M. Neuville (2000). CityShark: A user-friendly instrument dedicated to ambient noise (microtremor) recording for site and building response studies, *Seismol. Res. Lett.* **71,** 698–703.

Chávez-García, F. J., J. C. Castillo, and W. R. Stephenson (2002). 3D site effects: A thorough analysis of a high-quality dataset, *Bull. Seismol. Soc. Am.* **92,** 1941–1951.

Chávez-García, F. J., D. Raptakis, K. Makra, and K. Pitilakis (2000). Site effects at Eurosesstest-II. Results from 2D numerical modeling and comparison with observations, *Soil Dynam. Earthquake Engin.* **19,** 23–39.

Choukroune, P. (1992). Tectonic evolution of the Pyrenees, *Annu. Rev. Earth Planet. Lett.* **20,** 143–158.

Cornou, C., and P.-Y. Bard (2003). Site-to-bedrock over 1D transfer function ratio: An indicator of the proportion of edge-generated surface waves? *Geophys. Res. Lett.* **30,** 1453–1457.

Cornou, C., P.-Y. Bard, and M. Dietrich (2003). Contribution of dense array analysis to basin-edge-induced waves identification and quantification: Application to Grenoble basin, French Alps (II), *Bull. Seismol. Soc. Am.* **93,** 2624–2648.

Courboulex, F., C. Larroque, A. Deschamps, C. Kohrs-Sansorny, C. Gélis, J. L. Got, J. Charreau, J. F. Stéphan, N. Béthoux, J. Virieux, D. Brunel, C. Maron, A. M. Duval, J-L. Perez, and P. Mondielli (2007). Seismic hazard on the French Riviera: Observations, interpretations and simulations, *Geophys. J. Int.* **170,** 387–400.

Drouet, S., A. Souriau, and F. Cotton (2005). Attenuation, seismic moment and site effects for week motion events: Application to the Pyrenees, *Bull. Seismol. Soc. Am.* **95,** 1731–1748.

Dubos, N., A. Souriau, C. Ponsolles, and J. F. Fels (2003). Etude des effets de site dans la ville de Lourdes (Pyrénées, France) par la méthode des rapports spectraux, *Bull. Soc. Géol. Fr.* **174,** 33–44 (in French).

Dubos, N., M. Sylvander, A. Souriau, C. Ponsolles, S. Chevrot, J. F. Fels, and S. Benahmed (2004). Analysis of the May 2002 earthquake sequence in the central Pyrenees: Consequences for the evaluation of the seismic risk at Lourdes, France, *Geophys. J. Int.* **156,** 527–540.

ECORS Pyrenees Team (1988). The ECORS deep reflection seismic survey across the Pyrenees, *Nature* **331,** 508–510.

Endrun, B. (2010). Love wave contribution to the ambient vibration H/V amplitude peak observed with array measurements, *J. Seismol.*, doi 10.1007/s10950-010-9191-x.

Fäh, D., F. Kind, and D. Giardini (2001). A theoretical investigation of average H/V ratios, *Geophys. J. Int.* **145,** 535–549.

Fäh, D., M. Wathelet, M. Kristekova, H. B. Havenith, B. Endrun, G. Stamm, V. Poggi, J. Burjanek, and C. Cornou (2009). Using Ellipticity Information for Site Characterization, *Network of Research Infrastructures for European Seismology, Deliverable JRA4-D4*, EC project number 026130, 54 pp.

Goel, R. K., and A. K. Chopra (1998). Period formulas for concrete shear wall buildings, *J. Struct. Eng. ASCE* **124,** 426–433.

Guéguen, P., P.-Y. Bard, and C. S. Oliveira (2000). Experimental and numerical analysis of soil motions caused by free vibrations of a building model, *Bull. Seismol. Soc. Am.* **90,** 1464–1479.

Guéguen, P., C. Cornou, S. Garambois, and J. Banton (2007). On the limitation of the H/V spectral ratio using seismic noise as an exploration tool. Application to the Grenoble basin (France), *Pure Appl. Geoph.* **164,** 115–134.

Haghshenas, E., P. Y. Bard, and N. TheodulidisSESAME WP04 Team (2008). Empirical evaluation of microtremor H/V spectral ratio, *Bull. Earthq. Eng.* **6,** 75–108.

Hallier, S., E. Chaljub, M. Bouchon, and H. Sekiguchi (2008). Revisiting the basin-edge effect at Kobe during the 1995 Hyogo-Ken Nanbu earthquake, *Pure Appl. Geophys.* **165,** 1751–1760.

Hartzell, S., D. Carver, R. A. Williams, S. Harmsen, and A. Zerva (2003). Site response, shallow shear-wave velocity, and wave propagation at the San Jose, California, dense seismic array, *Bull. Seismol. Soc. Am.* **93,** 443–464.

Hartzell, S., L. Ramirez-Guzman, D. Carver, and Pengcheng Liu (2010). Short baseline variations in site response and wave-propagation effects and their structural causes: Four examples in and around the Santa Clara Valley, California, *Bull. Seismol. Soc. Am.* **100,** 2264–2286.

Hennino, R., N. Trégourès, N. M. Shapiro, L. Margerin, M. Campillo, B. A. van Tiggelen, and R. L. Weaver (2001). Observation of equipartition of seismic waves, *Phys. Rev. Lett.* **86,** 3447–3450.

Hirn, A., M. Daignières, J. Gallart, and M. Vadell (1980). Explosion seismic sounding of throws and dips in the continental Moho, *Geophys. Res. Lett.* **7,** 263–266.

Hisada, Y. (1994). An efficient method for computing Green's functions for a layered half-space with sources and receivers at close depths, *Bull. Seismol. Soc. Am.* **84,** 1456–1472.

Hisada, Y. (1995). An efficient method for computing Green's functions for a layered half-space with sources and receivers at close depths (Part 2), *Bull. Seismol. Soc. Am.* **85,** 1080–1093.

Hobiger, M. (2011). Polarization of surface waves: Characterization, inversion and application to seismic hazard assessment, *Ph.D. Thesis*, Grenoble University, 301 pp.

Hobiger, M., C. Cornou, N. Le Bihan, B. Endrun, F. Renalier, G. Di Giulio, A. Savvaidis, M. Wathelet, and P.-Y. Bard (2010). Joint inversion of Rayleigh wave ellipticity and spatial autocorrelation measurements, *SSA 2010 annual meeting*, 21–23 April, Portland, Oregon.

Kawase, H., and K. Aki (1990). Topography effect at the critical SV wave incidence: Possible explanation of damage pattern by the Whittier-Narrows, California, earthquake of 1 October 1987, *Bull. Seismol. Soc. Am.* **80,** 1–22.

Kawase, H. (1996). The cause of the damage belt in Kobe: "The basin-edge effect", constructive interference of the direct *S* wave with the basin-induced diffracted/Rayleigh wave, *Seismol. Res. Lett.* **67,** 25–34.

Komatitsch, D., and J. Tromp (1999). Introduction to the spectral-element method for 3-D seismic wave propagation, *Geophys. J. Int.* **139,** 806–822.

Komatitsch, D., and J.-P. Vilotte (1998). The spectral element method: An efficient tool to simulate the seismic response of 2D and 3D geological structures, *Bull. Seismol. Soc. Am.* **88,** 368–392.

Komatitsch, D., Q. Liu, J. Tromp, P. Süss, C. Stidham, and J. H. Shaw (2004). Simulations of ground motion in the Los Angeles basin based upon the spectral-element method, *Bull. Seismol. Soc. Am.* **94,** 187–206.

Komatitsch, D., S. Tsuboi, and J. Tromp (2005). The spectral-element method in seismology, in *Seismic Earth: Array Analysis of Broadband Seismograms*, American Geophysical Monograph **157,** 205–227.

Lachet, C., and P. Y. Bard (1994). Numerical and theoretical investigations on the possibilities and limitations of Nakamura's technique, *J. Phys. Earth* **42,** 337–397.

Lambert, J., A. Levret-Albaret, M. Cushing, and C. Durouchoux (1996). *Mille ans de séismes en France*, Ouest Editions, Nantes, France, 70 pp. (in French).

LeBrun, B., D. Hatzfeld, and P.-Y. Bard (2001). Site effects study in urban area: Experimental results in Grenoble, *Pure Appl. Geophys.* **158,** 2543–2557.

Lermo, J., and F. J. Chávez-García (1993). Site effect evaluation using spectral ratios with only one station, *Bull. Seismol. Soc. Am.* **83,** 1574–1594.

Levret, A., J. C. Backe, and M. Cushing (1994). Atlas of macroseismic maps for French earthquakes with their principal characteristics, *Nat. Hazards* **10,** 19–46.

Lomax, A., and R. Snieder (1994). Finding sets of acceptable solutions with a genetic algorithm with application to surface wave group dispersion in Europe, *Geophys. Res. Lett.* **21,** 2617–2620.

Lovati, S., M. Bakalovi, M. Massa, G. Ferretti, F. Pacor, and R. Paolucci (2010). Experimental approach for estimating seismic amplification effects at the top of a ridge and their interpretation on ground motion predictions: The case of Narni (central Italy), *Geophys. Res. Abstracts* **12,** EGU2010-4955-1.

Lysmer, J., and R. L. Kuhlemeyer (1969). Finite dynamic model for infinite media, *J. Engin. Mechanics Division, ASCE* **95,** no. EM4, 859–877.

Malischewsky, P. G., and F. Scherbaum (2004). Love's formula and H/V-ratio (ellipticity) of Rayleigh waves, *Wave Motion* **40,** 57–67.

Manakou, M. V., D. G. Raptakis, F. J. Chávez-García, P. I. Apostolidis, and K. D. Pitilakis (2010). 3D soil structure of the Mygdonian basin for site response analysis, *Soil Dynam. Earthquake Eng.* **30,** 1198–1211.

Margerin, L. (2009). Generalized eigenfunctions of layered elastic media and application to diffuse fields, *J. Acoust. Soc. Am.* **125,** 164–174.

Margerin, L., M. Campillo, B. A. van Tiggelen, and R. Hennino (2009). Energy partition of seismic coda waves in layered media: Theory and application to Pinyon Flats Observatory, *Geophys. J. Int.* **177,** 571–585.

Mozco, P., J. O. A. Robertsson, and L. Eisner (2007). The finite-difference time-domain method for modeling of seismic wave propagation, in *Advances in Wave Propagation in Heterogeneous Earth*, R.-S. Wu and V. Maupin (Editors) Elsevier, Amsterdam, Advances in Geophysics **48,** 421–516.

Nakamura, Y. (1989). A method for dynamic characteristics estimation of subsurface using microtremor on the ground surface, *Quarterly Report of Railway Technical Research Institute (RTRI), Japan* **30,** no. 1, 25–33.

Park, C. B., R. D. Miller, and J. Xia (1999). Multi-channel analysis of surface waves, *Geophysics* **64,** 800–808.

Parolai, S., P. Bormann, and C. Milkereit (2001). Assessment of the natural frequency of the sedimentary cover in the Cologne area (Germany) using noise measurements, *J. Earthquake Eng.* **5,** 541–564.

Parolai, S., M. Picozzi, S. M. Richwalski, and C. Milkereit (2005). Joint inversion of phase velocity dispersion and H/V ratio curves from seismic noise recordings using a genetic algorithm, considering higher modes, *Geophys. Res. Lett.* **32,** L01303, doi 10.1029/2004GL021115.

Pedersen, H. A., F. J. Sánchez-Sesma, and M. Campillo (1994). Three-dimensional scattering by two-dimensional topographies, *Bull. Seismol. Soc. Am.* **84,** 1169–1183.

Pequegnat, C., P. Gueguen, D. Hatzfeld, and M. Langlais (2008). The French Accelerometric network (RAP) and national data center (RAP-NDC), *Seismol. Res. Lett.* **79,** 79–89.

Perrouty, S. (2008). Mesures géophysiques du remplissage sédimentaire Quaternaire dans les vallées de Bagnères-de-Bigorre et d'Argelès-Gazost, *M2 report LMTG-University Toulouse III*, 30 pp. (in French).

Peterson, J. (1993). Observation and modeling of seismic background noise, *U.S. Geol. Surv. Tech. Rept. 93-322*, 1–95.

Phillips, W. S., and K. Aki (1986). Site amplification of coda waves from local earthquakes in central California, *Bull. Seismol. Soc. Am.* **76,** 627–648.

Picozzi, M., S. Parolai, and S. M. Richwalski (2005). Joint inversion of H/V ratios and dispersion curves from seismic noise: Estimating the *S*-wave velocity of bedrock, *Geophys. Res. Lett.* **32,** L11308, doi 10.1029/2005GL022878.

Pischiutta, M., G. Cultrera, A. Caserta, and L. Luzi (2010). Topographic effects on the hill of Nocera Umbra, central Italy, *Geophys. J. Int.* **182,** 977–987.

Pitarka, A., K. Irikura, T. Iwata, and H. Sekiguchi (1998). Three-dimensional simulation of the near-fault ground motion for the Hyogo-ken Nanbu (Kobe), Japan, earthquake, *Bull. Seismol. Soc. Am.* **88,** 428–440.

Rigo, A., A. Souriau, N. Dubos, M. Sylvander, and C. Ponsolles (2005). Analysis of the seismicity in the central part of the Pyrenees (France), and tectonic implications, *J. Seismol.* **9,** 211–222.

Satoh, T., H. Kawase, and S. Matsushima (2001). Differences between site characteristics obtained from microtremors, *S* waves, *P* waves, and codas, *Bull. Seismol. Soc. Am.* **91,** 313–334.

Scherbaum, F., F. K. Hinzen, and M. Ohrnberger (2003). Determination of shallow shear wave velocity profiles in the Cologne, Germany area using ambient vibrations, *Geophys. J. Int.* **152,** 597–612.

Souriau, A., and H. Pauchet (1998). A new synthesis of Pyrenean seismicity and its tectonic implications, *Tectonophysics* **290,** 221–244.

Souriau, A., A. Roullé, and C. Ponsolles (2007). Site effects in the city of Lourdes, France, from H/V measurements. Implications for seismic risk evaluation, *Bull. Seismol. Soc. Am.* **97,** 2118–2136.

Steidl, J. H., A. G. Tumarkin, and R. J. Archuleta (1996). What is a reference site? *Bull. Seismol. Soc. Am.* **86,** 1733–1748.

Stephenson, W. J., S. Hartzell, A. D. Frankel, M. Asten, D. L. Carver, and W. Y. Kim (2009). Site characterization for urban seismic hazard in lower Manhattan, New York City, from microtremor array analysis, *Geophys. Res. Lett.* **36,** L03301.

Strollo, A., S. Parolai, K.-H. Jäckel, S. Marzotari, and D. Bindi (2008). Suitability of short-period sensors for retrieveing reliable H/V peaks for frequencies less than 1 Hz, *Bull. Seismol. Soc. Am.* **98,** 671–681.

Sylvander, M., A. Souriau, A. Rigo, A. Tocheport, J.-P. Toutain, C. Ponsolles, and S. Benahmed (2008). The 2006 November, $M_L =$ 50 earthquake near Lourdes (France): New evidence for NS extension across the Pyrenees, *Geophys. J. Int.* **175,** 649–664.

Uebayashi, H. (2003). Extrapolation of irregular subsurface structures using the horizontal-to-vertical spectral ratio of long-period microtremors, *Bull. Seismol. Soc. Am.* **93,** 570–582.

Wathelet, M. (2008). An improved neighborhood algorithm: Parameter conditions and dynamic scaling, *Geophys. Res. Lett.* **35,** L09301, doi 10.1029/2008 GL033256.

Wathelet, M., D. Jongmans, M. Ohrnberger, and S. Bonnefoy-Claudet (2008). Array performances for ambient vibrations on a shallow structure and consequences over V_S inversion, *J. Seismol.* **12,** 1–19.

Wessel, P., and W. H. F. Smith (1991). Free software helps map and display data, *Eos Trans. AGU* **72,** 441.

CNRS and Université Paul Sabatier
Observatoire Midi-Pyrénées
14 Avenue Edouard Belin
31400—Toulouse, France
Annie.Souriau@dtp.obs-mip.fr
(A.S., L.M., M.C., J.M.)

ISTerre, Maison des géosciences
BP 53X, 38041
Grenoble Cedex, France
(E.C., C.C., M.W., C.P., M.L., P.G.)

Observatoire Midi-Pyrénées
57 Avenue d'Azereix
65007-Tarbes, France
(F.G., Ch.P.)

Manuscript received 20 October 2010

Bulletin of the Seismological Society of America, Vol. 105, No. 3, pp. –, June 2015, doi: 10.1785/0120140228

Earthquake Ground Motion in the Mygdonian Basin, Greece: The E2VP Verification and Validation of 3D Numerical Simulation up to 4 Hz

by E. Maufroy, E. Chaljub, F. Hollender,* J. Kristek, P. Moczo, P. Klin, E. Priolo, A. Iwaki,† T. Iwata, V. Etienne,‡ F. De Martin, N. P. Theodoulidis, M. Manakou, C. Guyonnet-Benaize, K. Pitilakis, and P.-Y. Bard

Abstract In a low-seismicity context, the use of numerical simulations becomes essential due to the lack of representative earthquakes for empirical approaches. The goals of the EUROSEISTEST Verification and Validation Project (E2VP) are to provide (1) a quantitative analysis of accuracy of the current, most advanced numerical methods applied to realistic 3D models of sedimentary basins (verification) and (2) a quantitative comparison of the recorded ground motions with their numerical predictions (validation). The target is the EUROSEISTEST site located within the Mygdonian basin, Greece. The site is instrumented with surface and borehole accelerometers, and a 3D model of the medium is available. The simulations are performed up to 4 Hz, beyond the 0.7 Hz fundamental frequency, thus covering a frequency range at which ground motion undergoes significant amplification. The discrete representation of material heterogeneities, the attenuation model, the approximation of the free surface, and nonreflecting boundaries are identified as the main sources of differences among the numerical predictions. The predictions well reproduce some, but not all, features of the actual site effect. The differences between real and predicted ground motions have multiple origins: the accuracy of source parameters (location, hypocentral depth, and focal mechanism), the uncertainties in the description of the geological medium (damping, internal sediment layering structure, and shape of the sediment-basement interface). Overall, the agreement reached among synthetics up to 4 Hz despite the complexity of the basin model, with code-to-code differences much smaller than predictions-to-observations differences, makes it possible to include the numerical simulations in site-specific analysis in the 3D linear case and low-to-intermediate frequency range.

Introduction: The EUROSEISTEST Verification and Validation Project (E2VP)

The estimation of site effects within the framework of a seismic-hazard study can involve different approaches, both empirical and numerical. However, in the context of low or moderate seismicity, the use of empirical approaches is difficult to implement due to the lack of representative earthquakes. Consequently, the application of numerical tools becomes essential. During the last decades, an important effort has been dedicated to develop accurate and computationally efficient numerical methods for predicting earthquake ground motion in heterogeneous media, especially in 3D (e.g., Moczo *et al.*, 2014). Henceforth, the progress in methods and the increasing capability of computers make it technically feasible to calculate realistic seismograms for frequencies of interest in seismic design applications (Kawase and Matsushima, 1998; Day *et al.*, 2001, 2003, 2005; Satoh *et al.*, 2001; Komatitsch *et al.*, 2004; Bielak *et al.*, 2010; Chaljub *et al.*, 2010).

However, before using the 3D ground-motion simulation codes for civil engineering design purposes, it is necessary to verify their accuracy and validate them for sedimentary basins (as they represent a typical situation for many important cities and critical facilities). Several international blind prediction tests were designed to compare numerical modeling methods and evaluate their capability to model earthquake ground motion in surface sedimentary structures. Beginning with the Turkey Flat, California (Cramer, 1995), and Ashigara Valley, Japan (e.g., Bard,

*Also at ISTerre, Univ. Grenoble Alpes, CNRS, IRD, IFSTTAR, BP 53, F-38041 Grenoble CEDEX 09, France.

†Now at National Research Institute for Earth Science and Disaster Prevention, 3-1 Tennodai, Tsukuba, Ibaraki 305-0006, Japan.

‡Now at Saudi Aramco, EXPEC Advanced Research Center. Dhahran, Saudi Arabia.

1992), blind tests focused on the effects of surface sediments; these were followed by the more comprehensive comparison exercises on the Osaka–Kobe basin area in Japan (Kawase and Iwata, 1998) and on the southern California area within the Southern California Earthquake Center (SCEC) framework (Day *et al.*, 2001, 2003, 2005; Bielak *et al.*, 2010), which also included the effects of extended sources and regional propagation in the low-frequency range. The Effects of Surface Geology 2006 (ESG2006) exercise focused on the Grenoble valley in the French Alps (Chaljub *et al.*, 2006, 2010; Tsuno *et al.*, 2006) and revealed that 3D numerical simulations were far from being a "press-button" tool. Among the lessons learned in this exercise, one was especially important for practical applications: predictions of the earthquake ground motion in complex geological structures should be made using at least two different but comparably accurate methods to enhance the reliability of the predictions. This conclusion is consistent with the well-known fact that no single method can indeed be considered as the best for all relevant medium-wavefield configurations (i.e., all important combinations of source characteristics and underground structures), in terms of accuracy and computational efficiency.

The ESG2006 exercise included only the verification of the numerical methods. We recall the concepts of verification and validation (e.g., Moczo *et al.*, 2014): verification of a numerical method may be defined as the demonstration of the consistency of the numerical method with the original mathematical–physical problem defined by the controlling equation, constitutive law, and initial and boundary conditions. The quantitative analysis of accuracy should be a part of the verification. Once the numerical method is analyzed and verified for accuracy, it should be validated using observations. In general, the validation may be defined as the demonstration of the capability of the theoretical model (i.e., the mathematical–physical model and its numerical approximation) to predict and reproduce observations.

The main motivation of the EUROSEISTEST Verification and Validation Project (E2VP) is a follow-up on this series of comparative exercises, with an extension to the validation part for the most advanced numerical modeling methods. E2VP is an international collaborative project (see Table 1), organized jointly by: the Aristotle University of Thessaloniki, Greece; the ITSAK (Institute of Engineering Seismology and Earthquake Engineering of Thessaloniki), Greece; the Cashima research project (supported by the French Alternative Energies and Atomic Energy Commission [Commisariat à l'énergie atomique et aux énergies alternatives, or CEA] and by the Laue-Langevin Institute [ILL], Grenoble); and ISTerre at Grenoble Alpes University, France. The E2VP target site is the Mygdonian basin near Thessaloniki, Greece, which is the international research and test site of many international seismological and earthquake-engineering projects. To foster the use of linear 3D numerical simulations in practical prediction, E2VP was designed to (1) evaluate the accuracy of the current most-advanced numerical methods when applied to realistic 3D models and (2) provide an objective, quantitative comparison between recorded earthquake ground motions and their numerical predictions. Part of the results obtained in these efforts is presented here.

Table 1
Teams and Institutions Contributing to the 3D Numerical Simulations of This Study

Institution	Country	Town	Team Acronym
Comenius University of Bratislava	Slovakia	Bratislava	CUB
Université Joseph Fourier	France	Grenoble	UJF
Disaster Prevention Research Institute, Kyoto University	Japan	Kyoto	DPRI
Istituto Nazionale di Oceanografia e Geofisica Sperimentale	Italy	Trieste	OGS
Université de Nice, Sophia Antipolis	France	Valbonne	UNICE
Bureau de Recherches Géologiques et Minières	France	Orléans	BRGM

The article is accompanied by the methodological study of Chaljub *et al.* (2015). It focuses on quantitative and qualitative analysis of accuracy (i.e., verification) of four numerical modeling methods in their application to stringent canonical models directly related to the model of the Mygdonian basin.

The Target Site: The Mygdonian Basin, EUROSEISTEST, Greece

The first step of E2VP was to identify a suitable test site, that is, a site coupling a good preexisting geological, geophysical, and geotechnical characterization with a sufficient number of available recordings from adequately deployed seismic stations. Such conditions are rarely fulfilled within the Euro-Mediterranean area, and the selection process resulted in decision for the EUROSEISTEST site, located 30 km east-northeast of Thessaloniki, northeastern Greece (see Fig. 1).

The site is located at the center of the Mygdonian sedimentary basin between the Volvi and Lagada lakes, in the epicentral area of the magnitude 6.5 event that occurred in 1978 and damaged the city of Thessaloniki. The Mygdonian basin has been extensively investigated within the framework of various European projects (Pitilakis *et al.*, 2009). A detailed 3D model is available based on works by Manakou *et al.* (2007, 2010). Dense instrumentation, including surface accelerometers (Fig. 1) and a vertical array of six sensors spread over a depth of about 200 m at the central TST site, produced numerous accelerograms (Pitilakis *et al.*, 2013).

The basin has been shaped by north–south extensive tectonics, with east–west-trending normal faults on each side. The velocity structure of the basin is well constrained along the central north-northwest–south-southeast profile crossing

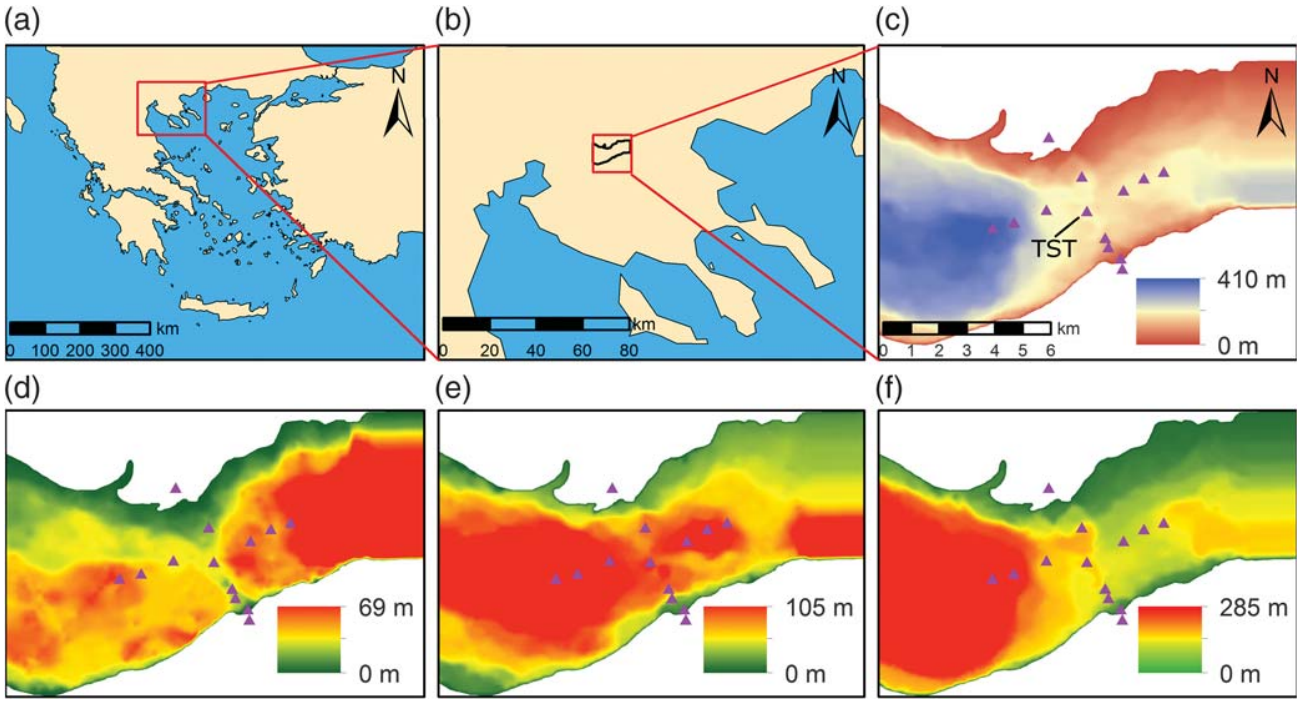

Figure 1. (a,b) Location of the EUROSEISTEST site within the Mygdonian basin in northeastern Greece; (c) total sediment thickness in the basin; thicknesses of (d) shallow layer 1 in the 3D model, (e) layer 2, and (f) deep layer 3 (see Table 2). Note the strong lateral variations and the asymmetries between the northern and southern edges, as well as between the western and eastern sides. The location of the EUROSEISTEST accelerometric array is represented by the purple triangles. The central accelerometric site TST appears as a saddle point, with a maximum of sediment thickness along a north–south profile and a minimum along an east–west profile.

the central TST site, based on a large number of geophysical and geotechnical measurements, surface and borehole seismic prospecting, electrical soundings, and microtremor recordings (Jongmans *et al.*, 1998; Raptakis *et al.*, 2000). Along that profile, the sediment thickness reaches its maximum at the TST site (196 m), and the *S*-wave velocity (V_S) increases from 130 m/s at the surface to about 800 m/s at a large depth. Because the velocity in the underlying bedrock is 2600 m/s, the velocity contrast at the sediment–bedrock interface is large. The 3D structure in the whole graben has been extrapolated from the central profile, taking into account information from many single-point microtremor measurements, array microtremor recordings, one east–west refraction profile, and old deep boreholes drilled for water exploration purposes (Raptakis *et al.*, 2005). The resulting detailed 3D model of the basin (Manakou, 2007; Manakou *et al.*, 2007, 2010) is 5 km wide and 15 km long, with the maximum sediment thickness reaching about 410 m. The TST site resembles a saddle point, with the sediment thickness increasing both eastward and westward, off the north-northwest–south-southeast central profile, which actually corresponds to a buried pass between two thicker sub-basins (Fig. 1). The slope of the northern basin edge is much gentler than the steep slope of the southern edge: the meshing of the 3D model thus requires specific attention and care, as the diffraction on the longer northern basin edge is very efficient. The whole area presents a rather smooth topography: a preliminary sensitivity study indicated only negligible impacts on ground motion (waveforms and engineering parameters), and it was decided to not include the topography in the main E2VP simulations. It was flattened, changing the elevation of each interface but keeping unchanged the local thickness of the various layers.

The mechanical properties of the 3D models are given in Table 2. We used two different velocity models (A and B). Realistic model A consists of three sediment layers with laterally varying thicknesses, according to the propositions by Manakou *et al.* (2007, 2010). Within these three layers, properties are constant (homogeneous). Model B keeps exactly the same geometry but replaces the homogeneous layers with increasing-velocity linear gradients to avoid any internal velocity jumps within the sedimentary filling. Model B is a smoothed version of model A and was designed only for the verification purposes of this study. Outside the basin, the crustal 1D velocity model of Papazachos (1998) has been considered for the regional propagation. The attenuation is assumed to be correctly represented by a frequency-independent quality factor Q and a reference frequency of 1 Hz.

Some features of the models deserve a special mention because of their impact on the difficulty of the numerical simulations: (1) the simultaneous existence of a soft shallow layer and of a high water table, with $V_S = 200$ m/s and *P*-wave–to–*S*-wave velocity ratio $V_P/V_S = 7.5$, and (2) a very hard bedrock leading to large impedance contrast and effi-

Table 2
Mechanical Properties of the Two 3D Models Used in the Present Study

Model	Layer	V_S (m/s)	V_P (m/s)	ρ (kg/m3)	Q_S	Q_κ
Layered model A (constant properties within layers)	1	200	1500	2100	20	∞
	2	350	1800	2200	35	∞
	3	650	2500	2200	65	∞
Smooth model B (linear increasing gradient within layers)	1	200–250	1500–1600	2100	20–25	∞
	2	250–500	1600–2200	2100–2130	25–50	∞
	3	500–900	2200–2800	2130–2250	50–90	∞
Bedrock		2600	4500	2600	260	∞

In layered model A, each layer has homogeneous properties but laterally varying thickness. Smooth model B is built with linear velocity gradients and without any discontinuity within the sediments. Model B is designed only for verification purposes and is therefore not used in the validation (model A being the realistic model). V_S, *S*-wave velocity; V_P, *P*-wave velocity; ρ, mass density; Q_S, shear quality factor; and Q_κ, bulk quality factor. The Q values are assumed to be frequency independent.

cient wave trapping. Model details were defined for a maximum simulation frequency of 4 Hz.

How to Objectively Quantify the Similarity between Two Signals?

There are many ways to compare two seismograms in the time or frequency domain: each depends on the quantities to be compared (from the whole signal to selected engineering parameters) and on the method used to compute the differences between quantities. Recently, Kristeková *et al.* (2006, 2009) developed misfit criteria based on the time–frequency (TF) representation of the seismic signals using the continuous wavelet transform with the Morlet wavelet. Provided the signals under comparison are not too different, the TF misfit criteria are sensitive either to differences in envelope (amplitude) or in phase. The TF misfit criteria are therefore particularly well suited for the comparison of numerical synthetics (computed for the same models with different methods), and they allow a proper characterization of the nature of the differences between seismograms.

As is well known, waveform differences between earthquake records and their numerical predictions can be relatively large; however, an objective and quantitative way of comparing signals is necessary. From an engineering viewpoint, Anderson (2004) proposed characterizing the similarity between two seismograms by a goodness-of-fit (GOF) based on 10 ground-motion parameters commonly used in earthquake engineering: the peak acceleration, peak velocity, peak displacement, Arias intensity, the integral of squared velocity, Fourier spectrum and acceleration response spectrum on a frequency-by-frequency basis, the shape of the normalized integrals of acceleration and velocity squared (Husid plots), and the cross correlation. The investigated frequency range can be split into narrow frequency subintervals to be evaluated separately. The agreement between the two compared seismograms is quantified on each parameter by a GOF value between 0 and 10, with 10 meaning perfect agreement. Anderson (2004) also introduced the following verbal scale for GOF: a score below 4 is a poor fit, a score of 4–6 is a fair fit, a score of 6–8 is a good fit, and a score over 8 is an excellent fit. The Anderson GOF may be considered a robust criterion for comparing recordings with their numerical predictions.

Considering the somewhat redundant character of some components of the original Anderson parameters, we restricted our comparison in the present study to five parameters. Three of them are representative of the signal amplitude in different frequency bands: peak value of the acceleration time series (peak ground acceleration [PGA], C1); spectral acceleration at intermediate frequencies (around 2 Hz, C2); and spectral acceleration at lower frequencies (around 0.5 Hz, C3). The other two are representative of the total amount of energy contained in the signal (cumulative absolute velocity [CAV], C4) and of the duration (relative significant duration [RSD], C5). Arguments for the selected characteristics and details on their computations are provided in the Appendix. For these five ground-motion parameters, the direct misfit between two signals is quantified in percentage. The misfit value is positive when the prediction overestimates the target (or reference) signal, and negative when the prediction underestimates the target signal.

In this article, we also follow the GOF procedure by Kristeková *et al.* (2009) that describe the envelope and phase GOF criteria based on the TF misfit criteria. Thus, we consider the GOF as

$$\mathrm{GOF} = 10\exp(-|M|), \tag{1}$$

in which M represents a single-valued misfit in the envelope or phase. GOF ranges from 0 (no fit) to 10 (perfect fit); further details may be found in Kristeková *et al.* (2009): to summarize, a GOF value of 8 corresponds to a misfit of 20%, and a GOF value of 6 to a misfit of 50%. The TF-based GOF values are considered only in the verification part of E2VP, as the numerical predictions are sometimes too different from the actual recordings.

Verification: Cross-Comparisons between Various 3D Numerical Predictions of Ground Motion in the Mygdonian Basin

Several teams contributed to the verification phase of E2VP. They used a variety of methods or implementations of the same method: finite-difference method (FDM), Fourier

Table 3
Applied 3D Methods Used by the EUROSEISTEST Verification and Validation Project (E2VP) Participants to This Study

Team and 3D Acronyms	Method	Characterization	Attenuation	Absorbing Boundary Conditions	References
CUB 3D01	FDM	Finite difference, fourth-order velocity-stress volume arithmetic and harmonic averages of density and moduli, arbitrary discontinuous staggered grid	GZB 4 relaxation mechanisms	CPML	Kristek *et al.* (2002, 2010); Moczo *et al.* (2002, 2004, 2014)
UJF 3D02	SEM	Spectral element, Legendre fourth-order polynomial Gauss–Lobatto–Legendre integration	GZB 3 relaxation mechanisms	Stacey (1988)	Chaljub *et al.* (2007); Peter *et al.* (2011)
DPRI 3D03	FDM	Finite difference, fourth-order velocity-stress nonuniform staggered grid	linear $Q(f)$ $f_0 = 2$ Hz, Graves (1996)	Clayton and Engquist (1977) A1 + Cerjan	Pitarka (1999)
OGS 3D04	FPSM	Fourier pseudospectral, vertically stretching staggered grid	GZB 3 relaxation mechanisms	CPML	Klin *et al.* (2010)
UNICE 3D09	DGM	Discontinuous Galerkin, velocity-stress second-order Lagrangian polynomials with tetrahedral mesh and homogeneous physical properties within elements	n.a.	CPML	Etienne *et al.* (2010)
BRGM 3D11	SEM	Spectral element, Legendre fourth-order polynomial Gauss–Lobatto–Legendre integration	Memory variables with eight relaxation mechanisms	Stacey (1988) paraxial P1 approximation	De Martin (2011)

All methods are second-order in time. GZB, generalized Zener body; CPML, convolutional perfectly matched layer (Martin and Komatitsch, 2009); n.a., not applicable. See also Data and Resources.

pseudospectral method (FPSM), spectral-element method (SEM), and discontinuous Galerkin method (DGM). Additional details on each method can be found in Tables 1 and 3.

In what follows, we compare the 3D ground-motion simulations obtained with each code for a virtual M_w 1.3 event occurring beneath the Mygdonian basin, considering both the layered model A and the smooth model B (Table 2). A double-couple point source is assumed at 5 km depth beneath the TST central site (blue star in Fig. 2), with normal faulting to match the typical regional focal mechanism (strike, 260°; dip, 40°; rake, −90°); the source time function is a Heaviside step function low-pass filtered below 3 Hz with a 10-pole causal Butterworth filter. For each source-model configuration, the teams were required to simulate 30 s of ground motion at 287 receivers (yellow triangles in Fig. 2). The required frequency range up to 4 Hz was intended to cover the low-to-intermediate frequencies at which ground motion is significantly affected by the basin.

Layered Model with Attenuation

Figure 3a shows velocity seismograms at the central TST site simulated by five teams for the layered model A, including attenuation. Note the good agreement of all numerical predictions at early arrivals (less than 6 s), especially on the vertical component, and the large differences in phase and amplitude at late arrivals. Some of those differences, in particular in the amplitude of the later arrivals, are attributed to the fact that the method of team 3D03 applies a frequency dependence of Q: it approximates the required model value only near the reference frequency f_0, and an almost linear increase of Q with frequency is applied above f_0, whereas other teams modeled the required constant Q. Globally, the numerical predictions by teams 3D01, 3D02, 3D04, and 3D11 are very close in the whole time window.

Figures 4 and 5 show maps of the envelope and phase GOFs (equation 1) evaluated at the virtual receivers for numerical predictions by teams 3D01, 3D02, 3D03, 3D04, and 3D11. The GOF values are evaluated in the 0.5–4.0 Hz frequency range as the weighted average for the horizontal components of the ground velocity in Figure 4 and for the vertical component in Figure 5. "Weighted average" means that the larger component is given a proportionally larger weight; such a weighting was considered to avoid meaningless values corresponding to large relative differences on very weak components (for instance on rock near the nodal planes). Each small colored circle represents a value of GOF between numerical predictions by two teams for the corresponding receiver. The color scale ranges from an extremely poor fit (red) to an excellent fit (blue). The GOF maps are useful in tracking differences between numerical predictions. Table 4 summarizes the weighted averages (with the same amplitude-dependent weighting) of GOF evaluated for rock and soil (sedimentary) sites for the investigated verification cases. Figure 4 and Table 4 show that the results obtained by teams 3D01, 3D02, 3D04, and 3D11 for layered model A with attenuation are the most similar, with GOF values in the basin mostly comprised between 6 and 8 (good fit). Outside the basin, the GOF values rise above 8 (excellent fit) at the rock sites.

The smaller values of GOF between the 3D03 and other synthetics are mainly due to the differently implemented attenuation. The GOF values for the basin are mostly between 4 and 6 (fair fit) but fall under 4 for some central receivers. The level of agreement is smaller for envelopes. This is understandable: the attenuation mostly affects the amplitudes of the waveform.

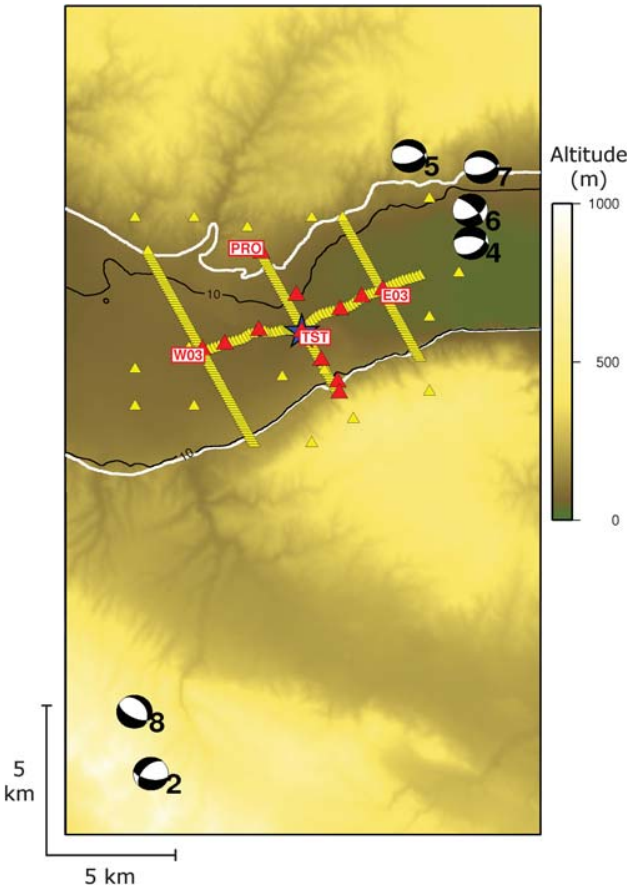

Figure 2. Detailed locations of the virtual central source (epicenter at the blue star) and of the six local real events (beachballs with event numbers) selected for the EUROSEISTEST Verification and Validation Project (E2VP) validation exercise and recorded by the EUROSEISTEST accelerometric network (red triangles), superimposed to the virtual receivers (yellow triangles) considered in the E2VP verification exercise. The white line denotes the basin edge, and the black line is the location where the sediment thickness equals 10 m. The background color scale corresponds to the free-surface elevation.

Layered Model without Attenuation

We next consider the case of the layered model A without attenuation to remove the differences caused by the implementation of attenuation. Consequently, the eventual differences should be mainly due to the discrete representation of material heterogeneities, to the numerical dispersion, and to spurious reflections from the boundaries of the numerical grid. Especially, the discrete representation and dispersion can considerably affect the solutions because locally generated surface waves propagate over relatively long distances in the perfectly elastic medium. The velocity seismograms at the central TST site simulated by the five teams are shown in Figure 3b. Dispersive surface waves dominate the waveforms. Large differences (in phase and amplitude) are observed on late arrivals (after 6 s), corresponding partly to surface waves diffracted off the valley edges and traveling toward the center of the basin without being attenuated.

Figure 6 shows the maps of envelope and phase GOFs (weighted average over the three components of ground velocity) between the numerical predictions by teams 3D01, 3D02, 3D03, 3D04, and 3D09. The overall level of GOFs is lower compared to the case with attenuation (see also the average GOF values for soil sites in Table 4). The general decrease of fit between the numerical predictions is mainly due to the large differences in late high-frequency arrivals, which are not attenuated compared to the case with attenuation. The phase GOF values are smaller than the amplitude GOFs: the numerical dispersion mostly affects the short-wavelength waves traveling over long distances.

Smooth Model without Attenuation

The presence of material interfaces in sediments in the layered model A certainly affects the generation and propagation of surface waves in sediments. The role of the material interfaces was pointed out by comparing the numerical predictions for the layered model A with and without attenuation. It is thus reasonable to include another comparison. The smooth model B has the same geometry of interfaces within sediments as the layered model A, but material parameters do not change at these interfaces. What changes at the interfaces is just the gradient (see the mechanical properties in Table 2). This is achieved by linear variations of parameters with depth inside layers.

Figure 3c shows the velocity seismograms at the central site TST, simulated in the smooth model B by teams 3D01, 3D02, 3D04, and 3D09. The similarity of the seismograms, including parts with surface-wave packets arriving at late times, is striking. The maps of the GOF values for the available predictions are shown in Figure 7, and the associated weighted average GOFs are given in Table 4 (see above for the weighting scheme). Compared to the GOF maps in Figure 6 for the elastic layered model A, it is clear that globally the GOF values for the smooth model B are considerably higher (see also Table 4 for the soil sites). Indeed, the GOF values obtained for the smooth model B are mostly above 6 in the basin and often rise above 8, whereas GOF values for the layered model A are one level lower (mostly above 4, often above 6, but almost all under 8). It is also noteworthy that the GOF values for the elastic smooth model B are larger than the GOF values for the layered model A with attenuation (compare Figs. 7 and 4). Material interfaces at which material parameters change discontinuously are thus clearly identified as one key factor that significantly affects the accuracy of the 3D numerical simulations. In other words (and from the optimistic viewpoint), it is not difficult to reach a very good level of agreement for the sedimentary basin with smooth variations of material parameters.

Discussion on the Comparison Criteria

Figure 8 displays the absolute values of misfits evaluated for the selected engineering criteria (C1–C5; see the Appendix) as a function of the GOF values evaluated according to equation (1) for the three basin models and for teams 3D01, 3D02, 3D04, 3D09, and 3D11. We can see a very satisfactory relation-

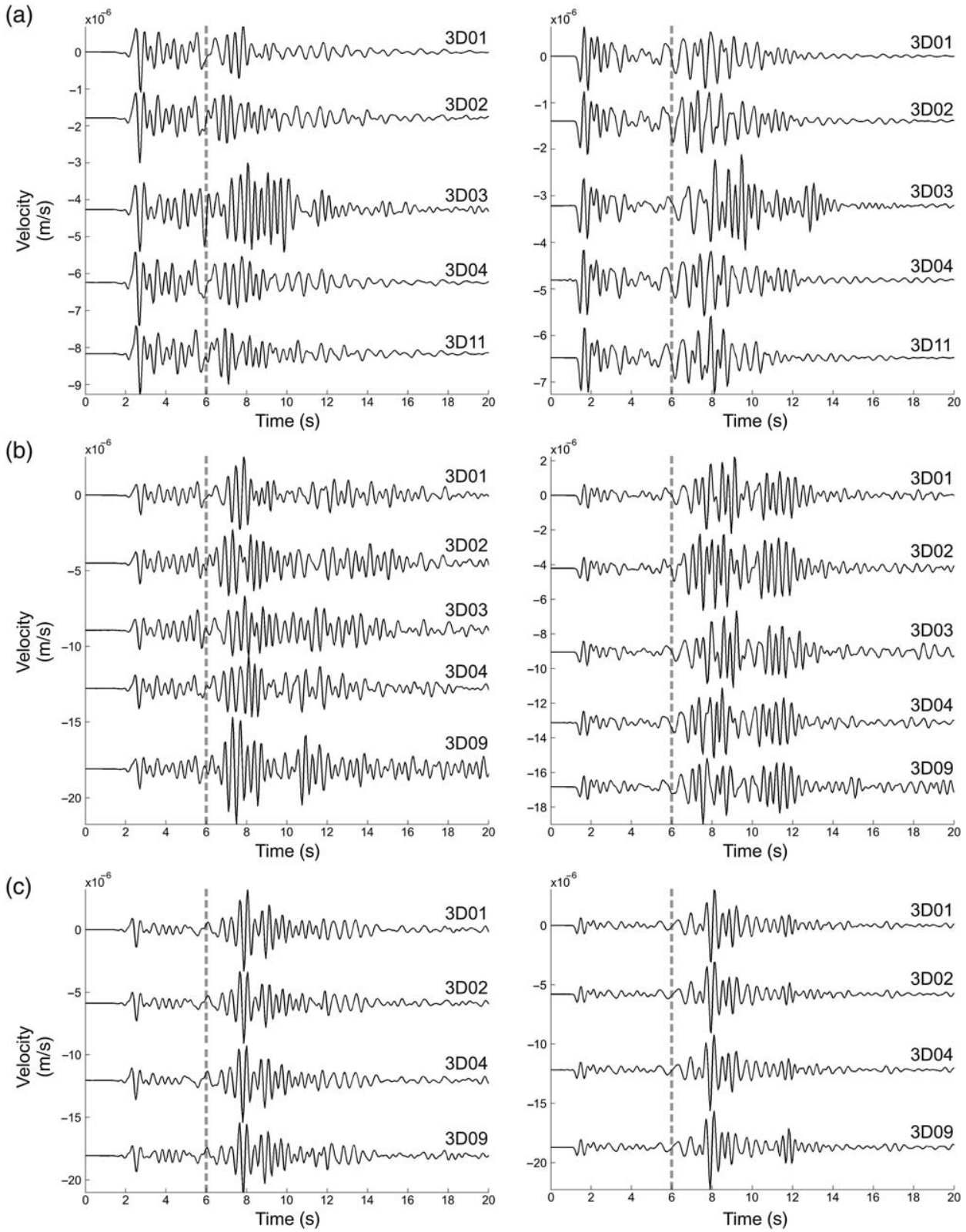

Figure 3. North–south (left) and vertical (right) components of synthetic ground velocity at central soil site TST, computed by four or five different teams for a virtual central event in three cases: (a) the viscoelastic simulation in layered model A, the pure elastic simulation in (b) the layered model A, and (c) the smooth model B. Most of the numerical predictions are consistent for the first 6 s, before the arrival of the later phases, among which surface waves diffracted off the valley edges. Note that team 3D03 did not implement the requested constant-Q viscoelastic rheology.

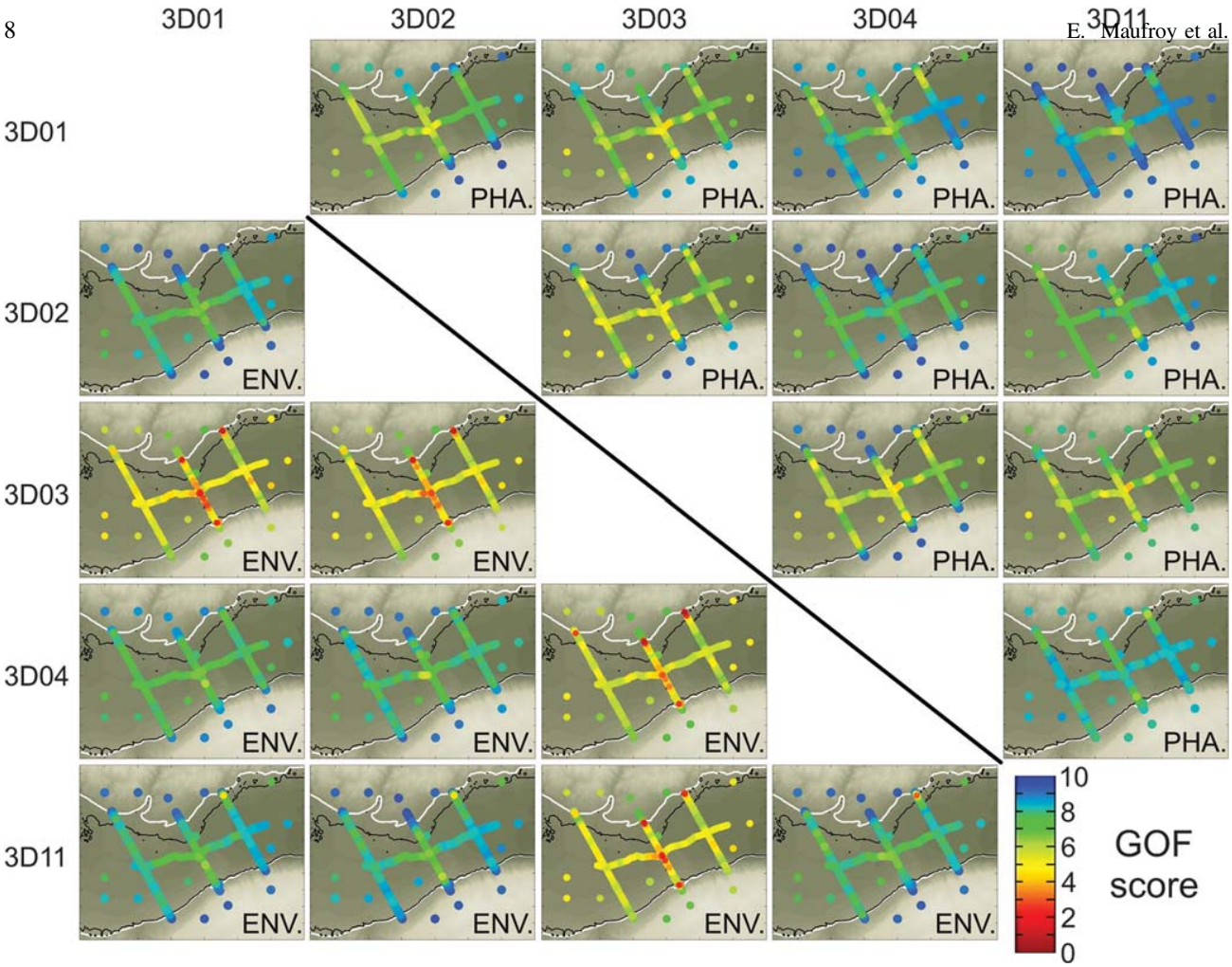

Figure 4. Locations of goodness-of-fit (GOF) values (following the GOF procedure by Kristeková *et al.*, 2009) for the viscoelastic rheology case in the layered model A of the Mygdonian basin. The scores are computed as the weighted average (see the Layered Model with Attenuation section) over both horizontal components of ground velocity for five different numerical predictions (by teams 3D01, 3D02, 3D03, 3D04, and 3D11). The bottom left block of plots displays the envelope scores (ENV.); the upper right block displays the phase scores (PHA.). Each colored dot corresponds to the envelope (amplitude) or phase GOF value computed in the whole frequency range (0–4 Hz) at the corresponding virtual receiver. Score 0 (red) corresponds to a very poor fit between the two numerical predictions of two teams, whereas score 10 (blue) corresponds to a perfect fit. The results of one team relative to the other teams are to be found on the line and column labeled by the team 3D acronym.

ship between the misfits (except for criterion C5) and GOFs: when a GOF decreases, the corresponding misfit increases. It is also clear that in terms of C1–C5 misfit criteria, the numerical predictions by all teams for the three models are close: no misfit exceeds 30% and most of them are below 20%. In particular, the misfits for the smooth model B are clearly lower than the misfits for the layered model A. We also see, as expected, a clear difference between the rock and soil sites: the level of agreement at the rock sites is significantly better (excellent in the GOF verbal classification) than at the soil sites for all the three models and for each criterion but C5.

The misfit for criterion C5 (RSD) correlates well with the GOF at the soil sites (solid symbols in Fig. 8), but a different trend appears at the rock sites (empty symbols in Fig. 8): the C5 misfit indicates disagreement, whereas the corresponding GOFs are all above 8 (excellent agreement). The higher C5 misfits at the rock sites are due to the fact that a small difference in duration between two signals gives a high misfit in percentage if the duration of the target signal is short. For example, the average signal durations in the elastic smooth model B (green symbols in Fig. 8) are equal to 1.34 s (team 3D01) and 0.99 s (team 3D02) at rock sites, whereas they increase to 18.07 s (3D01) and 18.29 s (3D02) at the soil sites. The average differences in duration between the numerical predictions of these two teams are equal to 0.36 s for the rock sites and 0.68 s for the soil sites. These differences are of the same order, but the relative misfits in percentage are higher at the rock sites (18.8%) where the duration is short compared to the longer duration at the soil sites (5.4% of misfit).

Based on these comparisons and analyses, we conclude that the selected ground-motion characteristics C1–C5, which are more relevant for earthquake-engineering purposes, make a reasonable and acceptable alternative to the GOFs (equation 1) for comparing dissimilar waveforms. We will thus use

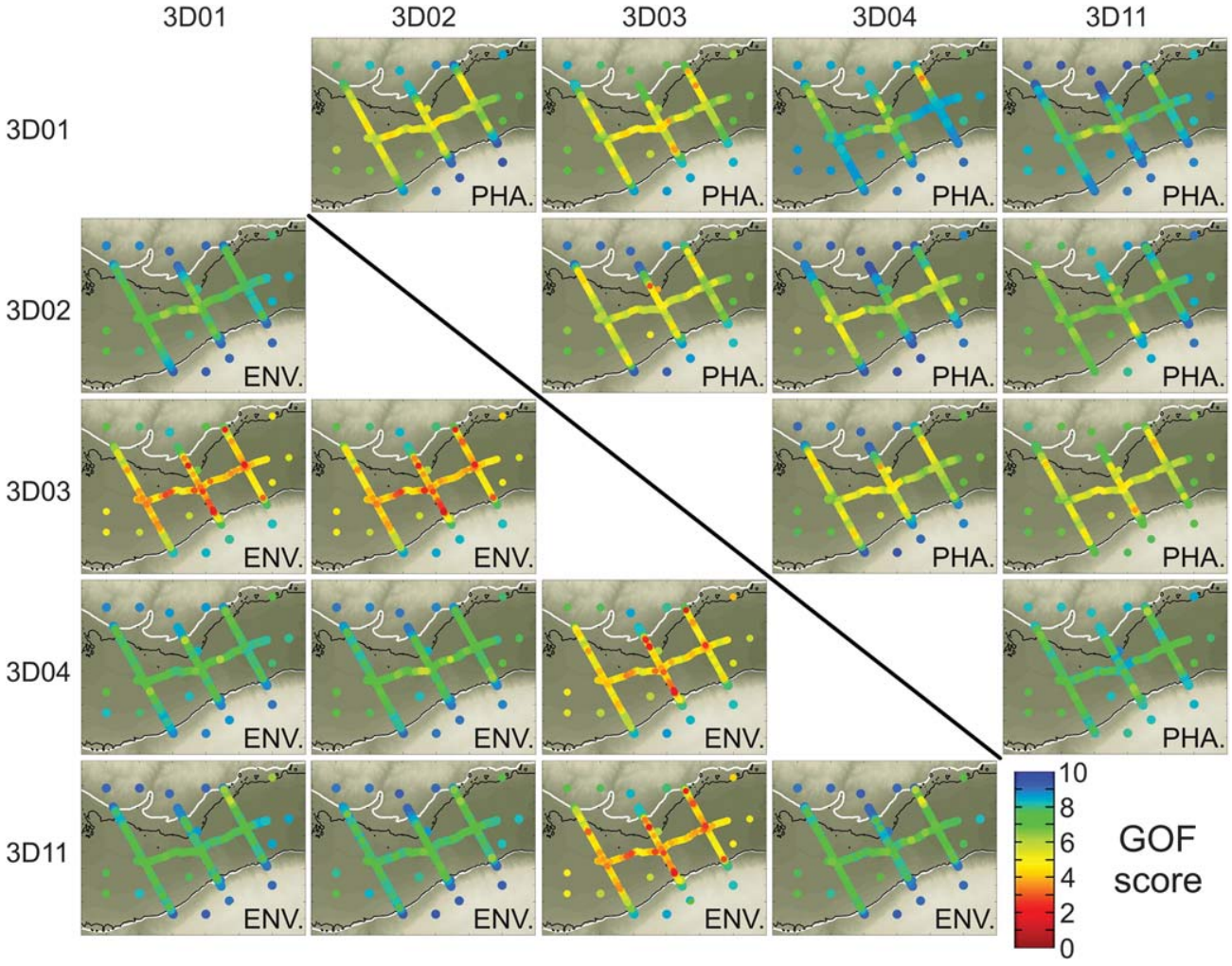

Figure 5. Same as Figure 4, but for the vertical component.

Table 4

Summary of Goodness-of-Fit (GOF) Values (Following the GOF Procedure by Kristeková *et al.*, 2009) Obtained for the Three Verification Cases Presented in This Article

		Receivers at Rock Sites				Receivers at Soil Sites			
		H component		*V* component		*H* component		*V* component	
		Env.	Ph.	Env.	Ph.	Env.	Ph.	Env.	Ph.
Layered model A, with *Q*	3D01–3D02	9.3	8.7	9.2	8.8	8.0	7.0	7.6	5.8
	3D01–3D03	6.6	8.2	8.1	8.2	5.6	6.9	4.8	5.8
	3D01–3D04	8.8	8.6	8.8	8.7	7.8	7.8	7.9	7.4
	3D01–3D11	9.2	9.5	9.2	9.3	8.1	8.6	8.0	8.0
Layered model A, no *Q*	3D01–3D02	9.2	8.8	9.0	8.8	6.7	5.6	6.5	4.5
	3D01–3D03	8.0	7.4	7.8	7.6	6.5	6.2	6.4	5.5
	3D01–3D04	8.7	8.2	8.7	8.3	6.6	4.9	6.2	4.7
	3D01–3D09	9.3	8.7	9.1	8.6	6.3	5.1	5.9	4.8
Smooth model B, no *Q*	3D01–3D02	9.6	9.6	9.3	9.5	8.2	8.4	8.2	8.6
	3D01–3D04	9.6	9.6	9.4	9.6	8.0	8.2	8.2	8.0
	3D01–3D09	9.6	9.6	9.3	9.4	7.8	7.4	7.6	7.1

The scores are given in envelope (Env.) and phase (Ph.) for each team relative to team 3D01. The values are weighted averages computed either on 19 rock sites or on 268 soil sites (weighting individual GOF values by the corresponding time–frequency amplitude to emphasize the GOF values of the most energetic points).

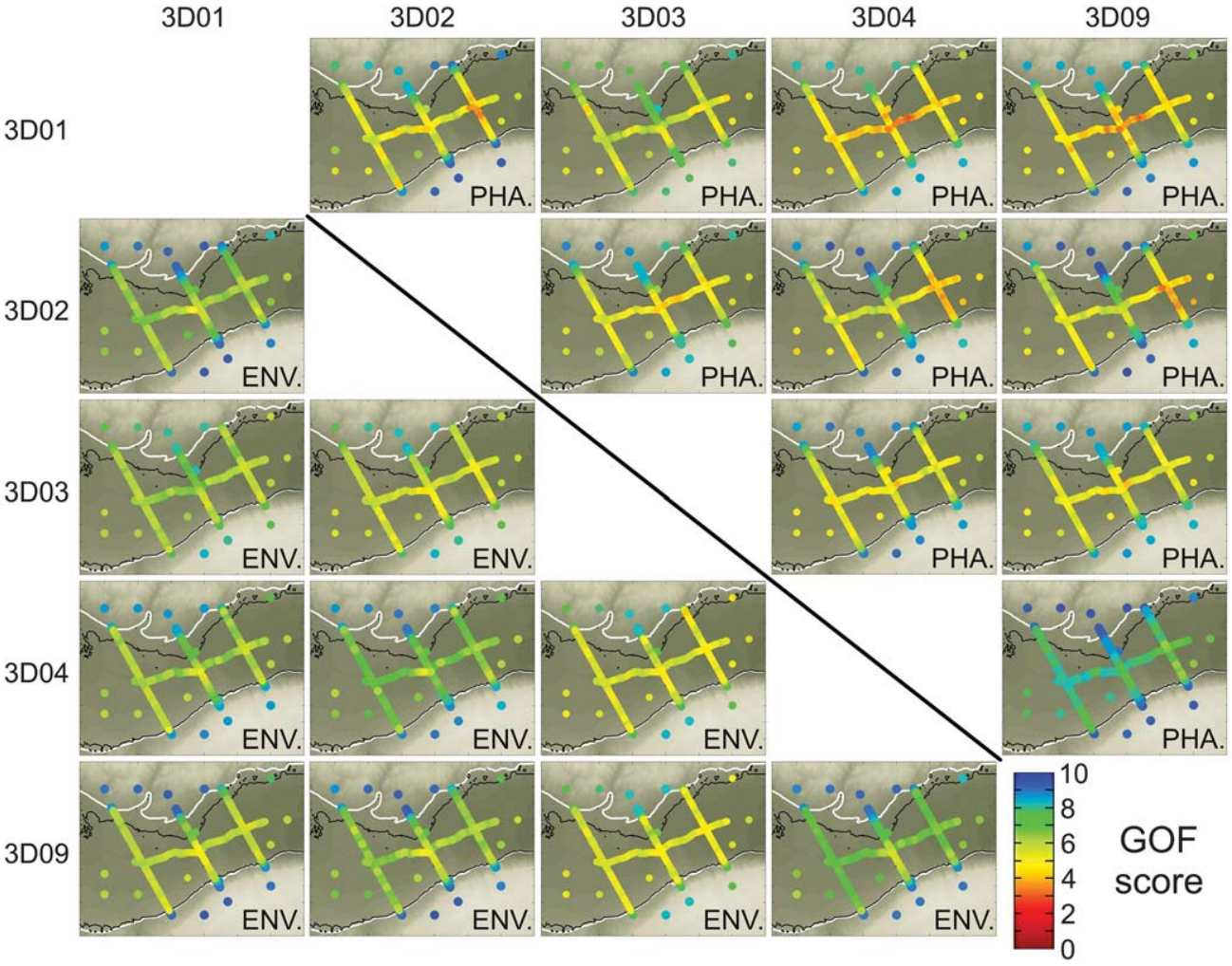

Figure 6. Same as Figure 4, but without attenuation. The scores are computed as the weighted average (see the Layered Model with Attenuation section) over the three components of ground velocity for five different numerical predictions (by teams 3D01, 3D02, 3D03, 3D04, and 3D09).

them for the validation phase (next section) to quantitatively compare recorded waveforms with their numerical predictions.

An Overall Evaluation

As already pointed out and clearly appearing in Figure 3, the velocity seismograms obtained by different teams differ from each other mostly for the layered model A without attenuation (with the exception of the 3D03 solution for model A with attenuation, due to their different implementation of the attenuation, as discussed previously). These differences among synthetics are well reflected by GOFs based on the TF misfits (equation 1). The selected (earthquake-engineering) criteria, as expected, provide a robust and different view on the level of agreement among the synthetics for the layered model A with and without attenuation. The C4 (CAV) misfits are relatively low for model A without attenuation, whereas the C5 (RSD) misfits are relatively low for model A with attenuation (see Fig. 8). The attenuation eventually improves prediction of the signal duration in the basin sediments.

Overall, given the complexity of the Mygdonian basin model, the level of similarity of all the 3D simulations up to 4 Hz (a rather high frequency with wavelengths as short as 50 m) is encouraging.

On the other hand, the verification phase of E2VP confirmed the previous experience of the ESG2006 comparative exercise for the complex model of the Grenoble valley (Chaljub *et al.*, 2010). Cross comparisons among methods and iterations (to remove technical errors and possibly to improve the method or code) are still necessary for a reliable numerical prediction of ground motion in complex models.

The discrete representation of continuous and discontinuous material heterogeneity, the attenuation model, the approximation of the free surface, and nonreflecting boundaries are identified as the main sources of differences among the numerical methods and/or codes. All of those key elements need proper implementation in the methods and codes for a sufficiently accurate simulation of ground motion at sites atop complex local sedimentary structures. A more detailed discus-

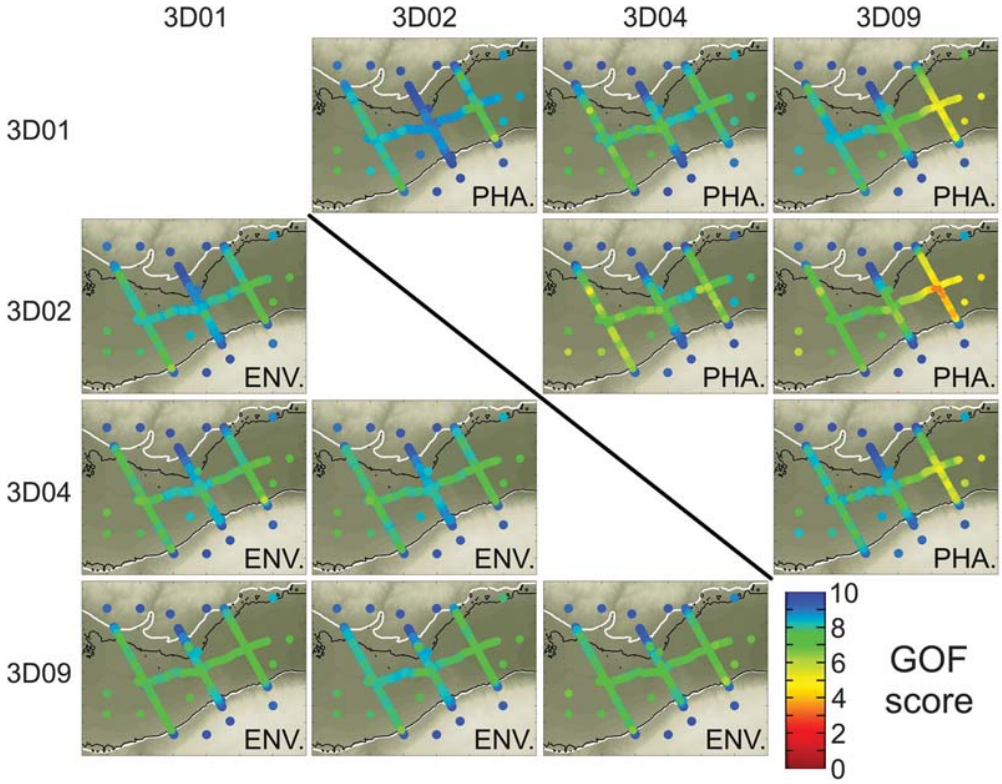

Figure 7. Same as Figure 4, but for the smooth model B, without attenuation. The scores are computed as the weighted average (see the Layered Model with Attenuation section) over the three components of ground velocity for four different numerical predictions (by teams 3D01, 3D02, 3D04, and 3D09).

sion of these factors and the way to reduce the related code-to-code differences are provided by Chaljub *et al.* (2015).

Implementation of attenuation into the 3D numerical simulations has a complex impact on the accuracy of the numerical predictions (e.g., compare the C4 and C5 misfits in Fig. 8). Importantly, a proper attenuation model apparently improves the level of agreement among different predictions in the sedimentary basin, as waveforms are not dominated by strong late arrivals of very dispersive surface waves.

Besides the attenuation, a smooth velocity distribution inside sediments allows reaching significantly improved levels of agreement among different predictions.

In conclusion of the verification phase, the encouraging level of agreement among numerical predictions up to 4 Hz, the subsequent identification of the factors affecting the accuracy of the simulations, and indications for correct handling of those factors (Chaljub *et al.*, 2015) support the use of the 3D numerical modeling approach for predicting ground motion, at least in the linear, low-to-intermediate frequency range, and provided it is performed wisely and carefully.

Validation: Comparison of 3D Numerical Predictions with Earthquake Recordings in the Mygdonian Basin

The next phase in E2VP is the validation part, consisting of a quantitative comparison between numerical predictions and actual recordings in the frequency range up to 4 Hz. The comparison was performed for six local weak-to-moderate magnitude events, spanning various azimuths, hypocenter depths, and distances. The earthquakes were recorded by the local array of surface and borehole accelerometers (see Fig. 2 and Table 5). Importantly for the numerical simulations, the hypocenters are located inside the 3D numerical box (as displayed in Fig. 2): the maximum size of this box was limited to roughly 20×30 km^2 to keep a reasonable computational time while going up to 4 Hz. This limited size excluded a number of more distant events with good signal-to-noise ratios, which will be included in a later study considering the improving capabilities of high-performance computers. Further requirements on the selected events were (1) available focal mechanism and (2) a sufficient number of high-quality recordings by the local seismic array. The synthetics to be compared with the records are computed for the 3D viscoelastic layered model A of the Mygdonian basin (Table 2).

Comparing Recordings and their Numerical Predictions for Event Number 4

The acceleration time histories recorded from the closest and largest event (number 4 in Fig. 2 and Table 5) are compared with the numerical predictions computed by three different teams at three receivers: the TST surface site at the center of the basin (soft soil, Fig. 9a), the TST 197 m deep borehole receiver (rock condition, Fig. 9b), and the surface

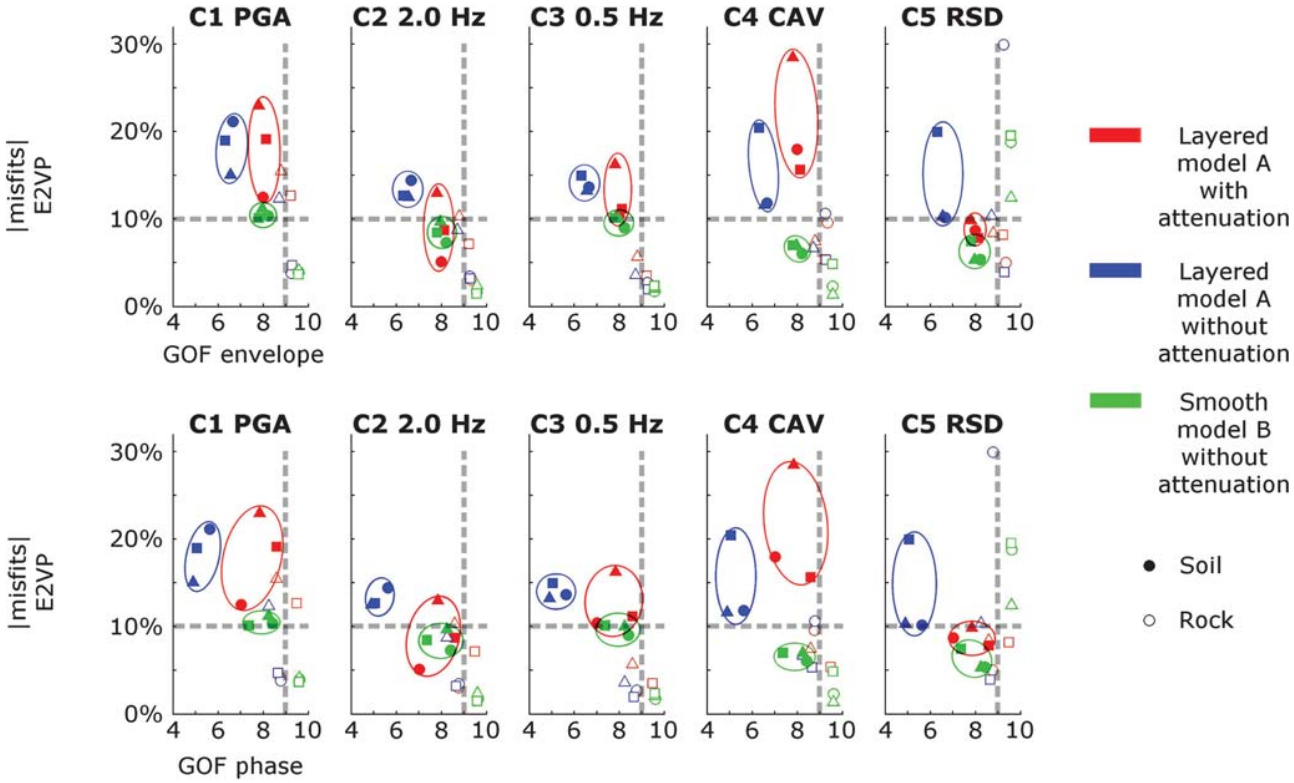

Figure 8. Comparison of GOF values (following the GOF procedure by Kristeková *et al.*, 2009) and horizontal absolute misfits obtained on the E2VP evaluation criteria C1–C5 (see the Appendix), for the three verification cases presented in this article and differentiated here by colors. The GOF values are computed as the weighted average over horizontal components of ground velocity in the envelope (top panels) and in phase (bottom panels) for team 3D01 relative to team 3D02 (circles), team 3D04 (triangles) and teams 3D11/3D09 (squares), depending on their availabilities. All values are weighted averages (weighting individual values by the corresponding time–frequency amplitude or target parameter, for GOF and C1–C5, respectively, to emphasize the misfits for the most important points), computed either on 19 rock sites (open symbols) or on 268 soil sites (solid symbols surrounded by an oval for each verification case).

site W03 located westward (soft soil, Fig. 9c). The numerical predictions look visually very similar to one another at each of these three sites. The highest level of agreement between recordings and numerical predictions is found on the north component of the surface and borehole receivers at the TST site, except for a slight time shift that is probably due to inaccuracy in the hypocenter location. These cases (i.e., event 4 and the TST site) are surely the best results of the whole validation exercise. At the opposite extreme, large discrepancies between recordings and numerical predictions appear in the waveforms at the W03 site, even if the maximum level of amplitude is relatively well predicted and if the same event is considered.

To have a global view of the agreement between recordings of the event 4 and their numerical predictions for all recording sites, the horizontal components are compared in terms of misfits on the E2VP criteria C1–C5 (Fig. 10). The positive and negative misfit values, respectively, mean over- and underestimation of 3D01's prediction with respect to the recordings. The misfit values are highly variable on the

Table 5

Characteristics of Six Selected Real Events that Occurred near the Mygdonian Basin, for which the Recordings by the EUROSEISTEST Accelerometric Array are Compared to 3D Numerical Predictions

Event Number	Date (yyyy/mm/dd) (hh:mm:ss)	Magnitude M_w	Depth (km)	Hypocentral Distance at Central Site TST (km)	Strike (°)	Dip (°)	Rake (°)
2	2004/11/19 21:01:04	2.8	6.9	17.2	100	60	−50
4	2005/09/12 19:08:30	4.4	5.0	8.2	53	43	−127
5	2005/09/20 17:41:20	3.1	6.0	9.2	72	55	−113
6	2005/10/09 07:12:05	3.9	6.0	9.3	61	55	−115
7	2005/10/09 12:30:22	3.4	5.0	9.7	72	55	−113
8	2006/08/17 04:27:31	3.8	10.0	17.2	329	34	−64

See locations of epicenters in Figure 2. Event 8 was not recorded at central site TST.

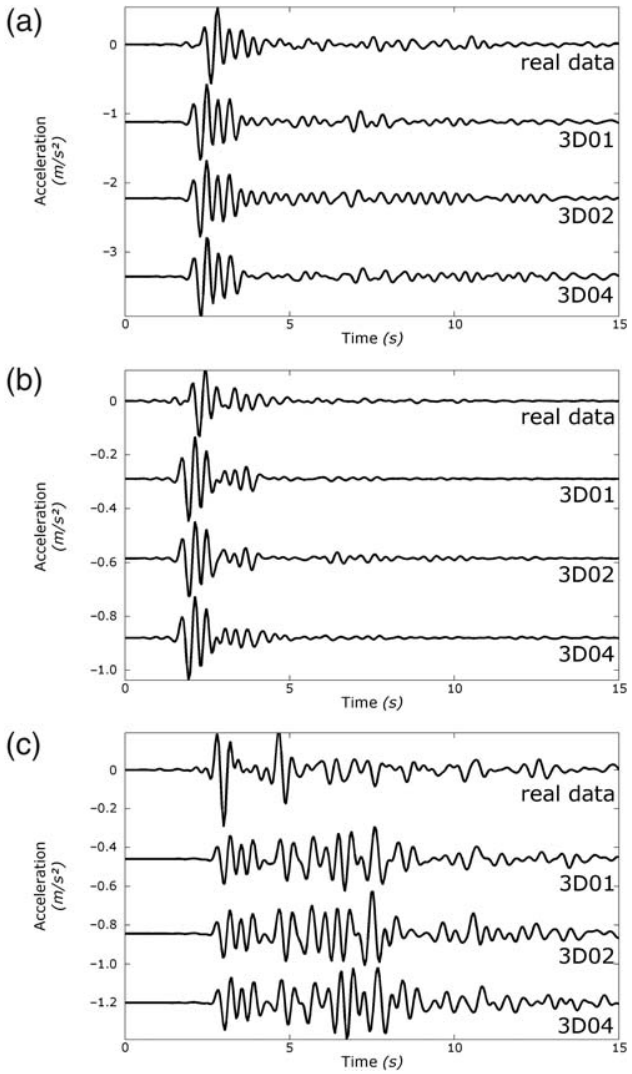

Figure 9. North–south component of observed and numerically predicted ground acceleration at (a) the central soil site TST at surface, (b) the corresponding 197 m depth borehole station, and (c) the west soil site W03, for the M_w 4.4 real event in the northeast (event 4 in Fig. 2 and Table 5). Every time series is Butterworth filtered between 0.5 and 4.0 Hz.

whole array: an almost perfect fit (~0%) is achieved on a few receivers, but some high misfits (greater than ±100%) are also observed. The misfit values are also highly variable from one criterion to another. The visual comparison of recordings with their numerical predictions (Fig. 9) indicates a good level of agreement at the surface soil site TST (central receiver in Fig. 10) and at the corresponding downhole sensor at 197 m depth (the vertical array of five receivers below TST is represented in Fig. 10 by a diagonal projection of points at the surface). The level of agreement at the surface soil site TST is indeed excellent (misfits closed to 0%) for criteria C1, C2, and C4 (intermediate-to-high frequencies and CAV intensity). The misfit value for C3 remains reasonable (below 20%). As for C5, it was previously shown (see the Discussion on the Comparison Criteria section) that the duration criterion can lead to relatively strong misfits if the duration of the seismic signal is short; it is precisely the case at TST for close-event 4. The misfits shown in Figure 10 for the borehole station also drop to a satisfactory level (absolute values for all criteria are below 30%). On the contrary, the recorded waveform and the numerical predictions at the western site of the array are really different (Fig. 9c). It is noteworthy that, even if the waveforms are different, the numerical prediction is still able to reproduce some of the characteristics of the ground motion: the fit at the western site is excellent for C3 (low frequencies) and good for C4 (CAV intensity).

The highest misfits observed in Figure 10 are easily explainable. The amplitude of the ground motion at the eastern soil site (far-right colored dot) is systematically overestimated by the numerical prediction regardless of the frequency band considered (criteria C1–C4). That receiver is the closest receiver to the seismic source, and the numerical prediction is thus especially impacted by even small uncertainties in source characteristics (for instance, a slight error in the hypocenter location). At the northern rock site, the numerical prediction considerably underestimates amplitude of the recorded waveform (regardless of frequency range; C1–C3) and intensity (C4). The location of the station PRO, relative to the epicenter of event 4, is close to the azimuth of the nodal planes of the focal mechanism (see Fig. 2). Rapid spatial variations of amplitude and intensity of the ground motion are expected for such short distances from this azimuth: therefore, the numerical prediction at PRO for event 4 is highly sensitive to weak uncertainties in the focal mechanism. The overprediction of duration at this site is fully consistent with the underestimation of the amplitude of the main signal, resulting in a Husid plot spread over a larger time.

Comparing Verification and Validation Misfits for All Six Events

Those misfit values show that the validation results are very variable, even inside one event. A global overview of the validation exercise allows comparing the level of agreement between recordings and their numerical predictions to the agreement reached among different synthetics. Figure 11a gathers misfit values based on the E2VP criteria for the verification exercise (misfits between synthetics obtained by different teams; blue-tone dots) and for the validation exercise (misfits between recordings and numerical predictions; red-tone dots) at all receivers for the six selected events (Fig. 2 and Table 5). The averaging over all receivers was obtained by (1) considering only absolute misfit values (L1 norm), so as to not balance overprediction at some sites by underprediction at others and (2) weighting the misfit value at each receiver by the value of the corresponding parameter, so as to emphasize the misfits for the most important points. An overall misfit around 25% is observed for the verification, whereas the misfit values are much higher for the validation (around 80%).

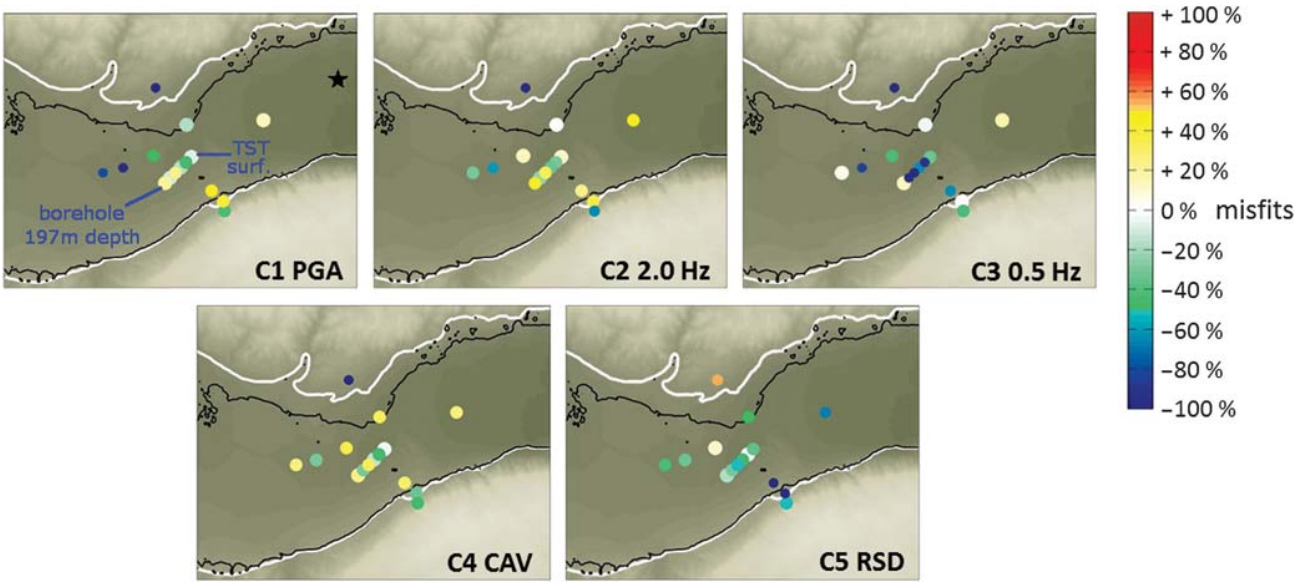

Figure 10. Maps of horizontal misfits on the E2VP evaluation criteria (see the How to Objectively Quantify the Similarity between Two Signals? section) between the recordings of real event 4 (black star; see also Fig. 2 and Table 5) and its numerical 3D prediction by team 3D01. C1 is based upon peak ground acceleration (PGA), C2 upon elastic spectral acceleration ranging between 1.5 and 3.0 Hz, C3 upon elastic spectral acceleration ranging between 0.375 and 0.750 Hz, C4 upon cumulative absolute velocity (CAV), and C5 upon 5%–95% relative significant duration. Each colored dot corresponds to the misfit obtained at the corresponding real receiver, the vertical array at TST being projected on the surface at the center of the map. Red/yellow tones are for overestimation of the numerical prediction compared to the recordings; blue/green tones are for underestimation.

Figure 11b provides a complementary comparison by considering only one surface soil site (TST) for five events (one of the six events was not recorded at TST). The verification misfits remain approximately at the same level (around 25%), whereas the validation misfits are reduced to approximately 60%. Finally, Figure 11c focuses on the average misfit for the biggest event (event 4) at all receivers. A reduction of the misfit values to about 10% is observed for the verification and to about 40% for the validation. This synthesis, shown in Figure 11, clearly demonstrates the robustness of the statement that the smallest differences between recordings and their numerical predictions are significantly larger than the usual distances between simulations.

Discussion: Can We Identify the Origins of the Validation Misfits?

The details of the waveforms are highly sensitive to the source parameters (hypocenter location and focal mechanism), to the shape of the sediment-basement interface, and to the internal sediment layering of the basin. Each of these items may affect the validation misfits. Are the misfits due predominantly to inaccuracies in the description of the sources and/or of the 3D model? Figure 12 shows maps of the misfit values for criterion C4 (CAV) between actual recordings and their numerical prediction by team 3D02 for the six selected events in Figure 2 and Table 5. A first assumption consists of assigning the origin of mismatch between recordings and their numerical predictions to the uncertainties in source parameters. One could then expect that the higher the magnitude, the lower the misfits because larger-magnitude earthquakes are usually better characterized than low-magnitude earthquakes (for events moderate enough to assume a point source). Figure 12 shows that the best validation agreement is indeed obtained for the largest-magnitude event (event 4, M_w 4.4). Nevertheless, the second largest magnitude (event 6, M_w 3.9) produces the worst validation results, whereas the two lowest-magnitude events (event 2, M_w 2.8; event 5, M_w 3.1) produce the second best results. Within our dataset (limited to few events), no clear relation appears between the validation misfits and the magnitude or the hypocentral distance of those earthquakes.

Another hypothesis is to relate the origin of misfits to the uncertainties in the 3D distribution of the model properties. Depending on the level of knowledge in the model, some stations should systematically produce low misfits and good validation results (where the model properties are accurately defined), while other stations should systematically produce strong misfits (where the model properties are poorly defined), provided that the local response is predominantly controlled by the local structure. Nothing similar can be observed in Figure 12.

To remove (some of) the errors due to uncertainties in source parameters and to focus on the prediction of the site effect alone, Figure 13 evaluates the prediction of the Fourier transfer function from the downhole sensor to the surface sensor at the central vertical array TST. The instrumental site-to-reference spectral ratio derived from the actual recordings of event 4 (gray line) is compared to those derived from

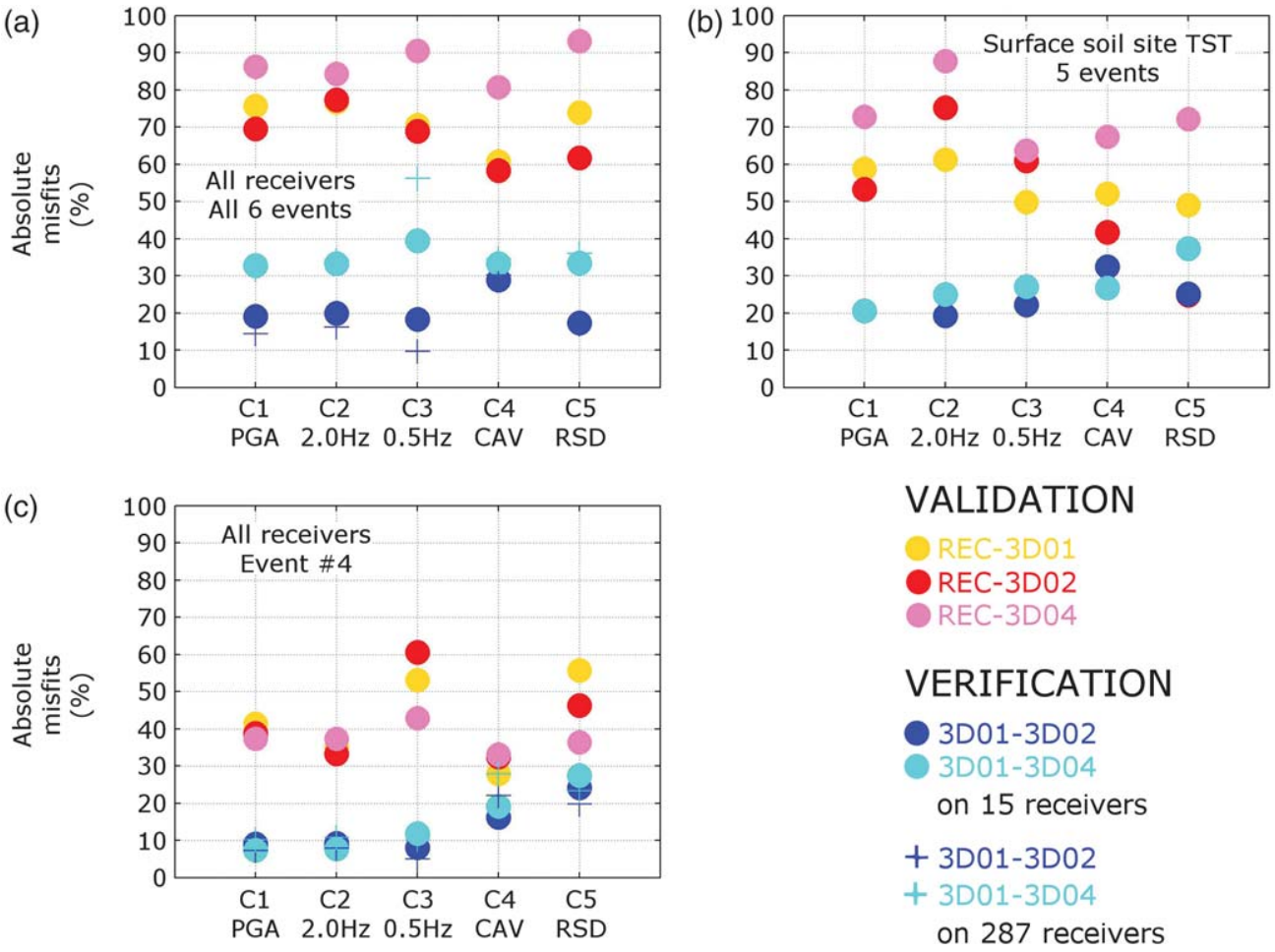

Figure 11. Summary of horizontal absolute misfits obtained on the E2VP evaluation criteria C1–C5 for the verification and validation exercises, considering different configurations: (a) average for the six selected events (Fig. 2 and Table 5) at all receivers; (b) average for the five events recorded at the central soil site TST; (c) average for the biggest event (event 4) at all receivers. Synthetics-to-synthetics misfits (verification, blue-tone dots) are compared to recordings-to-synthetics misfits (validation, warm-tone dots). The verification misfits in the left panels are computed by taking into account either the real array (limited to 15 surface receivers; solid circles) or the complete virtual array (287 receivers; crosses). A single value per array is obtained by calculating the weighted average of the absolute misfits over the considered receivers, weighting each individual misfit by the corresponding target value of the ground-motion parameter (to decrease the importance of weaker points).

3D synthetics (back lines). The frequencies at which amplification of ground motion occurs (around 0.75 Hz for the fundamental peak, 1.7 and 2.8 Hz for overtones, and around 1.0 Hz probably due to the excitation of local surface waves) are well reproduced in all synthetics. However, the amplitudes of these different maxima are not all accurately predicted. The overtone at 2.8 Hz and the contribution of the surface waves at 1 Hz are significantly underestimated. We estimate that the numerical predictions have well reproduced some features of the site effect, but not all.

Respective Influence of the Uncertainties in Source and Model

To deepen the analysis of the actual capability to numerically predict the site-effect component, synthetic time histories that could both maximize the impact of the numerical estimate of the site-effect component and minimize the effect of uncertainties in the source description are required. Toward that goal, we compute hybrid time histories: the complex synthetic spectral ratio between the surface and downhole TST sensors, as derived from the numerical computation (i.e., with both modulus and phase), is considered as the borehole–surface transfer function and is thus multiplied in the Fourier domain, with the actual signal recorded at the downhole sensor. The inverse Fourier transform returns a hybrid time history in the sense that the input signal is a real signal (integrating actual source parameters), whereas the site-effect part is coming from the numerical predictions. This way the effect of uncertainties in the source description is somehow removed (we consider the sensitivity of the transfer function to uncertainties in source parameters is very weak as long as the precision on hypocenter location remains

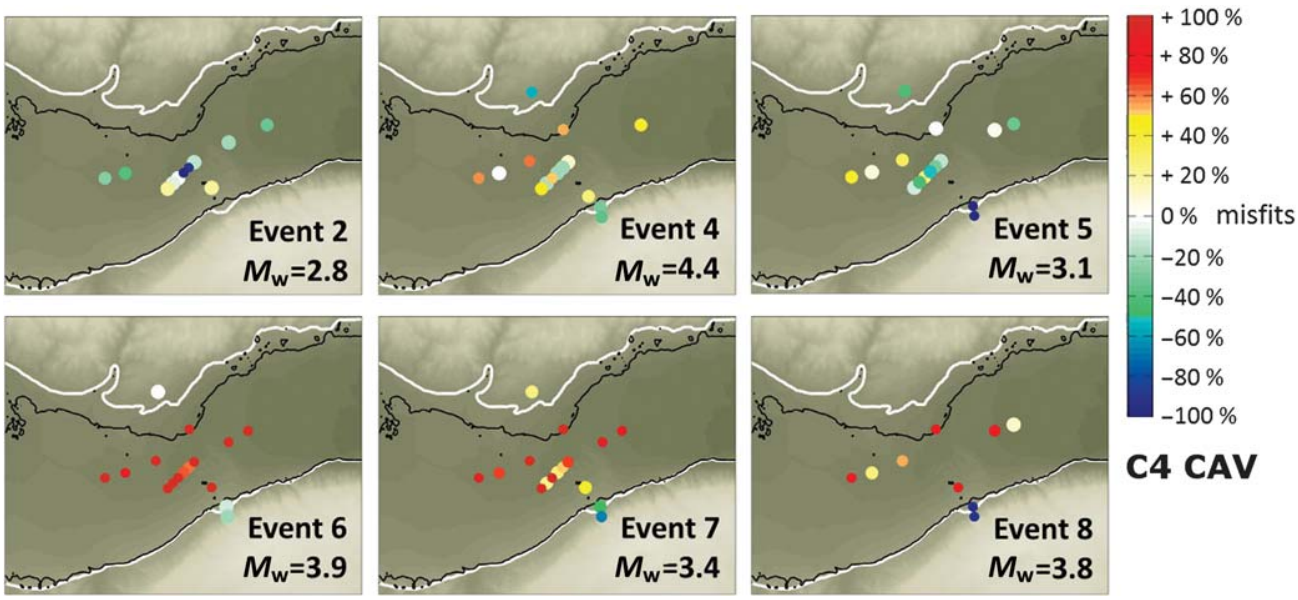

Figure 12. Locations of horizontal misfits for criterion C4 (CAV) between the real recordings of the six selected events (see Fig. 2 and Table 5) and their numerical 3D predictions by team 3D02. Each colored dot corresponds to the misfit obtained at the corresponding real receiver, the vertical array at TST being projected onto the surface at the center of the map. Red tones are for overestimation of the numerical prediction compared to the recordings, blue tones are for underestimation.

within a few kilometers; Chaljub *et al.*, 2014). The E2VP evaluation criteria are then applied between the actual recordings and the hybrid time histories computed at the surface soil site TST for five of the selected events (event 8 was not recorded at TST) using the actual recordings at the downhole rock site and the numerical transfer function predicted by three teams (3D01, 3D02, and 3D04). Figure 14 displays the misfits obtained following this procedure and their comparison to the previous validation misfits obtained between actual recordings and their fully numerical predictions. Figure 14a demonstrates that for all C1–C5 criteria, the absolute misfit values obtained with hybrid signals are significantly lower than the values obtained with fully numerical signals (around 35% instead of 60%). Because hybrid signals may be considered as free from effects of source uncertainties, one may conclude that the origins of discrepancies between actual recordings and their numerical predictions are likely to be almost equally balanced between uncertainties in source parameters and uncertainties in the 3D model description.

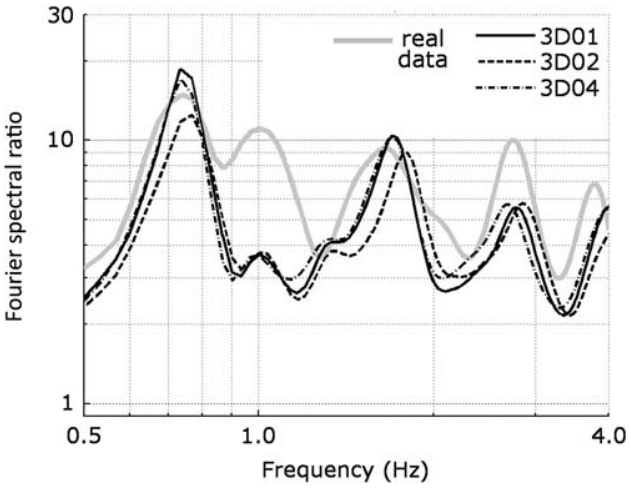

Figure 13. Fourier spectral ratios at the central site TST, computed between the surface receiver and the borehole receiver at 197 m depth for the average horizontal component recorded or numerically predicted for the M_w 4.4 event in the northeast (event 4 in Fig. 2 and Table 5). The results are shown for three different numerical predictions (black lines), to be compared to the real data (gray bold line). The spectral ratios from this event are representative of the median spectral ratios computed for the five selected events recorded at TST.

Figure 14b presents the same results with average computed over signed misfit values (the ± sign of the misfit value respectively indicating over- or underestimation of the target is kept; see the Appendix) and allows the process to be extended one step further: fully numerical predictions exhibit a trend to overestimate most parameters (C1–C4), whereas the hybrid predictions exhibit an opposite trend to underestimate the same parameters, in perfect agreement with the surface/downhole spectral ratios displayed in Figure 13. This suggests that: (1) In the present case, uncertainties in source description tend to produce overestimation of the ground motion in the E2VP validation exercise (that could be explained by an overestimation of the magnitude; for example, the signals used for magnitude estimation could be insufficiently corrected for site effects). (2) The site effect itself is globally underestimated at the TST site. That global trend for underestimating the actual amplification by all the 3D simulations at the TST site (it could not be investigated at other sites, as there is no other

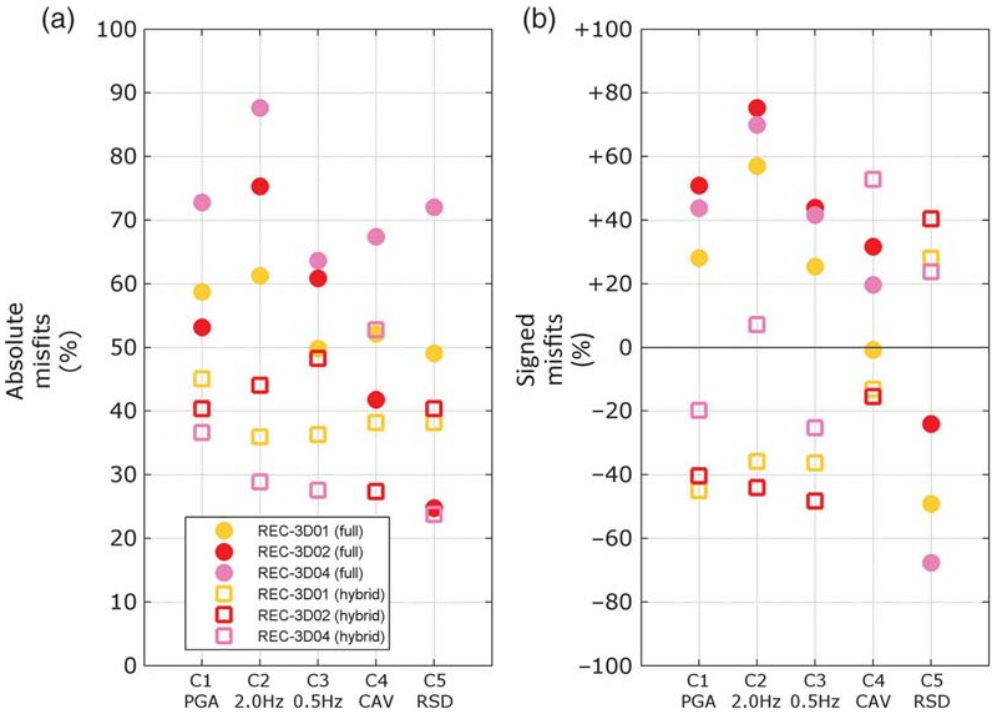

Figure 14. Average of (a) absolute misfit values and (b) signed misfit values obtained on the E2VP evaluation criteria C1–C5 for the five events recorded and numerically predicted by teams 3D01, 3D02, and 3D04 at the central soil site TST. The actual recordings are compared to fully numerical predictions (full circles) and to hybrid predictions (see the Respective Influence of the Uncertainties in Source and Model section; empty squares).

downhole sensor) could have several explanations: incorrect estimates of damping (too large values), incorrect internal sediment layering structure, overemphasis on the buried-pass or saddle-point structure just underneath the TST site (which would result in larger off-profile diffraction), or overestimation of the hypocentral depth, resulting in too-weak excitation of surface waves.

Conclusions

The participation of several computational teams from various parts of the world, with expertise in advanced numerical codes, allowed achievement of several major accomplishments in the verification and validation of 3D ground-motion simulation codes. A very good similarity, quantified with an objective scale, could be obtained among synthetics up to a frequency of 4 Hz despite the relative complexity of 3D models, which witnesses the accuracy of the corresponding numerical schemes. The existence of an excellent agreement between several completely independent codes, with code-to-code differences much smaller than predictions-to-observations differences, makes it possible and legitimate to include the numerical simulation approach in the toolbox for site-specific ground-motion estimation, at least in the 3D linear case and low-to-intermediate frequency range.

A careful verification exercise requires time, whereas a careful validation exercise also requires high-quality data. The most common outcome of the verification phase (similarly to the conclusions of Chaljub *et al.*, 2010) is that, without iterations and cross checking, different codes are very likely to provide significantly different results when applied to the same case study. As an immediate conclusion, too fast applications of 3D codes may yield wrong ground-motion estimates, potentially resulting in increased mistrust in end users. The lessons and experiences of E2VP draw attention to the following recommendations for a wise and careful use of such numerical simulation codes.

One should never be satisfied with only one computation from one single team, but should request several teams (at least two) with different numerical schemes to perform parallel computations of the same case. The corresponding results then can be considered reliable only if they agree beyond some quantitative threshold; a GOF threshold of 7 seems a reasonable value and roughly corresponds to misfit thresholds for the C1–C5 criteria within about 20%–25%.

Comparison of numerical predictions with actual data (*in situ* earthquake recordings) is always useful. Having sensitive *in situ* instrumentation (continuously recording broadband velocimeters or accelerometers) proves to be invaluable for checking the reliability of numerical simulation results, with a special emphasis on vertical arrays, which allow the site-effect component to be constrained. In addition to the availability of high-quality *in situ* recordings, the validation phase showed the importance of completing such data with high-quality metadata, concerning both the source parameters and the site model. Even though the need for additional infor-

mation and complementary surveys can always be identified, the site selected for the present project can be considered as one of the best-known sites, at least in the Euro-Mediterranean area. The results obtained here in terms of validation, and comparison with actual recordings should thus be representative of the top-ranking sites in terms of site investigations.

Even in such a well-known site, the prediction of several ground-motion parameters of engineering interest exhibits average differences around 60%–80%, with a minimum of 30%–40% for the larger magnitude, probably best-known event. Such values should be kept in mind when discussing the effects of missing elements in the numerical approach (e.g., nonlinearities). The gross characteristics of the amplification at the valley center are satisfactorily reproduced by the 3D model, both in terms of spectral contents and signal duration, although with a slight underestimation. In the present case, the differences between recordings and numerical predictions appear to have an approximately balanced origin shared between inaccuracies in source parameters (hypocenter location, magnitude, and focal mechanism), and uncertainties in the site model (geometry, velocity structure, and damping). Interestingly, in the present case, the former are associated with some overprediction of ground motion, whereas the latter would underestimate the site amplification. Such observations suggest a positive bias in magnitude estimates, which would be consistent with an underestimation of site effects at most observational stations. However, similar analyses on other sites are required to indicate whether such observations can be generalized or are specific to the considered site.

Two final comments concerning the validation phase are worth consideration. The first is related to the small number of candidate seismic events that could be considered (i.e., those within the numerical box). This is indeed a typical situation for moderate/weak seismicity areas. Future validation exercises would certainly benefit from the possibility of including more distant events, which implies either the increase of computing capabilities or the use of hybrid numerical schemes coupling computations at different scales (an excitation box).

The second comment deals with the consequences of these results on the use of numerical simulation for ground-motion prediction. In the case of a deterministic approach, a scenario earthquake would be defined: all the uncertainties affecting the validation and linked to source parameters (partially responsible for the large differences between recordings and their numerical predictions) should therefore be left aside, and only those linked to the propagation and site models should be considered; however, for sources of finite extent, an additional cause of variability should be taken into account as the detailed rupture kinematics cannot be deterministically predicted, but it should be tackled with some sensitivity study. In the case of a probabilistic approach, the use of numerical simulation would probably focus more on the determination of the site amplification function than on massive simulations with a wide range of source parameters (location and magnitude). Therefore, whatever the approach, the main focus is the determination of the site amplification. Further investigations of the validation of 3D numerical simulations should thus definitely favor the use of pairs of stations on the site of interest and on relevant nearby reference, including local vertical arrays, together with thorough geophysical and geotechnical surveys to provide the required details of the underground structure, not only for high frequencies and short wavelengths, but also for some still badly known parameters, such as material damping.

Data and Resources

Several numerical cases of the E2VP are made freely available to the seismological community at http://www.sismowine.org (last accessed February 2015). The real seismograms used in this study can be obtained from the EUROSEISTEST strong ground-motion database and web portal at http://euroseisdb.civil.auth.gr (last accessed June 2014; see also Pitilakis *et al.*, 2013). The spectral-element method (SEM) meshes were designed using the commercial software Cubit (https://cubit.sandia.gov; last accessed June 2014). The synthetic seismograms from team 3D11 were computed using the code EFISPEC3D (De Martin, 2011; http://efispec.free.fr; last accessed January 2014).

Acknowledgments

The authors thank all the participants of the EUROSEISTEST Verification and Validation Project and acknowledge the Cashima project (funded by Commissariat à l'énergie atomique et aux énergies alternatives [CEA] and Laue-Langevin Institute [ILL]) for its financial support. We thank Robert W. Graves and an anonymous reviewer for their careful review of this work.

The simulations of team 3D01 were performed in the Computing Centre of the Slovak Academy of Sciences using the supercomputing infrastructure acquired in project ITMS 26230120002 and 26210120002 (Slovak infrastructure for high-performance computing) supported by the Research and Development Operational Program funded by the European Regional Development Fund (ERDF). The simulations of team 3D02 were performed on the CIMENT infrastructure, Grenoble, France. The simulations of team 3D04 were performed on the computational resources of Consorzio Interuniversitario per il Calcolo Automatico (CINECA), Bologna, Italy. The simulations of team 3D09 were performed on the high-performance computing facilities of Institut du Développement et des Ressources en Informatique Scientifique (IDRIS)/Centre National de la Recherche Scientifique (CNRS) and of the Observatoire de la Côte d'Azur (OCA), France. This research was also partly funded by Bureau des Recherches Géologiques et Minières (BRGM) internal funds for project SEISMORISK.

References

Anderson, J. G. (2004). Quantitative measure of the goodness-of-fit of synthetic seismograms, *13th World Conf. on Earthquake Engineering Conf. Proc.*, Vancouver, British Columbia, Canada, 1–6 August, Paper Number 243.

Bard, P.-Y. (1992). Discussion session: Lessons, issues, needs and prospects, special theme session 5: Turkey Flat and Ashigara Valley experiments, *10th World Conf. on Earthquake Engineering Conf. Proc.*, Madrid, Spain, 19–24 July, 6985–6988.

Bielak, J., R. W. Graves, K. B. Olsen, R. Taborda, L. Ramírez-Guzmán, S. M. Day, G. P. Ely, D. Roten, T. H. Jordan, P. J. Maechling, *et al.* (2010). The ShakeOut earthquake scenario: Verification of three simulation sets, *Geophys. J. Int.* **180,** 375–404, doi: 10.1111/j.1365-246X.2009.04417.x.

Campbell, K. W., and Y. Bozorgnia (2010). A ground motion prediction equation for the horizontal component of cumulative absolute velocity (CAV) based on the PEER-NGA strong motion database, *Earthq. Spectra* **26,** no. 3, 635–650, doi: 10.1193/1.3457158.

Chaljub, E., C. Cornou, and P.-Y. Bard (2006). Numerical benchmark of 3D ground motion simulation in the valley of Grenoble, French Alps, *Third International Symposium on the Effects of Surface Geology on Seismic Motion*, Grenoble, France, 30 August–1 September, Paper Number SB1, Vol. 2.

Chaljub, E., D. Komatitsch, J.-P. Vilotte, Y. Capdeville, B. Valette, and G. Festa (2007). Spectral element analysis in seismology, in *Advances in Wave Propagation in Heterogeneous Media*, R.-S. Wu and V. Maupin (Editors), in Advances in Geophysics, R. Dmowska (Series Editor), Academic Press London, United Kingdom, Vol. 48, 365–419.

Chaljub, E., E. Maufroy, F. De Martin, F. Hollender, C. Guyonnet-Benaize, M. Manakou, A. Savvaidis, A. Kiratzi, Z. Roumelioti, and N. Theodoulidis (2014). How sensitive is earthquake ground motion to source parameters? Insights from a numerical study in the Mygdonian basin, EGU General Assembly, *Geophys. Res. Abstr.* **16,** EGU2014–11738.

Chaljub, E., E. Maufroy, P. Moczo, J. Kristek, F. Hollender, P.-Y. Bard, E. Priolo, P. Klin, F. De Martin, Z. Zhang, *et al.* (2015). 3-D numerical simulations of earthquake ground motion in sedimentary basins: Testing accuracy through stringent models, *Geophys. J. Int.* **201,** no. 1, 90–111, doi: 10.1093/gji/ggu472.

Chaljub, E., P. Moczo, S. Tsuno, P.-Y. Bard, J. Kristek, M. Käser, M. Stupazzini, and M. Kristeková (2010). Quantitative comparison of four numerical predictions of 3D ground motion in the Grenoble valley, France, *Bull. Seismol. Soc. Am.* **100,** no. 4, 1427–1455.

Clayton, R., and B. Engquist (1977). Absorbing boundary conditions for acoustic and elastic wave equations, *Bull. Seismol. Soc. Am.* **67,** no. 6, 1529–1540.

Cramer, C. H. (1995). Weak-motion observations and modeling for the Turkey Flat, U.S., site-effects test area near Parkfield, California, *Bull. Seismol. Soc. Am.* **85,** no. 2, 440–451.

Day, S. M., J. Bielak, D. Dreger, R. Graves, S. Larsen, K. B. Olsen, and A. Pitarka (2001). Tests of 3D elastodynamic codes: Final report for Lifelines project 1a01, *Technical Report*, Pacific Earthquake Engineering Research Center and Southern California Earthquake Center.

Day, S. M., J. Bielak, D. Dreger, R. Graves, S. Larsen, K. B. Olsen, and A. Pitarka (2003). Tests of 3D elastodynamic codes: Final report for Lifelines project 1a02, *Technical Report*, Pacific Earthquake Engineering Research Center.

Day, S. M., J. Bielak, D. Dreger, R. Graves, S. Larsen, K. B. Olsen, and A. Pitarka (2005). 3D ground motion simulations in basins: Final report for lifelines project 1a03, *Technical Report*, Pacific Earthquake Engineering Research Center.

De Martin, F. (2011). Verification of a spectral-element method code for the Southern California Earthquake Center LOH.3 viscoelastic case, *Bull. Seismol. Soc. Am.* **101,** no. 6, 2855–2865.

Electrical Power Research Institute (EPRI) (1988). A criterion for determining exceedance of the operating basis earthquake, *Report No. EPRI NP-5930*, Palo Alto, California.

Etienne, V., E. Chaljub, J. Virieux, and N. Glinsky (2010). An *hp*-adaptive discontinuous Galerkin finite-element method for 3-D elastic wave modeling, *Geophys. J. Int.* **183,** no. 2, 941–962, doi: 10.1111/j.1365-246X.2010.04764.x.

Graves, R. W. (1996). Simulating seismic wave propagation in 3D elastic media using staggered-grid finite differences, *Bull. Seismol. Soc. Am.* **86,** no. 4, 1091–1106.

Jongmans, D., K. Pitilakis, D. Demanet, D. Raptakis, J. Riepl, C. Horrent, K. Lontzetidis, and P.-Y. Bard (1998). EURO-SEISTEST: Determination of the geological structure of the Volvi basin and validation of the basin response, *Bull. Seismol. Soc. Am.* **88,** no. 2, 473–487.

Kawase, H., and T. Iwata (1998). A report on submitted results of the simultaneous simulation for Kobe, in *The Effects of Surface Geology on Seismic Motion, Recent Progress and New Horizon on ESG Study*, Vol. 3, Balkema/CRC Press, Leiden, The Netherlands.

Kawase, H., and S. Matsushima (1998). Strong motion simulation in Kobe during the Hyogo-ken Nanbu earthquake of 1995 based on a three-dimensional basin structure, *J. Struct. Constr. Eng. Trans. Architec. Inst.* **514,** 111–118.

Kempton, J. J., and J. P. Stewart (2006). Prediction equations for significant duration of earthquake ground motions considering site and near-source effects, *Earthq. Spectra* **22,** no. 4, 985–1013, doi: 10.1193/1.2358175.

Klin, P., E. Priolo, and G. Seriani (2010). Numerical simulation of seismic wave propagation in realistic 3-D geo-models with a Fourier pseudo-spectral method, *Geophys. J. Int.* **183,** no. 2, 905–922, doi: 10.1111/j.1365-246X.2010.04763.x.

Komatitsch, D., Q. Liu, J. Tromp, P. Süss, C. Stidham, and J. H. Shaw (2004). Simulations of ground motion in the Los Angeles basin based upon the spectral-element method, *Bull. Seismol. Soc. Am.* **94,** 187–206, doi: 10.1785/0120030077.

Kristek, J., P. Moczo, and R. J. Archuleta (2002). Efficient methods to simulate planar free surface in the 3D 4th-order staggered-grid finite-difference schemes, *Stud. Geophys. Geod.* **46,** no. 2, 355–381.

Kristek, J., P. Moczo, and M. Gális (2010). Stable discontinuous staggered grid in the finite-difference modeling of seismic motion, *Geophys. J. Int.* **183,** no. 3, 1401–1407, doi: 10.1111/j.1365-246X.2010.04775.x.

Kristeková, M., J. Kristek, and P. Moczo (2009). Time-frequency misfit and goodness-of-fit criteria for quantitative comparison of time signals, *Geophys. J. Int.* **178,** 813–825, doi: 10.1111/j.1365-246X.2009.04177.x.

Kristeková, M., J. Kristek, P. Moczo, and S. M. Day (2006). Misfit criteria for quantitative comparison of seismograms, *Bull. Seismol. Soc. Am.* **96,** no. 5, 1836–1850, doi: 10.1785/0120060012.

Manakou, M. (2007). Contribution to the determination of a 3D soil model for site response analysis, the case of the Mygdonian basin, *Ph.D. Thesis*, Department of Civil Engineering, Aristotle University of Thessaloniki, Greece.

Manakou, M., D. Raptakis, P. I. Apostolidis, F. J. Chávez-García, and K. Pitilakis (2007). The 3D geological structure of the Mygdonian sedimentary basin (Greece), *4th International Conference on Earthquake Geotechnical Engineering*, Thessaloniki, Greece, 25–28 June, Paper Number 1686.

Manakou, M., D. Raptakis, F. J. Chávez-García, P. I. Apostolidis, and K. Pitilakis (2010). 3D soil structure of the Mygdonian basin for site response analysis, *Soil Dynam. Earthq. Eng.* **30,** 1198–1211.

Martin, R., and D. Komatitsch (2009). An unsplit convolutional perfectly matched layer technique improved at grazing incidence for the viscoelastic wave equation, *Geophys. J. Int.* **179,** no. 1, 333–344, doi: 10.1111/j.1365-246X.2009.04278.x.

Moczo, P., J. Kristek, and M. Gális (2004). Simulation of the planar free surface with near-surface lateral discontinuities in the finite-difference modeling of seismic motion, *Bull. Seismol. Soc. Am.* **94,** no. 2, 760–768.

Moczo, P., J. Kristek, and M. Gális (2014). *The Finite-Difference Modelling of Earthquake Motions Waves and Ruptures*, Cambridge University Press, Cambridge, United Kingdom.

Moczo, P., J. Kristek, V. Vavryčuk, R. J. Archuleta, and L. Halada (2002). 3D heterogeneous staggered-grid finite-difference modeling of seismic motion with volume harmonic and arithmetic averaging of elastic moduli and densities, *Bull. Seismol. Soc. Am.* **92,** no. 8, 3042–3066.

Papazachos, C. B. (1998). Crustal *P*- and *S*-velocity structure of the Serbo-macedonian Massif (northern Greece) obtained by non-linear inversion of traveltimes, *Geophys. J. Int.* **134,** 25–39, doi: 10.1046/j.1365-246x.1998.00558.x.

Peter, D., D. Komatitsch, Y. Luo, R. Martin, N. Le Goff, E. Casarotti, P. Le Loher, F. Magnoni, Q. Liu, C. Blitz, *et al.* (2011). Forward and adjoint simulations of seismic wave propagation on fully unstructured hexahedral meshes, *Geophys. J. Int.* **186,** no. 2, 721–739, doi: 10.1111/j.1365-246X.2011.05044.x.

Pitarka, A. (1999). 3D elastic finite-difference modeling of seismic motion using staggered grids with nonuniform spacing, *Bull. Seismol. Soc. Am.* **89,** no. 1, 54–68.

Pitilakis, K., G. Manos, D. Raptakis, A. Anastasiadis, K. Makra, and M. Manakou (2009). The EUROSEISTEST experimental test site in Greece, *EGU General Assembly*, Vienna, Austria, 19–24 April.

Pitilakis, K., Z. Roumelioti, D. Raptakis, M. Manakou, K. Liakakis, A. Anastasiadis, and D. Pitilakis (2013). The EUROSEISTEST strong ground motion database and web portal, *Seismol. Res. Lett.* **84,** no. 5, 796–804.

Raptakis, D., F. J. Chávez-García, K. Makra, and K. Pitilakis (2000). Site effects at Euroseistest-I: Determination of the valley structure and confrontation of observations with 1D analysis, *Soil Dynam. Earthq. Eng.* **19,** 1–22.

Raptakis, D., M. Manakou, F. J. Chávez-García, K. Makra, and K. Pitilakis (2005). 3D configuration of Mygdonian basin and preliminary estimate of its site response, *Soil Dynam. Earthq. Eng.* **25,** 871–887.

Satoh, T., H. Kawase, T. Sato, and A. Pitarka (2001). Three-dimensional finite-difference waveform modeling of strong motions observed in the Sendai basin, Japan, *Bull. Seismol. Soc. Am.* **91,** 812–825, doi: 10.1785/0120000086.

Stacey, R. (1988). Improved transparent boundary formulations for the elastic-wave equation, *Bull. Seismol. Soc. Am.* **78,** no. 6, 2089–2097.

Trifunac, M. D., and A. G. Brady (1975). On the correlation of seismic intensity scales with the peaks of recorded strong ground motion, *Bull. Seismol. Soc. Am.* **65,** no. 1, 139–162.

Tsuno, S., E. Chaljub, and P.-Y. Bard (2006). Grenoble valley simulation benchmark: Comparison of results and main learning, *Third International Symposium on the Effects of Surface Geology on Seismic Motion*, Grenoble, France, 30 August–1 September, Paper Number SB2, Vol. 2.

Appendix

The E2VP Ground-Motion Evaluation Criteria

To evaluate the extent of similarity between two mismatched signals within the EUROSEISTEST Verification and Validation Project (E2VP), we elaborated comparisons based on a series of complementary ground-motion parameters, each one emphasizing a different characteristic of the waveforms. To keep a reasonable number of parameters, the E2VP evaluation criteria are restricted to five parameters (three for amplitude/frequency content, one for energy, and one for duration) chosen as followed: (1) C1, peak ground acceleration (PGA); (2) C2, elastic spectral acceleration in intermediate frequencies, arithmetic average over 1.5–3.0 Hz; (3) C3, elastic spectral acceleration in low frequencies, arithmetic average over 0.375–0.750 Hz; (4) C4, cumulative absolute velocity (CAV); and (5) C5, relative significant duration (RSD) between 5% and 95% of the Arias intensity.

Criteria C1–C3 evaluate the amplitude of the signal in different frequency bands. These different frequency bands are chosen according to the observed characteristics of the real signals at the center of the Mygdonian basin: the frequency range evaluated by C3 includes the fundamental resonance frequency of the basin, whereas C2 covers the two higher modes.

Criterion C4 is based on the CAV, which is defined as the integral of the absolute value of the acceleration time series (Electrical Power Research Institute [EPRI], 1988):

$$\mathrm{CAV} = \int_0^{D_{\max}} |a(t)|dt, \tag{A1}$$

in which $|a(t)|$ is the absolute value of the acceleration time series at time t and $D_{\max}$ represents the total duration of the time series. Anderson (2004) proposed the Arias intensity and the energy integral as ground-motion parameters representative of the signal's intensity; both parameters are computed from the square of the acceleration or velocity time series. CAV is chosen as an alternative in the E2VP evaluation procedure because this parameter is of the same dimension as the three amplitude and frequency-content criteria C1, C2, and C3, therefore giving misfit values of the same order. CAV was found to be the instrumental intensity measure that best correlates with the onset of structural damage to engineered structures (EPRI, 1988; Campbell and Bozorgnia, 2010).

The duration criterion C5 is based on the RSD, which is defined as the time interval over which a specified amount of energy is dissipated. One common measure of the significant duration is the time interval between 5% and 95% of the Arias intensity I_A (Trifunac and Brady, 1975; Kempton and Stewart, 2006):

$$I_A = \left(\frac{\pi}{2g}\right) \int_0^{D_{\max}} a^2(t)dt, \tag{A2}$$

in which $a(t)$ is the acceleration time history, g is the acceleration of gravity, and $D_{\max}$ represents the total duration of the time series. The 5%–95% RSD is chosen in the E2VP evaluation procedure because it does not account for the timing of arrival of the different phases of energy. A slight time shift is frequently encountered when comparing recordings with their numerical predictions, possibly due to some mislocation of the source or to uncertainties in the bedrock velocity structure. That problem, easily identified by comparing arrival times at rock sites, does not affect the impact of ground motion on structures and is therefore of a secondary importance with respect to the E2VP purposes.

Prior to the computation of the misfits, the same processing is performed on both time series to be compared. They are cut to the same duration in time (generally to the shorter length of the numerical prediction, or 30 s in the present study). Both are band-pass filtered using a sixth-order Butterworth filter with corner frequencies of 0.05 Hz and of the maximum frequency available in the numerical prediction (4 Hz in the present study).

The comparison of two signals involves a prediction (a synthetic ground motion) being compared to the target, which is either the corresponding real recording or another prediction (eventually considered as a reference signal). The misfit δ_P between the target and its prediction for one ground-motion parameter P is therefore expressed in percentage of the target parameter P_{target} with the logarithm formulation

$$\delta_P = \left(\frac{(\log(P_{\mathrm{pred.}}/P_{\mathrm{target}})}{\log(2)}\right) \times 100. \tag{A3}$$

This calculation of the misfit δ_P gives symmetrical values for under- or overestimation of the target value: δ_P is negative when the prediction underestimates the target and positive when the prediction overestimates the target.

In the E2VP evaluation procedure, the horizontal components of the ground motion are handled differently, depending on the considered ground-motion parameter. At first, each parameter is estimated over distinct horizontal components, giving two horizontal values per ground motion. Both C4 and C5 are based on the integral of the acceleration time series; therefore, the two horizontal values of the corresponding parameter (CAV and RSD) are directly added together prior to the comparison. Concerning C1–C3, the horizontal components of the target signal are systematically rotated, ranging from 0° to 355°, with an angle increment of 5°, to determine the rotation of components that maximizes the value of the considered parameter. This systematic exploration is performed on the acceleration time series for C1 and on the elastic spectral acceleration for C2 and C3. Once the maximizing rotation angle is determined, the same rotation is applied to the predictive signal. The comparison finally occurs on the horizontal component rotated to maximize the value of the target parameter.

University Grenoble Alpes
ISTerre, CNRS, IRD, IFSTTAR
BP 53, F-38041 Grenoble CEDEX 09
France
emeline.maufroy@ujf-grenoble.fr
emmanuel.chaljub@ujf-grenoble.fr
pierre-yves.bard@ujf-grenoble.fr
(E.M., E.C., P.-Y.B.)

CEA Cadarache
French Alternative Energies and Atomic Energy Commission
DPIE/SA2S/GAS
Bât. 352, F-13108 St. Paul Les Durance
France
fabrice.hollender@cea.fr
cedric.guyonnet-benaize@hotmail.fr
(F.H., C.G.-B.)

Comenius University Bratislava
Faculty of Mathematics, Physics and Informatics
Geophysical Institute
Slovak Academy of Sciences
Mlynská dolina F2
84248 Bratislava 4
Slovakia
kristek@fmph.uniba.sk
moczo@fmph.uniba.sk
(J.K., P.M.)

Istituto Nazionale di Oceanografia e di Geofisica Sperimentale (OGS)
Centro di Ricerche Sismologiche
Borgo Grotta Gigante 42/c
I-34010 Sgonico (Trieste)
Italy
pklin@inogs.it
epriolo@inogs.it
(P.K., E.P.)

Disaster Prevention Research Institute
Kyoto University
Gokasho, Uji
Kyoto 611-0011
Japan
iwaki@bosai.go.jp
iwata@egmdpri01.dpri.kyoto-u.ac.jp
(A.I., T.I.)

Université de Nice Sophia-Antipolis
Centre National de la Recherche Scientifique (CNRS)
IRD, Observatoire de la Côte d'Azur
GEOAZUR, UMR 7329
Sophia-Antipolis
F-06560 Valbonne
France
vincent.etienne@aramco.com
(V.E.)

Bureau des Recherches Géologiques et Minières (BRGM)
Direction Risques et Prévention
Unité Risques Sismique et Volcanique
3 avenue Claude Guillemin
BP 36009
F-45060 Orléans CEDEX 2
France
f.demartin@brgm.fr
(F.D.)

Institute of Engineering Seismology & Earthquake Engineering (ITSAK-EPPO)
P.O. Box 53 Finikas
GR-55102 Thessaloniki
Greece
ntheo@itsak.gr
(N.P.T.)

Aristotle University of Thessaloniki
P.O. Box 424
GR-54124 Thessaloniki
Greece
manakou@civil.auth.gr
kpitilak@civil.auth.gr
(M.M., K.P.)

Manuscript received 29 July 2014;
Published Online 19 May 2015

SCIENTIFIC REPORTS

OPEN

Long Duration of Ground Motion in the Paradigmatic Valley of Mexico

V. M. Cruz-Atienza[1], J. Tago[2], J. D. Sanabria-Gómez[3], E. Chaljub[4,5], V. Etienne[6], J. Virieux[4,5] & L. Quintanar[1]

Received: 20 June 2016
Accepted: 15 November 2016
Published: 09 December 2016

Built-up on top of ancient lake deposits, Mexico City experiences some of the largest seismic site effects worldwide. Besides the extreme amplification of seismic waves, duration of intense ground motion from large subduction earthquakes exceeds three minutes in the lake-bed zone of the basin, where hundreds of buildings collapsed or were seriously damaged during the magnitude 8.0 Michoacán earthquake in 1985. Different mechanisms contribute to the long lasting motions, such as the regional dispersion and multiple-scattering of the incoming wavefield from the coast, more than 300 km away the city. By means of high performance computational modeling we show that, despite the highly dissipative basin deposits, seismic energy can propagate long distances in the deep structure of the valley, promoting also a large elongation of motion. Our simulations reveal that the seismic response of the basin is dominated by surface-waves overtones, and that this mechanism increases the duration of ground motion by more than 170% and 290% of the incoming wavefield duration at 0.5 and 0.3 Hz, respectively, which are two frequencies with the largest observed amplification. This conclusion contradicts what has been previously stated from observational and modeling investigations, where the basin itself has been discarded as a preponderant factor promoting long and devastating shaking in Mexico City.

The seismic response of the Valley of Mexico has been for many years a paradigmatic study case in earthquake seismology and engineering. After the devastation of Mexico City (MC) in 1985, when more than 15,000 people died due to a magnitude 8.0 earthquake beneath the coast of Michoacán, more than 450 km away from the city, scientists have attempted to explain site effects such as the extraordinary amplification of seismic waves and the extremely long duration of ground motion in the sedimentary basin where most of the city is located (Fig. 1). Amplification of ground motion due to local soil conditions is a well-known phenomenon. In the Valley of Mexico, spectral amplification for subduction earthquakes (i.e., with epicentral distances greater than 300 km) at soft-soil sites range from 10 to 50 at frequencies between 0.2 and 0.7 Hz with respect to hard-rock sites[1,2]. However, the hard-rock sites also experience large amplifications of about 10 due to regional site effects (quantified from attenuation relationships) associated with the volcanic arc deposits where the valley is embedded[3,4]. This means that absolute spectral amplifications in the lake-bed zone of the Valley of Mexico may reach values from 100 to 500, which are probably the largest ever reported worldwide[4].

Long-lasting ground motion in the Valley of Mexico

While the amplification of seismic waves in the Valley of Mexico has been satisfactorily explained by regional and local soil conditions[5–12], the physical reasons for the long duration of ground motion remain an open question. Initial efforts addressing this issue considered two-dimensional wave propagation models in small-basin configurations with realistic attenuation properties. Results from these exercises led to conclude that surface-waves trains generated at the edges of the basin[10,13,14] suffer a rapid decay as they propagate, and thus to discard this mechanism as a possible explanation for the long seismic records[7,15]. This conclusion invoked the existence of regional-scale effects producing the elongation of the incoming wavefield to Mexico City from subduction earthquakes, such as multipathing of seismic waves due to scatterers in the crust and surroundings of the basin[16,17], and seismic energy entrapment in both the accretionary prism near the source region and the Transmexican Volcanic Belt (TMVB)[18,19]. The interaction between the incoming wavefield and the local basin conditions may

[1]Instituto de Geofísica, Universidad Nacional Autónoma de México, Mexico. [2]Facultad de Ingeniería, Universidad Nacional Autónoma de México, Mexico. [3]Escuela de Física, Universidad Industrial de Santander, Bucaramanga, Colombia. [4]Univiversité de Grenoble Alpes, ISTerre, F-38058 Grenoble, France. [5]CNRS, ISTerre, F-38058 Grenoble, France. [6]ARAMCO, Advanced Research Center, Saudi Arabia. Correspondence and requests for materials should be addressed to V.M.C.-A. (email: cruz@geofisica.unam.mx)

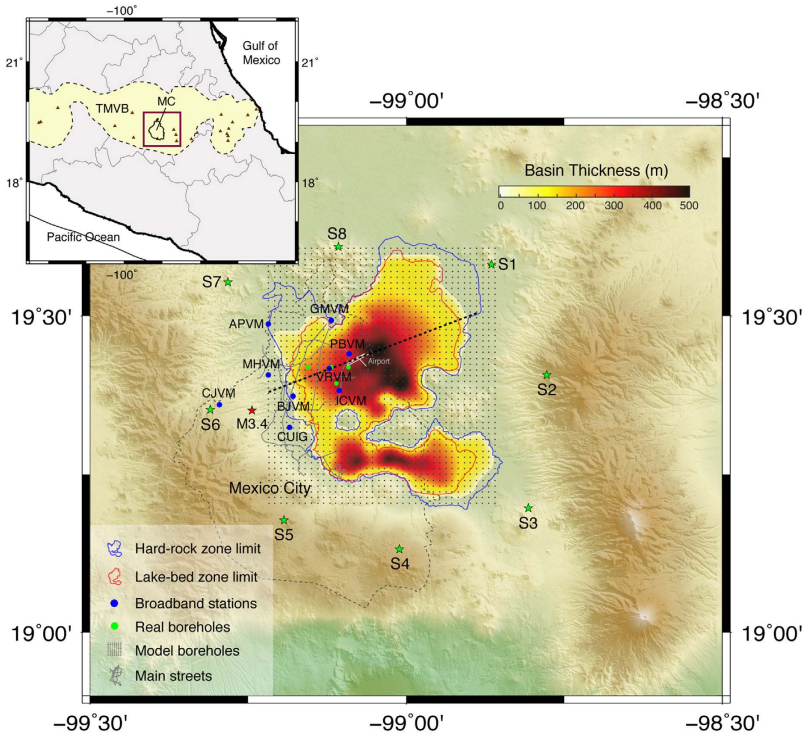

Figure 1. Topographic setting of Mexico City (MC) and the Valley of Mexico. Color scale corresponds to the basin thickness (i.e., the basin contact with the Oligocene volcanics of the Transmexican Volcanic Belt, TMVB). Stars show the epicenters for the vertical body forces applied at the free surface (green) and the magnitude 3.4 earthquake of December 1, 2014 (red). This figure has been created using the Generic Mapping Tools (GMT) Version 5.3.0, http://gmt.soest.hawaii.edu.

also elongate the ground motion when the resonant frequencies of the basin coincide with the dominant periods of the wavefield[20].

Although our current understanding of the duration of ground motion in the lake-bed zone of MC is clearly rooted in the nature of the incoming wavefield, the actual effects produced by the sedimentary basin itself have been underestimated. Figure 2a shows the seismic records ($f < 1$ Hz) of a magnitude 3.4 earthquake that occurred ~4 km below the city on December 1, 2014 (Fig. 1). These unprecedented records were possible thanks to a recently-installed permanent broadband network (blue circles) in the Valley of Mexico operated by the Servicio Sismológico Nacional (SSN). Despite the small magnitude of the event, ground motion in the basin lasted more than two minutes (e.g. at lake-bed sites VRVM, ICVM and PBVM). This can be better appreciated in the band-pass filtered signals at 0.3 Hz, where the long coda is dominated by the harmonic beating widely reported in the literature for subduction earthquakes recorded in MC[16,21]. In contrast, this beating is barely present at hard-rock sites such as CUIG and CJVM, where the motion is dominated by a single wave package with duration no longer than 20 s. This observation strongly suggests that ground motion in the lake-bed zone experiences very long durations in the absence of regional-scale effects. Local basin conditions are thus preponderant in the duration of ground shaking across the basin at frequencies where the amplification of seismic waves is the largest. The leading question of this work is thus raised about the mechanisms allowing long-lasting wave propagation within a highly dissipative sedimentary basin. Two main hypotheses may be advanced: (1) the basin incoming wavefield suffers from multiple-scattering even at a local scale, and/or (2) the sedimentary basin itself enhances sustained wave trains generation and efficient propagation.

Though certainly true, hypothesis one does not seem to have first order implications in the duration of ground motion at the lake-bed zone, as revealed by the absence of significant seismic energy in the coda of hard-rock sites (Fig. 2). On the other hand, considering the highly dissipative and fluid saturated sediments that cover large part of the basin (see next section), a plausible idea supporting hypothesis two is the efficient propagation of seismic energy in the deep basin, carried by surface-waves overtones. In this work we examine this argument based on realistic 3D wave propagation modeling to understand whether local soil conditions within the basin may explain the observed long seismic records.

A basin model for the Valley of Mexico

The Valley of Mexico is located in the southern and volcanically active part of the TMVB (Fig. 1). This region is composed by Oligocene volcanics overlaying Cretaceous limestones. On top of these formations within the valley, there are Miocene volcanics overlain by a ~100 m thick sequence of tuffs or sands, gravel and recent lava flows[11,22], averaging a thickness of ~2 km for the TMVB above the Cretaceous limestones[12,23]. Geotechnically speaking, this geologic setting corresponds to the hill zone of the valley (region outside the blue contour in Fig. 1), which may

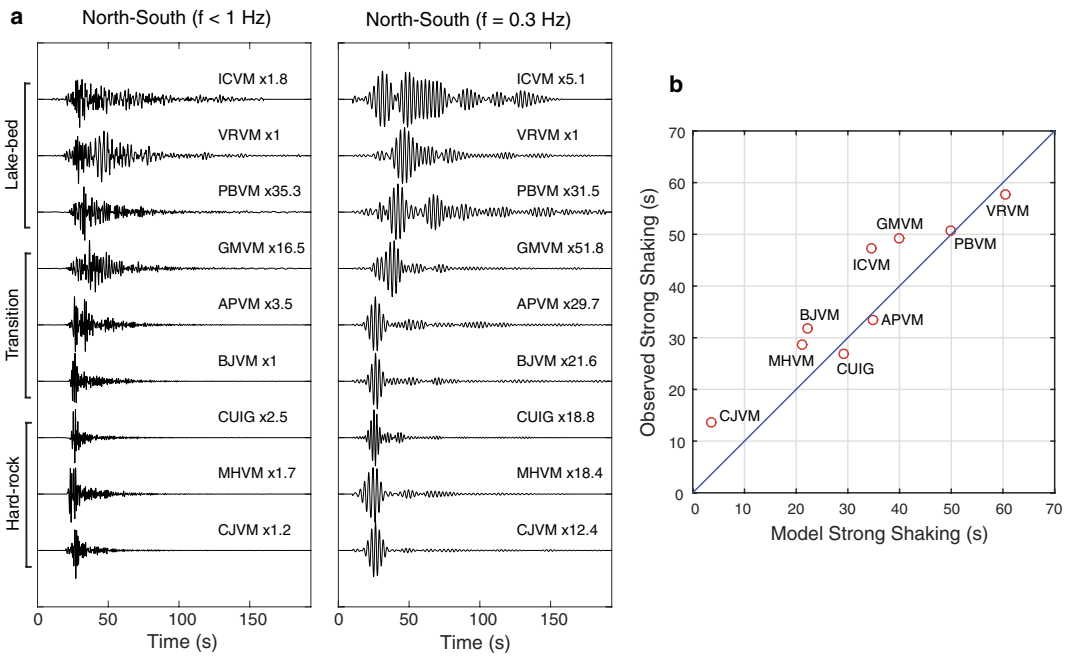

Figure 2. (**a**) Observed velocity seismograms in two different frequency bands at nine broadband seismic stations for a M3.4 earthquake with 4 km depth (see Fig. 1). Records are aligned with the P-wave arrival and scaled with the factors given for each trace. Notice the long seismic records in the lake-bed stations. (**b**) Observed and modeled durations of the strong shaking phase for f < 1 Hz. The corresponding synthetic seismograms are shown in Figure A2.

be considered hard-rock sites (e.g. CUIG, MHVM and CJVM). The stratigraphy of the MC basin is essentially the same as in the hill zone except for the absence of recent lava flows and the presence of clays with high water content of 10 to about 100 m thickness[24,25]. The basin is geotechnically known as the lake-bed zone of the valley (region within the red contour in Fig. 1) and it is where the largest amplification of ground motion is observed. The transition region in between the lake-bed and the hard-rock zones is mainly composed by alluvial deposits. The composition and thickness of the surficial clay deposits changes laterally within the basin[8,22]. However, shear-wave speed measurements on core samples from different boreholes in the lake-bed zone show extremely low values in these deposits (i.e. 30–100 m/s), with an average thickness of about 50 m[24]. Laboratory tests[26] and field estimates[27] also show that the clays are highly dissipative, with very low shear Q values ranging from 10 to 50. These observations led to a four-layer velocity model for the basin with very high Vp/Vs values on top to explain experimental data from several earthquakes[28]. We adopt this model for the lake-bed zone in our calculations (Figure A1a and Table A1).

Observations within the basin show that depths (H) to the deep, geotechnically consistent deposits are proportional to the natural vibration periods (T_0) of the sites (i.e., $H = (\beta/4)^*T_0)^3$. These periods are thus proportional to the thickness of the surficial clay layers that we have assumed constant in our model. However, to confine the underlying deep-basin deposits in depth, from a large data set of natural vibration periods across the basin[2,29] and assuming an average shear-wave speed (β) of 400 m/s, we generated the bed-rock geometry shown in Fig. 1. This interface represents, in our model, the contact between the basin deposits and the Oligocene volcanics of the TMVB (i.e., fourth interface in Figure A1a). A cross section of our basin model along the dotted line of Fig. 1 is shown later in section "Dominance of surface waves overtones". Regarding the crustal structure surrounding the basin, we adopted a 1D model determined from the inversion of receiver functions at the CUIG site[30], which includes a relatively low-velocity layer on top, associated with the ~2 km thick TMVB (see Figure A1a and Table A1). To minimize numerical errors, the interfaces of the model were vertically homogenized before discretizing the model by averaging the S- and P-slownesses and densities[31] (circles in Figure A1a). The homogenization length is 50 m, which is about half of the minimum wavelength in the surficial clay layers. Using the computational method introduced in the next section we calibrated, by trial and error, the attenuation properties of the seismic model so that the durations of the intense phases of ground motions (i.e., time between 5% and 95% of the Arias intensity)[32] observed for the M3.4 earthquake in nine stations are similar to those predicted by our model assuming a 4 km depth reverse faulting below the epicenter (Figs 2b and A2), as suggested by the first P-wave arrivals. These properties, which are in accordance with laboratory and field measurements[26,27], are such that Qs = 0.3*Vs for Vs < 400 m/s and Qs = 0.1*Vs otherwise, with Qp = 2*Qs everywhere (Table A1).

Computational method for viscoelastic wave propagation

Simulating the propagation of seismic waves in extreme sedimentary basins represents a big challenge. In our seismic model for the Valley of Mexico, the S-wavelength at 1 Hz shortens from 4.8 km in the deep crust to only 50 m in the top layer of the basin during propagation. To obtain an accurate solution of the elastodynamic

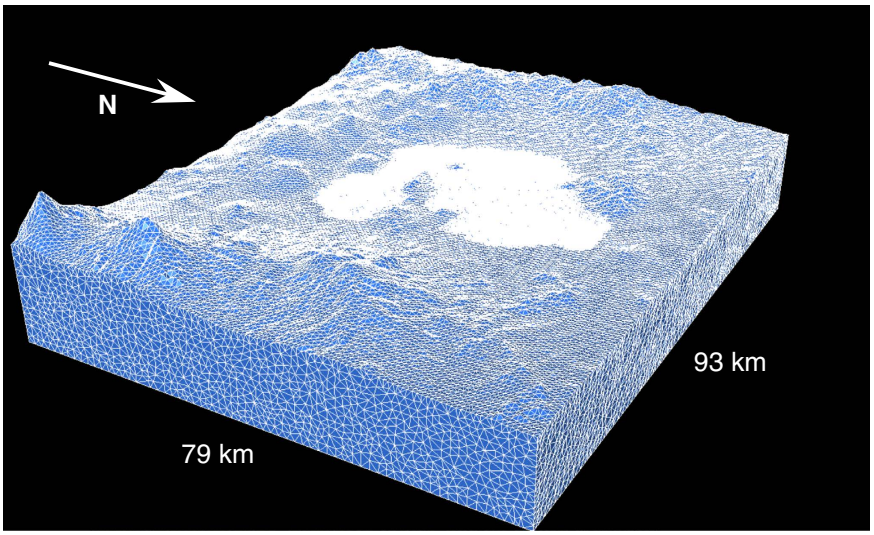

Figure 3. Top ~10 km of the unstructured tetrahedral mesh used in the study. Notice that the elements honor the basin geometry and the actual topography of the terrain (compare with Fig. 1). The mesh considered for the simulations reaches 50 km depth. This figure has been created using the TetView Linux software Version 1.0, http://wias-berlin.de/software/tetgen/tetview.html.

equations governing the propagating waves with such modulation, the numerical scheme must handle powerful capabilities to sample the wavefield efficiently in the whole simulation domain. For this reasons we have developed an hp-discontinuous Galerkin finite element method (DG-FEM) called GEODG3D that handles both unstructured domain decompositions (h-adaptivity) and different approximation orders per element in space (p-adaptivity)[33–35]. GEODG3D is an extension for viscoelastic wave propagation of a method previously introduced for elastic waves[33]. It solves the velocity-stress formulation of the visco-elastodynamic equations in three dimensions with rock quality factors, Qs and Qp, chosen to be nearly constant in the frequency range of interest (i.e., $f < 1$ Hz). For a detailed description of the viscoelastic model and the DG-FEM see Methods.

To maximize the integration time step imposed by the Courant stability criterion, GEODG3D locally adapts the elements' approximation order depending on both the elastic properties of the medium and the size of the tetrahedra (p-adaptivity) (Figure A3a). For decomposing the simulation domain in tetrahedral elements, we followed a meshing strategy that guarantees the same numerical accuracy across the whole domain[33]. Given a maximum resolvable frequency (1 Hz in this work) and starting from a regular coarse mesh, the strategy iteratively refines the elements until the accuracy criterion (i.e., 3 elements per minimum wavelength; Figure A5) is satisfied locally in at least 99.8% of the elements (h-adaptivity) (Figure A3b). Figure 3 shows the resulting mesh for the upper part of the simulation domain, where the elements are clearly adapted to both the actual topography and the extremely low velocities of the basin (compare with Fig. 1). Numerical verification (Figure A4) and convergence analysis (Figure A5) of the GEODG3D viscoelastic solver have been thoroughly done[35], finding excellent results for different international benchmark problems (see Section 3 of Methods). Table A2 provides useful numbers related to the tetrahedral mesh and discretization parameters used in all simulations of this study.

Dominance of surface waves overtones

Observational evidence for the dominance of surface waves overtones in the Valley of Mexico shows that peak displacements in the lake-bed zone between 0.3–0.5 Hz at different borehole depths (green circles in Fig. 1) for several subduction earthquakes are in accordance with theoretical eigenfunctions for the Rayleigh-waves first overtones in the basin model of Table A1[28]. These observations, which are shown later in section "Dominance of surface waves overtones", reveal that seismic energy barely decays with depth. Furthermore, surface waves dispersion diagrams generated from the correlation of ambient noise in the lake-bed zone also show the overwhelming dominance of first overtones[36]. To understand the physical reason explaining these observations and to quantify the implications in terms of ground motion duration, we first analyzed Green's functions in our 3D model of the Valley of Mexico (Fig. 3) for eight vertical forces applied at the free surface around the basin (green stars in Fig. 1). The sources radiation thus corresponds to P- and S-waves followed by a dominant Rayleigh train. In order to quantify the effect of attenuation, we performed the simulations for both the elastic and the viscoelastic cases up to 220 s in the UNAM supercomputer Miztli. Velocity snapshots for the viscoelastic simulation with source S6 are shown in Fig. 4, where amplification, diffraction and generation of surface waves at the basin edges are clearly observed.

Figure 5 shows normalized seismic profiles at 0.5 Hz with 500 m spacing for source S6 along the dashed line of Fig. 1. In the elastic case (Fig. 5a), three main pulses are observed. Two of them propagate from the basin edges with speed of ~66 m/s, and the other emerges at ~10 km of the array with a speed of 260 m/s. Considering the Rayleigh waves group-velocity dispersion curves for shallow and deep basin locations (circles in Figure A1b), speeds clearly correspond to the fundamental mode (R0) and first overtones (R1), respectively. It is striking that

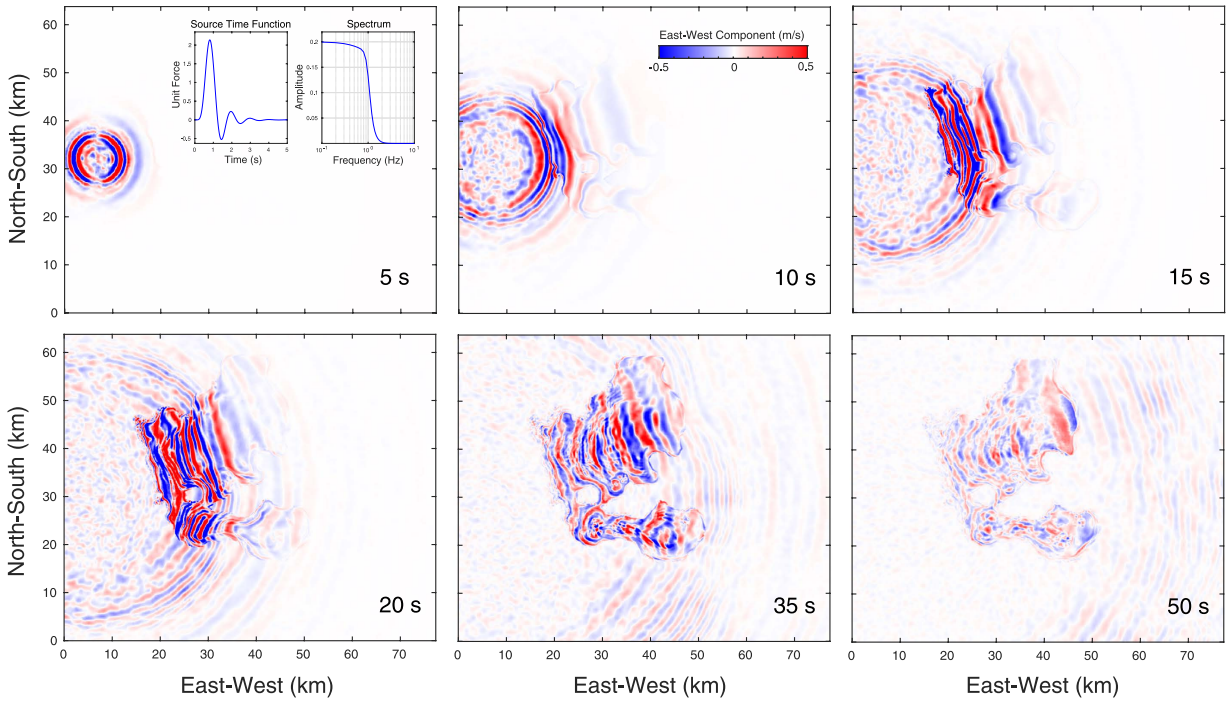

Figure 4. Snapshots of the Green's function for the vertical body force S6 (see Fig. 1) described by the inset time history with flat spectrum up to 1 Hz. Notice the topographic scattering, the generation and propagation of wave trains at different speeds within the basin, and their multiple diffractions. This figure has been created using the Matlab software Version R2016a, http://www.mathworks.com/.

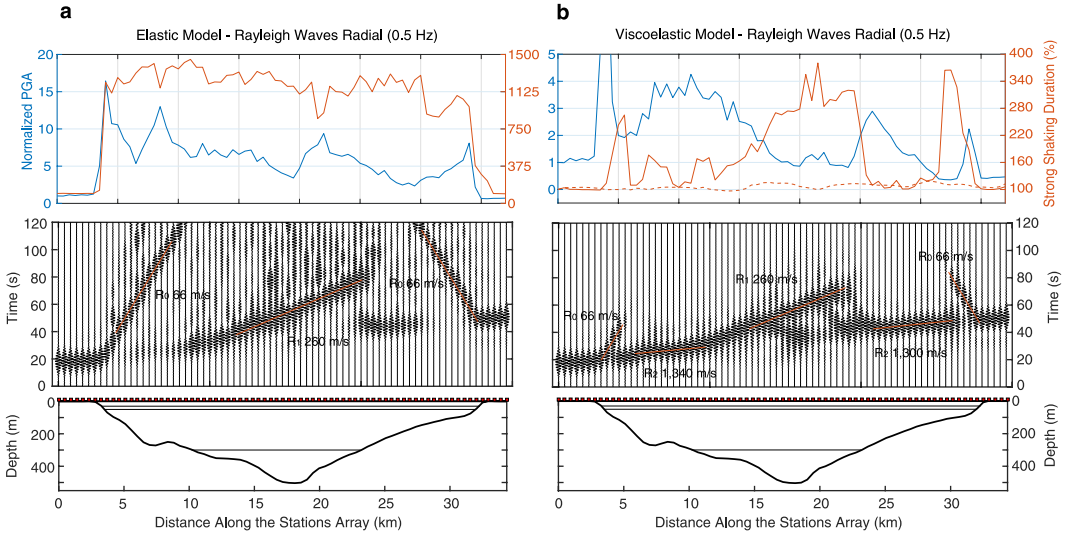

Figure 5. Seismic sections of the radial-component at 0.5 Hz for source S6 along the linear array shown in Fig. 1 for the elastic (**a**) and viscoelastic (**b**) models. A cross section of the basin model is shown at the bottom. On top, peak ground accelerations (PGAs, radial component) along the array (blue) normalized by the value at the station with smallest epicentral distance. Durations of the strong shaking phase along the array (orange) as percentages of the duration of the incoming wavefield (i.e., the duration measured at the station with smallest epicentral distance). As a reference, the dashed line indicates the durations considering only the 1D regional structure (i.e., in the absence of the basin).

even in the absence of attenuation, the first overtone dominates in the deep basin (i.e., between 10 and 23 km along the array). Unlike the elastic case, attenuation rapidly dissipates the fundamental mode and makes the overtones dominant along almost the whole array in the viscoelastic simulation (Fig. 5b). The most prominent wave train in the shallow basin regions propagates with the speed of the bedrock fundamental mode (i.e., ~1,300 m/s,

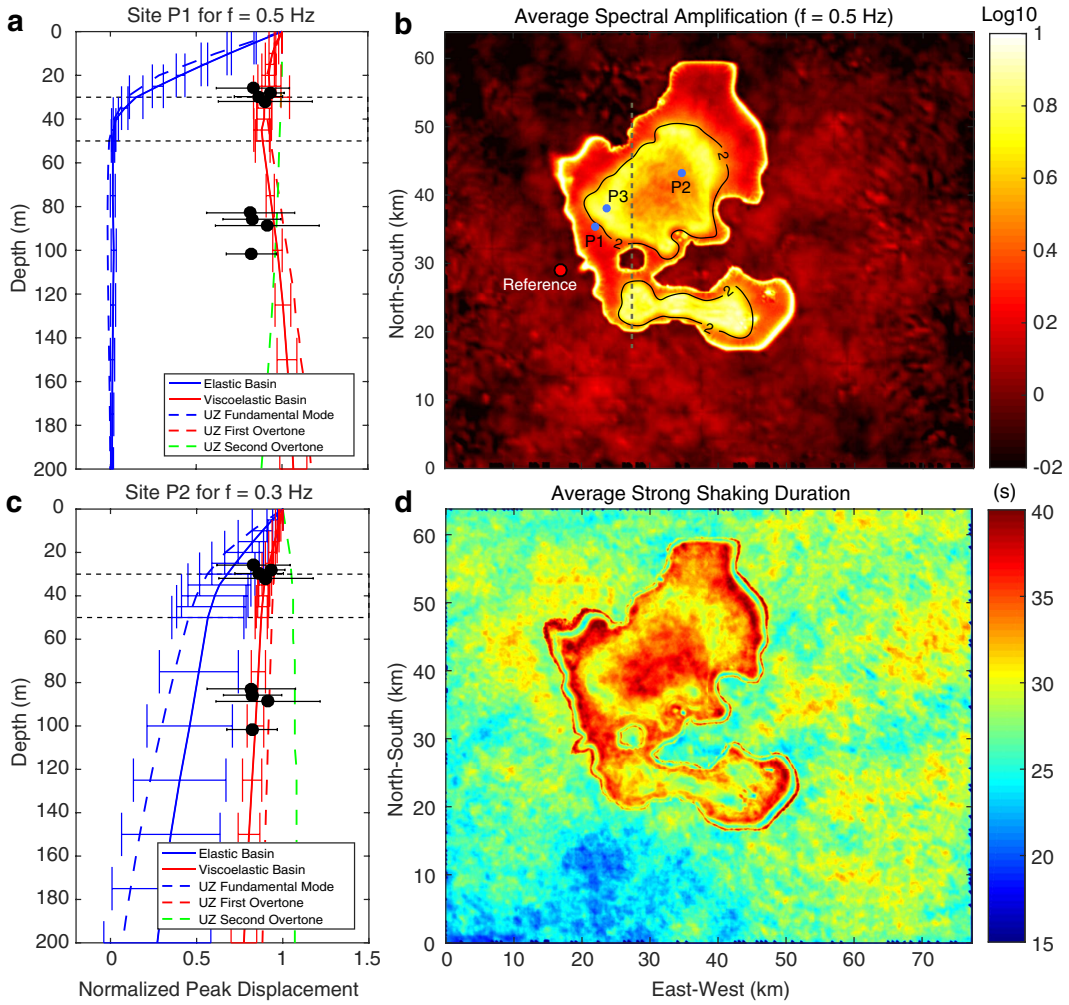

Figure 6. (**a,c**) Comparison of average eigenfunctions for the 8 sources with standard deviation bars for both elastic (blue solid) and viscoelastic (red solid) simulations at two representative sites, P1 and P2, and different frequencies. Dashed lines show theoretical eigenfunctions for the vertical component of Rayleigh waves in the model of Figure A1a (Table A1) for the fundamental mode (blue) and the first (red) and second (green) overtones. Normalized peak vertical displacements observed in different boreholes (green dots in Fig. 1) are shown with black circles and error bars (after Shapiro *et al.*, 2001). (**b**) Fourier spectral amplifications (geometric mean of both horizontal components) at 0.5 Hz with respect to the CUIG site (Fig. 1) averaged for the 8 sources. The black contour corresponds to the 2 s dominant-period. (**d**) Duration of the strong shaking phase for $f < 1$ Hz averaged for the 8 sources. This figure has been created using the Matlab software Version R2016a, http://www.mathworks.com/.

Figure A1b). This means that the incident R0 suffers a mode conversion to become the second overtone (R2) when transduced into the basin, and that such overtone dominates the ground motion at shallow regions thanks to the rapid dissipation of the basin fundamental mode, R0. Around 12 km along the array, the R1 becomes dominant when surface waves propagate from shallow to deeper parts of the basin, revealing the strong influence of the deep sediments.

A systematic analysis is necessary to conclude that overtones dominate the ground motion in the whole basin model. We thus analyzed the wavefields from the eight sources at a regular network of boreholes with 1 km spacing (gray dots in Fig. 1). From the seismograms at the network we computed and averaged synthetic eigenfunctions of Rayleigh waves for all sources in each borehole. To do so we normalized vertical displacements along the boreholes by the corresponding peak values at the free surface and at the same absolute time[28]. Figure 6a and c show the average eigenfunctions with standard deviation bars for both the elastic (blue solid lines) and viscoelastic (red solid lines) simulations at two representative sites, P1 and P2, and different frequencies. In the unrealistic elastic simulations and shallow basin regions (i.e., <250 m deep; e.g. at site P1), the energy at 0.5 Hz decays very rapidly with depth (see Figure A6a) and, consequently, the corresponding eigenfunctions fit the expected shape for the fundamental mode (dashed blue line in Fig. 6a). In contrast, in the realistic viscoelastic simulations the energy efficiently travels in depth so that the eigenfunctions fit the theoretical shape for the first and second overtones (dashed red and green lines). Something similar happens in the deep basin at 0.3 Hz (e.g., at site P2), where the elastic and viscoelastic eigenfunctions follow the expected shapes for the fundamental and

first overtone, respectively (dashed lines in Fig. 6c and Figure A6b). Although it is difficult to identify propagating pulses in the seismic profiles at 0.3 Hz (Figure A7), eigenfunctions at shallow regions reveal that ground motion is dominated by the first and/or second overtones in both the elastic and viscoelastic cases (Figure A9d). In deeper locations and 0.5 Hz, while the viscoelastic simulations are clearly dominated by the first and/or second overtones, variability of the elastic eigenfunctions reveals a contested dominance between the fundamental and higher modes (Figure A9b). In conclusion, ground motion between 0.3 and 0.5 Hz in the viscoelastic model are dominated, across the whole basin, by surface-waves overtones as data from real boreholes suggest[29] (black circles in Fig. 6a,c). The strong attenuation in the top clay layers is responsible for this propagation regime by dissipating the fundamental mode (Figure A6). RMS differences of the elastic and viscoelastic averaged eigenfunctions in the whole borehole network are shown in Figures A9a and A9c, where the shallow and deep regions of the basin are clearly distinguished by yellow colors. In those regions and frequencies, the attenuation plays a major role promoting the overtones dominance.

Implications for the duration of ground motion

Since the attenuation decreases with depth, seismic energy in the deep basin carried by overtones can propagate long distances. Basin-transduced surface waves and generation of wave trains at the basin edges, in addition to the wavefield dispersion and diffraction across the 3D structure, should then elongate the duration of ground motion. The top panels of Figs 5 and A7 show durations of the strong shaking phase for Rayleigh waves along the seismic profile for source S6. In the realistic viscoelastic model, durations grow as the basin becomes deeper, reaching values of 170–280% and 290–500% of the incoming field duration at 0.5 and 0.3 Hz, respectively. A similar situation is found for Love waves (transverse component) as shown in Figure A8, where relative durations vary as 160–280% at 0.5 Hz and 200–500% at 0.3 Hz along almost the whole array. Results for Love waves where obtained applying a 1.5 km depth double-couple strike-slip point source at location S6. In shallow regions (i.e. $<$300 m deep), peak ground accelerations (PGAs) are the largest, although significant amplification also occurs far from the source, between 22 and 28 km of the array for Rayleigh waves. As expected, amplification of single wave packages in the shallow basin region shortens the strong shaking duration. This is clear in both figures from the anti-correlation of PGA and durations along the profile. Horizontal spectral amplifications (geometric mean of both horizontal components) at 0.5 Hz with respect to the CUIG site averaged for all sources reach values larger than 10 along two ring-like regions encompassed by the 2 s dominant-period contour (Fig. 6b). These estimates are in qualitative agreement with empirical values of spectral accelerations at the same frequency[37] and suggest that regions with largest amplification may be explained by the geometry of the deep basin. Significantly larger amplifications (up to 25) are found at the lake-bed representative site P3 (Fig. 6b) around ~1.8 and ~3.2 s (Figure A10), which are two periods with similar amplification levels (with respect to CUIG) for subduction earthquakes at near by locations[2]. These results give confidence in our model predictions in terms of amplification patterns in the valley.

Average durations of horizontal strong shaking in regions with large amplification are relatively small for the reason explained above (Fig. 6d). However, durations in most regions of the basin exceed 40 s as observed in the lake-bed stations for the M3.4 earthquake (Fig. 2). Although much smaller in amplitude, ground motions at hard-rock are also long due to the scatter effect of the basin in the opposite side of the source. This is clearly seen in Figure A11, where ground motion duration inside and outside the basin is the same within the shadow-like region, proving that seismic energy recorded at hard-rock sites does not necessarily correspond to the incoming wavefield of the basin, as suggested by several authors[5,8,16]. Our simulations show that duration of ground motion is remarkably lengthened at frequencies with the largest amplification in the lake-bed (i.e., between ~0.2 and ~0.7 s) (Figs 5, A7 and A8). Long shaking duration at these frequencies may cause large structural damage in Mexico City due to the accumulation of yielding cycles that lengthen the natural vibration periods of the structures. Such mechanism makes these periods to approach those of the soil promoting structural failure, as observed during the devastating 1985 earthquake where more than three hundred 9–12 story, relatively small buildings collapsed[38,39].

In conclusion, our results demonstrate that waves overtones dominate the ground motion in the lake-bed zone of the Valley of Mexico and that this propagation regime strongly contributes to the elongation of intense shaking (i.e., duration of both Rayleigh and Loves waves longer than 170% and 290% of the incoming field duration at 0.5 and 0.3 Hz, respectively) at frequencies where the largest amplification is observed. The bedrock fundamental mode is transduced into the basin and converted into overtones (first and second modes) that dominate the ground motion. The structure of the deep basin is responsible for this mechanism, proving that local basin conditions remarkably increase the duration of strong motion in the lake-bed despite the highly dissipative surficial sediments. Our results imply that duration of the incoming wavefield from subduction earthquakes should be significantly shorter than the observed duration in the lake-bed zone. This conclusion contradicts what has been previously stated from observational and theoretical studies considering the ground motion at hard-rock sites as the basin incoming wavefield. The contradiction can be explained if the seismic coda at those sites is dominated by multiple-scattered local waves generated at the basin, as suggested by our simulations.

References

1. Singh, S. K. *et al.* The Mexico Earthquake of September 19, 1985—A Study of Amplification of Seismic Waves in the Valley of Mexico with Respect to a Hill Zone Site. *Earthquake Spectra* **4,** 653–673, doi: 10.1193/1.1585496 (1988).
2. Reinoso, E. & Ordaz, M. Spectral Ratios for Mexico City from Free-Field Recordings. *Earthquake Spectra* **15,** 273–295, doi: 10.1193/1.1586041 (1999).
3. Singh, S. K., Mena, E. & Castro, R. Some aspects of source characteristics of the 19 September 1985 Michoacan earthquake and ground motion amplification in and near Mexico City from strong motion data. *Bulletin of the Seismological Society of America* **78,** 451–477 (1988).

4. Ordaz, M. & Singh, S. K. Source spectra and spectral attenuation of seismic waves from Mexican earthquakes, and evidence of amplification in the hill zone of Mexico City. *Bulletin of the Seismological Society of America* **82,** 24–43 (1992).
5. Sánchez-Sesma, F., Chávez-Pérez, S., Suárez, M., Bravo, M. A. & Pérez-Rocha, L. E. The Mexico Earthquake of September 19, 1985—On the Seismic Response of the Valley of Mexico. *Earthquake Spectra* **4,** 569–589, doi: 10.1193/1.1585491 (1988).
6. Campillo, M., Bard, P. Y., Nicollin, F. & Sánchez-Sesma, F. The Mexico Earthquake of September 19, 1985—The Incident Wavefield in Mexico City during the Great Michoaca´n Earthquake and Its Interaction with the Deep Basin. *Earthquake Spectra* **4,** 591–608, doi: :10.1193/1.1585492 (1988).
7. Bard, P. Y., Campillo, M., Chávez-García, F. J. & Sánchez-Sesma, F. The Mexico Earthquake of September 19, 1985—A Theoretical Investigation of Large- and Small-scale Amplification Effects in the Mexico City Valley. *Earthquake Spectra* **4,** 609–633, doi: 10.1193/1.1585493 (1988).
8. Seed, H. B., Romo, M. P., Sun, J. I., Jaime, A. & Lysmer, J. The Mexico Earthquake of September 19, 1985—Relationships Between Soil Conditions and Earthquake Ground Motions. *Earthquake Spectra* **4,** 687–729, doi: 10.1193/1.1585498 (1988).
9. Kawase, H. & Aki, K. A study on the response of a soft basin for incident S, P, and Rayleigh waves with special reference to the long duration observed in Mexico City. *Bulletin of the Seismological Society of America* **79,** 1361–1382 (1989).
10. Chávez-García, F. J. & Bard, P.-Y. Site effects in Mexico City eight years after the September 1985 Michoacán earthquakes. *Soil Dynamics And Earthquake Engineering* **13,** 229–247 (1994).
11. Singh, S. K. *et al.* Is there truly a "hard" rock site in the Valley of Mexico? *Geophysical Research Letters* **22,** 481–484, doi: 10.1029/94GL03298 (1995).
12. Shapiro, N. M. *et al.* Surface-wave propagation across the Mexican Volcanic Belt and the origin of the long-period seismic-wave amplification in the Valley of Mexico. *Geophysical Journal International* **128,** 151–166, doi: 10.1111/j.1365-246X.1997.tb04076.x (1997).
13. Bard, P.-Y. & Bouchon, M. The seismic response of sediment-filled valleys. Part 2. The case of incident P and SV waves. *Bulletin of the Seismological Society of America* **70,** 1921–1941 (1980).
14. Kawase, H. Site effects on strong ground motions. *International Handbook of Earthquake and Engineering Seismology*, Part B, Lee, W. H. K. & Kanamori, H. (eds.) Academic Press, London, 1013–1030 (2003).
15. Chávez-García, F. J., Ramos-Martínez, J. & Romero-Jiménez, E. Surface-wave dispersion analysis in Mexico City. *Bulletin of the Seismological Society of America* **85,** 1116–1126 (1995).
16. Singh, S. K. & Ordaz, M. On the origin of long coda observed in the lake-bed strong-motion records of Mexico City. *Bulletin of the Seismological Society of America* **83,** 1298–1306 (1993).
17. Barker, J. S., Campillo, M., Sánchez-Sesma, F. J., Jongmans, D. & Singh, S. K. Analysis of wave propagation in the Valley of Mexico from a dense array of seismometers. *Bulletin of the Seismological Society of America* **86,** 1667–1680 (1996).
18. Shapiro, N. M., Olsen, K. B. & Singh, K. On the duration of seismic motion incident onto the Valley of Mexico for subduction zone earthquakes. *Geophysical Journal International* **151,** 501–510, doi: 10.1046/j.1365-246X.2002.01789.x (2002).
19. Cárdenas-Soto, M. & Chávez-García, F. J. Regional Path Effects on Seismic Wave Propagation in Central Mexico. *Bulletin of the Seismological Society of America* **93,** 973–985, doi: 10.1785/0120020083 (2003).
20. Chávez-García, F. J. & Salazar, L. Strong Motion in Central Mexico: A Model Based on Data Analysis and Simple Modeling. *Bulletin of the Seismological Society of America* **92,** 3087–3101, doi: 10.1785/0120010231 (2002).
21. Bodin, P., Gomberg, J., Singh, S. K. & Santoyo, M. Dynamic deformations of shallow sediments in the Valley of Mexico, Part I: Three-dimensional strains and rotations recorded on a seismic array. *Bulletin of the Seismological Society of America* **87,** 528–539 (1997).
22. Pérez-Cruz, G. Estudio sismológico de reflexión del subsuelo de la ciudad de México. *MSc Thesis, Faculty of Engineering, Universidad Nacional Autónoma de México, Mexico* (1988).
23. Havskov, J. & Singh, S. K. Shallow crustal structure below Mexico City. *Geofísica Internacional* **17,** 222–229 (1977-78).
24. Singh, S. K., Santoyo, M., Bodin, P. & Gomberg, J. Dynamic deformations of shallow sediments in the Valley of Mexico, Part II: Single-station estimates. *Bulletin of the Seismological Society of America* **87,** 540–550 (1997).
25. Ovando-Shelley, E., Romo, M. P. & Ossa, A. The sinking of Mexico city: Its effects on soil properties and seismic response. *Soil Dynamics and Earthquake Engineering* **24,** 333–343 (2007).
26. Romo, M. P. & Ovando-Shelley, E. Modeling the dynamic behavior of Mexican clays. *Eleventh World Conf. Earthquake Engineering, Acapulco, Mexico* no. 1028 (1996).
27. Jongmans, D., Demanet, D., Horrent, C., Campillo, M. & Sánchez-Sesma, F. J. Dynamic soil parameters determination by geophysical prospecting in Mexico City: implication for site effect modeling. *Soil Dynamics and Earthquake Engineering* **15,** 549–559 (1996).
28. Shapiro, N. M., Singh, S. K., Almora, D. & Ayala, M. Evidence of the dominance of higher-mode surface waves in the lake-bed zone of the Valley of Mexico. *Geophysical Journal International* **147,** 517–527, doi: 10.1046/j.0956-540x.2001.01508.x (2001).
29. Lermo, J., Rodríguez, M. & Singh, S. K. The Mexico Earthquake of September 19, 1985—Natural Period of Sites in the Valley of Mexico from Microtremor Measurements and Strong Motion Data. *Earthquake Spectra* **4,** 805–814, doi: 10.1193/1.1585503 (1988).
30. Cruz-Atienza, V. M., Iglesias, A., Pacheco, J. F., Shapiro, N. M. & Singh, S. K. Crustal Structure below the Valley of Mexico Estimated from Receiver Functions. *Bulletin of the Seismological Society of America* **100,** 3304–3311, doi: 10.1785/0120100051 (2010).
31. Chaljub, E. *et al.* 3-D numerical simulations of earthquake ground motion in sedimentary basins: testing accuracy through stringent models. *Geophysical Journal International* **201,** 90–111, doi: 10.1093/gji/ggu472 (2015).
32. Arias, A. A measure of earthquake intensity. *Hansen RJ (ed) Seismic design for nuclear power plants*. MIT Press, Cambridge, Massachusetts, 438–483 (1970).
33. Etienne, V., Chaljub, E., Virieux, J. & Glinsky, N. An hp-adaptive discontinuous Galerkin finite-element method for 3-D elastic wave modelling. *Geophysical Journal International* **183,** 941–962, doi: 10.1111/j.1365-246X.2010.04764.x (2010).
34. Tago, J., Cruz-Atienza, V. M., Virieux, J., Etienne, V. & Sánchez-Sesma, F. J. A 3D hp-adaptive discontinuous Galerkin method for modeling earthquake dynamics. *Journal of Geophysical Research: Solid Earth* **117,** n/a-n/a, doi: 10.1029/2012JB009313 (2012).
35. Tago, J. Modelado de la dinámica de la fuente sísmica y de la propagación de ondas viscoelásticas con el método de Galerkin discontinuo. *Ph.D. Thesis, Universidad Nacional Autónoma de México, Mexico*, p. 250 (2012).
36. Rivet, D., Campillo, M., Sanchez-Sesma, F., Shapiro, N. M. & Singh, S. K. Identification of surface wave higher modes using a methodology based on seismic noise and coda waves. *Geophysical Journal International* **203,** 856–868, doi: 10.1093/gji/ggv339 (2015).
37. Singh, S., Iglesias, A., Ordaz, M., Pérez-Campos, X. & Quintanar, L. Estimation of Ground Motion in Mexico City from a Repeat of the M∼7.0 Acambay Earthquake of 1912. *Bulletin of the Seismological Society of America* **101,** 2015–2028 (2011).
38. Hall, J. F. & Beck, J. L. Structural damage in Mexico City. *Geophysical Research Letters* **13,** 589–592, doi: 10.1029/GL013i006p00589 (1986).
39. Beck, J. L. & Hall, J. F. Factors contributing to the catastrophe in Mexico City during the earthquake of September 19, 1985. *Geophysical Research Letters* **13,** 593–596, doi: 10.1029/GL013i006p00593 (1986).

Acknowledgements

We thank Michel Campillo for fruitful and enlightening discussions, Shri K. Singh for his comments and criticism on the manuscript, and Pierre-Yves Bard and Francisco Sánchez-Sesma for their advices in the results interpretation. We also thank Vladimir Kostoglodov for helpful layout and editorial advises, Eduardo Reinoso

for the basin isoperiod map and useful information and Arturo Cárdenas for the installation and maintenance of the seismic network of the Valley of Mexico. The HPC-GA grant of the Marie Curie International Research Staff Exchange Scheme has supported this work under call FP7-PEOPLE-2011-IRSES. The calculations presented in this article were performed using the supercomputer Miztli of the National Autonomous University of Mexico (UNAM) under grant number SC16-1-IR-87 and the Froggy platform from the CIMENT HPC center of Grenoble Alpes University which is supported by the Rhône-Alpes region (grant CPER07_13 CIRA), the OSUG@2020 labex (reference ANR10 LABX56) and the Equip@Meso project (reference ANR-10-EQPX-29-01). J.D.S-G. acknowledges the financial support from the Universidad Industrial de Santander of Colombia and the Seismology Department of UNAM for its hospitality during the time of this project.

Author Contributions

V.M.C.-A. designed the study, performed the computational simulations, interpreted the results and wrote the manuscript. J.T. implemented and adapted the viscoelastic solver and interpreted the results. J.D.S.-G. generated the numerical mesh, performed the computational simulations and interpreted the results. E.C. interpreted the results and performed the basin model homogenization. V.E. generated the numerical mesh. J.V. interpreted the results. L.Q. provided the seismic data. All authors contributed with discussions and improvements of the manuscript.

Additional Information

Supplementary information accompanies this paper at http://www.nature.com/srep

Competing financial interests: The authors declare no competing financial interests.

How to cite this article: Cruz-Atienza, V. M. *et al.* Long Duration of Ground Motion in the Paradigmatic Valley of Mexico. *Sci. Rep.* **6**, 38807; doi: 10.1038/srep38807 (2016).

Publisher's note: Springer Nature remains neutral with regard to jurisdictional claims in published maps and institutional affiliations.

Supplementary Information

of "Long Duration of Ground Motion in the Paradigmatic Valley of Mexico"

V.M. Cruz-Atienza, J. Tago, J.D. Sanabria-Gómez, E. Chaljub,
V. Etienne, J. Virieux and L. Quintanar

August 26, 2016

In this section we introduce the mathematical and computational models used to simulate the wave propagation in the Valley of Mexico. First, we introduce the model for a viscoelastic rheology and how we couple the corresponding constitutive relationship with the equation of motion to get the hyperbolic system describing the viscoelastic wave propagation. Then, we introduce the system discretization following a discontinuous Galerkin strategy, and present the computational model verification and convergence analysis based on different international benchmark problems. We also include all tables and supplementary figures referred in the main text of the manuscript.

1 Viscoelastic model for waves propagation

The stress-strain constitutive relationship in an isotropic viscoelastic medium can be defined as

$$\begin{aligned}\sigma_{ij}(t) &= \delta_{ij}\delta_{kl}\int_{-\infty}^{t}\lambda(t-\tau)\partial_t\epsilon_{kl}(\tau)d\tau \\ &\quad +(\delta_{ik}\delta_{jl}+\delta_{il}\delta_{jk})\int_{-\infty}^{t}\mu(t-\tau)\partial_t\epsilon_{kl}(\tau)d\tau,\end{aligned} \tag{1}$$

where $\sigma_{ij}(t)$ is the stress tensor, $\lambda(t)$ and $\mu(t)$ are the Lamé relaxation functions and $\epsilon_{kl}(t)$ is the strain tensor.

To avoid the unaffordable computation of the time convolutions in equation (1), for each Lamé relaxation function we will model the viscoelastic rheology as a *Generalized Maxwell Body* (GMB-EK) with n *Maxwell Bodies* (MB) and 1 *Hooke Body* (HB) connected in parallel[4]. In the frequency domain, the relaxation functions can be written as

$$\lambda(\omega) = \lambda_U\left(1-\sum_{l=1}^{n}Y_l^{\lambda}\frac{\omega_l}{\omega_l+i\omega}\right) \tag{2}$$

$$\mu(\omega) = \mu_U\left(1-\sum_{l=1}^{n}Y_l^{\mu}\frac{\omega_l}{\omega_l+i\omega}\right), \tag{3}$$

where λ_U and μ_U are the unrelaxed Lamé parameters that correspond to the instantaneous elastic response of the viscoelastic material, Y_l^{λ} and Y_l^{μ} are the anelastic coefficients and ω_l are the relaxation frequencies for the l^{th} MB. The anelastic coefficients, Y_l^{λ} and Y_l^{μ}, gather some physical properties of the propagation medium[11] and its computation will be explain in Section 1.1.

We use the inverse Fourier transformation to express the Lamé relaxation functions (equations (2) and (3)) in the

time domain, so that convolutions in equation (1) may be written as:

$$\int_{-\infty}^{t} \lambda(t-\tau)\partial_t \epsilon_{kl}(\tau)d\tau = \lambda_U \epsilon_{kl} - \lambda_U \sum_{m=1}^{n} Y_m^{\lambda} \zeta_m^{kl}(t) \tag{4}$$

$$\int_{-\infty}^{t} \mu(t-\tau)\partial_t \epsilon_{kl}(\tau)d\tau = \mu_U \epsilon_{kl} - \mu_U \sum_{m=1}^{n} Y_m^{\mu} \zeta_m^{kl}(t), \tag{5}$$

where we define the anelastic functions as

$$\zeta_m^{kl}(t) = \omega_m \int_{-\infty}^{t} \epsilon_{kl}(\tau) \exp^{-\omega_m(t-\tau)} d\tau \qquad m = 1, \cdots, n \quad k, l \in \{1, 2, 3\}, \tag{6}$$

and, because of the exponential term in equation (6), the time evolution of the anelastic functions can be associated with their own ODE[8]:

$$\partial_t \zeta_m^{kl}(t) + \omega_m \zeta_m^{kl}(t) = \omega_m \epsilon_{kl}(t) \qquad m = 1, \cdots, n \quad k, l \in \{1, 2, 3\}. \tag{7}$$

By substituting equations (4) and (5) into equation (1) our constitutive relationship becomes

$$\begin{aligned} \sigma_{ij}(t) &= \delta_{ij}\delta_{kl}\lambda_U \epsilon_{kl}(t) + (\delta_{ik}\delta_{jl} + \delta_{il}\delta_{jk})\mu_U \epsilon_{kl}(t) \\ &\quad - \sum_{m=1}^{n} (\delta_{ij}\delta_{kl}\lambda_U Y_m^{\lambda} \zeta_m^{kl}(t) + (\delta_{ik}\delta_{jl} + \delta_{il}\delta_{jk})\mu_U Y_m^{\mu} \zeta_m^{kl}(t)). \end{aligned} \tag{8}$$

To avoid having the physical properties involved in the fluxes computation[1] (see Section 2), we define the stress vector as $\vec{\sigma} = (\omega, \omega', \omega'', \sigma_{xy}, \sigma_{xz}, \sigma_{yz})^t$ with $\omega = \frac{1}{3}(\sigma_{xx}+\sigma_{yy}+\sigma_{zz})$, $\omega' = \frac{1}{3}(2\sigma_{xx}-\sigma_{yy}-\sigma_{zz})$ and $\omega'' = \frac{1}{3}(-\sigma_{xx}+2\sigma_{yy}-\sigma_{zz})$. This change of variable allows to express equation (8) in the following matrix form as

$$\Lambda \vec{\sigma} = \sum_{\theta \in \{x,y,z\}} \partial_\theta \mathcal{N}_\theta \vec{u} - \sum_{l=1}^{n} \mathcal{A}_l \vec{\zeta_l} \tag{9}$$

where $\vec{u} = (u_x, u_y, u_z)^t$ is the displacement vector and $\vec{\zeta_l} = (\zeta_l^{xx}, \zeta_l^{yy}, \zeta_l^{zz}, \zeta_l^{xy}, \zeta_l^{xz}, \zeta_l^{yz})^t$ is the anelastic function vector for the l^{th} MB. Matrix $\Lambda = \text{diag}[3/(3\lambda_U + 2\mu_U), (3/2\mu_U), 3/(2\mu_U), 1/\mu_U, 1/\mu_U, 1/\mu_U]$, which gathers the physical properties of the medium, is given by the unrelaxed Lamé parameters, λ_U and μ_U, and $\mathcal{N}_\theta$ are constant real matrices defined as

$$\mathcal{N}_x = \begin{pmatrix} 1 & 2 & -1 & 0 & 0 & 0 \\ 0 & 0 & 0 & 1 & 0 & 0 \\ 0 & 0 & 0 & 0 & 1 & 0 \end{pmatrix}^T \quad \mathcal{N}_y = \begin{pmatrix} 0 & 0 & 0 & 1 & 0 & 0 \\ 1 & -1 & 2 & 0 & 0 & 0 \\ 0 & 0 & 0 & 0 & 0 & 1 \end{pmatrix}^T \quad \mathcal{N}_z = \begin{pmatrix} 0 & 0 & 0 & 0 & 1 & 0 \\ 0 & 0 & 0 & 0 & 0 & 1 \\ 1 & -1 & -1 & 0 & 0 & 0 \end{pmatrix}^T.$$

Matrix $\mathcal{A}$, associated with the anelastic term of equation (8), is given by

$$\mathcal{A}_l = \begin{bmatrix} \mathcal{A}_l^1 & \mathcal{A}_l^1 & \mathcal{A}_l^1 & 0 & 0 & 0 \\ 2\mathcal{A}_l^2 & -\mathcal{A}_l^2 & -\mathcal{A}_l^2 & 0 & 0 & 0 \\ -\mathcal{A}_l^2 & 2\mathcal{A}_l^2 & -\mathcal{A}_l^2 & 0 & 0 & 0 \\ 0 & 0 & 0 & 2\mathcal{A}_l^2 & 0 & 0 \\ 0 & 0 & 0 & 0 & 2\mathcal{A}_l^2 & 0 \\ 0 & 0 & 0 & 0 & 0 & 2\mathcal{A}_l^2 \end{bmatrix}, \tag{10}$$

where $\mathcal{A}_l^1 = \frac{3\lambda_U Y_l^{\lambda} + 2\mu_U Y_l^{\mu}}{3\lambda_U + 2\mu_U}$ and $\mathcal{A}_l^2 = Y_l^{\mu}$.

To obtain the first part of the hyperbolic system of partial differential equations governing the propagation of viscoelastic waves, we just applied the time derivative to equation (9):

$$\Lambda\partial_t\vec{\sigma} = \sum_{\theta\in\{x,y,z\}} \partial_\theta \mathcal{N}_\theta \vec{v} - \sum_{l=1}^{n} \mathcal{A}_l \vec{\xi}_l, \tag{11}$$

where $\vec{v} = \partial_t\vec{u} = (v_x, v_y, v_z)^t$ is the velocity vector, and $\vec{\xi}_l = \partial_t\vec{\zeta}_l = (\xi_l^{xx}, \xi_l^{yy}, \xi_l^{zz}, \xi_l^{xy}, \xi_l^{xz}, \xi_l^{yz})^t$, is the time derivative of the anelastic functions vector $\vec{\zeta}_l$ that for simplicity, we will still call the anelastic function vector. Then the ODE associated with $\vec{\xi}_l$ is given by

$$\partial_t\vec{\xi}_l + \omega_l\vec{\xi}_l = \omega_l \sum_{\theta\in\{x,y,z\}} \partial_\theta \mathcal{O}_\theta \vec{v}, \tag{12}$$

where

$$\mathcal{O}_x = \begin{bmatrix} 1 & 0 & 0 & 0 & 0 & 0 \\ 0 & 0 & 0 & 0.5 & 0 & 0 \\ 0 & 0 & 0 & 0 & 0.5 & 0 \end{bmatrix}^T \quad \mathcal{O}_y = \begin{bmatrix} 0 & 0 & 0 & 0.5 & 0 & 0 \\ 0 & 1 & 0 & 0 & 0 & 0 \\ 0 & 0 & 0 & 0 & 0 & 0.5 \end{bmatrix}^T \quad \mathcal{O}_z = \begin{bmatrix} 0 & 0 & 0 & 0 & 0.5 & 0 \\ 0 & 0 & 0 & 0 & 0 & 0.5 \\ 0 & 0 & 1 & 0 & 0 & 0 \end{bmatrix}^T. \tag{13}$$

To complete the hyperbolic system and keep track of the time-varying velocity field, we incorporate the equation of motion. This equation can be written in matrix form[1] as

$$\rho\partial_t\vec{v} = \sum_{\theta\in\{x,y,z\}} \partial_\theta \mathcal{M}_\theta \vec{\sigma} + \vec{f}, \tag{14}$$

where ρ is the medium density, $\vec{f}$ is the external force vector and $\mathcal{M}_\theta$ are constant real matrices defined as

$$\mathcal{M}_x = \begin{pmatrix} 1 & 1 & 0 & 0 & 0 & 0 \\ 0 & 0 & 0 & 1 & 0 & 0 \\ 0 & 0 & 0 & 0 & 1 & 0 \end{pmatrix} \quad \mathcal{M}_y = \begin{pmatrix} 0 & 0 & 0 & 1 & 0 & 0 \\ 1 & 0 & 1 & 0 & 0 & 0 \\ 0 & 0 & 0 & 0 & 0 & 1 \end{pmatrix} \quad \mathcal{M}_z = \begin{pmatrix} 0 & 0 & 0 & 0 & 1 & 0 \\ 0 & 0 & 0 & 0 & 0 & 1 \\ 1 & -1 & -1 & 0 & 0 & 0 \end{pmatrix}.$$

Thus, equations (11) and (14) constitute the hyperbolic system fully describing the viscoelastic wave propagation.

1.1 Computation of the anelastic coefficients

The computation of the anelastic coefficients, Y_l^λ and Y_l^μ, in equations (2) and (3) is done such that the quality factors, Q_φ, for $\varphi \in \{\lambda, \mu\}$, are approximated over a frequency range of interest. The inverse of the quality factor is defined for each Lamé relaxation function (equations (2) and (3)) as

$$Q_\varphi^{-1}(\omega) = \frac{\mathrm{Im}\varphi(\omega)}{\mathrm{Re}\varphi(\omega)} = \sum_{l=1}^{n} \frac{\omega_l\omega + Q^{-1}(\omega)\omega_l^2}{\omega_l^2 + \omega^2} Y_l^\varphi \qquad \varphi \in \{\lambda, \omega\}. \tag{15}$$

To approximate a nearly constant $Q_\varphi(\omega)$ in a given frequency range, we set the relaxation frequencies ω_l in the frequency range of interest with a logarithmically equidistant spacing[4]. A constant Q has been proved to be a good approximation for most geophysical applications[9]. Nonetheless, the following procedure can also be applied for any frequency dependency of Q[10]. Once the relaxation frequencies are spread along the frequency range, we used a least square method to determine the anelastic coefficients in equation (15) that better fit the function $Q_\varphi(\omega)$.

In practice, seismologists describe the rocks anelastic dissipation through the quality factors Q_α and Q_β associated with the P- and S- waves, respectively. After computing their corresponding coefficients Y_l^α and Y_l^β, we can compute

those related with the Lamé parameters using the transformations

$$Y_l^{\lambda} = \left(1 + \frac{2\mu}{\lambda}\right) Y_l^{\alpha} - \frac{2\mu}{\lambda} Y_l^{\beta} \qquad \text{and} \qquad Y_l^{\mu} = Y_l^{\beta}. \tag{16}$$

For our simulations, we have considered three MB (i.e., three relaxation frequencies) to approximate constant Q_α and Q_β in the frequency range [0.01 5.0] Hz, which is a reasonable choice for our modeling purposes. The more relaxation frequencies we consider the better is the approximation of the given function $Q_\varphi(\omega)$. However, it is important to notice that increasing the amount of relaxation frequencies implies a significant increment in the memory storage requirements and computational time.

2 hp-Discontinuous Galerkin method

Before solving the hyperbolic system given by equations (11) and (14), we first need to decompose the physical domain, Ω, into K elements, so that

$$\Omega \simeq \Omega_h = \sum_{i=1}^{K} D_i \tag{17}$$

where each D_i is a straight-sided tetrahedron whose union constitutes a geometrically conforming mesh .

We approximate the velocity and stress vectors in every tetrahedron, D_i $\forall i \in \{1, \ldots, K\}$, using a nodal interpolation[6] as

$$\hat{\vec{v}}_i(\vec{x}, t) = \sum_{j=1}^{d_i} \vec{v}_{i_j}(\vec{x}_j, t)\varphi_{i_j}(\vec{x}) \tag{18}$$

$$\hat{\vec{\sigma}}_i(\vec{x}, t) = \sum_{j=1}^{d_i} \vec{\sigma}_{i_j}(\vec{x}_j, t)\varphi_{i_j}(\vec{x}), \tag{19}$$

where $\vec{x} \in D_i$, t is the time and d_i is the number of nodes supporting the interpolation Lagrangian polynomial basis functions, φ_{i_j}, associated to the j-node located at $\vec{x}_j$.

Using the nodal interpolations (18) and (19), we can apply a discontinuous Galerkin approach[5] to equations (11) and (14) and get

$$\begin{aligned} \rho_i(\mathcal{I}_3 \otimes \mathcal{K}_i)\frac{\vec{v}_i^{n+\frac{1}{2}} - \vec{v}_i^{n-\frac{1}{2}}}{\Delta t} &= -\sum_{\theta \in \{x,y,z\}} (\mathcal{M}_\theta \otimes \mathcal{E}_{i\theta})\vec{\sigma}_i^n \\ &\quad + \frac{1}{2}\sum_{k \in N_i} \left[(\mathcal{P}_{ik} \otimes \mathcal{F}_{ik})\vec{\sigma}_i^n + (\mathcal{P}_{ik} \otimes \mathcal{G}_{ik})\vec{\sigma}_k^n\right] \end{aligned} \tag{20}$$

$$\begin{aligned} (\Lambda_i \otimes \mathcal{K}_i)\frac{\vec{\sigma}_i^{n+1} - \vec{\sigma}_i^n}{\Delta t} &= -\sum_{\theta \in \{x,y,z\}} (\mathcal{N}_\theta \otimes \mathcal{E}_{i\theta})\vec{v}_i^{n+\frac{1}{2}} - \sum_{l=1}^{n} (\mathcal{A}_{i_l} \otimes \mathcal{K}_i)\vec{\xi}_{i_l}^{n+\frac{1}{2}} \\ &\quad + \frac{1}{2}\sum_{k \in N_i} \left[(\mathcal{Q}_{ik} \otimes \mathcal{F}_{ik})\vec{v}_i^{n+\frac{1}{2}} + (\mathcal{Q}_{ik} \otimes \mathcal{G}_{ik})\vec{v}_k^{n+\frac{1}{2}}\right] \end{aligned} \tag{21}$$

where the matrices involved are: the mass matrix

$$(\mathcal{K}_i)_{rj} = \int_{V_i} \varphi_{i_r}\varphi_{i_j} dV \qquad j, r \in [1, d_i],$$

the stiffness matrix

$$(\mathcal{E}_{i\theta})_{rj} = \int_{V_i} (\partial_\theta \varphi_{i_r}) \varphi_{i_j} dV \qquad j, r \in [1, d_i] \qquad \theta \in \{x, y, z\},$$

the flux matrices

$$\begin{aligned} (\mathcal{F}_{ik})_{rj} &= \int_{S_{ik}} \varphi_{i_r} \varphi_{i_j} dS \qquad j, r \in [1, d_i] \\ (\mathcal{G}_{ik})_{rj} &= \int_{S_{ik}} \varphi_{i_r} \varphi_{k_j} dS \qquad r \in [1, d_i] \qquad j \in [1, d_k]. \end{aligned}$$

and the auxiliary flux matrices

$$\begin{aligned} \mathcal{P}_{ik} &= \sum_{\theta \in \{x,y,z\}} n_{ik_\theta} \mathcal{M}_\theta \\ \mathcal{Q}_{ik} &= \sum_{\theta \in \{x,y,z\}} n_{ik_\theta} \mathcal{N}_\theta, \end{aligned}$$

where $\mathcal{I}_3$ is the 3x3 identity matrix, $\otimes$ represent the tensor product, and n_{ik_θ} is the component along the θ axis of the unit normal vector $\vec{n}_{ik}$ of the element face S_{ik} which points from the i- to the k-element.

The size of these matrices depends on the order of the polynomial basis used for the nodal interpolation. The flux terms of the i^{th}-tetrahedron are computed following a non-dissipative centered scheme with its N_i adjacent elements. Besides, thanks to the change of variable previously introduced, the fluxes of equation (21) do not involve the physical properties of the neighboring elements but only their velocity fields.

In our method, we have implemented P0, P1 and P2 (i.e. constant, linear and quadratic) approximation orders that can be individually assigned to each tetrahedron D_i depending on its characteristic size and medium properties (i.e., p-adaptivity). Staggered time integration is performed through a second-order explicit leap-frog scheme, which allows the alternation of velocities and stresses during computation. The order of approximation used for time integration matches the highest approximation order for the spatial interpolation (*i.e.* P2).

To solve the ODE's governing the anelastic functions (12), we approximate these functions using a nodal interpolation and the same Galerkin approach introduced before for equations (11) and (14), to get

$$\begin{aligned} (\mathcal{I}_6 \otimes \mathcal{K}_i) \frac{\vec{\xi}_{i_l}^{n+\frac{1}{2}} - \vec{\xi}_{i_l}^{n-\frac{1}{2}}}{\Delta t} &= -\omega_l \left((\mathcal{I}_6 \otimes \mathcal{K}_i) \vec{\xi}_{i_l}^{n-\frac{1}{2}} + \sum_{\theta \in \{x,y,z\}} (\mathcal{O}_\theta \otimes \mathcal{E}_{i\theta}) \vec{v}_i^{n-\frac{1}{2}} \right) \\ &\quad + \omega_l \frac{1}{2} \sum_{k \in N_i} \left[(\mathcal{R}_{ik} \otimes \mathcal{F}_{ik}) \vec{v}_i^{n-\frac{1}{2}} + (\mathcal{R}_{ik} \otimes \mathcal{G}_{ik}) \vec{v}_k^{n-\frac{1}{2}} \right] \end{aligned} \tag{22}$$

where $\mathcal{R}_{ik} = \sum_{\theta \in \{x,y,z\}} n_{ik_\theta} \mathcal{O}_\theta$. It is important to notice that the discontinuous Galerkin approximation used for the ODE's allows us to honour the p-adaptivity of the scheme.

In order to achieve good accuracy for P2 elements, the unstructured model discretization must warranty 3 tetrahedra per minimum wavelength[5] (see Figure A5). On the other hand, the scheme stability is given by an heuristic criterion[7] given by

$$\Delta t < \min_i \left(\frac{1}{2k_i + 1} \cdot \frac{2r_i}{\alpha_i} \right) \tag{23}$$

where r_i is the radius of the sphere inscribed in the element indexed by i, α_i is the $P-$wave velocity in the element and k_i is the polynomial degree used in the element.

Our Discontinuous Galerkin Finite Element Method (DG-FEM) (i.e., the GEODG3D code) thus has two main features that make it a very flexible and powerful numerical tool. One is the h-adaptivity, which allows working with unstructured tetrahedral meshes geometrically adapted to the physical properties of the medium and the free surface topography, so that the accuracy criterion is satisfied locally (Figures 3a and A3b). The other is the p-adaptivity, that allows choosing the most convenient order of approximation per tetrahedron to relax as much as possible the stability condition (i.e., to maximize the integration time step). A nice example of p-adaptivity is given in Figure A3a, where the elements right below the basin, which have a very little characteristic size and relatively high wave speeds, are low approximation order (i.e., P1 or P0). This numerical approach was developed in recent years during the PhD thesis of Tago (2012)[12], where more methodological and numerical details are provided.

3 Model verification and convergence

To verify the correctness of the solutions yielded by the GEODG3D code, we solved two international benchmarks problems. Solutions were compared with those from AXITRA[2], a semi-analytical discrete wave number method. The benchmarks correspond to the elastic and viscoelastic versions of the Layer Over an Homogeneous half-space problems, LOH1 and LOH3, respectively[3].

For the LOH3 benchmark, the viscoelastic moduli were exactly the same in both the AXITRA and GEODG3D simulations. This choice allows quantifying approximation errors associated only to the implementation of the attenuation model for a given number of relaxation mechanisms and thus for the same $Q(\omega)$ functions. In this benchmark problem, the top layer is 1000 m thick and the physical properties of the whole model are given in Table A3. We approximated the frequency-independent quality factors Q_α and Q_β with three relaxation mechanisms. Receivers are located in the free surface ($z = 0$) with positions relative to the epicenter ($x \rightarrow$ North and $y \rightarrow$ East) given in Table A4. A double-couple point source is located 2000 m below the free surface with all components of its moment tensor equal to zero except $M_{xy} = M_{yx}$, with moment value $M_0 = 10^{18}\ Nm$. The Moment rate time history is a Gaussian pulse given by

$$\frac{1}{t_r\sqrt{\pi}} \exp \frac{-(t-t_0)^2}{t_r^2}, . \tag{24}$$

where t is the time, $t_r = 0.05\ s$ is the rise time and $t_0 = 0.25\ s$ is the origin time. The source spectrum is almost flat up to 10 Hz so all the frequencies below have almost the same amplitude. Solutions should be compared up to 5.0 Hz.

All solutions were computed using P2 elements in the physical domain, approximately ten P1 elements in the Convolutional Perfectly Matched Layer (CPML)[5] region and free surface boundary conditions on top of the model. The characteristic size of the tetrahedra used for both the structured and the unstructured meshes was 100 m, as suggested in the benchmarks descriptions[3]. This choice is convenient for our method since the number of elements per minimum wavelength, n_λ, is about three, which corresponds to the accuracy criterion for our method[5] (see Figure A5).

Figure A4 shows the comparison of the three velocity components in the farthest three receivers (*i.e.* located about 32 times the minimum wavelength from the epicenter) using an unstructured mesh. The time series were filtered using a two-pass four-pole Butterworth filter in the frequency band $[1 - 5]\ Hz$. The agreement between solutions is excellent (i.e., error of about 1.2%).

We performed a convergence analysis of the GEODG3D method based on both the elastic (LOH1) and the viscoelastic (LOH3) benchmarks considering structured and unstructured meshes. The Normalized Root Mean Square (NRMS)

function was used to quantify the error between our solutions and the AXITRA reference solutions. This function is given by

$$NRMS(v_\theta^{DG-FEM}, v_\theta^{AXITRA}) = \frac{\sqrt{(\sum_{i=1}^{n}(v_{\theta_i}^{DG-FEM} - v_{\theta_i}^{AXITRA})^2)/n}}{max(v_\theta^{AXITRA}) - min(v_\theta^{AXITRA})}, \tag{25}$$

where n is the length of the seismograms vectors and $\theta \in \{x, y, z\}$. Components with no signals were excluded in the NRMS computation. For the rest of receivers we computed the NRMS in the three velocity components and averaged them to have a single misfit value.

Figure A5 presents NRMS values computed for the following four simulation cases: 1) the LOH1 benchmark with structured mesh, 2) the LOH1 benchmark with unstructured mesh, 3) the LOH3 benchmark with structured mesh and 4) the LOH3 benchmark with unstructured mesh. NRMS values are reported as a function of the number of elements per minimum wavelength, n_λ, associated with the cutoff frequency of 5 Hz. Linear regressions are also plotted in the log-log scale. The resulting slopes give the convergence rates of the solutions with respect to n_λ. For the unstructured viscoelastic case (i.e., for conditions similar to our simulations in the Valley of Mexico) the convergence rate is 2.98.

Four main conclusions detach from Figure A5: 1) viscoelastic solutions are systematically better than the elastic ones no matter we use structured or unstructured meshes; 2) the convergence rate of both viscoelastic and elastic solutions is virtually the same and depends on the kind of mesh we use; 3) the convergence rate is significantly higher in unstructured meshes no matter we solve the elastic or viscoelastic equations (*i.e.* convergence rate about 1.8 times higher); and 4) numerical errors are lower than 2% and 1.2% in structured and unstructured meshes, respectively, provided that $n_\lambda >= 3$ no matter we solve the elastic or viscoelastic equations.

References

1. Benjemaa, M., N. Glinsky-Olivier, V. M. Cruz-Atienza, and J. Virieux, 3-d dynamic rupture simulations by a finite volume method, *Geophys. J. Int.*, *178*(1), doi:10.1111/j.1365-246X.2009.04088.x, 2009.

2. Bouchon, M., and O. Coutant, Calculation of synthetic seismograms in a laterally varying medium by the boundary element-discrete wavenumber method, *Bull. Seismol. Soc. Am.*, *84*, 1869–1881, 1994.

3. Day, S. M., J. Bielak, D. Dreger, R. Graves, S. Larsen, K. Olsen, and A. Pitarka, Test of 3D elastodynamics codes: Final report for lifelines project 1A02, *Tech rept.*, Pacific Earthquake Engineering Research Center, Berkeley, California, 2003.

4. Emmerich, H., and M. Korn, Incorporation of attenuation into time-domain computations of seismic wave fields, *Geophysics*, *52*(9), doi:10.1190/1.1442386, 1987.

5. Etienne, V., E. Chaljub, J. Virieux, and N. Glinsky, An hp-adaptive discontinuous Galerkin finite-element method for 3-D elastic wave modelling, *Geophys. J. Int.*, *183*(2), doi:10.1111/j.1365-246X.2010.04764.x, 2010.

6. Hesthaven, J. S., and T. Warburton (Eds.), *Nodal Discontinuous Galerkin Methods: Algorithms, Analysis and Applications*, 1st ed., 515 pp., Springer, 2008.

7. Kaser, M., and M. Dumbser, A highly accurate discontinuous Galerkin method for complex interfaces between solids and moving fluids, *Geophysics*, *73*(3), 23–35, 2008.

8. Kristek, J., and P. Moczo, Seismic-Wave Propagation in Viscoelastic Media with Material Discontinuities: A 3d Fourth-Order Staggered-Grid Finite-Difference Modeling, *Bull. Seism. Soc. Am.*, *93*, doi:10.1785/0120030023, 2003.

9. Liu, H. P., D. L. Anderson, and H. Kanamori, Velocity dispersion due to anelasticity; implications for seismology and mantle composition, *Geophys. J. Roy. Astr. Soc.*, *47*, 41–58, 1976.

10. Liu, P., and R. J. Archuleta, Efficient Modeling of Q for 3D Numerical Simulation of Wave Propagation, *Bull. Seismol. Soc. Am.*, *96*(4), 1352–1358, 2006.

11. Moczo, P., and J. Kristek, On the rheological models used for time-domain methods of seismic wave propagation, *Geophys. Res. Lett.*, *32*(L01306), doi:10.1029/2004GL021598, 2005.

12. Tago, J., Modelado de la dinámica de la fuente sísmica y de la propagación de ondas viscoelásticas con el método de Galerkin discontinuo, Ph.D. thesis, UNAM, Mexico, 2012.

Table A1 Velocity structure considered in this study. Green shaded layers correspond to those inside the 3D basin geometry shown in Figure 1. Blue shaded layers correspond to the 1D structure where the basin is embedded. Thicknesses indicated with stars correspond to the deepest point of the basin. They vary depending on the basin geometry.

H (km)	Vp (km/s)	Vs (km/s)	Rho (gr/cm^3)	Qp	Qs
0.03	0.8	0.05	2.0	30.0	15.0
0.02	1.2	0.1	2.0	60.0	30.0
0.25	2.0	0.4	2.05	80.0	40.0
0.25*	2.5	0.8	2.05	160.0	80.0
1.42*	2.70	1.56	2.20	312.0	156.0
2.34	5.51	3.18	2.53	636.0	318.0
10.97	6.00	3.46	2.69	692.0	346.0
27.62	6.68	3.86	2.91	772.0	386.0
∞	8.31	4.80	3.43	960.0	480.0

Table A2 Numerical information of a typical viscoelastic simulation. The UNAM supercomputing platform Miztli has 40 Gb Infiniband interconextion and processors Intel Xeon E5-2670 with frequency of 2.6 to 3.3 GHz.

Maximum resolved frequency	1 Hz
Size of the simulation domain	93.3 x 79.7 x 50.3 km
Length of the CPML layer	8 km
Number of mesh elements	12.25 million
Elements within the basin	97.04 %
P0 elements	10.41 %
P1 elements	12.85 %
P2 elements	76.75 %
Minimum element size	0.49 m
Maximum element size	737 m
Integration time step	0.00036 s
Number of time steps	514,995
Number of parallel processors	512
Computing elapsed time	23.7 hr

Table A3: Medium parameters of the LOH3 benchmark

	α (m/s)	β (m/s)	ρ (kg/m^3)	Q_α	Q_β
layer	4000	2000	2600	120	40
halfspace	6000	3464	2700	180	80

Table A4: Receivers location of the LOH1 and LOH3 benchmarks

Receiver	1	2	3	4	5	6	7	8	9
x (m)	0	0	0	490	3919	7348	577	4612	8647
y (m)	693	5543	10392	490	3919	7348	384	3075	5764

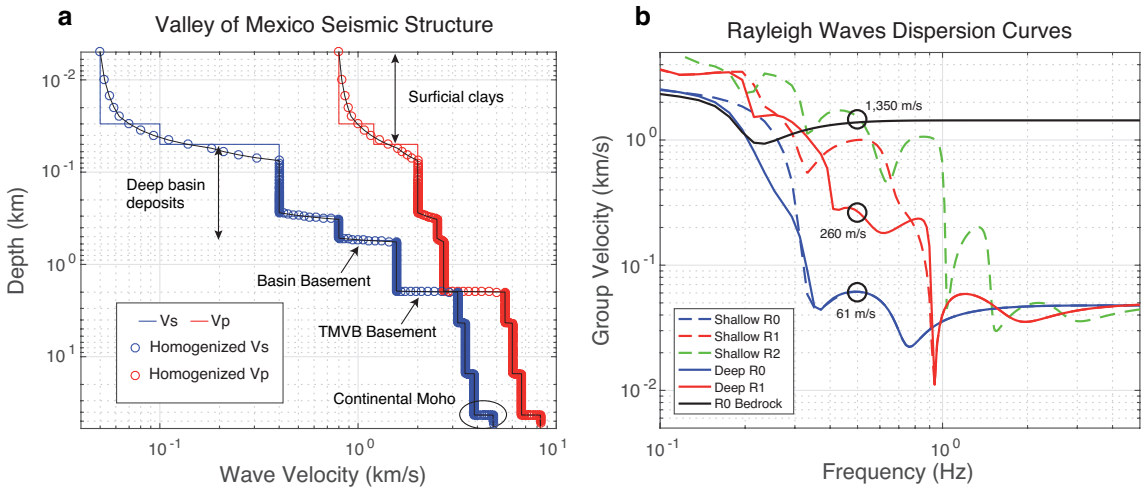

Figure A1 (a) Velocity structure used in the numerical model (see Table A1). Depth of the basin basement varies in space according to the basin thickness shown in Figure 1. Circles show the homogenized velocity structure used for the model discretization. (b) Rayleigh waves dispersion curves for the vertical component of the fundamental (R0, blue) and first overtone (R1, red) at shallow (250 m thick; dashed) and deep (500 m thick; solid) basin sites.

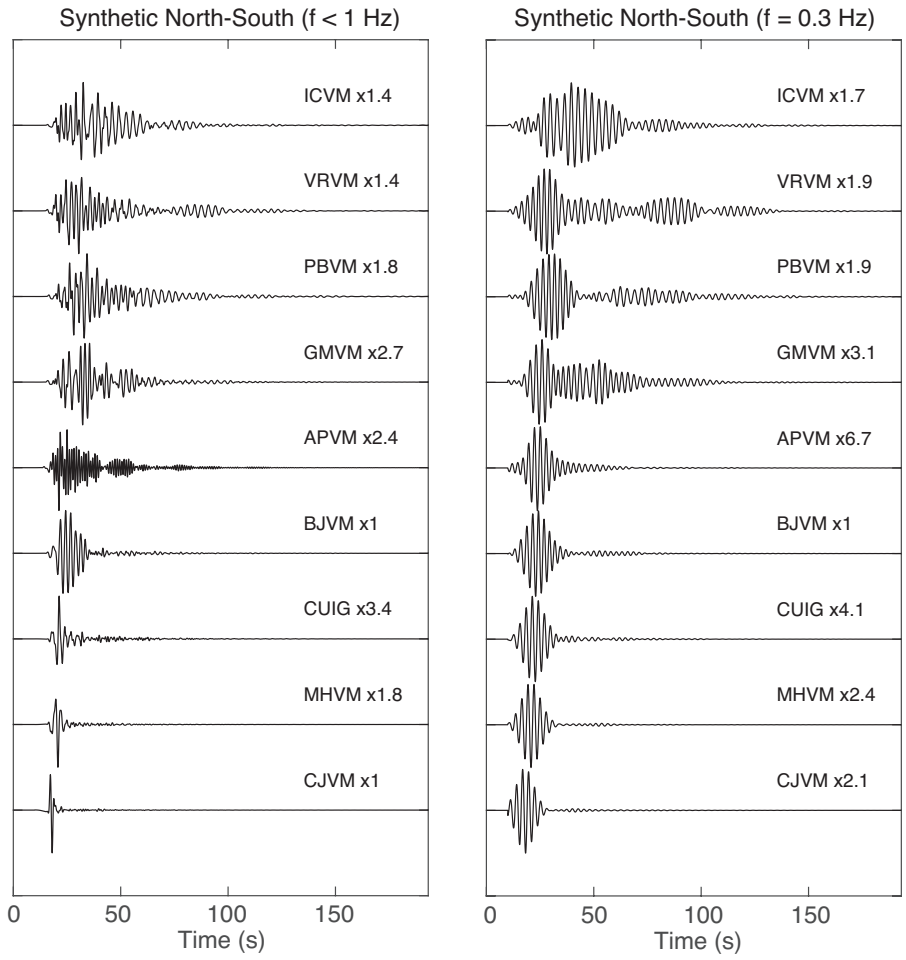

Figure A2 Synthetic velocity seismograms computed at nine broadband stations for the M3.4 earthquake with 4 km depth (Figure 1). The source is a vertical dip-slip dislocation with strike to the north and source time function shown in the inset of Figure 4. Records are aligned with the P-wave arrival. Durations of the strong shaking phases for f < 1 Hz are compared with real observations in Figure 1b.

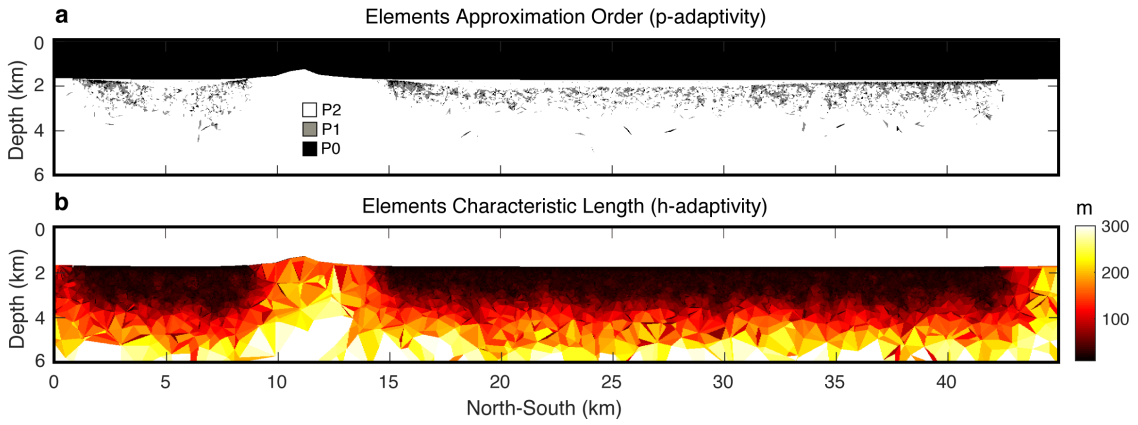

Figure A3 (a) Cross-section of the discrete model along the dashed line of Figure 6b. The distribution of the elements approximation order (i.e., p-adaptivity) is indicated with three different colors. Notice the concentration of low-order elements right below the interface with highest impedance contrasts (i.e., below the shallower basin regions close to its borders). (b) Same cross-section showing the tetrahedral mesh refinement within the basin (h-adaptivity).

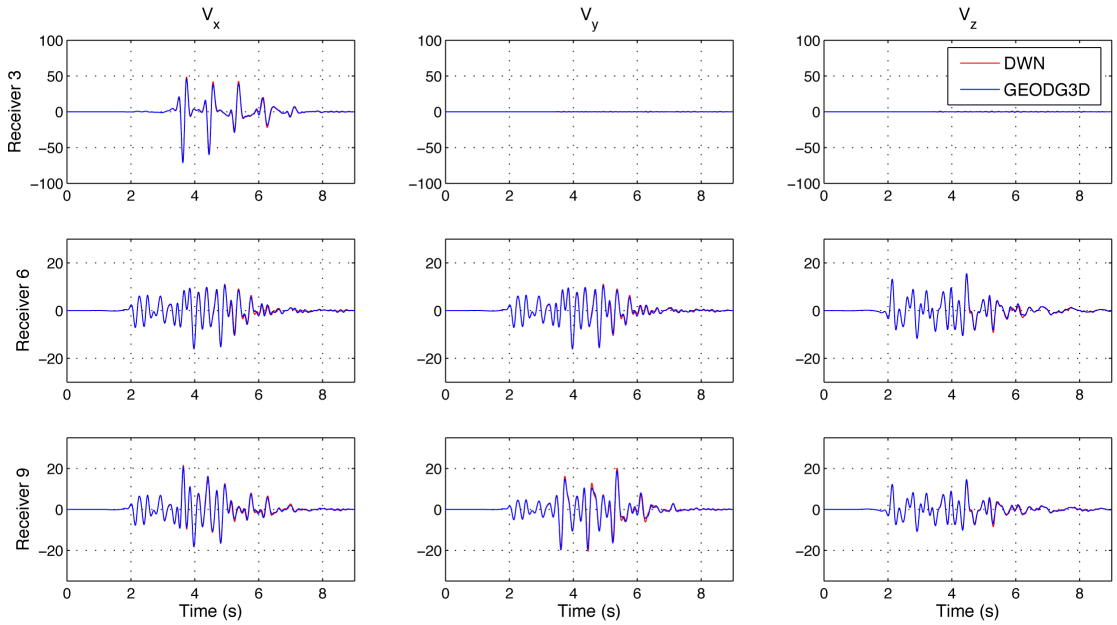

Figure A4 Comparison of synthetic seismograms (bandpass filtered between 1 and 5 Hz) computed with the Discontinuous Galerkin GEODG3D method (blue) and the Discrete Wave Number method (DWN, red) for the viscoelastic benchmark "Layer Over a Halfspace 3" (LOH3) of the Southern California Earthquake Center (SCEC) described by Day et al. (2003). Both solutions were computed with exactly the same viscoelastic modulus for three relaxation mechanisms so the signals misfit only responds to numerical approximation errors. The GEODG3D solution was computed using a P2 unstructured mesh with characteristic size of 100 m. The three receivers are located at distances from the source of about 32 times the minimum wavelength.

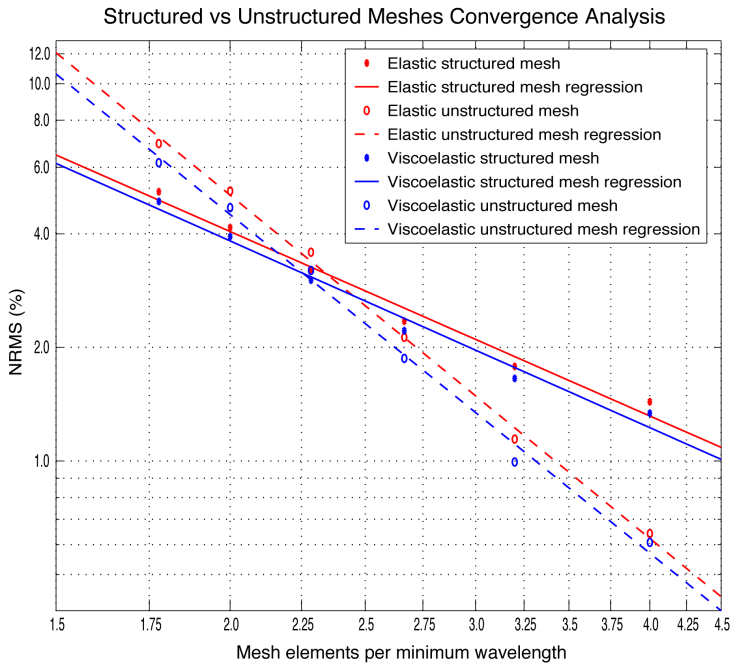

Figure A5 Convergence analysis for GEODG3D elastic (red) and viscoelastic (blue) methods considering structured (solid) and unstructured (dashed) meshes. Problems used were the LOH1 and LOH3 (Day et al., 2003) taking the DWN solutions as references. Viscoelastic solutions are always better that the elastic. Convergence rate in unstructured meshes (slope of 2.98) is significantly higher than the corresponding value for structured meshes (slope of 1.64). This is due to the numerical anisotropy induced by the regularity of elements in the structured mesh.

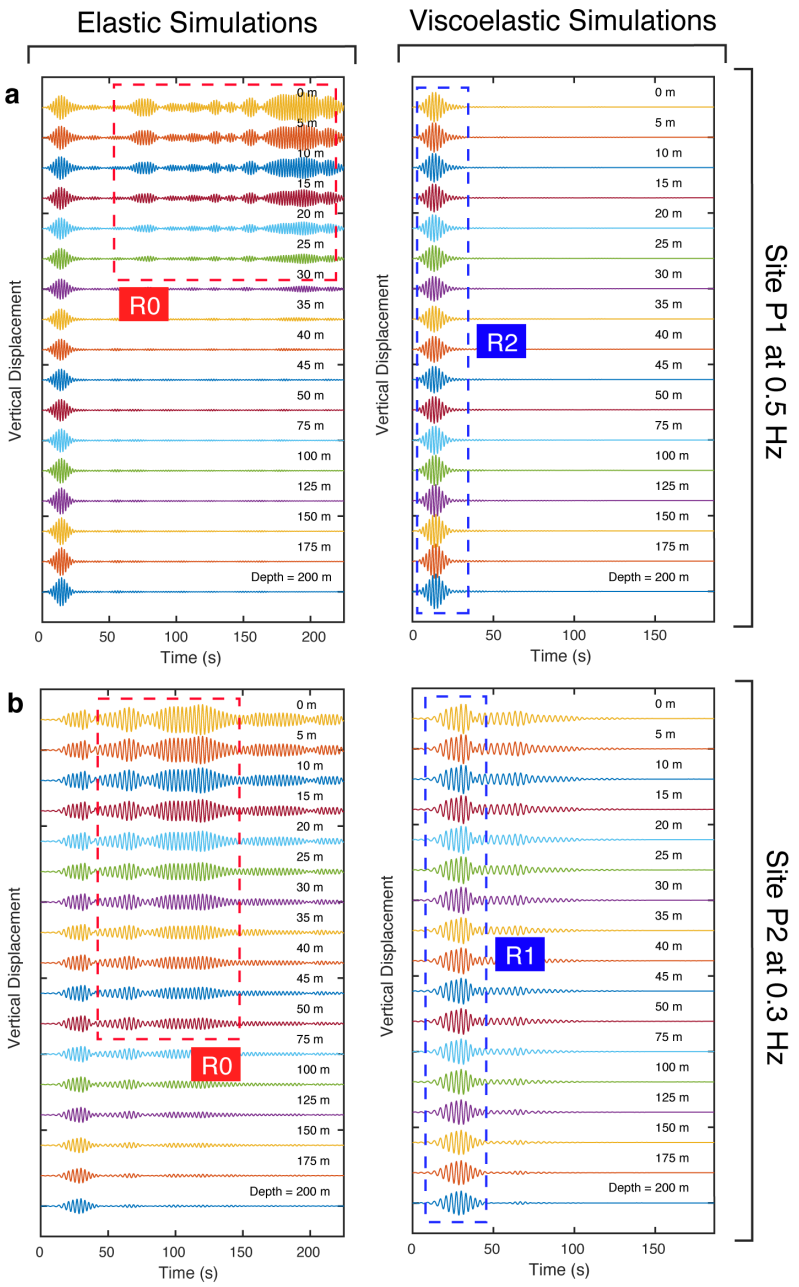

Figure A6 Synthetic borehole seismograms at sites P1 and P2 (see Figure A9) for two different frequencies. While the energy of the fundamental mode (R0) decays rapidly with depth (red rectangles), that of the first and second overtones (R1 and R2) persists along the entire depth of the borehole. Compare the amplitudes of the wave packages with the eigenfunctions of Figures 6a and 6c.

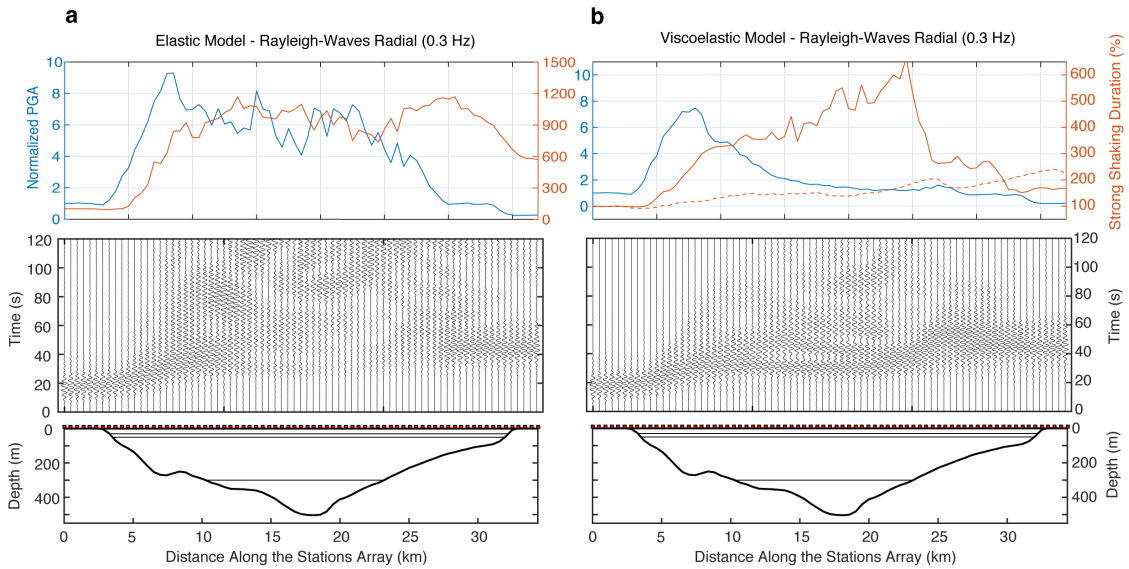

Figure A7 Same as Figure 5 but for f = 0.3 Hz.

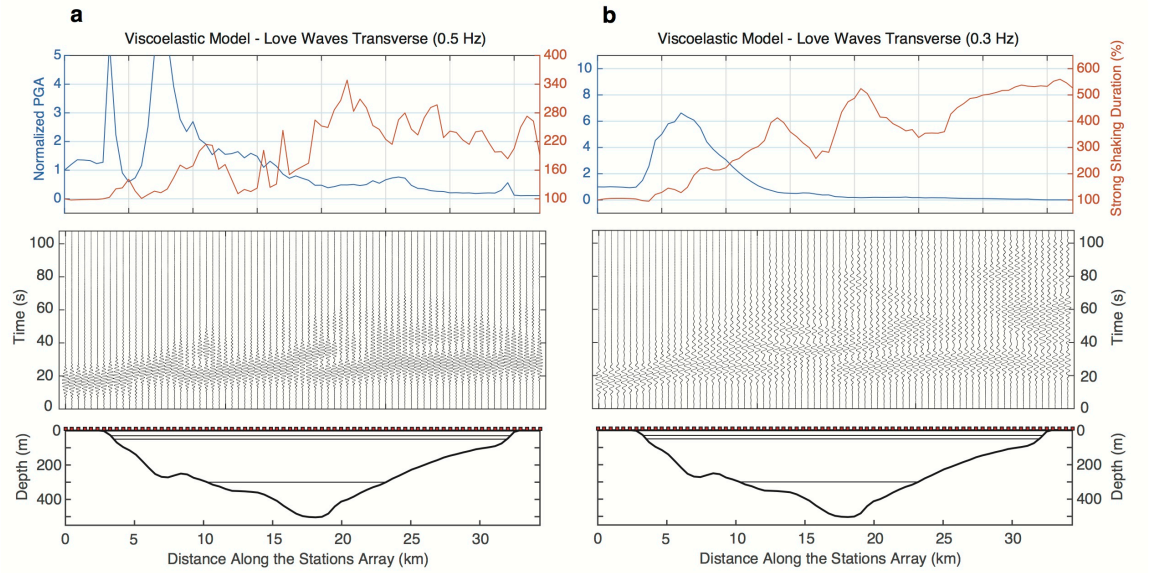

Figure A8 Same as Figure 5 but for Love waves in the viscoelastic model at (a) f = 0.5 Hz and (b) f = 0.3 Hz. This simulation corresponds to a 1.5 km depth double-couple strike-slip point source at location S6.

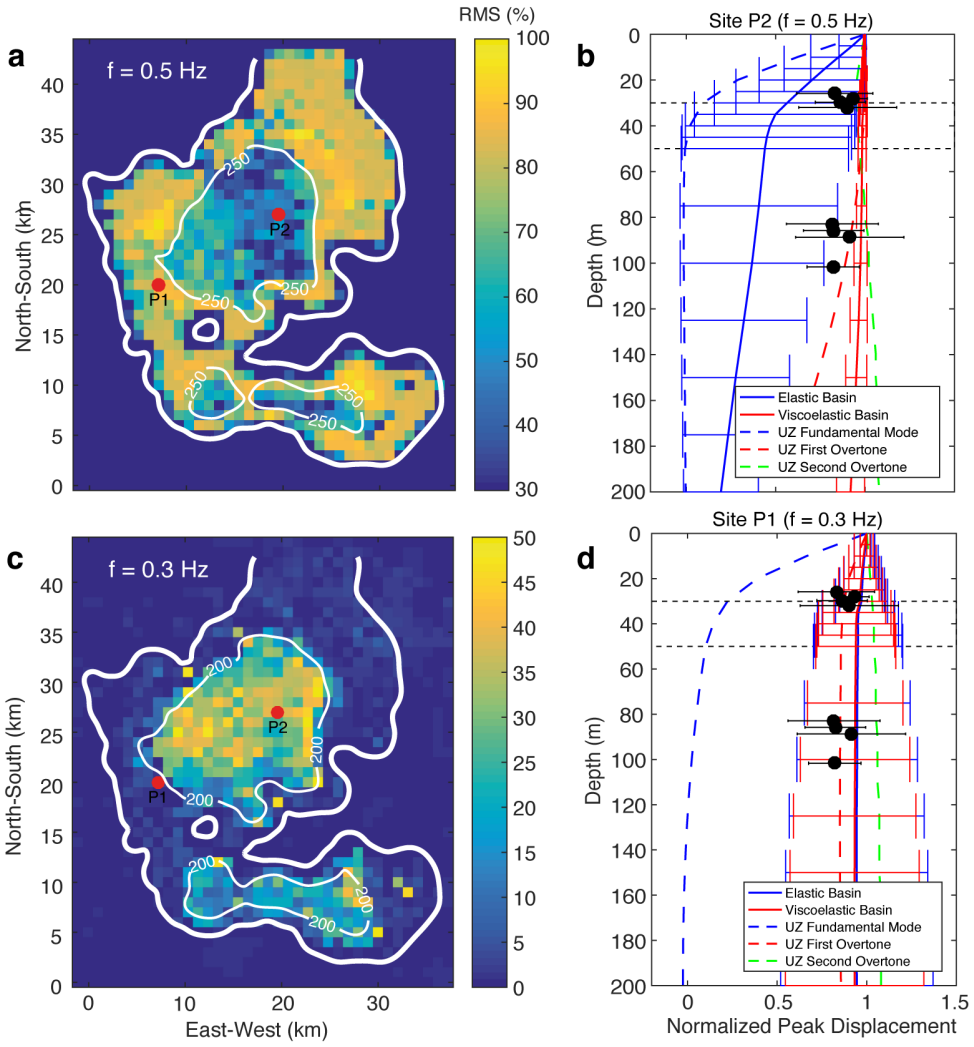

Figure A9 (a) and (c) RMS differences of the averaged (for the eight sources) elastic and viscoelastic eigenfunctions computed in the whole borehole network shown in Figure 1 for two different frequencies. White contours delineate the basin geometry at fixed depths in meters. Yellow colors depict regions where attenuation plays a major role resulting in the dominance of Rayleigh waves first overtones. (b) and (d) Same as Figure 6 but for frequencies of 0.3 and 0.5 Hz at representative sites P1 and P2. Notice the dominance of first overtones at 0.3 Hz for both elastic and viscoelastic models in shallow basin regions (i.e., at P1). This figure has been created using the Matlab software Version R2016a, http://www.mathworks.com/.

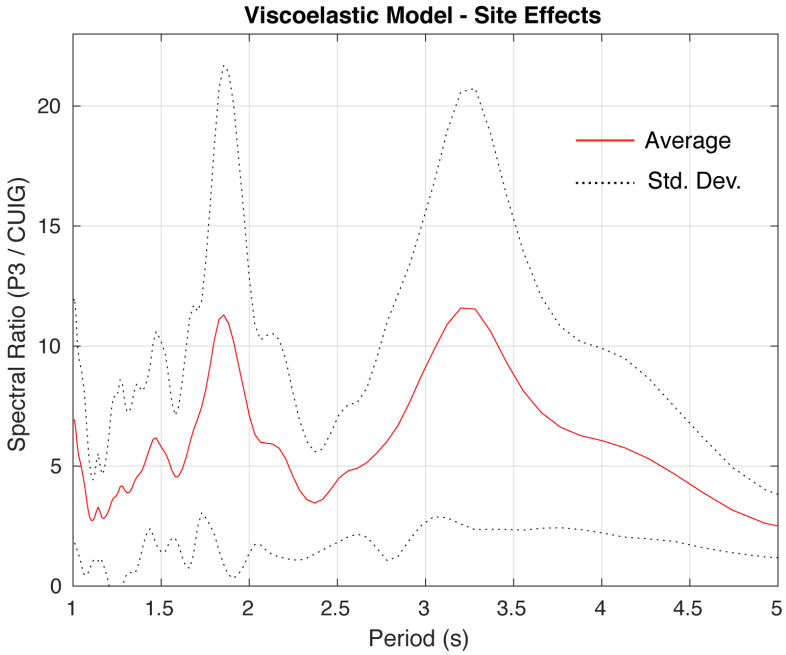

Figure A10 Average horizontal spectral amplification for the eight sources (solid red line) and standard deviations (black dotted lines) at the lake-bed representative site P3 (Figure 6) with respect to the hard-rock CUIG site.

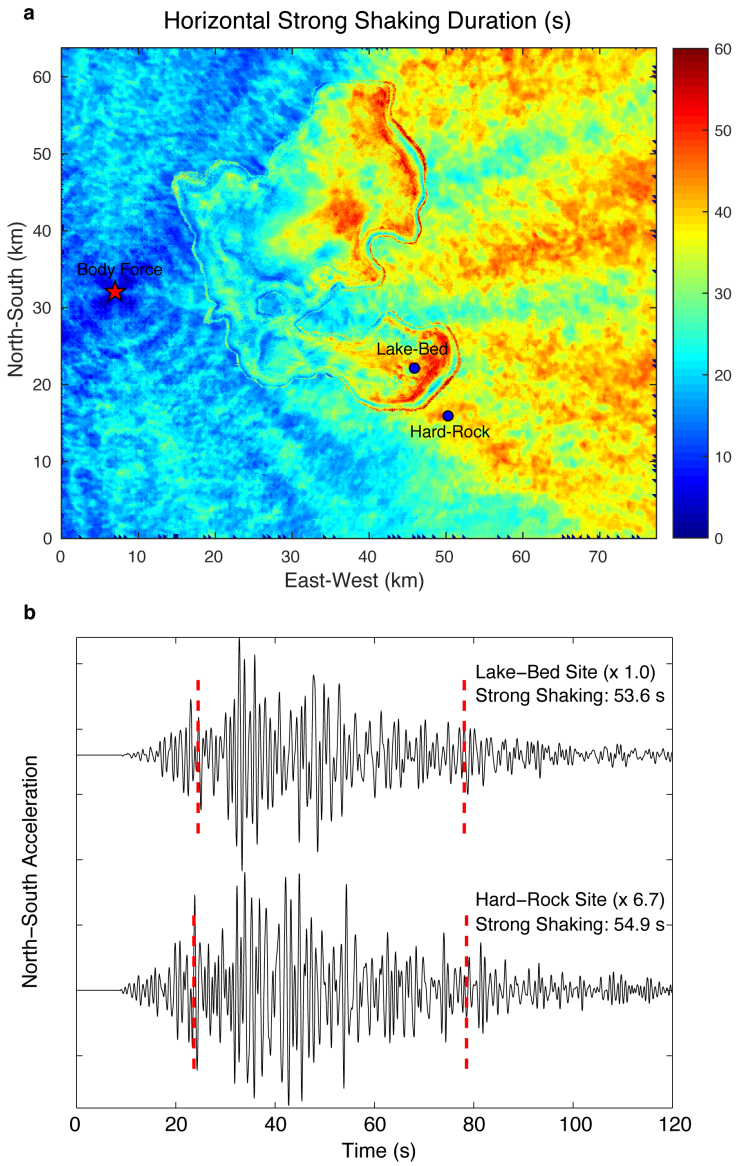

Figure A11 (a) Duration of the strong shaking phase of the Green's function due to source S6 (Figures 1 and 4) averaged for both horizontal components and f < 1 Hz. Notice the long duration of ground motions in both the sedimentary basin and the external shadow region. (b) Seismograms computed in two close sites, one in the lake-bed zone and the other at hard-rock within the seismic shadow. Red dashed lines indicate the strong shaking phase computed form the Arias intensity. Although very different in amplitude, durations of their strong phases are almost the same. This figure has been created using the Matlab software Version R2016a, http://www.mathworks.com/.

IV.4 Sensitivity analyses and variability of EGM predictions

1. Hallier, S., Chaljub, E., Bouchon, M., & Sekiguchi, H., 2008. Revisiting the basin-edge effect at Kobe during the 1995 Hyogo-Ken Nanbu earthquake, *Pure Appl. Geophys.*, **165**, 1751–1760.
2. Causse, M., Chaljub, E., Cotton, F., Cornou, C., & Bard, P.-Y., 2009. New approach for coupling k^2 and empirical Green's functions: application to the blind prediction of broad-band ground motion in the Grenoble basin, *Geophys. J. Int.*, **179**(3), 1627–1644.
3. Imtiaz, A., Causse, M., Chaljub, E., & Cotton, F., 2015. Is Ground-Motion Variability Distance Dependent? Insight from Finite-Source Rupture Simulations, *Bull. Seismol. Soc. Am.*.
4. Maufroy, E., Chaljub, E., Hollender, F., Bard, P.-Y., Kristek, J., Moczo, P., Martin, F. D., Theodoulidis, N., Manakou, M., Guyonnet-Benaize, C., Hollard, N., & Pitilakis, K., 2016. 3D numerical simulation and ground motion prediction: Verification, validation and beyond – Lessons from the E2VP project, *Soil. Dyn. Earthq. Eng.*, **91**, 53–71.

Pure appl. geophys. 165 (2008) 1751–1760
0033–4553/08/091751–10
DOI 10.1007/s00024-008-0404-y

Pure and Applied Geophysics

Revisiting the Basin-edge Effect at Kobe During the 1995 Hyogo-Ken Nanbu Earthquake

Soline Hallier,[1] Emmanuel Chaljub,[1] Michel Bouchon,[1] and Haruko Sekiguchi[2]

Abstract—The basin edge effect, i.e., the interference of the direct S wave with the surface wave diffracted off the basin edge has been invoked by many authors to explain the damage distribution during the January 17, 1995 Hyogo-Ken Nanbu (Kobe) earthquake. Here we present the results of numerical experiments obtained with the spectral element method in 2-D geometry. Our results confirm that the amplification of horizontal motion close to the basin edge can be twice as large as the one measured in the center of the basin. This additional amplification is shown to depend strongly on the edge geometry and on frequency, due to physical dispersion of diffracted surface waves. In particular we obtain maximal amplification around 3 Hz, at frequencies critical for buildings.

Key words: Site effect, basin edge, numerical modelling, spectral element method, Kobe.

1. Introduction

The Hyogo-Ken Nanbu (Kobe) earthquake (M = 7.2) of January 17, 1995 caused considerable damage in the area of Kobe, in particular in a localized zone referred to as the damage, or disaster, belt where most buildings collapsed. The damage belt is a 1 km-wide and 30 km-long area with WSW-ENE orientation, located about 1 km from the Rokko fault (see Fig. 1). In order to explain this peculiar damage distribution, Kawase (1996) invoked a wave propagation effect which he referred to as the basin edge effect. The basin edge effect is caused by the constructive interference between the direct *S*-wave impinging on the basin and the surface wave diffracted off the basin edge. It produces an amplification pattern consistent with the observations, i.e., parallel to the fault, localized at a finite distance from the fault and affecting mainly the horizontal motion in the direction normal to the fault. Maximum values of ground velocity recorded during the Kobe earthquake are given in Table 1.

Many authors have confirmed this effect for the Kobe event, based upon numerical simulations either in 2-D (e.g., Pitarka *et al.*, 1996, 1997) or 3-D geometry

[1] Laboratoire de Géophysique Interne et Tectonophysique, CNRS, Université Joseph Fourier, Grenoble, France.
[2] AFRC, Geological Survey of Japan, Tsukuba, Japan.

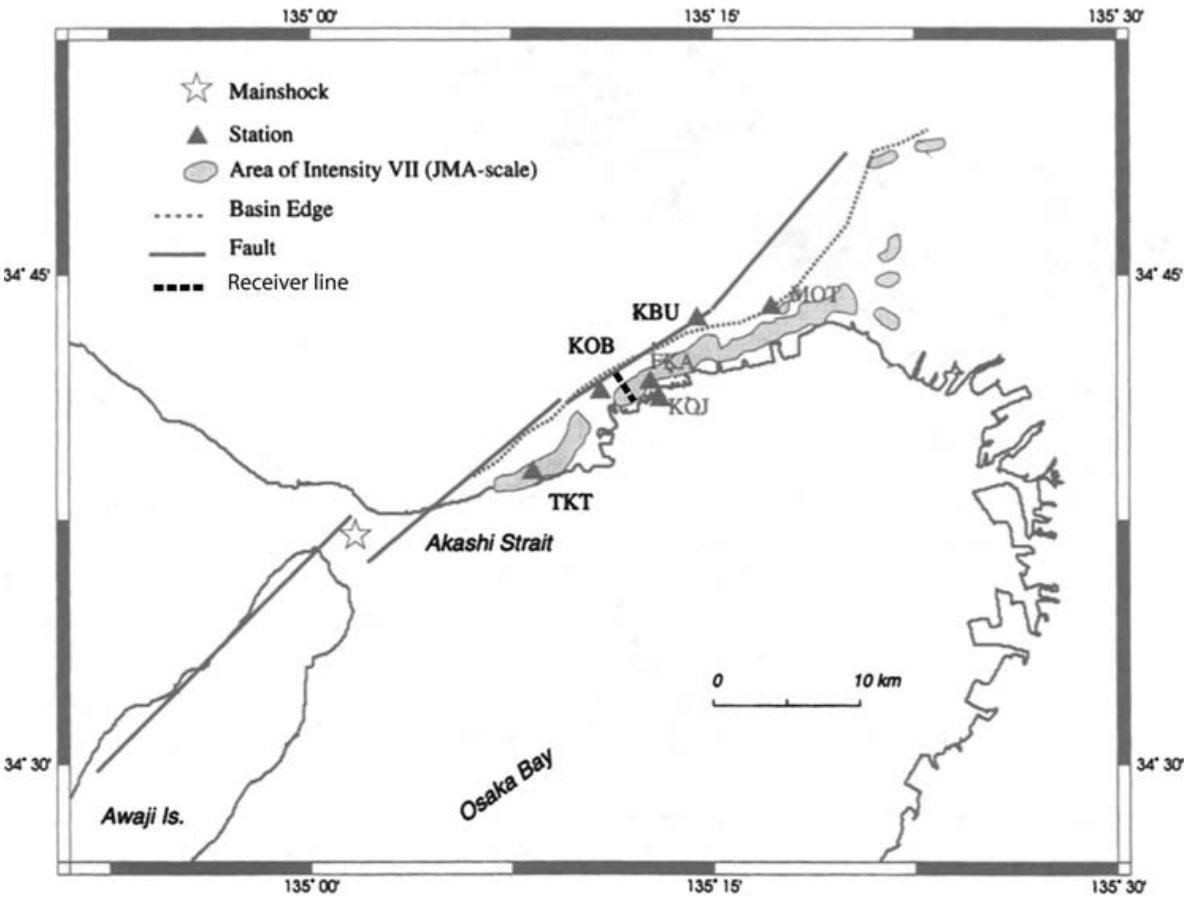

Figure 1
Map of the Osaka basin showing the disaster belt of the Kobe event (shaded zone) defined as the area where the JMA intensity exceeded VII. The Rokko and Nojima faults are indicated with black lines and the epicenter with a star. The basin edge is indicated with a black dotted line. The studied profile, perpendicular to the basin edge, is indicated with a black dashed line (digitized from PITARKA *et al.*, 1998).

Table 1

Values of the peak velocity (in m/s) recorded at stations shown in Figure 1 during the Kobe earthquake. Radial corresponds to the component perpendicular to the fault and transverse corresponds to the component parallel to the fault. Note the large amplification of the radial component at station TKT, located within the damage belt

Station	Radial	Transverse	Vertical
KBU	0.36	0.39	0.18
KOJ	0.86	0.38	0.34
KOB	1.02	0.56	0.49
TKT	1.57	0.63	0.13

(e.g., FURUMURA and KOKETSU, 2000; PITARKA *et al.*, 1998; HISADA *et al.*, 1998). Most of these studies were restricted to low frequencies, i.e., less than 2 Hz in 2-D and less than 1 Hz in 3-D. This upper frequency bound was imposed by available computational resources (especially in 3-D).

In this paper, we present the results of numerical experiments conducted with the spectral element method (SEM) (e.g., KOMATITSCH and VILOTTE, 1998; KOMATITSCH and TROMP, 1999; CHALJUB *et al.*, 2007) with the objective of better understanding the basin edge effect in the Kobe area and of quantifying its dependence on the basin-edge geometry. The SEM is particularly well suited for this study since it can naturally handle the sharp contrast between the basin and the bedrock, in particular at the basin edge, and because it provides great accuracy in modeling surface wave propagation. Our simulations consider a 2-D geometry and are valid for frequencies up to 4 Hz. We do not account for the complexity of the source process (see e.g., WALD, 1996; SEKIGUCHI *et al.*, 1996a,1996b, for details) as we only focus on the edge effect, which as stated previously is a 2-D propagation effect.

2. Numerical Model

We consider the basin geometry and the velocity model given in PITARKA *et al.* (1996) and represented in the left part of Figure 2. Note that the shape of the basin edge in the original model of PITARKA *et al.* (1996) is more complex than the one shown in Figure 2. The influence of the edge geometry on the basin edge effect will be discussed in the remainder of the paper.

The values of density, P and *S* velocities and quality factors Q_P and Q_S are given in Table 2. The model is piecewise homogeneous, with non-flat interfaces between the layers. The shallowest layer is 50-m thick, with minimal *S* velocity of 300 m/s. The phase and group velocities of the fundamental Rayleigh mode for this velocity model are shown in the right part of Figure 2.

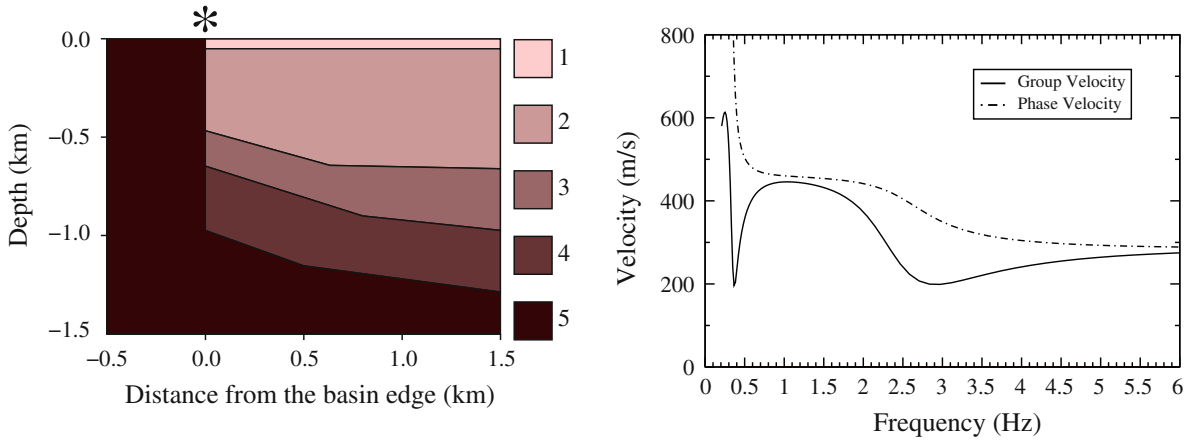

Figure 2
Left: Close view of the Kobe model used in this study showing the geometry of the basin edge and the different zones of the model whose numbers are defined in Table 2. The position of the epicenter is indicated with an asterisk. Right: Theoretical group (solid line) and phase (dashed line) velocities of the fundamental Rayleigh mode for the velocity model given in Table 2.

Table 2

Definition of the piecewise homogeneous basin model used in our calculations (after PITARKA et al. 1996). The physical interfaces are flat in the center of basin, but have significant slope close to the basin edge. The "maximum depth" refers to the interface depth 1500 m from the basin edge

Layer	Maximum depth (m)	ρ (kg/m^3)	V_P (m/s)	V_S (m/s)	Q_P	Q_S
1	50	1600	1500	300	60	30
2	705	2000	1600	500	160	80
3	1173	2200	2000	1100	300	150
4	1785	2200	4200	2850	440	220
5	∞	2400	5700	3200	2000	1000

In order to model P $-$ *S*V wave propagation in the Kobe model with the SEM, we designed a simple structured mesh of quadrangles that honors all the physical interfaces defined above. In each element, we use a polynomial order $N = 4$ for both spatial directions. For calculations accurate up to 4 Hz, the mesh contains 150×60 elements, and we impose a number of 5 points (one element) per minimal wavelength.

We consider a shear dislocation source, located at 10-km depth beneath the basin edge. The source time function is a smoothed step function which radiates a displacement field with a flat spectrum in the frequency band considered in our calculations.

We define 51 surface receivers located every 50 m between -500 m and 2000 m relative to the basin edge. The receiver line is perpendicular to the basin edge and its position in the Osaka basin is shown in Figure 1.

We record the ground velocity on the vertical component and on the horizontal component perpendicular to the basin edge. To quantify the edge effect, we introduce an aggravation factor which we define as the ratio of the horizontal (perpendicular to the basin edge) peak ground velocity (PGV) within the basin to the horizontal PGV at a reference receiver located in the basin, 1500 m from the basin edge.

3. Results

3.1. Frequency Dependence

The interference of the diffracted surface wave with the direct *S* wave forms the basin-edge effect, but since the surface wave is dispersive the interference is expected to depend on frequency as well.

Figure 3 shows the horizontal (perpendicular to the basin edge) and vertical components of ground velocity recorded along the receiver line and filtered between 2 and 4 Hz. Due to the radiation pattern of the source, the main incoming phase is an *S* wave with almost vertical incidence, which is clearly seen on the horizontal component. The vertical component is dominated by energy diffracted off the basin edge and traveling as surface (Rayleigh) waves. The dashed line indicates the group velocity of the

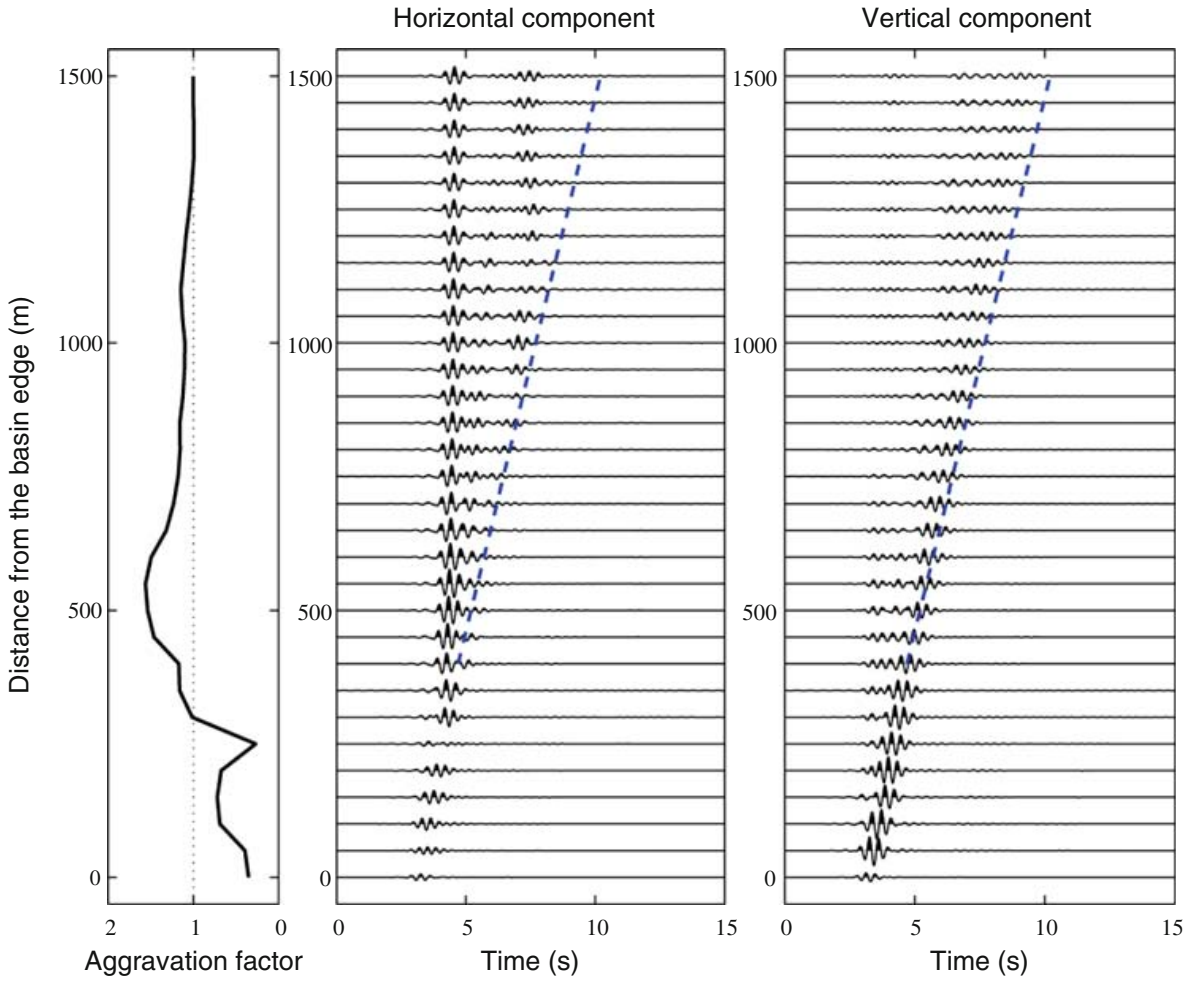

Figure 3

Left: Spatial variation of the aggravation factor calculated along the receiver line perpendicular to the basin edge for the frequency band [2 Hz, 4 Hz]. Middle and right: Synthetic seismograms filtered between 2 and 4 Hz of horizontal and vertical ground velocity. The vertical component is dominated by the surface wave diffracted off the basin edge. The dashed line indicates the Rayleigh energy arrival with group velocity about 200 m/s which corresponds to the Airy phase seen around 3 Hz in Figure 2.

high-frequency Airy phase seen around 3 Hz in Figure 2. The interference of the *S* wave with this surface arrival corresponds to a maximum aggravation factor of 1.6 which occurs about 550 m from the basin edge. Note that previous studies of the basin-edge effect in Kobe have focused on the low frequency interference and have ignored the possible interference with the high-frequency Airy phase.

The same results filtered between 0 and 2 Hz are shown in Figure 4. The dashed line shows an energy arrival with group velocity of 440 m/s, which corresponds to the plateau seen around 1 Hz in the group velocity curve of Figure 2. The interference of the *S* wave with this low frequency Rayleigh wave takes place further away from the edge, around 850 m, on a 450 m wide area and leads to a maximum value of the aggravation factor of about 1.4. These results are in good agreement with those of KAWASE (1996) and PITARKA *et al.* (1997, 1998). As discussed by KAWASE (1996), the zone with aggravated

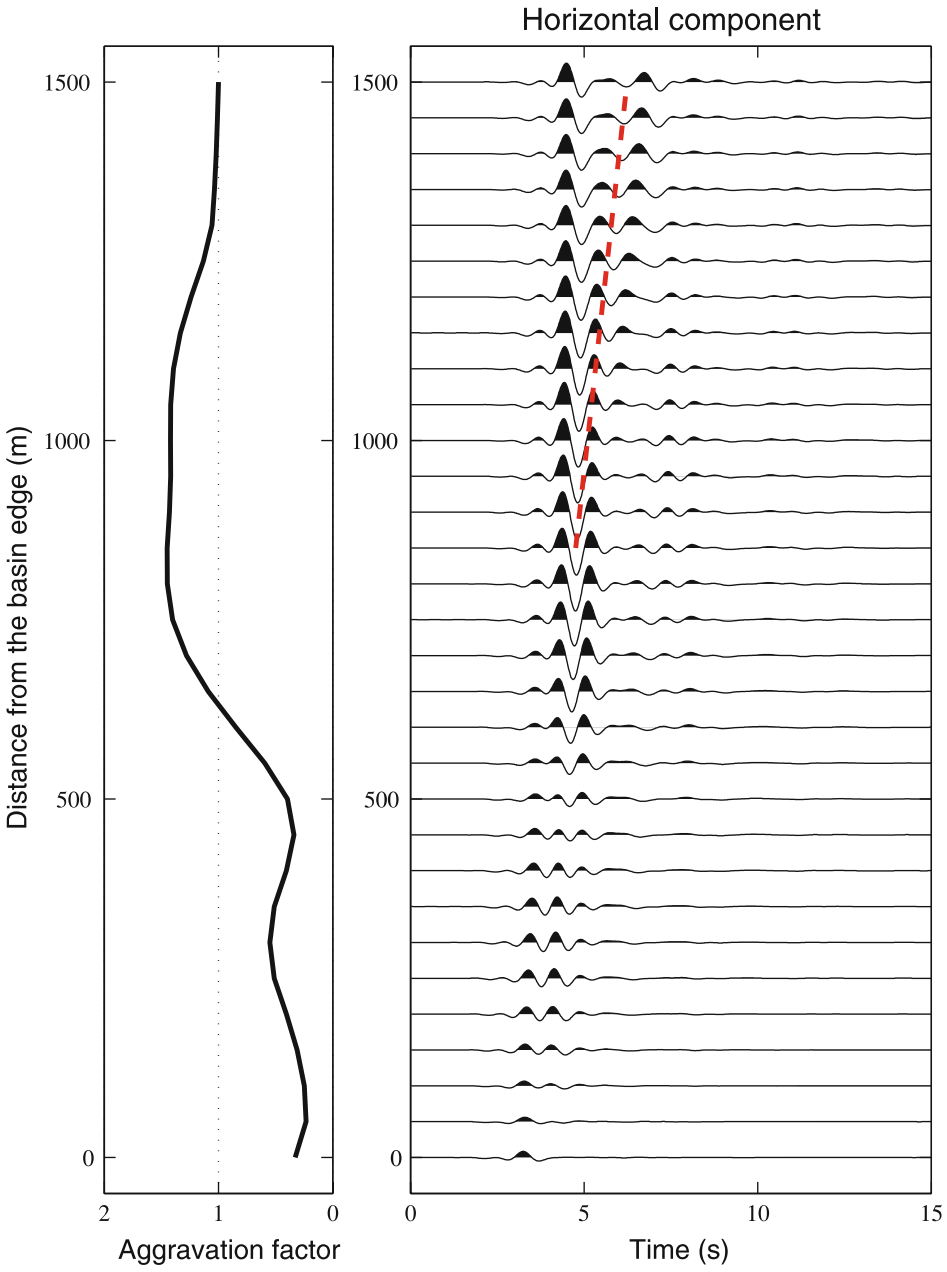

Figure 4
Left: Spatial variation of the aggravation factor calculated along the receiver line perpendicular to the basin edge for the frequency band [0 Hz, 2 Hz]. Right: Synthetic seismograms filtered between 0 and 2 Hz of horizontal ground velocity. The dashed line indicates the Rayleigh energy arrival with group velocity about 440 m/s which interferes with the direct *S* wave about 850 m from the basin edge.

PGV predicted by low-frequency 2-D numerical simulations is not as large as the observed damage belt (around 1200 m for the latter in the area considered by KAWASE (1996) and in this study, compared to about 600 m for numerical predictions). Figure 3 suggests that if the input motion had enough energy above 2 Hz, then the high-frequency interference could have increased the width of the zone with aggravated PGV (by about 200 m) and shifted it closer to the basin edge.

3.2. *Effect of Edge Geometry*

The geometry of the basin edge is known to affect the energy diffracted towards the basin (see e.g., BARD and BOUCHON, 1980a,1980b; AOI *et al.*, 1995) and is therefore expected to change the characteristics of the basin-edge interference. For example, NARAYAN (2005) found a systematic decrease of the amplitude of diffracted Love waves with decreasing slope of the basin edge. In his study, the geometry of the basin is restricted to edges tilted towards the bedrock. Here we test all possible orientations for the basin edge, including the case in which the edge is tilted towards the basin. We refer to the geometry considered by NARAYAN (2005) as shape A, to the case of a vertical edge as shape B, and to the last case as shape C (see top panel of Fig. 5). Shapes A, B and C are typical of basins bounded by normal, strike-slip and thrust faults, respectively. In our simulations, the A and C shapes are obtained by shifting the position of the basin edge at the surface by 400 m in the direction of the bedrock and basin, respectively. The slope of the edge, defined as the angle between the basin edge and the surface, is 68° for the A and C shapes. For each basin geometry, the zero offset corresponds to the basin edge position at the surface and the reference basin site is located 1500 m from the edge. The source position is unchanged in all cases. We plot the aggravation factor as a function of the distance from the basin edge for three frequency bands: low frequency (LF) [0 Hz, 2 Hz], high frequency (HF) [2 Hz, 4 Hz] and broadband (BB) [0 Hz, 4 Hz].

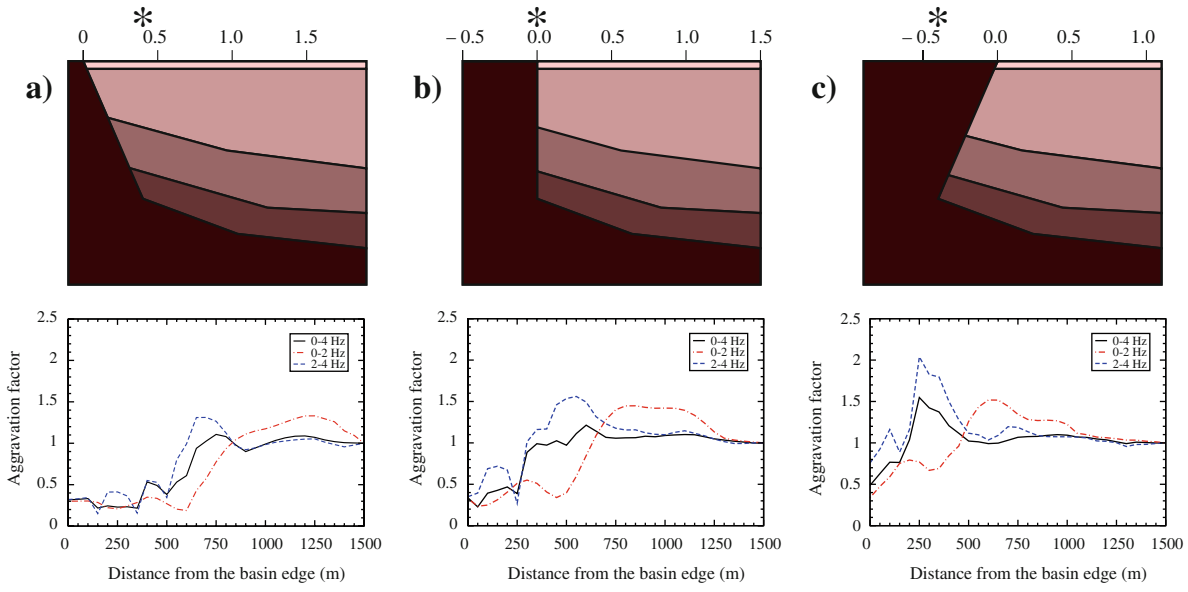

Figure 5

Top: The three geometries of the basin edge considered in this study. The basin edge can be either vertical B, tilted towards the bedrock A or towards the basin C. The position of the epicenter is indicated with an asterisk. Bottom: Ratio of the horizontal PGV measured in the basin to the horizontal PGV measured at the reference basin site. The analysis is performed in three frequency bands: [0 Hz, 4 Hz] (solid line), [0 Hz, 2 Hz] (dash-dotted line) and [2 Hz, 4 Hz] (dashed line). The basin-edge effect occurs in both the low-frequency and the high-frequency bands (see text).

The distance to the basin edge of the zone with increased PGV depends slightly on the edge geometry: It is shifted by about 250 m for A and C shapes, compared to the case of a straight edge. This is because the diffraction of the Rayleigh wave involves the structure of the basin edge at depth, whereas we measure the distance to the basin edge at the surface. Note that like NARAYAN (2005), we found no significant dependence of the amplitude of the diffracted Rayleigh wave on the slope of the basin edge.

For shape A, the aggravation factors reach values of : 1.35 (LF), 1.35 (HF) and 1.15 (BB). For the HF band and LF band, the maximum values of the aggravation factor are obtained 650 m and 1250 m from the basin edge, respectively. The overall pattern obtained for vertical edge (B shape) is similar to that of shape A.

The amplification pattern is somehow different for shape C as the basin-edge effect is now dominated by the HF interference. The aggravation factor due to the basin-edge effect is unchanged in the LF band (around 1.5), but it reaches 2.1 in the HF band. Numerical tests (not shown here) suggest that this extra amplification is due to the focusing of the direct *S* wave by the shape of the basin edge. The focusing of the direct *S* due to the particular shape of the basin edge is likely to occur for all frequencies, however it is only at high frequency that it adds to the interference with the diffracted Rayleigh wave and therefore leads to an enhanced basin-edge effect.

The basin edge geometry in the Kobe area is most likely of shape C (PITARKA *et al.*, 1996). The basin-edge effect should therefore have had a high-frequency part with a constructive interference closer to the fault. The fact that this interference has not been reported is due either to the fact that high-frequencies have only been slightly excited by the Kobe main shock, or simply because of the lack of recordings very close to the fault. Such HF basin-edge effect could in principle have been recorded on aftershocks of the Kobe event by deploying a receiver line perpendicular to the basin edge (see e.g., ADAMS *et al.*, 2003). Such analysis could have helped to identify *a posteriori* the importance of the basin-edge effect in the dramatic occurrence of the disaster belt.

4. Conclusions

We have presented a numerical study of the basin-edge effect in the Kobe area based upon the spectral element method. We have shown that the basin-edge effect can occur over a wide frequency band, and that it is influenced by the shape of the basin edge. With the velocity model of the Kobe area, the direct *S* wave is shown to interfere with the surface wave at two possible locations in two distinct frequency bands: the first interference occurs at low frequency (between 0 Hz and 2 Hz) about 600 m from the fault, the second occurs closer to the fault (about 250 m) and at higher frequency (between 2 Hz and 4 Hz). Aggravation factors measured on ratios of horizontal peak ground velocity reach about 1.5 and 2.1 for the low-frequency and high-frequency interferences, respectively. These values suggest that the basin-edge effect has contributed to the occurrence of the damage belt on a frequency band wider than previously reported.

Acknowledgments

The computations shown in this paper are based on a 2-D spectral element code modified from an original version written by D. Komatitsch. The dispersion curves shown in this paper are obtained from the computer programs in seismology of Robert B. Herrmann. S. H. greatly acknowledges the seismic risk team at LGIT for extra financial support during the summer of 2006. The author acknowledges the support of the French Agence Nationale de la Recherche (ANR), under grant ACTS-Taiwan 'Active Tectonics and Seismic Hazard in Taiwan'.

References

Adams, B. M., Osborne, N. M., and Taber, J. J. (2003), *The basin-edge effect from weak ground motions across the fault-bounded edge of the Lower Hutt Valley, New Zealand*, Bull. Seismol. Soc. Am. *93,* 2703–2716.

Aoi, S., Iwata, T., Irikura, K., and Sanchez-Sesma, F. J. (1995), *Waveform inversion for determining the boundary shape of a basin structure*, Bull. Seismol. Soc. Am. *85,* 1445–1455.

Bard, P.-Y. and Bouchon, M. (1980a), *The seismic response of sediment-filled valleys. Part 1: The case of incident SH waves*, Bull. Seismol. Soc. Am. *70,* 1263–1286.

Bard, P.-Y. and Bouchon, M. (1980b), *The seismic response of sediment-filled valleys. Part 2: The case of incident P and SV waves*, Bull. Seismol. Soc. Am. *70*, 1921–1941.

Chaljub, E., Komatitsch, D., Vilotte, J.-P., Capdeville, Y., Valette, B., and Festa, G., *Spectral element analysis in seismology*. In *Advances in Wave Propagation in Heterogeneous Media* (eds. R.-S. Wu and V. Maupin), *Advances in Geophysics* (Elsevier 2007).

Furumura, T. and Koketsu, K. (2000), *Parallel 3-D simulation of ground motion for the 1995 Kobe earthquake: The component decomposition approach*, Pure and Appl. Geophys. *157,* 2047–2062.

Hisada, Y., Bao, H., Bielak, J., Ghattas, O., and O'Hallaron, D. R. (1998), *Simulations of long-period ground motions during the 1995 Hyogoken-Nanbu (Kobe) earthquake using 3D finite element method*. In *Proc. a 2nd Intern. Symp. a Effect of Surface Geology on Seismic Motion*, Yokohama, Japan.

Kawase, H. (1996), *The cause of the damage belt in Kobe: "The basin-edge effect," constructive interference of the direct S wave with the basin-induced diffracted Rayleigh waves*, Seismol. Res. Lett. *67*, 25–34.

Komatitsch, D. and Tromp, J. (1999), *Introduction to the spectral element method for three-dimensional seismic wave propagation*, Geophys. J. Int. *139*, 806–822.

Komatitsch, D. and Vilotte, J. P. (1998), *The spectral-element method: an efficient tool to simulate the seismic response of 2D and 3D geological structures*, Bull. Seismol. Soc. Am. *88*, 368–392.

Narayan, J. P. (2005), *Study of basin-edge effects on the ground motion characteristics using 2.5-D modeling*, Pure Appl. Geophys. *162,* 273–289.

Pitarka, A., Irikura, K., Iwata, T., and Kagawa, T. (1996), *Basin structure effects in the Kobe area inferred from the modeling of ground motions from two aftershocks of the january 17, 1995 Hyogo-Ken Nanbu earthquake*, J. Phys. Earth *44,* 563–576.

Pitarka, A., Irikura, K., and Iwata, T. (1997), *Modelling of ground motion in the Higashinada (Kobe) area for aftershock of the 1995 january 17 Hyogo-Ken Nanbu, Japan, earthquake*, Geophys. J. Int. *131*, 231–239.

Pitarka, A., Irikura, K., Iwata, T., and Sekiguchi, H. (1998), *Three-dimensional simulation of the near-fault ground motion for the 1995 Hyogo-Ken Nanbu (Kobe), Japan, earthquake*, Bull. Seismol. Soc. Am. *88*, 428–441.

Sekiguchi, H., Irikura, K., Iwata, T., Kakehi, Y., and Hoshiba, M. (1996a), *Determination of the location of faulting beneath Kobe during the 1995 Hyogo-Ken Nanbu, Japan, earthquake from near-source particle motion*, Geophys. Res. Lett. *23*, 387–390.

Sekiguchi, H., Irikura, K., Iwata, T., Kakehi, Y., and Hoshiba, M. (1996b), *Minute locating of faulting beneath Kobe and the waveform inversion of the source process during the 1995 Hyogo-Ken Nanbu, Japan, earthquake using strong ground motion records*, J. Phys. Earth *44*, 473–487.

WALD, D. (1996), *Slip history of the 1995 Kobe, Japan, earthquake determined from strong motion, teleseismic, and geodetic data*, J. Phys. Earth *44*, 489–503.

(Received March 20, 2008, revised August 10, 2008)

Geophysical Journal International

Geophys. J. Int. (2009) **179,** 1627–1644 doi: 10.1111/j.1365-246X.2009.04354.x

New approach for coupling k^{-2} and empirical Green's functions: application to the blind prediction of broad-band ground motion in the Grenoble basin

Mathieu Causse, Emmanuel Chaljub, Fabrice Cotton, Cécile Cornou and Pierre-Yves Bard

Laboratoire de Géophysique Interne et de Tectonophysique (LGIT), CNRS, Université Joseph Fourier, Observatoire des Sciences de l'Univers de Grenoble, Institut de recherche pour le Développement, Laboratoire Central des Ponts-et-Chaussées, France. E-mail: mathieu.causse@obs.ujf-grenoble.fr

Accepted 2009 August 3. Received 2009 May 13; in original form 2008 June 2

SUMMARY

We present a new approach for performing broad-band ground motion time histories (0.1–30 Hz) of a future earthquake in a sedimentary basin. Synthetics are computed with an hybrid scheme combining reciprocity-based 3-D-spectral element method simulations at low frequencies and empirical Green's functions (EGF) at high frequencies. The combination between both deterministic and empirical parts results in a set of hybrid Green's functions, summed according to a new k^{-2} kinematic model algorithm. The summation technique enables to remove the high-frequency artefacts that appear above the EGF corner frequency. The ground motion variability is assessed by generating a variety of source parameter sets selected from *a priori* probability density functions. This leads to a population of response spectra, from which the median spectral acceleration and standard deviation values are derived. The method is applied to simulate a M_W 5.5 event in the deep Grenoble basin (French Alps). The comparison with EC8 regulations suggests the need of specific design spectra in the Grenoble valley.

Key words: Earthquake ground motions; Site effects; Europe.

INTRODUCTION

Synthesizing time histories of ground motion in urban areas is useful to design specific structures and to estimate potential damages for a future earthquake. This is particularly true in European alpine valleys where moderate earthquakes may have large consequences caused by large 2-D/3-D site effects. The Grenoble city is a typical example of alpine valley: first, historic seismicity shows the possibility of M_W 5.5 events at the vicinity of the city (≈20 km); second, this deep sedimentary valley exhibits large complex site effects (Lebrun *et al.* 2001; Cornou *et al.* 2003; Guéguen *et al.* 2006b; Drouet *et al.* 2007). In order to analyse seismic hazard in the Grenoble valley, a M_W 5.5 scenario earthquake occurring on the Belledonne border fault south of the city is assumed (Thouvenot *et al.* 2003). The source proximity makes it necessary to use a finite-extent source description. The ground motion predictions are thus performed with a new approach coupling the k^{-2} source model (Herrero & Bernard 1994) and hybrid Green's functions (HGF), that incorporate 3-D site effects. This new procedure provides an estimation of the ground motion variability.

Ground motion characteristics are strongly affected by the velocity structure. The lack of detailed knowledge of the propagation medium makes it usually difficult to use numerical methods for estimating ground motion at high frequency (generally above 1–2 Hz). An alternative approach is then the empirical Green's functions (EGF) method (Hartzell 1978), when good quality small earthquake recordings are available. This method automatically includes propagation and site effects, under the assumption of the soil response linearity. Nevertheless it is inadequate for assessing low-frequency ground motion, because of the often bad signal-to-noise ratio in the small event recordings below 1 Hz. Thus, several authors (Kamae *et al.* 1998; Pulido & Kubo 2004; Pacor *et al.* 2005) proposed to calculate broad-band ground motion with a hybrid scheme combining deterministic and stochastic approaches: low-frequency Green's functions are evaluated by numerical algorithms whereas high-frequency Green's functions are obtained from filtered white noise. In this paper, a hybrid method is also proposed. First, low-frequency ground motion (<1 Hz) is modelled with 3-D spectral element method (Komatitsch & Vilotte 1998; Komatitsch & Tromp 1999; Komatitsch *et al.* 2004; Chaljub *et al.* 2007) calculations based on reciprocity. Second, the good quality recordings of a M_L 2.8 earthquake provided by the 2005 Grenoble experiment (Chaljub *et al.* 2006) and the French permanent accelerometric network (http://www-rap.obs.ujf-grenoble.fr),

are used as EGFs to simulate high-frequency ground motion (1–30 Hz). The advantage of such a combination is that both methods are adequate for simulating specific site effects.

In addition, in the relevant frequency range for earthquake engineering and within a few fault lengths, ground-motion simulations highly depend on the rupture process complexity. Thanks to its ease of application, kinematic modelling remains the best way to perform physically based ground motion predictions. Moreover, Hartzell *et al.* (2005) compared a class of kinematic models based on fractal distribution of subevent sizes with a simple slip-weakening dynamic model and concluded that at present the kinematic simulations match better the 1994 Northridge ground motion than the dynamic ones. A now classical approach is a self-similar rupture model in which the spatial static slip distribution is described in the wavenumber domain by a k^{-2} power-law decay (Herrero & Bernard 1994; Bernard *et al.* 1996). This model leads to the commonly observed ω^{-2} displacement amplitude spectrum decay under the two constraints that the rupture front propagates with a constant rupture velocity and that the rise time is inversely proportional to the wavenumber k. Ground motion is next computed by summing up the HGF according to a k^{-2} source model. In order to couple k^{-2} model and the EGF method, a specific summation algorithm is developed. It enables to correct the high-frequency artefacts that appear above the EGF corner frequency. Finally, source parameters are defined with probability density functions and the resulting ground motion variability is assessed by means of the Latin Hypercube Sampling (LHS) method. The ground motion sensitivity to source parameters and to EGF uncertainties is thoroughly investigated. As a result, median and standard deviation of the spectral acceleration (SA) are predicted on nine stations within the Grenoble valley in the frequency range [0.1–30 Hz]. In order to test the reliability of the ground motion predictions, simulations on rock station are compared to the empirical ground motion equations developed by Bragato & Slejko (2005) and to the stochastic method of Pousse *et al.* (2006). The comparison of the predictions at sediments stations with Eurocode eight suggests the need of specific design spectra in the framework of the Grenoble basin.

SOURCE MODEL

Static slip distribution

The complexity of the static slip is described with a self-similar distribution of slip heterogeneities. Following Herrero & Bernard (1994) the static slip is supposed to have a k^{-2} asymptotic decay in the wavenumber domain beyond the corner wavenumber k_c, inversely proportional to the ruptured fault dimension. For a rectangular fault plane with length L and width W we define the slip amplitude spectrum in a way similar to Somerville *et al.* (1999) and Gallovic & Brokesova (2004)

$$D_k(k_x, k_y) = \frac{\bar{D}LW}{\sqrt{1+\left[\left(\frac{k_x L}{K}\right)^2+\left(\frac{k_y W}{K}\right)^2\right]^2}}, \quad (1)$$

where k_x and k_y are the wavenumbers along the strike and the dip directions, respectively, $\bar{D}$ refers to the mean slip and K is a dimensionless constant controlling the corner wavenumber $k_c = K/\sqrt{(L^2+W^2)}$. The parameter K is fundamental because it determines the amplitude of the slip heterogeneities generating the high-frequency source energy. At low wavenumber $[k_x^2 + k_y^2 \leq (1/L)^2 + (1/W)^2]$ the slip spectrum phases are chosen to concentrate the slip on the fault centre whereas for high wavenumbers, phases are random. Consequently, the static slip is the sum of a deterministic and a stochastic part. The deterministic part of the slip generates a smooth asperity with mean slip $\bar{D}$, the size of which depends on the corner wavenumber, that is, the dimensionless parameter K. Large values of K lead to a small asperity. The main asperity is then added to the high wavenumber slip contributions, corresponding to a set of zero mean slip heterogeneities. This leads to a variety of heterogeneous slip models. All the details to generate the static slip distributions can be found in Appendix A.

Since for a given wavenumber $k > k_c$, the slip fluctuation amplitudes are proportional to K^2, K controls the roughness of the static slip. Fig. 1 displays examples of static slip distributions obtained for different K values. The case $K = 0.35$ results in one large smooth asperity covering the whole fault plane. For $K = 1.4$ the maximum slip increases and a large part of the fault has zero slip. Consequently, the gradient of the slip distribution increases as well and static slip is rougher. This emphasizes the link between K and the average static stress drop $\Delta\sigma$. To better illustrate this correlation,

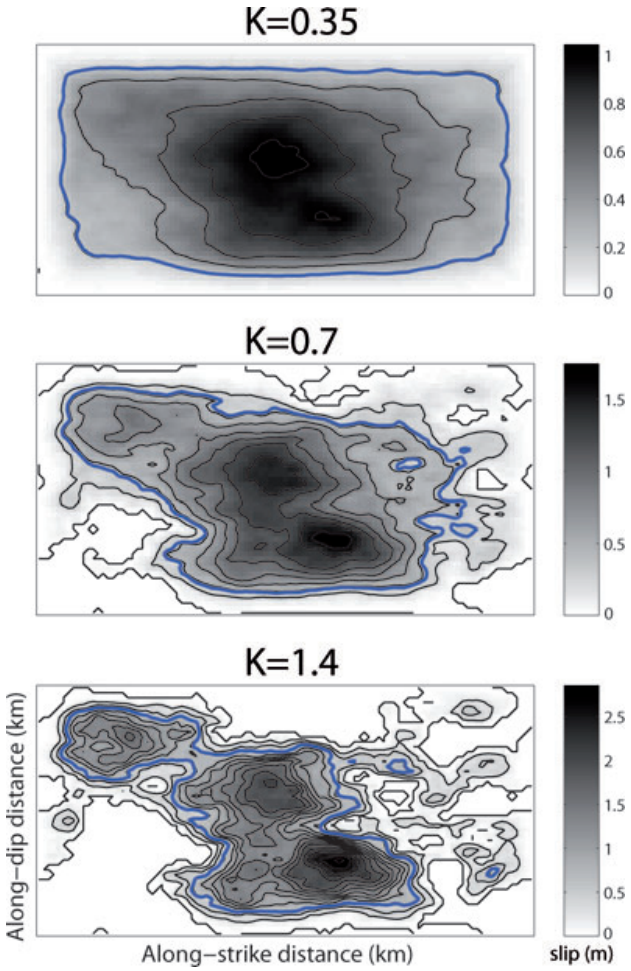

Figure 1. Example of static slip distributions for different K values. The mean slip is $\bar{D} = 0.4$ m in all cases. The blue line defines the area with slip above $0.2D_{max}$. To calculate the static stress drop values, we assume $C_f = 1$ and $\mu = 10^{10}$ N m. The $\Delta\sigma$ values are 18, 34 and 65 bars for $K = 0.35$, 0.7 and 1.4, respectively.

we calculate $\Delta\sigma$ following Kanamori & Anderson (1975):

$$\Delta\sigma = C_f \mu \frac{\bar{D}}{\tilde{L}}, \tag{2}$$

where C_f is a non-dimensional shape factor ($C_f \approx 1$ in all cases), μ is the rigidity and $\tilde{L}$ represents the characteristic length of the rupture area. We define $\tilde{L}$ as the square root of the main slip area, defined by the fault surface with slip over 20 per cent of the maximum slip. This simple test shows the average static stress drop increase with K (see legend of Fig. 1 for more details).

Source kinematics

Following Bernard *et al.* (1996), we model the rupture process as a 'self-healing' slip pulse of width L_0 propagating at constant rupture velocity v. For wavenumbers $k < \frac{1}{2L_0}$, the rise time is $\tau_{\max} = L_0/v$ whereas for higher wavenumbers, the rise time is inversely proportional to k. These choices ensure the commonly observed flat level of the acceleration amplitude spectrum beyond the corner frequency F_c. Gallovic & Brokesova (2004) derived a general equation of the ground motion acceleration spectrum for a 2-D rectangular fault model with a k-dependent rise time. They developed an analytical formula of the amplitude spectrum for a line fault in a homogeneous elastic medium, in the Fraunhoffer's approximation. The authors show evidence of two characteristic frequencies. First, the corner frequency can be expressed as

$$F_c = \frac{vC_dK}{L}, \tag{3}$$

where $C_d = \frac{1}{1-(v/c)\cos\Theta}$ is the directivity coefficient (Ben-Menahem 1961). Θ denotes the directivity angle, defined as the angle between the rupture front propagation and the source–receiver direction, and c is the shear wave velocity. The second characteristic frequency is defined as: $F_t = (vC_d)/(2L_0)$. Beyond F_t, the high-frequency energy comes from the coherent summation of the small-scale ruptures within the slip band. Gallovic & Burjanek (2007) showed that such constructive interferences result in overestimated high-frequency directivity effects. Thus, following Bernard & Herrero (1994) and Gallovic & Burjanek (2007), we assign the small-scale heterogeneities ($k > \frac{1}{2L_0}$) random rupture directions to reduce the high-frequency spectral level dependence on the rupture propagation direction. According to Gallovic & Burjanek (2007), at frequencies above the transition frequency

$$F_0 = \frac{v}{L_0} = \frac{1}{\tau_{\max}}, \tag{4}$$

the acceleration amplitude spectral level for $\Theta = 0^\circ$ and $\Theta = 180^\circ$ is such that

$$A_o = 4\pi^2 C_s M_o \left(\frac{v}{L}\right)^2 \cdot K^2 \cdot \mathrm{RMS}\left[C_d(\Theta)^2 X(C_d(\Theta)/2)\right], \tag{5}$$

where C_s contains the propagation information and radiation pattern and X is the amplitude spectrum of the slip velocity function corresponding to unit slip and a one second rise time. In this paper, a Gaussian function with standard deviation $\sigma = \tau_{\max}/10$ is assumed for the slip velocity function. For $\Theta = 90^\circ$, the spectral level is flat above the corner frequency. It is given by

$$A_{\Theta=90^\circ} = 4\pi^2 C_s M_o \left(\frac{v}{L}\right)^2 \cdot K^2 \cdot X(1/2). \tag{6}$$

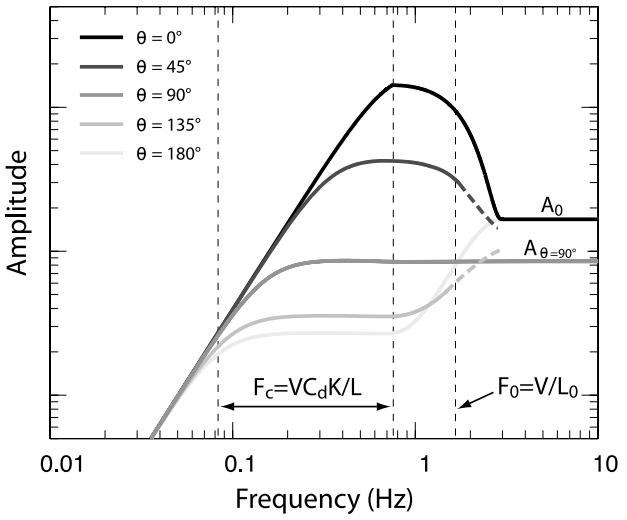

Figure 2. Representation of the acceleration spectra for different values of the directivity angle Θ. A Gaussian slip velocity function with standard deviation $\sigma = \tau_{\max}/10$ is assumed. In this example, $L = 20$ km, $K = 1$, $L_0 = 0.1L$, $v = 3000\ \mathrm{m\,s^{-1}}$ and $v/c = 0.8$. Introducing rupture incoherence does not modify the spectrum for $\Theta = 90^\circ$. Nevertheless, for $\Theta = 0^\circ$ and 180°, the directivity coefficient is the quadratic sum of $C_d{}^2$ coefficients with variable Θ (Bernard & Herrero 1994). To obtain the curves for $\Theta = 0^\circ$ and 180°, following Gallovic & Burjanek (2007), the theoretical spectra for a classical k^{-2} model are modified by setting their level to A_0 above the frequency $2f_0$. A cosine function is then applied between frequencies $f_0/2$ and $2f_0$ to ensure a smooth transition. The high-frequency levels for the other values of Θ range from $A_{\Theta=90^\circ}$ to A_0.

The levels obtained for the other values of Θ range from A_0 to $A_{\Theta=90^\circ}$. A representation of the ground acceleration amplitude spectrum is given in Fig. 2. The whole rupture process is illustrated on Fig. 3. Note that the resulting slip velocity functions exhibits negative values at some points, which is physically unrealistic. Ruiz *et al.* (2007) developed a recombination scheme of the Fourier slip components to get slip velocity functions compatible with earthquake dynamic (e.g. Tinti *et al.* 2005). Nevertheless, studying the shape of this function is not the purpose of our study and we do not apply any other correction than removing the negative static slip values.

SUMMATION ALGORITHM

The simulated event ground motion displacement $U(r, t)$ at position r is numerically expressed according to the discretized representation theorem (Aki and Richards 2002)

$$U(r,t) = \sum_{ij} \frac{\mu_{ij} a_{ij}}{m_{o_{ij}}} s_{ij}(t - t_{r_{ij}}) * G_{ij}(r,t), \tag{7}$$

where μ_{ij}, a_{ij}, $m_{o_{ij}}$ and $G(r, t)_{ij}$ refer to the rigidity, area, seismic moment and Green's function at the subfault (i, j), respectively. The slip histories $s_{ij}(t)$ and the rupture times $t_{r_{ij}}$ arise from the k^{-2} source model described above. In this study $G_{ij}(r, t)$ is replaced with the recording of a small earthquake $u(r, t)$ used as EGF. According to Hartzell (1978) the summation is valid only below the EGF corner frequency f_c. The small event is supposed to follow a k^{-2} model as well. In the following $(l, w, K_S, \bar{d}, m_o)$ stands for the fault length, width, K value, mean dislocation and seismic moment of the small event, respectively.

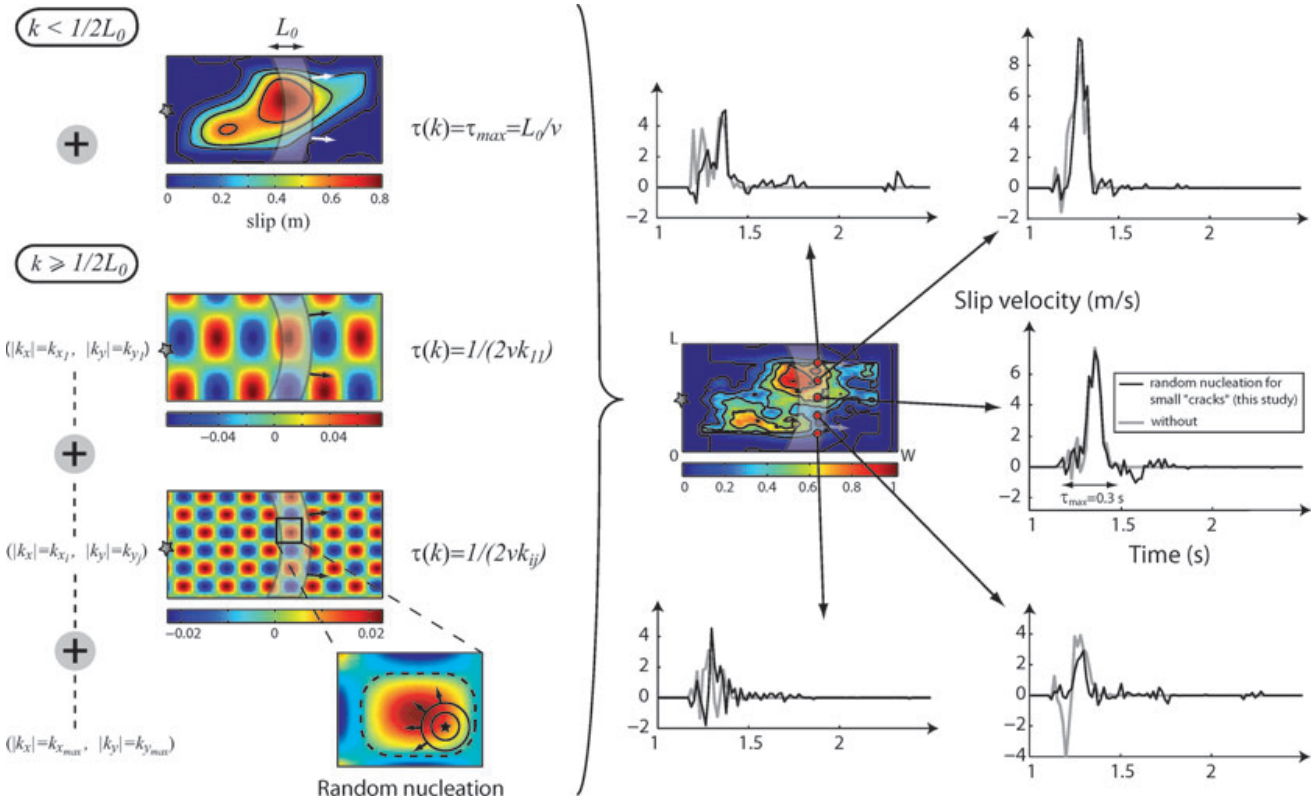

Figure 3. Representation of the rupture process, modelled as a slip pulse propagating at constant rupture velocity v. The slip distribution is split into its low and high components at frequency $k = \frac{1}{2L_0}$. The low wavenumber slip has a rise time equal to $\tau_{\max} = L_0/v$. The high wavenumber slip is composed of a set of heterogeneities of different scales, considered as independent subevents. These subevents start slipping as the main rupture front reaches one point, randomly chosen, from which a secondary rupture front propagates (see bottom left box). The slip duration for a given subevent is proportional to its wavenumber. The figure also displays example of resulting slip velocity functions, compared with the functions that would be obtained from a classical k^{-2} model (without random nucleation points). In this example, $L = 5$ km, $W = 2.5$ km, $\bar{D} = 0.2$ m, $K = 1$ and $\tau_{\max} = 0.3$ s.

Fault plane discretization

The EGF fault plane is assumed to be a square. Its length is determined from the corner frequency. The EGF is supposed to be small enough ($M_{\mathrm{L}} = 2.8$ in this study) to neglect directivity effects. This common assumption is controversial (e.g. Boatwright 2007) and is discussed in the section 'EGF uncertainties'. Thus, assuming a k^{-2} model, the EGF corner frequency is such that

$$f_{\mathrm{c}} = \frac{vK_S}{l}. \tag{8}$$

Assessing the rupture length implies to determine the K_S value. An approximation of K_S can be obtained by considering the model of Brune (1970), which gives for a circular fault: $f_{\mathrm{c}} = 0.33c/r_{fge}$, where c is the shear wave velocity and r_{fge} is the fault radius. In the case of a square fault plane, the conservation of the EGF rupture surface between a square and a circular fault gives: $f_{\mathrm{c}} = 0.33\sqrt{\pi}c/l$. By considering: $v = 0.8c$, which is consistent with dynamic rupture modelling, we get: $f_{\mathrm{c}} \approx 0.74v/l$. This suggests $K_S \approx 0.74$. Thus, from eq. (8), we obtain the small earthquake rupture length.

The dimensions of the target event fault plane are next assessed using the scaling laws between small and large earthquakes. The classical law of Brune (1970), based on the assumption of self-similarity between the small and the large events, gives

$$\frac{L}{l} = \frac{W}{w} = \frac{\bar{D}}{\bar{d}} = N, \text{ with} N = \left(\frac{M_0}{m_0}\right)^{1/3}. \tag{9}$$

M_0 denotes the seismic moment of the target event. Note that eq. (9) is valid provided that both events have the same K value. In other words, the choices $L = W = N \cdot l$ and $K = K_S$ lead to a target event stress drop equal the EGF one. In our procedure, L and W are fixed. Consequently, the natural variability of the simulated event stress drop is accounted for by a deviation from $K = K_S$. The choice of the K value distribution will be discussed later. The fault plane discretization parameters can be found in Table 1.

Summation along dislocation rise-time

As explained above, the static slip consists in a deterministic part, with mean slip $\bar{D}$ and a stochastic zero mean high wavenumber part. It leads us to split the summation along the dislocation rise-time in two parts. The number of EGFs to sum on a given subfault (i, j) is: $N_{ij} = N_{\mathrm{DET}_{ij}} + N_{\mathrm{STO}_{ij}}$, where DET and STO indicies stand for deterministic and stochastic slip, respectively. $N_{\mathrm{DET}_{ij}}$ is such that $\sum_{ij} N_{\mathrm{DET}_{ij}} = N^3$ and $N_{\mathrm{STO}_{ij}} = \sum_k \frac{1}{\bar{d}} |D_{k_{ij}}|$, where $D_{k_{ij}}$ is the slip contribution of the kth spectrum component at the subfault (i, j). The global summation algorithm can be expressed as

$$U(r, t) = R(t) * u(r, t), \tag{10}$$

Table 1. Fault plane discretization and EGF parameters. N_L, N_W and N_D denotes the EGF number to sum along the strike, the dip and the dislocation rise time, respectively.

Parameters	Value
M_0	2.2×10^{17} N m
m_0	2.0×10^{13} N m
L/W	2
f_c	12 Hz
l	0.160 km
N_L	36
N_W	18
N_D	18
Target event strike	120°
EGF strike	160°
Dip	90°
EGF focal depth	3 km

Notes: The seismic moments of the EGF and the simulated event are directly obtained from the moment magnitude. We assume that local magnitude and moment magnitude are the same for the EGF. The corner frequency f_c is assessed from the EGF displacement amplitude spectrum.

where the site-dependent apparent source-time function (ASTF) $R(t)$ is

$$R(t) = \sum_{i=1}^{N}\sum_{j=1}^{N}\frac{r}{r_{ij}}\left[\sum_{q=1}^{N_{\mathrm{DET}_{ij}}}\delta(t - t_{r_{ij}} - t_{s_{ij}} - t_{\mathrm{DET}_q}) + \sum_{q=1}^{N_{\mathrm{STO}_{ij}}} p\cdot\delta(t - t_{r_{ij}} - t_{s_{ij}} - t_{\mathrm{STO}_q})\right]. \quad (11)$$

The indice q denotes the summation along the dislocation rise time. The constant p is defined according to: $p = 1$ for $D_{k_{ij}} > 0$ and $p = -1$ for $D_{k_{ij}} < 0$. At last the term $t_{s_{ij}}$ is introduced to account for the different subfault/receiver S-wave traveltime delays and r/r_{ij} is the geometric spreading factor.

Summation process beyond the EGF corner frequency

Beyond f_c the main event energy is purely stochastic because the EGF summation becomes incoherent. Hence the ASTF spectral level is flat and corresponds approximately to the square root of the total number of EGFs to sum up. Thus the resulting high-frequency level is not in agreement with the desired level for the source model. The theoretical level expected for $f \geq f_c$ is Θ-dependent (see section 'Source kinematics'). However, for simplicity, we assume that this level is the same whatever the value of Θ is. We then set the acceleration spectrum level to its maximum value A_0 (note that after eqs (5) and (6), the largest error induced corresponds to a factor of $A_0/A_{\Theta=90^\circ} \approx 2$). Consequently, the theoretical ASTF level is supposed to be (see Appendix B)

$$|R(f \geq f_c)_{\mathrm{theo}}| = \beta N K^2, \quad (12)$$

where $\beta \approx 3.5$.

Following Kohrs-Sansorny *et al.* (2005), the number of EGFs to sum along the dislocation rise time is modified to reproduce the required high-frequency spectral level. The following procedure is proposed (see Appendix C): (1) the EGF dislocation d is adapted so that the average number of EGF summed on each subfault is not N but $[\frac{\alpha(N)}{\beta}]^2 \cdot \frac{N^2}{K^2}$, where $\alpha(N) = 2\sqrt{\ln\left(\frac{N-1}{4}\right)}$ and $\beta \approx 3.5$; (2) the deterministic slip contribution to the ASTF is low-pass filtered to keep only the zero mean slip fluctuations contributions beyond f_c and (3) the spectrum is divided by $[\frac{\beta}{\alpha(N)}]^2 \cdot \frac{K^2}{N}$ to conserve the seismic moment.

Resulting ASTF

Fig. 4(a) displays the effects of the above-described EGF summation scheme correction on the average ASTF amplitude spectra. The spectra are calculated for an unilateral rupture and a rectangular fault with $L/W = 2$. This fault ratio is in agreement with the results of Somerville *et al.* (1999) and will be kept in the following. Fig. 4(a) shows that the high-frequency procedure based on the assumption of a square fault plane holds for $L/W = 2$ and the target high-frequency level is reached. Note that in addition to the misestimation of the high-frequency spectral level, an other type of numerical artefact appears due to the finite distances between the small-event sources (Bour & Cara 1997). It corresponds to a peak occurring approximatively at: $f_p = vC_d/l$ (Fig. 4b). In order to reduce this peak, a random component is introduced in the rupture velocity v. v is thus uniformly distributed in the interval $[v - 100\ \mathrm{m\,s^{-1}},\ v + 100\ \mathrm{m\,s^{-1}}]$. Are also shown the effects of the source (Figs 4c and d). These figures show that the main theoretical characteristics of the amplitude spectrum for a line fault are preserved (i.e. corner frequencies, Θ, K and $\tau_{\max}$-dependence of the model). It should be noticed that $R(f)$ phases are necessarily stochastic beyond f_c. Nevertheless this is consistent with the rupture process that is purely stochastic above F_0.

GREEN'S FUNCTIONS

EGFs

On 2005 October 1 a small earthquake occurred on the southern tip of the Belledonne border fault, about 15 km south of the Grenoble city ($M_L = 2.8$, Local magnitude Sismalp, http://sismalp.obs.ujf-grenoble.fr). This event has been recorded by the French accelerometric permanent network and by a temporary array from the French mobile network (INSU/CNRS), composed of velocimetric sensors (CMG40T, with a flat response from 20 to 60 s) and deployed in the Grenoble city from 2005 June 15 to October 30 (Chaljub *et al.* 2006). These good quality recordings provide an opportunity to simulate the effects of a moderate sized earthquake with the EGF method. Velocities are first differentiated to get the ground acceleration. Twenty-seven three-component accelerograms are then used as EGFs to compute ground motion at nine stations in the Grenoble city (Fig. 5). Seven of the stations are installed on soft soil within the sediment-filled valley, while two are located at rock sites. The hypothesized scenario is a M_W 5.5 left-lateral strike slip event. The fault plane is supposed to be vertical with a strike of 120°. The small earthquake characteristics and the rupture plane discretization parameters are displayed in Table 1. Note that the strike of the small event (160°) is different from that of the target event. Indeed a value of 120° seems more appropriate for a M_W 5.5 scenario in the Laffrey area (Thouvenot *et al.* 2003). In order to account for differences in focal mechanism, a simple procedure is applied to correct the EGF radiation pattern. It has been observed that the radiation pattern of small earthquakes is frequency dependent and characterized by a transition from the theoretical double-couple

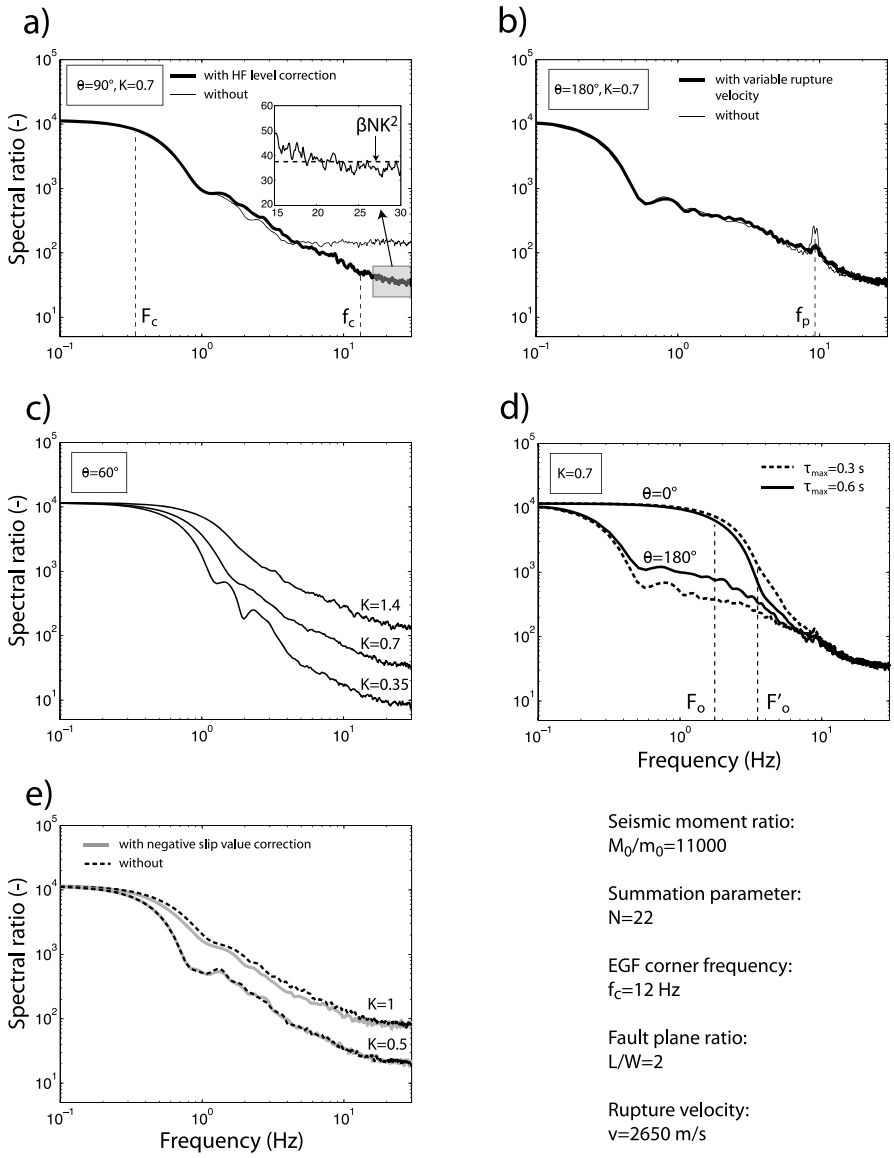

Figure 4. Average apparent source-time function spectra (quadratic mean of 100 simulated spectra) in the case of an unilateral rupture and a rectangular fault plane with $L/W = 2$. The parameters used to compute the spectra are in agreement with the Grenoble application. They are displayed at the bottom right. (a) Effect of the high-frequency spectral level correction. The dashed line in the zoomed box indicates the expected theoretical level. (b) Effect of the addition of a random component to the rupture velocity. (c) Effect of the roughness parameter K. (d) Effect of the angle Θ and the rise time $\tau_{\max}$. Frequencies f_0 and f'_0 denotes the transition frequencies for $\tau_{\max} = 0.6$ and 0.3 s, respectively. (e) Effect of removing the negative slip value.

radiation pattern at low frequencies to a totally isotropic radiation pattern at high frequencies (Satoh 2002). Following Pulido & Kubo (2004) we assume a radiation pattern with a linear variation from 1 to 3 Hz between the theoretical double-couple radiation and a spherical radiation. We only consider the contributions of the *SH* and *SV* waves. The theoretical radiation patterns F^{SH} and F^{SV} are given in Aki and Richards (2002) (equations 4.90 and 4.91). To estimate the take-off angle, an homogeneous medium is hypothesized. Finally, to assess the contributions of the *SH* and *SV* waves to the different ground motion components, we assume a vertically incident wave-field, which is the most plausible given the impedance contrast ($\approx$4) between the bedrock and the sedimentary basin. This leads to a frequency-dependent factor used to correct the EGF amplitude spectrum. This factor equals 1 above 3 Hz and does not change the vertical component. The EW and NS-component modifications at 1 Hz do not exceed a factor of 5, except for station G15 for which a change in the fault azimuth shifts from a maximum to a node of the *SH* radiation pattern, and the EW-component correction factor equals 0.05. The resulting EGF amplitude spectrum modification is large but significantly improves the fit between the 3-D simulation and the EGFs (Fig. 6a).

EGF uncertainties

The small event input parameters (moment magnitude $M_{\rm W}$, corner frequency $f_{\rm c}$ and K value K_s) are only known with large uncertainties. Here we analyse the influence of a potential parameter value misestimation on the simulated ground motion. More precisely, the sensitivity to each EGF parameter is investigated by looking ASTF

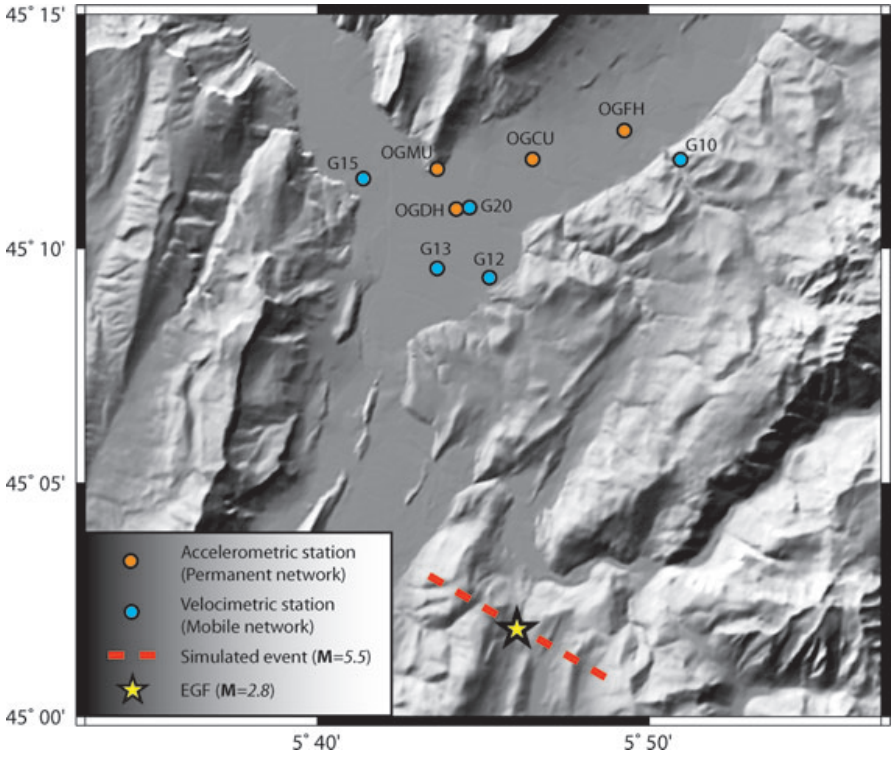

Figure 5. Map of the Grenoble valley, station and fault location.

changes when varying the given parameter around its supposed best estimate value, while keeping the other parameters unchanged. First, the M_W reference value is chosen by assuming $m_L = M_W$ for small events, which leads to $M_W = 2.8$. A deviation of plus or minus 0.2 from the M_W reference value results in a change of a factor 2 in the seismic moment value m_0, and consequently, in the number of EGF to sum up. Therefore, the simulations are largely sensitive to the M_W value at low frequency (Fig. 7a). Furthermore, the corner frequency controls the EGF rupture length l (eq. 8), and consequently, the target event fault plane dimension. For instance, underestimating the f_c value leads to increased rupture length L and decreased target event corner frequency f_c. Since the number of summed EGF is unchanged, the f_c uncertainty does not concern the low-frequency and high-frequency expected spectral levels (Fig. 7b). Finally, Fig. 7(c) shows the effects of varying the K_s value, assuming self-similarity between the small and the target events ($K = K_s$). As f_c is kept constant, changing K_s also affects the rupture lengths l and L.

In addition, it has been assumed that the small event is not affected by directivity effects. If this hypothesis is rejected, first, the simple correction applied to account for the EGF fault strike modification (initial estimated value of 160° set equal to 120°, see section 'EGFs') should also include a modification of f_c. Nevertheless, the procedure applied in this study to simulate ground motion above f_c ensure that the expected ASTF spectral level at f_c is obtained, whatever the f_c value is. Consequently, the particular EGF directivity effects are not expected to significantly modify the simulation results. Second, although the Θ values differ from one station to the other (Fig. 5), the f_c reference value has been set from the data recorded at OGMU rock station and is supposed to be the same for all the stations. However, the difference in the Θ values is not large. Thus, once again, this approximation is expected to bring only minor modifications on ground motion. Using several EGFs would ensure that the potential small event directivity effects are averaged. However, in moderate seismicity area like the Grenoble basin, very few events are available.

HGFs

Since the EGFs have a satisfactory signal-to-noise ratio (>2) only beyond about 1 Hz, they are not adequate to simulate the low-frequency ground motion. Consequently, low frequencies are computed with the spectral element method (SEM) and combined in the time domain with the EGFs to obtain a set of HGFs (Kamae *et al.* 1998). The SEM is a high-order method that combines the ability of finite element methods to handle 3-D geometries and the minimal numerical dispersion of spectral methods (Komatitsch & Vilotte 1998; Komatitsch & Tromp 1999). The reader is referred to Chaljub *et al.* (2007), Komatitsch *et al.* (2004), Lee *et al.* (2008) and Chaljub (2009) for details about the application of the SEM to ground motion estimation in sedimentary basins or valleys. The SEM is particularly well suited for ground motion estimation in alpine valleys because of its natural ability to account for free-surface topography and its accuracy to model the propagation of surface waves, such as those diffracted off the valley edges. The numerical prediction of ground motion with the SEM presented hereafter have been carefully validated by comparison with those of other advanced 3-D methods, during the numerical benchmark organized within the 2006 symposium on the effects of surface geology (ESG) on ground motion (Chaljub *et al.* 2009; Tsuno *et al.* 2009).

Deterministic ground motion calculations implicitly assume that the 3-D structure (i.e. the positions of the physical interfaces, seismic wave velocities, densities, attenuation factors, etc.) is known from the source region to the receivers. For the Grenoble area, we use a simple 1-D model of the crust combined with a 3-D model

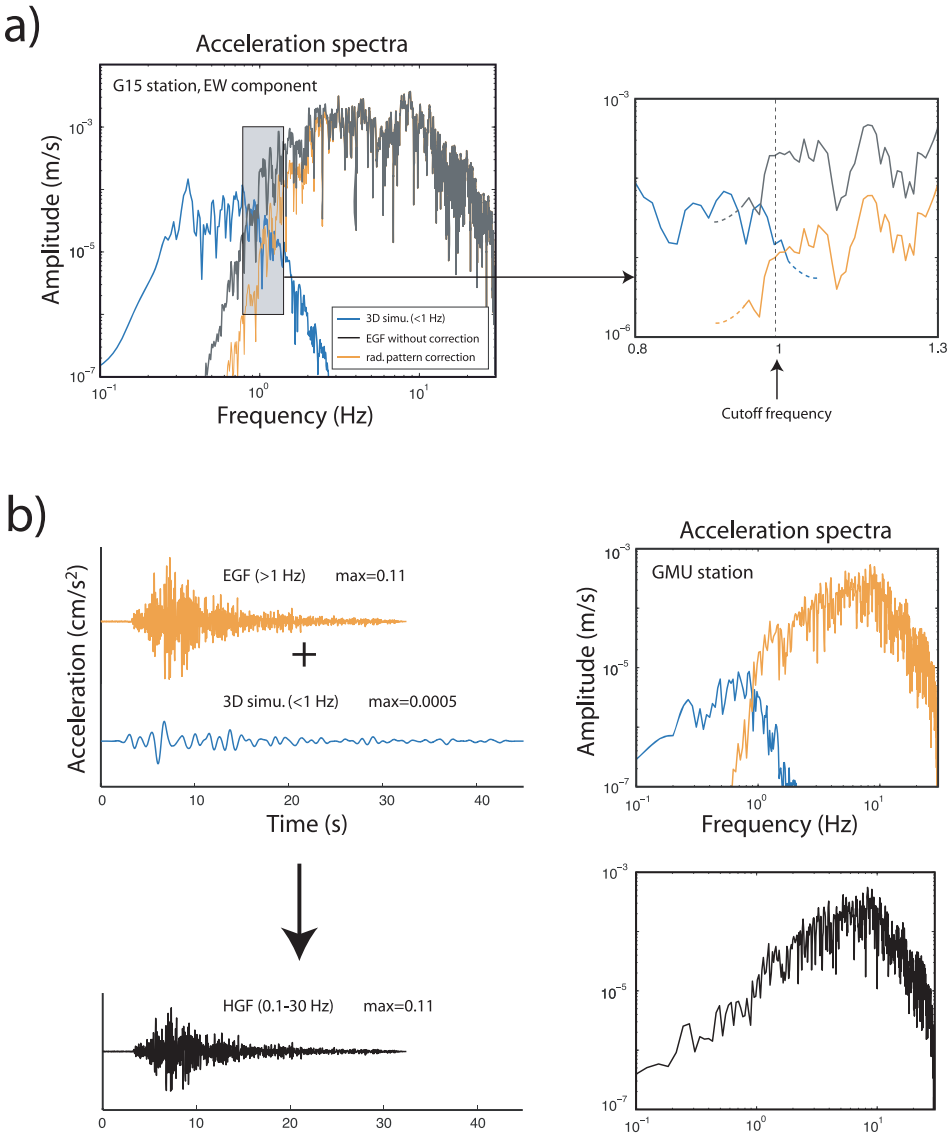

Figure 6. (a) Effect of the EGF radiation pattern correction on the fitting between the deteministic and the empirical ground motion. (b) Principle of the low-frequency ground motion simulation. 3D-simulations and EGFs are filtered and summed on each subfault to obtain a set of HGFs.

of the sedimentary valley. The crustal model is defined following Thouvenot *et al.* (2003) and given in Table 2.

The 3-D valley model is bounded by the sediment-bedrock interface obtained by Vallon (1999). Within the sedimentary cover, seismic velocities and densities are only allowed to vary with depth as

$$\begin{cases} a = 300.0 + 19.0 \times \sqrt{d}, \\ b = 1450.0 + 1.2 \times d, \\ \rho = 2140.0 + 0.125 \times d, \end{cases} \tag{13}$$

where depth d is given in m, P (resp. S) velocities a (resp. b) in m s^{-1} and mass density ρ in kg m^{-3}. Finally, we account for attenuation only in the sediments by assuming a finite shear quality factor $Q_\mu = 50$ and an infinite bulk quality factor Q_κ.

The depth dependence of seismic velocities given by eq. (13) relies on direct measurements made for depths larger than 40 m in a deep borehole drilled in 1999 in the eastern part of the valley (Nicoud *et al.* 2002). It also matches closely the values derived from a refraction profile in the western part of the valley (Cornou 2002; Dietrich *et al.* 2009). This is consistent with the early geological history of the valley since the deep part of the sedimentary cover (i.e. below about −30 m) was formed by the sedimentation of postglacial lacustrine deposits, a smooth process that did not produce strong lateral variations. The shallower part, filled by the deposits of the Isère and Drac rivers, is known to be much more heterogeneous and a continuous effort is deployed to map these lateral variations into a fully 3-D model of the valley. The 1-D model defined by eq. (13) provides a crude average of the shallow subsurface but it has been shown to explain reasonably well the ground motion characteristics for frequencies below 1.5 Hz, in particular the level of amplification between bedrock and sediments (Chaljub *et al.* 2004, 2005; Chaljub 2009) and the ambient noise propagation properties (Cornou *et al.* 2008).

In order to define the low frequency part of the HGFs, we need to compute the ground motion at a small number of stations (9 for

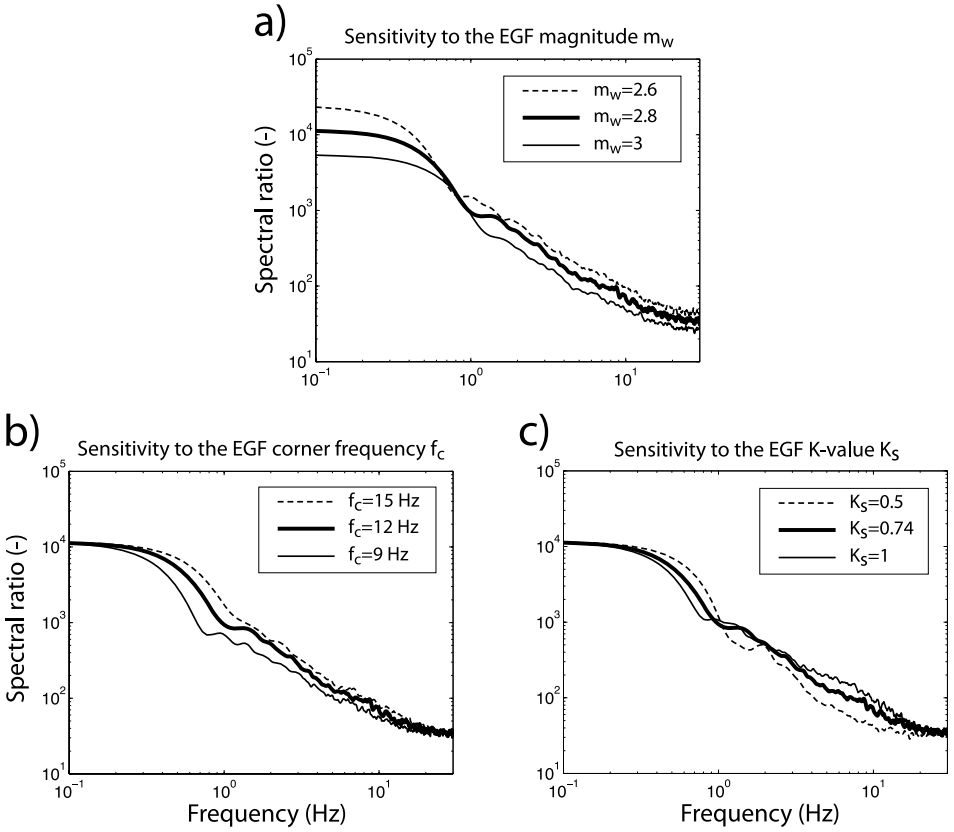

Figure 7. Sensitivity of the ASTF to the EGF parameters M_{W}, f_{c} and K_s. The assumed reference values are $M_{\mathrm{W}} = 2.8$, $f_{\mathrm{c}} = 12$ Hz and $K_s = 0.74$. The spectra correspond to the quadratic mean of 100 simulated spectra for $\Theta = 90^{\circ}$ and $\tau_{\max} = 0.6$ s.

Table 2. 1-D velocity and density model of the bedrock used for estimating the deterministic part of the hybrid Green's functions.

Depth of top layer (km)	α (km s^{-1})	β (km s^{-1})	ρ (g cm^{-3})	Quality factor
0	5.60	3.20	2.72	∞
3	5.92	3.43	2.72	∞
27	6.60	3.81	2.92	∞
35	8.00	4.45	3.32	∞

the results presented in this paper) due to a large number of point sources distributed on the fault plane. The fault plane is discretized into $36 \times 18 = 648$ square subfaults of length 160 m. It is therefore indicated to invoke the reciprocity of the wave equation and to switch the respective roles of sources and receivers, as suggested by Eisner & Clayton (2001), Graves & Wald (2001) and recently implemented by Zhao *et al.* (2006) for tomographic applications.

Let $\mathbf{x^R}$ stand for the position of one of the receivers. The ith component of the displacement field due to a double-couple punctual source located at $\mathbf{x^S}$ is

$$u_i\,(\mathbf{x^R}, t) = \frac{\partial\, G_{ji}}{\partial x_k^S}\,(\mathbf{x^R}, \mathbf{x^S}, t) * M_{jk}(\mathbf{x^S}, t), \tag{14}$$

where G is the Green's function and M gathers the seismic moment tensor and the source time function. Note that G has to be evaluated at the receiver position. Applying reciprocity yields

$$u_i\,(\mathbf{x^R}, t) = \frac{\partial\, G_{ij}}{\partial x_k^S}\,(\mathbf{x^S}, \mathbf{x^R}, t) * M_{jk}(\mathbf{x^S}, t), \tag{15}$$

where now the Green's function is the displacement field evaluated at the source position due to a unit force located at the receiver. The final seismic moment is described with a Heaviside function, scaled to the EGF magnitude ($M_{\mathrm{L}} = 2.8$).

Following eq. (15), we thus performed a total of 27 simulations, 3 unit forces in the x, y and z directions for each of the nine receivers, and recorded the spatial derivatives of the ground displacement at the 648 points defining the fault plane. The grid used for those calculations contains about 40 000 elements (2 600 000 points) and provides a sampling of at least five gridpoints per wavelength for frequencies up to 2 Hz. The computation of 90 s of these 157 464 derivatives of Green's functions required a continuous access to 32 CPUs during about 2 months.

Next, both deterministic and empirical parts of the Green's functions are summed in the time domain on each subfault by adjusting the P-waves arrival times (Fig. 6b). Numerical simulations and EGFs are, respectively, low-passed and high-passed filtered with a pair of complementary filters. A set of 648 three-component HFG is obtained for each station. Given that the EGFs do not have a satisfactory signal-to-noise ratio below 1 Hz and that deterministic Green's functions are calculated up to 2 Hz, the value of the filter cut-off frequency can be chosen within this range. Numerical simulations result in a set of Green's functions specific to the subfault-receiver path. This is not the case for the empirical part since the same EGF is used for each part of the fault plane. Nevertheless, the numerical simulation accuracy is strongly limited by the lack of detailed knowledge of the propagation medium. Therefore, the cut-off frequency is chosen to be 1 Hz (Fig. 6b).

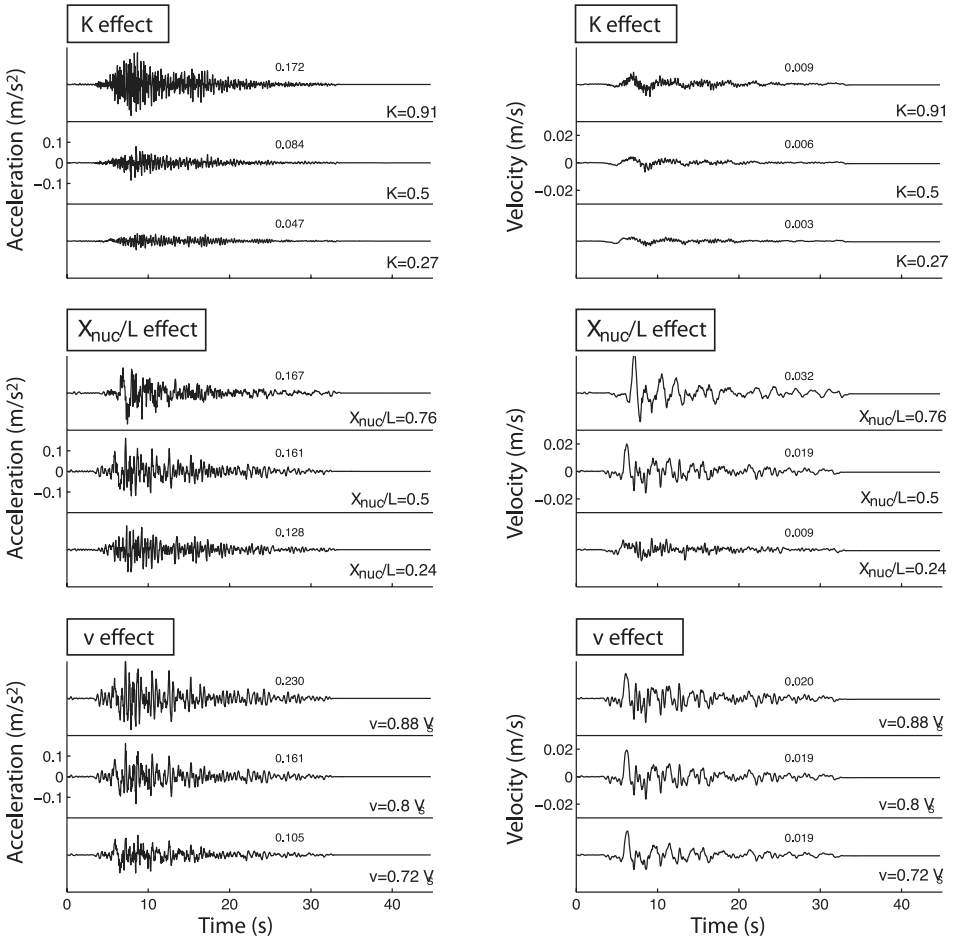

Figure 8. Sensitivity of the ground acceleration with respect to the variation by one standard deviation of the parameter K, the hypocentre abscissa $X_{\rm nuc}$ and the rupture velocity v. Acceleration and velocity time histories are the EW-components at station OGMU. The maximum value is indicated on the right of each time-series. $X_{\rm nuc}/L \leq 0.5$ corresponds to the northwestern part of the fault. In order to show the K effects, an antidirective unilateral rupture is supposed. This way the sensitivity to K can be observed not only on the ground acceleration but also on the velocity. To study the v effects, the hypocentre is set on the middle of the fault.

GROUND MOTION PREDICTIONS

Ground motion variability assessment

The ground motion prediction variability is evaluated by first defining the source parameter uncertainties and then calculating their effects on the SA. More precisely the k^{-2} model parameters are assigned probability density functions. The Latine hypercube sampling (LHS) method (McKay 1988) is next applied to select for each parameter a set of n values, chosen with respect to its distribution. These values are randomly combined for obtaining a set of n samples of source parameters (see Pavic *et al.* 2000, for more details). Finally, the resulting parameter combinations are used to simulate, with the aforementioned summation algorithm, a class of n response spectra, from which the median and standard deviation of SA are calculated. In this study, a value of $n = 50$ is taken. For each simulation the high wavenumber slip spectrum phases are randomly defined.

The source parameter distributions are assessed by investigating their scattering obtained from past kinematic inversion studies. Mai *et al.* (2005) have analysed the hypocentre position by studying a database of more than 80 finite-source rupture models and defined probability density functions that we used in this paper. Somerville *et al.* (1999) also detailed the characteristics of 15 crustal earthquake slip models, from which they derived a relation between the corner wavenumber $k_{\rm c} = K/L$ and the seismic moment. For a $M_{\rm W}$ 5.5 event, the relation gives a median K value of 0.5 with a standard error of 0.26. Taking this distribution, the $n = 50$ K-values range from 0.17 to 1.2. Consequently, according to the discussion of Appendix A, the slip model correction proposed to remove the negative slip areas can be applied. Next we supposed that the rupture velocity v is uniformly distributed between $0.7c$ and $0.9c$, where c is the share wave velocity. Finally, we assume a constant rise-time $\tau_{\rm max}$ equal to 0.25 s, which is the average value proposed by Somerville *et al.* (1999) for a $M_{\rm W}$ 5.5 earthquake. Fig. 8 displays the effects of the source parameters uncertainties on the ground acceleration and velocity at rock station OGMU. Are also shown examples of amplitude acceleration Fourier spectra for unilateral directive and antidirective ruptures (Fig. 9).

Simulation on rock and validation

In order to test the reliability of the ground motion predictions, simulations on rock site are compared to the empirical ground motions equations of Bragato & Slejko (2005) and to the stochastic

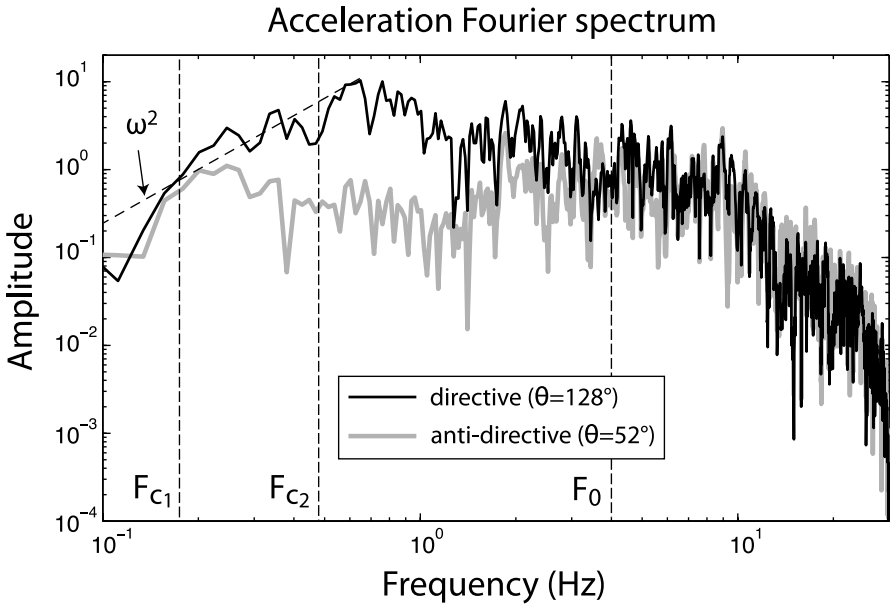

Figure 9. Example of amplitude acceleration Fourier spectra for unilateral directive and antidirective ruptures, at OGMU rock station (EW component). The slope is approximately ω^2 below F_{c_1} and F_{c_2} (theoretical corner frequency values for a non-directive and a directive propagation, respectively). The spectral level is flat and equal for both rupture types beyond the transition frequency F_0, and starts decreasing above about 10 Hz, due to the seismic wave attenuation.

method developed by Pousse *et al.* (2006). Both methods, based on real data, provide estimation of the ground motion median and standard deviation expected at a rock station. Bragato & Slejko (2005) empirical equations have been derived from a large data set of seismometric and accelerometric records collected in the Eastern Alps and are valid in the magnitude range 2.5–6.3 for distances of up to 130 km. Pousse *et al.* (2006) method generates time-domain accelerograms following a specific time envelope and based on the assumption that phases are random. The frequency content of the signal follows a modified ω^{-2} model. The method depends on four indicators (peak ground acceleration, strong-motion duration, Arias intensity and central frequency), empirically connected to Japanese data recorded by the K-net array.

Fig. 10 stands for the comparison between the EGF response spectra at rock stations (OGMU and G10) and Bragato & Slejko (2005) predictions. The good agreement between the data and Bragato & Slejko (2005) model in the frequency range 0.5–3 Hz, especially for station G10, shows that the EGF seismic moment estimation is correct. Discrepancies observed at frequencies above 3 Hz can be explained by the rock stiffness differences at stations OGMU and G10. $V_{S_{30}}$ is close to 2200 m s^{-1} at OGMU and 1500 m s^{-1} at G10, whereas Bragato & Slejko (2005) model includes softer rock types ($800 < V_{S_{30}} < 1500$ m s^{-1} on average; P. L. Bragato, 2008, personal communication). In the following station G10, which best fits the empirical model rock site definition, is kept as the reference rock station.

Comparison between our k^{-2} hybrid calculations, Bragato & Slejko (2005) predictions and Pousse *et al.* (2006) stochastic simulations is displayed on Fig. 11. Stochastic simulations are initially adjusted to adapt the definition of rock. Indeed the K-net array rock types used in Pousse *et al.* (2006) correspond to $V_{S_{30}} \approx 800$ m s^{-1}. Pousse *et al.* (2006) $V_{S_{30}}$ is thus set equal to 1500 m s^{-1}. Since the roughness parameter K median value is poorly constrained by Somerville *et al.* (1999) empirical model, ground motion predictions are shown not only for a median value $K = 0.5$ but also for

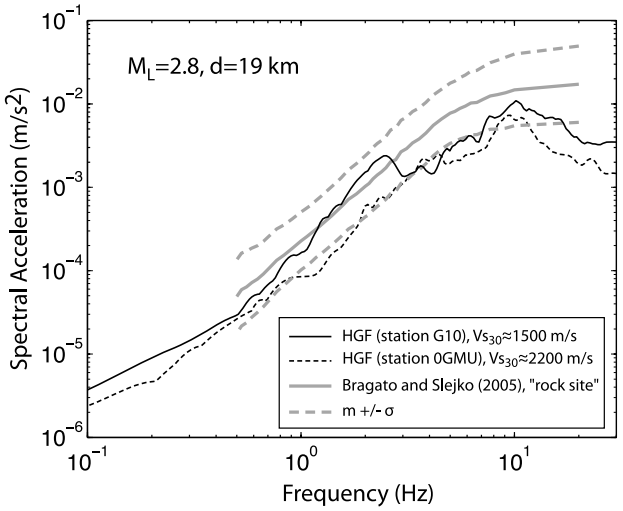

Figure 10. Comparison between the EGF response spectra at rock stations OGMU and G10 (EW component) and Bragato & Slejko (2005) empirical ground motion equations for a rock site, $M_{\mathrm{L}} = 2.8$ and an epicentral distance equal to 19 km.

$K = K_S = 0.74$ (self-similarity between the small and the simulated events) and for $K = 1$ [value used in the classical model of Herrero & Bernard (1994)]. First, for $K = 0.5$, our ground motion simulations well match Bragato & Slejko (2005) empirical equations in the frequency range 0.5–2 Hz and predict lower values for higher frequencies (Fig. 11a). This is consistent with the comparison between the EGF and the empirical equation predictions, showing a similar tendency (Fig. 10). The difference observed at high frequency decreases with an increasing K value. Second, a value of $K = 1$ is necessary to improve the agreement between k^{-2} hybrid simulations and Pousse *et al.* (2006) corrected response spectra. For

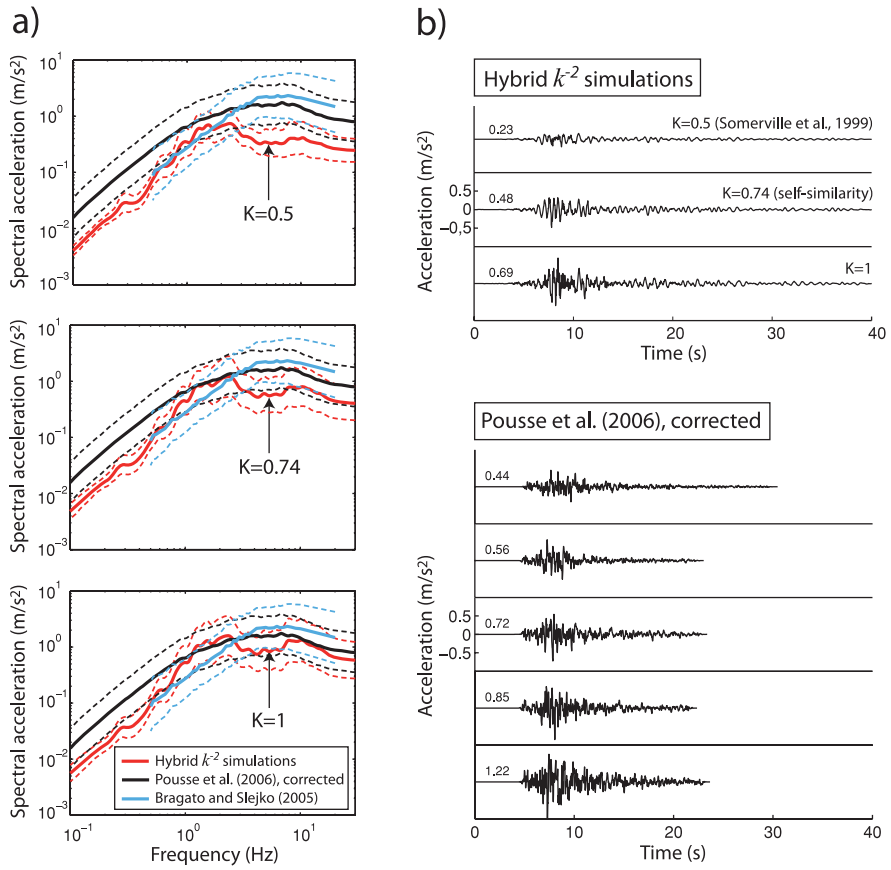

Figure 11. (a) Comparison between the response spectra obtained from our k^{-2} hybrid predictions (station G10, EW component), Bragato & Slejko (2005) empirical ground motion equations and Pousse *et al.* (2006) stochastic simulations, corrected according to Cotton *et al.* (2006) procedure ($V_{S_{30}} = 1500\ \mathrm{m\,s^{-1}}$). The dashed line correspond to the plus and minus standard deviation spectra. (b) Example of accelerograms (station G10, EW component) obtained from the k^{-2} hybrid procedure. Are also shown example of Pousse *et al.* (2006) corrected stochastic simulations. The six time-series span the median ground motion within ± 1 *SD*.

$K = 1$, the obtained time-series are also similar in terms of amplitude and duration (Fig. 11b). Note that below 1 Hz, the stochastic simulations exceed the other predictions of a factor of about 2. This difference may come from Pousse *et al.* (2006) procedure, that overestimates the acceleration Fourier amplitude below the corner frequency for moderate sized earthquakes (Fabian Bonilla, 2008, personal communication—see also fig. 8 of Pousse *et al.* 2006).

Despite the discrepancies observed at high frequency, one can conclude that our simulations are consistent with Bragato & Slejko (2005) empirical equations and the stochastic simulations, for the three tested K values.

Simulation on sediment

In order to simulate ground motion at sediment stations, a K value of 0.5 is kept, since it results from past earthquake analysis (Somerville *et al.* 1999, relationships). The comparison at the rock station G10 with Bragato & Slejko (2005) empirical equation results and Pousse *et al.* (2006) corrected simulations suggests that $K = 0.5$ does not lead to overestimated ground motion. Fig. 12 displays the accelerograms derived from median source parameter values at the 9 stations and Fig. 13 displays median and standard deviation of the simulated response spectra. The spectra are compared with the European regulation spectra (EC8) for rock site (category A in EC8 classification) or for standard to stiff soils (category B and C) for the stations located within the basin. First, our predictions exceed the EC8 spectra at some sites and some frequencies, especially at station OGDH, which exhibits two peaks at 0.3 and 2 Hz. The first peak, generated by 3-D simulations (<1 Hz), corresponds to the fundamental resonance frequency of the sedimentary basin (Lebrun *et al.* 2001; Guéguen *et al.* 2006a). This peak also clearly appears at stations OGFH, G15 and G20. This confirms the importance of coupling the EGF with 3-D numerical calculations. The second peak at 2 Hz has been well identified from geophysical and geotechnical surveys (Guéguen *et al.* 2006b, P. Guéguen and S. Garambois, unpublished manuscript) and from global inversion methods (Drouet *et al.* 2007). This is interpreted as the resonance effects within a surficial soft clay layer overlaying more competent sandy graver layers. Second, the spectral responses at stations G20 and OGDH, located only a few hundreds of meters away, obviously diverge beyond 1 Hz. This points out the large spatial variability of the high-frequency amplification effects, caused by fast lateral variations of the upper soft sediment layers (Tsuno *et al.* 2008). Such variations are observed from several drillings and surface wave measurements performed in this area. Third, the EC8 design spectra largely exceed our simulations at rock stations OGMU and G10. These results indicate that standard European regulations provide a frequency-dependent and site-dependent safety margin in the Grenoble basin. The use of HGFs suggests the need of specific design spectra in Grenoble,

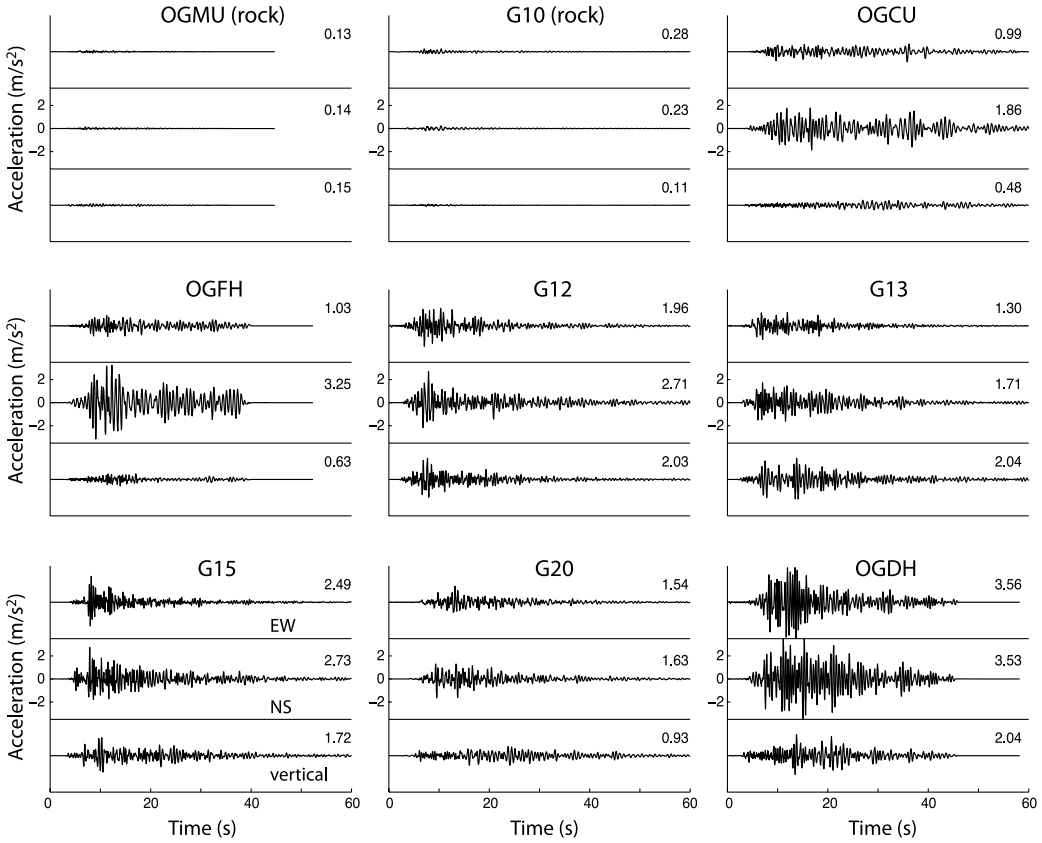

Figure 12. Simulated accelerograms for median parameter values. The maximum value is indicated on the right of each accelerogram.

with increased low-frequency level in the valley and much smaller spectra on rock. Microzonation studies are thus preferable in such a specific geological context.

CONCLUSION

A new method has been introduced for performing broad-band ground motion time histories from a finite-extent source model. This method includes specific site effects and is adequate for simulating ground motion in 3-D deep alluvial valleys. The ground acceleration is computed in the frequency range 0.1–30 Hz with a new approach coupling k^{-2} source model and HGFs, obtained by summing reciprocity-based SEM 3-D simulations ($<$1 Hz) and EGFs. A procedure is proposed to assess the ground motion prediction variability due to the source rupture process, from specific distributions of the k^{-2} model parameters. We used this new approach for predicting ground motion for a potential M_W 5.5 earthquake in the Grenoble valley. At sediment sites, the simulated response spectra significantly differ from one station to the other. At some sites simulations present large response spectra both at high-frequency ($>$1 Hz) and low-frequency ($\approx$0.3 Hz) and EC8 spectra are exceeded. This points out the interest of coupling EGFs and 3-D numerical simulations in such deep valleys.

The method presented relies on reliable estimation of the source model parameter distributions. Our ground motion estimations especially depends on the slip distribution roughness, controlled by the parameter K. In order to estimate the *a priori* K value distribution, Somerville *et al.* (1999) scaling laws have been used. Nevertheless, the reliability of these relationships may be questionable. First, Somerville *et al.* (1999) results have been derived from a small number of inverted source models (15) and the event magnitudes M_W range from 5.6 to 7.2, which decreases the K estimation robustness for a M_W 5.5 event. Second, the inverse problem parametrization often involves subjective decision resulting in highly different inverted slip images and there is no basis to distinguish between artefacts, smoothing constraints and real features (Beresnev 2003). The comparison made in Fig. 11 indicates that a median K value of 0.5 may result in underestimated ground motion. There is thus a need of improving earthquake model databases to better constrain source parameters for performing blind predictions. An other approach would have been to set the median K value equal to 1, which leads to the best fit between the predictions at rock station G10, Bragato & Slejko (2005) predictions and Pousse *et al.* (2006) corrected simulations. Such a calibration is also proposed by Causse *et al.* (2008). Nevertheless, this approach would not change the general conclusion on the comparison between the ground motion predictions at sediment stations and the EC8 design spectra.

ACKNOWLEDGMENTS

Mathieu Causse's grant is funded by CEA and CNRS. This work benefits from ANR-QSHA and SIRSEG(MEDAD) programs. Fabrice Cotton's work is supported by Institut Universitaire de France. All the computations presented in this paper were performed at the Service Commun de Calcul Intensif de l'Observatoire de Grenoble (SCCI). The authors would also like to thank the French

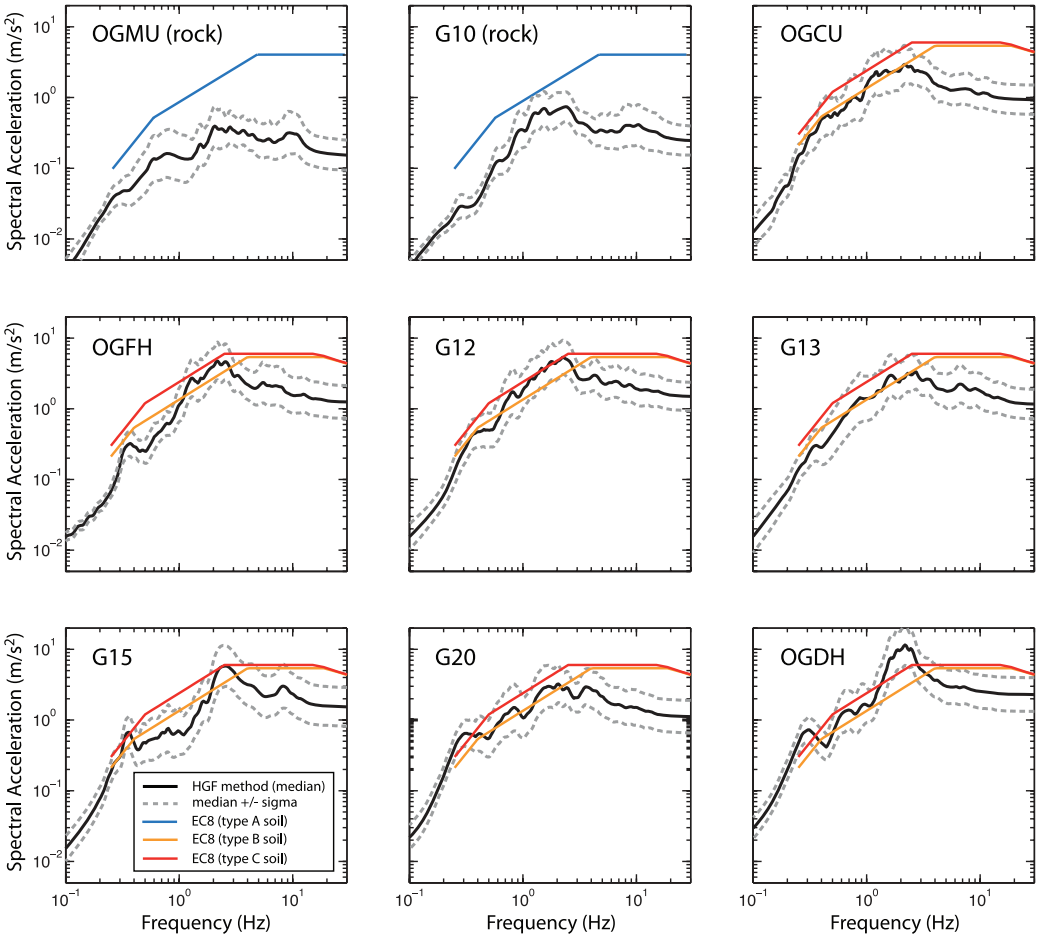

Figure 13. Simulated median and standard deviation of the spectral acceleration (EW component), compared with EC8 spectra. The median K value is $K = 0.5$, as suggested by Somerville *et al.* (1999) empirical model.

Accelerometric Permanent network and all the participants to the 2005 Grenoble experiment (Chaljub *et al.* 2006).

REFERENCES

Aki, K. & Richards, P.G., 2002. *Quantitative Seismology,* 2nd edn., University Science Books, Sausalito, CA.

Ben-Menahem, A., 1961. Radiation of seismic surface-waves from finite moving sources, *Bull. seism. Soc. Am.,* **51,** 401–435.

Beresnev, I.A., 2003. Uncertainties in finite-fault slip inversions: to what extent to believe? A critical review, *Bull. seism. Soc. Am.,* **93,** 2445–2458.

Bernard, P. & Herrero, A., 1994. Slip heterogeneity, body-wave spectra, and directivity of earthquake ruptures, *Annali Di Geofisica,* **XXXVII,** 1679–1690.

Bernard, P., Herrero, A. & Berge C., 1996. Modeling directivity of heterogeneous earthquake ruptures, *Bull. seism. Soc. Am.,* **86,** 1149–1160.

Boatwright, J., 2007. The persistence of directivity in small earthquakes, *Bull. seism. Soc. Am.,* **97,** 1850–1861.

Bour, M. & Cara, M., 1997. Test of a simple empirical Green's function method on moderate-sized earthquakes, *Bull. seism. Soc. Am.,* **87,** 668–683.

Bragato, P.L. & Slejko, D., 2005. Empirical ground motion attenuation relations for the eastern Alps in the magnitude range 2.5–6.3, *Bull. seism. Soc. Am.,* **95,** 252–276.

Brune, J.N., 1970. Tectonic stress and the spectra of seismic shear waves from earthquakes, *J. geophys. Res.,* **75,** 4997–5009.

Causse, M., Cotton, F., Cornou, C. & Bard P.-Y., 2008. Calibrating median and uncertainties estimates for a practical use of EGF technique, *Bull. seism. Soc. Am.,* **98,** 344–353.

Chaljub, E., 2009. Spectral element modeling of 3D wave propagation in the alpine valley of Grenoble, France, in *Third International Symposium on the Effects of Surface Geology on Seismic Motion,* Vol. 2, pp. 1467–1474, eds Bard, P.Y., Chaljub, E., Cornou, C., Cotton, F. & Guéguen, P., LCPC Editions.

Chaljub, E., Cornou, C., Guéguen, P., Causse, M. & Komatitsch, D., 2004. Spectral element modeling of 3D site effects in the alpine valley of Grenoble, France, in *Fall Meet. Suppl., Abstract S41C-07, EOS, Trans. Am. Geophys. Un.* **85**(47).

Chaljub, E., Cornou, C., Guéguen, P., Causse, M. & Komatitsch, D., 2005. Spectral-element modeling of 3D wave propagation in the alpine valley of Grenoble, France, in *Geophysical Research Abstracts,* Vol. 7, 05225. EGU 2nd General Assembly, Wien, Austria.

Chaljub, E. *et al.*, 2006. Measurement and variability study of site effects in the 3D glacial valley of Grenoble, French Alps, in LCPC Editions, editor, *Proceeding of the Third International Symposium on the Effects of Surface Geology on Seismic Motion,* number 154, Grenoble, France.

Chaljub, E., Komatitsch, D., Vilotte, J.P., Capdeville, Y., Valette, B. & Festa, G., 2007, Spectral element analysis in seismology, in *Advances in Wave Propagation in Heterogeneous Media,* Vol. 48, pp. 365–419, eds Wu, R. & Maupin, V., Advances in Geophysics, Elsevier - Academic Press.

Chaljub, E., Cornou, C. & Bard, P.Y., 2009. Numerical benchmark of 3D ground motion simulation in the valley of Grenoble, France, in *Third International Symposium on the Effects of Surface Geology on Seismic*

Motion, Vol. 2, pp. 1365–1376, eds Bard, P.Y., Chaljub, E., Cornou, C., Cotton, F. & Guéguen, P., LCPC Editions.

Cornou, C., 2002. Traitement d'antenne et imagerie sismique dans l'agglomération grenobloise (Alpes françaises): implications pour les effets de site, *PhD thesis*, Université Joseph Fourier, Grenoble I.

Cornou, C., Bard, P.Y. & Dietrich, M., 2003. Contribution of dense array analysis to basin-edge-induced waves identification and quantification. application to grenoble basin, french Alps (ii), *Bull. seism. Soc. Am.,* **93,** 2624–2648.

Cornou, C., Tsuno, S. & Chaljub, E., 2008. Real and synthetic ambient noise recordings in the Grenoble basin: reliability of the 3D numerical model, in *The 14th World Conference on Earthquake Engineering,* Beijing, China.

Cotton, F., Scherbaum, F., Bommer, J., Bungum, H. & Sabetta, F., 2006. Criteria for selecting and adapting ground motion models for specific target region. Application to Central Europe and rock sites, *J. Seism.,* **1,** 1–20.

Dietrich, M., Cornou, C., Ménard, G., Lemeille, F., Guyoton, F. & Guiguet, R., 2009. Seismic profiling and borehole measurements in the Isére valley near Grenoble, France—1: data acquisition and processing, in *Third International Symposium on the Effects of Surface Geology on Seismic Motion,* Vol. 2, pp. 1597–1608, eds Bard, P.Y., Chaljub, E., Cornou, C., Cotton, F. & Guéguen, P., LCPC Editions.

Drouet, S., Scherbaum, F., Cotton, F. & Souriau, A., 2007. A selection and ranking of ground motion models for seismic hazard analysis in the Pyrenees, *J. Seism.,* **11,** doi:10.1007/s10950-006-9039-6.

Eisner, L. & Clayton, R.W., 2001. A reciprocity method for multiple-source simulations, *Bull. seism. Soc. Am.,* **91,** 553–560.

Gallovic, F. & Brokesova, J., 2004. On strong ground motion synthesis with the k^{-2} slip distribution, *J. Seism.,* **8,** 211–224.

Gallovic, F. & Burjanek, J., 2007. High frequency directivity in strong ground motion modeling methods, *Ann. Geophys.,* **50,** 203–211.

Graves, R.W. & Wald, D.J., 2001. Resolution analysis of finite fault source inversion using one- and three-dimensional Green's functions. 1. Strong motions, *J. geophys. Res.,* **106,** 8745–8766.

Guéguen, P., Cornou, C., Garambois, S. & Banton, J., 2006a. On the limitation of the H/V spectral ratio using seismic noise as an exploration tool: application to the Grenoble valley (France), a small apex ratio basin, *Pure appl. Geophys.,* **164,** 1–20.

Guéguen, P., Garambois, S., Tadenuma, S., Lebrun, B. & Cotton, F. 2006b. Geotechnical, geophysical and seismological data used for the estimate of the highest amplified frequency in the basin of Grenoble, in *Proceeding of the Third International Symposium on the Effects of Surface Geology on Seismic Motion,* number 100, Grenoble, France.

Hartzell, S.H., 1978. Earthquakes aftershocks as Green's functions, *Geophys. Res. Lett.,* **5,** 1–4.

Hartzell, S.H., Guatteri, M., Mai, P.M., Liu, P.C. & Fisk, M., 2005. Calculation of broadband time histories of ground motion, part II: kinematic and dynamic modeling using theoretical Green's functions and comparison with the 1994 Northridge earthquake, *Bull. seism. Soc. Am.,* **95,** 614–645.

Herrero, A. & Bernard, P., 1994. A kinematic self-similar rupture process for earthquakes, *Bull. seism. Soc. Am.,* **84,** 1216–1228.

Kamae, K., Irikura, K. & Pitarka, A., 1998. A technique for simulating stroung ground motion using hybrid Green's functions, *Bull. seism. Soc. Am.,* **88,** 357–367.

Kanamori, H. & Anderson, D.L., 1975. Theoretical basis of some empirical relations in seismology, *Bull. seism. Soc. Am.,* **65,** 1073–1095.

Kohrs-Sansorny, C., Courboulex, F., Bour, M. & Deschamps, A., 2005. A two-stages method for strong ground motions simulations using stochastic summation of small earthquakes, *Bull. seism. Soc. Am.,* **94,** 314–319.

Komatitsch, D. & Tromp, J., 1999. Introduction to the spectral-element method for three-dimensional seismic wave propagation, *Geophys. J. Int.,* **139,** 806–822.

Komatitsch, D. & Vilotte, J.P., 1998. The spectral-element method: an efficient tool to simulate the seismic response of 2D and 3D geological structures, *Bull. seism. Soc. Am.,* **88,** 368–392.

Komatitsch, D., Liu, Q., Tromp, J., Süss, P., Stidham, C. & Shaw, J.H., 2004. Simulations of strong ground motion in the Los Angeles basin based upon the spectral-element method, *Bull. seism. Soc. Am.,* **94,** 187–206.

Lebrun, B., Hatzfeld, D. & Bard, P.Y., 2001. Site effects study in urban area: experimental results in Grenoble, *Pure appl. Geophys.,* **158,** 2543–2557.

Lee, S.J., Chen, H.W., Liu, Q., Komatitsch, D., Huang, B.S. & Tromp, J., 2008. Three-dimensional simulations of seismic-wave propagation in the Taipei basin with realistic topography based upon the spectral-element method, *Bull. seism. Soc. Am.,* **98**(1), 99999998–99999999. doi:10.1785/0120070033.

Mai, P.M., Spudich, P. & Boatwright, J., 2005. Hypocenter locations in finite-source rupture models, *Bull. seism. Soc. Am.,* **95,** 965–980.

McKay, M.D., 1988. Sensitivity and uncertainty analysis using a statistical sample of input values, in *Uncertainty Analysis*, pp. 145–186, ed. Ronen, Y., CRC Press, Boca Raton, Florida.

Nicoud, G., Royer, G., Corbin, J.-C., Lemeille, F. & Paillet, A., 2002. Creusement et remplissage de la vallée de l'Isère au Quaternaire récent. Apports nouveaux du forage GMB1 (1999) dans la région de Grenoble (France), *Géologie de la France,* **4,** 39–49, in French.

Pacor, F., Cultrera, G., Mendez, A. & Cocco, M., 2005. Finite fault modeling of strong ground motions using a hybrid deterministic-stochastic approach, *Bull. seism. Soc. Am.,* **95,** 225–240.

Pavic, R., Koller, M.G., Bard, P-Y. & Lacave-Lachet, C., 2000. Ground motion prediction with the empirical Green's function technique: an assessment of uncertainties and confidence level, *J. Seism.,* **4,** 59–77.

Pousse, G., Bonilla, L.F., Cotton, F. & Margerin, L., 2006. Nonstationary stochastic simulation of strong ground motion time histories including natural variability: application to the K-net japanese database, *Bull. seism. Soc. Am.,* **96,** 2103–2117.

Pulido, N. & Kubo, T., 2004. Near-fault strong motion complexity of the 2000 Tottori earthquake (Japan) from a broadband source asperity model, *Tectonophysics,* **390,** 177–192.

Ruiz, J., Baumont, D., Bernard, P. & Berge-Thierry, C., 2007. New approach in the kinematic k^{-2} source model for generating physical slip velocity functions, *Geophys. J. Int.,* **171,** 739–754.

Satoh, T., 2002. Empirical frequency-dependent radiation pattern of the 1998 Miyagiken-Nanbu earthquake in Japan, *Bull. seism. Soc. Am.,* **92,** 1032–1039.

Somerville, P. *et al.*, 1999. Characterizing crustal earthquake slip models for the prediction of strong ground motion, *Seism. Res. Lett.,* **70,** 59–80.

Thouvenot, F., Fréchet, J., Jenatton, L. & Gamond, J.F., 2003. The Belledonne border fault: identification of an active seismic strike-slip fault in the Western Alps, *Geophys. J. Int.,* **155,** 174–192.

Tinti, E., Fukuyama, E., Piatanesi, A. & Cocco, M., 2005. A kinematic source-time function compatible with earthquake dynamics, *Bull. seism. Soc. Am.,* **95,** 1211–1223.

Tsuno, S., Cornou, C. & Bard, P.Y., 2008. Superficial S-wave velocity and damping factor model determined by the MASW measurement in the Grenoble sedimentary basin, in *The 14th World Conference on Earthquake Engineering, Beijing*, *China*.

Tsuno, S., Chaljub, E. & Bard, P.Y., 2009. Grenoble simulation benchmark: Comparison of results and learnings, in *Third International Symposium on the Effects of Surface Geology on Seismic Motion,* Vol. 2, eds Bard, P.Y., Chaljub, E., Cornou, C., Cotton, F. & Guéguen, P., LCPC, 2009. Paper number SB2.

Vallon, M., 1999. Estimation de l'épaisseur d'alluvions et sédiments quaternaires dans la région grenobloise par inversion des anomalies gravimétriques (estimation of the alluvial and quaternary sediments thicknesses in the Grenoble region from inversion of gravimetric anomalies). Technical report, LGGE, Université Joseph Fourier, IPSN/CNRS, in French.

Zhao, L., Chen, P. & Jordan, T.H., 2006, Strain Green tensor, reciprocity, and their applications to seismic source and structure studies, *Bull. seism. Soc. Am.,* **96,** 1753–1763.

APPENDIX A: STATIC SLIP GENERATION

The static slip models are obtained by inverse Fourier transform from eq. (1). They result from the superposition of a deterministic

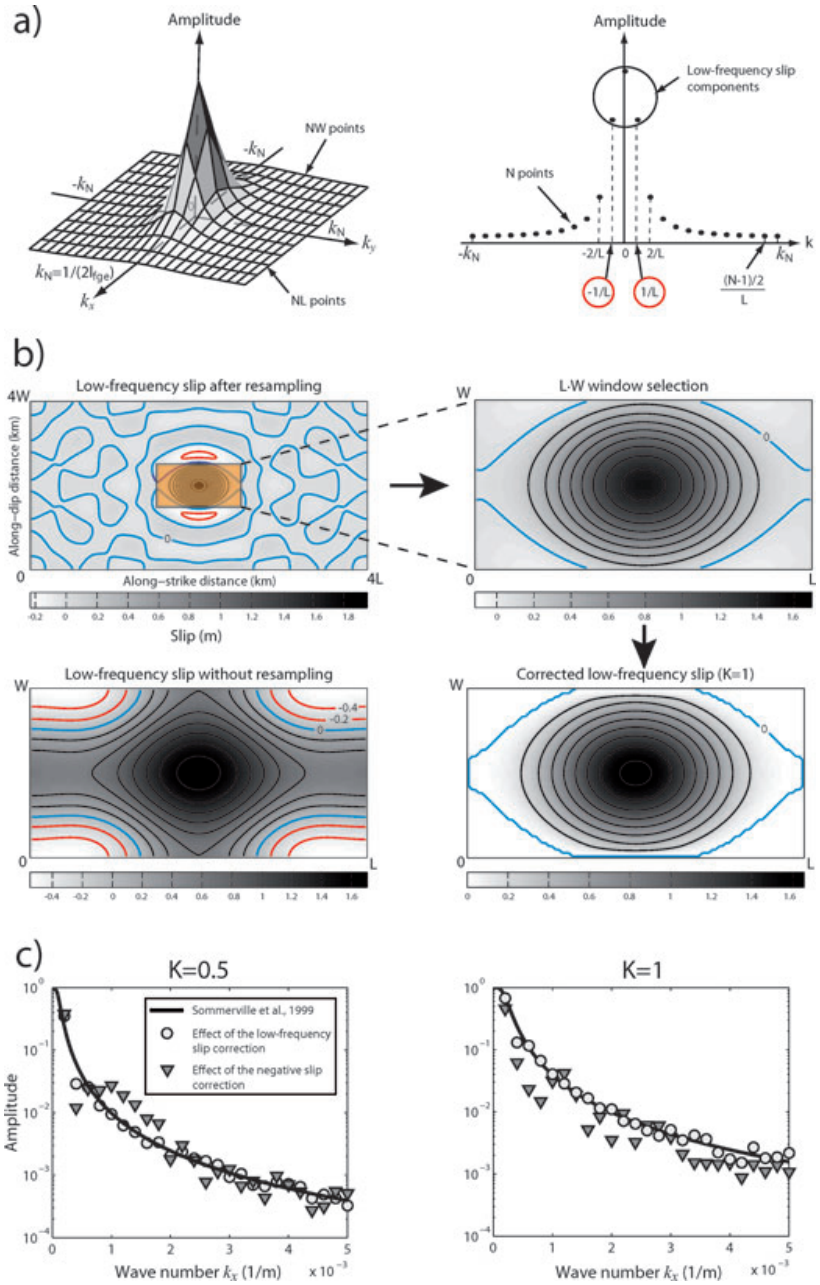

Figure 14. (a) Slip amplitude spectrum in 2-D (left-hand panel) and 1-D (right-hand panel). The deterministic slip ($k \leq 1/L$) is defined by only 3 points. (b) Deterministic slip correction procedure. The mean slip is 0.4 m and the K value equals 1. The space between the slip contourlines is 0.2 m. (c) Effect of the slip correction procedure on the amplitude slip spectrum. The curves correspond to the 1-D along-strike Fourier transforms. The larger the K value is, the larger the reduction induced by removing the negative slip is.

part ($k \leq k_c$) and a stochastic part ($k > k_c$). From numerical considerations the deterministic slip is defined in the Fourier domain by a limited number of points (only three points in 1-D, Fig. 14a). This results in spurious artefacts in the space domain, in particular strongly negative slip zones. A simple process is thus introduced to enhance the low wavenumber asperity features (Fig. 14b): (1) the low wavenumber slip amplitude spectrum is resampled using n times the original sampling rate. The resulting spatial slip covers a fictitious fault plane of size (nL, nW). In practice, we used $n = 4$; (2) the centre window of size (L, W) is selected; (3) the remaining negative slip areas and the fault edges are assigned zero slip and (4) a constant scaling factor is applied to conserve the mean slip. This procedure brings about only minor modifications on the slip amplitude spectrum (Fig. 14c).

The deterministic slip is next added the high wavenumber slip contributions. A classical problem of this superposition is the emergence of negative slip areas in the final slip distributions. In order to remove the unphysical negative slip values, the slip fluctuation amplitudes are just reduced at any point with negative slip to reach a zero slip. The slip is next tapered on the edges and normalized again to get the right mean slip. The effect of the negative slip removing is to decrease the slip spectrum amplitude at high frequency, and

consequently the source energy. However, this reduction remains weak for $K \leq 1$ because most of the slip is positive (Fig. 14c). Besides our tests show that the apparent source time function spectral decay is preserved and that the high-frequency energy decrease is also weak for $K \leq 1$ (*cf.* Section 'Summation Algorithm', Fig. 4e). For simulating with higher K values, negative slip values can be kept but the k^{-2} source model has to be considered as a purely mathematical tool providing the expected source spectrum characteristics.

APPENDIX B: CALCULATION OF THE THEORETICAL ASTF HIGH-FREQUENCY SPECTRAL LEVEL

From eq. (11), the ASTF amplitude spectrum is such that:

$$|R(f)| = |U(f)|/|u(f)|, \tag{B1}$$

where $U(f)$ and $u(f)$ denotes the simulated event and the EGF displacement spectra, respectively. Beyond the EGF corner frequency f_c, both events have a ω^{-2} spectral decay. Hence the theoretical ASTF amplitude spectrum is a plateau, the level of which is:

$$|R(f \geq f_c)|_{\text{theo}} = |U(f_c)|_{\text{theo}}/|u(f_c)|_{\text{theo}}. \tag{B2}$$

The theoretical displacement spectrum amplitude of the target event at frequency f_c is

$$|U(f_c)|_{\text{theo}} = \frac{A_o}{4\pi^2 f_c^2}. \tag{B3}$$

The A_o value is given by eq. (5) and the corner frequency of the small event, that is assumed to follow a k^{-2} model, is such that: $f_c = \frac{vK_S}{l}$, with $K_S \approx 0.74$ (eq. 8).

Besides, the propagation effects and radiation patterns and supposed to be the same for both EGF and simulated event. It leads to:

$$|u(f_c)|_{\text{theo}} = C_s m_o, \tag{B4}$$

After eqs (B2), (B3) and (B4), and by assuming that both events have the same rupture velocity, we obtain

$$|R(f \geq f_c)|_{\text{theo}} = \text{RMS}\left[C_d(\Theta)^2 X(C_d(\Theta)/2)\right]\left(\frac{M_o}{m_o}\right)\left(\frac{l}{L}\right)^2\left(\frac{K}{K_S}\right)^2. \tag{B5}$$

For a ratio $v/c = 0.8$ and for a Gaussian slip velocity function with a standard deviation $\sigma = \tau/10$ RMS$[C_d(\Theta)^2 X(C_d(\Theta)/2)] \approx 1.9$. Thus, eq. (B5) gives

$$|R(f_c)|_{\text{theo}} = \beta N K^2, \tag{B6}$$

with $\beta \approx 3.5$.

APPENDIX C: CALCULATION OF THE EGF NUMBER TO SUM FOR THE HIGH-FREQUENCY ASTF LEVEL CORRECTION

In order to obtain the expected level $|R(f \geq f_c)|_{\text{theo}}$, the average number of EGFs to sum along the rise time dislocation is adapted. This choice comes to assume a new EGF dislocation. Let d/γ be the modified EGF dislocation. At low frequency, the EGF summing up is coherent. Hence the ASTF amplitude becomes γN^3. To conserve the seismic moment, the whole spectrum is divided by γ. Besides, beyond f_c, the summation is incoherent. Therefore, the ASTF level becomes the square root of the EGF quadratic sum, each EGF being represented by a Dirac function with amplitude 1 or -1. This leads to

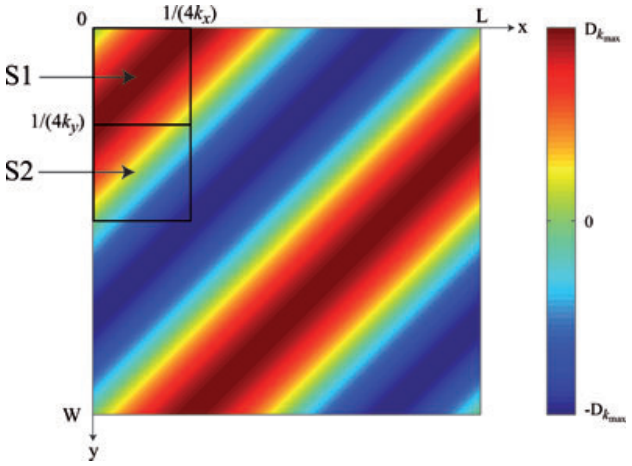

Figure 15. Representation of the slip distribution $D_k(x, y)$ for a given wavenumber k. The integrals I_1 and I_2 (eqs 26 and 27) represents the integrals of $|D_k(x, y)|$ over the surfaces S_1 and S_2, respectively.

$$|R(f \geq f_c)|_{\text{obs}} = \frac{1}{\gamma}\sqrt{\gamma(N_{\text{STO}} + N_{\text{DET}})}, \tag{C1}$$

where $N_{\text{DET}} = N^3$ and N_{STO} is the total number of summed EGF resulting from the stochastic slip heterogeneities. The deterministic slip contribution to the ASTF is low-pass filtered to keep only the stochastic slip contributions beyond f_c. Thus, eq. (C1) gives

$$|R(f \geq f_c)|_{\text{obs}} = \left(\frac{N_{\text{STO}}}{\gamma}\right)^{1/2}. \tag{C2}$$

N_{STO} calculation

In order to estimate N_{STO}, the surface slip density for a given wavenumber $k > 1/\sqrt{L^2 + W^2}$ is calculated. It is defined as

$$\rho_{s_k} = \frac{1}{LW}\int_0^L \int_0^W |D_k(x, y)|\text{d}x\text{d}y, \tag{C3}$$

where $D_k(x, y)$ represents the slip distribution for the wavenumber k. Using the integrals I_1 and I_2 of $|D_k(x, y)|$ over the surfaces S_1 and S_2, respectively (Fig. 15), we obtain

$$\begin{aligned}\rho_{s_k} &= \frac{1}{LW} \cdot 2(I_1 + I_2) \cdot 2Lk_x \cdot 2Wk_y \\ &= 8k_x k_y (I_1 + I_2),\end{aligned} \tag{C4}$$

with

$$\begin{aligned}I_1 &= 2D_k(k_x, k_y)\int_0^{\frac{1}{4k_x}} \int_0^{\frac{1}{4k_y}} \left|\sin[2\pi(k_x x + k_y y)]\right| \text{d}x\text{d}y \\ &= \frac{D_k(k_x, k_y)}{\pi^2 k_x k_y}\end{aligned} \tag{C5}$$

and

$$\begin{aligned}I_2 &= 2D_k(k_x, k_y)\int_0^{\frac{1}{4k_y}} \int_0^{\frac{1}{4k_y} - \frac{k_y}{k_x}} \left|\cos[2\pi(k_x x + k_y y)]\right| \text{d}x\text{d}y \\ &= \frac{(\pi - 2)}{2}\frac{D_k(k_x, k_y)}{\pi^2 k_x k_y}.\end{aligned} \tag{C6}$$

It leads to

$$\rho_{s_k} = \frac{4D_k(k_x, k_y)}{\pi}. \tag{C7}$$

The overall surfacic slip density ρ_s is obtain by summing all the high wavenumber contributions

$$\rho_s = 2\int_{k_{x\min}}^{k_{x\max}} \int_{k_{y\min}}^{k_{y\max}} \rho_{s_k} \mathrm{d}k_x \mathrm{d}k_y. \tag{C8}$$

From eq. (1) we come to

$$\rho_s \approx \frac{8}{\pi} DK^2 \int_{k_{x\min}}^{k_{x\max}} \int_{k_{y\min}}^{k_{y\max}} \frac{1}{k_x^2 + k_y^2} \mathrm{d}k_x \mathrm{d}k_y. \tag{C9}$$

In the following a square fault plane is assumed ($L = W$). Hence from numerical considerations (see Appendix A, Fig. 14a): $k_{x_{\min}} = k_{y_{\min}} = \frac{2}{l(N-1)}$ and $k_{x_{\max}} = k_{y_{\max}} = k_N = \frac{1}{2l}$. Next cartesian coordinates are replaced with polar coordinates (r, Θ) in eq. (C9). It leads to the following approximation:

$$\begin{aligned}\rho_s &\approx \frac{8}{\pi} \bar{D}K^2 \int_0^{\pi/2} \int_{\frac{2}{l(N-1)}}^{\frac{1}{2l}} \frac{1}{r^2\cos\Theta^2 + r^2\sin\Theta^2} r\,\mathrm{d}r\,\mathrm{d}\Theta \\ &\approx 4\bar{D}K^2 \ln\left(\frac{N-1}{4}\right).\end{aligned} \tag{C10}$$

Besides N_{STO} is related to ρ_s according to

$$N_{\mathrm{STO}} = \frac{\rho_s L^2}{\bar{d}l^2}. \tag{C11}$$

Then, inserting (C10) into (C11) we get

$$N_{\mathrm{STO}} \approx \alpha(N)^2 N^3 K^2, \tag{C12}$$

with $\alpha(N) = 2\sqrt{\ln\left(\frac{N-1}{4}\right)}$.

► *Calculation of the adapted EGF dislocation d/γ*

After eqs (C2) and (C12), the observed ATSF spectral level is:

$$|R(f \geq f_{\mathrm{c}})|_{\mathrm{obs}} = \frac{\alpha(N)}{\gamma^{1/2}} N^{3/2} K. \tag{C13}$$

Finally, after eq. (B6), the condition: $|R(f \geq f_{\mathrm{c}})|_{\mathrm{obs}} = |R(f_{\mathrm{c}})|_{\mathrm{theo}}$ leads to

$$\frac{\alpha(N)}{\gamma^{1/2}} N^{3/2} K = \beta N K^2. \tag{C14}$$

Consequently, the new EGF dislocation to be considered is d/γ with

$$\gamma = \left(\frac{\alpha(N)}{\beta}\right)^2 \frac{N}{K^2}, \tag{C15}$$

where $\alpha(N) = 2\sqrt{\ln\left(\frac{N-1}{4}\right)}$ and $\beta \approx 3.5$.

Bulletin of the Seismological Society of America, Vol. 105, No. 2A, pp. 950–962, April 2015, doi: 10.1785/0120140107

Is Ground-Motion Variability Distance Dependent? Insight from Finite-Source Rupture Simulations

by Afifa Imtiaz, Mathieu Causse, Emmanuel Chaljub, and Fabrice Cotton*

Abstract The ground-motion variability sigma is a fundamental component in probabilistic seismic-hazard assessment because it controls the hazard level at very low probabilities of exceedance. So far, most of the analyses based on empirical ground-motion prediction equations do not consider any distance dependency of sigma. This study aims to analyze the potential distance dependency of ground-motion variability, especially in the near-field region, where the variability is poorly constrained due to the lack of available records. We, therefore, investigate the distance dependency of sigma by performing numerical simulations of ground motion for some strike-slip events. Synthetic velocity seismograms (up to 3 Hz) have been generated from a suite of finite-source rupture models of past earthquakes. Green's functions were calculated for a 1D velocity structure using a discrete wavenumber technique (Bouchon, 1981). The within-event component of the ground-motion variability was then evaluated from the synthetic data as a function of distance. The simulations reveal that the within-event component of the ground motion shows a distance dependency, subject to the rupture type. For bilateral ruptures, the variability tends to increase with distance. On the contrary, in case of unilateral events, the variability decreases with distance.

Introduction

Empirical ground-motion prediction equations (GMPEs) developed by means of regression techniques from recorded strong-motion data, generally are based on very simple parameterization with magnitude (**M**), distance (d), and site category (s). The distribution of ground motion for a given **M**, d, and s is then represented in terms of a median and a standard deviation, referred to as the aleatory variability sigma, which is a fundamental component in probabilistic seismic-hazard analysis (PSHA). Sigma exerts a strong influence on the seismic-hazard level, especially for long return periods (Bommer and Abrahamson, 2006). It is therefore imperative to accurately constrain sigma to perform reliable seismic-hazard analyses.

In seismic-hazard studies two types of uncertainties, termed as aleatory variability and epistemic uncertainty, are considered. Aleatory variability is defined as the natural randomness in a process and is supposed to be irreducible. On the contrary, epistemic uncertainty refers to the scientific uncertainty in the model of the process caused by limited data and knowledge, which can theoretically be reduced to zero with models better explaining the data. Ideally, sigma should represent the aleatory ground-motion variability obtained from repeated events on the same fault and recorded at the same station. As such, it includes only the natural randomness of the source rupture process (Anderson and Brune, 1999). Nevertheless, the computation of sigma in GMPEs is typically performed from records at multiple stations from different earthquakes, and hence mixes various paths and site responses. In other words, the variability in ground motion due to differences in paths and site response is typically considered as aleatory whereas it should be treated as epistemic uncertainty. This assumption is commonly referred to as ergodic (Anderson and Brune, 1999).

Thanks to the increasing availability of strong-motion records, several recent studies propose to refine ground-motion variability analyses by splitting sigma into various component (e.g., Chen and Tsai, 2002; Al-Atik *et al.*, 2010; Rodriguez-Marek *et al.*, 2011; Edwards and Fäh, 2013). Following the notation of Al-Atik *et al.* (2010), the total variability can then be expressed as

$$\sigma_{\text{tot}} = \sqrt{\phi^2 + \tau^2}, \tag{1}$$

in which, ϕ refers to the within-event variability (due to the variability in site conditions and path effects for a given event recorded at various stations) and τ refers to the between-event variability (essentially due to the natural source randomness). The variability σ_{tot} can further be refined by extracting the contribution of site-specific effects from ϕ, to obtain the

*German Research Centre for Geosciences (GFZ), Telegrafenberg, 14473 Potsdam, Germany; fcotton@gfz-potsdam.de.

single-station standard deviation (or single-station sigma) defined as

$$\sigma_{ss} = \sqrt{\phi_{ss}^2 + \tau^2}. \quad (2)$$

The term ϕ_{SS} is then called the event-corrected single-station sigma. A very recent work by Rodriguez-Marek *et al.* (2013) addresses the issue of the variation of single station sigma with respect to region, magnitude, and distance. First, it is remarkable from their work that the mean values of ϕ_{SS} appear to be stable (average $\phi_{SS} \approx 0.45$) across the different regions (California, Taiwan, Japan, Switzerland, and Turkey). Second, the authors observe that ϕ_{SS} depends both on magnitude and distance. They propose various models to account for such potential dependencies for moment magnitude (M_w) 4.5–8 and for distances up to 200 km, opening some new insights for improving PSHA. Nevertheless, the reliability of such models at short distances (< 20 km) remains questionable due to the scarcity of near-field records of moderate-to-large events ($M_w > 6$) and potential large epistemic uncertainties associated with small event metadata (in particular depth).

The present article addresses the issue of the ground-motion variability using near-field kinematic-rupture simulations. Our strategy is to evaluate sigma from synthetic data as a function of distance. Our study focuses on the within-event component of sigma (ϕ) only. Various published kinematic source models of vertical strike-slip events are considered to represent the source process on the fault. Synthetic velocity time series are computed up to 3 Hz by convolving slip-rate functions with 1D Green's functions at stations placed at various azimuths and distances from the source. For each source model, we then extract ϕ for peak ground velocity (PGV) and study the variations of ϕ with respect to distance. It is important to note that the scope of our study is not to provide ground-motion variability values, to be directly incorporated in seismic-hazard analyses, which would require an unreasonably large number of source models and computation time. We limited our selection by considering vertical strike-slip events with $6 < M_w < 7$ only, to focus on the overall physical properties that are likely to influence the distance dependency of ϕ.

Although a variety of distance definitions are available, this work will use R_{JB}, the Joyner–Boore distance, defined as the shortest distance from the receiver to the surface projection of the fault plane (Joyner and Boore, 1981), enabling us to represent the finiteness of the fault in the region of the near-fault plane. The R_{JB} distance is equivalent to the rupture distance R_{rup} (closest distance to the rupture surface) for vertical strike-slip events, especially when the rupture is very close to the surface as for our selected fault models.

Ground-Motion Simulation

Kinematic Source Models

A total of 11 kinematic source models (i.e., the spatiotemporal distribution of slip on the fault plane), with magnitudes ranging from M_w 5.8 to 6.8, were generated for vertical strike-slip events. Eight of the source models are based on published models of past events, obtained using kinematic inversion of strong-motion observations, sometimes combined with Global Positioning System and/or Interferometric Synthetic Aperture Radar data. Although they were derived using various inversion techniques, most of them assume uniformity in rupture velocity and rise time (Table 1). These models were extracted from a database of finite-source rupture models available online (Mai and Thingbaijam, 2014; see Data and Resources). Among the eight models, six correspond to bilateral rupture and two to unilateral rupture. The classification of the models into bilateral/unilateral rupture is based on McGuire *et al.* (2002), who proposed to quantify rupture directivity using a directivity ratio (DR) computed from the second moments of the slip space–time distribution (see Appendix A). DR ranges from 0, for a 1D symmetric bilateral rupture with constant slip, to 1, for a unilateral rupture.

To properly compute ground motion up to 3 Hz, a fine grid is required to represent the slip history on the fault plane. Because the considered kinematic source models are defined on coarse grids (~2 km × 2 km), they have been interpolated on a smaller grid (e.g., 200 m × 200 m), ensuring at least five points per minimum wavelength. The interpolation procedure assumes self-similarity of the static slip beyond the Nyquist wavenumber of the original model by imposing a k^{-2} slope of the slip spectrum. The resulting numbers of subfaults are shown in Table 1.

These eight source models were complemented by three synthetic models produced using a k^{-2} description of the final slip (e.g., Causse *et al.*, 2009). The fault-plane configuration and other kinematic parameters (rise time and rupture velocity) are the same as the source model derived by Sekiguchi and Iwata (2002) for the 2000 Tottori earthquake (Table 1). The final slip on the fault plane is described in the wavenumber domain by a k^{-2} asymptotic decay beyond a corner wavenumber $k_c = K/L_c$, in which L_c is the characteristic rupture length and K is a nondimensional parameter. The parameter K expresses the degree of roughness of the slip heterogeneity. Thus we generated three source models characterized by a smooth slip distribution ($K = 0.4$), a rough one ($K = 1.6$) and an intermediate one ($K = 0.8$), so as to isolate the effect of the slip roughness on the ground-motion variability.

Source parameters and computed DRs of the eight models, extracted from the database of finite-source rupture models, are listed in Table 1. The corresponding source parameter distributions are provided in Figures 1 and 2. The images of the k^{-2} slip models are shown in Figure 3. In Table 1, magnitude (M_w) and hypocentral depth (H) of each event along with the length (L) and width (W) of the source model are given. SVF indicates the slip-velocity function considered. Each extracted model from the database was interpolated to a finer grid of subfaults, which is given by Nb. subfaults. In case of constant rupture velocity (V_R) and rise time (T_R), the corresponding values are indicated. Nb.TW refers to the number of time windows used in the inversion (Nb.TW > 1

Table 1
Information on the Kinematic Source Models from the Database

Event Name	Event Date (yyyy/mm/dd)	Author	M_w	H (km)	L (km)	W (km)	SVF	Nb. Subfaults	V_R (km/s)	Nb.TW	T_R (s)	DR
Fukuoka	2005/03/20	Asano and Iwata (2006)	6.7	14	26	18	Smooth ramp	10,248	2.1	6	3.5	0.06
Yamaguchi	1997/06/25	Miyakoshi *et al.* (2000)	5.8	8.2	16	14	Triangle	5,751	2.5	2	0.75	0.39
Kagoshimaen-hoku-seibu	1997/03/26	Horikawa (2001)	6.1	7.6	15	10	Triangle	15,251	2.5	1	0.3	0.10
Kagoshima	1997/03/26	Miyakoshi *et al.* (2000)	6.0	7.7	18	12	Triangle	14,065	2.5	2	0.75	0.36
Tottori	2000/10/06	Semmane *et al.* (2005)	6.7	14.5	32	20	Tanhyp	16,261	Variable	1	Variable	0.13
Tottori	2000/10/06	Sekiguchi and Iwata (2002)	6.8	7.8	34	17.6	Tanhyp	15,390	1.8	6	3.5	0.11
Imperial Valley	1979/10/15	Archuleta (1984)	6.5	8.0	35	13	Boxcar	211,031	Variable	1	Variable	0.95
Coyote Lake	1979/08/06	Liu and Helmberger (1983)	5.9	8.0	10	10	Triangle	10,404	2.8	1	0.5	0.60

M_w, magnitude; H, hypocentral depth; L, length; W, width of the source model; SVF, slip-velocity function; Nb. Subfaults, number of subfaults of the finer-grid fault model; V_R, rupture velocity; T_R, rise time; Nb.TW, number of time windows used in the inversion; DR, Directivity Ratio (DR $<$ 0.5 indicate bilateral and DR $>$ 0.5 indicate unilateral rupture).

in case of multi-time-window linear inversion; Hartzell and Heaton, 1983). The Kagoshimaen-hoku-seibu source model has been derived assuming constant rise time but variable rupture velocity. Nevertheless, this model has been simplified, considering an average constant rupture velocity, due to unavailability of the rupture time distribution in the source model database. The DR indicates the rupture type. Imperial Valley and Coyote Lake models (DR $>$ 0.5) can be considered as unilateral and the rest (DR $<$ 0.5) as bilateral.

Station Layout

A network of 135 hypothetical stations at various distances and azimuths was designed. The receiver configuration was set up for the R_{JB} (Joyner–Boore distance) distances 1, 3, 10, 20, 30, 60, and 100 km. We remind that R_{JB} and R_{rup} distances are the same for vertical strike-slip events with rupture reaching the surface. The receivers were positioned at the specified distances along a line parallel to the fault as well as beyond the ends of the fault extending radially outward. The locations of the stations were adapted to the respective rupture lengths of the source models. The station layout is illustrated in Figure 4 for the source model of the 2005 Fukuoka event (rupture length $L = 26$ km). The azimuth angle (θ) between the direction of the rupture propagation and the epicenter-receiver azimuth followed the definition provided in Somerville *et al.* (1997). Because we are considering strike-slip fault models only, the angle θ is measured from the epicenter to the station in the horizontal plane as illustrated in Figure 4.

Synthetic Ground-Motion Computation

Green's functions were computed considering 1D layered velocity structures (as used by the respective authors for source inversion, see Appendix B) using a discrete wavenumber technique (computer package AXITRA, Coutant, 1989). For the three synthetic k^{-2} source models, the chosen velocity structure is the one used by Sekiguchi and Iwata (2002) to derive the source model of the 2000 Tottori event. Synthetic ground motions are next computed by convolving the Green's functions with the slip history of all the subfaults, as defined in the 11 considered kinematic source models. The SVF were the same as those used by the authors. Finally three-component velocity time series were obtained at each receiver location, by summing the contributions from the different subfaults, for the respective source models. Because of the large extent of some of the faults considered in this study (number of subfaults, Table 1), the calculation of the ground motions were distributed on a computing grid to be achieved in a reasonable time. The principle of the decomposition of the computations is explained in Appendix C. The synthetics of the fault normal component from the 2005 Fukuoka model have been illustrated in Figure 5.

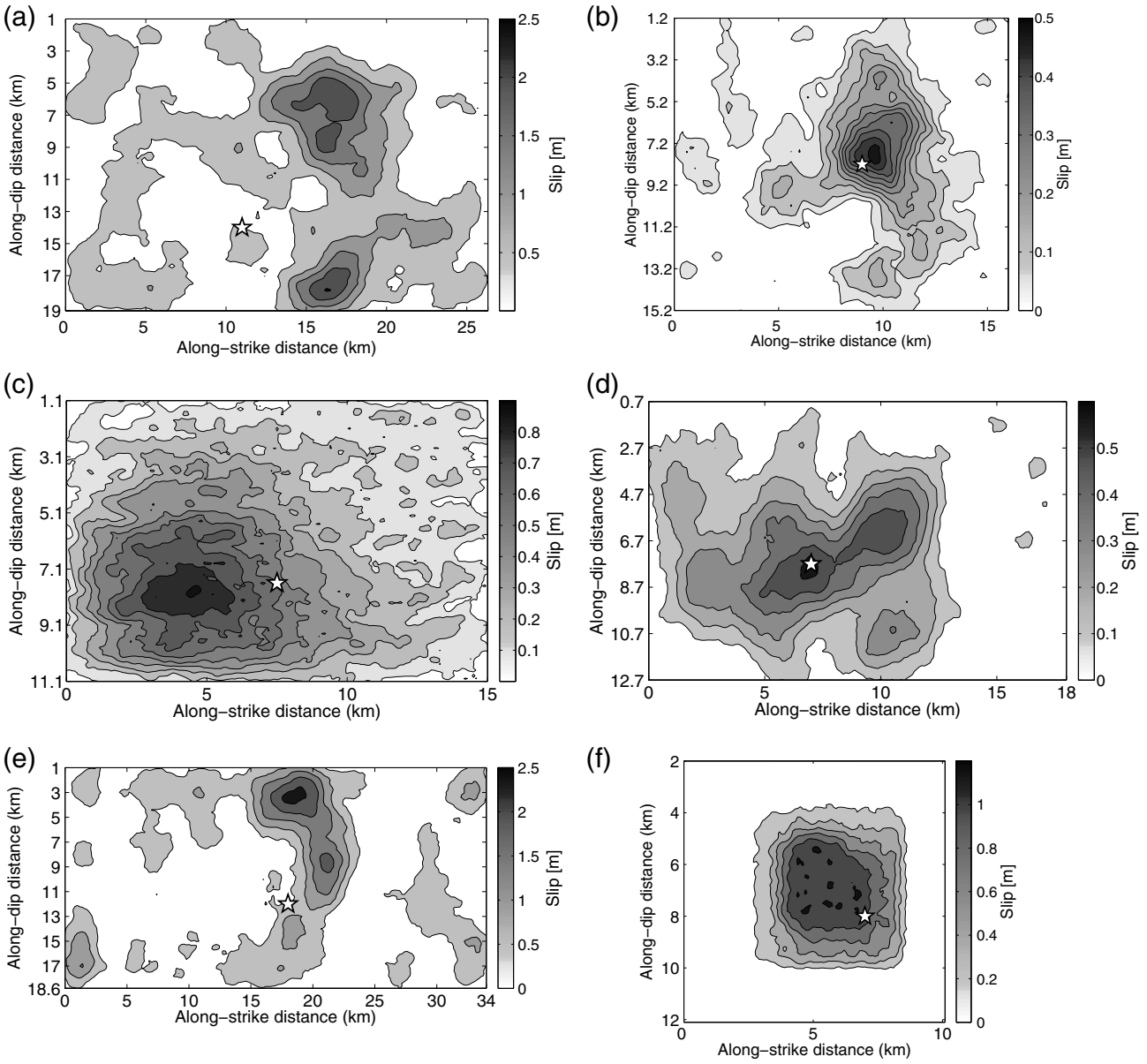

Figure 1. Slip images of the kinematic source models, having constant rupture velocity and rise time, extracted from the database of finite-source rupture models and interpolated to a finer grid. The models are (a) Fukuoka (2005), (b) Yamaguchi (1997), (c) Kagoshimaen-hoku-seibu (1997), (d) Kagoshima (1997), (e) Tottori (2000, Sekiguchi and Iwata), and (f) Coyote Lake (1979). The star symbol shows the location of the hypocenter. Contour lines represent lines of constant slip value.

PGV Calculation

We computed the PGV values as proposed by Boore *et al.* (2006), using the GMRotD50 definition. GMRotD50 is an orientation-independent geometric mean using period-dependent rotation angles. The two orthogonal components of the synthetic time series have been rotated from 1° to 90° in 1° steps, and the geometric mean for each pair of rotated time series were stored. Finally, PGV is taken as the median value of all the 90 geometric means. Ripperger *et al.* (2008) compared different PGV approximations from the two horizontal components and observed that GMRotD50 is a stable measure of the PGV showing a low dependence on the orientation of the horizontal components. Figure 6 shows the mean (with a standard deviation error bar) of ground motion in terms of natural log of PGV averaged over the different azimuths and along the R_{JB} distances for the fault models considered in this study. It is interesting to notice that in Figure 6b, the PGV values at $R_{JB} = 1$ km seems to indicate a slight reduction compared to those at $R_{JB} = 3$ km.

Analysis of PGV Within-Event Variability

We assessed the within-event component ϕ of the PGV variability (corresponding to a single source recorded at

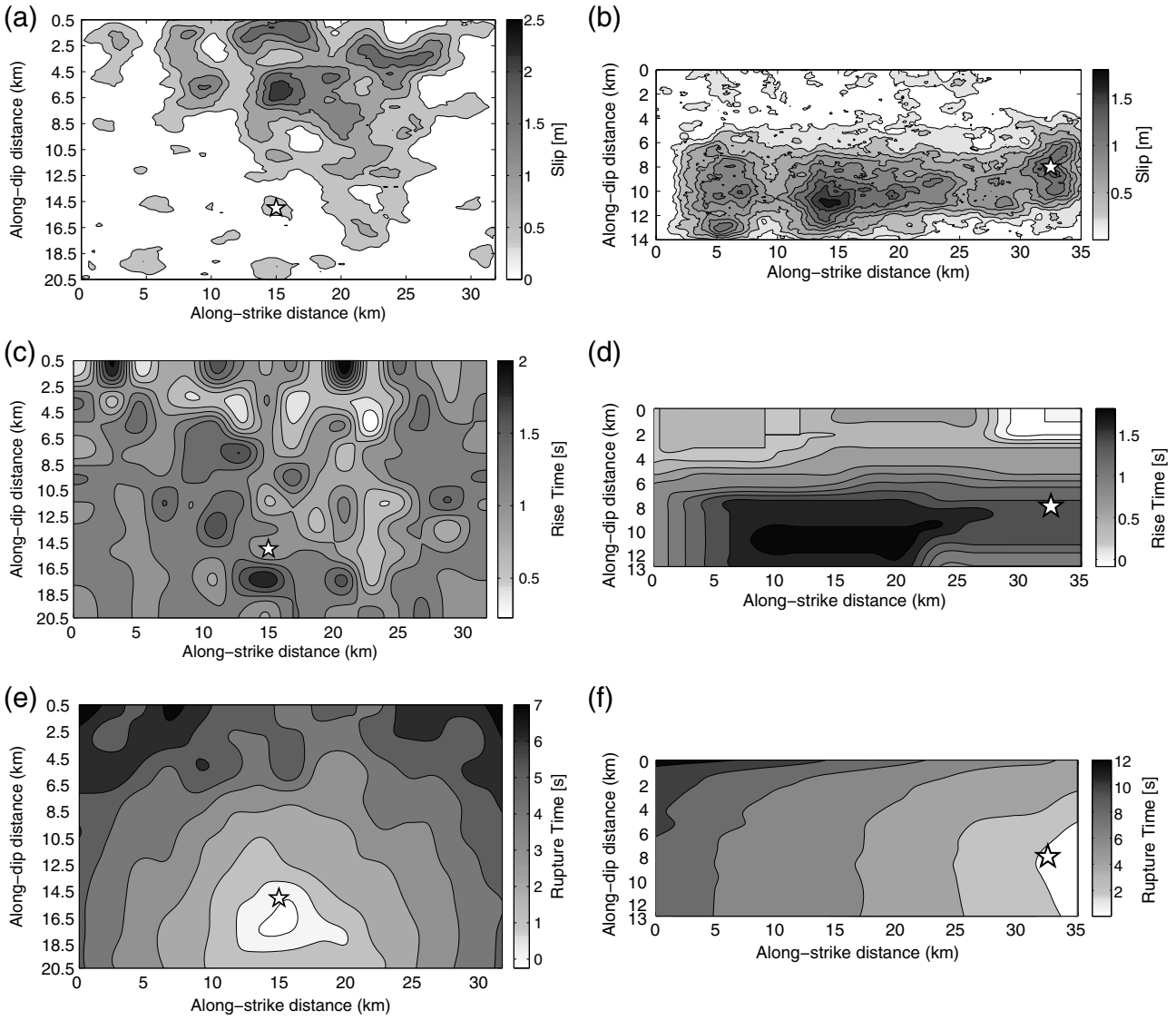

Figure 2. (a) Slip amplitude, (c) slip duration, (e) rupture front evolution images of Tottori (2000, Semmane *et al.*, 2005), and (b) slip amplitude, (d) slip duration, (f) rupture front evolution images of Imperial Valley (1979). Both kinematic source models have been extracted from the database of finite-source rupture models and then interpolated to a finer grid.

several stations) in this work. For each earthquake e, the variability at a distance R is calculated as the standard deviation of the residuals. The residuals are defined as

$$\delta_{e,R} = \ln(\mathrm{PGV})_{e,R,\theta} - \overline{\ln(\mathrm{PGV})_{\theta_{e,R}}}, \qquad (3)$$

in which $\ln(\mathrm{PGV})_{e,R,\theta}$ refers to the predictions for earthquake e at distance R and azimuth θ, and $\overline{\ln(\mathrm{PGV})_{\theta_{e,R}}}$ denotes the average over azimuths. Figure 7a illustrates the within-event ground-motion variability ϕ with varying distances for the selected source models from the finite-source rupture model database. Similarly, Figure 7b compares the variability for the three k^{-2} source models along with the two 2000 Tottori models.

We cannot ascertain any magnitude dependency of the variability due to the narrow magnitude range (M_w 5.82–6.83) considered. The most remarkable observation is that ϕ is dependent on distance. The distance dependency of ϕ exhibits two main regimes depending on the rupture type, that is, unilateral or bilateral (Fig. 7a). The perceptible trends of the PGV variability along with physical explanations on the origin of the variability are described below.

Variability Considering Bilateral Ruptures Only

We observe two main tendencies of ϕ considering bilateral rupture models only (i.e., with DR < 0.5), which could further be distinguished by the distance from the source.

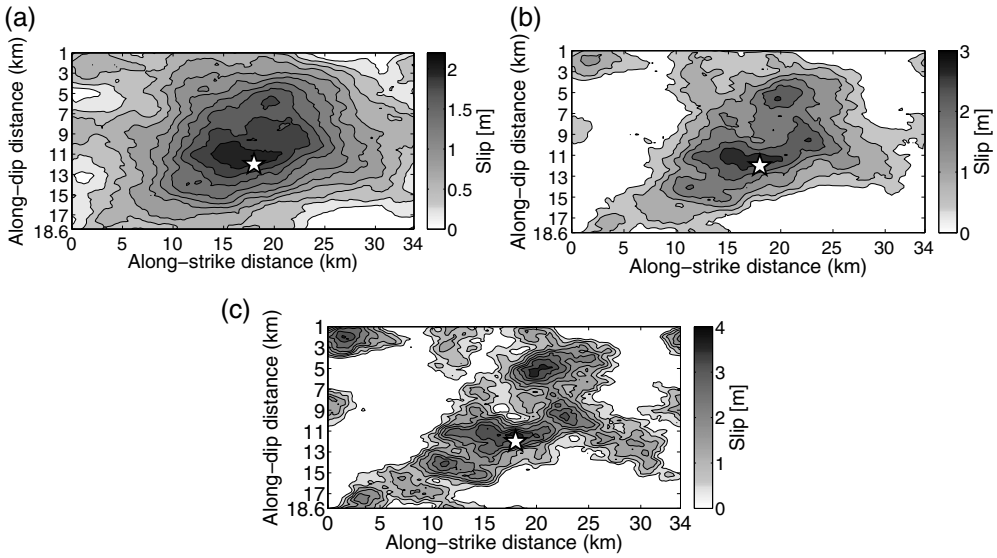

Figure 3. Slip images of the synthetic source models (a) k2-C04 (K = 0.4), (b) k2-C08 (K = 0.8), and (c) k2-C16 (K = 1.6), produced using k^{-2} descriptions of the final slip.

Variability in the Near Field (below $R_{JB} \sim 20$ km)

Considering the tendency of average values of within-event variability computed from nine bilateral models (the curve Avg-of-Bilateral-Models) in Figure 7a, variability ϕ demonstrates a fairly steady trend up to about 20 km from the source. However, the difference in the ϕ values among different rupture models is large (Fig. 8). This is because at short distances ϕ is controlled by source parameters such as location of main slip area, rupture initiation point, and hypocentral depth. A comparison of the results obtained for the Tottori event (models of Semmane *et al.*, 2005, and Sekiguchi and Iwata, 2002) and the synthetic k^{-2} source models (Fig. 7b) highlights the effect of the position of the main slip area. The source model derived for Tottori (Figs. 1e and 2a) considers the main slip area to be more widespread on the upper part in comparison to the synthetic k^{-2} source models, which assume the main slip area to be on the middle of the fault plane (Fig. 3). This may have caused the lower values of ϕ at 3 to ~20 km distance for the former models. Besides, the comparison between the three k^{-2} models (Fig. 7b) illustrates the effect of the different degrees of slip roughness (represented by the nondimensional parameter K). According to Causse *et al.* (2010), the natural variability of K can be described by a lognormal distribution with $\sigma_{\log(K)} = 0.12$. Thus, the values of K considered in our study ($K = 0.4$, $K = 0.8$, and $K = 1.6$) are expected to cover a wide range of potential degree of slip roughness ([median − 1.5 standard, median + 1.5 standard], that is ~85% of the potential values). The comparison indicates that the degree of slip roughness alone has little influence on the ground-motion variability in comparison to the position of the main slip area, except in the very near field (i.e., at 1 km), in which $\phi \sim 0.15$ for $K = 0.4$ and $\phi \sim 0.35$ for $K = 1.6$. The sensitivity to slip roughness is likely to depend on other source parameters (rise, time, and rupture velocity) and their potential correlations. For instance, large values of the rise time act as low-pass filters and could contribute to smoothing the effects of slip heterogeneities. On the other hand, shorter values of rise time (i.e., < 3.5 s) may tend to increase the sensitivity to slip roughness.

Variability in the Far Field (beyond $R_{JB} \sim 20$ km)

Interestingly, the ϕ values for the bilateral events seems to increase gradually above ~20 km distance (Fig. 7a). This tendency can be explained by the fact that in the far field extended sources behave like point sources, and accordingly, ϕ is essentially controlled by radiation pattern shape of *S* waves and Love waves. This is further investigated by analyzing the azimuth and distance dependency of the PGV values for the 2005 Fukuoka and 2000 Tottori (Semmane *et al.*, 2005) earthquakes. Figure 9a represents the PGV values at each receiver station for the respective azimuth angle θ at different R_{JB} distances. θ is the angle between the direction of rupture propagation and the epicenter-station azimuth (Somerville *et al.*, 1997). For distances larger than ~30 km, the PGV values over various azimuths along the station-array form a W-shape exhibiting radiation pattern effect. Following the *SH*-wave radiation pattern shape, we observe PGV maxima at azimuths 0°, 90°, and 180° and PGV minima at 45° and 135°. The slower decay of PGV maxima compared to that of PGV minima, with increasing distance (featuring the elongation of W-shape in Fig. 9a), eventually results in increased variability. Indeed PGV maxima are related to maximum *SH*-wave energy radiation at all distances, whereas the minima, that is, ground velocity at azimuths 45° and 135° are associated with a decrease of *SH*-wave energy radiation due to finite-source effects as distance increases.

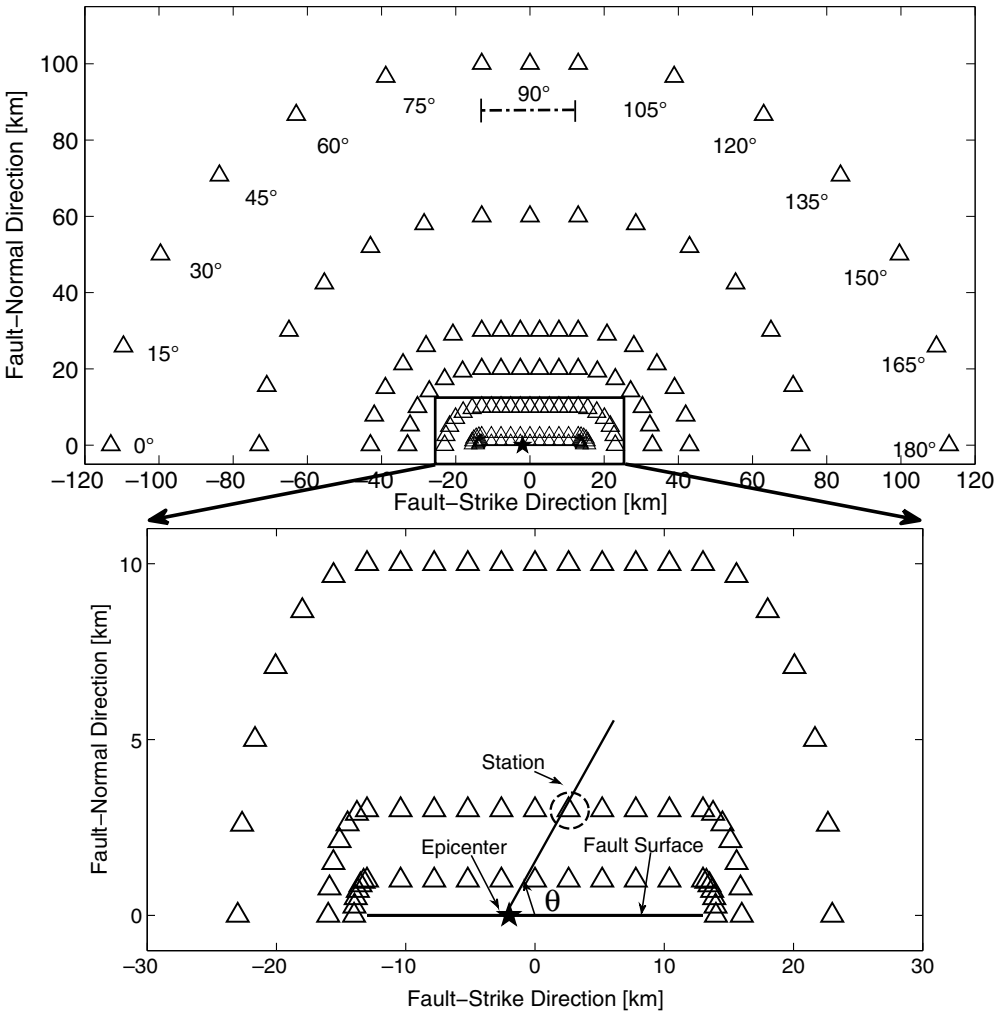

Figure 4. Station network for 2005 Fukuoka event with a zoom on the station very close to the fault (at 1, 3, and 10 km distance). The angle θ displayed on the zoomed plot represents the definition of azimuth angle between fault plane and ray path to site, according to Somerville *et al.* (1997). The radial angles (0°–180°) on the top layout represent the alignment direction of the stations at different distances, that is, the angle between the closest point on the fault and the station.

Variability Considering Unilateral Ruptures Only

Turning now to the two unilateral rupture models (i.e., with DR > 0.5) of the 1979 Imperial Valley and 1979 Coyote Lake earthquakes, we can observe that unlike the bilateral models, the variability exhibits a decreasing tendency with distance (Fig. 7a), implying higher ϕ values at shorter distances due to the presence of directivity effects. For unilateral events, strong forward-directivity effects (i.e., amplification of the PGV value) are expected for small values of the station-azimuth θ ($\theta < \sim 30°$). The dependence of directivity effects on θ is illustrated in Figure 9b, where the PGV values for the unilateral events are plotted against θ, at each R_{JB} distance. At short distances (<∼10 km) most of the stations are located in the 0°–30° azimuth region (15 out of 20 stations at 1 km) and thus associated with a strong PGV amplification due to forward-directivity effects. The large proportion of high peaked PGV values results in large variability ϕ at shorter distances. As the distance increases, fewer stations remain in the forward-directivity direction (3 out of 20 at 100 km) due to the smaller fault dimension relative to the fault-to-station distance, and hence the ϕ values decrease. At 100 km, the values of ϕ are of the same order as for bilateral events, meaning that the directivity of the rupture propagation is a second order effect far away from the source (i.e., beyond 2–3 rupture lengths).

Discussion and Conclusions

The ground-motion variability sigma is a fundamental component of PSHA studies, because small variations in sigma values can have a large influence on seismic-hazard analyses. So far GMPEs have considered sigma to be constant over distance. Though a few recent data analyses suggest that sigma is distance dependent, such studies remain, however, affected by the lack of strong-motion data recorded in the

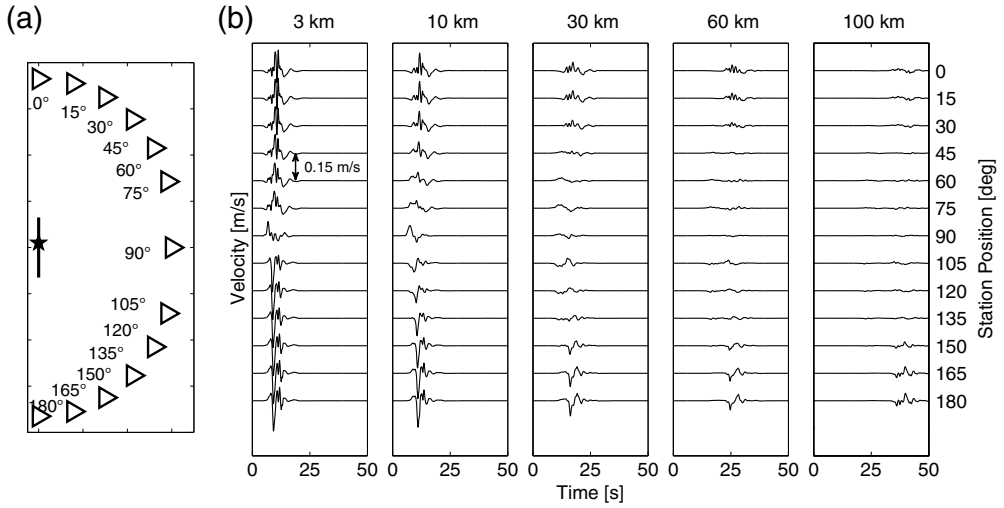

Figure 5. (a) An example of the station positions and (b) synthetic velocity time series on the fault-normal component of 2005 Fukuoka source model. Here, station position represents the station alignment (the angle between the closest point on the fault and the station) as illustrated in the station layout on the left.

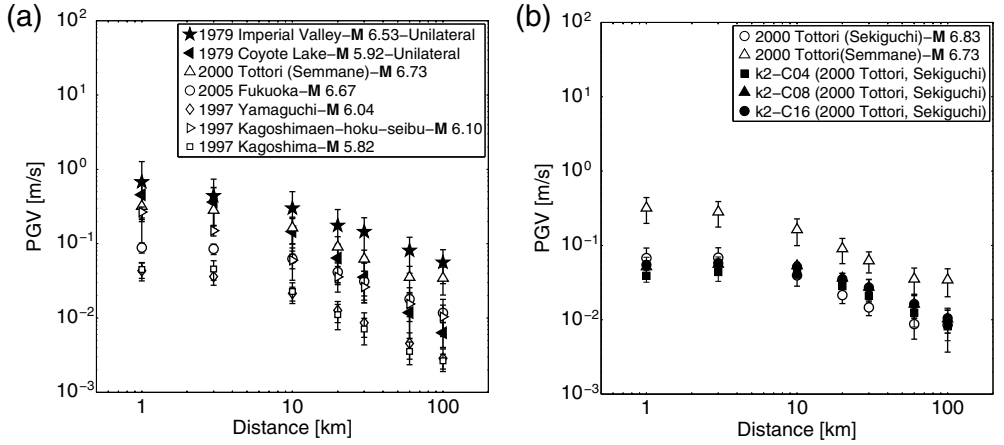

Figure 6. Mean ± standard values (bars showing one standard deviation band) of peak ground velocity (PGV) with varying R_{JB} distances for (a) source models from the finite-source rupture model database and (b) k^{-2} source models and 2000 Tottori models.

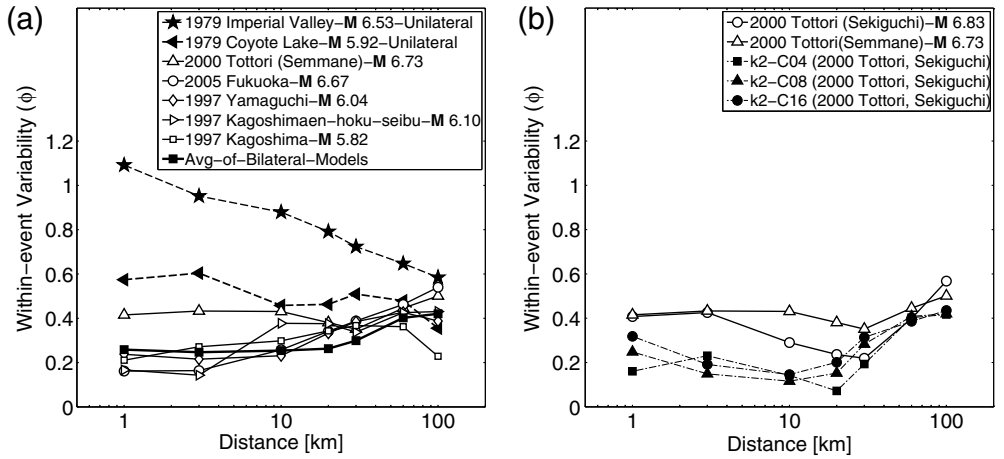

Figure 7. Within-event ground-motion variability (ϕ) with varying R_{JB} distances, for (a) source models from the finite-source rupture model database and (b) k^{-2} source models and 2000 Tottori event models.

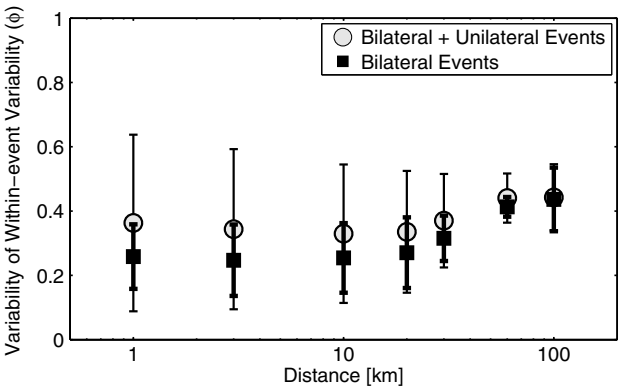

Figure 8. Mean ± standard (bars showing one standard deviation band) of the values of within-event ground-motion variability (ϕ) with varying R_{JB} distances, for the cases (1) bilateral and unilateral events combined and (2) only bilateral events.

near-source region (< 10–20 km). In this article, we have analyzed sigma from the viewpoint of simulations to complement real data studies and to investigate the influence of different source parameters on the resulting ground-motion variability. Ground motion, represented by the PGV, is computed from various kinematic source models and Green's functions computed for 1D-layered velocity models. Our study focuses on the within-event component ϕ of sigma. For simplicity, we have limited our study to vertical strike-slip faults.

Our results suggest that the within-event variability ϕ depends significantly on the rupture type, with unilateral ruptures resulting in larger ϕ values than bilateral ruptures, especially in the near-source region. Far away from the source (~100 km), this dependency vanishes and ϕ is steady ($\phi \sim 0.3$–0.5) for both kinds of ruptures. Thus the distance dependency of ϕ presents two main behaviors: (1) ϕ increases with distance for bilateral events and (2) ϕ decreases with distance for unilateral events. Interestingly, the range of within-event variability values provided by our numerical simulations in far field is consistent with the single station within-event variability (ϕ_{SS}) estimates obtained from real data by Rodriguez-Marek *et al.* (2013) ($\phi \sim 0.4$ at 100 km). It should be mentioned, however, that our ϕ estimations are not only single station but also single path because we assume a 1D velocity structure.

Using a global catalog of large shallow earthquakes, McGuire *et al.* (2002) found that approximately 80% of ruptures have DRs larger than 0.5, pointing out the overall predominance of unilateral ruptures. This shows the importance of considering directivity effects in the estimation of the between-event variability of ground motions. For a given earthquake scenario, prior knowledge about the rupture direction may contribute in refining the estimates of ϕ. The large variability, which we obtained at a short distance for unilateral ruptures, may, however, be strongly reduced if azimuth is considered as a predictor. This could be quantified by computing median ground motion from prediction models that account for directivity effects (e.g., Somerville *et al.*, 1997; Spudich and Chiou, 2008) or simply by assessing the variability in various azimuth ranges.

Our simulations are performed up to 3 Hz for simple 1D media. The ϕ values inferred in far field are essentially controlled by the shape of the wave radiation pattern. Nevertheless the radiation pattern effect, which is clearly observed in our synthetics, might be limited to lower frequency range (<~1 Hz) in real velocity structures. The theoretical four-lobe *S*-wave radiation pattern may be limited to low frequencies (< 1 Hz), with an isotropic pattern at high frequency due to the scattering of seismic waves (e.g., Liu and Helmberger, 1985; Takenaka *et al.*, 2003; Takemura *et al.*, 2009). In addition, according to Cho *et al.* (2010), observations suggest that far-field radiation patterns change from a distinct double-couple pattern, with strong directivity effects at low frequencies (< 1 Hz), to a more isotropic pattern with diminished directivity effects at high frequencies, putting forward the fact that directivity effects are also frequency dependent. This frequency dependence of directivity effects has been attributed to source incoherency by Bernard and Herrero (1994). Because our rupture models do not include any source of incoherency, the strong impact of directivity effects on the ϕ values computed from our synthetics may be weaker in the case of real earthquakes.

The results presented in this study are valid in a narrow magnitude range (~6 < M_w < ~7) and for vertical strike-slip events only. In addition, due to the small number of considered source models, the source variability may be underestimated and the inclusion of additional source models may then modify the observed overall trends. Considering additional unilateral rupture models would also strengthen the conclusions on the role of directivity effects. Finally, the cogency of our results relies on the validity of the inverted source models, which may be affected by uncertainties (e.g., Mai *et al.*, 2007), due to the nonuniqueness of the inverse problem, errors in the forward model, etc. Source inversion models derived from incomplete datasets and the ground-motion prediction at a site that is not considered in the inversion can be significantly biased. This is especially true if the prediction site is isolated as pointed out by Cirella and Spudich (2013). From a set of accelerograms recorded in the area of Niigata, the authors generated thousands of good source models (i.e., with a good level of data fit) of the 2007 Chuetsu earthquake that they used to predict ground motion at the Kashiwazaki-Kariwa nuclear power plant. They found that the ground-motion scatter at the power plant is of the order of the empirically observed between-event variability. Part of this scatter arises from particular choices to parameterize the inversion process, which are inherently user dependent. For instance, two of the source models considered in our study account for variability in slip, rupture velocity, and rise time, whereas the other models assume uniformity in rupture velocity and rise time (Table 1). These *a priori* choices partially constrain distributions and correlation patterns of source parameters, which may impact the ϕ values. However, the fact that we got nearly analogous estimation of

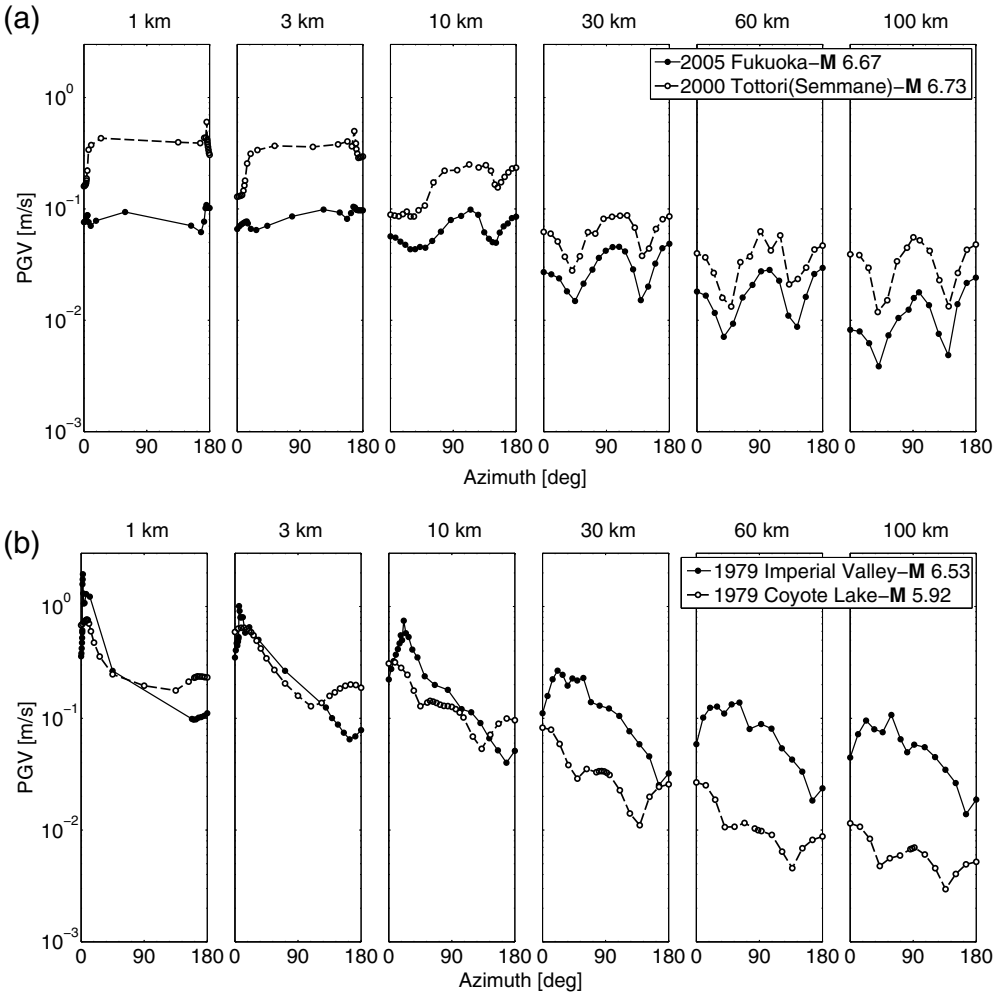

Figure 9. PGV values for the stations located at different azimuths along varying R_{JB} distances, for (a) bilateral and (b) unilateral events. Here azimuth represents θ, the angle between the epicenter and the station as illustrated in Figure 4.

ϕ from the two 2000 Tottori models, which were obtained by different authors inversion parameterization, adds credibility to our results. Furthermore, our study is intended to focus only on the variability of ground motion rather than its absolute value. The overall observed trends of the ground-motion variability have been related to global source features (rupture directivity, depth of the main slip area) that may still be captured by source inversions.

Data and Resources

The eight finite-source rupture models used in this study have been extracted from the finite-source rupture model database (Mai and Thingbaijam, 2014) available at http://equake-rc.info/SRCMOD/ (last accessed March 2014). This website is an online database of finite-fault rupture models of past earthquakes obtained using kinematic inversion of strong-motion data, sometimes combined with geodetic and/or data. The database provides the complete description of the space–time distribution of the coseismic slip, except from the model of Horikawa (2001) of the Kagoshimean-hoku-seibu event for which the rupture time distribution is not available.

Institut des Sciences de la Terre (ISTerre) is part of Labex OSUG@2020 (ANR10 LABX56). Most of the computations presented in this article were performed using the Grenoble University High Performance Computing (HPC) center, CIMENT, infrastructure (https://ciment.ujf-grenoble.fr; last accessed March 2014), which is supported by the Rhône-Alpes region (GRANT CPER07_13 CIRA: http://www.ci-ra.org; last accessed March 2014) and France-Grille (http://www.france-grilles.fr; last accessed March 2014). For the parallel computations of a large number of single jobs, we exploited the available resources of a local grid of HPC clusters (totalizing more than 3000 computing cores) in a best-effort mode, the grid middleware "cigri" (http://ciment.ujf-grenoble.fr/cigri; last accessed March 2014). The results were stored on a distributed data grid operated by the Integrated Rule-Oriented Data System (IRODS) (https://www.irods.org; last accessed March 2014).

Acknowledgments

We thank Martin Mai and an anonymous reviewer for very constructive and insightful feedback that helped us to considerably improve the article. We are thankful for the computation facilities we have been provided with from ISTerre and the Grenoble University High Performance Computing (HPC) center CIMENT.

References

Al-Atik, L., N. Abrahamson, J. J. Bommer, F. Scherbaum, F. Cotton, and N. Kuehn (2010). The variability of ground-motion prediction models and its components, *Seismol. Res. Lett.* **81,** 794–801, doi: 10.1785/gssrl.81.5.794.

Anderson, J. G., and J. N. Brune (1999). Probabilistic seismic hazard assessment without the ergodic assumption, *Seismol. Res. Lett.* **70,** no. 1, 19–28.

Archuleta, R. J. (1984). A faulting model for the 1979 Imperial Valley earthquake, *J. Geophys. Res.* **89,** no. B6, 4559–4585.

Asano, K., and T. Iwata (2006). Source process and near-source ground motions of the 2005 West Off Fukuoka Prefecture earthquake, *Earth Planet Space* **58,** 93–98.

Bernard, P., and A. Herrero (1994). Slip heterogeneity, body-wave spectra, and directivity of earthquake ruptures, *Ann. Geofisc.* **XXXVII,** 1679–1690.

Bommer, J. J., and N. A. Abrahamson (2006). Why do modern probabilistic seismic-hazard analyses often lead to increased hazard estimates? *Bull. Seismol. Soc. Am.* **96,** 1967–1977.

Boore, D. M., J. W. Lamprey, and N. A. Abrahamson (2006). Orientation-independent measures of ground motion, *Bull. Seismol. Soc. Am.* **96,** no. 4A, 1502–1511, doi: 10.1785/0120050209.

Bouchon, M. (1981). A simple method to calculate Green's functions for elastic layered media, *Bull. Seismol. Soc. Am.* **71,** no. 4, 959–971.

Causse, M., E. Chaljub, F. Cotton, C. Cornou, and P. Y. Bard (2009). New approach for coupling k-2 and empirical Green's functions: Application to the blind prediction of broadband ground-motion in the Grenoble basin, *Geophys. J. Int.* **179,** 1627–1644.

Causse, M., F. Cotton, and M. Mai (2010). Constraining the roughness degree of slip heterogeneity, *J. Geophys. Res.* doi: 10.1029/2009JB006747.

Chen, Y.-H., and C.-C. P. Tsai (2002). A new method for estimation of the attenuation relationship with variance components, *Bull. Seismol. Soc. Am.* **92,** no. 5, 1984–1991.

Cho, H., J. Hu, Y. Klinger, and E. M. Dunham (2010). Frequency dependence of radiation patterns and directivity effects in ground motion from earthquakes on rough faults, *Eos Trans. AGU*, (Fall Meet.), Abstract #S51A-1914.

Cirella, A., and P. Spudich (2013). Aleatory and epistemic uncertainties in interpolated ground motions—Example from the Kashiwazaki-Kariwa Nuclear Powaer Plant recordings of the July 16, 2007, Niigata-ken Chuetsu-oki, Japan, earthquake, *Geophys. Res. Abstr.*, EGU2013-5932.

Coutant, O. (1989). Program of numerical Simulation AXITRA, *Research Reports LGIT*, Université Joseph Fourier, Grenoble (in French).

Edwards, B., and D. Fäh (2013). A stochastic ground motion model for Switzerland, *Bull. Seismol. Soc. Am.* **103,** doi: 10.1785/0120110331.

Hartzell, S. H., and T. H. Heaton (1983). Inversion of strong ground motion and teleseismic waveform data for the fault rupture history of the 1979 Imperial Valley, California, earthquake, *Bull. Seismol. Soc. Am.* **73,** 1553–1583.

Horikawa, H. (2001). Earthquake doublet in Kagoshima, Japan: Rupture of asperities in a stress shadow, *Bull. Seismol. Soc. Am.* **91,** no. 1, 112–127.

Joyner, W. B., and D. M. Boore (1981). Peak horizontal acceleration and velocity from strong-motion records including records from the 1979 Imperial Valley, California, earthquake, *Bull. Seismol. Soc. Am.* **71,** no. 6, 2011–2038.

Liu, H., and D. V. Helmberger (1983). The near-source ground motion of the 6 August 1979 Coyote Lake, California, earthquake, *Bull. Seismol. Soc. Am.* **73,** no. 1, 201–218.

Liu, H., and D. V. Helmberger (1985). The 23:19 aftershock of the 15 October 1979 Imperial valley earthquake: More evidence for an asperity, *Bull. Seismol. Soc. Am.* **75,** 689–708.

Mai, P. M., and K. K. S. Thingbaijam (2014). SRCMOD: An online database of finite-fault rupture models, *Seismol. Res. Lett.* **85,** no. 6, doi: 10.1785/0220140077.

Mai, P. M., J. Burjanek, B. Delouis, G. Festa, C. Francois-Holden, D. Monelli, T. Uchide, and J. Zahradnik (2007). Source-inversion blind test: Initial results and further developments, *Eos Trans. AGU*, **88,** no. 52 (Fall Meet. Suppl.), Abstract S53C-08.

McGuire, J. J., L. Zhao, and T. H. Jordan (2002). Predominance of unilateral rupture for a global catalog of large earthquakes, *Bull. Seismol. Soc. Am.* **92,** no. 8, 3309–3317.

Miyakoshi, K., T. Kagawa, H. Sekiguchi, T. Iwata, and K. Irikura (2000). Source characterization of inland earthquakes in Japan using source inversion results, Paper read at *Proc. 12th World Conf. Earthq. Eng.*, Auckland, New-Zealand, 30 January–4 February 2000.

Ripperger, J., P. M. Mai, and J.-P. Ampuero (2008). Variability of near-field ground motion from dynamic earthquake rupture simulations, *Bull. Seismol. Soc. Am.* **98,** no. 3, 1207–1228, doi: 10.1785/0120070076.

Rodriguez-Marek, A., F. Cotton, N. Abrahamson, S. Akkar, L. Al-Atik, B. Edwards, G. Montalva, and M. Dawood (2013). A model for single-station standard deviation using data from various tectonic regions, *Bull. Seismol. Soc. Am.* **103,** 3149–3163, doi: 10.1785/0120130030.

Rodriguez-Marek, A., G. A. Montalva, F. Cotton, and F. Bonilla (2011). Analysis of single-station standard deviation using the KiK-net data, *Bull. Seismol. Soc. Am.* **101,** 1242–1258, doi: 10.1785/0120100252.

Sekiguchi, H., and T. Iwata (2002). Source process and near-fault ground motion of the 2000 Tottori-ken Seibu earthquake, *Monthly Chikyu* no. 38, 182–188 (in Japanese).

Semmane, F., F. Cotton, and M. Campillo (2005). The 2000 Tottori earthquake: A shallow earthquake with no surface rupture and slip properties controlled by depth, *J. Geophys. Res.* **110,** no. B3, B03306, doi: 10.1029/2004JB003194.

Somerville, P. G., N. F. Smith, R. W. Graves, and N. A. Abrahamson (1997). Modification of empirical strong ground motion attenuation relations to include the amplitude and duration effects of rupture directivity, *Seismol. Res. Lett.* **68,** 199–222.

Spudich, P., and B. S.-J. Chiou (2008). Directivity in NGA earthquake ground motion: Analysis using isochrone theory, *Earth. Spectra* **25,** 279–298.

Takemura, S., T. Furumura, and T. Saito (2009). Distortion of the apparent *S*-wave radiation pattern in the high-frequency wavefield: Tottori-Ken Seibu, Japan, earthquake of 2000, *Geophys. J. Int.* **178,** 950–961.

Takenaka, H., Y. Mamada, and H. Futamure (2003). Near-source effect on radiation pattern of high-frequency *S* waves: Strong *SH-SV* mixing observed from aftershocks of the 1997 northwestern Kagoshima, Japan, earthquakes, *Phys. Earth Planet. In.* **137,** nos. 1/4, 31–43.

Appendix A

Computation of Directivity Ratios

For each source model, we compute the directivity ratio (DR) as proposed by McGuire *et al.* (2002). From the space–time slip distribution, we first compute the second spatial moment $\hat{\mu}^{(2,0)}$, the second temporal moment $\hat{\mu}^{(0,2)}$, and the mixed moment $\hat{\mu}^{(1,1)}$ defined as

$$\hat{\mu}^{(2,0)} = \iint \dot{f}(\vec{r},t)(\vec{r}-\vec{r}_0)(\vec{r}-\vec{r}_0)^T dV dt, \qquad \text{(A1)}$$

$$\hat{\mu}^{(0,2)} = \iint \dot{f}(\vec{r},t)(t-t_0)^2 dV dt, \qquad \text{(A2)}$$

and

$$\hat{\mu}^{(1,1)} = \iiint \dot{f}(\vec{r},t)(\vec{r}-\vec{r}_0)(t-t_0)dVdt, \tag{A3}$$

in which $\dot{f}(\vec{r},t)$ is the space–time moment rate function, and $\vec{r}_0$ and t_0 refer to the spatial and temporal centroids.

Next, we determine the characteristic duration, expressed as

$$\tau_c = 2\sqrt{\hat{\mu}^{(0,2)}/M_0)} \tag{A4}$$

and the characteristic dimension in a direction $\vec{n}$, expressed as

$$x_c(\vec{n}) = 2\sqrt{\vec{n}^T(\hat{\mu}^{(2,0)}/M_0)\vec{n}}, \tag{A5}$$

in which M_0 denotes the seismic moment. The characteristic rupture length L_c is defined as $x_c(\vec{n}_1)$, the maximum value of $x_c(\vec{n})$, $\vec{n}_1$ being the Eigen vector associated with the largest eigen value. The ratio

$$\nu_c = L_c/\tau_c \tag{A6}$$

then represents the characteristic rupture velocity.

Finally, we compute the average velocity of the instantaneous spatial centroid:

$$\nu_0 = \hat{\mu}^{(1,1)}/\hat{\mu}^{(0,2)}. \tag{A7}$$

The DR is defined as the ratio ν_0/ν_c.

Appendix B

Velocity Models Used for Ground-Motion Computation

All the considered velocity models are the ones that have been used to perform source inversions, except the Imperial Valley earthquake, for which the model has been slightly simplified to reduce computation time. The velocity models considered in the ground-motion simulation are given in Table B1 for the bilateral models and in Tables B2 and B3 for unilateral models; V_P, V_S indicate the velocity and Q_P, Q_S the quality factor of P and S waves, respectively. D indicates density of the material in the layer.

For the Imperial Valley (1979) event, Archuleta (1984) assumes a model with velocity gradient as presented in Table B2. For the Green's function computation with Axitra program, different sublayers of the given velocity model were considered, which involved linear interpolation of the values. For example, the second layer (between 0.4 and 5 km) was divided into $N = 5$ sublayers of thickness $dh =$ 1150 m each, and values of the other parameters were taken at the middle of each sublayer. Similarly, the third layer (between 5 and 11 km depth) was divided into $N = 6$ sublayers of thickness $dh = 1000$ m. The fourth layer (between 11 and 11.1 km) marks the discontinuity. Finally, the fifth layer (between 11.1 and 12 km depth) was divided into $N = 2$ sublayers of thickness $dh = 450$ m. The final velocity model adopted is given in Table B3.

Table B1
Velocity Models of the Bilateral Events

Event Name	Depth (m)	V_P (m/s)	V_S (m/s)	D (kg/m^3)	Q_P	Q_S
Fukuoka (2005)	0	5500	3200	2600	∞	∞
	5000	6000	3460	2700	∞	∞
	18000	6700	3870	2800	∞	∞
Yamaguchi (1997)	0	5600	3300	2600	400	400
	3000	6000	3500	2700	450	450
	30000	6600	3800	2900	500	500
Kagoshimaen-hoku-seibu (1997)	0	2800	1620	2100	80	40
	500	4900	2830	2300	300	150
	5000	6000	3460	2700	300	150
	15000	6700	3870	3100	500	250
	35000	7800	4500	3400	1000	500
Kagoshima (1997)	0	3100	1800	2300	200	200
	500	4400	2500	2500	350	350
	3000	5900	3400	2700	450	450
	22000	7000	4000	3000	500	500
Tottori (2000, Semmane *et al.*, 2005)	0	5500	3180	2600	500	200
	2000	6050	3490	2700	500	200
	16000	6600	3810	2800	200	200
	38000	8030	4620	3100	500	200
Tottori (2000, Sekiguchi and Iwata, 2002)	0	5500	3179	2600	500	200
	2000	6050	3497	2700	500	200
	16000	6600	3815	2800	500	200
	38000	8000	4600	3000	500	200
	20000	8100	4620	3300	500	200

Table B2
Initial Velocity Model of Imperial Valley (1979) from Database

Event Name	Depth (m)	V_P (m/s)	V_S (m/s)	D (kg/m^3)	Q_P	Q_S
Imperial Valley (1979), Initial Model	0	1700	400	1800	∞	∞
	400	1800	700	1800	∞	∞
	5000	5650	3200	2500	∞	∞
	11000	5850	3300	2800	∞	∞
	11100	6600	3700	2800	∞	∞
	12000	7200	4150	2800	∞	∞

Appendix C

Computations of the Synthetic Ground Motions for Large Faults

The principle of the decomposition of the computations of ground motions for the large faults considered in this study is as follows:

Let F stand for one of those faults. F is further decomposed into N_s subfaults, such that the typical length of each subfault is a fifth of the minimum wavelength on F. Let N_r

Table B3
Velocity Models of the Unilateral Events

Event Name	Depth (m)	V_P (m/s)	V_S (m/s)	D (kg/m^3)	Q_P	Q_S
Imperial Valley	0	1700	400	1800	∞	∞
(1979),	400	1800	700	1800	∞	∞
Interpolated Model	1550	2281	1013	1888	∞	∞
	2700	3243	1638	2063	∞	∞
	3850	4206	2263	2238	∞	∞
	5000	5169	2888	2413	∞	∞
	6000	5667	3208	2525	∞	∞
	7000	5700	3225	2575	∞	∞
	8000	5733	3242	2625	∞	∞
	9000	5767	3258	2675	∞	∞
	10000	5800	3275	2725	∞	∞
	11000	5833	3292	2775	∞	∞
	11100	6225	3500	2800	∞	∞
	11550	6750	3813	2800	∞	∞
	12000	7050	4038	2800	∞	∞
Coyote Lake (1979)	0	3000	1500	2400	∞	∞
	500	5000	2800	2700	∞	∞
	3000	5700	3300	2780	∞	∞
	12000	6900	3300	3000	∞	∞
	60000	8100	4670	3200	∞	∞

(here $N_r = 135$) be the number of receivers, then the computation of the ground motions is done in three steps: (1) the components of all Green's functions relating the N_s subfaults to the N_r receivers are computed with the Axitra code (Coutant, 1989); (2) each Green's function is convolved in space and time to account both for the magnitude and focal mechanism of the subfault and for the imposed rupture kinematics; and (3) the contributions of the N_s subfaults are summed at each of the N_r receivers.

The $N_s \times N_r$ calculations needed by step (1) were done in parallel on the number of subfaults, that is, for each subfault the calculations at all receivers were gathered in a single job. For this purpose, we exploited the available resources of a local grid of High Performance Computing clusters (totalizing more than 3000 computing cores) in a best-effort mode thanks to the grid middleware "cigri." The results, consisting of one binary file per subfault, were stored on a distributed data grid operated by the IRODS system. The convolutions needed by step (2) were also distributed on the computing grid and stored again on the data grid. Finally, the reduce operation needed in step (3) was done for all receivers by successive grouping of the sources by packets, the size of which was controlled by the maximum number of binary files that would fit in the random access memory (RAM) of each computing node. For the example of the Imperial Valley calculations, each binary file containing the contribution of a single subfault at all receivers was about 16 MB, and the size of the source packets was 200 so that the summation could be done in a RAM of size 4 GB. For this event, which was the most demanding of all cases, the total time needed to compute the Green's functions was about 4000 hours of a single CPU core on an Intel E5-2670 with frequency 2.6 GHz.

Institut des Sciences de la Terre (ISTerre)
University Grenoble Alpes/CNRS/IRD/IFSTTAR
F-38000 Grenoble, France
afifa.imtiaz@ujf-grenoble.fr
mathieu.causse@ujf-grenoble.fr
emmanuel.chaljub@ujf-grenoble.fr
fabrice.cotton@ujf-grenoble

Manuscript received 16 April 2014;
Published Online 27 January 2015

Soil Dynamics and Earthquake Engineering xx (xxxx) xxxx–xxxx

Contents lists available at ScienceDirect

Soil Dynamics and Earthquake Engineering

journal homepage: www.elsevier.com/locate/soildyn

3D numerical simulation and ground motion prediction: Verification, validation and beyond – Lessons from the E2VP project

E. Maufroy[a], E. Chaljub[a], F. Hollender[b], P.-Y. Bard[a,*], J. Kristek[c,d], P. Moczo[c,d], F. De Martin[e], N. Theodoulidis[f], M. Manakou[g], C. Guyonnet-Benaize[h], N. Hollard[a], K. Pitilakis[g]

[a] University Grenoble Alpes, ISTerre, CNRS, IRD, IFSTTAR, Grenoble, France
[b] CEA, French Alternative Energies and Atomic Energy Commission, DEN, Saint Paul lez Durance, France
[c] Faculty of Math., Physics and Informatics, Comenius University, Bratislava, Slovakia
[d] Earth Science Institute, Slovak Academy of Sciences, Bratislava, Slovakia
[e] Bureau de Recherches Géologiques et Minières, Orléans, France
[f] ITSAK, Institute of Engineering Seismology and Earthquake Engineering, Thessaloniki, Greece
[g] Aristotle University of Thessaloniki, Thessaloniki, Greece
[h] Formerly CEA, Cadarache, France

ARTICLE INFO

Keywords:
Ground motion
Numerical simulation
Validation
Site effects
Goodness-of-fit
GMPE
Aleatory variability

ABSTRACT

The Euroseistest Verification and Validation Project (E2VP) is part of a series of complementary benchmarking exercises launched to better assess the ability of numerical simulation to accurately predict seismic ground motion. E2VP targeted more specifically the current, most-advanced numerical methods applied to realistic 3D, linear models of sedimentary basins through a quantitative comparison of the recorded and numerically-simulated ground motions. The target site, located within the Mygdonian basin near Thessaloniki, Greece, has been thoroughly investigated for two decades and a detailed, realistic 3D model has been derived from geological, geophysical and geotechnical investigations, while a dedicated instrumentation provided a significant number of surface and borehole recordings. Verification and validation tests up to a frequency of 4 Hz, much beyond the 0.4 Hz fundamental frequency of the deepest part of the graben, have been performed for a set of 19 local, small to moderate magnitude events. For careful and accurate enough computations, the model-to-model differences are smaller than the model-to-observations differences, the latter being controlled by uncertainties primarily in the crustal propagation model and source properties, and secondarily in the shallow structure. It is therefore recommended to prefer distant and/or deep events ($R > 10–20$ km, $Z > 8–10$ km) for validation exercises. Additional sensitivity tests illustrate the ability of carefully verified numerical simulation tools to provide an instructive insight at the structure of the so-called "aleatory" variability of ground motion, for both its within- and between-event components. The between-event variability is shown to be very sensitive to hypocenter location errors (even as low as ± 2 km), and to uncertainty in magnitude estimates. It explains the increase of aleatory variability for small magnitude events and emphasizes the usefulness of dense seismological networks. The within event, single-site variability is shown to be associated to an "epistemic" dependence of the 3D site response on the event back-azimuth, distance and depth, and calls for caution when interpreting single-station variabilities derived from a too small number of events.

1. Introduction

The rapid development of the simulation codes and computational facilities allowed considering the use of numerical-simulation tools as a valid option for predicting seismic ground motion, especially for poorly instrumented or moderate-seismicity countries lacking representative earthquake recordings. However, such an approach requires a careful evaluation of the actual performance of numerical simulation codes. This issue has been the topic of a few international studies, including blind prediction tests or comparative exercises, focused on various

* Correspondence to: ISTerre – Maison des Géosciences/Bâtiment OSUG C, CS 40700, 38058 GRENOBLE Cedex 9, France.
E-mail addresses: emeline.maufroy@univ-grenoble-alpes.fr (E. Maufroy), emmanuel.chaljub@univ-grenoble-alpes.fr (E. Chaljub), fabrice.hollender@cea.fr (F. Hollender), pierre-yves.bard@univ-grenoble-alpes.fr (P.-Y. Bard), Jozef.Kristek@fmph.uniba.sk (J. Kristek), moczo@fmph.uniba.sk (P. Moczo), F.DeMartin@brgm.fr (F. De Martin), ntheo@itsak.gr (N. Theodoulidis), manakou@civil.auth.gr (M. Manakou), cedric.guyonnet-benaize@hotmail.fr (C. Guyonnet-Benaize), Niels.Hollard@e.ujf-grenoble.fr (N. Hollard), kpitilak@civil.auth.gr (K. Pitilakis).

http://dx.doi.org/10.1016/j.soildyn.2016.09.047
Received 12 February 2016; Received in revised form 23 September 2016; Accepted 27 September 2016
Available online xxxx

sites. It started with the Turkey Flat, California (Cramer [1]), and Ashigara Valley, Japan (e.g., Bard [2]), blind tests focusing on effects of surface sediments, the results of which were presented during the first ESG conference in Odawara (Japan) in 1992. It was followed by more comprehensive comparison exercises on the Osaka/Kobe basin area in Japan (Kawase and Iwata, 1998 [3]), and on the Southern California area within the SCEC framework (Day et al. [4–6]; Bielak et al. [7]), which also included the effects of extended sources and regional propagation in the low frequency range ($f < 1$ Hz). Each of these cases had its own specificities (for instance, very low frequencies for the Osaka and SCEC exercises). A request issued in late 2003 by the French Nuclear Authority (ASN) to perform a 3D, NL simulation of site response for specific sites, was the initial impetus for a dedicated R & D program funded by CEA Cadarache and ILL (Laue-Langevin Institute, an international research center on neutron science based in Grenoble, and operating the most intense neutron source on Earth). It started with an international benchmarking exercise on the Grenoble basin (Chaljub et al. [8]; Tsuno et al. [9]; Chaljub et al. [10]), and was further deepened through the Euroseistest Verification and Validation Project (E2VP). Considering the lessons of the ESG2006 Grenoble benchmark, the E2VP project was launched in 2007 with two main objectives: (a) a quantitative analysis of the accuracy of current, most-advanced numerical methods applied to realistic 3D models of sedimentary basins, in the linear, small strain domain (3DL verification); (b) a quantitative comparison of the recorded and numerically-simulated ground motions (3DL validation). The selected target site was an extensional graben located in the Mygdonian basin near Thessaloniki, Greece, located in a seismically active zone, belonging to both Serbomacedonian massif and Circum Rodope zone (Fig. 1). A detailed, realistic 3D model of the basin and surrounding area had already been derived from a comprehensive set of geological, geophysical and geotechnical investigations, and the site instrumentation installed for about two decades provided a significant number of surface and borehole recordings.

This paper is intended to present a concise overview of the work accomplished since the launching of the E2VP project. This project has been organized in two phases, E2VP1 (2007–2010) and E2VP2 (2012–2014). As the main results of the first phase are reported in two recent papers (Chaljub et al. [11]; Maufroy et al. [12]), the present article puts more emphasis on the latest results, while reminding the overall process. The first section shortly reminds the main learnings of E2VP1, and its shortcomings as well. A few key issues were identified, which shaped the second phase E2VP2: its main components are presented in the following section, including an improvement of the source parameters for a larger set of validation events, an enlargement and refinement of the 3D model on the basis of newly compiled information and sometimes new measurements, and a comprehensive set of numerical simulations for close to 2000 point source locations and 15 receivers. These simulations aim first at the validation up to a frequency of 4 Hz, much beyond the 0.4 Hz fundamental frequency of the deepest part of the graben, for a set of 19 local, small to moderate magnitude events. The corresponding results are described in the following section, distinguishing the rock and sediment stations, and for the latter the absolute ground motion and the 3D site response. The next section is dedicated to the presentation of additional sensitivity tests, which illustrate the ability of carefully verified numerical simulation tools to provide an instructive insight at the structure of the so-called "aleatory" variability of ground motion: the between-event component is shown to be highly impacted by uncertainties in hypocentral location and magnitude, while the within event component is affected by the epistemic dependence of site response on source back-azimuth. The conclusion summarizes the main outcomes from the whole E2VP project, including recommendations regarding the organization of further validation exercises, the use of numerical simulation for ground motion prediction in engineering projects, and the analysis, interpretation and reduction of the aleatory variability in GMPEs.

2. From E2VP1 to E2VP2: the main steps

In short, the basic ideas of the project were, on the example of the Euroseistest site, to (1) quantify the "distance" between results of independent models and numerical schemes, and as much as possible to reduce them to the lowest possible level through a careful understanding of the differences; and (2) to compare this "cross-computation

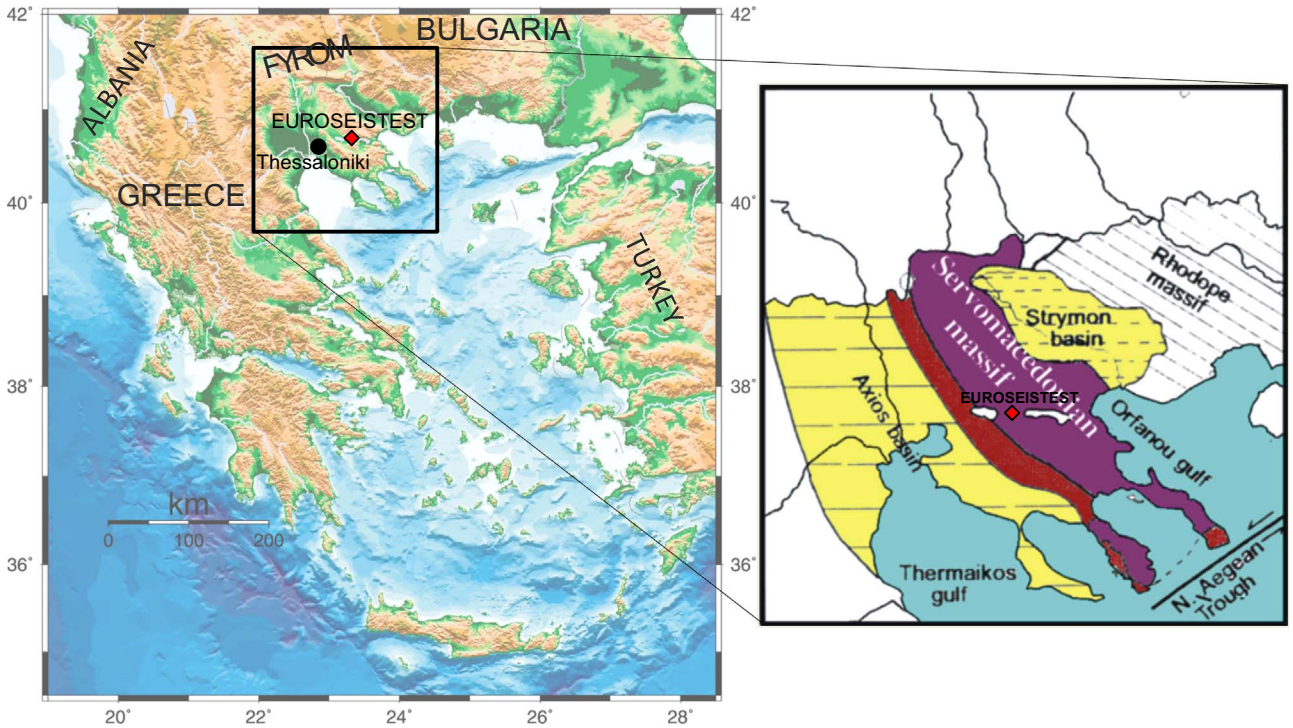

Fig. 1. Location of the Euroseistest site in North-Eastern Greece and first-order geological map of the surroundings of the Mygdonian basin. (For interpretation of the references to color in this figure legend, the reader is referred to the web version of this article.)

Table 1
Summary of main learnings from E2VP phase 1.

Main lessons about verification and validation studies	• Careful verification requires time and often to "go back to basics", while careful validation requires high quality data, i.e., including rich and high quality metadata. • No ground-motion simulation code accounting for wave propagation in complex media can be considered as press-button, neither in the linear, 3D domain, nor in the non-linear 2D - or even 1D - cases. The most common case is that, without iterations and cross-checking, different codes provide significantly different results when applied to the same case study. • Too fast applications of existing codes by non-expert users may yield wrong ground-motion estimates, potentially resulting in raising mistrust in end-users. This warning is applicable to all numerical simulation, including the simplest ones, but gets more and more important with increasing code sophistication. • Some codes currently used in engineering applications would deserve some significant improvements, or strong warnings on stringent validity limits, while even state-of-the-art codes (predominantly in the "academic" field) deserve constant upgrading.
Main recommendations for a wise use of numerical simulation codes	• One should never be satisfied with only one computation from one single team, but should request several teams (at least two) with different numerical schemes to perform parallel computations of the same case. Results should be considered as reliable only if they agree beyond some quantitative goodness-of-fit threshold. • These goodness-of-fit criteria should definitely be agreed upon by the engineering community in order to reach an objective of transparent quantitative comparison, which should replace sentences such as "one can see the very good agreement on the figure" • In the long run, it would be very valuable to assign a specific "quality label" to numerical codes and teams that did accept to run some of the now existing "canonical" cases with their own numerical code, which are freely available on web pages (http://www.sismowine.org/). Maintaining this kind of internet facility in the long run will be beneficial for the whole community. • External peer reviews are always useful in assessing the quality of results derived from highly sophisticated numerical codes. • Comparison with actual data (in-situ earthquake recordings), whenever possible, are always useful. Having sensitive in-situ instrumentation (continuously recording broad-band velocimeters or sensitive accelerometers) proves to be invaluable for checking the reliability of numerical-simulation results.

distance" to the "misfit" between simulation results and actual measured data for as many real events as possible. In order to keep track of overestimation or underestimation bias, a sign is included in this distance as detailed in Maufroy et al. [12]. The first phase E2VP1 (2007–2010) included a comprehensive series of cross-model verifications, with side computations on canonical models aimed at investigating the accuracy of numerical schemes under very stringent conditions – as detailed in Chaljub et al. [11] -, and a first round of comparison between observations and simulations for a small number (6) of local events, as reported in Maufroy et al. [12]. The computations were performed up to a frequency of 4 Hz: this remains limited compared to the frequency range of interest in earthquake engineering, but this is significantly higher than all previous similar exercises. It led to a number of lessons and recommendations on the use of the numerical-simulation approach, as listed in Table 1, but it also led to the identification of a few further issues that needed to be addressed in a second phase.

2.1. 3D linear modeling

The main focus and success of E2VP1 was thus on the use of 3D, linear simulation. The main results are summarized in Fig. 2. The code-to-code differences could be drastically reduced by the consideration of dedicated canonical models and stringent goodness-of-fit criteria comparing the waveforms in the time-frequency domain (Kristekova et al. [13]), leading to significant improvements in the numerical schemes (Chaljub et al. [11]). The simulation-to-observation differences could be quantified for only a limited number of events (6) because of the moderate seismicity and the limited extension of the 3D model considered by that time. For those events, the simulated and observed waveforms remain so different that another metrics was adopted to quantify their differences, on the basis of "engineering" parameters. After a careful analysis of the original Anderson's criteria (Anderson [14]), five parameters (C1 to C5) were selected (see Maufroy et al. [12]): pga (C1), the spectral acceleration at intermediate (C2) and low (C3) frequencies (averages in the [1.5–3 Hz] and [0.375–0.75 Hz] ranges, respectively), an "energy" indicator C4 (cumulative absolute velocity, CAV), and the Trifunac-Brady duration (RSD, Trifunac and Brady [15]) for C5. Parameters C1–C3 evaluate the amplitude of the signal in different frequency bands. These frequency bands are chosen according to the observed characteristics of the real signals at the center of the Mygdonian basin: the frequency range evaluated by C3 includes the fundamental resonance frequency of the basin, while C2 covers the two higher modes. C1 evaluates the highest frequencies available in the synthetics. C4 and C5 evaluate the total energy of the signal and its duration, respectively. The misfit was computed for each parameter in terms of relative increase or decrease compared to the measured values. Fig. 2 indicates that such an "engineering" distance is around 10–25% between different simulations, to be compared with misfit values in the range 40–80% between observations and simulations. As detailed in Maufroy et al. [12], these numbers do vary depending on the considered receiver (rock or valley), on the considered event, and on the engineering parameter, but the overall trends are robust, and emphasize both the usefulness of the prior verification part and the difficulty to obtain satisfactory, unbiased numerical predictions of ground motion.

Only very few events could be used for the validation: this is a typical situation for moderate/weak seismicity areas. It was therefore considered useful to include more events [from 6 to 19] in the second phase of the validation exercise (those shown in Fig. 1), which led to increase the size of the 3D model, as illustrated later in Fig. 6. In addition, the significant misfit between observations and simulations was shown to be partly due to uncertainties or errors in source parameters: the misfits on the sole site response component were found lower than those on absolute motion (Maufroy et al. [12]). It was thus decided first to improve as much as possible the location of the 19 selected events, and second to investigate through numerical simulation how the uncertainties in source parameters map on the variability of site-specific ground motion from local earthquakes.

2.2. Non-linear (NL) modeling

The first phase also included an comparison of 2D, NL simulations on a NS cross-section of Euroseistest. This attempt for a verification of NL codes proved however to be a failure, as code-to-code differences were too large with too many, too poorly identified origins. Yet, it is

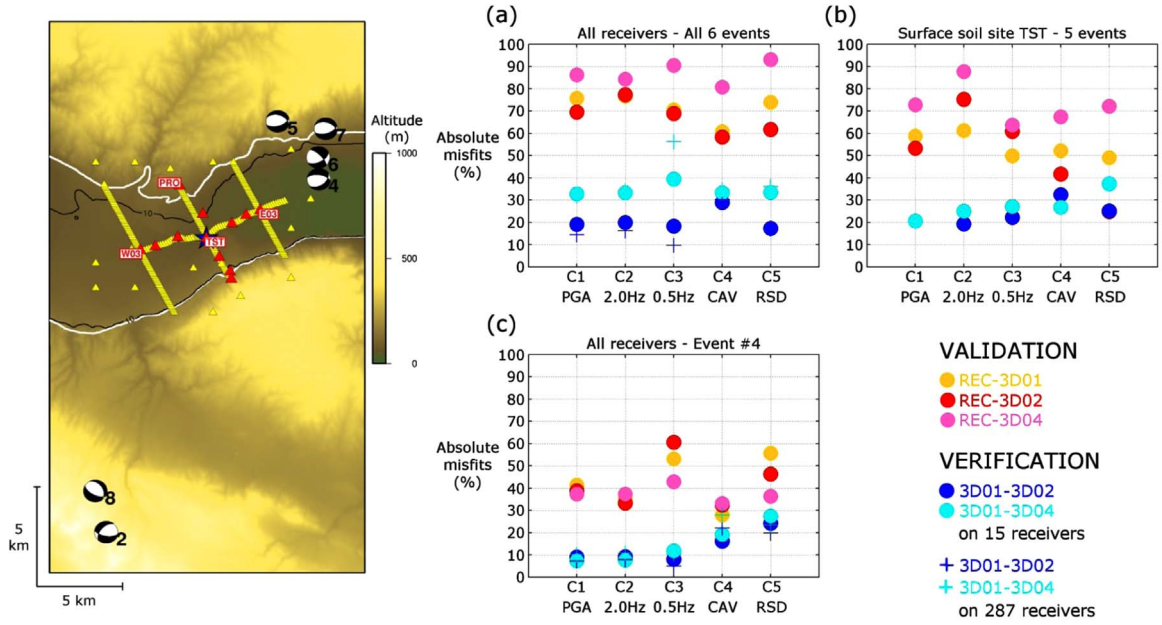

Fig. 2. Summary of horizontal absolute misfits obtained on the E2VP1 evaluation parameters C1–C5 (see text for their definition and Maufroy et al. [12] for more details) for the verification and validation exercises considering different configurations. Left: localization and focal mechanism of the 6 validation events (beachballs) and of the receivers used for the comparison (red and yellow triangles). Right: (a) average misfits for the 6 selected events at all receivers; (b) average misfits for the 5 events recorded at the central soil site TST; (c) average misfits for the biggest event #4 at all receivers. Synthetics-to-synthetics distances (verification, blue tones dots) are compared to recordings-to-synthetics misfits (validation, warm tones dots). The verification distances are computed for either the real array of 15 surface receivers (red triangles, solid circles) or the complete virtual array of 287 receivers (yellow triangles, crosses). A single value per array is obtained by calculating the weighted average of the absolute distances over the considered receivers (with weights proportional to the value of the corresponding ground-motion parameter). (For interpretation of the references to color in this figure legend, the reader is referred to the web version of this article.)

obvious that NL simulation codes deserve similar verification and validation efforts, especially as they are much more often used in engineering practice than 3D, linear simulation codes. Although non-linear site response was one of the major topics of the two pioneering blind tests initiated in the late 80′s for the sites of Ashigara Valley (Japan) and Turkey Flat (California), they were inconclusive because both sites lacked strong motion records involving significant non-linear behavior. A new benchmarking of 1D NL codes was performed in the last decade, based on the same Turkey Flat site that experienced a 0.3*g* motion during the 2004 Parkfield earthquake, and a few other sites with vertical array data (La Cienega, California; the KGWH02 KiK-net site in Japan, and Lotung in Taiwan). Its main findings, reported by Kwok et al. [16] and Stewart and Kwok [17], emphasized the key importance of the way these codes are used and of the required in-situ measurements. Significant differences between records and predictions have been identified as due to an incorrect velocity profile (although it was derived from redundant borehole measurements), a non-1D soil geometry (non-planar layers), and imperfections/deficiencies in the constitutive models, which were unable to represent the actual degradation curves for shear modulus and damping. The E2VP1 failure and these recent conclusions thus allowed to issue three main recommendations for future benchmarking exercises: a) NL verification should be performed on the simplest possible cases (1D soil columns and total stress, water-free, analysis); b) it should be performed on already instrumented sites having recorded large acceleration levels; c) it should be associated with careful in-situ surveys and lab tests designed in tight connection with the needs of the rheological models implemented in the various NL codes.

The second phase, E2VP2 (2012–2014). was thus designed to answer some of the identified issues related with 3D linear modeling, while two other projects were launched to address some other: the PRENOLIN project (Régnier et al. [18–20]) was designed to start answering the issues about NL modeling according to the E2VP1 lessons, and another benchmarking exercise, named “INTERPACIFIC”, was launched for a comparative assessment of the performance of various in-situ geophysical and geotechnical survey techniques (Garofalo et al. [21,22]). The present paper focuses exclusively on the new results related to 3D, linear modeling (E2VP2).

3. New validation phase E2VP2: model, data and simulations

This section presents the four main components of the additional work performed for this new phase, while the following sections will be dedicated to the presentation of the new results, in terms of validation and sensitivity analysis. The additional work started with the selection of a larger set of events and the re-assessment of their source parameters; the consideration of a lerger set of events implied an enlargement of the 3D model, which was therefore updated and implemented in an improved numerical code. The latter was then used for computing the ground motion associated not only to the new set of real events, but also for sensitivity studies allowing the investigate the deterministic impact of source location (distance, depth and back-azimuth) on ground motion characteristics, together with the impact of source parameter uncertainties on ground motion variability.

3.1. Improvement of source parameters for an increased number of local events (from 6 to 19)

This work included careful relocation and determination of focal mechanisms through waveform fitting of broad-band and accelerometric recordings with 1D synthetics computed by the discrete wavenumber method with the crustal velocity model proposed by Novotny et al. [23]. It is worth mentioning that for the events that were already considered in the first validation phase, the new source parameters can vary significantly with respect to the old ones: as an example, the largest event (Mw=4.4) used in the first phase was moved by 5 km vertically and 4.5 km horizontally to define the S3 event of phase 2. The resulting event parameters are listed in Table 2 and their location and focal mechanism are displayed in Fig. 3. Details on the relocation work may be found in appendix 3 of Maufroy et al. [24].

Table 2
Characteristics of the 19 selected real events that occurred near the Mygdonian basin, whose recordings by the Euroseistest accelerometric array are compared to 3D numerical predictions in the validation phase 2. Only the preferred solutions of the inversion for source parameters are shown.

Event ID	Date	Lat. (°)	Long. (°)	Depth (km)	Mag. Mw	TST hyp. dist. (km)	Strike (°)	Dip (°)	Rake (°)
S1	2006/05/10	40.5208	23.4052	5	4.38	19.3	245	54	−105
S2	2006/08/17	40.5433	23.1732	11	3.59	20.0	80	57	−149
S3	2005/09/12	40.7255	23.3408	10	4.40	12.8	281	52	−98
S4	2009/06/21	40.6895	23.1148	11	3.14	18.7	100	61	−102
S5	2012/10/21	40.6950	23.2580	11	3.44	11.9	81	53	−127
S6	2004/06/08	40.5520	23.5233	9	3.30	25.0	71	82	−121
S7	2004/07/15	40.6800	23.4378	7	3.70	14.4	73	53	−118
S8	2004/07/15	40.6952	23.4733	9	3.70	18.2	258	47	−96
S9	2004/11/09	40.7648	23.3520	3	3.10	12.7	253	46	−98
S10	2004/12/12	40.6760	23.2853	4	2.70	4.2	240	51	−89
S11	2005/04/20	40.8121	22.9129	4	3.50	36.1	103	58	−94
S12	2005/09/12	40.7012	23.3586	4	3.00	8.1	301	52	−77
S13	2005/10/09	40.7889	23.4375	8	3.40	20.2	64	74	−116
S14	2007/12/27	40.7230	23.1700	11	3.50	16.4	276	59	−95
S15	2008/08/28	40.6617	23.3292	3	2.80	4.4	80	48	−83
S16	2008/10/13	40.6120	23.4200	9	2.90	15.3	306	58	−52
S17	2009/10/05	40.6920	23.3850	10	3.40	13.1	63	60	−174
S18	2010/08/08	40.5603	23.5785	8	4.60	28.1	235	52	−157
S19	2011/07/25	40.6265	23.3047	5	2.80	6.6	14	84	0

3.2. Update and extension of the 3D model

The E2VP-phase 1 was based on the preexisting 3D model as proposed by Manakou [25] and Manakou et al. [26]. For E2VP-phase 2, a new 3D model was built “from scratch” in order to avoid any bias due to pre-existing interpretation choices. This new model has been extended to the whole Mygdonian basin by gathering all the available information complemented by a few additional specific measurements to constrain the bedrock geometry, the sedimentary thickness and the seismic velocity. An important point to mention in order to understand the “philosophy” of this E2VP2 validation effort, is that we did our best to build the new 3D model only on the basis of the available geological, geophysical and geotechnical data: there was no attempt to “retro-fit” the model in an *ad hoc* approach in order to optimize the fit between simulated ground motion and real records (an approach which was actually used in the first validation phase with the previous model). The objective is to be as close as possible to a realistic, blind prediction situation.

The compiled data include geology, hydrological and geotechnical boreholes (190 in total, out of which 59 reached the paleozoic basement at depths varying from 0 to 408 m), geophysical surveys (seismic refraction lines, controlled source/radio magneto-telluric surveys, array microtremor and H/V measurements). All available data were compiled in 3D using the geomodeller GOCAD (Caumon et al. [27];

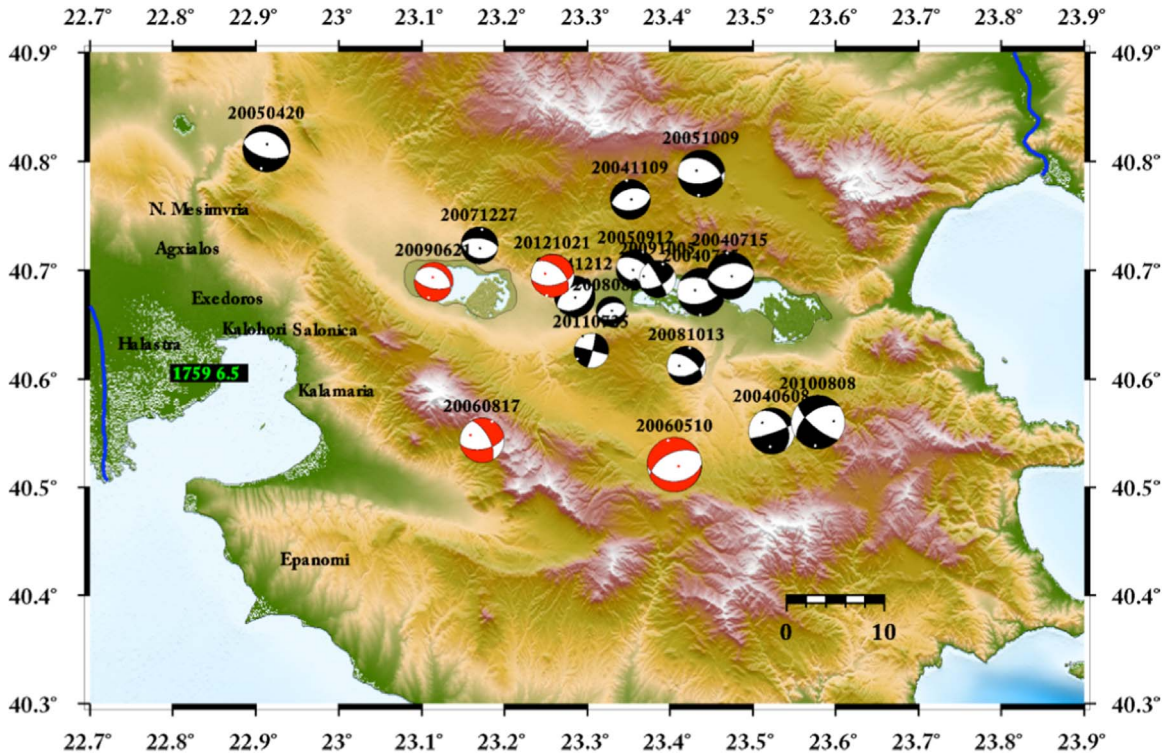

Fig. 3. Map of the 19 seismic events that were considered for the validation part of E2VP2. The focal mechanisms are indicated with beach-balls, the size of which is proportional to the magnitude of the event. Most of the events exhibit normal faulting, consistently with the extension regime of the area. (For interpretation of the references to color in this figure legend, the reader is referred to the web version of this article.)

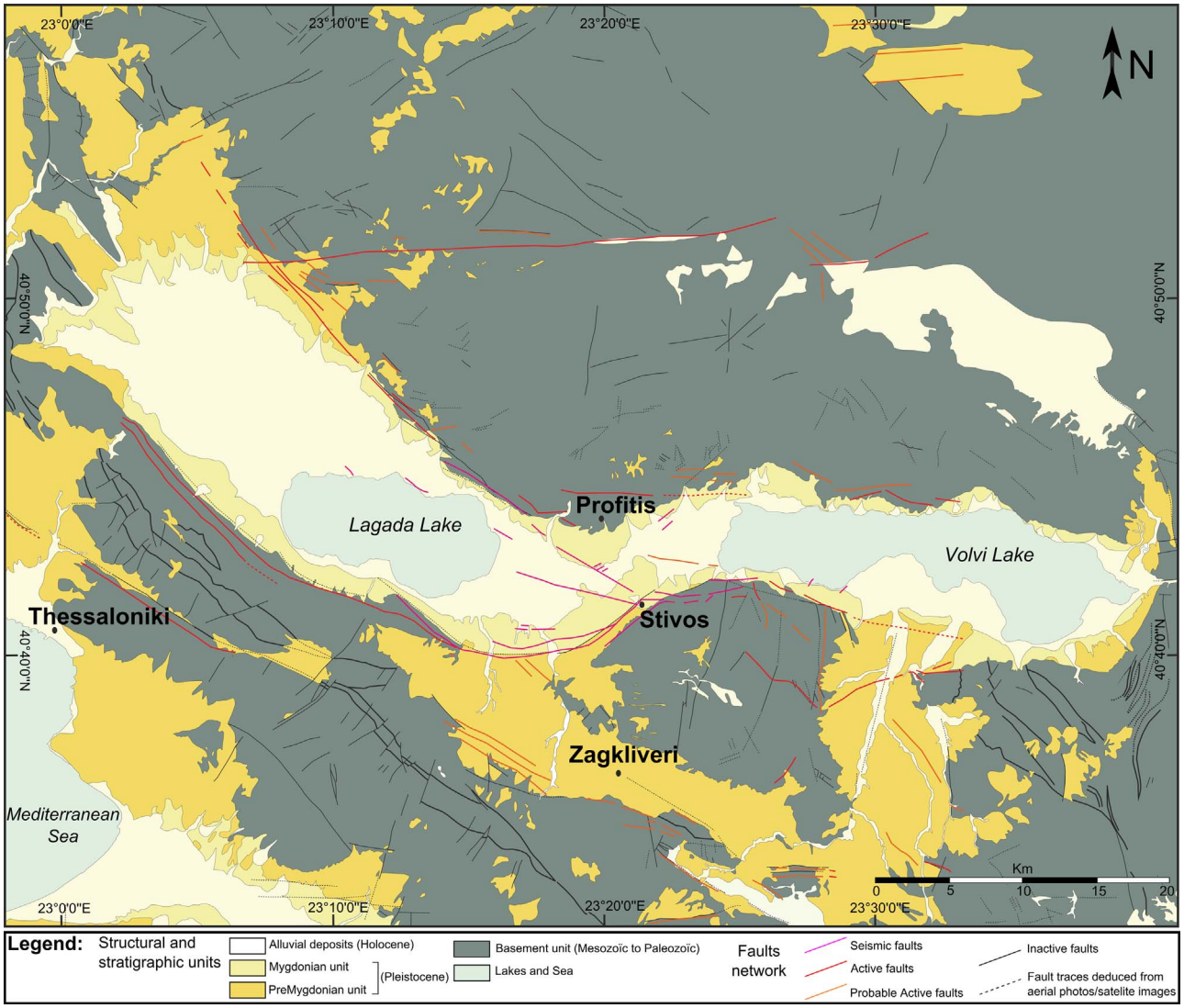

Fig. 4. Simplified structural sketch of the Mygdonian basin, modified from Mygdonian geological [29] and neotectonic maps [30], scales 1:50000–1:100000. (For interpretation of the references to color in this figure legend, the reader is referred to the web version of this article.)

Mallet [28]) to build a 3D geological model for the whole Mygdonian basin.

The main features of the resulting model are 1/the 3D geometry of the "geophysical" bedrock (i.e. Paleozoic basement), 2/the main faults surfaces and 3/the thickness maps of the entire filling of the Mygdonian basin. The present-day structure of the basin (shown in Fig. 4) is composed of three structural units, from shallower to deeper unit: (1) the Mygdonian system (2) the ProMygdonian system and (3) the Paleozoic basement (Manakou [25]; Manakou et al. [26]). The Mygdonian and ProMygdonian systems are two sedimentary units presenting significant lateral thickness variations, from 140 m in the eastern part (close to the Volvi Lake) to 400 m in the western part (close to the Lagada Lake). The Mygdonian system is composed of quaternary fluvial-lacustrine, deltaic, lacustrine, lagoonal and estuarine deposits (Sotiriadis et al. [31]), corresponding to Pleistocene and Holocene age. The ProMygdonian system is composed of conglomerates, sandstones, silt-sand and red-beds sediments (Raptakis et al. [32]), with a Tertiary age. These two sedimentary units overlay the Paleozoic basement, composed of gneiss, amphibolites, two-mica schists and marble intrusions. The overall thickness of the Mygdonian and ProMygdonian units is mapped in Fig. 5, together with the surface topography outside of the Mygdonian sedimentary filling.

These structural units are affected by a complex fault system. In the entire basin, the faults are mostly striking NW-SE, excepted in the eastern part (Volvi Lake) where the faults strike E-W and N-S. The main features are the 12 km long Vasiloudi - Gerakarou - Nikomidino - Stivos fault system, running through the southern and western part of the basin (F-GNSP for the main fault system and F-VL & F-Sx for its two segments, see Fig. 4). This fault system presents a constant dip to the North (70–80°), reduced to about 35° with increasing depth.

3.3. Update of the 3D simulation model (Spectral Element method)

3D simulations were performed with a spectral element code including an improved meshing and velocity homogeneization strategy, surface topography and intrinsic attenuation. The size of the computational domain is 69 km×69 km in the horizontal directions, and extends from the surface (with an elevation with respect to sea level varying from −6 m to 1181 m) down to a constant elevation plane at 30 km depth. The spectral element mesh was obtained using a robust, semi-automated procedure which produces a geometrically conforming, unstructured mesh of hexahedral elements, the sizes of which were tuned for a maximum frequency of 4 Hz and the associated wavelengths. The new model is characterized by a "double-gradient" velocity model, characterized by a first linear gradient from 130 m/s at surface

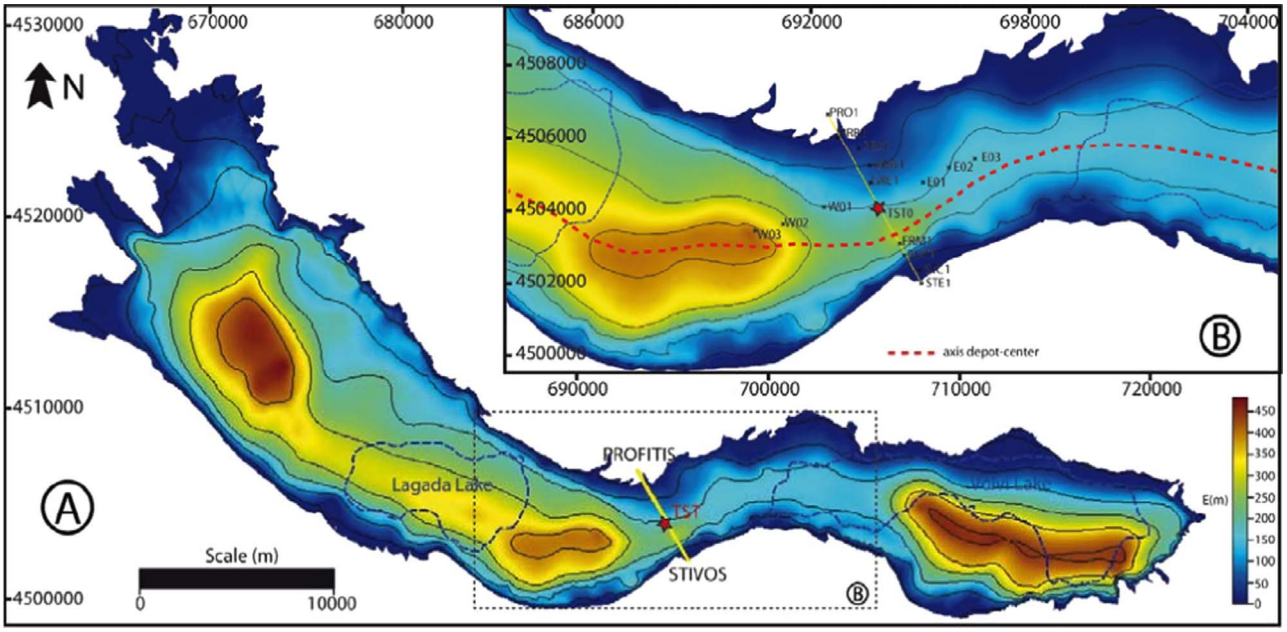

Fig. 5. Thickness of the whole sedimentary (quaternary+tertiary) series as derived form the 3D compilation of available data in 3D geomodelling. (For interpretation of the references to color in this figure legend, the reader is referred to the web version of this article.)

Table 3
V_S, V_P, ρ, Q_S and Q_P "anchor" values used to build E2VP2 properties model within the basin.

	Vs	*Vp*	*ρ*	*Qs*	*Qp*
Surface	130	1500	2075	=Vs/10	=max [Vp/20, Vs/5]
M/P limit	475	2100	2130		
Bedrock top	800	2700	2250		

to 475 m/s at an intermediate surface within the basin, and a second linear gradient from this intermediate surface (475 m/s) to the bedrock interface (with a sediment base velocity of 800 m/s). This intermediate surface, corresponding to a gradient change without velocity jump, could be associated to the Mygdonian/Premygdonian (M/P) limit. The corresponding velocity, unit mass and quality factors are listed in Table 3. The only abrupt velocity contrast thus corresponds to the sediment/bedrock interface, where the S-velocity jumps from 800 m/s to 2400 m/s. As specified in Maufroy et al. [33], the mesh does not follow neither the discontinuity of material parameters at the sediment-bedrock interface, nor the discontinuity of their first-order derivatives at the limit between the Pre-Mygdonian and Mygdonian sediments. Instead, those interfaces were homogenized by vertically averaging the S- and P- slownesses and mass density, as suggested in [10]. The size of the homogenization window is L=25 m, about half the minimum element size. The mesh contains about 6.5 million elements and, since the polynomial order is set to N=4, about 435 million grid points. The element size is kept smaller than the local minimum wavelength, that is, smaller than 50 m in the shallower basin part and 450 m in the bedrock, insuring at least 5 grid-points per wavelength for frequencies up to about 4 Hz.

For consistency, the bedrock velocity model has been taken identical to the velocity model used for the event relocation [23].

3.4. Ground motion simulations

This updated and improved model was then used for the simulation of the expected ground motion for various sets of events and receivers:

- A first set ("S1") was dedicated to the validation, i.e., the comparison between predictions and observations. It consists of the 19 selected events, with their actual, improved source parameters (magnitude range: 2.7–4.6; distance range: 0–30 km, as listed in Table 2), computed at the 15 receivers corresponding to actual strong motion instruments, as shown in Fig. 6.
- A second set ("S2") was dedicated to the investigation of the sensitivity of ground motion to the exact source location: each of the 19 events was recomputed for a total of 27 hypocentral positions, considering all combinations with a shift of the actual hypocenter by ± 2 km in each X, Y and Z direction. The resulting shifted hypocenters are thus located within a cubic box centered on the actual hypocenter location (as indicated in Table 2), and with a 4 km long edge.
- A large set ("S3") of 7*36*5=1260 virtual events arranged in 7 concentric circles from 2.5 to 30 km, 36 back-azimuths (10° step) and at 5 different depths from 2.5 to 15 km was considered to perform a comprehensive investigation of the sentivity of ground motion and site response to source location (i.e., distance, depth, and backazimuth) in a fully 3D environment. The corresponding focal mechanisms were randomly generated following a Gaussian distribution around the "average" normal faulting parameters in the Mygdonian basin area: strike=86 ± 18°, dip=52 ± 15°, rake=−101 ± 51°.
- Out of this "S3" set, a subset "S4" was extracted corresponding to a set of 52 actually occurred events ("real catalog", see below), which could not however be all used for the validation as a) the corresponding number of recordings was often too small, and b) the focal mechanism could not be determined with enough accuracy.

The three sets (S1–S3, including thus S4) were computed for the 15 receivers using the reciprocity theorem, which allows to limit the number of simulations to *3* times the number of receivers and thus saves computational time when the number of sources exceeds the number of receivers. As detailed in Causse et al. [34], the spatial derivatives of the 3D Green's functions are then convolved with the moment tensors to obtain the time series at the 15 receivers. The epicenter locations of sets S3 and S4 are displayed in Fig. 7.

4. New validation results

The set S1, corresponding to the nineteen seismic events listed in

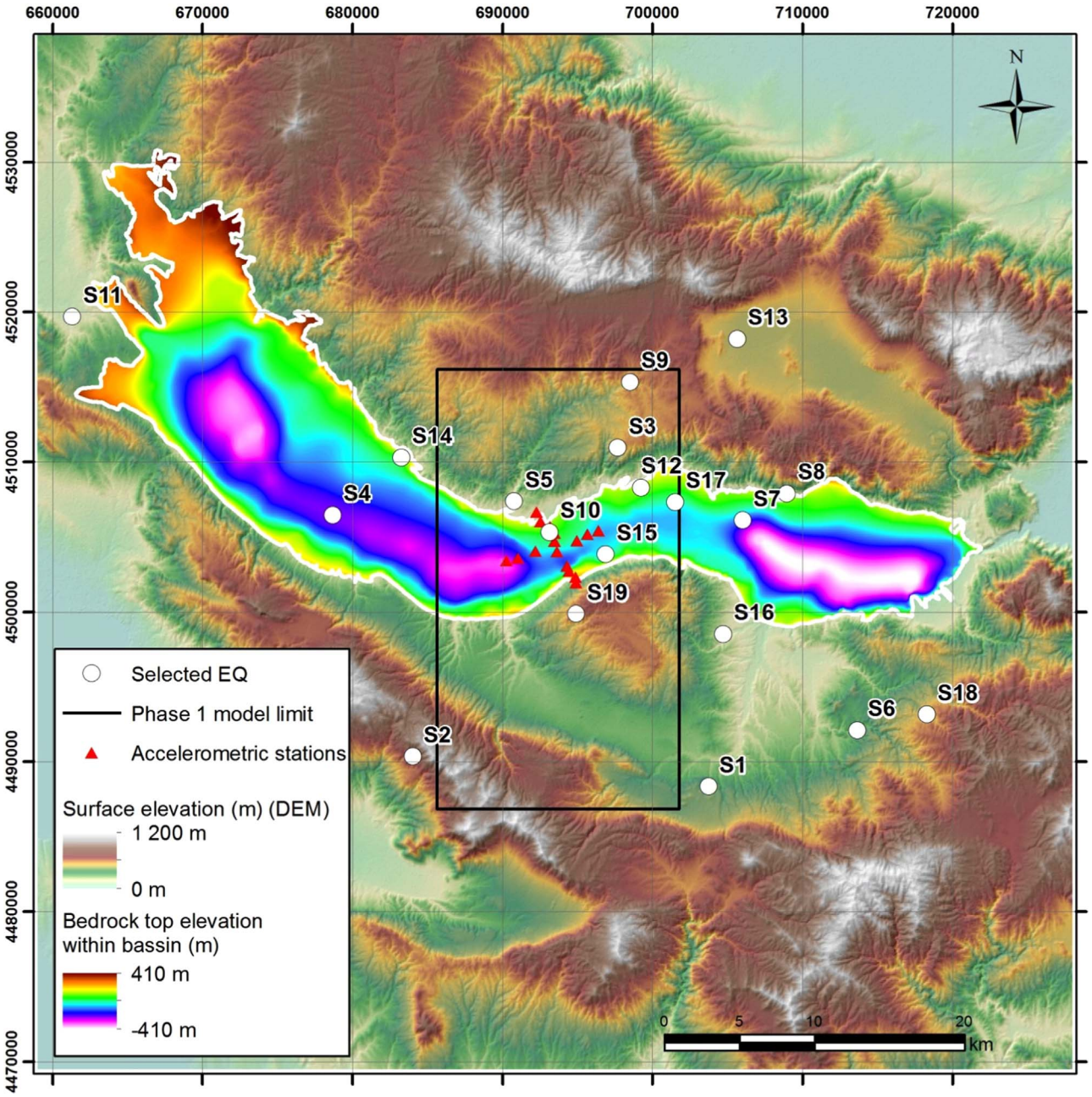

Fig. 6. Map of the whole model used for E2VP phase 2 modeling (box of 69×69 km), compared with the location of the area of the "phase 1" modeling box. The surface topography DEM et elevation of the top of the bedrock within the basin are also displayed. Also shown are the location of the 15 accelerometric stations used far the validation (red triangles), the 19 real events selected for the comparison between numerical predictions and actual recordings (white circles, with numbers referring to event IDs in Table 2. (For interpretation of the references to color in this figure legend, the reader is referred to the web version of this article.)

Table 2 and Fig. 3, well recorded by the Euroseistest accelerometric array, is considered in this section. The 3D numerical simulations of the 19 events are performed with the code EFISPEC3D (De Martin [35]) implementing the Spectral Element Method. They include the effects of surface topography and of frequency independent intrinsic attenuation, which was modeled using a Zener body with 3 relaxation mechanism distributed between 0.1 Hz and 4 Hz, as detailed in Moczo et al. [36].

Pre-processing of the data to perform the validation exercise includes: (1) filtering the real data with a Butterworth filter between 0.3 Hz (order 6) and 3.0 Hz (order 10), in order to get a similar frequency content between the recordings and the synthetics without contamination by high energy transients at frequencies higher than the maximum simulation frequency (4 Hz); (2) synchronization of recordings with the corresponding synthetics on the first *P*-wave arrival; (3) all couples of signals to be compared are cut to the same length in duration; and (4) a study of the signal-to-noise (SNR) ratio is performed on all recordings to determine the frequency band where that ratio is greater than 3: only recordings fulfilling such a SNR criterion over a frequency band [0.7–4 Hz] have been considered for the validation.

Differences between numerically-simulated seismograms and earthquake recordings were quantified as for E2VP Phase 1 on the basis of the 5 ground-motion parameters mentioned above. Arguments for the selected characteristics, details on their computations and on the way to handle the horizontal components are provided in Maufroy et al. [12]. The main results of this "blindly- oriented" validation exercise are summarized below, starting with the rock sites.

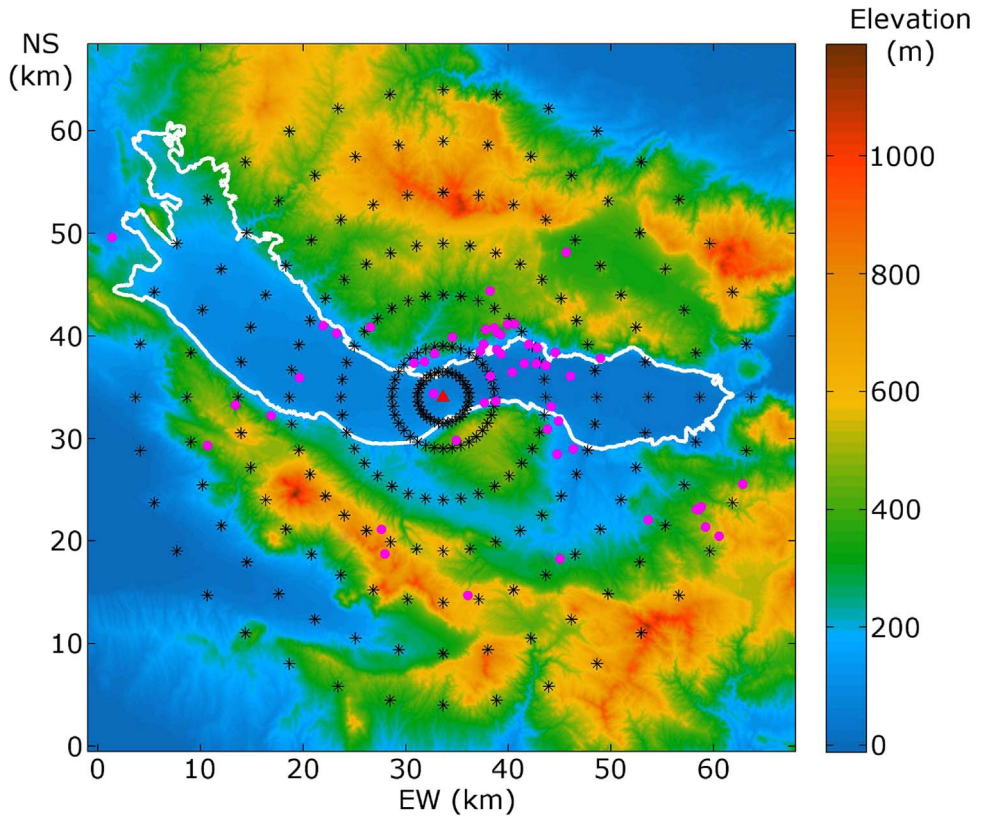

Fig. 7. Epicentral location of the "virtual" seismic sources considered in the numerical study. The response of the Mygdonian basin (bold white line) is computed for 1260 virtual sources (black circular crosses) located on seven concentric circles around the central soil site TST indicated by the red triangle, with back-azimuths equally distributed every 10°, and five different depths. 52 of these virtual locations are very close to real earthquakes recorded at some of the accelerometric stations: the epicentral locations of those 52 real events are depicted by the magenta dots. (For interpretation of the references to color in this figure legend, the reader is referred to the web version of this article.)

4.1. Validation results at rock sites

Results of the comparison between actual recordings and their numerical predictions at 3 rock sites in Euroseistest are given in Table 4. PRO is the northernmost station on a rock outcrop in the Profitis village, STE is the southernmost station on a rock outcrop south of the Stivos village, and TST5 is the deepest borehole sensor (depth 196 m) in the central vertical array. The level of misfit obtained on the 5 ground motion parameters Ci of the E2VP evaluation procedure is expressed by the average misfit computed for each of them from the selected events that were recorded at the corresponding rock site. The misfit values obtained here are similar or below in absolute value to the misfits obtained in the first validation phase at PRO and STE rock sites, giving a first confirmation that the surface ground motion outside the basin is in general well predicted by the numerical simulations. Only the borehole site TST5 exhibits anomalously high misfit values at the highest frequencies considered in the validation.

To get another viewpoint on the level of misfit outside the basin, Fig. 8 displays the Fourier spectral ratios computed between recordings and their numerical predictions for the events recorded at these 3 rock sites. Concerning northern rock site PRO (see Fig. 8a), the median ratio of observed ground motion over predicted is globally satisfactory (i.e., around and close to value 1), except for the lowest frequencies that are under-estimated. Reason for that low-frequency under-estimation of the ground motion at PRO is not yet understood. At southern rock site STE (Fig. 8b) the median ratio is satisfactorily close to 1 in all frequencies. It is noteworthy however that the validation results at STE can be bad for a few events (the colored lines giving the result for each individual event are far from the value 1 in a few cases).

Table 4
Average in % of horizontal misfits on the E2VP evaluation criteria between the actual recordings and their numerical predictions at 3 rock sites: northern rock site PRO, southern rock site STE and borehole TST5. The number of events recorded by each station and considered in the average is indicated in the last column.

	C1 PGA	C2 2.0 Hz	C3 0.5 Hz	C4 CAV	C5 RSD	Number of events
PRO	−21	−24	−54	−9	−73	9
STE	34	39	1	8	−124	17
TST5	128	129	53	88	−161	16

At borehole site TST5 (Fig. 8c) that is located close to the sediment-basement interface at 196 m depth, the actual ground motion appears to be significantly over-estimated by the synthetics at high frequencies. This can obviously significantly impact the ground motion prediction at the surface and center of the basin. Several tentative explanations can be considered. One possibility could be the new crustal-propagation model, as the model from Papazachos [37], used in E2VP phase 1, was later replaced by the model from Novotný et al. [23] also used in the improved characterization of the seismic sources. A comparative study for the two models, detailed in Maufroy et al. [24], indicates the E2VP2 crustal model induces only a slight increase (around 20% in general, possibly reaching up to 60% over some narrow frequency bands) of rock motion compared to the previous E2VP model. This effect, although it could participate, cannot fully explain the high-frequency overestimation found at borehole site TST5.

Another possibility is that borehole site TST5, located right below the sediments, might be significantly and inappropriately affected by the basin propagation in the new basin model of E2VP phase 2. The strongest argument in favor of that hypothesis is found in Fig. 8c. The average ratio (solid black line) exhibits, in addition to the overestimation trend at high frequencies, three troughs at frequencies around 0.75 Hz, 1.7 Hz and 2.7 Hz: these frequencies do coincide with the first 1D resonance frequencies in the basin at TST0. Such an excess

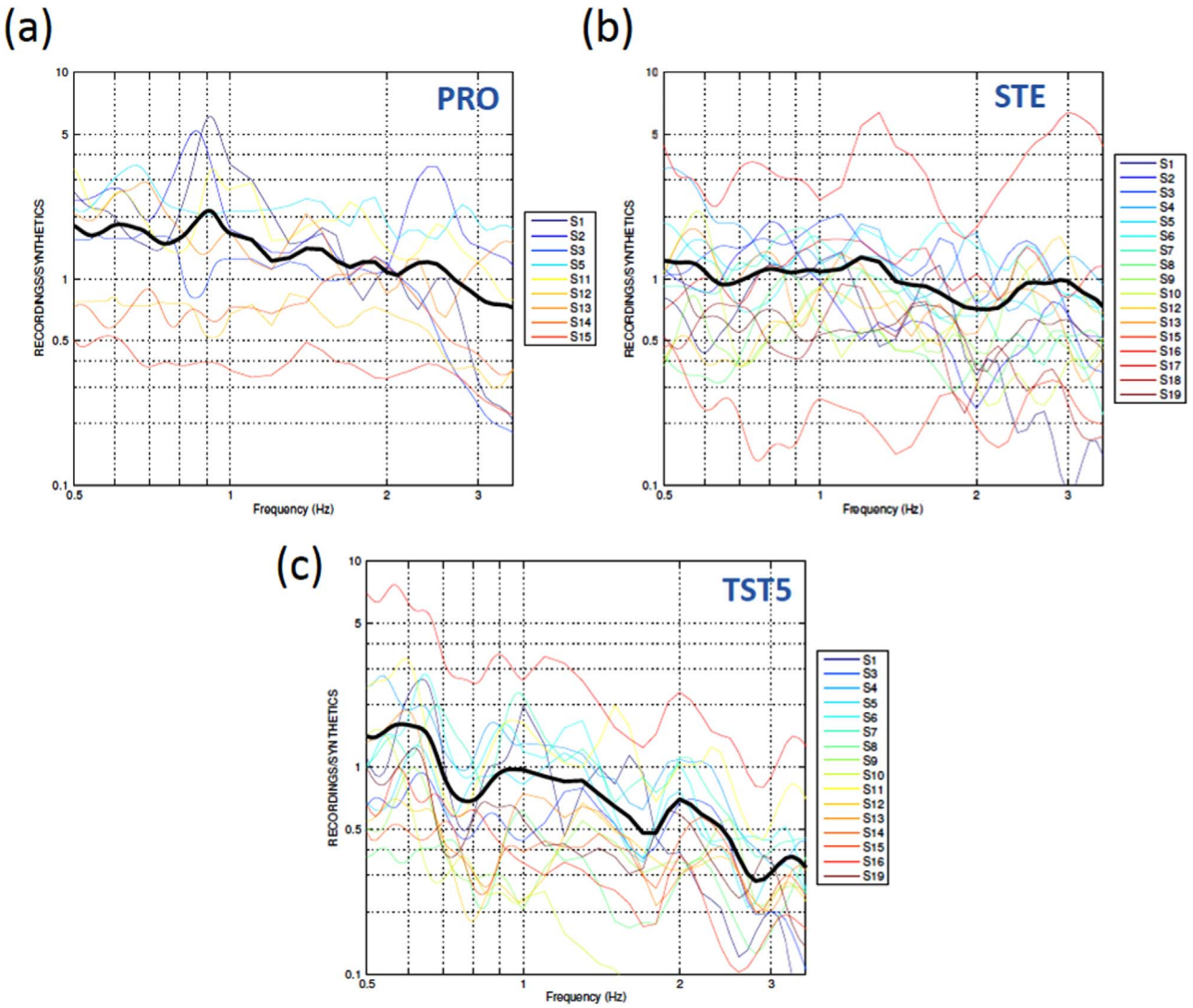

Fig. 8. Fourier spectral ratios between recordings and their numerical predictions at 3 rock sites: (a) northern rock site PRO, (b) southern rock site STE and (c) borehole TST5. Each colored line corresponds to one seismic event of the validation. The solid black line indicates the average ratio in each panel. (For interpretation of the references to color in this figure legend, the reader is referred to the web version of this article.)

footprint of the frequency-dependent site effect at TST, together with the overestimation trend at high frequency at TST5, might be indicative of a too weak attenuation in the new basin model, resulting in a too energetic feedback of energy radiating from the basin into the bedrock, especially at high frequency. Such an hypothesis should be also associated with an overamplification at TST0, which is partly the case, as seen in the following.

Finally a third possibility comes from the absence of scattering in the numerical model, the bedrock consisting of horizontally layered, homogeneous media. The signal duration (parameter C5) is found indeed to be under-predicted for each rock site, which is consistent both with the over prediction of amplitude parameters especially at high frequencies, and the absence of scattering.

4.2. Validation results in the Mygdonian basin

The same evaluation procedure has been applied to all stations for all selected events. The validation results have been detailed for each event, each site and each considered ground motion parameter as illustrated in Fig. 9 on the example of event S7 (one of the most satisfactory as seen in Table 5). They can also be summarized for each site and ground motion parameter as listed in Table 5 for the central site TST0. The detailed results for each event are available in Maufroy et al. [24].

In most cases the ground motion in the basin is significantly overestimated, while the signal duration (parameter C5) is almost systematically under-estimated. The last parameter is tightly related both to regional scattering – not accounted for in the modeling -, and to damping within the sediments, which is not constrained by any measurement. One way to investigate the preferential origin of this duration under-prediction is to have a special focus on the basin response.

Following the procedure of the first validation phase (Maufroy et al. [12]), “hybrid” time histories are computed to further investigate the ability of the numerical predictions to predict the site-response component of the ground motion. Hybrid time histories at TST0 are obtained by convolving the recorded signal at TST5 (which thus includes the actual source and path terms, in particular all the delayed arrivals from crustal scattering) with the site-effect part coming from the simulation (synthetic borehole-surface transfer function computed for the same event).

Hybrid time histories maximize the impact of numerical estimate of site-effect component and minimize the effect of uncertainties in source description or in crustal propagation. The validations misfits corresponding to such hybrid time histories are also listed in Table 5: such an approach can be found to significantly improve the fit on the

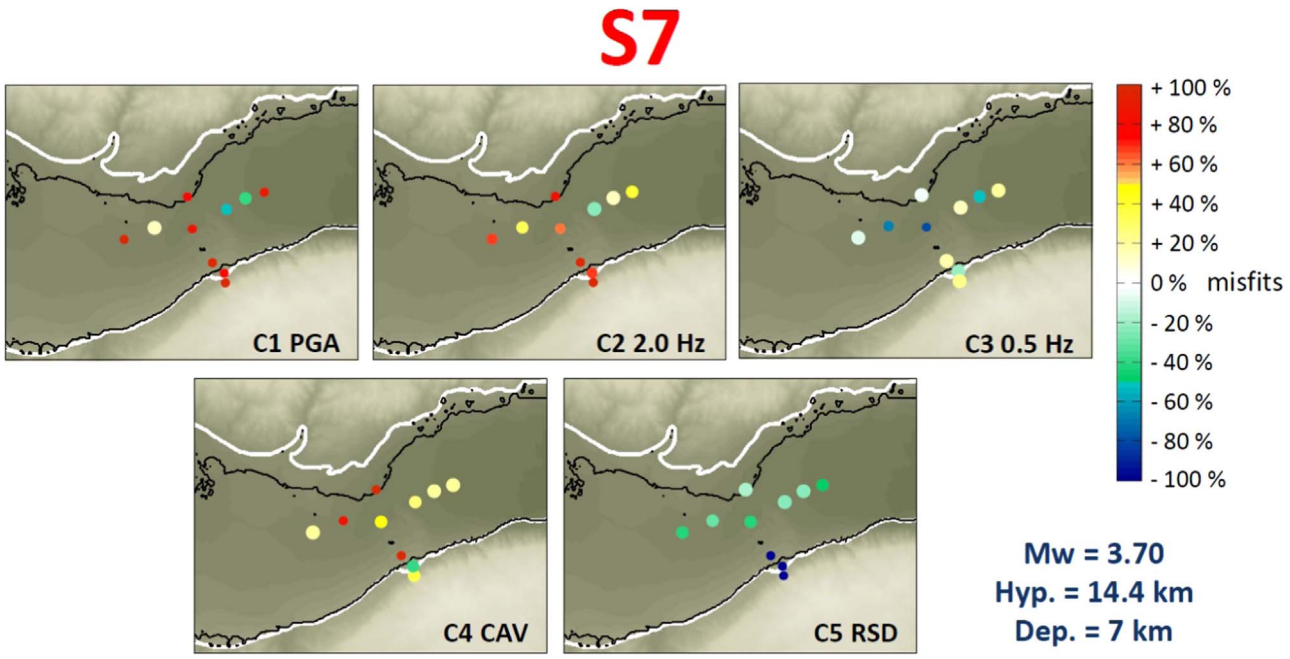

Fig. 9. Example map of horizontal misfits on the E2VP evaluation criteria between the recordings of the real event S7 (see Table 2 and Fig. 6) and its 3D numerical prediction. C1 is based upon peak ground acceleration, C2 upon elastic spectral acceleration ranging 1.5–3.0 Hz, C3 upon elastic spectral acceleration ranging 0.375–0.750 Hz, C4 upon cumulative absolute velocity and C5 upon 5–95% relative significant duration (see [12] for details). Each colored dot corresponds to the misfit obtained at the corresponding real surface receiver. Red/yellow tones are for overestimation of the recordings by the prediction; blue/green tones are for underestimation. (For interpretation of the references to color in this figure legend, the reader is referred to the web version of this article.)

amplitude-frequency parameters C1–C3, and on the energy parameter C4 as well – with however a remaining trend for over-prediction -, while the average misfit on duration C5 is moved from under-prediction to over-prediction. The misfit values obtained on criteria C1 to C3 for the hybrid time histories are significantly lower than for the full synthetics, being in absolute value closed to the values obtained in validation phase 1 (see Fig. 14 in Maufroy et al. [12]). The typical average misfit values encountered in phase 1 for hybrids were ranging from −20% to −50%. In the second phase, the corresponding average values equal 27%, 29% and 1% on C1–C3 respectively. However, when not taking into account events S10 and S15 (identified as being bad candidates for validation due to their proximity and low magnitude), those values decrease to 19%, 16% and −22% on C1–C3 respectively (–48% on C3 when considering only events with signal-to-noise ratio greater than 3). This represents a general improvement of the validation results on the site-effect component.

One important change from validation phase 1 to phase 2, is that the site-effect component was globally under-estimated in phase 1 (negative average misfit values for hybrid time histories at TST0), while it is now mostly over-estimated in phase 2 (positive average misfit values on C1 and C2). This observation, combined with the average misfit on duration, also supports the probable under-estimation of the damping value within the sediments.

The slight over-prediction of site response estimates also appear clearly on Fig. 10, which displays a comparison between the observed and computed surface/downhole transfer functions for various event

Table 5
Values of average horizontal misfits on the five engineering parameters Ci between the actual recordings at central soil site TST0 and their numerical predictions. Values in % evaluate the predictions by full synthetics vs. hybrid time histories (i.e. site response only). For each parameter Ci, the average is computed over the 16 events that were recorded both at TST0 and TST5, and over the 14 events excluding the worst ones S10 and S15.

	FULL SYN. **C1**	HYBRIDS **C1**	FULL SYN. **C2**	HYBRIDS **C2**	FULL SYN. **C3**	HYBRIDS **C3**	FULL SYN. **C4**	HYBRIDS **C4**	FULL SYN. **C5**	HYBRIDS **C5**
S1	154	10	129	11	27	−58	196	72	−39	92
S3	177	19	186	39	89	−48	156	13	−93	−63
S4	142	62	128	84	78	52	42	95	−169	−6
S5	147	32	166	35	40	−12	76	−4	−93	1
S6	128	81	117	104	−22	106	68	198	−44	98
S7	87	−24	63	−19	−77	−90	47	25	−41	64
S8	130	12	173	12	156	−73	192	62	−61	47
S9	186	−3	192	20	164	15	152	34	−70	27
S10	471	75	506	98	431	203	365	94	−205	101
S11	68	35	63	32	−65	4	61	66	4	47
S12	201	5	201	29	136	−72	146	−16	−48	−26
S13	243	46	153	−47	5	−134	123	−12	−109	−19
S14	234	2	214	−5	188	−1	184	−15	−57	15
S15	310	92	338	134	262	129	253	114	−102	29
S16	2	9	−119	−120	−143	−17	−72	31	−71	47
S19	99	−15	139	50	58	19	126	146	−69	53
AVERAGE	173	27	166	29	83	1	132	56	−79	32
AVERAGE without S10 S15	143	19	129	16	45	−22	107	50	−69	27

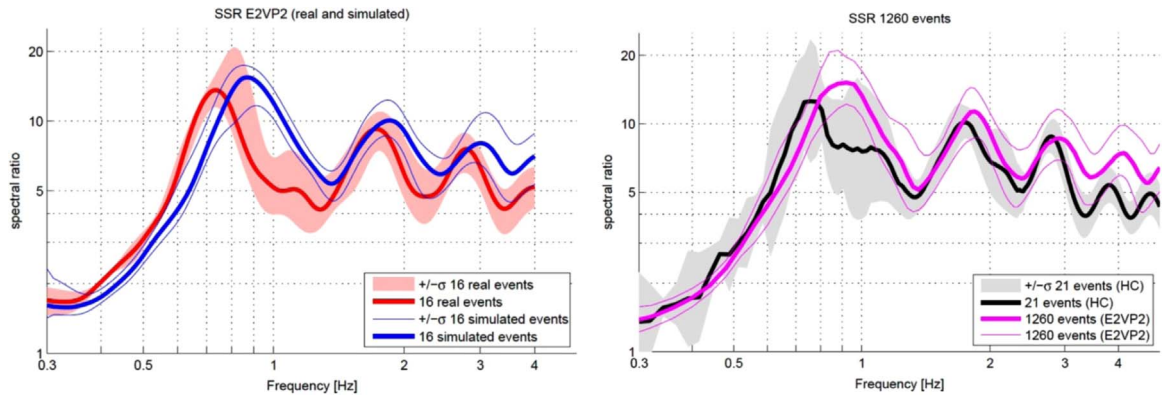

Fig. 10. Left: Median of SSR (Standard Spectral Ratios) at TST0 with TST5 as reference station, derived from the actual recordings of the 16 events of set S1 (solid red line, associated variability shown in pink), and for the corresponding E2VP2 simulations (bold blue line, associated variability shown by thin blue lines). Right: the same for another set of recordings (black line, 21 events with the best sigma to noise ratio, including more distant events outside the model box) compared with the predicted response for set S3 (solid magenta line, 1260 events on concentric circles and with various depth). (For interpretation of the references to color in this figure legend, the reader is referred to the web version of this article.)

subsets. Fig. 10a, corresponding to the 16 events of set S1 for which the TST0/TST5 ratio is available, exhibits a slight over-estimation of the site response by the E2VP2 numerical simulation, especially at frequencies between 1 and 1.5 Hz, together may be with a slight over estimation of the fundamental frequency. Fig. 10b compares the "best" instrumental estimate of TST5/TST0 transfer function, derived from a set of 21 pairs of recordings with high signal-to-noise ratio (including events from outside the model box), with the average transfer function obtained for the S3 simulation set (1260 events). An over-prediction in the same frequency range is still present, but it is also associated with a significantly larger variability of the site response (especially the observed one), and significant differences in the average instrumental ratios from the two sets of recordings. Although different, the average numerical and instrumental transfer functions are almost entirely located within the 16–84% variability range (i.e. within ± 1 standard-deviation) of each other, except around 1 Hz and beyond 3 Hz. The latter is probably indicative of an under-estimation of the damping in the sediments, while the former is probably a consequence of the high sensitivity of ground motion and site response to the source location (distance, depth and back-azimuth), which is investigated further in the next section.

5. Sensitivity studies and insight into the structure of the aleatory variability

One of the important outcome of the verification and validation exercise is the significantly smaller code-to-code distance compared to the code-to-data misfit. The latter is interpreted as resulting from errors or uncertainties in the source parameters and on the propagation model. It is therefore fully legitimate to use the numerical simulation approach to investigate, in a relative way, the sensitivity of ground motion and site response both to the variability in source parameters (i.e., the variability for a wide range of different hypocentral locations: epicentral distance, depth and backazimuth) and to the uncertainty in source parameters (i.e., to small changes in the magnitude and location parameters comparable to hypocentral location error). The synthetics obtained with the simulation approach for a large number of sources and receivers can also be used to generate some synthetic GMPEs, and to analyse the impact of the source uncertainties on the value of the aleatory variability in the light of the results of the sensitivity studies, investigating in particular how epistemic variabilities affect the within and between-event aleatory variability components.

5.1. Epistemic variability of site response

It is most often considered - at least implicitly - that site response can be decoupled from source and path effects. This section takes advantage of the S3 simulation set to investigate the sensitivity of the site response to some simple source-receiver attributes (back-azimuth, depth and distance) linked to the source-site crustal path and incoming wavefield, which may be a priori thought to impact the site response in a highly 3D environment. As a comprehensive analysis of this simulation set is provided in Maufroy et al. [33], only a short insight is provided here in relation with the impact of epistemic variability of site response on the "apparent" within-event aleatory variability. Fig. 11 displays the variability of surface/borehole transfer function with source back-azimuth and epicentral distance:

The amplification is found to exhibit a noticeable dependence on source back-azimuth. It is slightly larger around the two main peaks (0.7 Hz and 2 Hz) for southern events, and exhibits a smoother frequency-dependence for northern sources. The largest back-azimuth dependence is found for shallow, far sources while the smallest one consistently corresponds to deep, close sources (Fig. 11 bottom). This variability is related to the actual 3D geometry of the sediment-basement interface, with gentler slopes on the northern edge, and steeper slopes on the southern edges.

This dependency is frequency dependent: the variations with back-azimuth are the largest for the intermediate frequency range (around and just above the basin fundamental frequency), in between the fundamental and first higher 1D resonances, corresponding to the band mostly affected by edge-generated surface waves: their energy strongly depends on the incidence (source-depth) and back-azimuth of the incoming wavefield, in relation with the complex 3D geometry of the sediment-basement interface.

Though not shown here, the variability in site response is also found to be significantly larger when the reference is an outcropping rock at 2–3 km distance from the considered site, while it is minimum when the reference is at depth in the bedrock beneath the considered site. Vertical arrays are thus to be recommended, even though the "reference" motion at deep bedrock may significantly differ from an outcropping rock motion.

5.2. Sensitivity of ground motion to source location uncertainties

Besides the variability of site response related to large changes in back-azimuth and distance, we also investigated the impact of small changes in source location, mimicking the actual uncertainty in source location, on the variability of ground motion. The background objective is to provide a better guidance for the selection of appropriate events for future validation exercises, but it also improves our understanding of the aleatory variability of GMPEs. In that aim, we have considered the "S2" set, where the hypocentral locations of the 19 events of set S1 are moved at 27 different positions within a 4 km edge cubic box

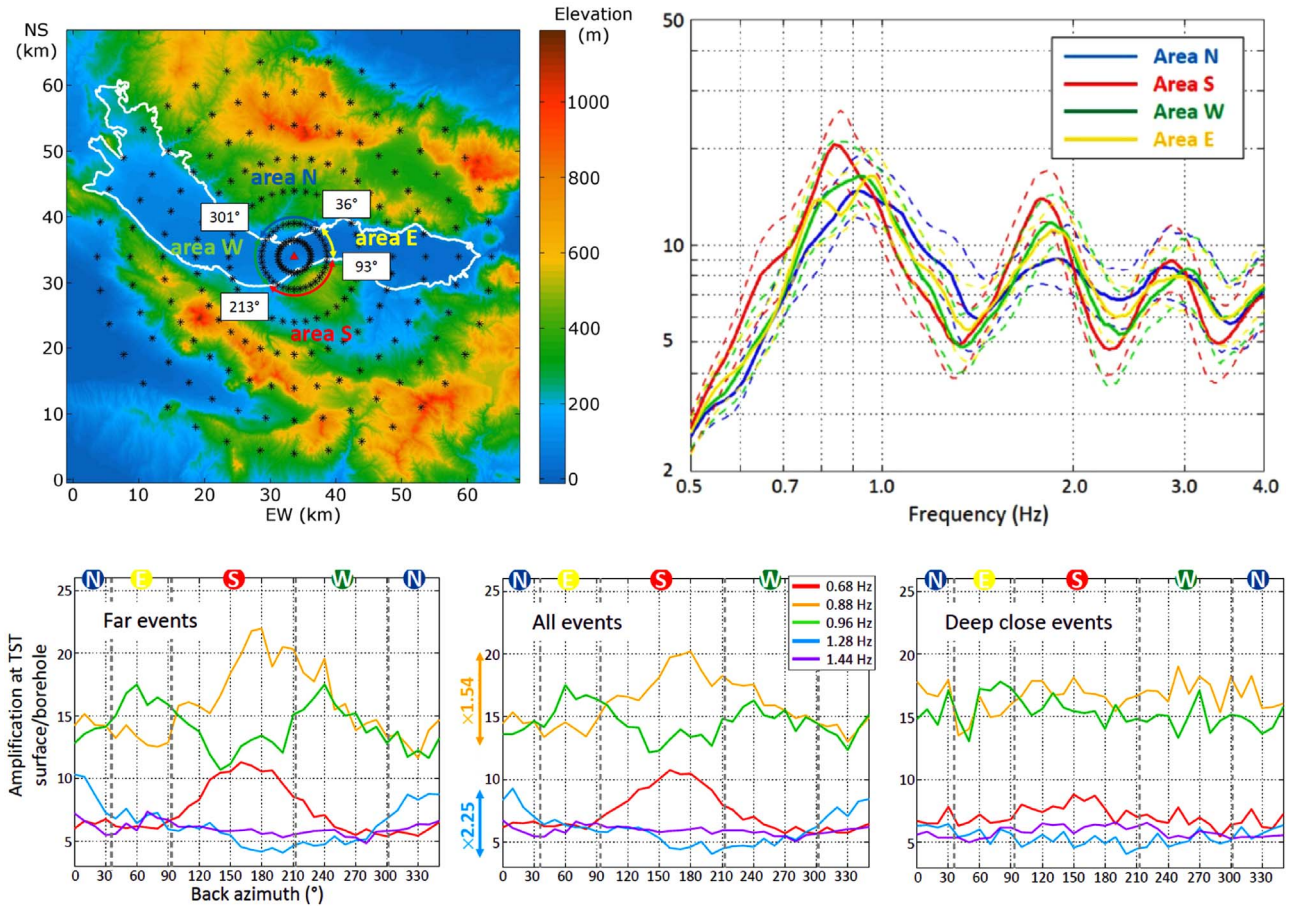

Fig. 11. Example impact of the source distance and backazimuth on the average amplification at the central TST site. Top left=Map of the basin and source location considered in this study. The basin contours are indicated by the bold white line and the surface elevation is given by the color scale. The location of the central receiver TST is shown by the red triangle, and the sources epicenters are shown by the circular setting of black crosses. Ground motions at TST are analyzed by considering 4 back-azimuth areas (N, E, S, and W) as described by the colored circular arrows; the areas are separated by the 4 back-azimuth values at TST (degrees labels) that correspond to the basin edges. Top right=average surface/borehole transfer functions for the 4 different back-azimuth ranges (solid lines=average, dotted lines=average ± one standard deviation. Bottom frames: details on the sensitivity to backazimuth for five different frequencies (color code), and three different event subsets, as indicated in the different frames (far events, all events and deep close events. (For interpretation of the references to color in this figure legend, the reader is referred to the web version of this article.)

centered on the best location estimate. The ± 2 km variability in each x, y and z direction is considered a reasonable and probably minimum estimate of the actual location uncertainty, especially for small magnitude events. For each event and each site, the variability of ground motion was estimated from the standard deviation of the acceleration response spectra for the 27 different hypocentral locations, at each frequency from 0.5 to 3.5 Hz, and then averaged over the whole frequency band. For each event, the site variabilities were averaged to provide an index of the "event" variability linked to the source location; this averaging was done separately for the four rock stations and the 11 sediment stations within the graben. The resulting values are summarized in Table 6, Fig. 12 displays the variability of acceleration spectra at site TST0 on the example of 4 different events corresponding to different depths and epicentral distances: event S10 is shallow (4 km) and close (4.2 km hypocentral distance), event S05 is deep and close (11 km and 11.9 km, respectively), event S11 is shallow and more distant (4 km, and 36 km, respectively), and event S02 is deep and distant (11 km and 20 km, respectively, see Table 2 and Fig. 3). Significant differences appear between the 4 events: the smallest variability is found for distant, deep, event S02, while the largest corresponds to the closer, shallow event S10.

A detailed look at Table 6 indicates that the variabilities at sediment and rock sites are very similar, and seem to be much more related to source location than to site response. This is further illustrated in Fig. 13, which compares the overall variabilities at sediment sites and at rock sites, together with the variability of the site transfer function. It shows that sediment and rock variabilities are comparable: their differences remain small compared to the large event-to-event variability of the sensitivity of ground motion to exact source location. Moreover, the ground motion variability is systematically larger, to much larger, than the corresponding variability of the rock-to-sediment transfer function: the former range from 0.07 to 0.30, while the latter lie between 0.04 and 0.10. Fig. 14 confirms that the ground motion variability is tightly related to the source distance and hypocentral depth: it is the largest for shallow, near sources, (variabilities larger than 0.25 for depths smaller than 5 km and epicentral distances smaller than 10 km) and the smallest for distant, deeper sources (variabilities below 0.10 for distances larger than 10 km and depth beyond 10 km, or distances beyond 20 km and depths larger than 8 km). One may notice that the site response variability also exhibits a slight decrease with increasing epicentral distance and hypocentral depth; It is however much less pronounced than for the response spectra. It may therefore be concluded that validation exercises focusing on absolute ground motion are much more difficult for very close events or very shallow, local events, unless there is a very dense local seismological array that allows to locate the events with a precision much smaller than the ± 2 km uncertainty considered here. Nevertheless, if the validation target is the site transfer function, even close and shallow events can be used.

Table 6
Sensitivity of ground motion to hypocentral location uncertainty. For the 19 events of set S1 (rows), the table lists the value of the average standard deviation (log10 scale) of the computed acceleration response spectra over the frequency range [0.5–3.2 Hz] for the 4 rock stations (Column #2), the 11 sediemnt stations (column #3) the deep borehole site at graben center (TST5, column #4) and the surface site at graben center (TST0, column #5); finally column #6 lists the corresponding values of the average variability of TST0/TST5 Fourier transfer functions over the same frequency range.

Event ID (S1 set)	Average rock	Average sediment	TST5	TST0	TST0/TST5
S01	0,126	0,141	0,131	0,129	0,081
S02	0,100	0,068	0,074	0,062	0,060
S03	0,101	0,082	0,089	0,086	0,040
S04	0,101	0,085	0,109	0,079	0,042
S05	0,244	0,219	0,294	0,246	0,069
S06	0,102	0,081	0,074	0,072	0,056
S07	0,208	0,230	0,241	0,236	0,072
S08	0,126	0,128	0,162	0,140	0,063
S09	0,263	0,276	0,234	0,240	0,065
S10	0,301	0,294	0,308	0,305	0,086
S11	0,203	0,224	0,217	0,223	0,066
S12	0,221	0,225	0,225	0,228	0,070
S13	0,114	0,106	0,124	0,114	0,058
S14	0,107	0,086	0,093	0,085	0,068
S15	0,254	0,294	0,271	0,286	0,101
S16	0,184	0,181	0,217	0,198	0,072
S17	0,157	0,113	0,171	0,132	0,049
S18	0,101	0,086	0,077	0,076	0,061
S19	0,243	0,216	0,242	0,226	0,077

5.3. Contributions to the understanding of aleatory variability

The previous sections show that the predicted ground motion exhibits an epistemic dependence on the source location, that the 3D site response varies with the source back-azimuth, and that the sensitivity to tiny changes in the source position very significantly impact the ground motion at short distances or for shallow sources. Such a complex and coupled dependence is not taken into account even in the latest, most sophisticated GMPEs. Considering that results of carefully verified numerical simulation codes are reliable, we thus used the results of the comprehensive set of 1260 virtual sources to derive synthetic GMPEs and to investigate how the above mentioned, well-identified, epistemic variability maps into the aleatory variability σ (and its within-event, φ, and between-event, τ, components). Basically, for each considered source, the numerically derived Green's functions were convolved with *ad hoc* source functions in order to simulate earthquakes with magnitude in the range 2–5. For the subsets corresponding to real events (S4 set corresponding to 52 real events), the magnitude was tuned to the real one; for all the other "virtual" events of the S3 set, the magnitude was assigned arbitrarily, in the limited range 2–5 however to be consistent with the point source assumption. These various sets of scaled synthetics were then used to derive GMPEs using the artificial neural network (ANN) approach described in Derras et al. [38] and Derras et al. [39]. The "standard" explanatory variables were the moment magnitude Mw, the epicentral distance D_{epi}, the hypocentral depth Z, and the V_{S30} site proxy. Alternative site proxies were also considered (fundamental frequency f_0, local sediment thickness h, average sediment velocity V_{Sh}), and additional source parameters as well (mainly the source back-azimuth

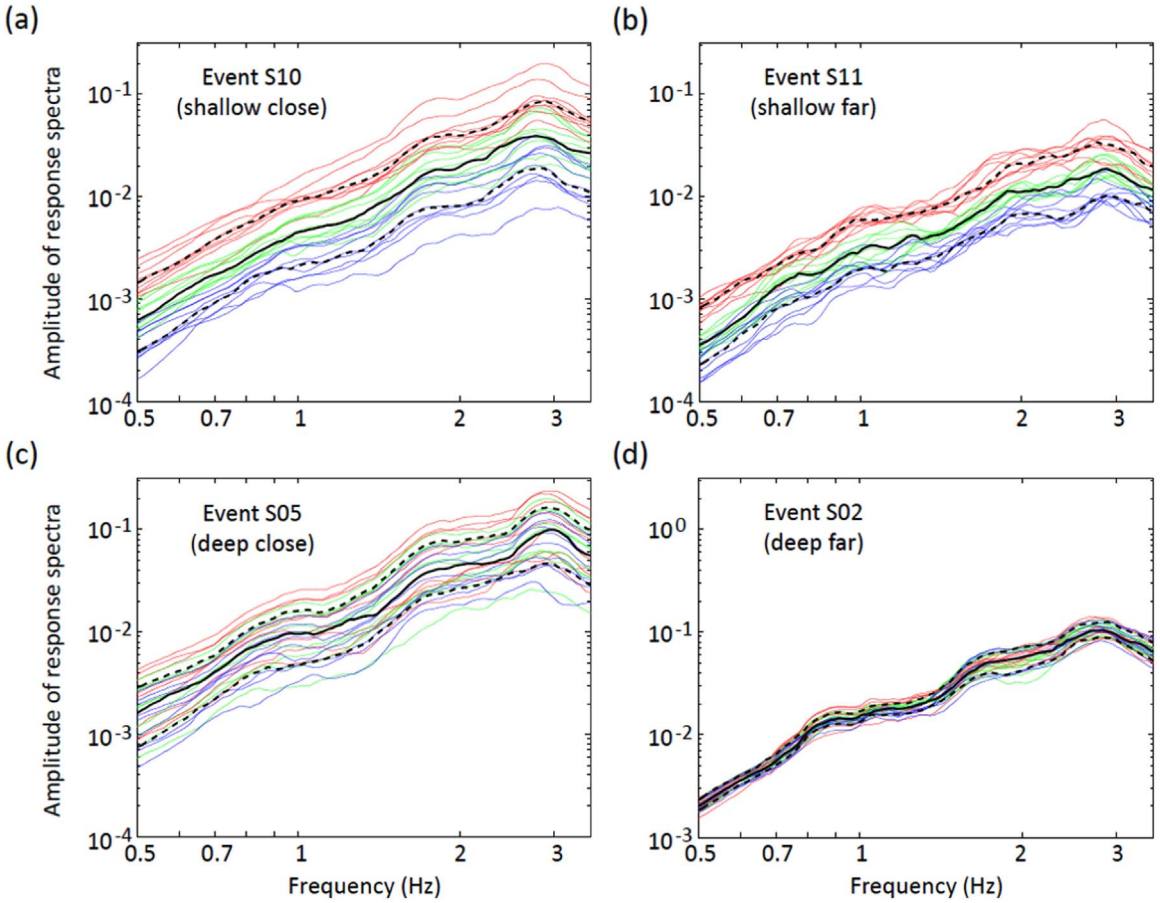

Fig. 12. Variability of the acceleration response spectra at TST0 site resulting from a ± 2 km variability in source location, for 4 different events of the S1 set. The color code corresponds to the hypocentral depth Z (red for $Z=Z_0-2$ km, green for $Z=Z_0$ and blue for $Z=Z_0+2$ km. The median response spectra is given in each panel by the solid black line, surrounded by the upper (84%) and lower (16%) percentiles as dashed black lines. (For interpretation of the references to color in this figure legend, the reader is referred to the web version of this article.)

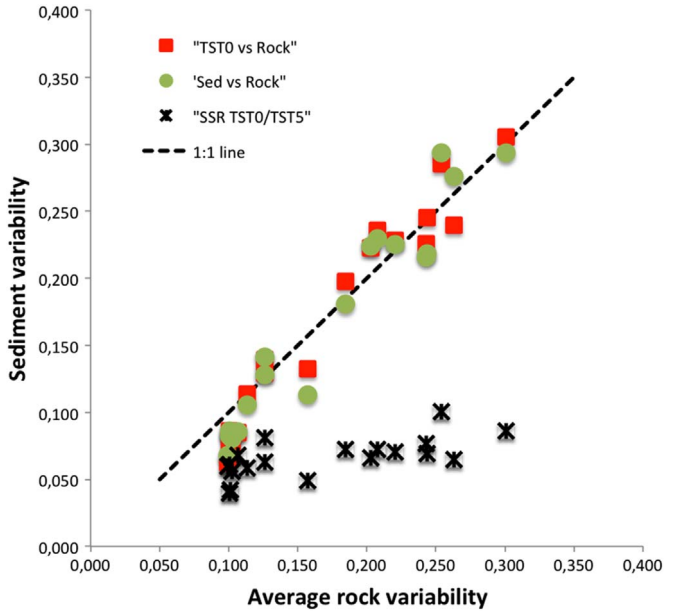

Fig. 13. Variability of the ground motion predictions resulting from a ± 2 km variability in source location, for the 19 different events of the S1 set. This variability is expressed in terms of standard deviations over the 0.5–3.3 Hz frequency range, of the predicted response spectra and TST0/TST5 transfer functions as listed in Table 6. The different symbols correspond to the average variability of response spectra at the central TST0 site (red squares), and for the 11 sediment sites (green circles), together with the variability of the TST0/TST5 transfer functions (black stars) plotted as a function of the corresponding average variability of response spectra for the 4 rock sites (abscissa). Each symbol corresponds to one of the 21 events of the S1 set. (For interpretation of the references to color in this figure legend, the reader is referred to the web version of this article.)

BAZ). The objectives were multifold:

– Compare the within and between- event variability levels between synthetics and real data (set S4).

– Investigate the effect of the size of the data set (small, S4, versus large, S3) on the values of within- and between-event variabilities.

– Investigate the effect of "controlled uncertainty" on magnitude or source localization on the between-event variability.

– Investigate the impact of various site proxies (V_{S30}, fundamental frequency f_0, local sediment thickness H, average sediment velocity V_{SH},) and of the corresponding uncertainties on the within-event variability.

– In such 3D basins, investigate the possible use of other source/site information, such as back-azimuth, in view of somewhat reducing the aleatory variability.

The results obtained so far are partly illustrated in Figs. 15 and 16 for two simple ground motion parameters, pga and pgv. Similar analyses were performed also for spectral ordinates at various oscillator frequencies (from 0.5 to 3.5 Hz), but are not significantly different from what is obtained for pga and pgv (note however that, as numerical predictions are valid only up to 4 Hz, "pga" corresponds to a limited frequency range). The main findings are summarized below.

i) The within and between event variabilities do exhibit a significant dependence on the data set. Fig. 15 displays the total, between- and within-event variabilities obtained for pga and pgv with a neural network considering moment magnitude, epicentral distance, depth and VS30 as explanatory variables, and for the two sets S3 and S4. All variabilities are shown to increase with the size of the data set. The between-event variability is found to be much larger (i.e., by about 50%) for the full S3 set than for the reduced S4 set; the size of the data set also slightly impacts the within-event variability, but to a much smaller extent (around 10–20%). The large increase of the between-event variability can be explained by the strong sensitivity of ground motion to hypocentral depth and distance. The increase of the within-event variability is consistent with the fact the S4 subset exhibits a skewed azimuthal distribution (see Fig. 7) and the observed sensitivity of site response to back-azimuth (Fig. 11). Such findings raise the attention on the need to consider a large set of recordings at a given site to have a reliable estimate of the within-event variability: in S3 set there are 1260 recordings per site, and 52 in S2 set. It thus invites to be cautious when working on too small data sets: both the between- and within-event variabilities may be underestimated, which may in turn also impact the estimates of single-site sigma. This should definitely be kept in mind in the derivation of GMPEs.

ii) It is also worth mentionning (see Maufroy et al. [40] for more details) that, for the S4 subset, the values of within and between-event variabilities are found somewhat lower on synthetics compared to their values derived from actual recordings. The corresponding values are listed in Table 7 (second and third columns). One of the reason of the lower within-event variabilities on the synthetics may come from the absence of uncertainty on the source parameters (magnitude and location). Therefore, different levels of uncertainties were artificially introduced in the magnitude and location values, without changing the corresponding synthetics computed with real, unperturbed magnitude and location. Magnitude values were randomly modified using a uniform distribution within [m−Δm, m+Δm], with Δm taken equal successively to 0.1, 0.2, 0.3, 0.4 and 0.5. For each Δm value, ten random sets of magnitude values were generated, and GMPEs derived on the corresponding sets of unchanged synthetics, with unchanged locations and distances, and modified magnitude values. The results are illustrated, on the example of the peak ground velocity PGV, in Fig. 16 left: as expected, the within-event estimate is left basically unchanged, while the between-event variability exhibits a significant, quasi-linear increase with Δm: it is doubled (from 0.12 to 0.24, log 10 values) for Δm=0.25, and tripled (up to 0.36) for Δm=0.5. Similar trends were obtained for other ground motion parameters (pga, spectral accelerations at various periods) and are not indicated here for conciseness.

iii) A similar analysis was performed to investigate the impact of uncertainties in source location. The actual locations were randomly modified using a uniform distribution centered on the actual one, with maximum deviations Δl in the x, y and z directions varying from 1 to 10 km. For each Δl value, ten random sets of modified locations were generated to avoid any set-specific bias. The right frame of Fig. 16 indicates that the within-event variability remains basically unchanged, while the between-event variability increases noticeably with source location uncertainty: the τ value increases by 25% (from 0.12 to 0.15) for a location uncertainty of ± 3 km, and by 50% (up to 0.18) for a location uncertainty of ± 5 km. Considering the average magnitude uncertainty (especially for moderate magnitude events) is at least 0.2, and the average location uncertainty is probably ranging from 2 to 5 km, our results indicate that a non negligible amount (i.e., increase by about 50–100%) of the between-event variability comes from source parameter uncertainties. The increase of variability at small magnitude reported in many recent GMPEs may therefore be a consequence of a larger location uncertainty, and investing in dense seismological networks for more precise localization may therefore constitute one of the most efficient ways to reduce sigma, especially for GMPEs including a large number of recordings from small magnitude events.

iv) The other types of source parameters that were considered for these synthetic GMPEs are the source depth Z and back-azimuth BAZ. It was found that, for the S4 data set, the τ value is significantly reduced when considering Z (from 0.2 to 0.10, i.e. by about 50%), and further reduced (from 0.10 to 0.075, 25%) when considering BAZ, while the φ value remains unchanged. Such

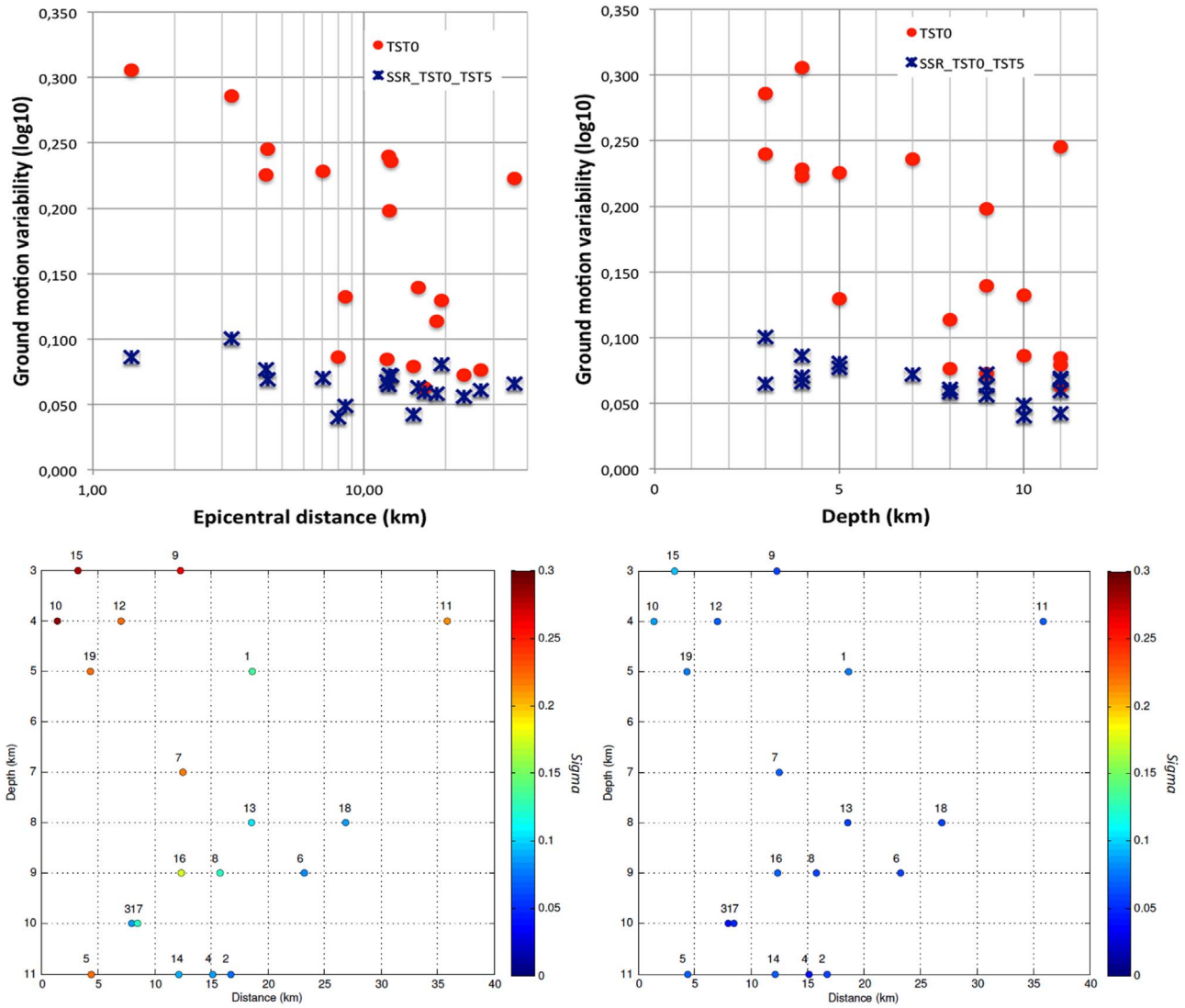

Fig. 14. Control of the ground motion variability due to source location uncertainty by epicentral distance and depth. The top row displays the dependence of variability on response spectra at TST0 (red circles) and Fourier transfer functions TST0/TST5 (blue stars) as a function of epicentral distance (left) and hypocentral depth (right). The bottom row displays the values of the variabilities of TST0 response spectra (left) and TST0/TST5 transfer functions (right) in the (epicentral distance/depth) plane: the color code indicates the corresponding variability (same scale for both plots); the labels on each symbol indicate the S1 event ID. (For interpretation of the references to color in this figure legend, the reader is referred to the web version of this article.)

results cannot be directly extrapolated to classical data sets used for the derivation of GMPEs; they however indicate that the twin parameter set (epicentral distance, depth) performs better in ground motion prediction than the sole hypocentral distance, and that, when considering a single site with a pronounced 3D underground structure, the source back-azimuth could be considered to further reduce the prediction uncertainty.

v) Finally, it was found that two site proxies, V_{S30} and f_0, perform almost equally well to account for site conditions, while the local sediment thickness H and average sediment velocity V_{SH}, which are sometimes proposed for alternative site classifications, perform much more poorly. A similar analysis was performed on the impact of uncertainties in the estimates of these site proxies on the within-event variability φ: it was found – on this particular data set – that the impact is very small, much smaller than the uncertainties on source parameters. As the number of sites is limited, and the associated geological conditions as well, further investigations are needed to generalize such results.

6. Conclusions

The use of numerical simulation has proved extremely powerful and useful for improving the understanding of the physics of ground motion from source to site. Using the simulation approach for design purposes requires much care and is much more demanding, especially when going to frequencies beyond 1 Hz. Verification and validation exercises such as E2VP will certainly be repeated in the future on other sites and datasets. In the same way as E2VP benefitted from lessons of previous similar benchmarking exercises, it is important to summarize the main lessons from the present project, and more specifically from its second phase, as the main results from E2VP1 are already summarized in Table 1.

Two important recommendations must first be mentioned, because they appeared as recurrent issues all along the 8-year life of the E2VP:

Numerical simulation codes require careful use and regular cross-checking, which proves to be a very efficient tool in securing the quality of the results, especially after code updates or improvements.

The most important aspects of accuracy of any numerical method and code that is applied for numerical prediction of earthquake ground motion in engineering projects, may be valuably verified through some

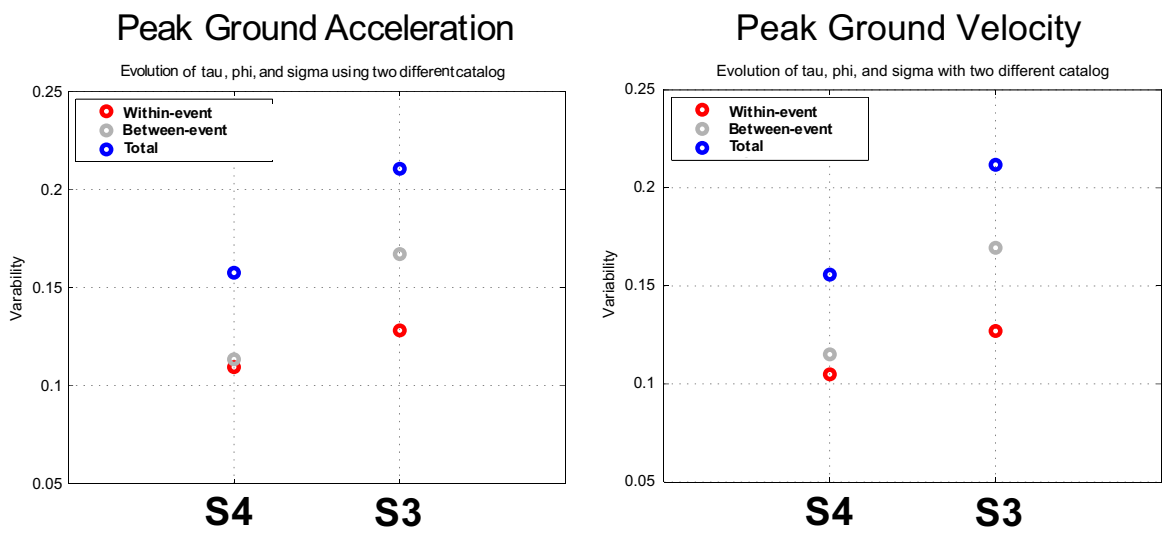

Fig. 15. Impact of data set size on the total (blue circle), within-event (red circle) and between-event (grey circle) variabilities. The S3 set and S4 subsets consist of 1260 events and 52 events, respectively, both recorded at 15 sites. The aleatory variabilities are displayed for the peak ground acceleration (left) and peak ground velocity (right).

stringent cases with already existing solutions. The canonical cases developed within E2VP, which are freely available to the seismological community (http://www.sismowine.org), can serve this purpose.

Most of the new work achieved during E2VP2 was related to validation. The comparison for the 19, relocated events has thus been found in average slightly improved for rock sites, and slightly deteriorated within the Mygdonian basin, with an overall trend for an overestimation. It was found once again that the sole site response ("hybrids") is better estimated. The significant overestimation in terms of signal amplitude (parameters C1–C4) thus comes mainly for the overestimation of the rock motion, also associated with an underestimation of signal duration (C5): both may come from the absence of scattering in the considered crustal model. When considering all the real receivers, the overall E2VP2 misfit values range between +50 and +150%, to be compared with the +40–80% of E2VP1 (on only 6 events), while the "site-response only" misfits now range around +20%, while they were around −40% for E2VP1. The modifications in the basin model have slightly improved the site response estimate, but the sensitivity to the source parameters and the associated uncertainties leads to conclude that the feasibility of validation up to frequencies around a few Hz (4 Hz in the present case) is still a real challenge, for several reasons.

- The predicted ground motion proves to be very sensitive to the exact position of the source – especially its depth and distance – for very close events and for local, shallow events: as it is unrealistic to expect a precision on localization smaller than 2 km (especially for the depth), it is therefore recommended, for validation purposes, to select events with epicentral distance R larger than 20 km and hypocentral depths Z larger than 8 km. Closer events (R > 10 km)

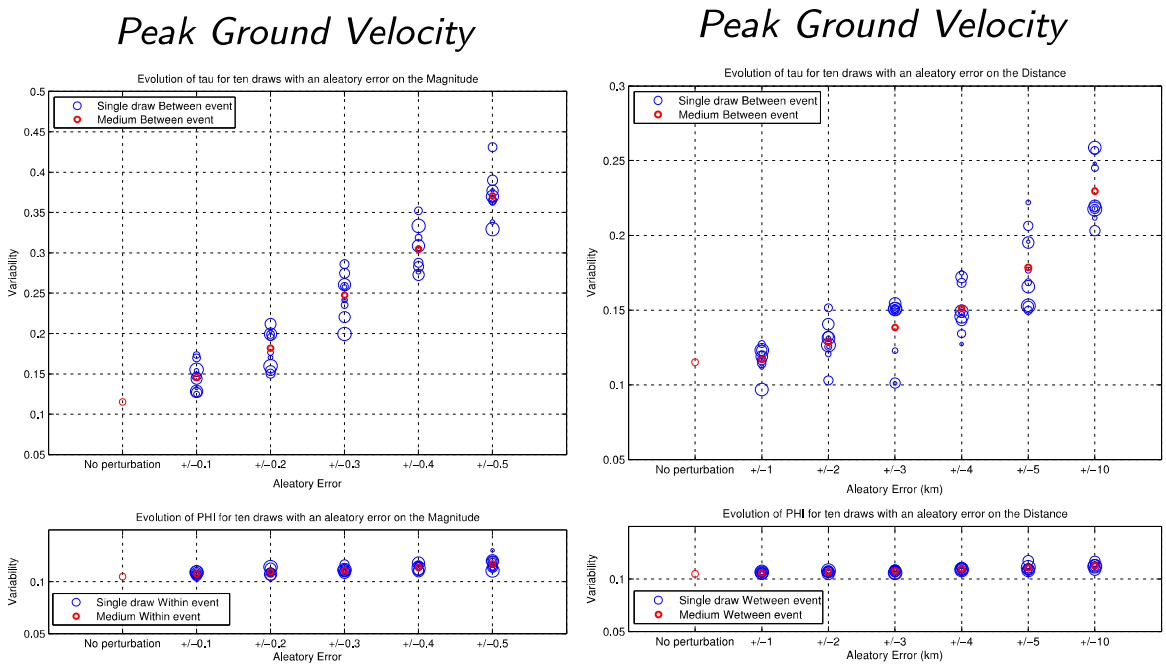

Fig. 16. Influence of the uncertainty on source parameters (magnitude, left; and location, right) on the aleatory variability components (between-event on top and within event on bottom). This influence is illustrated here for the PGV. The amount of uncertainties considered for the magnitude values and the source location are indicated on the abscissa. Each open blue symbol corresponds to one random generation of perturbated magnitude or location sets, while red circles correspond to the median values for the 10 random sets for one level of magnitude or location uncertainty. (For interpretation of the references to color in this figure legend, the reader is referred to the web version of this article.)

Table 7
Comparison of observed and "synthetic" variabilities for the S4 set. The observed values (second column) correspond to a specific GMPE derived on the basis of the S4 set by O.J. Ktenidou et al. (personal communication, see also Ktenidou et al. [41]). The synthetic values (columns 3–5) are derived with the neural network approach using the exact magnitude and location (column 3), randomly modified magnitudes (Δm= ± 0.2) and exact locations (column 4), and randomly modified locations (Δl= ± 3 km) and exact magnitudes (column 5).

	Observed, after relocation and with site information (VS30)	Synthetics, exact M and location	Synthetics, with exact location and magnitude error Δm= ± 0.2	Synthetics, with exact magnitude and location error Δl= ± 3 km
Between-event τ	0.18	0.12	0.18	0.15
Within-event φ	0.15	0.12	0.12	0.12
Total σ	0.24	0.16	0.22	0.19

can also be used, provided they are deeper (Z > 10 km)

- The misfit between observations and numerical predictions remain significantly larger than the distance between carefully selected, up-to-date, and carefully implemented numerical simulation codes. For the prediction of ground motion for expected events with a priori defined source characteristics, the numerical-simulation approach is fully legitimate in the toolbox for site-specific ground-motion estimation.
- The predictions-to-observations differences are significantly lower when considering only the site amplification, especially when the reference is at depth within a vertical array. This emphasizes the added value of "hybrid" approaches made possible by the availability of down-hole recordings and the invaluable usefulness of in-situ recordings: it seems today very difficult to predict site effects in a complex geometry context with only geological, geophysical and geotechnical information. Site instrumentation is strongly recommended, including also due attention to reference sites (downhole and outcropping rock as much as possible) for a proper "calibration" of the reference motion.
- The 3D site response however exhibits a significant dependency on the source back-azimuth, which partly explains the event-to-event variability of instrumental site-to-reference spectral ratios.

It is also worth to discuss these results in the light of a few recent studies reporting comparisons between strong motion recordings and low to intermediate frequency ground motion simulation for various moderate to significant size earthjqulkes: Chino Hills, California (2008, Mw 5.4, 336 receivers within 100 km distance, 0.1–4 Hz; Taborda and Bielak [42]), Po Plain, Italy (2012, Mw 6.0, 34 receivers within 30 km distance, 0.1–1.5 Hz; Paolucci et al. [43]), and South Napa, California (2014, Mw 6.0, 10 receivers within 20 km distance, 0.1–5 Hz; Gallovic [44]). The first two report Anderson-like [14] "goodness-of-fit" scores predominantly in the range 4–8 (i.e., basically "fair" and "good"), corresponding to simulation to recordings differences in the range 50–100%, while the last indicates PGV and response spectra ratios in the range [0.25–4]- thus with some gof scores below 4 ("poor" fit)-, most of them being in the range [0.5–2] (i.e., at least "fair"). Such average misfit values turn out to be slightly smaller than ours when considering full synthetics (see Table 5), and significantly larger when considering hybrid synthetics at the single receiver TST0, i.e., when focusing only on the 3D site response. One must keep in mind however that such a comparison must be done with caution. The values reported in these recent post-earthquake simulation studies correspond to one particular, rather large, event, while ours are an average for many smaller events. Another difference is that most often, in those studies, the target records have already been used to constrain the rupture history, while in our case the determination of source parameters is independent of the target recordings. The comparisons reported in these papers are performed after the event, and thus do not correspond to the case of a fully blind situation where the ground motion prediction is requested in advance of the event (which was actually the initial request from the French nuclear authority that launched all these benchmarking exercises).

In addition, the comprehensive sensitivity study also showed that, beyond the deterministic prediction of ground motion for a given earthquake scenario, carefully verified numerical simulation can provide a very instructive insight at the structure of the so-called "aleatory" variability of ground motion, for both its within- and between-event components. For the E2VP case, the between-event variability has been found very sensitive to hypocenter location errors (25% increase of τ for a location uncertainty of ± 3 km), and to uncertainty in magnitude estimates (doubling of τ for a Δm uncertainty of ± 0.25). Such a finding explains the increase of aleatory variability for small magnitude events in most recent GMPEs, and emphasizes the usefulness of dense seismological networks in order to reduce τ and σ. The within event, single-site variability is shown to be associated to an "epistemic" dependence of the 3D site response on the event back-azimuth (predominantly), and on distance and depth (more slighltly). This result calls for caution in the interpretation of single-station variabilities derived from a too small number of events: in the E2VP case, even 52 recordings at one site are not enough to fully capture the whole variability of site response when the azimuthal distribution is skewed.

Acknowledgements

We thank A. Kiratzi, Z. Roumelioti from AUTH for their efficient help in relocating the events, and O.J Ktenidou for her precious contribution about aleatory variability. We also thank an anonymous reviewer for his/her relevant comments and suggestions which helped improving the quality and clarity of the paper. The funding of this project was provided by CEA within the framework of the CASHIMA and SIGMA projects. The SEM calculations were performed using HPC resources from GENCI-TGCC under grants (2013–046060, 2014–046060) and using the Froggy platform from the CIMENT HPC center of Grenoble Alpes University (https://ciment.ujf-grenoble.fr, last accessed February 2016) which is supported by the Rhône-Alpes region (GRANT CPER07_13 CIRA), the OSUG@2020 labex (reference ANR10 LABX56) and the Equip@Meso project (reference ANR-10-EQPX-29-01) of the Programme Investissements d'Avenir supervised by the Agence Nationale pour la Recherche. The SPECFEM3D code used to produce the 3-D synthetic Green's functions is available at https://geodynamics.org/cig/software/specfem3d (last accessed September 2016).

References

[1] Cramer CH. Weak-motion observations and modeling for the Turkey Flat, U.S., site-effects test area near Parkfield, California. Bull Seismol Soc Am 1995;85(2):440–51.
[2] Bard P-Y. Discussion session: lessons, issues, needs and prospects, special theme session 5: Turkey Flat and Ashigara Valley experiments. In: Proceedings of the 10th world conference on earthquake engineering conference proceedings. 1992. p. 6985–88.
[3] Kawase H, Iwata T. A report on submitted results of the simultaneous simulation for Kobe. In: The effects of surface geology on seismic motion, recent progress and new horizon on ESG study. vol. 3. Balkema/CRC Press.
[4] Day SM, Bielak J, Dreger D, Graves R, Larsen S, Olsen KB, Pitarka A. Tests of 3D elastodynamic codes: final report for lifelines project 1a01, tech. rep., Pacific

Earthquake Engineering Research Center and Southern California Earthquake Center. 2001.
[5] Day SM, Bielak J, Dreger D, Graves R, Larsen S, Olsen KB, Pitarka A. Tests of 3D elastodynamic codes: final report for lifelines project 1a02, tech. rep., Pacific Earthquake Engineering Research Center. 2003.
[6] Day SM, Bielak J, Dreger D, Graves R, Larsen S, Olsen KB, Pitarka A. 3D ground motion simulations in basins: final report for lifelines project 1a03, tech. rep., Pacific Earthquake Engineering Research Center. 2005.
[7] Bielak J, Graves RW, Olsen KB, Taborda R, Ramírez-Guzmán L, Day SM, et al. The shakeout earthquake scenario: verification of three simulation sets. Geophys J Int 2010;180:375–404. http://dx.doi.org/10.1111/j.1365-246X.2009.04417.x.
[8] Chaljub E, Tsuno S, Bard P-Y. Numerical Benchmark of 3D ground motion simulation in the valley of Grenoble, French Alps. In: Bard P-Y, Chaljub E, Cornou C, Cotton F, Guéguen P (eds.), ESG2006 Proceedings. LCPC Editions, ISSN 1628-4704. Vol. 2. 2009. p. 1365–75.
[9] Tsuno S, Chaljub E, Bard P-Y. Grenoble simulation benchmark: comparison of results and main learnings. In: Bard P-Y, Chaljub E, Cornou C, Cotton F, Guéguen P (eds.), ESG2006 Proceedings. ISSN 1628-4704. Vol. 2, 2009. p. 1377–433.1436.
[10] Chaljub E, Moczo P, Tsuno S, Bard P-Y, Kristek J, Kaser M, et al. Quantitative comparison of four numerical predictions of 3D ground motion in the Grenoble valley, France. Bull Seism Soc Am 2010;100(4):1427–55.
[11] Chaljub E, Maufroy E, Moczo P, Kristek J, Hollender F, Bard P-Y, et al. 3-D numerical simulations of earthquake ground motion in sedimentary basins: testing accuracy through stringent models. Geophys J Int 2015;201(1):90–111. http://dx.doi.org/10.1093/gji/ggu472.
[12] Maufroy E, Chaljub E, Hollender F, Kristek J, Moczo P, Klin P, et al. Earthquake ground motion in the Mygdonian basin, Greece: the E2VP verification and validation of 3D numerical simulation up to 4 Hz. Bull Seism Soc Am V 2015;105:1398–418. http://dx.doi.org/10.1785/0120140228.
[13] Kristeková M, Kristek J, Moczo P. Time-frequency misfit and goodness-of-fit criteria for quantitative comparison of time signals. Geophys J Int 2009;178(2):813–25.
[14] Anderson JG. Quantitative measure of the goodness-of-fit of syn- thetic seismogramsProceedings of the 13th world conference on earthquake engineering, 2004 August 16. Canada: Vancouver, British Columbia; 2004, [Paper No. 243].
[15] Trifunac MD, Brady AG. On the correlation of seismic intensity scales with the peaks of recorded strong ground motion. Bull Seism Soc Am 1975;65(1):139–62.
[16] Kwok AO, Stewart JP, Hashash YM. Nonlinear ground-response analysis of Turkey Flat shallow stiff-soil site to strong ground motion. Bull Seismol Soc Am 2008;98:331–43.
[17] Stewart J, Kwok A. Nonlinear seismic ground response analysis: protocols and verification against array. Data PEER Annu Meet San Franc Present 2009:84.
[18] Régnier J, Bonilla LF, Bard PY, Kawase H, Bertrand E, Hollender F, Marot M, Sicilia D, Nozu A. PRENOLIN Project: a benchmark on numerical simulation of 1D non-linear site effect. 1 – verification phase based on canonical cases. 6ICEGE, Christchurch, New-Zealand; November 2015.
[19] Régnier J, Bonilla LF, Bard PY, Kawase H, Bertrand E, Hollender F, Marot M, Sicilia D, Nozu A. PRENOLIN Project: a benchmark on numerical simulation of 1D non-linear site effect. 2 – Results of the validation phase. 6ICEGE, Christchurch, New-Zealand; November 2015.
[20] Régnier J, Bonilla L-F, Bard P-Y, Bertrand E, Hollender F, Kawase H, Sicilia D, Arduino P, Amorosi A, Asimaki D, Boldini D, Chen L, Chiaradonna A, DeMartin F, Ebrille M, Elgamal A, Falcone G, Foerster E, Foti S, Garini E, Gazetas G, Gélis C, Ghofrani A, Giannakou A, Gingery JR, Glinsky N, Harmon J, Hashash Y, Iai S, Jeremić B, Kramer S, Kontoe S, Kristek J, Lanzo G, di Lernia A, Lopez-Caballero F, Marot M, McAllister G, Mercerat ED, Moczo P, Montoya-Noguera S, Musgrove M, Nieto-Ferro A, Pagliaroli A, Pisanò F, Richterova A, Sajana S, Santisi d'Avila MP, Shi J, Silvestri F, Taiebat M, Tropeano G, Verrucci L, Watanabe K. International benchmark on numerical simulations for 1D, non-linear site response (PRENOLIN): verification phase based on canonical cases. Bull Seism Soc Am 2016;106(5):2112–35. http://dx.doi.org/10.1785/0120150284.
[21] Garofalo F, Foti S, Hollender F, Bard PY, Cornou C, Cox BR, et al. InterPACIFIC project: comparison of invasive and non-invasive methods for seismic site characterization. Part I: intra-comparison of surface wave methods. Soil Dyn Earthq Eng 2016. http://dx.doi.org/10.1016/j.soildyn.2015.12.010.
[22] Garofalo F, Foti S, Hollender F, Bard P-Y, Cornou C, Cox BR, et al. Interpacific project: comparison of invasive and non-invasive methods for seuismic site characterization. Part II: intercomparison between surface-wave and borehole methods. Soil Dyn Earthq Eng 2016. http://dx.doi.org/10.1015/j.soil-dyn.2015.12.009.
[23] Novotný O, Zahradník J, Tselentis G-A. Northwestern Turkey earthquakes and the crustal structure inferred from surface waves observed in western Greece. Bull Seism Soc Am 2001;91(4):875–9.
[24] Maufroy E, Chaljub E, Hollender F, Bard P-Y, De Martin F, Roumelioti Z, Theodoulidis N, Guyonnet-Benaize C, Ktenidou O, Perron V. 3D ground motion simulations for site effects assessment: Learnings from Euroseistest Verification and Validation Project. Cashima/Sigma internal report number SIGMA-2014-D3-137. 2014. 79 pages (main texte) +131 pages (appendixes).
[25] Manakou M. Contribution to the determination of a 3D soil model for site response analysis. The case of the Mygdonian basin [Ph.D. thesis, in Greek with English abstract]. Thessaloniki (Greece): Department of Civil Engineering, Aristotle University of Thessaloniki; 2007.
[26] Manakou M, Raptakis D, Chávez-García FJ, Apostolidis PI, Pitilakis K. 3D soil structure of the Mygdonian basin for site response analysis. Soil Dyn Earthq Eng 2010;30:1198–211.
[27] Caumon G, Collon-Drouaillet P, Le Carlier de Veslud C, Viseur S, Sausse J. Surface-based 3D modelling of geological structures. Math Geosci 2009;41:927–45.
[28] Mallet JL, {G}eomodeling . Applied Geostatistics. New York, NY: Oxford University Press; 2002.
[29] I.G.M.E. Geological Maps of Greece, Scale 1:50.000. Sheets: Thessaloniki, Epanomi,Vasilika, Thermi, Polygiros, Zagliveri.
[30] Mountrakis D, et al. Special edition of the neotectonic map of Greece, Earthquake Planning and Protection Organization (OASP). Scale 1:100.000. Sheets: Langadas, Thessaloniki; 1995–1996.
[31] Sotiriadis L, Psiolovikos A, Vavliakis E, Syrides G. Some tertiary and quaternary basins of Macedonia/Greece. Formation and evolution. Clausthal Geol Abh 1983:21.
[32] Raptakis D, Manakou M, Chávez-García FJ, Makra K, Pitilakis K. 3D configuration of Mygdonian basin and preliminary estimate of its site response. Soil Dyn Earthq Eng 2005;25:871–87.
[33] Maufroy E, Chaljub E, Theodoulidis N, Roumelioti Z, Hollender F, Bard P-Y. Source-related variability of site response in the Mygdonian basin, Greece, from accelerometric recordings and 3D numerical simulations. Submitt Bull Seism Soic. Am, Minor Revis 2016.
[34] Causse M, Chaljub E, Cotton F, Cornou C, Bard P-Y. New approach for coupling k-2 and empirical Green's functions: application to the blind prediction of broadband ground motion in the Grenoble basin. Geophys J Int 2009. http://dx.doi.org/10.1111/j.1365-246X.2009.04354.x.
[35] De Martin F. Verification of a spectral-element method code for the Southern California Earthquake Center LOH.3 viscoelastic case. Bull Seismol Soc Am 2011;101(6):2855–65.
[36] Moczo P, Kristek J, Galis M. The finite-difference modelling of earthquake motions: waves and ruptures. Cambridge University Press; 2014.
[37] Papazachos CB. Crustal P- and S-velocity structure of the Serbomacedonian Massif (Northern Greece) obtained by non-linear inversion of traveltimes. Geophys J Int 1998;134:25–39. http://dx.doi.org/10.1046/j.1365-246x.1998.00558.x.
[38] Derras B, Bard PY, Cotton F, Bekkouche A. Adapting the neural network approach to PGA prediction: an example based on the KiK-net data. Bull Seism Soc Am 2012;102(4):1446–61. http://dx.doi.org/10.1785/0120110088.
[39] Derras B, Bard P-Y, Cotton F. Towards fully data driven ground-motion prediction models for Europe, in press and on line. Bull Earthq Eng 2014;12-1:495–516. http://dx.doi.org/10.1007/s10518-013-9481-0.
[40] Maufroy E, Chaljub E, Hollender F, Bard P-Y, Kristek J, Moczo P, De Martin F, Theodoulidis N, Manakou M, Guyonnet-Benaize C, Pitilakis K, Hollard N. Validating the numerical simulation approach for ground motion prediction: General framework and latest lessons from the E2VP project. In: vited theme lecture, 6ICEGE (Proceedings of the 6th international conference on earthquake geotechnical engineering). Christchurch, New-Zealand; November 1–4, 2015. paper #452, 19 pages.
[41] Ktenidou OJ, Roumelioti Z, Abrahamson NA, Cotton F, Pitilakis K. Ground motion uncertainty and variability (single-station sigma): insights from Euroseistest, Greece, 2014, Abstract S42B-03 presented at 2014 Fall Meeting, AGU (American Geophysical Union), San Francisco, Calif., 15–19 Dec. 2014
[42] Taborda R, Bielak J. Ground-motion simulation and validation of the 2008 Chino Hills, California, Earthquake. Bull Seismol Soc Am 2013;103(1):131–56.
[43] Paolucci R, Mazzieri I, Smerzini C. Anatomy of strong ground motion: near-source records and three-dimensional physics-based numerical simulations of the Mw 6.0 2012 May 29 Po Plain earthquake, Italy. Geophys J Int 2015;203:2001–20.
[44] Gallovic F. Modeling velocity recordings of the Mw 6.0 South Napa, California, Earthquake: unilateral event with weak high-frequency directivity. Seismol Res Lett 2016;87(1). http://dx.doi.org/10.1785/0220150042.

Chapter V

Appendices

V.1 Towards Seismic Scattering and Absorption Mapping

SSAM – Projet de Recherche Collaborative
Appel à projets générique 2016
Défi des autres savoirs
Seismic Scattering and Absorption Mapping

Contents

Abstract

Among the physical processes that control the amplitude of seismic waves, attenuation is probably the most poorly understood and undetermined factor. Deciphering and quantifying the mechanisms at the origin of wave attenuation represents a current frontier in seismology and allied fields. At the phenomenological level, attenuation processes fall into two categories: elastic processes such as scattering of seismic waves by small-scale heterogeneities; inelastic processes such as absorption and dissipation caused by the anleasticity of the geological materials or fluid flow. The separation of scattering and absorption phenomena is key to make the link between frequency-dependent attenuation of seismic waves and mechanisms of energy dissipation proposed in the rock physics literature. The objective of the proposal SSAM is to develop a genuine tomographic approach to the Mapping of Seismic Scattering and Absorption properties of Earth materials with applications to the structure and dynamics of the continental crust, and seismic hazard assessment. To carry out this research, we will elaborate on recent theoretical advances in the field of wave multiple scattering and random signal processing which pave the way for the development of an inversion technique exploiting diffuse seismic wavefields and ambient noise in the 0.05-30 Hz frequency band. This methodological proposal, which brings together experts in the theory of wave propagation in complex media, state-of-the-art numerical methods and seismic tomography relies on a three-fold approach: (i) At the theoretical level, our work is based on recent advances of the project coordinator in the field of radiative transfer of seismic waves, which let us foresee the possibility to separate scattering and absorption phenomena. (ii) State-of-the art numerical simulations of seismic wave propagation in heterogeneous media will facilitate the validation of the theoretical approach, will allow us to test our inversion tools in realistic situations and to extend our approach to the field of ambient noise. (iii) Combined with data analysis from dense seismic networks, our tomographic approach should provide high-resolution maps of the scattering and absorption properties of geological media at spatial scales ranging from the sedimentary basin to the continental crust of Western Europe. At the sedimentary basin scale, attenuation models will facilitate the quantification of the variability of ground motions in connection with the presence of small-scale heterogeneities, thereby reducing epistemic uncertainties in seismic hazard assessment. At the european scale, attenuation models will provide a novel high-resolution characterization of crustal rock properties, independent of the seismic velocity models. Together with the latter, scattering and absorption tomography has the potential to unravel the mechanisms underlying the creation of small-scale heterogeneities as well as the role of fluids in the dissipation of seismic energy.

Partner	Last Name	First Name	Current Position	Involvement in the project (PM)	Contribution to the project
IRAP	MARGERIN	Ludovic	CNRS Researcher (CR1)	28	Project Coordinator, theory and numerical implementation of sensitivity kernels for coda waves
IRAP	CALVET	Marie	Physicien Adjoint (Associate Professor)	15	Inverse problem and implementation of scattering/absorption tomography, geological interpretation of the results
IRAP	BYSTRICKY	Micha	Associate Professor	6	Interpretation of the results and relation with physical properties of rocks
IRAP			Master student then Ph.D student	5+36	Attenuation tomography of Europe
ISTerre	CHALJUB	Emmanuel	Physicien Adjoint	15,6	Design of heterogeneity models, numerical simulations of random wave fields
ISTerre	STEHLY	Laurent	Physicien Adjoint	12,6	Sensitivity functions for noise wavefields
ISTerre			Master student then Ph.D student	5+36	Sensitivity of noise to source distribution and attenuation tomography of the Argostoli Basin
ISTerre			Master student	5	Development of a software suite for distributed processing of seismic data
BRGM	DE MARTIN	Florent	Research Engineer	5,4	Numerical simulations and dissemination of scientific results
BRGM			IT Engineer	6	Construction of synthetic seismogram catalogue

Table 1 Summary table of the personnel involved in the project SSAM. Note: the "precariousness" rate (taux de précarité) R of our proposal is defined as the ratio between the research time of non-permanent participants supported by ANR and the research time of all participants, independent of their funding (the calculation excludes Ph.D and Master students). We find $R = (24+4)/(25.8+13.8+3.6+24+15.6+12.6+5.4+4) = 26.71\%$ which is below the rate of 30% recommended by ANR.

1 Context, position and objectives of the detailed proposal

Much of our knowledge about the natural resources and deep structure of the Earth's crust comes from high-resolution tomography of seismic velocities. But this technique, which has proven so effective, offers only an incomplete description of the medium properties. Any natural material contains small-scale heterogeneities, fundamentally unresolvable by velocity tomography, which scatter and absorb seismic energy and entail both attenuation and large variability of ground motions (see Figure 1). Deciphering and quantifying the mechanisms at the origin of attenuation represents a current frontier in seismology and allied fields. The objective of the proposal SSAM is to develop a genuine tomographic approach to the Mapping of Seismic Scattering and Absorption properties of Earth materials with applications to the structure and dynamics of the continental crust and seismic hazard assessment. While the outputs of our research have direct implications for the design of future hazard maps, our proposal focuses on the development of methodological tools that aim at the quantification of the basic processes -scattering and absorption-, which are responsible for the attenuation of seismic

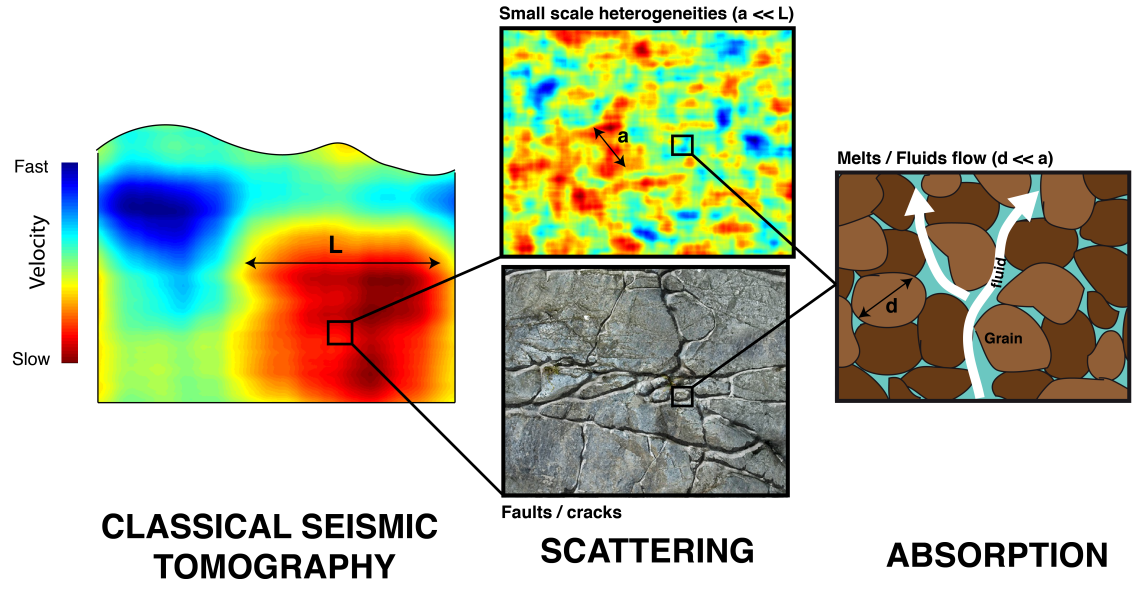

Figure 1 Schematic view of the processes and spatial scales involved in seismic wave attenuation. Scattering is caused by small-scale elastic fluctuations or mechanical discontinuities which cannot be resolved by classical tomographic methods. Absorption is caused by anelastic processes, such as viscous dissipation, fluid flow between fractures, or at the pore scale.

waves.

1.1 What can we learn from scattering/absorption tomography?

1.1.1 Implications for the structure and dynamics of the crust

A number of physical models have been proposed in the literature to explain the absorption of seismic energy (see e.g. Mavko et al. 2009, for a review). However, in practical applications, it remains difficult to pinpoint a particular mechanism. The principal obstacle to the characterization of absorption processes is the intrication between scattering attenuation caused by small-scale heterogeneities in the range [0.1-10]km and intrinsic attenuation. As evidenced by the long-lasting *seismic coda* (see Sato et al. 2012, for a review), multiple-scattering is prominent in the crust and masks the absorption processes.

Within the framework of the SSAM proposal, we will develop a new technique to map *separately* the scattering and absorption properties of geological media as a function of frequency. While previous attempts in this direction have previously been made, they all rely on a *regionalization* of the data and implicitly assume spatially *homogeneous* properties (see Sato et al. 2012, and references therein). As illustrated in Figure 1, absorption properties (in particular their frequency dependence) shed light on physical processes occurring at spatial scales that are completely inaccessible by standard methods. By combining our new measurements with the results of classical velocity tomography which are already available, we expect to put constraints on the presence, nature and topology of fluids that are thought to be ubiquitous in the crust. Let us remark that there is still a gap to bridge between mechanisms that are described at the laboratory scale and field measurements, simply because the range of frequencies does not usually overlap (Wang 2010; Adelinet et al. 2010). By mapping precisely the absorption properties of geological units, our approach may also be used to establish empirical attenuation laws that in turn may guide the development or discrimination of physical attenuation models that are relevant in the [0.05-30]Hz frequency band.

As illustrated in Figure 1, small-scale heterogeneities, which are prominent in the crust, are responsible for seismic wave scattering. Conversely, frequency-dependent scattering attenuation provides major constraints on the texture of geological media: media that are poor (resp. rich) in small scales have smooth (resp. rough) aspects. As tectonic processes are responsible for the creation of small-scale heterogeneities, they very likely leave specific imprints in the texture of the medium. Therefore, as previously demonstrated by the proposers

in the case of the Earth's inner core, detailed mapping of scattering properties may unravel key information on the dynamical processes at work in the crust (Monnereau et al. 2010).

1.1.2 Implications for seismic hazard

In the context of risk studies, the extreme variability of ground motion amplitude and duration observed over a broad range of spatial scales (100m-100km) is one of the fundamental sources of epistemic uncertainty in the evaluation of seismic hazard. Among the physical processes that control the amplitude of seismic waves, attenuation is probably the most poorly understood and undetermined factor, and plays an important role in various "hot" engineering seismology topics. For instance attenuation is identified as the controlling phenomenon of the kappa parameter which is used by engineers to characterize the high-frequency content of ground motions (Anderson and Hough 1984; Parolai et al. 2015). Scattering also controls the generation of surface waves at major surface heterogeneities such as alluvial deposits, topography and possibly buildings (Imtiaz et al. 2014). Despite its recognized importance, there is no routine measurement of attenuation in engineering applications. Scattering is most often ignored and absorption is usually taken as inversely proportional to the shear wave velocity, but this is only a convention hiding a lack of knowledge. The mapping of scattering and absorption properties will facilitate the design of realistic models of both frequency-dependent intrinsic attenuation and small-scale heterogeneity, and will push back the current frontiers of strong ground motion predictions for relevant targets such as sedimentary basins, thereby considerably reducing the epistemic uncertainty.

In the same context, the design of seismic hazard maps at regional or continental scale relies heavily on so-called "ground motion prediction equations" (GMPE) which require the knowledge of a frequency-dependent quality factor (e.g. Douglas 2003). Because attenuation displays short-scale (few tens of km) lateral variations in the crust, these GMPE often fail to predict the observed amplitudes thereby introducing large uncertainties in ground motion estimations. To overcome this limitation, next generation GMPE should obviously incorporate 2-D (3-D) spatial variations of the quality factor and will directly benefit from the kind of high-resolution attenuation models we aim to develop (Pasyanos 2015).

At a more local scale (i.e., site specific studies), attenuation mapping would facilitate the calibration of nonlinear soil models at intermediate strain levels $\approx 10^{-5}$-10^{-3} (Hartzell et al. 2004). After the dramatic nuclear accident triggered by the 2011 Tohoku earthquake, a better assessment of nonlinear site response is currently under deep investigation in the workpackage PRENOLIN of the SINAPS@ Project (funded by the ANR "Investissement d'Avenir - recherche en matière de sureté nucléaire et de radioprotection"). The attenuation factors that we intend to map at local scale could be directly used by such nonlinear models for calibration purposes.

1.2 Scattering and absorption tomography with random wave fields: proof of concept

1.2.1 Exploiting multiply-scattered waves: why?

A number of techniques have been devised to retrieve attenuation information from the modeling of direct seismic waves emitted by earthquakes. A major issue with the use of deterministic and ballistic signals lies in the fact that their amplitude is affected by multiple factors that are difficult to disentangle in practice: source radiation pattern, geometrical effects such as focussing/defocussing, site effects caused by surface layering, and last but not least attenuation. In addition, since both scattering –the effect of small-scale elastic fluctuations– and absorption –the dissipation of seismic energy– manifest themselves as an approximately exponential decay of direct wave amplitude with distance, it is not possible to separate their effects from attenuation measurements based on ballistic waves only. This feature is highly undesirable since scattering and dissipation convey independent and complementary information on the nature of the medium. Moreover, while absorption removes seismic energy from the medium and therefore reduces the overall amplitude of ground motions, scattering can entrap energy in the most heterogeneous regions, and entail a dramatic increase of the signal duration. In conclusion, whether one adopts a purely geophysical or more risk-oriented viewpoint, the separation of scattering and absorption effects is a crucial issue, and a real seismological challenge.

In this proposal, we argue that the modeling of scattered seismic signals, which are prominent in the short period seismic wave field (typically less than 20s), offers an elegant and efficient solution to the problem of mapping seismic attenuation. In particular, the tail portion of the seismogram known as the *seismic coda*, which is composed of waves multiply-scattered by crustal heterogeneities, displays a number of interesting features

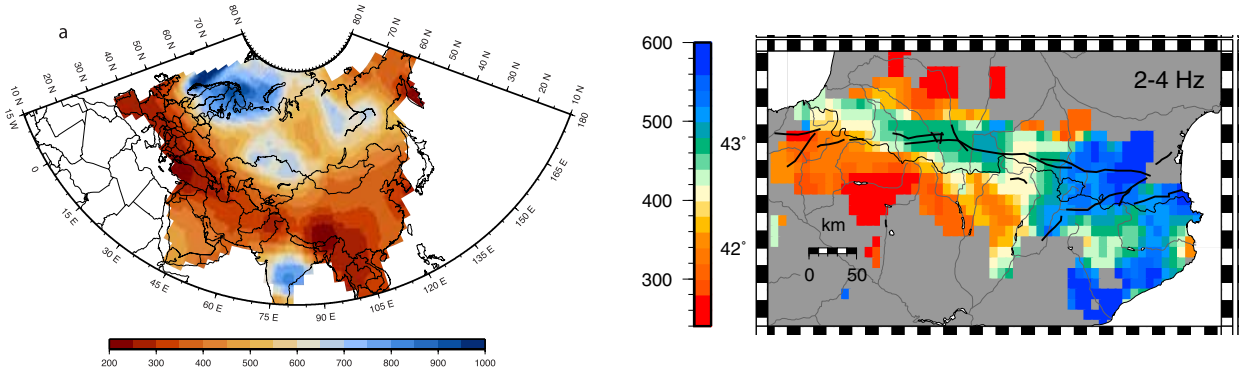

Figure 2 Left: map of the seismic coda wave quality factor Q_c for Eurasia (taken from Romanowicz and Mitchell 2007). Right: map of Q_c for the Pyrenees (Calvet et al. 2013). Red (blue) corresponds to high (low) attenuation.

for attenuation studies. In sharp contrast with ballistic arrivals, the rate of decay of the coda is not affected by the source mechanism or the local site effects, but is a sensitive function of the geological environment (Fehler and Sato 2003). Moreover, a number of observations as well as numerical experiments support the idea that scattering and absorption have distinct impacts on the shape of the seismic coda: increasing the scattering strength results in a broadening of the coda envelope, while increasing absorption yields a faster decay rate of the coda. These simple properties form the physical basis for the separation of scattering and absorption effects from coda waves.

The mathematical model relating the scattering and absorption properties of the medium to the spatio-temporal energy distribution of coda waves is known as the theory of radiative transfer (RT) or transport theory in short. This model has been adopted in a broad range of disciplines such as IR optical tomography, ultrasonics, astrophysics, to cite a few only. A concise introduction to radiative transfer methods in seismology can be found in Margerin (2005). At least three facts have limited the applications of RT theory to seismic data. First of all, because late arrivals explore a broad volume of the medium, it is widely believed that coda waves are inherently devoid of precise local information, and therefore inadequate for tomographic purposes. Second, efficient numerical methods to solve globally the transport equation have been lacking for a long time, even for the trivial case of a homogeneous scattering medium. Finally, the quantitative relation between spatial variations of scattering and /or absorption, or in other words the sensitivity of coda waves to a local change of propagation properties was not known. In the past two years, the project coordinator (PC) and his colleagues have made decisive progresses on all three fronts and are now in a position to develop a genuine tomography of scattering and absorption properties based on scattered seismic signals. All previous attempts at mapping scattering/absorption properties rely on the assumption that the propagation medium is statistically *homogeneous* in the region under investigation (Fehler et al. 1992; Hoshiba 1993; Sato et al. 2012), thereby severely limiting the spatial resolution of such approaches.

Thanks to the densification of seismic networks and the development of database facilities in Europe, we hope to take full advantage of our new theoretical approach. Figure 2 illustrates the tremendous gain of spatial resolution that may be achieved thanks to the use of earthquake data from dense permanent networks. This Figure represents a map of the decay rate of coda waves, quantified by the coda quality factor Q_c. On the left, we show a map of Q_c for the crust of Eurasia taken from the state-of-the-art Treatise on Geophysics (2007). Only very large scale variations correlated with mountain ranges and cratonic areas show up. Note that metropolitan France is represented by one red Pixel at this scale. The contrast with the Q_c map (right) obtained by our group for the Pyrenees is spectacular. We want to emphasize that this map is not the result of a tomography, but a mere representation of the observed variability of the coda decay obtained with the aid of earthquake data from permanent seismic networks. On this map, the sedimentary basins and the axial pyrenean zone show up clearly in the western part of the range, demonstrating a correlation with major geological units. But even more interesting is the sharp discontinuity between the eastern and western Pyrenees, which is not apparent in the geology and which suggests that attenuation studies may reveal previously undetected deep geological units.

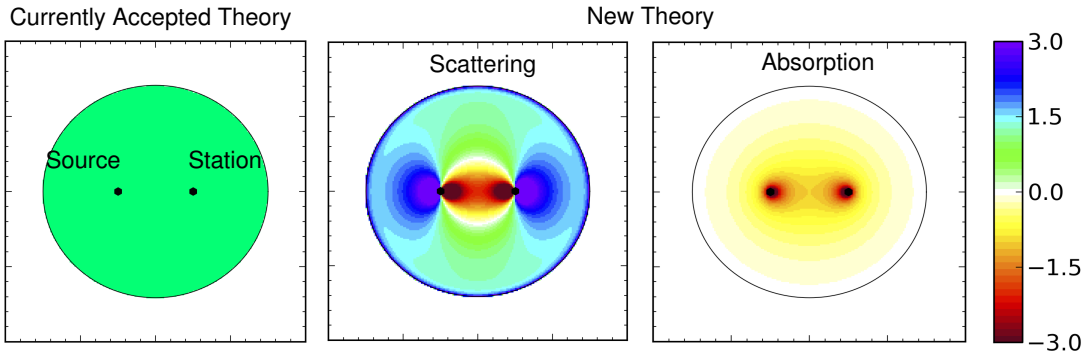

Figure 3 Map view of the sensitivity of coda waves to a perturbation of scattering and absorption properties in the medium. Left: the currently accepted view with uniform sensitivity and no distinction between attenuation mechanisms. Center: "true" sensitivity to scattering. Right: "true" sensitivity to absorption. Color scale in arbitrary units. The black line delimits the area sampled by the waves after twice the ballistic shear wave arrival time (Mayor et al. 2014).

Figure 2 therefore conveys two crucial messages: (1) there exist rapid spatial variations of attenuation in the crust that have remained undetected so far; (2) the massive deployments of seismic stations which took place in the last 15 years offer the opportunity to map these variations with unprecedented resolution. In seismically active regions which are the most interesting for both risk and geodynamic studies, earthquake records should suffice for our purposes. In more quiet regions, we will take advantage of the recent advances in signal-processing techniques which allow the passive reconstruction of the Green's function –including the scattered coda– from ambient noise records.

Figure 3 serves to illustrate the dramatic increase of spatial resolution that we may expect thanks to the tomographic technique we intend to develop. On this Figure, the black dots show the location of the source and station and the black ellipse delimits the area (volume) sampled by the waves at a given lapse time in the coda. In this case, we have chosen twice the travel time of ballistic shear waves, a value commonly found in the literature. The left plot shows the commonly accepted view on the spatial sensitivity of coda waves, which is uniformly distributed inside the causality ellipse. In the center we show the "true" sensitivity function of coda waves to scattering perturbations, derived from RT theory by our group (Mayor et al. 2014; Margerin et al. 2016). In red (blue) areas, an increase of the scattering level entails a decrease (increase) of the amplitude of the coda at the given lapse-time. The sensitivity displays fine spatial variations which are completely absent in the classical view. The approximation apparent in Figure 3 (left) added to the sparse data coverage in turn explain why all rapid spatial variations of attenuation are washed out in images such as the one shown on Figure 2 (left). Note also that the color scale in Figure 3 has been saturated to enhance the visibility: the sensitivity tends in fact to infinity as one approaches the source and station, which implies that coda waves are extremely sensitive to changes occurring in the vicinity of these 2 points. This feature is a strong argument in favor of the fact that coda waves are sensitive to *local* changes, contrary to what was believed so far. We have successfully implemented a simplified version of the kernel shown in Figure 3 (right) to obtain a map of the depth-averaged absorption properties of the crust in the Western Alps with a lateral resolution of about 100km, thereby demonstrating the feasibility of our project (Mayor et al. 2016). Let us finally remark that if we perturb absorption instead of scattering, a very different sensitivity function is obtained (Figure 3, right), which strongly supports the idea that separation of scattering and absorption effects is indeed possible with scattered waves. Sensitivity functions of the RT equation form the cornerstone of the linearized inversion strategy we intend to follow. However, it should be pointed out that the kernels shown in Figure 3 (center + right) need to be generalized in several ways. In the scientific program, we describe the necessary improvements and their technical solutions.

1.2.2 Exploiting the noise wave field: development and numerical validation

Following early developments in acoustics (Weaver and Lobkis 2001), it has been shown that the Green's function between distant seismic stations can be retrieved from the correlation of seismic noise (Shapiro and Campillo 2004). To take advantage of the recent developments in ambient noise processing, we will make every effort to extend our approach to the Greens Functions (GF) retrieved by cross-correlation. This is admittedly a theoretical and methodological challenge, but well worth pursuing in view of the potential benefits. One of the chief interests of analyzing noise records lies in the fact that they allow the reconstruction of GF between arbitrary pairs of seismic stations, thereby increasing tremendously the path coverage in regions of low seismic activity.

Recently, several studies have suggested that the attenuation of surface waves may be estimated using ambient noise data. Based on a semi-empirical model of the coherency of ambient noise, Prieto et al. (2009) built a 1D shear wave attenuation model of southern California. In Prieto's approach, the spatial decay of the envelope of the coherency is fitted with an exponential function containing a single spatial scale representing the attenuation length. This method was extended by Lawrence and Prieto (2011) to map the attenuation of Rayleigh waves in the western US in the 8-32s period band. It is worth emphasizing that the interpretation of the exponential term is a subject of heated debates, as it depends on a number of ingredients, including the spatial distribution of noise sources and the processing of data.

The amplitude of direct arrivals reconstructed by noise cross-correlations has also been analyzed by Prieto and Beroza (2008); Lin et al. (2011); Denolle et al. (2013). These authors have argued that the amplitude decay of Rayleigh waves with distance is similar for earthquake data and empirical Green's function reconstructed from noise cross-correlations. Nevertheless, the interpretation of the amplitude of direct waves reconstructed by cross-correlations remains quite controversial, since these waves are affected by the same factors as earthquake data, but with two additional complexities: (1) the noise source distribution varies in time and space, and (2) the processing technique has a strong impact on the retrieved amplitudes (e.g. Seats et al. 2012). It is well known that noise sources are not uniformly distributed at the surface of the Earth, leading to azimuthal variations in the strength of ambient noise sources. As a consequence, the amplitude of noise correlations depends heavily on the azimuth of the station pair considered. For this reason, it is difficult to map lateral variations of attenuation using station pairs having different orientations. Moreover, Cupillard and Capdeville (2010) have shown using numerical simulations that in the case of a non-uniform distribution of noise sources, the geometrical spreading of noise cross-correlations depends on the source distribution. If this effect is not properly taken into account, it can lead to erroneous attenuation measurements.

The emphasis of our research will be on the analysis of the *full* waveform of noise- based Green's function, including the coda. The analysis of the correlation properties of this coda by Stehly et al. (2008) supports the view that, very much like the coda of earthquakes, it is composed of multiply-scattered waves and may therefore be exploited to image scattering and absorption properties. Furthermore, the numerical study by Colombi et al. (2014) strongly suggests that coda waves are much less sensitive than direct waves to the azimuthal anisotropy of the noise source distribution. To clarify the interpretation of the amplitude of noise cross-correlations, we propose to follow an empirical approach based on numerical simulations. Contrary to previous investigations, we will to take into account the influence of scattering by small-scale heterogeneities of the medium which are widespread in the crust and which have been overlooked in most theoretical approaches so far. We will take advantage of the reciprocity of the wave equation to perform a joint numerical study of noise cross-correlation functions *and* coda waves in heterogeneous media *at no extra numerical cost*. How this may be achieved in practice is detailed in the technical section of this proposal.

The methodological developments will be greatly facilitated by the construction of a catalog of synthetic noise and coda waveforms based on state-of-the-art numerical simulations of wave propagation in scattering and absorbing media. This database, which will be built at an early stage of the project and made available to the seismological community, will serve two purposes: (1) Define the limits of validity and the spatial resolution of a linearized scattering/absorption tomography in a controlled situation. (2) Evaluate numerically the sensitivity kernels of noise-reconstructed coda waves w.r.t. the relevant physical parameters: scattering, absorption and noise source distribution. To build this catalog, we will calculate the GF of the wave equation in a variety of random heterogeneous media, for series of point-like white-noise sources distributed on a grid.

Exploiting the linearity of the wave equation, the action of the different sources can then be combined at will to analyze the influence of the noise source distribution on the retrieved GF amplitude. The same game can be played with the propagation medium by perturbing locally the variance of velocity fluctuations and/or the intrinsic quality factor quantifying the amount of absorption. To simulate major geophysical boundaries such as basin edges, more complex models combining small-scale heterogeneities with sharp discontinuities may also be considered. Armed with this catalog of synthetic seismograms, we should get a complete grasp of the scattering/absorption imaging capabilities of earthquake and noise-based coda waves.

1.3 Field applications

We envisage two applications of scattering and absorption tomography at quite different spatial scales. (1) During the FP7 2010-2014 European Project NERA, a dense network of 65 broad-band seismological stations was deployed in Argostoli, on the greek ionian island of Cephalonia, one of the highly seismogenically active zone in Europe. The network recorded 6 months of seismic noise and about 500 teleseismic, regional and local events with a high signal-to-noise ratio. The network geometry, characterized by interstation distance ranging from 5 m to 2 km (average 50 m) and sampling various geological units, provides a unique opportunity to understand the spatial variability of earthquake ground motion and its effect on large span structures. The ability to map small-scale heterogeneities and intrinsic attenuation is critical to better understand and model the amplification and duration lengthening of earthquake ground motion. The Argostoli site has also been chosen as a test site to study non-linear site response, for which the characterization of intrinsic attenuation is critical for the calibration of non-linear models at low deformation rates. The Argostoli dataset is available to the research community through the European portal EIDA since mid-2015.

(2) The second application is devoted to the mapping of scattering and absorption properties of the crust in Western Europe. This region has been very well instrumented : about 1300 permanent seismic stations (broadband velocimeters and accelerometers) and 30 temporary experiments have been deployed since 1996 ($\sim$1100 stations). Waveforms are already available through the European portal EIDA. We also note that within the timeline of our project, we expect a significant improvement of the spatial coverage in certain regions. In the case of Spain and south-western France for instance, the data of the Iberarray and Pyrope experiments should be released within the next one or two years. We may also benefit from the data acquired during the AlparrayFr experiment (2015-2019), funded by the ANR. Western Europe displays an incredible geological diversity, including old and recent mountain ranges, volcanic areas, subduction zones at different stages, and major active faults. To gain further understanding of the dynamical processes at the origin of this diversity, we need to go beyond velocity tomography. We anticipate that our tomographic approach, which quantifies independently absorption and scattering, can unravel key features that have been missed by seismic imaging so far.

1.4 Relation to other research projects.

To our knowledge, the SSAM proposal has no equivalent at the national, european or international level. Our research is completely original for several reasons: (i) Most notably, we develop of a new tomographic technique based on a recent theoretical result established by our group. (ii) The end products of our research are high-resolution scattering/absorption maps which are still lacking worldwide. (iii) Most seismological imaging techniques employed at the continental scale exploit direct waves at frequencies below 1Hz. We exploit specifically multiply-scattered signals in a broad frequency range [0.05-30]Hz, which is directly relevant to seismic hazard applications. (iv) The targets of our applications cover a broad range of scales: from the sedimentary basin to the continent.

Furthermore, we expect cross-fertilization between our project and other ongoing research programs. We have already noted that the output of our research will be useful to calibrate non-linear models such as those developed in the context of the Sinaps@ project funded by ANR. Attenuation mapping of the Argostoli basin will complement the velocity models that are developed in the framework of the European Research Project NERA. In turn, the outputs of this project will be particularly useful for our purposes, as a knowledge of the background velocity is required in our approach. Likewise, the European reference velocity model EPcrust (Molinari and Morelli 2011) will be fruitfully exploited to provide meaningful geological and geophysical interpretation of our results. In addition, we note that all the data that we analyze will be collected thanks to

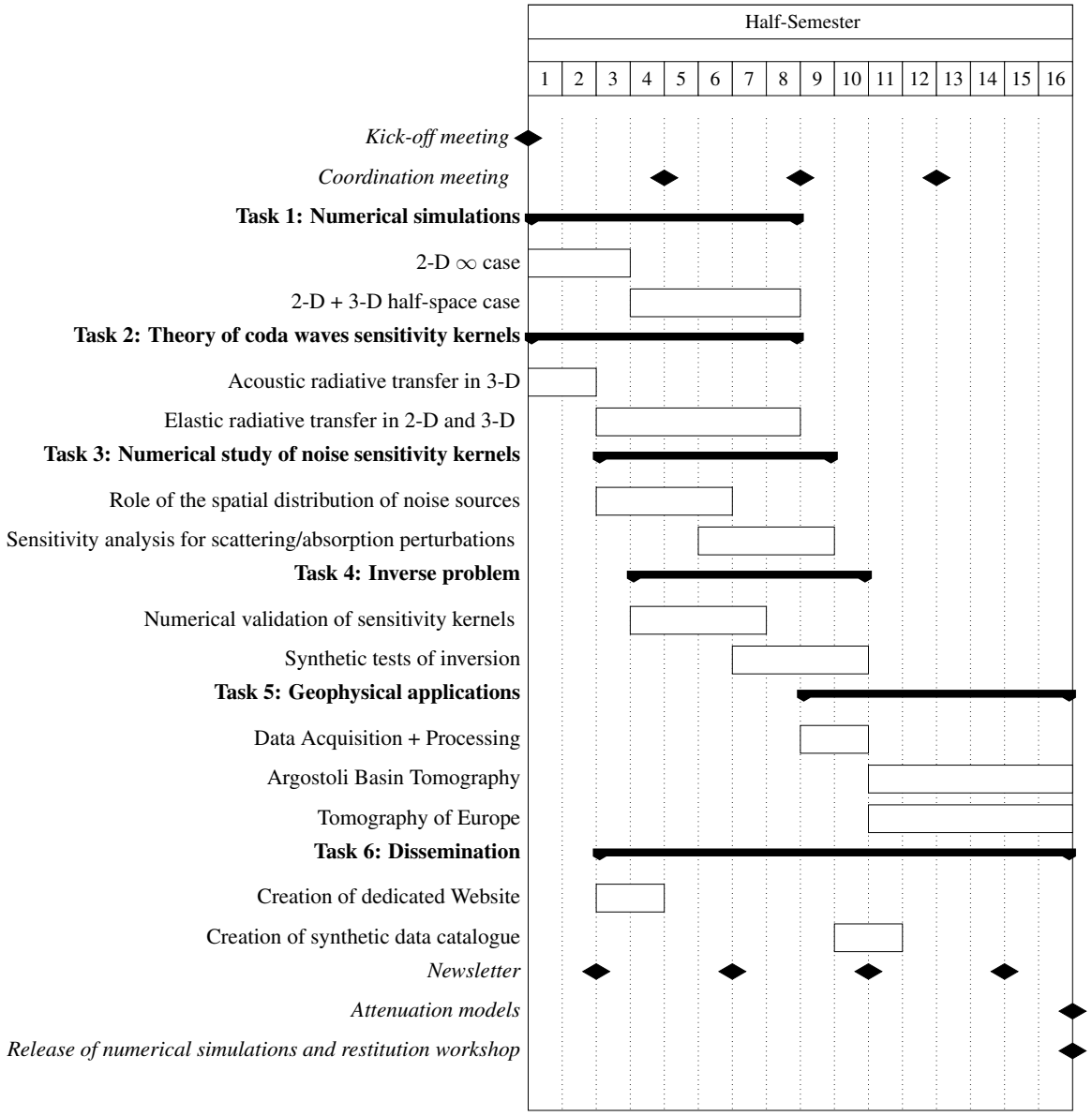

Table 2 Timeline of the SSAM project.

the EIDA infrastructure. In particular, we will take advantage of both the densification of permanent seismic networks (EPOS initiative of the european commission), and of past temporary experiments at the national level (e.g. the Pyrope experiment supported by ANR) or at the european level (e.g. Iberarray).

2 Scientific and technical program, organisation of the proposal

To successfully carry out the proposed research, we will need to pursue theoretical developments, numerical simulations and data analyses at different geophysical scales ranging from the sedimentary basin to the continent. In this section we describe in details the different tasks of our research program as well as their inter-connections. When specific risks have been identified, the back-up solutions -when available- are clearly indicated at the beginning of each task description. A kick-off meeting and three coordination meetings will be successively organized at IRAP, BRGM and ISTerre to discuss the results, monitor the workflow, and readjust the strategy if necessary. The exact schedule of these meetings will be discussed by the partners in the course of the project. These meeting will be supplemented with regular web conferences (at least one every six months) to ensure information exchange between the partners. Table 2 summarizes the timeline of the project. Further details on the connections and dependencies between tasks are provided in the text.

2.1 Task 1: Numerical simulations of random wave fields

Deliverables/Milestones: Data bank of synthetic seismograms in 2-D and 3-D spatially varying heterogeneous media.
Members involved: E. Chaljub (ISTerre) is responsible for the numerical developments and will supervise a Master student in charge of developing a software suite for the post-processing of the simulations. The heterogeneity models will be designed in collaboration with the PC. Cross-checks of the numerical simulations will be performed with F. De Martin (BRGM).
Back-up solution: Use Finite Difference instead of Spectral Elements to perform numerical simulations in continuous random media.

2.1.1 Preliminary remarks.

Numerical simulations are a very important component of this project and will serve different purposes: (i) In the case of earthquake coda waves, we have seen that a well established physical model -radiative transfer- has been developed which allows one to model the space-time distribution of energy in the coda with good accuracy. Nevertheless, our tomographic approach requires an essential linearization step which certainly limits its applicability. Numerical simulations will therefore be essential to delimit the domain of validity of our approach, to experiment different inversion strategies, and to determine the spatial resolution of attenuation models in a variety of controlled situations. (ii) In the case of ambient noise, the physical picture is not as clear as with multiply-scattered waves generated by earthquakes. The complex interplay between inhomogeneous spatial distribution of noise sources and scattering processes is a particularly challenging issue. We will use numerical simulations to study experimentally the sensitivity of the amplitude of direct and coda waves of noise correlograms to the relevant medium and source parameters. In this way, we hope to clarify the potential of noise data for attenuation studies.

It is very important to note that the numerical simulations will do double duty. In other words, ambient noise and coda waves may be studied in the same framework. The key to understand this point lies in the fact that noise sources are usually very short range (compared to other spatial length-scales) and may therefore be represented as white-noises. In this case, the cross-correlation C_{AB} of two random wavefields acquired at positions A and B may be obtained through a single surface or volume integral of Green's functions G:

$$C_{AB}(\tau) = \iint G(A,X;t)G(B,X;t+\tau)\,S(X)dXdt, \tag{1}$$

where the space integral is performed over the whole domain, its boundary or yet another subset, depending on the spatial distribution of noise sources, as encapsulated in the term $S(X)$. By the reciprocity theorem, $G(X,B;t) = G(B,X;t)$, the evaluation of the integral (1) requires only two numerical simulations with impulsive sources at A and B, respectively. The Green's functions synthesized in each simulation between A, or B, and all positions X may be analyzed separately to study coda waves. The simple but very important result (1) is a clear motivation for the joint study of coda and noise wave fields in heterogeneous media. Below, we explain how to cover a range of interesting geophysical situations with a *single* numerical input model.

2.1.2 Design of the heterogeneity models

In this section, we discuss the practical numerical implementation of the models of heterogeneity.

Discrete vs continuous models of heterogeneity. In the real Earth, both discrete scatterers (cracks, intrusions) and continuous fluctuations of elastic parameters are present. Numerically, however, considering the two types of models simultaneously would be impractical. The key to the success of our numerical experiments lies in the control of the scattering parameters of the model, and this is most easily achieved if we consider a single form of disorder at a time. The most important spatial scale of a scattering model is the scattering mean free path l, which controls the exponential rate of decay of the coherent wave and the generation of multiply-scattered waves (Sheng, 2006 for a review). In the temporal domain, one defines a mean free time $\tau = l/c$ (c is the wave speed) which represents the mean time between two scattering events in the heterogeneous medium. In order to have full control on the simulations, we must be able to determine *a priori* the value of the mean free path (or mean free time). Different techniques have been proposed in the literature to carry out this task,

which depend on the type of heterogeneity model. This point further justifies the separate treatment of the continous/discrete situations below.

(i) Models of continuous fluctuations are described by a power spectrum of heterogeneity which we denote by Φ. For a given elastic parameter, *e.g.* the rigidity μ, this power spectrum and the spatial correlation function C of the relative fluctuations $\delta\mu/\mu$ form a Fourier tranform pair:

$$C(\mathbf{x}) = \left\langle \frac{\delta\mu}{\mu}(\mathbf{r}+\mathbf{x})\frac{\delta\mu}{\mu}(\mathbf{r}) \right\rangle = \frac{1}{(2\pi)^d} \iiint \Phi(\mathbf{q}) e^{i\mathbf{q}\cdot\mathbf{x}} d\mathbf{q}, \tag{2}$$

where d is space dimension. In the Earth, there are both direct and indirect evidences that the power spectrum follows a power-law over a broad range of wave numbers, which is often modeled with the aid of a Von-Kármán function. Direct proof of this fact comes from the analysis of well-log data. Observation and modeling of high-frequency seismogram envelops ($f > 1$Hz) provide additional support for the Von-Kármán model, which is defined by:

$$\Phi(q) = \frac{8\pi^{3/2}\epsilon^2 a^3 \Gamma(\nu+3/2)}{\Gamma(\nu)(1+q^2a^2)^{\nu+3/2}}, \tag{3}$$

where ϵ^2 denotes the total variance of the fluctuations, a is the correlation length of the fluctuations, and ν is an exponent which controls the richness of the model in small-scale features.

(ii) While the continuous models are relatively easy to generate, they can be fully controlled only if the variance of the fluctuations is not too large, which permits the application of perturbation theory to calculate the mean free path. Therefore, to test models with strong scattering (high-contrast heterogenous media), it is also useful to implement models of discrete, distributed heterogeneities for which very accurate methods to calculate the mean free path have been developed (Sheng 2006). The chief difficulty in the generation of these models is the avoidance of scatterers overlap, which in turn entails spatial correlations between the scattering centers. This situation can be handled at the theoretical level but slightly complicates the calculation of the mean free path.

Spatial/temporal scaling of the models. Here, we give a typical example of a Von-Kármán random medium which allows us to cover a broad range of interesting scattering situations in a *single* numerical experiment. In the Earth, the mean free path depends strongly on the geological context and on the central frequency of the waves, but typical estimates for the crust lie in the range $10-500$km. Figure 4 shows the dependence of the mean free path upon a-dimensional frequency $ka = \omega a/c$ for a realistic Von-Kármán medium with $\nu = 0.25$, variance of the fluctuations $\epsilon^2 = 0.025$ and correlation length $a = 0.5$km. Scattering theory allows us to calculate very precisely the mean free path for this model:

$$l^{-1} = \frac{k^4}{16\pi^2} \int_{4\pi} \Phi\left(\frac{2\omega}{c}\sin\frac{\theta}{2}\right) \sin\theta d\theta d\phi, \tag{4}$$

where k is the central wavenumber of the waves (not to be confused with the wavenumber q describing the spatial fluctuations of the elastic parameters). It is very important to note that the mean free path is fully determined by the power spectrum of heterogeneities and that the whole range $l \in [10-500]$km may be covered by simulating the propagation of waves over a decade in frequency, as shown by Figure 4. By appropriately filtering the signal in different frequency bands, we will therefore be able to model the propagation of seismic waves in a variety of situations which are relevant to the propagation in the crust: the low-frequency regime $ka \in [0.5, 1]$ is representative of microseismic noise studies and the high-frequency regime $ka \in [1, 5]$ is typical of earthquake coda analyses. Table 3 displays the characteristic parameters obtained after choosing realistic values of the wave velocity c and the total simulation time window. The accuracy of the numerical results depends critically on the ability to represent the small scales in the model. Again, scattering theory allows us to precisely determine the maximal spatial frequency (or minimum fluctuation length) that needs to be correctly represented. We note in particular that formula (4) implies that the waves are sensitive to small-scale features of the medium up to the spatial frequency $q_{max} = 2\omega/c$ with ω the central frequency of the waves.

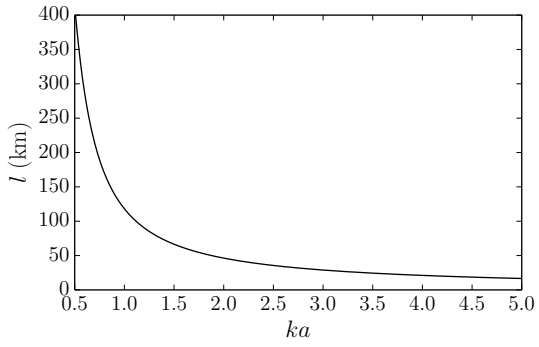

Figure 4 Frequency dependence of the mean free path in a Von-Kármán type heterogeneous medium with correlation length $a = 0.5$km.

Table 3 Typical parameters of the Von-Kármán model of Figure 4, assuming a background shear wave velocity $c = 3.14$ km/s and a time window $T = 250$ s. τ : mean free time, l : mean free path, λ : wavelength.

ka	0.5	1	5
l (km)	400	150	15
τ (s)	130	50	5
λ (km)	6.28	3.14	0.63
T/τ	2	5	50

Therefore, if we want to accurately simulate wave propagation for wavelengths larger than λ_{min}, we will have to filter out all the spatial fluctuations below $\lambda_{min}/2$ and to adapt the spatial resolution of the numerical grid accordingly (*i.e.* to roughly double the spatial resolution used for smooth media) to make sure that our results are both numerically accurate and physically sound.

2.1.3 Cross-Validation of numerical simulations in heterogeneous media

Recent studies have pointed out that numerical simulation of elastic wave propagation in complex 3D media was still far from being a press-button approach (e.g. Chaljub et al. 2010, 2015) implying that verification of the numerical codes is an important step prior to application to realistic cases. In this proposal, we will use two different simulation codes implementing the spectral element method in 2D and 3D: `specfem` (Peter et al. 2011) and `efispec` (De Martin 2011). Both codes have already been verified for a variety of realistic 3D applications (e.g. Chaljub et al. 2015). The calculations will be shared between the two codes and between different operators at ISTerre and BRGM in order to minimize the level of human error. We will also use a set of finite-difference codes developped by the team of P. Moczo at the Coemenius University of Bratislava[1] in order to verify the numerical implementation of continuous random media.

2.1.4 Numerical simulations: ∞ 2-D case

We will start by the simulation of scalar (SH) wave propagation in an unbounded viscoelastic medium with random properties as described in Figure 4 and Table 3. One of the main objectives is to understand the contribution of the sources of seismic noise to the Green's function reconstructed by cross-correlation, in particular to its coda. Around 10 simulations will be performed in order to be able to analyze pairs of receivers with inter-distances ranging between 1 and 10 seismic wavelengths. In order to cover a realistic range of source-receiver distances, we will use a squared 2D computational domain with 314 km side and will consider a uniform distribution of point sources (*i.e.* of receivers in the simulation thank to reciprocity) in the volume. According to the numbers given in Table 3, the spatial resolution of the numerical grid should be adapted to half the minimum seismic wavelength, i.e. 314 m (to be confirmed in the cross-validation step). For the spectral element method, using a polynomial order $N \in [4-5]$, this yields an element size equal to 314 m at most, so the total 2D domain will be meshed with 1000×1000 elements. Based upon preliminary calculations using the 2D version of `specfem` in a background homogeneous visco-elastic medium with $c = 3.14$ km/s, each simulation of 250 s of propagation requires about 150 hours of single core CPU time on Froggy, the latest machine available at the Grenoble University computing center[2]. This reasonable computational time will allow us to run all the SH calculations, including the computation of numerical noise sensitivity kernel (see task 3), using our local (Grenoble University and BRGM) computational resources.

To investigate in a systematic fashion the sensitivity of the coda to spatial variations of scattering/absorption

[1] `http://nuquake.eu/Computer_Codes/index.html`
[2] `https://ciment.ujf-grenoble.fr`

properties, the propagation medium will be divided up into cells of typical size $l/10$ to $l/5$. One cell at a time, we will modify the local scattering/absorption properties and simulate the propagation of waves in the perturbed medium. To increase the scattering strength, it suffices to locally boost the standard deviation of the fluctuations. Note that we have full control on the perturbation of the mean free path thanks to Eq. (4). Absorption is easily controlled by increasing (or decreasing) directly the quality factor. For each source/receiver simulation, we typically expect to carry out about 500 simulations to cover the whole domain of interest. To promote the synergy and interaction between the partners, the post-processing of synthetic data will be performed on a distributed data grid (further details are provided in section 2.6). A master student will be recruited and supervised by E. Chaljub to develop a software suite for distributed processing of distributed seismic data.

2.1.5 Numerical simulations in a half-space: 2-D + 3-D case

The next step will be to simulate P-SV wave propagation in a viscoelastic half-space with random distribution of shear and compressional wave speeds. As further detailed in Task 3, an important goal of these simulations is to clarify the impact of the source distribution on the amplitude of noise cross-correlation functions, as well as their sensitivity to spatial variations of absorption and scattering properties. Again, the medium will be divided up into cells where scattering/absorption properties will be successively perturbed. Based on preliminary $P-SV$ calculations performed with `specfem2D` in a background homogeneous viscoelastic medium with $V_S = 3.14$ km/s and $V_P = 5$ km/s, simulating 250 s of propagation requires about 500 hours of single core CPU time on Froggy. Given the number of simulations needed to compute the numerical noise sensitivity kernels (typically 500 per source-station configuration as outlined above), we will use both local and national (GENCI) computational resources for the $P-SV$ 2D calculations. Finally, we will also perform 3D simulations in viscoelastic random media in order to (i) test the radiative transfer sensitivity kernels developed in Task 2 in a realistic crustal configuration when a localized transition in absorption and/or scattering properties exists, (ii) understand the effect of a strong discontinuity of the background medium, such as a sedimentary basin, on the seismic and noise coda.

Our spectral element codes and processing pipelines are already operational in 3D. In particular, we have designed a semi-automated procedure to generate the spectral element meshes which adapt to the variations, even strong, of seismic velocities. We first build a conforming unstructured spectral element mesh with local refinement in the regions of interest (close to the surface, around a sedimentary basin), and then define a smooth velocity medium using simple homogenization tools. In Figure 5, we show an example of such mesh designed for the mygdonian basin in Greece. The computational domain is 65 km $\times$ 65 km $\times$ 30 km and the shear wave velocities are as low as 135 m/s in the top part of the sedimentary layers. Simulation of 30 s of propagation in this model for frequencies up to 4 Hz requires about 15000 hours of single core CPU on Curie (one of the GENCI machine with almost similar performance as Froggy). The same kind of calculations, adding random fluctuations outside of the basin and extending the runtime to 90 s (*i.e.* $\times$ 3) will be needed for the proposal. For this, we will rely on the computational resources available at the national level (GENCI) and ask for five millions single CPU hours on a massively parallel machine (Curie or equivalent). A specific proposal will be submitted to GENCI in spring 2016 through the dedicated website. Post-processing will be performed on a data grid as outlined above.

2.2 Task 2: Theoretical developments of coda waves sensitivity kernels

Deliverables/Milestone: numerical codes to calculate the sensitivity functions of coda waves to absorption and scattering in 3-D media, based on spectral solutions of the radiative transfer equation
Members involved: This task will be entirely performed by the PC at IRAP.
Back-up solution: Implementation of differential Monte-Carlo methods instead of spectral techniques.

The objective of task 2 is to extend the preliminary results shown in Figure 3 (acoustic 2-D case + isotropic scattering) to the full elastic 3-D case including the coupling between body and surface waves. The PC will invest a very significant amount of this research time to this task (70% in the first 2 years). Sensitivity kernels based on the equation of radiative transfer form the theoretical basis for the separation of scattering and absorption properties and will be implemented in a linearized inversion approach as described in task 4.

The development of a fully-coupled theory for the modeling of multiply-scattered waves is admittedly a very ambitious goal. Our research strategy will be based on a step-by-step approach, increasing the level of

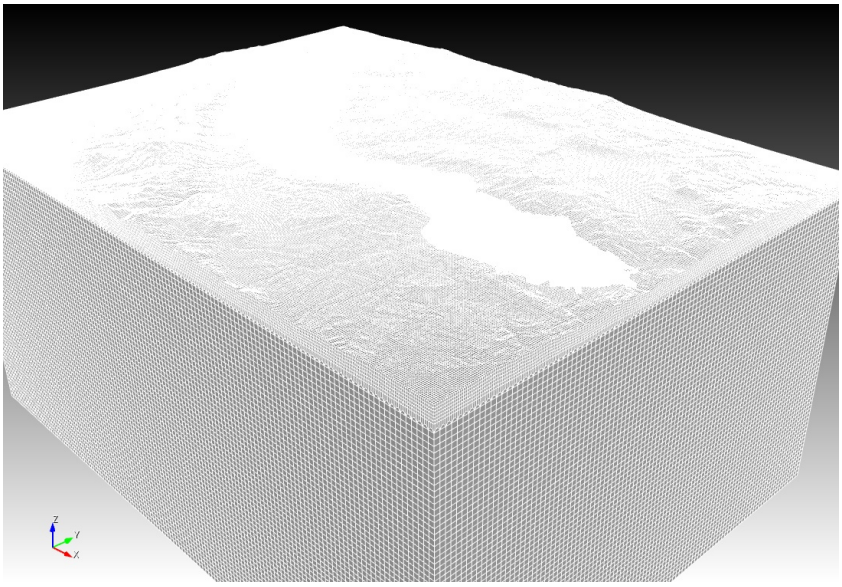

Figure 5 Spectral element mesh used for 3D numerical simulation of wave propagation in the Mygdonian basin (Greece) up to 4 Hz. The mesh is composed by 4,764,721 hexahedron elements and about 316 million Gauss-Lobatto-Legendre collocation points (i.e., around 950 million degrees of freedom). The mesh is refined twice: once when approaching the free surface and once again inside the low-velocity basin to respect the numerical dispersion relationship

complexity of the physical model progressively. Since the radiative transfer equation is not part of the standard curriculum of solid earth geophysicists, we provide a quick overview of the topic. At the formal level, transport equations in scattering and absorbing media take the following general form:

$$\frac{\partial \mathcal{I}(\mathbf{r},t,\mathbf{n})}{\partial t} + c\mathbf{n}\cdot\nabla\mathcal{I}(\mathbf{r},t,\mathbf{n}) + \left(\frac{1}{\tau_a(\mathbf{r})}+\frac{1}{\tau_s(\mathbf{r})}\right)\mathcal{I}(\mathbf{r},t,\mathbf{n}) = \frac{1}{\tau_s(\mathbf{r})}\int_{2\pi} p(\mathbf{n},\mathbf{n}')\mathcal{I}(\mathbf{r},t,\mathbf{n}')d\mathbf{n}' + S(\mathbf{r},t,\mathbf{n}) \tag{5}$$

Eq. (5) contains two timescales: the mean free time τ_s which quantifies the *scattering* properties, and the *absorption* time τ_a[3]. Because the Earth is not a simple heterogeneous medium, these timescales vary spatially. The transported quantity is the specific intensity $I(\mathbf{r},t,\mathbf{n})$, which represents the flux of energy in direction $\mathbf{n}$, at position $\mathbf{r}$ and time t. The term $S(\mathbf{r},t,\mathbf{n})$ represents the source of energy, and the function $p(\mathbf{n},\mathbf{n}')$ describes the angular dependence of the scattering. The latter is fully determined by the heterogeneity power spectrum Φ. Our goal is to retrieve the functions $\tau_s(\mathbf{r})$ and $\tau_a(\mathbf{r})$ from the spatio-temporal distribution of seismic energy. In the linearized approach, we introduce a reference medium whose scattering and absorption properties $(1/\tau_s^0, 1/\tau_a^0)$ are supposed to be known [4]. We then decompose $1/\tau_a$ as: $1/\tau_a(\mathbf{r}) = 1/\tau_a^0 + \delta(1/\tau_a(\mathbf{r}))$, where the term $\delta(1/\tau_s)$ is supposed to be small compared to $1/\tau_s^0$. A similar decomposition applies to $1/\tau_a$. The detected intensity in the reference and perturbed medium is denoted by I^0 and $I^0+\delta I$, respectively. The sensitivity kernels for scattering and absorption are then defined as:

$$\frac{\delta I(t)}{I_0(t)} = \int K_s(\mathbf{r},t)\delta(1/\tau_s(\mathbf{r}))d\mathbf{r} + \int K_a(\mathbf{r},t)\delta(1/\tau_a(\mathbf{r}))d\mathbf{r} \tag{6}$$

In other words, we have obtained a linear relation between the spatial variations of scattering and absorption properties and the detected intensity (see Mayor et al. 2014; Margerin et al. 2016, for technical details). The solution of the inverse problem, i.e., the retrieval of the scattering/absorption properties from the data is the subject of task 4. In what follows, we present the strategy adopted to calculate the kernels K_s and K_a in cases of increasing complexity.

[3] For waves of central frequency ω, the following relations with the traditional scattering and intrinsic quality factors hold: $Q_{sc} = \omega\tau_s$, $Q_i = \omega\tau_a$

[4] The determination of the reference medium is discussed in Task 4

2.2.1 Acoustic radiative transfer in 3-D

The calculation of the kernels K_s and K_a depends crucially on the knowledge of the Green's function of Eq. (5) in the reference medium. In the work of Mayor et al. (2014), we exploited an analytical solution of the problem in 2-D for a simplified model which assumes that the function p is constant (isotropic scattering). In view of applications to real data (and to facilitate the comparison with numerical works), it is of utmost importance to model the multiple scattering of waves in heterogeneous media with a Von-Kármán power spectrum. As previously noted, this requires the knowledge of the Green's function of Eq. (5) for a general function p, a problem which is notoriously difficult to solve either numerically or analytically. Fortunately, it was recently pointed out that Fourier methods "with a twist" can be successfully employed to obtain semi-analytical solutions of the transfer problem in the stationary case, or numerically stable series solution in the time-dependent case (Markel 2004; Panasyuk et al. 2006; Liemert and Kienle 2011). These new Fourier expansions are sometimes collectively referred to as the method of "rotated reference frames" because they exploit rotational symmetries of the transfer equation. The spectral approach turns the angular convolutions required to calculate the sensitivity functions (6) into simple multiplications, which represents a decisive computational advantage. In other words, once the Green's function has been discretized in the spectral domain, the extra-numerical work required to calculate the sensitivity functions is almost negligible. Therefore, in what follows the emphasis is put on the calculation of the Green's function of the radiative transfer equation based on spectral techniques.

In 2-D, the propagation direction $\mathbf{n}$ may be specified by a single angle. The basic idea of the modified Fourier method is to expand the specific intensity as follows: $I(\mathbf{r},t,\mathbf{n}) = \frac{I_0(\mathbf{r},t)}{2} + \sum_m I_m(\mathbf{r},t)\cos(m\phi_{\mathbf{r}})$. The difference with a standard expansion lies in the fact that the angle $\phi_{\mathbf{r}}$ is defined with respect to a reference frame which *rotates* with the position vector $\mathbf{r}$, hence the name of the method. Additional Fourier and Hankel transforms with respect to the time and space variables turn the equation of transfer into a simple tridiagonal system whose solution is almost trivial. The numerical cost grows only linearly with the integer N at which the Fourier series is truncated. We have successfully implemented a modified version of the method of rotated reference frames to extend the calculation of sensitivity functions to 2-D heterogeneous media of the Von-Kármán type (Margerin et al. 2016).

The extra effort to pass from the 2-D to the 3-D scalar case appears rather modest. Apart from a change of basis functions (Legendre polynomials instead of trigonometric functions, spherical Bessel functions instead of ordinary Bessel functions), all the nice properties of the method are preserved, in particular the tridiagonal form of the linear system of equations. We therefore expect to solve the 3-D scalar case rather rapidly. At the level of the radiative transfer equation, the free surface of the Earth imposes total specular reflection of the incident energy flows. This boundary condition may be very conveniently treated by the classical method of image. While the scalar model of scattering in a 3-D half-space is only an intermediate result, it already captures much of the essential physics. Indeed, numerical solutions of the elastic radiative transfer equation for coupled P and S waves obtained by the Monte-Carlo method have revealed two important facts (Margerin et al. 2000): (i) multiply-scattered signals are very rapidly dominated by shear waves[5]; this stems from the fact that mode coupling favors $P \to S$ over $S \to P$ conversions; (ii) Polarization of shear waves is very rapidly washed out and has a minor impact on the transport of waves. For this reason, the simple scalar model should already do a very good job at sufficiently high-frequencies where we expect the energy transport by Rayleigh waves to be negligible.

2.2.2 Elastic radiative transfer in 2-D and 3-D

The next step of our research will be devoted to the introduction of coupling between different wave modes. Several strategies may be envisaged which are summarized below. It should be noted at first that the *structure* of the radiative transfer equation (5) does not change if one considers two or more propagating modes instead of one. It may happen that some modes are degenerate, like for example shear waves in 3-D space, whose polarization spans a 2-D subspace. This gives rise to polarization effects, which, as explained above, are washed out rapidly in the multiple scattering process. We will therefore neglect these subtleties in our approach.

[5] A deeper asymptotic result known as equipartition stipulates that the energy density of S waves becomes larger than the one of P waves by a factor $2c_p^3/c_s^3$ ($t \to \infty$), with c_p and c_s the P and S wave speeds in the medium

Coupling between body waves in 2-D in-plane geometry (P-SV). We will first consider the coupling between P and S waves in 2-D. In this case, Eq. (5) becomes a 2-D integro-differential equation for the specific intensity vector (I_p, I_s), where I_p and I_s are the respective P and S intensity. The velocity c, the mean free time τ_s and the absorption time τ_a should accordingly be interpreted as diagonal matrices: $\mathbf{Diag}(c_p, c_s)$, $\mathbf{Diag}(\tau_s^p, \tau_s^s)$, $\mathbf{Diag}(\tau_a^p, \tau_a^s)$ with self-explanatory notations. The function p becomes a 2×2 matrix which describe mode conversions. We note again that this matrix function is fully specified by the power spectrum of heterogeneities Φ.

A preliminary investigation indicates that the application of the method of rotated coordinate frames to the vector transport equation yields a banded linear system in $2N$ unknown, where we recall that the Fourier expansion (2.2.1) is truncated for $m > N$. A variety of efficient techniques have been developed to solve this kind of linear problems, some of which are already implemented in compiler suites (eg Polizzi and Sameh 2006).We are therefore confident in the fact that the spectral approach can be both accurate and convenient in the vector case too. We therefore expect this work to be done in 6 months.The algorithm will first be developed in 2-D infinite space and the free surface will again be treated by the method of image. The sensitivity functions for absorption and scattering will be validated with the aid of the 2-D P-SV numerical simulations performed during task 1.

In principle it is possible to perturb the scattering and absorption properties of P and S waves separately. In the case of scattering, the perturbations of the P and S mean free times will be strongly correlated because these quantities are tied to the heterogeneity model. Concerning absorption properties, the situation is not as clear, although it is usually believed that shearing motions are responsible for most of the dissipation. At the theoretical level, we will be able to distinguish between perturbations of the inverse quality factors Q_κ and Q_μ, which in turn control the absorption times of P and S waves[6].

Coupling between body and surface waves The last 18 months of task 2 will be dedicated to the modeling of the coupling between body and surface waves. This part of the proposal is important to determine the depth-dependence of the sensitivity functions, which in turn depends on the relative importance of body and surface waves in the energy transport. A very promising approach to tackle this problem is the quasi-2D transport theory developed by Trégourès and Van Tiggelen (2002). This model applies in a waveguide geometry (e.g. crust over mantle) and is based on a surface wave decomposition of the elastic wavefield. In this approach, body waves and surface waves are treated on the same footing, the former being represented as a surface wave mode sum. As an additional bonus, this model allows one to straightforwardly incorporate depth-dependent properties. The quasi-2D transport equation is formally identical with Eq. (5). Similar to the P-S case discussed above, all quantities should be understood as vectors or matrices: the specific intensity is a n-dimensional vector, each component representing the intensity transported by mode i ($i \in \{0, 1, \cdots, n\}$); the velocity c, the mean free time τ_s and the absorption time τ_a are diagonal matrices with elements the group velocity, the scattering mean free times and the absorption time of the modes respectively. These last two quantities are fully determined by the power spectrum Φ and the quality factors Q_κ and Q_μ, respectively.

The formalism described above for coupled P-S waves extends straightforwardly to the quasi-2D equation of transport. However, the banded numerical system to be solved will become much larger since a large number of guided modes (typically 50 modes or more) will be necessary to represent accurately the body waves. We nevertheless foresee that the size of the system (typically 10000×10000) will still be manageable numerically. The calculations will be performed on the local computer center CALMIP[7]. We also would like to emphasize that there exist alternatives to the spectral technique we propose to implement. In particular, the PC has already developed a Monte-Carlo simulation code to solve the transport equation for coupled P and S waves in 3-D. This code may be extended to treat a more general system, coupling together a large number of modes. Differential Monte-Carlo methods (Lux and Koblinger 1991) may then be employed to calculate numerically the sensitivity kernels in a completely independent way. While Monte-Carlo methods suffer from several well-known drawbacks such as slow numerical convergence and lack of accuracy, they are relatively easy to implement and very flexible. Therefore, they form a viable alternative to the spectral techniques, which secures the numerical developments.

[6]The relations between the former and the latter are one-to-one

[7]http://www.calmip.univ-toulouse.fr

2.3 Task3: Numerical study of the sensitivity of the coda of ambient noise cross-correlations

Deliverable/Milestone: empirical sensitivity functions of the coda of noise cross-correlations for perturbations of scattering, absorption and source distribution.
Members involved: The task will be performed at ISTerre by a Master student then PhD student to be recruited, under the supervision of E. Chaljub and L. Stehly.

Preliminary remarks and key questions. Several theoretical works have put the forward the possibility to retrieve the full Green's function of an arbitrarily complex medium from the cross-correlation of noise wave fields acquired at arbitrarily distant stations. The main requirement is that the sources of seismic noise be homogeneously distributed within the medium, and/or that the scattering of seismic waves by heterogeneities within the Earth be strong enough to randomize the seismic wavefield outside of the target region (De Verdière 2009; Wapenaar et al. 2006). In practice this assumption is never completely fulfilled: noise sources are restricted to the free surface of the Earth implying that seismic noise is dominated by surface waves (Bernard 1952; Hasselmann 1963; Friedrich et al. 1998; Ekström 2001). Moreover, the distribution of noise sources and their temporal evolution are frequency dependent: above 1Hz, the seismic noise is mainly excited by human activities, whereas at longer period (> 1s) it is related to the interaction between the oceans and the solid earth (Gutenberg 1951; Ardhuin et al. 2015). This implies that the biases that may arise in the Green's function reconstruction are frequency dependent (Stehly et al. 2006). Although Stehly et al. (2008) have shown that coda waves are at least partially reconstructed by cross-correlating seismic noise in the 5-40s period band, the problem is still open and requires further investigations.

The aim of this work package is to evaluate the impact of a non-homogeneous distribution of noise sources on the amplitude of the coda reconstructed from noise correlations. More precisely, we will investigate how the sensitivity of the coda of noise cross-correlation is related to the distribution of noise sources. To address this question we will follow a systematic step-by-step approach as described below.

2.3.1 Sensitivity of the coda of noise cross-correlations to the spatial distribution of noise sources

The aim of this subtask is to compute the sensitivity of waveforms retrieved from noise correlations to perturbations of the source distribution only. To this end, we may exploit Eq. (6), which implies that the contribution to the correlation of a particular noise source located at X is simply proportional to the correlation of two Green's functions. Therefore, we may immediately express the sensitivity kernel K^n for the noise source distribution as:

$$K^n(X,\tau) = \int G(A,X;t)G(B,X;t+\tau)\,dt \tag{7}$$

This kernel quantifies the change in amplitude at time τ of the noise-based Green's function, induced by a perturbation of the distribution of noise sources at position X. Note that the sensitivity functions of other observables -such as the intensity of the signal reconstructed by cross-correlations- may also be straightforwardly evaluated numerically.

Figure 6 shows an example of a sensitivity kernel $K^n(X,\tau)$ computed in PREM (Dziewonski and Anderson 1981) for two stations located 800km apart and evaluated at the arrival time of the surface waves in the 20-25s period band. In Figure 6, we recognize three typical regions which have been previously described in the literature: (i) the "coherent area" is delimited by black dashed lines and corresponds to noise sources located 'near' the axis $A-B$, which contribute positively to the amplitude of the surface waves (Snieder 2004; Sabra et al. 2005; Roux et al. 2005). (ii) the "finite-frequency" area is delimited by red dashed lines, where the kernel shows spatial oscillations. (iii) outside of the coherent and finite-frequency areas the kernel takes negligible values. This result will be generalized to heterogeneous media using the synthetic Green's functions obtained during task 1. In this way, we will obtain a clear picture of the location of sources contributing to the reconstruction of different parts of the Green's function: direct waves, early coda and late coda. This preliminary study will help us analyze the interplay between medium perturbation and source perturbation that we consider next.

2.3.2 Sensitivity of the coda of noise cross-correlations to attenuation and scattering perturbations

Our next step is to determine under what conditions the coda of noise cross-correlations may be used to map the absorption and scattering properties in the medium. To quantify the impact of the noise sources, we will

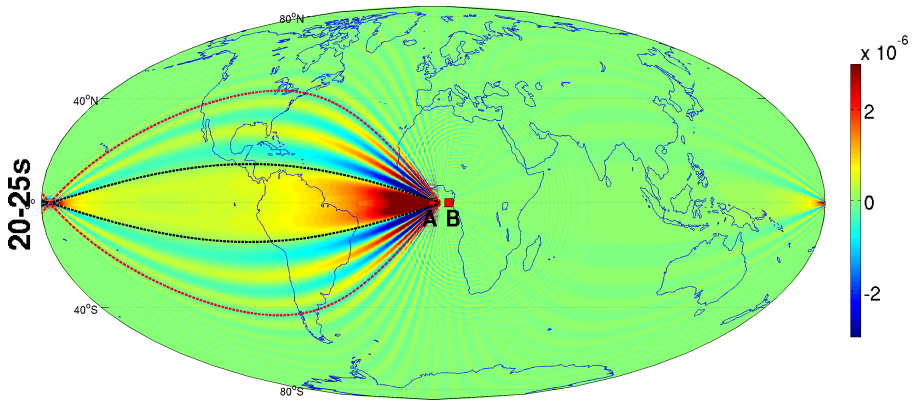

Figure 6 Amplitude sensitivity kernel of direct surface waves in the 20-25s period band for perturbations of the source distribution. The two stations are separated by 800 km and the PREM velocity model has been adopted.

consider different spatial distributions of practical importance: (i) Homogeneous distribution throughout the medium (ideal configuration). (ii) Homogeneous distribution on a ring surrounding the source and station. (iii) Asymmetric distribution on a ring to mimic directional noise sources. (iv) Single distant source of noise. (v) In the case of a half-space geometry: sources located at the surface only. Note that at the computational level, the only difference between the five cases pertains to the subset over which integral (1) is performed.

To evaluate the scattering and absorption sensitivity functions, the following brute force approach will be employed. (i) For given source-receiver configuration and noise distribution, compute the noise cross-correlation functions in a reference model that has homogeneous absorption and scattering properties. (ii) Next, successively perturb the absorption/scattering properties of the medium inside small cells covering the whole propagation medium. For each perturbation, compare the amplitude of the reference and perturbed coda waves at different lapse times (iii) From these measurements, obtain the sensitivity kernels of coda waves reconstructed from noise correlations w.r.t absorption/scattering perturbations for different lapse time in the coda. The steps (i)-(iii) are repeated for each noise source distribution, and for different source-station distances. In the framework of monitoring temporal changes of the medium with coda waves, similar numerical experiments have been successfully conducted by Obermann et al. (2013), which gives us confidence in our strategy.

The preceding procedure will be applied to various observables. We will consider in particular the intensity of the coda of noise cross-correlations and compare empirical sensitivity kernels with their theoretical counterparts derived in task 2. In the case of an ideal homogeneous distribution of sources, we expect to find good coincidence between the two approaches. By testing different spatial distribution of sources, we will determine to what extent the sensitivity functions obtained in the framework of transfer theory may be applied to their noise cross-correlations analog. In case of disagreement, our numerical approach will nevertheless allow us to employ empirical sensitivity kernels that are tailored to the local distribution of noise sources which may be inferred from array analysis as explained in task 5.

The numerical applications will parallel the development of theoretical sensitivity kernels as outlined in task 2. In this way, we reinforce the synergy between tasks 1-3 to take maximum advantage of the interdisciplinary approach. We will first perform a complete parametric study for scalar waves in a 2-D ∞ medium for both scattering and absorption perturbations. This study will give us access to the lateral variations of the sensitivity. Next, we will consider the 2-D P-SV half-space geometry and perform a complete parametric study to highlight the dependence of the sensitivity on the depth of the perturbations. As a full numerical study in 3-D is out of reach, we will use a few 3-D numerical simulations and results from task 2 as guides to combine empirically the lateral and depth dependent parts of the sensitivity.

2.4 Task 4: Inverse problem

Deliverable: inversion code to retrieve the spatial variations of scattering and absorption properties from the observed spatial variations of intensity.

Personnel involved: Task 4 will be mostly performed at IRAP by the Master/Ph.D. student under the super-

vision of M. Calvet and L. Margerin (earthquake coda wave tomography), and in collaboration with the PhD student and L. Stehly from ISTerre (noise coda wave tomography).

Back-up solution: At the time of writing, the outcome of task 3 has some uncertainty. If we find out that noise data are too sensitive to the spatial distribution of noise sources for tomographic applications, we will focus our efforts on earthquake data. Note that the methodology developed below is primarily intended to the inversion of earthquake data, but should work with minor adaptations for noise data too.

2.4.1 Preliminary step: numerical validation of sensitivity kernels

The first step of Task 4 pertains to earthquake coda waves only, and consists in the numerical validation of the sensitivity kernels developed during Task 2 with the aid of the numerical simulations obtained during Task 1. We will proceed by increasing the complexity of the models progressively. To begin with, we will exploit the 2-D scalar simulations in ∞ space, which allow for a complete parametric study. We will then move on to the 2-D P-SV half-space case. First, we will test the sensitivity functions obtained by considering propagating body waves only. We expect this model to give good results when the perturbations are located below the penetration depth of the Rayleigh waves. We will then pursue our investigations by testing the fully coupled theory including body and surface waves.

2.4.2 Definition of the reference heterogeneity model

In a linearized tomographic approach, we define perturbations of the medium properties with respect to a reference model. For our purposes, we therefore need to determine the spatially averaged scattering/absorption properties of the crust in the frequency band $[0.05 - 30]$ Hz, i.e. the scattering mean free time τ_s, the absorption time τ_a and the scattering anisotropy p, which are controlled by the heterogeneity power spectrum of the medium[8]. In the case of the european crust, we cannot rely on previous estimates of the scattering and absorption lengths published in the literature because the spatial coverage is too sparse and the scattering anisotropy p is usually undetermined. To construct our reference scattering and absorption model we will rely on a method that we recently developed, which is based on the direct modeling of the coda in various frequency bands (Calvet and Margerin 2013). This method has been successfully applied to a dataset from the Pyrenees and will be adapted to the case of a large-scale attenuation tomography as detailed below. Note that we plan to regionalize the reference model, a typical region having typical dimension $250 \times 250\text{km}^2$ or more.

Because attenuation properties are strongly frequency-dependent, we will analyze the signals in a series of narrow frequency bands (see Task 5 for further details). To account for site amplification and source magnitude, we will normalize both observed and computed coda enveloppes by the average value of the energy in a time window in the late coda (coda normalization approach, see Yoshimoto et al. 1993). The length and position of this window will be adapted depending on the epicentral distance range of the records. Seismic velocities will be fixed a priori based on the EPcrust model (Molinari and Morelli 2011) and the heterogeneity of the medium will be described by a Von-Kármán spectrum characterized by three parameters: the variance of the velocity fluctuations ϵ^2, the correlation length a and the exponent ν, as illustrated in Task 1. To synthesize coda enveloppes, the Green's functions of the radiative transfer equation will be computed using the numerical methods developed during Task 2.

In a first step, the range of acceptable values for τ_a will be estimated from the analysis of the coda quality factor Q_c at large lapse-time as proposed by Calvet and Margerin (2013). Next, a quantitative comparison between observed and computed enveloppes at short lapse time will be performed through a misfit function (various misfit functions will be tested). The important point to note is that the shape of the seismogram envelope near the ballistic arrivals contains crucial information on the heterogeneity power spectrum and mean free time τ_s (Gusev and Abubakirov 1996; Calvet and Margerin 2013). The time window will be optimized by testing various starting times and window lengths (Lacombe et al. 2003). Different approaches to the minimization of the misfit function will be tested such as the classical grid search method or the Levenberg-Marquardt algorithm. The results of individual envelopes fits may be subsequently spatially averaged to obtain the reference model but other strategies (involving e.g. some averaging of the data first) will be tested. The whole

[8]For simplicity, we present the case of a single propagation mode. The more general situation will be considered in the framework of the project.

procedure will be tested using the 3-D numerical simulations performed during task 1 in the crust and basin configurations, respectively.

2.4.3 Inversion strategy and synthetic tests

A key feature of our theoretical approach is to arrive at a *linear* relation (Eq. 6) between the observable in the coda (relative change of intensity) and the parameters of the model (scattering and absorption properties). The first step of the inversion process is to *discretize* the continuous formulation to convert it to a standard linear system involving matrices and vectors. For this purpose the use of Voxels appears as a reasonable first choice. To treat the singularities of the sensitivity kernels at the source and receiver, we may use some general normalization formulas derived for each kernel by Mayor et al. (2014). Outside of the Voxels containing the source and receiver, simple Riemann sums may be used to integrate the discretized kernels numerically. The result can then be compared to the value given by the normalization condition, which is obtained independently and does not require numerical integration. The difference between the two quantities may finally be reassigned to the source and receiver Voxels.

To solve the linear inverse problem, we will follow a common least-squares approach (see e.g. Tarantola 2005). Damping will be introduced through the covariance matrix of the model parameters. To optimize the choice of damping parameters, i.e. the correlation length and variance of the correlation function, the method of the L curve will be adopted as described by Hansen (1992). Because intensity fluctuates strongly in the coda[9], we will not try to invert directly for the time-dependent intensity. Like in the multiple lapse-time window technique (Fehler et al. 1992), we will average the intensity in consecutive time windows of typical duration a few tens of periods, in order to average out the statistical fluctuations.

Formula (6) also reveals that the detected intensity depends on both the scattering and absorption perturbations, which inevitably introduces cross-talk between the two quantities. Fortunately, our preliminary study demonstrates that the sensitivity to scattering perturbations decays rapidly in the coda, which alleviates the problem. We may also consider alternative observables which are specifically sensitive to scattering or absorption. In particular Carcolé and Sato (2010); Calvet and Margerin (2013); Mayor et al. (2016) have shown that the coda quality factor Q_c evaluated in late time windows in the coda is a good proxy for the intrinsic quality factor Q_i. Hence, preliminary measurements of Q_c may be used as a priori information on τ_a for the inverse problem. To test the inversion procedure, we will exploit the 3-D numerical simulations performed during task1 for the sedimentary basin and continental crust configurations. The numerical tests should give us a good idea of the spatial resolution of the method, and will facilitate the optimization of damping parameters when true data are considered.

2.5 Task5: Geophysical applications

Deliverable/Milestone: (i) 3D scattering and absorption maps for Central and Western Europe. (ii) Scattering and absorption model of the Argostoli Basin. (iii) Empirical attenuation-velocity laws for different geological units.
Members involved: Task 5.1 (European attenuation model and interpretation) will be performed by the Ph.D student, Marie Calvet and Micha Bystricky in collaboration with L. Margerin. Task 5.2 (Argostoli basin model) will be mostly performed at ISTerre by the Ph.D. student under the supervision of E. Chaljub and L. Stehly.
Back-up solution: If the conclusion of task 3 is negative (noise data cannot be used for attenuation tomography), we will use regional and earthquake data to carry out the attenuation tomography of Argostoli.

2.5.1 Large-scale application: the european crust

Knowledge of the crustal structure is crucial for many geophysical applications, such as upper-mantle tomographic studies which need crustal corrections, forward seismic wave propagation or location of seismic events. Recently, Molinari and Morelli (2011) have proposed a reference crustal model for the European Plate from a compilation of geological and geophysical data. This model (EPcrust) gives the P- and S-wave velocity in three layers (sediments, upper crust and lower crust) with a resolution of $0.5^\circ \times 0.5^\circ$ on a geographical latitude-longitude grid. We propose to develop a similar reference 3-D crustal model of scattering and absorption in

[9]Under the gaussian field assumption, the intensity obeys an exponential distribution for which the standard deviation is equal to the average value (see Sheng 2006)

the frequency band [0.05-30]Hz in a region delimited by North Africa to the south, Scandinavia to the north, (35°N-71°N), Spain to the west and Russia to the east (12°W- 42°E). Following the inversion strategy developed in Task 4, the attenuation model will be constructed by combining the analysis of earthquake and noise data in the [1-30]Hz and [0.05-1]Hz frequency bands, respectively.

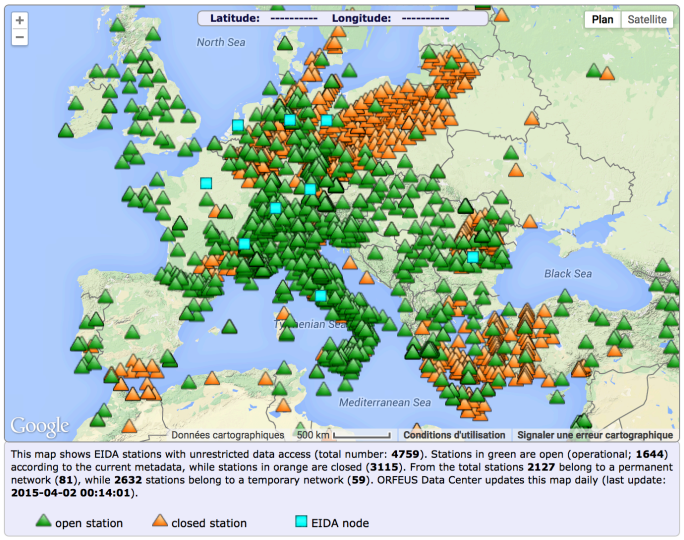

Figure 7 Location map of permanent and temporary seismic stations deployed in Central-Western Europe (http://www.orfeus-eu.org/eida/).

Data collection: Thanks to the installation of permanent broadband and accelerometric networks, as well as the deployment of numerous temporary experiments, Central and Western Europe have been very well instrumented since 1996 (Figure 7). Within the timeline of the project, the spatial coverage will be improved in France (RESIF project, PYROPE and AlparrayFR experiments) and in Spain (IberArray experiment). Continuous records are available at the European Integrated Data Archive (EIDA) through the Arklink protocol.

Earthquake records: For the Pyrenees, we have already collected about 10000 waveforms on ∼110 seismic stations for ∼700 earthquakes which occured between 2000 and 2010 with a local magnitude ranging from 2 to 5 (Calvet et al. 2013). This dataset will be complemented using catalogues from the European Mediterranean Seismological Centre (CSEM) or from national earthquake monitoring services. We will first collect earthquake records with a local magnitude greater than 3 and an epicentral distance smaller than 250 km. Selected records will start 30 seconds before the origin time of the earthquake with total duration 240 seconds. In order to improve the data coverage, we will add Lg records of larger-magnitude events (magnitude greater than 5.0) with epicentral distance ranging from 600km to 1000km and total duration about 800s. Based on the number of seismic stations available through the EIDA portal (> 3000), we anticipate that more than 500000 waveforms can be collected. All the waveforms will be deconvolved from the station response, and acceleration records will be integrated to get the three components of velocity. Next, seismograms will be filtered in five frequency bands: 1-2 Hz, 2-4 Hz, 4-8 Hz, 8- 16 Hz and 16-32 Hz (the last band will depend on the sampling rate of the records). Amplitude are then squared to obtain the coda energy envelope to be analyzed.

Noise records: Noise correlations will be used to study the attenuation of the european crust at lower frequency (typically 0.02-0.3 Hz), and will thus provide complementary information. The data processing will be adapted depending on the results of Task 3, but we can already present a general outline here. We will collect two years of continuous noise records at all available european broadband stations during the period 2013-2014 through the EIDA portal (∼400 broadband stations) as well temporary stations deployed during the CIFALPS experiment.[10] Cross-correlations will be computed between all ∼100000 pairs of stations day per day and averaged over two years. Noise records are known to be non-stationary. To address this issue, we will build two sets of correlations: (1) Standard correlations obtained without applying any processing to the noise records other than a quality control which consists in removing all segments of data that contain earthquake, glitches or others kinds of high amplitude transients. (2) 1-bit correlations : in this case data are filtered in narrow frequency bands and their sign calculated *before* computing the correlations. Although this is completely counter-intuitive, it has been shown theoretically and numerically that the relative amplitude of correlations computed in this way is preserved under broad assumptions (Cupillard and Capdeville 2010;

[10]CIFALPS is a dense seismic profile of 46 stations with an interstation spacing of 5 to 10 km deployed during 18 month from Bollène to the Po Plain.

Cupillard et al. 2011). All computations will be done at the computing center of the University of Grenoble using highly optimized codes developed by Albanne Lecointre and Xavier Briand in the framework of the ERC project Whisper.

Geophysical and geological interpretation of the results: The crustal structure of Western and Central Europe results from various lithospheric deformation episodes which have overprinted the Proterozoic East-European Craton and the Caledonian and variscan crustal domains since the late Paleozoic Age. Many different tectonic units have been identified: caledonian, variscan and alpine orogens, fault systems, magmatic provinces, mesozoic and cenozoic rifts, active volcanoes, subduction zones, deep sedimentary basins (Ziegler and Dèzes 2006), which are not systematically marked in the seismic velocity structure. High-resolution maps of absorption and scattering properties have the potential to reveal specific trends and systematic correlations between velocities and attenuation properties, thereby allowing a better investigation of the relation between seismic properties, geology and geodynamics. Furthermore, the frequency dependence of the absorption properties may allow us to pinpoint specific dissipation mechanisms, as described in the rock physics literature (e.g. Mavko et al. 2009, for a review). In the last six months of the project we plan to make a detailed comparison of the attenuation structure of Europe with available seismic velocity tomographies, gravity anomaly maps (distributed by the International Gravimetric Bureau - http://bgi.omp.obs-mip.fr), geological features, earthquake distribution, past tectonic activity and other available geophysical observations (as for example heat flux measurements distributed by the International Heat Flux Commission - http://www.heatflow.und.edu). The result of this comparison will allow us to discuss the origin of the small-scale heterogeneities in the crust and the emplacement/circulation of fluids in connexion with crustal processes. Particular attention will be paid to tectonic units where high-resolution velocity models have been developed (Pyrenees, Western Alps, Italian volcanoes), as well as major faults (as for example the North-Anatolian Fault system).

2.5.2 Small-scale application: the Argostoli basin

During the last four decades, the effects of topography and geological geometry of sedimentary basin on seismic ground motion have been the topic of many instrumental and numerical investigations. The velocity structure of sedimentary basins is usually rather well constrained but the high-frequency attenuation and the relative contributions of scattering and absorption are still undetermined. Yet, attenuation has a huge impact on the strong motion amplitude and duration which has to be considered in seismic hazard assessment. Nowadays, numerical facilities allow for high-frequency simulations of strong motions (see Task 1) including small-scale heterogeneities and viscoelastic effects. In this project, we propose to provide a high-frequency attenuation model for the Argostoli basin, which has been well instrumented in the framework of the FP7 2010-2014 European Project NERA. We believe that this model will be valorized through the SEISM Institute program SINAPS (http://www.institut-seism.fr/projets/sinaps) and will shed light on the variability of ground motions in the basin.

Data collection: Argostoli is a basin located in a small alluvial valley on Cephalonia Island, the most seismically active region in Greece. Argostoli and the surrounding villages were completely destroyed by an earthquake of magnitude 7.2 in August 1953. The Argostoli network consists of 64 broad-band stations which have been deployed from September 2011 to April 2012 (see figure 8). This network is organized around two profiles, respectively parallel and perpendicular to the major axis of the valley. The profiles are supplemented with two dense arrays. Array A is located near the south-western edge of the valley made of alluvial deposits, and consists of 21 broadband stations with inter-station spacing ranging from 5m to 160m. Array B is composed of 10 short-period stations located at the north-eastern edge of the valley. The two profiles are deployed across three distinct geolocial units: marine deposits from the pliocene (west), alluvial deposits from the holocene (center) and carbonate rocks (east) from the triassic. Geophysical (passive and active surface wave measurements, H/V measurements) and geological surveys have been already performed to constrain the geometry of the basin and the velocity structure beneath the seismic profile. In this project, we propose to supplement this model with attenuation measurements at high frequency. We will take advantage of the high density of stations (typically separated by less than one wavelength) to investigate variations of scattering and absorption properties among the three main geolocial units.

461 local events with a magnitude smaller than 5.0 have been already recorded at the Argostoli seismic

network within 80 km epicentral distance. These events have been relocated in the framework of the european project NERA and most of them occur to the north-east of Argostoli. The dataset will be available in 2015 through the EIDA portal. About 6 months of continuous noise records are available at all stations. We will compute the correlations of daily noise records between all station pairs in the 0.1-20 Hz frequency band, the inters-tation distance varying between a few meters to 2 km.

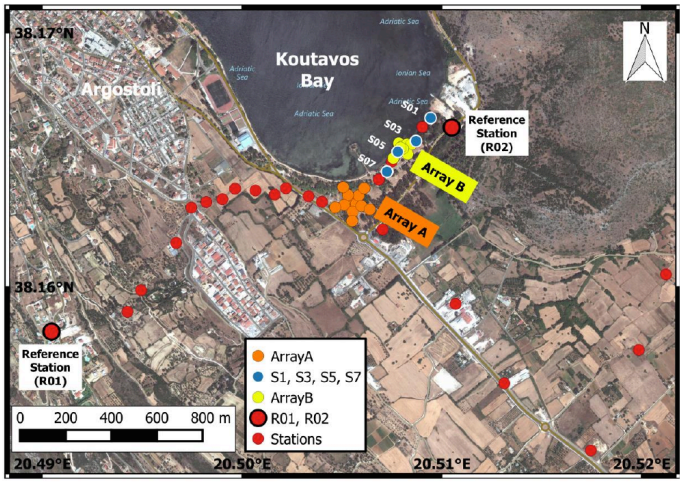

Figure 8 Map of the seismological network deployed at Argostoli (courtesy A. Imtiaz, ISTerre)

Earthquake records analysis In the case of the Argostoli basin, most of our efforts will be dedicated to the analysis of noise records. Nevertheless, depending on the results of task 3, we may have to analyze earthquake records as a back-up solution. In a first step will derive a regional model for the Cephalonia Island (absorption, scattering and heterogeneity spectra) from the analysis of local and regional earthquakes, following the methodology established during Task 4. To correct for site effects which may be prominent in Argostoli, we will employ the coda normalization technique which has proven very efficient (Yoshimoto et al. 1993). Clearly, the network geometry is not optimal to analyze data from distant earthquakes. Nevertheless we may try to exploit the high sensitivity of coda waves in the vicinity of the station. To do so, we have to adapt the tomographic technique. The natural idea that comes to mind is to use differential measurements, i.e., for each earthquake, take the difference between the intensity measured at two stations located on different geological units. In this way, we hope to remove the sensitivity to the attenuation structure in the source region. Using the linearity of our formulation, the sensitivity kernels for these type of measurements are readily obtained and only minor changes need to be brought to the inversion procedure. Hopefully, this differential approach may allow us to retrieve local changes in the scattering/absorption structure across the basin.

Noise records analysis Using arrays A and B (see Figure 8), we will perform a preliminary analysis of the noise directivity to estimate the spatial distribution of noise sources with respect to the Argostoli seismic network. Based on this analysis, we will be able to adapt the sensitivity functions for scattering/absorption to the distribution of noise sources. Regional estimates of the scattering properties which are required to evaluate the sensitivity functions of noise cross-correlation functions will be provided by independent analysis of earthquake data (see previous paragraph for details). Using the methodology developed in the framework of Task 4, the spatial variations of the coda of noise correlations will be inverted to retrieve spatial variations of scattering/absorption properties. For stations separated by typically more than 500m, cross-correlations will be used. These measurements may be complemented with auto-correlations to increase the sensitivity to the local structure. In addition to the analysis of the coda of noise cross-correlations, we also note that it should be relatively straightforward to map the lateral and depth variations of the velocity in the basin using Rayleigh wave dispersion. The combination of both type of measurements (velocity+ attenuation) will facilitate the geological interpretation of the results and may also provide a complete 3-D model as an input for realistic strong ground motion simulations.

2.6 Task 6: Sharing and dissemination of the results

Deliverables/Milestones: (i) Website of the project. (ii) Newsletter. (iii) Data bank of numerical simulations. (iv) Restitution workshop.

Members involved: F. De Martin (BRGM) in collaboration with the PC.

Sharing and dissemination will take place at different levels: (i) To facilitate data sharing between the

partners during the project; (ii) To ensure visibility towards both the scientific communities and the general public; (iii) To share with the international community of seismologists the catalogue of numerical simulations together with the appropriate tools to manipulate data.

2.6.1 Data sharing between the partners

During the project, data sharing between the different local computing centers of the partners will be done through the Integrated Rule-Oriented Data System (iRODS, http://irods.org). iRODS is an open source data management software used worldwide by research organizations and government agencies. It enables secure collaboration so that users can log in to their home grid to access data hosted on other partners' remote grid. Thanks to iRODS' metadata catalog that describes every file, directory, and storage resource in the data grid, the partners will efficiently share the raw results of their numerical simulations. Numerical simulations computed on national computing centers (GENCI) will be first transferred on ISTerre or BRGM local computing centers and then catalogued into their iRODS' home grid.

After post-processing and cleaning the raw results, they will be gathered and stored in a ready-to-use and secured catalogue at DataBRGM (https://data.brgm.fr). DataBRGM, designed by the BRGM's IT department over the past years, will ensure the sustainability of data created along the project. It is an operational web application created to allow BRGM researchers to preserve scientific data. This user-friendly web application allows each user to log in to a secured workspace where he can transfer, describe and manage data. Transfers can be done by drag&drop, upload to temporary FTP folder (for large sized files) or retrieval of distant data. The description of data is achieved through a form where metadata are defined (e.g., title, date, a short description, language and data producer, geographical information, keywords, etc.). For data management, the workspace allows the user to create, delete and duplicate data set. Each data uploaded in the application gets a permalink accessible through the Internet so that end-users can download it. This catalog of data could be a first step to build (after the end of the project) a dedicated numerical simulation database managed by a database management systems (e.g., MySQL).

2.6.2 Visibility towards the scientific community and outreach activities.

A public website of the project (e.g., www.anr-ssam.fr) will be set up and maintained by the partners. The template of this website will be based on the following ones proposed by BRGM IT department: http://spicy.brgm.fr/ or http://www.ultimateco2.eu/. The website will present the consortium and summarize the objectives of the project. Important deliverables such as scientific articles, proceedings, computer codes, attenuation maps, posters or presentations will be made publicly available. Beyond the scientific dissemination, outreach activities are planned such as the publication of newsletters (1 per year) and popularized articles. This website will also be linked to other websites devoted to seismic tomography.

2.6.3 Catalogue sharing with the seismological community

At the end of the project, all the partners are willing to widely distribute the results of their numerical simulations so that the international seismological community can reuse them for research purposes. To do so, we will deliver a catalogue of numerical simulations together with the tools developed during the project to post-process the data. The tools developed will allow end-users to request specific data (by metadata input) and to post-process them.

Budget justification for each partner

IRAP

- **Staff.** Ph.D. student (36 months). Implementation of scattering/absorption tomography and application to the european crust (Task 4+5). Cost: $34 \times 3 = \mathbf{102k€}$
- **Staff.** Master student (then Ph.D student), 6 months. Numerical validation of sensitivity kernels (Task 4): $0.55 \times 6 = \mathbf{3.3k€}$
- **Equipment.** Disks for local storage of earthquake and noise data (2.5k€) + workstation (3k€) + laptop for the Ph.D student (1.5k€) : **7k€**
- **Operating costs, missions, and dissemination.**
  Coordination meeting: we plan 1 meeting at BRGM and 1 meeting at IsTerre with 2 participants from

IRAP per meeting. Cost: $2 \times 2 \times 0.6 = \mathbf{2.4k€}$
Dissemination of results at international conferences (AGU, EGU): 2.8 kE per Conference.
We plan 2 conferences for the Ph.D student, L. Margerin and M. Calvet, 1 for M. Bystricky.
Total: $7 \times 2.8 = \mathbf{19.6k€}$.
For the dissemination of scientific results, preference will be given to journals that are free of charge. We nevertheless anticipate the possibility to publish in high impact factor journals. Publication fees: $2 \times 2 = \mathbf{4k€}$.
Software (Mathematica): 0.6kE per year: $\mathbf{2.4k€}$

- **Total aid requested (excluding operating costs)** $102 + 3.3 + 7 + 2.4 + 19.6 + 4 + 2.4 = \mathbf{140.7k€}$

ISTerre

- **Staff.** Ph.D Student, 36 months. Noise sensitivity kernels and tomography of the Argostoli basin (Task 3+5). Cost: $30804€ \times 3 = \mathbf{92.412k€}$
- **Staff.** Master student (then Ph.D student), 5 months. Sensitivity of the coda of noise cross-correlation functions to the distribution of noise sources (Task 3). Cost: $\mathbf{2.772k€}$.
- **Staff.** Master student, 5 months. Development of a software suite for distributed processing of distributed seismic data (Task 1+3+6). Cost: $\mathbf{2.772k€}$.
- **Equipment** Personal computer for the Ph.D student: $\mathbf{1.5k€}$.
- **Operating costs, missions and dissemination.** Networking activity: we plan 3 meetings during the project. They will be organized in Toulouse to cut down the costs. Approximate costs per participant: 1flight (150€) + 1 per diem (250€) = 400€. 3 participants (E. Chaljub, L. Stehly, Master student/Ph.D Student): $3 \times 0.4 \times 3 = \mathbf{3.6k€}$.
Dissemination of results at international conferences (AGU, EGU): 2.5 k€ per conference. We plan 3 conferences for the Ph.D student, 2 for L. Stehly and 2 for E. Chaljub. Total: $7 \times 2.5 = \mathbf{17.5k€}$.
Operational fees for the calculations and storage on the local HPC resources: $\mathbf{6.0k€}$.
University management fees (4%): $\mathbf{5.062k€}$.
- **Total aid requested.** $92.412 + 2 \times 2.772 + 1.5 + 3.6 + 17.5 + 6.0 + 5.062 = \mathbf{131.618k€}$.

BRGM

- **Staff.** Information Technology Research Engineer, 4 months. Creation of a catalogue and a database of numerical simulations. Cost: $\mathbf{30.508k€}$
- **Operating costs, missions, and dissemination.**
Creation of a website dedicated to the project by BRGM staff: $\mathbf{3.498k€}$.
Organisation of a one day restitution workshop (conference center rental fee; food and drink for about 100 invited scholars). Cost: $\mathbf{2k€}$.
Missions in Toulouse and Grenoble for networking activities (2 participants at 3 meetings). Total: $2 \times 3 \times$ [train (200€) + per diem (150€)] $= \mathbf{2.1k€}$
BRGM management fees: $\mathbf{1.524k€}$
- **Total aid requested:** $30.508 + 3.498 + 2.1 + 2 + 1.524 = \mathbf{39.631k€}$

Access to national computer centers (GENCI): As requested by ANR, a specific proposal will be submitted to GENCI through the dedicated web interface (http://www.edari.fr) in spring 2016. We will request 5 millions hours single CPU Time per year on the massively parallel computer CURIE (or an equivalent super-computer), for two years.

Description of the consortium

The research team brings together experts in numerical methods and high-performance computing, theory and processing of random signals, wave multiple scattering and inverse problems. The first two years of the project will be devoted to the development of a synthetic noise and coda waveform data bank. The large-scale numerical simulations will be performed at national computer centers (TGIR GENCI) and will be supervised by E. Chaljub (ISTERRE, UJF, Grenoble). E. Chaljub is a seismologist and applied mathematician who has made key contributions to the development and applications of the popular and versatile spectral element method

(SEM) from local hazard studies to global seismology. He has conducted extensive benchmarks of numerical methods in the framework of the european projects ESG2006 and E2VP. From this experience, he has acquired the firm conviction that numerical simulations should be cross-validated by researchers using different computer codes, even if based on the same numerical technique. For this reason, E. Chaljub will team up with F. de Martin, who is a junior research engineer at BRGM (Orléans). F. de Martin is an expert in numerical methods applied to seismic hazard assessment and has developed his own implementation of SEM. In collaboration with E. Chaljub and the BRGM Information System experts, he will supervise the computer science engineer in charge of defining the metadata format and of building the waveform catalogue.

The analysis of synthetic noise data will be conducted by L. Stehly (ISTERRE, UJF, Grenoble) and a PhD student to be recruited 6 months after the beginning of the project, to ensure that the construction of the data bank has matured. L. Stehly has made several pioneering contributions to the field of ambient noise seismology. He introduced the concept of iterated correlations, which allowed him to demonstrate the scattering origin of the coda of noise-based GF. He clarified the temporal and spatial variations of noise sources and documented the thickening of the crust under the western alps using ambient noise tomography. His recent focus has been on the application of advanced signal processing methods to improve the performance of seismic interferometry. In collaboration with E. Chaljub, he will supervise the PhD student in charge of extending the concept of sensitivity functions to the coda of ambient noise correlations, with applications to the absorption and scattering tomography of the Argostoli basin.

The Ph.D student in charge of the analysis of the coda of earthquake data, the development of the linearized tomography, and the applications to Western Europe will be recruited at IRAP (Toulouse) 1.5yr after the beginning of the project, to ensure that most of the theoretical and numerical tools are ready. He will be supervised by M. Calvet (IRAP, UPS, Toulouse) who is a seismologist with a strong background in seismic tomography and wave scattering. She has developed travel-time sensitivity kernels for the imaging of heterogeneous anisotropic media with application to the structure of the inner core. Using dense seismological data from the Pyrenees, she has put in evidence fine-scale spatial variations of scattering and absorption properties along the mountain range. These observations have motivated for a large part the theoretical development of sensitivity functions. Interpretation of the results of scattering/absorption tomography in the light of geophysical and rock physics data will be performed by M. Bystricky, who has a broad experience in experimental rheology and mineral physics.

L. Margerin (CNRS researcher, 44 y.o.) is the project coordinator and a seismologist with a strong expertise in seismic wave scattering. He is at the origin of the scattering/absorption sensitivity functions, and will extend this theory to 3-D anisotropically scattering media in the first 2 y. of the project. With M. Calvet, he will supervise the Ph.D student in Toulouse and will conceive the input heterogeneity models for the numerical simulations with E. Chaljub. L. Margerin has developed the first numerical Monte-Carlo solutions of radiative transfer equations for coupled P and S seismic waves in 3-D. He introduced the concept of energy leakage of coda waves and uncovered equipartition and weak localization of seismic waves, with application to site effect modeling, and the heterogeneity of volcanoes. He developed the first multiple-scattering model of precursory arrivals at the global scale and showed the existence of very weak small-scale fluctuations in the lower mantle. With his colleague M. Calvet, he developed a technique to calculate the scattering attenuation in multi-phase media which led to the discovery of inner core translation. His works (47 peer-reviewed articles, 7 book chapters) have been published in a variety of leading journals (including Phys. Rev. Lett. and Science) covering a broad range of disciplines[11]. In 2007, he received the Schlumberger Medal of the French Academy of Sciences for his contributions to seismic scattering.

3 Valorisation, protection and exploitation of results, global impact of the proposal

Valorisation, protection and exploitation of the results

Scientific dissemination will be carried out by taking part in international conferences and publishing peer-reviewed articles in scientific journals. At least one article to be published in a high impact factor journal is

[11] Most of the publications are available at: https://omp.academia.edu/LudovicMargerin

targeted. In accordance with the ANR commitment about the diffusion, the sharing and the archiving of the scientific production financed by public funds (see "ANR guide des déposants"), the pre-print version or the scientific production itself (with due respect for the publishers copyright policies and self-archiving) will be uploaded on the open archive website HAL (http://hal.archives-ouvertes.fr) or on a local institutional archive such as HAL-BRGM (https://hal-brgm.archives-ouvertes.fr/). During international meetings, the PC plans to co-organize special sessions dedicated to the problem of estimating attenuation across sub-fields of seismology (seismic tomography, seismic hazard assessment, and volcano-seismology). He has had previous experience in organizing such interdisciplinary events through his synergistic activities as Deputy Director of the CNRS research Group Mesoimage[12].

The catalogue of synthetic seismograms produced by the spectral-element method codes `specfem` (under GNU public license) and `efispec` (under CeCILL-V2/GNU-GPL-V3 licenses) will be disseminated under an open data license (e.g., Open Database Commons, Open Database License or "Licence Ouverte ETALAB", etc.). This license is to be discussed among the partners during coordination meetings. The tools for exploiting the catalogue, as well as the numerical codes to calculate the sensitivity kernels of multiply-scattered seismic waves in 2-D and 3-D will be in open access under the CeCILL and/or GNU public licenses mentioned above. Through this project, we are determined to share our catalogue and tools to enable transparent, reproducible and transdisciplinary research.

The final products of our project are frequency-dependent, 3-D models of absorption and scattering at two different scales: the european crust and the sedimentary basin of Argostoli. These models will be freely downloadable on the website of the project, and will complement the velocity model of Argostoli which is currently developed in the framework of the Sinaps project, as well as the crustal velocity model EPcrust.

A final workshop (one or two days event) will be organized to disseminate the project findings to targeted audiences (scientists, authorities and policy makers in the fields of seismology, geophysical exploration and risk assessment). We intend to host approximately 100 scientists to debate the results. The presentation of the catalogue of numerical simulations and of the tools to exploit the data will be presented as well. The future audience will be listed at the beginning of the project and maintained informed about the advancement by semestrial newsletters. In addition to the support requested from ANR (2k€), the workshop can be co-sponsored by the GDR "MesoImage" if extra-expenses are needed.

Since most participants of the project are affiliated with local Universities, they will be able to integrate the outputs of the project into their own classes. We are thinking in particular of the Erasmus Mondus Master at the University of Grenoble, which attracts students from all around the globe to study seismology and seismic hazard.

Global impact

In terms of strategy, the Risks and Prevention Department of BRGM as well as other public institutes or private companies involved in seismic risk, would benefit from the frequency-dependent attenuation tomography of Europe to produce future seismic hazard maps[13]. Indeed, it is widely recognized that the main cause for the variability of the ground motion amplitude at the regional scale is the attenuation structure of the crust. Incorporating 2-D or even 3-D spatial variation of attenuation into ground motion prediction equations should considerably reduce the epistemic uncertainty in seismic risk studies. At regional or local scales, the experience gained during the small-scale application (Argostoli basin) by implementing heterogeneous media into the spectral-element software `efispec` (currently used for advanced seismic microzoning studies in complex geological media) would help quantify the uncertainties associated with numerical predictions of ground motions.

Indirectly, the findings of the SSAM project would impact the results of the framework defined in the partnership agreement signed in June 2014 for five years between BRGM and the " Caisse centrale de réassurance" (CCR). In the domain of seismic risk, the objective of this partnership is to assess accurate financial costs of potential damages by improving the knowledge on seismic hazard and the vulnerability of buildings in the home country and overseas territory.

Other operational applications may be envisaged. With the rapid development and densification of seis-

[12] http://mesoimage.grenoble.cnrs.fr/

[13] The SHARE program of EU is a notable example

mic networks through the european initiative EPOS[14], more and more solid earth observatories are seeking to develop rapid inversions of source size and mechanism, as well as real-time predictions of peak ground accelerations caused by major seismic events. Again, we emphasize that a better knowledge of attenuation may be profitable to both aspects. At the regional scale, determination of the moment magnitude largely depends on a good estimation of attenuation, which controls the corner frequency of the source spectrum.

By making our numerical codes available to the seismological community, we expect an efficient and rapid transfer of our methodological developments towards allied fields such as volcano-seismology and exploration geophysics, where small-scale heterogeneities play a prominent role. The measurement of frequency-dependent absorption properties of geophysical media will bring novel independent constraints on the physical state of the medium, thereby facilitating the localization and characterization of melts and interstitial fluids.

To our knowledge, a catalogue of synthetic Green's functions calculated in heterogeneous media which are rich in small scales is a completely original product that could benefit to other imaging techniques based on multiply-scattered waves. The development of sensitivity functions for coda wave interferometry (CWI) is one possible example. In this technique, one exploits temporal (instead of spatial) changes of the coda to detect possible variations of medium properties. We anticipate that the sensitivity functions that we develop in the framework of scattering/absorption tomography could be adapted to CWI to improve on the spatial resolution of current monitoring techniques.

While a lot of efforts are directed towards seismic velocity tomography, the final images still lack a representation of small-scale heterogeneities, which are way below the current resolution of the best models. Independent of societal applications, the added value of our research is to retrieve novel information -scattering and absorption- from largely unexploited seismic signals -coda waves-. We are convinced that high-resolution attenuation models used in conjunction with more traditional velocity tomography will facilitate the identification of the geodynamical processes at the origin of the present-day structure of the crust.

References

Adelinet, M., J. Fortin, Y. Guéguen, A. Schubnel, and L. Geoffroy, 2010. *Geophys. Res. Lett.*, 37(2).

Anderson, J. G. and S. E. Hough, 1984. *Bulletin of the Seismological Society of America*, 74(5):1969–1993.

Ardhuin, F., L. Gualtieri, and E. Stutzmann, 2015. *Geophys. Res. Lett.*, 42:765–772.

Bernard, P., 1952. *Pont. Acad. Scient. Scripta Var*, 12:131–146.

Calvet, M. and L. Margerin, 2013. *Bulletin of the Seismological Society of America*, 103(3):1993–2010.

Calvet, M., M. Sylvander, L. Margerin, and A. Villaseñor, 2013. *Tectonophysics*, 608:428–439.

Carcolé, E. and H. Sato, 2010. *Geophys. J. Int.*, 180(1):268–290.

Chaljub, E., E. Maufroy, P. Moczo, J. Kristek, F. Hollender, P.-Y. Bard, E. Priolo, P. Klin, F. de Martin, Z. Zhang, W. Zhang, and X. Chen, 2015. *Geophys. J. Int.*, 201(1):90–111.

Chaljub, E., P. Moczo, S. Tsuno, P.-Y. Bard, J. Kristek, M. Kaser, M. Stupazzini, and M. Kristekova, 2010. *Bull. Seismol. Soc. Am.*, 100(4):1427–1455.

Colombi, A., J. Chaput, F. Brenguier, G. Hillers, P. Roux, and M. Campillo, 2014. *Comptes Rendus Geoscience*, 346(11):307–316.

Cupillard, P. and Y. Capdeville, 2010. *Geophys. J. Int.*, 181:1687–1700.

Cupillard, P., L. Stehly, and B. Romanowicz, 2011. *Geophys. J. Int.*, 184(3):1397–1414.

De Martin, F., 2011. *Bull. Seismol. Soc. Am.*, 101(6):2855–2865.

De Verdière, Y. C., 2009. *Nonlinearity*, 22:R45–R75.

Denolle, M., E. Dunham, G. Prieto, and G. Beroza, 2013. *J. Geophys. Res.*, 118:2102–2118.

Douglas, J., 2003. *Earth-Science Reviews*, 61(1):43–104.

Dziewonski, A. M. and D. L. Anderson, 1981. *Physics of the Earth and planetary interiors*, 25(4):297–356.

Ekström, G., 2001. *J. Geophys. Res.*, 106:26483–26494.

Fehler, M., M. Hoshiba, H. Sato, and K. Obara, 1992. *Geophys. J. Int.*, 108(3):787–800.

Fehler, M. and H. Sato, 2003. *Pure and applied geophysics*, 160(3-4):541–554.

Friedrich, A., F. Krüger, and K. Klinge, 1998. *J. of Seism.*, 2:47–64.

Gusev, A. A. and I. R. Abubakirov, 1996. *Geophysical Journal International*, 127(1):49–60.

Gutenberg, B., 1951. *American Meteorological Society*, pages 1303–1311.

Hansen, P. C., 1992. *SIAM review*, 34(4):561–580.

Hartzell, S., L. Bonilla, and R. A. Williams, 2004. *Bull. Seismol. Soc. Am.*, 94(5):1609–1629.

[14]http://www.epos-eu.org/

Hasselmann, K., 1963. *Rev. Geophys.*, 1:177–210.
Hoshiba, M., 1993. *J. Geophys. Res.*, 98(B9):15809–15824.
Imtiaz, A., C. Cornou, P. Bard, and A. Zerva, 2014. In *Second European Conference on Earthquake Engineering and Seismology (2ECEES)*.
Lacombe, C., M. Campillo, A. Paul, and L. Margerin, 2003. *Geophys. J. Int.*, 154(2):417–425.
Lawrence, J. and G. Prieto, 2011. *J. Geophys. Res.*, 116:B06302.
Liemert, A. and A. Kienle, 2011. *Journal of Physics A: Mathematical and Theoretical*, 44(50):505206.
Lin, F., M. Ritzwoller, and W. Shen, 2011. *Geophys. Res. Lett.*, 38:L11303.
Lux, I. and L. Koblinger, 1991. *Monte Carlo particle transport methods: neutron and photon calculations*, volume 102. CRC press Boca Raton.
Margerin, L., 2005. *Seismic Earth: Array Analysis of Broadband Seismograms*, pages 229–252.
Margerin, L., M. Campillo, and B. Van Tiggelen, 2000. *J. Geophys. Res.*, 105(B4):7873–7892.
Margerin, L., T. Planès, J. Mayor, and M. Calvet, 2016. *Geophys. J. Int.*, 204:650–666.
Markel, V. A., 2004. *Waves in random media*, 14(1):L13–L19.
Mavko, G., T. Mukerji, and J. Dvorkin, 2009. *The rock physics handbook: Tools for seismic analysis of porous media*. Cambridge university press.
Mayor, J., M. Calvet, L. Margerin, O. Vanderhaeghe, and P. Traversa, 2016. *Earth and Planetary Science Letters*, 439:71–80.
Mayor, J., L. Margerin, and M. Calvet, 2014. *Geophys. J. Int.*, 197(2):1117–1137.
Molinari, I. and A. Morelli, 2011. *Geophys. J. Int.*, 185(1):352–364.
Monnereau, M., M. Calvet, L. Margerin, and A. Souriau, 2010. *Science*, 328(5981):1014–1017.
Obermann, A., T. Planès, E. Larose, C. Sens-Schönfelder, and M. Campillo, 2013. *Geophysical Journal International*, 194(1):372–382.
Panasyuk, G., J. C. Schotland, and V. A. Markel, 2006. *Journal of Physics A Mathematical General*, 39:115–137.
Parolai, S., D. Bindi, and M. Pilz, 2015. *Bull. Seismol. Soc. Am.*, 105(2A):1049–1052.
Pasyanos, M., 2015. *Earthquake Spectra*, 31(4):2281–2300.
Peter, D., D. Komatitsch, Y. Luo, R. Martin, N. Le Goff, E. Casarotti, P. Le Loher, F. Magnoni, Q. Liu, C. Blitz, T. Nissen-Meyer, P. Basini, and J. Tromp, 2011. *Geophys. J. Int.*, 186(2):721–739.
Polizzi, E. and A. H. Sameh, 2006. *Parallel computing*, 32(2):177–194.
Prieto, G. and G. Beroza, 2008. *Geophys. Res. Lett.*, 35:L14304.
Prieto, G., J. Lawrence, and G. Beroza, 2009. *J. Geophys. Res.*, 114:B07303.
Romanowicz, B. and B. Mitchell, 2007. *Treatise on geophysics*, 1:731–774.
Roux, P., K. G. Sabra, W. A. Kuperman, and A. Roux, 2005. *J Acoust Soc Am*, 117(1):79–84.
Sabra, K. G., P. Roux, and W. A. Kuperman, 2005. *J. Acoust. Soc. Am.*, 117(1):164–174.
Sato, H., M. C. Fehler, and T. Maeda, 2012. *Seismic wave propagation and scattering in the heterogeneous earth*, volume 496. Springer.
Seats, K. J., J. F. Lawrence, and G. A. Prieto, 2012. *Geophys. J. Int.*, 188(2):513–523.
Shapiro, N. M. and M. Campillo, 2004. *Geophys. Res. Lett.*, 31:L07614.
Sheng, P., 2006. *Introduction to wave scattering, localization and mesoscopic phenomena*, volume 88. Springer Science & Business Media.
Snieder, R., 2004. *Phys. Rev. E*, 69(4 Pt 2):046610.
Stehly, L., M. Campillo, B. Froment, and R. Weaver, 2008. *J. Geophys. Res.*, 113(B12):11306.
Stehly, L., M. Campillo, and N. Shapiro, 2006. *J. Geophys. Res.*, 111:B10306.
Tarantola, A., 2005. *Inverse problem theory and methods for model parameter estimation*. SIAM.
Trégourès, N. P. and B. A. Van Tiggelen, 2002. *Physical Review E*, 66(3):036601.
Wang, Z., 2010. *Methods and Applications in Reservoir Geophysics*, 15:83–100.
Wapenaar, K., E. Slob, and R. Snieder, 2006. *Phys. Rev. Lett.*, 97(23):234301.
Weaver, R. L. and O. I. Lobkis, 2001. *Phys. Rev. Lett.*, 87(13):134301.
Yoshimoto, K., H. Sato, and M. Ohtake, 1993. *Geophysical Journal International*, 114(1):165–174.
Ziegler, P. and P. Dèzes, 2006. *Geological Society, London, Memoirs*, 32(1):43–56.